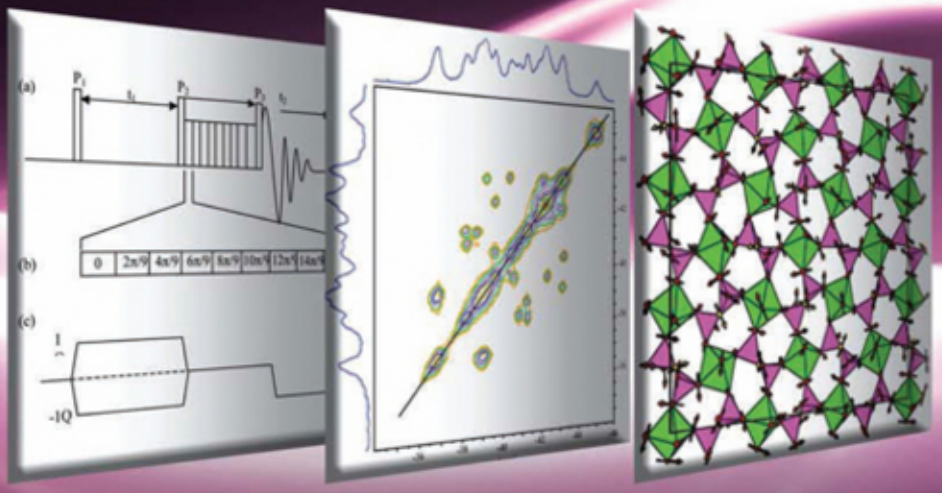
NMR | MRI

BIOLOGY | CHEMISTRY | MEDICINE | PHYSICS

NMR CRYSTALLOGRAPHY



Editors | Robin K. Harris | Roderick E. Wasylishen | Melinda J. Duer

WILEY

EMR

Visit the online Encyclopedia of Magnetic Resonance
at www.mrw.interscience.wiley.com/emr

NMR Crystallography

EMR Handbooks

Based on the *Encyclopedia of Magnetic Resonance* (EMR), this monograph series focuses on hot topics and major developments in modern magnetic resonance and its many applications. Each volume in the series will have a specific focus in either general NMR or MRI, with coverage of applications in the key scientific disciplines of physics, chemistry, biology or medicine. All the material published in this series, plus additional content, will be available in the online version of EMR, although in a slightly different format.

Forthcoming EMR Handbooks

Multidimensional NMR Methods for the Solution State
Edited by Gareth A. Morris and James W. Emsley
ISBN 978-0-470-77075-7

Solid State NMR Studies of Biopolymers
Edited by Ann E. McDermott and Tatyana Polenova
ISBN 978-0-470-72122-3

Handbook of RF Coils for MRI and NMR
Edited by John T. Vaughan and John R. Griffiths
ISBN 978-0-470-77076-4

Ultrafast Echo-time Imaging
Edited by Graeme M. Bydder, Felix W. Wehrli and Ian R. Young
ISBN 978-0-470-68835-9



Encyclopedia of Magnetic Resonance

Edited by Robin K. Harris, Roderick E. Wasylishen, Edwin D. Becker, John R. Griffiths, Vivian S. Lee, Ian R. Young, Ann E. McDermott, Tatyana Polenova, James W. Emsley, George A. Gray, Gareth A. Morris, Melinda J. Duer and Bernard C. Gerstein.

The *Encyclopedia of Magnetic Resonance* (EMR) is based on the original printed *Encyclopedia of Nuclear Magnetic Resonance*, which was first published in 1996 with an update volume added in 2000. EMR was launched online in 2007 with all the material that had previously appeared in print. New updates have since been and will be added on a regular basis throughout the year to keep the content up to date with current developments. Nuclear was dropped from the title to reflect the increasing prominence of MRI and other medical applications. This allows the editors to expand beyond the traditional borders of NMR to MRI and MRS, as well as to EPR and other modalities. EMR covers all aspects of magnetic resonance, with articles on the fundamental principles, the techniques and their applications in all areas of physics, chemistry, biology and medicine for both general NMR and MRI. Additionally, articles on the history of the subject are included.

For more information see: http://www.mrw.interscience.wiley.com/emr

NMR Crystallography

Editors

Robin K. Harris

University of Durham, Durham, UK

Roderick E. Wasylishen

University of Alberta, Edmonton, Alberta, Canada

Melinda J. Duer

University of Cambridge, Cambridge, UK

WILEY

A John Wiley and Sons, Ltd., Publication

This edition first published 2009
© 2009 John Wiley & Sons Ltd

Registered office

John Wiley & Sons Ltd, The Atrium, Southern Gate, Chichester, West Sussex, PO19 8SQ, United Kingdom

For details of our global editorial offices, for customer services and for information about how to apply for permission to reuse the copyright material in this book please see our website at www.wiley.com.

The right of the authors to be identified as the authors of this work has been asserted in accordance with the Copyright, Designs and Patents Act 1988.

All rights reserved. No part of this publication may be reproduced, stored in a retrieval system, or transmitted, in any form or by any means, electronic, mechanical, photocopying, recording or otherwise, except as permitted by the UK Copyright, Designs and Patents Act 1988, without the prior permission of the publisher.

Wiley also publishes its books in a variety of electronic formats. Some content that appears in print may not be available in electronic books.

Designations used by companies to distinguish their products are often claimed as trademarks. All brand names and product names used in this book are trade names, service marks, trademarks or registered trademarks of their respective owners. The publisher is not associated with any product or vendor mentioned in this book. This publication is designed to provide accurate and authoritative information in regard to the subject matter covered. It is sold on the understanding that the publisher is not engaged in rendering professional services. If professional advice or other expert assistance is required, the services of a competent professional should be sought.

Library of Congress Cataloging-in-Publication Data

NMR crystallography / editors, Robin K. Harris, Roderick E. Wasylishen, Melinda J. Duer.
p. cm.
Includes bibliographical references and index.
ISBN 978-0-470-69961-4
1. Crystallography. 2. Nuclear magnetic resonance spectroscopy. I. Harris, Robin Kingsley. II. Wasylishen, Roderick E. III. Duer, Melinda J.
QD906.7.N83N67 2009
548—dc22

2009031427

A catalogue record for this book is available from the British Library.

ISBN-13: 978-0-470-69961-4

Set in 9.5/11.5 pt Times by Laserwords (Private) Limited, Chennai, India
Printed and bound in Singapore by Markono Print Media Pte Ltd

Encyclopedia of Magnetic Resonance

Editorial Board

Editors-in-Chief

Robin K. Harris
University of Durham
Durham
UK

Roderick E. Wasylishen
University of Alberta
Edmonton, Alberta
Canada

Section Editors

SOLID-STATE NMR & PHYSICS

Melinda J. Duer
University of Cambridge
Cambridge
UK

Bernard C. Gerstein
Ames, IA
USA

SOLUTION-STATE NMR & CHEMISTRY

James W. Emsley
University of Southampton
Southampton
UK

George A. Gray
Varian Inc.
Palo Alto, CA
USA

Gareth A. Morris
University of Manchester
Manchester
UK

BIOCHEMICAL NMR

Ann E. McDermott
Columbia University
New York, NY
USA

Tatyana Polenova
University of Delaware
Newark, DE
USA

MRI & MRS

John R. Griffiths
Cancer Research UK
Cambridge Research
Institute
Cambridge
UK

Vivian S. Lee
NYU Langone Medical
Center
New York, NY
USA

Ian R. Young
Imperial College
London
UK

HISTORICAL PERSPECTIVES

Edwin D. Becker
National Institutes of Health
Bethesda, MD
USA

International Advisory Board

David M. Grant (Chairman)
University of Utah
Salt Lake City, UT
USA

Isao Ando
Tokyo Institute
of Technology
Tokyo
Japan

Adriaan Bax
National Institutes of Health
Bethesda, MD
USA

Chris Boesch
University Bern
Bern
Switzerland

Paul A. Bottomley
Johns Hopkins University
Baltimore, MD
USA

William G. Bradley
UCSD Medical Center
San Diego, CA
USA

Graeme M. Bydder
UCSD Medical Center
San Diego, CA
USA

Paul T. Callaghan
Victoria University
of Wellington
Wellington
New Zealand

Richard R. Ernst
Eidgenössische Technische
Hochschule (ETH)
Zürich
Switzerland

Ray Freeman
University of Cambridge
Cambridge
UK

Lucio Frydman
Weizmann Institute
of Science
Rehovot
Israel

Maurice Goldman
Villebon sur Yvette
France

Harald Günther
Universität Siegen
Siegen
Germany

Herbert Y. Kressel
Harvard Medical School
Boston, MA
USA

C. Leon Partain
Vanderbilt University Medical
Center
Nashville, TN
USA

Alexander Pines
University of California
at Berkeley
Berkeley, CA
USA

George K. Radda
University of Oxford
Oxford
UK

Hans Wolfgang Spiess
Max-Planck Institute
of Polymer Research
Mainz
Germany

Charles P. Slichter
University of Illinois
at Urbana-Champaign
Urbana, IL
USA

John S. Waugh
Massachusetts Institute
of Technology (MIT)
Cambridge, MA
USA

Bernd Wrackmeyer
Universität Bayreuth
Bayreuth
Germany

Kurt Wüthrich
The Scripps Research
Institute
La Jolla, CA
USA
and
ETH Zürich
Zürich
Switzerland

Contents

Contributors ix

Series Preface xiii

Volume Preface xv

Part A: Introduction 1

1 Crystallography & NMR: an Overview
Robin K. Harris 3
2 Tensors in NMR
S. Chandra Shekar, Alexej Jerschow 19
3 Computation of Magnetic Resonance Parameters for Crystalline Systems: Principles
Jonathan R. Yates, Chris J. Pickard 29
4 Experimental Characterization of Nuclear Spin Interaction Tensors
Jeremy J. Titman 41

Part B: Chemical Shifts 51

5 Magnetic Shielding & Chemical Shifts: Basics
Julio C. Facelli, Anita M. Orendt 53
6 Symmetry Effects at the Local Level
Matthias Bechmann, Angelika Sebald 63
7 Chemical Shift Computations for Crystalline Molecular Systems: Practice
Robin K. Harris, Paul Hodgkinson, Chris J. Pickard, Jonathan R. Yates, Vadim Zorin 81
8 Chemical Shifts & Solid-state Molecular-level Structure
Anita M. Orendt, Julio C. Facelli 99
9 Chemical Shift Anisotropy & Asymmetry: Relationships to Crystal Structure
James K. Harper 113

Part C: Coupling Interactions 125

10 Dipolar & Indirect Coupling: Basics
Roderick E. Wasylishen 127
11 Dipolar Recoupling: Heteronuclear
Christopher P. Jaroniec 137

12 Dipolar Recoupling: Homonuclear
Robert Tycko 163
13 Dipolar Coupling: Molecular-level Mobility
Detlef Reichert, Kay Saalwächter 177
14 Spin Diffusion in Crystalline Solids
Lyndon Emsley 195
15 Indirect Coupling & Connectivity
Anne Lesage 209
16 Nuclear Quadrupole Coupling: An Introduction & Crystallographic Aspects
Sharon E. Ashbrook, Stephen Wimperis 223

Part D: Crystal Structure Determination using NMR 243

17 Fundamental Principles of NMR Crystallography
Francis Taulelle 245
18 Interplay between NMR & Single-crystal X-ray Diffraction
Darren H. Brouwer 263
19 Combined Analysis of NMR & Powder Diffraction Data
Kenneth D.M. Harris, Mingcan Xu 275
20 Tensor Interplay
David L. Bryce 289

Part E: Properties of the Crystalline State 303

21 Intermolecular Interactions & Structural Motifs
Lindsay S. Cahill, Gillian R. Goward 305
22 Hydrogen Bonding in Crystalline Organic Solids
Steven P. Brown 321
23 Inorganic Non-stoichiometric Crystalline Systems & Atomic Ordering
Mark E. Smith 341
24 Rotational & Translational Dynamics
Christopher I. Ratcliffe 355
25 Intramolecular Motion in Crystalline Organic Solids
Paul Hodgkinson 375
26 Structural Phase Transitions
Kenneth R. Jeffrey, Glenn H. Penner 387

Part F: Applications of NMR to Crystalline Solids 415

27 Structural Biology
David A. Middleton 417
28 Organic & Pharmaceutical Chemistry
Marek J. Potrzebowski 435
29 Inorganic & Materials Chemistry
Ray Dupree 455
30 Geochemistry
Brian L. Phillips 463

Index 487

Contributors

Sharon E. Ashbrook — *School of Chemistry and EaStCHEM, University of St Andrews, St Andrews KY16 9ST, UK*
Chapter 16: Nuclear Quadrupole Coupling: An Introduction & Crystallographic Aspects

Matthias Bechmann — *Department of Chemistry, University of York, Heslington YO10 5DD, UK*
Chapter 6: Symmetry Effects at the Local Level

Darren H. Brouwer — *Department of Chemistry, Redeemer University College, Ancaster, Ontario L9K 1J4, Canada*
Chapter 18: Interplay between NMR & Single-crystal X-ray Diffraction

Steven P. Brown — *Department of Physics, University of Warwick, Coventry CV4 7AL, UK*
Chapter 22: Hydrogen Bonding in Crystalline Organic Solids

David L. Bryce — *Department of Chemistry, University of Ottawa, Ottawa, Ontario K1N 6N5, Canada*
Chapter 20: Tensor Interplay

Lindsay S. Cahill — *Department of Physics, University of Warwick, Coventry CV4 7AL, UK*
Chapter 21: Intermolecular Interactions & Structural Motifs

Ray Dupree — *Physics Department, University of Warwick, Coventry CV7 4AL, UK*
Chapter 29: Inorganic & Materials Chemistry

Lyndon Emsley — *Centre de RMN à Très Hauts Champs (CNRS / ENS-Lyon / UCB Lyon 1), Université de Lyon, 69100 Villeurbanne, France*
Chapter 14: Spin Diffusion in Crystalline Solids

Julio C. Facelli — *Department of Biomedical Informatics and Center for High Performance Computing, University of Utah, Salt Lake City, UT 84112-0190, USA*
Chapter 5: Magnetic Shielding & Chemical Shifts: Basics
Chapter 8: Chemical Shifts & Solid-state Molecular-level Structure

Gillian R. Goward — *Department of Chemistry, McMaster University, Hamilton, Ontario L8S 4M1, Canada*
Chapter 21: Intermolecular Interactions & Structural Motifs

James K. Harper *Department of Chemistry, University of Utah, Salt Lake City, UT 84112, USA*
Chapter 9: Chemical Shift Anisotropy & Asymmetry: Relationships to Crystal Structure

Kenneth D. M. Harris *School of Chemistry, Cardiff University, Cardiff CF10 3AT, UK*
Chapter 19: Combined Analysis of NMR & Powder Diffraction Data

Robin K. Harris *Department of Chemistry, University of Durham, Durham DH1 3LE, UK*
Chapter 1: Crystallography & NMR: an Overview
Chapter 7: Chemical Shift Computations for Crystalline Molecular Systems: Practice

Paul Hodgkinson *Department of Chemistry, University of Durham, Durham DH1 3LE, UK*
Chapter 7: Chemical Shift Computations for Crystalline Molecular Systems: Practice
Chapter 25: Intramolecular Motion in Crystalline Organic Solids

Christopher P. Jaroniec *Department of Chemistry, Ohio State University, Columbus, OH 43210, USA*
Chapter 11: Dipolar Recoupling: Heteronuclear

Kenneth R. Jeffrey *Department of Chemistry, University of Guelph, Guelph, Ontario N1G 2W1, Canada*
Chapter 26: Structural Phase Transitions

Alexej Jerschow *Department of Chemistry, New York University, New York, NY 10003, USA*
Chapter 2: Tensors in NMR

Anne Lesage *Laboratoire de Chimie, Ecole Normale Superieure de Lyon, 69364 Lyon 07, France*
Chapter 15: Indirect Coupling & Connectivity

David A. Middleton *School of Biological Sciences, University of Liverpool, Liverpool L69 7ZB, UK*
Chapter 27: Structural Biology

Anita M. Orendt *Center for High Performance Computing, University of Utah, Salt Lake City, UT 84112-0190, USA*
Chapter 5: Magnetic Shielding & Chemical Shifts: Basics
Chapter 8: Chemical Shifts & Solid-state Molecular-level Structure

Glenn H. Penner *Department of Chemistry, University of Guelph, Guelph, Ontario N1G 2W1, Canada*
Chapter 26: Structural Phase Transitions

Brian L. Phillips *Department of Geosciences, Stony Brook University, Stony Brook, NY 11794-2100, USA*
Chapter 30: Geochemistry

Chris J. Pickard — *School of Physics & Astronomy, University of St. Andrews, St. Andrews KY16 9SS, UK*
Chapter 3: Computation of Magnetic Resonance Parameters for Crystalline Systems: Principles
Chapter 7: Chemical Shift Computations for Crystalline Molecular Systems: Practice

Marek J. Potrzebowski — *Center of Molecular and Macromolecular Studies, Polish Academy of Sciences, 90-362 Łódź, Poland*
Chapter 28: Organic & Pharmaceutical Chemistry

Christopher I. Ratcliffe — *Steacie Institute for Molecular Sciences, National Research Council Canada, Ottawa, Ontario K1A 0R6, Canada*
Chapter 24: Rotational & Translational Dynamics

Detlef Reichert — *Institut für Physik, Martin-Luther-Universität Halle-Wittenberg, D-06108 Halle, Germany*
Chapter 13: Dipolar Coupling: Molecular-level Mobility

Kay Saalwächter — *Institut für Physik, Martin-Luther-Universität Halle-Wittenberg, D-06108 Halle, Germany*
Chapter 13: Dipolar Coupling: Molecular-level Mobility

Angelika Sebald — *Department of Chemistry, University of York, Heslington YO10 5DD, UK*
Chapter 6: Symmetry Effects at the Local Level

S. Chandra Shekar — *Department of Chemistry, New York University, New York, NY 10003, USA*
Chapter 2: Tensors in NMR

Mark E. Smith — *Department of Physics, University of Warwick, Coventry CV4 7AL, UK*
Chapter 23: Inorganic Non-stoichiometric Crystalline Systems & Atomic Ordering

Francis Taulelle — *Lavoisier Institute, University of Versailles-Saint-Quentin-en-Yvelines, 78035 Versailles, France*
Chapter 17: Fundamental Principles of NMR Crystallography

Jeremy J. Titman — *School of Chemistry, University of Nottingham, Nottingham NG7 2RD, UK*
Chapter 4: Experimental Characterization of Nuclear Spin Interaction Tensors

Robert Tycko — *Laboratory of Chemical Physics, National Institute of Diabetes and Digestive and Kidney Diseases, National Institutes of Health, Bethesda, MD 20892-0520, USA*
Chapter 12: Dipolar Recoupling: Homonuclear

Roderick E. Wasylishen — *Department of Chemistry, Gunning/Lemieux Chemistry Centre, University of Alberta, Edmonton, Alberta T6G 2G2, Canada*
Chapter 10: Dipolar & Indirect Coupling: Basics

Stephen Wimperis *Department of Chemistry and WestCHEM, University of Glasgow, Glasgow G12 8QQ, UK*
Chapter 16: Nuclear Quadrupole Coupling: An Introduction & Crystallographic Aspects

Mingcan Xu *School of Chemistry, Cardiff University, Cardiff CF10 3AT, UK*
Chapter 19: Combined Analysis of NMR & Powder Diffraction Data

Jonathan R. Yates *TCM Group, Cavendish Laboratory, University of Cambridge, Cambridge CB3 OHE, UK*
Chapter 3: Computation of Magnetic Resonance Parameters for Crystalline Systems: Principles
Chapter 7: Chemical Shift Computations for Crystalline Molecular Systems: Practice

Vadim Zorin *Department of Chemistry, University of Durham, Durham DH1 3LE, UK*
Chapter 7: Chemical Shift Computations for Crystalline Molecular Systems: Practice

Series Preface

The *Encyclopedia of Nuclear Magnetic Resonance* was published in eight volumes in 1996, in part to celebrate the fiftieth anniversary of the first publications in NMR in January 1946. Volume 1 contains an historical overview and ca. 200 short personal articles by prominent NMR practitioners, while the remaining seven volumes comprised ca. 500 articles on a wide variety of topics in NMR (including MRI). Two "spin-off" volumes incorporating the articles on MRI and MRS (together with some new ones) were published in 2000 and a ninth volume was brought out in 2002. In 2006, the decision was taken to publish all the articles electronically (i.e. on the World Wide Web) and this was carried out in 2007. Since then, new articles have been placed on the web every three months and a number of the original articles have been updated. This process is continuing. The overall title has been changed to the *Encyclopedia of Magnetic Resonance* to allow for future articles on EPR and to accommodate the sensitivities of medical applications.

The existence of this large number of articles, written by experts in various fields, is enabling a new concept to be implemented, namely the publication of a series of printed handbooks on specific areas of NMR and MRI. The chapters of each of these handbooks will comprise a carefully chosen selection of Encyclopedia articles relevant to the area in question. In consultation with the Editorial Board, the handbooks are coherently planned in advance by specially selected editors. New articles are written and existing articles are updated to give appropriate complete coverage of the total area. The handbooks are intended to be of value and interest to research students, postdoctoral fellows, and other researchers learning about the topic in question and undertaking relevant experiments, whether in academia or industry.

Robin K. Harris
University of Durham, Durham, UK

Roderick E. Wasylishen
University of Alberta, Edmonton, Alberta, Canada

November 2009

Volume Preface

Since the earliest days of NMR, it has been recognized that the technique can provide information on matters concerning the disposition of atoms in the unit cells of crystals. Thus, the distance between protons in the water molecules of gypsum, $CaSO_4 \cdot 2H_2O$, was determined by Pake and reported as 1.58 Å in 1948. However, the term NMR crystallography has only recently come into common usage, and even now causes raised eyebrows within some parts of the diffraction community. On the other hand, the power of solid-state NMR to give crystallographic information has considerably increased since the CPMAS suite of techniques was introduced in 1976. In the first years of the 21st century, the ability of NMR to provide information to support and facilitate the analysis of single-crystal and powder diffraction patterns has become widely accepted. Indeed, NMR can now be used to refine diffraction results and, in favorable cases, to solve crystal structures with minimal (or even no) diffraction data. The increasing ability to relate chemical shifts (including the tensor components) to the crystallographic location of relevant atoms in the unit cell via computational methods has added significantly to the practice of NMR crystallography. Of course, NMR will never replace diffraction techniques in the determination of atomic positions in crystal structures, but diffraction experts will increasingly welcome NMR as an ally in their structural analyses. Indeed, it may be that in future crystal structures will be determined by simultaneously fitting diffraction patterns and NMR spectra.

However, NMR can also supply information on crystal structures which is inaccessible or very difficult to obtain by diffraction methods. Prominent among such investigations is the determination of dynamics at the molecular level in crystalline materials. There are many NMR methods for studying such motion, including relaxation measurements as well as spectral features, and they cover a vast range of motional rates. NMR can frequently distinguish between static and dynamic disorders.

Thus NMR crystallography can and should be considered as both complementary and supplementary to diffraction crystallography. At the time of writing there are few reviews and no books on NMR crystallography. It therefore seems to be timely to produce this handbook. The chapters herein, though taken from articles in the electronic version of the *Encyclopedia of Magnetic Resonance*, were commissioned specifically with this handbook in mind. The editors have attempted to produce a coherent set of chapters covering most aspects of NMR crystallography in a reasonably uniform way. Of course, since each chapter has its specific authors (expert in the topics in question) there will undoubtedly be some small degree of overlap between them and possibly a few lacunae. However, the handbook should be of value not only to students and practitioners of solid-state NMR but also to the wider crystallographic community.

Some care has been taken to achieve consistency of symbols and notation, but there remain a few variations between chapters (for example, in the symbols used for dipolar coupling constants).

Finally, it may be noted that single-crystal NMR work, though feasible, is relatively unusual, so most studies involve microcrystalline/polycrystalline samples. Little information is sacrificed by this usage. Heterogeneous systems containing crystalline components are also amenable to study. Moreover, structural information at the molecular level (including geometrical data) can be obtained by NMR from amorphous and glassy materials, again with little loss. Although that situation is hinted at in various parts of the handbook, it is not specifically covered, though matters such as defect and other nonstoichiometric structures are discussed.

The handbook is organized into six parts. The first contains an overview and some chapters on

fundamental NMR topics. Next comes a part concentrating on chemical shifts, followed by one on coupling interactions. Part D contains chapters describing how NMR results relate to fundamental crystallography concepts and to diffraction methods. The fifth part concerns specific aspects of structure, such as hydrogen bonding, and also has chapters on questions of molecular-level mobility and phase transitions. Finally, the four chapters in the last part give applications of NMR crystallography to structural biology, organic and pharmaceutical chemistry, inorganic and materials chemistry, and geochemistry.

As mentioned above, the articles are also to be found, with minimal differences but changed format, in the online *Encyclopedia of Magnetic Resonance*, which is at:

http://www.mrw.interscience.wiley.com/emr.

The online versions also contain brief autobiographies of the article authors, a list of related Encyclopedia articles, and, in a number of cases, acknowledgements by the authors. They also have cross-references to Encyclopedia articles which are not part of this handbook. Additionally, article abstracts and key words can be found online.

We are grateful to all the authors involved in this handbook for their agreements to write the online articles which preceded the handbook, for their expert texts and for their cooperation in reaching this stage. We also thank the people at Wiley and at Laserwords for all their hard work in bringing the handbook to the point of publication.

We offer this handbook in the hope that it will not only provide valuable information for a wide range of scientists but that it will also stimulate further advances in NMR crystallography.

Robin K. Harris
University of Durham, Durham, UK

Roderick E. Wasylishen
University of Alberta, Edmonton, Alberta, Canada

Melinda J. Duer
University of Cambridge, Cambridge, UK

November 2009

PART A
Introduction

Chapter 1
Crystallography & NMR: an Overview

Robin K. Harris

Department of Chemistry, University of Durham, Durham DH1 3LE, UK

1.1	Introduction	3
1.2	Limitations of Diffraction Techniques	5
1.3	NMR and its Crystallographic Significance	7
1.4	Required Information	8
1.5	Concluding Remarks	16
	References	17

1.1 INTRODUCTION

Although there is no problem defining nuclear magnetic resonance (NMR), different people interpret the term *crystallography* differently. In particular, experts in diffraction studies of crystals frequently use the term as though it is synonymous with structural information obtained by diffraction methods. However, historically, crystals were studied and classified by their morphology alone. It became recognized, for example, that different habits can result from the same underlying symmetry.

The term *crystallography* is derived from the Greek words *crystallon*, meaning cold drop/frozen drop, and *graphein*, meaning "write". It refers to the experimental science of determining the arrangement of atoms in solids, specifically for what are now called *crystalline* solids. In older usage, it is simply the scientific study of crystals. The use of the words "atoms in solids" implies that amorphous solids may be included in "crystallography", but this is contentious and such systems will not, in general, be dealt with here. Moreover, the original usage of the word (dating from eighteenth century Latin "crystallographiæ" and French "cristallographie") referred to the external shape of crystals (morphology) rather than the internal structure, and this is still included in the normal meaning. Dictionaries define "crystallography" in various ways. Some include both internal arrangement and external morphology of crystals. Others discuss the properties of crystals and/or their classification. One of the simplest definitions states merely "the study of crystal form and structure".[1] Most dictionaries (as opposed to encyclopedias) do not mention diffraction in the definition.

Of course, studies of morphology alone tend to obscure the varied nature of the internal arrangements. A student first meeting crystallographic concepts may be lead to believe in crystalline perfection, i.e., the existence of perfect three-dimensional translational symmetry of a unit cell with fixed contents, belonging to a well-defined space group. Reality shows a greater variety of possibilities within the general idea of "crystallinity", questions of non-stoichiometric systems, disorder, defects, incommensurate cases, and molecular-level mobility all complicating the general situation. Moreover, the surface structure of crystals deviates from that of their bulk contents; surface structures are extremely important, since they govern interactions with the surrounding medium, as in all types of composite materials.

NMR Crystallography Edited by Robin K. Harris, Roderick E. Wasylishen and Melinda J. Duer © 2009 John Wiley & Sons, Ltd. ISBN: 978-0-470-69961-4

These facts clearly indicate the width of usage and applicability of the terms *crystallography* and *crystal structure*. As a result, many tools must be brought to fully understand both the macroscopic nature and atomic-level structure of crystalline materials. Over the last century, diffraction experiments have emerged as the primary way of determining the disposition of atoms in unit cells of crystals. When a new compound is synthesized and obtained in crystalline form, it is usually of high priority to determine its solid-state structure by means of single-crystal diffraction studies. Indeed, this is also frequently the key way of obtaining the *molecular* structure definitively for organic and organometallic compounds, though solution-state NMR is equally powerful for such determinations. Indeed, synthetic chemists are often not interested in crystallographic details other than the molecular structure. Single-crystal diffraction work is accepted as the "gold standard" for providing molecular structure (and the structure of network systems) for crystalline systems. It will undoubtedly remain so.

However, NMR has much to offer the crystallographer because it can both supplement and complement the diffraction results. The term NMR *crystallography* has come into common use in the last decade, though some diffraction experts decry it.[a] Historically, NMR has given crystallographic information since the earliest days of the technique. It was recognized, for example, that dipolar interactions could yield direct information on internuclear distances. This can be achieved easily when there are isolated pairs of protons in a crystal. In 1948 Pake[2] reported the line-pair separations of the water proton resonances for a single crystal of calcium sulfate dihydrate (gypsum), $CaSO_4 \cdot 2H_2O$, as a function of the crystal orientation in $\boldsymbol{B}_0$ (Figure 1.1). Thence, he derived the internuclear distance between the protons in the hydrate water molecules as 1.58 Å. This was at a time (1948) when detecting hydrogen atoms by X-ray diffraction was problematic (as it remained for many years – and even today this can cause difficulties in some cases). Pake also illustrated the lineshape for the proton spectrum of a polycrystalline sample of gypsum, which is of the type now well known as a *Pake doublet*, allowing internuclear distance information to be obtained even in the absence of a single crystal. An article a year later[3] illustrates the experimental powder pattern for $ClH_2C–CH_2Cl$ (Figure 1.2), together with a simulated Pake doublet (though this case does not really have isolated proton spin pairs). The same paper states the following in the introduction: "The development of experimental methods for observing nuclear magnetism has provided *a means of investigating* certain aspects of molecular and *crystal structure*" (italicization inserted here).

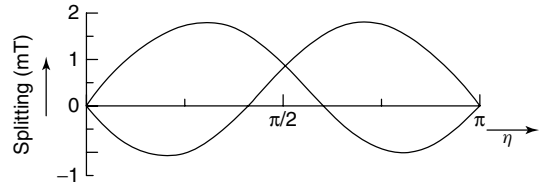


Figure 1.1. Proton line-pair separations for a single crystal of gypsum as a function of the angle, η, between the [100] direction and the applied magnetic field. (Reproduced from Ref. 2. © American institute of Physics, 1948.)

Today, NMR methods (and consequently the nature of results) have advanced enormously so that it is now feasible to solve crystal structures for polycrystalline samples, in favorable cases, by NMR means, given only the unit cell parameters and space group from diffraction work,[4] and to obtain structural information about crystalline proteins.[5] While no one would suggest that NMR will ever replace diffraction work, it can and does address crystallographic matters that diffraction methods struggle with. The complementarity of the two techniques is based on the fact that diffraction methods rely on the presence of long-range order, whereas NMR spectra reflect the local environment of the nucleus under study. This means that a combination of the two techniques is especially powerful (*see* **Chapters 18** and **19**). For instance, NMR can give structural information on imperfect crystalline situations (such as are mentioned above) and on crystal surfaces – all cases for which diffraction methods struggle to give definitive data. Indeed, the NMR techniques are not limited to crystalline materials; hence, information on molecular-level structure and local environment can be obtained for amorphous solids (and

[a]One referee objected to the term NMR *crystallography* in the title of a submitted paper as follows:

- Since the authors are dealing with powders rather than crystals, the use of the term *crystallography* is inappropriate.
- Crystallography specifically applies to diffraction of electromagnetic radiation.

Neither comment appears apposite!

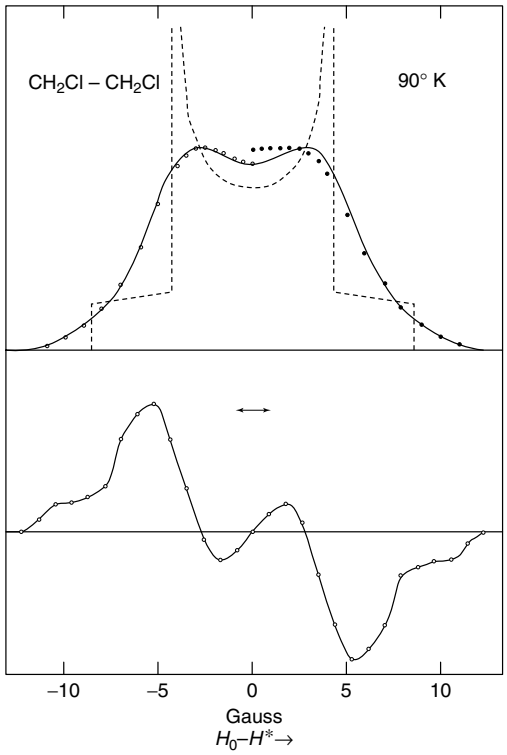
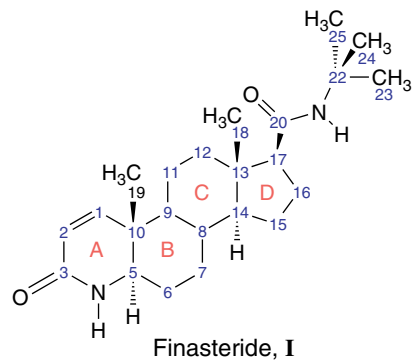


Figure 1.2. The proton magnetic resonance absorption line and its derivative for solid 1,2-dichloroethane at 90 K. The solid lines in both parts of the figure (the lower part being in derivative mode) represent experimental data. In the upper part of the figure, the open circles in the left half are theoretical values computed for a proton separation of 1.70 Å and the points in the right half are for 1.72 Å. The dashed curve is the theoretical lineshape for a crystal powder with a proton separation of 1.70 Å and in which magnetic interactions are confined to pairs of nuclei. The upper diagram illustrates the well-known "Pake doublet". (Reproduced from Ref. 3. © American institute of Physics, 1948.)

for heterogeneous systems) for which diffraction is largely inapplicable. Such systems provide important applications of NMR, but the present article is limited to crystalline materials (except for one case).

NMR work on single crystals is feasible (and yields detailed crystallographic information).[6] However, rather large crystals and special probes are required; hence, single-crystal NMR is not common (though more use is perhaps justified). Polycrystalline samples are normally studied, usually using magic-angle spinning. Fortunately, given the range of specialist pulse sequences available for deriving specific pieces of information, the loss of information incurred by not using single crystals is, in general, rather small. The remainder of this article will only involve polycrystalline systems.

One of the simplest uses of solid-state NMR in crystallography is to distinguish between habit (samples giving identical MAS spectra) and polymorphism (spectra being different) (*see* **Chapter 28**).[7] Polymorphism is ubiquitous throughout chemistry and its study is essential to many solid-state applications, especially in the pharmaceutical industry. Distinctions between polymorphs by NMR are generally clear-cut and are rendered particularly straightforward by taking advantage of the multinuclear nature of NMR. For example, ^{13}C spectra may reveal differences between samples that are not apparent from ^{15}N studies. The distinctions enable studies of phase transitions to be made by NMR (*see* **Chapter 26**). Another simple use of solid-state NMR is in detecting isomorphism. Thus, Figure 1.3 shows[8] that four samples of finasteride (see **I**) solvates are isomorphous while the remaining (acetic acid) one has a different structure. This example also demonstrates the superb direct chemical information given by NMR, i.e., the signals definitively determine the solvent molecules involved, in contrast to diffraction that, because of solvent molecule mobility in the solvates, can only show a volume of electron density of indiscriminate nature.



Finasteride, **I**

1.2 LIMITATIONS OF DIFFRACTION TECHNIQUES

Although it is stressed that the superb ability of diffraction techniques to obtain structural information

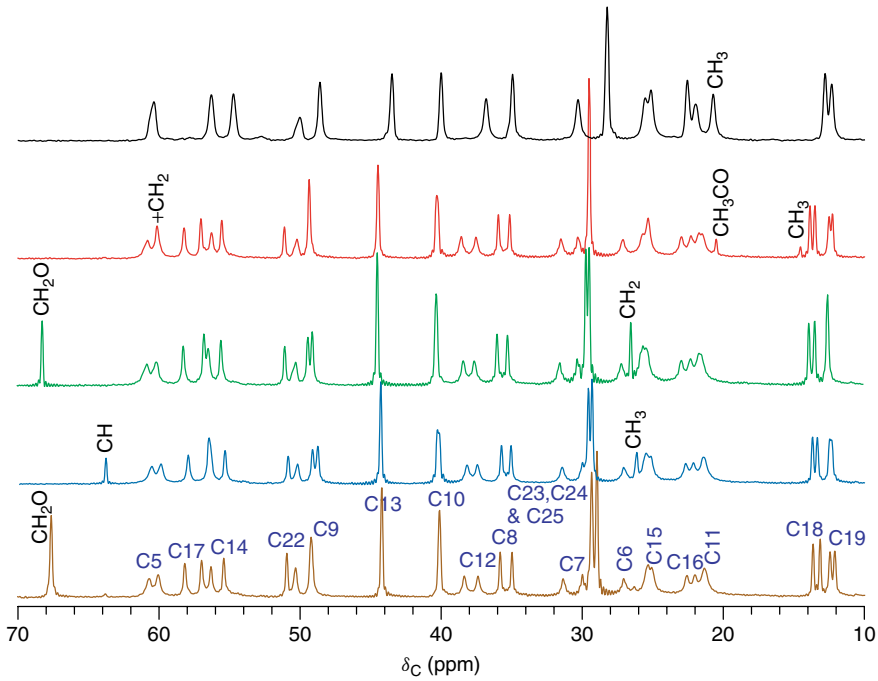


Figure 1.3. Carbon-13 CPMAS spectra of five solvates of finasteride (**I**). Top to bottom: acetic acid solvate; ethyl acetate hydrate solvate; THF hydrate solvate; isopropanol hydrate solvate; and dioxane hydrate solvate. Assignments are indicated for the solvent peaks. (Reproduced with permission from Ref. 8. © 2007, John Wiley & Sons Ltd.)

for crystalline materials (most importantly, the positions of atoms in the unit cell) is and will remain unsurpassed, there are certain inherent difficulties with obtaining some facets of crystallographic information from single-crystal diffraction experiments. These can be summarized as follows:

- For the best results, single crystals are required, which should be of the order of 0.001 mm^3 or greater (though with synchrotron radiation much smaller crystals can be effectively studied).
- The crystals need to be as perfect as possible, i.e., without substantial defects – though special techniques can cope with some imperfections (such as twinning).
- Disorder, either spatial or temporal, causes uncertainties.
- For X-ray diffraction (though not neutron diffraction), distinctions between atoms of different elements with similar atomic numbers are sometimes difficult to make (especially in isoelectronic cases).
- Historically, hydrogen atoms have been difficult to locate with accuracy, especially in the presence of heavy atoms.
- The crystal studied may not be representative of the bulk sample (though powder diffraction experiments can be used to clarify this matter).
- Amorphous solids cannot be adequately examined.

Advances in technology are rendering some of these difficulties less restrictive. In addition, in recent years, the power of powder diffraction techniques has been greatly increased so that it is feasible in many cases to obtain detailed crystal structures by this means.[9] This is particularly valuable, for example, for samples of small crystals embedded in an amorphous matrix, as is the case for many ceramic systems. Other advances in X-ray diffraction procedures allow electron distributions to be modeled in detail, and the location of hydrogen atoms is much improved. However, the fact remains that X rays locate electron density, not nuclei, though neutron diffraction does depend on the positions of atomic nuclei.

There are two major areas in which complementary information is desirable:

1. *Molecular-level mobility*: Most X-ray diffraction measurements that result in structure determinations now take place at 120 K. However, even at this temperature, there is significant mobility over the timescale of a typical diffraction experiment (generally ca. 4–6 h). Analysis of diffraction patterns can take some account of this (especially for vibrational motion) by using ellipsoids based on atomic displacement factors, though for X-ray measurements these actually depict electron density distributions. Site exchange (temporal disorder) by rapid jump motions can be accounted for by the use of fractional populations if the sites are distinguishable. However, when equivalent sites are involved, as with 120° rotations of tertiary butyl groups, the exchange cannot be easily detected by diffraction methods. Moreover, obtaining information on the kinetics of molecular-level motion is extremely difficult by diffraction techniques. In this context, most vibrations occur at a sufficiently high frequency that their effects on both diffraction patterns and NMR spectra can be ignored.
2. Purely spatial (i.e., static) disorder raises a different problem, in that, in principle, the structure is not properly spatially repetitive; hence, it is not possible in strict theory to define a space group except on an average basis. In such cases, the analysis of diffraction patterns results in structures with fractional occupations. Differently ordered domains are difficult to investigate.

1.3 NMR AND ITS CRYSTALLOGRAPHIC SIGNIFICANCE

The relationship of NMR to crystallography is a complex one (*see* **Chapter 17**). NMR parameters can provide substantial crystallographic information in both direct and indirect ways. Such information derives from the various NMR measurables (*see* **Chapters 2** and **4**), namely, the following:

- *Isotropic chemical shifts* (*see* **Chapters 5** and **8**): Traditionally, these have been used in the solution state to give direct information on molecular-level chemical structure. They can be used in similar manner for crystalline solids.[10] They can also define the number of nuclei in different environments for relevant nuclei in the crystal structure. This will determine the crystallographic asymmetric unit. In favorable circumstances, molecular symmetry and even space group information are obtained. In addition, chemical shifts often provide knowledge about intermolecular interactions, for example, the location of hydrogen bonds.
- *Full information on chemical shift tensors*: The anisotropy and asymmetry of the tensor relate directly to the detailed electronic environment of the atom concerned and hence correlate with the information obtainable from X-ray diffraction (*see* **Chapter 9**).
- *Dipolar coupling* (*see* **Chapter 10**): This spin–spin interaction gives interatomic distance information directly and provides a very powerful method of studying crystal structure. However, molecular-level motion can strongly affect the observed dipolar coupling constants (*see* **Chapter 13**) so that care needs to be taken in interpretation. When MAS is used, recoupling pulse sequences are frequently necessary to obtain dipolar coupling constants (*see* **Chapters 11** and **12**).
- *Isotropic indirect spin–spin coupling*[b] (*see* **Chapters 10** and **15**): This parameter gives information largely on conformational matters and is especially powerful for studies of molecular structure within crystals. However, its utility for solids has hitherto been muted because splitting patterns are often obscured by the linewidths in solids, particularly for (H,H) and long-range (C,H) coupling. On the other hand, coupling involving heavier atoms can be informative. Moreover, sophisticated measurements can reveal coupling across hydrogen bonds,[11] giving intermolecular relationships in crystals (*see* **Chapter 22**).
- *Quadrupolar coupling*: This interaction depends on electric field gradients (EFGs) at the nuclei, which in turn depend sensitively on the local environment. The anisotropy and asymmetry of the coupling provide additional information related to the site symmetry of the relevant nuclei in crystalline materials (*see* **Chapter 16**).
- *Relaxation times*: Three such processes are of particular importance for obtaining information on molecular-level motion (*see* **Chapters 13**, **24**

[b] In principle, indirect coupling is a tensor property, but its anisotropy and asymmetry have so far proved to be of limited use.

and **25**). These are (a) spin-lattice (otherwise known as *longitudinal*) relaxation, with characteristic time designated T_1; (b) spin-lattice relaxation in the rotating frame, designated time $T_{1\rho}$; and (c) spin–spin (otherwise known as *transverse*) relaxation, with time T_2. They have characteristic motional dependencies at rates of tens to hundreds of megahertz, tens of kilohertz, and low frequencies, respectively. The related phenomenon of spin diffusion also carries information about the solid state (*see* **Chapter 14**).

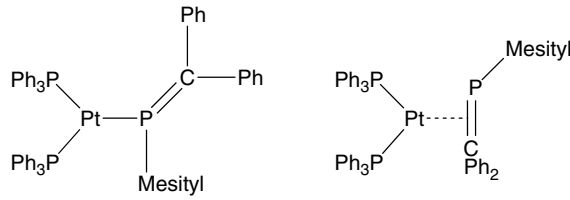
Other articles will explore these parameters in considerable detail. In this one, examples will be quoted to give the flavor of "NMR crystallography". The derived information can facilitate the complete structure determination from single-crystal or powder diffraction patterns. In many cases, the knowledge obtained is additional to that found from diffraction work. Applications of NMR crystallography have been made to structural biology (*see* **Chapter 27**), geochemistry (*see* **Chapter 30**), organic and pharmaceutical chemistry (*see* **Chapter 28**), and inorganic and materials chemistry (*see* **Chapter 29**).

1.4 REQUIRED INFORMATION

So what constitutes crystallographic information?

1.4.1 Molecular-Level Information

As mentioned above, one key aspect is the atomic bonding (connectivity) pattern, forming the molecules or networks. The long history of solution-state NMR in this context, predating most high-resolution solid-state NMR, indicated the potential of the technique for solids. That potential is now increasingly being fulfilled, especially by the use of isotropic chemical shifts. One aspect of importance lies in the fact that solid-state structures may not be identical to those in solution. A relatively early NMR example of this phenomenon was provided[12] by $Pt(PPh_3)_2(P(mesityl)=CPh_2)$ (**II**). Phosphorus-31 CPMAS spectra of the solid showed unambiguously (from chemical shifts) that this compound has an η^1-coordinated (see **IIa**) phosphaalkene ligand, in disagreement with the η^2 case (see **IIb**) indicated by NMR for the solution state. The CPMAS work confirmed single-crystal diffraction results, thus giving an example of solid-state NMR acting as a bridge between solution-state NMR and diffraction techniques.



IIa **IIb**

CPMAS NMR provides an easier route to *molecular* structure in solids than diffraction because the link between isotropic chemical shifts and bonding environments is direct and specific to each atom. The correlations between shifts and bonding have been exhaustively worked out over five decades from solution-state NMR data. Indeed, solution-state NMR is usually the preferred route to obtain molecular structure. Solid-state molecular-level structure determination can make use of the shift/structure correlations, but due regard has to be paid to specifically solid-state shift effects.

Indirect coupling can also play an important role in determining bonding patterns in crystalline solids (*see* **Chapter 15**), though, in contrast to solution-state work, this has mostly not involved (H,H) or (C,H) coupling. An early example of such usage was the determination[13] of the connectivity in the zeolite ZSM-39 via ^{29}Si COSY experiments (Figure 1.4). Recent pulse sequence developments[14] have extended the scope for such determinations via J coupling. Combinations of NMR experiments are sometimes necessary to provide full topological information on crystal structures.[15] Dipolar coupling can also be of assistance in determining molecular structure in crystalline materials, though it has to be remembered that, because it occurs through space, it does not, per se, distinguish between connectivity and intermolecular proximity.

Of course, there is more to molecular structure than connectivity. In particular, conformations of flexible chains are of importance – and these can be *expected* to differ between solution and crystalline states since conformational flexibility is normally inhibited in most solids. Solid-state NMR chemical shifts provide direct conformational information, as illustrated by the case of form II of oxybuprocaine

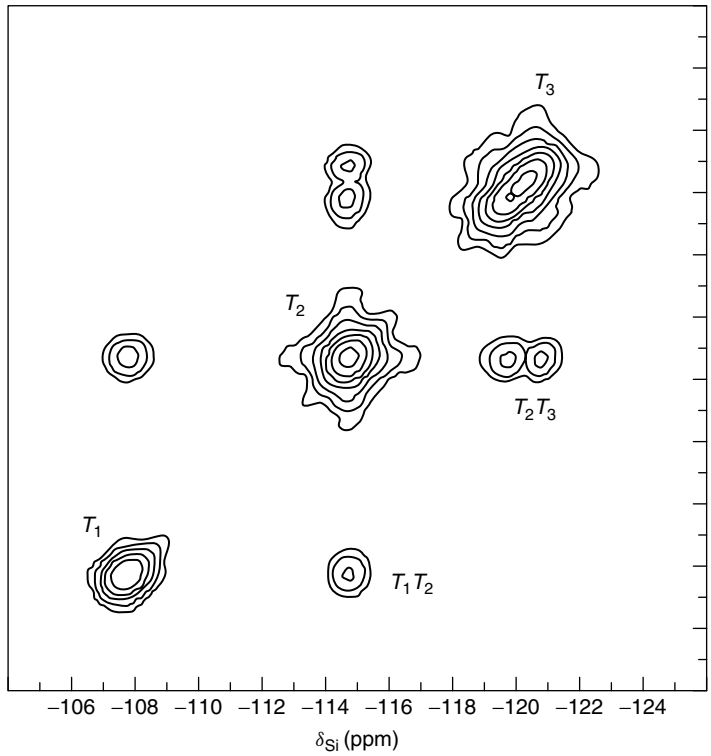
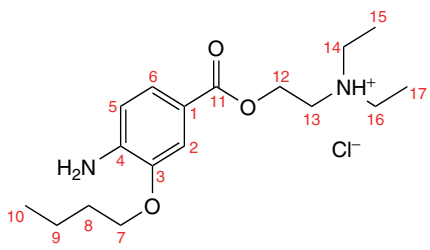


Figure 1.4. A two-dimensional homonuclear Si,Si connectivity plot for the zeolite ZSM-39, showing the connectivity (via oxygen) between the four different silicon sites. (Reprinted with permission from Ref. 13. © 1989 American Chemical Society.)

hydrochloride (**III**).[16] The ^{13}C CPMAS spectrum of this compound (Figure 1.5) shows the existence of signals at unusual shifts for an ethyl group, 4–7 ppm to low frequency of those for the solution state. These are consistent with the expected positions for a gauche–gauche conformation (influenced by the well-known "γ-gauche shielding effect").



Oxybuprocaine hydrochloride, **III**

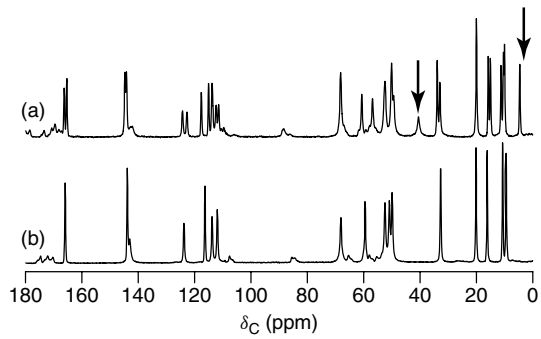
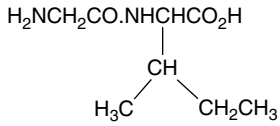


Figure 1.5. Carbon-13 CPMAS spectra of oxybuprocaine hydrochloride (**III**) form I (b) and form II (a), with arrows indicating the unusual positions for an ethyl group in the latter.

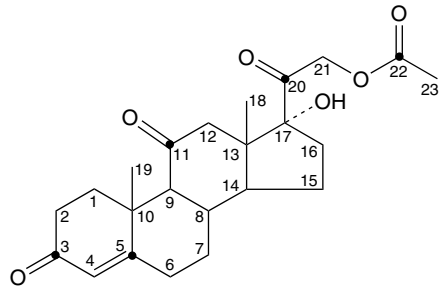
Dipolar coupling, being through space, can also give information on conformations – in principle more directly than "scalar" coupling can. Thus, Terao

and coworkers[17] were able to determine the complete molecular structure of glycylisoleucine (**IV**), involving six dihedral angles, via selective dipolar recoupling experiments. Chemical shifts and dipolar coupling constants are being increasingly used to determine the secondary structure of crystalline (and amorphous) proteins.[18]



Glycylisoleucine, **IV**

A second key aspect of crystallography concerns intermolecular interactions and the intermolecular environment. Here also, NMR has a strong role to play (*see* **Chapter 21**). One common stabilizing influence for crystal structures is the existence of intermolecular hydrogen bonding. The presence of such bonding and its location can frequently be attested by the chemical shift of a relevant nucleus (*see* **Chapter 22**). Thus, for form III of cortisone acetate (**V**), which has three molecules in the asymmetric unit, isotropic ^{13}C chemical shifts (assigned via measurements of the anisotropies and asymmetries) show[19] that two such molecules have hydrogen bonds involving the carbonyl group at position C3, while the third bonds through the carbonyl group at position C22. Intermolecular hydrogen bonding (NH–N) has also been detected by establishing the existence of indirect spin–spin (J_{NN}) coupling.[20]



Cortisone acetate, **V**

Additional information on atomic environments can come from the use of the tensorial nature of shielding (*see* **Chapter 9**). For example, experimental measurements of the anisotropy

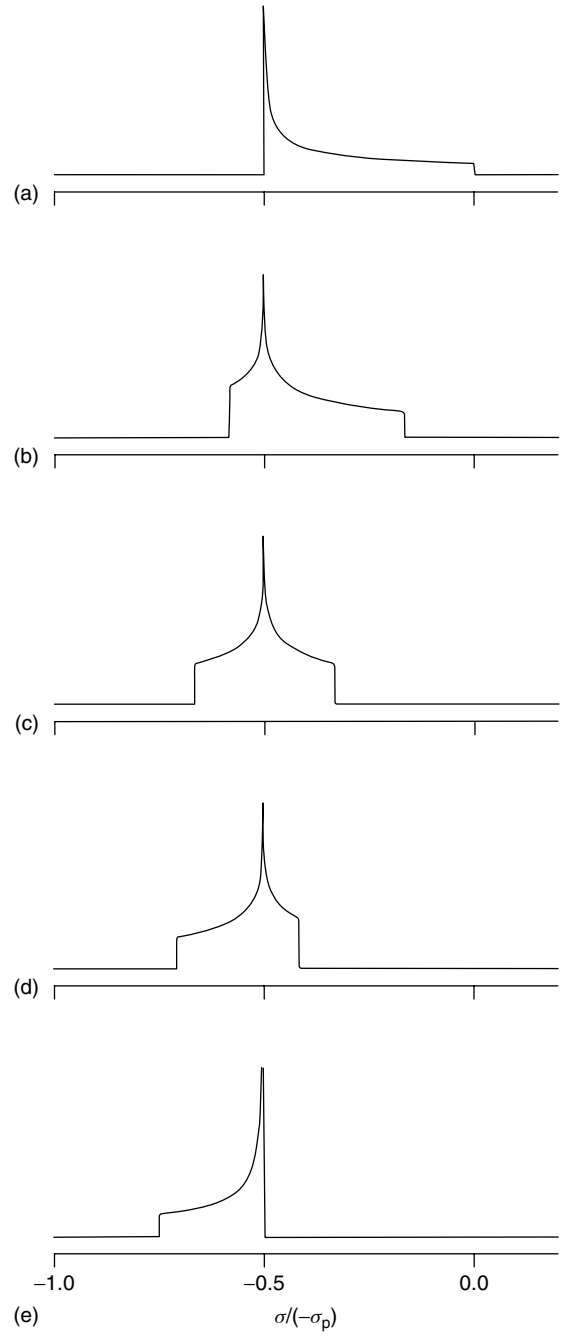


Figure 1.6. Schematic solid-state ^{199}Hg spectra for static samples, illustrating the effects of changes in mercury coordination from linear HgX_2 (top) to trigonal HgX_3 (bottom). (Reproduced with permission from Ref. 21. © 1997, Elsevier Science B.V.)

and asymmetry of ^{199}Hg chemical shifts allow the coordination of mercury in its crystalline compounds to be deduced from simple theoretical considerations.[21] Thus, Figure 1.6 shows the variation of bandshape expected as the local environment varies between linear HgX_2 and trigonal HgX_3. The compound $[Hg(S\text{-}2,3,5,6\text{-}Me_4C_6H)_3]^-$ illustrates this point: the measured values of the anisotropy and asymmetry of the ^{199}Hg chemical shift tensor indicate that the compound contains a distorted HgS_3 environment.

The multidimensional capability of NMR conveys considerable advantages and can reveal intermolecular effects. This is well seen for the simple case of methanol.[22] Two-dimensional spectra involving chemical shift anisotropy and spin diffusion for ^{13}C-enriched samples detect (Figure 1.7) differences in orientation between neighboring molecules because the spin-exchange process results in changes in the direction of the chemical shift principal axes. Moreover, there is a clear distinction between the α and β forms of methanol, which is not readily apparent in the one-dimensional spectra. The shape of the band for the β form in Figure 1.7(c) is simulated with the assumption that there is a 12° angle between C–O bond vectors in adjacent molecules. The simulated spectrum for the α form utilizes the crystal structure of Torrie *et al*.[23] It may be noted that the spectrum of the glassy sample shows rather random relative orientations of molecules in this case.[c]

Isotropic chemical shifts give immediate information about host–guest systems, including solvates. This includes recognition of the nature of the guest molecules (which may not be immediately apparent from diffraction patterns if the guests are highly

[c]While amorphous systems can scarcely come under the heading of "crystallography" and are not otherwise dealt with in this article, this example is included here to emphasize that NMR is not limited to crystalline systems.

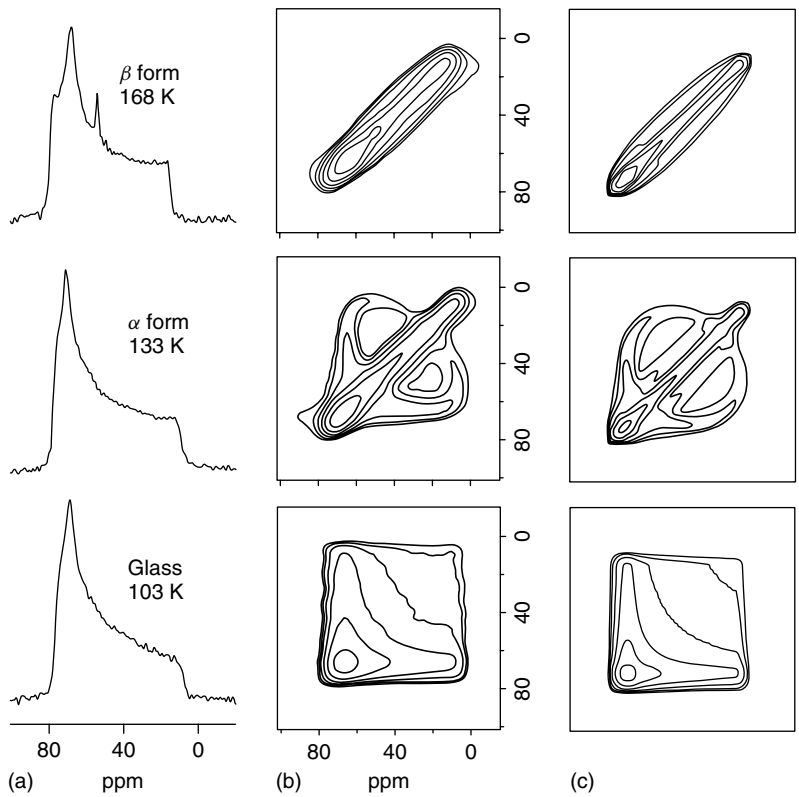


Figure 1.7. Carbon-13 spectra of static samples for three forms of methanol: (a) one-dimensional spectra; (b) experimental EXSY spectra (involving spin diffusion during the mixing time); and (c) simulated spectra.

mobile[8]). The relative positions of guest and host can also be addressed by studying the mutual effects on chemical shifts. In the case of incommensurate systems, which require considerations of n-dimensional ($n > 3$) "superspace" for diffraction analysis, NMR can again provide immediate information on the guest molecules and on the host molecules separately.

Dipolar coupling is, in principle, a prime source of intermolecular environment information (*see* **Chapter 10**). For cases of hydrogen bonding, good results can be obtained. For instance, for L-tyrosine hydrochloride an intermolecular C–O–H distance of 2.47 ± 0.07 Å was obtained by NMR,[24] which may be compared with the value 2.521 Å reported from neutron diffraction experiments. A truly intermolecular distance of <3 Å between aromatic protons has been found from double-quantum MAS work on a benzoxazine dimer.[25] N,C dipolar couplings have been used[26] to show the proximity of the α-helix of one molecule of a 56-amino acid protein to the N terminus of another molecule. Distances between carbon atoms in different fibrils of amyloid peptides have been explored by NMR.[27] However, in general, there are considerable difficulties in quantifying intermolecular internuclear distances via measurements of dipolar coupling because multiple interactions frequently complicate the evaluations, even in the case of selective isotopic enrichment. This means that diffraction-derived structures are usually required to understand the NMR results.

A third key element of crystallography, which is imperfectly addressed by diffraction techniques, is molecular-level mobility. NMR has many approaches to this problem (*see* **Chapters 24** and **25**), but a couple of examples will suffice at this point. In urea- and thiourea-inclusion compounds, the guest molecules are highly mobile, though in restricted ways. For the particular case of fluorocyclohexane as a guest, ring inversion is not greatly hindered by the channels, and variable-temperature ^{19}F spectra reveal[28] a classic coalescence phenomenon (Figure 1.8), from which the activation thermodynamic parameters can be derived.

Mobility information can come from quadrupolar spectra as well as those of spin-$^1/_2$ nuclides. Thus, molecular-level mobility can, in some circumstances, affect the linewidths of isotropic STMAS spectra but not isotropic MQMAS spectra[29] (Figure 1.9). Deuterium bandshapes of static samples are powerful indicators of mobility. For instance, they have been used[30] to accurately describe the nature of the motion

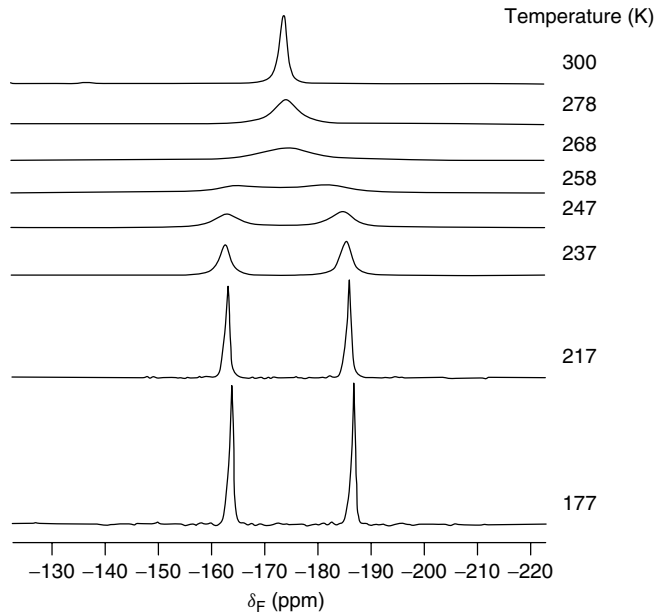


Figure 1.8. Experimental ^{19}F MAS spectra (with proton decoupling) of the fluorocyclohexane/thiourea inclusion compound for various temperatures, showing the coalescence of the axial and equatorial signals resulting from ring inversion.

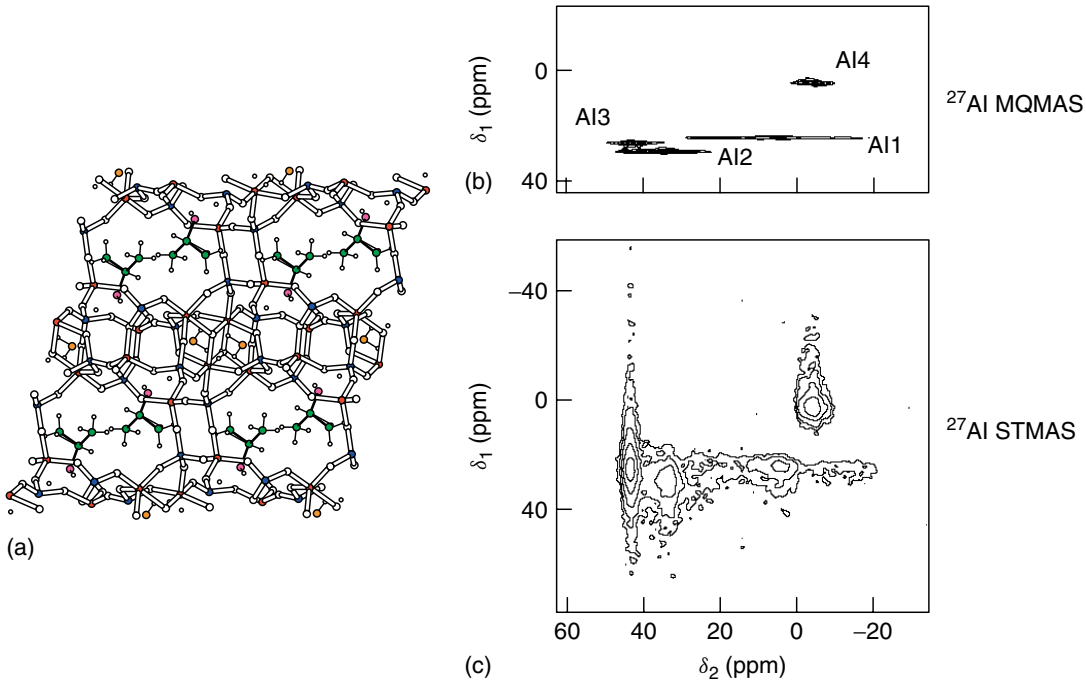


Figure 1.9. Structure of isopropylamine-ALPO-14 (a) and its two-dimensional ^{27}Al triple-quantum MQMAS (b) and STMAS (c) spectra, with the linewidths for the latter showing evidence of complex molecular mobility of the host:guest system.

of guest benzene and pyridine molecules within calixarene inclusion compounds. Note that, as in many cases, diffraction-derived structural information formed an important background to the investigation, but that the "added value" of NMR was essential to delineate the motional effects.

As already mentioned, relaxation times form another fruitful source of mobility information, extending down to lifetimes in the microseconds region.

1.4.2 Crystal Structure Information

The previous section has specifically dealt with *chemical* aspects of crystallography. However, NMR also provides detailed information of the more classical symmetry aspects of the subject.

Diffraction patterns are sometimes complicated by the existence of several independent molecules of the same species in the unit cell. Thus, information on the size of the asymmetric unit is valuable in advance of diffraction experiments. NMR is ideal for such determinations, since if there are, for example, two molecules in the asymmetric unit, then in principle all resonances will be split into two (though, of course, resolution may be inadequate in some cases) – a fact that is immediately recognizable. The case of form III of cortisone acetate has already been mentioned above. Figure 1.10 shows[31] the clear splitting for the resonance of C10 into three equal-intensity peaks. Of course, asymmetric units can be *smaller* than a complete molecule, as is the case for the trinuclear dimethyl chalcogenides, $(Me_2SnE)_3$, E = S, Se.[32] In this case, observation of a 2:1 or 1:2 doublet for ^{119}Sn (and ^{77}Se) shows that the asymmetric unit is half a molecule. However, additional crystallographic information is obtained by making use of the multinuclear nature of NMR; thus, observation of a 1:1:1 triplet for ^{13}C shows that the molecule has a C_2 symmetry axis rather than a mirror plane (Figure 1.11). NMR information on the content of the asymmetric unit is also of importance for understanding the crystal structure of network systems, as is the case for silicon carbide.

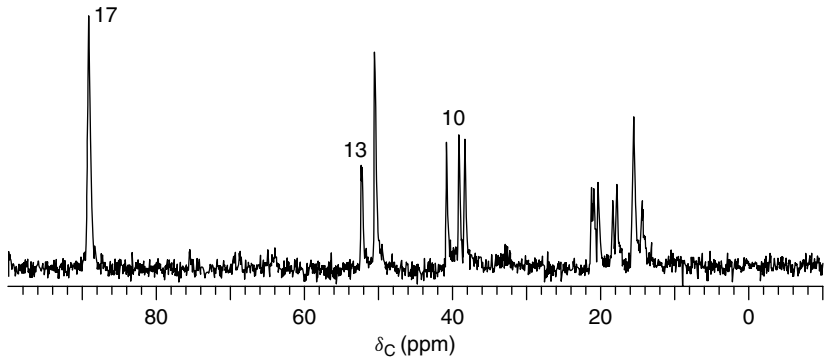


Figure 1.10. Portion of the dipolar dephased ^{13}C CPMAS spectrum of cortisone acetate (**V**), form III, showing the resonance of C10 split into three because there are three molecules in the asymmetric unit. Note that C13 only appears as a 1:2 doublet and the three components for C17 are not resolved. (Reproduced with permission from Ref. 31. © 1990, Elsevier Ltd.)

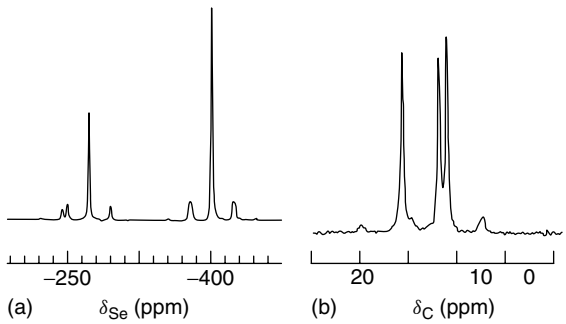


Figure 1.11. (a) Selenium-77 MAS spectrum of $(Me_2SnSe)_3$, showing that there is twofold but not threefold molecular symmetry and (b) carbon-13 spectrum of $(Me_2SnS)_3$, showing that the twofold symmetry is that of a rotation axis and not of a mirror plane. The small signals are either J_{SnSe} satellites or sinning sidebands.

This compound exists in a number of forms, known as *polytypoids*, which are distinguished by different modes of repetition of planes of atoms. Figure 1.12 shows the ^{29}Si spectra[33] of four such forms, two of which have only one pair of SiC atoms in the asymmetric unit, whereas the other two have two and three such pairs, respectively.

It should be stressed that the nature of NMR equivalence between nuclear sites needs to be understood (*see* **Chapter 6**). When two positions are related by a center of symmetry, then they are fully equivalent as far as mutual isotropic (*J*) coupling is concerned, and a single resonance is to be expected under MAS conditions (unless there is indirect coupling to other nuclei), in spite of such coupling. A single line is also expected under fast MAS conditions even when dipolar coupling (or anisotropic *J*) is involved. However, for static samples, the nuclei will still be subject to splittings arising from dipolar coupling (depending on the orientation of the internuclear vector with respect to the applied magnetic field), and this continues to be true under slow MAS conditions, thus leading to complex spectra. On the other hand, nuclei related by rotation axes or mirror planes will not, in general, be equivalent as far as isotropic J-coupling is concerned under static or slow MAS conditions, and dipolar coupling will even affect the spectra under fast MAS.

Quadrupole coupling tensors provide direct information on the site symmetry of atoms in crystal structures. Table 1.1 lists the EFG parameters of a central atom, M, for various coordination sites, as derived from a point-charge approximation[34] The parameter *A* is given in Reference 29. As for spectra of spin-$^1/_2$ nuclei, immediate information on the asymmetric unit can be obtained for quadrupolar nuclei. Thus, for $(CO)_5MnPbPh_3$ (of unknown crystal structure) ^{55}Mn MQMAS spectra at high magnetic field[35] (Figure 1.13) show that there are four independent molecules present, with slightly different quadrupolar parameters.

Interplay between different NMR tensors (e.g., between dipolar and shielding tensors) can supply additional information, such as the relative orientations of the two tensors, even from powder NMR experiments (*see* **Chapter 20**). This is particularly powerful if the orientation of one of those tensors in

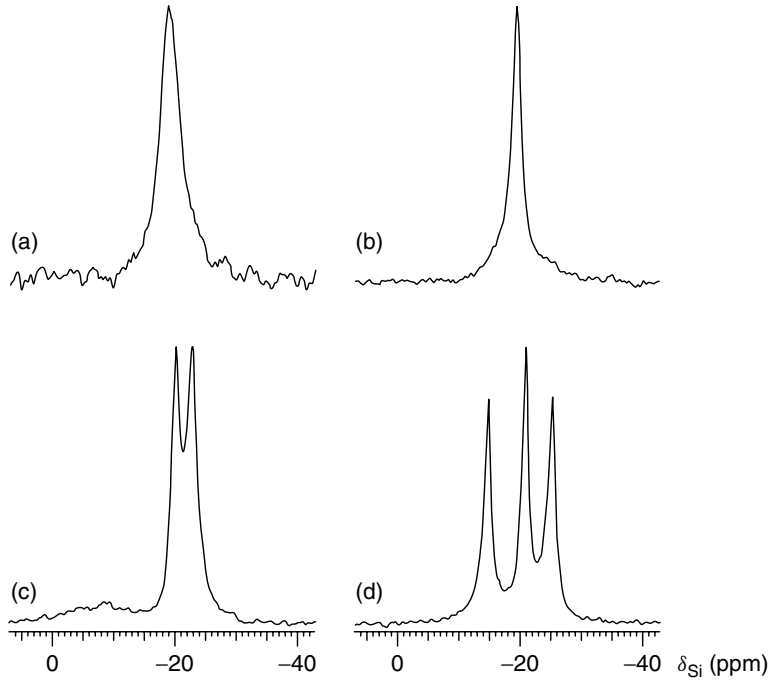


Figure 1.12. Silicon-29 MAS NMR spectra of four polytypes of silicon carbide, showing the differing numbers of silicon atoms in the asymmetric unit: (a) 3C; (b) 2H; (c) 4H; and (d) 6H.

Table 1.1. Electric field gradient parameters for a central atom with various coordinations

Complex	Symmetry	EFG_{PAS}	η_Q
MX_4	T_d	0	0
MX_3Y	C_{3v}	$-2A$	0
MX_2Y_2	C_{2v}	$\pm 2A$	1
MX_6	O_h	0	0
MX_5Y	C_{4v}	$-2A$	0
trans-MX_4Y_2	D_{4h}	$-4A$	0
cis-MX_4Y_2	C_{2v}	$2A$	0
mer-MX_3Y_3	C_{2v}	$\pm 3A$	1
fac-MX_3Y_3	C_{3v}	0	0

the crystal structure is known or can be deduced, as is the case for the dipolar coupling between directly bonded atoms.

There are various types of crystal structures that depart from the simple ideal of three-dimensional repetition. These include nonstoichiometric systems, defect structures, disordered structures, and incommensurate compounds. For all these cases, NMR can supply information that is not available from diffraction measurements (*see* **Chapter 23**). For instance, it can sometimes distinguish between spatial and temporal disorder by virtue of the different timescales available to the two techniques. This matter is further explored in **Chapter 25**, but one example here makes the point. The azobenzene dyestuff DR278 was shown by single-crystal diffraction techniques to contain the molecules in two different conformations (with unequal occupancies) in the unit cell. NMR demonstrated[36] unequivocally that there was exchange between the two forms (temporal disorder), and a combination of selective population inversion and bandshape analysis enabled the thermodynamic parameters for the exchange to be derived. Additionally, two-dimensional work provided the relative orientations of ^{15}N shielding principal axes in the two forms (consistent with the diffraction data).

Furthermore, where X-ray diffraction struggles to recognize the differences between neighboring atoms in the periodic table (especially when isoelectronic), NMR has no such problem; this is one aspect where the multinuclear character of NMR conveys a considerable advantage. It is particularly important for

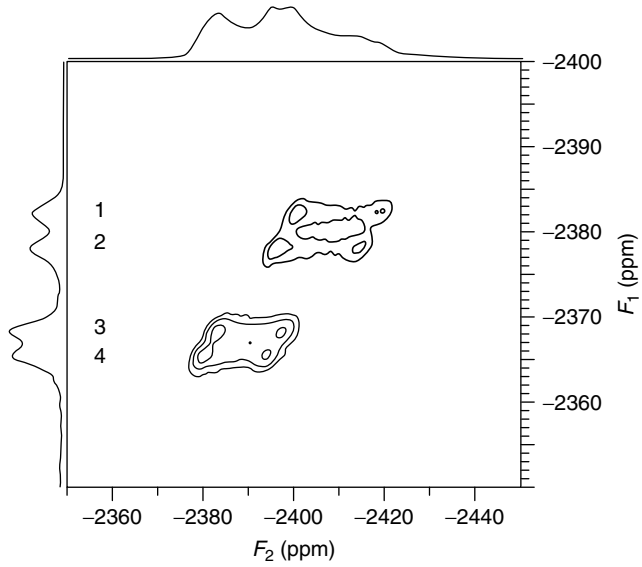


Figure 1.13. Manganese-55 two-dimensional triple-quantum MAS spectrum of $(CO)_5MnPbPh_3$, clearly showing that there are four nonequivalent sites for the molecule. (Reproduced with permission from Ref. 35. © 2006, American Chemical Society.)

ceramic materials and zeolites because of the electronic similarity of oxygen and nitrogen and of the SiN and AlO pairs of atoms. Thus, ^{15}N NMR has been used[37] to determine the ordering of anionic elements (nitrogen and oxygen) in J-phase yttrium silicon oxynitride, $Y_4Si_2O_7N_2$.

Simple NMR information on the number of atoms, ions, or molecules in the asymmetric unit can sometimes leads to evaluation of the space group. Thus, the through-bonds double-quantum MAS correlation ^{31}P spectrum of ZrP_2O_7 (Figure 1.14) shows[38] that the unit cell contains 13 unsymmetrical P_2O_7 units and the corresponding through-space case indicates that, in addition, there is one symmetrical P_2O_7 unit. This is consistent with a *Pbca* space group and not with the $Pa\bar{3}$ structure, which had been assumed earlier. The NMR information allowed the structure to be obtained from powder XRD data.

1.5 CONCLUDING REMARKS

Interplay between diffraction and solid-state NMR, as mentioned above, is now common. It usually consists merely of the NMR data being interpreted in terms of the structure determined by diffraction or by the two techniques being looked at in parallel, rather than seeing the information content gain by synergy. However, the future would seem to hold better promise. It has been demonstrated that structure solutions can be obtained by constraining the possible solutions to powder diffraction analysis according to NMR information, using a computer protocol that integrates the two types of information. The structure of form II of cortisone acetate has been obtained in this way[10] even though only a single piece of (semiquantitative) NMR information was included in the input. An analogous combination of NMR information, powder diffraction data, and computing methods has proved successful in determining the crystal structure of *N*-(*p*-tolyl)-dodecylsulfonamide.[39] Dipolar coupling results can form even more powerful constraints on crystal structures.[40] The ultimate goal may be to incorporate such computations into procedures to determine crystal structures by the simultaneous refinement of NMR and diffraction data.

In parallel with such developments, other advances are being made in the computation area. Specifically, shielding, indirect coupling, and quadrupolar coupling tensors can now be computed for solids by taking account of the repetition inherent in crystal structures (*see* **Chapter 3**). The planewave-pseudopotential approach, as used in

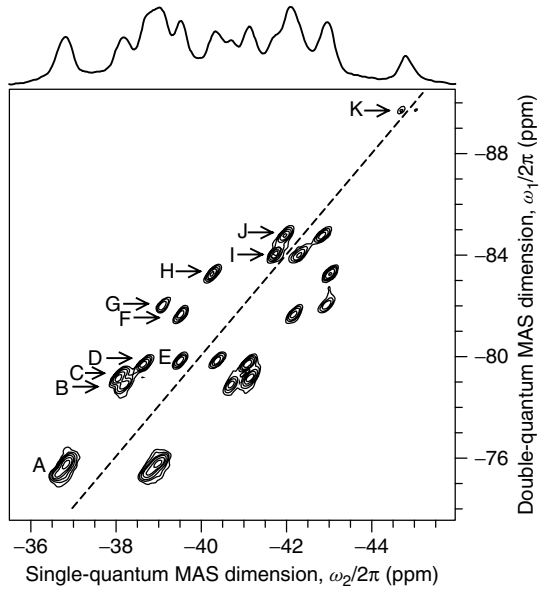


Figure 1.14. Phosphorus-31 two-dimensional through-bond double-quantum MAS correlation spectrum of ZrP_2O_7 obtained at 12 kHz spinning frequency using the refocused INADEQUATE experiment. The dashed line indicates the diagonal of the spectrum. The one-dimensional MAS spectrum is shown above the two-dimensional plot.

the CASTEP protocol,[41] is increasingly applied (*see* **Chapter 7**). This and other computational developments are revealing new understanding of the factors affecting NMR parameters in solids.

As mentioned earlier, it has now been possible to solve a complete crystal structure using NMR data[4] (together with unit cell parameters and the space group from a powder diffraction study). In this case, interatomic distances were obtained by ^{29}Si double-quantum dipolar recoupling experiments. An approach using NMR criteria to decide between computer-generated crystal structures (selected on the basis of lattice energy computations) has shown to have considerable potential for determining structures without diffraction input.[42] Significantly, this work made use of the full chemical shift tensor information. NMR crystallography imposes considerable constraints on allowed space groups in many cases, leading to full structure determination[43] (*see* **Chapter 17**). It has also been shown that in certain circumstances NMR data can reveal information more accurately than that by diffraction analysis. Thus, Facelli and Grant[44] used ^{13}C shielding tensors to prove that there was a lack of symmetry between atoms in naphthalene crystals, which accorded with the known space group, whereas the geometry as determined by the diffraction experiments suggested symmetry within experimental error. A combination of experimental chemical shift tensors and shielding computations has been used to improve the crystal structure of a zeolite obtained from powder XRD data, creating an "NMR crystallography structure refinement strategy".[45] Of course, these examples are unusual cases and NMR will certainly never replace diffraction techniques for the determination of crystal structures. However, it is equally certain that the importance of NMR to crystallography will grow as its ability to provide essential complementary information is increasingly recognized. The subject of NMR crystallography is thriving and is set to make further substantial contributions to our understanding of the nature of the crystalline state.

REFERENCES

1. A. Isaacs, J. Daintith, and E. Martin, eds, *Oxford Dictionary of Science*, 4th edn., Oxford University Press, ISBN 0192800981, 1999.
2. G. E. Pake, *J. Chem. Phys.*, 1948, **16**, 327–336.
3. H. S. Gutowsky, G. B. Kistiakowsky, G. E. Pake, and E. M. Purcell, *J. Chem. Phys.*, 1949, **17**, 972–981.
4. D. H. Brouwer, R. J. Darton, R. E. Morris, and M. H. Levitt, *J. Am. Chem. Soc.*, 2005, **127**, 10365–10370.
5. S. G. Zech, A. J. Wand, and A. E. McDermott, *J. Am. Chem. Soc.*, 2005, **127**, 8618–8626.
6. M. A. Kennedy and P. D. Ellis, *Concepts Magn. Reson.*, 1989, **1**, 35–47 and 109–129.
7. R. K. Harris, *Analyst*, 2006, **131**, 351–373.
8. A. Othman, J. S. O. Evans, I. R. Evans, R. K. Harris, and P. Hodgkinson, *J. Pharm. Sci.*, 2007, **96**, 1380–1396.
9. K. D. M. Harris, M. Tremayne, and B. M. Kariuki, *Angew. Chem. Int. Ed.*, 2001, **40**, 1626–1651.
10. R. K. Harris, *Solid State Sci.*, 2004, **6**, 1025–1037.
11. T. N. Pham, S. Masiero, G. Gottarelli, and S. P. Brown, *J. Am. Chem. Soc.*, 2005, **127**, 16018–16019.
12. H. W. Kroto, S. L. Klein, M. F. Meidine, J. F. Nixon, R. K. Harris, K. J. Packer, and P. Reams, *J. Organomet. Chem.*, 1985, **280**, 281–287.

13. C. A. Fyfe, H. Gies, and Y. Feng, *J. Am. Chem. Soc.*, 1989, **111**, 7702–7707.

14. A. Lesage, C. Auger, S. Caldarelli, and L. Emsley, *J. Am. Chem. Soc.*, 1997, **119**, 7867–7868.

15. V. Munch, F. Taulelle, T. Loiseau, G. Férey, A. K. Cheetham, S. Weigel, and G. D. Stucky, *Magn. Reson. Chem.*, 1999, **37**, S100–S107.

16. R. K. Harris, S. Cadars, L. Emsley, J. R. Yates, C. J. Pickard, R. K. R. Jetti, and U. J. Griesser, *Phys. Chem. Chem. Phys.*, 2007, **9**, 360–368.

17. K. Nomura, K. Takegoshi, T. Terao, K. Uchida, and M. Kainosho, *J. Am. Chem. Soc.*, 1999, **121**, 4064–4065.

18. A. E. McDermott, *Curr. Opin. Struct. Biol.*, 2004, **14**, 554–561.

19. E. A. Christopher, R. K. Harris, and R. A. Fletton, *Solid State NMR*, 1992, **1**, 93–101.

20. T. N. Pham, J. M. Griffin, S. Masiero, S. Lena, G. Gottarelli, P. Hodgkinson, C. Filip, and S. P. Brown, *Phys. Chem. Chem. Phys.*, 2007, **9**, 3416–3423.

21. G. A. Bowmaker, R. K. Harris, and S.-W. Oh, *Coord. Chem. Rev.*, 1997, **167**, 49–94.

22. R. Tycko and G. Dabbagh, *J. Am. Chem. Soc.*, 1991, **113**, 3592–3593.

23. B. H. Torrie, S.-X. Weng, and B. M. Powell, *Mol. Phys.*, 1989, **67**, 575–581.

24. B.-J. van Rossum, C. P. de Groot, V. Ladizhansky, S. Vega, and H. J. M. de Groot, *J. Am. Chem. Soc.*, 2000, **122**, 3465–3472.

25. I. Schnell, S. P. Brown, H. Y. Low, H. Ishida, and H. W. Spiess, *J. Am. Chem. Soc.*, 1998, **120**, 11784–11795.

26. J. J. Helmus, P. S. Nadaud, N. Höfer, and C. P. Jaroniec, *J. Chem. Phys.*, 2008, **128**, article no. 052314.

27. R. Tycko, *J. Chem. Phys.*, 2007, **126**, article no. 064506.

28. R. K. Harris, A. Nordon, and K. D. M. Harris, *Magn. Reson. Chem.*, 1999, **37**, 15–24.

29. S. Antonijevic, S. E. Ashbrook, S. Biedasek, R. I. Walton, S. Wimperis, and H. Yang, *J. Am. Chem. Soc.*, 2006, **128**, 8054–8062.

30. E. B. Brouwer, G. D. Enright, C. I. Ratcliffe, G. A. Facey, and J. A. Ripmeester, *J. Phys. Chem. B*, 1999, **103**, 10604–10616.

31. R. K. Harris, A. M. Kenwright, B. J. Say, R. R. Yeung, R. A. Fletton, R. W. Lancaster, and G. L. Hardgrove, *Spectrochim. Acta*, 1990, **46A**, 927–935.

32. R. K. Harris, and A. Sebald, *Magn. Reson. Chem.*, 1989, **27**, 81–87.

33. D. C. Apperley, R. K. Harris, G. L. Marshall, and D. P. Thompson, *J. Am. Ceram. Soc.*, 1991, **74**, 777–782.

34. O. H. Han and E. Oldfield, *Inorg. Chem.*, 1990, **29**, 3666–3669.

35. K. J. Ooms, K. W. Feindel, V. V. Terskikh, and R. E. Wasylishen, *Inorg. Chem.*, 2006, **45**, 8492–8499.

36. G. McGeorge, R. K. Harris, A. S. Batsanov, A. M. Chippendale, J. F. Bullock, and Z. Gan, *J. Phys. Chem. A*, 1998, **102**, 3505–3513.

37. D. S. B. Hauck, R. K. Harris, D. C. Apperley, and D. P. Thompson, *J. Mater. Chem.*, 1993, **3**, 1005–1006.

38. I. J. King, F. Fayon, D. Massiot, R. K. Harris and J. S. O. Evans, *Chem. Commun.*, 2001, 1766–1767.

39. M. Rajeswaran, T. N. Blanton, N. Zumbulyadis, D. J. Giesen, C. Conesa-Moratilla, S. T. Misture, P. W. Stephens, and A. Huq, *J. Am. Chem. Soc.*, 2002, **124**, 14450–14459.

40. D. A. Middleton, X. Peng, D. Saunders, K. Shankland, W. I. F. David, and A. J. Markvardsen, *Chem. Comm.*, 2002, 1976–1977.

41. J. R. Yates, C. J. Pickard, and F. Mauri, *Phys. Rev. B*, 2007, **76**, article no. 024401.

42. J. K. Harper and D. M. Grant, *Cryst. Growth Des.*, 2006, **6**, 2315–2321.

43. F. Taulelle, *Solid State Sci.*, 2004, **6**, 1053–1057.

44. J. C. Facelli and D. M. Grant, *Nature*, 1993, **365**, 325–327.

45. D. H. Brouwer, *J. Magn. Reson.*, 2008, **194**, 136–146.

Chapter 2
Tensors in NMR

S. Chandra Shekar and Alexej Jerschow

Department of Chemistry, New York University, New York, NY 10003, USA

2.1	Introduction	19
2.2	Cartesian to Spherical Tensors	19
2.3	Hamiltonians in Terms of Spherical Tensors of Rank 0, 1, 2	23
2.4	Matrix Elements for Spherical Tensors	26
	References	27

2.1 INTRODUCTION

Tensors are ubiquitous in NMR spectroscopy.[1–7] Spin tensors represent the quantum-mechanical operators, while the spatial tensors are used to describe the magnitude of the isotropic and anisotropic coupling interactions with the magnetic field, with other spins, and with an electric field gradient.[1–9] Contractions or scalar products between tensors are used to represent Hamiltonians, and the detection process with a quantum-mechanical detection operator. The use of irreducible spherical tensors is often described as a convenience of representation, but it is difficult to see its versatility from the outset. We aspire to present here step-by-step instructions for how to arrive at tensor representations and show the connections between cartesian and spherical tensors with an emphasis on how they are used in describing NMR experiments.

NMR Crystallography Edited by Robin K. Harris, Roderick E. Wasylishen and Melinda J. Duer © 2009 John Wiley & Sons, Ltd. ISBN: 978-0-470-69961-4

2.2 CARTESIAN TO SPHERICAL TENSORS

A cartesian second rank tensor $\boldsymbol{V}$, in three dimensions is a 3×3 matrix and is defined by the way its elements transform under a rotation of the coordinate axes. By definition,

$$V_{kl}^{R} = (\boldsymbol{R}^{\mathrm{T}}\boldsymbol{V}\boldsymbol{R})_{kl} = \sum_{m,n=1,2,3} R_{mk} R_{nl} V_{mn}, \quad k, l = 1, 2, 3 \tag{2.1}$$

where, $\boldsymbol{V}^{\mathrm{R}}$ is the tensor in the rotated coordinate system and $\boldsymbol{R}$ is the 3×3 rotation matrix.

$$\boldsymbol{R}^{\mathrm{T}}\boldsymbol{R} = \mathbf{1} = \boldsymbol{R}\boldsymbol{R}^{\mathrm{T}}, \quad \boldsymbol{R}^{-1} = \boldsymbol{R}^{\mathrm{T}} \tag{2.2}$$

$\mathbf{1}$ is the 3×3 unit matrix.

A very common and frequently used convenient parameterization of rotations is the Euler rotation.[1,2,7,8,10–14] In terms of the Euler triplet

$\Omega = (\alpha\beta\gamma)$, the rotation matrix is given by.[11,13,14]

$$\begin{aligned}\boldsymbol{R}(\alpha\beta\gamma) &= \boldsymbol{R}_z(\alpha)\boldsymbol{R}_y(\beta)\boldsymbol{R}_z(\gamma)\\ &= \begin{pmatrix} c_\alpha & -s_\alpha & 0\\ s_\alpha & c_\alpha & 0\\ 0 & 0 & 1\end{pmatrix}\begin{pmatrix} c_\beta & 0 & s_\beta\\ 0 & 1 & 0\\ -s_\beta & 0 & c_\beta\end{pmatrix}\\ &\times \begin{pmatrix} c_\gamma & -s_\gamma & 0\\ s_\gamma & c_\gamma & 0\\ 0 & 0 & 1\end{pmatrix}\\ &= \begin{pmatrix} c_\alpha c_\beta c_\gamma - s_\alpha s_\gamma & -c_\alpha c_\beta c_\gamma - s_\alpha c_\gamma & c_\alpha s_\beta\\ s_\alpha c_\beta c_\gamma + c_\alpha s_\gamma & -s_\alpha c_\beta s_\gamma + c_\alpha c_\gamma & s_\alpha s_\beta\\ -s_\beta c_\gamma & s_\beta s_\gamma & c_\beta\end{pmatrix}\end{aligned} \tag{2.3}$$

with $c_\theta = \cos\theta$ and $s_\theta = \sin\theta$.

From equation (2.1), it can be seen that all transformed elements depend on all the original elements. However, it turns out that we can combine the elements of $\boldsymbol{V}$ and group them into certain "symmetry" sets. Upon transformation, the elements of a given symmetry set transform among themselves, akin to angular momentum eigenfunctions in quantum mechanics in general and in NMR specifically. There are three such symmetry sets for a rank 2 cartesian tensor—an invariant set with one element, an "antisymmetric" set of three elements, a "symmetric" set of five elements. It is shown below that it is no coincidence that spherical harmonics (which are eigenfunctions of the orbital angular momentum operator) also have 1, 3, and 5 members for rank $l = 0,1,2$, respectively. Those combinations of cartesian tensor elements that possess the same transformation properties as the spherical harmonics of rank $l = 0,1,2$ are called *spherical tensors* of rank $l = 0,1,2$, respectively.[10]

Any 3×3 matrix, $\boldsymbol{V}$ can be expressed as a sum of isotropic $\boldsymbol{V}^0$, symmetric $\boldsymbol{V}^s \equiv \boldsymbol{S}$ and antisymmetric $\boldsymbol{V}^a \equiv \boldsymbol{A}$ matrices.[13]

$$\boldsymbol{V} = V^0\mathbf{1} + \boldsymbol{V}^a + \boldsymbol{V}^s \equiv V^0\mathbf{1} + \boldsymbol{A} + \boldsymbol{S} \tag{2.4}$$

The matrix elements of the different components can be derived as[13]

$$\begin{aligned} V^0 &= \frac{1}{3}\sum_{k=1,2,3} V_{kk}\\ V^s_{kl} \equiv S_{kl} &= \frac{1}{2}\left(V_{kl} + V_{lk} - \delta_{kl}2V^0\right)\\ V^a_{kl} \equiv A_{kl} &= \frac{1}{2}\left(V_{kl} - V_{lk}\right)\\ k, l &= 1, 2, 3\end{aligned} \tag{2.5}$$

Both the symmetric and antisymmetric parts above are traceless. The symmetric part, therefore, has only five independent elements while the antisymmetric counterpart has three.

Using equation (2.1) and the equivalent

$$V^R_{lk} = \sum_{m,n=1,2,3} R_{ml}R_{nk}V_{mn} = \sum_{m,n=1,2,3} R_{nl}R_{mk}V_{nm} \tag{2.6}$$

leads immediately to

$$A^R_{kl} = \frac{1}{2}(V^R_{kl} - V^R_{lk}) = \sum_{m,n=1,2,3} R_{mk}R_{nl}A_{mn} \tag{2.7}$$

$$S^R_{kl} = \frac{1}{2}(V^R_{kl} + V^R_{lk}) = \sum_{m,n=1,2,3} R_{mk}R_{nl}S_{mn} \tag{2.8}$$

proving that the elements of $\boldsymbol{A}$, $\boldsymbol{S}$ transform according to transformation equation (2.1) and hence, each is a cartesian tensor of rank 2. Though they share with spherical harmonics the trait that elements of a given symmetry set mix only among themselves under rotations, they do not transform exactly like spherical harmonics of rank 1 and rank 2.

The $2l + 1$ components of a spherical harmonic of rank 1 transform according to

$$Y^R_{ln} = \sum_{m=l,l-1,\ldots,l} Y_{lm}\mathcal{D}^l_{mn}, \quad n = l, l-1, \ldots, -l \tag{2.9}$$

with the Wigner rotation matrix elements having the form[10]

$$\begin{aligned}\mathcal{D}^l_{mn}(\Omega) &= \mathrm{e}^{-\mathrm{i}m\alpha}d^l_{mn}(\beta)\ \mathrm{e}^{-\mathrm{i}n\gamma},\\ m, n &= l, l-1, \ldots, -l\end{aligned} \tag{2.10}$$

d^l_{mn} are the reduced Wigner rotation matrix elements. Our immediate goal is to build upon these antisymmetric and symmetric cartesian rank 2 tensors and arrive at corresponding spherical tensors of rank 1 and rank 2.

In the following, we produce the interrelationships between the spherical tensor components and the cartesian counterparts. The spherical tensors will be represented by T_{lm}, which will denote a tensor of rank l and order m (and not a matrix element). It is important to remember that each T_{lm} can itself be represented in matrix form. The rank 0 spherical tensor has a particularly simple form.

2.2.1 Rank 0 Spherical Tensor

Direct application of equations (2.1) and (2.2) yields

$$\left(3V^0\right)^R = \sum_{k=1,2,3} V_{kk}^R = \sum_{m,n,k=1,2,3} R_{km} R_{kn} V_{mn} = \sum_{m,n=1,2,3} \delta_{mn} V_{mn} = \sum_{m=1,2,3} V_{mm} = 3V^0 \tag{2.11}$$

the well-known result that the trace of a matrix is invariant under rotations, and hence V^0 is unchanged and "unmixed". This is the spherical tensor $l = 0$.

$$T_{00} = V^0 \tag{2.12}$$

2.2.2 Rank 1 Spherical Tensors

From equation (2.5),

$$A_{kk} = 0, \qquad A_{lk} = -A_{kl} \tag{2.13}$$

which when used in equation (2.7) results in

$$A_{kl}^R = \sum_{p<q} A_{pq}(R_{pk}R_{ql} - R_{pl}R_{qk}) \tag{2.14}$$

2.2.2.1 The T_{10} Component

From equation (2.14)

$$A_{12}^R = A_{12}(R_{11}R_{22} - R_{12}R_{21}) + A_{13}(R_{11}R_{32} - R_{12}R_{31}) + A_{23}(R_{21}R_{32} - R_{22}R_{31}) \tag{2.15}$$

and using equation (2.3), after somewhat lengthy but straightforward algebra and trigonometry, we obtain

$$\begin{aligned} &-\mathrm{i}2(R_{11}R_{22} - R_{12}R_{21}) \\ &\quad = (R_{11} + \mathrm{i}R_{12})(R_{21} - \mathrm{i}R_{22}) - c.c. \\ &\quad = (c_\alpha\, c_\beta - \mathrm{i}s_\alpha)\mathrm{e}^{-\mathrm{i}\gamma}(s_\alpha\, c_\beta - \mathrm{i}c_\alpha)\mathrm{e}^{\mathrm{i}\gamma} - c.c. \\ &\quad = \mathrm{i}2[c_\alpha\, c_\beta\,(-c_\alpha) + (-s_\alpha)s_\alpha\, c_\beta] \\ &\quad \Longrightarrow R_{11}R_{22} - R_{12}R_{21} = c_\beta \end{aligned} \tag{2.16}$$

where c.c. denotes complex conjugate.

$$\begin{aligned} R_{11}R_{32} - R_{12}R_{31} &= -s_\beta s_\alpha \\ R_{21}R_{32} - R_{22}R_{31} &= s_\beta c_\alpha \end{aligned} \tag{2.17}$$

$$A_{12}^R = A_{12}c_\beta + (-A_{13}s_\alpha + A_{23}c_\alpha)s_\beta \tag{2.18}$$

But since

$$-A_{13}s_\alpha + A_{23}c_\alpha = \frac{1}{2}\left\{(A_{23} - \mathrm{i}A_{13})\mathrm{e}^{-\mathrm{i}\alpha} + (A_{23} + \mathrm{i}A_{13})\mathrm{e}^{\mathrm{i}\alpha}\right\} \tag{2.19}$$

A_{12}^R may be recast as

$$A_{12}^R = A_{12}c_\beta + \frac{1}{\sqrt{2}}(A_{23} - \mathrm{i}A_{13})\frac{1}{\sqrt{2}}s_\beta\mathrm{e}^{-\mathrm{i}\alpha} + \frac{1}{\sqrt{2}}(A_{23} + \mathrm{i}A_{13})\frac{1}{\sqrt{2}}s_\beta\mathrm{e}^{\mathrm{i}\alpha} \tag{2.20}$$

Using

$$d_{00}^1 = c_\beta, \qquad d_{10}^1 = -\frac{1}{\sqrt{2}}s_\beta \tag{2.21}$$

and exploiting the symmetry of the reduced Wigner rotation matrix,

$$d_{mn}^l = d_{-n-m}^l = (-)^{m+n}d_{nm}^l = (-)^{m+n}d_{-m-n}^l \tag{2.22}$$

along with equation (2.10), we are in a position to write

$$A_{12}^R = \sum_{m=1,0,-1} T_{1m}\mathcal{D}_{m0}^1(\Omega) \tag{2.23}$$

We now tentatively propose

$$T_{10} = A_{12}, \quad T_{1\pm1} = \mp\frac{1}{\sqrt{2}}(A_{23} \mp \mathrm{i}A_{13}) \tag{2.24}$$

In equation (2.24), it is seen that T_{10} transforms like the spherical harmonic Y_{10}.

2.2.2.2 The $T_{1\pm1}$ Component

Similarly, it can be confirmed that $T_{1\pm1}$ transform like $Y_{1\pm1}$, and the constructs for the rank 1 spherical tensor components in terms of the cartesian antisymmetric rank 2 tensor components given in equation (2.24) are indeed correct.

$$A_{23}^R \mp \mathrm{i}A_{13}^R = \sum_{p<q} A_{pq}\left\{(R_{p2}R_{q3} - R_{p3}R_{q2}) \mp \mathrm{i}(R_{p1}R_{q3} - R_{p3}R_{q1})\right\} \tag{2.25}$$

Using equation (2.3),

$$A^R_{23} \mp \mathrm{i}A^R_{13} = \mathrm{e}^{\mp \mathrm{i}\gamma}\Big\{A_{12}(-s_\beta) + \frac{1}{2}\Big[(A_{23} - \mathrm{i}A_{13})(\pm)\mathrm{e}^{-\mathrm{i}\alpha}(1 \pm c_\beta) + (A_{23} + \mathrm{i}A_{13})(\mp)\mathrm{e}^{+\mathrm{i}\alpha}(1 \mp c_\beta)\Big]\Big\} \tag{2.26}$$

But since

$$d_{01} = \frac{1}{\sqrt{2}}s_\beta, \quad d^1_{\pm 11} = \pm\frac{1}{2}(1 \pm c_\beta) \tag{2.27}$$

$$\mp\frac{1}{\sqrt{2}}(A^R_{23} \mp \mathrm{i}A^R_{13}) = \sum_{m=1,0,-1} T_{1m}\mathcal{D}^1_{m\pm 1}\ (\Omega) \tag{2.28}$$

completing the assignment of rank 1 spherical tensor components in terms of the cartesian tensor elements given in equation (2.24).

Therefore,

$$T^R_{1n} = \sum_{m=1,0,-1} T_{1m}\mathcal{D}^1_{mn}\ (\Omega) \tag{2.29}$$

2.2.3 Rank 2 Spherical Tensors

From equation (2.8), and using the fact that $\boldsymbol{S}$ is traceless,

$$\begin{aligned} S^R_{33} &= \frac{1}{2}s^2_\beta\{-S_{33} + (S_{11} - S_{22})c_{2\alpha}\} + S_{33}\ c^2_\beta \\ &\quad + S_{12}\ s^2_\beta s_{2\alpha} + (S_{13}\ c_\alpha + S_{23}s_\alpha)s_{2\beta}\ 2S^R_{33} \\ &= c.c. + \frac{1}{2}S_{33}(3c^2_\beta - 1) + (S_{13} + \mathrm{i}S_{23})s_{2\beta}\mathrm{e}^{-\mathrm{i}\alpha} \\ &\quad + \frac{1}{2}(S_{11} - S_{22} + \mathrm{i}2S_{12})\mathrm{e}^{-\mathrm{i}2\alpha}s^2_\beta \end{aligned} \tag{2.30}$$

Using

$$\begin{aligned} d^2_{00} &= \frac{1}{2}(3c^2_\beta - 1) \\ d^2_{10} &= -\sqrt{\frac{3}{8}}s_{2\beta}, \quad d^2_{20} = \sqrt{\frac{3}{8}}s^2_\beta \end{aligned} \tag{2.31}$$

along with equations (2.10) and (2.22)

$$\sqrt{\frac{3}{2}}S^R_{33} = \sum_{m=0,\pm1,\pm2} T_{2m}\mathcal{D}^2_{m0}(\Omega) \tag{2.32}$$

where we tentatively propose

$$\begin{aligned} T_{20} &= \sqrt{\frac{3}{2}}S_{33}, \quad T_{2\pm1} = \mp(S_{13} \pm \mathrm{i}S_{23}) \\ T_{2\pm2} &= \frac{1}{2}(S_{11} - S_{22} \pm \mathrm{i}2S_{12}) \end{aligned} \tag{2.33}$$

Therefore, T_{20} transforms like Y_{20}.

Similarly, it can be confirmed that the remaining T_{2q}'s transform like their corresponding spherical harmonics, and the constructs for the rank 2 spherical tensor components in terms of the cartesian antisymmetric rank 2 tensor components given in equation (2.33) are indeed correct.

2.2.4 Construction of Rank 0, 1, 2 Spherical Tensors from a Second Rank Cartesian Tensor

From equations (2.12), (2.24) and (2.33)

$$\begin{aligned} T_{00} &= V^0 \\ T_{10} &= V^a_{12} \qquad T_{1\pm1} = \pm\frac{1}{\sqrt{2}}(V^a_{23} \mp \mathrm{i}V^a_{13}) \\ T_{20} &= \sqrt{\frac{3}{2}}V^s_{33}, \quad T_{2\pm1} = \mp(T^s_{13} \pm \mathrm{i}T^s_{23}) \\ T_{2\pm2} &= \frac{1}{2}(V_{11} - V_{22} \pm \mathrm{i}2V^s_{12}) \end{aligned} \tag{2.34}$$

where the antisymmetric and symmetric second rank cartesian tensors $\boldsymbol{V}^a$, $\boldsymbol{V}^s$ are specified by equations (2.4) and (2.5).

Tensor definitions sometimes vary in their normalization constants and the definition of positive versus negative order components. The spherical tensor component constructs for rank 1 in equation (2.34) differ by a rank-dependent constant factor and a phase from those given in ref. 2. However, they agree with those by Varshalovich *et al.*,[13] except for a factor of $\sqrt{\frac{3}{2}}$ for T_{2m}. These differences are self-compensating in the sense that the final form of the Hamiltonian and observable quantities are the same.

The spherical tensors of rank $l = 0,1,2$ above, have identical transformation properties under rotations as the spherical harmonics of rank $l = 0,1,2$, namely,

$$T^R_{ln} = \sum_{m=l,l-1,..,l} T_{lm}\boldsymbol{\mathcal{D}}^l_{mn}, \quad n = l, l-1, \ldots, l \tag{2.35}$$

2.2.5 Spatial versus Spin Tensors

The treatment presented so far has made no distinction between spatial and spin tensors. While spatial tensors operate on real 3-D space, spin tensors operate on the space spanned by the basis functions of the angular momentum operators, which may be much higher dimensional. In three dimensions, which would correspond to a space spanned by angular momentum $L=1$, there is a direct correspondence between real and spin space. In order to make this distinction explicit, it is customary to use separate symbols for spin and spatial tensors. Typically, T_{LM} is used for spin tensors, and A_{LM}, R_{LM}, or V_{LM} for spatial tensors, but they are both part of a more general pattern, which is outlined in the following section. A generalization to unitary operations is normally introduced as well for spin tensors.

2.3 HAMILTONIANS IN TERMS OF SPHERICAL TENSORS OF RANK 0, 1, 2

One of the most basic parts of the Hamiltonian in NMR is the interaction term between the nuclear magnetic moment $\mu = \gamma \boldsymbol{I}$ and the magnetic field $\boldsymbol{B}$, where γ is the gyromagnetic ratio (not to be confused with the Euler angle γ that we have used earlier). The interaction can be written as

$$\mathcal{H} = -\boldsymbol{\mu} \cdot \boldsymbol{B} = -\gamma \boldsymbol{I} \cdot \boldsymbol{B} \tag{2.36}$$

$\boldsymbol{B}$ may be due to an externally applied magnetic field, or due to internally created fields. In the latter case, one may consider the dipolar coupling as the interaction of a spin with the magnetic field created by another nearby spin.

The magnetic field, external or internal, may be altered by orientation, or by shielding through the electrons, which can likewise be anisotropic.

A very general way a given vector (e.g., for an applied external steady uniform magnetic field $\boldsymbol{B} \equiv \boldsymbol{B}^0$) can be altered is by operating on it (multiplying it by) a square matrix of corresponding dimensions, which in three dimensions corresponds to a rank 2 cartesian tensor (say $\boldsymbol{V}$).

$$\boldsymbol{V} \cdot \boldsymbol{B} = \boldsymbol{B}^{\text{eff}} \tag{2.37}$$

We can call $\boldsymbol{V}$ a shielding or a coupling tensor depending on its origin, and replace equation (2.36) by

$$\mathcal{H} = -\boldsymbol{\mu} \cdot \boldsymbol{B}^{\text{eff}} = -\boldsymbol{\mu} \cdot \boldsymbol{V} \cdot \boldsymbol{B} = -\gamma \boldsymbol{I} \cdot \boldsymbol{V} \cdot \boldsymbol{B} \tag{2.38}$$

which is the template form of most NMR Hamiltonians.

2.3.1 Chemical Shift Interaction

$$\boldsymbol{\sigma} \cdot \boldsymbol{B} = \boldsymbol{B}^{\text{eff}} \tag{2.39}$$

σ is a rank 2 cartesian tensor due to the chemical environment, which "couples" the nuclear spin to the external magnetic field. σ can be understood in the following manner. The molecular electronic current density around the nuclear spin vector $\boldsymbol{I}$ will present it with an effective magnetic field as given by equation (2.39). As highlighted in the introduction section, $\boldsymbol{\sigma}$ can be decomposed into isotropic, symmetric, and antisymmetric parts. If the antisymmetric part is zero or can be ignored, $\boldsymbol{\sigma}$ can be diagonalized by a rotation and the diagonal elements σ_{pp}, $p=1$, 2, 3 are called the *principal values* of the shielding tensor, and the corresponding coordinate frame's unit vectors correspond to the *principal directions*. The Hamiltonian equation (2.38) for the chemical shift takes the form:

$$\begin{aligned} \mathcal{H}^{cs} &= -\gamma \boldsymbol{I} \cdot \boldsymbol{\sigma} \cdot \boldsymbol{B} = \omega \sum_{k,l=1,2,3} I_k \sigma_{kl} n_l \\ &= \omega \sum_{k,l=1,2,3} \sigma_{kl} V_{kl} \\ V_{kl} &= I_k n_l, \qquad \omega = -\gamma B, \qquad \boldsymbol{B} = B\boldsymbol{n} \end{aligned} \tag{2.40}$$

where the second rank tensor mixes the magnetic field and spin components. $\boldsymbol{n}$ is a unit vector.

2.3.2 Dipolar Coupling

In the dipolar interaction Hamiltonian involving two spins, the magnetic moment of either spin can be thought of as coming under the influence of the magnetic field arising from the magnetic dipole moment belonging to the other spin.[1,2,7,8,15,16] The expression for the magnetic field due to a magnetic dipole from spin S is

$$\boldsymbol{B}^{\text{eff}} = \frac{\mu_0}{4\pi} \frac{1}{r_{IS}^3} \{\boldsymbol{\mu}_S - \mathbf{3}(\boldsymbol{\mu}_S \cdot \boldsymbol{n})\boldsymbol{n}\} \tag{2.41}$$

where $\boldsymbol{r}_{IS} = r_{IS}\,\boldsymbol{n}$ is the vector from spin S to the point at which the field is evaluated and n is the unit vector in that direction with $n_{1,\,2,\,3}$ being its components[8] along the x, y, z-axes. μ_0 is the free space permeability, also known as the *magnetic constant*.

Inserting equation (2.41) into equation (2.38) gives for the dipolar Hamiltonian

$$\begin{aligned}\mathcal{H}^{\mathrm{d}} &= -\gamma_I \boldsymbol{I}\cdot\boldsymbol{B}^{\mathrm{eff}}\\ \boldsymbol{B}^{\mathrm{eff}} &= \hbar\frac{\mu_0}{4\pi}\frac{\gamma_S}{r_{IS}^3}\{\boldsymbol{S} - \mathbf{3}(\boldsymbol{S}\cdot\boldsymbol{n})\boldsymbol{n}\}\end{aligned} \tag{2.42}$$

The dipolar coupling Hamiltonian then becomes [1,2,7,8,15,16]

$$\begin{aligned}\mathcal{H}^{\mathrm{d}} &= \omega_{\mathrm{D}}\left\{\sum_{k=1}^{3} I_k S_k - 3\sum_{k,l=1}^{3} n_k n_l I_k S_l\right\}\\ &= \omega_{\mathrm{D}}\sum_{k,l=1}^{3}(\delta_{kl} - 3n_k n_l) I_k S_l\\ &= \omega_{\mathrm{D}}\sum_{k,1=1,2,3} D_{kl} I_k S_l \equiv \omega_{\mathrm{D}}\sum_{k,1=1,2,3} D_{kl} V_{kl}\\ &= \omega_{\mathrm{D}}\boldsymbol{I}\cdot\boldsymbol{D}\cdot\boldsymbol{S}\\ \omega_{\mathrm{D}} &= -\hbar\frac{\mu_0}{4\pi}\frac{\gamma_I\gamma_S}{r_{IS}^3},\\ D_{kl} &= \delta_{kl} - 3n_k n_l, \quad V_{kl} = I_k S_l\\ n_1 &= \sin\theta\cos\phi, \quad n_2 = \sin\theta\sin\phi,\\ n_3 &= \cos\theta\end{aligned} \tag{2.43}$$

which is the cartesian form that we will use as a starting point to derive the corresponding spherical tensor form. The polar angle θ and the azimuth ϕ specify the orientation of the dipole vector in spherical coordinates. Also, ω_{D} is the dipolar coupling constant and $\boldsymbol{D}$ is the dipolar coupling cartesian second-rank tensor.

2.3.3 Quadrupolar Interaction

Nuclei with spin $> 1/2$ are bestowed with an electric quadrupole moment.[1,2,6,8–10,15] If a nonvanishing electric field gradient exists at the nucleus, the resulting quadrupolar interaction is given by[1,2,6,8,9,15,16]

$$\begin{aligned}\mathcal{H}^{\mathbf{Q}} &= \omega_{\mathrm{Q}}\boldsymbol{I}\cdot\boldsymbol{U}\cdot\boldsymbol{I}\\ &= \omega_{\mathrm{Q}}\sum_{k,l=1,2,3} U_{kl} I_k I_l \equiv \omega_{\mathrm{Q}}\sum_{k,l=1,2,3} U_{kl} V_{kl}\\ \omega_{\mathrm{Q}} &= \frac{\mathrm{e}Q}{\hbar 6 I(2I-1)}\\ U_{lk} &= U_{kl}, \quad \sum_{k=1,2,3} U_{kk} = 0, \quad V_{kl} = I_k I_l\end{aligned} \tag{2.44}$$

Above, ω_{Q} describes the strength of the coupling determined by the nuclear quadrupolar moment eQ and $\boldsymbol{U}$ is the cartesian second rank electric field gradient tensor at the nucleus.

The above formulation of the quadrupolar interaction in cartesian form is less useful and less intuitive than the chemical shift and the coupling interactions. One can directly derive an expression for the quadrupolar interaction in terms of spherical tensors from a multipole expansion.[8,9]

2.3.4 General Expression for Hamiltonians

Typically, the coupling Hamiltonians between a nuclear spin with either magnetic fields or other spins can be expressed as a *contraction* of two second rank cartesian tensors:[1,2,10]

$$\mathcal{H} = \sum_{k,l=1,2,3} U_{kl} V_{kl} \tag{2.45}$$

where $\boldsymbol{U}$ and $\boldsymbol{V}$ are second rank cartesian tensors. From equation (2.1) it is seen that $\mathcal{H}$ is invariant under rotations, i.e., it is itself a rank 0 tensor.

From equation 2.4,

$$V_{kl} = V^0\delta_{kl} + V^a_{kl} + V^s_{kl} \tag{2.46}$$

which, when substituted into equation (2.45), using equation (2.5),

$$\mathcal{H} = 3U^0V^0 + \sum_{k,l=1,2,3} U^a_{kl}V^a_{kl} + U^s_{kl}V^s_{kl} \tag{2.47}$$

Here, $\mathcal{H}$ is decomposed in terms of isotropic, symmetric, and antisymmetric rank 2 cartesian tensors. The process of summing over the indices "averages" out and eliminates the cross terms between the different symmetry types. Inverting equation (2.34) yields

$$\begin{aligned}\sum_{k,l=1,2,3}^{k<l} U^a_{kl}V^a_{kl} &= \sum_{m=1,0,-1}(-)^m T_{1-m}(\boldsymbol{U})T_{1m}(\boldsymbol{V})\\ \sum_{k,l=1,2,3} U^s_{kl}V^s_{kl} &= \sum_{m=0,\pm1,\pm2}(-)^m T_{2-m}(\boldsymbol{U})T_{2m}(\boldsymbol{V})\end{aligned} \tag{2.48}$$

which when substituted back in to equation (2.47) leads to

$$\mathcal{H} = \sum_{l=0}^{2}(3-l)\sum_{m=l,l-1,..,l}(-)^m T_{l-m}(\boldsymbol{U})T_{lm}(\boldsymbol{V}) \tag{2.49}$$

Table 2.1. NMR interactions: $\lambda = CS$, D, and Q correspond respectively to chemical shift and dipolar interactions

λ	ω_λ	l	m	$T_{lm}(\boldsymbol{U})$	$T_{lm}(\boldsymbol{V})$
CS	$-\gamma B$	0	0	$\sigma^0 = \frac{1}{3}\sum_k \sigma_{kk}$	$\frac{1}{3}\boldsymbol{I}\cdot\boldsymbol{n}$
		1	0	$\frac{1}{2}(\sigma_{12}-\sigma_{21})$	$\frac{\mathrm{i}}{2}(I_+n_- - I_-n_+)$
			±1	$\pm\frac{1}{2\sqrt{2}}\{(\sigma_{23}-\sigma_{32})\mp\mathrm{i}(\sigma_{13}-\sigma_{31})\}$	$-\frac{\mathrm{i}}{2\sqrt{2}}(I_\pm n_z - I_z n_\pm)$
		2	0	$\sqrt{\frac{3}{2}}(\sigma_{33}-\sigma^0)$	$\sqrt{\frac{1}{6}}(3I_zn_z - \boldsymbol{I}\cdot\boldsymbol{n})$
			±1	$\mp\frac{1}{2}\{(\sigma_{13}+\sigma_{31})\pm\mathrm{i}(\sigma_{23}+\sigma_{32})\}$	$\mp\frac{1}{2}(I_\pm n_z + I_z n_\pm)$
			±2	$\frac{1}{2}\{(\sigma_{11}-\sigma_{22})\pm\mathrm{i}(\sigma_{12}+\sigma_{12})\}$	$\frac{1}{2}I_\pm n_\pm$
D	$-\hbar\frac{\mu_0}{4\pi}\frac{\gamma_I\gamma_S}{r_{IS}^3}$	0	0	0	$\frac{1}{3}\boldsymbol{I}\cdot\boldsymbol{S}$
		1	0	0	$\frac{\mathrm{i}}{2}(I_+S_- - I_-S_+)$
			±1	0	$-\frac{\mathrm{i}}{2\sqrt{2}}(I_\pm S_z - I_z S_\pm)$
		2	0	$\sqrt{\frac{3}{2}}(3\cos^2\theta-1)$	$\sqrt{\frac{1}{6}}(3I_zS_z - \boldsymbol{I}\cdot\boldsymbol{S})$
			±1	$\mp3\ \sin\theta\ \cos\theta\mathrm{e}^{\pm\mathrm{i}\phi}$	$\mp\frac{1}{2}(I_\pm S_z + I_z S_\pm)$
			±2	$\frac{3}{2}\sin^2\theta\mathrm{e}^{\pm\mathrm{i}2\phi}$	$\frac{1}{2}I_\pm S_\pm$
Q	$\frac{\mathrm{e}Q}{\hbar 6I(2I-1)}$	0	0	0	$\frac{1}{3}I(I+1)$
		1	0	0	$\frac{\mathrm{i}}{2}I_z$
			±1	0	$\pm\frac{\mathrm{i}}{2\sqrt{2}}(I_\pm I_z - I_z I_\pm)$
		2	0	$\sqrt{\frac{3}{2}}U_{33}$	$\sqrt{\frac{1}{6}}(3I_z^2 - I(I+1))$
			±1	$\mp\frac{1}{2}(U_{13}\pm\mathrm{i}U_{23})$	$\mp\frac{1}{2}(I_\pm I_z + I_z I_\pm)$
			±2	$\frac{1}{2}(U_{11}-U_{22}\pm\mathrm{i}2U_{12})$	$\frac{1}{2}I_\pm^2$

A given interaction (equations (2.40), (2.43), and (2.44) for CS, D, and Q, respectively) is expressed in terms of spherical components using equations (2.5), and (2.34) and the Hamiltonian is synthesized from equation (2.50). The following notation is used here: $(I, n)_k$; $k \equiv 1, 2, 3 \equiv x, y, z$; $(I, n)\pm = (I, n)_x \pm \mathrm{i}(I, n)_y$. See text for more details.

where $T_{lm}(\boldsymbol{U})$ and $T_{lm}(\boldsymbol{V})$ denote the irreducible tensors rising majestically out of their cartesian roots $\boldsymbol{U}$ and $\boldsymbol{V}$, respectively.

It is convenient to rewrite the above equation as

$$\mathcal{H}^{\lambda} = \omega_{\lambda} \sum_{l=0}^{2} (3-l) \sum_{m=l,l-1,..,l} (-)^{m} T_{l-m}(\boldsymbol{U}) T_{lm}(\boldsymbol{V}) \tag{2.50}$$

where λ denotes a given type of interaction and ω_{λ} its "*strength*".[1,2]

Using equations (2.5) and (2.34) in equation (2.50), a given type of interaction can be constructed in terms of spherical tensor components. As a demonstration, Table 2.1 provides the corresponding expressions for chemical shift, dipolar, and quadrupolar interactions.[1,2]

2.4 MATRIX ELEMENTS FOR SPHERICAL TENSORS

Different matrix normalizations are in use for the matrix representations of spherical tensors. Below, the matrix elements for spherical tensors T_{lm}; $l = 1, \ldots, 2I$; $m = 0, 1, \ldots, l$ are given for $I = 1$ and $I = \frac{3}{2}$ with the normalization typically used in NMR.[3,4] The matrices for negative order are obtained simply by[1–14]:

$$T_{l-m} = (-)^{m} T_{lm}^{\dagger} \tag{2.51}$$

2.4.1 $I = 1$

$$\begin{aligned}
T_{10} &= \begin{pmatrix} 1 & 0 & 0 \\ 0 & 0 & 0 \\ 0 & 0 & -1 \end{pmatrix} \\
T_{11} &= -\begin{pmatrix} 0 & 1 & 0 \\ 0 & 0 & 1 \\ 0 & 0 & 0 \end{pmatrix} \\
T_{20} &= \frac{1}{\sqrt{6}} \begin{pmatrix} 1 & 0 & 0 \\ 0 & -2 & 0 \\ 0 & 0 & 1 \end{pmatrix} \\
T_{21} &= \frac{1}{\sqrt{2}} \begin{pmatrix} 0 & -1 & 0 \\ 0 & 0 & 1 \\ 0 & 0 & 0 \end{pmatrix} \\
T_{22} &= \begin{pmatrix} 0 & 0 & 1 \\ 0 & 0 & 0 \\ 0 & 0 & 0 \end{pmatrix}
\end{aligned} \tag{2.52}$$

2.4.2 $I = \frac{3}{2}$

$$\begin{aligned}
T_{10} &= \frac{1}{2} \begin{pmatrix} 3 & 0 & 0 & 0 \\ 0 & 1 & 0 & 0 \\ 0 & 0 & -1 & 0 \\ 0 & 0 & 0 & -3 \end{pmatrix} \\
T_{11} &= -\sqrt{\frac{1}{2}} \begin{pmatrix} 0 & \sqrt{3} & 0 & 0 \\ 0 & 0 & 2 & 0 \\ 0 & 0 & 0 & \sqrt{3} \\ 0 & 0 & 0 & 0 \end{pmatrix} \\
T_{20} &= \sqrt{\frac{3}{2}} \begin{pmatrix} 1 & 0 & 0 & 0 \\ 0 & -1 & 0 & 0 \\ 0 & 0 & -1 & 0 \\ 0 & 0 & 0 & 1 \end{pmatrix} \\
T_{21} &= \sqrt{3} \begin{pmatrix} 0 & -1 & 0 & 0 \\ 0 & 0 & 0 & 0 \\ 0 & 0 & 0 & 1 \\ 0 & 0 & 0 & 0 \end{pmatrix} \\
T_{22} &= \sqrt{3} \begin{pmatrix} 0 & 0 & 1 & 0 \\ 0 & 0 & 0 & 1 \\ 0 & 0 & 0 & 0 \\ 0 & 0 & 0 & 0 \end{pmatrix} \\
T_{30} &= \frac{3}{2\sqrt{10}} \begin{pmatrix} 1 & 0 & 0 & 0 \\ 0 & -3 & 0 & 0 \\ 0 & 0 & 3 & 0 \\ 0 & 0 & 0 & -1 \end{pmatrix} \\
T_{31} &= -\frac{3}{\sqrt{10}} \begin{pmatrix} 0 & 1 & 0 & 0 \\ 0 & 0 & -\sqrt{3} & 0 \\ 0 & 0 & 0 & 1 \\ 0 & 0 & 0 & 0 \end{pmatrix} \\
T_{32} &= \frac{3}{2} \begin{pmatrix} 0 & 0 & 1 & 0 \\ 0 & 0 & 0 & -1 \\ 0 & 0 & 0 & 0 \\ 0 & 0 & 0 & 0 \end{pmatrix} \\
T_{33} &= -\frac{3}{\sqrt{2}} \begin{pmatrix} 0 & 0 & 0 & 1 \\ 0 & 0 & 0 & 0 \\ 0 & 0 & 0 & 0 \\ 0 & 0 & 0 & 0 \end{pmatrix}
\end{aligned} \tag{2.53}$$

REFERENCES

1. H. W. Spiess, Rotations of molecules and nuclear spin relaxation, in *NMR Basic Principles and Progress. Grundlagen und fortschritte*, eds P. Diehl, E. Fluck and R. Kosfeld, Springer-Verlag: Berlin, Heidelberg, New York, 1978, Vol. **15**, p. 55.
2. M. Mehring, *Principles of High Resolution NMR in Solids*, 2nd edn., Springer-Verlag: Berlin, Heidelberg, New York, 1983.
3. G. J. Bowden and W. D. Hutchison, *J. Magn. Reson.*, 1986, **67**, 403.
4. G. J. Bowden, W. D. Hutchison, and J. Khachan, *J. Magn. Reson.*, 1986, **67**, 415.
5. N. Müller, G. Bodenhausen, and R. R. Ernst, *J. Magn. Reson.*, 1987, **75**, 297.
6. G. Jaccard, S. Wimperis, and G. Bodenhausen, *J. Chem. Phys.*, 1985, **85**, 6282.
7. A. Jerschow, *J. Magn. Reson.*, 2005, **176**, 7.
8. A. Abragam, *Principles of Nuclear Magnetism*, Oxford University Press: London, 1961.
9. A. Jerschow, *Prog. NMR Spectrsc.*, 2005, **46**, 63.
10. M. E. Rose, *Elementary Theory of Angular Momentum*, John Wiley & Sons: New York, Chapman & Hall: London, 1957.
11. W.-K. Tung, *Group Theory in Physics*, World Scientific Publishing: Philadelphia, PA, 1985.
12. B. I. Silver, *Irreducible Tensor Methods'*, Academic Press: New York, 1976.
13. D. A. Varshalovich, A. N. Moskalev, and V. K. Khersonskii, *Quantum Theory of Angular Momentum*, World Scientific: Singapore, New Jersey, Hong Kong, 1988.
14. R. N. Zare, *Angular Momentum: Understanding Spatial Aspects in Chemistry and Physics'*, John Wiley & Sons, 1988.
15. M. Munowitz, *Coherence and NMR*, John Wiley & Sons, 1988.
16. M. Bak, J. T. Rasmussen, and N. C. Nielsen, *J. Magn. Reson.*, 2000, **147**, 296.

Chapter 3

Computation of Magnetic Resonance Parameters for Crystalline Systems: Principles

Jonathan R. Yates[1] and Chris J. Pickard[2]

[1]*TCM Group, Cavendish Laboratory, University of Cambridge, Cambridge CB3 OHE, UK*
[2]*School of Physics & Astronomy, University of St. Andrews, St. Andrews KY16 9SS, UK*

3.1	Introduction	29
3.2	Overview of the Planewave-Pseudopotential Approach	30
3.3	Shielding in a Periodic System	32
3.4	Other Magnetic Resonance Parameters	36
3.5	Examples	39
	References	40

3.1 INTRODUCTION

Magnetic resonance experiments of increasing sophistication probe the structure and dynamics of solid-state materials, for example, to determine the arrangement of atoms in a lattice, the packing of units in a molecular crystal, or the structure of a defect site. There is a clear need for quantitative theoretical support for these experiments, particularly to link the observed spectrum to the underlying microscopic structure. First-principles quantum-mechanical methods have the potential to provide this information. Indeed, traditional quantum-mechanical techniques have long been used to study isolated molecules and establish important links between structure and spectra. However, when one is interested in the magnetic response of extended systems, it is important to take into account the crystal nature of the material; attempts to extend quantum chemical approaches have been made, for example, by representing the effects of the crystal lattice through an arrangement of point charges, or by constructing an appropriately sized cluster of atoms or molecules. However, an alternative approach is to start from common material modeling techniques which exploit the translation symmetry inherent in crystals. The first of these was the use of the linear augmented plane wave (LAPW) approach to compute electric field gradients (EFGs). More recently, there has been a series of developments based on the planewave-pseudopotential technique and it is now possible to compute NMR chemical shifts and J-couplings, as well as electron paramagnetic resonance (EPR) $\boldsymbol{g}$-tensors and hyperfine couplings, for crystalline systems.

NMR Crystallography Edited by Robin K. Harris, Roderick E. Wasylishen and Melinda J. Duer © 2009 John Wiley & Sons, Ltd. ISBN: 978-0-470-69961-4

3.2 OVERVIEW OF THE PLANEWAVE-PSEUDOPOTENTIAL APPROACH

There are numerous first-principles methods applicable to either molecules or solid-state systems. The following section outlines the planewave-pseudopotential technique that has proved to be a useful platform for the prediction of solid-state magnetic resonance parameters. Further details can be found in the book by Martin[1] or in the review of Payne *et al.*[2]

3.2.1 Density Functional Theory

The behavior of a collection of electrons and nuclei can be predicted by solving the Schrödinger equation for the system:

$$\hat{H}\Psi = E\Psi \tag{3.1}$$

where the Hamiltonian describes the various electrostatic interactions between the particles. An important simplification can be made by noting that the mass of the nuclei is much greater than the electron mass. This leads to the Born–Oppenheimer approximation, in which the electronic and nuclear degrees of freedom can be separated. Even with this simplification, it is still impractical to solve equation (3.1) for anything other than the most trivial system. The difficulty lies in its many-body nature—the fact that the electronic degrees of freedom are coupled to each other.

The Kohn–Sham formulation of density functional theory (DFT) treats the electronic charge density ρ as the fundamental variable and exactly maps the many-body equation (3.1) onto a set of N equations involving single-particle wavefunctions,

$$-\frac{\hbar^2}{2m_e}\nabla^2\Psi(\boldsymbol{r}) + \upsilon_{\text{eff}}(\boldsymbol{r})\Psi(\boldsymbol{r}) = \varepsilon\Psi(\boldsymbol{r}) \tag{3.2}$$

where the Kohn–Sham potential, $\upsilon_{\text{eff}}(\boldsymbol{r})$ contains terms arising from the interaction with the ionic charges $V_{\text{ion}}(\boldsymbol{r})$, the Coulomb interaction energy of the charge density interacting with itself (known as the *Hartree energy*), and a potential V_{xc}, which describes the effects of exchange and correlation between the electrons:

$$\upsilon_{\text{eff}}(\boldsymbol{r}) = V_{\text{ion}}(\boldsymbol{r}) + \int \mathrm{d}\boldsymbol{r}'\frac{\rho(\boldsymbol{r}')}{|\boldsymbol{r}-\boldsymbol{r}'|} + V_{\text{xc}}[\rho(\boldsymbol{r})] \tag{3.3}$$

The set of independent particle equations (3.2) and (3.3) are amenable to computation, but at the price that the form of the potential V_{xc} is unknown. It is necessary to make physically motivated approximations in order to make progress. Fortunately, simple approximations have been shown to be adequate for many purposes. In solid-state studies, the most simple useful approximation is the local density approximation (LDA) in which the exchange-correlation energy at a given point is taken to be the same as in a uniform electron gas with the same charge density. For many properties, adding terms dependent on the gradient of the density (the generalized gradient approximation, GGA) provides an improvement. Numerous GGAs have been proposed; the one by Perdew, Burke, and Ernzerhof[3] (PBE) has been used for many solid-state NMR calculations. In quantum-chemical calculations based on localized orbital basis sets, it is common to use hybrid functionals, which include a proportion of Hartree–Fock exchange. In an extended basis, such as planewaves, hybrid functionals have a high computational cost. While hybrid functionals have been used to compute the ground-state structures of crystals, they have not yet been applied for the calculation of NMR chemical shifts in solids.

3.2.2 Bloch's Theorem

For any realistic crystal, the total number of electrons is vast. It is naturally desirable to exploit the translational symmetry of a crystalline material and consider only the crystallographic unit cell under periodic boundary conditions. That this is possible follows from Bloch's theorem:[a] As the potential has lattice periodicity (i.e., $\upsilon_{\text{eff}}(\boldsymbol{r}) = \upsilon_{\text{eff}}(\boldsymbol{r}+\boldsymbol{R})$ for all $\boldsymbol{R}$ where $\boldsymbol{R}$ is a lattice vector), then the eigenstates of the single-particle Hamiltonian can be written as

$$\Psi_{n,\boldsymbol{k}}(\boldsymbol{r}) = \mathrm{e}^{\mathrm{i}\boldsymbol{k}.\boldsymbol{r}}u_{n,\boldsymbol{k}}(\boldsymbol{r}) \tag{3.4}$$

where $u_{n,\boldsymbol{k}}$ is a function periodic in the unit cell such that $u_{n,\boldsymbol{k}}(\boldsymbol{r}) = u_{n,\boldsymbol{k}}(\boldsymbol{r}+\boldsymbol{R})$ for all lattice vectors $\boldsymbol{R}$. These Bloch states are labeled by their crystal momentum $\boldsymbol{k}$. The only unique values of $\boldsymbol{k}$ lie

[a]Named for Felix Bloch. This was result was derived by Bloch as part of his thesis work in 1928, long before his part in the history of NMR.

within the reciprocal unit cell, or equivalently and by convention, within the first Brillouin Zone (i.e., the Wigner–Seitz cell of the reciprocal lattice).

The problem of solving for an infinite number of electrons has become one of calculating for a finite number of bands at an infinite number of $\boldsymbol{k}$-points. However, physical properties are expected to smoothly vary with $\boldsymbol{k}$ and hence many integrals can be well approximated by a finite sampling of $\boldsymbol{k}$. A common scheme for Brillouin zone integration consists of the sets of regular integration grids introduced by Monkhorst and Pack.[4]

3.2.3 The Supercell Approximation

The application of periodic boundary conditions forces periodicity on the system studied. To address systems that do not have full three-dimensional translational symmetry—for example, in the study of disordered systems, defects, impurities, or the interaction of molecules and surfaces, the so-called supercell approximation can be used. Aperiodic systems are approximated by enclosing the region of interest in either bulk material (for a defect) or vacuum (for a molecule) and then periodically repeating this cell throughout space (Figure 3.1). The supercell must be large enough for the fictitious interactions between neighboring cells to be negligible.

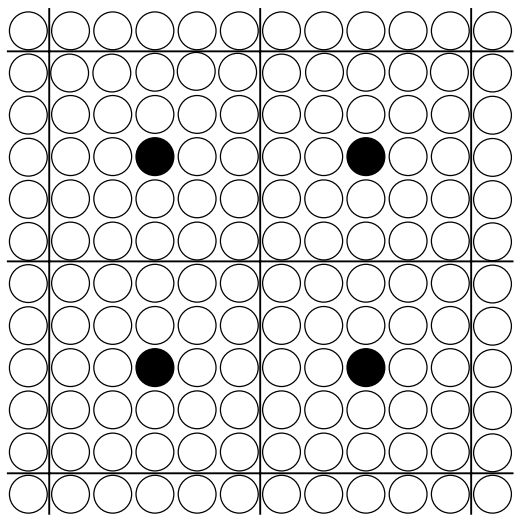


Figure 3.1. The supercell approximation: modeling a point defect within periodic boundary conditions.

3.2.4 The Planewave Basis Set

In order to solve the eigenvalue problem of equation (3.2) numerically, the eigenstates must be represented by some basis set. While there are many possible choices, the one made here is to use planewaves as the basis. There are many advantages in the use of planewaves: they form a mathematically simple basis, they naturally incorporate periodic boundary conditions, and, perhaps most importantly, planewave calculations can be taken systematically to convergence as a function of the size of the basis. The Kohn–Sham eigenstates are expressed as

$$\Psi_{n,\boldsymbol{k}}(\boldsymbol{r}) = \sum_{\boldsymbol{G}} c_{n,\boldsymbol{k}}(\boldsymbol{G}) \mathrm{e}^{\mathrm{i}(\boldsymbol{k}+\boldsymbol{G})\cdot\boldsymbol{r}} \tag{3.5}$$

where the sum is over all reciprocal lattice vectors $\boldsymbol{G}$. $c_{n,\boldsymbol{k}}(\boldsymbol{G})$ are the coefficients to be determined in solving equation (3.2). To truncate the basis set, the sum is limited to a set of reciprocal lattice vectors contained within a sphere with a radius defined by the cutoff energy, E_{cut}:

$$\frac{\hbar^2|\boldsymbol{k}+\boldsymbol{G}|^2}{2m} \leq E_{\mathrm{cut}} \tag{3.6}$$

Hence, the basis set is defined by the maximum kinetic energy component it contains. Physical quantities can be converged systematically by increasing E_{cut}. A fast-fourier transform (FFT) can be used to change the representation of the eigenstates from a sum of Fourier components to a uniform grid of points in the real-space unit cell. The use of numerically efficient FFTs is one key to the success of the planewave-pseudopotential formalism—it allows individual operations to be performed in the most efficient basis, e.g., the kinetic energy operator in Fourier space, and a local potential in real space.

3.2.5 The Pseudopotential Approximation

The electrons in an atom can be divided into two types—core electrons and valence electrons. The core electrons are tightly bound to the nucleus, while the valence electrons are more extended. A working definition for core electrons is that they are the

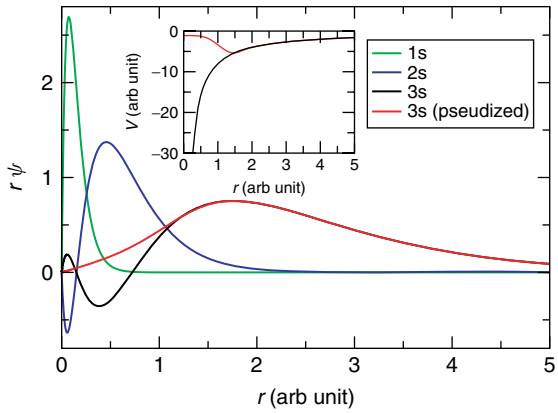


Figure 3.2. Si atomic orbitals: all-electron 1s, 2s, and 3s and the 3s pseudized orbital. Inset: all-electron potential and the corresponding potential felt by the pseudized 3s state.

ones that play no part in the interactions between atoms, while the valence electrons dictate most of the properties of the material. It is common to make the frozen core approximation; the core electrons are constrained not to differ from their free atomic nature when placed in the solid-state environment. This reduces the number of electronic degrees of freedom in an all-electron calculation. It is a very good approximation. A different, but physically related, approach is taken in the pseudopotential approximation. Since, in an all-electron calculation, the valence electron wavefunctions must be orthogonal to the core wavefunctions they necessarily have strong oscillations in the region near the nucleus (see the all-electron wavefunction in Figure 3.2). Given that a planewave basis set is to be used to describe the wavefunctions, these strong oscillations are undesirable—requiring many planewaves for an accurate description. Further, these oscillations are of very little consequence for the electronic structure in the solid, since they occur close to the nucleus. In the pseudopotential approach, only the valence electrons are explicitly considered, the effects of the core electrons being integrated within a new ionic potential. The valence wavefunctions need no longer be orthogonal to the core states, and so the orthogonality oscillations disappear; hence, far fewer planewaves are required to describe the valence wavefunctions. Numerous schemes to produce optimally soft pseudopotentials have been developed. Common choices are the norm-conserving potentials due to Troullier and Martins[5] and Vanderbilt's ultrasoft scheme.[6]

3.3 SHIELDING IN A PERIODIC SYSTEM

When a sample of matter is placed in a uniform external magnetic field electronic currents flow throughout the material. For an insulating nonmagnetic material, only the orbital motion of the electrons contribute to this current. The current density $\boldsymbol{j}(\boldsymbol{r})$, produces a nonuniform induced magnetic field in the material, which is given by the Biot–Savart law as

$$\boldsymbol{B}_{\text{in}}(\boldsymbol{r}) = \frac{\mu_0}{4\pi}\int \mathrm{d}^3 r' \boldsymbol{j}(\boldsymbol{r}') \times \frac{\boldsymbol{r}-\boldsymbol{r}'}{|\boldsymbol{r}-\boldsymbol{r}'|^3} \tag{3.7}$$

(note that we have used SI units throughout this article, which accounts for the different constants in these equations as compared to those in the original papers). The magnetic shielding tensor is defined as the ratio between this induced field and the external applied field

$$\boldsymbol{B}_{\text{in}}(\boldsymbol{r}) = -\boldsymbol{\sigma}(\boldsymbol{r})\boldsymbol{B}_{\text{ext}} \tag{3.8}$$

It is clear that the question of computing the shielding tensor is that of computing the induced electronic current. As the magnetic fields used in NMR experiments are small (in the sense that the corresponding Zeeman energy is a small term in the Hamiltonian), we can compute the induced current within perturbation theory, keeping quantities to linear order in the external field (we represent such linear quantities by a superscript (1)). To linear order, the current is given by

$$\begin{aligned}\boldsymbol{j}^{(1)}(\boldsymbol{r}') = 2\sum_{\text{o}} \big[&\langle \Psi_{\text{o}}^{(0)}|\boldsymbol{J}^{\text{p}}(\boldsymbol{r}')|\Psi_{\text{o}}^{(1)}\rangle \\ &+\langle \Psi_{\text{o}}^{(1)}|\boldsymbol{J}^{\text{p}}(\boldsymbol{r}')|\Psi_{\text{o}}^{(0)}\rangle\big] \\ &+ 2\sum_{\text{o}} \langle \Psi_{\text{o}}^{(0)}|\boldsymbol{J}^{\text{d}}(\boldsymbol{r}')|\Psi_{\text{o}}^{(0)}\rangle\end{aligned} \tag{3.9}$$

where the summation is over all occupied orbitals, the factor of 2 accounts for spin degeneracy and the current operator, $\boldsymbol{J}(\boldsymbol{r}')$, has been written as the sum of diamagnetic and paramagnetic terms,

$$\boldsymbol{J}(\boldsymbol{r}') = \boldsymbol{J}^{\text{d}}(\boldsymbol{r}') + \boldsymbol{J}^{\text{p}}(\boldsymbol{r}') \tag{3.10}$$

$$\boldsymbol{J}^{\text{d}}(\boldsymbol{r}') = \frac{e^2}{m_{\text{e}}}\boldsymbol{A}(\boldsymbol{r}')|\boldsymbol{r}'\rangle\langle\boldsymbol{r}'| \tag{3.11}$$

$$\boldsymbol{J}^{\text{p}}(\boldsymbol{r}') = -\frac{e}{2m_{\text{e}}}\boldsymbol{p}|\boldsymbol{r}'\rangle\langle\boldsymbol{r}'| + |\boldsymbol{r}'\rangle\langle\boldsymbol{r}'|\boldsymbol{p} \tag{3.12}$$

Within perturbation theory, $|\Psi_o^{(1)}\rangle$ is given by

$$|\Psi_o^{(1)}\rangle = \sum_e \frac{|\Psi_e^{(0)}\rangle\langle\Psi_e^{(0)}|}{\varepsilon - \varepsilon_e} H^{(1)}|\Psi_o^{(0)}\rangle = \mathcal{G}(\varepsilon_o^{(0)}) H^{(1)}|\Psi_o^{(0)}\rangle \quad (3.13)$$

where the Green function $\mathcal{G}(\varepsilon_o^{(0)})$ has been introduced. Using the symmetric gauge for the vector potential, $\boldsymbol{A}(\boldsymbol{r}) = 1/2\boldsymbol{B} \times \boldsymbol{r}$, the linear-order Hamiltonian is given by $H^{(1)} = e/m_e \boldsymbol{A} \cdot \boldsymbol{p}$ and we arrive at the following expression for the induced current,

$$\boldsymbol{j}^{(1)}(\boldsymbol{r}') = \frac{4e}{m_e} \sum_o \mathrm{Re} \left[\langle\Psi_o^{(0)}|\boldsymbol{J}^p(\boldsymbol{r}')\mathcal{G}(\varepsilon_o^{(0)})\boldsymbol{r}\boldsymbol{p}|\Psi_o^{(0)}\rangle\right] \cdot \boldsymbol{B} - \frac{e^2}{2m_e}\rho(\boldsymbol{r}')\boldsymbol{B} \times \boldsymbol{r}' \quad (3.14)$$

where $\rho(\boldsymbol{r}') = 2\sum_o \langle\Psi_o^{(0)}|\boldsymbol{r}'\rangle\langle\boldsymbol{r}'|\Psi_o^{(0)}\rangle$ is the ground-state charge density. So far, no distinction between finite and extended systems has been made. In the following sections, the conceptual and practical difficulties in applying equation (3.14) to extended systems are discussed.

3.3.1 The Position Operator Problem

For a finite system there is, in principle, no problem in computing the induced current directly from equation (3.14). However, for an extended system, there is an obvious problem with the second (diamagnetic) term of equation (3.14); the presence of the position operator, $\boldsymbol{r}$, will generate a large contribution far away from $\boldsymbol{r} = 0$, and the term will diverge in an infinite system. The situation is saved by recognizing that an equal but opposite divergence occurs in the first (paramagnetic) term of equation (3.14), and so only the sum of the two terms is well defined. Through the use of a sum rule, we arrive at an alternative expression for the current

$$\boldsymbol{j}^{(1)}(\boldsymbol{r}') = \frac{4e}{m_e} \sum_o \mathrm{Re} \left[\langle\Psi_o^{(0)}|\boldsymbol{J}^p(\boldsymbol{r}')\mathcal{G}(\varepsilon_o^{(0)})(\boldsymbol{r} - \boldsymbol{r}')\boldsymbol{p}|\Psi_o^{(0)}\rangle\right] \cdot \boldsymbol{B} \quad (3.15)$$

In an insulator the Green function $\mathcal{G}(\varepsilon_o^{(0)})$ is localized and so $\boldsymbol{j}^{(1)}(\boldsymbol{r}')$ remains finite at large values of $(\boldsymbol{r} - \boldsymbol{r}')$.

At this point, there still remains the question of the practical computation of the current, which for reasons of efficiency, it is desirable to work with just the part of the Bloch function, which is periodic in the unit cell ($u_{n,\boldsymbol{k}}$ in equation (3.4)). Equation (3.15) is not suitable for such a calculation as the position operator does not have the periodicity of the unit cell. One solution to this problem is to consider the response to a magnetic field with a finite wavelength, q. In the limit that $q \to 0$, the uniform field result is recovered. For a practical calculation, this enables one to work with the $u_{n,\boldsymbol{k}}$, at the cost that a calculation at a point in the Brillouin Zone $\boldsymbol{k}$ will require knowledge of the wavefunctions at $\boldsymbol{k} \pm \boldsymbol{q}$ (i.e., six extra calculations for the full tensor). A complete derivation was presented in Refs. 7, 8 leading to the final result for the current,

$$\boldsymbol{j}^{(1)}(\boldsymbol{r}') = \lim_{q\to 0} \frac{1}{2q}\left[\boldsymbol{S}(\boldsymbol{r}', q) - \boldsymbol{S}(\boldsymbol{r}', -q)\right] \quad (3.16)$$

where

$$\boldsymbol{S}(\boldsymbol{r}', q) = \frac{2e}{m_e N_k} \sum_{i=x,y,z} \sum_{o,\boldsymbol{k}} \mathrm{Re}\left[\frac{1}{i} \times \langle u_{o,\boldsymbol{k}}^{(0)}|\boldsymbol{J}^p_{\boldsymbol{k},\boldsymbol{k}+\boldsymbol{q}_i}(\boldsymbol{r}')\mathcal{G}_{\boldsymbol{k}+\boldsymbol{q}_i}(\varepsilon_{o,\boldsymbol{k}})\boldsymbol{B} \times \hat{\boldsymbol{u}}_i \cdot (\boldsymbol{p} + \boldsymbol{k})|u_{o,\boldsymbol{k}}^{(0)}\rangle\right] \quad (3.17)$$

$\boldsymbol{q}_i = q\hat{\boldsymbol{u}}_i$, N_k is the number of $\boldsymbol{k}$-points included in the summation and

$$\boldsymbol{J}^p_{\boldsymbol{k},\boldsymbol{k}+\boldsymbol{q}_i} = -\frac{e}{2m_e}(\boldsymbol{p} + \boldsymbol{k})|\boldsymbol{r}'\rangle\langle\boldsymbol{r}'| + |\boldsymbol{r}'\rangle\langle\boldsymbol{r}'|(\boldsymbol{p} + \boldsymbol{k} + \boldsymbol{q}_i) \quad (3.18)$$

An alternative solution to this problem was developed by Sebastiani.[9] Rather than compute the magnetic response using extended Bloch functions, a transformation to Wannier orbitals is made. As Wannier orbitals can be chosen to be well localized around a particular lattice site, it is then possible to apply equation (3.15) directly, using a position operator in the form of a saw-tooth function.

When a planewave basis set is used, $\boldsymbol{j}^{(1)}(\boldsymbol{r}')$ will be obtained on the points of the FFT grid. In general, these will not coincide with the positions of the nuclei, and so to compute the induced field, $\boldsymbol{B}^{(1)}(\boldsymbol{R})$, equation (3.7) and $\boldsymbol{j}^{(1)}(\boldsymbol{r}')$ are Fourier transformed into reciprocal space. The induced magnetic field can then be simply evaluated as

$$\boldsymbol{B}^{(1)}(\boldsymbol{G}) = \mu_0 \frac{i\boldsymbol{G} \times \boldsymbol{j}^{(1)}(\boldsymbol{G})}{G^2} \quad (3.19)$$

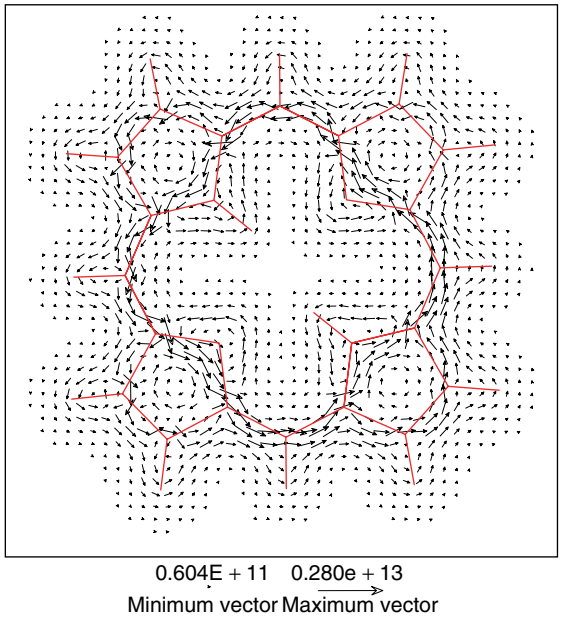


Figure 3.3. Current flow in porphyrin. Height above molecular plane is 0.53 (Bohr). Vectors are scaled such that minimum: 0.6 × 10^{11}nA T^{-1}Bohr^{-2}, maximum: 0.3 × 10^{13}nA T^{-1}Bohr^{-2}.

where $\boldsymbol{G}$ is a reciprocal lattice vector. $\boldsymbol{B}^{(1)}(\boldsymbol{R})$ is subsequently obtained by a explicit Fourier transform at the nuclear positions $\boldsymbol{R}$

$$\boldsymbol{B}^{(1)}(\boldsymbol{R}) = \sum_{\boldsymbol{G}} \mathrm{e}^{\mathrm{i}\boldsymbol{G}\cdot\boldsymbol{R}} \boldsymbol{B}^{(1)}(\boldsymbol{G}) \tag{3.20}$$

The computational work in evaluating this Fourier transform is very much smaller than that needed to obtain $\boldsymbol{j}^{(1)}(\boldsymbol{r}')$. As such, the cost of obtaining the shielding at a single atomic site is essentially identical to evaluating it at all atomic sites. Taking this further, it is also straightforward to obtain the shielding on an arbitrary set of points—the so-called nucleus independent chemical shift (NICS) or to make a map of the flow of the induced current; see Figure 3.3.

For $\boldsymbol{G} = 0$, equation (3.19) cannot be applied. Indeed the $\boldsymbol{G} = 0$ component of the induced magnetic field is not a bulk property;[10] rather it is determined by the induced currents on the surface of the sample. In particular, its value depends on the shape of the sample, and is determined by macroscopic magnetostatics. In order to compare with results from MAS experiments, a spherical sample should be assumed for which

$$\boldsymbol{B}^{(1)}(\boldsymbol{G} = \boldsymbol{0}) = \frac{2\mu_0}{3}\boldsymbol{\chi}\boldsymbol{B} \tag{3.21}$$

where $\boldsymbol{\chi}$ is the macroscopic magnetic susceptibility. $\boldsymbol{\chi}$ is directly provided by first-principles calculation, and can be used to adjust the shieldings for arbitrary sample shapes, should this be required.

Finally, we note that experiments typically measure the change in shielding relative to a reference standard—the chemical shift δ. The conversion is straightforward

$$\delta = -[\sigma - \sigma_{\mathrm{ref}}^{\mathrm{iso}}] \tag{3.22}$$

The shielding of the reference standard, $\sigma_{\mathrm{ref}}^{\mathrm{iso}}$, could be obtained by performing a calculation on the standard compound itself, but this is often not convenient—for example, if the reference is a liquid or solution. For this reason, most studies have obtained $\sigma_{\mathrm{ref}}^{\mathrm{iso}}$ as the intercept of a line of unit gradient fitted to a graph of calculated shieldings against experimental shifts.

3.3.2 Core States and Pseudopotentials

In the planewave-pseudopotential approach, it is implicit that the core electrons can be treated separately from the valence states in an atomic code. Historically, the validity of the frozen core approximation for NMR properties had been doubted, but a careful study by Gregor, Mauri, and Car[11] showed that, if the core and valence states are partitioned in a gauge-invariant way, the shielding of the core electrons is chemically insensitive. The contribution of the core electrons to chemical shifts can hence be neglected. If absolute shieldings are required, the core contribution is most conveniently calculated by setting the gauge origin at the atomic center, so that the tensor shielding is purely diamagnetic and given by the Lamb formula,

$$\sigma_{\alpha\beta} = \delta_{\alpha\beta}\frac{\mu_0 e^2}{4\pi m_{\mathrm{e}}}\int \mathrm{d}^3 r \frac{n(\boldsymbol{r})}{r} \tag{3.23}$$

where α and β are Cartesian coordinates and δ is the Kronecker delta As shown in Figure 3.2, the use of pseudopotentials implies a nonphysical form for the wavefunction in the region close to the nucleus. For this reason, a formalism based on pseudopotentials might appear a poor choice for the calculation of *nuclear* magnetic resonance parameters. The upper part of Figure 3.4 shows shieldings computed

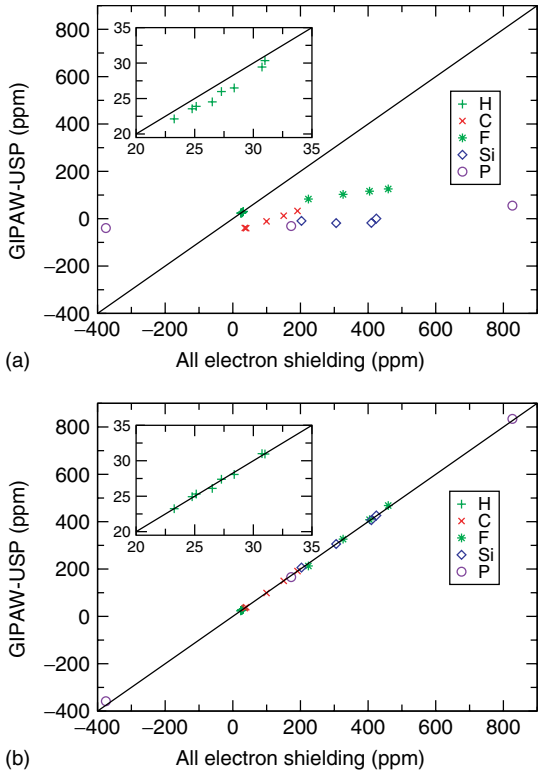


Figure 3.4. Isotropic magnetic shielding for nuclear sites in a range of molecules. The graphs show shieldings obtained by the GIPAW method and ultrasoft pseudopotentials plotted against all-electron shielding. The straight line represents perfect agreement. The upper figure (a) shows the contribution without GIPAW augmentation, the lower figure (b) plots the total contribution. (Reproduced from Ref. 13. © American Physical Society, 2007.)

for a range of isolated molecules by using only the pseudowavefunctions (i.e., neglecting the fact that the pseudowavefunction differs from the true all-electron wavefunction close to the nucleus), and the corresponding large basis set quantum-chemical calculations. For proton shieldings, the agreement is reasonable. For ^{13}C, the pseudopotential results reproduce the general trend of the all-electron shieldings although the slope is somewhat less than unity. Uncorrected pseudopotential calculations for proton and first row elements have been presented (see e.g., Ref. 12); the agreement can be improved by using rather hard pseudopotentials (i.e., a small matching radius). For the second row elements, Si and P, Figure 3.4 shows the impact of the pseudopotential approximation to be dramatic with almost all of the chemical sensitivity lost. In order to make direct comparison to experiment, it is therefore vital to correctly account for the use of pseudopotentials and to obtain shieldings with the accuracy of all-electron calculations.

The basis for such an approach was provided by projector augmented wave (PAW) method introduced by van de Walle and Blöchl.[14] In this scheme, a linear transformation $\mathcal{T}$ maps the valence pseudo wavefunctions $|\tilde{\Psi}\rangle$ onto the corresponding all-electron wavefunctions, $|\Psi\rangle = \mathcal{T}\,|\tilde{\Psi}\rangle$,

$$\mathcal{T} = \mathbf{1} + \sum_{\boldsymbol{R},n} [|\phi_{\boldsymbol{R},n}\rangle - |\tilde{\phi}_{\boldsymbol{R},n}\rangle]\langle\tilde{p}_{\boldsymbol{R},n}| \qquad (3.24)$$

$|\phi_{\boldsymbol{R},n}\rangle$ are all-electron atomiclike states obtained from a calculation on an isolated atom and $|\tilde{\phi}_{\boldsymbol{R},n}\rangle$ are the corresponding pseudized states. $\langle\tilde{p}_{\boldsymbol{R},n}|$ are a set of projectors such that $\langle\tilde{p}_{\boldsymbol{R},n}|\tilde{\phi}_{\boldsymbol{R}',m}\rangle = \delta_{\boldsymbol{R},\boldsymbol{R}'}\delta_{n,m}$. $\boldsymbol{R}$ labels the atomic site and n is a composite index that accounts for the angular momentum and the number of projectors. In simple terms, the PAW transformation works by computing the component of a certain atomic-like state (say 2p) in a pseudowavefunction, and replacing the pseudized component by its all-electron form. This may seem like a rather approximate procedure, but because the atomic states form a good basis for the wavefunction in the region close to the nucleus, it can be made highly accurate by using multiple projectors.

Within the PAW scheme, for an all-electron local or semilocal operator O, the corresponding pseudo-operator, $\widetilde{O}$, is given by

$$\widetilde{O} = O + \sum_{\boldsymbol{R},n,m} |\tilde{p}_{\boldsymbol{R},n}\rangle\big[\langle\phi_{\boldsymbol{R},n}|O|\phi_{\boldsymbol{R},m}\rangle - \langle\tilde{\phi}_{\boldsymbol{R},n}|O|\tilde{\phi}_{\boldsymbol{R},m}\rangle\big]\langle\tilde{p}_{\boldsymbol{R},m}| \qquad (3.25)$$

As constructed in equation (3.25), the pseudooperator $\widetilde{O}$ acting on pseudowavefunctions will give the same matrix elements as the all-electron operator O acting on all-electron wavefunctions.

For a system under a uniform magnetic field, PAW alone is not a computationally realistic solution. In using a set of localized functions, the gauge-origin problem, well known in quantum chemical approaches, has been introduced. In short, equation (3.25) will require an infinitely large number of projectors in order for the computed shieldings to be translationally invariant (i.e., independent of the choice of gauge origin). To address this problem, Pickard and Mauri[8] introduced a field-dependent transformation operator

$\mathcal{T}_{\boldsymbol{B}}$, which, by construction, imposes the translational invariance exactly:

$$\mathcal{T}_{\boldsymbol{B}} = \mathbf{1} + \sum_{\boldsymbol{R},n} \mathrm{e}^{\frac{\mathrm{i}e}{2\hbar}\boldsymbol{r}\cdot\boldsymbol{R}\times\boldsymbol{B}}[|\phi_{\boldsymbol{R},n}\rangle - |\tilde{\phi}_{\boldsymbol{R},n}\rangle]\langle\tilde{p}_{\boldsymbol{R},n}|\,\mathrm{e}^{-\frac{\mathrm{i}e}{2\hbar}\boldsymbol{r}\cdot\boldsymbol{R}\times\boldsymbol{B}} \quad (3.26)$$

The resulting approach is known as the *gauge including projector augmented wave* (GIPAW) method. Although originally formulated for norm-conserving pseudopotentials, the extension to the more computationally efficient ultrasoft pseudopotentials has been presented by Yates *et al.*[13] Figure 3.4 shows shieldings computed using ultrasoft pseudopotentials and the GIPAW scheme, together with large basis set quantum-chemical calculations. For the shieldings in these isolated molecules, the agreement is essentially perfect. For crystalline systems, validation of the technique comes only from comparison to NMR experiments; numerous studies have been made in recent years, just two are mentioned in section "Examples".

3.4 OTHER MAGNETIC RESONANCE PARAMETERS

3.4.1 Electric Field Gradient

For a quadrupolar nucleus (spin $I > 1/2$), the observed NMR response includes an interaction between the quadrupole moment of the nucleus (Q), and the electric field gradient (EFG) generated by its surroundings. The EFG is a second rank, symmetric, traceless tensor $V(\boldsymbol{r})$ given by

$$V_{\alpha\beta}(\boldsymbol{r}) = \frac{\partial E_\alpha(\boldsymbol{r})}{\partial r_\beta} - \frac{1}{3}\delta_{\alpha\beta}\sum_\gamma \frac{\partial E_\gamma(\boldsymbol{r})}{\partial r_\gamma} \quad (3.27)$$

where α,β,γ denote the Cartesian coordinates x,y,z and $E_\alpha(\boldsymbol{r})$ is the local electric field at the position $\boldsymbol{r}$, which can be calculated from the charge density $n(\boldsymbol{r})$:

$$E_\alpha(\boldsymbol{r}) = \int \mathrm{d}^3 r \frac{n(\boldsymbol{r})}{|\boldsymbol{r}-\boldsymbol{r}'|^3}(r_\alpha - r'_\alpha) \quad (3.28)$$

The EFG tensor is then equal to

$$V_{\alpha\beta}(\boldsymbol{r}) = \int \mathrm{d}^3 r \frac{n(\boldsymbol{r})}{|\boldsymbol{r}-\boldsymbol{r}'|^3}\left[\delta_{\alpha\beta} - 3\frac{(r_\alpha - r'_\alpha)(r_\beta - r'_\beta)}{|\boldsymbol{r}-\boldsymbol{r}'|^2}\right] \quad (3.29)$$

To compute the EFG tensor in a periodic system is less demanding than calculating either the shielding or indirect coupling tensors, as it requires only knowledge of the ground-state charge density, ground-state wavefunctions and the position of the ions in the unit cell—no linear response calculation is required.

The quadrupolar coupling constant, C_Q and the asymmetry parameter, η_Q can be obtained from the diagonalized electric field gradient tensor whose eigenvalues are labeled V_{XX}, V_{YY}, V_{ZZ}, such that $|V_{ZZ}|>|V_{XX}|>|V_{YY}|$:

$$C_Q = \frac{eV_{ZZ}Q}{h} \quad (3.30)$$

and

$$\eta_Q = \frac{V_{YY} - V_{XX}}{V_{ZZ}} \quad (3.31)$$

Within the planewave-pseudopotential approach, the charge density is expressed as the sum of three terms,[15] and there are correspondingly three distinct contributions to the EFG. First, there is a contribution arising from the ionic charges (sum of the nuclear and core-electron charge). From the site under consideration, this appears as an infinite lattice of point charges whose EFG contribution can be obtained using an Ewald summation. Secondly, there is the contribution of the pseudized valence charge density, which is evaluated by using a reciprocal space form of equation (3.29). Finally, there is a PAW contribution to account for the difference between the pseudo and all-electron charge densities on the atomic site under consideration.

3.4.2 Indirect Coupling

The indirect (or J) coupling manifests itself in splittings of the NMR resonance, or as a modulation of the spin-echo signal. Physically, the coupling arises from the interaction of two nuclei, K and L, with magnetic moments, μ_K and μ_L, mediated by the electrons in the system. The first complete analysis of this indirect coupling was provided by Ramsey[16,17] who showed that the J-coupling tensor, $\boldsymbol{J}_{KL}$, is obtained from the magnetic field induced at nucleus K due to the perturbative effect of nucleus L,

$$\boldsymbol{B}^{(1)}_{\mathrm{in}}(\boldsymbol{R}_K) = \frac{\hbar\gamma_K\gamma_L}{2\pi}\boldsymbol{J}_{KL}\cdot\boldsymbol{\mu}_L \quad (3.32)$$

where γ_K and γ_L are the gyromagnetic ratios of nuclei K and L. At the nonrelativistic level, two

distinct mechanisms contribute to $\boldsymbol{B}_{\text{in}}^{(1)}(\boldsymbol{R}_K)$. First, the nuclei interact via the electronic charge; the nucleus L induces an orbital current $\boldsymbol{j}^{(1)}(\boldsymbol{r})$ which, in turn, creates a magnetic field at nucleus K. The nuclei also interact via the electronic spin; the nucleus L inducing a polarization of the electronic spin, $\boldsymbol{m}^{(1)}(\boldsymbol{r})$, which also contributes to the magnetic field at nucleus K. $\boldsymbol{B}_{\text{in}}^{(1)}(\boldsymbol{R}_K)$ is given by

$$\begin{aligned}\boldsymbol{B}_{\text{in}}^{(1)}(\boldsymbol{R}_K) = &\frac{\mu_0}{4\pi}\int \boldsymbol{m}^{(1)}(\boldsymbol{r})\cdot\left[\frac{3\boldsymbol{r}_K\boldsymbol{r}_K - |\boldsymbol{r}_K|^2}{|\boldsymbol{r}_K|^5}\right]\mathrm{d}^3\boldsymbol{r}\\ &+\frac{\mu_0}{4\pi}\frac{8\pi}{3}\int \boldsymbol{m}^{(1)}(\boldsymbol{r})\delta(\boldsymbol{r}_K)\,\mathrm{d}^3\boldsymbol{r}\\ &+\frac{\mu_0}{4\pi}\int \boldsymbol{j}^{(1)}(\boldsymbol{r})\times\frac{\boldsymbol{r}_K}{|\boldsymbol{r}_K|^3}\,\mathrm{d}^3\boldsymbol{r}\end{aligned} \tag{3.33}$$

$\boldsymbol{r}_N = \boldsymbol{r} - \boldsymbol{R}_N$ with $\boldsymbol{R}_N$ the position of nucleus N; δ is the Dirac delta function.

The induced current can be computed using the equivalent expression for the shielding, equation (3.14), but using a vector potential of the form $\boldsymbol{A}(\boldsymbol{r}) = \frac{\mu_0}{4\pi}\frac{\boldsymbol{\mu}_L\times\boldsymbol{r}_L}{|\boldsymbol{r}_L|^3}$. $\boldsymbol{m}^{(1)}(\boldsymbol{r})$ can also be computed through perturbation theory,

$$\boldsymbol{m}^{(1)}(\boldsymbol{r}) = g\beta\left[\boldsymbol{n}_{\uparrow}^{(1)}(\boldsymbol{r}) - \boldsymbol{n}_{\downarrow}^{(1)}(\boldsymbol{r})\right] = 2g\beta\boldsymbol{n}_{\uparrow}^{(1)}(\boldsymbol{r}) \tag{3.34}$$

with g the Lande g-factor and β the Bohr magneton. $\boldsymbol{n}_{\uparrow}^{(1)}(\boldsymbol{r})$ ($\boldsymbol{n}_{\downarrow}^{(1)}(\boldsymbol{r})$) is the spin up (down) charge density given by $\boldsymbol{n}_{\uparrow}^{(1)}(\boldsymbol{r}) = 2\sum_{\text{o}} Re[\langle\Psi^{(0)}|\boldsymbol{r}\rangle\langle\boldsymbol{r}|\Psi_{\text{o}}^{(1)}\rangle]$. $|\Psi_{\text{o}}^{(1)}\rangle$ is given by

$$\begin{aligned}|\Psi_{\text{o}}^{(1)}\rangle &= \sum_{\text{e}}\frac{|\Psi_{\text{e}}^{(0)}\rangle\langle\Psi_{\text{e}}^{(0)}|}{\varepsilon-\varepsilon_{\text{e}}}H_{\text{M}}^{(1)}|\Psi_{\text{o}}^{(0)}\rangle\\ &= \mathcal{G}(\varepsilon_{\text{o}}^{(0)})H_{\text{M}}^{(1)}|\Psi_{\text{o}}^{(0)}\rangle\end{aligned} \tag{3.35}$$

with the first-order Hamiltonian given by the well-known Fermi-contact (FC) and spin-dipolar (SD) terms

$$H_{\text{M}}^{(1)} = H_{\text{FC}} + H_{\text{SD}} \tag{3.36}$$

$$H_{\text{FC}} = g\beta\frac{\mu_0}{4\pi}\frac{8\pi}{3}\boldsymbol{S}\cdot\boldsymbol{\mu}_L\delta(\boldsymbol{r}_L) \tag{3.37}$$

$$H_{\text{SD}} = g\beta\frac{\mu_0}{4\pi}\boldsymbol{S}\cdot\left(\frac{3\boldsymbol{r}_L(\boldsymbol{\mu}_L\cdot\boldsymbol{r}_L) - r_L^2\boldsymbol{\mu}_L\mathbf{1}}{|r_L|^5}\right) \tag{3.38}$$

where $\boldsymbol{S}$ is the Pauli spin operator and $\mathbf{1}$ the identity matrix. For analysis, it is common to divide the total J-coupling tensor into five components, although only the total tensor can be observed experimentally

$$\begin{aligned}\boldsymbol{J}_{KL} = &\boldsymbol{J}_{KL}^{\text{DSO}} + \boldsymbol{J}_{KL}^{\text{PSO}} + \boldsymbol{J}_{KL}^{\text{FC}}\\ &+\boldsymbol{J}_{KL}^{\text{SD}} + \boldsymbol{J}_{KL}^{\text{SD/FC}}\end{aligned} \tag{3.39}$$

DSO and PSO refer, respectively, to the diamagnetic and paramagnetic-induced current response. The first four terms arise from symmetric interactions, with the same coupling mechanism at the perturbing and receiving sites. The term $\boldsymbol{J}_{KL}^{\text{SD/FC}}$ is a cross term between the SD and FC interactions, which contributes only to the anisotropic part of $\boldsymbol{J}_{KL}$.

Joyce *et al.*[18] developed a technique to compute J-coupling tensors for solid-state systems using the planewave-pseudopotential formalism. PAW is used to provide all-electron accuracy; it is a strict test of the theory because the wavefunction reconstruction must be performed at both the perturbing and receiving nuclei.

Unlike the case of nuclear shielding, even for a truly periodic system, the J-coupling perturbation breaks the translational symmetry of the crystal, and a simulation supercell of sufficient size to inhibit the interaction of periodically repeated images of the perturbing site must be chosen. Often, the primitive crystallographic cell is large enough to give converged results; however, in some cases, it is necessary to consider a larger simulation cell containing two or more primitive cells. Initial results are promising; Table 3.1 shows computed and experimental ^{29}Si and ^{31}P NMR parameters for the silicophosphate

Table 3.1. Calculated NMR chemical shifts and J-coupling for the silicophosphate $Si_5O(PO_4)_6$. The experimental values are in brackets. (Calculasions from Ref. 18, experiment from Ref. 19)

Coupling	^{31}P (ppm)	^{29}Si (ppm)	$J^2_{\text{P-O-Si}}$ (Hz)
$J^2_{\text{P-O}_3\text{-Si}_1}$	−47.4 (−43.8)	−214.8 (−213.3)	−17.12 (15 ± 2)
$J^2_{\text{P-O}_2\text{-Si}_2}$		−218.7 (−217.0)	−16.26 (14 ± 2)
$J^2_{\text{P-O}_5\text{-Si}_2}$		−218.7 (−217.0)	−1.17 (4 ± 2)
$J^2_{\text{P-O}_4\text{-Si}_3}$		−128.6 (−119.1)	−14.13 (12 ± 2)

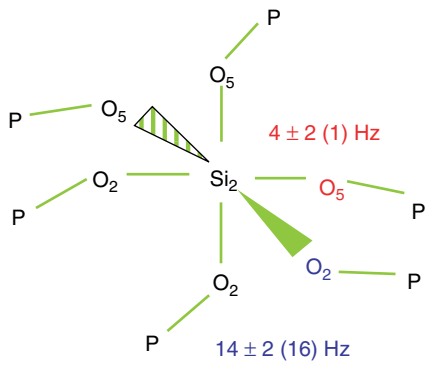


Figure 3.5. Schematic representation of the coupling pathways between Si_2 and P in $Si_5O(PO_4)_6$, showing the two experimental (calculated) J-couplings. (Reproduced from Ref. 13. © American Physical Society, 2007.)

$Si_5O(PO_4)_6$. Figure 3.5 highlights the two distinct coupling pathways between the P and Si_2 sites—the couplings are rather different in size and there is good agreement between experiment and calculation.

3.4.3 Metallic Systems

The shielding in metallic systems arises from two mechanisms. The familiar orbital response of the electrons, outlined in section, "Shielding in a Periodic System" and the Knight shift, which arises from a spin polarization induced by the external field. d'Avezac *et al.*[20] have presented a planewave-pseudopotential approach to compute the shielding in metals. This uses GIPAW to compute the orbital response and PAW for the Knight shift. Chemical shifts for the elemental metals Al, Li, and Cu have been presented, showing good agreement with experiment. The calculations are somewhat more demanding than the equivalent calculation for insulators, because a very fine sampling of the Brillouin Zone is required.

3.4.4 EPR

In crystalline materials, EPR can be used to study paramagnetic defects. EPR spectra of spin 1/2 centers have two contributions: the hyperfine tensor $\boldsymbol{A}$ and the g-tensor $\boldsymbol{g}$, which are defined through the following effective Hamiltonian

$$H_{\text{eff}} = \frac{\alpha}{2}\boldsymbol{S}\cdot\boldsymbol{g}\cdot\boldsymbol{B} + \sum_I \boldsymbol{S}\cdot\boldsymbol{A}_I\cdot\boldsymbol{I}_I \qquad (3.40)$$

where α is the fine structure constant and the summation I runs over all nuclei. The hyperfine tensor arises from the interaction of the nuclei with the ground-state spin density. This term has been calculated within the planewave-pseudopotential approach; indeed it was for this property that the PAW scheme was first introduced.[14] The tensor $\boldsymbol{g}$ arises from the interaction of the electronic spin with the external magnetic field. This term plays a somewhat similar role to the shielding in NMR; induced electronic currents in the sample modify the tensor $\boldsymbol{g}$ from its vacuum value. The GIPAW approach has been used to compute $\boldsymbol{g}$-tensors in several crystalline materials,[21] including defects in α-quartz and zirconia.

3.4.5 Heavy Elements and Relativistic Effects

The Schrödinger equation is nonrelativistic; it is valid only for particles whose velocity is much smaller than the speed of light. This is a good approximation for electrons in materials comprising of light elements, but as we descend the periodic table relativistic effects begin to play an important role because both the low-lying core states, and the valence states in the region close to the nucleus obtain high values of momentum. Relativity has a significant effect on the bonding and structural properties of materials containing heavy elements, and unsurprisingly it also has a large influence on their magnetic resonance parameters. In treating such elements, it is therefore necessary to move to a description based on the Dirac equation, which is able to account for the influence of special relativity on the electronic states.

Numerous quantum-chemical approaches incorporating relativistic effects have been developed. The use of pseudopotentials provides an alternative, simple, and computationally efficient route to including relativistic effects. In the initial construction of the pseudopotential, the free atom is treated relativistically, ensuring that the valence states have the correct relativistic eigenvalues. In the pseudopotential construction, it is usual to average over spin-orbit split states (the scalar-relativistic approximation), but it is possible to obtain pseudopotentials that include spin-orbit splitting. For bonding properties, it is sufficient to use only relativistic pseudopotentials; by

construction, the pseudovalence wavefunctions have low momentum throughout space and can be treated nonrelativistically. For the calculation of properties with a large contribution in the region close to the nucleus, it is necessary to use PAW operators modified to account for relativistic effects. Yates *et al.*[22] have used GIPAW operators modified using the zeroth order regular approximation (ZORA) to compute ^{77}Se and ^{125}Te shieldings. Within this scheme, a relativistic calculation on TeH_2 has the same computational cost as a nonrelativistic calculation on OH_2.

3.5 EXAMPLES

The methods described in this article have been applied to a wide range of solid materials from molecular crystals (e.g., pharmaceutical polymorphs and amino acids) to inorganic solids such as silicate glasses and perovskites. Applications to molecular crystals are presented in the article by Harris *et al.* (*see* **Chapter 7**), here two illustrative examples are briefly mentioned.

Figure 3.6 shows a Heteronuclear Multiple Quantum Coherence (HMQC) spectra of the disaccharide maltose, in comparison with GIPAW calculations treating the system first as an isolated molecule and then as a full periodic crystal. The excellent agreement between the crystalline calculation and experiment is sufficient to produce a full site assignment of the resonances. The significant differences between the isolated molecule and full crystal calculations show the importance of intramolecular interactions on the NMR parameters for this system. For maltose these changes have been shown to be due to the presence of so-called weak (C–H–O) hydrogen bonds.[23]

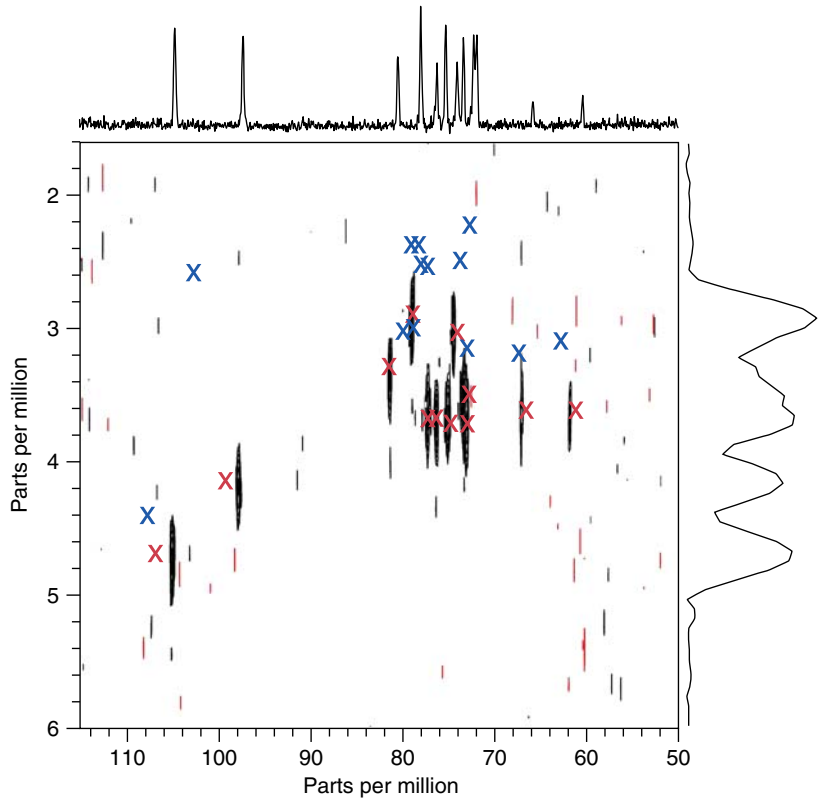


Figure 3.6. ^{13}C–^{1}H MAS *J*-HMQC solid-state NMR spectrum of maltose. The crosses show the positions of the peaks computed using the GIPAW method while treating the system as an isolated molecule (blue) and as a full crystal (red). (Reprinted with permission from Ref. 23. © (2005) American Chemical Society.)

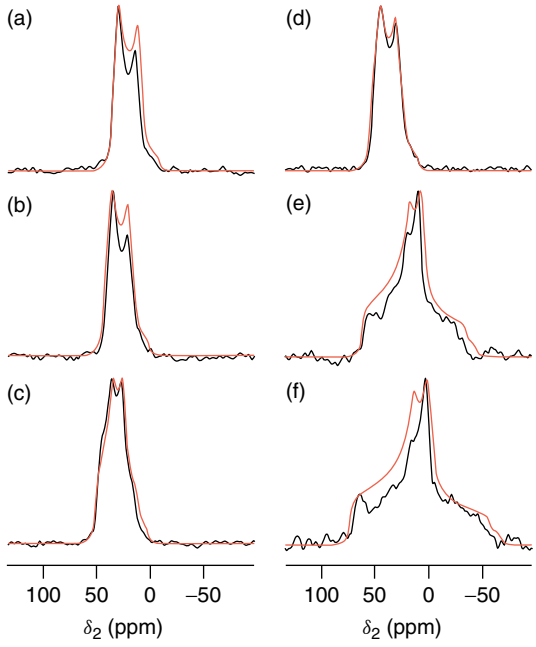


Figure 3.7. Cross-sections from the triple-quantum ^{17}O MAS spectrum of orthoenstatite. Shown in red are lineshapes simulated using NMR parameters computed using the GIPAW method. (Reprinted with permission from Ref. 24. © (2007) American Chemical Society.)

Figure 3.7 shows MAS line shapes extracted from an ^{17}O triple-quantum MAS spectrum of the $MgSiO_3$ polymorph orthoenstatite. These have characteristic quadrupolar lineshapes. In two cases, (b) and (c), the lineshape arises from the overlap of two resonances. Chemical shift and EFG tensors were computing using the planewave-pseudopotential approach, and the corresponding lineshapes, obtained using the calculated δ_{iso}, C_Q, and η_Q, are also shown in Figure 3.7. Again, the good agreement between theory and experiment allows a site assignment of the experimental resonances.[24]

REFERENCES

1. R. M. Martin, *Electronic Structure: Basic Theory and Practical Methods*, CUP: Cambridge, 2004.
2. M. C. Payne, M. P. Teter, D. C. Allen, T. A. Arias, and J. D. Joannopoulos, *Rev. Mod. Phys.*, 1992, **64**, 1045.
3. J. P. Perdew, K. Burke, and M. Ernzerhof, *Phys. Rev. Lett.*, 1996, **77**, 3865.
4. H. J. Monkhorst and J. D. Pack, *Phys. Rev., B*, 1976, **13**, 5188.
5. N. Troullier and J. L. Martins, *Phys. Rev., B*, 1991, **43**, 1993.
6. D. Vanderbilt, *Phys. Rev., B*, 1990, **41**, 7892.
7. F. Mauri, B. G. Pfrommer, and S. G. Louie, *Phys. Rev. Lett.*, 1996, **77**, 5300.
8. C. J. Pickard and F. Mauri, *Phys. Rev., B*, 2001, **63**, 245101.
9. D. Sebastiani and M. Parrinello, *J. Phys. Chem. A*, 2001, **105**, 1951.
10. F. Mauri and S. G. Louie, *Phys. Rev. Lett.*, 1996, **76**, 4246.
11. T. Gregor, F. Mauri, and R. Car, *J. Chem. Phys.*, 1999, **111**, 1815.
12. D. Sebastiani, *Mod. Phys. Lett.*, 2003, **17**, 1301.
13. J. R. Yates, C. J. Pickard, and F. Mauri, *Phys. Rev., B*, 2007, **76**, 024401.
14. C. G. van de Walle and P. E. Blöchl, *Phys. Rev., B*, 1993, **47**, 4244.
15. M. Profeta, F. Mauri, and C. J. Pickard, *J. Am. Chem. Soc.*, 2003, **125**, 541.
16. N. F. Ramsey and E. M. Purcell, *Phys. Rev.*, 1952, **85**, 143.
17. N. F. Ramsey, *Phys. Rev.*, 1953, **91**, 303.
18. S. A. Joyce, J. R. Yates, C. J. Pickard, and F. Mauri, *J. Chem. Phys.*, 2007, **127**, 204107.
19. C. Coelho, T. Azaïs, L. Bonhomme-Coury, G. Laurent, and C. Bonhomme, *Inorg. Chem*, 2007, **46**, 1379.
20. M. d'Avezac, N. Marzari, and F. Mauri, *Phys. Rev., B*, 2007, **76**, 165122.
21. C. J. Pickard and F. Mauri, *Phys. Rev. Lett.*, 2002, **88**, 086403.
22. J. R. Yates, C. J. Pickard, M. C. Payne, and F. Mauri, *J. Chem. Phys.*, 2003, **118**, 5746.
23. J. R. Yates, T. N. Pham, C. J. Pickard, F. Mauri, A. M. Amado, A. M. Gil, and S. P. Brown, *J. Am. Chem. Soc.*, 2005, **127**, 10216.
24. S. E. Ashbrook, A. J. Berry, D. J. Frost, A. Gregorovic, C. J. Pickard, J. E. Readman, and S. Wimperis, *J. Am. Chem. Soc.*, 2007, **129**, 13213.

Chapter 4

Experimental Characterization of Nuclear Spin Interaction Tensors

Jeremy J. Titman

School of Chemistry, University of Nottingham, Nottingham NG7 2RD, UK

4.1	Introduction	41
4.2	Measurements from Wideline Spectra	42
4.3	Spinning Sideband Analysis	44
4.4	Single Crystals	46
4.5	Reliability	46
4.6	Conclusion	49
	References	49

4.1 INTRODUCTION

There are three approaches to the measurement of the tensors that characterize anisotropic nuclear spin interactions in solid-state NMR. For powdered solids the principal values can be obtained directly from the singularities observed in the wideline spectrum, but this straightforward option suffers from spectral overlap for samples with several inequivalent sites. Hence, an analysis of the intensities of the rotational sidebands observed in the slow spinning MAS spectrum is often the method of choice instead. This approach has the added advantages of good sensitivity and the ability to remove interference effects arising from interactions much smaller than the MAS rate. Finally, if a single crystal is available, it can be mounted on a goniometer incorporated into the NMR probe, so that a series of spectra can be acquired as the crystal is rotated. This is the only approach that allows a direct determination of the orientations of the interaction tensors relative to the molecular frame.

This article considers these approaches in turn, with a particular focus on the data analyses required to obtain the tensor parameters from one-dimensional wideline and MAS spectra of powdered samples. In cases of spectral overlap a suitable two-dimensional NMR experiment is often used to improve resolution of the responses from inequivalent sites. Examples include the separation of overlapping spinning sideband manifolds by the 2-D PASS technique[1] or the resolution of second-order broadened central transitions of half-integer quadrupolar nuclei by MQMAS. Similarly, pulse sequences synchronized with the MAS rotor have been designed that allow interactions averaged by MAS to be reintroduced selectively. These so-called "recoupling" experiments are regularly used to measure heteronuclear or homonuclear dipolar couplings that might otherwise be obscured by the dominant chemical shift interaction. Sophisticated NMR techniques of this type are beyond the scope of this article, and they are dealt with elsewhere. Nevertheless, it should be noted that, in principle, the

NMR Crystallography Edited by Robin K. Harris, Roderick E. Wasylishen and Melinda J. Duer © 2009 John Wiley & Sons, Ltd. ISBN: 978-0-470-69961-4

methods for extracting tensor parameters from simple NMR spectra described here are equally valid for use with more complex experiments.

4.2 MEASUREMENTS FROM WIDELINE SPECTRA

In high field the shifts or splittings observed in solid-state NMR spectra due to the interaction of the nuclear spin with its surroundings vary with orientation in a characteristic fashion. For example, the frequency shift arising from the shielding interaction can be written as

$$\Delta\omega = -\sigma_{\mathrm{iso}}\omega_0 - \frac{\omega_0\zeta}{2} \times (3\cos^2\beta - 1 - \eta\sin^2\beta\cos 2\alpha) \quad (4.1)$$

where the isotropic shielding σ_{iso}, the anisotropy ζ and the asymmetry η are related to the principal values of the shielding tensor in ppm by

$$\sigma_{\mathrm{iso}} = 1/3(\sigma_{xx} + \sigma_{yy} + \sigma_{zz}), \quad \zeta = \sigma_{zz} - \sigma_{\mathrm{iso}}, \quad \eta = \frac{\sigma_{yy} - \sigma_{xx}}{\zeta} \quad (4.2)$$

and these are ordered so that

$$|\sigma_{zz} - \sigma_{\mathrm{iso}}| \geq |\sigma_{xx} - \sigma_{\mathrm{iso}}| \geq |\sigma_{yy} - \sigma_{\mathrm{iso}}| \quad (4.3)$$

The first-order quadrupolar splitting for a nucleus with spin I is given by

$$\omega_{\mathrm{Q}} = 1/2\left(\frac{3\chi}{4I(2I-1)}\right) \times (3\cos^2\beta - 1 - \eta_{\mathrm{Q}}\sin^2\beta\cos 2\alpha) \quad (4.4)$$

where the quadrupolar coupling constant χ and the asymmetry η_{Q} are related to the principal values of the EFG tensor by

$$\chi = \frac{\mathrm{e}QV_{zz}}{h}, \quad \eta_{\mathrm{Q}} = \frac{V_{yy} - V_{xx}}{V_{zz}} \quad (4.5)$$

with these ordered in a similar fashion. In each case the orientation of the principal axis system of the tensor relative to the $\boldsymbol{B}_0$ field is described by the Euler angles $\Omega = (\alpha, \beta, \gamma)$. As a consequence, the spectrum for a powdered solid takes a characteristic form in which contributions from different crystallites overlap to form a continuous lineshape. Pake[2] analyzed the lineshape arising from a pair of dipolar coupled spin-1/2 nuclei, and powder patterns are commonly observed for the chemical shift and in the first-order spectra of quadrupolar nuclei.

If a single interaction dominates and individual sites are resolved, the singularities observed give a direct measure of the principal values. When the patterns from different sites overlap, the experimental spectrum must be fitted to a superposition of calculated lineshapes using a nonlinear least-squares fitting procedure. The fitting parameters normally include line broadening and intensity scaling factors, in addition to the tensor parameters for each site. As is normally the case with a many-parameter minimization procedure, local minima must be distinguished from the global minimum by an initial grid search of the parameter surface. It should be noted that the reliability of the fit can be reduced drastically when the singularities of powder patterns from different sites are nearly coincident.[3]

Calculated lineshapes are easily generated by summing a number of single-crystallite contributions to the overall powder lineshape using expressions like equations (4.1) and (4.4), a procedure often described as "powder averaging". For the wideline case the orientations of the crystallites can be limited to a single octant of the unit sphere because of symmetry considerations.[4] The powder pattern is conveniently obtained by dividing the spectral width into discrete intervals and constructing a histogram of the number of crystallites contributing to a given frequency bin. The contribution of each crystallite is weighted by a factor that depends on its orientation, and line broadening is applied to the resulting spectrum by convolution with a Gaussian or Lorentzian lineshape function. If the crystallite orientations chosen for the summation are selected at random or fall on a uniform grid, then a dense mesh is required to reliably reproduce the experimental pattern, resulting in long computation times. For an iterative fitting procedure it is important that the calculations are as efficient as possible, so much effort has been expended on designing powder averaging schemes that allow a sparse sampling of the orientations without compromising the accuracy of the results. Recent examples are based on integration by a Gaussian spherical quadrature[4] or involve generating sets of orientations that are uniformly distributed over the unit sphere by minimizing a fictional repulsive potential between them.[5] Efficient powder averaging of this type can be further be combined with interpolation of the frequency between the chosen orientations to ensure that all bins receive the correct contributions.[6] As an illustration, Figure 4.1 shows (a) the carbon-13 wideline NMR spectrum of dimethoxymethane recorded

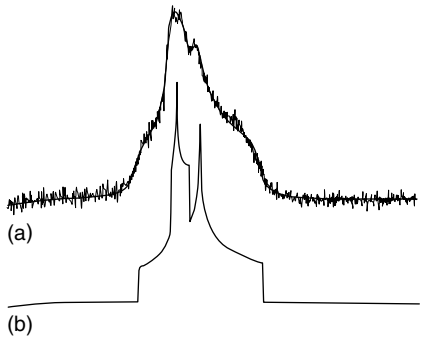


Figure 4.1. (a) Carbon-13 wideline NMR spectrum of dimethoxymethane recorded at a temperature of 25 K with a Larmor frequency of 20.1 MHz. (b) CSA powder patterns, shown without line broadening, obtained by a nonlinear least-squares fit combined with interpolation in the frequency domain, as described in the text. (Reproduced from Ref. 6. © American Institute of Physics, 1986.)

at a temperature of 25 K with a Larmor frequency of 20.1 MHz. This is compared with the calculated spectrum, obtained by interpolation and fitting as described above, which consists of the superposition of two CSA powder patterns, shown without line broadening in (b). Alternatively, powder averaging can be avoided by employing analytical expressions for the intensity of the type originally derived by Bloembergen and Rowland[7] for the Knight shift. These involve complete elliptical integrals of the first kind which can be evaluated numerically using a power series.

Since powder patterns usually cover a substantial frequency spread, an appropriate echo sequence is required to record undistorted spectra suitable for analysis. Wideline deuterium spectra obtained with a quadrupolar echo have been extensively used to quantify EFG tensors, because χ is normally small enough to give first-order lineshapes, but large enough that other interactions can be neglected. Sample preparation often involves selective deuteration to improve sensitivity, and this has the added advantage that a single powder pattern is observed in the wideline spectrum. In contrast, wideline measurements of carbon-13 shielding tensors in organic molecules at natural abundance are often impaired by overlap. In this situation the analysis of resolved MAS sidebands or the use of a two-dimensional NMR experiment that separates the overlapping powder patterns are more fruitful approaches. For abundant spin-1/2 nuclei, such as phosphorus-31, homonuclear dipolar couplings introduce systematic errors which must be explicitly taken into account when calculating lineshapes. For proton or fluorine-19 homonuclear decoupling via multiple pulse sequences, such as WAHUHA must be employed to remove the large dipolar couplings and reveal a CSA powder pattern.[8] Other systematic errors arise from incomplete heteronuclear decoupling, uneven cross-polarization efficiency and finite pulse amplitude effects.

For half-integer spin quadrupolar nuclei the first-order broadened satellite transitions can be used to measure the EFG tensor. However, this approach is limited to cases with small quadrupolar couplings, otherwise the satellites are too broad to be detected in the wideline spectrum. In these circumstances, the second-order quadrupolar broadening of the central transition provides an alternative measurement. The corresponding frequency is given by

$$\omega_{\mathrm{CT}} = \frac{1}{\omega_0}\left\{\frac{\chi}{4I(2I-1)}\right\}^2 \{4I(I+1)-3\} \times \sum_{\lambda=0,2,4}\sum_{\mu=-l}^{l} c_{\lambda,\mu}\exp(-\mathrm{i}\mu\alpha)\, d^{(\lambda)}_{\mu,0}(\beta) \quad (4.6)$$

where the $d^{(\lambda)}_{\mu,0}$ are the reduced Wigner rotation matrices of rank λ and the expansion coefficients $c_{\lambda,\mu}$ are given elsewhere. This expression can be used to calculate central transition lineshapes for fitting to experimental spectra by powder averaging in an analogous fashion to that above. A second-order isotropic contribution results from the $\lambda = 0$ term which augments the chemical shift, so that the resulting line position is usually incorporated as a fit parameter. The $\lambda = 4$ anisotropic term is not completely removed by MAS, so that a powder pattern remains which can be used to measure the EFG tensor with improved resolution, especially for high magnetic field and rapid spinning. Any residual sidebands can be folded onto the central transition by synchronizing the dwell time with the MAS rotor. In this case the powder pattern is calculated for fitting by assuming an infinite spinning rate.

Many software packages are available that can be used to measure interaction tensors from experimental spectra, particularly for the important cases of the CSA powder pattern for a spin-1/2 nucleus and the second-order broadened central transition of a half-integer spin quadrupolar nucleus under MAS.[9]

4.3 SPINNING SIDEBAND ANALYSIS

Maricq and Waugh[10] gave the first detailed analysis of the rotational sidebands that appear in MAS spectra. They distinguished between so-called "inhomogeneous" and "homogeneous" nuclear spin interactions in terms of the behavior observed when the MAS rate is slow compared to the anisotropy. In the inhomogeneous case, for example with a chemical shift or a first-order quadrupolar interaction, the eigenstates of the corresponding Hamiltonian are not affected by the spinning. In these circumstances, the FID assumes the form of a train of rotational echoes which, after Fourier transform, gives an array of well-defined spinning sidebands. The sideband intensity envelope contains information about the tensor parameters, so that their measurement is not compromised in exchange for the high site resolution afforded by MAS. Focusing on the chemical shift, Herzfeld and Berger[11] used the properties of Bessel functions to find an analytical expression for the powder-averaged intensity for the MAS sideband separated from the isotropic line by $n\omega_r$

$$I_n = \frac{1}{4\pi}\int_0^{\pi}\int_0^{2\pi} |F_n|^2 \sin\beta \, d\alpha \, d\beta \qquad (4.7)$$

where

$$F_n = \frac{1}{2\pi}\int_0^{2\pi} \exp\{i[-n\theta + \Delta_-\tau_-(\alpha,\beta,\theta) + \Delta_+\tau_+(\beta,\theta)]\}\, d\theta \qquad (4.8)$$

and

$$\Delta_+ = \frac{3\omega_0(\sigma_{iso} - \sigma_{zz})}{\omega_r}$$
$$\Delta_- = \frac{\omega_0(\sigma_{yy} - \sigma_{xx})}{\omega_r} \qquad (4.9)$$

The factors τ_- and τ_+ depend on the α and β Euler angles and are given elsewhere.

Owing to limitations in the computer resources available at the time, Maricq and Waugh rejected explicit calculations of the sideband intensities in powdered samples as the basis of an iterative method of matching the experimental sideband envelope. Instead, they proposed a discrete variant of the moment analysis originally described by Van Vleck[12] where the moments M_l are defined by

$$M_l = \omega_r^l \sum_{n=-\infty}^{+\infty} n^l I_n \Big/ \sum_{n=-\infty}^{+\infty} I_n \qquad (4.10)$$

where the second and third moments are independent of the MAS rate

$$M_2 = \frac{3\zeta^2}{20}(3+\eta^2), \quad M_3 = \frac{27\zeta^3}{140}(1-\eta^2) \qquad (4.11)$$

This approach relies on an accurate measurement of the intensities of all the sidebands arising from a particular site, but this is often not feasible owing to spectral overlap. In addition, the outer sidebands make an increasingly large contribution to the moments, but these are of low intensity and significantly affected by the noise.

To circumvent these problems, Herzfeld and Berger evaluated I_n by numerical integration of equations (4.7) and (4.8), and then plotted the ratios I_n/I_0 as a function of the ratio of a reduced span Ω/ω_r and the skew κ of the tensor defined as

$$\frac{\Omega}{\omega_r} = \frac{\omega_0(\sigma_{33} - \sigma_{11})}{\omega_r}$$
$$\kappa = \frac{\sigma_{11} + \sigma_{33} - 2\sigma_{22}}{\sigma_{33} - \sigma_{11}} \qquad (4.12)$$

With the principal components assigned so that $\sigma_{11} < \sigma_{22} < \sigma_{33}$, Ω is always positive, but κ varies between -1 and $+1$ with the extreme values corresponding to axially symmetric tensors. Contour plots of the ratio $I_{\pm n}/I_0$ were constructed by interpolating between points in a grid of 15 Ω/ω_r values between 0 and 15 and 21 κ values between -1 and 1. These were used as the basis of a graphical determination of the CSA tensor parameters, since the contours corresponding to each of the observed values of I_n/I_0 intersect at the correct values of Ω/ω_r and κ. If sideband manifolds from different sites overlap, this analysis can be limited to the well-resolved sidebands, since only the intensity ratio relative to the centerband needs to be measured.

The graphical approach is rarely used these days, but it forms the basis of a number of iterative fitting procedures for obtaining the shift tensor parameters. For example, de Groot *et al.* proposed using a precalculated grid of intensities to generate a simulated sideband pattern by convolution with an appropriate lineshape function.[13] This results in an efficient iteration loop when minimizing the χ^2 with the experimental spectrum using the linewidth, an intensity scaling factor and the isotropic shift as parameters in addition to ζ and η. Olivieri commented on the need for a rigorous statistical analysis to obtain standard deviations for the resulting tensor components and also pointed out the lack of precision associated with measurements of η in cases of near-axial

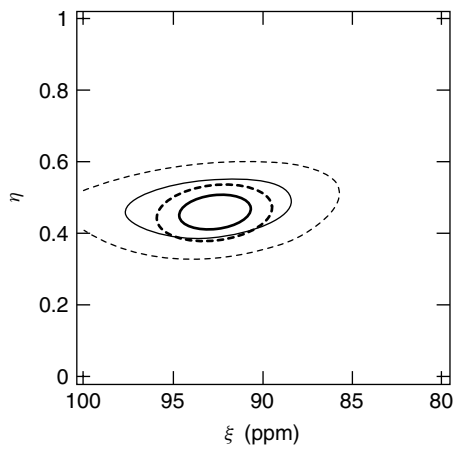


Figure 4.2. Plots of χ^2 as a function of the carbon-13 CSA tensor parameters ζ and η evaluated for the carbonyl C7 site in penicillin-V from sideband manifolds taken from 2-D-PASS experiments obtained at a Larmor frequency of 50.3 MHz and MAS rates of 1030 Hz (thick lines) and 800 Hz (thin lines). The boundaries of the 68.3% (dashed lines) and 95.4% (solid lines) joint confidence regions for ζ and η are shown. (Reproduced from Ref. 15. © Elsevier, 1998.)

symmetry.[14] As an alternative, Antzutkin *et al*. obtained the joint confidence limits on ζ and η from plots of the χ^2 error surface.[15] In this approach the single-crystallite FID was calculated directly in the time domain over a single rotor period for 51 values of the ratio ζ/ω_r between 10 and -10 and 11 values of η. The resulting signal was Fourier transformed and the amplitude evaluated at $n\omega_r$ up to $n = \pm 11$ before powder averaging to produce the required sideband intensities. These were collected and interpolated to provide a dense grid as a function of ζ/ω_r and η. The χ^2 between experimental and calculated intensities was then minimized for each point on the precalculated grid by altering only the intensity scaling factor. The resulting error surface was plotted, allowing the CSA parameters to be identified from the minimum and their joint confidence regions to be evaluated. As an illustration, Figure 4.2 shows plots of χ^2 as a function of the carbon-13 CSA tensor parameters ζ and η evaluated for the carbonyl C7 site in penicillin-V from data obtained at MAS rates of 1030 Hz (thick lines) and 800 Hz (thin lines). Because sidebands from different carbon-13 sites in penicillin-V overlap in the one-dimensional MAS spectrum, the intensities were obtained from a 2-D-PASS experiment. The boundaries of the 68.3% (dashed lines) and 95.4% (solid lines) joint confidence regions for ζ and η are shown. Sachleben reformulated the method of Antzutkin *et al*. in terms of Bayesian statistics by employing the posterior probability that the experimental sideband intensities can be described by particular values of ζ and η.[16] Bayes's theorem allows the posterior probability to be related to χ^2 assuming that the experimental noise is distributed as a Gaussian of standard deviation σ and the sidebands are well-separated from one another

$$p(\zeta, \eta) = N \exp\left\{-\frac{1}{2\sigma_{\text{noise}}^2} \sum_n \left(I_n - I_n^{\text{calc}}\right)^2\right\} \tag{4.13}$$

The Bayesian analysis allows the posterior probability distribution to be mapped into the entropy which allows a comparison of the information content of sideband manifolds recorded at different spinning speeds, as discussed further below.

All these approaches generate a look-up table of powder sideband intensities to minimize the computation necessary for each iteration in a least-squares fitting procedure. However, efficient methods for simulating MAS spectra by numerical evaluation of the Liouville-von Neumann equation allow the powder FID to be calculated directly during each iteration. In simulations the propagator U, which describes the spin dynamics, is usually approximated by the product

$$U = \prod_j \exp\{-\mathrm{i}H(j\tau)\tau\} \tag{4.14}$$

where τ is a short interval during which the time-dependent MAS Hamiltonian H is considered to be constant. Since the exponential operators in equation (4.14) are generated by diagonalizing the matrix representation of H, optimized linear algebra algorithms can be used to speed up the calculations.[17] Further efficiency gains can be made by exploiting symmetry, such as the time–translation relationship between the MAS rotor phase $\omega_r t$ and the Euler angle γ. Once again, the symmetry of the problem with respect to α and β is such that the powder average need only be evaluated over one octant of the unit sphere.[4] Taken together, all these developments make it feasible to calculate the MAS FID directly during each iteration while minimizing the χ^2 with the experimental data.

Several software packages are available that combine efficient simulations with least-squares fitting to

extract the CSA parameters and evaluate the associated errors from a statistical analysis.[18] As in the wideline case, precautions should be taken to avoid systematic errors. For example, distorted sideband intensities can arise from uneven cross-polarization efficiency, miscalibration of the magic angle and non-uniform molecular orientation distributions. In addition, dipolar couplings, particularly to quadrupolar nuclei such as nitrogen-14, have to be taken into account explicitly in simulations.

For half-integer spin nuclei with large quadrupolar couplings the second-order broadened central transition observed with rapid MAS provides the most convenient method for the measurement of the EFG tensor. However, when $\chi/[4I(2I-1)] \leq 50\,\text{kHz}$ the second-order lineshape is often obscured by contributions to the broadening from other interactions. For these relatively small quadrupolar couplings an alternative approach[19] involves recording the sideband manifolds arising from the first-order broadened satellite transitions which extend across spectral widths as large as 2 MHz. This requires rapid spinning often at rates in excess of 20 kHz and accurate setting of the magic angle to within $\pm 0.005^\circ$. Sideband intensities toward the edge of the spectrum are distorted because of their excitation by a finite amplitude radio-frequency pulse and by the narrow bandwidth of the high-Q MAS probe. These effects must be explicitly included when the sideband patterns are simulated to fit the experimental data when extracting the tensor parameters. As an illustration, Figure 4.3(a) shows an experimental sodium-23 NMR spectrum of sodium oxalate recorded at a MAS rate of 13.9 kHz which should be compared with the simulated satellite transition sideband manifold in Figure 4.3(b). Note that second-order effects have been included in these simulations to match the sideband lineshapes.

4.4 SINGLE CRYSTALS

Tensor principal values can be easily obtained from wideline or MAS spectra of powdered samples, but a direct measurement of the orientation of the principal axis system (PAS) with respect to the crystallographic axes is only possible using single crystals. In these experiments the crystal is mounted in a goniometer and NMR spectra are acquired as a function of rotation angle θ about an axis perpendicular to B_0. This procedure is repeated with the crystal mounted in three different orientations, and a rotation plot is constructed which displays the resonance frequency as a function of θ. As an illustration, Figure 4.4 shows three rotation plots[20] obtained from the rubidium-87 central transition of a single crystal of $RbClO_4$ which contains two magnetically inequivalent sites. The resonance frequency, in this case given by a combination of equation (4.1) for the chemical shift and equation (4.6) for the quadrupolar interaction to second order, can be expressed in the goniometer frame as a function of θ for each of the three crystal orientations. Hence, the matrices representing all the tensors involved can be extracted by fitting calculated rotation curves to the experimental data for each crystal orientation with all independent elements as adjustable parameters. In this case both the EFG and the CSA tensors have been obtained along with their relative orientation.

Single-crystal NMR can suffer from reduced sensitivity when the crystals are small, although efforts to overcome this limitation have been made recently by detecting the NMR signal with a microcoil.[21] On the other hand, the approach is useful in situations where wideline or MAS powder spectra yield poor results. Examples include measurements of weak homonuclear dipolar couplings in the presence of large shift anisotropies or of quadrupolar interactions strong enough to result in second-order broadening that substantially exceeds the accessible MAS rate.

4.5 RELIABILITY

Intuitively, it might be imagined that the reliability of the measured tensor parameters would be compromised at increased MAS rates due to the reduced number of sidebands observed. However, in many practical situations with moderate MAS this apparent loss of information content is more than compensated by an increase in the signal-to-noise ratio of the remaining sidebands. Therefore, Hodgkinson and Emsley set out to investigate systematically how the reliability varies with the MAS rate to establish the optimum value.[3] This was achieved by evaluating the normalized Cramér–Rao bounds $r(p_j)$ which provide lower limits on the standard deviations of the fit parameters p_j and can be obtained from the Fisher information matrix $\boldsymbol{F}$ by

$$r(p_j) = p_j \Big/ \sqrt{(\boldsymbol{F}^{-1})_{jj}} \tag{4.15}$$

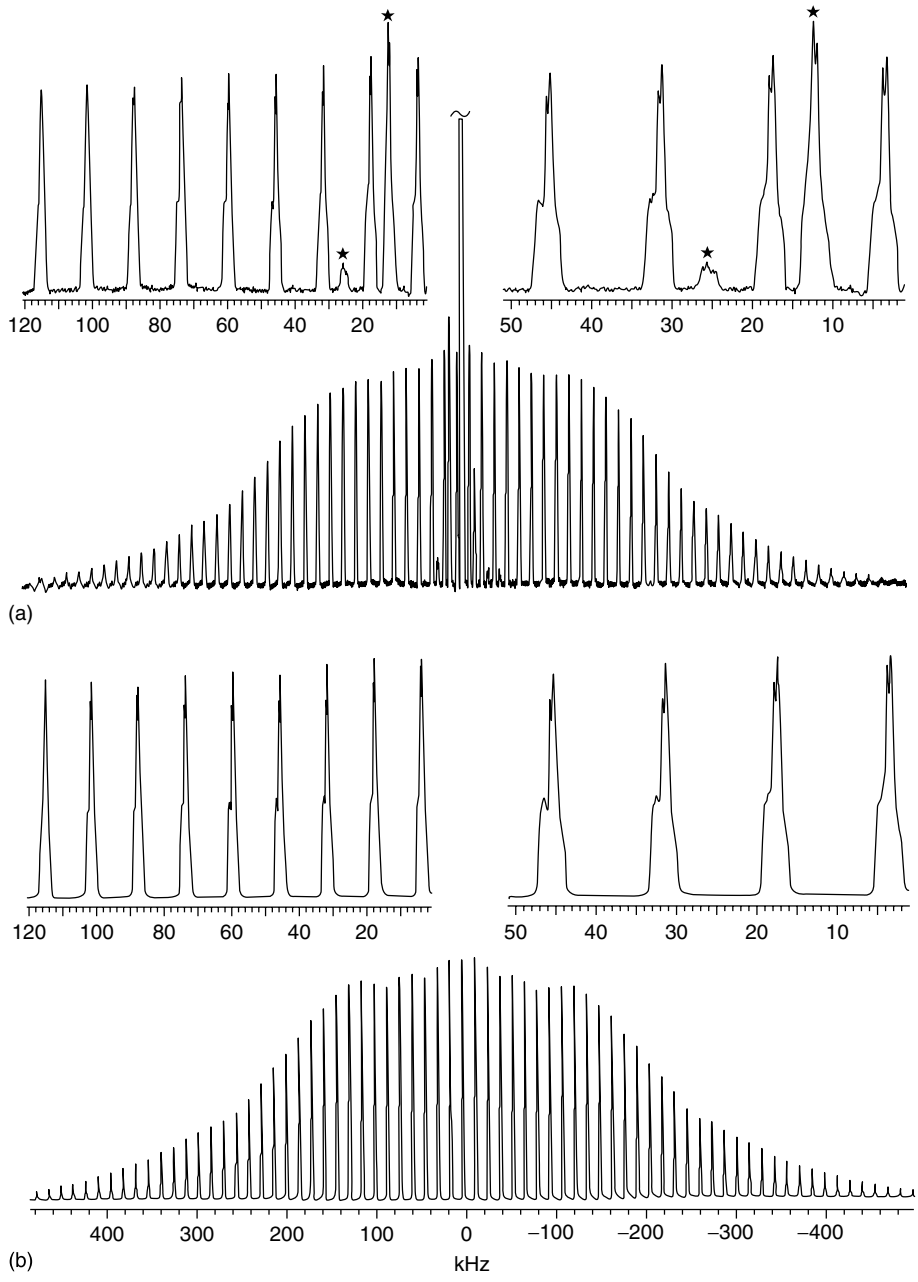


Figure 4.3. (a) Experimental Na-23 NMR spectrum of sodium oxalate recorded at a Larmor frequency of 105.8 MHz and a MAS rate of 13.9 kHz with insert showing lineshapes for the spinning sidebands. (b) Simulated satellite sideband spectrum calculated using $\chi = 2.5$ MHz and $\eta = 0.74$ and experimental parameters $Q = 200$ and $\omega_1/2\pi = 40$ kHz. Sidebands arising from the central transition are denoted by asterisks. Note that the simulated spectrum does not include the narrow central transition observed experimentally. (Reproduced from Ref. 19. © Elsevier, 1991.)

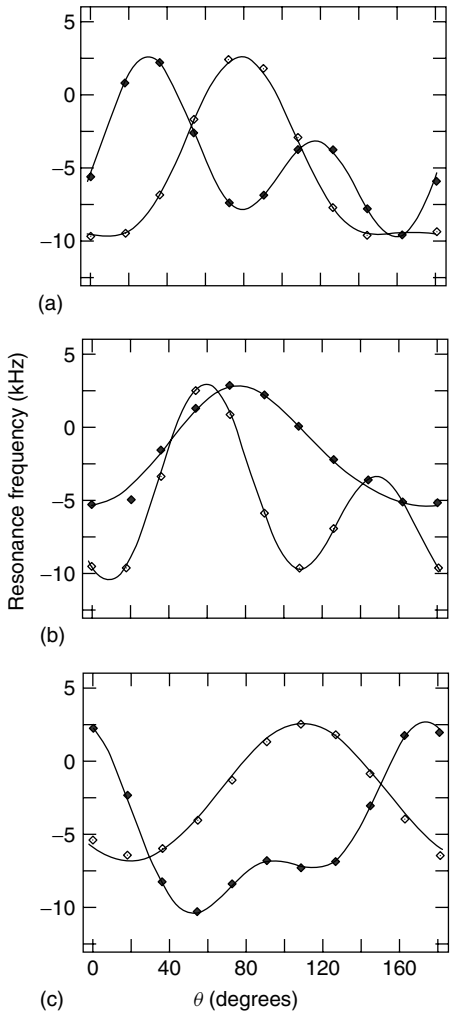


Figure 4.4. Rotation plots obtained from the rubidium-87 central transition of a single crystal of $RbClO_4$ rotating about the (a) $-x$, (b) y, and (c) $-z$ axis of the goniometer frame, respectively. The experimental resonance frequencies recorded at a Larmor frequency of 130.9 MHz for the two magnetically inequivalent sites (open and filled diamonds) have been fitted to theoretical curves to obtain the EFG and CSA tensors, as well as their relative orientation. (Reproduced from Ref. 20. © Elsevier, 1996.)

For the CSA tensor, in addition to ζ and η, the isotropic shift, the linewidth and an intensity scaling factor are the usual fit parameters. All the p_j are correlated with one another to some extent, but the reliabilities scale linearly with the ratio of the experimental noise to the intensity factor and are largely independent of the isotropic shift. Provided the FID is not truncated, the sampling parameters do not affect the $r(p_j)$ and the linewidth has a scaling effect. Hence, under normal conditions, $r(\zeta)$ and $r(\eta)$ are significant functions only of a scaled anisotropy ζ/ω_r and the asymmetry. Plots of the reliabilities as a function of η and a reduced MAS rate ω_r/ζ are shown in Figure 4.5. The former (a) demonstrates the somewhat unexpected conclusion that across nearly the whole range of η the global maximum in the reliability for the anisotropy occurs at ω_r/ζ close to 0.4. This

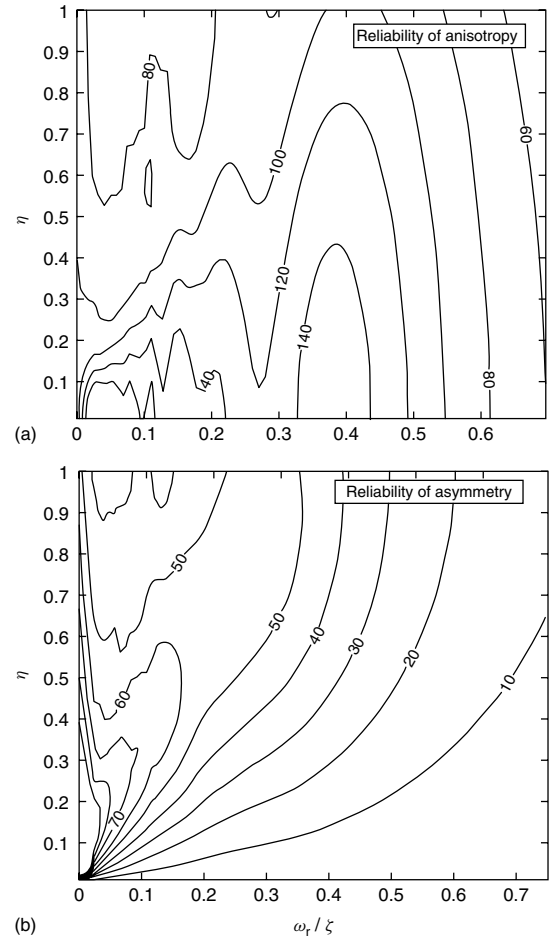


Figure 4.5. Contour plots of the reliability of (a) the anisotropy $r(\zeta)$ and (b) the asymmetry $r(\eta)$ for the chemical shift tensor as a function of η and the reduced MAS rate ω_r/ζ. (Reproduced from Ref. 3. © American Institute of Physics, 1997.)

means that so long as $\eta > 0.1$ there is a constant optimum number of sidebands for analysis equal to about 6. Similarly, when $\eta < 0.1$, the most reliable measurements of ζ are obtained with ω_r/ζ around 0.05, corresponding to about 20 sidebands. On the other hand, the most reliable measurement of the asymmetry is obtained from a wideline spectrum, since $r(\eta)$ (b) always reaches its global maximum when ω_r/ζ tends to zero. However, if $\eta > 0.3$ there is a further local maximum for ω_r/ζ between 0.2 and 0.3, corresponding to an analysis of between 6 and 10 sidebands. In the case of interactions that result in a Pake pattern, the situation is rather different. Similar plots of $r(\chi)$ and $r(\eta_Q)$ for a first-order quadrupolar interaction show that a global maximum in the reliability for the quadrupole coupling occurs with ω_r/χ close to 0.25, but only across a restricted range of η_Q between 0.2 and 0.75. However, when $\eta_Q = 0$, as in the case of the inherently symmetric dipolar tensor, the most reliable measurement of the anisotropy is obtained from the wideline spectrum, since once again $r(\eta_Q)$ reaches its global maximum as ω_r/χ approaches zero.

In summary, for determinations of the anisotropy of the chemical shift a MAS sideband analysis is significantly more reliable than a wideline measurement for all values of η. However, a wideline spectrum is the method of choice for determination of the dipolar coupling and of χ for near symmetric first-order quadrupolar tensors. In most other situations the difference in reliability between a sideband analysis with the optimum number of sidebands and a wideline measurement is marginal. Similar conclusions were obtained from a Bayesian analysis of the information content of chemical shift sideband manifolds.[16] These demonstrated that, taking both ζ and η into account, the minimum entropy or maximum information content of a MAS spectrum occurs for ζ/ω_r between 2 and 3 with only a slight variation with signal-to-noise ratio. Hence, a MAS spectrum with 5–7 sidebands gives the most reliable determination of both ζ and η from a single measurement.

4.6 CONCLUSION

This article has discussed the methods for measuring the tensors that describe nuclear spin interactions in solid-state NMR with a particular focus on the analysis of one-dimensional wideline and MAS spectra of powdered samples. Current approaches usually employ nonlinear least-squares fitting of a simulated spectrum to the experimental data. In the MAS case simulated sideband intensities are sometimes obtained from a precalculated grid to minimize the computation required during each iteration of the fitting procedure. However, efficient powder averaging schemes and calculation strategies that use symmetry indicate that this approach is no longer necessary. Errors must be obtained either from a statistical analysis or by exploring the full χ^2 surface. For interactions that result in a Pake pattern the wideline spectrum generally provides the most reliable determination of the tensor, while for the CSA the total information content is greatest in a MAS spectrum with approximately 6 sidebands.

REFERENCES

1. For a review see: O. N. Antzutkin, *Prog. Nucl. Magn. Reson. Spectrosc.*, 1999, **35**, 203.
2. G. E. Pake, *J. Chem. Phys.*, 1948, **16**, 327.
3. P. Hodgkinson and L. Emsley, *J. Chem. Phys.*, 1997, **107**, 4808.
4. M. Edén and M. H. Levitt, *J. Magn. Reson.*, 1998, **132**, 220.
5. M. Bak and N. C. Nielsen, *J. Magn. Reson.*, 1997, **125**, 132.
6. D. W. Alderman, M. S. Solum, and D. M. Grant, *J. Chem. Phys.*, 1986, **84**, 3717.
7. N. Bloembergen and T. J. Rowland, *Acta Metall.*, 1953, **1**, 731.
8. H. Raber, G. Brunger, and M. Mehring, *Chem. Phys. Lett.*, 1973, **23**, 400.
9. Recent examples include: MatNMR, J. D. van Beek, *J. Magn. Reson.*, 2007, **187**, 19; DMFit, D. Massiot, F. Fayon, M. Capron, I. King, S. Le Calvé, B. Alonso, J.-O. Durand, B. Bujoli, Z. Gan, and G. Hoatson, *Magn. Reson. Chem.*, 2002, **440**, 70.
10. M. Matti Maricq and J. S. Waugh, *J. Chem. Phys.*, 1979, **70**, 3300.
11. J. Herzfeld and A. E. Berger, *J. Chem. Phys.*, 1980, **73**, 6021.
12. J. H. van Vleck, *Phys. Rev.*, 1968, **74**, 1168.
13. H. J. M. de Groot, S. O. Smith, A. C. Kolbert, J. M. L. Courtin, C. Winkel, J. Lugtenburg, J. Herzfeld, and R. G. Griffin, *J. Magn. Reson.*, 1991, **91**, 30.
14. A. C. Olivieri, *J. Magn. Reson.*, 1996, **123**, 207.

15. O. N. Antzutkin, Y. K. Lee, and M. H. Levitt, *J. Magn. Reson.*, 1998, **135**, 144.

16. J. R. Sachleben, *J. Magn. Reson.*, 2006, **183**, 123.

17. For example BLAS, L. S. Blackford, J. Demmel, J. Dongarra, I. Duff, S. Hammarling, G. Henry, M. Heroux, L. Kaufman, A. Lumsdaine, A. Petitet, R. Pozo, K. Remington, and R. C. Whaley, *ACM Trans. Math. Soft.*, 2002, **28**, 135.

18. For example SIMPSON, M. Bak, J. T. Rasmussen, and N. C. Nielsen, *J. Magn. Reson.*, 2000, **147**, 296.

19. J. Skibsted, N. C. Nielsen, H. Bildsøe, and H. J. Jakobsen, *J. Magn. Reson.*, 1991, **95**, 88.

20. T. Vosegaard, J. Skibsted, H. Bildsøe, and H. J. Jakobsen, *J. Magn. Reson.*, 1996, **122**, 111.

21. T. Vosegaard, P. Daugaard, E. Hald, and H. J. Jakobsen, *J. Magn. Reson.*, 2000, **142**, 379.

PART B
Chemical Shifts

Chapter 5
Magnetic Shielding & Chemical Shifts: Basics

Julio C. Facelli[1,2] and Anita M. Orendt[2]

[1]*Department of Biomedical Informatics, University of Utah, Salt Lake City, UT 84112-0190, USA*
[2]*Center for High Performance Computing, University of Utah, Salt Lake City, UT 84112-0190, USA*

5.1	Introduction	53
5.2	Symmetry Properties of the Shielding Tensor	54
5.3	Theory of Magnetic Shielding	55
5.4	Calculations of Magnetic Shielding	56
	References	58

5.1 INTRODUCTION

Perhaps the most important discovery after the successful detection of the nuclear magnetic resonance (NMR) signal was the observation that the nuclear spin resonance frequencies depend on the chemical or electronic environment of the nuclei,[1,2] or as Ramsey states in his landmark papers[3,4] of 1950: "In measurements of nuclear magnetic moments, a correction must be made for the magnetic field arising from the motions of the molecular electrons which are induced by the externally applied field." Ramsey realized that a correction using only Lamb's diamagnetic theory developed for atoms was inadequate for molecules because there are additional shielding contributions arising from the second-order paramagnetism. To address this problem he developed the necessary theoretical framework to explain and eventually to calculate the "chemical effect" that would become the chemical shift commonly used for structural elucidation.

It should be noted that magnetic shielding, $\boldsymbol{\sigma}$, is a tensor property, i.e., it depends on the molecular orientation with respect to the external magnetic field, a fact that becomes apparent by the orientation dependence of the spectra of stationary single crystals or the wide resonances observed in stationary powders.[5] The magnetic shielding tensor describes the change in the local magnetic field at the position of the nucleus due to the interaction between the electrons and the external magnetic field. This change in the local magnetic field can produce shielding or deshielding of the nucleus. In the first case, the local magnetic field is increased with respect to the external field, while in the second case the local field is decreased. In principle, shielding is referenced to the situation for a bare nucleus, unless otherwise stated.

In practice, NMR experiments do not measure the magnetic shielding directly, instead the common practice is to measure chemical shifts, $\boldsymbol{\delta}$, as the change of the resonance frequency of a nucleus relative to a given standard. However, the shielding is the magnetic property that can be defined quantum mechanically and calculated directly; conversions being made later give chemical shifts that can be compared with experimental measurements. This conversion involves calculating the shielding of the reference compound. Following the IUPAC recommendation,[6] the

NMR Crystallography Edited by Robin K. Harris, Roderick E. Wasylishen and Melinda J. Duer © 2009 John Wiley & Sons, Ltd. ISBN: 978-0-470-69961-4

relation between the chemical shift and magnetic shielding is given by

$$\delta_i = \frac{(\sigma_{\text{ref}} - \sigma_i)}{(1 - \sigma_{\text{ref}})} \tag{5.1}$$

In equation (5.1), δ_i is the measured chemical shift, σ_{ref} is the shielding of the reference compound used in the NMR experiment, and σ_i is the shielding of the measured compound. The determination of the value of σ_{ref} is quite difficult, as it involves the estimation of the paramagnetic contribution to the magnetic shielding in the center of mass of the molecule using its relationship with the spin rotational constant along with the calculation of the corresponding diamagnetic part using quantum mechanical methods. The procedure for selecting primary and secondary reference compounds has been extensively discussed by Jameson and Mason.[7] Figure 5.1 depicts the correlation between ^{13}C chemical shifts and shieldings of the most common organic groups.

The material presented in this article is restricted to chemical shifts and shielding calculations of diamagnetic molecules. When the molecular electronic ground state is not a singlet, i.e., when unpaired electrons are present in the sample, additional mechanisms contributing to the magnetic shielding should be considered.[8]

5.2 SYMMETRY PROPERTIES OF THE SHIELDING TENSOR

The components of the magnetic shielding tensor are given by

$$\sigma_{\alpha\beta} = \frac{\partial^2 E}{\partial \mu_\alpha \partial B_\beta} \tag{5.2}$$

In equation (5.2), E is the total electronic energy of the molecule, $\boldsymbol{B}$ is the external magnetic field, and μ is the magnetic moment of the nucleus of interest. Two important observations that can be made from equation (5.2): (1) the magnetic shielding tensor is an antisymmetric tensor because exchanging the indices α and β in equation (5.2) leads to a different quantity. Note that this permutation exchanges the components of the magnetic moment μ and magnetic field $\boldsymbol{B}$, with respect to which the derivative of the energy is calculated, i.e.,

$$\sigma_{\alpha\beta} = \frac{\partial^2 E}{\partial \mu_\alpha \partial B_\beta} = \frac{\partial^2 E}{\partial B_\beta \partial \mu_\alpha} \neq \frac{\partial^2 E}{\partial \mu_\beta \partial B_\alpha} = \sigma_{\beta\alpha} \tag{5.3}$$

This property of the tensor should not be confused with the fact that the first-order response function to the shielding interaction, i.e., the NMR spectrum, is sensitive only to the symmetric part of the tensor and that the antisymmetric components contribute only to the second-order response, i.e., the relaxation of the spin magnetization.[9,10] (2) When using perturbation theory for the expansion of the molecular

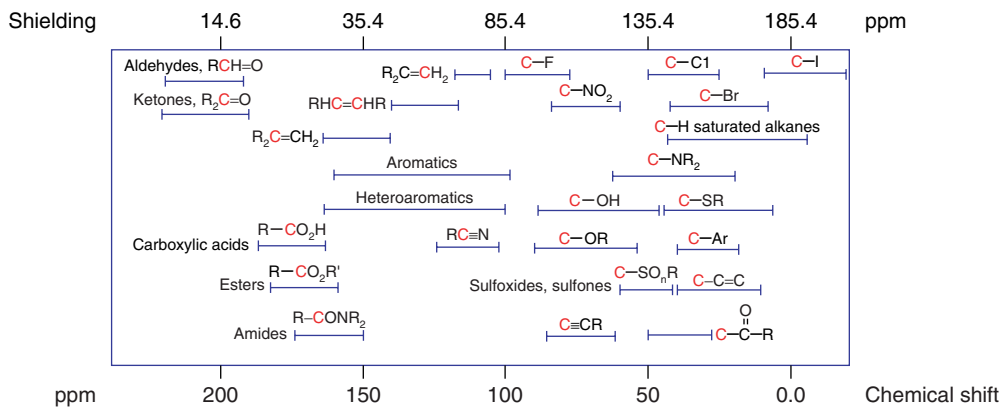


Figure 5.1. Correlation between the ^{13}C chemical shifts and shieldings for the most common organic groups. The shieldings were obtained from the chemical shifts by using the original literature value for the absolute shielding of carbon monoxide, 3.20 ppm, which correspond to an absolute shielding for the secondary standard, tetramethyl silane (TMS) of 185.4 ppm[7].

energy in powers of the external magnetic field and the nuclear magnetic moment, the magnetic shielding tensor components can be identified as the coefficients in the expansion that are bilinear terms in the nuclear magnetic moment and the external magnetic field. The magnetic shielding tensor has nine independent components, but this number may be reduced by the molecular or crystal symmetry.[11]

5.3 THEORY OF MAGNETIC SHIELDING

The theory and modeling of magnetic shielding have been described in numerous publications,[12–40] including a very comprehensive volume edited by Kaupp *et al*.[41] To obtain exact expressions for the calculation of magnetic shielding using the nonrelativistic Born-Oppenheimer approximation,[42] it is necessary to include the vector potentials representing the external magnetic field and the dipolar field from the magnetic moment of the nucleus into the electronic Hamiltonian. In the gauge of Coulomb, the vector potential defining these fields at the position of the electron k can be expressed as follows:

$$\boldsymbol{A}_k(\boldsymbol{r}) = \frac{1}{2}\boldsymbol{B} \times \boldsymbol{r}_k + \frac{(\boldsymbol{\mu}_N \times \boldsymbol{r}_{Nk})}{r_{Nk}^3} \qquad (5.4)$$

In equation (5.4), the origin of the vector potential is at the position $\boldsymbol{O}$, while $\boldsymbol{r}_k$ and $\boldsymbol{r}_{Nk}$ are defined according to Figure 5.2. Note that for simplicity we are considering that only one nucleus in the molecule has a nonzero magnetic moment.

Following the standard procedures for the inclusion of magnetic interactions into the electronic Hamiltonian, the full electronic Hamiltonian in the presence of these two magnetic fields is given by equation (5.5), where c is the speed of light in the vacuum.

$$H = \frac{1}{2}\sum_k \left[\frac{1}{\mathrm{i}}\nabla_k - \frac{1}{c}A_k(\boldsymbol{r})\right]^2 + \boldsymbol{V}(\boldsymbol{r}) \qquad (5.5)$$

Using the properties of the Coulomb gauge, i.e., $\nabla \cdot \boldsymbol{A} = 0$, the expansion of this Hamiltonian leads to six terms; of these only three are relevant to the calculation of magnetic shielding. These terms are as follows:

$$H_\alpha^{(1,0)} = \frac{-\mathrm{i}}{2c}\sum_k L_{k_\alpha} = \frac{-\mathrm{i}}{2c}\sum_k (\boldsymbol{r_k} \times \nabla_k)_\alpha \qquad (5.6)$$

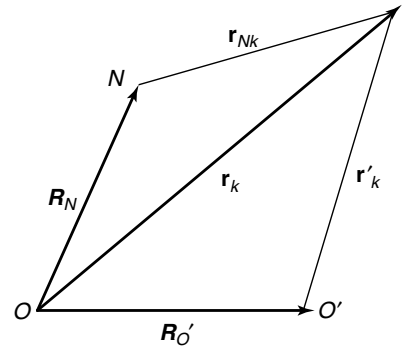


Figure 5.2. Coordinate system used to illustrate the gauge origin dependence of the diamagnetic and paramagnetic contributions of the magnetic shielding. O is the origin of coordinates, O' is the new origin of coordinates, $\boldsymbol{R}_{O'}$ is the position of the new origin of coordinates with respect to the original one, $\boldsymbol{R}_N$ is the position of the nucleus N, $\boldsymbol{r}_k$ is the position of the electron with respect to O, $\boldsymbol{r}_{Nk}$ is the position of the electron with respect to the nucleus N, and $\boldsymbol{r}'_k$ is the position of the electron relative to the new origin of coordinates O'.

$$H_\alpha^{(0,1)} = \frac{-\mathrm{i}}{c}\sum_k \frac{L_{Nk_\alpha}}{r_{Nk}^3} = \frac{-\mathrm{i}}{2c}\sum_k \frac{(\boldsymbol{r}_{Nk} \times \nabla_k)_\alpha}{r_{Nk}^3} \qquad (5.7)$$

$$H_{\alpha\beta}^{(1,1)} = \frac{1}{c^2}\sum_k \frac{(\boldsymbol{r}_k \cdot \boldsymbol{r}_{Nk}\delta_{\alpha\beta} - r_{k_\alpha} \cdot r_{Nk_\beta})}{r_{Nk}^3} \qquad (5.8)$$

If we restrict our analysis to closed-shell molecules, for which the electronic ground state is of the $\boldsymbol{\Sigma}$ type, $H^{(1,0)}$ and $H^{(0,1)}$ have zero contribution to the energy using first-order Raleigh–Schrödinger (RS) perturbation theory. This leaves no terms of order $1/c$ contributing to the magnetic shielding. The third term, $H^{(1,1)}$, gives a nonzero contribution using first-order RS perturbation theory, which is proportional to $1/c^2$. A second contribution of order $1/c^2$ can be obtained, at second order, from the cross term between $H^{(1,0)}$ and $H^{(0,1)}$. Using the definition of magnetic shielding given by equation (5.2), we can identify the diamagnetic and paramagnetic contributions to the magnetic shielding as these two first- and second-order terms in the RS perturbation expansion. The final expressions for the diamagnetic and paramagnetic contributions in the Coulomb

gauge are given by

$$\sigma^{\mathrm{d}}_{\alpha\beta}(O) = \frac{1}{2c^2}\left\langle \psi_0 | (\boldsymbol{r}_k \cdot \boldsymbol{r}_{Nk}\delta_{\alpha\beta} - r_{k_\alpha} r_{Nk_\beta}) r_{Nk}^{-3} | \psi_0 \right\rangle \tag{5.9}$$

$$\sigma^{\mathrm{p}}_{\alpha\beta}(O) = \frac{-1}{2c^2} \sum_n \frac{1}{E_n - E_0} \times \left\langle \psi_0 | \boldsymbol{L}_{k_\alpha} | \psi_n \right\rangle \langle \psi_n | \boldsymbol{L}_{Nk_\beta} r_{Nk}^{-3} | \psi_0 \rangle + \mathrm{C.C.} \tag{5.10}$$

We have thus indicated explicitly that equations (5.9) and (5.10) are valid when the origin of the vector potential is at the position O. The sum in equation (5.10) is over all the excited states of the molecule. Before discussing the methods available for the practical evaluation of equations (5.9) and (5.10), it is important to understand the behavior of the diamagnetic and paramagnetic terms under a translation of the origin of coordinates. Both the terms, as shown by equations (5.9) and (5.10), exhibit an explicit dependence on the origin of coordinates used in the calculations. For exact and variational wave functions in a complete space, these dependences cancel each other making the total magnetic shielding independent of the origin of coordinates.[14,17,18] Unfortunately, this is not true for a finite expansion of the wave function and serious complications arise in magnetic shielding calculations as a consequence of the imperfect cancellation of origin-dependent terms in the diamagnetic and paramagnetic components.

Several methods have been proposed to mitigate the gauge problems, to make the results formally gauge invariant for incomplete basis sets and to produce better results when using moderate size basis sets. The most common approach is to use the London or gauge invariant (or including) atomic orbitals (GIAOs), in the atomic expansion of the molecular orbitals.[21,24,25] Other popular methods are as follows: individual gauge for localized orbitals (IGLO),[34,35,43] localized orbitals local origin (LORG),[28,44] individual gauges for atoms in molecules (IGAIM),[45] and continuous gauge transformation (CSGT).[46] While the methods mentioned above take different approaches to mitigate the gauge problem, all of them are exact and converge to the same magnetic shielding values in the limit of very large basis.[37] Of course, the converged values are identical to those obtained with the common origin method when the same extended basis is used in the calculations. However, more important for practical applications is that these methods produce better results when using modest basis sets.[15,47]

5.4 CALCULATIONS OF MAGNETIC SHIELDING

Today there are two major approaches to the calculation of the magnetic shielding, which are based on the two predominant types of electronic structure methods in use: those based on Hartree–Fock theory and its systematic improvements using perturbation methods to include the electronic correlation,[42] which will be labeled "traditional ab initio methods" and those based on density functional theory (DFT).[48] The reader is referred to the recent reviews by Gauss and Stanton[49] and Wilson[50] for update comprehensive reviews of these two complementary methodologies. For accurate calculations of magnetic shieldings the first approach is preferred because it provides a systematic path to improve the calculated results; however, this systematic improvement arrives with a considerable increase in the computational cost of the calculations. Therefore, in practice highly precise calculations of magnetic shielding using traditional ab initio methods are restricted to small molecules of relatively minor interest to practicing chemists. The best calculations available using traditional ab initio methods for a representative set of small molecules with shieldings spanning over 1500 ppm show an agreement between theory and experiment with the observed standard deviation of 11.3 ppm, which corresponds to a relative error of 0.7%.[15,47] For medium size and large molecules the computational limitations of the traditional ab initio methods make calculations based on DFT, with their relatively low computational cost and increasingly improved performance, highly competitive. As a result, DFT methods have become the dominant approach for modeling chemical shifts for medium to large molecules. While DFT does not provide a systematic way to improve the results, recently introduced exchange correlation functionals designed to reproduce chemical shifts (KT1, KT2, and KT3)[51–54] give results that are comparable to those from the best electronic structure calculations. Even the greatly popular hybrid B3LYP functional has proven a very reliable and practical tool for chemical shift calculations.[15,47] DFT calculations can be used to calculate the chemical shifts in extraordinarily large molecular systems; for instance, using

linear scaling techniques a calculation including more than 1000 atoms has been reported[55] for *N*-methyl nicotinamide within a molecular guest-clip system, including the surrounding water molecules.

In spite of the success of the magnetic shielding calculations discussed above, there are several limitations in the current methods that should be considered. These limitations can be broadly divided as those inherent to the approximations used in the calculations and those due to the lack of knowledge of the molecular or crystalline structure.

In the first category, the greatest deficiency of the current methods is the neglect of relativistic corrections. This is of minor consequence when dealing with the molecules including first- or second-row atoms, but may become a significant problem when the molecule includes atoms beyond the third row of the periodic table. There is consistent evidence that the relativistic effects on magnetic shielding are significant for heavy atoms. For instance, these effects have been shown to range from 0.1% in He to 83% in Rn.[56] Unfortunately, their importance on chemical shifts, i.e., relative shieldings or their anisotropies, is not well documented. While there is a great deal of literature dealing with relativistic effects on magnetic shielding calculations, there are no well-established methods that can be used routinely. Moreover, the most common approximations to take into account these effects have not been implemented in the most popular software used for magnetic shielding calculations. Therefore, calculation of magnetic shielding in molecules containing heavy atoms remains mostly the realm of very specialized research groups;[57] however, this situation may change with the recent implementation of shielding calculations using the zeroth-order regular approximation (ZORA)[58,59] approach in the Amsterdam Density Functional (ADF) (http://www.scm.com/) package. Details of the recent advances in relativistic effects on magnetic shielding calculations have been presented in Vaara's recent review paper.[56]

The second methodological challenge in the calculation of NMR magnetic shielding is associated with the uncertainties in the molecular or crystalline geometry and the effects that the lattice may have on the NMR magnetic shielding. The first problem is a consequence of the great sensitivity of the magnetic shieldings to the molecular geometry, a fact that has been known for some time.[60,61] This sensitivity has been instrumental in using NMR chemical shift information to elucidate structural problems,[62] but at the same time it can lead to unacceptable large errors in the calculated magnetic shieldings due to the uncertainties in the position of hydrogen atoms determined by common structural methods such as X-ray diffraction. It has become common practice to optimize the position of the hydrogen atoms, determined by X-ray diffraction, before performing shielding calculations for molecular solids. This has been justified by the lack of accuracy in the determination of the position of hydrogens by standard X-ray crystallography techniques.[61] Unfortunately, the practice of using optimized or partially optimized structures to calculate NMR magnetic shieldings leads to significant questions about possible cancellation of errors between the method used to optimize the geometry and the one used to calculate the NMR magnetic shielding. It is conceivable that good agreement could be achieved due to the use of an optimized geometry that underestimates the interatomic bond distances, in conjunction with a method to calculate NMR magnetic shieldings that also underestimates the shielding or vice versa. Note that almost always the derivative of the magnetic shielding with respect to the interatomic bond distances is negative, $\partial\sigma/\partial r \leq 0$.[63] This situation has been discussed in the case of the calculations of the ^{15}N chemical shifts of $^{15}NO_2$ in aminonitropyridines, aminonitropyrimidines, and their *N*-oxides.[64] Zhang *et al*. have recently presented a comprehensive study of these issues at the popular B3LYP level of calculation.[65]

The inclusion of intermolecular effects in the calculation of magnetic shielding has attracted a great deal of attention over the years[12,20,38,66–68] but no "off the shelf" method is available to take into account these effects in solids. Unfortunately, in many cases the intermolecular interactions cannot be neglected without losing the quantitative agreement between experimental and calculated results, as shown in a recent comprehensive review on intermolecular effect on shielding.[69] In these situations, it is necessary to exercise care and complement the standard methods available to calculate magnetic shieldings with appropriate ways to take into account the intermolecular effects. The methods available to calculate solid-state effects can be classified into those that use the cluster models,[70] the electrostatic models,[71–76] and periodic boundary conditions.[77] Cluster models, which represent the solid-state effects by a finite number of neighboring molecules, are the least desirable because they greatly

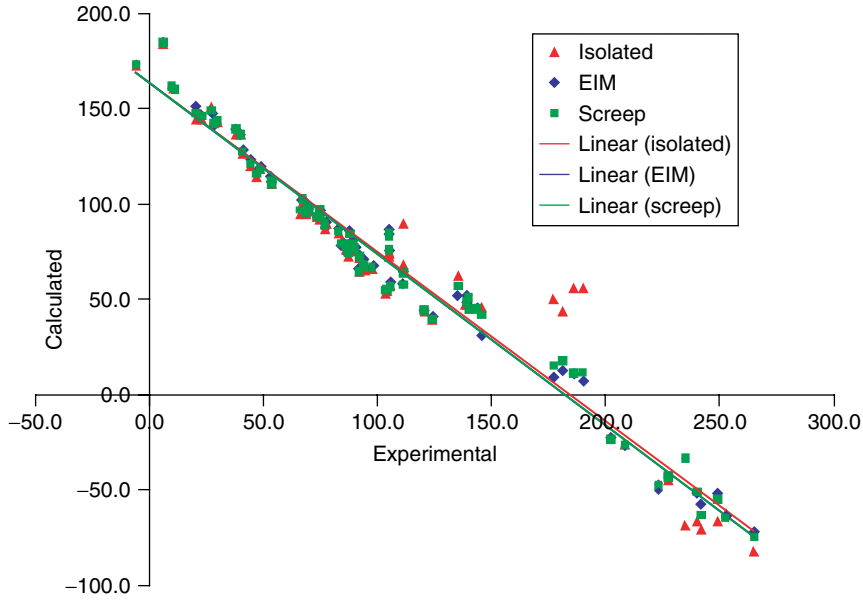


Figure 5.3. Correlation between ^{13}C experimental chemical shifts and the shieldings calculated for isolated molecules and including the intermolecular effects using two different electrostatic methods. The shieldings are in absolute part per million, i.e., referenced to the bare nucleus. The chemical shifts are in part per million referenced to TMS.[71] (Reproduced from Ref. 71. © Wiley, 2004.)

increase the size of the calculations and require an arbitrary definition of the molecules or fragments that are included in the calculation. Electrostatic models, which represent the environment by a finite charge distribution, are quite effective as they do not require significant additional computational resources. The success of these methods is well documented in a recent publication of our research group.[71] As depicted in Figure 5.3, these methods can be very effective when the intermolecular effects are dominated by electrostatic interactions but they fail when other effects are important.[78]

The periodic boundary conditions methods are certainly the most desirable because they include automatically all possible intermolecular effects. Recently two research groups have introduced theories and implemented programs for calculating magnetic shielding in periodic systems using DFT.[77] Sebastiani and coworkers have used the Carr-Parrinello Molecular Dynamics CPMD[79] code to implement the calculation of chemical shifts with periodic boundary conditions.[40,80–83] Mauri *et al.* have also developed the gauge-including projector augmented wave (GIPAW) method to calculate NMR magnetic shielding using periodic boundary conditions,[39,84–91] that has been implemented in the proprietary (NMR-)CASTEP code. Details of the latter method are given elsewhere in this Handbook (*see* **Chapters 3** and **7**). The use of these theories may make ad hoc methods unnecessary in the calculation of the intermolecular effects in crystalline solids, because such effects are intrinsically included in the calculations.

Nowadays the calculation of magnetic shielding can be performed routinely and they are reliable enough to assist in the elucidation of molecular and crystal structural problems. This is demonstrated in several related articles in this handbook on NMR crystallography.

REFERENCES

1. E. M. Purcell, *Phys. Rev.*, 1949, **76**, 1262.
2. H. L. Anderson, *Phys. Rev.*, 1949, **76**, 1460.
3. N. F. Ramsey, *Phys. Rev.*, 1950, **77**, 567.
4. N. F. Ramsey, *Phys. Rev.*, 1950, **78**, 699.

5. D. M. Grant, in *Encyclopedia of Nuclear Magnetic Resonance*, eds-in-chief D. M. Grant and R. K. Harris, Wiley & Sons: London, 1996, Vol. **2**, p 1298.
6. R. K. Harris, E. D. Becker, S. M. Cabral de Mendez, P. Granger, R. E. Hoffman, and K. W. Zilm, *Pure Appl. Chem.*, 2008, **80**, 59.
7. J. Mason, *Multinuclear NMR*, Plenum Press: New York, 1987.
8. I. Berini, C. Luchiant, and G. Parigu, *Solution NMR of Paramagnetic Molecules*, Elsevier: Amsterdam, 2001.
9. J. C. Facelli, A. M. Orendt, D. M. Grant, and J. Michl, *Chem. Phys. Lett.*, 1984, **112**, 147.
10. F. A. L. Anet and D. J. O'Leary, *Concepts Magn. Reson.*, 1991, **3**, 193.
11. A. D. Buckingham and S. M. Malm, *Mol. Phys.*, 1971, **22**, 1127.
12. C. J. Jameson and A. C. de Dios, in *Specialist Periodical Reports on Nuclear Magnetic Resonance*, eds G. A. Webb, Royal Society: London, 2004, Vol. **33**, 47.
13. G. A. Webb, in *Encyclopedia of Nuclear Magnetic Resonance*, eds-in-chief D. M. Grant and R. K. Harris, John Wiley & Sons: London, 1996, Vol. **7**, p 4307.
14. J. C. Facelli, in *Encyclopedia of Nuclear Magnetic Resonance*, eds-in-chief D. M. Grant and R. K. Harris, John Wiley & Sons: London, 2002, Vol. **9**, p 323.
15. J. C. Facelli, *Concepts Magn. Reson.*, 2004, **20A**, 42.
16. J. C. Facelli and A. C. De Dios (eds), *Proceedings of the Second International Symposium held at the 216th National Meeting of the American Chemical Society, August 23–26, 1998*, ACS Symposium Series: Boston, MA, 1999.
17. J. C. Facelli, in *Encyclopedia of Nuclear Magnetic Resonance*, eds-in-chief D. M. Grant and R. K. Harris, John Wiley & Sons: London, 1996, Vol. **7**, p 4299.
18. J. C. Facelli, in *Encyclopedia of Nuclear Magnetic Resonance*, eds-in-chief D. M. Grant and R. K. Harris, John Wiley & Sons: London, 1996, Vol. **7**, p 4327.
19. A. C. de Dios and C. J. Jameson, *Annu. Rep. NMR Spectrosc.*, 1994, **29**, 1.
20. A. C. de Dios and E. Oldfield, *Solid State Nucl. Magn. Reson.*, 1996, **6**, 101.
21. P. Pulay and J. F. Hinton, in *Encyclopedia of Nuclear Magnetic Resonance*, eds-in-chief D. M. Grant and R. K. Harris, John Wiley & Sons: London, 1996, Vol. **7**, p 4334.
22. P. Lazzeretti, M. Malagoli, and R. Zanasi, in *Encyclopedia of Nuclear Magnetic Resonance*, eds-in-chief D. M. Grant and R. K. Harris, John Wiley & Sons: London, 1996, Vol. **7**, p 4318.
23. M. Bühl, M. Kaupp, O. L. Malkina, and V. G. Malkin, *J. Comput. Chem.*, 1999, **20**, 91.
24. J. R. Cheeseman, G. W. Trucks, T. A. Keith, and M. J. Frisch, *J. Chem. Phys.*, 1996, **104**, 5497.
25. R. Ditchfield, *Mol. Phys.*, 1974, **27**, 789.
26. H. Fukui, *Prog. Nucl. Magn. Reson. Spectrosc.*, 1997, **31**, 317.
27. J. Geertsen, *Chem. Phys. Lett.*, 1991, **179**, 479.
28. A. E. Hansen and M. Bilde, in *Encyclopedia of Nuclear Magnetic Resonance*, eds-in-chief D. M. Grant and R. K. Harris, John Wiley & Sons: London, 1996, Vol. **7**, p 4292.
29. V. G. Malkin, O. L. Malkina, and D. R. Salahub, *Chem. Phys. Lett.*, 1994, **221**, 91.
30. V. G. Malkin, O. L. Malkina, L. A. Eriksson, and D. R. Salahub, in *Modern Density Functional Theory*, eds J. M. Seminario and P. Politzer, Elsevier Science: Amsterdam, 1995, Vol. **2**, 273.
31. D. B. Chesnut, *Annu. Rep. NMR Spectrosc.*, 1989, **21**, 51.
32. D. B. Chesnut, *Annu. Rep. NMR Spectrosc.*, 1994, **29**, 71.
33. D. B. Chesnut, in *Reviews in Computational Chemistry*, eds K. B. Lipkowitz and D. B. Boyd, VCH Publishers: New York, 1996 245, Vol. **8**, 245.
34. W. Kutzelnigg, U. Fleischer, and M. Schindler, *NMR Basic Princ. Prog.*, 1990, **23**, 165.
35. W. Kutzelnigg, U. Fleischer, and C. van Wüllen, in *Encyclopedia of Nuclear Magnetic Resonance*, eds-in-chief D. M. Grant and R. K. Harris, John Wiley & Sons: London, 1996, Vol. **7**, p 4284.
36. U. Fleischer, C. van Wüllen, and W. Kutzelnigg, in *Encyclopedia of Computational Chemistry*, eds P. von Ragué Schleyer, John Wiley & Sons: London, 1998, p 1827.
37. G. Schreckenbach, *Theor. Chim. Acta*, 2002, **108**, 246.
38. T. Helgaker, M. Jaszuński, and K. Ruud, *Chem. Rev.*, 1999, **99**, 293.
39. F. Mauri, B. G. Pfrommer, and S. G. Louie, *Phys. Rev. Lett.*, 1996, **77**, 5300.
40. D. Sebastiani, G. Goward, I. Schnell, and M. Parrinello, *Comp. Phys. Commun.*, 2002, **147**, 707.

41. M. Kaupp, M. Bühl, and V. Malkin, *Calculation of NMR and EPR Parameters. Theory and Applications*, Wiley-VCH: Weinheim, 2004.
42. J. Simons and J. Nichols, *Qunatum Mechanics in Chemistry*, Oxford University Press: New York, 1997.
43. W. Kutzelnigg, *Isr. J. Chem.*, 1980, **19**, 193.
44. J. C. Facelli, D. M. Grant, T. D. Bouman, and A. E. Hansen, *J. Comp. Chem.*, 1990, **11**, 32.
45. T. A. Keith and R. F. W. Bader, *Chem. Phys. Lett.*, 1992, **194**, 1.
46. T. A. Keith and R. F. W. Bader, *Chem. Phys. Lett.*, 1993, **210**, 223.
47. J. C. Facelli, in *Handbook of Modern NMR*, ed. G. A. Webb, Kluwer Academic Publishers: London, 2006.
48. R. G. Parr and W. Yang, *Density-Functional Theory of Atoms and Molecules*, Oxford University Press: Oxford, 1989.
49. J. Gauss and J. F. Stanton (eds) *Electron-correlated Approaches for Calculation of Chemical Shifts*, John Wiley & Sons, Inc., 2002.
50. P. J. Wilson, *Annu. Rep. NMR Spectrosc.*, 2003, **49**, 118.
51. T. W. Keal and D. J. Tozer, *J. Chem. Phys.*, 2003, **119**, 3015.
52. T. W. Keal and D. J. Tozer, *J. Chem. Phys.*, 2004, **121**, 5654.
53. T. W. Keal, D. J. Tozer, and T. Helgaker, *Chem. Phys. Lett.*, 2004, **391**, 374.
54. M. J. Allen, T. W. Keal, and D. J. Tozer, *Chem. Phys. Lett.*, 2003, **380**, 70.
55. J. K. F. K. Christian Ochsenfeld, *Angew. Chem., Int. Ed. Engl.*, 2004, **43**, 4485.
56. J. Vaara, *Phys. Chem. Chem. Phys.*, 2007, **9**, 5399.
57. J. I. Melo, M. C. Ruiz de Azua, C. G. Giribet, G. A. Aucar, and R. H. Romero, *J. Chem. Phys.*, 2003, **118**, 471.
58. J. Autschbach and T. Ziegler, in *Encyclopedia of Nuclear Magnetic Resonance*, eds-in-chief D. M. Grant and R. K. Harris, John Wiley & Sons: London, 2002, Vol. **9**, 306.
59. J. Autschbach, in *Principles and Applications of Density Functional Theory in Inorganic Chemistry*, eds N. Kaltsoyannis and J. E. McGrady, Springer-Verlag GmbH: Berlin, 2004, Vol. **112**, p 1.
60. J. C. Facelli and D. M. Grant, *Nature*, 1993, **365**, 325.
61. D. M. Grant, F. Liu, R. J. Iuliucci, C. G. Phung, J. C. Facelli, and D. W. Alderman, *Acta Crystall.*, 1995, **B51**, 540.
62. J. K. Harper, J. C. Facelli, D. H. Barich, G. McGeorge, A. E. Mulgrew, and D. M. Grant, *J. Am. Chem. Soc.*, 2002, **124**, 10589.
63. C. J. Jameson and H. J. Osten, *Annu. Rep. NMR Spectrosc.*, 1986, **17**, 1.
64. K. L. Anderson, L. H. Merwin, W. S. Wilson, and J. C. Facelli, *Int. J. Mol. Sci.*, 2002, **3**, 858.
65. Y. Zhang, A. Wu, X. Xu, and Y. Yan, *J. Phys. Chem.*, 2007, **111**, 9431.
66. C. J. Jameson, A. K. Jameson, H. Parker, S. M. Cohen, and C.-L. Lee, *J. Chem. Phys.*, 1978, **68**, 2861.
67. N. A. Besley and J. D. Hirst, *J. Am. Chem. Soc.*, 1999, **121**, 8559.
68. S. Chalmet and M. F. Ruiz-Lopez, *J. Chem. Phys.*, 1999, **111**, 1117.
69. A. M. Orendt and J. C. Facelli, *Annu. Rep. NMR Spectrosc.*, 2007, **62**, 115.
70. J. C. Facelli, R. J. Pugmire, and D. M. Grant, *J. Am. Chem. Soc.*, 1996, **118**, 5488.
71. N. Di Fiori, A. M. Orendt, M. C. Caputo, M. B. Ferraro, and J. C. Facelli, *Magn. Reson. Chem.*, 2004, **42**, S41.
72. D. M. Schneider, M. C. Caputo, M. B. Ferraro, and J. C. Facelli, *Int. J. Mol. Sci.*, 2000, **1**, 75.
73. D. Solis and M. B. Ferraro, *Theor. Chem. Acc.*, 2000, **104**, 323.
74. D. Solis, M. B. Ferraro, and J. C. Facelli, *J. Mol. Struct.*, 2002, **602-603**, 159.
75. D. Stueber, F. N. Guenneau, and D. M. Grant, *J. Chem. Phys.*, 2001, **114**, 9236.
76. D. Stueber, A. M. Orendt, J. C. Facelli, R. W. Parry, and D. M. Grant, *Solid State Nucl. Magn. Reson.*, 2002, **22**, 29.
77. C. J. Pickard and F. Mauri, in *Calculation of NMR and EPR Parameters*, ed. M. Kaupp, M. Bühl and V. G. Malkin, Wiley-VCH Verlag GmbH & Co. KGaA, Weinhein, 2004.
78. A. M. Orendt, J. C. Facelli, and D. M. Grant, *Chem. Phys. Lett.*, 1999, **302**, 499.
79. M. Parrinello and W. Andreoni, CPMD V3.9, http://www.cpmd.org/. Copyright IBM Corp 1990-2006, Copyright MPI fuer Festkoerperforschung Stuttgart, 1997–2001.

80. J. Schmidt, A. Hoffmann, H. W. Spiess, and D. Sebastiani, *J. Phys. Chem.*, 2006, **110**, 23204.

81. D. Sebastiani, *Chem. Phys. Chem. Phys.*, 2006, **7**, 164.

82. D. Sebastiani, G. Goward, I. Schnell, and H. W. Spiess, *J. Mol. Struct.*, 2003, **625**, 283.

83. D. Sebastiani and U. Rothlisberger, *J. Phys. Chem.*, 2004, **108**, 2807.

84. M. Benoit, M. Profeta, F. Mauri, C. J. Pickard, and M. E. Tuckerman, *J. Phys. Chem.*, 2005, **109**, 6052.

85. F. Buda, P. Giannozzi, and F. Mauri, *J. Phys. Chem.*, 2000, **104**, 9048.

86. C. Gervais, R. Dupree, K. J. Pike, C. Bonhomme, M. Profeta, C. J. Pickard, and F. Mauri, *J. Phys. Chem.*, 2005, **109**, 6960.

87. C. Gervais, M. Profeta, F. Babonneau, C. J. Pickard, and F. Mauri, *J. Phys. Chem.*, 2004, **108**, 13249.

88. C. Gervais, M. Profeta, V. Lafond, C. Bonhomme, T. Azais, H. Mutin, C. J. Pickard, F. Mauri, and F. Babonneau, *Magn. Reson. Chem.*, 2004, **42**, 445.

89. T. Gregor, F. Mauri, and R. Car, *J. Chem. Phys.*, 1999, **111**, 1815.

90. C. J. Pickard and F. Mauri, *Phys. Rev. B*, 2001, **63**, 245101.

91. M. Profeta, M. Benoit, F. Mauri, and C. J. Pickard, *J. Am. Chem. Soc.*, 2004, **126**, 12628.

Chapter 6
Symmetry Effects at the Local Level

Matthias Bechmann and Angelika Sebald

Department of Chemistry, University of York, Heslington YO10 5DD, UK

6.1	Introduction	63
6.2	Spin Systems and Interactions	63
6.3	Magnetic Shielding Tensors in Single Crystals	67
6.4	Magnetic Shielding Tensors in Polycrystalline Powders	72
6.5	Summary and Miscellaneous	77
	References	78

6.1 INTRODUCTION

This article outlines the general behavior patterns of nuclear spin systems in solid materials. The basic rules about, and the differences between, spin systems in solution- and solid-state NMR are explained. The various solid-state NMR spin-system circumstances will be examined step by step, starting with the NMR properties of spin systems in oriented single crystals. The same set of circumstances will be revisited for polycrystalline powder samples, both for stationary samples and for samples under magic-angle spinning (MAS) conditions. Finally, a brief summary is given, including some comments on various topics omitted from the main discussion for the sake of clarity. With one exception of a "real world" example for illustration, our entire discussion is, in general terms, aiming to illustrate the principles rather than focusing on particular cases. Also, RF pulse sequences and how their properties relate to the properties of spin systems are almost entirely excluded from our discussion. We trust, however, that many exciting applications and aspects of the general principles outlined in this article will be found in the numerous contributions to this Handbook.

NMR Crystallography Edited by Robin K. Harris, Roderick E. Wasylishen and Melinda J. Duer © 2009 John Wiley & Sons, Ltd. ISBN: 978-0-470-69961-4

6.2 SPIN SYSTEMS AND INTERACTIONS

6.2.1 Spin Systems and Interactions in Standard Solution-state NMR

Symmetry governs the appearance and properties of all NMR spectra. Let us first briefly consider the standard situation in solution-state NMR, ignoring more complicated cases such as partial alignment of molecules or relaxation mechanisms. The standard situation typically deals with (relatively) small molecules dissolved in nonviscous liquids, accompanied by rapid isotropic tumbling and translational motion of the molecules in solution. In the absence of steric hindrance effects, in this scenario molecules will tend to assume, on average, the highest possible molecular symmetry. We consider molecules as finite three-dimensional objects. The appropriate mathematical tool to describe the symmetry properties of finite objects is represented by the symmetry point groups. There is an infinitely large number of such symmetry groups but, obviously, only a finite number of these will be of practical importance. The

name *point group symmetry* refers to the fact that all symmetry operations in these groups leave at least one point of the object unchanged and, hence, do not describe any translational properties. A direct consequence of molecular motion in solution is that in NMR we directly observe only the isotropic averages of the various anisotropic NMR interactions. In particular, when assessing spin systems in solution-state NMR, only isotropic magnetic shielding (or isotropic chemical shift) and isotropic indirect coupling (J coupling) need to be taken into account as these are the only two directly observable parameters. Presence or absence of equivalence by symmetry of atomic sites/nuclear spins in a molecule determines the number and the integrated intensity of resonance signals in NMR (the latter statement assuming suitable data acquisition). Two (or more) spins in a molecule are said to be *chemically equivalent* if their sites are related by a (point group) symmetry operation applicable to the entire molecule. Chemically equivalent spins have identical isotropic magnetic shielding values. After determination of the molecular point group symmetry and identification of sets of chemically equivalent spins in a molecule (if present), J coupling comes into play to identify *magnetically equivalent* spins. First of all, it is a necessary prerequisite for at least two sets of at least two chemically equivalent spins each to be present in a molecule in order to enable the presence of magnetic equivalence. Whether or not two spins are magnetically equivalent is determined by the symmetry of their J-coupling pathways with all members of another set of chemically equivalent spins in the molecule: if one member of one set of chemically equivalent spins has identical J-coupling pathways with *all* members of another set of chemically equivalent spins, then this is true (by symmetry) for all members of the set – and it applies to both sets of spins. If that is the case, then each set is composed of magnetically equivalent spins.

These two levels of equivalence by symmetry in solution-state NMR are, by convention, indicated by the so-called alphabet notation; more extended and elaborate descriptions and numerous examples can be found in many textbooks.[1] Operating with finite objects/molecules and just two NMR parameters, isotropic magnetic shielding and J coupling, the standard solution-state NMR situation provides a crisp and clear-cut recipe for the classification of spin systems. Also, it is quite straightforward to assign "typical" or "general" properties to the NMR spectra originating from different types of spin systems. As a general trend, spin systems involving sets of magnetically equivalent spins in conjunction with sizable differences of isotropic magnetic shielding values, produce simple, so-called first-order spectra ("what you see is what you get"). In contrast, the NMR spectra obtained for spin systems with similar isotropic magnetic shielding values and inequivalent J-coupling pathways give rise to more complicated NMR spectra in solution, which do not normally lend themselves to analysis "by inspection". It is fair to say that the meaning of the terms chemical and magnetic equivalence in solution-state NMR is generally accepted. It is also fair to say that, while the spin-system situation encountered in standard solution-state NMR is rather straightforward and surely accounts for the huge success of solution-state NMR in its role as a routine analytical tool (one of its many roles), the simplicity comes at a price: it wastes a fairly large part of the information carried by the anisotropic NMR interactions in principle. This brief encounter with spin systems in solution-state NMR may act as a reminder that the solution-state spin-system concept, based on just two scalar quantities, will require major adaption when dealing with solid matter.

6.2.2 Spin Systems and Interactions in Solid-state NMR

Moving on from the standard solution-state NMR scenario to solid-state NMR, of course, symmetry properties still rule. However, the overall situation is now quite different on two accounts: (i) the solid state is characterized by (much) reduced degrees of motion of molecules/particles, in particular, lack of translational motion, with all concomitant effects of the anisotropic NMR interactions not being reduced to their isotropic averages anymore; (ii) in the solid state, more often than not we will lose the "comfort zone" of being able to restrict ourselves to dealing solely with finite objects/molecules and will have to consider extended lattices instead. We now inspect these two points in more detail. Even before we start, it is obvious that the spin-system concepts in solid-state NMR will be significantly different from the solution-state NMR situation.

Crystalline solids are characterized by so-called long-range order, that is, periodicity in three-dimensional space.[2] We can imagine a crystalline solid as being built by arranging a large number of identical building blocks in

three-dimensional space by following certain building plans and by making sure that the construction results in a space-filling arrangement. Obviously, building an object in this way requires translation to be taken into account if we want to describe the symmetry properties of such an, in principle, infinitely large object. The appropriate mathematical tools for describing the symmetry properties of infinitely large objects are *lattices*. Given that we normally deal with very large numbers of molecules making up a macroscopic crystal, of the order of Avogadro's number, it is certainly a very good approximation if we use mathematical tools here for the description of infinite objects. Owing to the requirement of finding space-filling arrangements, there is only a finite number of lattices suitable to cover space completely. For instance, there are only five such plane lattice types in two-dimensional space. In three-dimensional space, there is also only a finite number of lattices that permit space-filling repetition of building blocks. These are the 14 Bravais lattices.[3] They are obtained by stacking the two-dimensional plane lattices on top of each other in different ways. With the lattices describing the translational symmetry properties of solids, we have not yet considered the contents of these fictional building blocks. These contents (sometimes referred to as *motifs*), for example, a molecule, come with their own set of symmetry properties and being (or taken as) a finite object, the basic contents of the building blocks are characterized by their point group symmetry properties as well as symmetry operations such as glide planes or screw axes that can be applied to the motifs but not the lattices – for the lattices have to retain their proper rotational (only one-, two-, three-, four-, and sixfold rotations are permitted) and reflection symmetries.[4] Take, for example, the N_2 molecule: one of the symmetry operations applicable to the molecule is a C_∞ rotation around the molecular axis – permitted as far as the motif in crystalline N_2 is concerned, but a noncrystallographic symmetry operation not in line with the symmetry restrictions on lattices. The full description of a three-dimensional structure requires both elements of point and space-group symmetries. As there is only a finite number of three-dimensional lattices, we end up with a finite number of so-called crystallographic space groups, of which there are 230.[5] The smallest unit necessary to generate the entire three-dimensional structure from a set of symmetry operations is commonly called the *asymmetric unit*. This could be an entire molecule, or half a molecule, or just a small section of an otherwise infinitely large arrangement of ions in an inorganic solid. By and large, it is the asymmetric unit that is probed by solid-state NMR (except when direct-dipolar coupling is present; see below) as we are not able to detect translational symmetry in a homogeneous magnetic field. Because of this, the usage of the term *NMR crystallography* has been criticized – and this criticism is justified if we understand the term crystallography in the sense in which it is used in diffraction experiments. The signal generation and amplification in diffraction experiments primarily stems from the periodicity of the translationally repeated units, whereas the signal generation and amplification in NMR originates from the myriads of asymmetric units present in the sample. Even at this highly qualitative level, it is obvious that diffraction techniques and solid-state NMR are naturally geared to complement each other for purposes of structure determination. With diffraction techniques, in particular X-ray diffraction, being a very mature field for the study of structure, there are numerous textbooks and highly specialized monographs available dealing with the symmetry properties of crystalline matter at all levels.[6–8]

Solid materials lack the high degree of molecular motion present in nonviscous liquids. In terms of structure this usually means that in molecular crystals the molecular symmetry is lower than in solution. Although "solid" does not automatically imply "absolutely rigid", still the lack of rapid and isotropic molecular motion means that all *anisotropic* NMR interactions are present because of the lack of spatial averaging. These interactions include magnetic shielding (MS), direct dipolar coupling (D), indirect coupling (J), and quadrupolar coupling (Q). We mostly concentrate on magnetic shielding in the absence and presence of direct dipolar coupling and only briefly comment about the role of indirect dipolar coupling. Further, the discussion assumes that we deal with diamagnetic solids, and relaxation as well as magnetic susceptibility effects are ignored.

To start with, we briefly review several concepts and conventions necessary to describe the anisotropic NMR interactions themselves as well as relate these quantities to the NMR signals we observe. The anisotropic interactions $\lambda =$ MS, D, J are mathematically described by second-rank tensors $\boldsymbol{A}^\lambda$, and $\lambda =$ Q is represented by a fourth rank tensor.

The following conventions apply to the uniform treatment of all these anisotropic NMR interactions (later on it will become clear why it is necessary to have this unified approach).[9] The isotropic part $A^{\lambda}_{\mathrm{iso}}$, the anisotropy $A^{\lambda}_{\mathrm{aniso}}$, and the asymmetry parameter η^{λ} relate to the principal elements of the interaction tensor $\boldsymbol{A}^{\lambda}$ according to $A^{\lambda}_{\mathrm{iso}} = (A^{\lambda}_{xx}+A^{\lambda}_{yy}+A^{\lambda}_{zz})/3$; $A^{\lambda}_{\mathrm{aniso}} = A^{\lambda}_{zz} - A^{\lambda}_{\mathrm{iso}}$; and $\eta^{\lambda} = (A^{\lambda}_{yy}-A^{\lambda}_{xx})/A^{\lambda}_{\mathrm{aniso}}$ with $|A^{\lambda}_{zz} - A^{\lambda}_{\mathrm{iso}}| \geqslant |A^{\lambda}_{xx} - A^{\lambda}_{\mathrm{iso}}| \geqslant |A^{\lambda}_{yy} - A^{\lambda}_{\mathrm{iso}}|$. η^{λ} can assume values between 0 and 1. The interaction $\lambda =$ MS involves three quantities, the external magnetic field $\boldsymbol{B}_0$, the nuclear spin, and its electronic environment. The three-dimensional electronic surroundings of the nucleus modify the magnetic field experienced at the site of the nucleus according to $\boldsymbol{B}_{\mathrm{induced}} = \boldsymbol{A}^{\mathrm{MS}} \cdot \boldsymbol{B}_0$ (actually, the electrons shield the nuclei from the applied magnetic field; this is why we prefer to refer to this interaction as magnetic shielding rather than chemical shift). Both $\boldsymbol{B}_0$ and $\boldsymbol{B}_{\mathrm{induced}}$ are three-component vectors and these two quantities are related by the tensor

$$\boldsymbol{A}^{\mathrm{MS}} = \begin{pmatrix} A^{\mathrm{MS}}_{xx} & A^{\mathrm{MS}}_{xy} & A^{\mathrm{MS}}_{xz} \\ A^{\mathrm{MS}}_{yx} & A^{\mathrm{MS}}_{yy} & A^{\mathrm{MS}}_{yz} \\ A^{\mathrm{MS}}_{zx} & A^{\mathrm{MS}}_{zy} & A^{\mathrm{MS}}_{zz} \end{pmatrix}$$

$\boldsymbol{B}_{\mathrm{induced}}$ is not necessarily parallel to $\boldsymbol{B}_0$ except for three special directions. These are the so-called principal axes of the magnetic shielding tensor, $\{A^{\mathrm{MS}}_{xx}, A^{\mathrm{MS}}_{yy}, A^{\mathrm{MS}}_{zz}\}$. Figure 6.1 illustrates how these special directions relate to different orientations in $\boldsymbol{B}_0$. Assignment of the principal axes is always such that the direction of its z-axis corresponds to the principal value, A^{MS}_{zz}, furthest away from $A^{\mathrm{MS}}_{\mathrm{iso}}$, whereas its y-axis corresponds to the principal value, A^{MS}_{yy}, closest to $A^{\mathrm{MS}}_{\mathrm{iso}}$. The isotropic part $A^{\mathrm{MS}}_{\mathrm{iso}}$ of the magnetic shielding tensor is the same as the quantity "isotropic chemical shift" (allowing for a change of sign) observed in solution-state NMR. Together, the anisotropy $A^{\mathrm{MS}}_{\mathrm{aniso}}$ and the asymmetry parameter η^{MS} describe the shape of the magnetic shielding tensor $\boldsymbol{A}^{\mathrm{MS}}$. Different tensors $\boldsymbol{A}^{\mathrm{MS}}$ usually display different principal axes systems.

Nuclei with spin $S > 1/2$ experience an electric interaction with surrounding electric fields, which gives rise to the quadrupolar-coupling interaction Q. What has been said earlier about the properties of $\boldsymbol{A}^{\mathrm{MS}}$ equally applies to the tensor $\boldsymbol{A}^{\mathrm{Q}}$.

Both interactions $\lambda =$ D, J represent magnetic interactions between nuclear spins. Direct dipolar coupling D is a direct through-space interaction. Its interaction tensor $\boldsymbol{A}^{\mathrm{D}}$ is characterized by $\eta^{\mathrm{D}} = 0$ (an axially symmetric tensor), $A^{\mathrm{D}}_{\mathrm{iso}} = 0$ (hence not directly observable in solution-state NMR), and the anisotropy is better known as the dipolar coupling constant $b_{12} = A^{\mathrm{D}}_{\mathrm{aniso}} = -\mu_0\gamma_1\gamma_2\hbar/(4\pi r^3_{12})$ where 1, 2 refers to the two nuclear spins coupled to each other, γ_1, γ_2 are the respective magnetogyric ratios and r is the internuclear distance between spins 1 and 2. The line connecting spins 1 and 2 coincides with the direction of the unique component $\boldsymbol{A}^{\mathrm{D}}_{zz}$ of the dipolar coupling tensor. $\boldsymbol{A}^{\mathrm{D}}$ provides direct and model-free quantitative structural information in the form of internuclear distances. The indirect dipolar coupling interaction $\lambda =$ J is a so-called through-bond interaction, mediated by the shared electrons in chemical bonds between two coupled spins. The tensor $\boldsymbol{A}^{\mathrm{J}}$ is characterized by a nonvanishing isotropic value $A^{\mathrm{J}}_{\mathrm{iso}}$, identical with the quantity "J coupling" commonly observed in solution-state NMR. The shape of the tensor A^{J} is *not* necessarily axially symmetric, and its anisotropy is often very difficult or impossible to distinguish from simultaneous direct dipolar coupling contributions.

We apply a uniform recipe to specify the mutual orientations of the NMR interaction tensors, similar in spirit to the uniform description of the shapes of the various NMR interaction tensors, and to "walk" through the various different principal axes systems

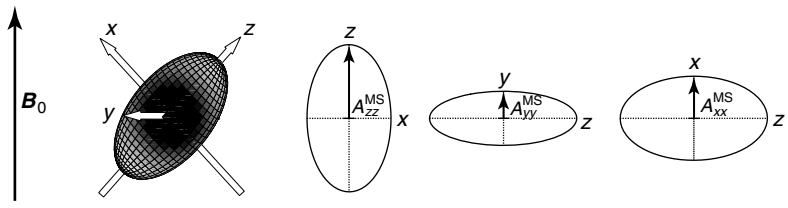


Figure 6.1. Ellipsoid representing $\boldsymbol{A}^{\mathrm{MS}}$ in a general orientation in frame L; also shown are the projections of the three special orientations of $\boldsymbol{A}^{\mathrm{MS}}$ for which $\boldsymbol{B}_0$ is parallel to the directions of the three principal axes, $\{A^{\mathrm{MS}}_{xx}, A^{\mathrm{MS}}_{yy}, A^{\mathrm{MS}}_{zz}\}$ of $\boldsymbol{A}^{\mathrm{MS}}$.

involved in solid-state NMR. The tools employed here are sets of Euler angles, $\Omega^{\lambda}_{\mathrm{FF}'} = \{\alpha^{\lambda}_{\mathrm{FF}'}, \beta^{\lambda}_{\mathrm{FF}'}, \gamma^{\lambda}_{\mathrm{FF}'}\}$ where F and F′ refer to a starting principal axes frame (F) and a target principal axes frame (F′).[10] Figure 6.2 illustrates the procedure. The three necessary successive rotations are (i) a rotation α around the z-axis of frame F, (ii) a rotation β around the y_*-axis of the new (temporary) frame resulting from the α rotation, (iii) a rotation γ around the z_{**}-axis of the frame resulting from the β rotation to arrive at the target frame F′. Not only do we have to deal with several anisotropic NMR interactions, each of which comes with its own principal axes frame, we also need to employ several more frames of reference to get us from the principal axes frame of an NMR interaction tensor to start with, all the way to the NMR signal we observe. This whole journey employs successive sets of Euler rotations $\Omega^{\lambda}_{\mathrm{FF}'}$. We encounter the following frames: P^{λ}, the principal axes frame of the interaction tensor $\boldsymbol{A}^{\lambda}$ (in particular, with $\lambda = \mathrm{MS}$, D); molecular and/or crystal frames of reference, M and C respectively (in solid-state NMR, these frames, depending on the sample/spin system, can often by defined in the most convenient way and it is often the case that a particular frame P^{D} can serve as a crystal/molecular "frame of choice"); the laboratory frame of reference, L (where we observe our NMR signals, the z-direction of which is the direction of the $\boldsymbol{B}_0$ vector). Finally, when using MAS techniques (see below), we need yet another frame of reference, the rotor frame R. Its z-axis is along the axis of the sample holder. The angle subtended between this z-axis and the z-direction of the $\boldsymbol{B}_0$ vector is the "magic angle" $\beta_{\mathrm{RL}} = 54.74^{\circ}$ when using MAS. The frame R is different from the other frames of reference in that it is time dependent due to the rotation of the rotor, yielding $\alpha_{\mathrm{RL}} = -\omega_{\mathrm{r}} t$ where ω_{r} is the spinning frequency in rad s^{-1}. Accordingly, $\Omega_{\mathrm{RL}}(t) = \{-\omega_{\mathrm{r}} t, \beta_{\mathrm{RL}}, 0\}$ under MAS conditions. Figure 6.3 presents an overview of the multitude and the hierarchies of the frames of references encountered in solid-state NMR.

We are now equipped with all the definitions and concepts necessary to explore the behavior of different spin systems in a range of solid-state NMR circumstances. We first consider oriented single crystals, and then move on and revisit the same set of spin systems in stationary polycrystalline powder samples, followed by examination of the situation for polycrystalline powder samples under MAS conditions.

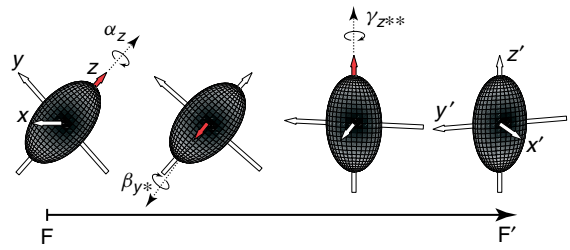


Figure 6.2. The successive Euler rotations $\Omega^{\lambda}_{\mathrm{FF}'} = \{\alpha^{\lambda}_{\mathrm{FF}'}, \beta^{\lambda}_{\mathrm{FF}'}, \gamma^{\lambda}_{\mathrm{FF}'}\}$ for the transformation from frame F to frame F′.

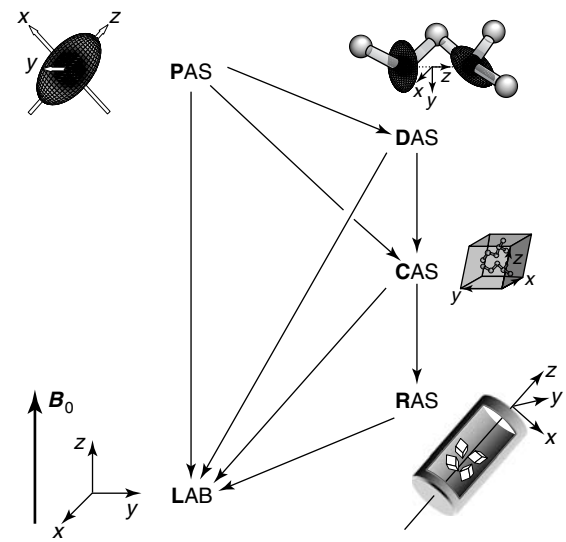


Figure 6.3. The complete chain of frames of reference encountered in solid-state NMR. Depending on circumstances, some steps may be omitted. For NMR experiments on polycrystalline powder samples, often a conveniently defined frame D can act as a (pseudo) frame of reference C.

6.3 MAGNETIC SHIELDING TENSORS IN SINGLE CRYSTALS

6.3.1 Only Magnetic Shielding Present

If magnetic shielding is the only anisotropic NMR interaction present, this leaves us with several specific situations regarding shape and orientation of the MS tensor.[11,12] The chain of frame transformations here only requires three steps, from $\mathrm{P}^{\mathrm{MS}} \rightarrow \mathrm{C} \rightarrow \mathrm{L}$

(see Figure 6.3). There are several different cases as follows:

1. There is only a single spin in the asymmetric unit, experiencing magnetic shielding anisotropy. In the general case, the MS tensor $\boldsymbol{A}^{\mathrm{MS}}$ has no particular alignment with respect to the symmetry elements of the unit cell. The NMR spectrum consists of a single peak for a given orientation of the crystal. The resonance position in the spectrum (resonance frequency) depends on the orientation of $\boldsymbol{A}^{\mathrm{MS}}$ with respect to $\boldsymbol{B}_0$. Variation of the crystal orientation varies the orientation of $\boldsymbol{A}^{\mathrm{MS}}$ in L and, therefore, causes the position of the resonance line to shift. Orienting the crystallographic axes system C of the single crystal in the laboratory frame L of the NMR experiment makes it possible to assign a specific resonance frequency to a particular crystal orientation. An array of experiments, executing NMR measurements at various different crystal orientations, then makes it possible to completely map the shape *and* orientation of $\boldsymbol{A}^{\mathrm{MS}}$ with respect to the crystallographic axes system[9] (see Figure 6.4). This general situation does not impose any restrictions on either shape or orientation of A^{MS}.
2. There is only a single spin in the asymmetric unit but now its location exhibits special site symmetry. As before, for each orientation of the crystal in the L frame, one sharp resonance is observed and its position varies with the orientation of the crystal in L, as before. However, now the properties of $\boldsymbol{A}^{\mathrm{MS}}$ have to reflect the site symmetry, and depending on the site symmetry there will be constraints on the shape and/or orientation of $\boldsymbol{A}^{\mathrm{MS}}$. A MS tensor sitting on an n-fold proper rotation axis C_n with $n = 3, 4, 6$ has to have the direction of its largest value principal axis, $\left|A_{zz}^{\mathrm{MS}}\right|$, oriented along the C_n axis. In addition, $\boldsymbol{A}^{\mathrm{MS}}$ has to display rotational symmetry around this axis, enforcing $\eta^{\mathrm{MS}} = 0$. For a twofold rotation axis, C_2, the direction of one of the three principal axes of $\boldsymbol{A}^{\mathrm{MS}}$ (not necessarily $\left|A_{zz}^{\mathrm{MS}}\right|$, though) needs to be oriented along the C_2 axis, but there are no restrictions on the shape of the tensor. For an MS tensor located on a mirror plane σ, its orientation has to be such that the directions of two of its principal axes lie in the symmetry plane and, hence, the direction of the third tensor component needs to be perpendicular to that plane. The shape of the tensor can be arbitrary. For spins residing on an inversion center i, no constraints are imposed on the shape or orientation of $\boldsymbol{A}^{\mathrm{MS}}$ since MS tensors themselves are invariant under inversion transformations. Constraints imposed by n-fold improper rotation axes S_n with $n = 3, 4, 6$ are identical to the constraints imposed by the corresponding proper rotation operations C_n, enforcing a prolate shape ($\eta^{\mathrm{MS}} = 0$) of the MS tensor with the direction of its component $\left|A_{zz}^{\mathrm{MS}}\right|$ aligned with the direction of the S_n axis. A twofold improper rotation axis S_2 enforces no constraints on the shape or orientation of an MS tensor: S_2 is equivalent to the symmetry operation of a center of inversion.
3. A very special situation is encountered if $\boldsymbol{A}^{\mathrm{MS}}$ is located on a site of cubic symmetry. Just as cubic crystals displaying isotropic optical properties, A^{MS} on a site of cubic symmetry is isotropic and the corresponding resonance position in NMR spectra will be independent of the orientation of the crystal in frame L. In practice, this is a rather rare condition.
4. We also have to consider the situation where there is more than one spin species present. If all of these are independent of each other (that is, not related by symmetry to each other), then the corresponding MS tensors will each follow their own, site-specific behavior as explained earlier for single spins experiencing magnetic shielding anisotropy. For an arbitrary orientation of the single crystal in L, there will be as many individual sharp resonances in the NMR spectrum as there are independent sites, and each of these resonances will individually trace their orientation-dependent MS pattern as one records spectra for an array of orientations of the single crystal. Finally, we can also encounter a situation where MS tensors are related *to each other* by a symmetry operation. If two MS tensors are related to each other by inversion symmetry, then the shape *and* orientation of these two tensors have to be identical. As long as these two MS tensors reside on locations without special site symmetries, their mutual relationship does not impose any restrictions as to what these tensorial properties are (shape and orientation in frame C). If we record single-crystal NMR spectra for different crystal orientations, this pair of MS tensors will only give rise to one resonance for each crystal orientation, tracing the identical shape and orientation of both tensors. (Two tensors $\boldsymbol{A}^{\mathrm{MS}}$ related by inversion symmetry are

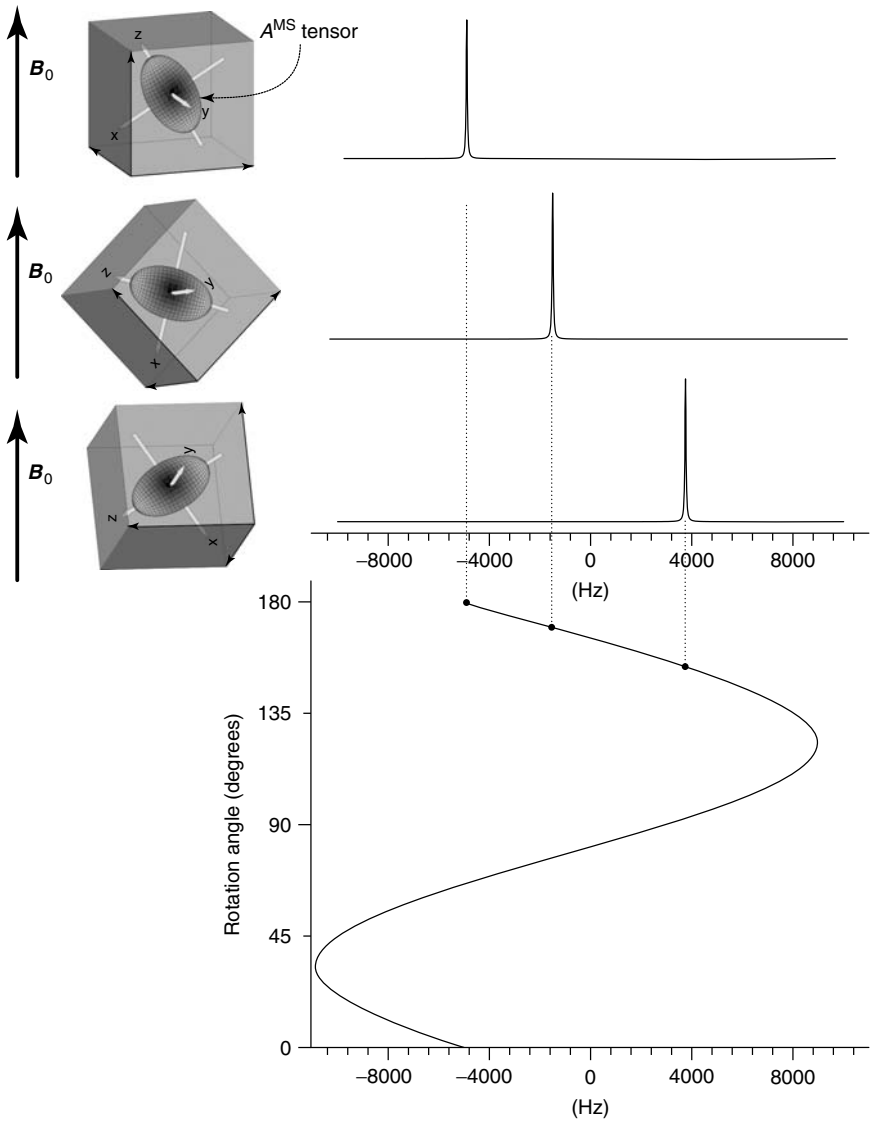


Figure 6.4. Sketch of the effect of varying the orientation of a single crystal in frame L on the NMR spectrum of a single tensor $\boldsymbol{A}^{\mathrm{MS}}$.

called "magnetically equivalent" by Haeberlen in Ref. 9, in a different sense from the meaning of the term magnetic equivalence when used in solution-state NMR). The situation is slightly different if two MS tensors are related to each other by either a twofold axis of rotation or by a mirror plane. These conditions require the shapes of the two MS tensors to be identical and they impose restrictions on the possible *mutual* orientations of the tensors (this point is discussed later) but do not necessarily impose any other restrictions as to the allowed shape of the two MS tensors. In the crystal environment, the mutual symmetry relationship obeyed by these two MS tensors, however, leads them to have nonidentical orientations in frame C. If we record single-crystal NMR spectra for such pairs of MS tensors, we will observe two resonances for arbitrary crystal

orientations in frame L, and the two rotation patterns obtained from recording NMR spectra of a full set of crystal orientations will yield identical values A_{iso}^{MS} and A_{aniso}^{MS} for these two MS tensors.

5. For nuclei with $S > 1/2$, the above-discussed points about symmetry constraints on the shape and orientation of the MS tensor equally apply to the quadrupolar-coupling tensor $\boldsymbol{A}^{Q}$. In the absence of symmetry constraints (scenario 1), the two tensors $\boldsymbol{A}^{MS}$ and $\boldsymbol{A}^{Q}$ associated with one spin are independent of each other. In the presence of local symmetry constraints, both tensors $\boldsymbol{A}^{MS}$ and $\boldsymbol{A}^{Q}$ simultaneously need to conform to these constraints. In practice, often the magnitude of quadrupolar coupling greatly exceeds the magnitude of the remaining NMR interactions and thus strongly dominates the NMR properties of a given spin system. In consequence, solid-state NMR involving quadrupolar nuclei is predominantly concerned with the spectroscopy of isolated spins. This is in contrast to the situation for spin systems composed of nuclei with $S = 1/2$, where the simultaneous presence of magnetic shielding and dipolar coupling interactions is a very common situation. Accordingly, the following discussion focuses on spin systems composed of nuclei with $S = 1/2$.

6.3.2 Magnetic Shielding and Dipolar Coupling Present

By adding direct dipolar coupling D to the scenario, we automatically have to consider more than one MS tensor. The chain of frame transformations now requires an additional step involving $P^{MS} \rightarrow P^{D} \rightarrow C \rightarrow L$ (see Figure 6.3). Direct dipolar coupling is neither restricted to *intramolecular* couplings nor does the coupling network stop at the boundaries of asymmetric units or unit cells. By its direct through-space nature, $\boldsymbol{A}^{D}$ essentially couples every spin with every other spin in the crystal. Depending on the density of the coupling network, we may have to see the single crystal as one strongly coupled entity of mutually coupled, very large numbers of nuclear spins. Fortunately, the r^{-3} dependence of the direct dipolar coupling constant b_{12} makes it a rather short-range interaction allowing often (but by no means always) for reasonable assumptions about the spatial isolation of spins and clusters of spins from each other. Importantly, it also opens a route to the tailor-made synthesis of samples containing isolated spin systems, for instance, by specific ^{13}C enrichment in combination with co-crystallization with unenriched material. For the sake of clarity, we assume the presence of isolated spin pairs in the following discussion. However, we would like to emphasize that "real-world" spin systems will often be far more complicated than this model situation.

Take an isolated homonuclear pair of spins dipolar coupled to each other, and further assume both spins to be identical and not to experience anisotropic magnetic shielding. Now the only orientation-dependent interaction is the dipolar coupling tensor $\boldsymbol{A}^{D}$. NMR spectra of this spin pair for a range of orientations of the single crystal in frame L give rise to two resonances for each crystal orientations (the so-called dipolar splitting). Figure 6.5 illustrates this case: upon changing the orientation of the single crystal (and thus changing the orientation of $\boldsymbol{A}^{D}$), the positions of the two resonances shift but always remain symmetric around the center of the spectrum (as $\eta^{D} = 0$). An array of NMR experiments for different orientations of the crystal in frame L maps the complete tensor $\boldsymbol{A}^{D}$. This type of spin system is assumed in the famous paper by Pake[13] in describing the ^{1}H NMR spectra of H_2O molecules in gypsum. Let us now assume that the two dipolar-coupled spins no longer have identical values A_{iso}^{MS} but still the only orientation-dependent interaction in the spin pair is $\boldsymbol{A}^{D}$. With a very large difference in values $A_{iso}^{MS_1}$ and $A_{iso}^{MS_2}$, this would represent a heteronuclear spin pair; for homonuclear spin pairs, this difference could be anything from very small to rather large. In either case, this inequality causes an additional splitting of the two resonances tracing $\boldsymbol{A}^{D}$, resulting in four peaks in the various NMR spectra of the oriented single crystal, but the splitting pattern remains symmetric around the center of the spectrum. Again, a complete set of single-crystal NMR spectra fully maps $\boldsymbol{A}^{D}$. If we break the symmetry of the spin system even further by allowing the two spins to experience anisotropic magnetic shielding, the symmetry of the distribution of the four peaks around the center of the spectrum is also lost. A complete set of NMR spectra recorded for many different orientations of the crystal in frame L now maps simultaneously and completely all three tensors, $\boldsymbol{A}^{D}$ as well as $\boldsymbol{A}^{MS_1}$ and $\boldsymbol{A}^{MS_2}$, which will, in general, have independent principal axes systems.

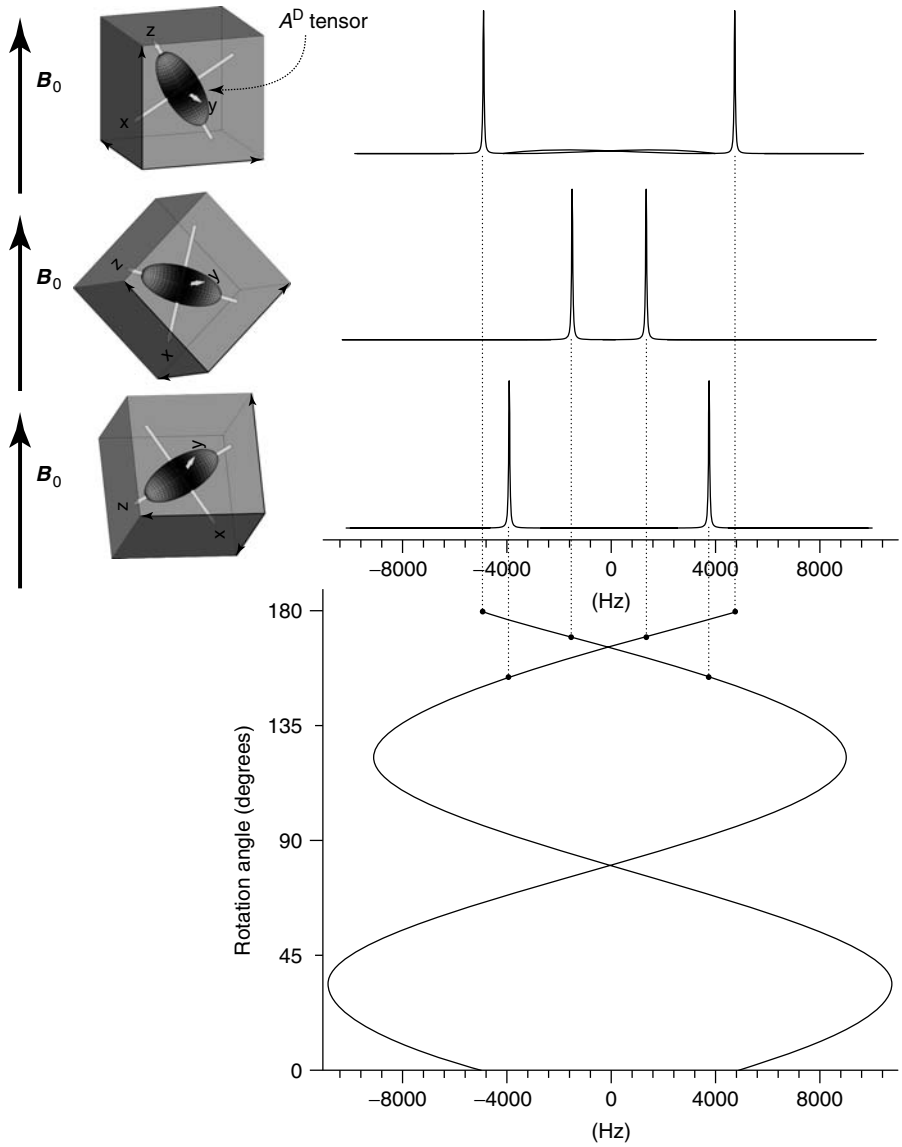


Figure 6.5. Sketch of the effect of varying the orientation of a single crystal in frame L on the NMR spectrum originating from the orientation dependence of the dipolar coupling tensor $\boldsymbol{A}^{\mathrm{D}}$ if the two coupled spins have identical values $A_{\mathrm{iso}}^{\mathrm{MS}}$ and there is no magnetic shielding anisotropy.

These different types of dipolar-coupled spin pairs can be observed regardless of whether the entire spin pair belongs to one asymmetric unit in the crystal structure or whether the two halves of the spin pair are located in two adjacent asymmetric units. In a more realistic application scenario (that is, in the absence of the knowledge of the crystal structure), it is hence not possible from NMR spectra alone to distinguish these two cases from each other. A "real-world" example in Figure 6.6 may help to illustrate the point. The mono-ammonium salt of maleic acid crystallizes in space-group *Pbcm*. Half of the maleate anion constitutes the asymmetric unit, with the two halves of the molecule being related by

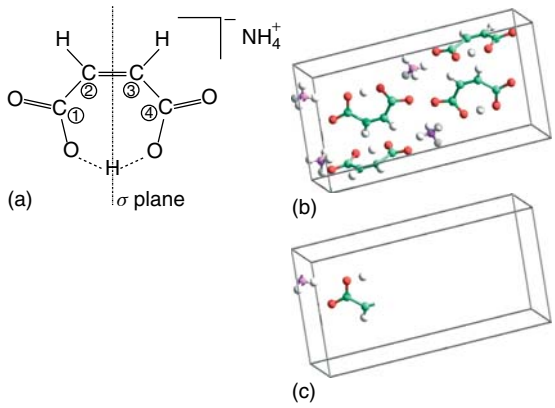


Figure 6.6. Sketch (a) of the molecular structure of mono-ammonium maleate, highlighting the symmetry plane σ; also shown (b) are the packing of molecular units in the crystallographic unit cell[14] and the asymmetric unit consisting of half a molecule (c).

symmetry (by a mirror plane perpendicular to the molecular plane).[14] Accordingly, homonuclear direct dipolar coupling between the ^{13}C MS tensors of the spin pairs 1/4 and 2/3 span across the border of the asymmetric unit, and each of the 1/4 and the 2/3 pairs of ^{13}C MS tensors in the maleate anion must, in addition, reflect their mutual symmetry relationship. In the previous section, assuming absence of direct dipolar coupling, we had characterized two such MS tensors related by symmetry as having identical shapes but different orientations, with some restrictions as to the possible mutual orientations. In the presence of $\boldsymbol{A}^{\mathrm{D}}$ and with the direction of its unique component $|A_{zz}^{\mathrm{D}_{23}}|$ (or, similarly $|A_{zz}^{\mathrm{D}_{14}}|$) perpendicular to the mirror plane, one can particularly conveniently see the orientational constraints on such a pair of MS tensors. The mirror plane requires for the $\mathrm{P}^{\mathrm{MS}} \rightarrow \mathrm{P}^{\mathrm{D}}$ transformation that $\alpha_{\mathrm{PD}}^{\mathrm{MS}_2} = -\alpha_{\mathrm{PD}}^{\mathrm{MS}_3}$, $\beta_{\mathrm{PD}}^{\mathrm{MS}_2} = -\beta_{\mathrm{PD}}^{\mathrm{MS}_3} + \pi$, $\gamma_{\mathrm{PD}}^{\mathrm{MS}_2} = \gamma_{\mathrm{PD}}^{\mathrm{MS}_3}$ for the mono-ammonium maleate ^{13}C spin system.[15] If two MS tensors $\boldsymbol{A}^{\mathrm{MS}_1}$ and $\boldsymbol{A}^{\mathrm{MS}_2}$ are related by a C_2 axis, their orientations relative to the principal axes frame of $\boldsymbol{A}^{\mathrm{D}}$ are $\alpha_{\mathrm{PD}}^{\mathrm{MS}_2} = \alpha_{\mathrm{PD}}^{\mathrm{MS}_1}$, $\beta_{\mathrm{PD}}^{\mathrm{MS}_2} = \beta_{\mathrm{PD}}^{\mathrm{MS}_1} + \pi$, $\gamma_{\mathrm{PD}}^{\mathrm{MS}_2} = -\gamma_{\mathrm{PD}}^{\mathrm{MS}_1} + \pi$.[16] Of course, a complete set of NMR spectra for different orientations of the single crystal in the frame L will fully characterize again all three interaction tensors present, and again a general orientation of the crystal will give rise to four resonances in the NMR spectrum.

6.4 MAGNETIC SHIELDING TENSORS IN POLYCRYSTALLINE POWDERS

We have seen that solid-state NMR experiments on oriented single crystals permit us to map directly and completely the shape and orientation of anisotropic NMR interactions. However, suitable single-crystalline materials are not the most commonly available form of samples for NMR experiments. Polycrystalline powders offer a far more accessible form of solid samples for NMR studies and we now examine the impact of this choice of sample on solid-state NMR spectra and their information content. All the relationships and transformations as illustrated above for oriented single crystals still hold, but we need to examine how much of this information we can actually retrieve from NMR experiments for polycrystalline powder samples.

6.4.1 Stationary Samples

We have seen earlier that recording NMR spectra of an oriented single crystal for a large number of individual crystal orientations in the L frame enabled us to completely map the shape and orientation of, say, a single MS tensor. The way in which we generated this information is a sequential approach and it works to the full extent because the spatial relationship between the frames C and L is known. A polycrystalline powder consists of a very large number of crystallites in all possible orientations in L. If we record the NMR spectrum of such a sample, we get the (orientation-dependent) NMR signatures of all these crystallite orientations simultaneously. We no longer observe a sharp resonance signal but broad signals (consisting of many individual resonances) with distinct features, usually called *powder patterns* are seen. We are now well equipped to understand the origin of the intensity distribution in such powder patterns (see Figure 6.7) as reflecting probabilities of MS tensor orientations, and the sharp singularities representing the eigenvalues of the MS tensor where only one type of spin experiencing magnetic shielding anisotropy is present. Different values of the asymmetry parameter η^{MS} in combination with different values of the anisotropy parameter $A_{\mathrm{aniso}}^{\mathrm{MS}}$ give rise to a range of typical powder patterns, as is briefly summarized in Figure 6.8. In comparison with oriented single crystals, we obviously have gained ease

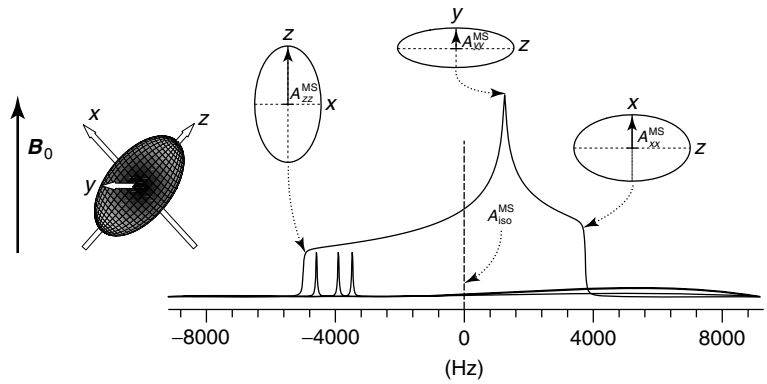


Figure 6.7. Sketch of the powder pattern of a single tensor $\boldsymbol{A}^{\mathrm{MS}}$ symbolizing the origin of the broad peak from multiple individual crystallites in the powder (three inset sharp resonances); also shown are the singularities as corresponding to the principal values $\{A_{xx}^{\mathrm{MS}},\ A_{yy}^{\mathrm{MS}},\ A_{zz}^{\mathrm{MS}}\}$ and $A_{\mathrm{iso}}^{\mathrm{MS}}$.

of sample preparation at the expense of spectral resolution. We still can obtain information about the shape of the MS tensor from the powder pattern, but we have lost access to the orientational information related to frame C by using a polycrystalline powder sample (for example, we can no longer distinguish a case of two MS tensors having identical shapes but differing orientations from a single MS tensor – both cases will result in a powder pattern solely reflecting η^{MS} and $A_{\mathrm{aniso}}^{\mathrm{MS}}$). As soon as there is more than one MS tensor in the asymmetric unit, even in the absence of dipolar coupling interactions, it becomes obvious that overlapping powder patterns in NMR spectra represent a serious limitation, as can be seen in Figure 6.8(e) where we assume three independent MS tensors to be present.

The trend of being able to retrieve only partial information from polycrystalline powder samples about the MS tensor continues when we consider spin systems in the presence of direct dipolar coupling. As before with the MS-tensor-only cases, we observe broad powder patterns with characteristic features that reflect some of the properties of the underlying spin systems. Figure 6.9 illustrates this point by sketching some such typical powder patterns. The main characteristic now is that we sample a powder average of the distribution of $\boldsymbol{A}^{\mathrm{D}}$ over all possible crystallite orientations. The MS tensors (necessarily more than one) involved have their defined individual orientations relative to the dipolar coupling tensor. However, $\eta^{\mathrm{D}} = 0$, and this rotational symmetry of $\boldsymbol{A}^{\mathrm{D}}$ means that for the general case of a dipolar-coupled pair of MS tensors in a powder sample, we can only retrieve some of the orientational information about the MS tensors: the powder patterns only encode the relative orientation of the two MS tensors. The Euler angles $\alpha_{\mathrm{PD}}^{\mathrm{MS}_1}$, $\beta_{\mathrm{PD}}^{\mathrm{MS}_1}$, $\alpha_{\mathrm{PD}}^{\mathrm{MS}_2}$, and $\beta_{\mathrm{PD}}^{\mathrm{MS}_2}$ are determined but only the difference $|\gamma_{\mathrm{PD}}^{\mathrm{MS}_1} - \gamma_{\mathrm{PD}}^{\mathrm{MS}_2}|$ may be retrieved from NMR experiments on isolated spin pairs in powder samples. This information retrieval from a powder pattern is more complete when the two MS tensors are related to each other by C_2 or mirror plane symmetry (see above), or if there are more than two MS tensors coupled to each other, as more parameters will then be encoded with increasingly more constraints imposed on them.

Where do we stand now? (i) The convenience of using polycrystalline powder samples has erased all orientation information for MS tensors in the absence of additional direct dipolar coupling; (ii) the presence of $\boldsymbol{A}^{\mathrm{D}}$ greatly helps us to retrieve much more information about MS tensors from powder samples – almost complete information, in fact – but at the expense of a rapidly growing number of parameters necessary to fully describe the spin system at hand; (iii) lack of spectral resolution and/or definition of features of powder patterns and/or overlapping powder patterns are obviously a very serious constraint. We need much improved spectral resolution for powder samples (at least comparable to the spectral resolution in NMR experiments on oriented single crystals) while maintaining – if possible – all the information about shapes and orientations of MS tensors that is, in principle, obtainable from polycrystalline powder

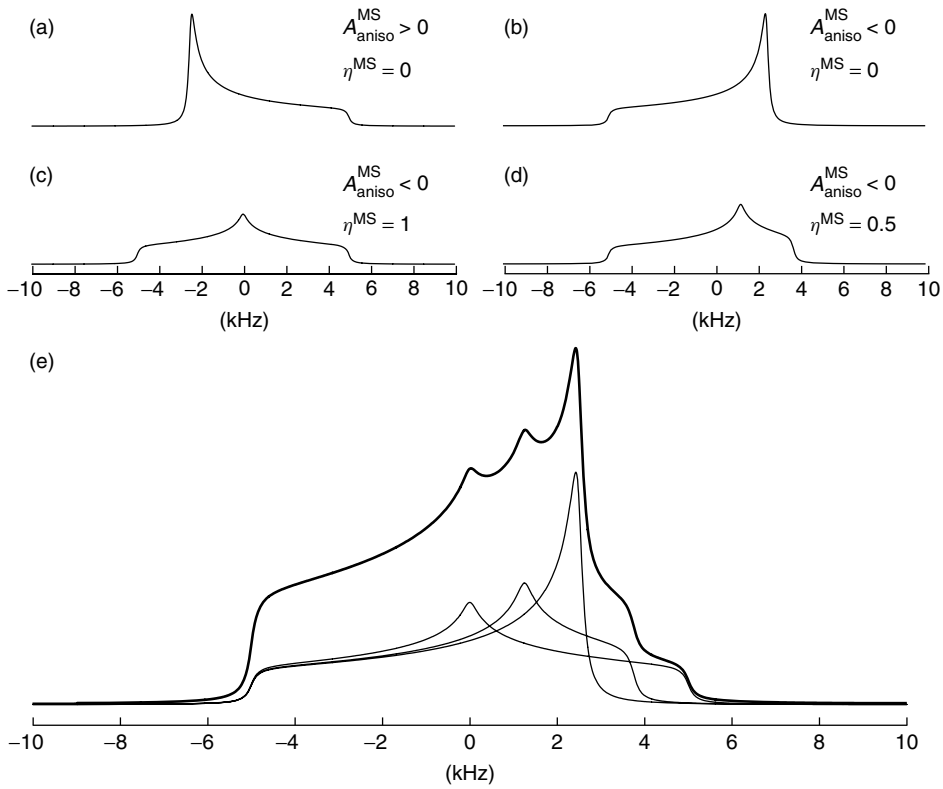


Figure 6.8. Illustration of a variety of powder patterns of a single tensor $\boldsymbol{A}^{MS}$ (a–d) and multiple tensors $\boldsymbol{A}^{MS}$ (e). The respective values of A^{MS}_{aniso} and η^{MS} are shown; (e) is the superposition of powder patterns (b–d) and symbolizes problematic spectral overlap in the presence of multiple tensors $\boldsymbol{A}^{MS}$.

samples. The way to achieve this goal is actually to make matters even more complicated by introducing time dependence of the NMR Hamiltonian and yet another principal axes system (see Figure 6.3) by moving on to so-called MAS NMR.

6.4.2 Polycrystalline Powders under Magic-angle Spinning Conditions

Rotating the sample during an NMR experiment around an axis that is inclined at an angle $\arctan\sqrt{2} \approx 54.74^\circ$ to the $\boldsymbol{B}_0$ direction is commonly referred to as *magic-angle spinning* (*MAS*).[17] In a nutshell, the effect of MAS is to average the anisotropic components of the interaction tensors by imposing time dependence on the NMR Hamiltonian. One could consider MAS (single axis of rotation) as a very crude approximation to the averaging effects resulting from (isotropic) molecular motion in nonviscous liquids. The extent to which averaging of the anisotropic components of the NMR interaction tensors occurs under MAS conditions is not only a function of the rotation speed ω_r of the sample; in addition, it depends on a symmetry property of the now time-dependent Hamiltonian, that is, whether the Hamiltonian commutes with itself $\left([H(t'), H(t'')] = 0\right)$ at all times t', t'', or not $\left([H(t'), H(t'')] \neq 0\right)$.[18,19] Here, we do not digress and discuss the properties of time-dependent NMR Hamiltonians any further; full descriptions can be found in the literature.[18–22] This section is subdivided according to the commutation properties of $H(t)$. We note that the commutation properties of $H(t)$ under MAS lead to a slight reshuffle of the spin-system scenarios as inspected and revisited so far in the absence of MAS: cases we used to consider separately before now are together in one

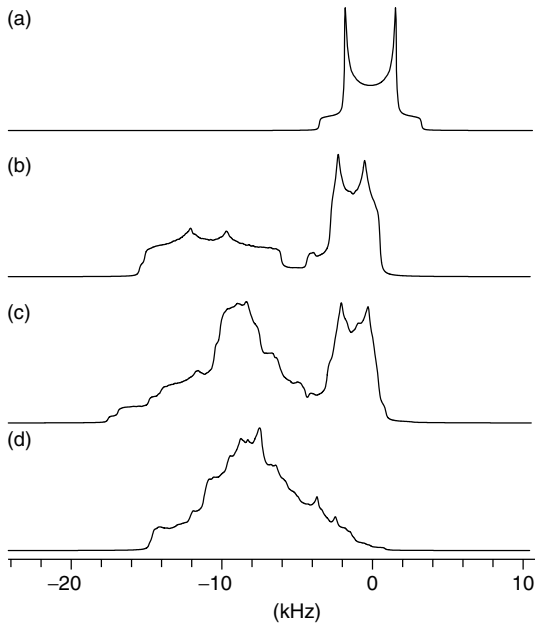


Figure 6.9. Illustration of a range of powder patterns from simultaneous presence of $\boldsymbol{A}^{\mathrm{MS}}$ and $\boldsymbol{A}^{\mathrm{D}}$ in several different spin systems. (a) Assuming $A_{\mathrm{aniso}}^{\mathrm{MS}_1} = A_{\mathrm{aniso}}^{\mathrm{MS}_2} = 0$ and $A_{\mathrm{iso}}^{\mathrm{MS}_1} = A_{\mathrm{iso}}^{\mathrm{MS}_2}$, $A_{\mathrm{aniso}}^{\mathrm{D}} = -2296$ Hz. (b) to (d) are simulations based on "real world" ^{13}C spin systems and their properties; all simulations assume $\omega_0/2\pi = -50$ MHz. (b) the 2,3-^{13}C spin in sodium pyruvate,[37] (c) the three-spin 1,2,3-^{13}C system in sodium pyruvate,[37] the four-spin 1,2,3,4-^{13}C system in mono-ammonium maleate.[15]

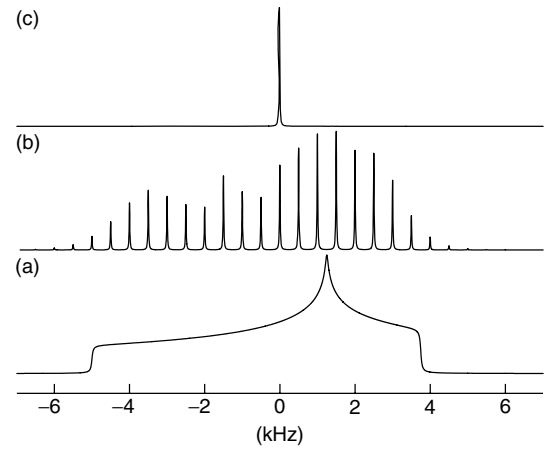


Figure 6.10. Sketch symbolizing the effect of MAS (b, c) on a powder pattern originating from a single species $\boldsymbol{A}^{\mathrm{MS}}$ ($A_{\mathrm{aniso}}^{\mathrm{MS}} = -5$ kHz, $\eta^{\mathrm{MS}} = 0.5$) (a); (b) illustrates the "slow-spinning regime" ($\omega_{\mathrm{r}}/2\pi = 500$ Hz), (c) corresponds to the "fast-spinning regime" ($\omega_{\mathrm{r}}/2\pi = 20$ kHz).

group of cases, whereas cases we previously grouped together now fall in separate groups. Our sample is still the same polycrystalline powder as before and, in principle, comes with the same information content. We focus on how much of this information we can extract from NMR spectra obtained under MAS conditions.

1. *Cases where* $\left[H(t'), H(t'')\right] = 0$
   These cases include single or multiple MS tensors in the absence of direct dipolar coupling, as well as dipolar-coupled spin systems where the differences in magnetic shielding between the coupled spins are large and greatly exceed the magnitude of the dipolar coupling interactions (typically found in, for instance, a heteronuclear spin pair). All these cases have in common that fast MAS reduces the anisotropic interaction tensors to their isotropic average, $A_{\mathrm{iso}}^{\mathrm{MS}}$ for the magnetic shielding tensors involved (the same quantity as commonly observed in solution-state NMR), and $A_{\mathrm{iso}}^{\mathrm{D}} = 0$ for the (heteronuclear) dipolar coupling interaction. What qualifies here as fast-spinning regime has a straightforward meaning: the rotation frequency of the sample $\omega_{\mathrm{r}}/2\pi$ must exceed the frequency spread of the anisotropic interaction. Depending on the case at hand, "fast spinning" could be anything from a few hundred hertz all the way to several tens of kilohertz. The spin-system cases in this category have something else in common, namely, the effect of sample spinning on the NMR spectrum if $\omega_{\mathrm{r}}/2\pi$ does *not* exceed the frequency spread of the powder pattern. In all these cases, the static powder pattern will be broken up into so-called spinning sidebands (see Figure 6.10) occurring at integer multiples of the rotation frequency around the resonance at $A_{\mathrm{iso}}^{\mathrm{MS}}$ – and each spinning sideband is a sharp, featureless signal. Generally, the occurrence of spinning sidebands, as well as the fact that for a polycrystalline powder all spinning sidebands are in-phase, can be traced back to averaging over the angle γ_{PR} over a period of rotation.[23,24] On inspecting Figure 6.10, one can see that the envelope of the intensity distribution of the spinning sideband pattern in this so-called slow-spinning regime resembles the shape of the corresponding powder pattern

that one would observe for a stationary sample. Analyzing these intensity patterns for MS tensors in the absence of dipolar coupling interactions by various methods,[25] quantitative information about A^{MS}_{aniso} and η^{MS} can be obtained. For a heteronuclear spin pair, in a regime where $\omega_r/2\pi > A^{D}_{aniso}$ *and* $\omega_r/2\pi < A^{MS}_{aniso}$, we can recover A^{MS}_{aniso} and η^{MS} of the observed MS tensor, whereas a spinning regime with $\omega_r/2\pi < A^{D}_{aniso}$ *and* $\omega_r/2\pi < A^{MS}_{aniso}$ gives access to both A^{MS}_{aniso} and η^{MS} and the Euler angles α^{MS}_{PD}, β^{MS}_{PD}.

Obviously, using MAS is largely beneficial, even if the benefits are at the cost of a much more complicated Hamiltonian as compared to NMR experiments on stationary powder samples. First of all, it is much more straightforward and more precise to determine A^{MS}_{iso}. We gain in terms of spectral resolution as well as in terms of achievable signal-to-noise ratio. Furthermore, we can retrieve all those parameters describing shape and orientation of the interaction tensors of a spin system from MAS NMR spectra that we previously identified as encoded in the powder patterns of stationary samples. Finally, MAS gives us yet another experimental variable as we can record NMR spectra at various different spinning speeds, optimized for a particular purpose. Also, if there happens to be a large number of independent sites/MS tensors in the asymmetric unit, leading in the slow-spinning regime to an MAS NMR spectrum crowded by numerous isotropic signals, each accompanied by a set of spinning sidebands, clever use of timing of certain sets of RF pulses (such as TOSS or PASS) can nicely disentangle these sets of spinning sidebands from each other.[24,26,27] In contrast, overlapping powder patterns in the NMR spectra of stationary samples cannot be so easily disentangled. At least for spin systems for which $\left[H(t'), H(t'')\right] = 0$ under MAS conditions, by and large, we only gain from switching from NMR experiments on stationary samples to MAS NMR experiments.

2. *Cases where* $\left[H(t'), H(t'')\right] \neq 0$

It remains to investigate if this favorable situation of loss-free gains is also true for spin systems under MAS conditions where $\left[H(t'), H(t'')\right] \neq 0$. These cases include spin systems where two (or more) MS tensors experience direct dipolar coupling interactions and where differences in magnetic shielding do *not* vastly exceed A^{D}_{aniso}. This is typically the case for homonuclear dipolar-coupled spin systems. The characteristic behavior for such spin systems under MAS conditions is that the fast-spinning regime is much harder, if not impossible, to reach experimentally. Even spinning frequencies $\omega_r/2\pi$ which considerably exceed the magnitude/frequency spread of the interaction tensors do not usually qualify as fast spinning. As a consequence, the averaging effect of MAS is, in some sense, less complete than for spin systems characterized by a self-commuting Hamiltonian. This is illustrated in Figure 6.11 where one can see that $\omega_r/2\pi = 2.5A^{D}_{aniso}$ does not lead to sharp and featureless spinning sidebands. Of course, the Hamiltonian is still periodically time dependent due to the MAS rotation and, hence, we still see spinning sidebands. However, in contrast to the $\left[H(t'), H(t'')\right] = 0$ cases, the spinning sidebands are considerably broader and have structure, reminiscent of differently scaled versions of the underlying static powder patterns, their structure changing with spinning sideband order. This is illustrated in Figure 6.12. The smaller the differences in A^{MS}_{iso} values involved, the harder it becomes to reach anything resembling a fast-spinning regime. A special case identified previously was for dipolar-coupled homonuclear spin

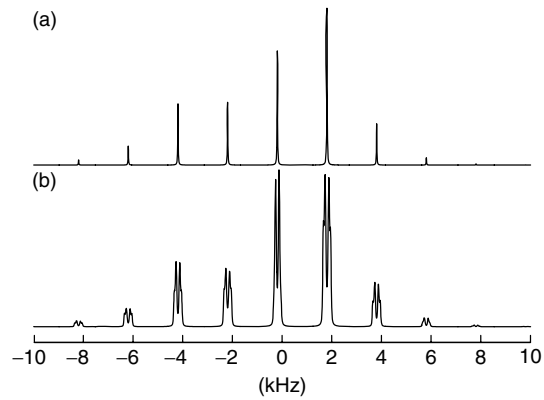


Figure 6.11. Illustration of the effect of absence (a) and presence (b) of homonuclear dipolar coupling on spinning sidebands in MAS NMR spectra. Underlying parameters: $\omega_r/2\pi = 2$ kHz, $A^{D}_{aniso} = -791$ Hz, $A^{MS_1}_{aniso} = A^{MS_2}_{aniso} = -6399$ Hz, $\eta^{MS_1} = \eta^{MS_2} = 0.35$. Only in the absence of $\boldsymbol{A}^{D}$ does MAS yield sharp and featureless spinning sidebands, even if $\omega_r/2\pi > A^{D}_{aniso}$ as assumed here.

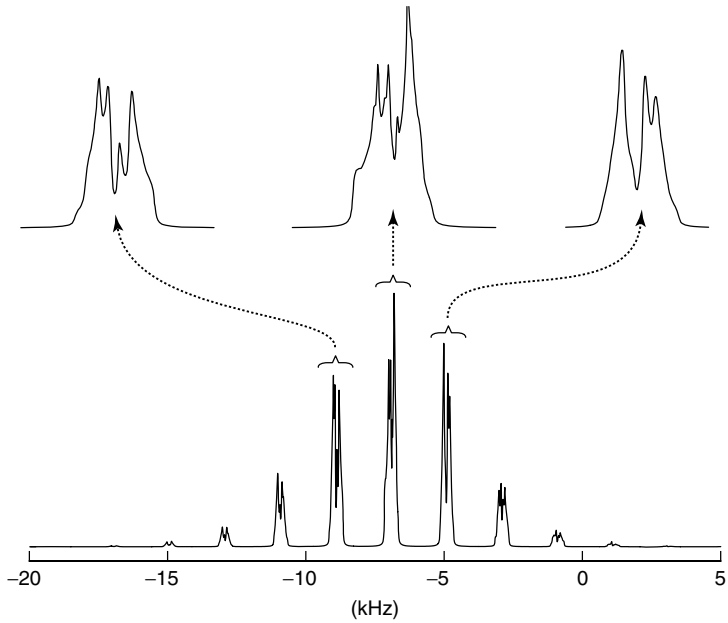


Figure 6.12. Simulated MAS NMR spectrum ($\omega_0/2\pi = -50$ MHz, $\omega_r/2\pi = 2$ kHz) based on the ^{13}C parameters of the 2,3-^{13}C spin pair in mono-ammonium maleate,[15] highlighting the rich structure of spinning sidebands for tightly dipolar-coupled homonuclear spin systems.

pairs, where the two MS tensors are related to each by symmetry (see above). Here, $\Delta A_{iso}^{MS} = 0$ but the two tensors have nonidentical orientations (mirror plane and C_2 axis) or identical orientations (inversion symmetry). In MAS NMR, spin pairs where the two MS tensors are related by a mirror plane or C_2 axis are known as fulfilling the $n = 0$ rotational resonance condition.[28] The incompleteness of the averaging by MAS is particularly prevalent for this kind of dipolar-coupled spin system, extending to spin systems with small differences ΔA_{iso}^{MS}.[29]

Are these findings of incomplete averaging good news or bad news regarding our ability to characterize both shape and orientation of $\boldsymbol{A}^{MS}$ from MAS NMR spectra? As it turns out, all parameters that we identified previously as encoded in powder patterns of stationary samples can be retrieved from MAS NMR spectra of spin systems governed by a nonself-commuting Hamiltonian. This is a nearly complete set of all parameters describing the shape *and* orientation of MS tensors in such spin systems for powder patterns. That is the good news if we are actually interested in characterizing the properties of the MS tensors, especially as now we can operate in a much larger and technically more forgiving (relative) window of spinning speeds ω_r in order to create this wanted information. The persistence of the encoding of *all* anisotropic interaction parameters, even at (relatively) fast-spinning conditions, is a far less welcome property if one is primarily interested in determining internuclear distances from the MAS NMR experiments. Then one would prefer all the signatures of shapes and orientations of the MS tensors to be absent from MAS NMR spectra[30,31] (determining internuclear distances from MAS NMR experiments continues to be an area of much activity) – but that can be rather difficult, if not impossible, to achieve in practice (building selectivity into MAS NMR pulse sequences is an important aspect).

6.5 SUMMARY AND MISCELLANEOUS

We can summarize our findings as follows: we obviously lose the information about *absolute* interaction

tensor orientations in frame C when switching from oriented single crystals to (polycrystalline) powders. If this information is vital, then there is no choice but to carry out NMR experiments on oriented single crystals. Luckily, however, the vast majority of solid-state NMR application areas is primarily concerned with generating information about magnitudes and *relative* orientations of NMR interaction tensors. This information is encoded to a very large extent in NMR experiments conducted on powder samples, with MAS adding plenty of further degrees of experimental freedom without destroying information. Regarding the precision of data analysis about relative interaction tensor orientations from MAS NMR experiments, in our view, MAS NMR can easily compete with single-crystal NMR, perhaps not for all kinds of spin systems but for a very reasonable range. It all depends strongly on the relative magnitudes of the interaction tensors present. Relative magnitudes span the whole range from spin systems dominated by $\boldsymbol{A}^{\mathrm{D}}$, with $\boldsymbol{A}^{\mathrm{MS}}$ playing a less important role (typically, ^{1}H and ^{19}F spin systems), to spin systems where $\boldsymbol{A}^{\mathrm{D}}$ and $\boldsymbol{A}^{\mathrm{MS}}$ carry similar weights (typically, ^{13}C or ^{31}P in many different compounds), to spin systems that are strongly or even completely dominated by $\boldsymbol{A}^{\mathrm{MS}}$ (typically, heavy isotopes such as ^{195}Pt or ^{119}Sn). We have briefly mentioned indirect dipolar coupling $\boldsymbol{A}^{\mathrm{J}}$ (see above) but chosen not to include it in the discussion. It is obvious that the role of J coupling in solid-state NMR is far less prominent to this date than its role in solution-state NMR. Nevertheless, $\boldsymbol{A}^{\mathrm{J}}$ does play a role in solid-state NMR as well. Particularly $A^{\mathrm{J}}_{\mathrm{iso}}$ is being more incorporated into all kinds of one- and two-dimensional MAS NMR experiments inspired by the arsenal of solution-state NMR pulse sequences.[32] As far as $A^{\mathrm{J}}_{\mathrm{aniso}}$ is concerned, it has been mainly a topic of academic interest[33] (and debate as well). $A^{\mathrm{J}}_{\mathrm{aniso}}$ is of little concern for spin systems where $A^{\mathrm{J}}_{\mathrm{aniso}} \ll A^{\mathrm{D}}_{\mathrm{aniso}}$, as is typically the case for ^{13}C spin systems. Anisotropy of J coupling does, however, present a problem for the determination of internuclear distances based on experimental measurements aiming at $A^{\mathrm{D}}_{\mathrm{aniso}}$ for spin systems with $A^{\mathrm{J}}_{\mathrm{aniso}} \gtrapprox A^{\mathrm{D}}_{\mathrm{aniso}}$. Then only the combined effects of $(A^{\mathrm{J}}_{\mathrm{aniso}} + A^{\mathrm{D}}_{\mathrm{aniso}})$ are observed, even preventing the meaningful determination of internuclear distances entirely in some circumstances.[34]

At this point in time, calculations (ab initio and otherwise) of $\boldsymbol{A}^{\mathrm{MS}}$ have gathered quite some momentum as compared to the situation just a few years back.[35] It seems rather obvious that combined approaches featuring experimental work as well as calculations will become more established. Such combined approaches may also include concepts and ideas which did not originally start in the world of NMR, an example here being concepts about "continuous symmetry"[36] and how these relate to physical properties such as $\boldsymbol{A}^{\mathrm{MS}}$. We have completely omitted one very big point from our discussion: dynamic properties of solid materials. Obviously, different types and frequencies of dynamic-disorder events can fully or partially average NMR interaction tensors $\boldsymbol{A}^{\lambda}$. Sometimes this could be a blessing (for instance, $\boldsymbol{A}^{\mathrm{MS}}$ encoding valuable information about the geometry and mechanisms of exchange processes in solid materials) or it could equally be a curse (for instance, preventing structural studies by causing some degrees of averaging of $\boldsymbol{A}^{\mathrm{D}}$). Dynamic disorder in solid materials in the context of solid-state NMR is a big topic, especially so since this technique can probe timescales and disorder mechanisms not readily accessible to other experimental techniques. Finally, continued methodological progress improving spectral resolution for quadrupolar nuclei[38,39] will greatly help to develop and extend solid-state NMR studies to include experiments dealing with the simultaneous presence of several anisotropic NMR interactions *including* $\boldsymbol{A}^{\mathrm{D}}$.[40]

REFERENCES

1. M. H. Levitt, '*Spin Dynamics*', Wiley: Chichester, 2001.
2. J. F. Nye, '*Physical Properties of Crystals*', Oxford University Press, Oxford, 1985.
3. J. Martinet, '*Perfect Lattices in Euclidean Spaces*', Springer: Berlin, London, 2003.
4. H. F. Franzen, '*Physical Chemistry of Inorganic Crystalline Solids*', Springer: Berlin, Heidelberg, 1986.
5. it.iucr.org, '*International Tables for Crystallography*', Springer: Berlin, 2005, Vols. **A-G**.
6. W. Clegg, '*Crystal Structure Determination*', Oxford Science Publications: Oxford, 1998.
7. G. H. Stout and L. H. Jensen, '*X-Ray Structure Determination. A Practical Guide*', John Wiley & Sons: New York, 1989.
8. M. F. C. Ladd and R. A. Palmer, '*Structure determination by X-ray crystallography*', Plenum Press: New York, 1977.

9. U. Haeberlen, '*Advances in Magnetic Resonance*', Academic Press: New York, 1976, Suppl. 1.
10. (a) A. R. Edmonds, '*Angular Momentum in Quantum Mechanics*', Princeton University Press: Princeton, 1974; (b) D. M. Brink and G. R. Satchler, '*Angular Momentum*', Clarendon Press: Oxford, 1993.
11. J. Weil, T. Buch, and J. Clapp, *Adv. Magn. Reson.*, 1973, **6**, 183–257.
12. J. B. Robert and L. Wiesenfeld, *Phys. Rep.*, 1982, **86**, 363–401.
13. G. E. Pake, *J. Chem. Phys.*, 1948, **16**, 327–336.
14. L. Golic and I. Leban, *Croat. Chim. Acta*, 1982, **55**, 41–45.
15. S. Dusold, H. Maisel, and A. Sebald, *J. Magn. Reson.*, 1999, **141**, 78–90.
16. (a) S. Dusold, W. Milius, and A. Sebald, *J. Magn. Reson.*, 1998, **135**, 500–513; (b) M. Bechmann, S. Dusold, F. Geipel, A. Sebald, and D. Sellmann, *J. Phys. Chem A*, 2005, **109**, 5275–5280.
17. (a) E. R. Andrew, A. Bradbury, and R. G. Eades, *Nature*, 1959, **183**, 1802; (b) I. J. Lowe, *Phys. Rev. Lett.*, 1959, **2**, 285–287.
18. A. Schmidt and S. Vega, *J. Chem. Phys.*, 1992, **96**, 2655–2680.
19. M. H. Levitt, D. P. Raleigh, F. Creuzet, and R. G. Griffin, *J. Chem. Phys.*, 1990, **92**, 6347–6364.
20. M. Mehring, '*Principles of High Resolution NMR in Solids*', Springer-Verlag: Berlin, Heidelberg, 1983.
21. M. J. Duer, '*Introduction to Solid-State NMR Spectroscopy*', Blackwell: Oxford, 2004.
22. (a) S. A. Smith, W. E. Palke, and J. T. Gerig, *Concepts Magn. Reson.*, 1992, **4**, 107–144; (b) S. A. Smith, W. E. Palke, and J. T. Gerig, *Concepts Magn. Reson.*, 1992, **4**, 181–204; (c) S. A. Smith, W. E. Palke, and J. T. Gerig, *Concepts Magn. Reson.*, 1993, **5**, 151–177; (d) M. Edén, *Concepts Magn. Reson. A*, 2003, **17A**, 117–154; (e) M. Edén, *Concepts Magn. Reson. A*, 2003, **18A**, 1–23.
23. M. H. Levitt, *J. Magn. Reson.*, 1989, **82**, 427–433.
24. O. N. Antzutkin, *Progr. NMR Spectrosc.*, 1999, **35**, 203–266.
25. (a) J. Herzfeld and A. E. Berger, *J. Chem. Phys.*, 1980, **73**, 6021–6030; (b) M. M. Maricq and J. S. Waugh, *J. Chem. Phys.*, 1979, **70**, 3300–3316; (c) M. Bak, J. T. Rasmussen, and N. C. Nielsen, *J. Magn. Reson.*, 2000, **147**, 296–330.
26. W. T. Dixon, *J. Chem. Phys.*, 1982, **77**, 1800–1809.
27. W. T. Dixon, *J. Magn. Reson.*, 1981, **44**, 220–223.
28. M. M. Maricq and J. S. Waugh, *J. Chem. Phys.*, 1979, **70**, 3300–3316.
29. M. Bechmann and A. Sebald, *J. Magn. Reson.*, 2005, **173**, 296–304.
30. (a) A. E. Bennett, R. G. Griffin, and S. Vega, Recoupling of homo- and heteronuclear dipolar interactions in rotating solids, in '*Solid-State NMR IV: Methods and Applications of Solid-State NMR*', NMR Basic Principles and Progress, ed. B. Blümich, Springer Verlag: Berlin, 1994, Vol. **33**, pp 1–78; (b) S. Dusold and A. Sebald, Dipolar recoupling under magic-angle-spinning conditions, in '*Annual Reports on NMR Spectroscopy*', ed. G. Webb, Academic Press: London, 2000, Vol. **41**, pp 185–264.
31. M. H. Levitt, Symmetry-based pulse sequences in magic angle spinning solid-state NMR, in '*Encyclopedia of Nuclear Magnetic Resonance*', ed. D. M. Grant and R. K. Harris, Wiley: Chichester, 2002, Vol. **9**, pp 165–196.
32. D. Sakellariou and L. Emsley, Through-bond experiments in solids, in '*Encyclopedia of Nuclear Magnetic Resonance*', ed. D. M. Grant and R. K. Harris, Wiley: London, 2002.
33. J. Vaara, J. Jokisaari, R. E. Wasylishen, and D. L. Bryce, *Progr. Nucl. Magn. Reson. Spectrosc.*, 2002, **41**, 233–304.
34. S. Dusold and A. Sebald, *Molec. Phys.*, 1998, **95**, 1237–1245.
35. M. Kaupp, M. Bühl, and V. G. Malkin, Calculation of NMR and EPR parameters, in '*Theory and Applications*', ed. M. Kaupp, M. Bühl and V. G. Malkin, Wiley-VCH: Weinheim, 2004.
36. A. Steinberg, M. Karni, and D. Avnir, *Chem. Eur. J.*, 2006, **12**, 8534–8538.
37. S. Dusold and A. Sebald, *J. Magn. Reson.*, 2000, **145**, 340–356.
38. L. Frydman and J. S. Harwood, *J. Am. Chem. Soc.*, 1995, **117**, 5367–5368.
39. Z. Gan, *J. Chem. Phys.*, 2001, **114**, 10845–10853.
40. A. Jerschow, *Monatshefte für Chemie*, 2002, **133**, 1–16.

Chapter 7

Chemical Shift Computations for Crystalline Molecular Systems: Practice*

Robin K. Harris[1], Paul Hodgkinson[1], Chris J. Pickard[2], Jonathan R. Yates[3] and Vadim Zorin[1]

[1]*Department of Chemistry, University of Durham, Durham DH1 3LE, UK*
[2]*School of Physics & Astronomy, University of St. Andrews, St. Andrews KY16 9SS, UK*
[3]*TCM Group, Cavendish Laboratory, University of Cambridge, Cambridge CB3 0HE, UK*

*This article is a revised and updated version of 'Chemical shift computations on a crystallographic basis: some reflections and comments', published as *Magn. Reson. Chem.* 2007, ***45***, S174–S186.

7.1	Computational Details	82
7.2	General Aspects	83
7.3	Practical Uses of the Computations	87
7.4	Conclusions	96
	References	96

The first-principles (or ab initio) prediction of chemical shifts has long been practised in the quantum chemical community.[1,2] However, most effort has been directed toward the accurate calculation of shielding in relatively small, isolated molecules. Experimentally, there is an increasing interest in the use of magic-angle spinning (MAS) techniques to measure nuclear magnetic resonance parameters in extended systems (ordered crystals, amorphous solids, even large biomolecules), and there is a corresponding demand for computations of chemical shifts in crystalline materials to support experiment.

Any extension of traditional quantum chemical approaches to such situations faces considerable challenges: modeling a solid as a "large molecule" or cluster is fraught with difficulties. While NMR is most immediately sensitive to local environments, there are situations where long-range effects are significant (e.g., arising from electrostatics and ring currents), and the choice of cluster, in particular its termination, is critical if the calculations are to be kept to a manageable size. However, such approaches have been usefully applied to studies of chemical shifts in systems such as molecular crystals,[3] supramolecular assemblies,[4] and organometallic compounds.[5] Cluster models have also been combined with classical point-charge arrays to simulate the long-range electrostatic effects of crystal lattices.[6,7]

It is clearly very attractive to formally and efficiently exploit the translational repetition inherent in

NMR Crystallography Edited by Robin K. Harris, Roderick E. Wasylishen and Melinda J. Duer © 2009 John Wiley & Sons, Ltd. ISBN: 978-0-470-69961-4

crystals, and, in the last decade, such a method for the prediction of magnetic resonance parameters has been developed.[8] Perhaps unsurprisingly, the method has its origins in the solid-state physics community, and makes extensive use of theoretical techniques developed to describe the behavior of electrons in crystals. The method, known as the *gauge-including projector augmented wave* (GIPAW) method, has two essential ingredients.

The first[9] deals with the problem of calculating the quantum mechanical response of electrons in a crystal to an externally applied uniform magnetic field. Formally, this requires expectation values of the position operator to be evaluated, which is problematic because the position operator cannot be represented under periodic boundary conditions. In contrast to traditional molecule-based methods, plane waves are used to form a basis set, implying that, as the high spatial frequencies of a wave function increase, so does the size of the basis set required, and hence the computational cost. This would limit calculations to those systems containing only light elements if the nuclear Coulomb potential is used to describe the interaction between the ions and electrons. However, chemical intuition suggests that neither the tightly bound core electrons nor the form of the wave function near the nucleus strongly influence most chemical properties. This observation is exploited by the second essential ingredient of the GIPAW method (and the origin of its name), namely the use of pseudopotentials to represent the interaction between core and valence states. Pseudopotentials permit both the removal of the core electrons from the calculation and the smoothing of the valence wave functions near the nucleus. However, while the core electrons have very little chemically sensitive contribution to shielding,[10] the behavior of the valence wave function near the nucleus is critical to describing the shielding, and a naive pseudopotential theory would fail for all but the lightest elements. Fortunately, the projector augmented wave (PAW) method of van der Walle and Blöchl[11] allows the straightforward reconstruction of all-electron wave functions from their pseudoequivalents. The GIPAW method is simply an extension of this theory appropriate for systems in an external magnetic field. This approach has also been rapidly adopted by the experimental community, and it is timely to review the impact it has had on the study of organic molecular crystals. This is the subject of this article. However, it should be noted that the GIPAW method has also been applied with success to framework materials, where structural correlations are likely to be better defined.[12,13]

The principles of computing chemical shifts by the GIPAW method are reviewed in **Chapter 3**. The present article is concerned with their practical application for crystalline molecular organic compounds.

7.1 COMPUTATIONAL DETAILS

Magnetic resonance parameters, such as chemical shifts, can be measured with extreme accuracy. This achievement places considerable demands on any theoretical approach to their prediction—the experimental accuracy must be matched by the fidelity of the calculation. At the same time, most of the scientific problems attacked by the solid-state NMR community involve complex materials containing many inequivalent atomic sites. The computational requirements can be considerable, frequently needing the resources of institutional computer clusters or national supercomputing facilities. The successful simulator must balance the requirements of accuracy with available computing resources.

The plane-wave pseudopotential approach has been developed so that most of the parameters that control the quality of the calculation, principally the sampling of the Brillouin zone and the size of the basis set, have a predictable impact on both the computational cost and on precision. Thus, calculations can be systematically improved until the desired precision is achieved (or the computational resources are exhausted). In addition, the parameters influence the calculations largely independently, thus simplifying an exploration of parameter space.

A true crystal contains an infinite number of atoms, and hence electrons. It is therefore implausible to consider every electronic state in the system. Bloch's theorem provides a convenient way to handle this situation. The translational symmetry of a crystal allows the infinite number of electronic wave functions to be treated as a finite number of bands at an infinite number of "*k*-points" in the first Brillouin zone of the crystal's reciprocal lattice. The properties of these bands vary smoothly throughout the Brillouin zone, and integral quantities (such as the total energy and the current response to an applied magnetic field) can be calculated by sampling at a finite number

of *k*-points. As the Brillouin zone exists in reciprocal space, it is large for a crystal with a small unit cell, and compact for large complex crystals. Rather than monitoring the total number of *k*-points in a calculation, it is more appropriate to converge the quantities of interest with respect to the sampling *density* (in reciprocal space) of *k*-points. This number is then transferable between different crystals of a similar type. As a rule, because there is less dispersion in the energy bands, molecular crystals do not require as dense a sampling as, for example, a semiconductor. The computational cost of the calculation scales proportionally to the number of *k*-points employed. This number may be reduced by exploiting any additional symmetry in the crystal structure, although for organic molecular crystals the amount of symmetry is typically modest. The positioning of the initial *k*-point is also of importance for convergence. The "gamma point", (0,0,0), should be avoided.

In contrast to local-orbital-based methods, the plane-wave basis set may be systematically converged, the degree of convergence being controlled by a single parameter: the plane-wave cutoff energy, E_{cut}. The plane-wave basis set consists of all those plane waves with a kinetic energy less than that specified by the cutoff. For a well-designed code, the computational cost scales as $N \ln N$ with the number of plane waves N, where N is proportional to $E_{\text{cut}}^{3/2}$.

The rate of convergence with respect to the basis-set size is controlled by the degree to which smooth pseudopotentials can be constructed. This depends on the particular pseudopotential scheme used, and also on the elements in the system of interest. For molecular crystals, the "hardest" element encountered is typically the oxygen atom, which requires a higher cutoff energy for convergence. The GIPAW scheme was originally implemented using norm-conserving pseudopotentials, but the method has now been extended to take advantage of "ultrasoft" pseudopotentials.[14] This pseudopotential scheme (due to Vanderbilt[15]) is considered to be both the most accurate and computationally efficient, and is recommended. In addition, it is theoretically closely related to the (GI)PAW schemes for all-electron reconstruction.

The one choice of parameter for which there is no predictable improvement is that of the density functional used to describe the electronic exchange and correlation. There is a vast quantum chemical literature devoted to divining the most appropriate density functional for given situations. However, there may be considerable advantage in sticking to a single functional for many calculations to learn its strengths and weaknesses. The generalized gradient approximation (GGA) due to Perdew, Burke, and Ernzerhof (PBE)[16] has been widely used to date for the computation of shielding in crystalline materials, with good results. However, the KT3 functional has also been used.[17] As an example, Table 7.1 compares data obtained using the two functionals for the β form (a monohydrate) of testosterone, the structure of which is shown later. While most PBE results are within a few ppm of the experimental values, the computed shift for C5 is wildly in error when the proton positions are optimized. However, the forces on all the atoms, including C5, are moderately low (<0.6 eV Å^{-1}), so the problem does not arise from errors in the diffraction results. The computed shift for C5 using the KT3 functional is substantially better, though still not good. Indeed, the overall situation is clearly much improved with KT3, though some of this is apparent rather than real (the PBE data being distorted by the effect of the C5 result on the choice of the reference shift). The reason for the differences is not understood, but it may arise from inadequacies of PBE in dealing with conjugated systems. Clearly, results need to be carefully evaluated (see below) if they are to prove useful.

It should be noted that, when studies using different exchange-correlation functionals are compared, there will be significant differences in the reference shielding values, but these are not important in Table 7.1 because, in each case, the average computed shielding is linked to the average experimental shift. Small variations in reference shielding also occur when different forms of pseudopotentials are used.

7.2 GENERAL ASPECTS

It is not straightforward to compare chemical shifts obtained by the GIPAW method with experimental results since there are a number of uncertain features, even apart from the details of the computational methods:

Temperature effects need to be carefully considered. The computations are carried out for static molecular situations, in effect at 0 K and neglecting zero-point motion (clearly not realistic for

Table 7.1. Computed and experimental isotropic chemical shifts (in ppm) for β testosterone, showing the substantial variations between computed results using the PBE and KT3 functionals. Proton positions (Only) were optimized prior to computation of the shielding

Atomic number	Experimental chemical shift	PBE computed chemical shift	PBE difference	KT3♦ computed chemical shift	KT3 difference
1	35.25	32.30	2.95	33.48	1.77
2	35.25	32.79	2.46	33.64	1.61
3	200.15	203.82	−3.67	195.66	4.49
4	124.65	127.46	−2.81	122.35	2.30
5	173.75	188.12	14.37	179.93	−6.18
6	33.45	32.88	0.57	34.04	−0.59
7	33.45	34.08	−0.63	34.87	−1.42
8	35.25	33.25	2.00	35.27	−0.02
9	54.65	55.99	−1.34	55.25	−0.60
10	39.35	40.48	−1.13	43.65	−4.30
11	20.95	18.62	2.33	21.22	−0.27
12	35.25	34.30	0.95	34.84	0.41
13	43.55	41.98	1.57	44.45	−0.90
14	51.55	51.41	0.14	50.81	0.74
15	23.95	20.43	3.52	22.58	1.37
16	28.75	26.28	2.47	27.83	0.92
17	80.65	85.88	−5.23	85.23	−4.58
18	12.55	6.98	5.57	9.43	3.12
19	16.85	12.13	4.72	14.74	2.11

♦Unpublished data by S.J. Clark, R.K. Harris, P. Hodgkinson, D. Jochym and V. Zorin.

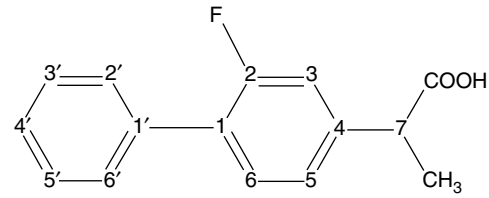
comparison with experimental results, either from NMR or from diffraction). The crystal structures that are input to a first-principles calculation are generally determined these days at approximately 120 K, while older reports involve ambient temperatures. There would appear to be two related problems here. One is that this diffraction-derived structure will not actually be properly energy-minimized for 0 K. Lattice vibrations, for instance, cause changes in unit-cell dimensions with temperature. It is possible to adjust the unit-cell dimensions in a computation, but this is not often desirable. The second problem is that the NMR parameters will be computed for artificially fixed atomic positions, whereas the observed values will be averaged over any motion at the molecular level. In particular, vibrations of hydrogen bonds—both intra- and intermolecular—are likely to have substantial repercussions on shielding. An unsymmetrical double potential minimum for a proton in a hydrogen bond would be expected to be a particular problem. There may be substantial motion, even at 120 K, not purely vibrational in nature. For instance, internal rotation about C–CH_3 bonds or of phenyl (or phenylene) rings about their axes may be rapid compared to the diffraction recording time, but would not be apparent from the crystal structure if they occur with a jump motion. However, such motions can be readily taken into account, e.g., by averaging the computed chemical shifts for the three methyl hydrogens or for the two ortho carbons for a phenyl group. It is, in principle, possible to take account of molecular motion of a non-jump type, for example by performing a molecular dynamics simulation and averaging the chemical shifts from the resulting ensemble of structures. This is a computationally demanding approach. Low-frequency vibrational motions (both intra- and inter-molecular), especially those with large amplitudes, might be expected to introduce significant changes in chemical shifts with temperature (as has been observed experimentally). It has been shown by computation that zero-point corrections to chemical shifts can be significant, and that thermal effects, in general, are

particularly noticeable for shielding anisotropies. However, owing to the high computational cost, most simulations use static structures unless, for example, the object is to study a material where dynamics is known to be particularly important. It may be noted that Sebastiani and coworkers[18–20] have studied the effects of dynamics at the molecular level on NMR parameters, with particular emphasis on proton chemical shifts.

A second set of problems arises from the way in which diffraction results are incorporated into the computations. After atomic coordinates derived from diffraction studies are fed into the computational process, it is possible to optimize the geometry (i.e., to minimize the energy) by allowing the positions of atoms within the unit cell and (if required) unit-cell parameters to vary. The latter option is not normally taken since diffraction-fixed values are acceptable, but rescaling of the lattice parameters and subsequent geometry optimization has been carried out[21] in the case of ferrierite. During geometry optimization, ab initio forces on the atoms are calculated and used to adjust atomic positions. These computations are iterated until the structures converge, using three criteria: thus, optimization proceeds until energy reduction is less than a set amount, geometry changes fall below a certain specified tolerance, and all the forces on the atoms are reduced to less than a given value (see below). Changes in the displacement between successive steps should be less than 0.002 Å and the change in energy should be less than 2×10^{-5} eV. Different initial structures may converge to slightly different situations, but the tolerance values can be decreased until the effect on the subsequently calculated shieldings becomes acceptably low. The optimized geometry is usually found to differ from the diffraction-produced positions. Should one optimize before computing the shielding tensors or not at all? One might argue on a case-by-case basis, but we believe that normally the best procedure is to fix the positions of the heavy atoms and unit-cell parameters at their diffraction-derived values, but to allow the hydrogen atom positions to be optimized. Certainly, this is best for relatively old X-ray diffraction reports, in which the hydrogen positions are often uncertain or even simply assumed to be "at reasonable positions". For instance, as Table 7.2, which gives results[22] for the compound flurbiprofen **(I)**, shows, various bond

Table 7.2. Bond lengths involving hydrogen atoms for X-ray, H-optimized and fully optimized structures of flurbiprofen[22]

Bond	Bond length		
	X-ray	Calculated (only H atoms relaxed)	Calculated (all atoms relaxed)
O–H	1.286	1.023	1.036
O···H	1.358	1.618	1.522
O–H···O	2.641	2.641	2.559
Methyl C–H	1.128	1.091	1.091
Aromatic C–H	1.132	1.083	1.084
C7–H	1.149	1.090	1.092



(I)

lengths to hydrogen can be radically different following optimization of hydrogen positions only. This can be particularly the case for hydrogen bonds. Hydrogen positions have a sensitive influence on the chemical shifts of nearby ^{13}C nuclei. Much smaller changes occur when all the atom positions are relaxed. However, even the latter can have significant effects on chemical shifts, as shown in Table 7.3, but there is a danger of accidental cancelation of errors if full optimization is used, thus obscuring the true situation. There is less justification for the strategy of proton position optimization for neutron-diffraction-derived structures or for cases with modern X-ray results. The procedures relating to geometry optimization can be rationalized by a careful consideration of the forces acting on the atoms. If these are small (as is usually the case for structures derived from neutron diffraction), there is little need to optimize geometry. If they are large (say >1.0 eV Å^{-1}) for the crystal structure as taken from diffraction data (which commonly occurs for hydrogen atoms, with forces sometimes tens of eV Å^{-1}), then it is certainly wise to optimize the hydrogen positions. If the forces remain large after this action, then optimization of the heavy-atom

Table 7.3. Calculated and experimental ^{13}C chemical shifts (in ppm from the calculated shift of tetramethylsilane) for flurbiprofen[22]

Site[a]	Calculated		Experimental
	H-relaxed	All relaxed	
C1′ (Q)	141.84	136.26	136.6
C1 (Q)	131.69	128.16	128.4
C4 (Q)	142.22	139.34	140.6
CF	162.77	162.89	160[b]
COOH (Q)	179.58	190.18	184.0
C3	116.32	114.76	117.1
C5	122.64	120.57	123.7
C4′	128.04	127.71	—
C2′	131.22	129.07	—
C3′	131.22	128.56	129.0[c]
C5′	127.31	125.87	—
C6′	133.05	128.99	—
C6	133.66	129.69	—
C7	46.79	43.99	46.6
Methyl C8	10.21	10.26	16.1

[a](Q) indicates quaternary carbon.
[b]A doublet arising from C, F indirect isotropic coupling ($|J| = 250$ Hz).
[c]Unresolved.

positions may be desirable. The NMR results used for comparison with computations are commonly obtained at ambient probe temperature (only rarely at 120 K), so nowadays there is the additional problem of relating computed data based on a structure determined at a different temperature from that of the observed chemical shifts. Variable-temperature diffraction or NMR experiments may be needed to overcome this difficulty. An alternative strategy may be attempted when unit-cell parameters are known (from powder diffraction experiments) for the temperature at which the NMR results were measured, while the full crystal structure was determined at a lower temperature. In such cases, it may be feasible to fix the unit-cell size at the value for the higher temperature, use the atomic coordinates from the diffraction work and then carry out optimization.

Thirdly, GIPAW computations provide shielding constants, which need to be converted to chemical shifts for comparison with experiment. In effect, this implies use of a reference, although this does not need to be explicitly involved. If there is only a single nucleus to be computed (e.g., for F in a monofluorinated compound such as flurbiprofen),[22] then there is no alternative to computing the shielding of a reference compound, which introduces uncertainties because the reference and sample compound normally have very different structures, leading to significant errors in the computed chemical shift differences. However, if many shifts are computed for the same nuclide of a system, as is usually the case for ^{13}C, then alternative strategies can be applied. Thus, plotting computed shielding against experimental shift should yield a straight line which, when extrapolated to zero shift, will give the shielding of the reference. This technique can also be used if many chemically related compounds with a single relevant nucleus (e.g., many monofluorinated systems) are studied. However, there is a secondary problem since such plots should ideally have unit slope, but they rarely do in practice. Thus, one can either constrain the slope to unity before extrapolation or use the fitted slope for extrapolation. Different shielding constants for the reference are obtained. For combined computed shielding versus experimental shift plots for the α and β forms of testosterone (see below),[23] the slope is 1.06. When this plot is extrapolated to zero shift, the shielding of the reference is found to be 172.56 ppm, whereas when the slope is constrained to unity, this is 169.17 ppm (naturally, the RMS error of the plots is better when no constraint is placed on the slope, 2.25 versus 3.97 ppm). Finally, one can simply set the average computed shielding constant to the average experimental chemical shift. This is equivalent to the extrapolation procedure when unit slope is assumed. Of course, such a method is fine if the experimental points are evenly spread over a large shift range. If that is not the case, then bunching of the signals may produce biasing. Therefore, on occasion, one might want to exclude some signals to get a better distribution across the spectrum and therefore a more reliable reference chemical shift.

Deviations between computed and experimental results arise from three different sources, namely, (i) inadequacies in the computational procedures, (ii) errors or uncertainties in the diffraction-produced crystal structures, and (iii) errors in the experimental NMR data. The latter two types are usually relatively small except for hydrogen positions and for the problem of temperature comparisons, as discussed above.

Of course, deviations of points from straight-line experimental/computed shift plots depend on whether the slope is constrained to unity or not.

It should be noted that the output of a GIPAW calculation, as implemented in the NMR–CASTEP code, separately reports the isotropic bulk magnetic susceptibility (IBMS) contribution to shielding, which can be of importance when comparing chemical shifts of different compounds under certain types of referencing procedures.[24] It has the same value for all nuclei (of whatever nuclide) in the sample, so that internal comparisons of shifts for a given compound are always unaffected. Moreover, such effects are eliminated by MAS.[25] Therefore, the final listing of shielding data in NMR–CASTEP does not include the IBMS contribution, thereby facilitating comparisons between computer-derived chemical shifts for different crystalline solids.

7.3 PRACTICAL USES OF THE COMPUTATIONS

7.3.1 Accuracy of Comparisons between Computed and Experimental Results

A comparison of computed and experimental results in individual cases has some intrinsic interest (see Figure 7.1, modified from Ref. 26, which shows the combined ^{13}C results for two polymorphs of methylnitroacetanilide (**II**)), especially for theoreticians, though it is of relatively little value, per se, to the spectroscopist or structural chemist. Examination of results shows that, whereas, in general, the order of the computed shifts matches that of the experimental results, the differences between corresponding values can be high. The RMS difference between the computed and experimental ^{13}C shifts for (**II**), for instance, is 2.9 ppm, but this falls to 1.3 ppm when the methyl resonances are excluded. In other cases, more extreme differences occur for individual resonances, as discussed above for testosterone. As a result of such problems, attention is often directed away from individual results and toward shift differences between corresponding carbons of molecules that differ as little as possible, as discussed below.

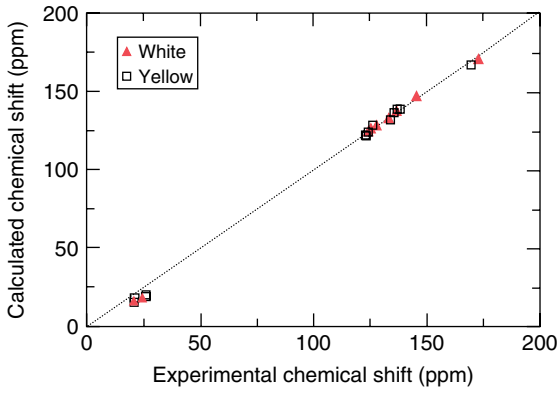
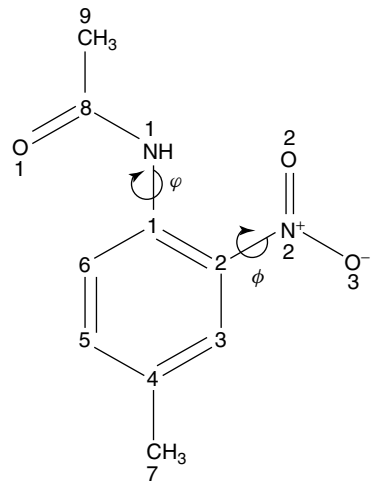


Figure 7.1. Experimental versus calculated (NMR–CASTEP) isotropic ^{13}C chemical shifts for the white and yellow forms of **II**.[24] The straight line represents perfect agreement (unit slope) between calculation and experiment.

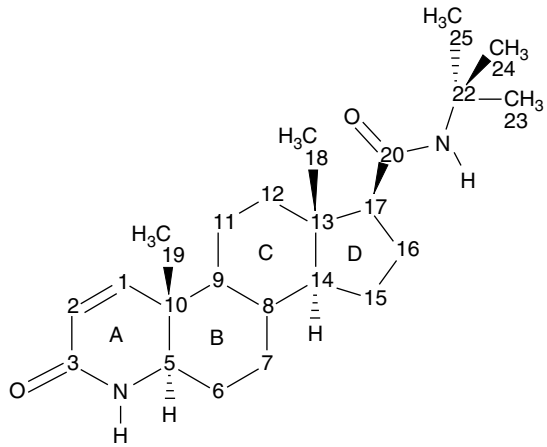


(II)

7.3.2 Assignment of NMR Signals

While there are many experimental ways of assigning NMR spectra, ambiguous or doubtful cases can arise, especially for solids, where the range of experiments can be lower than that for solutions (and resolution is certainly poorer). In fact, solid-state assignments are often made by analogy with those for corresponding solutions. However, this is dangerous because it ignores the effects of crystal packing and of differences in geometry or conformation—identifying which may be the object of the exercise! Computing can help, as in the case of Form I of finasteride

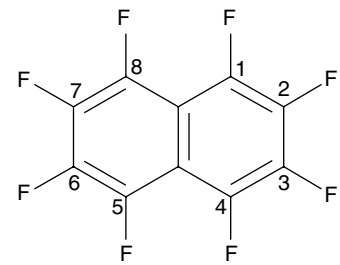
(III)[27]. There is disagreement in the literature regarding the assignments of ^{13}C signals at 164.3 and 169.3 ppm. Wenslow *et al*.[28] assign the former to C3 and the latter to C20, but Morzycki *et al*.[29] reversed this assignment, using arguments based on expectations of hydrogen-bonding changes between solution and solid states. Both carbons are quaternary, so simple dipolar dephasing experiments cannot distinguish between them. We have carried out GIPAW computations on finasteride Form I. The computed shift for C3 is 161.7 ppm and that for C20 is 166.6 when hydrogen positions alone are optimized. The sign of the difference strongly supports the original assignments of Wenslow *et al*.,[28] and the magnitude is in excellent agreement with experiment. This assignment has now been confirmed by INADEQUATE experiments,[30] which establish atomic connectivities. However, these experiments took six days of a high-field spectrometer. Computers are more readily available than state-of-the-art solid-state NMR spectrometers; thus, in principle, precious spectrometer time can be saved through the use of computing!



(III)

7.3.3 Multinuclear Aspects

GIPAW computations give simultaneous results for all nuclei in the system under consideration. Several publications present data for nuclides other than ^{13}C[17,22,31–34] (although the present article largely focuses on applications to organic molecular solids for which only a handful of elements are normally relevant). As an example of computation on a different nuclide, we mention here recent work which used GIPAW calculations to fully assign the ^{19}F spectrum of octafluoronaphthalene **(IV)** to the crystallographically distinct sites of its ambient-temperature structure.[17] The problem was demanding because the chemical shift range is very narrow (about 7 ppm) and fluorine is one of the more challenging atoms for first-principles calculations; a high cutoff energy of 1110 eV was required to ensure convergence. Despite optimization of all the atomic positions and the use of different density functional theory (DFT) functionals, agreement with experimental results was only partial. Two-dimensional correlation experiments were required to confirm that the predicted pattern of correlations was indeed correct. Note that the combination of calculation and experiment was necessary for unambiguous assignment; although the correlation experiments could only provide *relative* assignments of correlated pairs of peaks, they were essential in confirming the validity of the calculations (as in the INADEQUATE case discussed above). Since calculations are of most interest precisely in difficult cases, it is expected that correlation experiments will continue to play a key role in applying the first-principles calculations to NMR problems.



(IV)

It is worth noting that the article on octafluoronaphthalene[17] also discusses the use of the GIPAW method to provide other NMR-related physical parameters such as the anisotropy of the bulk magnetic susceptibility (ABMS), which can make a significant contribution to solid-state MAS NMR linewidths. Application of first-principles calculation to quadrupolar nuclei also provides additional information in the form of predicted quadrupole parameters. Indeed, assignments become significantly more robust when different types of parameters are used together. For example, Yates

et al.[34] and Gervais *et al.*[32,33] showed that ^{17}O quadrupole coupling constants could be used in conjunction with ^{17}O chemical shifts to make unambiguous assignments in cases where overlap of the isotropic shifts made assignment on the basis of shift values alone impossible.

The value of GIPAW calculations in providing results for all nuclides in a system is emphasized by heteronuclear multidimensional experiments. Thus, for terbutaline sulfate **(V)** (anhydrate B modification), GIPAW data can be overlaid on a ^{13}C, ^{1}H HETCOR spectrum, as shown in Figure 7.2. As usual, the one-dimensional proton spectrum is poorly resolved, but two dimensions can improve matters. GIPAW results predict where the hydrogen bond resonance involving aromatic hydroxyl groups should appear. They also allow assignment for the doublet lines of C8 (which arise from the fact that there are two molecules in the asymmetric unit): specifically, it is shown that the high-frequency ^{13}C peak is associated with the high-frequency resonances for the attached protons.

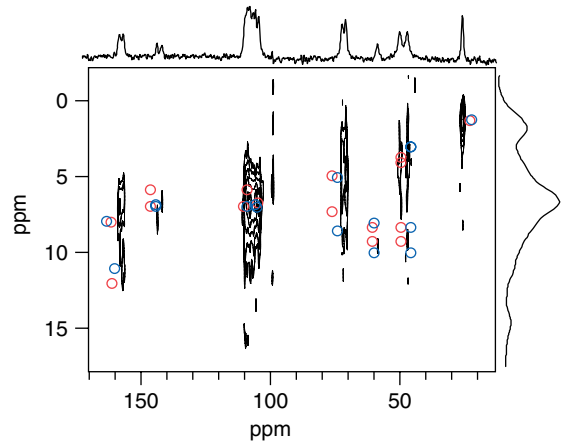
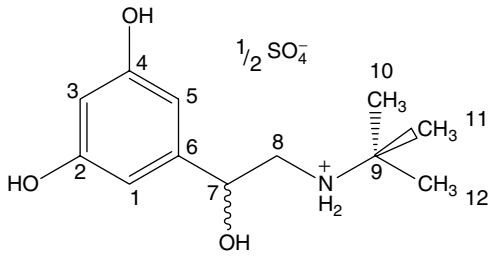


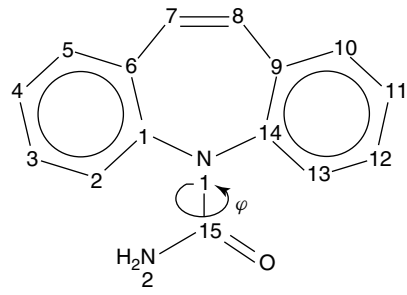
Figure 7.2. ^{13}C, ^{1}H HETCOR plot for the anhydrate B modification of terbutaline sulphate **(V)**, with NMR–CASTEP computed chemical shifts overlaid as circles. The red and blue circles correspond to the two independent molecules of the crystallographic asymmetric unit (see Section 7.3.5).



(V)

7.3.4 Molecular-Level Mobility/Rigidity

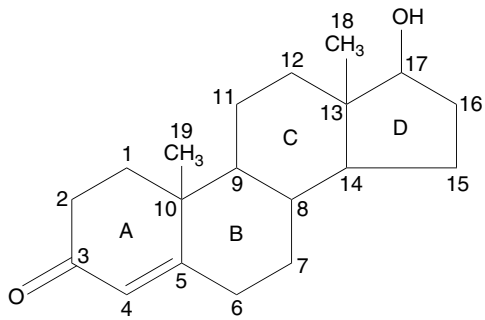
A situation of particular interest occurs when a molecule has intramolecular mobility in the solution state but is rigid in the solid. A common case arises for phenyl or *para*-phenylene rings, for which the solution state generally gives only 3 or 2 different shifts for CH carbons, respectively (ortho protons in a phenyl ring, for example, being equivalent). If the rings are relatively rigidly positioned in the solid state, the influence of packing normally results in the appearance of 5 and 4 CH resonances for phenyl and phenylene systems, respectively. There is no experimental way (at least for microcrystalline powder samples, as normally used for MAS NMR) of assigning the components of an ortho doublet, for example, to the two crystal sites involved. However, computation can often achieve this readily. For the *P*-monoclinic form of carbamazepine **(VI)**, there is an analogous "crystallographic splitting" for the resonances of C1 and C14, because of the fixed position of the acetamido group—in contrast to the situation for a solution at ambient temperature. The experimental splitting is 3.3 ppm (sign unknown),[35] while GIPAW computation gives 3.1 ppm (with the sign defined), allowing assignment of the two signals to specific atomic positions in the crystal structure[36]—the low-frequency component relates to C1.



(VI)

7.3.5 The Crystallographic Asymmetric Unit

Cases of particular interest arise when there is more than one independent molecule of the same chemical species in the crystallographic unit cell (*see* **Chapter 1**). Connectivity experiments, such as INADEQUATE, can link resonances for the same independent molecule, but only computing can then assign the independent molecules to their correct crystallographic site. Since the computation involves differences between closely similar molecules (i.e., the same chemical species), many of the uncertainties are minimized. At the same time, the shift differences are quite small, so that such cases provide a good test of the power of GIPAW. This situation has been demonstrated[23] for the (anhydrous) form of testosterone **(VII)**, which has two molecules in the asymmetric unit, designated *U* and *V* (Figure 7.3). Since the molecules in question are chemically identical, though crystallographically different, comparison between the computational results should be more accurate than when comparing those between different compounds.



(VII)

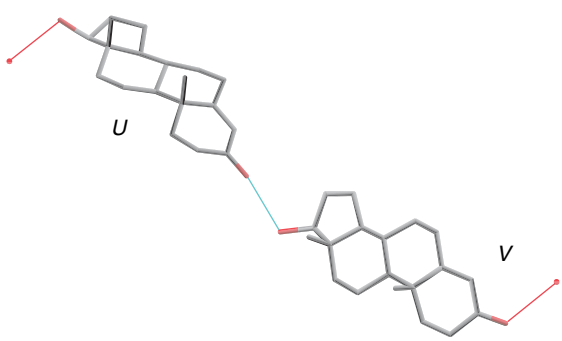


Figure 7.3. The two independent molecules in the α form of testosterone.[35]

Table 7.4. Computed and experimental ^{13}C crystallographic splittings for α-testosterone[a]

	Splitting (ppm)	
Carbon number	Computed	Experimental
1	−0.10	−1.01
2	1.74	+0.79
3	−0.33	±1.50[b]
4	1.69	±0.50[b]
5	−0.16	−1.45
6	1.22	±0.26
7	0.50	+0.15[c]
8	1.59	+0.48
9	−0.13	−1.12
10	1.11	+0.46
11	−1.23	+0.97
12	−0.50	−1.63
13	−0.19	+0.10[c]
14	−0.00	−0.72
15	0.50	±0.10[b]
16	0.17	+0.33[c]
17	−3.40	−2.34
18	0.14	−0.54
19	0.73	+0.64

[a]Signs given as *U*–*V*.
[b]Signs not accessed experimentally.
[c]The splitting sign is not certain on the simple basis of the experimental data, although suggested. Of course, changing the sign of these entries would affect other pairs including C17 (see Ref. 26).

Table 7.4 shows[23] the results (following optimization of proton positions) for the crystallographic splitting, with the signs for the computed shifts given as *U*–*V*. The connectivities between atoms were established, as far as possible, by INADEQUATE experiments, thus linking signals for the two independent molecules separately. The relative signs of the experimental splittings agree with those from computation for each of the four carbon atoms where the experimental splitting is more than 1 ppm and its relative sign is known, provided one of the two possible assignments of experimental resonances to *U* and *V* molecules is made (as in the table). The correct sign is also found for nearly all the remaining carbon signals of known relative experimental sign. While the magnitudes of the splittings are not

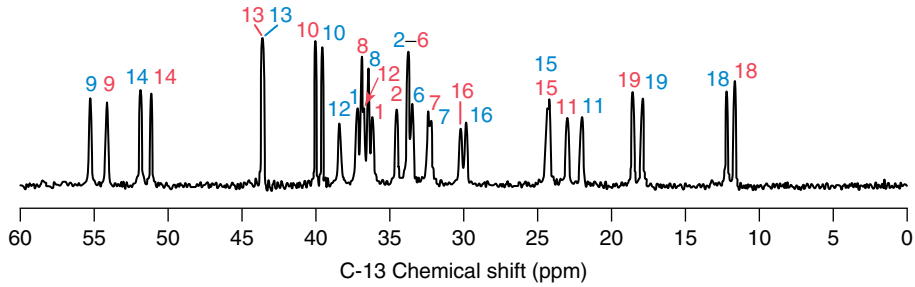


Figure 7.4. Aliphatic region of the ^{13}C spectrum for the α form of testosterone **(VII)**, showing the assignment of the doublet lines to the two independent molecules, as demonstrated by an INADEQUATE experiment combined with computation of the chemical shifts. Blue numbers correspond to molecule *V*, whereas red numbers refer to molecule *U* (see Figure 7.3). (Reproduced from Ref. 37. © Royal Society of Chemistry, 1973, 1978.)

well reproduced, one can be moderately confident that the assignments to *U* and *V* molecules are correct, though the result for C11 remains anomalous. At least the principle is established that signals may be linked to specific crystallographic sites (Figure 7.4) for cases with crystallographic splittings by combining two-dimensional NMR correlation experiments with computation. A similar approach was used[38] for vitamin-D**3**, which also had two molecules in the asymmetric unit. In that case, apparently disordered regions of the crystal structure were refined using plane-wave pseudopotential calculations, though chemical shifts were computed on a molecular basis.

7.3.6 Polymorphic Forms

Polymorphs form a particularly important class of systems, especially for pharmaceutical industry (*see* **Chapters 28**). They can normally be characterized by their NMR spectra since both geometry and packing differences affect chemical shifts. These small differences are ideal for testing the power of the computational methods. Since the molecules are the same chemically, computations of the shift differences between analogous nuclei should be relatively accurate, since some of the causes of error get partially canceled, as has already been emphasized. This has indeed proved to be the case[23] for the α and β forms of testosterone (though, strictly speaking, these are not polymorphs, the β form being a monohydrate). Table 7.5 shows the experimental and computed ^{13}C shift differences between the α and β forms. The relative signs of the experimental differences agree with those from computation in 10 out of the 13 cases where the experimental magnitude is greater than 0.5 ppm. This is an impressive result, given that it is based on relatively old diffraction-derived crystal structures, requiring geometry optimization for the protons.

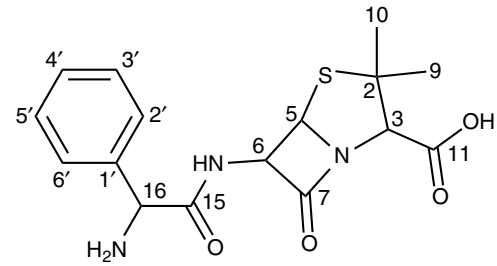
Table 7.5. Computed and experimental ^{13}C shift differences between the α and β forms of testosterone, given as $\alpha - \beta$[23]

	Shift (ppm)	
Carbon number	Computed	Experimental[a]
1	3.02	1.4
2	−1.12	−1.2
3	1.16	1.8
4	0.70	0.7
5	−5.21	−2.4
6	1.29	0.1
7	−1.46	−1.2
8	1.84	1.4
9	−0.69	0.0
10	−0.20	0.4
11	1.72	1.5
12	2.80	2.3
13	−0.04	0.0
14	0.13	−0.1
15	1.81	0.3
16	−0.04	1.2
17	−1.11	0.8
18	0.76	−0.7
19	2.35	1.3

[a]The old published experimental shifts for the β form have been increased by 0.50 ppm to account for a systematic difference between the new and old values for the α form.

7.3.7 Shielding Tensor Components

Another useful test of the accuracy of the computational methods lies in consideration of the full shielding tensor, as has been extensively investigated by the Grant and coworkers using molecule-based programs[3,40–43] (*see* **Chapter 9**). GIPAW computations automatically produce the individual tensor components and thus the anisotropy and asymmetry of shielding, which are, in essence, differences in shielding values for the same nucleus. This is the third case where comparison of chemical shifts for the same chemical entity (indeed, for anisotropies, the identical molecule in different orientations with respect to the applied magnetic field) is involved, so that it provides a good test of the efficacy of the computations. Several uncertainties in the NMR (referencing) and the molecular situation (e.g., only one geometry) are minimized, resulting in an expectation of increased accuracy from that point of view and throwing the burden of accuracy on the validity of the computations. Some GIPAW results for anisotropies have been reported for α testosterone,[23] phenylphosphonic acid[32] and for several amino acids.[33]



(VIII)

In Table 7.6, we report the computed shielding parameters for the antibiotic ampicillin **(VIII)** and compare them with the experimental results of Antzutkin *et al*.[44] The details of the computation are identical to those reported in Ref. 22. The agreement between the computed and experimental parameters is generally good, both for the isotropic shifts and for the anisotropies and asymmetries. The greatest

Table 7.6. Computed and experimental ^{13}C chemical shift parameters for ampicillin

	Computed			Experimental[44]		
	Isotropic shift[a]	Anisotropy[a,b]	Asymmetry[c]	Isotropic shift[a]	Anisotropy[a,b]	Asymmetry[c]
C9	24.22	−24.92	0.86	30.2 ± 0.1	−22.9 ± 0.5	0.94 ± 0.06
C11	162.99	69.35	0.68	173.3 ± 0.1	67.1 ± 0.5	0.93 ± 0.02
C1′	134.89	−125.81	0.54	135.5 ± 0.1	−115.5 ± 1.0	0.61 ± 0.02
C2	64.95	46.39	0.81	64.8 ± 0.1	42.0 ± 0.3	0.76 ± 0.02
C2′[d]	130.03	−117.14	0.75	130.0 ± 0.1	−104.6 ± 1.0	0.79 ± 0.02
C3′[d]	130.01	−130.86	0.68	129.2 ± 0.1	−115.3 ± 0.4	0.72 ± 0.01
C4′	130.10	−130.01	0.70	132.2 ± 0.1	−121.9 ± 1.5	0.68 ± 0.02
C5′[d]	134.09	−137.26	0.63	129.2 ± 0.1	−115.3 ± 0.4	0.72 ± 0.01
C6′[d]	126.31	−132.21	0.63	127.1 ± 0.1	−116.9 ± 1.3	0.64 ± 0.02
C3	77.36	28.42	0.31	73.4 ± 0.5	−31.6 ± 0.7	0.60 ± 0.11
C5	63.10	38.22	0.82	65.3 ± 0.5	36.5 ± 2.9	0.66 ± 0.29
C7	170.47	89.38	0.59	175.2 ± 0.5	93.2 ± 1.5	0.53 ± 0.04
C10	18.81	−28.55	0.54	28.9 ± 0.1	−28.6 ± 0.5	0.56 ± 0.08
C15	163.61	85.67	0.68	170.2 ± 0.5	89.1 ± 2.0	0.73 ± 0.04
C6	49.86	30.31	0.73	57 ± 1	N/A	N/A
C16	55.87	7.40	0.73	57 ± 1	N/A	N/A

[a]In ppm.
[b]Defined as $\delta_{ZZ} - \delta_{iso}$.
[c]Defined as $(\delta_{YY} - \delta_{XX})/(\delta_{ZZ} - \delta_{iso})$.
[d]Simultaneous interchange of the computed values for C2′ with C6′ and C3′ with C5′ may be made, since the relationship of the phenylene ring carbon positions to the experimental shifts is ambiguous.

differences between computed and experimental isotropic shifts occur at the ends of the shift range as both the methyl and carbonyl resonances are underestimated by 10 ppm. For the anisotropy (Figure 7.5), some deviation is found for the aromatic sites, and there is also a major puzzle for C3, for which the computation seems to give the wrong sign even though the asymmetry is not near 1. It is instructive to view the computed resultsas a plot of anisotropy *versus* isotropic shift as in Figure 7.6. In such a plot, the systematic nature of the errors in the computed

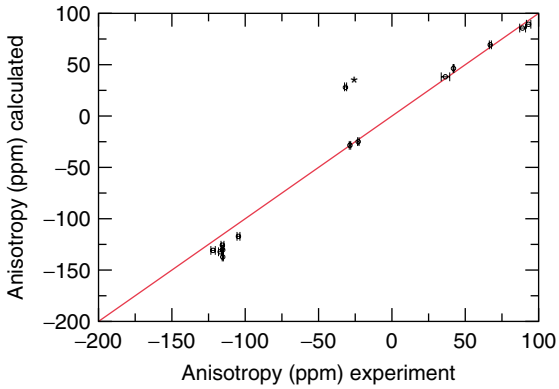


Figure 7.5. Comparison of computed and experimental chemical shift anisotropies for ampicillin. The anomalous value for C3 is indicated by an asterisk. The line is of unit slope.

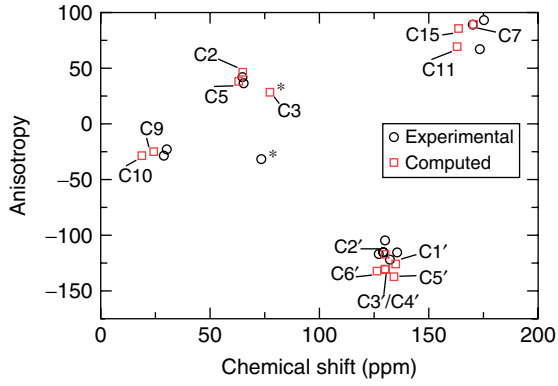


Figure 7.6. Two-dimensional comparison of computed and experimental results for ampicillin, using both isotropic chemical shifts and anisotropies. The sites of the computed peaks are labeled. The asterisks denote the C3 site whose anisotropy differs in sign between experiment and computation.

results is evident. From Figure 7.6, we can assign the two methyl sites, C9 and C10, to the peaks at 30.2 and 28.9 ppm respectively, in agreement with the assignment in Ref. 44, which reversed that of Ref. 45. Distinctions between the resonances of the aromatic ring sites are less clear because the differences are small. Clearly, using two independent parameters provides a way to compensate for the errors in the computations, leading to more reliable assignments; instead of using chemical shifts anisotropy information, related approaches have used quadrupolar parameters[33,46] or a two-dimensional MAS-J-HMQC spectrum correlating ^{13}C and ^{1}H chemical shifts.[31]

7.3.8 Effects of Crystal Packing

It is of considerable interest to determine to what extent observed differences between chemical shifts for isolated molecules (often approximated by dilute solutions in noninteracting solvents) and those for crystalline solids occur for intramolecular reasons (differences in geometry or conformation) or because of the environment (crystal packing) in the solid (intermolecular reasons) (*see* **Chapter 21**). Additional NMR experiments to differentiate between these effects may be impossible, but computation can be of considerable value. It is feasible to undertake GIPAW computations on effectively isolated molecules (by the use of large vacuum supercells) with the same general geometry as in the crystalline state, so addressing the question. Of course, there may be issues around the matter of optimization of hydrogen positions in cases where intermolecular hydrogen bonding occurs, but these can be addressed by suitable variations in the computing protocol. This is one example where computation can be used as a "thought" experiment.

Yates *et al.*[31] have taken this concept further for maltose **(IX)** anomers and have shown that the computed change in the CH and CH_2 proton chemical shifts when comparing the full crystal and an isolated molecule is a quantitative measure of weak intermolecular C–H···O hydrogen bonding (see Figure 7.7). The computed shift changes were found to be up to 2 ppm (~10% of the typical range of ^{1}H shifts in solids); moreover, there was a clear correlation between a large chemical shift change and both a short H···O distance (<2.7 A) and a CHO

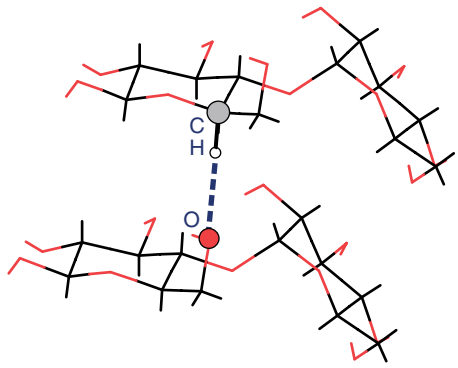
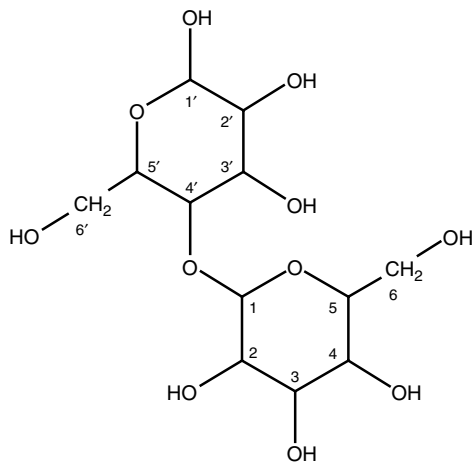


Figure 7.7. The weak inter-molecular C–H···O hydrogen-bonding arrangement associated with the H4 proton in the anhydrous α-maltose structure. (Reproduced from Ref. 29. © Royal Society of Chemistry, 2002.)

bond angle $<130^{\circ}$, thus showing that directionality is important in C–H···O hydrogen bonding (see Figure 7.8).



(IX)

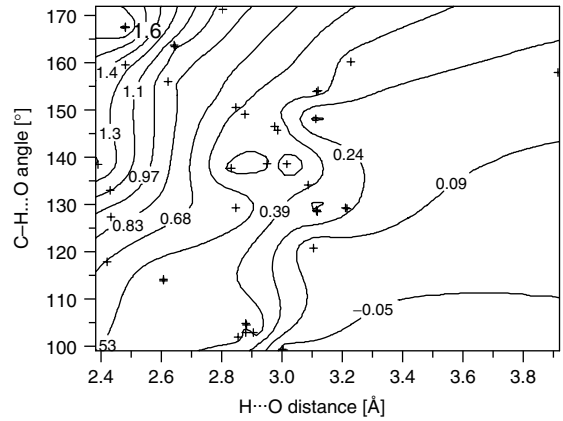


Figure 7.8. A contour plot showing the dependence of the calculated molecule-to-crystal change in chemical shift $\Delta\delta_{iso}(^1H)$ on CH–O bond length and bond angle for anomers of the disaccharide maltose. The crosses correspond to all CH and CH_2 ^1H nuclei in anhydrous α-maltose, anhydrous β-maltose, and β-maltose monohydrate. The contours of constant $\Delta\delta_{iso}(^1H)$ were obtained by fitting to these points. (Reproduced from Ref. 29. © Royal Society of Chemistry, 2002.)

7.3.9 Solvates and Cocrystals

A similar question arises for solvates and cocrystals, the latter being essentially solvates where the pure "solvent" compound is solid at ambient temperature (*see* **Chapter 28**). What influence do the solvent molecules have on the chemical shifts? Experimentally, one might not be able to obtain data for the host structure without the solvent since desolvation often produces an entirely different structure. However, in the computations one can artificially remove the solvent molecules from the host structure and recompute the chemical shifts (another type of "thought" experiment). Of course, this may again raise questions about geometry optimization, but possible variations on this theme can be tried. Table 7.7 contains computation results for the acetic acid solvate of finasteride **(III)**. In this compound, the acetic acid molecule acts as a H-bond donor to the C1 carbonyl oxygen atom and as a H-bond acceptor from the NH nitrogen atom at position 2. Data are included in Table 7.6 for the full solvate (with the proton positions optimized), for the solvate with the solvent artificially removed (retaining the optimized proton positions) and again for the solvate with the solvent artificially removed but with the proton positions reoptimized. It can be seen that the effect of the solvent is, in this case, relatively small, being between −3.1 ppm for C2 and +4.0 ppm for C1 (but with most resonances shifted by less than 0.6 ppm in magnitude). The additional effect of reoptimizing proton positions is smaller, ranging from −0.4 ppm for C1 to +0.5 ppm for C3 (but with all

Table 7.7. Carbon-13 chemical shifts (in ppm) of the finasteride acetic acid solvate: NMR–CASTEP results

Position	Computed CS[a]	Computed CS without solvent	Solvent effect	Computed CS without solvent[b]	Reoptimisation effect	Solvent effect[c]
1	162.1	158.1	4.0	157.7	−0.4	4.4
2	124.8	127.9	−3.1	128.1	0.2	−3.3
3	166.3	164.9	1.4	165.4	0.5	0.9
5	62.1	62.3	−0.2	62.2	−0.1	−0.1
6	24.3	27.1	−2.8	27.0	−0.1	−2.7
7	30.2	30.2	0.0	30.2	0.0	0.0
8	35.5	35.6	−0.1	35.6	0.0	−0.1
9	49.6	49.4	0.2	49.4	0.0	0.2
10	41.4	42.3	−1.0	42.3	0.0	−0.9
11	19.4	19.6	−0.3	19.6	0.0	−0.2
12	36.7	37.8	−1.1	38.0	0.2	−1.3
13	45.5	45.1	0.5	45.1	0.0	0.4
14	56.1	55.8	0.3	55.8	0.0	0.3
15	25.6	25.6	0.0	25.6	0.0	0.0
16	21.2	22.0	−0.8	22.1	0.1	−0.9
17	57.3	58.7	−1.4	58.8	0.1	−1.5
18	9.9	9.7	0.2	9.6	−0.1	0.3
19	9.2	9.7	−0.5	9.7	0.1	−0.5
20	170.0	169.7	0.3	169.8	0.1	0.2
22	50.6	50.5	0.2	50.4	−0.1	0.2
23[d]	25.0	25.0	0.0	24.9	−0.1	0.1

[a]Proton positions optimized.
[b]Proton positions reoptimized after removal of solvent.
[c]Including reoptimization.
[d]Average of C23, C24, and C25.

other values 0.2 ppm or less in magnitude). It is not altogether easy to rationalize the apparent effects of the solvent molecules on the chemical shifts of the host shown by the computations, but it should be noted that the major effects are seen for C1, C2, and C6, which are in the region affected by hydrogen bonding. There is no C–OH group in finasteride to act as donor in hydrogen bonding with the "solvent" molecule, so reoptimization is not expected to have a major effect on any ^{13}C chemical shift.

A second example in which solvent molecules (in this case, water) have been removed by a virtual process from a solvate during GIPAW computations involves the β form of testosterone (VII), which is a monohydrate. Table 7.8 contains the data. The changes in chemical shift are, on the whole, small, the biggest values (greater than 1.0 ppm in magnitude) being associated with the atoms (C3, C5, and C17) involved in the hydrogen bonding (C5 by conjugation). There appears to be a general shift of 0.4 ppm when the water is removed.

7.3.10 Hydrogen Bonding

As discussed earlier, one can compute the chemical shift with variation of the position of a hydrogen atom within a hydrogen bond (*see* **Chapter 22**). This procedure can be used to locate the position of the proton in cases where the diffraction-based refinement of the crystal structure does not involve such atoms (but where the hydrogen atoms are reported at "chemically reasonable positions"). Such shift computations were carried out[47] for methylnitroacetanilide **(II)** (but in that case using the Gaussian program and a molecular cluster) and the N···H distance estimated to be 1.03 ± 0.02 Å. The method was validated for L-histidine hydrochloride monohydrate, where neutron diffraction data were available. Of course, this

Table 7.8. NMR–CASTEP computations of carbon-13 chemical shifts (in ppm) for β testosterone with the published structure and with water molecules removed

Atom number	Full structure	Water removed	Difference[a]
C1	31.9	32.0	0.6
C2	32.3	32.9	1.0
C3	203.4	201.2	−1.8
C4	127.0	126.8	0.2
C5	187.7	184.2	−3.0
C6	32.4	32.0	0.0
C7	33.6	33.4	0.2
C8	32.8	32.5	0.1
C9	55.5	55.4	0.3
C10	40.0	39.6	0.1
C11	18.2	18.2	0.4
C12	33.9	33.1	−0.3
C13	41.5	41.4	0.3
C14	51.0	51.0	0.4
C15	20.0	18.8	−0.8
C16	25.8	25.2	−0.2
C17	85.4	87.7	2.7
C18	6.5	6.4	0.3
C19	11.7	10.6	−0.6

[a]Corrected for a general shift of −0.4 ppm.

approach assumes a fixed position for the hydrogen atom, whereas in reality it is vibrating in a potential well, which could have an asymmetric double minimum, but some form of weighted averaging of results for different hydrogen positions can, in principle, be applied.

7.4 CONCLUSIONS

Computations of chemical shifts can reveal new information, inaccessible by experimental methods. Hence, gains can be made in understanding the link between chemical shifts and crystal structure. Computation thus becomes a vital tool in the application of NMR to crystallography. Currently, the accuracy of the computations allows firm conclusions to be made in some situations, but in others it is not yet possible to use the results with complete confidence. Developments in theory and computation should allow more challenging situations to be addressed in future. In this sense, NMR provides some very sensitive tests of theory and presents a challenge to theoreticians to further improve the computational methodology. The current aim is to consistently reduce discrepancies between computed and experimental shifts for ^{13}C resonances to below 2 ppm. Questions regarding temperature consistency between diffraction and NMR results and of molecular-level mobility need to be resolved, and further work is required.

REFERENCES

1. T. Helgaker, M. Jaszuski, and K. Ruud, *Chem. Rev.*, 1999, **99**, 293.
2. J. Gauss and J. F. Stanton, *Adv. Chem. Phys.*, 2002, **123**, 355.
3. J. C. Facelli and D. M. Grant, *Nature*, 1993, **365**, 325.
4. C. Ochsenfeld, S. P. Brown, I. Schnell, J. Gauss, and H. W. Spiess, *J. Am. Chem. Soc.*, 2001, **123**, 2597.
5. R. Salzmann, C. J. Ziegler, N. Godbout, M. T. McMahon, K. S. Suslick, and E. Oldfield, *J. Am. Chem. Soc.*, 1998, **120**, 11323.
6. A. C. De Dios and E. Oldfield, *Chem. Phys. Lett.*, 1993, **205**, 108.
7. D. Stueber, *Concepts Magn. Reson.*, 2006, **28**, 347.
8. C. J. Pickard and F. Mauri, *Phys. Rev. B*, 2001, **63**, article no. 245101.
9. F. Mauri, B. G. Pfommer, and S. G. Louie, *Phys. Rev. Lett.*, 1996, **77**, 5300.
10. T. Gregor, F. Mauri, and R. Car, *J. Chem. Phys.*, 1999, **111**, 1815.
11. C. G. Van der Walle and P. E. Blöchl, *Phys. Rev. B*, 1993, **47**, 4244.
12. S. E. Ashbrook, A. J. Berry, D. J. Frost, A. Gregorovic, C. J. Pickard, J. E. Readman, and S. Wimperis, *J. Am. Chem. Soc.*, 2007, **129**, 13213.
13. A. Soleilhavoup, M. R. Hampson, S. J. Clark, J. S. O. Evans, and P. Hodgkinson, *Magn. Reson. Chem.*, 2007, **45**, S144.
14. J. R. Yates, C. J. Pickard, and F. Mauri, *Phys. Rev. B*, 2007, **76**, article no. 024401.
15. D. Vanderbilt, *Phys. Rev. B*, 1990, **41**, 7892.
16. J. P. Perdew, K. Burke, and M. Ernzerhof, *Phys. Rev. Lett.*, 1996, **77**, 3865.
17. A. J. Robbins, W. T. K. Ng, D. Jochym, T. W. Keal, S. J. Clark, D. J. Tozer, and P. Hodgkinson, *Phys. Chem. Chem. Phys.*, 2007, **9**, 2389.

18. Y. J. Lee, B. Bingl, T. Murakhtina, D. Sebastiani, W. H. Meyer, G. Wegner, and H. W. Spiess, *J. Phys. Chem. B*, 2007, **111**, 9711.
19. D. Sebastiani and U. Rothlisberger, *J. Phys. Chem. B*, 2004, **108**, 2807.
20. J. Schmidt and D. Sebastiani, *J. Chem. Phys.*, 2005, **123**, article no. 074501.
21. M. Profeta, F. Mauri, and C. J. Pickard, *J. Am. Chem. Soc.*, 2003, **125**, 541.
22. J. R. Yates, S. E. Dobbins, C. J. Pickard, F. Mauri, P. Y. Ghi, and R. K. Harris, *Phys. Chem. Chem. Phys.*, 2005, **7**, 1402.
23. R. K. Harris, S. A. Joyce, C. J. Pickard, S. Cadars, and L. Emsley, *Phys. Chem. Chem. Phys.*, 2006, **8**, 137.
24. R. K. Harris, E. D. Becker, S. M. Cabral de Menezes, R. Goodfellow, and P. Granger, *Pure Appl. Chem.*, 2001, **73**, 1795.
25. D. L. VanderHart, in *'Encyclopedia of Nuclear Magnetic Resonance'*, eds D. W. Grant and R. K. Harris, John Wiley & Sons: Chichester, 1996, Vol. 5, p. 2938.
26. R. K. Harris, P. Y. Ghi, R. B. Hammond, C. Y. Ma, K. J. Roberts, J. R. Yates, and C. J. Pickard, *Magn. Reson. Chem.*, 2006, **44**, 325.
27. O. Othman, J. S. O. Evans, I. R. Evans, R. K. Harris, and P. Hodgkinson, *J. Pharm. Sci.*, 2007, **96**, 1380.
28. R. M. Wenslow, M. W. Baum, R. G. Ball, J. A. McCauley, and R. J. Varsolona, *J. Pharm. Sci.*, 2000, **89**, 1271.
29. J. W. Morzycki, I. Wawer, A. Gryszkiewicz, J. Maj, L. Siergiejczyk, and A. Zaworska, *Steroids*, 2002, **67**, 621.
30. A. Lesage, M. Bardet, and L. Emsley, *J. Am. Chem. Soc.*, 1999, **121**, 10987.
31. J. R. Yates, T. N. Pham, C. J. Pickard, F. Mauri, A. M. Amado, A. M. Gil, and S. P. Brown, *J. Am. Chem. Soc.*, 2005, **127**, 10216.
32. C. Gervais, M. Profeta, V. Lafond, C. Bonhomme, T. Azais, M. Mutin, C. J. Pickard, F. Mauri, and F. Babonneau, *Magn. Reson. Chem.*, 2004, **42**, 445.
33. C. Gervais, R. Dupree, K. J. Pike, C. Bonhomme, M. Profeta, C. J. Pickard, and F. Mauri, *J. Phys. Chem. A*, 2005, **109**, 6960.
34. J. R. Yates, C. J. Pickard, M. C. Payne, R. Dupree, M. Profeta, and F. Mauri, *J. Phys. Chem. A*, 2004, **108**, 6032.
35. R. K. Harris, P. Y. Ghi, H. Puschmann, D. C. Apperley, U. J. Griesser, R. B. Hammond, C.-Y. Ma, K. J. Roberts, G. J. Pearce, J. R. Yates, and C. J. Pickard, *Org. Process Res. Dev.*, 2005, **9**, 902.
36. J. N. Lisgarten, R. A. Palmer, and J. W. Saldanha, *J. Crystallogr. Spectrosc. Res.*, 1989, **19**, 641.
37. P. J. Roberts, R. C. Petterson, G. M. Sheldrick, N. W. Isaacs, and O. Kennard, *J. Chem. Soc., Perkin Trans. 2*, 1973, 1978.
38. R. A. Olsen, J. Struppe, D. W. Elliott, R. J. Thomas, and L. J. Mueller, *J. Am. Chem. Soc.*, 2003, **125**, 11784.
39. R. K. Harris, *Analyst*, 2006, **131**, 351.
40. R. J. Iuliucci, J. C. Facelli, D. W. Alderman, and D. M. Grant, *J. Am. Chem. Soc.*, 1995, **117**, 2336.
41. J. K. Harper, D. M. Grant, Y. G. Zhang, P. L. Lee, and R. Von Dreele, *J. Am. Chem. Soc.*, 2006, **128**, 1547.
42. J. K. Harper and D. M. Grant, *Cryst. Growth Des.*, 2006, **6**, 2315.
43. J. K. Harper, D. H. Barich, E. M. Heider, and D. M. Grant, *Cryst. Growth Des.*, 2005, **5**, 1737.
44. O. N. Antzutkin, Y. K. Lee, and M. H. Levitt, *J. Magn. Reson.*, 1998, **135**, 144.
45. N. J. Clayden, C. M. Dobson, L.-Y. Lian, and J. M. Twyman, *J. Chem. Soc., Perkin Trans. 2*, 1986, **35**, 1933.
46. S. J. Clark, M. D. Segall, C. J. Pickard, P. J. Hasnip, M. J. Probert, K. Refson, and M. C. Payne, *Z. Krystallogr.*, 2005, **220**, 567.
47. R. K. Harris, P. Y. Ghi, R. B. Hammond, C.-Y. Ma, and K. J. Roberts, *Chem. Commun.*, 2003, **22**, 2834.

Chapter 8

Chemical Shifts & Solid-state Molecular-level Structure

Anita M. Orendt[1] and Julio C. Facelli[1,2]

[1]*Center for High Performance Computing, University of Utah, Salt Lake City, UT 84112-0190, USA*
[2]*Department of Biomedical Informatics, University of Utah, Salt Lake City, UT 84112-0190, USA*

8.1	Introduction	99
8.2	Molecular Structure	100
8.3	Tautomeric Form	100
8.4	Bond Lengths	101
8.5	Bond Angles	103
8.6	Dihedral Angles	103
8.7	Steric Crowding	106
8.8	Concluding Remarks	108
	References	109

8.1 INTRODUCTION

The importance of NMR chemical shifts for obtaining information about molecular structure has been evident since the first observation of the sensitivity of the chemical shift to the electronic environment of the nucleus. The chemical shift of a given nucleus in a compound is affected by the cumulative effect of the electrons of the atoms surrounding the nucleus of interest and the nature of the interaction between these electrons and this nucleus. Tables of the chemical shift ranges of nuclides in different bonding situations are given in many works; herein we cite only one.[1] Typical ranges of chemicals shifts widely vary between different nuclides: the range, for diamagnetic samples, is about 15 ppm for ^{1}H, several hundred parts per million for ^{13}C, around 1000 ppm for ^{15}N and ^{17}O, and several thousands of parts per million for nuclei such as ^{81}Br, ^{129}Xe, ^{207}Pb. In the first two sections of this article, a few examples of how chemical shift measurements can be used to obtain structural information, such as confirmation of the structure of the molecule or its tautomeric form, are highlighted; this is of particular importance in the solid state where the definition of the molecular unit might not be obvious. In the remaining sections, the focus is on the sensitivity of chemical shifts to specific geometrical features for a given bonding arrangement, namely bond lengths, bond angles, and dihedral angles as well as the effects of steric crowding. Although the relationship between structure and chemical shifts is usually complex, there are many cases in which simple rules have been obtained either by empirical correlations or by molecular modeling.

The early work on ^{13}C solution-state isotropic shifts highlighted the manner in which structural effects could be quantified in a number of different classes of compounds.[2] With the advent of the techniques of cross polarization[3] and magic-angle spinning,[4–6] this type of work was extended to

NMR Crystallography Edited by Robin K. Harris, Roderick E. Wasylishen and Melinda J. Duer © 2009 John Wiley & Sons, Ltd. ISBN: 978-0-470-69961-4

isotropic chemical shifts measured from solids. The use of solid-state measurements is often advantageous as there are cases where the bonding environment or tautomeric form changes between solution and solid state. In addition, a number of effects, such as the freezing of conformations, the existence of polymorphism, multiple molecules per asymmetric unit, or different phases are observed only in the solid state. In these cases, there are often distinct differences observed between the values of the chemical shifts obtained from solution-state and solid-state measurements, sometimes leading to assignment difficulties.[7]

Finally, it should be mentioned that the measurement of the principal values of the shift tensor in a powdered solid or the full tensor in a single crystal allows a more detailed picture of the three-dimensional nature of the electronic environment.[8] This is important because, in a number of cases,[9,10] it has been shown that an effect observed in the isotropic shift is due to a change in only one of the three tensor components, and as such the effect is three times as large in this one component. In other cases,[11,12] there is little or no effect observed in the isotropic shift, but there are effects that cancel among the components, with one or more shifting to higher chemical shift values and others to lower chemical shift values. While this article briefly discusses some cases where principal values are studied, the reader is directed to **Chapter 9** for a more detailed account of the sensitivity of principal values to structural parameters.

The use of quantum chemical calculations of the magnetic shielding tensor is crucial in the study of the relationship between chemical shifts, whether isotropic or a tensor component, and structure. Calculations serve two main purposes: they allow for the assignment of a chemical shift to a particular nucleus in the compound of interest, necessary for further analysis in cases where this information has not been obtained experimentally, and they allow for the systematic study of one independent effect in ways that are not always possible in experiments, by performing calculations with changes of a single structural parameter.

What follows is by no means a complete review of all the literature on this topic; instead, a representative selection of cases is used to highlight the manner in which chemical shifts are influenced by structural features.

8.2 MOLECULAR STRUCTURE

One of the earliest solid-state MAS spectra showed that PCl_5 in its stable form actually exists as a mixture of PCl_4^+ and PCl_6^-, contrary to what has been observed in earlier solution-state NMR but consistent with the crystal structure.[13,14] The solution-state ^{31}P NMR showed one resonance at 80 ppm, whereas in the solid state, there were two resonances observed at −96 and 281 ppm. A similar situation, as was mentioned in the initial chapter of this handbook, was observed in the coordination of a phospha-alkene ligand to a platinum: in solution state, an η^2-complex was observed whereas by solid-state measurements, an η^1-complex was determined to exist, again confirmed by an X-ray structure.[15] A difference of 278 ppm is observed in the chemical shift of the phospha-alkene phosphorus between the two bonding arrangements, allowing the assignment of the type of bonding and therefore, the molecular structure to be made readily. These examples serve as illustrations of the importance of using solid-state NMR measurements to confirm the structure of a sample in the solid state instead of assuming that it will be the same as in solution.

Although the above examples illustrate drastic changes in bonding arrangements leading to very large changes in chemical shifts between solution and the solid state, often more modest changes are observed. One such case is the chemical shift of the carbonyl carbon in carboxylic acids, which has been shown to depend on the protonation state of this group.[12] This effect, observed in a series of amino acids and dipeptides in both the protonated and deprotonated forms, has been observed as a small change of around 4 ppm measured isotropic shift. The δ_{11} and δ_{22} components, however, show much larger changes, with the former changing from 242 to 257 ppm and the latter from 177 to 155 ppm, on average from a set of approximately 35 amino acids and amino-acid hydrochloride salts. These large, reproducible changes allow for a reliable method to assign a protonation state of a carboxylate carbon on the basis of the NMR measurement of the ^{13}C chemical shift principal values.

8.3 TAUTOMERIC FORM

The chemical shift measured or calculated for compounds with multiple tautomeric forms can provide

valuable information on the form that exists or about any tautomeric averaging that might be occurring. As with the case of conformational averaging that is discussed below, there are many cases where averaging occurs in solution but in the solid state, only one form exists, especially if the spectrum is recorded at low temperatures. In the following, we focus on a couple of examples that illustrate this effect.

As shown in Figure 8.1, a series of ^{15}N shielding values shows distinct changes in both the isotropic and the principal components between a protonated and nonprotonated nitrogen in both five- and six-membered nitrogen heterocyclic compounds.[16]

Nitrogen heterocyclic compounds such as imidizoles, pyrazoles,[17] and triazoles contain both protonated and nonprotonated nitrogens. For imidizole,[18] a single ^{15}N peak at 186 ppm is observed in solution, indicative of averaging, whereas in the solid state, only one form exists, with two ^{15}N peaks – one observed at 150 ppm (protonated) and the second at 222 ppm (nonprotonated). Similar effects are observed for the imidizole ring in histidine.

Chemical shift values have also been used to assign tautomeric forms present in other forms of tautomerism such as keto-enol[19,20] and ketone-hemiketal.[21]

8.4 BOND LENGTHS

The dependence of chemical shift on bond length has been explored with shielding surfaces or plots of chemical shift versus bond length for a variety of diatomic and other small molecules.[22,23] The use

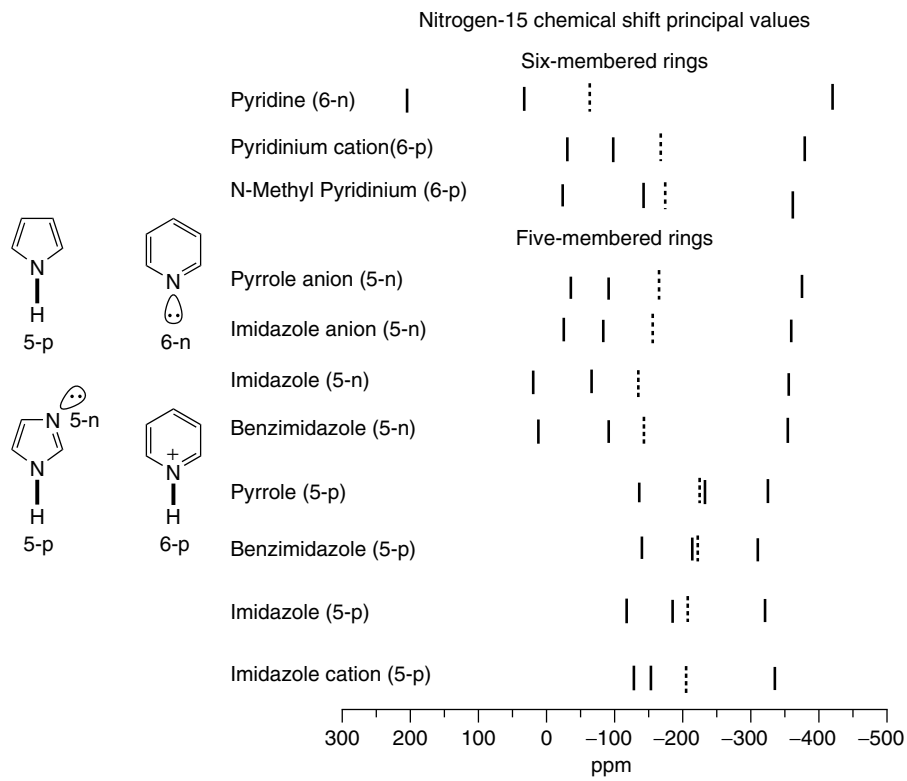


Figure 8.1. Schematic of nitrogen types in five-and six-membered heterocyclic rings along with typical isotropic (dotted lines) and principal components (solid lines) for representative compounds of each type. (Reproduced from Ref. 16. © American Chemical Society, 1997.)

of theory is critical in the study of how chemical shifts are influenced by bond length as a series of quantum chemical calculations changing a specific bond length can be readily done, a task that is impossible to do experimentally for a range of bond lengths without introducing other changes that also affect the chemical shifts. It should be noted that experimentally the dependence of chemical shifts on bond lengths can be explored over a narrow range of bond length, for small molecules, with the use of isotopic labeling.[24,25] These experiments and calculations can also serve to show the effect of rotational/vibrational stretching of bonds on the chemical shift.[26]

Results are typically reported as derivatives of the nuclear shielding with respect to bond length, $\partial^n\sigma/\partial r^n$. The first derivative is nearly always found to be negative, i.e., chemical shifts move to higher values as the bond length is increased, and its magnitude depends both on the atoms involved and the type of bonding. It should also be noted that although the dependence of chemical shift on bond length is not linear over a large range, for practical purposes (in the vicinity of typical bond lengths for a given atomic pair and bonding type) it can be treated as such. The trends are as follows: (i) the first derivatives become smaller when one of the atoms is hydrogen as against the case when both are heavy atoms and (ii) as the multiplicity of the bond increases, the magnitude of the derivatives become larger.[23] In the case of carbon isotropic chemical shifts, these derivatives are in the range of about -50 ppm Å^{-1} for C–C single bonds to about -300 ppm Å^{-1} for multiple or aromatic C–C bonds. This type of analysis has also been expanded to the study of more complex molecules such as amino acid residues,[27] where calculations have been done to explore the dependence of the C^{α} and C^{β} chemical shifts on various bond lengths in glycine, alanine, and valine. The magnitude of the calculated derivatives highlights the need to have accurate geometries when using shielding calculations to interpret experimental results.

Grant *et al*. explored the sensitivity of the calculated chemical shift tensor components to C–H bond distances and showed that in a number of different molecules (for example, perylene,[28] acenaphthene,[29] pentaerythritol,[30] and methyl-β-D-glucopyranoside[31]), the agreement between theoretical shielding values and experimental chemical shifts could be substantially improved by using the most exact information available for the hydrogen atom positions in molecules. As is widely known, X-ray diffraction generally does not provide accurate positions for hydrogen atoms, whereas neutron diffraction does; therefore, the best agreement is obtained by using neutron diffraction

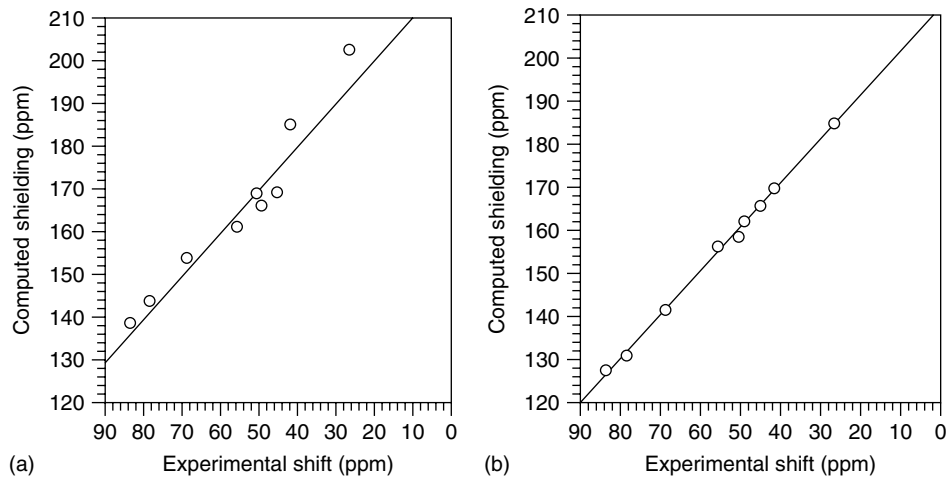


Figure 8.2. Plot of computed versus experimental chemical shifts in pentaerythritol for (a) X-ray atomic positions, with an rms agreement between experiment and theory of 4.45 ppm and (b) neutron diffraction atomic positions with an rms of 0.86 ppm. (Reproduced from Ref. 30. © American Chemical Society, 1997.)

structures when available. In the absence of neutron diffraction structures, the use of theory to optimize the position of hydrogen atoms in an X-ray structure is shown to be the best option. In most cases, the improvement in the agreement between experiment and theory was substantial – for example, in pentaerythritol,[30] as shown in Figure 8.2, using the X-ray structure for all atom positions gave a root mean square (rms) difference of 4.45 ppm between experimental and theoretical chemical shift principal values, whereas a neutron structure gave an rms of 0.86 ppm; using the X-ray structure with optimized hydrogen atom positions gives an rms of 1.19 ppm.

In many cases, uncertainties in the molecular geometries can produce uncertainties in the calculated shielding values that are larger than the experimental errors and comparable to the error due to approximations used in the calculations,[32] making the comparison between calculated and experimental chemical shifts challenging.

8.5 BOND ANGLES

As with bond lengths, the influence of bond angles on chemical shifts has also been explored, though to a much lesser extent, by using calculations to generate shielding surfaces as a function of angle.[22] In the same study of amino acids mentioned in the previous section, the effect of the backbone bond-angle variations in several different glycine, alanine, and valine residues[27] was also studied. Although the variation with bond length can generally be, as mentioned in the previous section, approximated as a linear function over a typical bond-length range for a given type of bond, the dependence on angle shows a significant curvature even over a $\pm 10^\circ$ range. The variations of the first derivative with respect to the angle are less than 1 ppm per degree in the amino acid residues mentioned above.

In the case of pentaerythritol,[30] the CCC angle in the solid, where the tetrahedral symmetry is not maintained because of distortion from the OH groups, was shown to have a dependence on the difference between the perpendicular and parallel components of the central carbon's shift tensor. In calculations of the shielding tensor, this difference showed a 2.7 ppm per degree linear dependence on the angle; this dependence resulted in a predicted CCC angle of 106.6° versus the 107.1° angle measured via neutron diffraction.

The effect of the CCX angle (where X = C, O, S) on the isotropic and principal values of the methylene carbon was explored for a set of cycloalkanes, cycloalkenes, and heterocyclic compounds.[10] For the compounds studied, the local symmetry of the CH_2 group dictates the orientation. Calculations showed one component bisecting the HCH angle, one perpendicular to the HCH plane, and the third perpendicular to the CCX plane (designated δ_{CC}), as shown in Figure 8.3. Experimentally, it was known that in cyclopropane,[33] with a small CCC angle of 49.8°, the δ_{CC} component is found to be -36 ppm (δ_{33}), while in *n*-eicosane,[34] CCC angle of 110.0°, it was 51 ppm (δ_{11}). The other two components stay in the same rank ordering and show much less variation, such that essentially the entire isotropic difference between these two compounds is reflected in the changes in the δ_{CC} component. In this study of 22 different compounds, some of which even include electronic effects by introducing an O or S atom in the α-position relative to the methylene carbon, these trends were still observed, as shown in Figure 8.3. The scatter observed between the lines calculated for cyclopropane and propane is due to other factors affecting the chemical shifts of these compounds, factors which cannot be isolated in the experimental measurements.

8.6 DIHEDRAL ANGLES

Numerous studies on the dependence of chemical shifts on dihedral angles exist in the literature, mainly due to the large role these angles play in determining the overall structure of a molecule. The scope of this article only allows for the mention of a select few; therefore, readers are directed to the annual specialist periodical reports on NMR compiled by Jameson and collaborators for a more comprehensive list.[35] It should be noted that, as with bond lengths and bond angles, it is difficult to experimentally isolate only a change in a dihedral angle. Calculations, on the other hand, allow for the study of chemical shift only due to the dihedral angle change as long as the change in the dihedral angle is not accompanied by a reoptimization of the rest of the molecule.

Grant and Paul[2] first studied the so-called γ effect, the dependence of the carbon chemical shift on the spatial orientation of a substituent in the γ position, in solution; using linear regression to separate a number of substituent effects, they found an effect of about

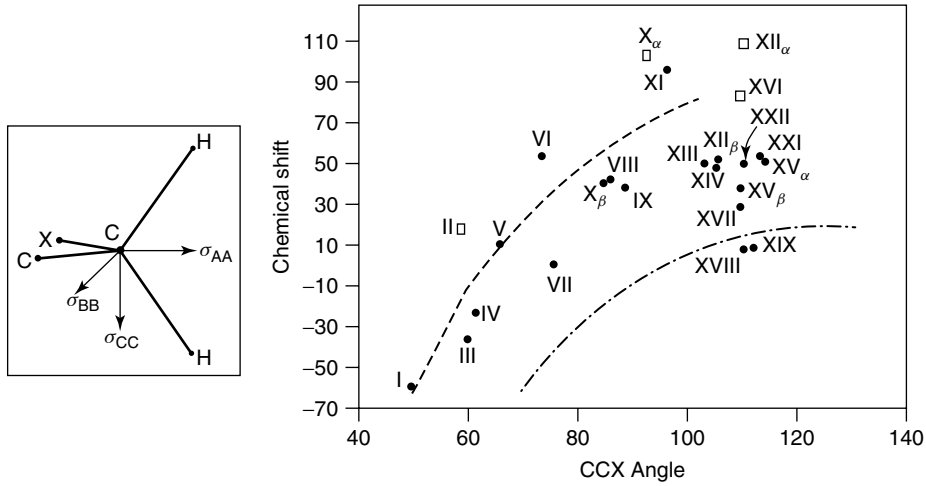


Figure 8.3. Relationship between δ_{CC} component and CCX angle (see insert) for as set of 22 methylene carbons; cases where X=O are designated as squares. Dashed lines are the calculated angular dependence as a function of CCC angle for the central carbon of (a) cyclopropane and (b) propane. (Reproduced from Ref. 10. © American Chemical Society, 1985.)

3 ppm between the ^{13}C isotropic chemical shifts of carbons in alkanes between compounds with a γ carbon in the gauche versus trans position. However, owing to molecular motion leading to conformational averaging in solution, this is an effect that can be better studied in the solid where the averaging is usually removed. This was done in 1981, when a measurement on powdered syndiotactic polypropene showed two distinct methylene carbon resonances separated by 8.7 ppm whereas only a single peak was observed in solution;[36] from the structure, it was determined that one of the peaks in the solid was because of a methylene with two gauche γ-carbon neighbors, whereas the other was for a methylene with two trans γ-carbon neighbors. This effect was also measured by a comparison of the isotropic chemical shifts of the methyl carbon of *cis*- and *trans*-2-butene,[37] which showed a difference of 7 ppm. The tensor components, measured at about 20 K, showed that this difference is entirely in one component with a 21 ppm difference (27 ppm in *trans*- and 6 ppm in *cis*-butene); calculations show that this component is the one perpendicular to the molecular plane.

In anisole,[38] by freezing the liquid, one gets six carbon aromatic shift tensors as the degeneracy observed in the liquid state between the two ortho and two metacarbons due to conformational averaging is lifted, with the two ortho carbons showing an isotropic chemical shift difference of 7.0 ppm and

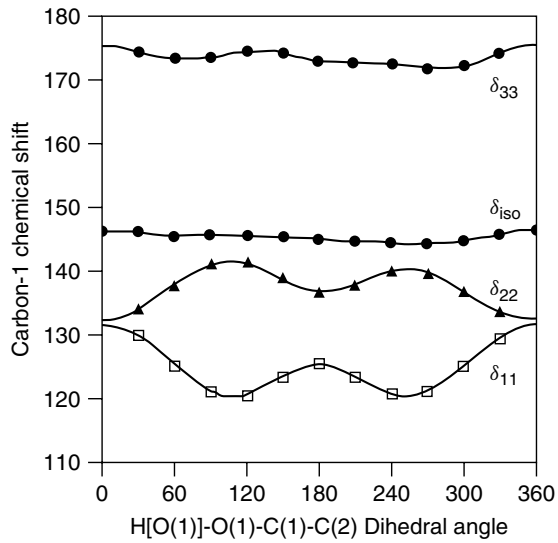


Figure 8.4. The values of the principal components of the chemical shift tensor and isotropic chemical shifts of C_1 of meso-erythritol as a function of the $H-O-C_1-C_2$ dihedral angle. (Reproduced from Ref. 11. © American Chemical Society, 1995.)

the two meta about 1.3 ppm. In the principal components of the shielding tensor, the effect is observed as lower chemical shifts in both the δ_{11} and δ_{33} components of the ortho carbon cis to the methyl

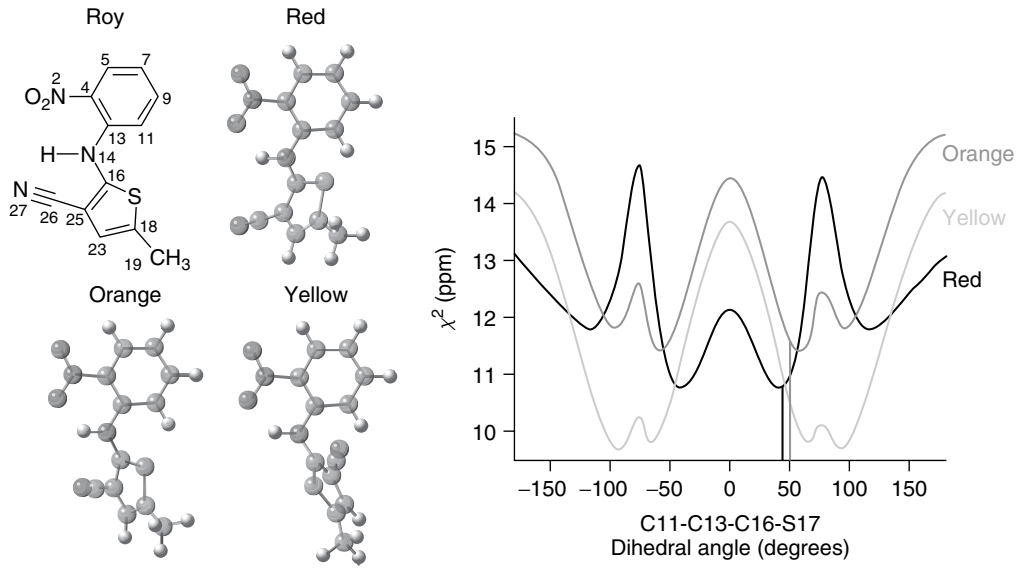


Figure 8.5. ROY polymorphs and chemical structure, showing that variation between the polymorphs occurs in the dihedral angle C11-C13-C16-S17. The variation of the least-squares comparison (χ^2) of ^{13}C and ^{15}N NMR data as a function of this angle; X-ray angles are marked as vertical lines. (Reproduced from Ref. 44. © American Chemical Society, 2006.)

group relative to the trans ortho carbon. The effect of methoxy orientation on the ^{13}C chemical shift tensor has also been measured on a number of polysubstituted methoxybenzenes (1,2,3-tri, 1,4-di, and 1,3,5-tri) via single-crystal NMR experiments,[39] with similar results.

Calculations have been used to explore the dihedral angle defining the orientation of the OH hydrogen in several compounds.[11,40–43] In a single-crystal study on meso-erythritol (1,2,3,4-butanetetrol),[11] the variation of the isotropic chemical shift and the principal components of C_1 with respect to the dihedral angle of the C_1 hydroxy H relative to carbon chain are given in Figure 8.4. As can be observed from this figure, neither the isotropic chemical shifts nor the δ_{33} components are sensitive to the dihedral angle, whereas the effects on the remaining two components mirror each other. Such plots can be generated and used to predict the dihedral angle.

Another case where dihedral angles play an important role is with conformational polymorphism. An example of this is the so-called "ROY" polymorphs of 5-methyl -2-[(2-nitrophenyl)amino]-3-thiophenecarbonitrile.[44] The three polymorphs, shown in Figure 8.5, have red, orange, and yellow colors while mainly differing in the dihedral angle between the phenyl and thiophene ring. Calculations of the shielding tensors were completed as a function of this dihedral angle; from a least-squares fit between the experimental ^{13}C and ^{15}N principal values of the three forms and these calculated values, predicted dihedral angles were obtained for each form. The plot of the variation of the fit with angle and a comparison with the X-ray dihedral angle is shown in Figure 8.5.

The same variation in dihedral angles that gives rise to conformational polymorphism can also be observed in the cases where independent molecules per asymmetric unit differ only by conformation. This has been recently observed by Harris *et al*. in a study of the mod II polymorphic form of oxybuprocaine hydrochloride.[45] This molecule exhibits a high degree of conformational flexibility, with one of the molecules in the asymmetric unit being "stretched out" while the second is in a "bent" conformation. This leads to differences in most of the carbon chemical shifts between the two forms, with the isotropic chemical shifts showing differences of up to 4.2 ppm. It can also be noted that one of the conformational changes observed is the γ effect mentioned earlier because of a gauche arrangement of substituents.

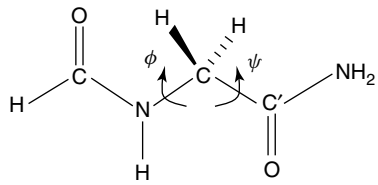


Figure 8.6. Capped amino acid fragment for glycine showing Ramachandran angles.

The use of chemical shifts to determine molecular conformation is perhaps most widely used in the study of the structure of amino acids, peptides, and proteins, both in the solution and in the solid state. This field has been extensively reviewed.[46–48] Although there has also been some effort on the use of ^{15}N[49] and ^{1}H chemical shifts,[50] most of the work is focused on using ^{13}C chemical shift parameters (using isotropic shifts, chemical shift anisotropy, or tensor components) of the C^{α} and C^{β} carbons in the determination of the Ramachandran angles ϕ, ψ (shown in Figure 8.6) to establish the backbone structure and the determination of the various χ angles to determine the orientation of the side chains.[51,52] Calculations of the relationship of isotropic chemical shifts to the ϕ, ψ angles have also been used for the further refinement of structures obtained from solution-state NMR methods.

Oldfield *et al*. have published a number of studies on the relationship between structure and chemical shifts in peptide fragments, including the effects of the backbone and side-chain dihedral angles.[27,53] The work of his group in this field, discussed below, has demonstrated the dominance of the local nature of shielding, in suggesting that calculations on models of individual amino acids can be used to predict the shifts in larger peptides.[54–57] In a typical study, model fragments are used for an amino acid in a peptide. The fragments typically consist of an N-formyl amino acid amide, as shown in Figure 8.6. Studies have shown that the effects of truncation and capping on the calculated chemical shift values relative to the experimentally measured values are minimal. In addition, it has also been shown that the C^{α} carbon isotropic shifts in these compounds are dominated by the effect of the torsion angles, suggesting that changes in other geometrical factors such as bond length and angles that may accompany the change of the dihedral angle may be neglected. Both of these observation support the generation of shielding surfaces based on the changes only in the ϕ, ψ angles. A representative shielding surface is shown in Figure 8.7.

Strohmeier and Grant[58] applied Oldfield's methodology, using the principal values of both the ^{13}C and the ^{15}N chemical shift tensors to determine the backbone conformation of melanostatin, L-Pro-L-Leu-Gly amide. The C^{α} tensor components on capped fragments were used to establish the backbone ϕ, ψ angles; these surfaces were then refined with information on the orientation of the C^{α} components relative to the C–N bond derived from $^{13}C-^{14}N$ coupling and the C^{β} shift components. This work also reported the X-ray structure of this compound to allow for a comparison. Figure 8.8 shows the agreement between theory and experiment ($\Delta\chi^2$) for the Ramachandran surfaces for both the glycine and leucine fragments. The places with lower $\Delta\chi^2$ values correspond to the angles at which there is the best agreement between experiment and theory.

The application of chemical shifts to study conformation in biological systems is not limited to only peptides and proteins – it has also been used in the analyses of nucleic acids,[59–61] nucleosides/nucleotides,[62] and polysaccharides.[63] For polysaccharides, the angles describing the glycosidic linkages have been well correlated to the isotropic ^{13}C chemical shifts of the carbons involved in the linkage. Sergeyev and Moyna[64] have calculated chemical shielding surfaces for oligoscaccharides and used the surfaces along with the experimental solid-state isotropic ^{13}C chemical shifts and NMR pseudopotential energy surfaces as constraints to model the linkage angles; results were within 10° from known X-ray structures.

8.7 STERIC CROWDING

Early solution-state NMR on methylated benzenes[65] and cyclohexanes[66,67] showed that the hydrogen–hydrogen interactions between nearby methyl group hydrogens can lead to predictable changes in the ^{13}C chemical shift of the methyl carbon. Li and Chesnut[68,69] extended this type of study to other groups of molecules, including aliphatic phosphines, amines, substituted hydrocarbons, and alcohols as well as to cyclic and bicyclic systems such as decalins, bicyclo[2.2.1]heptanes, and bicycle[2.2.2]octanes, finding that the effect shows good correlation with van der Waal terms, which,

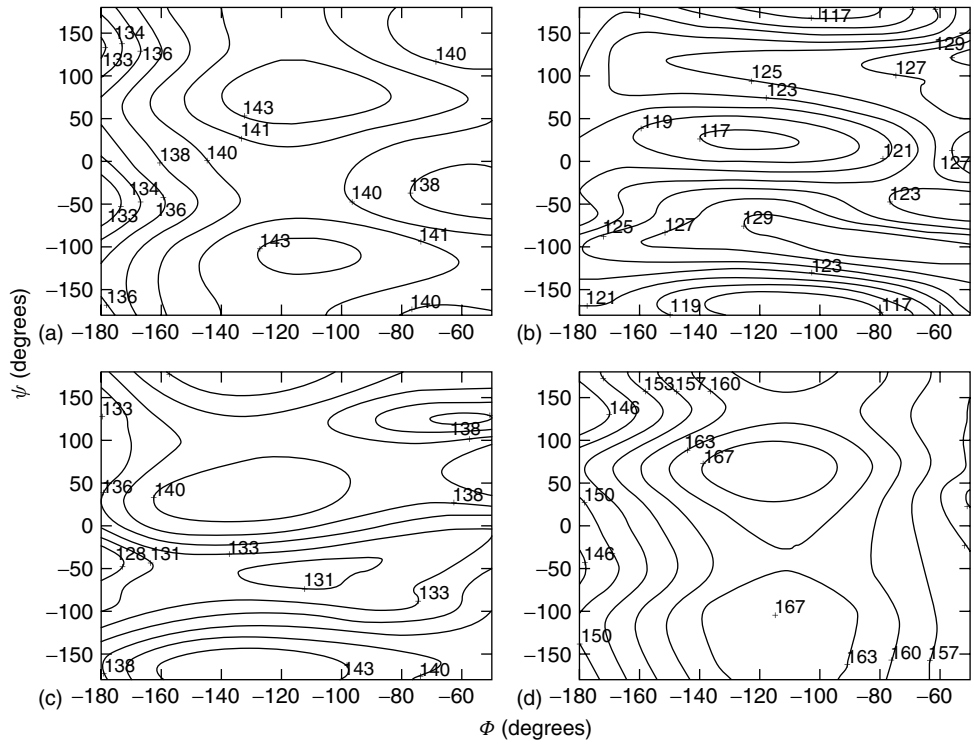


Figure 8.7. Computed (a) isotropic component and tensor components for (b) δ_{11}, (c) δ_{22}, (d) δ_{33} shift surfaces for C^{α} in N-formyl tyrosine amide using a side-chain orientation defined by $\chi_1 = -60^\circ$ and $\chi_2 = -85^\circ$. (Reproduced from Ref. 57. © American Chemical Society, 2002.)

in turn, show a strong repulsion at short interatomic distances, available from molecular modeling.

In the methyl benzene compounds,[65] the factor analysis of the ^{13}C methyl carbon chemical shift assigned a 4.43 ppm effect due to the interaction of two ortho groups such that the CH of one methyl group was bisecting the HCH of the other methyl group (2-1 ortho conformation). If the two methyl groups were oriented such that the two hydrogens of each CH_3 faced each other (2-2 conformation), then the effect was 1.87 ppm. A similar analysis of the ring carbons on a set of 15 methylated cyclohexanes[66] resulted in, among other substituent effects, parameters of 3.44 ppm due to geminal dimethyl substitution, 2.28 ppm for 1,2 equatorial–equatorial, and 3.07 ppm for 1,2 equatorial–axial, showing the sensitivity of the chemical shift to the steric effects.

The steric effect on the methyl carbons in methylated cyclohexanes[70] was also evaluated using a static measurement of the tensor component data on methyl groups either axial or equatorial. The differences were found to lie nearly completely in one component, namely, the component that theory places perpendicular to the $C_{ring}-C_{methyl}-H$ molecular symmetry plane, as indicated in Figure 8.9.

NMR studies of steric effects have been completed on methoxy substituted benzenes in solution[71,72] and in the solid state using single-crystal NMR techniques.[39] In these compounds, the methoxy group is generally found to be coplanar with the aromatic ring to allow for overlap between the oxygen atom nonbonding orbital and the aromatic π system. In the presence of an ortho substituent, as is the case in 1,2-dimethoxy benzene, a steric effect of about −6 ppm is observed for the oxygen isotropic chemical shift, attributed to the interaction of the lone pairs on the oxygen. In the case of two ortho substituents, as in 1,2,3-trimethylbenzene, the steric interactions force the methyl of the central group out of the plane. Both ^{13}C and ^{17}O isotropic shifts show good correlations both with the various angles that describe the orientation of the methoxy group as well as with the

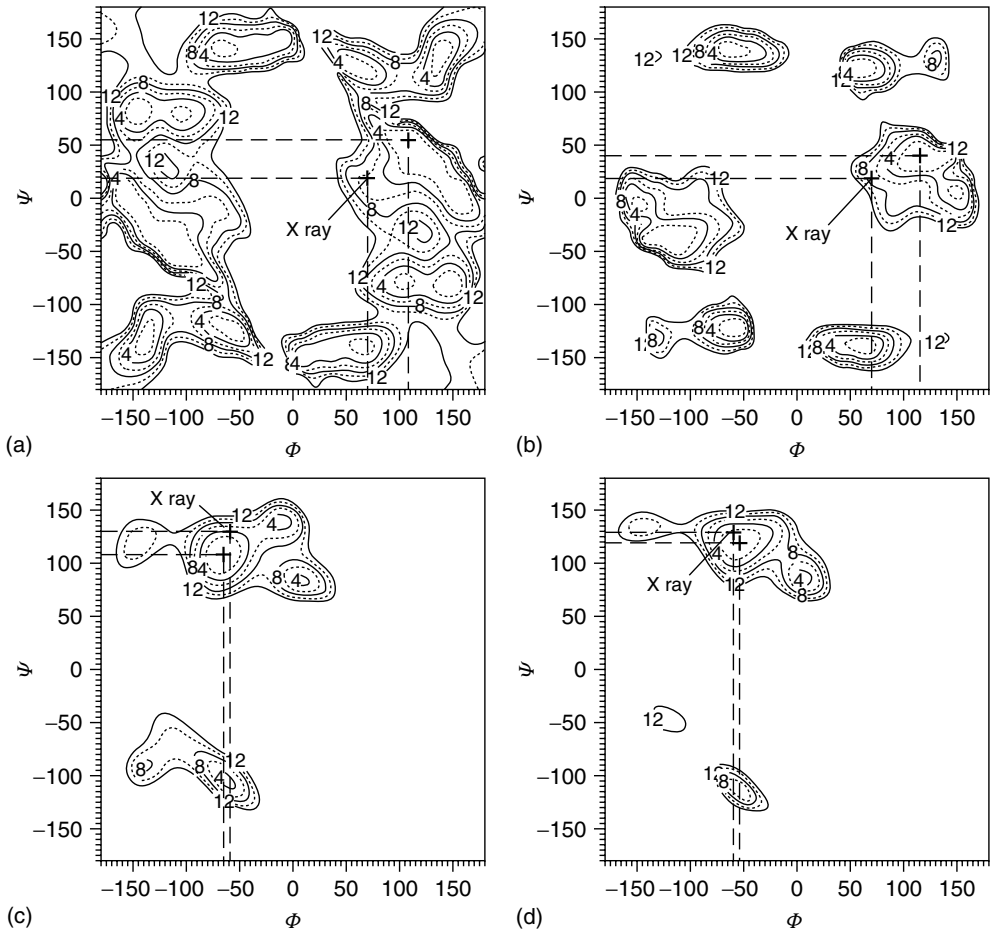


Figure 8.8. $\Delta\chi^2$ (measure of agreement between experimental and calculated chemical shifts) Ramachandran surfaces for (a) Gly C^{α} principal shift values, (b) Gly C^{α} principal shift values and CN bond vector orientation, (c) Leu C^{α} principal shift values, and (d) Leu C^{α} principal values and CN bond vector orientation. (Reproduced from Ref. 58. © American Chemical Society, 2004.)

bond order of the aromatic carbon to methoxy oxygen bond. In the analysis of the principal components of the aromatic carbons in a series of methoxybenzenes, the steric effect is observed in all three components, but is predominately (−11 ppm) in the component perpendicular to the aromatic ring.[39]

8.8 CONCLUDING REMARKS

Although the relationship between molecular-level structure and chemical shifts is in many cases not conducive to simple interpretation, there are still many examples, some of which are presented in this article, that demonstrate the high sensitivity of chemical shifts to individual molecular-level structural features such as tautomeric form, bond lengths, bond angles, and dihedral angles. This sensitivity to structural parameters has also been confirmed in many cases by quantum chemical calculations of the magnetic shielding tensor. These calculations, although complex, are an invaluable tool both to aid in the interpretation of experimental shift data as it relates to structure and to explore shift-structure relationships not amenable to experimental study. While this article has focused on molecular structure, other articles

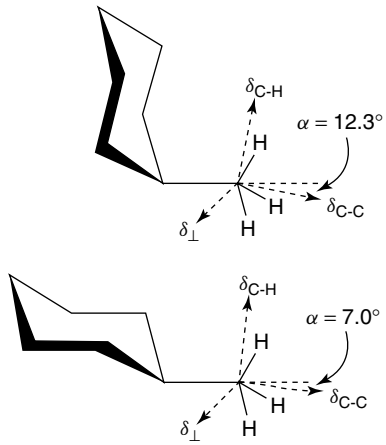


Figure 8.9. The orientation of the methyl ^{13}C chemical shift tensor for the axial and equatorial conformations of methylcyclohexane. (Reproduced from Ref. 70. © American Chemical Society, 1995.)

in this handbook discuss the effect of intermolecular interactions on the chemical shift. The reader is, therefore, cautioned to keep in mind that the intra- and intermolecular effects do not occur in isolation; on the contrary, they are interdependent and jointly determine the measured chemical shift.

REFERENCES

1. J. Mason, *Multinuclear NMR*, Plenum Press: New York, 1987.
2. E. G. Paul and D. M. Grant, *J. Am. Chem. Soc.*, 1963, **85**, 1701–1702.
3. A. Pines, M. G. Gibby, and J. S. Waugh, *Chem. Phys. Lett.*, 1972, **15**, 373–376.
4. I. Lowe, *Phys. Rev. Lett.*, 1959, **2**, 285–287.
5. E. R. Andrew, A. Bradbury, and R. G. Eades, *Nature*, 1958, **182**, 1659.
6. E. R. Andrew, A. Bradbury, and R. G. Eades, *Nature*, 1959, **183**, 1802–1803.
7. D. M. Grant, J. C. Facelli, D. W. Alderman, and M. H. Sherwood, in *Nuclear Magnetic Shieldings and Molecular Structure*, ed J. A. Tossell, Kluwer Academic Publishers: Dordrecht, 1993, 367–384.
8. J. C. Facelli and D. M. Grant, *Top. Stereochem.*, 1989, **19**, 1–61.
9. Z. Ma, M. D. Halling, M. S. Solum, J. K. Harper, A. M. Orendt, J. C. Facelli, R. J. Pugmire, D. M. Grant, A. W. Amick, and L. T. Scott, *J. Phys. Chem. A*, 2007, **111**, 2020–2027.
10. J. C. Facelli, A. M. Orendt, A. J. Beeler, M. S. Solum, G. Depke, K. D. Malsch, J. W. Downing, P. S. Murthy, D. M. Grant, and J. Michl, *J. Am. Chem. Soc.*, 1985, **107**, 6749–6754.
11. F. Liu, C. G. Phung, D. W. Alderman, and D. M. Grant, *J. Am. Chem. Soc.*, 1995, **117**, 9323–9328.
12. Z. Gu and A. McDermott, *J. Am. Chem. Soc.*, 1993, **115**, 4282–4285.
13. E. R. Andrew, A. Bradbury, R. G. Eades, and G. J. Jenks, *Nature*, 1960, **188**, 1096–1097.
14. R. E. Andrew, *Phil. Trans. Roy. Soc. London Ser. A*, 1981, **299**, 505–520.
15. H. W. Kroto, S. I. Klein, M. R. Meidine, J. F. Nixon, R. K. Harris, K. J. Packer, and P. Reams, *J. Organomet. Chem.*, 1985, **280**, 281–287.
16. M. S. Solum, K. L. Altman, M. Strohmeier, D. A. Berges, Y. Zhang, J. C. Facelli, R. J. Pugmire, and D. M. Grant, *J. Am. Chem. Soc.*, 1997, **119**, 9804–9809.
17. F. Aguilar-Parrilla, F. Mannle, H.-H. Limbach, J. Elguero, and N. Jagerovic, *Magn. Reson. Chem.*, 1994, **32**, 699–702.
18. M. Munowitz, W. W. Bachovchin, J. Herzfeld, C. M. Dobson, and R. G. Griffen, *J. Am. Chem. Soc.*, 1982, **104**, 1192–1196.
19. I. Bolz, C. Moon, V. Enkelmann, G. Brunklaus, and S. Spange, *J. Org. Chem.*, 2008, **73**, 4783–4793.
20. R. D. Curtis and R. E. Wasylishen, *Can. J. Chem.*, 1991, **69**, 834–838.
21. R. J. Iuliucci, J. Clawson, J. Z. Hu, M. S. Solum, D. Barich, D. M. Grant, and C. M. V. Taylor, *Solid State NMR*, 2003, **24**, 23–38.
22. C. J. Jameson and A. Cd. Dios, in *Nuclear Magnetic Shieldings and Molecular Structures*, ed J. A. Tossell, Kluwer Academic Publishers: Dordrecht, 1993, p 95–116.
23. A. C. de Dios and C. J. Jameson, *Ann. Rep. NMR Spectrosc.*, 1994, **29**, 1–69.
24. R. E. Wasylishen, J. O. Friedrich, S. Mooibroek, and J. B. Macdonald, *J. Chem. Phys.*, 1985, **83**, 548–551.
25. C. J. Jameson, Isotope effects on chemical shifts and coupling constants, in *Encyclopedia of Nuclear Magnetic Resonance*, eds-in-chief D. M. Grant and R. K. Harris, John Wiley & Sons: London, 1996, **4**, 2638–2655.

26. D. B. Chesnut and D. W. Wright, *J. Comput. Chem.*, 1991, **12**, 546–559.
27. A. C. de Dios, J. G. Pearson, and E. Oldfield, *J. Am. Chem. Soc.*, 1993, **115**, 9768–9773.
28. R. J. Iuliucci, C. G. Phung, J. C. Facelli, and D. M. Grant, *J. Am. Chem. Soc.*, 1996, **118**, 4880–4888.
29. R. J. Iuliucci, J. C. Facelli, D. W. Alderman, and D. M. Grant, *J. Am. Chem. Soc.*, 1995, **117**, 2336–2343.
30. F. Liu, A. M. Orendt, D. W. Alderman, and D. M. Grant, *J. Am. Chem. Soc.*, 1997, **119**, 8981–8984.
31. D. M. Grant, F. Liu, R. J. Iuliucci, C. G. Phung, J. C. Facelli, and D. W. Alderman, *Acta Crystallogr.*, 1995, **B51**, 540–546.
32. J. C. Facelli and D. M. Grant, *Nature*, 1993, **365**, 325–327.
33. K. W. Zilm, A. J. Beeler, D. M. Grant, J. Michl, T. C. Chou, and E. L. Allred, *J. Am. Chem. Soc.*, 1981, **103**, 2119–2120.
34. D. L. Vanderhart, *J. Chem. Phys.*, 1976, **64**, 830–834.
35. C. J. Jameson and A. C. de Dios, in *Specialist Periodical Reports on Nuclear Magnetic Resonance*, ed G. A. Webb, Royal Society: London, 2007, Vol. **36**, 50–71.
36. A. Bunn, M. A. E. Cudby, R. K. Harris, K. J. Packer and B. J. Say, *J. Chem. Soc. Chem. Commun.*, 1981, 15–16.
37. M. S. Solum, J. C. Facelli, J. Michl, and D. M. Grant, *J. Am. Chem. Soc.*, 1986, **108**, 6464–6470.
38. J. C. Facelli, A. M. Orendt, Y. J. Jiang, R. J. Pugmire, and D. M. Grant, *J. Phys. Chem.*, 1996, **100**, 8268–8272.
39. C. M. Carter, J. C. Facelli, D. W. Alderman, D. M. Grant, N. K. Dalley, and B. E. Wilson, *J. Chem. Soc., Faraday Trans. 1*, 1988, **84**, 3673–3690.
40. J. K. Harper and D. M. Grant, *J. Am. Chem. Soc.*, 2000, **122**, 3708–3714.
41. J. K. Harper, A. E. Mulgrew, J. Y. Li, D. H. Barich, G. A. Strobel, and D. M. Grant, *J. Am. Chem. Soc.*, 2001, **123**, 9837–9842.
42. J. K. Harper, J. C. Facelli, D. H. Barich, G. McGeorge, A. E. Mulgrew, and D. M. Grant, *J. Am. Chem. Soc.*, 2002, **124**, 10589–10595.
43. J. K. Harper, D. H. Barich, J. Z. Hu, G. A. Strobel, and D. M. Grant, *J. Org. Chem.*, 2003, **68**, 4609–4614.
44. J. R. Smith, W. Xu, and D. Raftery, *J. Phys. Chem. B*, 2006, **110**, 7766–7776.
45. R. K. Harris, S. Cadars, L. Emsley, J. R. Yates, C. J. Pickard, R. K. R. Jetti, and U. J. Griesser, *Phys. Chem. Chem. Phys.*, 2007, **9**, 360–368.
46. E. Oldfield, *J. Biomol. NMR*, 1995, **5**, 217–225.
47. Y. Shen and A. Bax, *J. Biomol. NMR*, 2007, **38**, 289–302.
48. A. C. de Dios and E. Oldfield, Chemical shifts in biochemical systems, in *Encyclopedia of Nuclear Magnetic Resonance*, eds-in-chief D. M. Grant and R. K. Harris, John Wiley & Sons: London, 1996, Vol. **2**, 1330–1336.
49. H. Le and E. Oldfield, *J. Biomol. NMR*, 1994, **4**, 341–348.
50. D. S. Wishart, B. D. Sykes, and F. M. Richards, *J. Mol. Biol.*, 1991, **222**, 311–333.
51. S. Neal, M. Berjanskii, H. Zhang, and D. S. Wishart, *Magn. Reson. Chem.*, 2006, **44**, S158–S167.
52. J. A. Vila, D. R. Ripoll, and H. A. Scheraga, *J. Phys. Chem. B*, 2007, **111**, 6577–6585.
53. A. C. de Dios and E. Oldfield, *J. Am. Chem. Soc.*, 1994, **116**, 5307–5314.
54. H.-B. Le, J. G. Pearson, A. C. de Dios, and E. Oldfield, *J. Am. Chem. Soc.*, 1995, **117**, 3800–3807.
55. J. Heller, D. D. Laws, M. Tomaselli, D. S. King, D. E. Wemmer, A. Pines, R. H. Havlin, and E. Oldfield, *J. Am. Chem. Soc.*, 1997, **119**, 7827–7831.
56. R. H. Havlin, H. Le, D. D. Laws, A. C. de Dios, and E. Oldfield, *J. Am. Chem. Soc.*, 1997, **119**, 11951–11958.
57. H. Sun, L. K. Sanders, and E. Oldfield, *J. Am. Chem. Soc.*, 2002, **124**, 5486–5495.
58. M. Strohmeier and D. M. Grant, *J. Am. Chem. Soc.*, 2004, **126**, 966–977.
59. X.-P. Xu and S. C. F. Au-Yeung, *J. Chem. Phys. B*, 2000, **104**, 5641–5650.
60. H. Precechtelova, M. L. Munzarova, P. Novak, and V. Sklenar, *J. Phys. Chem. B*, 2007, **111**, 2658–2667.
61. R. Ghose, J. P. Marino, K. B. Wiberg, and J. H. Prestegard, *J. Am. Chem. Soc.*, 1994, **116**, 8827–8828.
62. M. Ebrahimi, P. Rossi, C. Rodgers, and G. S. Harbison, *J. Magn. Reson.*, 2001, **150**, 1–9.
63. H. Saito, Polysaccharide solid state NMR, in *Encyclopedia of Nuclear Magnetic Resonance*, eds-in-chief D. M. Grant and R. K. Harris, John Wiley & Sons: London, 1996, Vol. **6**, 3740–3745.
64. I. Sergeyev and G. Moyna, *Carbohydr. Res.*, 2005, **340**, 1165–1174.

65. W. R. Woolfenden and D. M. Grant, *J. Am. Chem. Soc.*, 1966, **88**, 1496–1502.

66. D. K. Dalling and D. M. Grant, *J. Am. Chem. Soc.*, 1967, **89**, 6612–6622.

67. D. K. Dalling and D. M. Grant, *J. Am. Chem. Soc.*, 1972, **94**, 5318–5324.

68. S. Li and D. B. Chesnut, *Magn. Reson. Chem.*, 1985, **23**, 625–638.

69. S. Li and D. B. Chesnut, *Magn. Reson. Chem.*, 1986, **24**, 93–100.

70. A. Soderquist, J. C. Facelli, W. J. Horton, and D. M. Grant, *J. Am. Chem. Soc.*, 1995, **117**, 8441–8446.

71. R. R. Biekofsky, A. B. Pomilio, R. H. Contreras, D. G. De Kowalewski, and J. C. Facelli, *Magn. Reson. Chem.*, 1989, **27**, 158–161.

72. R. R. Biekofsky, A. B. Pomilio, R. H. Contreras, A. M. Orendt, and J. C. Facelli, *J. Phys. Chem.*, 1990, **94**, 7418–7423.

Chapter 9

Chemical Shift Anisotropy & Asymmetry: Relationships to Crystal Structure

James K. Harper

Department of Chemistry, University of Utah, Salt Lake City, UT 84112, USA

9.1	Introduction	113
9.2	Direct Encoding of Lattice Structure in Shift Tensors	115
9.3	Indirect Reflections of Lattice Structure in NMR Tensor Data	118
9.4	Refinement of Established Crystal Structures	119
9.5	Deriving Full Crystal Structures	121
	References	122

9.1 INTRODUCTION

NMR crystallography emphasizes the extraction of crystallographic information from solid-state nuclear magnetic resonance (SSNMR) data (*see* **Chapters 1** and **17**). For many years certain lattice features have been derived from SSNMR data. However, recent work has expanded these structural hints into full crystal structures in certain powdered solids,[1–10] portending more general and routine crystallographic analyses from SSNMR data. Presently, much of the reported work includes data from a second analysis method such as X-ray powder diffraction, but analyses involving only SSNMR data as experimental information have also been completed and demonstrated that accurate structures can be obtained without diffraction data.[11,12] Naturally, the question arises regarding which experiments provide the maximum insight into lattice structure. To date, experiments emphasizing isotropic shifts,[2,3,6,7] dipolar[1,2,4,13–17] and scalar couplings,[9,17] and shift tensor principal component values[5,8,10,18] have been explored as means of deriving structure. Descriptions of the use of isotropic shifts,[19] dipolar couplings[20,21] and spin diffusion[22] to evaluate crystal structures are given elsewhere in this handbook (*see* **Chapters 11**, **12**, **14** and **19**). Here, emphasis is placed on using the SSNMR shift tensor data to obtain crystallographic information. In this report, chemical shift (δ) is used rather than shielding (σ) in all discussions since shift is the value that is measured experimentally.

The chemical shift is a second-rank tensor quantity. A discussion of the shift tensor is given elsewhere,[23,24] (*see* **Chapter 2**) but key features are summarized here for convenience. The experimentally measurable part of the shift tensor is a real symmetric 3×3 matrix given by equation (9.1).

$$\begin{bmatrix} \delta_{xx} & \delta_{xy} & \delta_{xz} \\ \delta_{xy} & \delta_{yy} & \delta_{yz} \\ \delta_{xz} & \delta_{yz} & \delta_{zz} \end{bmatrix} \tag{9.1}$$

NMR Crystallography Edited by Robin K. Harris, Roderick E. Wasylishen and Melinda J. Duer © 2009 John Wiley & Sons, Ltd. ISBN: 978-0-470-69961-4

Since the observable part of the shift tensor is symmetric with $\delta_{ij} = \delta_{ji}$, six parameters can be measured per nucleus. To obtain all the six values, however, large single crystals are usually required. Hence, emphasis is often placed on the diagonalized form of tensor equation (9.2) with three values that can be measured in powdered solids.

$$\begin{bmatrix} \delta_{11} & 0 & 0 \\ 0 & \delta_{22} & 0 \\ 0 & 0 & \delta_{33} \end{bmatrix} \tag{9.2}$$

The three nonzero values in equation (9.2) are referred to as principal components and are defined in the "Mehring notation" such that $\delta_{11} \geq \delta_{22} \geq \delta_{33}$.[25] These principal components represent shielding in the three orthogonal directions of a Cartesian coordinate system. However, orientations of the shielding components relative to the molecule are lost in the diagonalization procedure; therefore, the values are ordered serially. The isotropic shift (δ_{iso}) is the average of the three principal components. In this article, emphasis will be placed primarily on analyses involving principal components. Comparable analyses involving the six values per nucleus of the full tensor are usually more informative,[26] but when this data can be obtained, high-quality crystals with established diffraction structures are typically available. Since the emphasis here is to assess what structural information SSNMR can provide, principal component methods will be emphasized.

Principal component data are often reported simply as the δ_{11}, δ_{22}, and δ_{33} values. However, information regarding the anisotropy and symmetry of the shielding tensor is given by other parameters defined in terms of the principal components. Presently, $\Delta\sigma$ or ζ (equations (9.3) and (9.4), respectively) are recommended to describe anisotropy with η (equation 9.5) used to represent asymmetry.[25] The acceptance of two expressions for anisotropy reflects the extensive use of both in the early literature. In fact, $\Delta\sigma$ and ζ differ only by a weighting factor with $\Delta\sigma = 3/2\zeta$.

$$\Delta\sigma = \delta_{11} - \frac{1}{2}(\delta_{22} + \delta_{33}) \tag{9.3}$$

$$\zeta = \delta_{11} - \delta_{iso} \tag{9.4}$$

$$\eta = \frac{\delta_{22} - \delta_{33}}{\delta_{11} - \delta_{iso}} \tag{9.5}$$

Equations (9.3)–(9.3) are used when $|\delta_{33} - \delta_{iso}| \leq |\delta_{11} - \delta_{iso}|$. In cases where $|\delta_{33} - \delta_{iso}| \geq |\delta_{11} - \delta_{iso}|$, alternative expressions are recommended having the δ_{11} and δ_{33} components interchanged. In 1993, two additional expressions, the span (Ω) and skew (κ), were introduced[27] and these parameters are now reported by some authors.

A summary of current recommendations and the rational for these choices is given elsewhere.[25] From the standpoint of extracting crystallographic information from tensor principal components, it is worth emphasizing that some lattice interactions only influence a single component. Thus, any mathematical combination of principal components can cause unintended cancellations or reinforcements (vide infra). This is commonly recognized when it comes to the isotropic shift where averaging the principal components usually reduces the informative power. However, the same reduction of information can occur in forming the span, skew, anisotropy, or asymmetry. This is illustrated by O–H···O hydrogen-bonded dimers where the O···O separation was found to correlate strongly with a single principal component.[28] However, when principal components were combined to form $\Delta\sigma$ the observed correlation was lost. Similar sensitivity of structural features to a single principal component is found in other hydrogen-bonded moieties such $^{13}C{=}O$'s[29–31] and in the recently observed purely magnetic intermolecular effects in certain aromatic systems.[32] Thus, while it is informative to report the span, skew, or other related parameters, to give only these values, as is sometimes done, reduces the ability to extract structural information. Therefore, it is advisable to also report experimental data as individual principal components in all studies.

In the following sections the discussion is organized to first consider reflections of the lattice structure in tensor principal components. Two cases are distinguished, direct effects and indirect effects. Quantifying these effects depends strongly on theoretical methods for calculating shift tensors in model compounds. A description of these techniques is given elsewhere in this volume.[33,34] (*see* **Chapters 3** and **7**) Next, an account of how tensor principal components have been used to refine established structures is given. Tensors are shown to allow refinements that are generally superior to those obtained from powder diffraction methods and to improve single-crystal structures at some sites. Finally, a discussion of how tensor shifts have been used to derive complete crystal structure is included.

9.2 DIRECT ENCODING OF LATTICE STRUCTURE IN SHIFT TENSORS

Chemical shift tensors usually reflect structure over only a short range of a few angstroms.[23] This strong emphasis on nearby structure makes tensor data extremely useful for establishing internal structural features such as conformation, but leaves them somewhat insensitive to lattice structure. However, some types of lattice information are directly reflected in tensor values. Two approaches have been used to evaluate lattice effects. In the early studies, tensor values were measured for a series of structures containing the same functional group in varied environments. These data were then compared to diffraction structures and structural features correlated with tensor data. This method cannot be used when diffraction structures are unavailable and, more recently, a second approach has been developed to simulate lattice effects. This method involves computation of shift tensors for model compounds using quantum mechanical methods and comparison of these values to experimental data. When a model compound has an established geometry from the diffraction data, computed tensor values for the isolated molecule are expected to fit experimental data very well unless lattice interactions are present. Conversely, poor fits at some sites indicate that those positions reflect details of the lattice environment. The direct lattice effects that are, perhaps, most relevant to crystallographic studies are electrostatic and hydrogen bonding. Factors influencing NMR shifts in solids have been the topic of a recent review[35] so only selected details that are relevant to extracting crystallographic information from tensor data will be discussed here.

In the following discussion, direct effects are defined as those requiring the inclusion of lattice detail in computed model structures to accurately simulate experimental tensor data. In contrast, indirect effects can be accurately modeled from computations on an individual molecule, i.e., by comparing calculated tensor values from a gas-phase structure with experimental values. Indirect effects are usually conformational differences of a molecular structure in the solid from its gas-phase minimum due to lattice forces.

9.2.1 Effects of Electrostatic Fields

Information about lattice structure can become encoded in tensor data when formally charged or polar sites are present in the lattice. These sites produce an electrostatic potential that can strongly alter tensor values. Such effects act over a long distance since the potential is proportional to $1/\langle r \rangle$, where r is the distance of the nucleus from the polar or charged site. All atoms in a molecule, however, do not reflect this effect equally and it appears that atoms that are charged or polarizable are most influenced. Presently, it has been demonstrated that the electrostatic potential can be modeled accurately in a variety of ways to account for this interaction.[35] More importantly, from a crystallographic point of view, these studies typically make use of crystallographic coordinates to model the effect through means such as placement of point charges surrounding a central molecule. Hence, the tensor data contain information about crystal structure, at least at certain sites, and this information may provide a path to lattice structure.

An early example of the sensitivity of tensors to lattice involves Hg-199 tensor data. Comparison of experimental ^{199}Hg tensor values with diffraction structures allowed the influence of additional ligands near a central ^{199}Hg to be assessed. In compounds involving the grouping HgX_2, predictable variations in the anisotropy and asymmetry were correlated with electronic changes due to the presence of one or two neighboring ligands in the lattice.[36] Although this work required actual transfer of electron density from these ligands to the central ^{199}Hg, these studies extrapolated the results to the point where no electron transfer from ligands was possible and reported significant changes in anisotropy and asymmetry even when electron transfer was small (Figure 9.1). Thus, this work anticipated more wide-ranging studies where the effect is primarily electrostatic.

A more general approach for treating electrostatic effects involves theoretical methods to model the lattice. Such techniques are now often used when computing tensors. These methods are of three general types: models that represent the lattice as an electrical field, representations that explicitly include neighboring molecules, and full crystal models that are designed to include all the possible lattice interactions through periodic boundary conditions. These computations have been invaluable in demonstrating when lattice effects must be included and quantifying the extent to which they can modify NMR shifts.[35] They are, however, usually limited to a comparison of tensors computed for an individual molecule versus the same molecule surrounded by

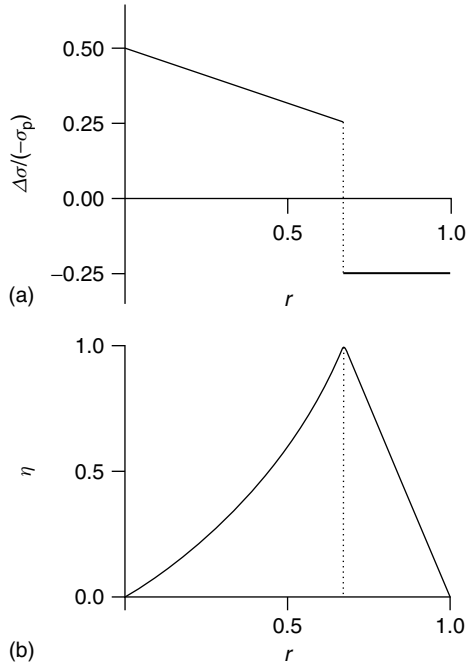


Figure 9.1. Variations in the anisotropy ($\Delta\sigma$) and asymmetry (η) of ^{199}Hg tensor in a compound with the grouping HgX_2 as a function of an electronic factor r (see Ref. 36), resulting when a neighbouring ligand (X) approaches the Hg. Zero contributions to the ^{199}Hg valence orbital electron density from the additional ligand occur at $r = 0$ (HgX_2), with a maximum effect at $r = 1$ (HgX_3). (Reproduced from Ref. 36. © Elsevier, 1997.)

an array of point charges or other representation of the lattice. Of course, this inclusion of lattice detail requires knowledge of the crystal structure for the molecule being evaluated. When the experimental NMR analysis involves a molecule with no known crystal structure, however, little appears to be known regarding the ability to differentiate among several candidate structures that include lattice effects in the calculation. Since determining structure in unknowns is one of the ultimate goals of NMR crystallography, an extension of these methods to unknowns is desirable. It is noteworthy that the ability to generate a nearly exhaustive set of possible crystal structures for a given molecule has now been demonstrated[37,38] and tensor data have been shown to vastly reduce the number of feasible candidate structures in the case of uncharged molecules.[11] Extension of these techniques to molecules having large electrostatic potentials portends the ability to derive full crystal structures from the information encoded in experimental tensor values.

9.2.2 The Influence of Hydrogen Bonding

Hydrogen bonding at certain atomic sites within a molecule can cause the tensor values of those sites to change dramatically relative to the same site with no hydrogen bonding present.[35] Thus, proximity of hydrogen-bonded molecules in a lattice and their partial orientation can be directly evaluated from tensor data. Tensor data have a distinct advantage over isotropic values when evaluating NMR data for evidence of hydrogen bonding. First, the shift variations are of a larger magnitude. More important, however, is the fact that hydrogen bonding in a given functional group causes characteristic change in only certain principal components, usually those perpendicular to the X–^{1}H · · ·Y hydrogen-bonding direction. Thus, hydrogen bonding at a position can often be identified solely from changes in specific tensor components relative to model compounds.

This characteristic signature of hydrogen bonding in tensor data is illustrated by COOH groups in amino acids where O· · ·H distances obtained from neutron and X-ray diffraction data have been shown to be strongly correlated with experimentally determined δ_{22} tensor components from the COOH carbon (Figure 9.2).[29] In this case, changes as large as 26 ppm toward higher frequencies were observed as O· · ·H separation decreased. This information provides a highly detailed view of hydrogen bonding around the carboxyl group that allows adjacent molecules in the lattice to be partially oriented. Of course, the influence of hydrogen bonding on tensors is not limited to the COOH group and the effect of hydrogen bonding on tensors has also been reported for the other carbon types[30,31,39] as well as ^{1}H,[28,40–44] and ^{15}N.[45–49] If crystallographic information is to be obtained from tensor data, it is crucial to know which atomic sites are likely to reflect hydrogen bonding. Therefore, a summary of functional groups that have been reported to change upon hydrogen bonding is given here ordered by nucleus type.

The ^{13}C nucleus reflects hydrogen bonding primarily when it appears in a carbonyl (C=O) acting as a hydrogen-bond acceptor in groups such as carboxylic acids[29] and amides.[30,31] In these moieties, variation in the δ_{22} and, to a lesser extent,

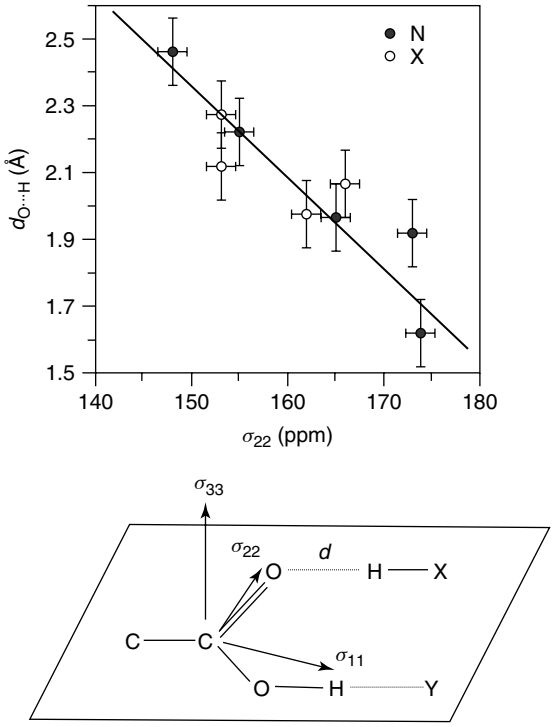


Figure 9.2. Hydrogen bonding in carboxylic acids is strongly reflected in ^{13}C δ_{22} principal components (top plot). In this case, the δ_{22} value (listed as σ_{22} above) reflects the O···H separation in the C–O···H bond with higher frequency shifts indicating shorter hydrogen bonds. The H···Y bonding has little effect on the δ_{22} component, demonstrating that electronic changes are greatest in hydrogen bond acceptors, as predicted by Ditchfield.[28] Filled and open circles denote neutron and X-ray diffraction data, respectively. Orientations of the ^{13}C principal axes are illustrated in the lower figure. (Reproduced from Ref. 29. © American Chemical Society, 1994.)

the δ_{11} principal components indicate hydrogen bonding. Some carbon–carbon double bonds also reflect hydrogen bonding, in particular those that are conjugated to a carbonyl[39] or that are part of certain aromatic systems.[50–52] Remarkably, ^{13}C tensors of carbohydrates do not appear to directly reflect hydrogen bonding even though most carbons have attached OH's that are involved in hydrogen bonds. This has been demonstrated for several carbohydrates by the unusually high-quality fit of computed tensors to experimental data when neutron diffraction structures are used in gas-phase calculations.[11,53–56] This result emphasizes that not all hydrogen-bonded groups reflect this bonding in tensor values even when the bonds are moderately strong.

Studies on ^{15}N tensor values and hydrogen bonding have primarily focused on nitrogen heterocycles such as nucleic acids. In these products, nonprotonated ^{15}N's are strongly influenced at the δ_{11} component and become more shielded upon hydrogen bonding. With protonated ^{15}N's, the δ_{22} value moves to higher frequencies upon hydrogen bonding.[45–49] Limited work on ammonium cations (RNH_3^+)[57] and neutral NH_2[58] groups has shown that these groups also reflect hydrogen bonding. However, the data are presently too limited to draw general conclusions. Overall, ^{15}N appears to be more sensitive than ^{13}C to hydrogen bonding as indicated by the larger magnitude of shift changes that occur upon bonding.

Information regarding hydrogen bonding is also reflected in ^{1}H tensors. In this case, the δ_{33} component usually lies along the X–^{1}H···Y bonding axis, so the δ_{11} and δ_{22} tensors components strongly reflect changes in hydrogen bonding.[28,40–44] The δ_{11} and δ_{22} components become less shielded with increasing hydrogen bond strength, while δ_{33} grows more shielded (Figure 9.3). Thus, small-span tensors for protons that can hydrogen bond (e.g., O–^{1}H) indicate little or no hydrogen bonding, while large spans suggest stronger hydrogen bonding. This information has been demonstrated to be of direct crystallographic relevance in the case of $Ca(OH)_2$ and $Mg(OH)_2$ where the measured value of $(\delta_{11} + \delta_{22})/2$ was used to infer that no hydrogen bonding occurred in either lattice.[44] Because the δ_{11} and δ_{22} components most strongly reflect hydrogen bonding, the isotropic variation is dominated by these values and, therefore, the isotropic shift also moves toward higher frequencies upon hydrogen bonding, albeit with less sensitivity. Presently, isotropic variation is most commonly used to monitor hydrogen bonding in solids.

From a practical viewpoint, experimental tensor data can be evaluated for hydrogen bonding simply by computing tensor values for the structure represented as an individual molecule and then comparing these values with the experimental data. Choosing an individual molecule for the calculation omits all lattice detail, so poor fits at sites that can hydrogen bond indicate probable hydrogen bonding to the lattice. Thus, for ^{13}C, computed carbonyl tensors fitting poorly at δ_{22} and to a lesser extent at δ_{11} indicate hydrogen bonding at that carbonyl. Likewise, large errors in computed ^{15}N tensors in heterocyclic aromatic compounds at the δ_{11} (unprotonated) or δ_{22}

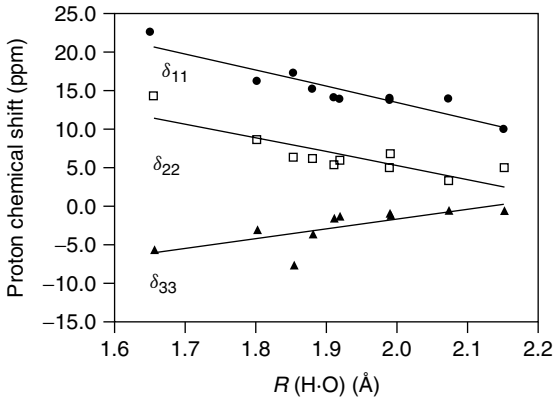


Figure 9.3. Changes in principal components of ^{1}H shifts reflect H···O separations in water found in different crystalline hydrates. The δ_{11} and δ_{22} values are most sensitive to hydrogen bonding and move toward higher frequencies, changing approximately 20 ppm for each angstrom decrease in H···O separation. (Reproduced from Ref. 40. © American Chemical Society.)

(protonated) components point to the presence of hydrogen bonding at these sites. Since ^{1}H has a much smaller anisotropy than the other nuclei, the errors in computed principal components may be comparable to the shift variation present. Hence, perhaps the most reliable way to establish hydrogen bonding from ^{1}H tensors is to search for large discrepancies between calculated and experimental ^{1}H tensor spans.

Clear identification of hydrogen bonding in tensor data is most strongly seen when the nucleus is involved in a single hydrogen bond per nucleus. The presence of multiple hydrogen bonds at a site can alter the trends described here. Nevertheless, poor fits between computed and experimental data remain useful in suggesting the presence of one or more lattice partners. Additional complications in identifying hydrogen bonding from tensor data can arise when working with flexible molecules because conformational variation can also cause large tensor shifts. In this case, mapping the conformational space with conformational varied trial structures will often provide a structure with good fits at hydrogen-bonding sites if the variation arises primarily from conformational effects. However, such mapping will be unable to produce a fit if hydrogen bonding also contributes significantly to the change. Internal hydrogen bonding is a third difficulty, but rules predicting when internal hydrogen bonding is expected to occur have been described[59] and can be consulted to prevent confusion over whether or not a hydrogen bond is intramolecular or intermolecular.

When tensor data indicate hydrogen bonding at a given site, this fact can be exploited to establish crystallographic detail. For example, in the case of ambuic acid, a monocarboxylic acid, a poor fit of experimental δ_{11} and δ_{22} tensor data to a gas-phase model structure suggested hydrogen bonding at the COOH.[5] Prior precedent indicated that such moieties almost invariably interlink forming a twofold or 2_1-screw axis involving the COOH.[60] Accordingly, only space groups containing these symmetry elements were evaluated, eliminating 60% of possible space groups from consideration. A full crystal structure was obtained from these NMR constrained data when used in conjunction with synchrotron X-ray powder diffraction data.

9.3 INDIRECT REFLECTIONS OF LATTICE STRUCTURE IN NMR TENSOR DATA

The direct encoding of lattice structure described in the section entitled "Direct Encoding of Lattice Structure in Shift Tensors" is only found in certain materials and even in these materials, only at charged or polarizable atomic sites. Thus, many experimentally measured tensor values will not directly reflect lattice structure. In these materials lattice forces still act on a molecule and can cause conformational changes in a structure that differ significantly from the gas-phase minimum. Since conformational changes can cause large variations in principal components, tensor data provide indirect evidence regarding the presence and, in some cases, the identity of neighboring molecules in the lattice.

The influence of conformational variation on tensor values can be seen through theoretical means by rotating a bond of interest over its entire conformational range while computing tensors at regular intervals. In many cases, a plot of computed tensor values versus dihedral angle reveals the complicating feature that the curves are degenerate with multiple conformational angles corresponding to a given tensor value (Figure 9.4).[55] Hence, many nuclear sites will have multiple fits of equal quality to experimental data. Fortunately, this degeneracy is usually only found when a single atomic site is examined. When data

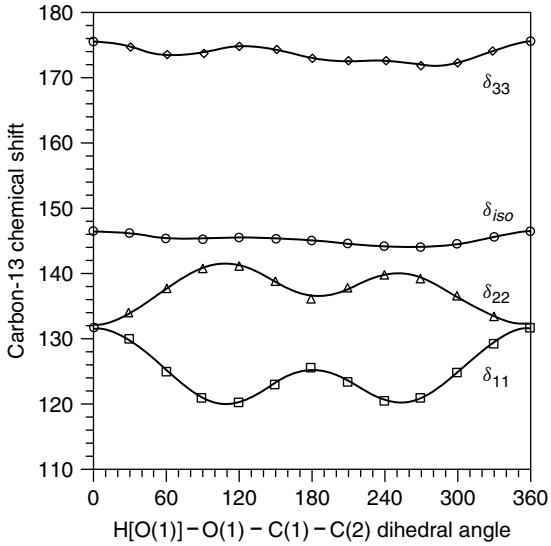


Figure 9.4. Computed principal components for C1 at all possible C2–C1–O–H dihedral angles in *meso*-erythritol illustrating the degeneracy often observed when a single site is evaluated. Many functional groups exhibit this feature and have multiple dihedral angles that match a given experimental principal value. Evaluating additional plots for nearby sites (e.g., C2) usually helps eliminate this ambiguity. (Reproduced from Ref. 55. © American Chemical Society, 1995.)

from multiple sites are combined, the unique relationship of principal value versus dihedral angle at each site ensures that destructive interference occurs allowing for a clear selection of a best fit to experimental data.[61] Selectivity increases as more sites are included up to a point, but since conformational changes have an influence that is short range, usually only sites within two bonds of a rotation axis aid selectivity.

Perhaps the most structurally informative interaction of a nucleus with the lattice is an attractive interaction involving a flexible group. For example, the OH hydrogen can rotate away from the gas-phase minimum energy structure to form a hydrogen bond, either as an acceptor or a donor. In the case of ^{13}C shifts, this rotation is strongly reflected in the δ_{11} and δ_{22} values of the C–OH moiety that involve an sp^3 carbon.[55] Thus, tensors have been used to locate hydroxy hydrogens in several products with an estimated accuracy of $\pm 12^\circ$.[62] This assignment is of crystallographic relevance since it implies that a donor or acceptor group of a neighboring molecule must be located within approximately 4 Å of the OH. Since hydrogen bonds have a well-defined geometry,[63] this assignment also roughly specifies orientation of the hydrogen-bonded partner. In many molecules only a few ways of making such pairings are possible because not many groups can hydrogen bond. Thus such conformational predictions serve to significantly reduce possible lattice arrangements.

As with polar groups, tensor data are also sensitive to conformation in nonpolar regions. It might be anticipated that such groups, which can only interact weakly with intermolecular sites, would have little energetic motivation to move from their minimum energy structures. In fact, nonpolar regions of molecules are quite likely to deform from gas-phase minima and when doing so allows stronger interactions such as hydrogen bonds to form. It is precisely the lack of strong interactions with adjacent lattice sites that makes these groups energetically easier to rotate away from minimum energy conformations and allows the occurrence of unexpected conformations. Hence, both polar and nonpolar regions of organic molecules can be expected to reflect lattice in this manner. A more complete discussion of this topic is given in this volume (*see* **Chapter 8**).[64]

While it is clear that indirect reflections of lattice structure in tensor data can provide conformational assignments, a major difficulty arises in trying to predict the identity of the neighboring groups that are causing conformational changes. The prediction of lattice structures that are consistent with the assigned conformations has been pursued by several approaches. A discussion of this topic is given later in the section entitled "Deriving Full Crystal Structures".

9.4 REFINEMENT OF ESTABLISHED CRYSTAL STRUCTURES

Tensor data are known to have an unusually high sensitivity to structure, possibly because shielding in a single direction can be measured, undiluted by the averaging inherent to isotropic shifts. This sensitivity is illustrated by naphthalene (Figure 9.5) where single-crystal neutron diffraction identifies the structure as one having D_{2h} point group symmetry.[65] However, tensors calculated using the coordinates obtained from the diffraction data fit experimental data poorly.[66,67] A structure deformed from D_{2h} to

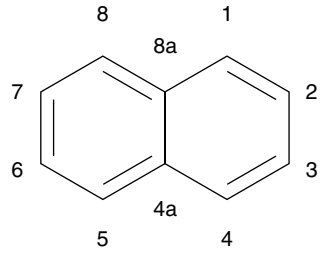


Figure 9.5. Naphthalene showing carbon numbering.

C_i symmetry was proposed to account for the differences. An alternative view ascribing differences to an asymmetrical distribution of closest neighbors in the lattice was found to make only a small contribution. Although the initial analysis was performed using the six values per nucleus of the full tensor, principal components also reflect the C_i symmetry (Table 9.1),[68] with particularly large differences found at C1 and C4, positions expected to be equivalent in D_{2h} symmetry. These data for naphthalene are purported to reflect geometrical variations smaller than the reported errors in the diffraction parameters. This study and a second closely related analysis of acenaphthene[67,69] suggest that tensor data can detect very minor defects even in neutron diffraction structures. Naturally, this result suggests the possibility of refining structures against tensor data and some work has been pursued with the goal of further refining known crystal structures.

Among the first SSNMR refinements of established X-ray diffraction structures were modifications of proton positions in carbohydrates.[56,67] Proton locations are not well determined in typical X-ray data and the reported C–H bond lengths for the carbohydrates studied was consistently too short. Although this error was small (≈ 0.1 Å) it was strongly reflected in the ^{13}C tensor data. Refinement of the proton positions was accomplished using a geometry optimization computation that allowed only hydrogen positions to move. Remarkably, refinement of protons from neutron diffraction data was also demonstrated using five carbohydrates.[70] In this case the C–H separation decreased by only 0.025 Å, on average upon refinement, but the root mean square (RMS) fit to experimental tensor data improved from 4.99 to 2.40 ppm. This sensitivity of tensors to hydrogen positions suggests that errors in heavier atom positions should also be reflected by tensor data.

Recently, the first examples of refinement of atoms other than hydrogen by SSNMR tensor data were reported.[5,10] In one case, a structure derived from X-ray powder diffraction data was found to have structural errors based on poor fits between tensors computed using the diffraction structure and experimental data.[5] Tensor data were available for all carbons, allowing specific regions needing refinement to be easily identified. Structural changes at only poorly fit positions significantly improved the tensor fit but the figure of merit of the diffraction refinement (Figure 9.6) was insensitive to these improvements. Although this refinement was monitored using ^{13}C tensor values, oxygen positions were also modified and this change was reflected in ^{13}C fits.

Table 9.1. Experimental ^{13}C principal components of naphthalene showing the differences in shifts at C1 and C4 and also at C2 and C3

Position	δ_{11}	δ_{22}	δ_{33}
C1, C8	224.7	140.3	22.8
C2, C7	227.6	139.3	11.1
C3, C6	227.6	138.2	10.4
C4, C5	223.9	145.6	20.4
C4a, C8a	208.5	202.2	−5.9

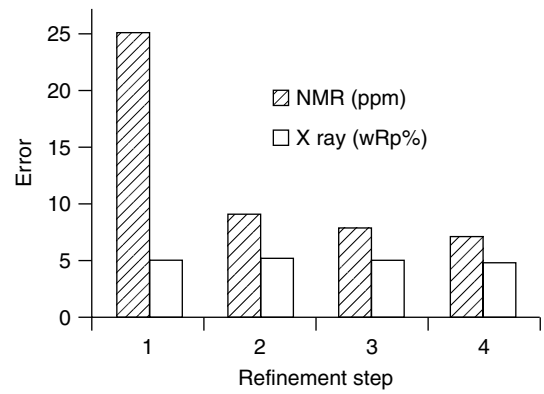


Figure 9.6. A structure for ambuic acid derived from X-ray powder diffraction (XRPD) methods (refinement step 1) shows large errors in computed NMR tensors despite the excellent XRPD fit. Subsequent geometry refinements (steps 2–4) show a significant improvement in the SSNMR error. The corresponding XRPD error is insensitive to these structural changes. (Reproduced from Ref. 5. © American Chemical Society, 2006.)

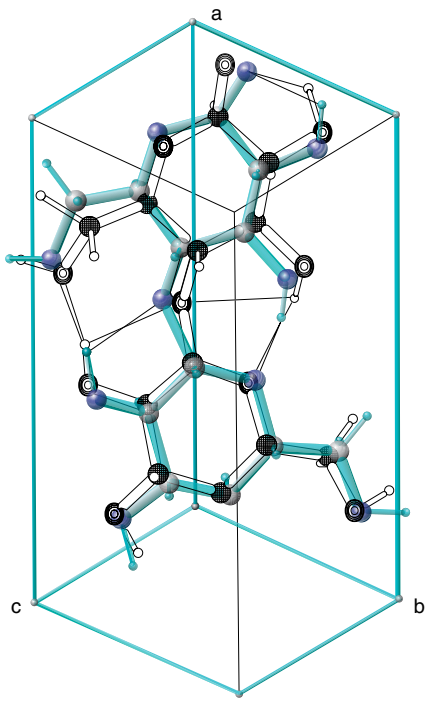


Figure 9.7. A least-squares superposition of the cellulose I_α structures derived from neutron fiber diffraction data (transparent model) and from SSNMR. The SSNMR model utilized the neutron diffraction structure as a starting point then refined the coordinates using ^{13}C isotropic chemical shifts as target functions. The vastly superior fit between measured and computed tensors for the refined structure provides strong evidence of improvement in the structure. The RMS difference for all atoms is 0.57 and 0.37 Å for nonhydrogen atoms alone. (Reproduced from Ref. 10. © American Chemical Society, 2006.)

A second study demonstrated that atomic positions determined from fiber diffraction could also be refined using SSNMR data.[10] In this case, the structure of cellulose I_α, established from X-ray and neutron diffraction data, was refined using isotropic ^{13}C shifts as target functions. Computed ^{13}C tensor data for the final refined structure matched the experimental tensor data far better than tensors calculated from the original diffraction structure, providing strong evidence of a structural improvement. Changes were noted at most positions as shown in Figure 9.7. Thus, structures derived from powder and fiber diffraction methods can apparently be further refined using tensor data.

An extension of heavy atom refinement to other nuclei has recently been reported using ^{29}Si tensors in zeolites.[8] In this case an iterative approach was used to refine a structure obtained from $^{29}Si/^{29}Si$ double-quantum SSNMR data. This method involved a systematic procedure for comparing computed tensor data to experimental values at each step and produced a final structure that was of comparable quality to one independently obtained from single-crystal X-ray diffraction. This ^{29}Si study further refined a structure originally derived from another SSNMR approach, suggesting that tensor data may also be used to improve structures derived from dipolar coupling data alone.

9.5 DERIVING FULL CRYSTAL STRUCTURES

The discussion so far has focused on deriving certain structural features from tensor data. Recently, however, complete structures of individual molecules with all conformational details have been reported from SSNMR data.[5,15,71–74] Of course, knowledge of these structures establishes a key portion of a complete crystal structure, amounting to a determination of the point group of the molecule. Subsequently, work has begun with the goal of deriving entire lattice structures from these SSNMR data.

Initial work involving tensor data has combined the NMR predicted structure with X-ray powder diffraction data.[5] X-ray powder methods require an initial model such as that provided by the NMR data. This combination has been previously used with isotropic shift[2,3,6,7] and dipolar-coupling[4] data to derive structure and it appears to be a significant improvement over structural solution from powder diffraction data alone.

With tensor data, several alternative paths were explored before a structure was found that was consistent with both the powder diffraction and SSNMR data. Although this process was somewhat inefficient and guided by intuition rather than a systematic search, the process served to identify deficiencies in the structure derived from diffraction alone as arising primarily from errors in bond lengths and valence angles involving nonhydrogen atoms. Dihedral angles predicted from X-ray powder methods were found to be quite accurate.

An alternative approach for deriving complete crystal structures has also been explored involving

crystal structure prediction. This technique computationally predicts a large set of possible crystal structures for a given molecule using only knowledge of atomic connectivity and no diffraction data.[75–77] Usually structures are predicted in only the most commonly observed space groups; however, methods capable of predicting structures in all 230 space groups have been reported.[78–80] An early combination of SSNMR data with crystal structure prediction data involved an analysis of four carbohydrates.[11] Tensor principal components were computed for all crystal structures predicted, 422 total, and compared with the experimental data. Nearly 90% of the structures considered possible from lattice energy considerations were eliminated at high probability using the tensor data. In three of the four carbohydrates, only 10 or fewer possible structures were retained. In addition, the correct structure was ranked in the top five in most cases. Most significantly, perhaps, these prediction methods demonstrate that even simple molecules have access to an incredible variety of crystal structures. Remarkably, even conformationally rigid individual molecules were found to fit well in several distinct space groups. This last point is of particular significance to SSNMR studies because it is tempting to assume that only a single space group will be compatible with a rigid structure assigned from NMR data. This study demonstrates the potential for NMR crystallography using only SSNMR data, but suggests caution in selecting a single best fit until a wide variety of crystal structures have been evaluated.

An alternative use of crystal structure prediction involves first predicting a structure from SSNMR data then using this structure to generate candidate structures. This method has the advantage that only space groups consistent with the determined point group must be considered. Additionally, the rather serious problem of treating flexible molecules in the prediction process are eliminated or at least reduced to a few candidate conformations. This approach has been used with an inorganic structure proposed from isotropic data[2] and prior work[11] suggests that similar studies that include tensor data may have greater selectivity.

REFERENCES

1. D. H. Brouwer, R. J. Darton, R. E. Morris, and M. H. Levitt, *J. Am. Chem. Soc.*, 2005, **127**, 10365.
2. J. Dutour, N. Guillou, C. Huguenard, F. Taulelle, C. Mellot-Draznieks, and G. Férey, *Solid State Sci.*, 2004, **6**, 1059.
3. M. Rajeswaren, T. N. Blanton, N. Zumbulyadis, D. J. Giesen, C. Conesa-Moratilla, S. T. Misture, P. W. Stephens, and A. Huq, *J. Am. Chem. Soc.*, 2002, **124**, 14450.
4. D. A. Middleton, X. Peng, D. Saunders, K. Shankland, W. I. F. David, and A. J. Markvardsen, *Chem. Commun.*, 2002, 1976.
5. J. K. Harper, D. M. Grant, Y. Zhang, P. L. Lee, and R. Von Dreele, *J. Am. Chem. Soc.*, 2006, **128**, 1547.
6. R. K. Harris, P. Y. Ghi, R. B. Hammond, C. Y. Ma, K. J. Roberts, J. R. Yates, and C. J. Pickard, *Magn. Reson. Chem.*, 2006, **44**, 325.
7. E. D. L. Smith, R. B. Hammond, M. J. Jones, K. J. Roberts, J. B. O. Mitchell, S. L. Price, R. K. Harris, D. C. Apperley, J. C. Cherryman, and R. Docherty, *J. Chem. Phys. B*, 2001, **105**, 5818.
8. D. H. Brouwer, *J. Am. Chem. Soc.*, 2008, **130**, 6306.
9. I. J. King, F. Fayon, D. Massiot, R. K. Harris, and J. S. O. Evans, *Chem. Commun.*, 2001, 1766.
10. R. Witter, U. Sternberg, S. Hesse, T. Kondo, F. T. Koch, and A. S. Ulrich, *Macromolecules*, 2006, **39**, 6125.
11. J. K. Harper and D. M. Grant, *Cryst. Growth Des.*, 2006, **6**, 2315.
12. F. Taulelle, *Solid State Sci.*, 2004, **6**, 1053.
13. C. J. Pickard, E. Salager, G. Pintacuda, B. Elena, and L. Emsley, *J. Am. Chem. Soc.*, 2007, **129**, 8932.
14. B. Elena, G. Pintacuda, N. Mifsud, and L. Emsley, *J. Am. Chem. Soc.*, 2006, **128**, 9555.
15. B. Elena and L. Emsley, *J. Am. Chem. Soc.*, 2005, **127**, 9140.
16. N. Mifsud, B. Elena, C. J. Pickard, A. Lesage, and L. Emsley, *Phys. Chem. Chem. Phys.*, 2006, **8**, 3418.
17. R. K. Harris, S. Cadars, L. Emsley, J. R. Yates, C. J. Pickard, R. K. R. Jetti, and U. Greisser, *Phys. Chem. Chem. Phys.*, 2007, **9**, 360.
18. D. H. Brouwer and G. D. Enright, *J. Am. Chem. Soc.*, 2008, **130**, 3095.
19. K. D. M Harris and M. Xu, in *Encyclopedia of Magnetic Resonance*, eds-in-chief R. K. Harris and R. E. Wasylishen, Wiley: Chichester, 2008. DOI: 10.1004/9780470034590.emrstm1004

20. C. P. Jaroniec, in *Encyclopedia of Magnetic Resonance*, eds-in-chief R. K. Harris and R. E. Wasylishen, Wiley: Chichester, 2008. DOI: 10.1011/9780470034590.emrstm1011
21. R. Tycko, in *Encyclopedia of Magnetic Resonance*, eds-in-chief R. K. Harris and R. E. Wasylishen, Wiley: Chichester, 2008. DOI: 10.1070/9780470034590.emrstm1070
22. L. Emsley, in *Encyclopedia of Magnetic Resonance*, eds-in-chief R. K. Harris and R. E. Wasylishen, Wiley: Chichester, 2008. DOI: 10.1010/9780470034590.emrstm1010
23. D. M. Grant, in *Encyclopedia of Nuclear Magnetic Resonance*, eds D. M. Grant and R. K. Harris, Wiley: Chichester, 1996, Vol. **2**, p 1298.
24. S. C. Shekar and A. Jerschow, in *Encyclopedia of Magnetic Resonance*, eds-in-chief R. K. Harris and R. E. Wasylishen, Wiley: Chichester, 2008. DOI: 10.1050/9780470034590.emrstm1050
25. R. K. Harris, E. D. Becker, S. M. Cabral de Menezes, P. Granger, R. E. Hoffman, and K. W. Zilm, *Pure Appl. Chem.*, 2008, **80**, 59.
26. F. Liu, C. G. Phung, D. W. Alderman, and D. M. Grant, *J. Am. Chem. Soc.*, 1995, **117**, 8251.
27. J. Mason, *Solid State NMR*, 1993, **2**, 285.
28. C. M. Rohlfing, L. C. Allan, and R. Ditchfield, *J. Chem. Phys.*, 1983, **79**, 4958.
29. Z. Gu, R. Zambrano, and A. McDermott, *J. Am. Chem. Soc.*, 1994, **116**, 6368.
30. S. Ando, I. Ando, A. Shoji, and T. Ozaki, *J. Am. Chem. Soc.*, 1988, **110**, 3380.
31. N. Asakawa, S. Kuroki, H. Kurosu, I. Ando, A. Shoji, and T. Ozaki, *J. Am. Chem. Soc.*, 1992, **114**, 3261.
32. Z. Ma, M. D. Halling, M. S. Solum, J. K. Harper, A. M. Orendt, J. C. Facelli, R. J. Pugmire, D. M. Grant, A. W. Amick, and L. T. Scott, *J. Phys. Chem. A*, 2007, **111**, 2020.
33. J. R. Yates and C. J. Pickard, in *Encyclopedia of Magnetic Resonance*, eds-in-chief R. K. Harris and R. E. Wasylishen, Wiley: Chichester, 2008. DOI: 10.1009/9780470034590.emrstm1009
34. R. K. Harris, P. Hodgkinson, C. J. Pickard, J. R. Yates and V. Zorin, in *Encyclopedia of Magnetic Resonance*, eds-in-chief R. K. Harris and R. E. Wasylishen, Wiley: Chichester, 2008. DOI: 10.1008/9780470034590.emrstm1008
35. A. M. Orendt and J. C. Facelli, *Ann. Rep. NMR Spectrosc.*, 2007, **62**, 115.
36. G. A. Bowmaker, R. K. Harris, and S.-W. Oh, *Coord. Chem. Rev.*, 1997, **167**, 49.
37. P. G. Karamertzanis and C. C. Pantelides, *J. Comput. Chem.*, 2005, **26**, 304.
38. P. G. Karamertzanis and C. C. Pantelides, *Mol. Phys.*, 2007, **105**, 273.
39. E. A. Christopher, R. K. Harris, and R. A. Fletton, *Solid State NMR*, 1992, **1**, 93.
40. G. Wu, C. J. Freure, and E. Verdurand, *J. Am. Chem. Soc.*, 1998, **120**, 13187.
41. R. E. J. Sears and R. Kaliaperumal, *J. Chem. Phys.*, 1990, **93**, 2959.
42. B. Berglund and R. W. Vaughan, *J. Chem. Phys.*, 1980, **73**, 2037.
43. R. Ditchfield, *J. Chem. Phys.*, 1976, **65**, 3123.
44. R. Kaliaperumal, R. E. J. Sears, Q. W. Ni, and J. E. Furst, *J. Chem. Phys.*, 1989, **91**, 7387.
45. K. L. Anderson-Altmann, C. G. Phung, S. Mavromoustakos, Z. Zheng, J. C. Facelli, C. D. Poulter, and D. M. Grant, *J. Phys. Chem.*, 1995, **99**, 10454.
46. J. Z. Hu, J. C. Facelli, D. W. Alderman, R. J. Pugmire, and D. M. Grant, *J. Am. Chem. Soc.*, 1998, **120**, 9863.
47. J. C. Facelli, R. J. Pugmire, and D. M. Grant, *J. Am. Chem. Soc.*, 1996, **118**, 5488.
48. Y. Wei, A. C. de Dios, and A. E. McDermott, *J. Am. Chem. Soc.*, 1999, **121**, 10389.
49. J. Czernek, R. Fiala, and V. Sklenár, *J. Magn. Reson.*, 2000, **145**, 142.
50. Y. Wei, A. C. de Dios, and A. E. McDermott, *J. Am. Chem. Soc.*, 1999, **121**, 10389.
51. M. Strohmeier, D. Stueber, and D. M. Grant, *J. Phys. Chem. A*, 2003, **107**, 7629.
52. D. H. Barich, J. S. Clawson, D. Stueber, M. Strohmeier, R. J. Pugmire, and D. M. Grant, *J. Phys. Chem. A*, 2002, **106**, 11375.
53. F. Liu, C. G. Phung, D. W. Alderman, and D. M. Grant, *J. Magn. Reson. A*, 1996, **120**, 242.
54. F. Liu, C. G. Phung, D. W. Alderman, and D. M. Grant, *J. Magn. Reson. A*, 1996, **120**, 231.
55. F. Liu, C. G. Phung, D. W. Alderman, and D. M. Grant, *J. Am. Chem. Soc.*, 1995, **117**, 9323.
56. F. Liu, A. M. Orendt, D. W. Alderman, and D. M. Grant, *J. Am. Chem. Soc.*, 1997, **119**, 8981.
57. M. Strohmeier, D. Stueber, and D. M. Grant, *J. Phys. Chem. A*, 2003, **107**, 7629.

58. K. L. Anderson, L. H. Merwin, W. S. Wilson, and J. C. Facelli, *Int. J. Mol. Sci.*, 2002, **3**, 858.

59. M. C. Etter, *Acc. Chem. Res.*, 1990, **23**, 120.

60. L. Leiserowitz, *Acta Crystallogr.*, 1976, **B32**, 775.

61. J. K. Harper and D. M. Grant, *J. Am. Chem. Soc.*, 2000, **122**, 3708.

62. J. K. Harper, A. E. Mulgrew, J. Y. Li, D. H. Barich, G. A. Strobel, and D. M. Grant, *J. Am. Chem. Soc.*, 2001, **123**, 9837.

63. G. A. Jeffery, in *An Introduction to Hydrogen Bonding*, ed. D. G. Truhlar, Oxford University Press: New York, 1997, p 12.

64. A. M. Orendt and J. C. Facelli, in *Encyclopedia of Magnetic Resonance*, eds-in-chief R. K. Harris and R. E. Wasylishen: Wiley, Chichester, 2008. DOI: 10.1057/9780470034590.emrstm1057

65. G. S. Pawley and E. A. Yeats, *Acta Crystallogr.*, 1969, **B25**, 2009.

66. J. C. Facelli and D. M. Grant, *Nature*, 1993, **365**, 325.

67. D. M. Grant, F. Liu, R. J. Iuliucci, C. G. Phung, J. C. Facelli, and D. W. Alderman, *Acta Crystallogr.*, 1995, **B51**, 540.

68. M. S. Sherwood, J. C. Facelli, D. W. Alderman, and D. M. Grant, *J. Am. Chem. Soc.*, 1991, **113**, 750.

69. R. J. Iuliucci, J. C. Facelli, D. W. Alderman, and D. M. Grant, *J. Am. Chem. Soc.*, 1995, **117**, 2336.

70. F. Liu, C. G. Phung, D. W. Alderman, and D. M. Grant, *J. Am. Chem. Soc.*, 1996, **118**, 10629.

71. C. M. Rienstra, L. Tucker-Kellogg, C. P. Jaroniec, M. Hohwy, M. T. Reif, B. T. McMahon, T. Lozano-Perez, and R. G. Griffin, *Proc. Natl. Acad. Sci. U.S.A.*, 2002, **99**, 10260.

72. F. Castellani, B. J. van Rossum, A. Diehl, M. Schubert, and H. Oschkinat, *Nature*, 2002, **420**, 98.

73. C. P. Jaroniec, C. E. MacPhee, V. S. Bajaj, M. T. McMahon, C. M. Dobson, and R. G. Griffin, *Proc. Natl. Acad. Sci. U.S.A.*, 2003, **101**, 711.

74. E. M. Heider, J. K. Harper, and D. M. Grant, *Phys. Chem. Chem. Phys.*, 2007, **9**, 1.

75. W. D. S. Motherwell, H. L. Ammon, J. D. Dunitz, A. Dzyabchenko, P. Erk, A. Gavezzotti, D. W. M. Hofmann, F. J. J. Leusen, J. P. M. Lommerse, W. T. M. Mooij, S. L. Price, H. Scheraga, B. Schweizer, M. U. Schmidt, B. P. van Eijck, P. Verwer, and D. E. Williams, *Acta Crystallogr.*, 2002, **B58**, 647.

76. J. P. M. Lommerse, W. D. S. Motherwell, H. L. Ammon, J. D. Dunitz, A. Gavezzotti, D. W. M. Hoffmann, F. J. J. Leusen, W. T. M. Mooji, S. L. Price, B. Schweizer, M. U. Schmidt, B. P. van Eijck, P. Verwer, and D. E. Williams, *Acta Crystallogr.*, 2000, **B56**, 697.

77. G. M. Day, W. D. S. Motherwell, H. L. Ammon, S. X. M. Boerrigter, R. G. Della Valle, E. Venuit, A. Dzyabchenko, J. D. Dunitz, B. Schweizer, B. P. van Eijck, P. Erk, J. C. Facelli, V. E. Bazterra, D. W. M. Hofmann, F. J. J. Leusen, C. Liang, C. C. Pantelideas, P. G. Karamertzanis, S. L. Price, T. C. Lewis, H. Nowell, A. Torrisi, H. A. Scheraga, Y. A. Arnautova, M. U. Schmidt, and P. Verwer, *Acta Crystallogr.*, 2005, **B61**, 511.

78. H. R. Karfunkel, Z. J. Wu, A. Burkhard, G. Rihs, D. Sinnreich, H. M. Buerger, and J. Stanek, *Acta Crystallogr.*, 1996, **B52**, 555.

79. F. J. J. Leusen, *Cryst. Growth*, 1996, **166**, 900.

80. W. T. M. Mooji, B. P. van Eijck, S. L. Price, P. Verwer, and J. Kroon, *J. Comp. Chem.*, 1998, **19**, 459.

PART C
Coupling Interactions

Chapter 10
Dipolar & Indirect Coupling: Basics

Roderick E. Wasylishen

Department of Chemistry, Gunning/Lemieux Chemistry Centre, University of Alberta, Edmonton, Alberta T6G 2G2, Canada

10.1	Introduction	127
10.2	Characterization of Indirect Spin–Spin Coupling Interactions in Solids	129
10.3	Characterization of Dipolar Spin–Spin Coupling Interactions in Solids	131
10.4	Conclusions	134
	References	135

10.1 INTRODUCTION

Nuclear spin–spin coupling interactions are capable of providing a wealth of information about the connectivity and spatial relationship among atoms in solid materials. The purpose of this article is to help the reader appreciate what the fundamental spin–spin coupling interactions are and how their characterization provides important structural information. After a brief qualitative description of the fundamental nuclear spin–spin coupling interactions, a few examples are provided to illustrate how their measurement can be related to solid-state structure. More examples or applications of the information derived from spin–spin coupling interactions are presented elsewhere in this handbook (e.g., *see* **Chapters 11**, **12** and **15**).

NMR Crystallography Edited by Robin K. Harris, Roderick E. Wasylishen and Melinda J. Duer © 2009 John Wiley & Sons, Ltd. ISBN: 978-0-470-69961-4

There are two fundamental spin–spin coupling interactions that can, in principle, occur between any pair of nuclear spins in a solid.[1] First, the two nuclear spins may interact via a direct-dipolar interaction analogous to the classical interaction between two magnetic point dipoles, μ_N and $\mu_{N'}$.[2–5] The direct-dipolar interaction can, in part, be characterized by the direct-dipolar coupling constant, R_{DD}, which is defined in frequency units (hertz) by equation (10.1):

$$R_{DD} = \left(\frac{\mu_0}{4\pi}\right)\left(\frac{\hbar}{2\pi}\right)\gamma_N\gamma_{N'}\langle r_{NN'}{}^{-3}\rangle \qquad (10.1)$$

where μ_0 is the permeability constant, $4\pi \times 10^{-7}$ kg m s^{-2} A^{-2}, $\hbar$ is Planck's constant divided by 2π, and γ_N and $\gamma_{N'}$ are the magnetogyric ratios of nuclei N and N', respectively. Of note, several authors define R_{DD} as given in equation (10.1), but with a minus sign in front of the expression (e.g., see Ref. 4). It is important to recognize that the magnitude of the direct-dipolar interaction depends on the average inverse cube separation of the two magnetic dipoles.

The second fundamental spin–spin coupling interaction involves a transfer of spin polarization via electrons, and does not depend on internuclear separation in any obvious manner. Because the indirect spin–spin coupling between two nuclear spins depends on their intervening electronic framework, one must rely on first-principles quantum chemistry computations to calculate reliable indirect spin–spin coupling constants. Furthermore, a general second-rank tensor is required to fully describe the

indirect spin–spin coupling between two nuclei, N and N'. Since most high-resolution NMR experiments yield one-third the trace of the indirect spin–spin coupling tensor, $J(N, N')$, it is the value of the isotropic indirect spin–spin coupling, $J(N, N')$, that is the focus of most experimental studies. It is sometimes convenient to express the isotropic spin–spin coupling constant, $J(N, N')$, in terms of a reduced indirect spin–spin coupling constant, $K(N, N')$, which only depends on the electronic structure of the molecule (equation (10.2)):

$$J(N, N') = \left(\frac{h}{4\pi^2}\right)\gamma_N\gamma_{N'}K(N, N') \qquad (10.2)$$

The importance of equation (10.2) is illustrated by considering the ^{31}P NMR spectrum of a 1 : 1 complex of silver nitrate and triphenylphosphine shown in Figure 10.1.[6] The spectrum acquired with magic-angle sample spinning exhibits an inner doublet due to spin–spin coupling with ^{107}Ag (natural abundance 51.839%, $\gamma(^{107}\text{Ag}) = -1.08892 \times 10^7$ rad s^{-1} T^{-1}), $|^1J(^{107}\text{Ag},^{31}\text{P})| = 707$ Hz, and an outer doublet due to spin–spin coupling with ^{109}Ag (natural abundance 48.161%, $\gamma(^{109}\text{Ag}) = -1.25186 \times 10^7$ rad s^{-1} T^{-1}), $|^1J(^{109}\text{Ag},^{31}\text{P})| = 815$ Hz. To a very good approximation, K(Ag, P) is independent of the silver isotope involved in spin–spin coupling to ^{31}P, and thus the experimental ratio, $^1J(^{109}\text{Ag},^{31}\text{P})/^1J(^{107}\text{Ag},^{31}\text{P}) \approx 1.15$ is in excellent agreement with the expected ratio, $\gamma(^{109}\text{Ag})/\gamma(^{107}\text{Ag})$, which is 1.14964. It is important to note that the spectrum in Figure 10.1 contains no information about the signs of $^1J(^{109}\text{Ag},^{31}\text{P})$ and $^1J(^{107}\text{Ag},^{31}\text{P})$; however, first-principles quantum calculations indicate the sign of ^1K(Ag, P) is positive so that the signs of $^1J(^{109}\text{Ag},^{31}\text{P})$ and $^1J(^{107}\text{Ag},^{31}\text{P})$ must be negative. Using the experimental values of $^1J(^{109}\text{Ag},^{31}\text{P})$ and $^1J(^{107}\text{Ag},^{31}\text{P})$, the reduced silver–phosphorus coupling constant, ^1K(Ag, P), is approximately 357×10^{20} N A^{-2} m^{-3} (or equivalently in units of T^2 J^{-1}). Note that this reduced indirect spin–spin coupling constant allows one to compare ^1K(Ag, P) with ^1K(Cu, P) or ^1K(Au, P) in related complexes, for example. It is well known that if one compares ^1K(X, P) values within any group of the periodic table, they increase as the atomic number of X increases, so one expects $^1K(\text{Au, P}) > {}^1K(\text{Ag, P}) > {}^1K(\text{Cu, P})$ in a series of related molecules (e.g., 1 : 1 coinage metal–phosphine complexes).[7]

The theoretical foundation of indirect spin–spin coupling is well established.[8–15] In the past decade, there has been considerable progress in calculating indirect spin–spin coupling tensors; however, accurately reproducing experimental indirect spin–spin coupling tensors in all but the simplest molecules remains a theoretical challenge.[9–15] Nevertheless, as discussed later in this article and elsewhere,[7,15] many valuable empirical relationships between indirect spin–spin coupling constants and molecular structure have been established.

As shown below, both the direct and indirect spin–spin coupling interactions are bilinear in the

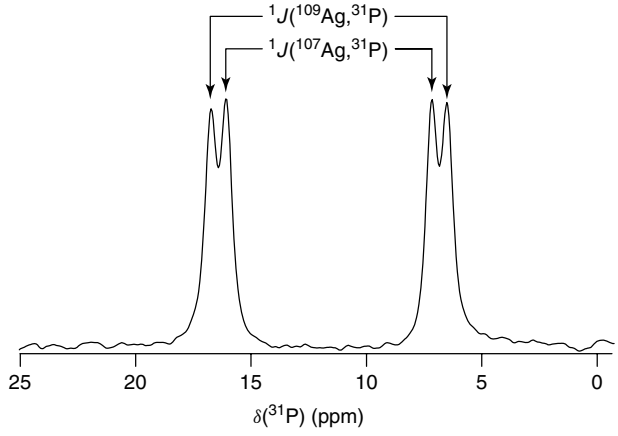


Figure 10.1. Phosphorus-31 NMR spectrum of solid $AgNO_3 \cdot PPh_3$, acquired at 213 K using a 4.70 T instrument with a spinning frequency of 3 kHz.

nuclear spin operators. Although, in principle, every spin of a sample is spin–spin coupled to all other spins in the sample via the direct-dipolar interaction, it is instructive to focus on an "isolated" spin pair. For example, for the silver–triphenylphosphine complex mentioned above, under conditions of ^{1}H decoupling the ^{107}Ag, ^{31}P and ^{109}Ag, ^{31}P spin pairs may be considered "isolated" to a good approximation. For an isolated spin pair, the spin–spin coupling Hamiltonian may be represented by

$$h^{-1}\hat{H} = R_{DD}\boldsymbol{I}_N \cdot \boldsymbol{D}(N, N') \cdot \boldsymbol{I}_{N'} + \boldsymbol{I}_N \cdot \boldsymbol{J}(N, N') \cdot \boldsymbol{I}_{N'} \qquad (10.3)$$

where $\boldsymbol{I}_N$ and $\boldsymbol{I}_{N'}$ are the nuclear spin angular momentum vectors, $\boldsymbol{D}(N, N')$ is the direct-dipolar tensor which, in the absence of motion, is an axially symmetric traceless tensor.[16] It should be noted that anisotropic vibrations can result in subtle vibrationally induced asymmetry in the dipolar tensor.[17,18] On the other hand, $\boldsymbol{J}(N, N')$ is a general second-rank tensor with up to nine independent components.[19] Because of the form of the two terms in equation (10.3), it is difficult to experimentally characterize direct-dipolar and indirect spin–spin coupling tensors independently. In fact, experimentally it is impossible to separately measure $R_{DD}(N, N')$ and the anisotropy of the indirect spin–spin coupling tensor, $\Delta J(N, N')$.[19,20] Instead, assuming the $\boldsymbol{J}$ and $\boldsymbol{D}$ tensors are coincident, experiments provide $R_{eff}(N, N')$, which is defined by equation (10.4),

$$R_{eff}(N, N') = R_{DD}(N, N') - \Delta J(N, N')/3 \qquad (10.4)$$

For most spin pairs involving only first- or second-row elements, $\Delta J(N, N')/3$ is small and, in practice, generally ignored. In the following section, we briefly outline some relatively straightforward experiments designed to characterize indirect and direct spin–spin coupling interactions.

10.2 CHARACTERIZATION OF INDIRECT SPIN–SPIN COUPLING INTERACTIONS IN SOLIDS

Isotropic indirect spin–spin coupling constants, often referred to as *scalar spin–spin coupling constants*, are traditionally obtained from magic-angle spinning (MAS) experiments.[21,22] Under conditions of rapid MAS, the direct-dipolar interaction is averaged to zero because the trace of the dipolar tensor is zero. The measurement of $^{1}J(^{103}\text{Rh}, ^{31}\text{P})$ and $^{1}J(^{31}\text{P}, ^{19}\text{F})$ for [*tris* (dimethylphenylphosphine)] (2,5-norbornadiene) rhodium(I) hexafluorophosphate from a routine ^{31}P NMR experiment acquired with MAS is illustrated in Figure 10.2.[23] Note that all three phosphine ligands are nonequivalent in the solid state and that there is one unique molecule in the asymmetric unit. Also, note that although splittings due to $^{2}J(^{31}\text{P}, ^{31}\text{P})$ cannot be resolved in the 1-D experiment, they are resolved in a 2-D ^{31}P J-resolved experiment (Figure 10.3). The principles of homonuclear 2-D J-resolved NMR spectroscopy are discussed in most NMR texts.[24] Inhomogeneity effects are effectively eliminated using J-spectroscopy techniques, thereby yielding NMR linewidths that correspond to the real spin–spin relaxation time, T_2. Several 2-D techniques including COSY, INADEQUATE, SECSY, etc., have been used to establish homonuclear J-connectivity in solids where small splittings due to J-coupling are unresolved (*see* **Chapter 15**). For example, in a recent publication, Florian *et al.*[25] demonstrated that $^{2}J(^{29}\text{Si}, ^{29}\text{Si})$ values as small as 1.5 Hz could be measured in 2-D J-resolved experiments. This and many other articles serve to dispel the common misconception that T_2 values in solids are short. For solids, it is convenient to define a time constant, T_2^{CPMG}, describing the decay of an echo train in a Carr–Purcell–Meiboom–Gill (CPMG) experiment carried out with MAS and RF decoupling schemes and contrast this time constant with that following single-pulse excitation (often denoted as T_2'). Invariably, T_2^{CPMG} is considerably longer than T_2' – even for quadrupolar nuclei. It is beyond the scope of this article to discuss the origins of line broadening in solid-state NMR spectroscopy, but it is important to recognize that any technique that takes advantage of the long values of T_2^{CPMG} compared to T_2' will yield enhanced resolution and in many cases improved signal-to-noise ratios.[26]

As illustrated in Figures 10.1 and 10.2, heteronuclear indirect spin–spin coupling constants can often be measured in standard 1-D solid-state NMR experiments with MAS. One interesting difference between NMR studies of isotropic liquids and solids is that in the solid state, indirect spin–spin constants involving quadrupolar nuclei are readily determined.[27–29] This is a consequence of the much longer spin–lattice relaxation times for quadrupolar nuclei in the solid state compared to those for isotropic liquids. For

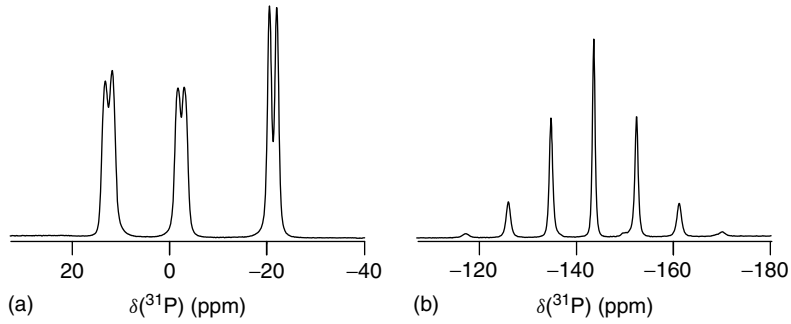


Figure 10.2. Phosphorus-31 NMR spectrum of solid [*tris*-(dimethylphenylphosphine)](2,5-norbornadiene) rhodium(I) hexafluorophosphate, acquired at 4.70 T with a spinning frequency of 6 kHz. The region of the spectrum containing the contribution from the three magnetically distinct phosphine ^{31}P nuclei is shown in (a) and that arising from the ^{31}P nucleus of the PF_6^- anion is shown in (b).

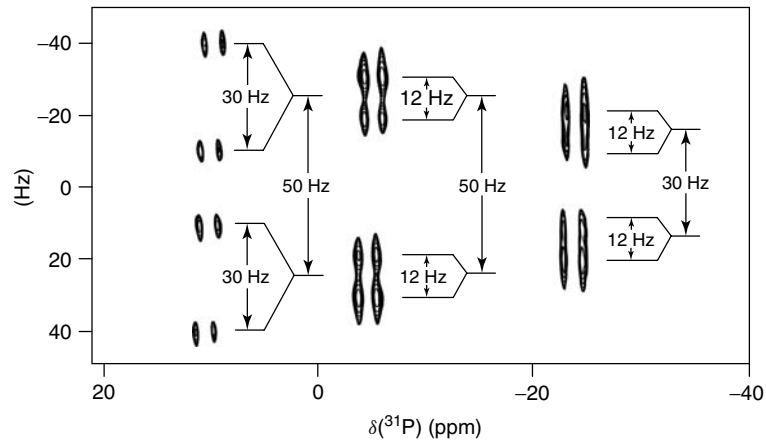


Figure 10.3. 2-D ^{31}P *J*-resolved NMR spectrum of solid [*tris*-(dimethylphenylphosphine)](2,5-norbornadiene) rhodium(I) hexafluorophosphate, obtained at 4.70 T with a spinning frequency of 8 kHz; 64 t_1 increments were acquired. (Adapted from Ref. 23. © Royal Society of Chemistry, 2008.)

example, the ^{113}Cd NMR spectrum of a cadmium thiocyanate hexamethylenetetramine complex, $Cd(SCN)_2 \cdot C_6H_{12}N_4 \cdot 2H_2O$, obtained with MAS shows a complex multiplet resulting from ^{113}Cd coupling to three ^{14}N nuclei (Figure 10.4).[30] Two of the nitrogen nuclei originate from directly bonded thiocyanate ligands, $^1J(^{113}Cd, ^{14}N) = 80$ Hz, while the third is a nitrogen from a hexamethylenetetramine ligand, $^1J(^{113}Cd, ^{14}N) = 95$ Hz. A study of 12 different cadmium thiocyanate complexes indicated that $^1J(^{113}Cd, ^{14}N)$ values appear to be related to the cadmium–nitrogen bond length (*see* Figure 10.5). Similar empirical correlations between $^1J(^{63/65}Cu, ^{31}P)$ and bond length have also been proposed.[31]

In recent years, considerable progress has been realized in the development of through-bond correlation NMR experiments that rely on J-coupling (*see* **Chapter 15**). For example, Lesage and Emsley[32] have used two related 2-D techniques for transferring magnetization between ^{13}C and ^{1}H nuclei using indirect ^{13}C,^{1}H spin–spin couplings. The sequences, dubbed MAS-J-HMQC and MAS-J-HSQC, respectively, differ in that the first utilizes heteronuclear multiple coherences while the second allows single-quantum (SQ) coherences to evolve during the indirect detection time. Frequency-switched Lee–Goldburg (FSLG) homonuclear decoupling is used to remove ^{1}H,^{1}H dipolar-coupling during this

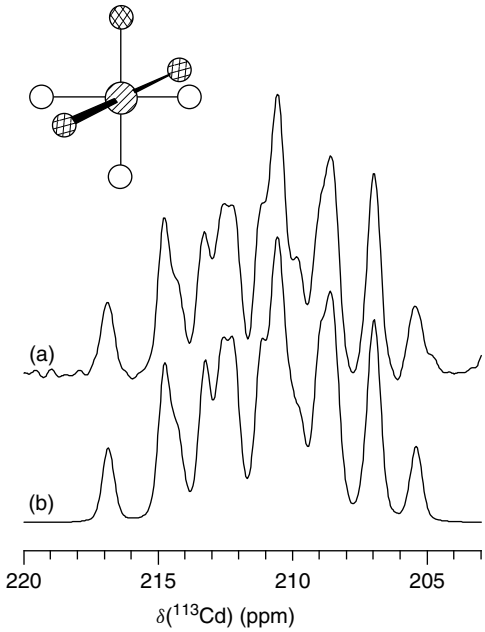


Figure 10.4. Isotropic region of the ^{113}Cd CP/MAS NMR spectrum of $Cd(SCN)_2 \cdot C_6H_{12}N_4 \cdot 2H_2O$, showing spin–spin coupling of ^{113}Cd with three ^{14}N nuclei: (a) experimental spectrum and (b) calculated spectrum. (Reproduced from Ref. 30. © American Chemical Society, 1994.)

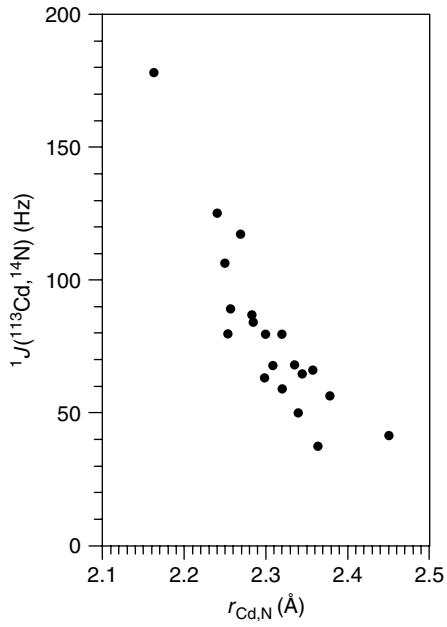


Figure 10.5. Dependence of ^1J (^{113}Cd,^{14}N) on the Cd–N distance. (Reproduced from Ref. 30. © American Chemical Society, 1994.)

period while MAS insures that chemical shifts and indirect spin–spin couplings are averaged to their isotropic values. Both experiments work well but the SQ scheme provides better ^1H resolution (e.g., splittings due to $J(^{13}C,^1H)$ are apparent). Emsley and coworkers[33] have also demonstrated the feasibility of proton to carbon INEPT (insensitive nuclei enhanced by polarization transfer) based on indirect spin–spin coupling. Related experiments involving "dilute" spin pairs were reported earlier by Fyfe and coworkers.[34]

Massiot *et al.*[35] and others[36] have demonstrated that it is possible to obtain $^2J(^{31}P, ^{27}Al)$ values using J-resolved experiments; furthermore, they demonstrated that these couplings can be used to generate MAS-J-HMQC correlation spectra. Amoureux *et al.*[37] have recently provided a useful summary of correlation NMR spectroscopy experiments on quadrupolar nuclei. These involve both through-bond (J) and through-space (dipolar) spin–spin coupling.

This section is concluded with a simple example illustrating the use of $^1J(^{107/109}Ag,^{13}C)$ values in demonstrating "head-to-tail" disorder of cyanide anions in solid silver cyanide, a linear polymer, $[Ag(CN)]_\infty$.[38] Figure 10.6 illustrates that it is impossible to simulate the observed ^{13}C NMR spectrum obtained with MAS by assuming one unique site (i.e., perfect "head-to-tail" disorder). The NMR results indicated that $30 \pm 10\%$ of the silver sites are disordered, i.e., either –NC–Ag–CN– or –CN–Ag–NC– as opposed to –NC–Ag–NC–; information that is unavailable from diffraction experiments.[39]

10.3 CHARACTERIZATION OF DIPOLAR SPIN–SPIN COUPLING INTERACTIONS IN SOLIDS

Consider an isolated spin pair of nuclei that interact with one another via the direct-dipolar interaction. It is often most convenient to express the dipolar Hamiltonian of such a spin pair in spherical coordinates.[1] It is well known that in this coordinate system, the

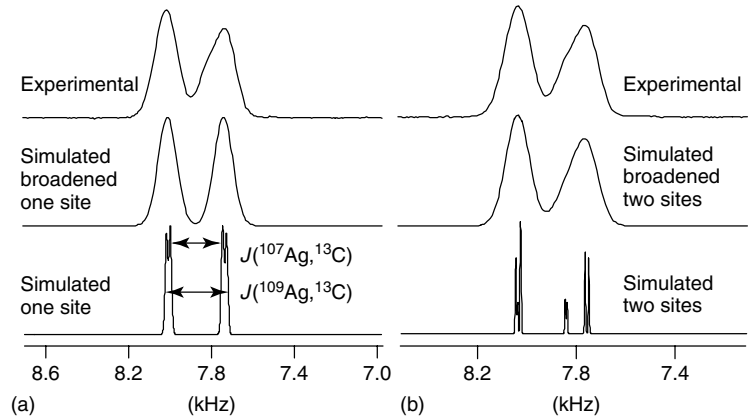


Figure 10.6. (a) Experimental ^{13}C MAS NMR isotropic resonance (the MAS spinning sidebands have been added to the isotropic centerband) for $Ag^{13}C^{15}N$. The simulated isotropic resonance of the ^{13}C MAS NMR spectrum of solid $Ag^{13}C^{15}N$ based on a typical $J_{iso}(^{109}Ag,^{13}C)$ of 280 Hz and the corresponding $J_{iso}(^{107}Ag,^{13}C)$, 243 Hz, are shown on the left for a single carbon site. The J-coupling between ^{13}C and the two silver isotopes results in four peaks, as shown in the unbroadened spectrum. The asymmetry of the reconstructed experimental isotropic ^{13}C resonance shown in part (a) cannot be reproduced on the basis of a one-site model, as evidenced by the disagreement between the experimental spectrum and the broadened "one-site" simulated spectrum. The simulated isotropic resonances of the ^{13}C MAS NMR spectrum of solid $Ag^{13}C^{15}N$ based on a two-site model, where the isotropic chemical shift and silver–carbon J-coupling are slightly different for carbon sites depending on the orientation of the nearest neighbor cyanide ligand, are shown in part (b). The experimental spectrum is successfully simulated as the sum of two distinct ^{13}C sites in an approximate ratio 2 : 1. (Reproduced from Ref. 38. © American Chemical Society, 2002.)

dipolar interaction between spin "1" and "2" can be expressed as a sum of six terms known as the *dipolar alphabet* (e.g., *see* Chapter 4 of text by R.K. Harris Ref. 16); however, only two terms are required to predict the NMR spectrum of an isolated spin pair, equation (10.5),

$$h^{-1}\hat{H}_{DD} = R_{DD}\{[-\boldsymbol{I}_{1z}\boldsymbol{I}_{2z}(3\cos^2\theta - 1)] + \frac{1}{4}[\boldsymbol{I}_1^+\boldsymbol{I}_2^- + \boldsymbol{I}_1^-\boldsymbol{I}_2^+](3\cos^2\theta - 1)\} \quad (10.5)$$

The first term in equation (10.5) involving the operators $\boldsymbol{I}_{1z}$ and $\boldsymbol{I}_{2z}$ is known as the "A" term of the dipolar alphabet while the second term involving raising and lowering operators is the "B" or "flip-flop" term. In equation (10.5), θ is defined as the angle between the dipolar vector, $\boldsymbol{r}_{1,2}$, and the applied magnetic field, $\boldsymbol{B}_0$. As discussed in reference,[1] it is only necessary to consider the "A" term to predict the NMR spectrum of a heteronuclear dipolar coupled spin pair, while for a homonuclear spin pair one must also consider the term involving the flip-flop operator. For a stationary sample containing an isolated spin pair, the dipolar interaction leads to a characteristic "Pake doublet". If the isolated spin pair is a heteronuclear spin pair, the separation between the "horns" of the Pake doublet is R_{eff}; however, for spin pairs that are magnetically equivalent, the analogous separation is $3R_{eff}/2$.

The ^{13}C NMR spectrum of a stationary sample of methyl-^{13}C triphenylphoshonium iodide acquired with ^1H decoupling (Figure 10.7) exhibits a "Pake doublet" as a result of the ^{13}C–^{31}P dipolar interaction. The powder pattern is broadened because of intermolecular ^{13}C–^{31}P and ^{13}C–^{13}C dipolar interactions. In this case, the magnetic shielding experienced by the carbon nuclei is essentially "isotropic". Also, it should be noted that, in principle, indirect spin–spin coupling, $^1J(^{31}P,^{13}C)$, also contributes to the powder pattern shown in Figure 10.7; however, from MAS spectra $^1J(^{31}P,^{13}C) \approx 50$ Hz, which is much smaller than $R_{eff}(^{31}P,^{13}C) \approx 2130$ Hz. If one does consider both the direct and indirect coupling constants, the separation between the "horns" is $R_{eff}(^{31}P,^{13}C) + J(^{31}P,^{13}C)$ while the separation between the outer shoulders is $-2R_{eff}(^{31}P,^{13}C) + J(^{31}P,^{13}C)$. Obviously when one examines the NMR spectra of spin pairs, the spectra are generally

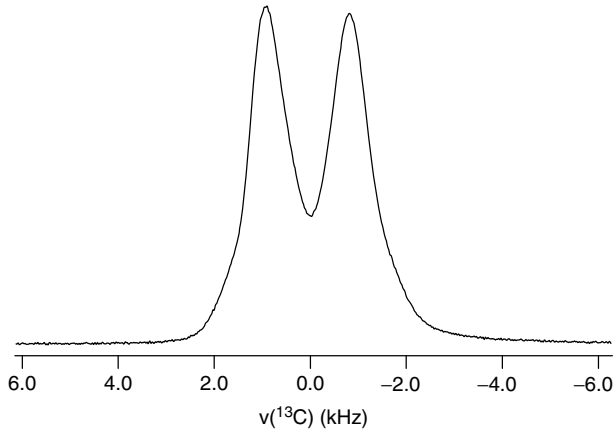


Figure 10.7. Methyl-carbon region of the ^{13}C NMR spectrum of a stationary solid sample of methyl-^{13}C-triphenylphosphonium iodide, acquired at 7.05 T.

complicated by anisotropic magnetic shielding. One can frequently analyze the NMR spectra of systems containing "isolated" spin pairs – particularly if spectra are obtained at more than one applied magnetic field strength.[40–43] For homonuclear spin pairs, the 2-D spin-echo experiment is invaluable in isolating spin–spin coupling interactions from anisotropic magnetic shielding. This is illustrated in Figure 10.8 for two different molybdenum organometallic complexes containing the tetraphenyldiphosphine (tpdp) ligand.[43]

The examples presented above are situations where the direct-dipolar coupling constants are relatively large because they involve directly bonded spin pairs. While interesting, it is obviously more important to develop techniques that are capable of measuring smaller dipolar-coupling constants (to provide longer internuclear distances), preferably from high-resolution NMR experiments that utilize MAS. Several ingenious techniques have been developed to recouple the dipolar interactions under MAS conditions. Here we use "recouple" to emphasize that under rapid MAS conditions, the dipolar interaction involving spin pairs is normally averaged to zero. Dipolar recoupling techniques have been extensively reviewed (e.g., *see* **Chapters 11** and **12**).[44–47] Chapter 3 of Duer's text[5] provides an excellent introduction to these methods and is also recommended. It is important to recognize that because of the nature of the dipolar Hamiltonian, the recoupling techniques for homonuclear spin pairs differ from those designed for heteronuclear spin pairs.

Invariably, heteronuclear dipolar recoupling schemes are based on an echo experiment. Most important is the rotational-echo, double-resonance (REDOR) experiment developed by Gullion and Schaefer,[48] which uses rotor-synchronous π-pulse trains to recover the dipolar interaction. A particularly lucid description of the REDOR experiment has been provided by Garbow and Gullion.[47] Using the $^{31}P-^{19}F$ REDOR experiment, Olsen *et al*.[49] have measured $^{31}P-^{19}F$ distances of 7–14 Å in DNA-drug complexes (note that in order to measure a $^{31}P-^{19}F$ separation of 14 Å, it is necessary to measure a dipolar-coupling constant of 16.6 Hz). Most applications of the REDOR experiment have involved pairs of spin-$\frac{1}{2}$ nuclei; however a related technique, rotational-echo, adiabatic passage, double resonance (REAPDOR) has been developed to measure dipolar-coupling constants between spin-$\frac{1}{2}$ nuclei and quadrupolar nuclei (e.g., a $^{17}O-^{13}C$ spin pair).[50–52]

Since the early days of MAS NMR,[53] it has been recognized that homonuclear spin pairs that are dipolar coupled to one another are recoupled under conditions of rotational resonance, RR (equation (10.6)).[54]

$$n\ \nu_r = (\nu_1^{iso} - \nu_2^{iso}) \qquad (10.6)$$

Here n is an integer, generally 1–3, ν_r is the MAS frequency, and ν_1^{iso} and ν_2^{iso} are the isotropic resonance frequencies of spins "1" and "2", respectively. Qualitatively, when the rotational resonance condition is satisfied, the "flip-flop" term

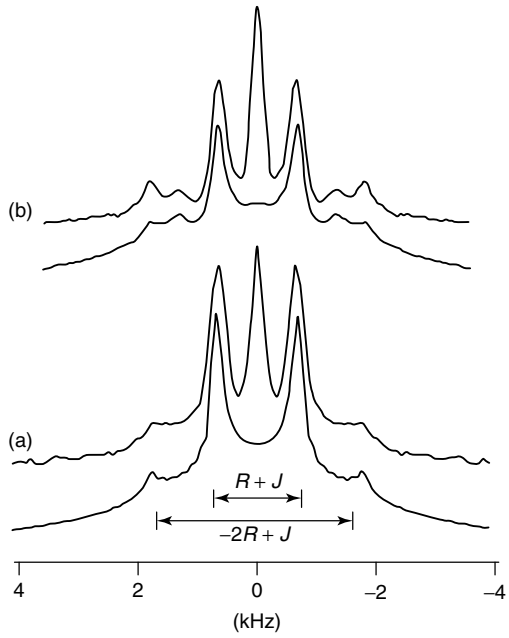


Figure 10.8. F_1 projections from 2-D ^{31}P spin-echo NMR spectra of powder samples of (a) *fac*-(OC)$_3$(η^2-phen)Mo(η^1-tpdp), and (b) *fac*-(OC)$_3$(η^2-Me$_2$phen)Mo(η^1-tpdp), obtained at 4.70 T. In (b), residual chemical shift effects cause additional peaks to appear, while (a) can be interpreted on the basis of the AX approximation. (Reproduced from Ref. 43. © American Chemical Society, 1999.)

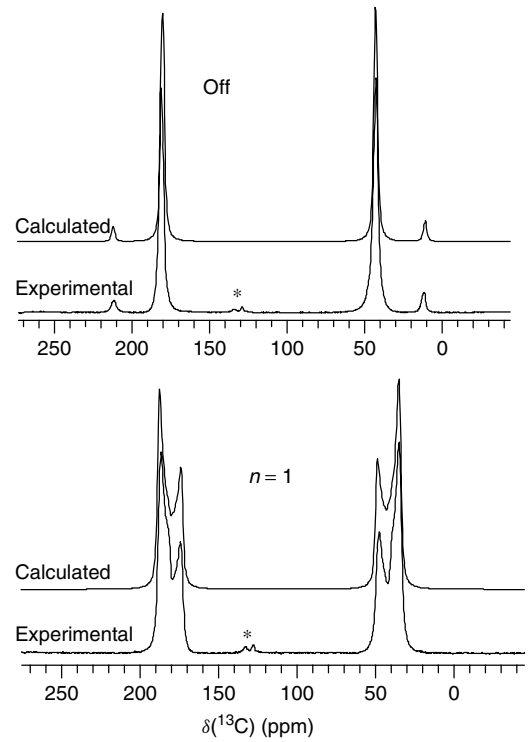


Figure 10.9. Off RR and $n = 1$ RR ^{13}C CP/MAS spectra of phenylacetic-$^{13}C_2$ acid (99%). $B_0 = 4.7$ T, $\nu_0 = 50.3$ MHz, number of acquisitions = 256. The "off RR" spectrum was acquired with variable-amplitude CP, $\nu_r = 9.0$ kHz. Signal due to naturally abundant ^{13}C in the phenyl ring is indicated by asterisks. (Reproduced from Ref. 55. © American Chemical Society, 2000.)

in equation (10.5) becomes time independent and contributes to the observed spectrum. The ^{13}C NMR spectrum of phenylacetic acid-$^{13}C_2$ (Figure 10.9) provides a striking example of the effect of satisfying the $n = 1$ condition.[55] In addition to influencing the line shape, there is an enhanced rate of exchange of Zeeman magnetization between sites "1" and "2" under conditions of rotational resonance which, in practice, is more useful to the experimentalist. The rotational resonance experiment is an example of a chemical-shift-dependent dipolar recoupling experiment. Dipolar coupling can also be reintroduced by RF pulses as illustrated in the dipolar recovery at the magic angle (DRAMA) experiment[56] and the related MELODRAMA experiment.[57] These experiments are most often performed as 2-D experiments in which a recoupling sequence is applied synchronously with MAS during the evolution period. Levitt has developed an elegant set of symmetry principles that are important in developing recoupling schemes.[58] In a recent investigation of disorder in AuCN, the supercycled $SR26_4^{11}$ sequence of Levitt was used to establish $^{13}C-^{13}C$ through-space connectivity.[59] The measurement and applications of through-space connectivity experiments is discussed in this handbook (e.g., *see* **Chapters 11** and **12**).

10.4 CONCLUSIONS

With the availability of improved NMR instrumentation, solid-state NMR spectroscopists will continue to develop clever techniques to extract both direct and indirect spin–spin coupling constants from complex solid materials. For successfully relating observed

indirect spin–spin coupling constants with molecular structure, accurate theoretical calculations of indirect spin–spin coupling tensors would be required. Significant progress in this area has been realized (e.g., *see* **Chapter 3**).[60] Clearly, further progress in this area will have a significant impact on NMR crystallography. Finally, it is clear that many of the powerful multidimensional NMR techniques used to elucidate molecular structure in isotropic liquids can be modified and extended to provide valuable structural information in the solid state.

REFERENCES

1. R. E. Wasylishen, Dipolar and indirect coupling tensors in solids, in '*The Encyclopedia of Nuclear Magnetic Resonance*', eds D. M. Grant and R. K. Harris, John Wiley & Sons: Chichester, 1996, pp 1685–1695.
2. P. Atkins and R. Friedman, '*Molecular Quantum Mechanics*', 4th edn., Oxford University Press: Oxford, 2005, Chapter 13, pp 436–472.
3. G. Lippens and J. Jeener, *Concepts Magn. Reson.*, 2001, **13**, 8.
4. M. H. Levitt, '*Spin Dynamics*', John Wiley & Sons: Chichester, 2001.
5. M. J. Duer, in '*Solid-State NMR Spectroscopy*', ed. M. J. Duer, Blackwell Science: Oxford, 2002, 46–56.
6. S.-W. Oh, G. M. Bernard, R. E. Wasylishen, R. McDonald, and M. J. Ferguson, *Can. J. Chem.*, 2005, **83**, 1721.
7. C. J. Jameson, in '*Multinuclear NMR*', ed. J. Mason, Plenum Press: New York, 1987, Chapter 4, pp 89–131.
8. N. F. Ramsey, *Phys. Rev.*, 1953, **91**, 303.
9. P. Pyykkö, *Theor. Chem. Acc.*, 2000, **103**, 214.
10. P. Pyykkö, in '*Calculation of NMR and EPR Parameters – Theory and Applications*', eds M. Kaupp, M. Bühl, and V. G. Malkin, Wiley-VCH Verlag GmbH & Co. KGaA: Weinheim, Vol. **103**, Chap. 2, pp 7–19, 214.
11. J. Vaara, J. Jokisaari, R. E. Wasylishen, and D. L. Bryce, *Prog. Nucl. Magn. Reson. Spectrosc.*, 2002, **41**, 233.
12. L. B. Krivdin and R. H. Contreras, *Annu. Rep. Nucl. Magn. Reson. Spectrosc.*, 2007, **61**, 133.
13. T. Helgaker, M. Jaszuński, and M. Pecul, *Prog. Nucl. Magn. Reson. Spectrosc.*, 2008, **53**, 249.
14. H. Fukui, in '*Nuclear Magnetic Resonance – Specialist Periodical Reports*', eds G. A. Webb, The Royal Society of Chemistry: Cambridge, 2008, Vol. **37**, pp 124–144.
15. K. Kamieńska-Trela and J. Wójcik, in '*Nuclear Magnetic Resonance – Specialist Periodical Reports*', eds G. A. Webb, The Royal Society of Chemistry: Cambridge, 2008, Vol. **37**, pp 145–179.
16. R. K. Harris, '*Nuclear Magnetic Resonance Spectroscopy*', Longman Scientific & Technical: Essex, England, 1986, Appendix 4.
17. J. M. Millar, A. M. Thayer, D. B. Zax, and A. Pines, *J. Am. Chem. Soc.*, 1986, **108**, 5113.
18. T. Nakai, J. Ashida, and T. Terao, *Mol. Phys.*, 1989, **67**, 839.
19. R. E. Wasylishen, Indirect nuclear spin-spin coupling tensors, in '*The Encyclopedia of Nuclear Magnetic Resonance*', Advances in NMR, eds D. M. Grant and R. K. Harris, 2002, Vol. **9**, pp 274–282.
20. D. L. Bryce and R. E. Wasylishen, *Acc. Chem. Res.*, 2003, **36**, 327.
21. E. R. Andrew and L. F. Farnell, *Mol. Phys.*, 1968, **15**, 157.
22. E. R. Andrew, *Prog. Nucl. Magn. Reson. Spectrosc.*, 1972, **8**, 1.
23. G. M. Bernard, K. W. Feindel, R. E. Wasylishen, and T. S. Cameron, *Phys. Chem. Chem. Phys.*, 2008, **10**, 5552.
24. R. R. Ernst, G. Bodenhausen, and A. Wokaun, '*Principles of Nuclear Magnetic Resonance in One and Two Dimensions*', Oxford Science Publications, Clarendon Press: Oxford, 1987, Chap. 7.
25. P. Florian, F. Fayon, and D. Massiot, *J. Phys. Chem. C*, 2009, **113**, 2562.
26. J. W. Wiench, V. S.-Y. Lin, and M. Pruski, *J. Magn. Reson.*, 2008, **193**, 233 and references therein.
27. K. Eichele, R. E. Wasylishen, J. S. Grossert, and A. C. Olivieri, *J. Phys. Chem.*, 1995, **99**, 10110.
28. A. Jerschow, *Monatsh. Chem.*, 2002, **133**, 1481.
29. G. Szalontail, *Monatsh. Chem.*, 2002, **133**, 1575.
30. K. Eichele and R. E. Wasylishen, *Inorg. Chem.*, 1994, **33**, 2766.
31. J. H. Nelson, *Concepts Magn. Reson.*, 2002, **14**, 19.
32. A. Lesage and L. Emsley, *J. Magn. Reson.*, 2001, **148**, 449.

33. B. Elena, A. Lesage, S. Steuernagel, A. Böckmann, and L. Emsley, *J. Am. Chem. Soc.*, 2005, **127**, 17296.
34. C. A. Fyfe, K. C. Wong-Moon, Y. Huang, and H. Grondey, *J. Am. Chem. Soc.*, 1995, **117**, 10397.
35. D. Massiot, F. Fayon, B. Alonso, J. Trebosc, and J.-P. Amoureux, *J. Magn. Reson.*, 2003, **164**, 160.
36. K. Kanehashi, T. Nemoto, and K. Saito, *J. Non-Cryst. Solids*, 2007, **353**, 4227.
37. (a) J.-P. Amoureux, J. Trébosc, L. Delevoye, O. Lafon, B. Hu, and Q. Wang, *Solid State Nucl. Magn. Reson.*, 2009, **35**, 12; (b) B. Hu, J. Trébosc, and J.-P. Amoureux, *J. Magn. Reson.*, 2008, **192**, 112.
38. D. L. Bryce and R. E. Wasylishen, *Inorg. Chem.*, 2002, **41**, 4131.
39. S. J. Hibble, S. M. Cheyne, A. C. Hannon, and S. G. Eversfield, *Inorg. Chem.*, 2002, **41**, 1042.
40. K. W. Zilm and D. M. Grant, *J. Am. Chem. Soc.*, 1981, **103**, 2913.
41. R. K. Harris, K. J. Packer, and A. M. Thayer, *J. Magn. Reson.*, 1985, **62**, 284.
42. W. P. Power and R. E. Wasylishen, *Annu. Rep. Nucl. Magn. Reson. Spectrosc.*, 1991, **23**, 1.
43. K. Eichele, G. C. Ossenkamp, R. E. Wasylishen, and T. S. Cameron, *Inorg. Chem.*, 1999, **38**, 639.
44. S. L. Grage and A. Watts, *Annu. Rep. Nucl. Magn. Reson. Spectrosc.*, 2007, **60**, 191.
45. I. Schnell, *Prog. Nucl. Magn. Reson. Spectrosc.*, 2004, **45**, 145.
46. M. Baldus, *Prog. Nucl. Magn. Reson. Spectrosc.*, 2002, **41**, 1.
47. J. R. Garbow and T. Gullion, '*Carbon-13 NMR Spectroscopy of Biological Systems*', ed. N. Beckmann, Academic Press: San Diego, 1995.
48. T. Gullion and J. Schaefer, *J. Magn. Reson.*, 1989, **81**, 196.
49. G. L. Olsen, E. A. Louie, G. P. Drobny, and S. T. Sigurdsson, *Nucleic Acids Res.*, 2003, **31**, 5084.
50. T. Gullion, *Chem. Phys. Lett.*, 1995, **246**, 325.
51. T. Gullion, *J. Magn. Reson. A*, 1995, **117**, 326.
52. L. Chopin, S. Vega, and T. Gullion, *J. Am. Chem. Soc.*, 1998, **120**, 4406.
53. E. R. Andrew, A. Bradbury, R. G. Eades, and V. T. Wynn, *Phys. Lett.*, 1963, **4**, 99.
54. D. P. Raleigh, M. H. Levitt, and R. G. Griffin, *Chem. Phys. Lett.*, 1988, **146**, 71.
55. D. L. Bryce and R. E. Wasylishen, *J. Phys. Chem. A*, 2000, **104**, 7700.
56. R. Tycko and G. Dabbagh, *Chem. Phys. Lett.*, 1990, **173**, 461.
57. B. Q. Sun, P. R. Costa, D. Kocisko, P. T. Lansbury, and R. G. Griffin, *J. Chem. Phys.*, 1995, **102**, 702.
58. M. H. Levitt, *J. Chem. Phys.*, 2008, **128**, 052205.
59. K. J. Harris and R. E. Wasylishen, *Inorg. Chem.*, 2009, **48**, 2316.
60. M. Kaupp, M. Bühl, and V. G. Malkin, eds, '*Calculation of NMR and EPR Parameters – Theory and Applications*', Wiley-VCH Verlag GmbH & Co. KGaA: Weinheim, 2004.

Chapter 11
Dipolar Recoupling: Heteronuclear

Christopher P. Jaroniec

Department of Chemistry, Ohio State University, Columbus, OH 43210, USA

11.1	Introduction	137
11.2	MAS Hamiltonian	138
11.3	Heteronuclear Dipolar Recoupling in Spin Pairs	141
11.4	Heteronuclear Dipolar Recoupling in Multispin Systems	147
11.5	Conclusions	157
	References	158

11.1 INTRODUCTION

Currently, high-resolution and high sensitivity NMR spectra of various types of polycrystalline solid samples containing spin-1/2 nuclei, such as ^{31}P, ^{13}C, and ^{15}N, can be recorded on a relatively routine basis. This is made possible by the combined effects of (i) high static magnetic fields up to ~22 T (950 MHz proton frequency), (ii) magic-angle spinning (MAS)[1–3] which involves the rapid rotation of the sample (at frequencies up to ~70 kHz) about an axis tilted relative to the magnetic field at an angle $\tan^{-1}\sqrt{2} \approx 54.74^{\circ}$, (iii) cross-polarization (CP) from protons,[4,5] and (iv) efficient proton decoupling.[6–8] MAS facilitates the acquisition of high-resolution solid-state nuclear magnetic resonance (SSNMR) spectra by effectively averaging the anisotropic parts of nuclear spin interactions that can be represented by second-rank tensors[9]: chemical shifts and through-space dipole–dipole couplings for spin-1/2 systems. Consequently, in order for these interactions – which are the primary source of information about three-dimensional molecular structure – to be detected and quantified under MAS conditions, they must be reintroduced or "recoupled" into the spectra. This type of recoupling can generally be achieved by the concurrent application of radiofrequency (RF) pulse sequences that appropriately manipulate the spin parts of the chemical shift and dipolar Hamiltonians and interfere with their spatial averaging due to MAS – note, however, that, in certain cases, purely MAS-driven recoupling is also possible.[10–13]

As thoroughly discussed elsewhere,[14–18] beginning in the late 1980s, a number of major advances have been made in the development of MAS NMR pulse schemes designed to recouple homonuclear and heteronuclear dipolar interactions as well as chemical shift anisotropies (CSA), with most of the initial dipolar recoupling schemes geared toward isolated spin-1/2 pairs, such as ^{13}C–^{13}C, ^{13}C–^{31}P, or ^{13}C–^{15}N, incorporated at specific sites in the sample by using various isotopic labeling approaches. Several of these dipolar recoupling schemes including rotational echo double resonance (REDOR),[19,20] rotational resonance (R^2),[11,12] and dipolar recoupling with a windowless sequence (DRAWS)[21] permit highly accurate and precise measurements of dipolar couplings as low as ~20–30 Hz to be performed. This yields quantitative, site-specific

NMR Crystallography Edited by Robin K. Harris, Roderick E. Wasylishen and Melinda J. Duer © 2009 John Wiley & Sons, Ltd. ISBN: 978-0-470-69961-4

internuclear distance restraints up to ~6–8 Å (note that the range of accessible distances can be further increased to ~10–15 Å by using selective ^{19}F labeling[22]) with uncertainties of a few tenths of an angstrom, and, as a result, these methods have had and continue to have tremendous impact on the SSNMR characterization of molecular structures of challenging biological systems[15,22–25] such as protein–protein and protein–ligand complexes,[26–28] membrane proteins,[29–31] surface-bound peptides,[32] and high-molecular-weight peptide and protein aggregates.[24,33–35]

Notwithstanding the numerous successful applications of homonuclear and heteronuclear dipolar recoupling techniques to biological solids containing "magnetically dilute" spin-1/2 pairs, there is a compelling motivation for pursuing analogous types of experiments in highly or uniformly ^{13}C,^{15}N (U-^{13}C,^{15}N) labeled molecules. The primary advantage offered by multispin systems of this type is that a multitude of site-resolved structural restraints can, in principle, be extracted by using one or few samples, as is done routinely in the context of modern biomolecular solution-state NMR.[36,37] Indeed, in recent years, by taking advantage of the principles of multidimensional spectroscopy[38] and improved sample-preparation methods,[39–42] highly resolved MAS NMR spectra were reported for a number of U-^{13}C,^{15}N enriched biological macromolecules, which paved the way for the detailed characterization of molecular structure and dynamics in these systems and demonstrated the general feasibility of such studies.[43–45] To illustrate the resolution and sensitivity of SSNMR spectra that can be obtained for U-^{13}C,^{15}N labeled biological molecules of varying complexity at, by today's standards, moderate magnetic fields ($\omega_0/2\pi \sim 500$ MHz for protons) and MAS rates ($\omega_r/2\pi \sim 10$ kHz), in Figure 11.1 we show 1-D ^{13}C and ^{15}N CP-MAS spectra of a three-residue peptide, formyl-Met-Leu-Phe (f-MLF),[46,47] and 2-D ^{15}N–^{13}C SPECIFIC-CP[48] correlation spectra of amyloid fibrils formed by residues 23–144 of human prion protein (huPrP23-144).[49]

In instances where the recoupling of nominally large, one-bond dipolar interactions (Table 11.1) is of interest, the original pulse schemes developed for selectively isotope labeled samples can often be applied directly to U-^{13}C,^{15}N labeled ones with minimal or no modifications. Examples of such applications include magnetization transfer in multidimensional chemical shift correlation experiments,[50,51] characterization of conformational dynamics[52–59] (*see* **Chapter 13**), and measurements of relative dipole tensor orientations, which yield protein backbone and side-chain dihedral angle restraints.[60–74] On the other hand, quantitative measurements of structurally interesting, weak dipolar interactions (i.e., dipolar coupling constant $< \approx 100$ Hz; internuclear distance $> \approx 3$ Å) within tightly coupled spin-1/2 clusters are generally less straightforward because of the potential interference from multiple direct and indirect spin–spin couplings, which contain little useful structural information themselves, yet are oftentimes comparable to or larger than the weak dipolar couplings of interest– in addition to the one-bond dipolar couplings listed in Table 11.1, these interactions include two-bond ^{13}C–^{13}C and ^{13}C–^{15}N dipolar couplings of ~500 Hz and ~200 Hz, respectively, as well as one-bond ^{13}C–^{13}C J-couplings (~30–60 Hz).

In this article, we focus on heteronuclear dipolar recoupling and discuss several recent SSNMR methods, which alleviate some of the major problems associated with the presence of strong dipolar and J-couplings in U-^{13}C,^{15}N enriched molecules and enable the accurate and precise measurements of multiple weak ^{13}C–^{15}N dipolar couplings. These methods, which include frequency-selective REDOR[75,76] and several 3-D transferred echo double resonance (TEDOR) variants,[77–79] are based on the well-known and closely related REDOR[19,20] and TEDOR[80] heteronuclear recoupling schemes, specifically selected for this purpose because they are particularly robust with respect to various experimental imperfections including finite pulse durations, resonance offsets, and RF inhomogeneity.[81–87] Applications of these techniques to U-^{13}C,^{15}N-enriched biological solids, ranging from small peptides and globular proteins in the microcrystalline phase to amyloid aggregates and membrane-associated proteins, are also highlighted.

11.2 MAS HAMILTONIAN

The Hamiltonian describing a system of coupled spin-1/2 nuclei placed in a strong static magnetic field and subjected to MAS and time-dependent RF fields can be written as[14,16]

$$\hat{H}(t) = \hat{H}_D(t) + \hat{H}_J + \hat{H}_{CS}(t) + \hat{H}_{RF}(t) \qquad (11.1)$$

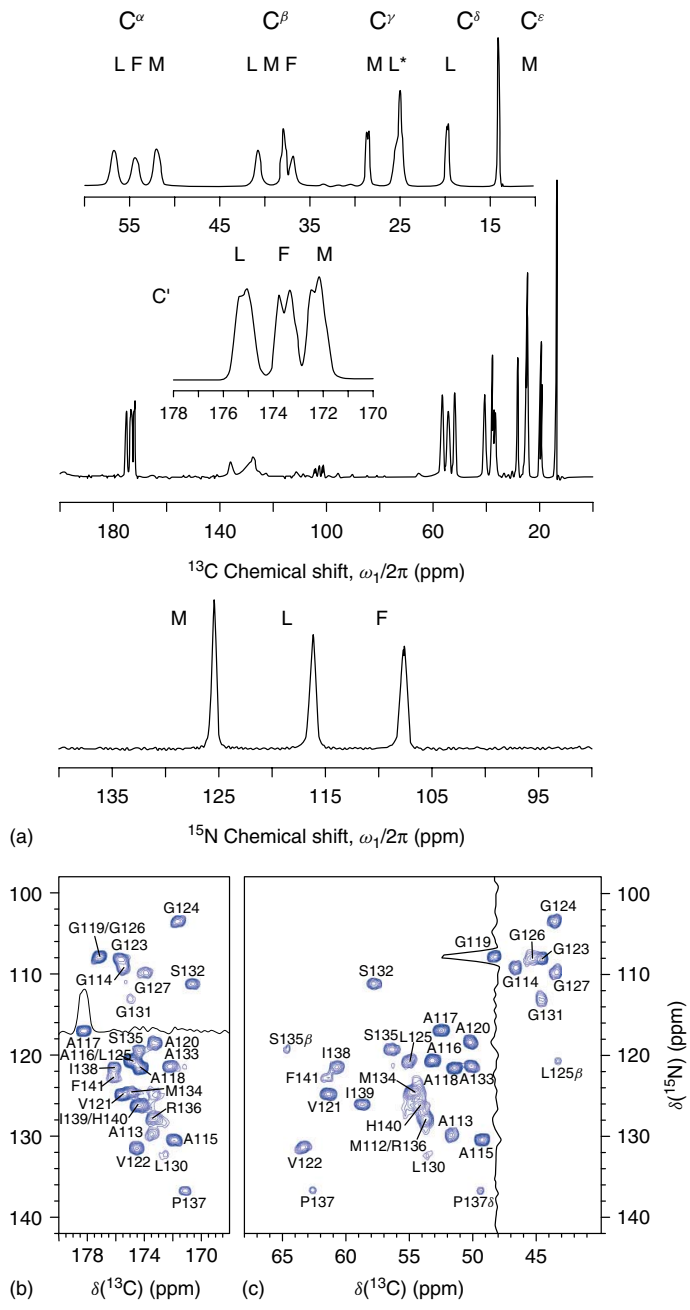


Figure 11.1. (a) 1-D ^{13}C and ^{15}N CPMAS spectra of formyl-U-^{13}C,^{15}N-Met-Leu-Phe recorded at 500 MHz ^{1}H frequency and 8.9 kHz MAS rate. (Adapted from Ref. 47. © American Chemical Society, 2000) (b) 2-D $^{15}N-^{13}C'$ and (c) $^{15}N-^{13}C\alpha$ spectra of U-^{13}C,^{15}N–huPrP23-144 amyloid fibrils recorded at 500 MHz ^{1}H frequency and 11.1 kHz MAS rate. Note that only residues comprising the relatively rigid core region of the amyloid fibrils are detected in these spectra. (Reproduced with permission from J. J. Helmus, K. Surewicz, P. S. Nadaud, W. K. Surewicz, and C. P. Jaroniec, *Proc. Natl. Acad. Sci. USA*, 2008, **105**, 6284. © The National Academy of Sciences of the USA, 2008.)

Table 11.1. Typical magnitudes of selected one-bond dipolar couplings in peptides and proteins

Nucleus I	Nucleus S	$I-S$ distance, r_{IS} (Å)	$I-S$ Dipolar coupling, $b_{IS}/2\pi$ (Hz)
^{1}H	^{13}C	1.12	21 500
^{1}H	^{15}N	1.04	10 825
^{13}C	^{13}C	1.52	2165
^{13}C′	^{15}N	1.33	1300
^{13}Cα	^{15}N	1.45	1005

where the $\hat{H}_{\mathrm{D}}(t)$, $\hat{H}_{\mathrm{J}}$, $\hat{H}_{\mathrm{CS}}(t)$, and $\hat{H}_{\mathrm{RF}}(t)$ terms represent direct dipolar (through-space) spin–spin couplings, indirect (through-bond) spin–spin couplings, chemical shift interactions, and applied RF fields, respectively. The individual Hamiltonian terms for a homonuclear spin system are given by

$$\hat{H}_{\mathrm{D}}(t) = \sum_{i<j} \omega_{ij}^{\mathrm{D}}(t)[3\hat{I}_{iz}\hat{I}_{jz} - \hat{\boldsymbol{I}}_i \cdot \hat{\boldsymbol{I}}_j] \tag{11.2}$$

$$\hat{H}_{\mathrm{J}} = \sum_{i<j} \omega_{ij}^{\mathrm{J}} \hat{\boldsymbol{I}}_i \cdot \hat{\boldsymbol{I}}_j \tag{11.3}$$

$$\hat{H}_{\mathrm{CS}}(t) = \sum_{i} \omega_{i}^{\mathrm{CS}}(t)\hat{I}_{iz} \tag{11.4}$$

$$\hat{H}_{\mathrm{RF}}(t) = \sum_{i} |\omega_{i}^{\mathrm{RF}}(t)|[\hat{I}_{ix}\cos\phi_i(t) + \hat{I}_{iy}\sin\phi_i(t)] \tag{11.5}$$

For heteronuclear spin pairs (and homonuclear spins, for which the absolute chemical shift difference greatly exceeds the magnitude of the spin–spin interaction, i.e., $|\omega_i^{\mathrm{CS}}(t) - \omega_j^{\mathrm{CS}}(t)| \gg |\omega_{ij}^{\mathrm{D}}(t)|, |\omega_{ij}^{\mathrm{J}}|$), the dipolar and J-coupling terms simplify to

$$\hat{H}_{\mathrm{D}}(t) = \sum_{i<j} \omega_{ij}^{\mathrm{D}}(t) 2\hat{I}_{iz}\hat{I}_{jz} \tag{11.6}$$

$$\hat{H}_{\mathrm{J}} = \sum_{i<j} \omega_{ij}^{\mathrm{J}} \hat{I}_{iz}\hat{I}_{jz} \tag{11.7}$$

In equations (11.2–11.7), indices i and j refer to different nuclear spins, $\hat{I}_x$, $\hat{I}_y$, and $\hat{I}_z$ are the spin angular momentum operators, $\omega_{ij}^{\mathrm{J}} = 2\pi J_{ij}$ where J_{ij} is the isotropic J-coupling constant in Hz (anisotropic J-coupling terms are assumed to be negligible), and $\omega_i^{\mathrm{RF}}(t) = -\gamma_i B_i^{\mathrm{RF}}(t)$ and are the RF-field angular nutation frequency (determined by the nuclear gyromagnetic ratio, γ_i, and RF-field amplitude, $B_i^{\mathrm{RF}}(t)$) and phase $\phi_i(t)$, respectively. The time-dependent coefficients $\omega_i^{\mathrm{CS}}(t)$ and $\omega_{ij}^{\mathrm{D}}(t)$ can be conveniently expressed as Fourier series:

$$\omega_i^{\mathrm{CS}}(t) = \sum_{m=-2}^{2} \omega_{\mathrm{CS}_i}^{(m)} \exp(\mathrm{i}m\omega_{\mathrm{r}}t) \tag{11.8}$$

$$\omega_{ij}^{\mathrm{D}}(t) = \sum_{m=-2}^{2} \omega_{\mathrm{D}_{ij}}^{(m)} \exp(\mathrm{i}m\omega_{\mathrm{r}}t) \tag{11.9}$$

with

$$\omega_{\lambda}^{(m)} = \omega_{\mathrm{iso}}^{\lambda}\delta_{m,0} + \delta^{\lambda}\left\{ D_{0,-m}^{(2)}(\Omega_{\mathrm{PR}}^{\lambda}) - \frac{\eta^{\lambda}}{\sqrt{6}}[D_{-2,-m}^{(2)}(\Omega_{\mathrm{PR}}^{\lambda}) + D_{2,-m}^{(2)}(\Omega_{\mathrm{PR}}^{\lambda})]\right\} \times d_{-m,0}^{(2)}(\beta_{\mathrm{RL}}) \tag{11.10}$$

where $\lambda = \mathrm{CS}_i$ or D_{ij}, ω_{r} is the rotor frequency in angular units, $\delta_{m,0}$ is the Kronecker delta, and $\omega_{\mathrm{iso}}^{\lambda}$, δ^{λ}, and η^{λ} are the isotropic value, anisotropy, and asymmetry parameter of interaction λ. The Wigner rotation matrices, $D_{m',m}^{(l)}(\Omega_{\mathrm{AB}}^{\lambda})$, describe the coordinate transformation between axis systems A and B, according to a set of three Euler angles $\Omega_{\mathrm{AB}}^{\lambda} = \{\alpha_{\mathrm{AB}}^{\lambda}, \beta_{\mathrm{AB}}^{\lambda}, \gamma_{\mathrm{AB}}^{\lambda}\}$:[88,89]

$$D_{m',m}^{(l)}(\Omega_{\mathrm{AB}}^{\lambda}) = \exp(-\mathrm{i}m'\alpha_{\mathrm{AB}}^{\lambda}) d_{m',m}^{(l)}(\beta_{\mathrm{AB}}^{\lambda}) \times \exp(-\mathrm{i}m\gamma_{\mathrm{AB}}^{\lambda}) \tag{11.11}$$

where $d_{m',m}^{(l)}(\beta_{\mathrm{AB}}^{\lambda})$ is the reduced Wigner matrix. The coordinate systems most relevant to the description of MAS NMR experiments in polycrystalline solids are denoted as P (principal axis frame), C (crystallite-fixed frame), R (rotor-fixed frame), and L (laboratory frame). Note that, for simplicity, equation (11.10) assumes that the principal axis frame coincides with the crystallite-fixed frame.

For the dipolar coupling between spins i and j we have

$$\omega_{\mathrm{iso}}^{\mathrm{D}_{ij}} = \eta^{\mathrm{D}_{ij}} = 0 \tag{11.12}$$

$$\delta^{\mathrm{D}_{ij}} = b_{ij} = -\left(\frac{\mu_0}{4\pi}\right)\frac{\gamma_i\gamma_j\hbar}{r_{ij}^3} \tag{11.13}$$

where b_{ij} is the dipolar coupling constant in angular frequency units and r_{ij} is the internuclear distance. Thus, for macroscopic sample rotation exactly at the magic angle, $\beta_{\mathrm{RL}} = \tan^{-1}\sqrt{2}$, the Fourier coefficients in equations (11.8–11.10) are given by

$$\omega_{\mathrm{D}_{ij}}^{(0)} = b_{ij}\frac{(3\cos^2\beta_{\mathrm{PR}}^{ij} - 1)}{2}\frac{(3\cos^2\beta_{\mathrm{RL}} - 1)}{2} = 0 \tag{11.14}$$

$$\omega_{\mathrm{D}_{ij}}^{(\pm 1)} = -\frac{1}{2\sqrt{2}} b_{ij}\sin(2\beta_{\mathrm{PR}}^{ij})\exp(\pm \mathrm{i}\gamma_{\mathrm{PR}}^{ij}) \tag{11.15}$$

$$\omega_{\mathrm{D}_{ij}}^{(\pm 2)} = \frac{1}{4} b_{ij}\sin^2\beta_{\mathrm{PR}}^{ij}\exp(\pm \mathrm{i}2\gamma_{\mathrm{PR}}^{ij}) \tag{11.16}$$

Analogous expressions can also be obtained for the chemical shift interaction,[3,14,17] where $\omega_{\mathrm{iso}}^{\mathrm{CS}_i}$, δ^{CS_i}, and η^{CS_i} are, in general, nonzero. Altogether, equations (11.8–11.16) demonstrate the well-known result that MAS effectively averages anisotropic nuclear spin interactions described by second-rank tensors[1–3] – the time-independent Fourier coefficients, $\omega_{\lambda}^{(0)}$, vanish when β_{RL} is the magic angle, and the $\omega_{\lambda}^{(\pm 1)}$ and $\omega_{\lambda}^{(\pm 2)}$ coefficients oscillating at ω_{r} and $2\omega_{\mathrm{r}}$ are averaged to zero with the period of one and one-half rotor cycle, respectively.

11.3 HETERONUCLEAR DIPOLAR RECOUPLING IN SPIN PAIRS

In this section, we briefly review several methods designed to reintroduce heteronuclear dipolar interactions under MAS in isolated spin pairs, with the main focus on rotary resonance recoupling (R^3)[90,91] and REDOR.[19,20] These initial recoupling schemes have not only been utilized for a variety of diverse applications,[16,22] but their introduction has also motivated the development of a multitude of new dipolar recoupling methodologies – indeed, as noted above, the recoupling techniques designed to measure weak $^{13}\mathrm{C}$–$^{15}\mathrm{N}$ dipolar couplings in U-$^{13}\mathrm{C}$,$^{15}\mathrm{N}$ labeled systems, which are discussed in the following section, are all derived from the REDOR recoupling scheme. To gain basic insight into how the application of RF pulse sequences can interfere with MAS to reintroduce heteronuclear dipolar couplings, in the following, we consider a simple system of two coupled nuclear spins of different types, denoted by I_1 and I_2, in the absence of chemical shift and J-coupling interactions.

11.3.1 Rotary Resonance Recoupling

R^3 involves the observation of the NMR signal for spin species I_1, in the presence of continuous-wave RF irradiation applied to spin species I_2, where the RF nutation frequency is set to a small integer multiple of the MAS frequency ($\omega_2^{\mathrm{RF}} = n\omega_{\mathrm{r}}$).[90,91] The corresponding Hamiltonian, assuming that ω_2^{RF} has phase x, is given by

$$\hat{H}(t) = \omega_{12}^{\mathrm{D}}(t)2\hat{I}_{1z}\hat{I}_{2z} + n\omega_{\mathrm{r}}\hat{I}_{2x} \tag{11.17}$$

The combined effects of MAS and rotor-synchronized RF pulse sequences on nuclear spin dynamics can be conveniently analyzed within the framework of the average Hamiltonian theory (AHT)[92,93] – this involves the transformation of $\hat{H}(t)$ into an interaction frame where the $\hat{H}_{\mathrm{RF}}(t)$ term vanishes, followed by calculation of the effective (or average) Hamiltonian describing the internal nuclear spin interactions (i.e., chemical shifts, dipolar, and J-couplings). For the R^3 experiment, the interaction frame dipolar Hamiltonian is given by

$$\begin{aligned}\tilde{\hat{H}}_{\mathrm{D}}(t) &= \mathrm{e}^{\mathrm{i}n\omega_{\mathrm{r}}t\hat{I}_{2x}}\hat{H}_{\mathrm{D}}(t)\mathrm{e}^{-\mathrm{i}n\omega_{\mathrm{r}}t\hat{I}_{2x}} \\ &= \sum_{m=-2}^{2}\left\{\omega_{\mathrm{D}_{12}}^{(m)}\left[\mathrm{e}^{\mathrm{i}(m+n)\omega_{\mathrm{r}}t} + \mathrm{e}^{\mathrm{i}(m-n)\omega_{\mathrm{r}}t}\right]\hat{I}_{1z}\hat{I}_{2z}\right. \\ &\quad \left. - i\omega_{\mathrm{D}_{12}}^{(m)}\left[\mathrm{e}^{\mathrm{i}(m+n)\omega_{\mathrm{r}}t} - \mathrm{e}^{\mathrm{i}(m-n)\omega_{\mathrm{r}}t}\right]\hat{I}_{1z}\hat{I}_{2y}\right\}\end{aligned} \tag{11.18}$$

and the lowest-order effective Hamiltonian, $\overline{\hat{H}}_{\mathrm{D}}^{(0)}$, is obtained as the average of the interaction frame Hamiltonian over the pulse sequence cycle time (one rotor period, τ_{r}, in this case):

$$\overline{\hat{H}}_{\mathrm{D}}^{(0)} = \frac{1}{\tau_{\mathrm{r}}}\int_0^{\tau_{\mathrm{r}}}\mathrm{d}t\,\tilde{\hat{H}}_{\mathrm{D}}(t) \tag{11.19}$$

Since all integrals of the form $\int_0^{\tau_{\mathrm{r}}}\mathrm{d}t\exp[\mathrm{i}(m \pm n)\omega_{\mathrm{r}}t]$ that appear in equations (11.18) and (11.19) vanish unless a rotary resonance condition $m \pm n = 0$ is satisfied, the lowest-order average dipolar Hamiltonian is given by

$$\overline{\hat{H}}_{\mathrm{D}}^{(0)} = (\omega_{\mathrm{D}_{12}}^{(-n)} + \omega_{\mathrm{D}_{12}}^{(n)})\hat{I}_{1z}\hat{I}_{2z} - \mathrm{i}(\omega_{\mathrm{D}_{12}}^{(-n)} - \omega_{\mathrm{D}_{12}}^{(n)})\hat{I}_{1z}\hat{I}_{2y} \tag{11.20}$$

This result indicates that dipolar coupling terms corresponding to coefficients $\omega^{(\pm 1)}$ and $\omega^{(\pm 2)}$ (cf.

equations (11.15) and (11.16)) are reintroduced under MAS when the RF nutation frequency equals ω_r and $2\omega_r$, respectively – otherwise $\overline{\hat{H}}_D^{(0)} = 0$ and heteronuclear decoupling is predicted at this level of AHT treatment. For example, for $n = \pm 1$ R^3 we have

$$\overline{\hat{H}}_D^{(0)} = \tilde{\omega}_{12}^D(\cos\gamma_{PR}^{12} 2\hat{I}_{1z}\hat{I}_{2z} - \sin\gamma_{PR}^{12} 2\hat{I}_{1z}\hat{I}_{2y}) \quad (11.21)$$

where the orientation-dependent effective dipolar coupling, $\tilde{\omega}_{12}^D$, is given by

$$\tilde{\omega}_{12}^D = -\frac{1}{2\sqrt{2}} b_{12} \sin(2\beta_{PR}^{12}) \quad (11.22)$$

With the initial density operator $\hat{\rho}(0) = \hat{I}_{1x}$, the evolution under the average Hamiltonian in equation (11.21) yields an observable I_1-spin signal of the following form:

$$S(\tau_{mix}) = \langle \hat{I}_{1x} \rangle(\tau_{mix}) = \langle \cos(\tilde{\omega}_{12}^D \tau_{mix}) \rangle \quad (11.23)$$

where $\langle \cdots \rangle$ indicates the powder average, and, consequently, the magnitude of the I_1–I_2 dipolar coupling constant, b_{12}, can be extracted in a straightforward manner by inspecting the I_1-spin evolution in the time or frequency domain (Figure 11.2). Note that the magnitude of the dipolar interaction recoupled by R^3 is independent of the Euler angle γ_{PR}^{12} – this property of the recoupling sequence, commonly referred to

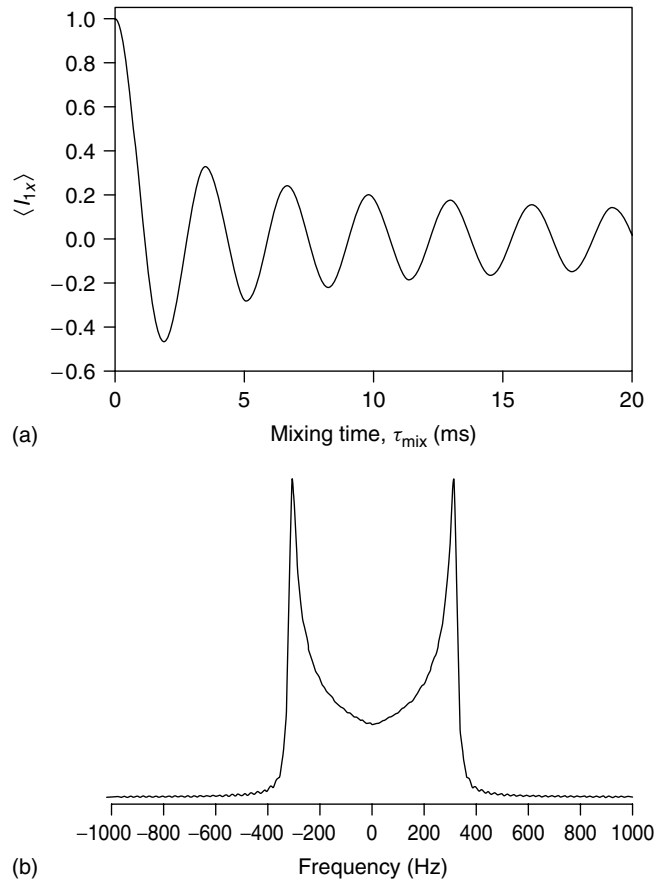


Figure 11.2. Simulated I_1-spin dipolar dephasing trajectory (a) and spectrum (b) corresponding to a $n = \pm 1$ rotary resonance recoupling experiment. The simulation was performed by the stepwise numerical propagation of the density operator for a heteronuclear I_1–I_2 (^{13}C–^{15}N) spin pair with a dipolar coupling constant, $b_{12}/2\pi = 900$ Hz, in the absence of chemical shifts and J-coupling, as implemented within the SIMPSON program.[95] The MAS rate and I_2-spin RF nutation frequency were set to 25 kHz.

as *γ-encoding*,[94] leads to particularly pronounced dipolar oscillations as seen in Figure 11.2(a).

The simple analysis above clearly demonstrates the emergence of dipolar recoupling conditions resulting from the interference between MAS and applied RF fields, and also provides a reasonable approximation to the I_1-spin dynamics in cases where the I_1–I_2 dipolar coupling is the dominant interaction. However, typically, the spin dynamics during R^3 are far more complicated owing to their strong concurrent dependence on the chemical shift tensor parameters of the I_2-spin. This stems from the fact that R^3 also reintroduces I_2-spin CSA terms (described by an effective Hamiltonian analogous to $\overline{\hat{H}}_D^{(0)}$, but with $\hat{I}_{1z}$ omitted and $\tilde{\omega}_{12}^D$ replaced by $\tilde{\omega}_2^{CS}$), which, in general, do not commute with the I_1–I_2 dipolar coupling and lead to significant distortions of the $n = \pm 1$ and ± 2 R^3 dipolar trajectories as well as the appearance of additional, albeit weaker, higher order ($|n| > 2$) rotary resonances.[14,16,91] Another potential disadvantage associated with R^3 is its sensitivity to RF inhomogeneity.[90,91]

While R^3 itself may oftentimes not be the method of choice for quantitative measurements of heteronuclear dipolar couplings, several closely related schemes have been proposed to alleviate the problems associated with the dependence of R^3 dipolar dephasing trajectories on the CSA parameters of the irradiated spin as well as RF inhomogeneity.[63,96,97] For example the SPI-R^3 sequence,[63] which involves the application of a rotary resonant RF field to the I_2-spin $\omega_2^{RF} = n\omega_r$ that is also continuously phase inverted during successive rotor cycles, is relatively insensitive to both I_2 CSA and RF inhomogeneity. Such rotor-synchronized $\pm x$ phase alternation of ω_2^{RF} has no effect on the $\hat{I}_{1z}\hat{I}_{2z}$ term in equation (11.21) but repeatedly changes the sign of the $\hat{I}_{1z}\hat{I}_{2y}$ term, meaning that after every two rotor periods the latter term is averaged to zero. The lowest order average dipolar Hamiltonian for $n = \pm 1$ SPI-R^3 is thus given by

$$\overline{\hat{H}}_D^{(0)} = \tilde{\omega}_{12}^D 2\hat{I}_{1z}\hat{I}_{2z} \tag{11.24}$$

with

$$\tilde{\omega}_{12}^D = -\frac{1}{2\sqrt{2}} b_{12} \sin(2\beta_{PR}^{12}) \cos\gamma_{PR}^{12} \tag{11.25}$$

More importantly, since the effective chemical shift Hamiltonian for SPI-R^3, $\overline{\hat{H}}_{CS}^{(0)} \propto \hat{I}_{2z}$, now commutes with $\overline{\hat{H}}_D^{(0)}$, it has no influence on I_1-spin dynamics to lowest order – i.e., the I_1 dipolar dephasing trajectory, $S(\tau_{mix}) = \langle \cos(\tilde{\omega}_{12}^D \tau_{mix}) \rangle$, reports primarily on the magnitude of b_{12}. We note here that although the attenuation of the effects of I_2-spin CSA and RF inhomogeneity by SPI-R^3 is associated with the fact that the pulse sequence is no longer γ-encoded ($\tilde{\omega}_{12}^D$ in equation (11.25) depends on both β_{PR}^{12} and γ_{PR}^{12}), which leads to somewhat less pronounced dipolar oscillations, this does not have a significant negative impact on the accurate determination of heteronuclear dipolar couplings.

11.3.2 Rotational Echo Double Resonance

While R^3 and related pulse schemes discussed in the previous section are all windowless, heteronuclear dipolar recoupling can also be achieved by applying sequences of discrete, rotor-synchronized 180° pulses to one or both spin species. This idea forms the basis for the REDOR technique developed by Gullion and Schaefer.[19,20] A typical implementation of REDOR, with all 180° recoupling pulses – two per rotor period – applied to the nonobserved I_2 spin species (usually ^{15}N in the context of ^{13}C–^{15}N spin pair labeled samples) is shown in Figure 11.3. Note that the I_1 signal during REDOR is generally observed as a spin-echo – therefore, for the pulse sequence in Figure 11.3 the entire group of ^{15}N 180° pulses following the 180° ^{13}C pulse is time-shifted by $\tau_r/2$ relative to the pulses preceding the ^{13}C 180° to prevent the refocusing of the recoupled ^{13}C–^{15}N dipolar interaction.

Assuming ideal δ-function 180° pulses for the time being, the interaction frame dipolar Hamiltonian for the REDOR scheme is given by

$$\tilde{\hat{H}}_D(t) = f(t)\omega_{12}^D(t) 2\hat{I}_{1z}\hat{I}_{2z} \tag{11.26}$$

where $\omega_{12}^D(t)$ is defined in equation (11.9), and the function $f(t)$ toggles between the values of ± 1 during subsequent delays between 180° pulses. A straightforward calculation of the lowest order average dipolar Hamiltonian using equation (11.19), assuming the 180° pulses are applied on the I_2 channel at $\tau_r/2$ intervals as shown in Figure 11.3, yields

$$\overline{\hat{H}}_D^{(0)} = \tilde{\omega}_{12}^D 2\hat{I}_{1z}\hat{I}_{2z} \tag{11.27}$$

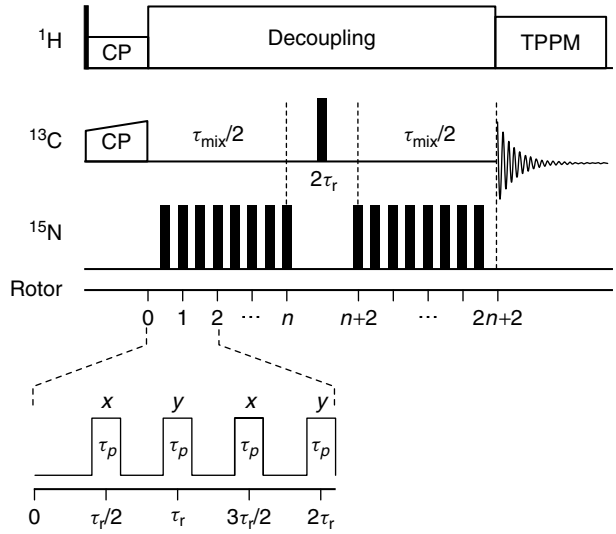


Figure 11.3. A typical implementation of the REDOR pulse sequence.[19,20] The particular implementation shown is especially relevant to studies of U-^{13}C,^{15}N labeled molecules. Narrow and wide black rectangles correspond to 90° and 180° pulses. During the REDOR experiment a ^{13}C spin-echo is generated following ^{1}H–^{13}C CP. The echo intensity is modulated during the period τ_{mix} according to the magnitude of the ^{13}C–^{15}N dipolar coupling, reintroduced by applying a train of rotor-synchronized 180° pulses on the ^{15}N channel as indicated in the figure. The ^{15}N pulse phases are usually set according to the *xy*-4 (*xyxy*) or *xy*-8 (*xyxy yxyx*) schemes,[81] which offer a high degree of compensation for pulse imperfections. Note that REDOR experiments generally involve the acquisition of two separate spin-echo trajectories: the dipolar dephased trajectory (S) using the pulse scheme shown in the figure, and a reference trajectory (S_0) that accounts for the transverse relaxation of ^{13}C coherences not related to ^{13}C–^{15}N dipolar dephasing. The S_0 trajectory is typically recorded in the absence of ^{15}N 180° pulses, although implementations that involve the application of an additional ^{15}N refocusing 180° pulse[85] or the time-shifting of a part of the ^{15}N 180°-pulse train can also been used[76,86] (cf. Figure 11.5). The resulting REDOR trajectories are then displayed as S/S_0 or $\Delta S/S_0 = 1 - S/S_0$.

with

$$\tilde{\omega}_{12}^{D} = -\frac{\sqrt{2}}{\pi} b_{12} \sin(2\beta_{PR}^{12}) \sin \gamma_{PR}^{12} \qquad (11.28)$$

Note that the form of the effective dipolar Hamiltonian for REDOR closely resembles that for $n = \pm 1$ SPI-R^3 (see equations (11.24) and (11.25)), with the main difference being the magnitude of the dipolar scaling factor ($\frac{\sqrt{2}}{\pi} \approx 0.45$ for REDOR vs. $\frac{1}{2\sqrt{2}} \approx 0.35$ for SPI-R^3; a higher scaling factor is generally advantageous). This indicates that, in analogy to SPI-R^3, the REDOR scheme shown in Figure 11.3 is also relatively insensitive to the recoupled I_2-spin CSA.

In practice, REDOR experiments are susceptible to various experimental imperfections including resonance offsets and RF inhomogeneity – particularly challenging are the measurements of weak dipolar couplings, which require the application of tens to hundreds of rotor-synchronized 180° pulses. This major problem was addressed shortly following the introduction of REDOR via the design of *xy*-type 180° pulse phasing schemes (e.g., *xy*-4: *xyxy*, *xy*-8: *xyxy yxyx*, etc.; see Figure 11.3), which offer a very high degree of compensation for such experimental imperfections.[81,82] More recently, additional improvements involving the use of composite 180° pulses have also been proposed.[87] Altogether, these developments have resulted in REDOR being a particularly robust heteronuclear dipolar recoupling pulse scheme, which has been successfully applied for the measurements of weak dipolar couplings in a number of complex biological systems.[16,22]

An additional potential concern related to the use of REDOR-type methods, which is not a factor for windowless recoupling schemes, is related to the effect of finite 180° pulse lengths on the recoupling

performance. This is a rather important issue, given that many modern SSNMR experiments routinely take advantage of high MAS rates in the ~10–40 kHz regime to achieve optimal spectral resolution and sensitivity. For example, for the REDOR scheme in Figure 11.3 implemented with a typical I_2-spin RF nutation frequency, $\omega_2^{RF}/2\pi = 50$ kHz, but at an MAS rate of 30 kHz instead of the usual 5–6 kHz, ~60% of the rotor period would be occupied by RF irradiation. The effects of finite pulses on the spin dynamics during REDOR have been analyzed using Floquet theory[83] as well as AHT and numerical simulations.[84] The overall conclusion of these studies is that finite pulse effects do not negatively impact the performance of REDOR recoupling provided that *xy*-4 type 180° pulse phasing schemes are employed, which is virtually always the case. We summarize below the AHT treatment for REDOR *xy*-4 and related sequences, which yields analytical expressions describing the spin dynamics in the presence of finite pulse effects[84] – for purpose of comparison, we also discuss a hypothetical implementation of REDOR where all pulse phases are x. Finally, an experimental demonstration of the finite pulse effects for REDOR *xy*-4 type schemes is provided.

In general, the interaction frame Hamiltonian for the REDOR sequence in Figure 11.3 in the presence of finite 180° pulses of arbitrary phase can be written:

$$\tilde{\hat{H}}_D(t) = \omega_{12}^D(t)[f(t)2\hat{I}_{1z}\hat{I}_{2z} + g(t)2\hat{I}_{1z}\hat{I}_{2x} + h(t)2\hat{I}_{1z}\hat{I}_{2y}] \quad (11.29)$$

In analogy to equation (11.26), the function $f(t)$ toggles, albeit in a continuous manner, between ± 1 during subsequent delays between pulses regardless of the details of the pulse phase cycling scheme. The functions $g(t)$ and $h(t)$ are a direct consequence of the finite pulses – they can only be nonzero during the pulses and their values depend on the details of the phase cycling scheme. For example, for REDOR *xy*-4 both $g(t)$ and $h(t)$ take on nonzero values, while $g(t)$ is always zero if all recoupling pulses have phase x. Although the presence of terms proportional to operators $\hat{I}_{2x}$ and/or $\hat{I}_{2y}$ in the effective dipolar Hamiltonian would generally be expected to have a negative impact on the performance of REDOR recoupling – these terms would not only significantly perturb the dipolar dephasing trajectories predicted for δ-function pulses but their appearance would also indicate the concurrent recoupling of noncommuting I_2 CSA terms – it turns out that for REDOR *xy*-4 and extensions thereof these transverse I_2-spin terms are averaged to zero with a cycle time of two rotor periods. The resulting lowest order average dipolar Hamiltonian for REDOR *xy*-4 with finite pulses is

$$\overline{\hat{H}}_D^{(0)} = \tilde{\omega}_{12}^D 2\hat{I}_{1z}\hat{I}_{2z} \quad (11.30)$$

where

$$\tilde{\omega}_{12}^D = -\frac{\sqrt{2}}{\pi}\kappa b_{12}\sin(2\beta_{PR}^{12})\sin\gamma_{PR}^{12} \quad (11.31)$$

Note that the effective dipolar Hamiltonian for finite pulse REDOR *xy*-4 is nearly identical to the Hamiltonian for δ-pulse REDOR (cf. equations (11.27) and (11.28)). The only difference is the factor κ in equation (11.31), which describes the finite pulse effects and is given by

$$\kappa = \frac{\cos(\varphi\pi/2)}{1-\varphi^2} \quad (11.32)$$

where φ is the fraction of the rotor period occupied by the pulses:

$$\varphi = \frac{2\tau_p}{\tau_r} \quad (11.33)$$

For δ-pulse REDOR we have $\varphi = 0$, which gives $\kappa = 1$, and, as expected, equation (11.31) reduces to equation (11.28). At the other extreme, in the case of windowless RF irradiation (i.e., $\varphi = 1$) we obtain $\lim_{\varphi\to 1}\kappa = \pi/4$. This yields the effective dipolar coupling of

$$\tilde{\omega}_{12}^D = -\frac{1}{2\sqrt{2}}b_{12}\sin(2\beta_{PR}^{12})\sin\gamma_{PR}^{12} \quad (11.34)$$

which is analogous to the expression obtained for SPI-R^3 (cf. equation (11.25)). For a typical intermediate case involving rapid MAS (e.g., $\omega_2^{RF}/2\pi =$ 50 kHz and $\omega_r/2\pi = 30$ kHz), we have $\varphi \approx 0.61$ and $\kappa \approx 0.92$ – i.e., AHT predicts that the dipolar coupling is reduced by only ~8% relative to that expected in the δ-pulse limit. Given that this additional scaling of the dipolar coupling can be readily accounted for in simulations by simply specifying the value of φ, the finite pulse effects for REDOR *xy*-4 and its extensions are relatively harmless.

For comparison, we briefly consider below a finite pulse version of the REDOR scheme

where all 180° pulses on the I_2 channel have phase x. In this case, transverse I_2-spin terms appear in the average dipolar Hamiltonian, which leads to significant perturbations of the REDOR dipolar dephasing trajectories as well as increased dependence of these trajectories on I_2 CSA parameters. The lowest order average dipolar Hamiltonian in this case is given by

$$\overline{\hat{H}}_{\mathrm{D}}^{(0)} = -\frac{\sqrt{2}}{\pi}\kappa b_{12}\sin(2\beta_{\mathrm{PR}}^{12}) \times [\sin\gamma_{\mathrm{PR}}^{12} 2\hat{I}_{1z}\hat{I}_{2z} + \varphi\cos\gamma_{\mathrm{PR}}^{12} 2\hat{I}_{1z}\hat{I}_{2y}] \tag{11.35}$$

which leads to the observable signal of the form

$$S(\tau_{\mathrm{mix}}) = \langle\cos(\sqrt{\Omega^2 + \Phi^2}\tau_{\mathrm{mix}})\rangle \tag{11.36}$$

with

$$\Omega = -\frac{\sqrt{2}}{\pi}\kappa b_{12}\sin(2\beta_{\mathrm{PR}}^{12})\sin\gamma_{\mathrm{PR}}^{12} \tag{11.37}$$

$$\Phi = -\frac{\sqrt{2}}{\pi}\varphi\kappa b_{12}\sin(2\beta_{\mathrm{PR}}^{12})\cos\gamma_{\mathrm{PR}}^{12} \tag{11.38}$$

Note that in the case of windowless x-phase RF irradiation ($\varphi = 1$, $\kappa = \pi/4$) the observable signal in equations (11.36–11.38) reduces to the $\gamma_{\mathrm{PR}}^{12}$ -independent expression obtained for $n = \pm 1$ R^3 (cf. equations (11.22) and (11.23)).

In Figure 11.4, we provide an experimental verification of the finite pulse effects for REDOR xy-4 type sequences.[84] Figure 11.4(a) shows representative experimental and simulated REDOR S/S_0 trajectories for 2-^{13}C,^{15}N-glycine, recorded under experimental conditions where 20% ($\varphi = 0.2$; $\omega_2^{\mathrm{RF}}/2\pi =$ 50 kHz and $\omega_{\mathrm{r}}/2\pi = 10$ kHz) and 61% ($\varphi = 0.61$; $\omega_2^{\mathrm{RF}}/2\pi = 25$ kHz and $\omega_{\mathrm{r}}/2\pi \approx 15.1$ kHz) of the rotor period is occupied by RF pulses. These trajectories clearly demonstrate the minor scaling of the dipolar oscillation frequency predicted above by AHT. Figure 11.4(b) shows the quantitative analysis of these data, where we plot the effective dipolar coupling extracted from several REDOR dephasing trajectories recorded for φ values in the range 0.1 to 0.61. The experimental dipolar couplings are generally found to be in good agreement with the corresponding values predicted by the AHT analysis.

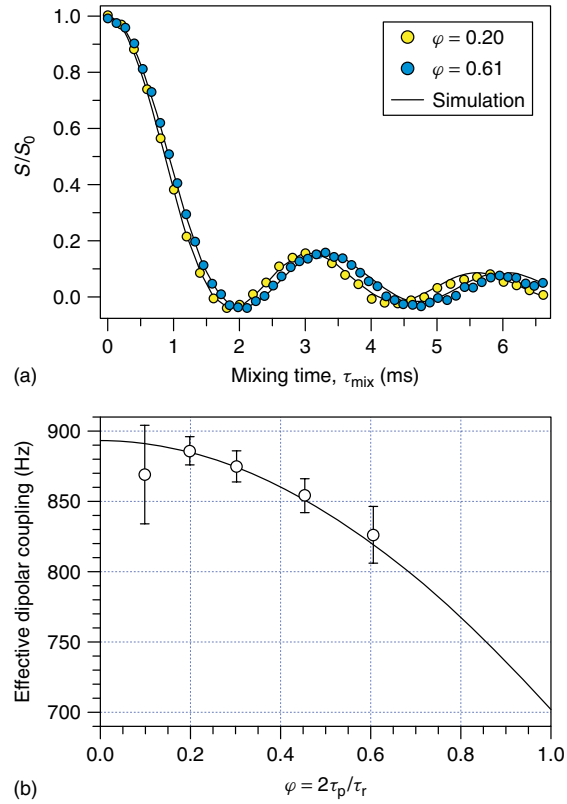


Figure 11.4. Finite pulse effects in REDOR experiments. (a) Representative experimental and simulated REDOR S/S_0 trajectories for 2-^{13}C,^{15}N-glycine. The trajectories shown were recorded under experimental conditions, where 20% ($\varphi = 0.20$; yellow circles) or 61% ($\varphi = 0.61$; blue circles) of the rotor cycle is occupied by the REDOR 180° pulses on the ^{15}N channel. (b) Plot of the measured effective ^{15}N–^{13}Cα dipolar couplings, $b_{IS}^{\mathrm{eff}}/2\pi$, in 2-^{13}C,^{15}N-glycine as a function of the fraction of the rotor cycle occupied by REDOR pulses, φ. The error bars are $\pm 2\sigma$. The solid line corresponds to a b_{IS}^{eff} vs. φ curve predicted using average Hamiltonian theory, $b_{IS}^{\mathrm{eff}}/2\pi = (b_{IS}/2\pi) \times \cos(\varphi\pi/2)/(1 - \varphi^2)$, where $b_{IS}/2\pi = 894$ Hz is the dipolar coupling expected in the δ-pulse limit. (Adapted from Ref. 84. © Elsevier, 2000.)

11.3.3 Symmetry-Based Pulse Sequences

Recently, starting with a scheme designed to achieve broadband γ-encoded homonuclear ^{13}C–^{13}C double-quantum dipolar recoupling,[98] Levitt and coworkers have introduced a family of general rotor-synchronized symmetry-based recoupling pulse

sequences.[99–101] In the context of heteronuclear dipolar recoupling, some of these symmetry-based sequences can be viewed as extensions of the R^3 and REDOR schemes. The two most widely explored symmetry classes are denoted CN_n^ν and RN_n^ν, where N, n, and ν are referred to as the symmetry numbers of the pulse sequence. In the case of CN_n^ν sequences, a total of N C-elements or cycles, each corresponding to a rotation of nuclear spins by an integer multiple of 360°, are incorporated into n rotor periods. Concurrently, the RF phases of subsequent C-elements are incremented with respect to each other by the angle $2\pi\nu/N$. The implementation of RN_n^ν sequences is similar to CN_n^ν sequences in that N R-elements are accommodated within n rotor periods. However, each R-element induces a 180° rather than a 360° rotation of the nuclear spins, and the RF phase is alternated between the values of $\pm\pi\nu/N$ rather than being repeatedly incremented.

While a detailed discussion of the various symmetry-based pulse schemes is beyond the scope of this article, the fundamental principle behind sequences of this type is that, by satisfying periodic symmetry relationships between the mechanical sample rotation due to MAS and RF rotations imposed by the pulse sequence, the space and spin trajectories for the different nuclear spin interactions (represented by quantum numbers l and m, and λ and μ, respectively) can be synchronized to generate an average Hamiltonian that suppresses all $\{l, m, \lambda, \mu\}$ combinations except for the desired ones. This means that it is possible to design pulse schemes, which permit highly selective recoupling of the nuclear spin interactions of interest. For example, we have noted above that in addition to recoupling heteronuclear dipolar couplings both SPI-R^3 and REDOR schemes also recouple the CSA of the irradiated spins. While such CSA recoupling is unavoidable for single-channel pulse sequences designed to achieve heteronuclear dipolar recoupling, both REDOR and SPI-R^3 can also reintroduce homonuclear dipolar couplings between the irradiated spins, which may interfere with heteronuclear dipolar evolution in some spin systems. Certain symmetry-based pulse sequences ($R12_3^1$, $R16_4^1$, etc.) generate an effective dipolar Hamiltonian $\overline{\hat{H}}_{\mathrm{D}}^{(0)} \propto \hat{I}_{1z}\hat{I}_{2z}$ that is analogous to that for REDOR and SPI-R^3, but with concurrent suppression of homonuclear dipolar couplings. An alternative approach to suppressing homonuclear dipolar couplings in REDOR and SPI-R^3 experiments, based on the symmetries $C3_3^1$ and $C7_7^1$, has also been proposed.[102]

11.4 HETERONUCLEAR DIPOLAR RECOUPLING IN MULTISPIN SYSTEMS

While measurements of interatomic distances in heteronuclear $^{13}C-^{15}N$ spin pairs using SSNMR methods described in the section "Heteronuclear Dipolar Recoupling Spin Pairs" are relatively routine nowadays,[16,22] the extension of these experiments to U-^{13}C,^{15}N labeled systems has generally not been straightforward owing to the presence of multiple homonuclear and heteronuclear spin–spin couplings. This problem is particularly exacerbated for measurements of weak $^{13}C-^{15}N$ dipolar couplings, which correspond to structurally interesting distances of greater than ~3 Å. For example, as discussed in more detail below, if the REDOR scheme in Figure 11.3 were applied to a molecule containing multiple coupled ^{13}C and ^{15}N nuclei, the resulting ^{13}C dephasing trajectories would be dominated by the strongest $^{13}C-^{15}N$ dipolar interactions. Furthermore, the simultaneous evolution of ^{13}C magnetization under the ~30–60 Hz one-bond $^{13}C-^{13}C$ J-couplings would lead to an additional modulation of these trajectories and generate antiphase ^{13}C coherences, especially for long mixing times ($\tau_{\mathrm{mix}} \gtrsim$ 10–15 ms), as well as significant lineshape perturbations caused by the refocusing of antiphase coherences into observable ^{13}C magnetization during detection.[75] Although several extensions of the REDOR technique that can report on the different $^{13}C-^{15}N$ dipolar couplings present in multispin systems have been proposed,[103–108] these schemes are not generally applicable to U-^{13}C,^{15}N peptides and proteins – this is primarily related to the fact that most of these experiments involve the application of 180° pulse trains on the ^{13}C channel, which would also reintroduce the large ~2 kHz one-bond $^{13}C-^{13}C$ dipolar couplings that are normally efficiently averaged by rapid MAS.[109,110]

In this section, we discuss several recently developed SSNMR techniques that alleviate the aforementioned problems and facilitate the accurate and precise measurements of multiple weak heteronuclear $^{13}C-^{15}N$ dipolar couplings in U-^{13}C,^{15}N labeled molecules. These techniques are based on the highly experimentally robust REDOR scheme

discussed in the section "Rotational Echo Double Resonance". Although REDOR does not formally suppress homonuclear dipolar couplings between the irradiated ^{15}N spins as noted in the section "Symmetry-based Pulse Sequences", this effect can be safely neglected when considering the evolution of ^{13}C magnetization for U-^{13}C,^{15}N enriched polypeptides, where typical ^{15}N–^{15}N dipolar couplings are small, $b_{NN}/2\pi < 50$ Hz, and the amide ^{15}N nuclei resonate in a relatively narrow frequency range. Moreover, since the basic principles behind these new techniques are quite general, alternate implementations employing pulse sequences that generate an analogous REDOR-like effective heteronuclear dipolar Hamiltonian, $\overline{\hat{H}}_D^{(0)} \propto \hat{I}_{1z}\hat{I}_{2z}$ (e.g., SPI-R^3 or the appropriate symmetry-based schemes), can also be readily envisioned.

11.4.1 Frequency-Selective REDOR

The effective Hamiltonian describing the spin–spin couplings within a system of n ^{13}C spins and m ^{15}N spins during the REDOR pulse sequence can be written:

$$\overline{\hat{H}} = \sum_{i=1}^{n}\sum_{j=1}^{m} \tilde{\omega}_{ij}^{D} 2\hat{C}_{iz}\hat{N}_{jz} + \sum_{i<j} \pi J_{ij} 2\hat{C}_{iz}\hat{C}_{jz} \tag{11.39}$$

where operators $\hat{\boldsymbol{C}}$ and $\hat{\boldsymbol{N}}$ represent ^{13}C and ^{15}N spins, respectively, J_{ij} is the ^{13}C–^{13}C J-coupling constant and the expression for $\tilde{\omega}_{ij}^{D}$, assuming that the principal axis frame for each interaction coincides with the crystallite-fixed frame, is given in equation (11.31). The evolution of transverse magnetization for the ith ^{13}C spin (i.e., $\hat{\rho}(0) = \hat{C}_{ix}$) under this effective Hamiltonian yields the observable powder-averaged signal:

$$S(\tau_{mix}) = \left\langle \prod_j \cos(\tilde{\omega}_{ij}^{D}\tau_{mix}) \right\rangle \prod_{j\neq i} \cos(\pi J_{ij}\tau_{mix}) \tag{11.40}$$

Since the observable ^{13}C coherences evolve simultaneously as products of cosine terms involving all relevant spin–spin couplings, the strongest couplings tend to dominate the evolution making the accurate quantification of weak heteronuclear dipolar couplings virtually impossible.

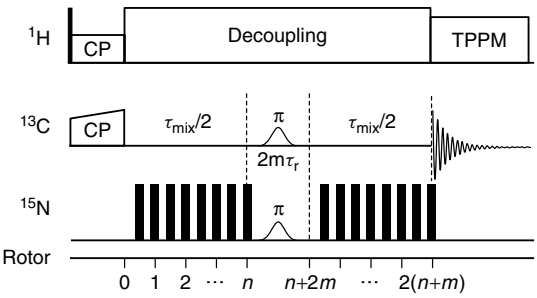


Figure 11.5. Frequency-selective REDOR pulse sequence.[76] The recoupling of individual ^{13}C–^{15}N spin pairs in U-^{13}C,^{15}N labeled molecules with concurrent suppression of ^{13}C–^{13}C J-couplings is achieved by using a pair of rotor-synchronized frequency-selective (e.g., Gaussian-shaped) 180° pulses applied simultaneously on the ^{13}C and ^{15}N channels as indicated in the figure. The REDOR dipolar dephasing S trajectory is recorded using the pulse scheme as shown, and the reference S_0 trajectory is recorded in the absence of the selective ^{15}N pulse. See the caption to Figure 11.3 for additional details of the REDOR pulse sequence.

Given that the effective Hamiltonian in equation (11.39) is a sum of commuting bilinear terms, it can be refocused by using spin-echo techniques. This idea forms the basis for the frequency-selective rotational echo double resonance (FS-REDOR) scheme[75,76] shown in Figure 11.5. FS-REDOR consists of a pair of rotor-synchronized, frequency-selective (e.g., Gaussian-shaped) 180° pulses applied simultaneously on the ^{13}C and ^{15}N channels and bracketed by two identical REDOR periods, of length $\tau_{mix}/2$ each, during which all ^{13}C–^{15}N dipolar and ^{13}C–^{13}C J-couplings evolve. Assuming that the selective 180° pulses are applied at frequencies of spins C_k and N_l, the effective Hamiltonian for the entire pulse sequence that is relevant to the evolution of spin C_k is given by

$$\overline{\hat{H}} = \tilde{\omega}_{kl}^{D} 2\hat{C}_{kz}\hat{N}_{lz} \tag{11.41}$$

leading to the observable C_k signal, which is equivalent to that expected for conventional REDOR for an isolated ^{13}C–^{15}N spin pair:

$$S(\tau_{mix}) = \langle \hat{C}_{kx} \rangle(\tau_{mix}) = \langle \cos(\tilde{\omega}_{kl}^{D}\tau_{mix}) \rangle \tag{11.42}$$

These results imply that within a system of many coupled ^{13}C and ^{15}N nuclei it is, in principle, possible to isolate a single ^{13}C–^{15}N dipolar coupling

of interest and suppress all other $^{13}C-^{15}N$ dipolar interactions as well as $^{13}C-^{13}C$ J-couplings, provided that the chemical shifts of the relevant ^{13}C and ^{15}N spins are such that they can be irradiated in a frequency-selective manner. In practice, bandwidths in the ± 2000 to ± 200 Hz regime have been obtained for 1–10 ms Gaussian-shaped pulses.[76] Note also that the selectivity of the FS-REDOR experiment can potentially be tuned further by using longer, weaker pulses with different shapes, albeit with an accompanying loss in spectral sensitivity due to transverse ^{13}C relaxation.

The FS-REDOR technique and extensions thereof have been successfully applied to several U-^{13}C,^{15}N enriched amino acids and peptides,[76,111–113] including the detection of a critical salt bridge between

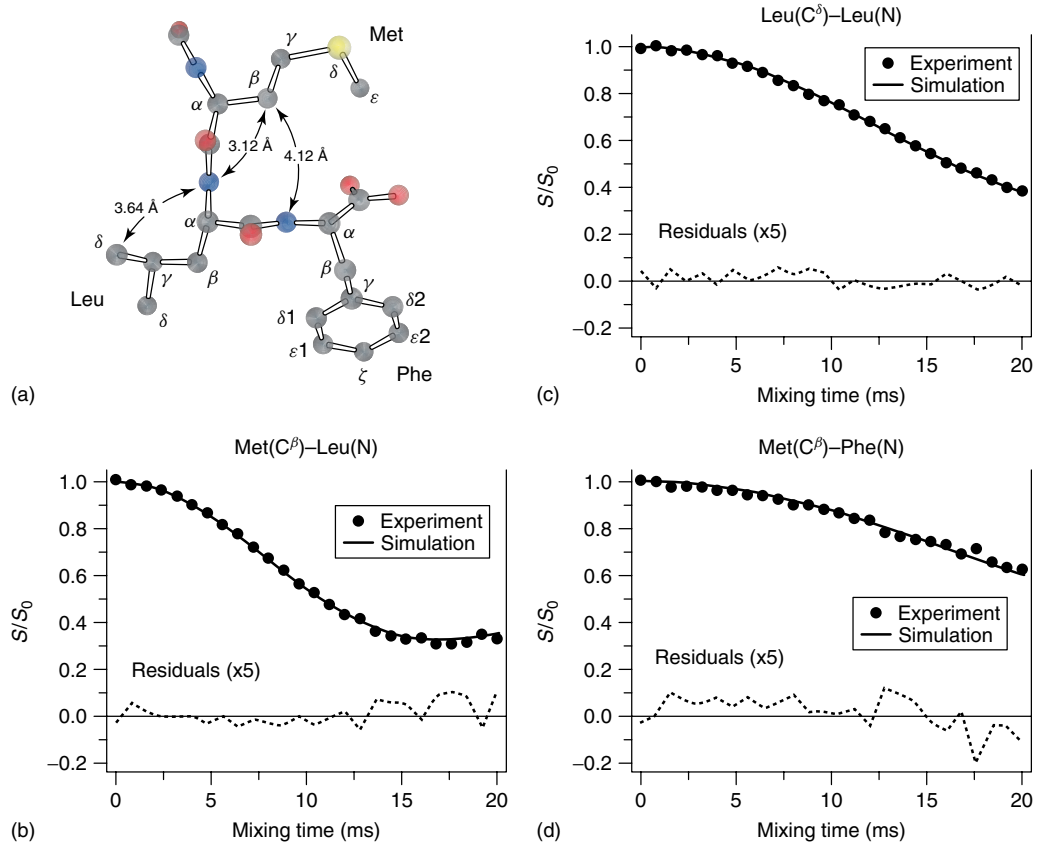


Figure 11.6. Representative frequency-selective REDOR measurements of $^{13}C-^{15}N$ distances in formyl-U-^{13}C,^{15}N-Met-Leu-Phe.[76,111] (a) Structural model of f-MLF based on the published X-ray structure of the methyl ester analog, f-MLF–OMe[114] (no X-ray structure is available for f-MLF), displaying the distances determined in panels (b)–(d). Experimental FS-REDOR S/S_0 curves and simulations are shown for (b) Met(Cβ)–Leu(N), (c) Leu(Cδ)–Leu(N), and (d) Met(Cβ)–Phe(N), and correspond to distances of 3.12 ± 0.03, 3.64 ± 0.09, and 4.12 ± 0.15 Å, respectively. Data were recorded at 500 MHz ^1H frequency and 10.0 kHz MAS rate. For the measurements shown, resonant frequency-selective Gaussian pulses of 2 ms (Met $^{13}C\beta$), 4 ms (Leu $^{13}C\delta$), and 10 ms (Leu or Phe ^{15}N) were used to selectively recouple appropriate spin pairs. The measurements were performed in a sample prepared by cocrystallizing f-U-^{13}C,^{15}N-MLF with natural abundance f-MLF in a 1:9 ratio, to minimize the interference from intermolecular $^{13}C-^{15}N$ couplings. (Reproduced with permission from C. M. Rienstra, L. Tucker-Kellogg, C. P. Jaroniec, M. Hohwy, B. Reif, T. Lozano-Perez, B. Tidor, and R. G. Griffin, *Proc. Natl. Acad. Sci. USA*, 2002, **99**, 10260. © The National Acedemy of Sciences of the USA, 2002.)

the side chains of residues Asp-23 and Lys-28 in Alzheimer's β-amyloid fibrils.[112] In Figure 11.6, we show several representative FS-REDOR measurements of $^{13}C-^{15}N$ dipolar couplings (corresponding to distances in the ~3–4 Å regime) for a three-residue peptide, formyl-U-^{13}C,^{15}N-Met-Leu-Phe (see spectra in Figure 11.1a). These data clearly indicate that multiple $^{13}C-^{15}N$ dipolar couplings and $^{13}C-^{13}C$ J-couplings, that would normally significantly perturb the REDOR dephasing trajectories, are efficiently suppressed by FS-REDOR – notably, markedly different dipolar dephasing trajectories are obtained for the Met(Cβ) site by simply changing the frequency of the ^{15}N selective pulse from Leu(N) (Figure 11.6b) to Phe(N) (Figure 11.6d), and both trajectories are completely free of the effects of the large ~200 Hz two-bond Met(Cβ)–Met(N) coupling. Altogether, FS-REDOR measurements in f-MLF have enabled the quantitative determination of 16 $^{13}C-^{15}N$ distances between ~2.5 and 6 Å, with typical precision (2σ) of ~0.1–0.3 Å. The $^{13}C-^{15}N$ distances determined by SSNMR were generally found to be in good agreement with the corresponding distances obtained using X-ray diffraction for the methyl ester analog of f-MLF[114] as illustrated in Figure 11.7(a) (note that no X-ray structure is available for f-MLF). Indeed, in combination with a set of backbone and side-chain torsion angle restraints, the FS-REDOR $^{13}C-^{15}N$ distance restraints were used to determine a high-resolution SSNMR structure for f-MLF[111] (Figure 11.7b).

While the applications of FS-REDOR to the structural studies of small U-^{13}C,^{15}N enriched peptides (or larger systems, segmentally labeled with U-^{13}C,^{15}N amino acids) displaying well-resolved ^{13}C and ^{15}N spectra are relatively straightforward, analogous studies of larger U-^{13}C,^{15}N labeled proteins are typically considerably more challenging owing to increased spectral crowding. Nevertheless, in certain cases where the resonances of primary interest are sufficiently well resolved, FS-REDOR techniques can be extended to address interesting structural questions in such systems.[115,116] Figure 11.8 illustrates an application of this type, where FS-REDOR was used to determine long-range (~4–5 Å) distances between the $^{13}C\gamma$ side-chain carbons of two aspartic acid residues and a Schiff base ^{15}N in the active site of a 26 kDa U-^{13}C,^{15}N labeled integral membrane protein, bacteriorhodopsin (bR).[115] This FS-REDOR experiment in bR was facilitated by the fact that the Schiff base ^{15}N has a unique chemical shift of ~165 ppm in the light-adapted form of the protein (i.e., ~30–60 ppm downfield of backbone amide resonances), and that Cγ signals for the Asp-85 and Asp-212 residues of interest are relatively well resolved from each other as well as from Cγ resonances arising from the remaining Asp residues.

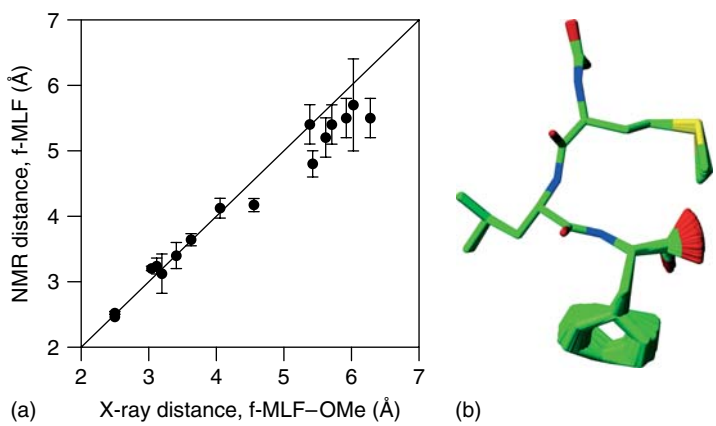


Figure 11.7. (a) Comparison of $^{13}C-^{15}N$ distances in formyl-U-^{13}C,^{15}N-Met-Leu-Phe measured by using frequency-selective REDOR[76,111] with the corresponding X-ray distances in f-MLF–OMe.[114] The uncertainties in NMR distances correspond to $\pm 2\sigma$. (b) Representative subset of f-MLF structures (PDB entry 1Q7O) calculated on the basis of SSNMR torsion angle and FS-REDOR $^{13}C-^{15}N$ distance restraints. (Reproduced with permission from C. M. Rienstra, L. Tucker-Kellogg, C. P. Jaroniec, M. Hohwy, B. Reif, T. Lozano-Perez, B. Tidor, and R. G. Griffin, *Proc. Natl. Acad. Sci. USA*, 2002, **99**, 10260. © The National Acedemy of Sciences of the USA, 2002.)

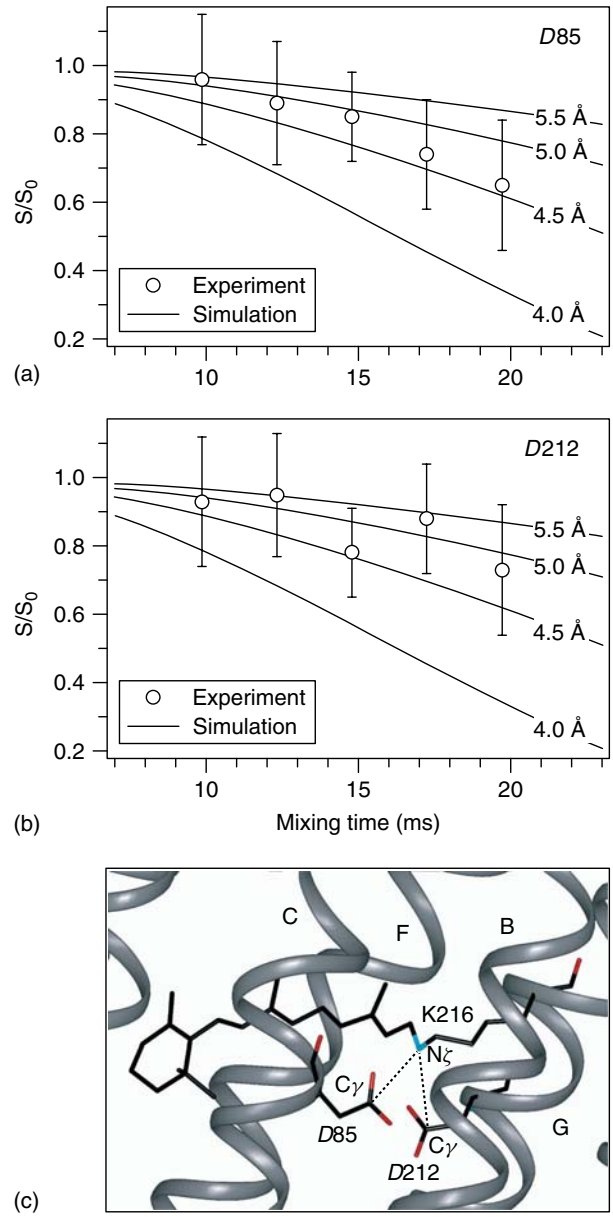


Figure 11.8. Frequency-selective REDOR distance measurements from the Schiff base (Lys-216 Nζ) to (a) Asp-85 Cγ and (b) Asp-212 Cγ in light-adapted U-^{13}C,^{15}N labeled bacteriorhodopsin. Spectra were recorded at 317 MHz ^{1}H frequency and 6.5 kHz MAS rate; the total experiment duration was ~10 days. The best-fit distances extracted from the experimental FS-REDOR S/S_0 trajectories are 4.7 ± 0.3 Å for Asp-85 and 4.9 ± 0.5 Å for Asp-212 – the corresponding distances in several X-ray structures of bR (PDB entries 1BRR,[117] 1QHJ,[118] and 1C3W[119]) are in the range 4.3–5.0 Å for Asp-85 and 4.0–4.4 Å for Asp-212. (c) Structural model of the bR active site based on X-ray diffraction studies, showing α-helices B, C, F, and G, the chromophore (comprising retinal with its Schiff base linkage to Lys-216), and the Asp-85 and Asp-212 side chains. The distances between the Schiff base ^{15}N and Asp ^{13}Cγ, measured by FS-REDOR, are indicated by dotted lines. (Adapted from Ref. 115. © American Chemical Society, 2001.)

11.4.2 3-D TEDOR Techniques

A more general approach toward the simultaneous measurement of multiple heteronuclear $^{13}C-^{15}N$ dipolar couplings in U-^{13}C,^{15}N labeled polypeptides with arbitrary ^{13}C and ^{15}N chemical shifts is based on multidimensional heteronuclear correlation (HETCOR) spectroscopy. In the simplest implementation of a 3-D HETCOR scheme, a series of 2-D $^{15}N-^{13}C$ chemical shift correlation spectra are acquired as a function of a $^{15}N-^{13}C$ dipolar magnetization transfer (or mixing) period – note, however, that an additional chemical shift dimension can also be readily incorporated into these schemes for increased spectral resolution.[79] Consequently, for each resolved ^{13}C site, C_i, cross peaks located at frequencies $(\Omega_{N_j}, \Omega_{C_i})$ with $j = 1, 2, \ldots$ are observed in the 2-D spectra for C_i-N_j pairs exhibiting sufficiently strong dipolar couplings – more importantly, in the context of quantitative measurements, the information about C_i-N_j distances is encoded in the full cross-peak buildup trajectories recorded as a function of the mixing time.

Several 3-D $^{15}N-^{13}C$ HETCOR schemes based on REDOR mixing and 90° ^{13}C and ^{15}N magnetization transfer pulses have been proposed[77–79,120] on the basis of the original TEDOR sequences developed by Schaefer and coworkers.[80,121] Of these 3-D TEDOR experiments, the "out-and-back" type schemes with ^{13}C detection, that avoid the recoupling of $^{13}C-^{13}C$ dipolar interactions by minimizing the RF irradiation on the ^{13}C channel are the most promising for applications to U-^{13}C,^{15}N labeled molecules.[77–79] In addition, for measurements of weak $^{13}C-^{15}N$ couplings requiring relatively long mixing times, these schemes must be compensated for spectral artifacts caused by homonuclear $^{13}C-^{13}C$ J-evolution. One such scheme, shown in Figure 11.9 and referred to as 3-D ZF-TEDOR,[78] employs two z-filter periods to suppress undesirable antiphase and multiple quantum coherences generated by the evolution of transverse ^{13}C magnetization under one-bond $^{13}C-^{13}C$ J-couplings. The importance of eliminating these undesirable ^{13}C coherences is illustrated in Figure 11.10 for a model dipeptide, U-^{13}C,^{15}N-acetyl-Val-Leu (ac-VL). Specifically, in the absence of the z-filter periods spurious cross peaks and phase-twisted lineshapes are observed in the 2-D $^{15}N-^{13}C$ spectra, particularly for longer mixing times (Figure 11.10(a)–(c)), which precludes the accurate determination of the actual cross-peak positions and intensities. On the other hand, the insertion of z-filters as indicated in Figure 11.9 restores pure absorption-mode correlation spectra that can be readily analyzed for all mixing times (Figure 11.10(d)–(f)).

The spectra in Figure 11.10(d)–(f) illustrate the utility of 3-D ZF-TEDOR for simultaneously detecting multiple structurally interesting $^{13}C-^{15}N$ dipolar couplings in U-^{13}C,^{15}N enriched biomolecules. For example, the relative intensities of correlations between valine Cγ1 and Cγ2 and both amide ^{15}N sites obtained for different mixing times immediately provide valuable qualitative information about the rotameric state of the side chain for that residue. Quantitative estimates of the $^{13}C-^{15}N$ distances

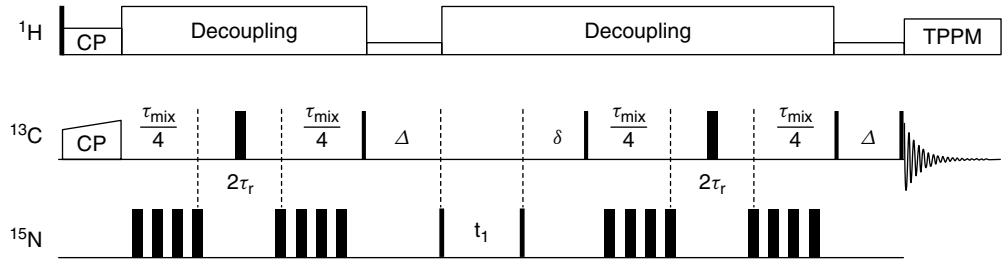


Figure 11.9. 3-D z-filtered TEDOR (ZF-TEDOR) pulse sequence.[78] Narrow and wide black rectangles correspond to 90° and 180° pulses. The delay δ ensures that the total delay between the REDOR dipolar mixing periods is equal to an integer number of rotor cycles, which is required for the efficient reconversion of $^{13}C-^{15}N$ antiphase coherences into observable ^{13}C magnetization. The z-filter periods Δ eliminate undesirable multiple quantum and antiphase spin coherences generated by $^{13}C-^{13}C$ J-evolution – in the studies discussed here, the z-filter periods were of minimum duration ($\Delta = 200$ μs) and utilized a weak RF field applied concurrently on the ^{1}H channel ($\omega_{RF} \approx \omega_r$) to rapidly dephase transverse ^{13}C spin coherences. However, alternate z-filter implementations can also be employed.[79,122]

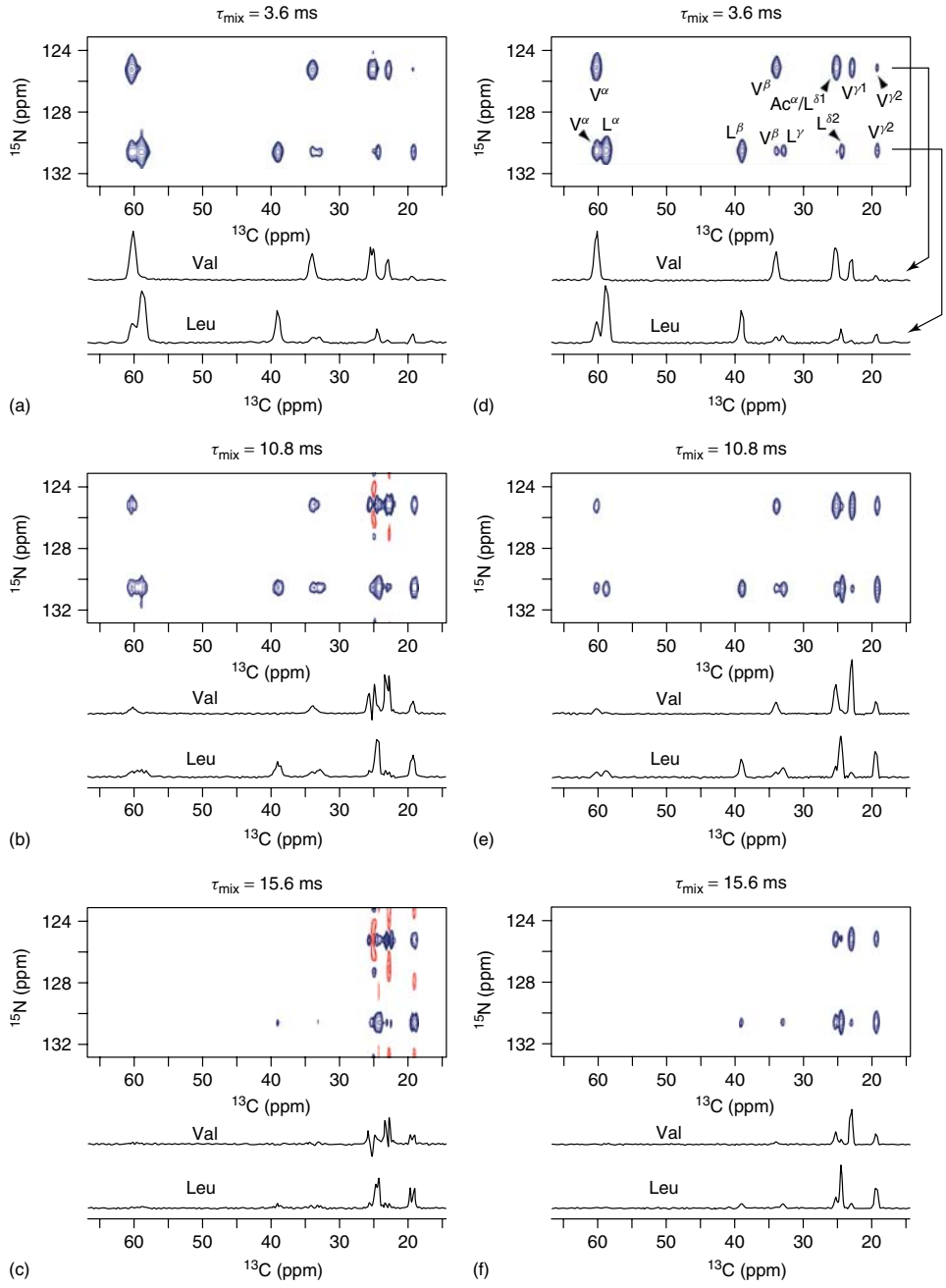


Figure 11.10. Representative 2-D planes from 3-D TEDOR experiments in U-^{13}C,^{15}N labeled acetyl-Val-Leu corresponding to dipolar mixing times of 3.6, 10.8, and 15.6 ms. Spectra were recorded at 500 MHz ^{1}H frequency and 10.0 kHz MAS rate, using the pulse scheme in Figure 11.9 implemented without (a)–(c) or with (d)–(f) z-filter delays. Positive and negative contours are shown in blue and red, respectively. These spectra demonstrate that the use of z-filters in 3-D TEDOR experiments performed on U-^{13}C,^{15}N labeled molecules eliminates the detrimental effects of ^{13}C–^{3}C J-couplings and leads to pure absorption-mode spectra. (Adapted from Ref. 78. © American Chemical Society, 2002.)

can be obtained by monitoring the complete cross-peak buildup trajectories, with the C_i-N_j cross-peak intensity as a function of τ_{mix} given by

$$I_{ij}(\tau_{mix}) = \Lambda_i e^{-\Gamma_i \tau_{mix}} \left\langle \sin^2\left(\frac{\tilde{\omega}_{ij}^{D}\tau_{mix}}{2}\right) \times \prod_{k\neq j} \cos^2\left(\frac{\tilde{\omega}_{ik}^{D}\tau_{mix}}{2}\right)\right\rangle \prod_{l\neq i} \cos^2(\pi J_{il}\tau_{mix}/2) \tag{11.43}$$

where Λ_i is the cross-peak amplitude scaling factor, and Γ_i is the relaxation rate constant for C_i spin coherences. While 3-D TEDOR-type schemes simultaneously restore the dipolar couplings between a given ^{13}C spin and all nearby ^{15}N nuclei, the cross-peak buildup trajectories are found to be determined primarily by the active dipolar coupling responsible for the appearance of the cross peak at frequencies $(\Omega_{N_j}, \Omega_{C_i})$ in the 2-D spectra and represented by the sine squared term in equation (11.43). Moreover, although 3-D ZF-TEDOR suppresses most of the detrimental $^{13}C-^{13}C$ J-evolution effects, the cross-peak intensities are still modulated by $^1J_{CC}$, which reduces the spectral sensitivity and, in practice, restricts the useful $^{15}N-^{13}C$ mixing times to $\tau_{mix} \sim 8-14$ ms depending on the value of $^1J_{CC}$. Finally, we note that the cross-peak buildup trajectories exhibit a formal dependence on the relative orientations of the active and passive $^{13}C-^{15}N$ dipolar couplings – this is somewhat problematic since the relative dipolar tensor orientations are generally unknown and to include them as fit parameters would be impractical. Fortunately, it is possible to use instead a simple analytical model based on Bessel function expansions of REDOR NMR signals[123] that depends only on the dipolar coupling magnitudes and is completely free of geometric parameters. According to this model, the C_i-N_j cross-peak intensity as a function of τ_{mix} can be approximated as[78]

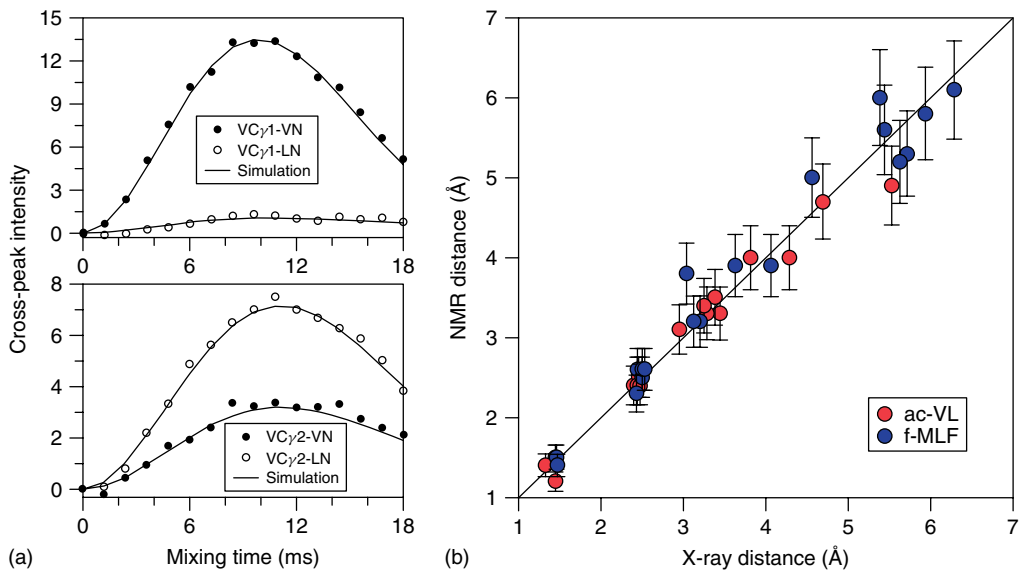


Figure 11.11. (a) Representative 3-D ZF-TEDOR cross-peak buildup trajectories for U-^{13}C,^{15}N-acetyl-Val-Leu, reporting on the dipolar couplings between Val $^{13}C\gamma1$ or $^{13}C\gamma2$ and Val ^{15}N or Leu ^{15}N. The $^{13}C-^{15}N$ distances extracted from the trajectories are as follows: Val(Cγ1)–Val(N): 3.1 Å; Val(Cγ1)–Leu(N): 4.7 Å; Val(Cγ2)–Val(N): 4.0 Å; Val(Cγ2)–Leu(N): 3.5 Å (Reproduced from Ref. 78. © American Chemical Society, 2002). (b) Comparison of $^{13}C-^{15}N$ distances in U-^{13}C,^{15}N-acetyl-Val-Leu and formyl-U-^{13}C,^{15}N-Met-Leu-Phe measured by using 3-D ZF-TEDOR[78] with the corresponding X-ray distances (f-MLF X-ray distances refer to f-MLF–OMe, cf. Figures 11.6 and 11.7). Uncertainties in the NMR distances correspond to ±10% of the measured distance (see Ref. 78 for a detailed discussion). Note that U-^{13}C,^{15}N labeled ac-VL and f-MLF peptides used in this study were diluted in a 1:4 and 1:9 ratio, respectively, in corresponding natural abundance peptides, to minimize the effects of intermolecular $^{13}C-^{15}N$ couplings.

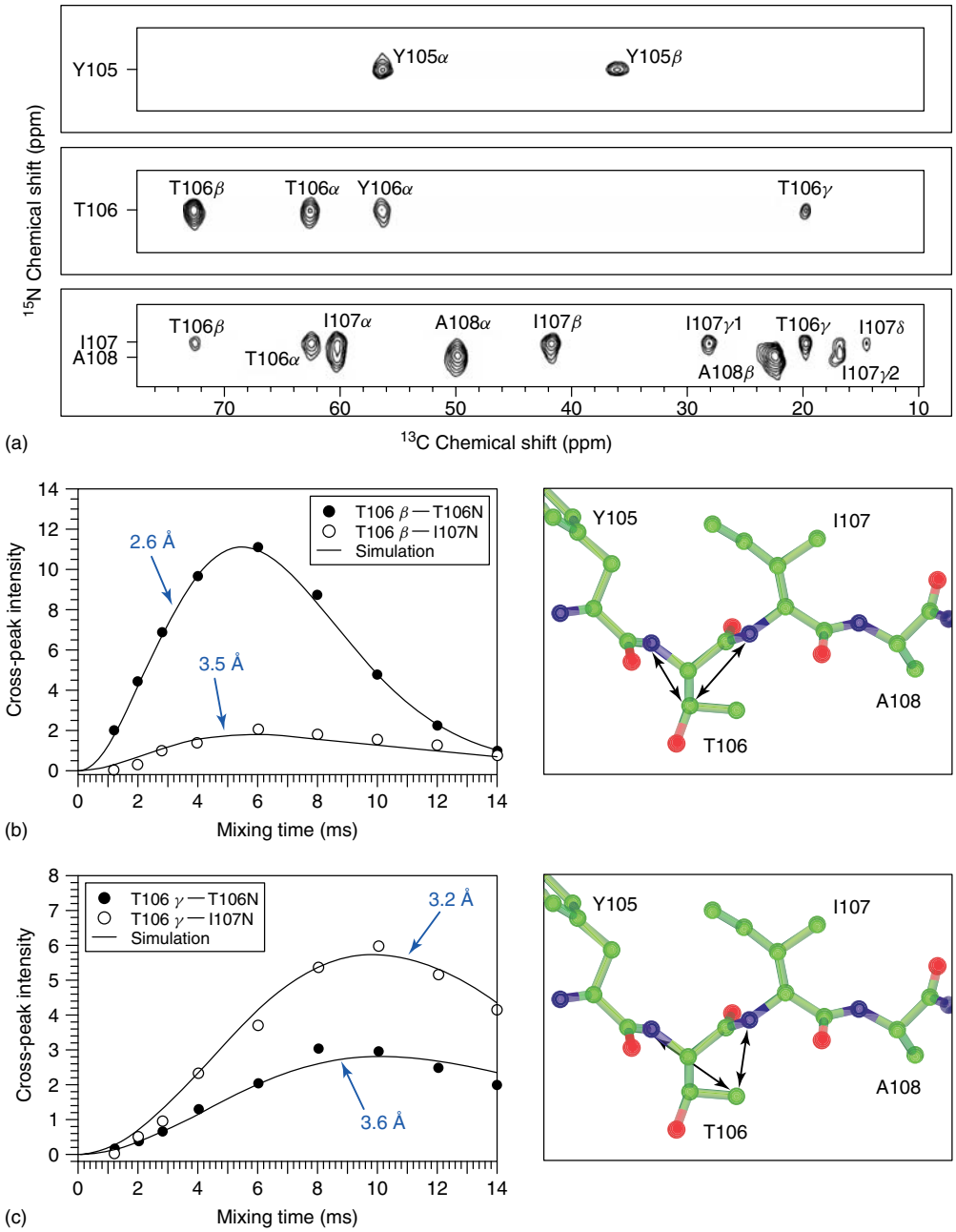


Figure 11.12. Representative 3-D ZF-TEDOR $^{13}C-^{15}N$ distance measurements for transthyretin 105–115 (amino acid sequence YTIAALLSPYS) amyloid fibrils, containing a U-^{13}C,^{15}N labeled four-residue stretch Y105–A108. (a) Strips from a 2-D $^{15}N-^{13}C$ correlation spectrum recorded with a mixing time $\tau_{mix} = 6.0$ ms. Resonance assignments are based on Ref. 124. (b) Experimental and simulated trajectories for the T106(Cβ)–T106(N) and T106(Cβ)–I107(N) cross peaks as a function of the dipolar mixing time, and the relevant molecular fragment displaying the measured distances. (c) Same as panel (b) but for T106(Cγ). (Reproduced with permission from C. P. Jaroniec, C. E. MacPhee, V. S. Bajaj, M. T. McMahon, C. M. Dobson, and R. G. Griffin, *Proc. Natl. Acad. Sci. USA*, 2004, **101**, 711. © The National Academy of Sciences of the USA, 2004.)

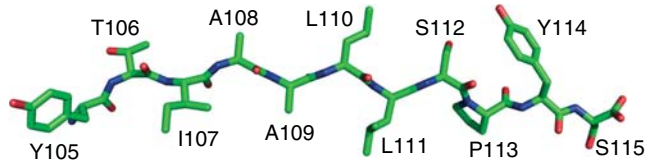


Figure 11.13. High-resolution three-dimensional structure of transthyretin 105–115 in amyloid fibrils determined using MAS SSNMR techniques (PDB entry 1RVS).[125] The structure was determined using 76 experimental restraints, recorded primarily on three peptide samples that were U-^{13}C,^{15}N labeled in overlapping stretches of four residues: Y105–A108, A108–L111, and L111–Y114. The experimental restraints included 35 ^{13}C–^{15}N distances in the ~2.5–6 Å regime determined mostly using 3-D ZF-TEDOR, and 41 backbone torsion angle restraints (on 19 ϕ and ψ angles) based on dipolar tensor correlation techniques and isotropic chemical shifts.

$$I_{ij}(\tau_{\text{mix}}) \approx \Lambda_i e^{-\Gamma_i \tau_{\text{mix}}} \{1 - [J_0(\sqrt{2} b_{ij} \tau_{\text{mix}}/2\pi)]^2\} \times \prod_{k \neq j} \{1 + [J_0(\sqrt{2} b_{ik} \tau_{\text{mix}}/2\pi)]^2\} \times \prod_{l \neq i} \cos^2(\pi J_{il} \tau_{\text{mix}}/2) \qquad (11.44)$$

where $J_0(x)$ is a Bessel function of zeroth order. For spin systems exhibiting highly resolved spectra all cross-peak trajectories corresponding to a given ^{13}C site can be fit simultaneously with a set of expressions similar to equation (11.44), which reduces the number of independent fit parameters and results in highest quality fits[78] – however, given that the most important features of the cross-peak buildup trajectories are primarily determined by the active dipolar coupling, in systems exhibiting more significant spectral overlap, individual trajectories can be modeled as discussed in Ref. 79. Finally, we note that the use of this approximate analytical model, as opposed to the analytical AHT result given in equation (11.43), is generally expected to be the major source of error in the measurements of ^{13}C–^{15}N distances in the 3–5 Å regime, with typical uncertainties on the order of ~10–15% of the measured distance.[78]

Figure 11.11(a) shows representative experimental and simulated 3-D ZF-TEDOR trajectories for ac-VL. These data illustrate that ^{13}C–^{15}N dipolar couplings corresponding to distances up to ~5 Å can be readily determined using this method, and that the simulation model in equation (11.44) provides a reasonable description of the experimental cross-peak buildup trajectories. In Figure 11.11(b), all ^{13}C–^{15}N distances measured in ac-VL and f-MLF by using 3-D ZF-TEDOR[78] are compared with the corresponding X-ray diffraction distances – overall, the two sets of distances show a remarkably high degree of agreement. To demonstrate an application of 3-D ZF-TEDOR to a more challenging biological system, in Figure 11.12, we show representative spectra, as well as the experimental and simulated cross-peak buildup trajectories for a segmentally U-^{13}C,^{15}N labeled amyloidogenic peptide corresponding to residues 105–115 of transthyretin.[124,125] In fact, these 3-D ZF-TEDOR distance measurements provided a set of critical restraints used to determine the high-resolution peptide structure in amyloid fibrils (Figure 11.13).[125]

Despite the $^1J_{CC}$-modulation of cross-peak intensities, which attenuates the spectral sensitivity and somewhat limits the range of accessible dipolar mixing times, the 3-D ZF-TEDOR scheme shown in Figure 11.9 and applied to U-^{13}C,^{15}N labeled samples is highly useful owing to its ability to rapidly provide a large number of ^{13}C–^{15}N distance restraints. In addition, several approaches have been proposed to suppress the ^{13}C–^{13}C J-modulation of cross-peak intensities in 3-D TEDOR experiments, resulting in increased sensitivity and/or resolution spectra at the expense of the number of ^{13}C–^{15}N dipolar couplings that can be simultaneously determined in a single experiment. These approaches include the use of (i) selective ^{13}C refocusing pulses,[78] (ii) constant-time (CT)- or semiconstant-time (SCT)-type pulse sequence elements of duration $\sim 1/^1J_{CC}$ to refocus the J-evolution,[79] and (iii) biosynthetic labeling schemes that yield proteins fully enriched with ^{15}N, but ^{13}C-labeled only at specific sites for different residues[126,127] – this type of "magnetic dilution" abolishes most one-bond ^{13}C–^{13}C J-couplings and allows the 3-D ZF-TEDOR scheme to be applied with no additional modifications.[128] As an example of this type of methodology, Figures 11.14 and 11.15 show an application of 3-D and 4-D SCT-TEDOR

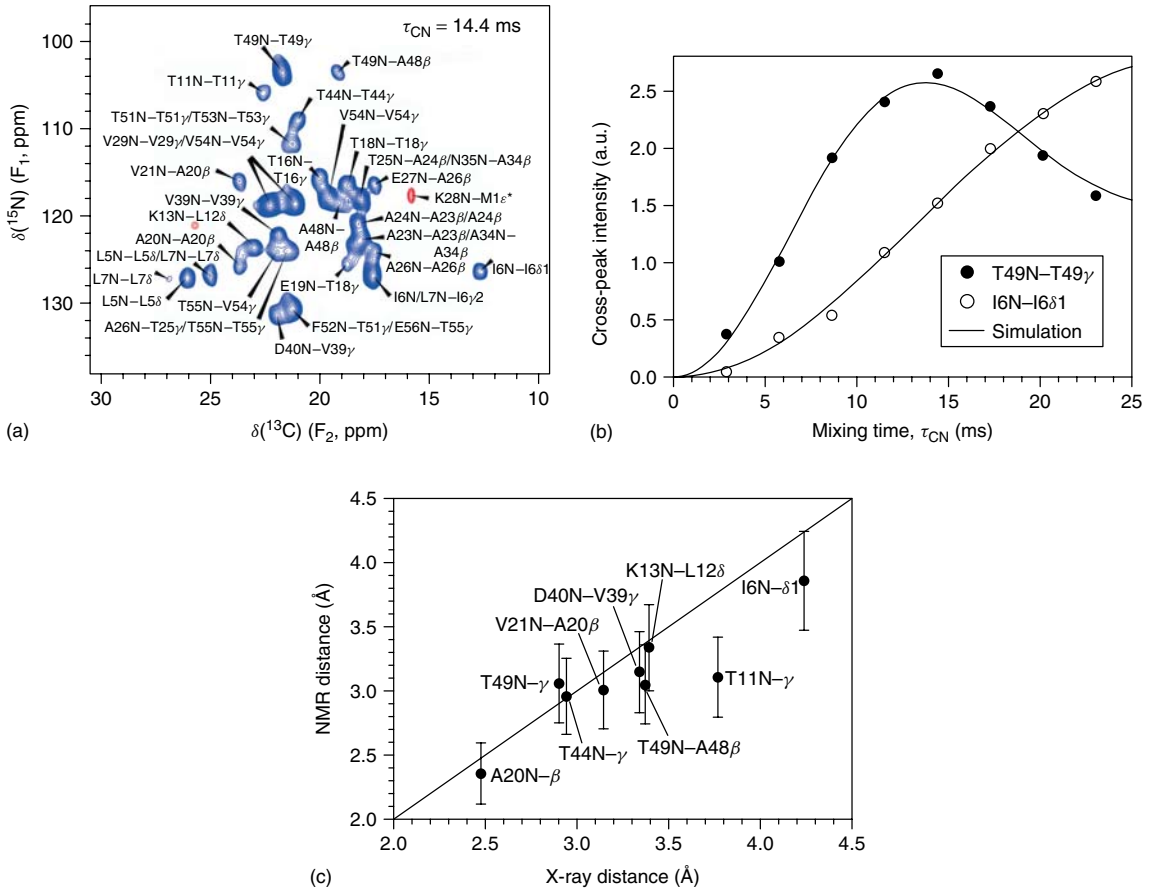


Figure 11.14. (a) 2-D slice from a 3-D SCT-TEDOR experiment on protein GB1 corresponding to the $^{15}N-^{13}C^{methyl}$ chemical shift correlation spectrum recorded with a dipolar mixing time 14.4 ms. Positive and negative cross peaks are drawn in blue and red, respectively. (b) Representative trajectories of cross-peak intensity as a function of the mixing time for T49N–T49γ and I6N–I6δ1 cross peaks, corresponding to $^{15}N-^{13}C$ distances in the ~3–4 Å range. Best-fit simulations using an analytical model are also shown (–). (c) Comparison of selected $^{15}N-^{13}C$ distances in GB1 determined using X-ray diffraction and 3-D SCT-TEDOR. Error bars correspond to ±10% of the measured distance. (Reproduced from Ref. 79. © American Institute of Physics, 2008.)

schemes to the determination of multiple distance restraints between amide ^{15}N sites and side-chain ^{13}C methyl groups of alanine, isoleucine, leucine, methionine, threonine, and valine residues in the 56-amino acid B1 immunoglobulin binding domain of protein G (GB1) in the microcrystalline phase.[79] Remarkably, these experiments provide both intra- and intermolecular $^{13}C-^{15}N$ dipolar coupling restraints, which yield information about the side-chain dihedral angles and the packing of protein molecules within the crystal lattice.

11.5 CONCLUSIONS

Recent advances in MAS SSNMR instrumentation and methodology as well as sample-preparation protocols have facilitated the widespread studies of highly or uniformly $^{13}C,^{15}N$ enriched peptides and small to medium-sized proteins, including a number of important biological systems that pose significant challenges for traditional high-resolution techniques. Measurements of long-range (greater than ~3 Å) internuclear distance restraints in these systems

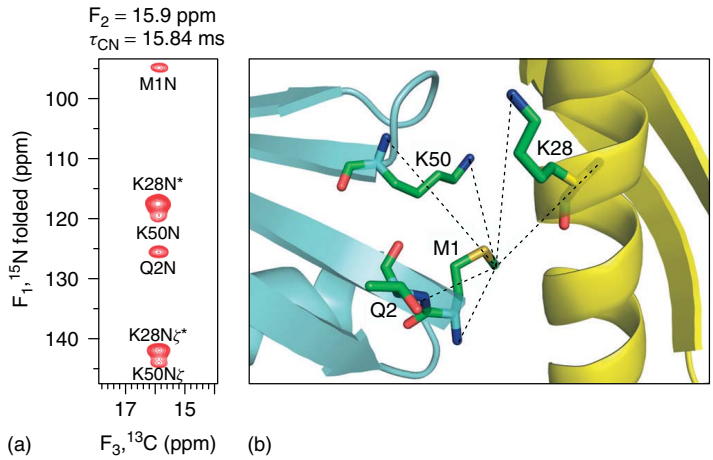


Figure 11.15. (a) Small (F_1,F_3)-region taken from the 3-D ^{15}N–$^{13}C^{methyl}$–^{13}C correlation spectrum of protein GB1 at the M1ε frequency in F_2, showing the correlations between M1ε and the neighboring ^{15}N nuclei. Six cross peaks were observed in this region and assigned on the basis of the GB1 ^{13}C and ^{15}N chemical shifts,[55] combined with the analysis of published GB1 crystal structures.[129] The four intramolecular correlations correspond to dipolar contacts between M1ε and M1N (NH_3^+), Q2N, K50N, and K50Nζ, and the two remaining cross peaks (indicated by asterisks) have been assigned to intermolecular contacts with K28N and K28Nζ. (b) Structural model of GB1 in the trigonal lattice (PDB entry 1PGB),[129] which qualitatively accounts for the observed cross-peak pattern, with the relevant M1ε – N distances indicated by dotted lines. The neighboring GB1 molecules in the crystal lattice are shown in ribbon representation in cyan and yellow, and residues M1, Q2, K50, and K28 are shown in stick representation (the atom-types for these residues are colored as follows: C = green, O = red, N = blue, S = yellow). (Reproduced from Ref. 79. © American Institute of Physics, 2008.)

by using dipolar recoupling techniques have the capacity to provide site-specific atomic-level insights about their three-dimensional structure and intermolecular interactions. In this article, we discussed several recent REDOR-based heteronuclear dipolar recoupling methods, which are experimentally robust and straightforward to implement and analyze, and which enable the accurate and precise measurements of multiple, weak ^{13}C–^{15}N dipolar couplings in U-^{13}C,^{15}N enriched peptides and proteins. In addition to the specific applications highlighted here, a multitude of analogous applications of these and related methods to other biological systems can also be readily envisaged.

REFERENCES

1. E. R. Andrew, A. Bradbury, and R. G. Eades, *Nature*, 1959, **183**, 1802.
2. I. J. Lowe, *Phys. Rev. Lett.*, 1959, **2**, 285.
3. M. M. Maricq and J. S. Waugh, *J. Chem. Phys.*, 1979, **70**, 3300.
4. A. Pines, M. G. Gibby, and J. S. Waugh, *J. Chem. Phys.*, 1973, **59**, 569.
5. E. O. Stejskal, J. Schaefer, and J. S. Waugh, *J. Magn. Reson.*, 1977, **28**, 105.
6. A. E. Bennett, C. M. Rienstra, M. Auger, K. V. Lakshmi, and R. G. Griffin, *J. Chem. Phys.*, 1995, **103**, 6951.
7. A. Detken, E. H. Hardy, M. Ernst, and B. H. Meier, *Chem. Phys. Lett.*, 2002, **356**, 298.
8. M. Ernst, *J. Magn. Reson.*, 2003, **162**, 1.
9. M. Mehring, '*Principles of High Resolution NMR in Solids*', Springer-Verlag: Berlin, 1983.
10. E. R. Andrew, S. Clough, L. F. Farnell, T. A. Gledhill, and I. Roberts, *Phys. Lett.*, 1966, **21**, 505.
11. D. P. Raleigh, M. H. Levitt, and R. G. Griffin, *Chem. Phys. Lett.*, 1988, **146**, 71.
12. M. H. Levitt, D. P. Raleigh, F. Creuzet, and R. G. Griffin, *J. Chem. Phys.*, 1990, **92**, 6347.
13. M. G. Colombo, B. H. Meier, and R. R. Ernst, *Chem. Phys. Lett.*, 1988, **146**, 189.

14. A. E. Bennett, R. G. Griffin, and S. Vega, in '*NMR Basic Principles and Progress*', ed. B. Blumich, Springer-Verlag: Berlin, 1994, Vol. **33**, p 1.
15. R. G. Griffin, *Nat. Struct. Biol.*, 1998, **5**, 508.
16. S. Dusold and A. Sebald, *Annu. Rep. NMR Spectrosc.*, 2000, **41**, 185.
17. B. J. Wylie and C. M. Rienstra, *J. Chem. Phys.*, 2008, **128**, 052207.
18. M. J. Duer, '*Introduction to Solid-State NMR Spectroscopy*', Blackwell Science: Oxford, 2004.
19. T. Gullion and J. Schaefer, *J. Magn. Reson.*, 1989, **81**, 196.
20. T. Gullion and J. Schaefer, *Adv. Magn. Reson.*, 1989, **13**, 57.
21. D. M. Gregory, D. J. Mitchell, J. A. Stringer, S. Kiihne, J. C. Shiels, J. Callahan, M. A. Mehta, and G. P. Drobny, *Chem. Phys. Lett.*, 1995, **246**, 654.
22. L. M. McDowell and J. Schaefer, *Curr. Opin. Struct. Biol.*, 1996, **6**, 624.
23. S. O. Smith, K. Aschheim, and M. Groesbeek, *Q. Rev. Biophys.*, 1996, **29**, 395.
24. R. Tycko, *Q. Rev. Biophys.*, 2006, **39**, 1.
25. F. A. Kovacs, D. J. Fowler, G. J. Gallagher, and L. K. Thompson, *Concepts Magn. Reson.*, 2007, **30A**, 21.
26. A. E. McDermott, F. Creuzet, R. G. Griffin, L. E. Zawadzke, Q. Z. Ye, and C. T. Walsh, *Biochemistry*, 1990, **29**, 5767.
27. L. M. McDowell, C. A. Klug, D. D. Beusen, and J. Schaefer, *Biochemistry*, 1996, **35**, 5395.
28. D. P. Weliky, A. E. Bennett, A. Zvi, J. Anglister, P. J. Steinbach, and R. Tycko, *Nat. Struct. Biol.*, 1999, **6**, 141.
29. F. Creuzet, A. McDermott, R. Gebhard, Kvd. Hoef, M. B. Spijker-Assink, J. Herzfeld, J. Lugtenburg, M. H. Levitt, and R. G. Griffin, *Science*, 1991, **251**, 783.
30. S. O. Smith, R. Jonas, M. Braiman, and B. J. Bormann, *Biochemistry*, 1994, **33**, 6334.
31. B. Isaac, G. J. Gallagher, Y. S. Balazs, and L. K. Thompson, *Biochemistry*, 2002, **41**, 3025.
32. J. R. Long, J. L. Dindot, H. Zebroski, S. Kiihne, R. H. Clark, A. A. Campbell, P. S. Stayton, and G. P. Drobny, *Proc. Natl. Acad. Sci. U S A*, 1998, **95**, 12083.
33. P. T. Lansbury, P. R. Costa, J. M. Griffiths, E. J. Simon, M. Auger, K. J. Halverson, D. A. Kocisko, Z. S. Hendsch, T. T. Ashburn, R. G. S. Spencer, B. Tidor, and R. G. Griffin, *Nat. Mol. Biol.*, 1995, **2**, 990.
34. T. L. S. Benzinger, D. M. Gregory, T. S. Burkoth, H. Miller-Auer, D. G. Lynn, R. E. Botto, and S. C. Meredith, *Proc. Natl. Acad. Sci. U S A*, 1998, **95**, 13407.
35. F. Shewmaker, R. B. Wickner, and R. Tycko, *Proc. Natl. Acad. Sci. U S A*, 2006, **103**, 19754.
36. K. Wüthrich, '*NMR of Proteins and Nucleic Acids*', Wiley: New York, 1986.
37. J. Cavanagh, W. J. Fairbrother, A. G. Palmer, M. Rance, and N. J. Skelton, '*Protein NMR Spectroscopy: Principles and Practice*', Elsevier, Academic Press: San Diego, 2007.
38. R. R. Ernst, G. Bodenhausen, and A. Wokaun, '*Principles of Nuclear Magnetic Resonance in One and Two Dimensions*', Oxford University Press: Oxford, 1987.
39. H. B. R. Cole, S. W. Sparks, and D. A. Torchia, *Proc. Natl. Acad. Sci. U S A*, 1988, **85**, 6362.
40. A. McDermott, T. Polenova, A. Bockmann, K. W. Zilm, E. K. Paulsen, R. W. Martin, and G. T. Montelione, *J. Biomol. NMR*, 2000, **16**, 209.
41. J. Pauli, B. van Rossum, H. Forster, H. J. M. de Groot, and H. Oschkinat, *J. Magn. Reson.*, 2000, **143**, 411.
42. R. W. Martin and K. W. Zilm, *J. Magn. Reson.*, 2003, **165**, 162.
43. A. E. McDermott, *Curr. Opin. Struct. Biol.*, 2004, **14**, 554.
44. C. E. Hughes and M. Baldus, *Annu. Rep. NMR Spectrosc.*, 2005, **55**, 121.
45. A. Bockmann, *Angew. Chem. Int. Ed.*, 2008, **47**, 6110.
46. M. Hong and R. G. Griffin, *J. Am. Chem. Soc.*, 1998, **120**, 7113.
47. C. M. Rienstra, M. Hohwy, M. Hong, and R. G. Griffin, *J. Am. Chem. Soc.*, 2000, **122**, 10979.
48. M. Baldus, A. T. Petkova, J. Herzfeld, and R. G. Griffin, *Mol. Phys.*, 1998, **95**, 1197.
49. J. J. Helmus, K. Surewicz, P. S. Nadaud, W. K. Surewicz, and C. P. Jaroniec, *Proc. Natl. Acad. Sci. U S A*, 2008, **105**, 6284.
50. M. Baldus, *Prog. NMR Spectrosc.*, 2002, **41**, 1.
51. S. K. Straus, *Philos. Trans. R. Soc. London, Ser. B*, 2004, **359**, 997.

52. I. Schnell and H. W. Spiess, *J. Magn. Reson.*, 2001, **151**, 153.
53. D. Huster, L. S. Xiao, and M. Hong, *Biochemistry*, 2001, **40**, 7662.
54. M. Hong, X. L. Yao, K. Jakes, and D. Huster, *J. Phys. Chem. B*, 2002, **106**, 7355.
55. W. T. Franks, D. H. Zhou, B. J. Wylie, B. G. Money, D. T. Graesser, H. L. Frericks, G. Sahota, and C. M. Rienstra, *J. Am. Chem. Soc.*, 2005, **127**, 12291.
56. J. L. Lorieau and A. E. McDermott, *J. Am. Chem. Soc.*, 2006, **128**, 11505.
57. J. L. Lorieau and A. E. McDermott, *Magn. Reson. Chem.*, 2006, **44**, 334.
58. M. Hong, *J. Phys. Chem. B*, 2007, **111**, 10340.
59. J. L. Lorieau, L. A. Day, and A. E. McDermott, *Proc. Natl. Acad. Sci. U S A*, 2008, **105**, 10366.
60. X. Feng, Y. K. Lee, D. Sandström, M. Eden, H. Maisel, A. Sebald, and M. H. Levitt, *Chem. Phys. Lett.*, 1996, **257**, 314.
61. Y. Ishii, T. Terao, and M. Kainosho, *Chem. Phys. Lett.*, 1996, **256**, 133.
62. M. Hong, J. D. Gross, and R. G. Griffin, *J. Phys. Chem. B*, 1997, **101**, 5869.
63. P. R. Costa, J. D. Gross, M. Hong, and R. G. Griffin, *Chem. Phys. Lett.*, 1997, **280**, 95.
64. X. Feng, M. Eden, A. Brinkmann, H. Luthman, L. Eriksson, A. Gräslund, O. N. Antzutkin, and M. H. Levitt, *J. Am. Chem. Soc.*, 1997, **119**, 12006.
65. X. Feng, P. J. E. Verdegem, Y. K. Lee, D. Sandström, M. Edén, P. Bovee-Geurts, W. J. de Grip, J. Lugtenburg, H. J. M. de Groot, and M. H. Levitt, *J. Am. Chem. Soc.*, 1997, **119**, 6853.
66. M. Hong, J. D. Gross, C. M. Rienstra, R. G. Griffin, K. K. Kumashiro, and K. Schmidt-Rohr, *J. Magn. Reson.*, 1997, **129**, 85.
67. M. Hong, J. D. Gross, W. Hu, and R. G. Griffin, *J. Magn. Reson.*, 1998, **135**, 169.
68. B. Reif, M. Hohwy, C. P. Jaroniec, C. M. Rienstra, and R. G. Griffin, *J. Magn. Reson.*, 2000, **145**, 132.
69. C. M. Rienstra, M. Hohwy, L. J. Mueller, C. P. Jaroniec, B. Reif, and R. G. Griffin, *J. Am. Chem. Soc.*, 2002, **124**, 11908.
70. J. C. Lansing, M. Hohwy, C. P. Jaroniec, A. F. L. Creemers, J. Lugtenburg, J. Herzfeld, and R. G. Griffin, *Biochemistry*, 2002, **41**, 431.
71. V. Ladizhansky, M. Veshtort, and R. G. Griffin, *J. Magn. Reson.*, 2002, **154**, 317.
72. V. Ladizhansky, C. P. Jaroniec, A. Diehl, H. Oschkinat, and R. G. Griffin, *J. Am. Chem. Soc.*, 2003, **125**, 6827.
73. W. T. Franks, B. J. Wylie, S. A. Stellfox, and C. M. Rienstra, *J. Am. Chem. Soc.*, 2006, **128**, 3154.
74. W. T. Franks, B. J. Wylie, H. L. Schmidt, A. J. Nieuwkoop, R. M. Mayrhofer, G. J. Shah, D. T. Graesser, and C. M. Rienstra, *Proc. Natl. Acad. Sci. U S A*, 2008, **105**, 4621.
75. C. P. Jaroniec, B. A. Tounge, C. M. Rienstra, J. Herzfeld, and R. G. Griffin, *J. Am. Chem. Soc.*, 1999, **121**, 10237.
76. C. P. Jaroniec, B. A. Tounge, J. Herzfeld, and R. G. Griffin, *J. Am. Chem. Soc.*, 2001, **123**, 3507.
77. C. A. Michal and L. W. Jelinski, *J. Am. Chem. Soc.*, 1997, **119**, 9059.
78. C. P. Jaroniec, C. Filip, and R. G. Griffin, *J. Am. Chem. Soc.*, 2002, **124**, 10728.
79. J. J. Helmus, P. S. Nadaud, N. Hofer, and C. P. Jaroniec, *J. Chem. Phys.*, 2008, **128**, 052314.
80. A. W. Hing, S. Vega, and J. Schaefer, *J. Magn. Reson.*, 1992, **96**, 205.
81. T. Gullion, D. B. Baker, and M. S. Conradi, *J. Magn. Reson.*, 1990, **89**, 479.
82. T. Gullion and J. Schaefer, *J. Magn. Reson.*, 1991, **92**, 439.
83. A. Schmidt and S. Vega, *Isr. J. Chem.*, 1992, **32**, 215.
84. C. P. Jaroniec, B. A. Tounge, C. M. Rienstra, J. Herzfeld, and R. G. Griffin, *J. Magn. Reson.*, 2000, **146**, 132.
85. J. C. C. Chan and H. Eckert, *J. Magn. Reson.*, 2000, **147**, 170.
86. T. K. Weldeghiorghis and J. Schaefer, *J. Magn. Reson.*, 2003, **165**, 230.
87. N. Sinha, K. Schmidt-Rohr, and M. Hong, *J. Magn. Reson.*, 2004, **168**, 358.
88. M. E. Rose, '*Elementary Theory of Angular Momentum*', Wiley: New York, 1957.
89. J. J. Sakurai, '*Modern Quantum Mechanics*', Addison-Wesley: Redwood City, 1985.
90. T. G. Oas, R. G. Griffin, and M. H. Levitt, *J. Chem. Phys.*, 1988, **89**, 692.

91. M. H. Levitt, T. G. Oas, and R. G. Griffin, *Isr. J. Chem.*, 1988, **28**, 271.
92. U. Haeberlen and J. S. Waugh, *Phys. Rev.*, 1968, **175**, 453.
93. U. Haeberlen, '*High-Resolution NMR in Solids: Selective Averaging*', Academic Press: New York, 1976.
94. N. C. Nielsen, H. Bildsøe, H. J. Jakobsen, and M. H. Levitt, *J. Chem. Phys.*, 1994, **101**, 1805.
95. M. Bak, J. T. Rasmussen, and N. C. Nielsen, *J. Magn. Reson.*, 2000, **147**, 296.
96. K. Takegoshi, K. Takeda, and T. Terao, *Chem. Phys. Lett.*, 1996, **260**, 331.
97. R. Fu, S. A. Smith, and G. Bodenhausen, *Chem. Phys. Lett.*, 1997, **272**, 361.
98. Y. K. Lee, N. D. Kurur, M. Helmle, O. G. Johannessen, N. C. Nielsen, and M. H. Levitt, *Chem. Phys. Lett.*, 1995, **242**, 304.
99. A. Brinkmann, M. Eden, and M. H. Levitt, *J. Chem. Phys.*, 2000, **112**, 8539.
100. A. Brinkmann and M. H. Levitt, *J. Chem. Phys.*, 2001, **115**, 357.
101. M. H. Levitt, *J. Chem. Phys.*, 2008, **128**, 052205.
102. J. C. C. Chan, *Chem. Phys. Lett.*, 2001, **335**, 289.
103. A. E. Bennett, L. R. Becerra, and R. G. Griffin, *J. Chem. Phys.*, 1994, **100**, 812.
104. A. E. Bennett, C. M. Rienstra, P. T. Lansbury, and R. G. Griffin, *J. Chem. Phys.*, 1996, **105**, 10289.
105. T. Gullion and C. H. Pennington, *Chem. Phys. Lett.*, 1998, **290**, 88.
106. O. Liivak and D. B. Zax, *J. Chem. Phys.*, 2000, **113**, 1088.
107. O. Liivak and D. B. Zax, *J. Chem. Phys.*, 2001, **115**, 402.
108. J. Schaefer, *J. Magn. Reson.*, 1999, **137**, 272.
109. T. Gullion and S. Vega, *Chem. Phys. Lett.*, 1992, **194**, 423.
110. A. E. Bennett, J. H. Ok, R. G. Griffin, and S. Vega, *J. Chem. Phys.*, 1992, **96**, 8624.
111. C. M. Rienstra, L. Tucker-Kellogg, C. P. Jaroniec, M. Hohwy, B. Reif, T. Lozano-Perez, B. Tidor, and R. G. Griffin, *Proc. Natl. Acad. Sci. U S A*, 2002, **99**, 10260.
112. A. T. Petkova, Y. Ishii, J. J. Balbach, O. N. Antzutkin, R. D. Leapman, F. Delaglio, and R. Tycko, *Proc. Natl. Acad. Sci. U S A*, 2002, **99**, 16742.
113. L. B. Andreas, A. K. Mehta, and M. A. Mehta, *J. Am. Chem. Soc.*, 2007, **129**, 15233.
114. E. Gavuzzo, F. Mazza, G. Pochetti, and A. Scatturin, *Int. J. Pept. Protein Res.*, 1989, **34**, 409.
115. C. P. Jaroniec, J. C. Lansing, B. A. Tounge, M. Belenky, J. Herzfeld, and R. G. Griffin, *J. Am. Chem. Soc.*, 2001, **123**, 12929.
116. L. Kaustov, S. Kababya, V. Belakhov, T. Baasov, Y. Shoham, and A. Schmidt, *J. Am. Chem. Soc.*, 2003, **125**, 4662.
117. L. O. Essen, R. Siegert, W. D. Lehmann, and D. Oesterhelt, *Proc. Natl. Acad. Sci. U S A*, 1998, **95**, 11673.
118. H. Belrhali, P. Nollert, A. Royant, C. Menzel, J. P. Rosenbusch, E. M. Landau, and E. Pebay-Peyroula, *Structure*, 1999, **7**, 909.
119. H. Luecke, B. Schobert, H. T. Richter, J. Cartailler, and J. K. Lanyi, *J. Mol. Biol.*, 1999, **291**, 899.
120. E. R. H. van Eck and W. S. Veeman, *J. Magn. Reson. A*, 1994, **109**, 250.
121. A. W. Hing, S. Vega, and J. Schaefer, *J. Magn. Reson. A*, 1993, **103**, 151.
122. L. Chen, R. A. Olsen, D. W. Elliott, J. M. Boettcher, D. H. Zhou, C. M. Rienstra, and L. J. Mueller, *J. Am. Chem. Soc.*, 2006, **128**, 9992.
123. K. T. Mueller, *J. Magn. Reson. A*, 1995, **113**, 81.
124. C. P. Jaroniec, C. E. MacPhee, N. S. Astrof, C. M. Dobson, and R. G. Griffin, *Proc. Natl. Acad. Sci. U S A*, 2002, **99**, 16748.
125. C. P. Jaroniec, C. E. MacPhee, V. S. Bajaj, M. T. McMahon, C. M. Dobson, and R. G. Griffin, *Proc. Natl. Acad. Sci. U S A*, 2004, **101**, 711.
126. D. M. LeMaster and D. M. Kushlan, *J. Am. Chem. Soc.*, 1996, **118**, 9255.
127. F. Castellani, B. van Rossum, A. Diehl, M. Schubert, K. Rehbein, and H. Oschkinat, *Nature*, 2002, **420**, 98.
128. A. J. Nieuwkoop, B. J. Wylie, W. T. Franks, G. J. Shah, and C. M. Rienstra, *J. Chem. Phys.*, 2009, submitted.
129. T. Gallagher, P. Alexander, P. Bryan, and G. L. Gilliland, *Biochemistry*, 1994, **33**, 4721.

Chapter 12
Dipolar Recoupling: Homonuclear

Robert Tycko

Laboratory of Chemical Physics, National Institute of Diabetes and Digestive and Kidney Diseases, National Institutes of Health, Bethesda, MD 20892-0520, USA

12.1 Introduction 163
12.2 Theoretical Background and Notation 163
12.3 Dipolar Recoupling by RF Pulses Alone 165
12.4 Chemical-Shift-Dependent Dipolar Recoupling 168
12.5 Symmetry Principles in Homonuclear Dipolar Recoupling 170
12.6 Frequency-Selective Homonuclear Dipolar Recoupling 171
12.7 Other Recent Developments 173
References 175

12.1 INTRODUCTION

In high field, nuclear magnetic dipole–dipole couplings are averaged to zero by magic-angle spinning (MAS). Since dipole–dipole couplings are valuable structural parameters, techniques for restoring these couplings under MAS have been a subject of active research since the late 1980s. Such techniques, which take the form of RF pulse sequences that are applied in synchrony with sample rotation, are called *dipolar recoupling* techniques. This article focuses on recoupling techniques for homonuclear dipole–dipole couplings, i.e., couplings between like nuclei (e.g., ^{13}C–^{13}C couplings).

Dipolar recoupling techniques are commonly used for at least three purposes. First, dipolar recoupling techniques permit quantitative measurements of coupling constants and hence internuclear distances. Second, dipolar recoupling techniques can be applied during the mixing periods of two-dimensional or multidimensional pulse sequences to permit dipole-driven spin polarization transfers that produce crosspeak signals. Third, dipolar recoupling techniques can be used to excite double-quantum or multiple-quantum coherences, e.g., for double-quantum or multiple-quantum filtering.

This article is not intended as an exhaustive review of homonuclear dipolar recoupling techniques and their applications. Instead, the goal is to introduce and briefly explain a limited number of key concepts. In the following sections, several distinct recoupling mechanisms are discussed and illustrated by specific recoupling sequences. Symmetry principles that have been used to guide the development of recoupling techniques are briefly reviewed. Finally, recent developments in frequency-selective recoupling, stochastic recoupling, and three-spin recoupling are discussed.

12.2 THEORETICAL BACKGROUND AND NOTATION

Consider a nuclear spin Hamiltonian in the usual rotating frame that contains terms describing

NMR Crystallography Edited by Robin K. Harris, Roderick E. Wasylishen and Melinda J. Duer © 2009 John Wiley & Sons, Ltd. ISBN: 978-0-470-69961-4

interactions with applied RF fields, homonuclear dipole–dipole couplings, and both anisotropic and isotropic chemical shifts:

$$H(t) = H_{\mathrm{RF}}(t) + H_{\mathrm{D}}(t) + H_{\mathrm{CSA}}(t) + H_{\mathrm{iso}} \quad (12.1)$$

All Hamiltonian terms are expressed in angular frequency units in this chapter.

Under MAS, the dipole–dipole coupling oscillates at the MAS angular frequency ω_{r} and at $2\omega_{\mathrm{r}}$:

$$\begin{aligned} H_{\mathrm{D}}(t) = [&A(\alpha,\beta)\cos(\omega_{\mathrm{r}}t+\gamma) \\ &+ B(\alpha,\beta)\sin(\omega_{\mathrm{r}}t+\gamma) \\ &+ C(\alpha,\beta)\cos(2\omega_{\mathrm{r}}t+2\gamma) \\ &+ D(\alpha,\beta)\sin(2\omega_{\mathrm{r}}t+2\gamma)] \\ &\times (3I_{z1}I_{z2} - \boldsymbol{I}_1\cdot\boldsymbol{I}_2) \end{aligned} \quad (12.2)$$

In equation (12.2), $\boldsymbol{I}_1$ and $\boldsymbol{I}_2$ are spin angular components for two dipole–coupled nuclei. The angles α, β, and γ are Euler angles that describe the orientation of the molecule or crystallite containing these nuclei relative to the MAS rotor, with γ being the angle about the rotor's rotation axis. The factors A–D contain the dependence on the dipolar coupling constant and crystallite orientation but should not be confused with the "dipolar alphabet", i.e., the components of the full dipolar coupling Hamiltonian, which are often labelled A–F. Explicit expressions for $H_{\mathrm{D}}(t)$ can be found elsewhere.[1] Clearly, the time average of $H_{\mathrm{D}}(t)$ over one rotation period τ_{r} is zero. The chemical shift anisotropy (CSA) has a similar time dependence and also averages to zero:

$$\begin{aligned} H_{\mathrm{CSA}}(t) = [&A'(\alpha,\beta)\cos(\omega_{\mathrm{r}}t+\gamma) \\ &+ B'(\alpha,\beta)\sin(\omega_{\mathrm{r}}t+\gamma) \\ &+ C'(\alpha,\beta)\cos(2\omega_{\mathrm{r}}t+2\gamma) \\ &+ D'(\alpha,\beta)\sin(2\omega_{\mathrm{r}}t+2\gamma)]I_z \end{aligned} \quad (12.3)$$

with coefficients A', B', C', and D' also being functions of molecule or crystallite orientation. The isotropic chemical shift is contained in $H_{\mathrm{iso}} = \omega_I I_z$, independent of time and orientation. In systems of two or more spins, the Hamiltonian contains terms as in equations (12.2) and (12.3) for each spin. The RF term has the form

$$H_{\mathrm{RF}}(t) = \omega_1(t)[I_x\cos\phi(t) + I_y\sin\phi(t)] \quad (12.4)$$

with the RF amplitude $\omega_1(t)$ and phase $\phi(t)$ having time dependences that are under experimental control.

Dipolar recoupling techniques are generally developed and analyzed with average Hamiltonian theory[2] (AHT), which is applicable under MAS when $H_{\mathrm{RF}}(t)$ is periodic with period $\tau = k\tau_{\mathrm{r}}$, with k being an integer, and when $U_{\mathrm{RF}}(\tau) = 1$. $U_{\mathrm{RF}}(t)$ is the net rotation of spin angular momenta produced by the RF pulses up to time t:

$$\begin{aligned} U_{\mathrm{RF}}(t) = \vec{T}\exp\Bigg\{-\mathrm{i}\int_0^t \mathrm{d}t'\omega_1(t')\big[&I_x\cos\phi(t') \\ &+ I_y\sin\phi(t')\big]\Bigg\} \end{aligned} \quad (12.5)$$

where $\vec{T}$ is the time-ordering operator. In an interaction representation with respect to $H_{\mathrm{RF}}(t)$, the spin Hamiltonian becomes

$$\tilde{H}(t) = \tilde{H}_{\mathrm{D}}(t) + \tilde{H}_{\mathrm{CSA}}(t) + \tilde{H}_{\mathrm{iso}} \quad (12.6)$$

with

$$\tilde{H}_{\mathrm{D}}(t) = U_{\mathrm{RF}}(t)^{-1}H_{\mathrm{D}}(t)U_{\mathrm{RF}}(t) \quad (12.7)$$

$$\tilde{H}_{\mathrm{CSA}}(t) = U_{\mathrm{RF}}(t)^{-1}H_{\mathrm{CSA}}(t)U_{\mathrm{RF}}(t) \quad (12.8)$$

$$\tilde{H}_{\mathrm{iso}} = U_{\mathrm{RF}}(t)^{-1}H_{\mathrm{iso}}U_{\mathrm{RF}}(t) \quad (12.9)$$

$U_{\mathrm{RF}}(t)^{-1}$ acts on the spin angular momentum operators in $H_{\mathrm{D}}(t)$, $H_{\mathrm{CSA}}(t)$, and $H_{\mathrm{iso}}(t)$, making them time dependent with period τ. In recoupling techniques, the time dependence of the spin operators induced by the RF pulses interferes with the spatial time dependence from MAS (which is also periodic with τ), in general preventing $\tilde{H}_{\mathrm{D}}(t)$ and/or $\tilde{H}_{\mathrm{CSA}}(t)$ from averaging to zero (for dipolar recoupling and/or CSA recoupling). The overall evolution operator is

$$\begin{aligned} U(t) = U_{\mathrm{RF}}(t)\vec{T}\exp\Bigg\{-\mathrm{i}\int_0^t \mathrm{d}t'\big[&\tilde{H}_{\mathrm{D}}(t') \\ &+ \tilde{H}_{\mathrm{CSA}}(t') + \tilde{H}_{\mathrm{iso}}(t')\big]\Bigg\} \end{aligned} \quad (12.10)$$

which becomes

$$\begin{aligned} U(n\tau) = \Bigg[\vec{T}\exp\Bigg\{-\mathrm{i}\int_0^\tau \mathrm{d}t'\big[&\tilde{H}_{\mathrm{D}}(t') + \tilde{H}_{\mathrm{CSA}}(t') \\ &+ \tilde{H}_{\mathrm{iso}}(t')\big]\Bigg\}\Bigg]^n \end{aligned} \quad (12.11)$$

at multiples of the period.

If all Hamiltonian terms in equation (12.11) are sufficiently small compared with ω_{r}, then the time-ordering operator becomes unimportant and the overall evolution operator is determined to a good

approximation by the average Hamiltonian:

$$U(n\tau) = \exp\left\{-\mathrm{i}\left[\frac{1}{\tau}\int_0^{\tau} \mathrm{d}t'\left[\tilde{H}_{\mathrm{D}}(t') + \tilde{H}_{\mathrm{CSA}}(t') + \tilde{H}_{\mathrm{iso}}(t')\right]\right]n\tau\right\} \tag{12.12}$$

Dipolar recoupling sequences are then designed to make the time averages of $\tilde{H}_{\mathrm{CSA}}(t)$ and $\tilde{H}_{\mathrm{iso}}(t)$ zero, but the time average of $\tilde{H}_{\mathrm{D}}(t)$ nonzero.

Alternatively, if $\tilde{H}_{\mathrm{CSA}}(t)$ and $\tilde{H}_{\mathrm{iso}}(t)$ are not sufficiently small, one can transform to a second interaction representation with respect to these terms, in which the dipole–dipole coupling becomes

$$\tilde{\tilde{H}}_{\mathrm{D}}(t) = U_{\mathrm{CS}}(t)^{-1}\tilde{H}_{\mathrm{D}}(t)U_{\mathrm{CS}}(t) \tag{12.13}$$

with

$$U_{\mathrm{CS}}(t) = \exp\left\{-\mathrm{i}\int_0^{t} \mathrm{d}t'\left[\tilde{H}_{\mathrm{CSA}}(t') + \tilde{H}_{\mathrm{iso}}(t')\right]\right\} \tag{12.14}$$

Dipolar recoupling is then determined by the time average of $\tilde{\tilde{H}}_{\mathrm{D}}(t)$.

12.3 DIPOLAR RECOUPLING BY RF PULSES ALONE

12.3.1 Delta-Function Pulses

A simple illustrative example of homonuclear dipolar recoupling is provided by the DRAMA (dipolar recovery at the magic angle) sequence[3] shown in Figure 12.1(a). DRAMA works in the delta-function pulse limit, i.e., when RF pulse lengths are negligible compared with τ_{r}. In this limit, rotations induced by the RF pulses are considered to be instantaneous, making $U_{\mathrm{RF}}(t)$ a piecewise-constant operator. Over the period $2\tau_{\mathrm{r}}$, it can be readily shown that $\tilde{H}_{\mathrm{CSA}}(t)$ and $\tilde{H}_{\mathrm{iso}}(t)$ average to zero, and the average dipole–dipole coupling is

$$\begin{aligned}\tilde{H}_{\mathrm{D,ave}} = 3(I_{y1}I_{y2} - I_{z1}I_{z2}) &\times \left\{\frac{A}{2\pi}[\sin(\omega_{\mathrm{r}}\tau_2 + \gamma) - \sin(\omega_{\mathrm{r}}\tau_1 + \gamma)]\right.\\ &- \frac{B}{2\pi}[\cos(\omega_{\mathrm{r}}\tau_2 + \gamma) - \cos(\omega_{\mathrm{r}}\tau_1 + \gamma)]\\ &+ \frac{C}{4\pi}[\sin(2\omega_{\mathrm{r}}\tau_2 + 2\gamma)\\ &- \sin(2\omega_{\mathrm{r}}\tau_1 + 2\gamma)]\\ &- \frac{D}{4\pi}[\cos(2\omega_{\mathrm{r}}\tau_2 + 2\gamma)\\ &\left.- \cos(2\omega_{\mathrm{r}}\tau_1 + 2\gamma)]\right\}\end{aligned} \tag{12.15}$$

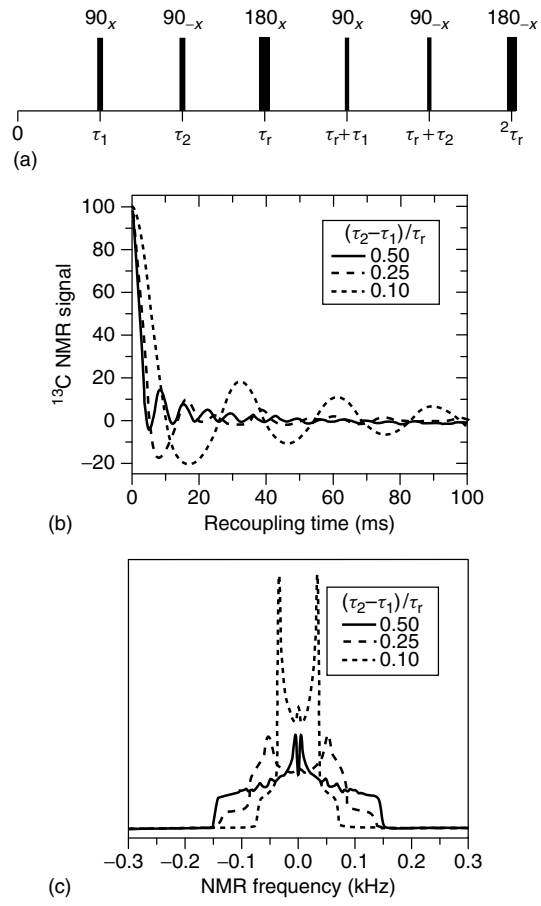


Figure 12.1. (a) RF pulse sequence for DRAMA recoupling. (b) Simulated time-domain signals under DRAMA recoupling for several values of the spacing between $\pi/2$ pulses as a fraction of the MAS rotor period. Simulations assume a pair of ^{13}C nuclei with a 2.60 Å separation, no chemical shifts, and $\tau_{\mathrm{r}} = 100$ μs, and are orientationally averaged. (c) Dipolar powder patterns, obtained by Fourier transformation of the time-domain signals.

Equation (12.15) illustrates several general features of dipolar recoupling. First, $\tilde{H}_{\mathrm{D,ave}}$ is proportional to the spin operator $(I_{y1}I_{y2} - I_{z1}I_{z2})$, which contains both double-quantum and zero-quantum terms. In contrast, the original coupling H_{D} is proportional to

the spin operator $(3I_{z1}I_{z2} - \boldsymbol{I}_1 \cdot \boldsymbol{I}_2)$, which contains only zero-quantum terms. Dipole–dipole couplings created by recoupling techniques can contain zero-quantum, single-quantum, or double-quantum terms, depending on the details of the technique. Second, the orientation dependence of $\tilde{H}_{\mathrm{D,ave}}$ is different from the dependence $A(\alpha,\beta)\cos\gamma + B(\alpha,\beta)\sin\gamma + C(\alpha,\beta)\cos 2\gamma + D(\alpha,\beta)\sin 2\gamma$ for the dipole–dipole coupling in a static sample (obtained from equation (12.2) by setting ω_r to zero). Therefore, dipolar powder pattern lineshapes recorded with dipolar recoupling techniques (or the corresponding time-domain signals before Fourier transformation) are generally different from the standard Pake patterns observed in static samples.[4,5] Under DRAMA, the powder pattern lineshape for a pair of coupled spin-1/2 nuclei approaches a Pake pattern in the limit $\omega_\mathrm{r}(\tau_2 - \tau_1) \ll 1$. Outside this limit, the lineshape depends on the spacing between $\pi/2$ pulses. Third, the dipolar scaling factor, i.e., the magnitude of the recoupled dipole–dipole interaction, depends on the details of the recoupling sequence. For DRAMA, the scaling factor is smallest when $\omega_\mathrm{r}(\tau_2 - \tau_1)$ is small and largest when $\omega_\mathrm{r}(\tau_2 - \tau_1) = \pi$. Figure 12.1(b) and (c) shows simulated time-domain signals and lineshapes for several values of $\omega_\mathrm{r}(\tau_2 - \tau_1)$.

12.3.2 Finite Pulses

Figure 12.2(a) shows a recoupling sequence with $\tau = 4\tau_\mathrm{r}$ that consists of one π pulse per rotor period, originally called *SEDRA*[6] (*simple excitation for the dephasing of rotational echo amplitudes*) or *RFDR*[7,8] (RF-*driven recoupling*) and originally analyzed in the delta-function pulse limit, where the recoupling effect depends on chemical shift differences (see below). When isotropic and anisotropic chemical shift differences are small, this sequence still produces dipolar recoupling (but no chemical shift or CSA recoupling) when the pulse lengths are a significant fraction of τ_r. The recoupling effect then depends on the time dependence of $\tilde{H}_\mathrm{D}(t)$ during the pulses themselves.[9] For RFDR in this finite-pulse limit (i.e., fpRFDR), it can be shown that

$$\begin{aligned}\tilde{H}_{\mathrm{D,ave}} = \Bigg\{ & \frac{3(\omega_\mathrm{r}^2 + 4\omega_1^2)}{16\pi(\omega_\mathrm{r}^2 - 4\omega_1^2)}[\sin(\omega_\mathrm{r}\tau_\mathrm{p} + \gamma) - \sin\gamma]A \\ & - \frac{3(\omega_\mathrm{r}^2 + 4\omega_1^2)}{16\pi(\omega_\mathrm{r}^2 - 4\omega_1^2)}[\cos(\omega_\mathrm{r}\tau_\mathrm{p} + \gamma) \\ & - \cos\gamma]B + \frac{3(\omega_\mathrm{r}^2 + \omega_1^2)}{16\pi(\omega_\mathrm{r}^2 - \omega_1^2)} \\ & \times [\sin(2\omega_\mathrm{r}\tau_\mathrm{p} + 2\gamma) - \sin 2\gamma]C \\ & - \frac{3(\omega_\mathrm{r}^2 + \omega_1^2)}{16\pi(\omega_\mathrm{r}^2 - \omega_1^2)}[\cos(2\omega_\mathrm{r}\tau_\mathrm{p} + 2\gamma) \\ & - \cos 2\gamma]D \Bigg\} [3I_{z1}I_{z2} - \boldsymbol{I}_1 \cdot \boldsymbol{I}_2] \end{aligned} \tag{12.16}$$

where τ_p is the π pulse length and $\omega_1 = 1/2\tau_\mathrm{p}$. Figure 12.2(b) and (c) shows simulated time-domain signals and lineshapes for several values of $\omega_\mathrm{r}\tau_\mathrm{p}$. Again, the scaling factor and lineshape depend on the details, with the lineshape approaching a Pake pattern when $\omega_\mathrm{r}\tau_\mathrm{p} \ll 1$.

A useful feature of fpRFDR is the fact that $\tilde{H}_{\mathrm{D,ave}}$ is proportional to $(3I_{z1}I_{z2} - \boldsymbol{I}_1 \cdot \boldsymbol{I}_2)$, as for a static sample. This allows techniques developed for homonuclear dipole-coupled spin systems in static solids to be adapted to MAS experiments, including time-reversal-based multiple-quantum spectroscopy[10] and homonuclear decoupling.[11] This operator form also permits sensitivity-enhanced two-dimensional solid-state NMR with transverse mixing.[12]

12.3.3 Continuous RF Irradiation

Figure 12.3(a) shows the 2Q-HORROR[13] (double-quantum homonuclear rotary resonance) homonuclear dipolar recoupling sequence, which consists of a block of continuous RF irradiation at $\omega_1 = \omega_\mathrm{r}/2$ for an even number of rotor periods, sandwiched between phase-shifted delta-function $\pi/2$ pulses. This sequence averages isotropic and anisotropic chemical shifts to zero, and produces

$$\begin{aligned}\tilde{H}_{\mathrm{D,ave}} = \frac{3}{8}\big[& (I_{+1}I_{+2} + I_{-1}I_{-2})(A\cos\gamma + B\sin\gamma) \\ & + i(I_{+1}I_{+2} - I_{-1}I_{-2})(-A\sin\gamma + B\cos\gamma)\big] \end{aligned} \tag{12.17}$$

where $I_\pm = I_x \pm \mathrm{i}I_y$ as usual. Equation (12.17) shows that 2Q-HORROR produces pure double-quantum recoupling, with the interesting feature that the magnitude of the recoupled interaction is proportional to $(A^2 + B^2)^{1/2}$ and hence is independent of γ. Recoupling sequences with this property are called γ-*encoded*. The relatively simple orientation dependence produced by γ-encoded recoupling

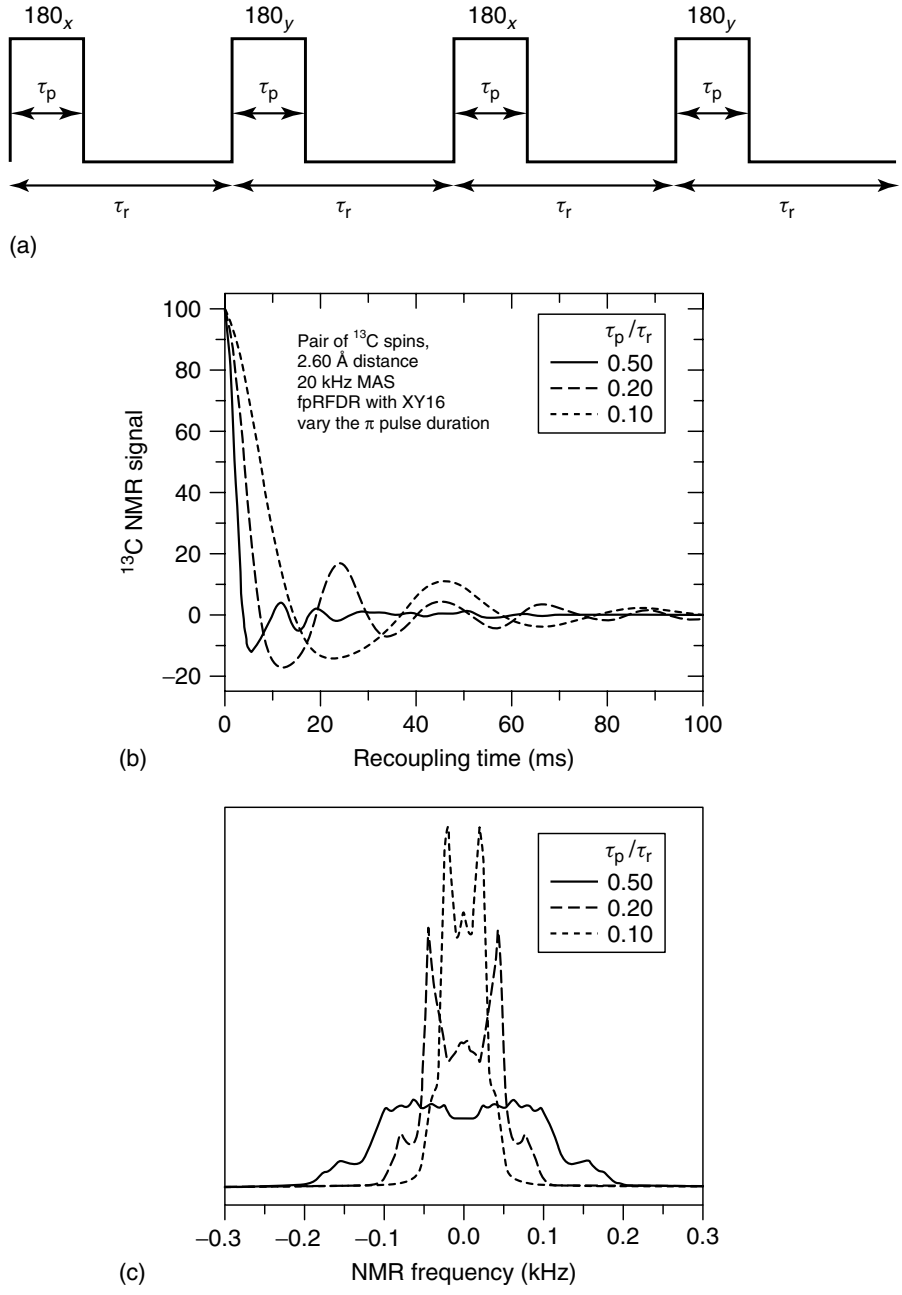


Figure 12.2. (a) RF pulse sequence for fpRFDR recoupling. (b,c) Simulated time-domain signals and dipolar powder patterns for several values of the π pulse duration as a fraction of the MAS rotor period. Simulations assume a pair of ^{13}C nuclei with a 2.60 Å separation, no chemical shifts, and $\tau_r = 50$ μs, and are orientationally averaged.

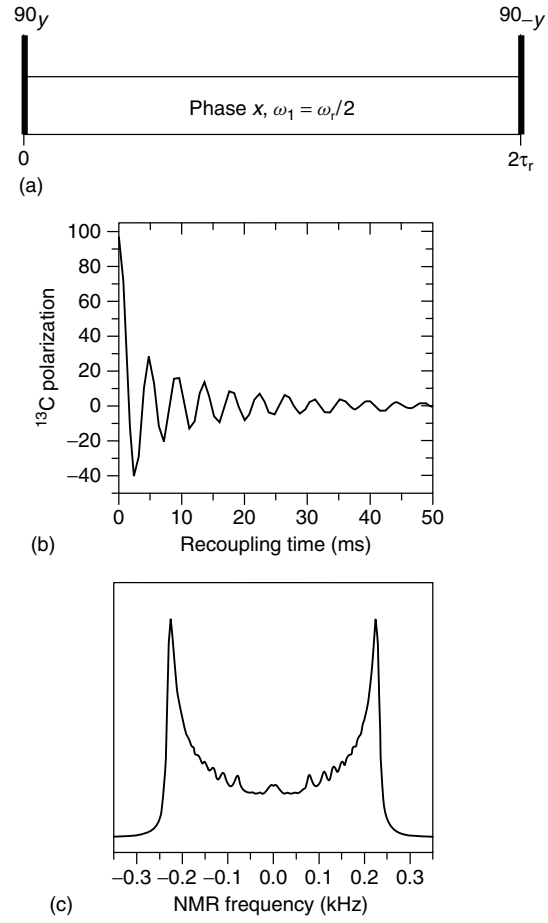


Figure 12.3. (a) RF pulse sequence for 2Q-HORROR recoupling. (b) Simulated time dependence of longitudinal spin polarization under 2Q-HORROR recoupling, assuming a pair of ^{13}C nuclei with a 2.60 Å separation, no chemical shifts, and $\tau_r = 100$ μs. (c) Dipolar powder pattern, obtained by Fourier transformation of the time dependence in part (b).

sequences leads to a powder pattern with sharp "horns", corresponding to a time-domain signal with strong oscillations, as shown in Figure 12.3(b). The strong oscillations can produce high double-quantum filtering efficiencies and can facilitate precise measurements of internuclear distances.

A gradual increase or decrease of the RF amplitude through the condition $\omega_1 = \omega_r/2$ can produce efficient spin polarization transfers by an adiabatic mechanism. The DREAM[14] (dipolar recoupling enhanced by amplitude modulation) technique takes advantage of this effect.

12.4 CHEMICAL-SHIFT-DEPENDENT DIPOLAR RECOUPLING

12.4.1 Rotational Resonance

Recoupling techniques described above average isotropic and anisotropic chemical shifts to zero, but only to lowest order. When isotropic shift differences or CSA are not small compared with ω_r, as is often the case, the performance of homonuclear dipolar recoupling techniques can be severely degraded by higher order chemical shift effects, preventing distance measurements, reducing double-quantum filtering efficiencies, and attenuating crosspeaks in multidimensional spectra. The development of recoupling sequences that are compatible with high-speed MAS or are less sensitive to chemical shifts for other reasons is therefore a recurring theme.

Alternatively, recoupling sequences that rely explicitly on chemical shift differences can be employed. The simplest example is the rotational resonance effect,[15,16] in which spin pairs are recoupled in the absence of RF pulses when their difference in isotropic chemical shifts is an integral multiple of ω_r. As discussed above, when chemical shifts are large, it is productive to view dipole–dipole couplings in an interaction representation with respect to the chemical shifts. For a pair of spins and without RF pulses, equation (12.14) becomes

$$\begin{aligned} U_{CS}(t) = \exp\left\{-\frac{i}{2}\int_0^t dt' H_{CSA-}(t')\right\} \\ \times \exp\left\{-\frac{i}{2}\int_0^t dt' H_{CSA+}(t')\right\} \\ \times \exp\left\{-\frac{i}{2}\Delta_{12}(I_{z1} - I_{z2})t\right\} \\ \times \exp\left\{-\frac{i}{2}\Sigma_{12}(I_{z1} + I_{z2})t\right\} \end{aligned} \tag{12.18}$$

with $\Delta_{12} = \omega_{I1} - \omega_{I2}$, $\Sigma_{12} = \omega_{I1} + \omega_{I2}$, and

$$\begin{aligned} H_{CSA\pm}(t) = \big[&(A'_1 \pm A'_2)\cos(\omega_r t + \gamma) \\ &+ (B'_1 \pm B'_2)\sin(\omega_r t + \gamma) \\ &+ (C'_1 \pm C'_2)\cos(2\omega_r t + 2\gamma) \\ &+ (D'_1 \pm D'_2)\sin(2\omega_r t + 2\gamma)\big] \\ &\times (I_{z1} \pm I_{z2}) \end{aligned} \tag{12.19}$$

and equation (12.13) becomes

$$\begin{aligned}\tilde{\tilde{H}}_{\mathrm{D}}(t) = \exp\left\{\frac{\mathrm{i}}{2}\int_0^t \mathrm{d}t' H_{\mathrm{CSA}-}(t')\right\} \\ \times \exp\left\{\frac{\mathrm{i}}{2}\Delta_{12}(I_{z1}-I_{z2})t\right\} H_{\mathrm{D}}(t) \\ \times \exp\left\{-\frac{\mathrm{i}}{2}\Delta_{12}(I_{z1}-I_{z2})t\right\} \\ \times \exp\left\{-\frac{\mathrm{i}}{2}\int_0^t \mathrm{d}t' H_{\mathrm{CSA}-}(t')\right\}\end{aligned} \tag{12.20}$$

Note that chemical shift terms proportional to $I_{z1}+I_{z2}$ commute with $H_{\mathrm{D}}(t)$ and therefore vanish from equation (12.20). The remaining terms commute with the $I_{z1}I_{z2}$ terms in $H_{\mathrm{D}}(t)$, which are therefore not recoupled. When $\Delta_{12} = n\omega_{\mathrm{r}}$, the average Hamiltonian becomes

$$\begin{aligned}\tilde{\tilde{H}}_{\mathrm{D,ave}} = \frac{1}{\tau_{\mathrm{r}}}\int_0^{\tau_{\mathrm{r}}} \mathrm{d}t\big[A\cos(\omega_{\mathrm{r}}t+\gamma) \\ + B\sin(\omega_{\mathrm{r}}t+\gamma) + C\cos(2\omega_{\mathrm{r}}t+2\gamma) \\ + D\sin(2\omega_{\mathrm{r}}t+2\gamma)\big] \\ \times \exp\left\{\frac{\mathrm{i}}{2}\int_0^t \mathrm{d}t' H_{\mathrm{CSA}-}(t')\right\} \\ \times \exp\left\{\frac{\mathrm{i}}{2}\Delta_{12}(I_{z1}-I_{z2})t\right\} \\ \times (I_{x1}I_{x2}+I_{y1}I_{y2}) \\ \times \exp\left\{-\frac{\mathrm{i}}{2}\Delta_{12}(I_{z1}-I_{z2})t\right\} \\ \times \exp\left\{-\frac{\mathrm{i}}{2}\int_0^t \mathrm{d}t' H_{\mathrm{CSA}-}(t')\right\}\end{aligned} \tag{12.21}$$

Considering only isotropic shifts, equation (12.21) yields

$$\begin{aligned}\tilde{\tilde{H}}_{\mathrm{D,ave}} = -\tfrac{1}{4}[(A+\mathrm{i}B)\mathrm{e}^{-\mathrm{i}\gamma}\delta_{1,n} \\ + (C+\mathrm{i}D)\mathrm{e}^{-2\mathrm{i}\gamma}\delta_{2,n}]I_{+1}I_{-2} \\ - \tfrac{1}{4}[(A-\mathrm{i}B)\mathrm{e}^{\mathrm{i}\gamma}\delta_{1,n} \\ + (C-\mathrm{i}D)\mathrm{e}^{2\mathrm{i}\gamma}\delta_{2,n}]I_{-1}I_{+2}\end{aligned} \tag{12.22}$$

so that rotational resonance recoupling occurs only at $n = 1$ and $n = 2$. CSA differences produce higher Fourier components in the interaction representation, leading to higher order rotational resonances.[17]

Equation (12.22) depends on the relation

$$\begin{aligned}\exp\{\mathrm{i}(I_{z1}-I_{z2})\theta\}(I_{x1}I_{x2}+I_{y1}I_{y2}) \\ \times \exp\{-\mathrm{i}(I_{z1}-I_{z2})\theta\} \\ = \frac{1}{2}\left(\mathrm{e}^{2\mathrm{i}\theta}I_{+1}I_{-2} + \mathrm{e}^{-2\mathrm{i}\theta}I_{-1}I_{+2}\right)\end{aligned} \tag{12.23}$$

which shows that chemical shift differences modulate the "flip-flop" operators in $H_{\mathrm{D}}(t)$, and therefore recouple only the flip-flop terms. The resulting average Hamiltonian in equation (12.22) is a zero-quantum coupling, but is not the same as the zero-quantum coupling in equation (12.16).

12.4.2 Delta-Function RFDR/SEDRA

Rotational resonance conditions can be broadened significantly by trains of π pulses that are synchronized with MAS, as in Figure 12.2(a). In the delta-function pulse limit, π pulses separated by $m\tau_{\mathrm{r}}$ have no direct effect on $H_{\mathrm{D}}(t)$ but transform $H_{\mathrm{CSA}}(t)$ and H_{iso} to

$$\begin{aligned}\tilde{H}_{\mathrm{CSA}}(t) + \tilde{H}_{\mathrm{iso}}(t) = -H_{\mathrm{CSA}}(t) - H_{\mathrm{iso}}(t) \\ \text{for } 0 < t < m\tau_{\mathrm{r}} \\ = H_{\mathrm{CSA}}(t) + H_{\mathrm{iso}}(t) \\ \text{for } m\tau_{\mathrm{r}} < t < 2m\tau_{\mathrm{r}}\end{aligned} \tag{12.24}$$

Equation (12.20) then becomes

$$\begin{aligned}\tilde{\tilde{H}}_{\mathrm{D}}(t) = \exp\left\{-\frac{\mathrm{i}}{2}\int_0^t \mathrm{d}t' H_{\mathrm{CSA}-}(t')\right\} \\ \times \exp\left\{-\frac{\mathrm{i}}{2}\Delta_{12}(I_{z1}-I_{z2})t\right\} H_{\mathrm{D}}(t) \\ \times \exp\left\{\frac{\mathrm{i}}{2}\Delta_{12}(I_{z1}-I_{z2})t\right\} \\ \times \exp\left\{\frac{\mathrm{i}}{2}\int_0^t \mathrm{d}t' H_{\mathrm{CSA}-}(t')\right\}, \\ \text{for } 0 < t < m\tau_{\mathrm{r}} \\ \exp\left\{-\frac{\mathrm{i}}{2}\int_{t-m\tau_{\mathrm{r}}}^{m\tau_{\mathrm{r}}} \mathrm{d}t' H_{\mathrm{CSA}-}(t')\right\} \\ \times \exp\left\{-\frac{\mathrm{i}}{2}\Delta_{12}(I_{z1}-I_{z2}) \right. \\ \left. \times\ (2m\tau_{\mathrm{r}}-t)\right\} H_{\mathrm{D}}(t) \\ \times \exp\left\{\frac{\mathrm{i}}{2}\Delta_{12}(I_{z1}-I_{z2})(2m\tau_{\mathrm{r}}-t)\right\} \\ \times \exp\left\{\frac{\mathrm{i}}{2}\int_{t-m\tau_{\mathrm{r}}}^{m\tau_{\mathrm{r}}} \mathrm{d}t' H_{\mathrm{CSA}-}(t')\right\}, \\ \text{for } m\tau_{\mathrm{r}} < t < 2m\tau_{\mathrm{r}}\end{aligned} \tag{12.25}$$

Equation (12.25) shows that $\tilde{\tilde{H}}_{\mathrm{D}}(t)$ is periodic with period $2m\tau_{\mathrm{r}}$ regardless of the chemical shift difference Δ_{12}. The same is not true in equation (12.20). Therefore, the rotor-synchronized π pulse train leads to a nonzero $\tilde{\tilde{H}}_{\mathrm{D,ave}}$ for nearly any value of Δ_{12}. Considering only isotropic chemical shifts,

$$\begin{aligned}\tilde{\tilde{H}}_{\mathrm{D,ave}} = \Bigg(& -\frac{\Delta_{12}\sin(m\Delta_{12}\tau_{\mathrm{r}}/2)}{m\tau_{\mathrm{r}}(\omega_{\mathrm{r}}^2-\Delta_{12}^2)}(A\cos\gamma + B\sin\gamma) \\ & -\frac{\Delta_{12}\sin(m\Delta_{12}\tau_{\mathrm{r}}/2)}{m\tau_{\mathrm{r}}(4\omega_{\mathrm{r}}^2-\Delta_{12}^2)} \\ & \times (C\cos 2\gamma + D\sin 2\gamma)\Bigg) \\ & \times [\exp(-\mathrm{i}m\Delta_{12}\tau_{\mathrm{r}}/2)I_{+1}I_{-2} \\ & + \exp(\mathrm{i}m\Delta_{12}\tau_{\mathrm{r}}/2)I_{-1}I_{+2}] \end{aligned} \tag{12.26}$$

Because π trains produce homonuclear dipolar recoupling in both the delta-function limit and the finite-pulse limit (by two distinct mechanisms), the SEDRA/RFDR/fpRFDR technique is one of the more robust recoupling techniques, effective over wide ranges of chemical shifts and MAS frequencies. In experiments, the phases of the π pulses are usually chosen to follow an XY-4 or higher XY-*n* phase pattern, because XY-*n* phase patterns compensate for RF inhomogeneity, resonance offsets, and other pulse imperfections.[18]

12.5 SYMMETRY PRINCIPLES IN HOMONUCLEAR DIPOLAR RECOUPLING

12.5.1 Levitt's *C* and *R* Sequences

Levitt and coworkers have developed an approach to the development of recoupling sequences that relies on general symmetry properties of pulse sequences, leading to selection rules that reveal which types of interactions can be recoupled by a sequence with a given symmetry. Two classes of symmetry-based sequences have been described: (i) "*C*" sequences are comprised of RF blocks (called *C elements*) that produce no net rotation of spin angular momenta.[19,20] The *C* element is repeated N times in n rotor periods, with overall RF phase shifts that increase in units of $\phi = 2\pi\nu/N$, where N, n, and ν are positive integers. The symmetry is represented by the symbol CN_n^{ν}; (ii) "*R*" sequences are comprised of RF blocks (called *R elements*) that produce a net rotation by π around x in the rotating frame.[21] The *R* element is repeated an even number N times in n rotor periods, alternating between an R_{ϕ} version and a $R'_{-\phi}$ version. For the R_{ϕ} version, all RF pulses in the *R* element are phase-shifted by $\phi = \pi\nu/N$. For the $R'_{-\phi}$ version, all RF pulses in the *R* element are first reversed in sign, then phase-shifted by $-\phi$. The symmetry is represented by the symbol RN_n^{ν}.

Selection rules are derived by considering a rotating-frame spin Hamiltonian under MAS that is a sum of terms of the form $H_{m\lambda 0}(t) = A_m \mathrm{e}^{\mathrm{i}m\omega_{\mathrm{r}}t}T_{\lambda 0}$. A_m is a function of the Euler angles α, β, γ discussed above; m is -2, -1, 1, or 2. $T_{\lambda 0}$ is an irreducible tensor operator element of rank λ, i.e., one member of a set of $2\lambda+1$ operators $T_{\lambda\mu}$ that transform among themselves under rotations, with $\mu = -\lambda, -\lambda+1, \ldots, \lambda-1, \lambda$. For dipole–dipole couplings, $\lambda = 2$; for chemical shifts, $\lambda = 1$. Leaving aside most mathematical details, one evaluates the average Hamiltonian for a *C* or *R* sequence by combining contributions from the NC blocks or $N/2$ pairs of R_{ϕ} and $R'_{-\phi}$ blocks. For *C* sequences, one finds that the coefficient of $T_{\lambda\mu}$ in the contribution from the kth *C* block that arises from $H_{m\lambda 0}(t)$ is the same as the contribution from the first *C* block, apart from a phase factor $\exp\{-\mathrm{i}2\pi(k-1)(\mu\nu - mn)/N\}$. Because the following relation is true for any positive integer N:

$$\sum_{k=1}^{N} \mathrm{e}^{-\mathrm{i}2\pi(k-1)q/N} = \begin{cases} N, & q = NZ \\ 0, & q \neq NZ \end{cases} \tag{12.27}$$

where Z is some other integer, the quantity $\mu\nu - mn$ must be an integer multiple of N for the average Hamiltonian to contain a nonzero $T_{\lambda\mu}$ term arising from $H_{m\lambda 0}(t)$. This is the selection rule for CN_n^{ν} sequences.

For *R* sequences, one finds that the coefficient of $T_{\lambda\mu}$ in the contribution from the kth *R* block that arises from $H_{m\lambda 0}(t)$ is the same as the contribution from the first block, apart from a phase factor $(-1)^{(k-1)\lambda}\exp\{-\mathrm{i}2\pi(k-1)(\mu\nu - mn)/N\}$. If λ is even, the net coefficient of $T_{\lambda\mu}$ is zero (i.e., no recoupling) unless $mn - \mu\nu$ is an even multiple of $N/2$. If λ is odd, the net coefficient of $T_{\lambda\mu}$ is zero unless $mn - \mu\nu$ is an odd multiple of $N/2$. These are the selection rules for RN_n^{ν} sequences.

The *C*7 and POST-*C*7 sequences[19,20] are important examples of *C* sequences for homonuclear dipolar recoupling. For these sequences (which differ only in the details of the *C* block itself), $N = 7$,

$n = 2$, and $\nu = 1$, implying the selection rule that $\mu - 2m$ be a multiple of seven. Terms with $\mu = 2$ and $m = 1$ or $\mu = -2$ and $m = -1$ are recoupled, corresponding to double-quantum dipolar recoupling. Terms with $\mu = 0$ and $\mu = 1$ are not recoupled, corresponding to the absence of CSA recoupling and the absence of both zero-quantum and one-quantum dipolar recoupling. The fact that only a single pair of dipolar terms are recoupled implies that the magnitude of the recoupled dipole–dipole interactions is independent of γ, i.e., $C7$ and POST-$C7$ are γ-encoded.

Many examples of RN_n^{ν} recoupling sequences have been reported.[22] The fpRFDR sequence described above is a very simple example, for which $n = 4$, $N = 4$, and $\nu = 1$. Consistent with the earlier discussion, the symmetry selection rules indicate that dipole–dipole couplings ($\lambda = 2$) can be recoupled in a zero-quantum ($\mu = 0$) form, with $|m| = 1$ or $|m| = 2$. Chemical shifts ($\lambda = 1$; $|\mu| = 0$ or 1) cannot be recoupled.

12.5.2 Symmetry-Based Constant-Time Recoupling

Another useful symmetry property of recoupling sequences involves their behavior when all pulses are cyclically displaced in time.[1] Suppose a recoupling sequence consists of two successive periods P_1 and P_2 of duration τ_1 and τ_2, with $\tau_1 + \tau_2 = n\tau_r$. It can be shown that the effect of a cyclic displacement of all pulses within $n\tau_r$ by τ_1, such that P_2 now occurs before P_1, is to change the average Hamiltonian contribution arising from the term $H_{m\lambda 0}(t)$ from $\hat{H}_{\lambda m,\mathrm{ave}}$ to $\hat{H}_{\lambda m,\mathrm{ave}} = \mathrm{e}^{-\mathrm{i}m\omega_r\tau_1} U_1(\tau_1)\tilde{H}_{\lambda m,\mathrm{ave}} U_1(\tau_1)^{-1}$, where $U_1(\tau_1)$ is the net rotation produced by the RF pulses in P_1.

Why is this useful? As an example, consider a general recoupling sequence that ends in two periods of length $\tau_r/3$. During these final two periods, either no pulses are applied (as in Figure 12.4a) or the applied pulses produce a net rotation of 2π. For such a sequence, two successive cyclic displacements by $\tau_r/3$ multiply the average Hamiltonian by $\mathrm{e}^{\mathrm{i}2m\pi/3}$ and $\mathrm{e}^{\mathrm{i}4m\pi/3}$. For $m = \pm 1$ and $m = \pm 2$, the total average Hamiltonian for the pulse sequence obtained by concatenating the original sequence with the two displaced versions will be zero. As shown in Figure 12.4(b), this provides a simple means of performing "constant-time" dipolar recoupling measurements, i.e., measurements in which the effective dipolar evolution period τ_{eff} is varied without changing the total pulse sequence length and the total number of RF pulses. Constant-time techniques[1,11,23] have reduced sensitivity to transverse spin relaxation and other effects, allowing quantitative measurements of relatively long internuclear distances. Figure 12.4(c) shows one example, in which a backbone $^{15}\mathrm{N}$–$^{15}\mathrm{N}$ distance is used to constrain the ψ torsion angle in a polypeptide.

12.6 FREQUENCY-SELECTIVE HOMONUCLEAR DIPOLAR RECOUPLING

12.6.1 Rotational Resonance and Related Approaches

In samples with many like nuclei, e.g., uniformly or multiply $^{13}\mathrm{C}$-labeled peptides and proteins, techniques that recouple all spin pairs simultaneously are usually not useful for quantitative determination of internuclear distances. This is because the individual pairwise couplings do not commute with one another and therefore interfere with one another in a nonlinear manner. In effect, stronger couplings shut off (or "truncate") weaker couplings, for example, preventing measurements of multiple-bond $^{13}\mathrm{C}$–$^{13}\mathrm{C}$ distances when directly bonded $^{13}\mathrm{C}$ pairs are present. To circumvent this problem, a variety of methods that recouple only spin pairs with specific chemical shifts or chemical shift differences have been demonstrated. The simplest method is rotational resonance, which recouples spin pairs when their isotropic chemical shift difference equals a multiple of ω_r. Although originally used for distance measurements in selectively labeled samples, rotational resonance has been shown to be effective in uniformly labeled samples as well.[24,25]

Spin pairs whose chemical shift differences are close to, but not exactly on, a rotational resonance condition can be recoupled with "band-selective" techniques, such as RFDR with widely separated π pulses.[26] Equation (12.26) shows that recoupling under RFDR requires that the chemical shift difference Δ_{12} be close to a rotational resonance condition when the π pulse spacing $m\tau_r$ is large. Alternatively, rotational resonance conditions can be broadened in a controlled manner by application of weak RF pulse trains with suitable phase or amplitude modulations,

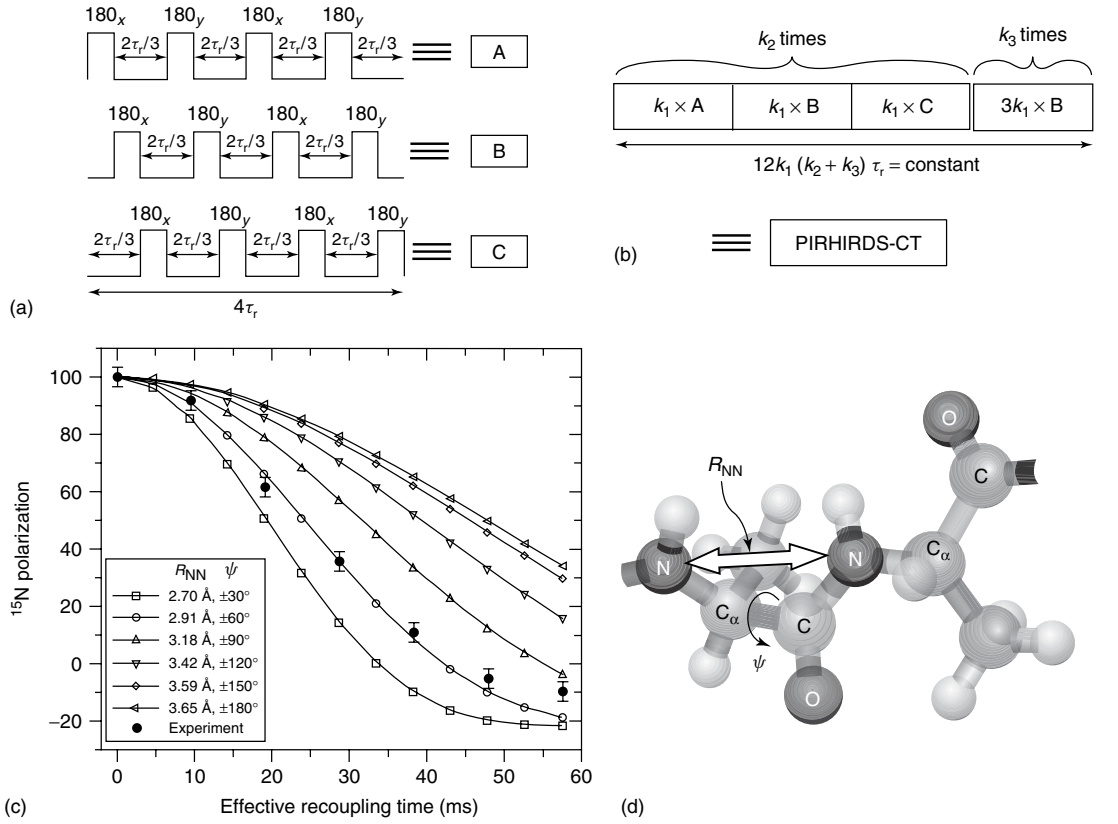


Figure 12.4. (a) Three variants of fpRFDR, related by cyclic displacements in time. Lengths of π pulses are $\tau_r/3$. (b) Constant-time recoupling technique, called *PITHIRDS-CT*, constructed from the fpRFDR variants. With $k_3 = 0$, there is no net recoupling. As k_3 is incremented and k_2 is decremented, the effective recoupling time becomes $12k_1k_3\tau_r$, while the total pulse length and total number of RF pulses remains constant. (c) Simulated PITHIRDS-CT data (open symbols) for ^{15}N pairs with the indicated internuclear distances, and experimental data (filled circles with error bars) for the 17-residue helical peptide MB($i + 4$)EK in lyophilized form, synthesized with uniform ^{15}N and ^{13}C labeling of two sequential amino acids, namely, Ala8 and Ala9. Experiments were performed at 14.1 T with $\tau_r = 50$ μs and with indirect detection of ^{15}N polarizations through ^{13}C NMR signals of α-carbons.[1] (d) Molecular model for a polypeptide, showing the relationship between the backbone ^{15}N–^{15}N distance and the ψ torsion angle. (Reproduced from Ref. 1 © American Institute of Physics, 2007.)

with the RF carrier frequency near the average of the NMR frequencies of the two coupled spins.[27]

Frequency-selective homonuclear recoupling can also be achieved far from rotational resonance conditions by an effect known as *rotational resonance in the tilted rotating frame* (RRTR). In RRTR experiments,[28,29] one adjusts the amplitude and carrier frequency of an applied RF field so that the effective field strengths for a pair of coupled spins in the rotating frame differ by ω_r or $2\omega_r$, or so that the sum of the effective field strengths is ω_r or $2\omega_r$.

12.6.2 Selectivity Induced by Chemical Shift Evolution Periods

Nonselective homonuclear recoupling techniques can be converted to frequency-selective techniques by alternation of nonselective recoupling blocks with periods of free evolution under isotropic chemical shifts.[30,31] This approach has been called SEASHORE (*Shift Evolution Assisted Selective HOmonuclear REcoupling*). If the

recoupling blocks have duration $p\tau_r$ and produce a double-quantum dipole–dipole Hamiltonian of the form $H_{DQ} = d_{12}I_{+1}I_{+2} + d_{12}{}^*I_{-1}I_{-2}$, with d_{12} being the effective coupling constant for the spin pair, i.e., the dipolar coupling constant for the spin pair multiplied by the appropriate scaling factor for the DQ recoupling pulse sequence employed. If a period $k\tau_r$ is inserted after each recoupling block, then the overall evolution operator for M repetitions of the recoupling block can be written as

$$\begin{aligned}
&U(Mp\tau_r + Mk\tau_r)\\
&\quad = \exp\{-i(\omega_{I1}I_{z1} + \omega_{I2}I_{z2})k\tau_r\}\\
&\quad \times \exp\{-i(d_{12}I_{+1}I_{+2} + d_{12}{}^*I_{-1}I_{-2})p\tau_r\}\ldots\\
&\quad \times \exp\{-i(\omega_{I1}I_{z1} + \omega_{I2}I_{z2})k\tau_r\}\\
&\quad \times \exp\{-i(d_{12}I_{+1}I_{+2} + d_{12}{}^*I_{-1}I_{-2})p\tau_r\}\\
&\quad = \exp\{-i(\omega_{I1}I_{z1} + \omega_{I2}I_{z2})Mk\tau_r\}\prod_{q=0}^{M-1}\\
&\quad \times \exp\{-i(d_{12}e^{iq\phi_{12}}I_{+1}I_{+2}\\
&\quad + d_{12}{}^*e^{-iq\phi_{12}}I_{-1}I_{-2})p\tau_r\}\\
&\quad \approx \exp\{-i(\omega_{I1}I_{z1} + \omega_{I2}I_{z2})Mk\tau_r\}\\
&\quad \times \exp\left\{-i\left[d_{12}\left(\sum_{q=0}^{M-1}e^{iq\phi_{12}}\right)I_{+1}I_{+2}\right.\right.\\
&\qquad \left.\left. + d_{12}{}^*\left(\sum_{q'=0}^{M-1}e^{iq'\phi_{12}}\right)I_{-1}I_{-2}\right]p\tau_r\right\} \qquad (12.28)
\end{aligned}$$

with $\phi_{12} = (\omega_{I1} + \omega_{I2})k\tau_r$. Equation (12.28) is essentially an AHT analysis of the effect of the chemical shift evolution periods on the dipole–dipole interaction, valid in the limit $|d_{12}|Mp\tau_r \ll 1$. The chemical shift periods induce a phase modulation of coupling constant $d_{12}{}^*$. The final line in equation (12.28) shows that this phase modulation tends to average out the dipole–dipole couplings unless ϕ_{12} is a multiple of 2π. In a many-spin system with nearly arbitrary NMR frequencies, it is generally possible to find values of $k\tau_r$ and the NMR carrier frequency such that only a desired pair of spins remains recoupled under SEASHORE, with all other homonuclear couplings being strongly attenuated. In principle, the SEASHORE approach is effective at arbitrarily high magnetic fields and high MAS frequencies, provided that a recoupling sequence that produces pure double-quantum couplings with the form of H_{DQ} can be found.

If the recoupling blocks produce a zero-quantum coupling of the form $H_{ZQ} = d_{12}(3I_{z1}I_{z2} - \boldsymbol{I}_1 \cdot \boldsymbol{I}_2)$, then a similar argument[31] shows that alternation with periods of chemical shift evolution truncates this coupling to $H'_{ZQ} = 2d_{12}I_{z1}I_{z2}$ unless $(\omega_{I1} - \omega_{I2})k\tau_r$ is a multiple of 2π. With this truncated form, frequency-selective π pulses can be used to refocus all but the desired homonuclear couplings. Other approaches to the truncation of homonuclear couplings for various purposes have been described.[32,33]

12.7 OTHER RECENT DEVELOPMENTS

12.7.1 Stochastic Homonuclear Dipolar Recoupling

Distance measurements in solution NMR rely on nuclear Overhauser effects (NOEs), in which rapidly fluctuating dipole–dipole couplings drive mutual spin flip transitions. The couplings are averaged to zero by molecular tumbling. If the fluctuations of different pairwise couplings are statistically uncorrelated, different couplings do not interfere with one another, even though the Hamiltonian terms for the different couplings do not commute with one another at each instant in time. Under these conditions, spin polarization transfers in a many-spin system can be described by a rate matrix with pairwise rates proportional to $1/r_{ij}{}^6$, with r_{ij} being the distance between nuclei i and j.

A similar effect can be achieved in solids by stochastic dipolar recoupling (SDR) techniques, in which random variables are introduced into RF pulse sequences in such a way that the recoupled dipole–dipole interactions fluctuate randomly, even in the absence of molecular motions. SDR experiments reported to date[34,35] utilize pulse sequences similar to those in SEASHORE experiments (see above), except that the RF carrier frequency is chosen randomly in each chemical shift evolution period, as shown in Figure 12.5(a). Phase factors in equation (12.28) then become random variables that average to zero in an incoherent manner and are nearly uncorrelated for different spin pairs as long as each spin has a distinct NMR frequency.[34] For two-spin systems, SDR produces exponential-like signal decays or polarization transfers, as in Figure 12.5(b). In two-dimensional NMR experiments with SDR, the build up of crosspeak volumes with increasing mixing time can be described by a rate matrix.[35] Since this is a $N \times N$ matrix for an N-spin system,

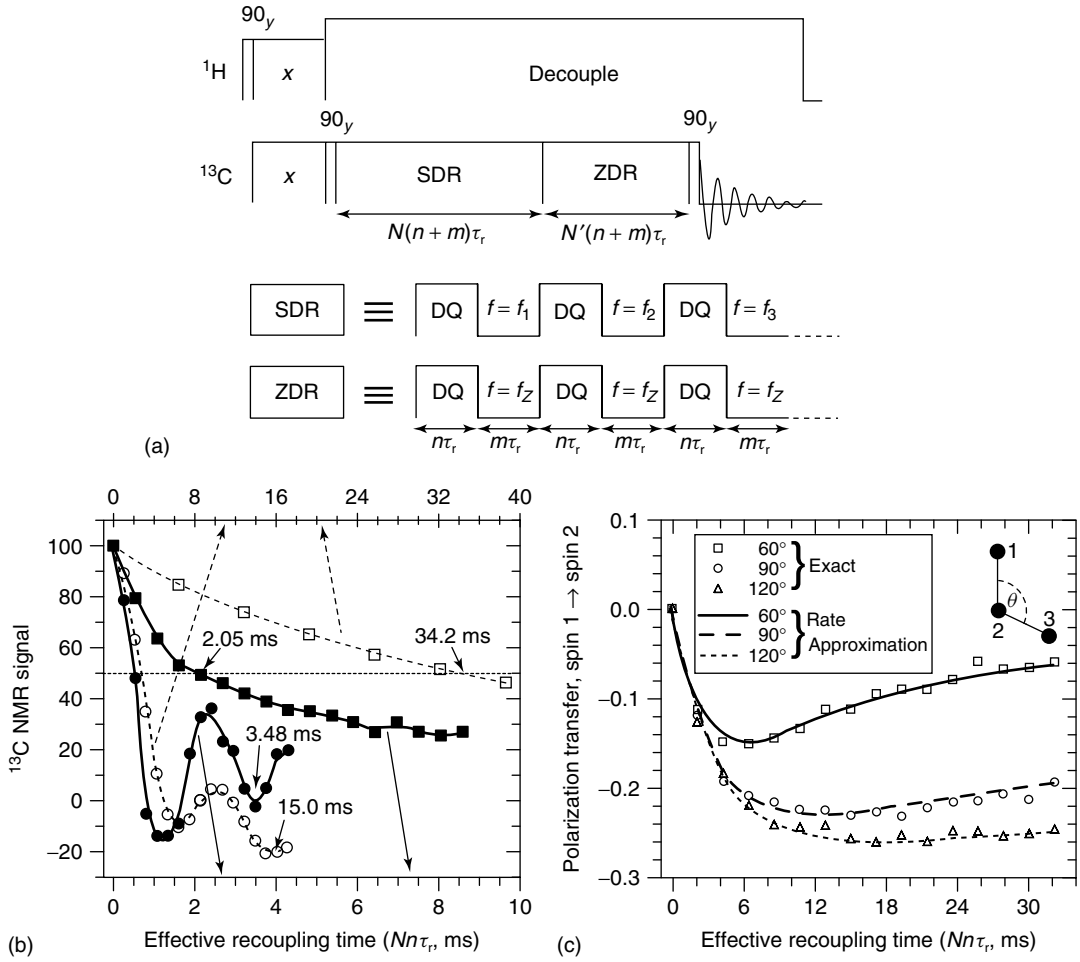


Figure 12.5. (a) RF pulse sequence for stochastic dipolar recoupling (SDR) in solid-state ^{13}C NMR. After standard $^{1}H-^{13}C$ cross-polarization and a $\pi/2$ pulse to rotate ^{13}C polarization to the z axis, the SDR sequence is applied, consisting of alternating periods of double-quantum recoupling and chemical shift precession. RF carrier frequencies f_k during chemical shift precession periods are chosen by a random number generator within the pulse program. In the ZDR (zero dipolar recoupling) period, the RF carrier frequency is set to a value f_z that produces no recoupling, according to the SEASHORE principle.[31] Lengths of SDR and ZDR periods are varied to produce a constant-time technique. (b) Experimental recoupling data at 9.39 T for two doubly labeled compounds in powder form,[35] namely, 2,3-$^{13}C_2$-L-alanine (filled symbols, $^{13}C-^{13}C$ distance $r = 1.54$ Å) and sodium bisulfite adduct of $^{13}C_2$-acetone (open symbols, $r = 2.51$ Å). Under coherent recoupling with the POST-C7 technique[20] (circles), signals oscillate with periods proportional to r^3. Under stochastic recoupling (squares), signals decay monotonically, with decay times proportional to r^6 as expected for a NOE-like rate process. (c) Simulated spin polarization transfers under SDR in a three-spin system with the indicated geometry, comparing full quantum mechanical simulations (symbols) with rate matrix simulations (lines). (Adapted from Refs. 34 and 35.)

while the Hamiltonian matrix is a $2^N \times 2^N$ matrix, simulations of polarization transfers under SDR are computationally feasible even when such simulations under coherent recoupling sequences are impossible. As shown in Figure 12.5(c), rate matrix simulations are in excellent agreement with full quantum mechanical simulations, although the rate matrix ignores the noncommutivity of different pairwise couplings. In principle, SDR methods represent a powerful approach to quantitative distance measurements in many-spin systems, distinct from frequency-selective recoupling approaches.

12.7.2 RF-Assisted Spin Diffusion, Proton-Mediated Exchange, and Three-Spin Recoupling

Many recent efforts to determine full structures of proteins or similar systems by solid-state NMR have relied on the detection of proximities (rather than precise distances) between pairs of ^{13}C nuclei in uniformly or multiply labeled samples, using various forms of multidimensional spectroscopy. Two techniques have been particularly useful. The first is called either DARR[36] (*dipolar-assisted rotational resonance*) or RAD[37] (RF-*assisted diffusion*). In two-dimensional DARR/RAD experiments, one applies an RF field to protons with amplitude $\omega_{1H} = \omega_r$. This field recouples both ^{1}H–^{1}H and ^{1}H–^{13}C dipole–dipole couplings, broadening the ^{13}C NMR lines and accelerating ^{13}C–^{13}C polarization transfers by spin diffusion, especially at high MAS frequencies. With mixing periods in the 0.2–1.0 s range, crosspeaks connecting ^{13}C nuclei that are roughly $6 - 8$ Å apart can be detected. The second technique is called either *proton-mediated* ^{13}C–^{13}C *exchange* or CHHC *spectroscopy*.[19,20] In proton-mediated ^{13}C–^{13}C exchange experiments, one transfers polarization among ^{13}C nuclei in a three-step process, consisting of ^{13}C $\rightarrow$^{1}H cross-polarization, ^{1}H $\leftrightarrow$^{1}H spin diffusion, and ^{1}H $\rightarrow$^{13}C cross-polarization. Crosspeaks connecting ^{13}C nuclei whose directly bonded protons are within roughly 3 Å of one another can be detected under typical conditions.

Recently, an alternative approach called PAR[38] (*proton-assisted recoupling*) has been proposed and demonstrated, with the possible advantages of greater structural selectivity and stronger crosspeak intensities. In PAR experiments, one applies RF fields to both ^{13}C (ω_{1C}) and ^{1}H (ω_{1H}) spins, with amplitudes chosen to avoid direct ^{1}H–^{13}C recoupling (e.g., $|\omega_{1C} - \omega_{1H}| = \omega_r$ or $|\omega_{1C} - \omega_{1H}| = 2\omega_r$) and direct ^{13}C–^{13}C recoupling (e.g., $\omega_{1C} = \omega_r/2$ or $\omega_{1C} = \omega_r$) conditions. The average dipole–dipole coupling Hamiltonian for a system of coupled ^{13}C and ^{1}H nuclei is then zero under MAS. However, the lowest order correction to the average Hamiltonian may be nonzero and can be of significant magnitude if the couplings are not vanishingly small compared with ω_r. According to the principles of AHT,[2] the lowest order correction involves commutators of the various Hamiltonian terms with one another, in the interaction representation with respect to the two applied RF fields. In particular, for a system comprised of two ^{13}C spins (I_1 and I_2) and one ^{1}H spin (S), the lowest order correction contains a term proportional to $[I_{z1}S_z, I_{y2}S_y] = -iI_{z1}I_{y2}S_x$ (and other similar terms) if the RF fields are applied along the rotating frame x axes. Such terms can produce transverse polarization transfers between ^{13}C spins that are coupled to a common ^{1}H spin. Selection of ω_{1C} and ω_{1H} to maximize these polarization transfers involves a combination of theory and empirical optimization.

REFERENCES

1. R. Tycko, *J. Chem. Phys.*, 2007, **126**, 064506.
2. U. Haeberlen and J. S. Waugh, *Phys. Rev.*, 1968, **175**, 453.
3. R. Tycko and G. Dabbagh, *Chem. Phys. Lett.*, 1990, **173**, 461.
4. M. Engelsberg and C. S. Yannoni, *J. Magn. Reson.*, 1990, **88**, 393.
5. G. E. Pake, *J. Chem. Phys.*, 1948, **16**, 327.
6. T. Gullion and S. Vega, *Chem. Phys. Lett.*, 1992, **194**, 423.
7. A. E. Bennett, C. M. Rienstra, J. M. Griffiths, W. G. Zhen, P. T. Lansbury, and R. G. Griffin, *J. Chem. Phys.*, 1998, **108**, 9463.
8. A. E. Bennett, J. H. Ok, R. G. Griffin, and S. Vega, *J. Chem. Phys.*, 1992, **96**, 8624.
9. Y. Ishii, *J. Chem. Phys.*, 2001, **114**, 8473.
10. N. A. Oyler and R. Tycko, *J. Phys. Chem. B*, 2002, **106**, 8382.
11. Y. Ishii, J. J. Balbach, and R. Tycko, *Chem. Phys.*, 2001, **266**, 231.
12. R. Tycko, *ChemPhysChem*, 2004, **5**, 863.

13. N. C. Nielsen, H. Bildsoe, H. J. Jakobsen, and M. H. Levitt, *J. Chem. Phys.*, 1994, **101**, 1805.

14. R. Verel, M. Ernst, and B. H. Meier, *J. Magn. Reson.*, 2001, **150**, 81.

15. E. R. Andrew, S. Clough, L. F. Farnell, T. D. Gledhill, and I. Roberts, *Phys. Lett.*, 1966, **21**, 505.

16. D. P. Raleigh, M. H. Levitt, and R. G. Griffin, *Chem. Phys. Lett.*, 1988, **146**, 71.

17. M. H. Levitt, D. P. Raleigh, F. Creuzet, and R. G. Griffin, *J. Chem. Phys.*, 1990, **92**, 6347.

18. T. Gullion, D. B. Baker, and M. S. Conradi, *J. Magn. Reson.*, 1990, **89**, 479.

19. Y. K. Lee, N. D. Kurur, M. Helmle, O. G. Johannessen, N. C. Nielsen, and M. H. Levitt, *Chem. Phys. Lett.*, 1995, **242**, 304.

20. M. Hohwy, H. J. Jakobsen, M. Eden, M. H. Levitt, and N. C. Nielsen, *J. Chem. Phys.*, 1998, **108**, 2686.

21. M. Carravetta, M. Eden, X. Zhao, A. Brinkmann, and M. H. Levitt, *Chem. Phys. Lett.*, 2000, **321**, 205.

22. M. H. Levitt, *J. Chem. Phys.*, 2008, **128**, 052205.

23. A. E. Bennett, D. P. Weliky, and R. Tycko, *J. Am. Chem. Soc.*, 1998, **120**, 4897.

24. A. T. Petkova and R. Tycko, *J. Magn. Reson.*, 2004, **168**, 137.

25. P. T. F. Williamson, A. Verhoeven, M. Ernst, and B. H. Meier, *J. Am. Chem. Soc.*, 2003, **125**, 2718.

26. G. Goobes, G. J. Boender, and S. Vega, *J. Magn. Reson.*, 2000, **146**, 204.

27. J. C. C. Chan and R. Tycko, *J. Chem. Phys.*, 2004, **120**, 8349.

28. K. Nomura, K. Takegoshi, T. Terao, K. Uchida, and M. Kainosho, *J. Am. Chem. Soc.*, 1999, **121**, 4064.

29. K. Takegoshi, K. Nomura, and T. Terao, *Chem. Phys. Lett.*, 1995, **232**, 424.

30. Y. Mou and J. C. C. Chan, *Chem. Phys. Lett.*, 2006, **419**, 144.

31. A. K. Paravastu and R. Tycko, *J. Chem. Phys.*, 2006, **124**, 194303.

32. N. Khaneja and N. C. Nielsen, *J. Chem. Phys.*, 2008, **128**, 015103.

33. I. Marin-Montesinos, G. Mollica, M. Carravetta, A. Gansmuller, G. Pilelo, M. Bechmann, A. Sebald, and M. H. Levitt, *Chem. Phys. Lett.*, 2006, **432**, 572.

34. R. Tycko, *J. Phys. Chem. B*, 2008, **112**, 6114.

35. R. Tycko, *Phys. Rev. Lett.*, 2007, **99**, 187601.

36. K. Takegoshi, S. Nakamura, and T. Terao, *Chem. Phys. Lett.*, 2001, **344**, 631.

37. C. R. Morcombe, V. Gaponenko, R. A. Byrd, and K. W. Zilm, *J. Am. Chem. Soc.*, 2004, **126**, 7196.

38. G. De Paepe, J. R. Lewandowski, A. Loquet, A. Bockmann, and R. G. Griffin, *J. Chem. Phys.*, 2008, **129**, 245101.

Chapter 13
Dipolar Coupling: Molecular-level Mobility

Detlef Reichert and Kay Saalwächter

Institut für Physik, Martin-Luther-Universität Halle-Wittenberg, D-06108 Halle, Germany

13.1	Introduction	177
13.2	Basics	179
13.3	Averaged Dipolar Couplings—Fast Motions	181
13.4	Dynamic Lineshape–Intermediate Motions	182
13.5	Site-Resolved Heteronuclear and Homonuclear Dipolar Couplings	183
13.6	Double-Quantum Experiments	190
13.7	Dipolar Exchange NMR—Slow Motions	191
13.8	Summary	191
	References	191

13.1 INTRODUCTION

The majority of reported nuclear magnetic resonance (NMR) studies naturally aim at obtaining *structural* data, for the relevant NMR interactions like chemical shift and dipolar coupling primarily provide information on the chemical structure and spatial organization of the sample material. Limited *dynamic* information can be gained from such data only, for example, for conformational transitions that alter the values of the isotropic chemical shifts. However, the majority of dynamic studies rely on anisotropic NMR interactions like the anisotropic chemical shift and the quadrupolar and—last but not least—the dipolar coupling (*see* **Chapter 10**). Soon after NMR was discovered and long before the discovery of the chemical shift and the J-coupling (which provide the basis of chemical applications), the relation between molecular dynamics and NMR relaxation parameters was elucidated. Likewise, the broadening of the NMR lines due to the dipole–dipole coupling and the influence of molecular dynamic processes on this broadening were discovered early on: it was realized that the observed wide absorption lines were due to static dipolar interactions.[1,2] In isotropic liquids, however, much narrower lines were detected and it was understood this is due to the averaging of static interactions. A stochastic reorientational motion (as is the typical case for a thermally activated process in matter) can be described by the correlation function of motion, which correlates a dynamic variable at two points in time, say at t and $t+\tau$, and averages over a sufficient number of different t. For dipolar coupling, the simplest analytical expression reads

$$C(\tau) = \langle r^6 \rangle \left\langle \frac{1}{r^3(t)} P_2\left(\cos\theta(t)\right) \times \frac{1}{r^3(t+\tau)} P_2\left(\cos\theta(t+\tau)\right) \right\rangle_t \quad (13.1)$$

where r is the internuclear distance and $P_2(\cos\theta) = (3\cos^2\theta - 1)/2$ is the second-order Legendre polynomial (for simplicity, we neglect here the contributions of higher order Legendre polynomials/Wigner functions). For isotropic samples and fixed intermolecular

NMR Crystallography Edited by Robin K. Harris, Roderick E. Wasylishen and Melinda J. Duer © 2009 John Wiley & Sons, Ltd. ISBN: 978-0-470-69961-4

vectors, equation (13.1) simplifies to

$$C(\tau) = \langle P_2(\cos\theta(0)) \cdot P_2(\cos\theta(\tau)) \rangle \quad (13.2)$$

where θ is the angle between the principal axis of the interaction tensor (the internuclear vector) and the applied magnetic field at time zero and τ. The meaning of equation (13.1) is demonstrated in Figure 13.1: for short τ, the value of the dynamic variable does not change and the product of the values of the dynamic variable is always positive and adds up on average to a certain positive value (commonly normalized to 1); however, for long τ, the product of the dynamic variable at different points in time separated by τ can be positive or negative, and thus averages to zero over the sample. The time average of $P_2(\cos\theta)$ is zero when the orientation angle θ follows an isotropic diffusion process; the correlation function of motion in this case becomes an exponential function that decays to zero

$$C(\tau) = \mathrm{e}^{-\frac{\tau}{\tau_c}} \quad (13.3)$$

where τ_c is the correlation time. If, however, the motion is fast but anisotropic, the averaging is incomplete, leaving an order parameter plateau

$$C(\tau) = (1 - S^2)\exp\left(-\frac{\tau}{\tau_c}\right) + S^2 \quad (13.4)$$

where S^2 is related to a residual coupling $S^2 \propto \langle\omega_D\rangle^2 \propto D_{res}^2$ from which the geometry of the motional process can be derived (see below). The static-limit dipolar frequency is given by $\omega_D = D_{stat} P_2(\cos\theta)$ for the heteronuclear case, but for the homonuclear case an additional factor of $\frac{2}{3}$ appears. D_{stat} is the static-limit dipolar coupling constant, defined for two nuclei i and j as $\frac{\mu_0}{4\pi}\gamma_i\gamma_j\frac{h}{2\pi}r_{ij}^{-3}$(expressed in rad s^{-1}). Averaging over time-dependent orientations $\theta(t)$, assuming uniaxial symmetry, yields the residual coupling $\langle\omega_D\rangle = D_{res} P_2(\cos\beta)$, where β now describes the orientation of the motion-averaged dipolar coupling tensor. The reduced coupling constant D_{res} is directly accessible. It is therefore straightforward to use simple temperature-dependent measurements of linewidths for the study of dynamic processes: the

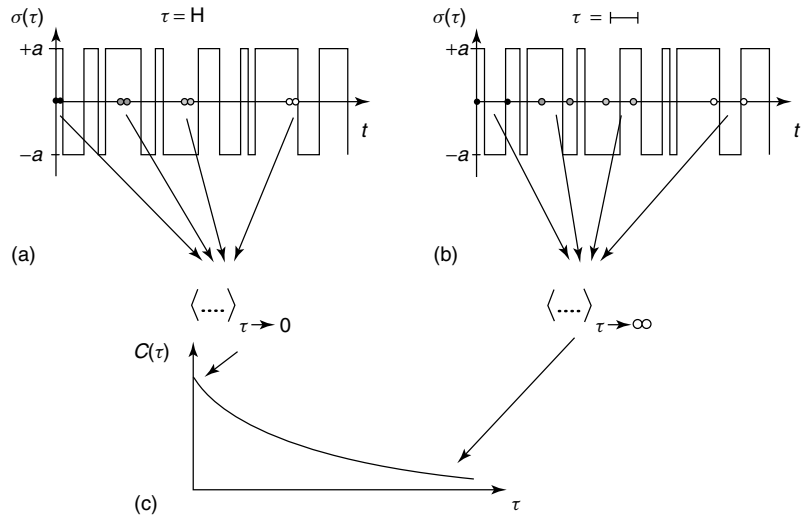


Figure 13.1. Schematic illustration of the meaning of the correlation function of motion, $C(\tau)$. The dynamic variable $\sigma(t)$ can take two distinct values $+a$ and $-a$, which vary by a random dynamic process. For simplicity, $C(\tau)$ is defined here as $C(\tau) = \langle\sigma(t)\cdot\sigma(t+\tau)\rangle$. In the two upper charts (a and b), $\sigma(t)$ is shown. For illustration, the gray circles mark points in time at which the products $\sigma(t)\cdot\sigma(t+\tau)$ are taken for two values of τ (shown as bars) at four values of t. Note that for short τ, the probability of finding $\sigma(t)$ in the same state is high while for long τ, the probability of finding $\sigma(t)$ in the one or in the other state is approximately equal. The averages of the products $\sigma(t)\cdot\sigma(t+\tau)$ thus yield $4a^2$ for the short τ value (a) and $(a^2 - a^2 - a^2 + a^2) = 0$ for the longer τ value (b). The final correlation function of motion for this example is an exponential function (c), see equation (13.3).

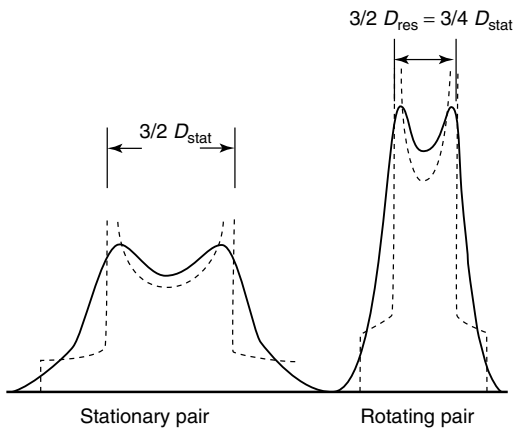


Figure 13.2. Theoretical line shapes for a dipolar-coupled nuclear spin pair with like spins $I = 1/2$ when stationary and when in motion about an axis perpendicular to the internuclear axis. (Reproduced from Ref. 11. © American Institute of Physics, 1950.)

temperature dependence of the second moment of the dipolar interaction, which is proportional to the dipolar linewidth, allows the identification of different motional modes, the frequency of which moves through the dynamic window of the method on increasing the temperature.[1] It is interesting to note that the introduction of magic-angle spinning (MAS), certainly the most influential innovation in solid-state NMR, was initiated by the idea of checking the effect of motion on the second moment: according to theory,[2] the second moment must remain constant even under motion and thus the spectral narrowing must be accompanied by the formation of spinning sidebands (ssb) appearing at *random* frequency positions, determined by the stochastic nature of the molecular process, and are invisible due to their vanishing spectral intensity. In contrast, a coherent motion like sample spinning should produce the ssbs at fixed frequency positions and thus should become observable in the NMR spectrum. This experiment was performed at an angle of 90° (rather at the magic angle),[3] and the idea was later developed to what became known as *magic angle spinning*.[4,5] Any molecular reorientation leads to an alteration of the resonance frequencies and thus of the NMR data, and is therefore detectable. Parameters of molecular dynamics are quantified by the timescale as well as the geometry of the process that causes alterations of the orientation angle θ of, in this case, the uniaxially symmetric dipolar interaction tensor with respect to the external magnetic field. The time dependence of the correlation function of motion, in particular, the autocorrelation function of $P_2(\cos\,\theta)$, contains the potentially available dynamic information. The shape of the correlation function can be as simple as a single exponential for an isotropic reorientation or as complicated as a multicomponent and nonexponential function for more complicated motions in larger and structured molecules. In most cases, this information is not completely accessible and approximations have to be made.

Currently available dynamic solid-state NMR methods span a dynamic range of more than 10 orders of magnitude and also provide information about the geometry of the dynamic processes, i.e., about the amplitude of reorientations (detailed information on jump angles), the number of interchanging sites, or even the details of the correlation function of motion. The extraction of this information from the experimental NMR data often requires a simplified assumption of the correlation function of motion or a motional model for which the relation between relaxation time and correlation function has to be calculated or relies on the simulation of spectra or other NMR data and comparison with the experimental data. In few cases of exchange-NMR experiments, the dynamic information can be extracted completely model-free. While the early experiments were mostly "low-resolution" experiments on abundant nuclei (like ^{1}H), the possibility of isotopic labeling as well as advances in line-narrowing approaches and multidimensional NMR provide an increased molecular resolution and sensitivity, making dynamic NMR a unique tool for the detailed investigation of dynamic processes in organic solids, and in which the dipolar coupling plays a major role.

13.2 BASICS

The cornerstone of all experiments and approaches described below is the dependence of the resonance frequency of a nucleus on the orientation of the internuclear vector versus the external magnetic field that is induced by the local field of a neighboring nucleus. In the static case, any NMR spectrum governed by dipolar coupling is the superposition of resonance lines located at the frequencies determined by the dipolar coupling constant and the orientation versus the external magnetic field, and is a superposition of all possible orientations that

occur in the sample. From this, it is immediately apparent that the spectrum contains information about macroscopic orientations, too; however, henceforth we assume isotropic materials, that is, all molecular orientations present in a random statistical distribution. Also, we further consider $^1H-^1H$ or ^1H-X couplings only, since other couplings are more insensitive and often inconvenient to measure in organic solids. It should be noted that whenever isotopic labeling is feasible, one should consider ^2H experiments since they provide the best tools for extracting dynamic information on all timescales.

Dynamic solid-state NMR spans a dynamic window from very fast processes with correlation times of nanoseconds down to very slow motions that occur on the timescale of seconds. Therefore, different experimental approaches have been developed. For dipolar coupling, one basically needs to distinguish different time regimes that are defined by the ratio of the rate of reorientation (that is inversely proportional to the correlation time of motion, τ_c) versus the dipolar coupling constant D_{stat}:

(a) slow motion: $(\tau_c)^{-1} \ll D_{stat}$
(b) intermediate motion: $(\tau_c)^{-1} \simeq D_{stat}$
(c) fast motion: $(\tau_c)^{-1} \gg D_{stat}$

In turn, these conditions roughly translate into the relation between the transverse relaxation time T_2^{stat} in the static case and the inverse of the dynamic rate, i.e., τ_c:

(a) slow motion: $\tau_c \gg T_2^{stat}$
(b) intermediate motion: $\tau_c \simeq T_2^{stat}$
(c) fast motion: $\tau_c \ll T_2^{stat}$

Since T_2^{stat} approximately equals the lifetime of the NMR signal (length of the free induction decay, (FID) time), the different regimes correspond to the following: (A) The FID decays faster as compared to the average lifetime of a certain molecular orientation, (C) the rate of reorientation is faster as compared to any frequency component of the FID, or (B) an appreciable number of reorientations happens during the lifetime of the FID. Fast processes in the range of the inverse Larmor frequency efficiently stimulate transitions of spins between their Zeeman levels and drive NMR relaxation. Thus, these experiments provide accurate information about fast motions with correlation times on the order of the inverse Larmor frequency, while in the absence of molecular dynamic processes, only spin dynamics like spin diffusion that do not contain information about the molecular dynamics contribute substantially to the relaxation data and make a faithful determination of molecular dynamic parameters difficult. Since there are excellent texts on NMR relaxation, we will not deal with such experiments here. Also, these fast processes lead to an averaging of the experimentally determined dipolar coupling that provides dynamic information, see below. Slower motion, however, can be either investigated by relaxation experiments in lower effective fields or one can make use of the fact that processes with correlation times on the order of the lifetime of the solid-state NMR signal, i.e., microseconds, have an effect on the appearance of the NMR spectrum due to a modulation of the resonance frequencies or interference with external perturbations. Even slower processes are the domain of exchange experiments that basically provide access to processes with correlation times as long as the relaxation time T_1.

Historically, the first "dipolar" experiments were carried out on abundant spins with large gyromagnetic ratio, i.e., ^1H and ^{19}F. In particular for ^1H, the dominant interaction is the homonuclear $^1H-^1H$ interaction that leads to an overall spectral width of about 40 kHz in a typical organic solid, in contrast to the chemical shift effects that are as small as a few tens of hertz at the external field strengths used in those days. Basically, it is possible to calculate the effects of a molecular reorientation on the experimental dipolar spectrum using standard procedures like exchange theory;[6] however, for the case of the dipolar interaction in solids, this is strictly true only for isolated spins forming a spin pair. The problem in real systems is that many closely spaced protons interact with each other; there are hardly any isolated $^1H-^1H$ pairs that would yield spectra that match theory and enable a quantitative calculation of the line shape. Though theoretical attempts were made to increase the number of spins in the calculation, the usual approach was to convolute the theoretical two-spin spectrum with a broad Gaussian or Lorentzian function that results in a rather featureless broad line[7] (see Figure 13.2) from which in most cases the second moment of the line shape was extracted. In Figure 13.3, temperature-dependent dipolar spectra and the extracted linewidth are shown for hexamethylbenzene.[8] The "onset" of the ring rotation, i.e., the temperature at which the inverse correlation time of the rotation becomes similar to the dipolar coupling constant and a substantial line narrowing happens, is also detected in the DSC trace. The application of temperature-dependent line

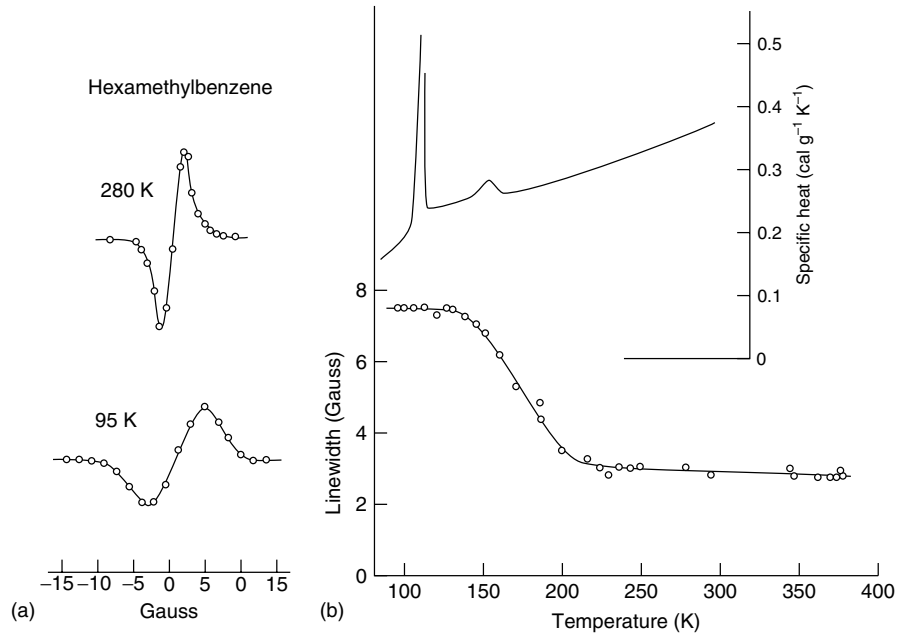


Figure 13.3. (a) ^{1}H Resonance line derivates for hexamethylbenzene (HMB). (b) Variation with temperature of the resonance linewidth and of the specific heat for HMB. The drop of linewidth between 150 and 200 K is due to the sixfold rotation of the molecule, which is also visible in the DSC trace by the hump between 135 and 165 K. The peak at 108 K is due to a structural change of the crystal lattice, which is unobservable by NMR. (Reproduced from Ref. 8. © American Institute of Physics, 1950.)

shapes and the measurements of second moment in more complex organic solids like polymers followed soon after[9,10]. In these temperature-dependent experiments, this line is narrowed down close to a temperature at which the motional rate of the thermally activated process approaches and eventually exceeds the dipolar coupling constant; however, this basically provides a single data point in the activation diagram. In addition, the transition from the static lineshape to the narrow line happens over a certain temperature range, so the accuracy in both temperature and rate is fairly limited. No detailed information about the geometry of the process is available either, except a rough estimate about the anisotropy of the reorientation: if the dynamic process happens to be isotropic, the limit is the natural linewidth related to the applied external field, while for anisotropic motions, a larger linewidth is obtained. Qualitatively, the smaller the amplitude of the reorientation, the closer the fast-limit linewidth to that of the rigid limit.

It should be noted that there is experimental evidence that dynamic parameters can be obtained not only by recording spectra at different temperatures (and thus motional rates of thermally activated processes) but also by changing parameters of the NMR experiment like the decoupling efficiency, inducing an "exchange narrowing" analogous to the classical motional narrowing.[12] However, this approach does not seem to have found applications in real systems.

13.3 AVERAGED DIPOLAR COUPLINGS—FAST MOTIONS

The most common quantitative approach is to apply a general model (see also model-free approach[13,14]) that defines a so-called dynamic order parameter S as the ratio of the averaged versus the full dipolar coupling

$$S = \langle P_2(\cos\theta)\rangle = \frac{D_{\text{res}}}{D_{\text{stat}}} \tag{13.5}$$

where $\langle \ldots \rangle$ means the time average and D_{stat} and D_{res} are the static-limit and residual dipolar coupling constants, respectively, as defined in the Introduction.

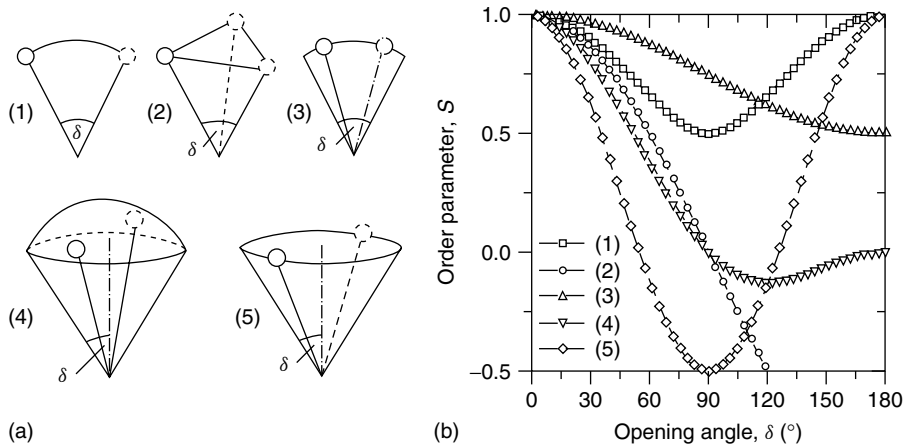


Figure 13.4. Dependence of the order parameter of motion, S, equation (13.5), on the topology (angle δ) of the molecular motion. (a) Sketches of the jump geometries. (1) Jumps about an angle δ between two equivalent sites. (2) Jumps about angles δ between three sites at the corners of an equilateral triangle. (3) Diffusion on an arc with the opening angle δ. (4) Diffusion inside a cone with the opening angle $2 \cdot \delta$ (5) Diffusion on a cone with the opening angle $2 \cdot \delta$. (b) Dependence of S versus δ. Note that for the case (2), δ is only defined between 0 and 120° where complete transverse isotropy is achieved ($S = -1/2$).

S is a measure of the anisotropy of the molecular reorientation and ranges from one for a completely rigid system (or a vanishing reorientation angle), passing zero for an isotropic motion down to $-1/2$ for transverse isotropy, i.e., the motion occurs in a plane perpendicular to the reference orientation. For special topologies of motion, a quantitative relation between the reorientation angle and S can be drawn,[15,16] as shown in Figure 13.4 where this relation is displayed for two- and three-site jump motions as well as planar diffusion and diffusion within a cone and on a cone, respectively. If such models are not applicable, at least anisotropic jump motions can be distinguished from rotational diffusions or relative information obtained by comparing different samples, etc. However, it should be noted that from averaged dipolar couplings measured in the fast limit, no information about the timescale of the motion can be obtained.

13.4 DYNAMIC LINESHAPE–INTERMEDIATE MOTIONS

If the rate of the process does not satisfy the condition for a fast process, i.e., if there are motionally induced frequency alterations during the lifetime of the FID, equation (13.5) cannot be applied anymore and, therefore, easy determination of dynamic parameters is not possible. However, the experimental parameters like the dipolar spectrum now contain information about the topology of the process and additionally about the timescale of the process. In principle, the NMR time-domain signal (F) can now be written as

$$F(t) = M_0 \left\langle \exp\left(i \int_0^t \omega(t')\, \mathrm{d}t' \right) \right\rangle \qquad (13.6)$$

where in a dynamic system, the resonance frequency ω that is determined by anisotropic interactions now is a random function of time as a result of the motion. For single spin pairs, and in particular the related case of ^{2}H NMR experiments with models relying on jumps between a limited number of sites, theoretical solutions based on exchange matrices are straightforward and well established in the literature.[17] More generally, following the well-known Anderson and Weiss (A–W) approach[18] of "random frequency modulation", approximate and rather simple analytical solutions are possible. The theory is based on a Gaussian resonance frequency distribution, which is due to the distribution of the dipolar local fields, and requires that the resonance frequency varies in time due to a random thermal process. The simplest model usually adopted is

isotropic rotational diffusion, which has a particularly simple, monoexponential correlation function. While the Gaussian frequency distribution naturally arises for the multispin scenario of a proton system, it turns out that the short-time behavior of just a spin pair (Pake-like frequency distribution) performing N-site jumps can still reasonably well be described by such an *ansatz*.[19] Details are addressed below. The A–W approach is an underestimated and powerful tool, as it provides simple analytical equations to describe frequency or time-domain data,[20] and even the time dependence in MAS experiments can be accommodated.[21] There are a number of extensions to the model[22–24] and applications to extract dynamic parameters from organic solids, in particular rubbery materials and of adsorbed molecules.[24–35]

13.5 SITE-RESOLVED HETERONUCLEAR AND HOMONUCLEAR DIPOLAR COUPLINGS

In addition to the disturbing multispin effects described above, experiments on abundant nuclei (like ^{1}H) in typical organic solids are often too unselective: one of the powers of NMR: its chemical selectivity thus molecular resolution, is lost due to the unfavorable ratio of the strong dipolar interaction between the spins that broadens the spectra and the small chemical shift that provides the spectral resolution. It is therefore generally desirable to separate the information from structure (chemical shift) and dynamics (dipolar coupling) in a two-dimensional manner.[36] For organic solids at natural abundance, dipolar experiments should be combined with high-resolution conditions provided by MAS, and a wealth of homonuclear and heteronuclear dipolar recoupling experiments, providing precise values for the coupling constants, have been designed in the past decades (*see* **Chapters 11** and **12**).[37] However, most of these experiments are used to obtain structural information (distances), and only a few (in fact less sophisticated) approaches have gained importance in dynamic studies and deserve special attention: cross-polarization (CP) dynamics, separated-local field (SLF) and related recoupling techniques, and homonuclear double-quantum (DQ) experiments. The former two approaches rely on the heteronuclear dipolar coupling between abundant (like ^{1}H) and rare spins (like ^{13}C). In a CP experiment, the increase of rare-spin magnetization occurs with the buildup time T_{CH} that is—similar to the relaxation time $T_{1\rho}$—sensitive to dynamic processes in the kilohertz range[38] and correlates to important mechanical parameters like dynamic moduli.[39,40] The measurement of T_{CH} became rather popular in dynamic investigations of organic solids; however, care must be taken in the interpretation of the data.[41] SLF experiments measure chemical shifts and dipolar coupling separately but in a way that they can be correlated.[36,42–44] Popular versions of SLF experiments are dipolar-rotational spin echoes (DRSE)[44–47] and wide-line separation (WISE) experiments.[48] An early example of DRSE is shown in Figure 13.5, where the dipolar spectra of a backbone and a ring carbon in polystyrene (PS) are compared: the latter exhibits a smaller dipolar coupling, due to the averaging by the flip motion. The WISE approach was first suggested as a dynamic filter[49] to separate mobile and rigid components in ^{13}C spectra and has later found broad application in polymer science.[50] WISE data from a block-copolymer of PS and poyldimethylsiloxane (PDMS) are shown in Figure 13.6: the different widths in the dipolar dimension reveal different mobilities of the glassy PS and the rubbery PDMS. Further developments of WISE include the suppression of the disturbing ^{1}H-spin diffusion during the CP step that would transfer the ^{1}H magnetization to different carbons and thus spoil the molecular resolution of the method.[51] The work of Frydman[52] deserves particular attention; it has shown that SLF experiments are possible even without homonuclear decoupling building blocks and for multispin systems: when sufficiently fast MAS rates are employed, quantitative dipolar sideband patterns from directly bonded spin pairs can be acquired in the absence of ^{1}H–^{1}H multiple-pulse homonuclear decoupling even for "real" organic solids. A special SLF version is the so-called PISEMA technique:[53] it works for static samples and is usually applied to oriented biological materials in which the X nucleus is usually a ^{15}N nucleus in a selectively isotopically enriched sample. The necessary spectral resolution is achieved by the isotopic labeling (reducing the number of resonances) and oriented samples (to avoid the broad anisotropic lines in the direct dimension). However, this experimental approach is restricted to specially labeled and prepared samples and hence to a few laboratories around the world.

SLF variants that deserve attention are the efficient DIPSHIFT experiment[54,55] (which is basically the DRSE experiment suggested by Schaefer *et al*.[46]

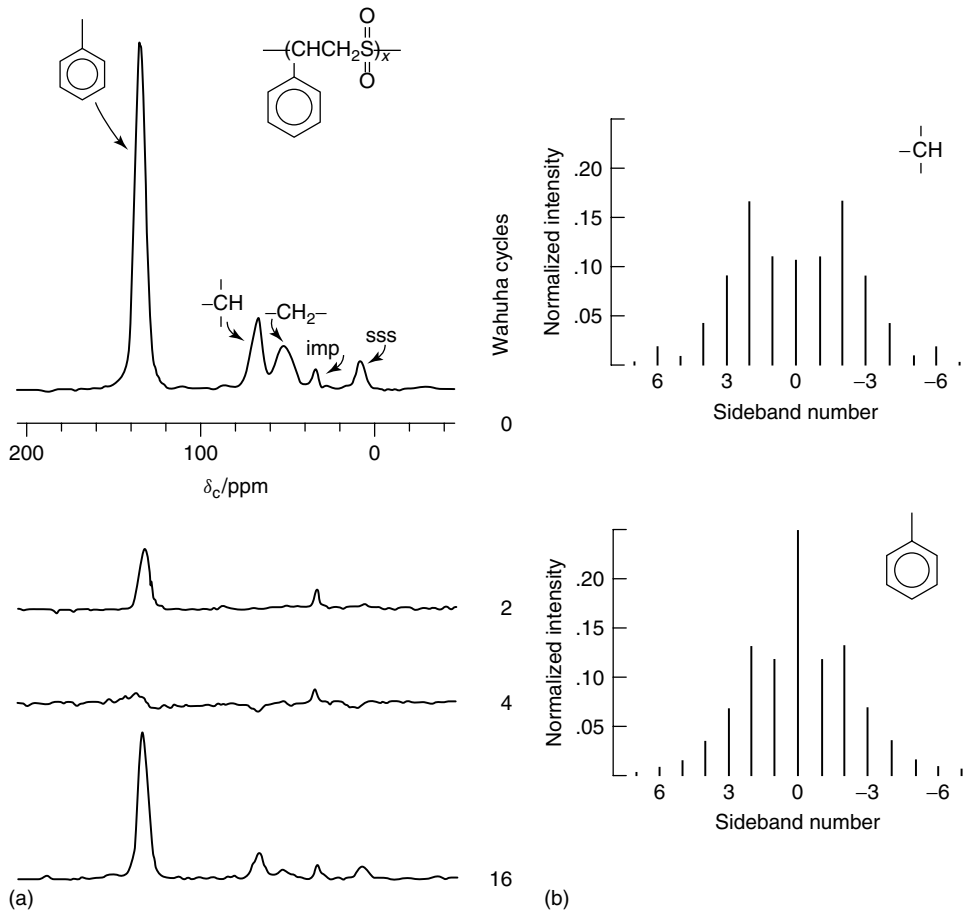


Figure 13.5. ^{13}C DRSE spectra of poly(styrene-*co*-sulfone). The homonuclear decoupling was achieved by the WAHUHA sequences, and the ^{13}C spectra depending on the number of WAHUHA cycles are shown in (a). This number plays the role of the increment t_1 in the indirect dimension. (b) Dipolar sideband patterns for two CH pairs. (Reproduced from Ref. 46. © American Chemical Society, 1984.)

but running it in a more efficient mode) and the Lee-Goldberg CP (LG–CP) experiment.[56] In these experiments, the homonuclear dipolar coupling is efficiently reduced by the irradiation of homonuclear ^1H decoupling sequences like MREV or LG decoupling. In turn, only the heteronuclear dipolar coupling between the X nuclei (for example, ^{13}C) and the ^1H remains. In principle, every ^{13}C still interacts with a number of ^1H. However, owing to the strong distance dependence of the dipolar coupling, only the closest protons play a major role in the experiment. When applied to protonated carbons with a well-defined number of bonded ^1H, these experimental schemes can be analyzed in terms of theoretical models that are well developed. All these experiments are 2-D experiments that provide the (normally) well-resolved ^{13}C MAS spectrum in the direct and the $^{13}C–^1H$ dipolar spectrum in the indirect dimension. The DIPSHIFT experiment is particularly efficient as it produces a $^{13}C–^1H$ dipolar MAS spectrum that is periodic with the MAS period, τ_r, and thus, it is only necessary to sample few data points during a single τ_r. Furthermore, the second Fourier transform over the dipolar dimension is omitted, as it does not add additional information but might result in some artifacts like a zero-frequency peak. Thus, even samples with low signal intensity can be investigated in natural isotopic abundance.[57,58]

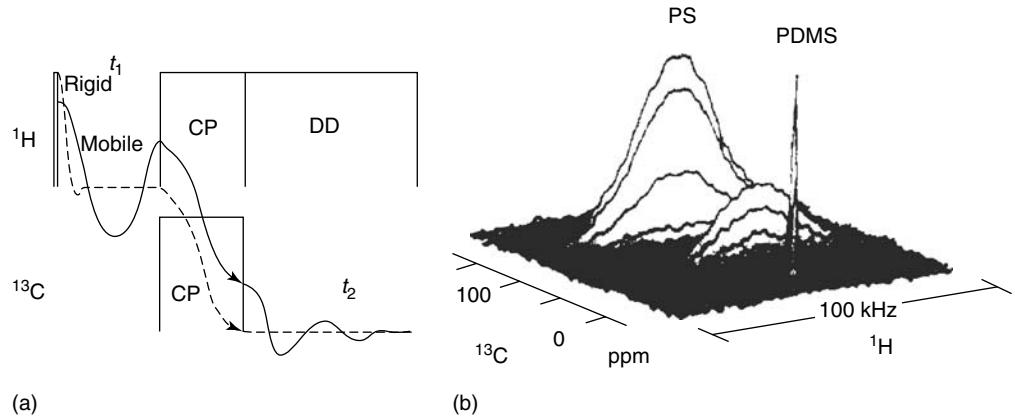


Figure 13.6. (a) Pulse sequence of the WISE experiment and (b) WISE spectrum of poly(styrene-*co*-dimethylsiloxane). In (a), the modulation of the carbon signals by the rigid and mobile protons is demonstrated. This appears in the indirect dimension as the dipolar linewidth (b). (Reproduced from Ref. 50. © American Chemical Society, 1992.)

For τ_c on the order of 10^{-5} s or less, all these experiments determine the dipolar coupling strength that is reduced by fast molecular dynamics. Information about the amplitude of the molecular process can be extracted from the reduction ratio with respect to the static value of the dipolar coupling in terms of an order parameter that contains the information about the anisotropy of the molecular reorientation, equation (13.5). Again, no information about the rate of motion can be made in this regime. Figure 13.7 displays calculated DIPSHIFT dephasing curves for different apparent dipolar couplings, which might be caused by fast but anisotropic molecular motions with different topologies (order parameters). The apparent T_2 relaxation of these curves is due to imperfections of the homonuclear decoupling sequences and residual couplings. LG–CP data are displayed in Figure 13.8 where the dipolar oscillations can be seen nicely. Please note the different apparent couplings, due to different amplitudes of motion, that are manifested in the different periods of these oscillations.

A related class of experiments are heteronuclear dipolar recoupling techniques based on the famous rotational-echo double-resonance (REDOR) technique (*see* **Chapter 11**)[59] which can be quantitatively applied to the ^{1}H–X case if sufficiently fast MAS (usually $\sim$30 kHz) is used. It is particularly robust and easy to set up (only the 90° pulse length must be calibrated carefully), and the common denominator is that the signal modulation over a single rotor period in an indirect dimension, or the Fourier transform of its extension yielding a sideband spectrum, can be used to extract (motionally averaged) dipolar couplings. There are in fact many variants in this class of techniques, including the combination with indirect ^{1}H detection for signal enhancement, and a particularly efficient SLF-type variant termed REREDOR.[60] Schematic pulse sequences and sideband patterns due to the rotor modulation in the indirect dimension are shown in Figure 13.9. An instructive early application of the recoupled polarization-transfer-heteronuclear multiple-quantum correlation (REPT-HMQC) variant to a liquid-crystal system is presented in Figure 13.10.[61] In the meantime, these experiments have found many further applications on complex organic solids.[62–64] However, a comparison of these indeed user-friendly experiments with LG-CP[65] demonstrated that the latter is in fact superior, since LG-CP benefits from the better signal intensity from larger rotors (no fast MAS required, so rotors larger than 2.5 mm can be used), In this way, more accurate dipolar coupling information can be obtained, however, at the expense of a more elaborate setup of the NMR experiment.

If the motional rate approaches the value of the dipolar coupling constant, the dipolar spectrum is no longer periodic with τ_r, for the incoherent dynamic process interferes with the coherent MAS rotation and leads to a substantial broadening of the dipolar spectrum or an exchange decay of the signal in the indirect dimension, as it does in 1-D NMR spectra in the intermediate-motional regime. To the best of our knowledge, there has been no investigation of

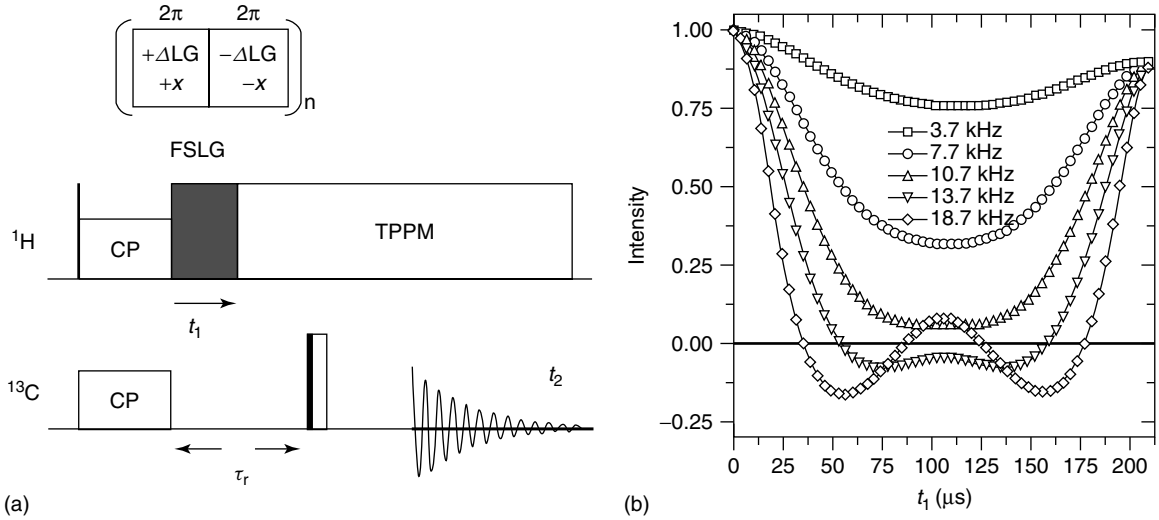


Figure 13.7. (a) Pulse sequence of the DIPSHIFT experiment. The homonuclear decoupling is efficiently achieved by frequency-switched LG decoupling (FSLG). The pulse at τ_r on the carbon channel serves to refocus the evolution due to the chemical shift. (b) DIPSHIFT dephasing curves. The data were calculated at a spinning rate of 4711 Hz, a T_2 of 2 ms, and for the dipolar couplings indicated in the figure.

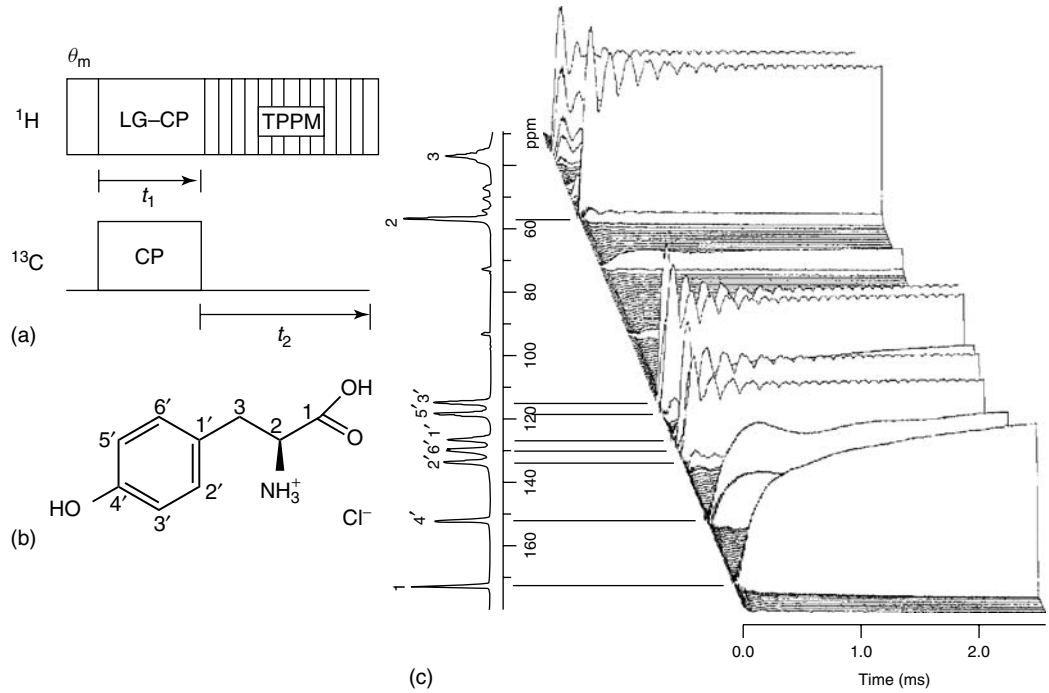


Figure 13.8. (a) Pulse sequence of the LG–CP experiment. (b) Molecular structure and atom numbering of tyrosine · HCl. (c) 2-D LG–CP data. The dipolar couplings can be calculated from the dipolar oscillations. Note the longer period of the oscillations from the nonprotonated carbon 4′. (Reproduced from Ref. 56. © American Chemical Society, 2000.)

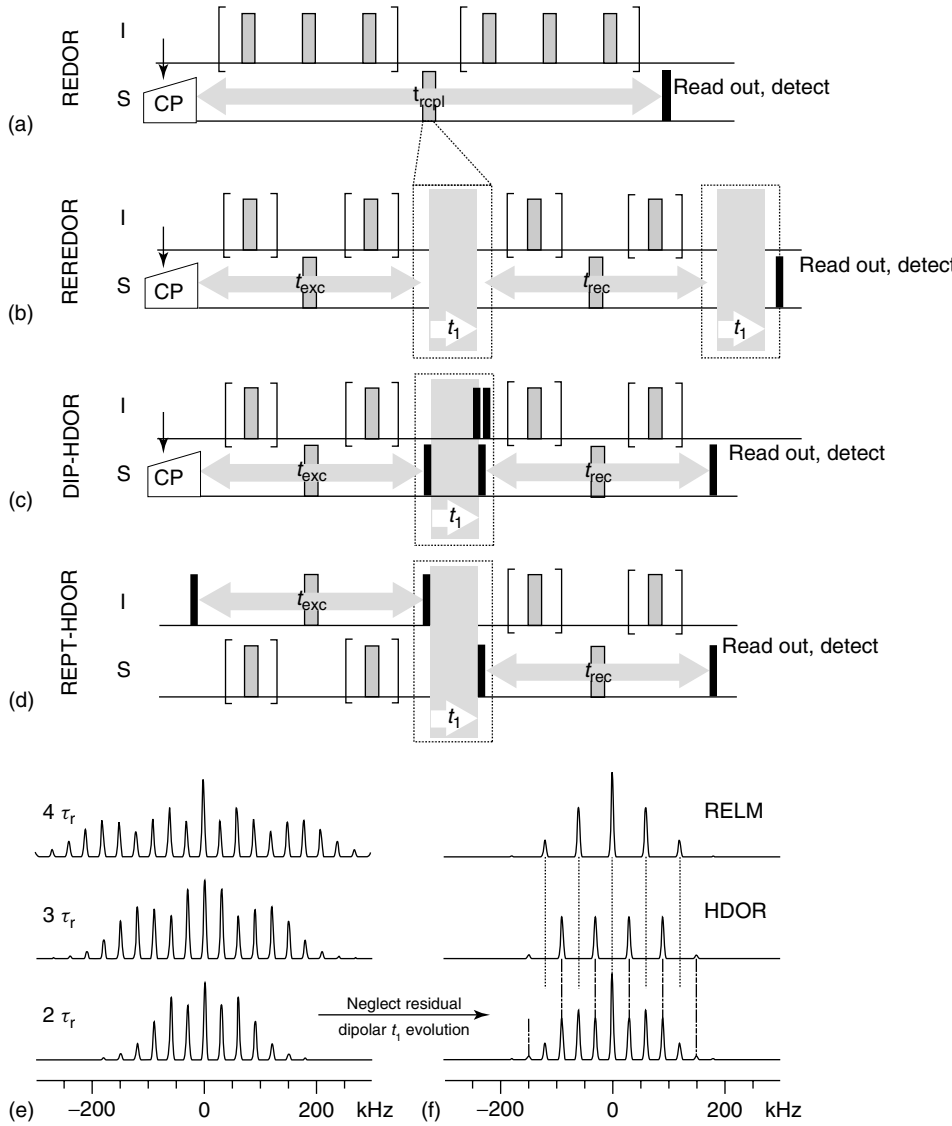


Figure 13.9. (a–d) Variants of REDOR-based ^{1}H–X recoupling experiments with dipolar modulation in t_1 and their relation to the original REDOR. The REPT (recoupled polarization transfer) variant includes an INEPT-type polarization transfer from ^{1}H to X and does not require an initial CP. (e–f) REREDOR sideband patterns (left) for different recoupling times, and the relationship to sidebands from heteronuclear dipolar-order rotor-encoding (HDOR) and rotor-encoding of longitudinal magnetization (RELM) is also shown. The former selects coherences modulated as $<\sin \phi(N\tau_r, 0) \sin \phi(N\tau_r, t_1)>$ (where $\phi(N\tau_r, t_1)$ is the REDOR-recoupled t_1-rotor-encoded dipolar phase), while the latter contributes $<\cos \phi(N\tau_r, 0) \cos \phi(N\tau_r, t_1)>$. The REREDOR manifold is a combination of the two and thus is more sensitive and accurate. (Reproduced from Ref. 60. © Elsevier, 2002.)

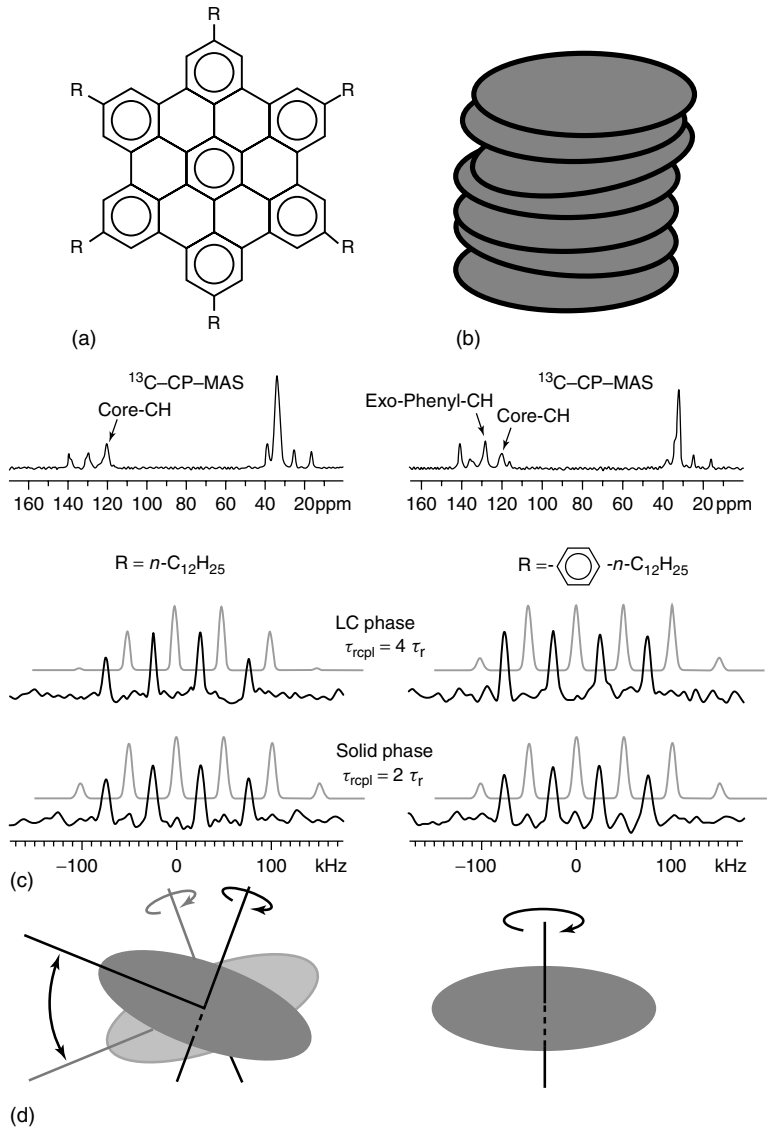


Figure 13.10. ^{1}H–^{13}C REPT-HMQC experiments on hexabenzocoronenes (HBC).[61] The technique is an earlier variant of REPT-HDOR (Figure 13.9f), with interchanged 90° pulses flanking t_1 and an additional 180° pulse on ^{13}C in the middle of t_1—it has additional (here unnecessary) ^{1}H chemical shift information in t_1, For the given purpose, REREDOR (Figure 13.9b) is nowadays more recommendable.[62] (a) Molecular structure of the HBC. (b) Schematic display of molecular stacking of HBCs. Each gray disc is a molecule as shown in (a). (c) The patterns are the sum projections over the core CH signals in the 2-D spectra of HBC-n-$C_{12}H_{25}$ and HBC Ph-n-$C_{12}H_{25}$, respectively. Experimental temperatures were 35 °C for the solid phase and 120 °C for the LC phase. The MAS spectra on top were recorded at a MAS rate of 12 kHz while for the REPT-HMQC experiments, 25 kHz was used. The inserts are simulated spectra. (d) Visualization of motional modes of a single disc in the stacks. While the HBC with the Ph-n-$C_{12}H_{25}$ side chains performs a rotation around an axis perpendicular to the plane of the molecule only, the one with the -n-$C_{12}H_{25}$ side chains appears to do an additional wiggle in the plane of the molecule. This was concluded from the reduced ^{1}H–^{13}C coupling, which can be qualitatively inferred from the reduced intensity of the outer dipolar sidebands.

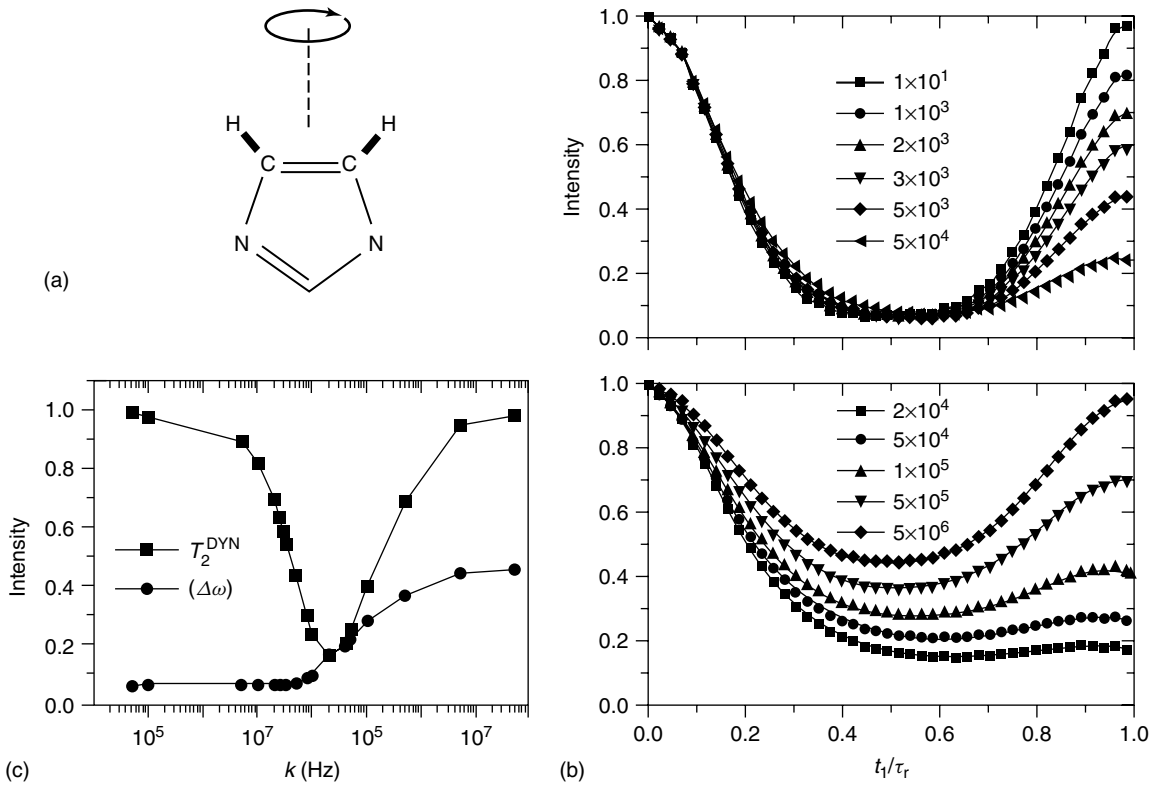


Figure 13.11. Simulated dynamic DIPSHIFT data. (a) Molecular structure of the imidazole molecule, performing two-site jumps of the molecule, which alters the orientation of the CH bond with dipolar coupling of 23 kHz at the basal carbon by 64°. (b) Simulation of DIPSHIFT dephasing curves for jump rates as indicated in the figure. (c) Apparent T_2^{DYN} and apparent dipolar coupling, $\langle \Delta\omega \rangle$ as explained in the text (calculated from the data shown in (b)).

this issue so far, and filling this gap was the concern of recent work of the authors.[19] To calculate the spectra, the A–W approach or its refinements can be used. More elaborate approaches that include the effect of the MAS rotation and the molecular reorientation are available nowadays.[19,66,67] Likewise, the application of the numerical approaches to LG-CP is straightforward. We like to note that though these approaches are computationally demanding, they work for any motional model. In particular, they do not rely on the assumptions made for the A–W theory. In Figure 13.11, we show simulations for DIPSHIFT experiments on the basal carbon of imidazole for jump rates ranging from the static to the fast-limit case. When the jump rate approaches the values of the C–H dipolar coupling, a kind of dynamic T_2 appears, i.e., the value of the dipolar signal at $t_1 = \tau_r$ does not reach that at $t_1 = 0$, indicating the loss of periodicity of the signal. At jump rates close to 10^4 Hz, the apparent dipolar coupling that can be related to the value of the signal at $t_1 = \tau_r/2$ starts to decrease, in concert with an increase of the apparent T_2. For convenience, these effects are parameterized in Figure 13.11(c) as $T_2^{\mathrm{DYN}} = \frac{I(\tau_r)}{I(0)}$ and $\langle \Delta\omega_D \rangle = \frac{I(\tau_r/2)}{I(0)}$. A comparison between the numerical approach and the A–W theory can be found in[19] where simple analytical procedures based on the A–W approximation are presented. In order to establish limits of validity of the A–W based formulas, a comparison with spin dynamics simulations based on the solution of the stochastic Liouville-von-Neumann equation[68] is presented. It is shown that at short evolution times (less than 30% of the rotor period) the A–W based formulas are suitable for fitting the DIPSHIFT curves and extracting kinetic parameters even in the case of jump-like motions. However, full spin dynamics simulations

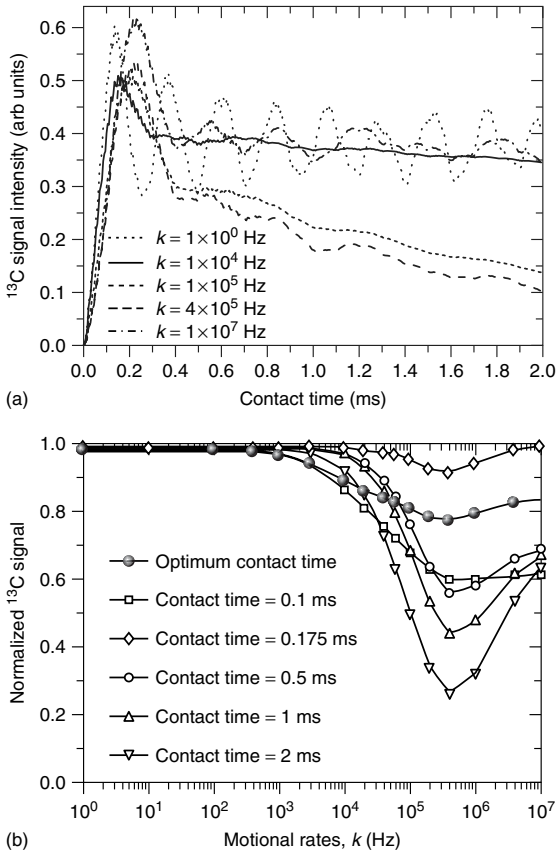


Figure 13.12. (a) Simulated ^{1}H–^{13}C cross-polarization buildup curves at selected motional rates for a CH spin pair. The superposed exponential decay for larger rates (fast limit) is a $T_{1\rho}$ effect. (b) Cross-polarization intensities as a function of the motional rates for selected contact times. The optimum contact time is that one that results in the highest CP efficiency, i.e., it has to be optimized for each jump rate.

provide a more reliable treatment and extend the frequency range of the molecular motions accessible by SLF experiments. Also, the effect of molecular motion on LG–CP (as shown by numerical simulations in Figure 13.12a) as well as on the important issue of CP efficiencies was investigated in this article. In particular, if cross-polarization is used as the excitation method, the presence of a distribution of motional correlation times leads to a bias in the fitted distribution because of the signal decay during the contact time (CT). This holds in particular for segments deep in the intermediate-motional regime (with rates of $\sim10^4$ to 10^5 Hz), which are suppressed in the resulting carbon spectrum, while segments with little (or fast but anisotropic) mobility are overrepresented (see Figure 13.12b).

We like to place a short comment here: although the DIPSHIFT experiment is more efficient in terms of experimental time, it seems to have difficulties when there is overlap of signals resulting from different molecular dynamics leading to different dipolar dephasings. In these cases, it appears difficult to separate the different contributions in the DIPSHIFT dephasing curves, since—at least in the fast limit when the signal is periodic with τ_r—two components with differently averaged coupling can hardly be distinguished from a single component with an in-between coupling. In contrast, in LG-CP experiments, these components would appear in the dipolar dimension (in time domain) with different initial slopes and dipolar oscillations (or alternatively with different widths of the well-structured line shapes when a Fourier transform in t_1 is performed) and can easily be told apart.

13.6 DOUBLE-QUANTUM EXPERIMENTS

One alternative way of dealing with the complex coupling topology in abundant dipolar-coupled spin systems is the excitation of higher-quantum coherences. Many applications in solid-state NMR were pioneered by Pines in the 1980s.[69] The buildup of *DQ* coherences in particular serves to extract information on the dipolar coupling between the *two* spins in question. Effects due to the time-dependent modulations of pair couplings were first reported for DQ experiments on ^{19}F.[70]

Advances in NMR hardware recently paved the way for ultrafast MAS experiments with commercially available MAS rates of 35 kHz,[71] and recently even up to 70 kHz.[72] Such spinning rates, in combination with high fields, enable solid-state ^{1}H experiments with considerably improved (as compared to wide-line experiments) but still limited spectral resolution. These MAS rates efficiently suppress the homonuclear dipolar interaction between more remote nuclei but affect those between next-neighbour nuclei much less.[73,74] DQ-MAS experiments select only those nuclei with nearby like spins and reveal spatial correlations between such spins. The precise value of the dipolar coupling

that carries information on structure and, importantly, the geometry of fast motions, can reliably be extracted from DQ sideband intensities.[75,76] DQ-MAS techniques proved particularly useful in characterizing the anisotropy of mesogenic molecules in liquid crystals,[77] or fast-moving polymer chains in elastomers,[78] polymer melts,[79] and block copolymers.[80] A number of applications of such experiments to different complex macro- and supramolecular systems has recently been reviewed.[81] However, the limited resolution still leaves them far from being generally applicable methods—they are restricted to cases in which the molecular moiety in question is well resolved in the ^{1}H MAS spectrum. Moreover, apart from a pioneering scaling analysis of the relationship between polymer chain dynamics and DQ intensities,[79] DQ-MAS techniques have to date not been used to elucidate the actual *timescale* of fast-to-intermediate motions.

In relatively simple systems such as single-component polymer melts or elastomers, chemical selectivity is often not an important issue. Then, static DQ methods have in fact proven to be more quantitative with respect to the precise absolute determination of weak motionally reduced (residual) ^{1}H–^{1}H dipolar couplings.[82] The absence of complications due to the additional MAS timescale then even allows for a much simpler quantitative treatment of intermediate-motional effects in DQ experiments (in terms of Anderson–Weiss theory),[33] and an application to chain dynamics in elastomers is described in Ref. 34.

13.7 DIPOLAR EXCHANGE NMR—SLOW MOTIONS

The slow motion regime (A) is commonly called the *static case*, i.e., although there might be an appreciable amount of molecular mobility, it is too slow to be observed in NMR spectra ("it is slow on the NMR timescale"). Such dynamic processes can, however, be observed in so-called exchange experiments[83,84] or specific NMR relaxation experiments.[85] The application of the dipolar interaction in the framework of exchange experiments, i.e., the observation of the reorientation of a dipolar vector connecting two nuclei during time periods much longer than the lifetime of the FID and quantitative interpretation is in principle possible; however, it requires the existence of spin pairs, as otherwise, magnetization exchange processes (spin diffusion, etc.) dominate and severely restrict the dynamic range. This can be facilitated by isotopic labeling, inserting the desired spins into the molecules,[86] or by experimental conditions that suppress multispin interactions. Such situations can be found—for example—in ^{1}H-depleted substances where only few ^{1}H spins are around, and the interaction between remote nuclei is further suppressed by very fast MAS.[87,88] Experiments of the latter kind are in progress and will certainly be reported soon. The methodology of DQ experiments has been extended to DQ–DQ exchange experiments permitting the investigation of slow motion.[89] Generally, applications of exchange-type experiments utilizing the dipolar coupling are rare and are thus not discussed here at length.

13.8 SUMMARY

Homo- and heteronuclear dipolar couplings belonged to the tool box of dynamic solid-state NMR from the early days of NMR. Owing to the progress in NMR hardware, the development progressed from low-resolution wide-line spectra via separated-local field experiments, employing cross-polarization and MAS, to DQ experiments under very fast MAS. Although the most accurate NMR tool for dynamic studies is still the exploration of the quadrupolar coupling in ^{2}H NMR experiments, organic solids at natural isotopic abundance are clearly most preferably studied by use of dipolar couplings.

REFERENCES

1. E. R. Andrew and R. G. Eades, *Proc. R. Soc. London, Ser. A: Math. Phys. Sci.*, 1953, **218**, 537.
2. G. E. Pake, *Solid State Phys.: Adv. Res. Appl.*, 1956, **2**, 1.
3. E. R. Andrew, A. Bradbury, and R. G. Eades, *Nature*, 1958, **182**, 1659.
4. E. R. Andrew, A. Bradbury, and R. G. Eades, *Nature*, 1959, **183**, 1802.
5. I. J. Lowe, *Phys. Rev. Lett.*, 1959, **2**, 285.
6. H. S. Gutowsky, D. W. McCall, and C. P. Slichter, *J. Chem. Phys.*, 1953, **21**, 279.
7. H. S. Gutowsky, G. B. Kistiakowsky, G. E. Pake, and E. M. Purcell, *J. Chem. Phys.*, 1949, **17**, 972.

8. E. R. Andrew, *J. Chem. Phys.*, 1950, **18**, 607.
9. W. P. Slichter, *Makromol. Chem.*, 1959, **34**, 67.
10. K. H. Illers and R. Kosfeld, *Makromol. Chem.*, 1960, **42**, 44.
11. H. S. Gutowsky and G. E. Pake, *J. Chem. Phys.*, 1950, **18**, 162.
12. M. Mehring, G. Sinning, and A. Pines, *Z. Phys. B: Condens. Matter*, 1976, **24**, 73.
13. G. Lipari and A. Szabo, *J. Am. Chem. Soc.*, 1982, **104**, 4559.
14. G. Lipari and A. Szabo, *J. Am. Chem. Soc.*, 1982, **104**, 4546.
15. V. Fedotov and H. Schneider, in *'NMR Basic Principles and Progress'*, eds P. Diehl, E. Fluck, H. Günther, R. Kosfeld and J. Seelig, Springer: Berlin, 1989, Vol. **21**, p 1.
16. A. G. Krushelnitsky, G. Hempel, and D. Reichert, *Biochim. Biophys. Acta: Proteins Proteomics*, 2003, **1650**, 117.
17. K. Schmidt-Rohr and H. W. Spiess, *'Multidimensional Solid-State NMR and Polymers'*, Academic Press: London, 1994.
18. P. W. Anderson and P. R. Weiss, *Rev. Mod. Phys.*, 1953, **25**, 269.
19. E. deAzevedo, K. Saalwächter, O. Pascui, A. Desouza, T. J. Bonagamba, and D. Reichert, *J. Chem. Phys.*, 2008, **128**, 104505.
20. R. Kimmich, *NMR-Tomography, Diffusometry, Relaxometry*, Springer: Berlin, 1998.
21. J. Hirschinger, *Concepts Magn. Reson., Part A*, 2006, **28A**, 307.
22. M. Goldman, T. Tabti, C. Fermon, J. F. Jacquinot, and G. Saux, *J. Magn. Reson., Ser. A*, 1993, **103**, 288.
23. J. Seliger, *J. Magn. Reson., Ser. A*, 1993, **103**, 175.
24. J. I. Kaplan, *Phys. Rev., A*, 1980, **22**, 1022.
25. W. Hiller and H. Schneider, *Acta Polym.*, 1988, **39**, 276.
26. R. Kimmich, G. Schnur, and M. Kopf, *Prog. Nucl. Magn. Reson. Spectrosc.*, 1988, **20**, 385.
27. F. Engelke, T. Kind, D. Michel, M. Pruski, and B. C. Gerstein, *J. Magn. Reson.*, 1991, **95**, 286.
28. D. Fenzke, B. C. Gerstein, and H. Pfeifer, *J. Magn. Reson.*, 1992, **98**, 469.
29. T. P. Kulagina, V. M. Litvinov, and K. T. Summanen, *J. Polym. Sci., Part B: Polym. Phys.*, 1993, **31**, 241.
30. D. Freude, H. Ernst, and I. Wolf, *Solid State Nucl. Magn. Reson.*, 1994, **3**, 271.
31. W. Kuhn, P. Barth, S. Hafner, G. Simon, and H. Schneider, *Macromolecules*, 1994, **27**, 5773.
32. R. C. Ball, P. T. Callaghan, and E. T. Samulski, *J. Chem. Phys.*, 1997, **106**, 7352.
33. K. Saalwächter, *J. Chem. Phys.*, 2004, **120**, 454.
34. K. Saalwächter and A. Heuer, *Macromolecules*, 2006, **39**, 3291.
35. B. S. Douglass, R. J. Cormier, and P. T. Callaghan, *Phys. Rev. E.*, 2007, **75**.
36. R. K. Hester, J. L. Ackerman, B. L. Neff, and J. S. Waugh, *Phys. Rev. Lett.*, 1976, **36**, 1081.
37. S. Dusold and A. Sebald, *Annu. Rep. NMR Spectrosc.*, 2000, **41**, 185.
38. D. G. Cory and W. M. Ritchey, *Macromolecules*, 1989, **22**, 1611.
39. A. A. Parker, J. J. Marcinko, P. Rinaldi, D. P. Hedrick, and W. M. Ritchey, *J. Appl. Polym. Sci.*, 1993, **48**, 677.
40. J. J. Marcinko, A. A. Parker, Y. T. Shieh, and W. M. Ritchey, *J. Appl. Polym. Sci.*, 1992, **45**, 391.
41. I. Klur, J. F. Jacquinot, F. Brunet, T. Charpentier, J. Virlet, C. Schneider, and P. Tekely, *J. Phys. Chem., B*, 2000, **104**, 10162.
42. E. F. Rybaczewski, B. L. Neff, J. S. Waugh, and J. S. Sherfinski, *J. Chem. Phys.*, 1977, **67**, 1231.
43. M. Linder, A. Hohener, and R. R. Ernst, *J. Chem. Phys.*, 1980, **73**, 4959.
44. M. G. Munowitz, R. G. Griffin, G. Bodenhausen, and T. H. Huang, *J. Am. Chem. Soc.*, 1981, **103**, 2529.
45. J. Schaefer, R. A. Mckay, and E. O. Stejskal, *J. Magn. Reson.*, 1983, **52**, 123.
46. J. Schaefer, M. D. Sefcik, E. O. Stejskal, R. A. Mckay, W. T. Dixon, and R. E. Cais, *Macromolecules*, 1984, **17**, 1107.
47. S. Swanson, S. Ganapathy, S. Kennedy, P. M. Henrichs, and R. G. Bryant, *J. Magn. Reson.*, 1986, **69**, 531.
48. N. Zumbulyadis, *Phys. Rev., B*, 1986, **33**, 6495.
49. P. Tekely, D. Nicole, J. Brondeau, and J. J. Delpuech, *J. Phys. Chem.*, 1986, **90**, 5608.
50. K. Schmidt-Rohr, J. Clauss, and H. W. Spiess, *Macromolecules*, 1992, **25**, 3273.
51. X. H. Qiu and P. A. Mirau, *J. Magn. Reson.*, 2000, **142**, 183.

52. D. McElheny, E. Devita, and L. Frydman, *J. Magn. Reson.*, 2000, **143**, 321.
53. C. H. Wu, A. Ramamoorthy, and S. J. Opella, *J. Magn. Reson., Ser. A*, 1994, **109**, 270.
54. A. C. Kolbert, H. J. M. De Groot, M. H. Levitt, M. G. Munowitz, J. E. Roberts, G. S. Harbison, J. Herzfeld, and R. G. Griffin, in *'Multinuclear Magnetic Resonance in Liquids and Solids-Chemical Applications'*, eds P. Granger and R. K. Harris, Kluwer Academic Publishers: Dordrecht, 1990, p 339.
55. M. Hong, J. D. Gross, and R. G. Griffin, *J. Phys. Chem., B*, 1997, **101**, 5869.
56. B. J. Van Rossum, C. P. De Groot, V. Ladizhansky, S. Vega, and H. J. M. De Groot, *J. Am. Chem. Soc.*, 2000, **122**, 3465.
57. P. Barre, S. Yamaguchi, H. Saito, and D. Huster, *Eur. Biophys. J. Biophys. Lett.*, 2003, **32**, 578.
58. D. Reichert, O. Pascui, E. R. deAzevedo, T. J. Bonagamba, K. Arnold, and D. Huster, *Magn. Reson. Chem.*, 2004, **42**, 276.
59. T. Gullion and J. Schaefer, *J. Magn. Reson.*, 1989, **81**, 196.
60. K. Saalwächter and I. Schnell, *Solid State Nucl. Magn. Reson.*, 2002, **22**, 154.
61. A. Fechtenkotter, K. Saalwächter, M. A. Harbison, K. Mullen, and H. W. Spiess, *Angew. Chem., Int. Ed.*, 1999, **38**, 3039.
62. M. M. Elmahdy, G. Floudas, M. Mondeshki, H. W. Spiess, X. Dou, and K. Müllen, *Phys. Rev. Lett.*, 2008, **100**, 107801.
63. M. Schulz-Dobrick, T. Metzroth, H. W. Spiess, J. Gauss, and I. Schnell, *ChemPhysChem*, 2005, **6**, 315.
64. A. Rapp, I. Schnell, D. Sebastiani, S. P. Brown, V. Percec, and H. W. Spiess, *J. Am. Chem. Soc.*, 2003, **125**, 13284.
65. J. Becker, A. Comotti, R. Simonutti, P. Sozzani, and K. Saalwächter, *J. Phys. Chem., B*, 2005, **109**, 23285.
66. A. Schmidt, S. O. Smith, D. P. Raleigh, J. E. Roberts, R. G. Griffin, and S. Vega, *J. Chem. Phys.*, 1986, **85**, 4248.
67. A. Schmidt and S. Vega, *J. Chem. Phys.*, 1992, **96**, 2655.
68. K. Saalwächter and I. Fischbach, *J. Magn. Reson.*, 2002, **157**, 17.
69. J. Baum, M. Munowitz, A. N. Garroway, and A. Pines, *J. Chem. Phys.*, 1985, **83**, 2015.
70. D. A. Lathrop and K. K. Gleason, *Macromolecules*, 1993, **26**, 4652.
71. H. J. Jacobson, *'Encyclodedia of Nuclear Magnnetic Resonance'*, John Wiley & Sons: Chichester, 1996, Vol. **1**, p 398.
72. A. Samoson, T. Tuherm, J. Past, A. Reinhold, T. Anupold, and N. Heinmaa, *Top. Curr. Chem.*, 2005, **26**, 15.
73. H. Geen, J. J. Titman, J. Gottwald, and H. W. Spiess, *Chem. Phys. Lett.*, 1994, **227**, 79.
74. S. Hafner and H. W. Spiess, *Concepts Magn. Reson.*, 1998, **10**, 99.
75. J. Gottwald, D. E. Demco, R. Graf, and H. W. Spiess, *Chem. Phys. Lett.*, 1995, **243**, 314.
76. U. Friedrich, I. Schnell, S. P. Brown, A. Lupulescu, D. E. Demco, and H. W. Spiess, *Mol. Phys.*, 1998, **95**, 1209.
77. S. P. Brown, I. Schnell, J. D. Brand, K. Mullen, and H. W. Spiess, *J. Am. Chem. Soc.*, 1999, **121**, 6712.
78. R. Graf, D. E. Demco, S. Hafner, and H. W. Spiess, *Solid State Nucl. Magn. Reson.*, 1998, **12**, 139.
79. R. Graf, A. Heuer, and H. W. Spiess, *Phys. Rev. Lett.*, 1998, **80**, 5738.
80. T. Dollase, R. Graf, A. Heuer, and H. W. Spiess, *Macromolecules*, 2001, **34**, 298.
81. S. P. Brown and H. W. Spiess, *Chem. Rev.*, 2001, **101**, 4125.
82. K. Saalwächter, *Prog. Nucl. Magn. Reson. Spectrosc.*, 2007, **51**, 1.
83. A. D. Bain, *Prog. Nucl. Magn. Reson. Spectrosc.*, 2003, **43**, 63.
84. Z. Luz, P. Tekely, and D. Reichert, *Prog. Nucl. Magn. Reson. Spectrosc.*, 2002, **41**, 83.
85. A. G. Krushelnitsky, A. E. Mefed, A. A. Kharitonov, and V. D. Fedotov, *Appl. Magn. Reson.*, 2001, **20**, 207.
86. W. G. Hu, C. Boeffel, and K. Schmidt-Rohr, *Macromolecules*, 1999, **32**, 1611.
87. M. Hologne, V. Chevelkov, and B. Reif, *Prog. Nucl. Magn. Reson. Spectrosc.*, 2006, **48**, 211.
88. V. Chevelkov, K. Rehbein, A. Diehl, and B. Reif, *Angew. Chem., Int. Ed.*, 2006, **45**, 3878.
89. I. Schnell, A. Watts, and H. W. Spiess, *J. Magn. Reson.*, 2001, **149**, 90.

Chapter 14
Spin Diffusion in Crystalline Solids

Lyndon Emsley

Centre de RMN à Très Hauts Champs (CNRS / ENS-Lyon / UCB Lyon 1), Université de Lyon, 69100 Villeurbanne, France

14.1	Introduction	195
14.2	The Mechanism of Spin Diffusion	196
14.3	Experiments to Measure Spin Diffusion	197
14.4	Modeling Spin Diffusion	197
14.5	Applications of Spin Diffusion to NMR Crystallography	201
14.6	Conclusion	205
	References	206

14.1 INTRODUCTION

Structural characterization of powdered samples is of ever-increasing importance for a wide range of contemporary materials-related problems, including, for example, the characterization of inorganic framework materials or of polymorphic pharmaceutical compounds.

While X-ray diffraction remains the method of choice for the structure determination of single-crystals, three main approaches are used for the crystallographic characterization of powders: powder X-ray (or neutron) diffraction, computationally based structure prediction techniques, and solid-state NMR.

NMR Crystallography Edited by Robin K. Harris, Roderick E. Wasylishen and Melinda J. Duer © 2009 John Wiley & Sons, Ltd. ISBN: 978-0-470-69961-4

In this respect, the field of NMR crystallography has seen very rapid growth over the past few years. Impressive results have been shown for NMR structure determination in inorganic framework materials.[1] In the field of molecular crystals, there has been particular progress toward structure *validation* methods by developing approaches to assign natural abundance solid-state NMR spectra, and then combining this with state-of-the art DFT chemical shift calculation methods.[2] These validation methods allow the assignment of a given powder form to a known crystal structure (usually obtained from single-crystal X-ray diffraction). These approaches are particularly effective, and have even been used to identify polymorphs in the presence of excipient mixtures in pharmaceutical tablet formulations.

Moreover, recently introduced approaches not only validate a structure but also offer the possibility of *complete ab initio structure determination* in molecular powders using combined NMR and computational methods. It has been shown how proton spin-diffusion (PSD) curves can be analyzed in terms of molecular conformation and crystal packing,[3] and shown that PSD data can be incorporated as restraints in a molecular modeling-based structure determination.[4,5]

In parallel to the development of proton spin diffusion to solve the structures of small molecules, there has been very rapid development in solid-state NMR approaches to determine the structures of biologically relevant solids, such as crystalline proteins[6] or fibril forming peptides,[7,8] or membrane included proteins.[9]

All these developments have principally relied so far on distance constraints that are derived from either proton spin diffusion or proton-driven carbon spin diffusion.

In this article, we review the role of spin diffusion in NMR crystallography.

14.2 THE MECHANISM OF SPIN DIFFUSION

If the energy levels that are connected by a dipolar coupling (e.g., the $\alpha\beta$ and $\beta\alpha$ levels in a two spin $I = 1/2$ system) have the same energy, then magnetization exchange (spin diffusion) can occur spontaneously (Figure 14.1). This is not usually the case. However, nuclear spin diffusion still occurs readily in solids because of the presence of a dense network of dipolar coupled nuclear spins. This allows for energy-conserving flip–flop transitions and is responsible for the transport of the magnetization. Bloembergen described the phenomenon in the very early days of NMR,[10] but it was with the introduction of multidimensional NMR experiments that it became easily observable. Spin diffusion can be in general separated into the study of *spatial transport of polarization (spatial spin diffusion)*[11–13] or to the study of *polarization exchange between different resonances in a spectrum (spectral spin diffusion)*.[11] The two processes are formally almost identical, and the information obtained is complementary. Here we focus on spectral spin diffusion. An excellent review on spin diffusion has been published by Meier.[11]

In the following, we see how experiments to observe spin diffusion are relatively easy to perform, yet their interpretation is difficult, primarily because the number of dipolar couplings contributing to the process is large.

In organic solids, we usually differentiate two different types of spectral spin diffusion:

1. *Proton Spin Diffusion* (PSD): In most protonated solids, under all but the fastest magic angle spinning conditions, the effective proton–proton dipolar couplings are significant compared to the (relatively limited) chemical shift differences, and so the dipolar couplings to the other protons produce a strong driving force for spin diffusion between two protons. Proton spin diffusion is usually fast.
2. *Proton-Driven Spin Diffusion* (PDSD): Generally, for nuclei such as phosphorus-31, carbon-13, silicon-29, or nitrogen-15, chemical shift differences are significantly larger than the residual homonuclear dipolar couplings under magic angle spinning. Spin diffusion is then quenched. However, in the presence of heteronuclear dipolar couplings to protons, a flip–flop process between the heteroatoms (e.g., two carbon-13 nuclei) can be compensated for by a change of state in the coupled protons, leading to a process with an overall conservation of energy. This process is referred to as *proton-driven spin diffusion*, and although not usually as efficient as pure PSD, it can lead to quite fast spin diffusion between heteroatoms.

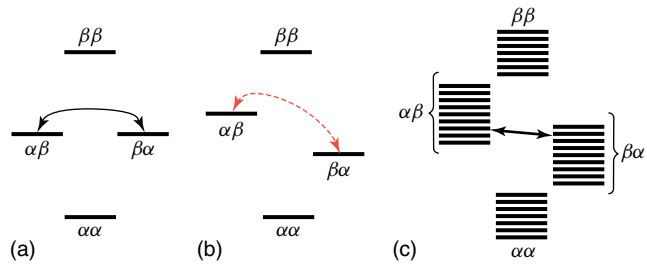


Figure 14.1. Energy levels for a two spin system. (a) When the two spins are equivalent, the $\alpha\beta$ and $\beta\alpha$ states are degenerate. The dipolar coupling between the two nuclei induces an energy-conserving "flip–flop" transition between these two states, and magnetization transfer (spin diffusion) occurs. (b) When the two spins are not equivalent, the transition is not energy conserving and its probability is low. Spin diffusion is quenched. (c) When the two inequivalent spins are coupled to (many) other spins, the energy levels of the two spin system are split (broadened) by these couplings and an overlap can occur between some of the levels $\alpha\beta$ and $\beta\alpha$. Transitions between these levels are now allowed and spin diffusion can occur. (Figure courtesy of D. Sakellariou.)

Theoretical approaches to the two processes are broadly similar.

Before moving on, it is worth noting at this point that processes such as cross polarization or REDOR can be viewed as heteronuclear radio frequency-driven spin diffusion, and homonuclear dipolar recoupling sequences can be viewed as homonuclear radio frequency-driven spin diffusion. A description of the spin dynamics that they induce shares many of the theoretical aspects of ordinary spin diffusion.

In conclusion, we see that for both processes, the spin diffusion rate depends not only on the dipolar couplings between the exchanging nuclei but also on their couplings to the environment. We see in the following section how this dramatically complicates the extraction of useful information.

14.3 EXPERIMENTS TO MEASURE SPIN DIFFUSION

Monitoring of spectral spin diffusion is relatively easy using 2-D experiments. The three most commonly used experiments to measure spin diffusion are shown in Figure 14.2 and all are derivatives of basic two-dimensional exchange spectroscopy. Figure 14.2(a) shows the sequence required for measuring PSD, and is probably the most experimentally demanding of the three. In this scheme, high-resolution proton NMR spectra are correlated in t_1 and t_2 by a spin diffusion time τ_{SD}.

As shown, high-resolution proton spectra require the application of homonuclear dipolar decoupling sequences under MAS. The experiment was first proposed by Caravatti *et al*.[14] in 1985 but was basically left unused until quite recently because sufficiently robust homonuclear decoupling sequences were not available. This situation has changed with the introduction of PMLG[15] and DUMBO[16,17] decoupling together with NMR consoles having state-of-the art electronics. Currently, PSD experiments are perfectly feasible, and examples are discussed in detail in the following sections.

PSD experiments are recorded almost exclusively under MAS, because static lineshapes are not sufficiently characteristic for protons to be of great use.

In isotopically enriched samples, PSD can be observed indirectly with the CHHC (or NHHC or other variants) experiment shown in Figure 14.2(c).[18,19] Carbon-13 (for example) MAS spectra are correlated by a short back CP step from carbon to protons, a PSD time τ_{SD}, and another CP step to return the magnetization to carbon. This combines the structural pertinence of PSD with the high resolution of the carbon-13 spectrum, and is a method of choice when isotopic enrichment is available (typically for proteins).

Figure 14.2(b) shows the experiment suitable to record PDSD correlation spectra.[20] This is a simple exchange spectroscopy sequence, which is particularly simple to implement and is the primary reason why the PDSD experiment is now so widely used. Note that the PDSD experiment can be carried out both under MAS and for static samples, because there are cases where the carbon-13 lineshapes are well defined enough by the chemical shift anisotropy to provide detailed crystallographic information, as we see in the following.

14.4 MODELING SPIN DIFFUSION

Because spin diffusion is mainly induced by the homonuclear dipolar interaction, it is in principle possible to determine the internuclear distance from measured spin-diffusion rates. However, in practice, it turns out to be extremely difficult to derive models for spin diffusion behavior. Three main approaches have been explored: first principles, numerical, and phenomenological.

Before summarizing each approach, we should mention that spin diffusion is a fully coherent process. The models developed below will invariably at some point give up reversibility in the description of the dynamics in order to simplify the problem. However, we note that the process is reversible, and that this has been convincingly demonstrated experimentally.[21]

14.4.1 Numerical Approaches

Because analytical approaches are not currently sufficient, the apparently simplest approach would be to use numerical simulations to predict spin diffusion rates. Here the problem is that the number of spins contributing to the polarization transfer dynamics is much larger than the number of spins that can be included in an exact density matrix simulation with the current computing resources. Toward this end,

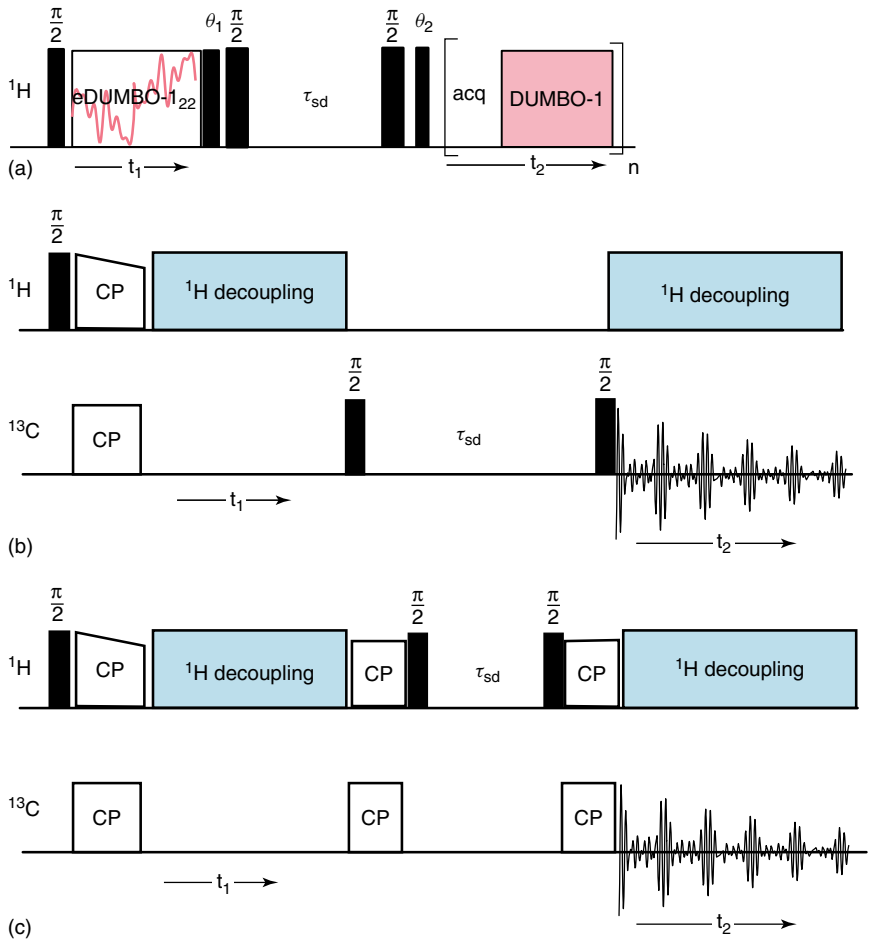


Figure 14.2. Pulse sequences for measuring (a) PSD with proton detection, (b) carbon–carbon PDSD, and (c) PSD with carbon detection (CHHC).

the spin diffusion problem has been one of the key driving forces for improved approaches to NMR simulations. The results have included simulation packages such as libcmatrix[22] or SPINEVOLUTION[23] optimized for large numbers of spins. Other developments have included the use of approximate propagation methods,[24] or the incorporation of symmetry considerations, and notably spatial periodicity.[25] The result is that today simulations can be run in a reasonable time for between 12 and15 spins, but 20 spins is still well out of reach. This limit of just over 10 spins has produced some interesting results related to spin diffusion,[26] including the reproduction of smooth spin diffusion curves. However, these approaches are not yet good enough to reproduce the fine details of spin diffusion dynamics required to determine molecular geometry. This is probably because there is now considerable evidence to show that typically more than 100 surrounding spins contribute to an ordinary spin diffusion curve.[3,27]

14.4.2 First Principles Approaches

The theoretical study of proton-driven spin diffusion is complicated because of the strong interactions between multiple bodies. Several first principle theoretical approaches in the past have been proposed, with

the most successful being the method of second order perturbation theory introduced by Suter and Ernst[28,29] and the method of memory functions introduced by Henrichs *et al*.[30] The case of MAS was treated within the framework of perturbation theory by Kubo and McDowell.[31]

The idea of Suter and Ernst was to link the isolated spin system with a bath of extraneous spins, in a manner analogous to semiclassical relaxation theory.[32] For relaxation, the environment is described by a stochastic process averaged over the ensemble, whereas in spin diffusion in solids, the coupling to the bath (first order) is coherent.[21]

We do not discuss the complex detail of these different approaches. For the current purpose, it is sufficient to say that in general a form for the equation of motion can, within certain limits, be obtained, which predicts that the rate of spin diffusion between two spins is given by a form given in equation (14.1):

$$W^{(2)} = -D^2 g^{(23)}(\Delta\omega) \qquad (14.1)$$

where D is the dipolar coupling constant between the two spins (which depends on the inverse third power of the internuclear distance) and $g^{(23)}(\Delta\omega)$ is the so-called zero-quantum lineshape, evaluated at the frequency $\Delta\omega$, the difference between the chemical shifts of the two spins. This is a deceptively simple result. In reality, it is extremely difficult to evaluate $g^{(23)}$, which depends on many factors including crystallite orientations, magic angle spinning speeds, and most importantly, the dipolar couplings to (all) other spins.

Much effort has been made to evaluate the zero-quantum lineshape function, including clever approximate methods. Although this has proved useful for some applications, no general approach has been found, and there is no existing approach suitable for detailed molecular structural studies.

14.4.3 Phenomenological Approaches

All of the structural studies based on either PSD or PDSD so far have used either an essentially qualitative analysis of spectra or an analysis based on a phenomenological description of spin diffusion in which we assume a simple exponential rate behavior for the exchange between two spins of the form given in equation (14.2)

$$k_{ij} = \sum_{\lambda \text{ molecules}} \left(\frac{\mu_0 \gamma_H^2 \hbar}{4\pi}\right)^2 \frac{A}{\left(r_{ij}^6\right)}, \quad i \neq j \qquad (14.2)$$

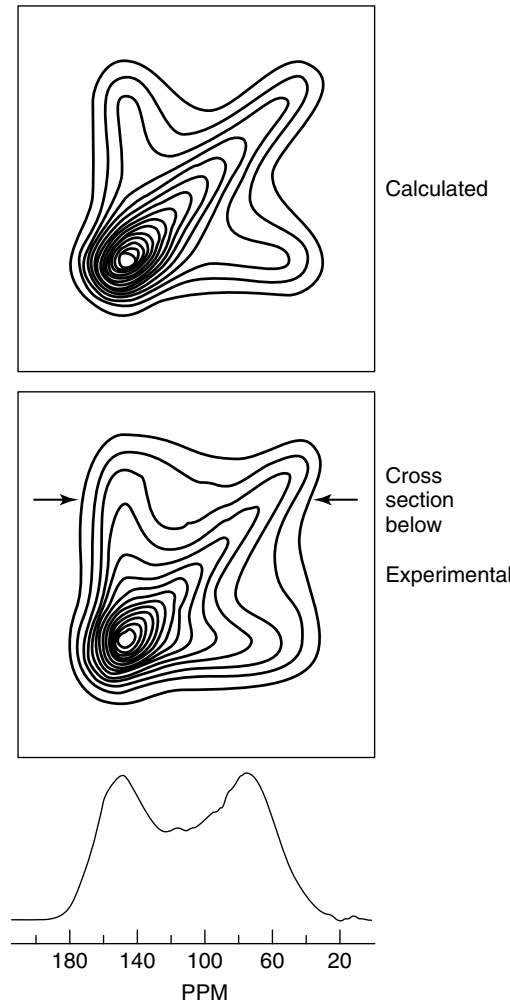


Figure 14.3. Two-dimensional, phase-sensitive, spin diffusion spectra of ^{13}C-labeled zinc acetate dihydrate. The spectrum at the top is a calculated spectrum. The spectrum at the bottom is a slice taken at the position indicated in the experimental spectrum shown in the middle. The spectrometer frequency for carbon was 25 MHz, and the mixing time for spin diffusion to occur was 0.5 s. Spin diffusion essentially goes to completion during this period. (Reproduced from Ref. 34. © Elsevier, 1984.)

and where the intensity of a cross peak in the spectrum is then simply given by a matrix equation as in equation (14.3):

$$P_{ij}(\tau_{SD}) = \exp(-\boldsymbol{K} \cdot \tau_{SD})_{ij} \cdot M_z^{j,0} \qquad (14.3)$$

where $M_z^{j,0}$ is the volume of the diagonal peaks for $\tau_{SD} = 0$ s and $\boldsymbol{K}$ is the exchange rate constant matrix, the elements of which are given by equation (14.2). Each cross peak build-up curve is thus in fact a sum of different curves arising from dipolar interaction with many different equivalent molecules. Full details of this approach have been published elsewhere.[3,4]

This approach is found to be surprisingly accurate and robust.[4,5] It has been used not only in its full

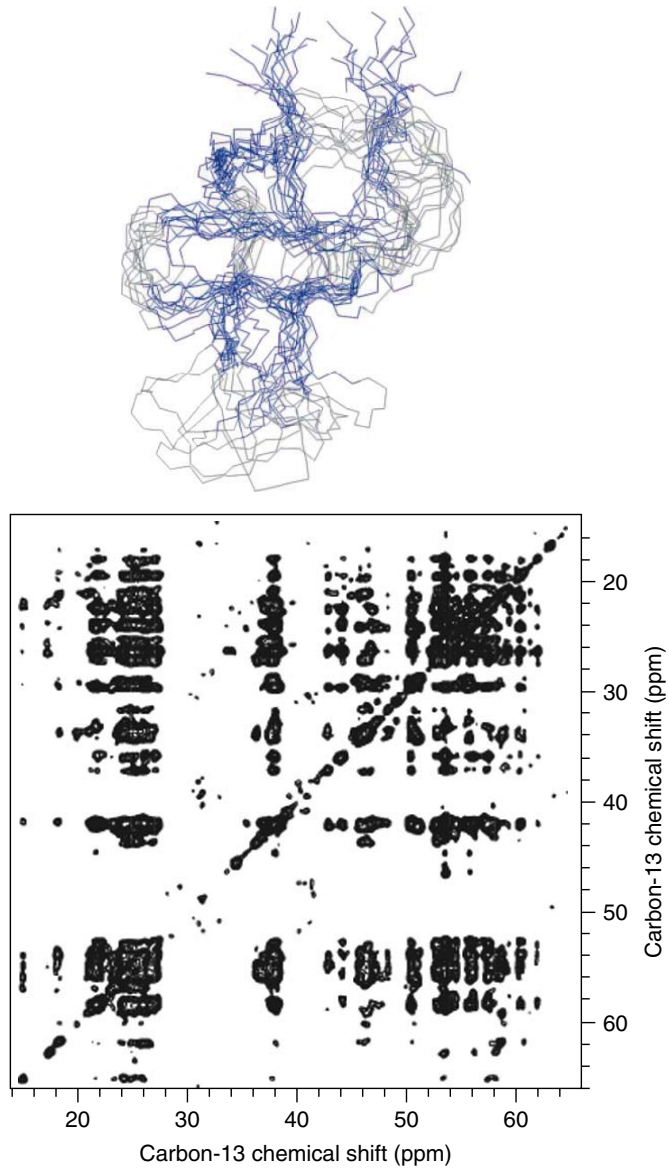


Figure 14.4. PDSD spectrum of the SH3 protein, and the resulting three-dimensional structure. (Reproduced from Ref. 6. © Nature Publishing Group, 2002.)

form, but also in a regime of the initial rates, where the sum over the crystalline lattice can be neglected. Examples are given in the following section.

14.5 APPLICATIONS OF SPIN DIFFUSION TO NMR CRYSTALLOGRAPHY

14.5.1 Results for Static Samples

The earliest examples of the use of spin diffusion for determining molecular conformations were introduced together with the two-dimensional PDSD method. Using a qualitative analysis of the peak shapes in static carbon–carbon PDSD spectra, Edzes and Bernards were able to clearly determine the relative chain orientations in crystalline polyethylene.[33] Henrichs and Linder[34] used a quantitative analysis of the 2-D lineshape in the same type of static carbon-13 experiment to determine the relative orientation of the two molecules of zinc acetate in the unit cell of the crystal structure. The spectrum they used and the best-fit simulation are shown in Figure 14.3.

A more recent example of this approach was demonstrated by Tycko and Dabbagh[35] to study the molecular orientational ordering in methanol glass.

14.5.2 Protein Structures from PDSD and CHHC Data

There has recently been a strong renaissance in the interest for spin diffusion as a structural tool, following the introduction of methods for preparing microcrystalline samples of solid proteins suitable for NMR. This allowed Oschkinat and coworkers[6] to measure 2-D PDSD spectra for the SH3 protein of the kind shown in Figure 14.4. By interpreting the cross peak intensities simply as a qualitative distance constraint in molecular modeling, in the same way as NOESY cross peak intensities are often used in liquid-state NMR protein structure determination, they were then able to determine the first solid-state protein structure by NMR. Since then, a series of protein structures have been determined in this way, using primarily PDSD or CHHC data, in conjunction with other structural restraints.[36] Recently, this approach has been extended to the successful structure determination of a fibril forming peptide, HET-S.[8]

14.5.3 Small Molecule Structures from Quantitative Initial Rate Analysis of CHHC Data

In parallel to the development of PDSD and CHHC experiments for protein structures, Baldus and coworkers[37,38] have shown two very nice examples of the determination of the molecular conformation in crystalline powders of two small molecules using a quantitative analysis of CHHC data. In this case,

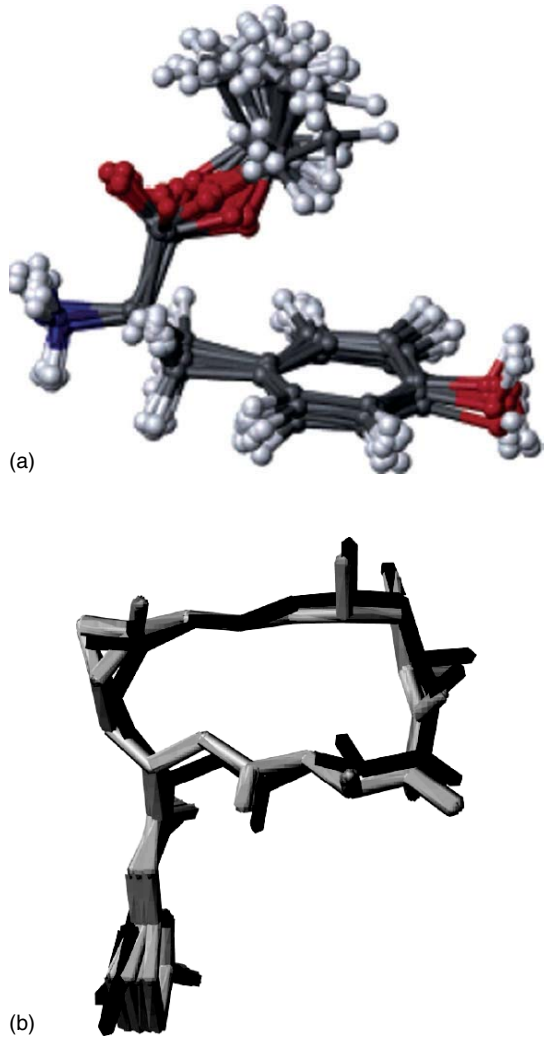


Figure 14.5. Molecular conformations of (a) tyrosine ethyl ester and (b) epithilone B, determined from CHHC PSD data.[37,38]

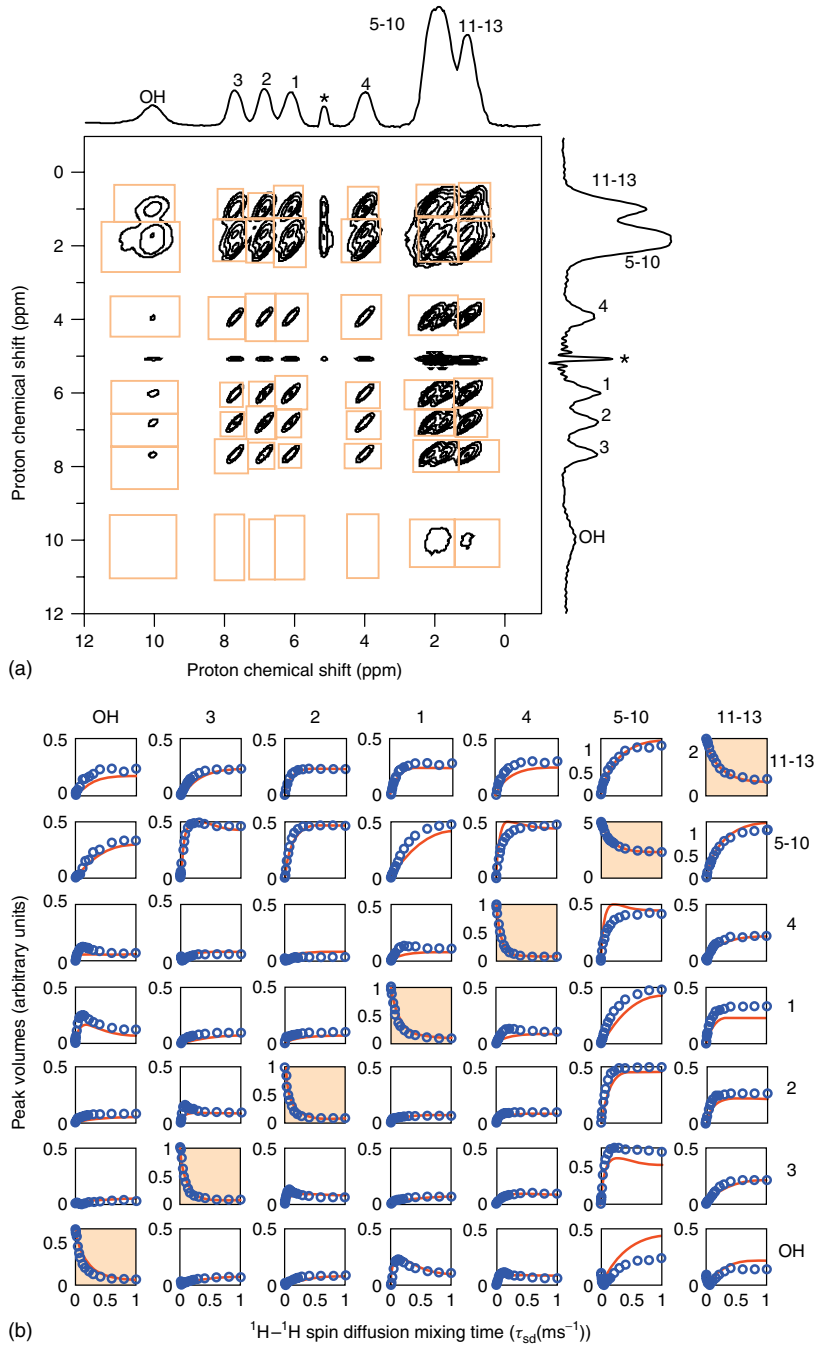
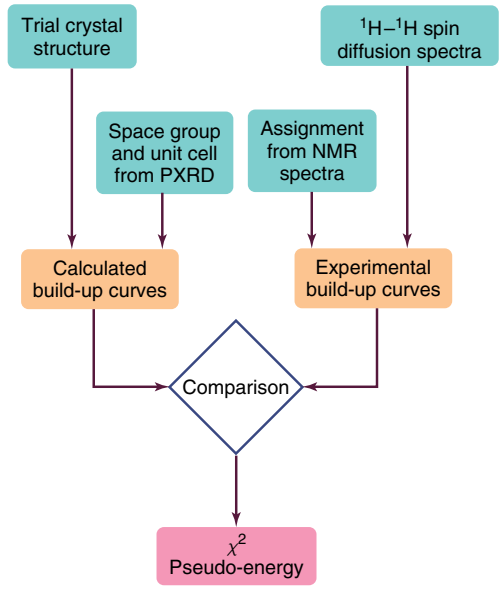


Figure 14.6. (a) 2-D ^{1}H-^{1}H spin-diffusion spectrum of thymol with τ_{SD} = 1 ms. Boxes indicate the regions used for integration of each cross peak. Asterisks indicate the carrier frequency artefacts. (b) PSD build-up curves determined from a series of spectra with different mixing times. The solid lines correspond to curves back calculated using Equation 14.2 from the known crystal structure. (Reproduced from Ref. 5. © Royal Society of Chemistry, 2008.)

they have used a rate matrix approach to spin diffusion, analogous to equation 14.2, but where the rates are limited only to intramolecular terms, and where the analysis is limited to the initial rate regime. In this regime, the cross peak intensities are indeed expected to be dominated by the influence of the nearest neighbors, and to provide thus a way to determine the local conformation. In the case of tyrosine ethyl ester[37] and epithilone B,[38] this indeed provided the basis for the determination of accurate structures, as illustrated in Figure 14.5. This is clearly a very attractive approach, with the only drawback being that it requires carbon-13 isotopic labeling of the molecule, to observe CHHC connectivities.

14.5.4 Full Crystal Structure Determination from Quantitative Full Matrix Determination of PSD

In principle, complete crystal structures, including both molecular conformation and crystal packing, can be determined from spin diffusion data. This has recently been demonstrated for two examples using PSD data.[4,5] Figure 14.6(a) shows a spin diffusion spectrum of thymol obtained with the sequence of Figure 14.1(a).[5] Each peak in the 2-D spectrum provides information about dipolar-driven magnetization exchange. For example, the cross peak in the top left corner of the spectra is the result of magnetization exchanged from the magnetically equivalent CH_3 protons evolving at the lowest chemical shift during t_1 to the OH protons evolving at the highest chemical shift during t_2. The dynamics of these magnetization exchanges can be followed by recording the evolution of the $^1H-^1H$ spin-diffusion spectrum when varying the spin-diffusion delay τ_{SD}. The measured volume of each peak in the 2-D spectrum is plotted as a function of the spin-diffusion delay τ_{SD} to obtain a series of build-up curves in Figure 14.6(b).



Scheme 14.1. Schematic routine for the use of $^1H-^1H$ spin-diffusion data in powder crystallography. (Reproduced from Ref. 5. © Royal Society of Chemistry, 2008.)

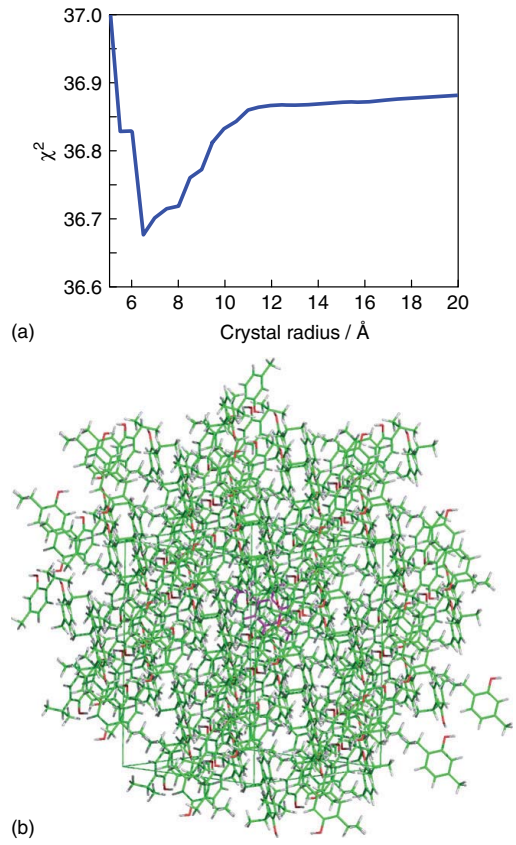


Figure 14.7. (a) Goodness-of-fit coefficient χ^2 as a function of the calculated crystal radius and (b) cluster corresponding to the 15 Å crystal radius. (Reproduced from Ref. 5. © Royal Society of Chemistry, 2008.)

The scheme for crystal structure determination is given in Scheme 14.1 and uses the coordinates of a single molecule of a trial structure as input. Symmetry-related molecules are generated from the coordinates to build a full unit cell. Space group and unit cell parameters are taken from the powder X-ray diffraction data. A larger part of the crystal is then generated by repeated translations of the full unit cell. The calculated build-up curves using equation 14.2 are then fit to the experimental ones by adjusting the only variable parameter, the phenomenological scaling factor A.

The size of the crystal used in the calculation plays an important role in the accuracy of the result when the full rate matrix analysis is used (as opposed to the initial rate approach used in the previous section). Figure 14.7 shows that pairs of spins distant from each other by up 15 Å continue to make a significant contribution to χ^2. This corresponds to generating about 60 molecules and defining 10 646 distances between atom pairs to be included in the calculation (Figure 14.7b). This clearly illustrates how the spin-diffusion data depend not only on the intramolecular distances (essential for determining the molecular conformation) but also on the intermolecular distances, essential for determining the crystal packing.

The full rate matrix analysis of the PSD curves can be combined with molecular modeling to determine the crystal structure. The general method used for the modeling stage of the determination of the crystal structure is to start with structures with random atomic coordinates, which are optimized using van der Waals forces and the experimental PSD term, which is obtained via the difference between the back calculated PSD curve and the experimental values.

Sixteen of the 42 lowest energy structures found in this way for thymol are shown in Figure 14.8(a). The structures cover a spread in χ^2 which is estimated roughly to be the uncertainty in the determination as defined by the noise level in the spectral data.[5] In this case, the result of the modeling procedure was an ensemble with an all-atom standard deviation in coordinates within the ensemble of 0.25 Å. The all-atom root-mean-square-deviation (rmsd) is 0.32 Å between the average structure of the ensemble and the reference single-crystal X-ray diffraction determined structure.

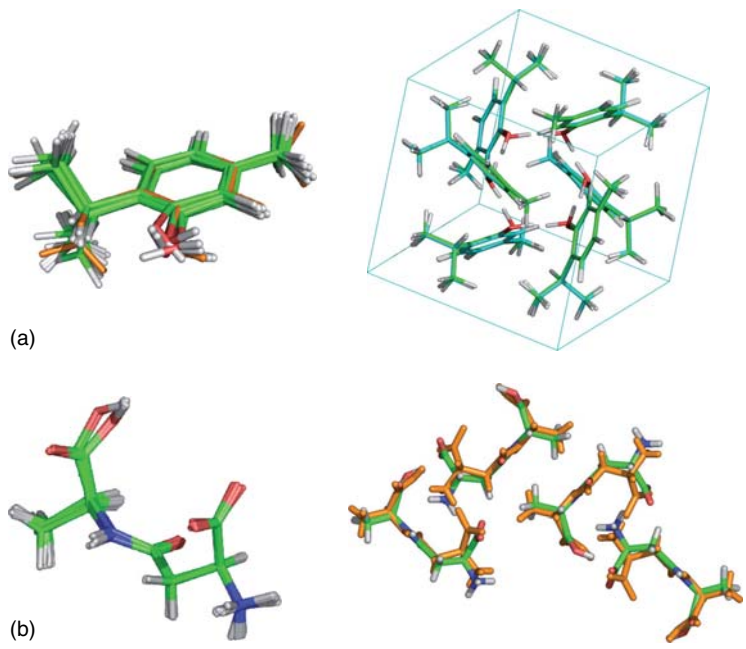


Figure 14.8. Crystal structures determined by PSD for (a) thymol[5] and (b) β-L-Asp-Ala.[4] In both cases the molecular confirmation is shown on the left, and the full unit cell on the right (with the comparison to the known structures).

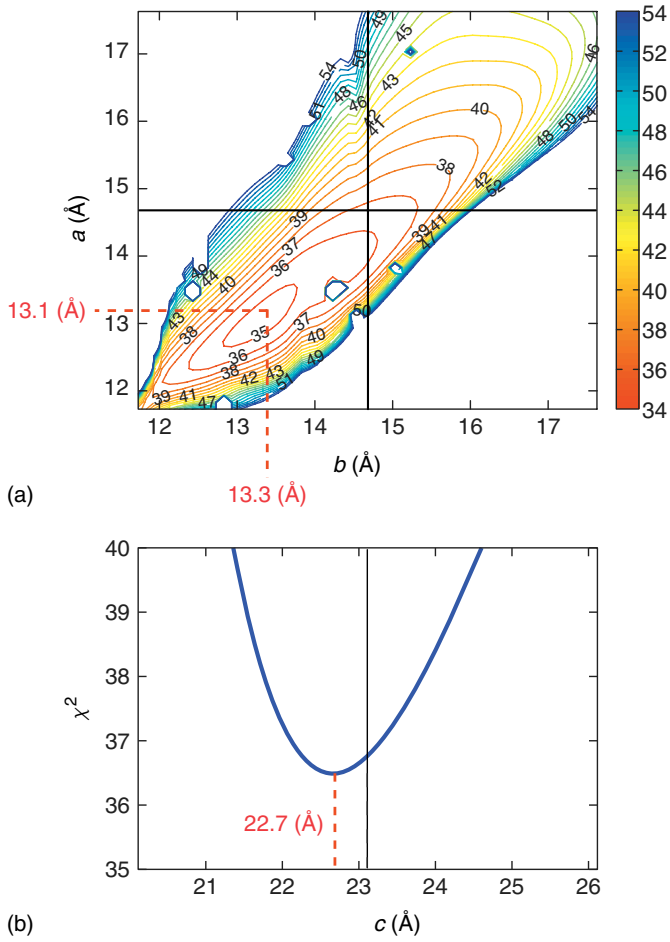


Figure 14.9. Sensitivity of PSD data to the unit cell parameters in thymol. (a) The joint variation of a and b. For this space group ($R\bar{3}$), $a = b$, which is found to be the best agreement with the data. (b) c is varied. The solid lines indicate the X-ray determined unit cell parameters. (Figure courtesy of Elodie Salager.)

Figure 14.8(b) shows the crystal structure determined by PSD for β-L-asp-ala.

14.5.4.1 Sensitivity to Unit Cell Parameters

In the above examples, the full crystal structure determination was achieved by including the unit cell parameters as known. Indeed, in favorable circumstances, the unit cell dimensions, and possibly the space group, can be determined from powder X-ray diffraction. However PSD data are also sensitive to the packing of the molecules. In Figure 14.9, we see that as the unit cell dimensions are changed for thymol, the best agreement is found for unit cell parameters within a few percent of the single-crystal X-ray diffraction determined values.

14.6 CONCLUSION

NMR powder crystallography using spin diffusion is clearly a very powerful technique for studying molecular organization in solids. This can vary from qualitative analysis of spin diffusion for polymer structures or proteins to a complete quantitative analysis for full crystal structure determination.

Currently, resolution in the proton spectrum is the limiting factor for wider application of the PSD method. The achievement of better ^{1}H NMR resolution by improving the homonuclear decoupling sequences and using higher spinning speeds in the future should increase the range of powdered materials that are amenable to this type of study. CHHC does not have this drawback, but instead requires isotopic enrichment.

Note that the result of the molecular modeling step for both CHHC and PSD approaches can then be used as the starting point for DFT refinement, to yield a final structure which can be validated using a comparison of calculated and experimental NMR chemical shifts. For the dipeptide β-L-Asp-Ala, a structure was obtained in this way that deviates from the known crystal structure by an all-atom rmsd of only 0.13 Å.[39] In the case of thymol, the structure found in this way for the powdered sample was identical to the single-crystal X-ray determined structure.

Most importantly, in many cases, the powder can be studied as is, without any modification and at natural abundance, and in particular when the powder under study may not be suitable for other structure determination methods, or can undergo changes in polymorphs during sample preparation. This is of widespread interest in many areas, and particularly in pharmaceutical chemistry.

REFERENCES

1. D. H. Brouwer, *J. Am. Chem. Soc.*, 2008, **130**, 6306.
2. R. K. Harris, P. Hodgkinson, C. J. Pickard, J. R. Yates, and V. Zorin, *Magn. Reson. Chem.*, 2007, **45**, S174.
3. B. Elena and L. Emsley, *J. Am. Chem. Soc.*, 2005, **127**, 9140.
4. B. Elena, G. Pintacuda, N. Mifsud, and L. Emsley, *J. Am. Chem. Soc.*, 2006, **128**, 9555.
5. E. Salager, R. S. Stein, C. J. Pickard, B. Elena, and L. Emsley, *Phys. Chem. Chem. Phys.*, 2009. DOI: 10.1039/b821018g.
6. F. Castellani, B. van Rossum, A. Diehl, M. Schubert, K. Rehbein, and H. Oschkinat, *Nature*, 2002, **420**, 98.
7. R. Tycko, *Curr. Opin. Struct. Biol.*, 2004, **14**, 96.
8. C. Wasmer, A. Lange, H. Van Melckebeke, A. B. Siemer, R. Riek, and B. H. Meier, *Science*, 2008, **319**, 1523.
9. A. Lange, K. Giller, S. Hornig, M. F. Martin-Eauclaire, O. Pongs, S. Becker, and M. Baldus, *Nature*, 2006, **440**, 959.
10. N. Bloembergen, *Physica*, 1949, **15**, 386.
11. B. H. Meier, *Adv. Magn. Opt. Reson.*, 1994, **18**, 1.
12. W. R. Zhang and D. G. Cory, *Phys. Rev. Lett.*, 1998, **80**, 1324.
13. K. W. Eberhardt, S. Mouaziz, G. Boero, J. Brugger, and B. H. Meier, *Phys. Rev. Lett.*, 2007, **99**, 4.
14. P. Caravatti, P. Neuenschwander, and R. R. Ernst, *Macromolecules*, 1985, **18**, 119.
15. E. Vinogradov, P. K. Madhu, and S. Vega, *Chem. Phys. Lett.*, 2002, **354**, 193.
16. D. Sakellariou, A. Lesage, P. Hodgkinson, and L. Emsley, *Chem. Phys. Lett.*, 2000, **319**, 253.
17. B. Elena, G. de Paepe, and L. Emsley, *Chem. Phys. Lett.*, 2004, **398**, 532.
18. A. Lange, S. Luca, and M. Baldus, *J. Am. Chem. Soc.*, 2002, **124**, 9704.
19. A. Lange, K. Seidel, L. Verdier, S. Luca, and M. Baldus, *J. Am. Chem. Soc.*, 2003, **125**, 12640.
20. N. M. Szeverenyi, M. J. Sullivan, and G. E. Maciel, *J. Magn. Reson.*, 1982, **47**, 462.
21. S. Zhang, B. H. Meier, and R. R. Ernst, *Phys. Rev. Lett.*, 1992, **69**, 2149.
22. P. Hodgkinson, personal communication, 2000.
23. M. Veshtort and R. G. Griffin, *J. Magn. Reson.*, 2006, **178**, 248.
24. R. Bruschweiler and R. R. Ernst, *J. Magn. Reson.*, 1997, **124**, 122.
25. P. Hodgkinson, D. Sakellariou, and L. Emsley, *Chem. Phys. Lett.*, 2000, **326**, 515.
26. V. E. Zorin, S. P. Brown, and P. Hodgkinson, *Mol. Phys.*, 2006, **104**, 293.
27. D. Sakellariou, P. Hodgkinson, S. Hediger, and L. Emsley, *Chem. Phys. Lett.*, 1999, **308**, 381.
28. D. Suter and R. R. Ernst, *Phys. Rev. B*, 1982, **25**, 6038.
29. D. Suter and R. R. Ernst, *Phys. Rev. B*, 1985, **32**, 5608.
30. P. M. Henrichs, M. Linder, and J. M. Hewitt, *J. Chem. Phys.*, 1986, **85**, 7077.
31. A. Kubo and C. A. McDowell, *J. Chem. Soc., Faraday Trans. 1*, 1988, **84**, 3713.

32. A. Abragam, *Principles of Nuclear Magnetism*, Oxford University Press: London, 1961

33. H. T. Edzes and J. P. C. Bernards, *J. Am. Chem. Soc.*, 1984, **106**, 1515.

34. P. M. Henrichs and M. Linder, *J. Magn. Reson.*, 1984, **58**, 458.

35. R. Tycko and G. Dabbagh, *J. Am. Chem. Soc.*, 1991, **113**, 3592.

36. A. Bockmann, *Angew. Chem. Int. Ed.*, 2008, **47**, 6110.

37. K. Seidel, M. Etzkorn, L. Sonnenberg, C. Griesinger, A. Sebald, and M. Baldus, *J. Phys. Chem. A*, 2005, **109**, 2436.

38. A. Lange, T. Schupp, F. Petersen, T. Carlomagno, and M. Baldus, *Chemmedchem*, 2007, **2**, 522.

39. C. J. Pickard, E. Salager, G. Pintacuda, B. Elena, and L. Emsley, *J. Am. Chem. Soc.*, 2007, **129**, 8932.

Chapter 15
Indirect Coupling & Connectivity

Anne Lesage

Laboratoire de Chimie, Ecole Normale Superieure de Lyon, 69364 Lyon 07, France

15.1	Introduction	209
15.2	Homonuclear Through-Bond Correlation Spectroscopy	210
15.3	Heteronuclear Through-Bond Correlation Spectroscopy	216
15.4	Conclusions	220
	References	220

15.1 INTRODUCTION

By combining cross polarization (CP) from protons, magic angle spinning (MAS), and proton decoupling, high sensitivity and high-resolution NMR spectra of low γ nuclei like ^{13}C, ^{15}N, or ^{31}P can be recorded routinely for both crystalline and amorphous solid samples. The unambiguous assignment of the resonances often constitutes the first step into a detailed structural investigation of materials by solid-state NMR spectroscopy.

For carbon-13-enriched samples, the assignment of the one-dimensional (1-D) ^{13}C spectra is relatively straightforward and was traditionally obtained by using carbon–carbon multidimensional correlation experiments, which relied on *dipolar-driven* magnetization transfer between pairs of neighboring carbon atoms. In contrast to liquid-state NMR spectroscopy, where experiments like correlation spectroscopy (COSY) or total correlation spectroscopy (TOCSY) usually constitute the first step toward assignment and structure determination, homonuclear correlation techniques, that rely on indirect couplings to probe *through-bond* connectivities in solid samples and therefore lead to unambiguous assignment of carbon resonances, have been only recently implemented. This was because (i) the through-bond J-couplings are usually much smaller than the (unaveraged) through-space dipolar interactions between adjacent nuclei (for a pair of directly bound ^{13}C nuclei, the scalar coupling typically ranges between 30 and 170 Hz compared to about 2 kHz for the dipolar coupling) and because (ii) this scalar interaction is of the same order of magnitude (in crystalline compounds) or much smaller (in amorphous solids) than the apparent linewidth. Several correlation techniques that yield homonuclear through-bond correlations are now available, and have been shown to constitute useful alternative techniques to dipolar recoupling methods. In parallel, it has been demonstrated that homonuclear scalar couplings could be measured with high accuracy, thereby providing an additional structural probe.

Proton NMR spectra constitute another, much more sensitive source of structural information, in particular for solid materials at natural abundance. Notably, the carbon resonances can be correlated with the chemical shift of the adjacent proton nuclei by applying two-dimensional (2-D) carbon–proton heteronuclear chemical shift correlation spectroscopy (HETCOR). Solid-state carbon–proton correlation

NMR Crystallography Edited by Robin K. Harris, Roderick E. Wasylishen and Melinda J. Duer © 2009 John Wiley & Sons, Ltd. ISBN: 978-0-470-69961-4

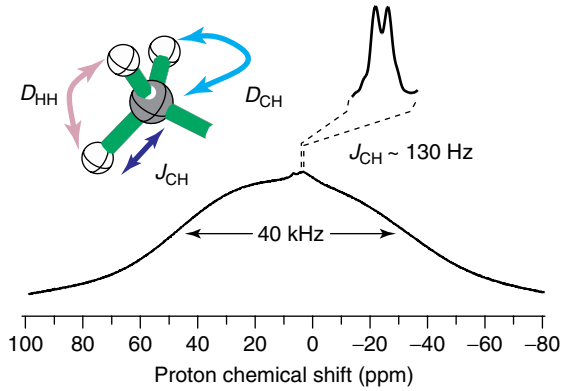


Figure 15.1. Schematic comparison between the size of the anisotropic dipolar interactions present in a solid sample and the size of an indirect scalar coupling interaction. The bottom spectrum is a static proton spectrum recorded on L-alanine, while the spectrum above represents a typical J_{CH} splitting.

experiments are usually based on a dipolar-coupling-driven magnetization transfer. Various schemes for polarization transfer have been proposed, ranging from simple Hartman–Hahn CP to more sophisticated multiple-pulse sequences. In the indirect dimension, proton linewidths are usually reduced by very fast MAS or, more efficiently, by using combined rotation and multiple-pulse spectroscopy (CRAMPS) techniques, which partially average out the homonuclear proton–proton dipolar couplings.

Until the end of the 1990s, the isotropic J_{CH} couplings were not employed in solid-state NMR of rigid solids. Like their homonuclear analogs, they are also much smaller than the dipolar interactions (for a pair of directly bound ^{13}C and ^{1}H nuclei, the scalar coupling typically ranges between 100 and 280 Hz compared to about 20 kHz for the dipolar interaction), and therefore were thought to be unresolvable in strongly coupled systems. This is illustrated schematically in Figure 15.1, which compares the size of the anisotropic interactions in a static proton spectrum with that of an isotropic indirect $^{1}H-^{13}C$ coupling. Owing to improvements in the efficiency of proton–proton homonuclear decoupling sequences, it was shown, however, that the heteronuclear $^{1}H-^{13}C$ scalar couplings could be resolved in strongly coupled spin systems and therefore used in spectral editing or correlation experiments in a way similar to liquid-state NMR techniques.

15.2 HOMONUCLEAR THROUGH-BOND CORRELATION SPECTROSCOPY

Two approaches can be distinguished to obtain homonuclear through-bond correlation spectra in solids. The first approach relies on the fact that when the inhomogeneous linewidth of carbon-13 resonances (or rather the contribution of all interactions that are described by a Hamiltonian linear in I_z) is refocused, (i.e., removed) by a π pulse in a simple spin-echo period, the scalar couplings can be resolved and standard solution-state pulse sequences can be employed like the incredible natural abundance double-quantum transfer experiment (INADEQUATE) or COSY. The second approach consists of applying a mixing period (a train of pulses synchronized with the rotor frequency) in which the Hamiltonian is reduced to an isotropic scalar coupling Hamiltonian in analogy with TOCSY liquid-state techniques.

15.2.1 The Inadequate Experiment for Solids

Capitalizing on previous work on plastic crystals,[1–3] glasses, and zeolites,[4–6] Emsley and coworkers demonstrated in 1997 that a ^{13}C INADEQUATE experiment was feasible on ordinary crystalline organic solid samples[7] and, 2 years later, introduced the refocused INADEQUATE technique, which was shown to be also practicable on disordered samples (see below).[8]

Figure 15.2(a) shows the pulse sequence for the refocused INADEQUATE experiment. After CP from ^{1}H, the ^{13}C magnetization evolves during the delay, 2τ under the homonuclear J-coupling Hamiltonian (in angular frequency units).

$$\hat{H} = 2\pi \sum_{i<j} J_{ij} \hat{I}_{iz} \hat{I}_{jz} \qquad (15.1)$$

The $^{13}C-^{13}C$ homonuclear dipolar couplings are removed by fast MAS, and the chemical shift is refocused by the 180° pulse. The double-quantum coherence created by the first carbon 90° pulse evolves during t_1 at the sum frequency of the two spins, $\omega_{DQ} = \omega_{SQ}^{A} + \omega_{SQ}^{B}$, and is converted back into an antiphase transverse coherence by the last 90° pulse, which evolves during the second $\tau-\pi-\tau$ delay into an in-phase signal before detection. As in solution-state NMR, directly bonded carbon-13

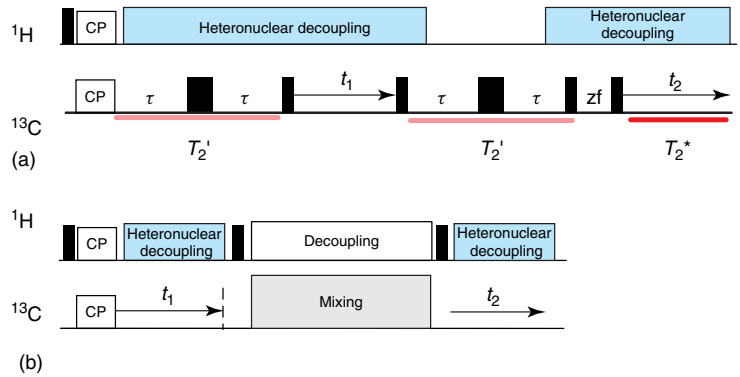


Figure 15.2. (a) Pulse sequence for the solid-state 2-D refocused INADEQUATE experiment. Thin vertical lines indicate 90° pulses and thick vertical lines correspond to 180° pulses. Under ideal conditions, the degree of conversion into double-quantum coherences is maximum for $\tau = 1/4J_{CC}$ and is zero for $\tau = 1/2J_{CC}$. The refocusing delay τ is set as an integral number of rotor periods to rigorously refocus the chemical shift interaction. A z-filter block is inserted at the end of the experiments in order to suppress antiphase magnetization before direct detection in t_2.[10] (b) Pulse sequence for the TOBSY experiment. The mixing block consists of rotor-synchronized RF pulses, while high-power on-resonance or off-resonance Lee–Goldburg irradiation is applied on the protons.

resonances are identified by the fact that they generate a common double-quantum frequency in ω_1. Note that an alternative experiment, the INADEQUATE-CR (composite refocusing),[9] which uses composite pulses, has been proposed to channel the magnetization into one line of the J-doublet, α or β, thereby reducing the number of resonances in ω_2.

A few years later, a closely related method, uniform-sign cross-peak (UC) double-quantum-filtered correlation spectroscopy (2QF-COSY), was introduced for solids by Mueller and coworkers.[11–13] In this experiment, the indirect t_1 evolution takes place before the first $\tau-\pi-\tau$ delay and before the filtering of the double-quantum coherences, which results in a single-quantum–single-quantum chemical shift correlation framework. Both methods, the refocused INADEQUATE and the uniform-sign cross-peak double-quantum-filtered correlation spectroscopy (UC2QF-COSY) techniques, have been demonstrated to be robust for establishing direct scalar connectivities in isotopically enriched organic samples, and have been applied to characterize the structure of systems as complex as the polymer phase of CsC_{60},[14] for example, to detect hydrogen bonds in solids through $^{15}N-^{15}N$ connectivities,[15,16] and to establish through-bond correlations in large biomolecular systems.[17–19] Carbon-13 INADEQUATE and UC2QF-COSY experiments have also been shown to be applicable on nonlabeled compounds.[12,20–23] By way of illustration, Figure 15.3 shows an extract in the aliphatic area of a 2-D refocused INADEQUATE spectrum recorded on natural abundance cholesteryl acetate. This spectrum allows straightforwardly the unambiguous assignment of all carbon resonances for the two molecules of the unit cell.

The validity of the assumption that, in solid-state INADEQUATE-type spectra, correlation peaks are only observed for bonded pairs of nuclei has been investigated in detail both experimentally and theoretically by Fayon *et al.*[24] These authors have shown that a double quantum (DQ) correlation is indeed indicative of a through-bond connectivity as soon as the isotropic chemical shifts of the two nuclei are different and rotational resonance conditions are avoided. However, DQ peaks may be observed even in the absence of a through-bond J-coupling in the specific case where the isotropic chemical shifts are the same, with a nonzero dipole–dipole coupling tensor and chemical shift anisotropy tensors that have different magnitudes or/and orientations.

We also note that triple-quantum–single-quantum INADEQUATE- and COSY-type spectra of solid samples can also be obtained under MAS, and have been shown to provide an improved description of the ^{31}P connectivities in phosphate glasses.[25]

As discussed in several papers, the efficiency of the INADEQUATE technique[8,17,21,26] and related

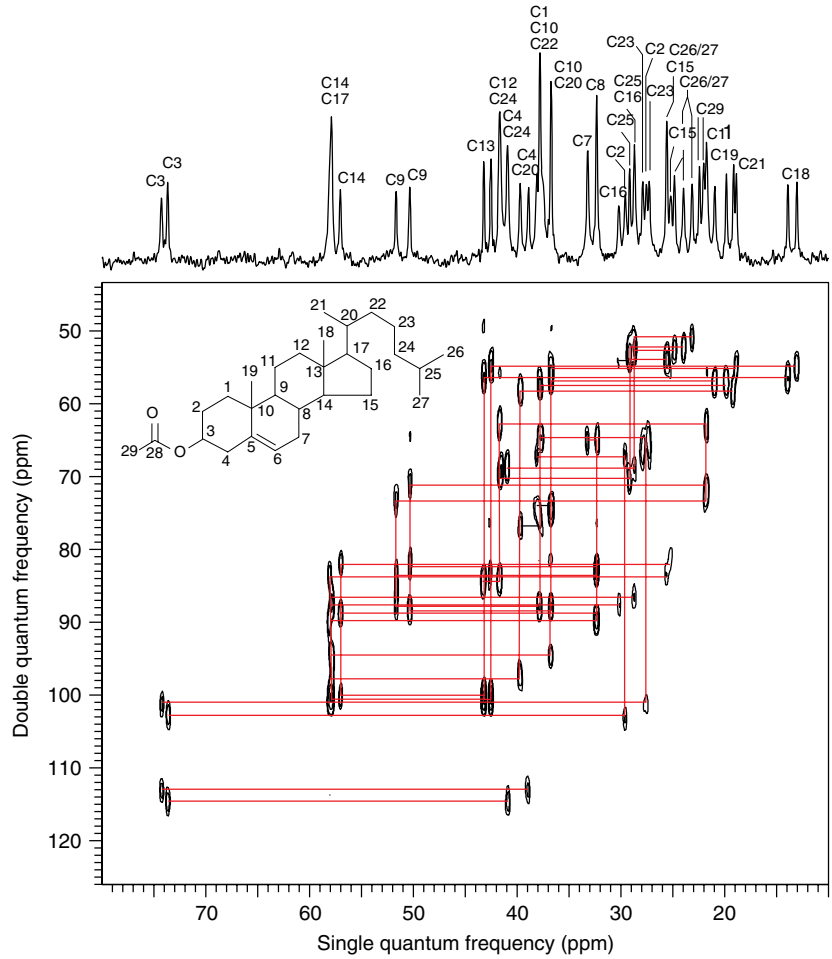


Figure 15.3. Extract from the aliphatic region of a carbon-13 refocused INADEQUATE spectrum recorded on natural abundance powdered cholesteryl acetate (this compound crystallizes with two molecules in the unit cell). The experiment was performed with a 4-mm double-tuned MAS probe at an MAS rate of 12.5 kHz with a proton RF field strength of 100 kHz. The τ delay was set to 4 ms. The total experimental time was 9 days. The one-dimensional CP/MAS spectrum (four scans) is shown above the 2-D map. The assignment of the carbon-13 resonances is straightforward and unambiguous since two bonded nuclei share a common frequency in the double-quantum dimension at the sum of their individual frequencies. (Reproduced from Ref. 20. © Wiley VCH, 2004.)

experiments[13] depends mainly on the decay of the ^{13}C transverse magnetization during the $\tau-\pi-\tau$ blocks. During these delays, as the π pulses refocus all the linear spin interactions (e.g., due to a chemical shift distribution, imperfect decoupling, or magnetic field inhomogeneity), the lifetime of transverse coherences T_2', or the so-called refocused linewidth Δ' (equal to $1/\pi T_2'$), is strongly dependent on the efficiency of the decoupling sequence applied on the proton spins. (Note that the refocused dephasing time T_2' can be measured in a simple spin-echo experiment and that large differences, of several orders of magnitude, between the apparent linewidth T_2^* and the refocused linewidth have been observed on both crystalline and amorphous samples.) In particular, it has been shown that, through a careful optimization of the heteronuclear decoupling sequence, the transverse coherence lifetimes can be significantly increased, leading to a dramatic improvement in the sensitivity of INADEQUATE experiments.[17,21]

15.2.2 The TOBSY Experiments

The second approach for obtaining through-bond correlations consists of applying a mixing period (successive radio frequency (RF) pulses synchronized with the MAS) for magnetization transfer during which the Hamiltonian is reduced to an isotropic mixing Hamiltonian of the form (in angular frequency units):

$$\hat{H} = 2\pi \sum_{i<j} J_{ij} \hat{\boldsymbol{I}}_i \cdot \hat{\boldsymbol{I}}_j \qquad (15.2)$$

The corresponding experiments are referred to as total through-bond correlation spectroscopy (TOBSY) experiments and the corresponding pulse sequence is shown in Figure 15.2(b). The first TOBSY experiment[27–29] (as well as the terminology) was introduced by Meier and coworkers in 1996 and uses variants of broadband wonderful alternating phase technique for zero residual splittings (WALTZ) decoupling pulses, synchronized with the rotor period, to remove chemical shift and dipolar terms and to allow polarization transfer through exclusively the $^{13}C-^{13}C$ indirect couplings. The resulting 2-D spectrum displays cross peaks between all spins that are coupled through scalar couplings (directly or relayed) that exceed a certain threshold.

A few years later, improved scalar isotropic mixing sequences were designed on the basis of symmetry principles. The $C9_3^1$ sequence and some of its variants developed by Titman and coworkers[30] were shown to be more suitable for use with relatively fast MAS and to give improved magnetization transfer efficiencies. Hardy *et al*. also proposed a series of improved TOBSY schemes, allowing through-bond COSY at MAS frequencies up to 50 kHz like the $\mathrm{POST}-C9_6^1$ scheme,[31] while Chan *et al*. showed that mixing schemes based on the *R* symmetry element[32,33] could also be used for through-bond polarization transfer (the $R30_6^{14}$ scheme, for example) and were especially robust with respect to RF inhomogeneity and resonance offset.[34] More recently, isotropic mixing sequences consisting of adiabatic pulses were introduced.[35,36] Note that while efficient correlations are achieved in TOBSY-type experiments, they usually require high RF power on the proton channel (typically three times the value of the RF power applied during the mixing scheme). The practicability of running TOBSY experiment at fast MAS without proton decoupling, however, has been recently demonstrated.[37]

By way of an example, Figure 15.4 shows a TOBSY spectrum recorded on uniformly ^{13}C-labeled antamanide, with a mixing time of 12.4 ms. Direct as well as relayed cross peaks are obtained, which allow one to unambiguously assign all amino acid spin systems from this single spectrum.

15.2.3 Through-Bond Correlations in Disordered Materials

Refocused INADEQUATE and UC2QF-COSY experiments have been successfully applied in disordered organic solids where the linewidths greatly exceed the value of the scalar coupling.[8,38–42] Interestingly, it was shown that, under efficient heteronuclear decoupling conditions, highly resolved 1-D spectra could be extracted from 2-D through-bond correlation spectra.[43] This is the case when the two chemical shift distributions caused by local structural disorder are correlated as illustrated schematically in Figure 15.5(a).

Figure 15.5(b) shows the refocused INADEQUATE spectrum of an 11% ^{13}C-enriched cellulose sample. The spectrum clearly shows that the chemical shifts of coupled pairs of carbon nuclei are strongly correlated, but that they are all by no means correlated in the same way. For example, the C3 and C2 resonances are strongly correlated with an almost constant positive slope. In contrast, the C6 and C5 resonances have a different type of correlation, where it appears that when C5 is shifted by ΔHz, C6 is shifted by $-0.2\ \Delta$Hz. Correlated chemical shift distributions have been also observed in disordered phosphates[38,41] and silicate materials.[44]

It has been recently shown that two-dimensional chemical shift conditional probability distributions could be extracted from experimental NMR correlation spectra of disordered solids and that they provide a new source of structural information characteristic of disordered solids, which is much more sensitive to structure than the individual atom chemical shift distributions.[26]

15.2.4 Measuring Homonuclear Scalar Couplings

Scalar couplings provide potential valuable structural information about bonding types or conformations.

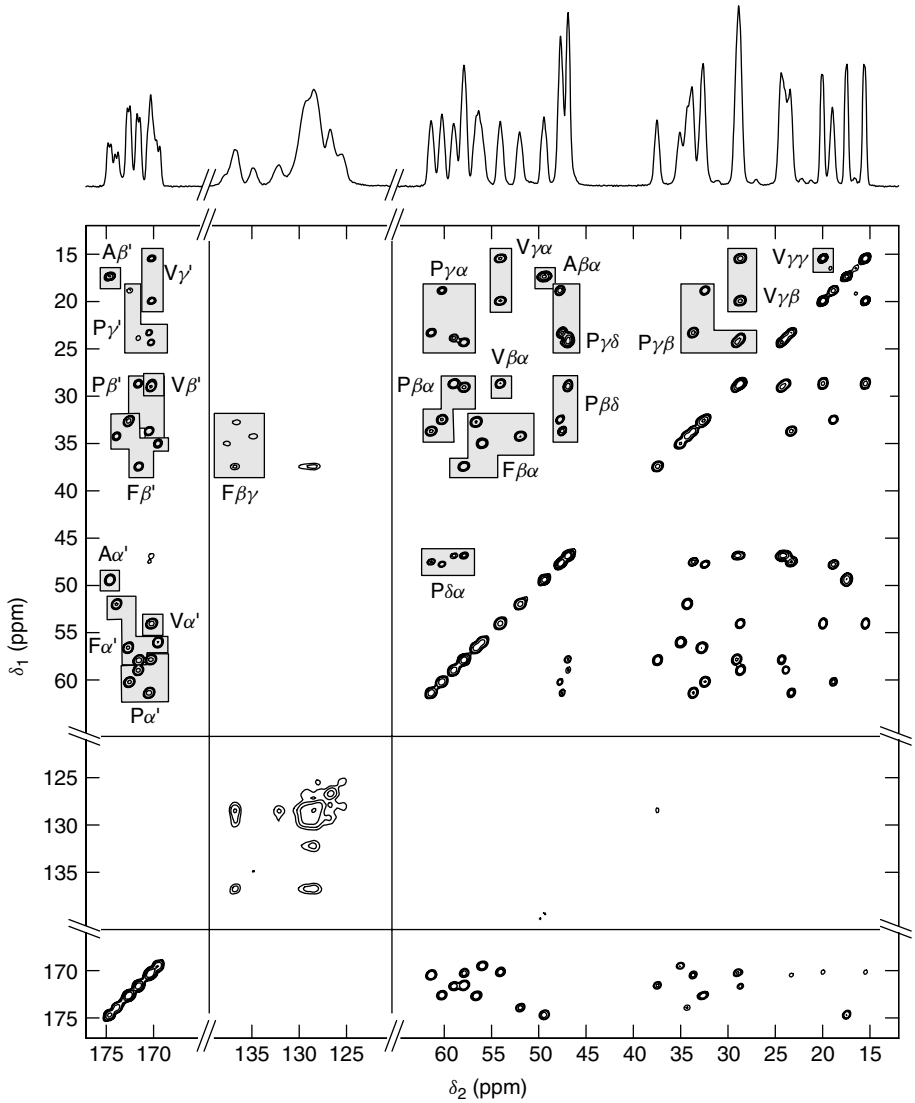


Figure 15.4. Two-dimensional carbon-13 TOBSY spectrum of the cyclic decapeptide [U−^{13}C, ^{15}N] antamanide using the $WiW9^{1}_{24}$ scheme during the mixing time at a MAS frequency of 26.67 kHz. The mixing time was set to 12.4 ms. During the adiabatic TOBSY sequence, off-resonance continuous wave decoupling was applied on protons with an RF amplitude of 160 kHz, while the root mean square (rms) RF amplitude was 76 kHz on carbons. Intense cross peaks allow one to readily assign the resonances in the spectrum to spin systems and amino acid types, as indicated. (Reproduced from Ref. 35. © Elsevier Science, 2003.)

A variety of methods, including multidimensional techniques, have been proposed in liquid-state NMR to determine quantitatively the value of indirect couplings. In solid-state NMR, under MAS, the homonuclear J-coupling between isolated spin 1/2 nuclei can be simply determined from the cosine modulation of signal intensity in rotor-synchronized spin-echo experiments. The corresponding pulse sequence is shown in Figure 15.6(a). Replacing the τ delays by an indirect evolution time $t_1/2$ leads to a 2-D experiment analogous to homonuclear J-resolved spectroscopy in solution-state NMR.

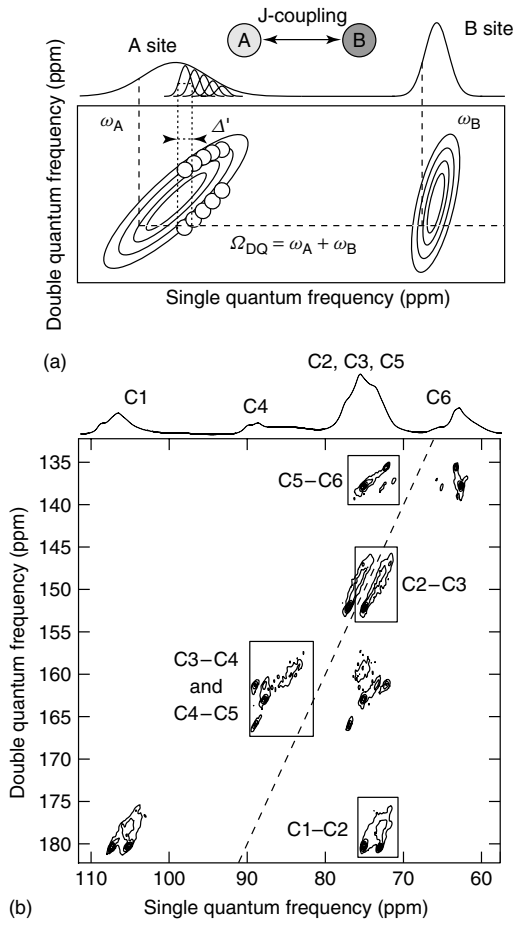


Figure 15.5. (a) Schematic refocused INADEQUATE spectrum of a directly bonded two-spin model system in a disordered sample where the single-quantum frequencies are inhomogeneously distributed over a certain range of chemical shifts. The intrinsic linewidth, Δ', corresponds to the linewidth of the individual NMR resonances in the distribution (the so-called refocused linewidth). Different chemical shift correlations between the two sites A and B give rise to different shapes for the two correlation peaks on the 2-D refocused INADEQUATE spectrum. Slices extracted along ω_2 provide spectra with higher resolution than the conventional 1-D CP/MAS spectrum. (b) The 2-D refocused INADEQUATE spectrum of an 11% ^{13}C-enriched cellulose sample extracted from wood. Acquisitions were made under ^{1}H decoupling at 100 kHz and a MAS frequency of 12.5 kHz. The τ period was set to 2.4 ms. Various highly resolved 2-D patterns are observed for the different sites, reflecting the correlations between the changes in chemical shifts induced by disorder for adjacent nuclei. Conditional probability matrices, reflecting these correlations, can be extracted from the boxed peaks. (Reproduced from Ref. 26. © American Chemical Society, 2005.)

Two-dimensional spin-echo experiments have been widely applied in the 1990s, notably to determine ^{31}P–^{31}P indirect couplings in organic and organometallic compounds.[46–48] More recently, it has been recognized by the works of Brown *et al*. that the spin-echo modulation provides an accurate and robust experimental way for measuring small homonuclear scalar couplings in solid compounds, including in cases where no splittings due to the J-coupling were observed in the normal cross polarization magic angle spinning (CP/MAS) spectrum.[45,49] This is related to the fact that all the NMR interactions linear in I_z (notably due to a chemical shift distribution) are refocused by the π pulse, and that, as for the INADEQUATE-type experiments, the refocused linewidths Δ'_2 and the corresponding transverse lifetimes of coherences are the relevant parameters in terms of indirect resolution and sensitivity.

Figure 15.6(b) and (c) illustrates the measurement of small hydrogen-bond-mediated ^{15}N–^{15}N J-couplings in small crystalline organic molecules. Using this approach, accurate measurements of J_{CC} couplings were reported in a series of carbon-13 selectively labeled rhodopsin isotopomers, revealing electronic perturbations in the conjugated chain.[50]

The principle of the spin-echo modulation in MAS solid-state NMR has been described in detail by Duma and coworkers,[51] who showed theoretically that, except for the case of total magnetic equivalence, the modulation of the spin echoes might indeed be used to estimate indirect couplings with high accuracy even in the presence of large chemical shift anisotropy (CSA) and dipole–dipole interactions. Interestingly, the authors pointed out that the interference between the CSA and the dipole–dipole (DD) coupling tends to restore the J-splitting in solids; in particular, in the case where the two isotropic shifts are identical.

We note that Cadars *et al*. have recently applied the spin-echo experiment in combination with two-dimensional correlation spectroscopy in order to determine two-dimensional J-coupling distributions in disordered samples.[52] Notably, 2-D $^2J(^{31}\text{P–N–}^{31}\text{P})$ coupling distributions were clearly identified in a bis-phosphino amine powdered sample, with values ranging from 23 to 30 Hz (with error bars between $\pm$0.2 and $\pm$1.5 Hz), and interpreted in terms of variation of the P–N–P bond angle.

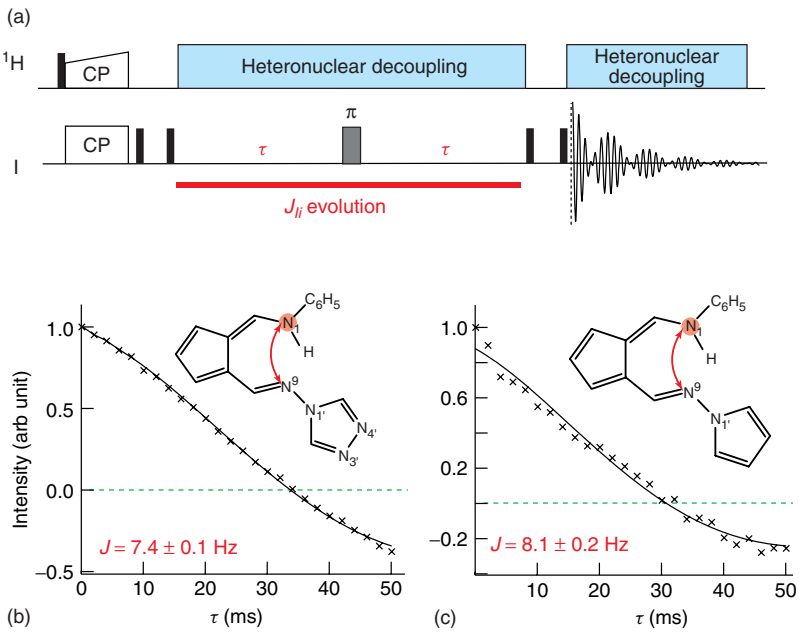


Figure 15.6. (a) Pulse sequence for the spin-echo experiment, suitable for measuring homonuclear J-couplings in isolated pairs of spin-$\frac{1}{2}$ nuclei in solids. For a given nucleus, bonded to a nonequivalent neighbor, the dependence of the resonance intensity on the spin-echo delay, τ, is given by $S(\tau) = A\cos(2\pi J\tau)\exp(-2\tau/T_2')$. The first Z-filter allows a proper definition of the time origin for the modulation, while the second one is used to remove antiphase coherences. Spin-echo modulation curves as a function of the echo period for the nitrogen-15 resonance of site N1 for (b) triazole and (c) pyrrole derivatives, together with the best-fit analytical curves. (Reproduced from Ref. 45. © Royal Society of Chemistry, 2002.)

Finally, our group proposed a modified version of the simple spin-echo experiment, suitable for measuring homonuclear scalar couplings in isotopically enriched solids (i.e., in multiple spin system).[53] This experiment, which includes selective pulses, was demonstrated for the measurement of $^2J(^{29}\text{Si}-\text{O}-^{29}\text{Si})$ couplings in a 50% ^{29}Si-enriched surfactant-templated layered silicate.

15.3 HETERONUCLEAR THROUGH-BOND CORRELATION SPECTROSCOPY

15.3.1 Resolving Heteronuclear Scalar Couplings in Rigid Solids

Carbon–proton (or nitrogen–proton) scalar couplings can be resolved by combining relatively fast sample rotation with an efficient homonuclear ^{1}H–^{1}H dipolar decoupling sequence. Indeed, under homonuclear proton decoupling (and assuming fast radio-frequency averaging compared to the MAS timescale), the proton–proton dipolar interaction is averaged to zero to first order. The remaining inhomogeneous interactions, i.e., the chemical shift and the heteronuclear couplings, are averaged by MAS to their isotropic components, leaving, to first order, only the isotropic chemical shift and the heteronuclear scalar couplings. This leads to a simplified effective Hamiltonian, similar to a "liquid-state" NMR Hamiltonian, which can be written as:

$$\hat{H} = \delta_S \hat{S}_z + \lambda \sum_n^N \delta_I^n \hat{I}_{nz} + \lambda \pi J_{IS} \sum_n^N 2\hat{I}_{nz}\hat{S}_z \quad (15.3)$$

where I and S represent the proton and carbon spins respectively. The proton isotropic chemical shift and the heteronuclear scalar couplings are multiplied by a scaling factor λ. The scaling factor varies according to the dipolar decoupling sequence that is used, and is close to $1/\sqrt{3}$ for

the frequency-switched Lee Goldburg (FSLG)[54] decoupling sequence and its phase-modulated Lee Goldburg (PMLG) variants,[55] as well as for the decoupling using mind-boggling optimization (DUMBO)-type decoupling sequences.[56,57] In weakly coupled systems, like plastic crystals for which the rotation of the molecule within the crystallographic cell averages out the intramolecular dipolar couplings, the J_{CH} scalar couplings can be observed quite straightforwardly under weak homonuclear proton decoupling, as already shown by Terao and coworkers in the 1980s.[58–60]

Figure 15.7 shows experimental carbon lineshapes observed under DUMBO-1 homonuclear decoupling[56] for a methyl, a methylene, and a methine carbon of rigid solid compounds. As expected, the CH_3 carbon resonance is split into a quartet line (with a more or less 1 : 3 : 3 : 1 intensity distribution), while the CH_2 and CH carbons display respectively a triplet and a doublet structure. We note, however, that the nonaveraged terms of the dominant dipolar interactions lead to a significant residual broadening of the resonances (or a relatively fast transverse decay of the carbon-13 coherences under homonuclear decoupling), as well as to slight deviations of the J-multiplet structure from the ideal liquid-like expected one. This renders the quantitative measurements of heteronuclear scalar couplings extremely difficult in strongly coupled systems. Such quantitative measurements are nevertheless possible in more mobile systems, as shown recently for a range of surface organometallic catalysts.[61]

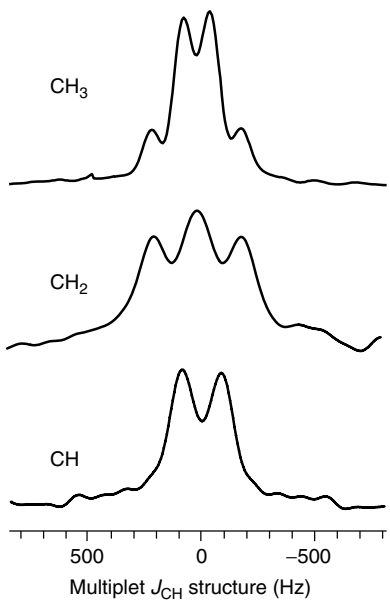


Figure 15.7. Carbon-13 *J*-multiplet patterns as observed under homonuclear decoupling for CH_3, CH_2, and CH groups. These spectra were respectively recorded on powder samples of 2-^{13}C-sodium acetate, 2-^{13}C-glycine, and 2-^{13}C-alanine. DUMBO-1 decoupling was applied during the direct acquisition of the NMR signal at a radio-frequency field strength of 100 kHz and a spinning frequency of 12.5 kHz.

15.3.2 The MAS-J-HMQC Experiment

On the basis of the observation that heteronuclear scalar couplings could be resolved in rigid solids, spectral editing techniques have been developed for solids,[62,63] and a new family of HETCOR experiments have been proposed, which rely on a polarization transfer using the heteronuclear J-couplings. The first experiment to be developed was the magic-angle spinning-J-heteronuclear multiple quantum correlation (MAS-J-HMQC) technique,[64] whose pulse sequence is shown in Figure 15.8(a). After CP from protons (*I* spins), the magnetization of carbons (*S* spins) evolves during the delay τ under only the isotropic J_{CH}-coupling Hamiltonian (since during this period a homonuclear decoupling sequence is applied on protons). Thus, for a pair of covalently bonded $^1H-^{13}C$ spins, the carbon magnetization evolves from in-phase (S_x) into antiphase ($2I_zS_y$) coherence with respect to its attached proton. This antiphase carbon coherence is converted into a heteronuclear multiple-quantum (MQ) coherence ($2I_xS_y$) by the 90° proton pulse. The proton chemical shift is then encoded by allowing these MQ coherences to evolve during the indirect evolution time t_1. The carbon chemical shift evolution during t_1 (and during the periods τ) is refocused by the 180° ^{13}C pulse applied in the middle of the pulse sequence. At the end of the evolution time t_1, the MQ coherences are converted back into antiphase carbon coherences by the 90° pulses, and these coherences evolve during the second period τ to become in-phase observable carbon coherences. A two-dimensional Fourier transform of the time domain signal gives chemical shift correlations between pairs of bonded protons in ω_1 and carbons in ω_2. A similar experiment, the MAS-J-HSQC experiment,[65] has been proposed, which involves the

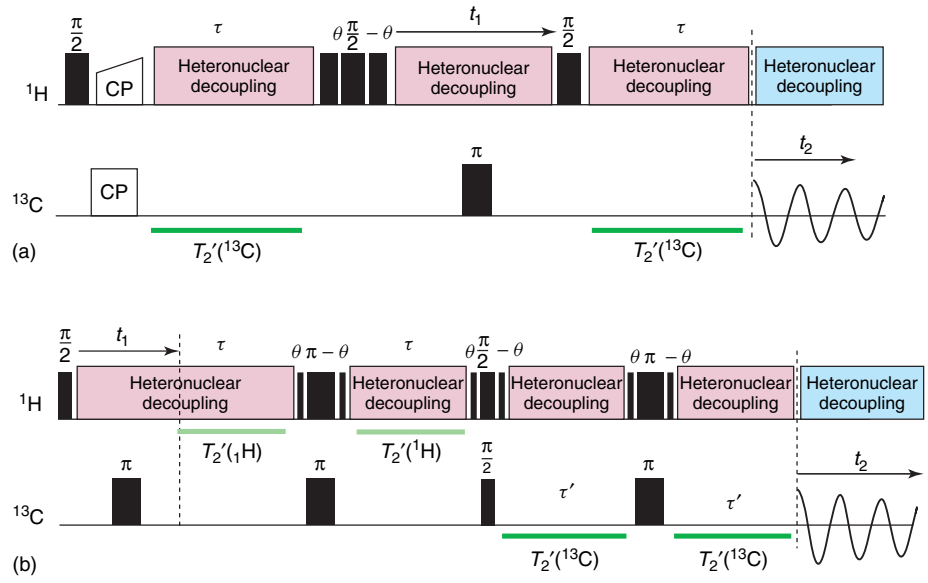


Figure 15.8. Pulse sequences for the 2-D (a) MAS-J-HMQC and (b) INEPT-HSQC heteronuclear through-bond correlation experiments. The successive dephasing periods are indicated by green lines together with the corresponding transverse dephasing times. For fully ^{13}C-labeled compounds, a major enhancement in sensitivity was experimentally reported for the INEPT-HSQC experiment when compared to the 2-D MAS-*J*-HMQC, while for natural abundance samples similar efficiencies were observed.

evolution of antiphase heteronuclear single-quantum proton coherences in t_1. Note that these experiments are quite analogous to certain versions of the liquid-state heteronuclear multiple-quantum correlation (HMQC) and heteronuclear single-quantum correlation (HSQC) experiments.

Figure 15.9(a) shows the MAS-J-HMQC spectrum recorded on cholesteryl acetate at natural abundance. As expected, this spectrum displays one-bond correlations between pairs of attached proton and carbon nuclei. In particular, no correlations are observed for the quaternary carbons. Despite the very small proton chemical shift range in the high-field region of the spectrum, the resolution of the 2-D map is outstanding and allows the unambiguous assignment of all the proton chemical shifts in the molecule. Note that, since the dispersion of the proton spectrum is small, a dipolar HETCOR spectrum on this sample would probably be too complicated to be useful and that the proton spectrum cannot be analyzed by one-dimensional spectroscopy. The MAS-J-HMQC experiment has been thus successfully applied to characterize a variety of medium-sized organic molecules.[20,66,67]

15.3.3 The INEPT-HSQC Experiment

The MAS-J-HMQC and MAS-J-HSQC experiments involve only the evolution of the relatively long-lived carbon transverse coherences during the fixed intervals τ. In other words, there is no evolution of the short-lived proton coherences during these periods. Recent improvements in CRAMPS techniques for averaging out proton homonuclear dipolar interactions, and in particular the development of a new generation of phase-modulated decoupling schemes, such as the eDUMBO-1 sequences,[57] contributed to a significant increase in proton transverse coherence lifetimes $T_2'(^1H)$ with values up to 10 ms. The use of these efficient line-narrowing techniques allowed the direct implementation of a solid-state version of refocused insensitive nuclei enhanced by polarization transfer (INEPT) experiments for solids.[68]

The pulse sequence for the solid-state 2-D insensitive nuclei enhanced by polarization transfer-heteronuclear single-quantum correlation (INEPT-HSQC) experiment is shown in Figure 15.8(b). The original liquid-state technique was simply adapted

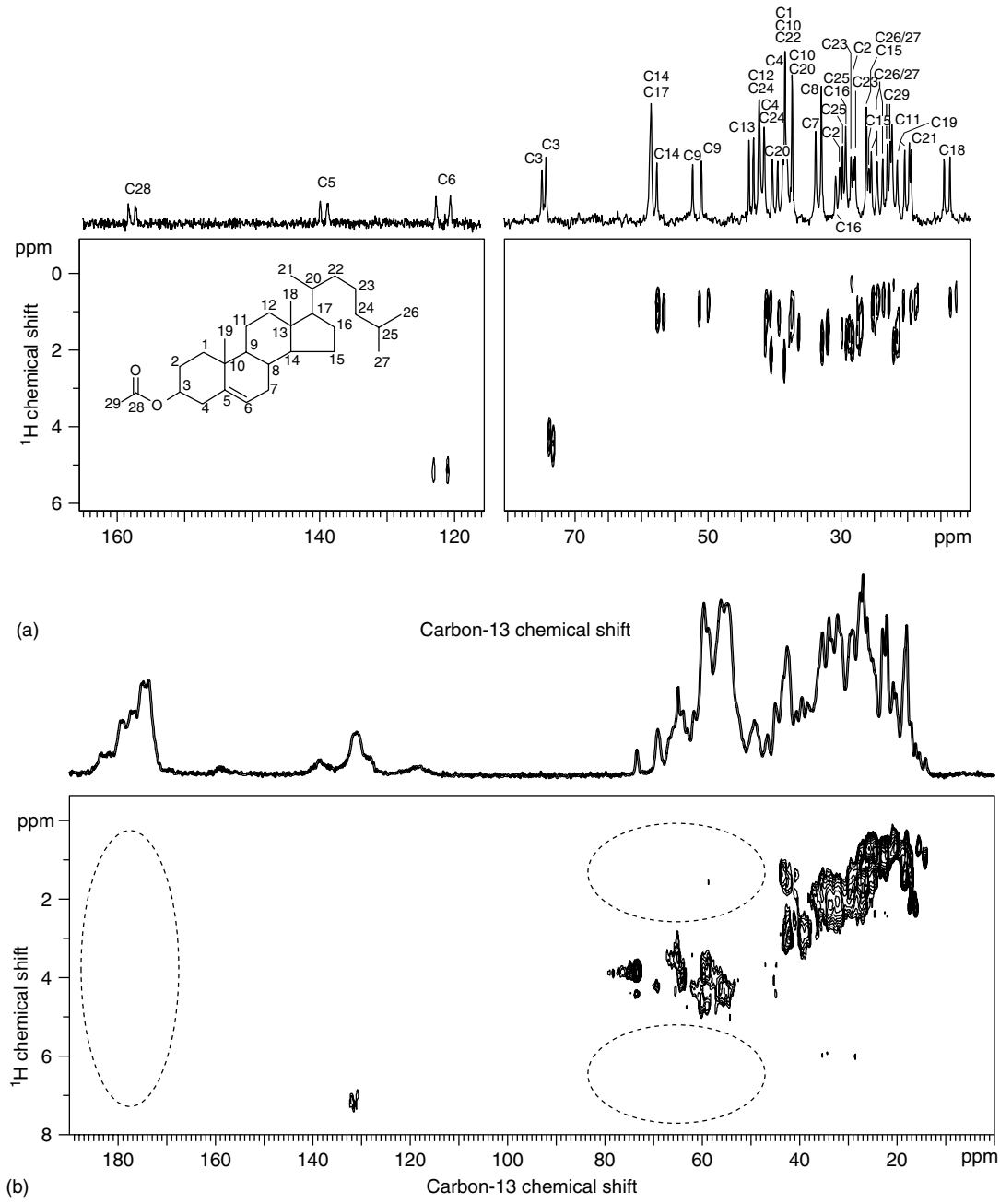


Figure 15.9. (a) Two-dimensional MAS-J-HMQC spectrum of cholesteryl acetate at natural abundance. The spinning frequency was 15 kHz and τ was 1.3 ms. A total of 140 t_1 increments with 320 scans each were collected. (Reproduced from Ref. 64. © American Chemical Society, 1998.) (b) Two-dimensional ^{1}H–^{13}C INEPT-HSQC spectrum of microcrystalline Crh, at ν_r = 22 kHz. A total of 192 transients were collected for each t_1 point (128 μs increment) with a recycle delay of 3 s. The 1-D ^{13}C CP/MAS is shown for comparison on top of the 2-D data. The dotted circles correspond to regions that would contain two-bond correlations. (Reproduced from Ref. 68. © American Chemical Society, 2005.)

for rotating solids by adding proton homonuclear decoupling during the τ and τ' transfer periods so that only the scalar couplings are preserved during these delays and affect coherence transfer. For a pair of bonded (^{1}H, ^{13}C) nuclei, after the first $\tau-\pi-\tau$ period, antiphase proton coherence with respect to the attached carbon is created, which is converted by the two simultaneous 90° pulses into antiphase carbon coherence. This antiphase ^{13}C coherence is then refocused during the second $\tau-\pi-\tau$ period into observable ^{13}C magnetization. Similar to that for the MAS-J-HMQC experiment, a two-dimensional Fourier transform of the time domain signal gives isotropic chemical shift correlations between pairs of attached nuclei.

Figure 15.9(b) shows the 2-D INEPT-HSQC spectrum recorded on a sample of uniformly ^{13}C-labeled microcrystalline Crh, an 85-residue dimeric protein.[69] This spectrum was obtained with good sensitivity in a reasonable experimental time (here 21 h). Particularly, an excellent selectivity for both the 1-D and 2-D INEPT data is observed with respect to the carbonyl resonances or the potential two-bond transfers in the aliphatic region, which are completely absent in the 2-D spectrum. As exemplified recently on powdered pharmaceutical compounds,[70] the refocused INEPT experiment, in combination with high-resolution proton double-quantum experiments, is a powerful tool for the complete assignment of the proton and carbon-13 NMR spectra of medium-sized molecules at natural abundance.

It should be pointed out that the sensitivity of the through-bond HETCOR experiments described above is directly related to the values of the evolution periods τ and τ', but, more importantly, to the carbon and, for the INEPT experiment, to the proton transverse coherence lifetimes T'_2 under homonuclear decoupling, or, in other words, to the efficiency of the homonuclear decoupling sequence applied during the τ and τ' delays.

15.4 CONCLUSIONS

Through-bond solid-state NMR spectroscopy has developed over the last 10 years as a useful complementary technique to dipolar-based correlation methods. By providing highly selective connectivities, correlation experiments based on homonuclear or heteronuclear indirect couplings allow the unambiguous identification of ^{13}C, ^{31}P, ^{15}N, ^{29}Si, or ^{1}H chemical shifts in powdered organic solids. While the direct dipolar couplings may vary considerably within a compound (in particular, if some groups are more mobile than others), the J-couplings are usually uniform over the molecule, leading to a more homogeneous transfer. Important applications of INADEQUATE- and INEPT-type techniques notably involve solid materials, where local dynamics partly average out the dipolar couplings.

Through-bond experiments rely on the application of efficient, state-of-the-art, heteronuclear, or homonuclear decoupling techniques. This research area will continue to experience major advances in the coming years, notably with the introduction of new hardware, such as very fast MAS and high RF capability probes. These developments will lead to a consequent sensitivity improvement of scalar connectivities, thereby extending the range of solid materials in which through-bond experiments will become practicable.

REFERENCES

1. T. A. Early, B. K. John, and L. F. Johnson, *J. Magn. Reson.*, 1987, **75**, 134.
2. R. Benn, H. Grondey, C. Brevard, and A. Pagelot, *J. Chem. Soc., Chem. Commun.*, 1988, **2**, 102.
3. G. D. Gray, C. H. W. Jones, and R. D. Sharma, *J. Magn. Reson.*, 1991, **91**, 186.
4. C. A. Fyfe, H. Gies, and Y. Feng, *J. Chem. Soc., Chem. Commun.*, 1989, **17**, 1240.
5. C. A. Fyfe, Y. Feng, H. Gies, H. Grondey, and G. T. Kokotailo, *J. Am. Chem. Soc.*, 1990, **112**, 3264.
6. C. T. G. Knight, R. J. Kirkpatrick, and E. Oldfield, *J. Non-Cryst. Solids*, 1990, **116**, 140.
7. A. Lesage, C. Auger, S. Caldarelli, and L. Emsley, *J. Am. Chem. Soc.*, 1997, **119**, 7867.
8. A. Lesage, M. Bardet, and L. Emsley, *J. Am. Chem. Soc.*, 1999, **121**, 10987.
9. R. Verel, J. D. van Beek, and B. H. Meier, *J. Magn. Reson.*, 1999, **140**, 300.
10. S. Cadars, J. Sein, L. Duma, A. Lesage, T. N. Pham, J. H. Baltisberger, S. P. Brown, and L. Emsley, *J. Magn. Reson.*, 2007, **188**, 24.
11. L. Mueller, D. W. Elliott, K. C. Kim, C. A. Reed, and P. D. W. Boyd, *J. Am. Chem. Soc.*, 2002, **124**, 9360.

12. R. A. Olsen, J. Struppe, D. W. Elliott, R. J. Thomas, and L. J. Mueller, *J. Am. Chem. Soc.*, 2003, **125**, 11784.
13. L. J. Mueller, D. W. Elliott, G. M. Leskowitz, J. Struppe, R. A. Olsen, K. C. Kim, and C. A. Reed, *J. Magn. Reson.*, 2004, **168**, 327.
14. G. Grasso, T. M. De Swiet, and J. J. Titman, *J. Phys. Chem., B*, 2002, **106**, 8676.
15. S. P. Brown, M. Perez-Torralba, D. Sanz, R. M. Claramunt, and L. Emsley, *J. Am. Chem. Soc.*, 2002, **124**, 1152.
16. T. N. Pham, S. Masiero, G. Gottarello, and S. P. Brown, *J. Am. Chem. Soc.*, 2005, **127**, 16018.
17. G. De Paepe, N. Giraud, A. Lesage, P. Hodgkinson, A. Böckmann, and L. Emsley, *J. Am. Chem. Soc.*, 2003, **125**, 13938.
18. L. L. Chen, R. A. Olsen, D. W. Elliott, J. M. Boettcher, D. H. H. Zhou, C. M. Rienstra, and L. J. Mueller, *J. Am. Chem. Soc.*, 2006, **128**, 9992.
19. L. Chen, J. M. Kaiser, T. Polenova, J. Yang, C. M. Rienstra, and L. J. Mueller, *J. Am. Chem. Soc.*, 2007, **129**, 10650.
20. J. Brus and A. Jegorov, *J. Chem. Phys., A*, 2004, **108**, 3955.
21. G. De Paepe, A. Lesage, S. Steuernagel, and L. Emsley, *ChemPhysChem*, 2004, **5**, 869.
22. R. K. Harris, S. A. Joyce, C. J. Pickard, S. Cadars, and L. Emsley, *Phys. Chem. Chem. Phys.*, 2006, **8**, 137.
23. R. K. Harris, S. Cadars, L. Emsley, J. R. Yates, C. J. Pickard, R. K. R. Jetti, and U. J. Griesser, *Phys. Chem. Chem. Phys.*, 2007, **9**, 360.
24. F. Fayon, D. Massiot, M. H. Levitt, J. J. Titman, D. H. Gregory, L. Duma, L. Emsley, and S. P. Brown, *J. Chem. Phys.*, 2005, **122**, 194313.
25. F. Fayon, C. Roiland, L. Emsley, and D. Massiot, *J. Magn. Reson.*, 2006, **179**, 49.
26. S. Cadars, A. Lesage, and L. Emsley, *J. Am. Chem. Soc.*, 2005, **127**, 4466.
27. M. Baldus and B. H. Meier, *J. Magn. Reson.*, 1996, **121**, 65.
28. M. Baldus, R. J. Iuliucci, and B. H. Meier, *J. Am. chem. Soc.*, 1997, **119**, 1121.
29. M. Baldus and B. H. Meier, *J. Magn. Reson.*, 1997, **128**, 172.
30. A. S. D. Heindrichs, H. Geen, C. Giordani, and J. J. Titman, *Chem. Phys. Lett.*, 2001, **335**, 89.
31. E. H. Hardy, R. Verel, and B. H. Meier, *J. Magn. Reson.*, 2001, **148**, 459.
32. M. Carravetta, M. E. X. Zhao, A. Brinkmann, and M. H. Levitt, *Chem. Phys. Lett.*, 2000, **321**, 205.
33. A. Brinkmann and M. H. Levitt, *J. Chem. Phys.*, 2001, **115**, 357.
34. J. C. C. Chan and G. Brunklaus, *Chem. Phys. Lett.*, 2001, **349**, 104.
35. E. H. Hardy, A. Detken, and B. H. Meier, *J. Magn. Reson.*, 2003, **165**, 208.
36. J. Leppert, O. Ohlenschlager, M. Gorlach, and R. Ramachandran, *J. Biomol. NMR*, 2004, **29**, 167.
37. Y. Mou, J. C. H. Chao, and J. C. C. Chan, *Solid-State NMR*, 2006, **29**, 278.
38. F. Fayon, G. L. Saout, L. Emsley, and D. Massiot, *Chem. Commun.*, 2002, **16**, 1702.
39. F. Fayon, I. J. King, R. K. Harris, R. K. B. Gover, J. S. O. Evans, and D. Massiot, *Chem. Mater.*, 2003, **15**, 2234.
40. H. Kono, T. Erata, and M. Takai, *Macromolecules*, 2003, **36**, 5131.
41. F. Fayon, I. J. King, R. K. Harris, J. S. O. Evans, and D. Massiot, *C. R. Chimie*, 2004, **7**, 351.
42. H. Kono, Y. Numata, T. Erata, and M. Takai, *Macromolecules*, 2004, **37**, 5310.
43. D. Sakellariou, S. P. Brown, A. Lesage, S. Hediger, M. Bardet, C. A. Meriles, A. Pines, and L. Emsley, *J. Am. Chem. Soc.*, 2003, **125**, 4376.
44. N. Hedin, R. Graf, S. C. Christiansen, C. Gervais, R. C. Hayward, J. Eckert, and B. F. Chmelka, *J. Am. Chem. Soc.*, 2004, **126**, 9425.
45. S. P. Brown, M. Perez-Torralba, D. Sanz, R. M. Claramunt, and L. Emsley, *Chem. Commun.*, 2002, **17**, 1852.
46. T. Allman, *J. Magn. Reson.*, 1989, **83**, 637.
47. A. Kubo and C. A. McDowell, *J. Chem. Phys.*, 1990, **92**, 7156.
48. G. Wu and R. E. Wasylishen, *Inorg. Chem.*, 1992, **31**, 145.
49. S. P. Brown and L. Emsley, *J. Magn. Reson.*, 2004, **171**, 43.
50. W. C. Lai, N. McLean, A. Gansmuller, M. A. Verhoeven, G. C. Antonioli, M. Carravetta, L. Duma, P. H. M. Bovee-Geurts O. G. Johannessen, H. J. M. de Groot, J. Lugtenburg, L. Emsley, S. P. Brown, R. C. D. Brown, W. J. DeGrip, and M. H. Levitt, *et al*., *J. Am. Chem. Soc.*, 2006, **128**, 3878.

51. L. Duma, W. C. Lai, M. Carravetta, L. Emsley, S. P. Brown, and M. H. Levitt, *ChemPhysChem*, 2004, **5**, 815.
52. S. Cadars, A. Lesage, M. Trierweiler, L. Heux, and L. Emsley, *Phys. Chem. Chem. Phys.*, 2007, **9**, 92.
53. S. Cadars, A. Lesage, N. Hedin, B. F. Chmelka, and L. Emsley, *J. Phys. Chem., B*, 2006, **110**, 16982.
54. M. Lee and W. Goldburg, *Phys. Rev., A*, 1965, **140**, 1261.
55. E. Vinogradov, P. H. Madhu, and S. Vega, *Chem. Phys. Lett.*, 1999, **314**, 443.
56. D. Sakellariou, A. Lesage, P. Hodgkinson, and L. Emsley, *Chem. Phys. Lett.*, 2000, **319**, 253.
57. B. Elena, G. de Paepe, and L. Emsley, *Chem. Phys. Lett.*, 2004, **398**, 532.
58. T. Terao, H. Miura, and A. Saika, *J. Chem. Phys.*, 1981, **75**, 1573.
59. T. Terao, H. Miura, and A. Saika, *J. Am. Chem. Soc.*, 1982, **104**, 5228.
60. T. Terao, H. Miura, and A. Saika, *J. Magn. Reson.*, 1982, **49**, 365.
61. F. Blanc, C. Coperet, A. Lesage, and L. Emsley, *Chem. Soc. Rev.*, 2008, **37**, 518.
62. A. Lesage, S. Steuernagel, and L. Emsley, *J. Am. Chem. Soc.*, 1998, **120**, 7095.
63. D. Sakellariou, A. Lesage, and L. Emsley, *J. Magn. Reson.*, 2001, **151**, 40.
64. A. Lesage, D. Sakellariou, S. Steuernagel, and L. Emsley, *J. Am. Chem. Soc.*, 1998, **120**, 13194.
65. A. Lesage and L. Emsley, *J. Magn. Reson.*, 2001, **148**, 449.
66. A. Lesage, P. Charmont, S. Steuernagel, and L. Emsley, *J. Am. Chem. Soc.*, 2000, **122**, 9739.
67. J. R. Yates, T. N. Pham, C. J. Pickard, F. Mauri, A. M. Amado, A. M. Gil, and S. P. Brown, *J. Am. Chem. Soc.*, 2005, **127**, 10216.
68. B. Elena, A. Lesage, S. Steuernagel, A. Bockmann, and L. Emsley, *J. Am. Chem. Soc.*, 2005, **127**, 17296.
69. A. Bockmann, A. Lange, A. Galinier, S. Luca, N. Giraud, M. Juy, H. Heise, R. Montserret F. Penin, and M. Baldus, *et al*., *J. Biomol. NMR*, 2003, **27**, 323.
70. N. Mifsud, B. Elena, C. J. Pickard, A. Lesage, and L. Emsley, *Phys. Chem. Chem. Phys.*, 2006, **8**, 3418.

Chapter 16

Nuclear Quadrupole Coupling: An Introduction & Crystallographic Aspects

Sharon E. Ashbrook[1] and Stephen Wimperis[2]

[1]*School of Chemistry and EaStCHEM, University of St Andrews, St Andrews KY16 9ST, UK*
[2]*Department of Chemistry and WestCHEM, University of Glasgow, Glasgow G12 8QQ, UK*

16.1 Introduction 223
16.2 Theory of Quadrupolar Coupling 224
16.3 Computation of Quadrupolar Parameters 224
16.4 Effect on NMR Spectra 226
16.5 Measurement by NMR 230
16.6 Use in NMR Crystallography 233
16.7 Conclusions 239
References 239

16.1 INTRODUCTION

As schoolchildren, we were all told that the ocean tides are raised by the pull of the Moon's gravity. Unfortunately, this explanation fails on at least three counts: (i) the Earth rotates on its axis every 24 h, yet there are not one but *two* high tides a day, (ii) the pull of the Sun's gravity on the Earth is much greater than that of the Moon's (and hence the Earth orbits the Sun, not the Moon), and (iii) lakes and inland seas experience no tides whatsoever. The correct explanation is that tides are an induced quadrupolar distortion of the Earth's oceans (hence two high and two low tides a day) caused by the gravitational *field gradient* of the Moon across the diameter of the Earth (which, owing to the much shorter distance between the Earth and the Moon, is far greater than that of the Sun).

Although on a very different length scale, and involving charges rather than masses and electric rather than gravitational fields, this is essentially the same phenomenon as the quadrupolar coupling that dominates NMR spectra of spin $I > 1/2$ nuclei. Atomic nuclei possess a nonspherical distribution of electric charge and hence an electric quadrupole moment (intrinsic in this case, not induced) that can interact with any electric field gradient across the nucleus arising from the surrounding electronic and nuclear environment. This interaction or coupling perturbs the energies of the nuclear spin states, giving rise to spectroscopically observable frequency shifts that can range up to many MHz or even a few GHz in magnitude.[1]

Over the last 30 or 40 years, solid-state NMR spectroscopy of quadrupolar nuclei such as ^{2}H, ^{14}N ($I = 1$), ^{7}Li, ^{11}B, ^{23}Na ($I = \frac{3}{2}$), ^{17}O, ^{27}Al ($I = \frac{5}{2}$) and the measurement of quadrupolar couplings by solid-state NMR have become well established,[2] although continuing interest in the subject has been stimulated by an impressive stream of new experimental techniques for achieving high-resolution spectra.[3–8] In this article, we will discuss the quadrupolar interaction in the context of the recent interest in determining crystallographic information by solid-state NMR.

NMR Crystallography Edited by Robin K. Harris, Roderick E. Wasylishen and Melinda J. Duer © 2009 John Wiley & Sons, Ltd. ISBN: 978-0-470-69961-4

First, we briefly review the nature of the quadrupolar interaction and discuss how quadrupolar couplings can be calculated and measured experimentally. Then, with these foundations in place, we describe, principally by means of examples, how quadrupolar couplings can be used to provide information about the arrangement of atoms in a crystalline solid.

16.2 THEORY OF QUADRUPOLAR COUPLING

Although small, the atomic nucleus has finite size and, hence, rather than a point electrical charge, we must consider a charge distribution. If this distribution is nonspherical and the centers of mass and charge coincide, the nucleus will possess an electric monopole or point charge (described by a tensor operator of rank $\ell = 0$), an electric quadrupole moment ($\ell = 2$), an electric hexadecapole moment ($\ell = 4$), and so on. There is some experimental evidence for nuclear electric moments with $\ell > 2$ and, to quote Abragam,[9] "there is no reason ... to doubt their existence", but it is the quadrupole moment that is principally responsible for perturbing the energies of the nuclear spin states.

The nuclear quadrupole moment interacts with the electric field gradient (EFG) across the nucleus.[1] Starting with the classical electrostatic interaction of the nuclear and surrounding charge distributions, Slichter replaces the nuclear charge density with its operator equivalent and, after much mathematical manipulation, arrives at the nuclear spin Hamiltonian for the quadrupolar coupling in an arbitrary x, y, z reference frame,[10]

$$H_{\mathrm{Q}} = \frac{eQ}{6I(2I-1)\hbar} \sum_{\alpha,\beta=x,y,z} V_{\alpha\beta}\left\{\frac{3}{2}(I_\alpha I_\beta + I_\beta I_\alpha) - \delta_{\alpha\beta} I(I+1)\right\} \tag{16.1}$$

where $\delta_{\alpha\beta}$ is the Kronecker delta and eQ is the nuclear quadrupole moment (units of C m^2). (As noted by Slichter,[10] it is interesting that the rank $\ell = 2$ nuclear quadrupole moment is described by a single parameter, implying that only its cylindrically symmetric component is of relevance here.) The quantity $V_{\alpha\beta}$ (units of V m^{-2}) is a component of the rank $\ell = 2$ Cartesian EFG tensor $\boldsymbol{V}$,

$$V_{\alpha\beta} = \left(\frac{\partial^2 \phi}{\partial\alpha\partial\beta}\right)_{r=0} \tag{16.2}$$

where ϕ is the electrostatic potential at the nucleus generated by the surrounding charge density. In its principal axis system (PAS), $\boldsymbol{V}$ is diagonal, with three nonzero elements V_{XX}, V_{YY}, and V_{ZZ}. By convention, we choose $|V_{ZZ}| \geq |V_{YY}| \geq |V_{XX}|$, and define the principal field gradient

$$eq = V_{ZZ} \tag{16.3}$$

and the axial asymmetry parameter

$$\eta_{\mathrm{Q}} = (V_{XX} - V_{YY})/V_{ZZ} \tag{16.4}$$

Using these, the quadrupolar Hamiltonian in equation (16.1) can be written in its PAS as

$$H_{\mathrm{Q}}^{\mathrm{PAS}} = \frac{e^2 qQ}{4I(2I-1)\hbar}\left\{3I_Z{}^2 - I(I+1) + \eta_{\mathrm{Q}}(I_X{}^2 - I_Y{}^2)\right\} \tag{16.5}$$

It can now easily be verified that $H_{\mathrm{Q}} = 0$ for $I = \frac{1}{2}$. As a result of the Laplace equation, $V_{XX} + V_{YY} + V_{ZZ} = 0$, another case where H_{Q} vanishes is that of cubic symmetry in the nuclear surroundings, when $V_{XX} = V_{YY} = V_{ZZ} = 0$. The Laplace equation also restricts the asymmetry parameter to the range $0 \leq \eta_{\mathrm{Q}} \leq 1$.

It is customary to tidy up the constants at the front of equation (16.5) by defining a quadrupolar coupling constant C_{Q} (in units of Hz)

$$C_{\mathrm{Q}} = e^2 qQ/h \tag{16.6}$$

In this case, the term *coupling* refers to the interaction of the nuclear quadrupole moment eQ and the principal field gradient eq and not, of course, to an interaction between two nuclear spins.

16.3 COMPUTATION OF QUADRUPOLAR PARAMETERS

The nuclear quadrupole moment eQ is an experimentally determined quantity. Computation of parameters such as C_{Q} and η_{Q} therefore becomes a question of calculating the $V_{\alpha\beta}$ components of the EFG tensor.

If SI units are used, Slichter[10] states that a point charge e at a position x, y, z generates a $V_{\alpha\beta}$ component at $r = 0$ (the nucleus) of

$$V_{\alpha\beta} = \frac{e}{4\pi\varepsilon_0 r^3}\left(\frac{3\alpha\beta}{r^2} - \delta_{\alpha\beta}\right) \tag{16.7}$$

where α or $\beta = x$, y, z as before and $r^2 = x^2 + y^2 + z^2$. The $V_{\alpha\beta}$ components arising from several

point charges may simply be summed to give a total. Therefore, it is quite straightforward (and instructive) to read the x, y, z coordinates of the atoms constituting one or more unit cells of an ionic crystal into a spreadsheet program, assign charges to these atoms (e.g., $+e$ for Na^+, $-e$ for Cl^-, $+2e$ for Ca^{2+}, $-2e$ for O^{2-}, etc.), and compute the full EFG tensor $\boldsymbol{V}$ at the origin, which may be placed on the nucleus of interest. The tensor $\boldsymbol{V}$ may then be diagonalized, the principal values used to obtain C_Q and η_Q, and the eigenvectors used to obtain the orientation of the EFG tensor in the crystal frame.

The value of C_Q obtained by finding $V_{ZZ} = eq$ using this "point-charge model" and then inserting it into equation (16.6) may be an order of magnitude or more smaller than that measured experimentally, particularly for a nucleus in a heavy atom. This is a consequence of the fact that, so far, the effect of the electrons in the orbitals around the nucleus of interest has been ignored. In a fully ionic solid, these closed-shell electrons will have spherical symmetry (and hence contribute zero-field gradient) until polarized by the EFG arising from the external point charges. If we call this latter field gradient $\boldsymbol{V}^{\text{ext}}$ and the additional, induced field gradient arising from the distorted closed shell $\boldsymbol{V}^{\text{ind}}$, then we have $\boldsymbol{V}^{\text{ind}} = -\gamma_\infty \boldsymbol{V}^{\text{ext}}$ and

$$\begin{aligned} \boldsymbol{V}^{\text{tot}} &= \boldsymbol{V}^{\text{ext}} + \boldsymbol{V}^{\text{ind}} \\ &= (1 - \gamma_\infty)\boldsymbol{V}^{\text{ext}} \end{aligned} \tag{16.8}$$

where $\boldsymbol{V}^{\text{tot}}$ is the total EFG tensor experienced by the nucleus and γ_∞ is a proportionality constant known as the Sternheimer antishielding factor,[10] which has been calculated to be small and positive for Li^+ ($\gamma_\infty \approx +0.25$ and hence shielding, not antishielding) but large and negative for heavier ions, such as Na^+ ($\gamma_\infty \approx -4$), O^{2-} ($\gamma_\infty \approx -14$), and Rb^+ ($\gamma_\infty \approx -50$).

Even including the Sternheimer antishielding factor as a correction, the point-charge model rarely provides results that agree well with experiment as it does not take into account any degree of covalency, i.e., interactions between atoms arising from the outer or valency electrons. As a result, there has been much interest in the use of electronic structure calculations for the numerical computation of EFG tensors. A detailed discussion of these quantum-mechanical methods is outside the scope of this article but it can be noted that, from an NMR spectroscopy perspective, they are popularly divided into two basic types:

1. Methods where a cluster of atoms is defined around the atom of interest and either Hartree–Fock theory or density functional theory (DFT) used to obtain the ground-state electronic wavefunction. The EFG tensor is then computed from the charge density (proportional to the square of the wavefunction in the Born interpretation). In order to obtain a good approximation to a crystalline solid, the defined cluster must be as large as possible and/or embedded in a lattice of point charges. This cluster approach can be implemented, for example, using the well-known quantum chemistry program GAUSSIAN.[11]
2. Methods that use a planewave basis set to exploit the periodicity of an infinite crystalline solid made up of repeating unit cells (see **Chapter 3**).[12] Normally DFT is used for the electronic structure calculation, with examples including the WIEN2k[13] and CASTEP[14] programs. The former calculates the all-electron wavefunction directly, while the latter replaces the core electrons with a pseudopotential for greater computational efficiency and then reconstructs the all-electron wavefunction using the projector augmented wave (PAW) method. These codes do not require definition of a cluster and have high accuracy as a result of the wavefunction extending throughout the infinite solid.

An important point to note with all these "first-principles" quantum-mechanical methods is that the EFG is a property of the ground-state electronic wavefunction and that, unlike the chemical shift or the indirect spin–spin coupling, its computation does not require knowledge of any excited states. Thus, despite recent improvements in the computation of chemical shifts, it should always be the case that the quadrupolar NMR parameters will be computed with greater time efficiency and (probably) accuracy.

Finally, although very definitely not one of the first-principles methods discussed above, it is worth noting that attempts have been made to calculate EFG tensors, and hence quadrupolar NMR parameters, from electron density maps yielded by advanced X-ray diffraction (XRD) techniques.[15] From the perspective of crystallography, however, it is the reverse of this process that is of greater interest: experimental measurements of quadrupolar NMR parameters yield EFG tensors and knowledge

of these could be used to improve the quality of XRD-derived electron density maps.

16.4 EFFECT ON NMR SPECTRA

The effect of the quadrupolar interaction, as expressed by the Hamiltonian H_Q, on nuclear spin energy levels subject to a Zeeman interaction and, hence, on NMR spectra has been extensively discussed in many places[1] and is only briefly reviewed here.

The general approach is to form the total nuclear spin Hamiltonian H by adding together the Zeeman, H_Z, and the quadrupolar, H_Q, Hamiltonians and then treat the latter as a small perturbation on the former:

$$H = H_Z + H_Q \tag{16.9}$$

where

$$H_Z = \omega_0 I_z \tag{16.10}$$

To proceed further, we now need to express H_Q in the laboratory axis system defined by H_Z and the best way of doing this is to take H_Q^{PAS} in (equation (16.5)) (where $\boldsymbol{V}$ is parameterized by just two terms, eq and η_Q) and rotate it into the laboratory frame. This rotation can be performed in a number of ways but one popular method is to rewrite H_Q^{PAS} in terms of spherical tensor operators, $T_{\ell,m}$,

$$H_Q^{PAS} = \frac{\sqrt{3}\pi C_Q}{2\sqrt{2}I(2I-1)}\left(T_{2,0} + \frac{\eta_Q}{\sqrt{6}}(T_{2,2} + T_{2,-2})\right) \tag{16.11}$$

where we have used the $\{T_{\ell,m}\}$ defined in[1] and exploit the convenient transformation properties of spherical tensors under rotation,

$$R(\alpha,\beta,\gamma)T_{\ell,m}R^{-1}(\alpha,\beta,\gamma) = \sum_{m'=-\ell}^{\ell} D^{\ell}_{m',m}(\alpha,\beta,\gamma)\, T_{\ell,m'} \tag{16.12}$$

where α, β, γ are the Euler angles and $D^{\ell}_{m',m}(\alpha,\beta,\gamma)$ is a Wigner rotation matrix element.[16] Using equations (16.11) and (16.12) the laboratory-frame quadrupolar Hamiltonian can then be written as

$$H_Q^{Lab} = \frac{\sqrt{3}\pi C_Q}{2\sqrt{2}I(2I-1)} \sum_{m'=-2}^{2} \left(D^2_{m',0}(\alpha,\beta,\gamma) + \frac{\eta_Q}{\sqrt{6}}\left(D^2_{m',2}(\alpha,\beta,\gamma) + D^2_{m',-2}(\alpha,\beta,\gamma)\right)\right) T_{2,m'} \tag{16.13}$$

If the eigenstates, $|i\rangle$, and eigenvalues, $\varepsilon_i^{(0)}$, of H_Z are known, i.e.,

$$H_Z|i\rangle = \varepsilon_i^{(0)}|i\rangle \tag{16.14}$$

and if H_Z dominates H_Q then time-independent perturbation theory[17] states that the energy, ε_i (here in units of s^{-1}), of an eigenstate of H in equation (16.9) is given by

$$\varepsilon_i = \varepsilon_i^{(0)} + \varepsilon_i^{(1)} + \varepsilon_i^{(2)} + \ldots \tag{16.15}$$

where

$$\varepsilon_i^{(1)} = \langle i|H_Q^{Lab}|i\rangle \tag{16.16}$$

and

$$\varepsilon_i^{(2)} = \sum_{i\neq j} \frac{\langle i|H_Q^{Lab}|j\rangle\langle j|H_Q^{Lab}|i\rangle}{\varepsilon_i^{(0)} - \varepsilon_j^{(0)}} \tag{16.17}$$

A first-order correction to an energy, $\varepsilon_i^{(1)}$, in equation (16.16) simply consists of a diagonal element of H_Q^{Lab} in equation (16.13). Since $T_{2,0}$ is the only diagonal $\ell = 2$ tensor operator, we can write a first-order quadrupolar Hamiltonian:

$$\begin{aligned} H_Q^{(1)} &= \frac{\sqrt{3}\pi C_Q}{2\sqrt{2}I(2I-1)}\left(D^2_{0,0}(\alpha,\beta,\gamma) + \frac{\eta_Q}{\sqrt{6}}\left(D^2_{0,2}(\alpha,\beta,\gamma) + D^2_{0,-2}(\alpha,\beta,\gamma)\right)\right) T_{2,0} \\ &= \omega_Q\left(I_z^2 - \frac{1}{3}I(I+1)\right) \end{aligned} \tag{16.18}$$

where

$$\omega_Q = \frac{\omega_Q^{PAS}}{2}(3\cos^2\beta - 1 + \eta_Q \sin^2\beta\cos 2\gamma) \tag{16.19}$$

with

$$\omega_Q^{PAS} = \frac{3\pi C_Q}{2I(2I-1)} \tag{16.20}$$

Note that, unlike H_Q^{PAS} or H_Q^{Lab}, $H_Q^{(1)}$ is orientationally dependent.

Observable NMR transitions have $\Delta m = m_i - m_j = \pm 1$ where m is the magnetic quantum number:

$$I_z|i\rangle = m_i\hbar|i\rangle \tag{16.21}$$

Up to first order, therefore, the frequencies of the observable transitions for a spin I nucleus are given by

$$\begin{aligned}\varepsilon_i - \varepsilon_{i+1} &= \left(\varepsilon_i^{(0)} - \varepsilon_{i+1}^{(0)}\right) + \left(\varepsilon_i^{(1)} - \varepsilon_{i+1}^{(1)}\right) \\ &= \omega_0 + \omega_Q(m_i^2 - m_{i+1}^2)\end{aligned} \tag{16.22}$$

Thus, in the NMR spectrum of a single crystal, two transitions would be found for a spin $I = 1$ with frequencies of $\omega_0 + \omega_Q$ and $\omega_0 - \omega_Q$, three transitions for a spin $I = \frac{3}{2}$ with frequencies of $\omega_0 + 2\omega_Q$, ω_0, and $\omega_0 - 2\omega_Q$, and so on. In each case, in this "Ernstian"[1,18] convention, the splitting between adjacent resonances in the quadrupolar multiplet is $2\omega_Q$. (In another widely used convention, the splitting between adjacent transitions is defined

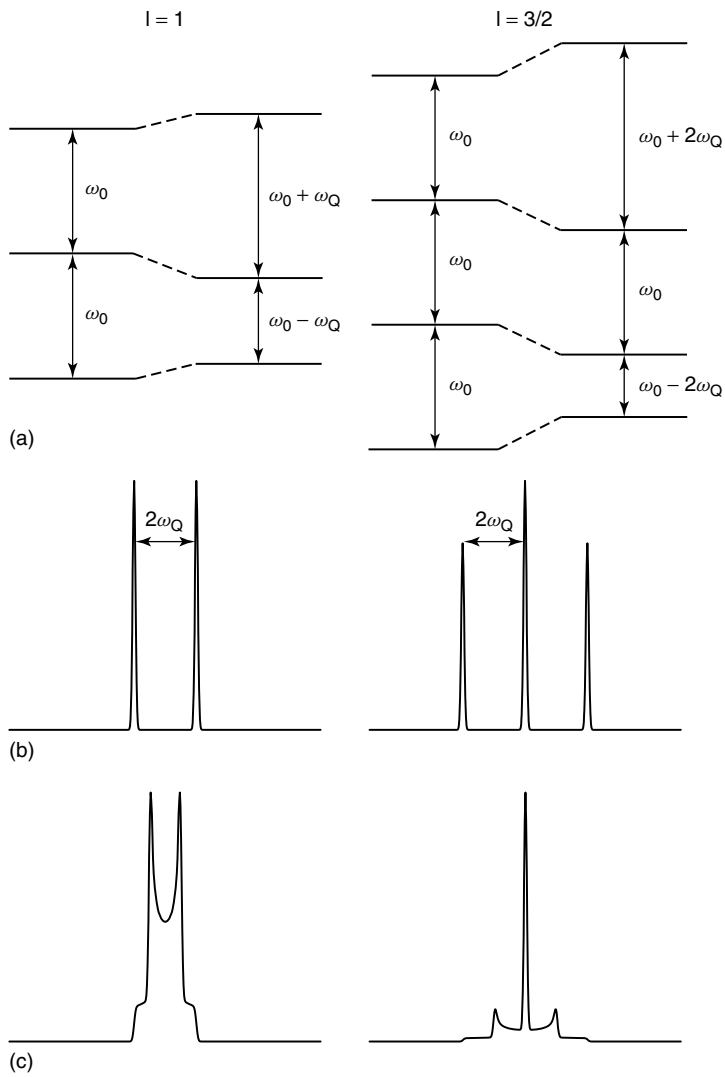


Figure 16.1. (a) First-order perturbation of the Zeeman energy levels by the quadrupolar coupling for spin quantum number $I = 1$ and $\frac{3}{2}$. (b) Simulations of the resulting (single-crystal) NMR spectra with $2I$ nondegenerate transitions separated by $2\omega_Q$. (c) Corresponding powder NMR spectra.

as ω_Q.) In a powdered sample, all orientations of $\boldsymbol{V}$ with respect to B_0 are present simultaneously and the full NMR spectrum is obtained from the average in equations (16.18) and (16.19) of β from 0 to π and (if $\eta_Q \neq 0$) γ from 0 to 2π. Figure 16.1 shows schematic energy levels and simulated single crystal and powder NMR spectra for $I=1$ and $\frac{3}{2}$, calculated up to first order. Note that for a half-integer spin quadrupolar nucleus ($I = \frac{3}{2}$, $\frac{5}{2}$, $\frac{7}{2}$, etc.), the $m = +\frac{1}{2} \leftrightarrow -\frac{1}{2}$ or "central" transition is not broadened in the powder spectrum.

Typical values of $\omega_Q^{PAS}/2\pi$ observed in solid-state NMR spectroscopy range up to ~10 MHz while $\omega_0/2\pi$ is typically 100 MHz. Therefore, second-order corrections to the energy levels are often important and equation (16.17) has to be evaluated. After simplification of the products of Wigner rotation matrix elements,[16] the following is obtained:

$$\varepsilon_i^{(2)} = \frac{\left(\omega_Q^{PAS}\right)^2}{2\omega_0} \times \left(A_{I,m_i}^{(0)} B^{(0)} + A_{I,m_i}^{(2)} B^{(2)}(\beta,\gamma) + A_{I,m_i}^{(4)} B^{(4)}(\beta,\gamma)\right) \tag{16.23}$$

where the spin and magnetic quantum number-dependent coefficients, $A_{I,m_i}^{(\ell)}$, are given in Table 16.1 for spins $I = \frac{3}{2}$ and $\frac{5}{2}$, and the orientation-dependent coefficients are

$$B^{(0)} = \left(1 + \frac{{\eta_Q}^2}{3}\right) \tag{16.24a}$$

$$B^{(2)}(\beta,\gamma) = \left(1 - \frac{{\eta_Q}^2}{3}\right) d_{0,0}^2(\beta) - \frac{2\sqrt{2}}{\sqrt{3}} \eta_Q \, d_{2,0}^2(\beta) \cos 2\gamma \tag{16.24b}$$

$$B^{(4)}(\beta,\gamma) = \left(1 + \frac{{\eta_Q}^2}{18}\right) d_{0,0}^4(\beta) + \frac{\sqrt{10}}{3} \eta_Q \, d_{2,0}^4(\beta) \times \cos 2\gamma + \frac{35}{9\sqrt{70}} {\eta_Q}^2 \, d_{4,0}^4(\beta) \cos 4\gamma \tag{16.24c}$$

where $d_{m',m}^{\ell}(\beta)$ is a reduced Wigner rotation matrix element.[16] The two most noticeable effects of the inclusion of this second-order quadrupolar interaction are (i) that the $m = +\frac{1}{2} \leftrightarrow -\frac{1}{2}$ central transition of a half-integer quadrupolar spin is now broadened in the powder spectrum, although this broadening is typically much smaller (~kHz) than the first-order broadening of the "satellite" transitions (~MHz), and (ii) that its center of mass is shifted away from the Larmor frequency ω_0 by an amount $A_{I,\frac{1}{2}}^{(0)} B^{(0)} (\omega_Q^{PAS})^2/\omega_0$. Figure 16.2 shows schematically the effects of the second-order correction on the spin $I = \frac{3}{2}$ energy levels and simulations of the resulting powder central-transition lineshape for $\eta_Q = 0$ and $\eta_Q = 1$.

Nowadays, most modern solid-state NMR experiments are performed on powdered materials under conditions of magic angle spinning (MAS). The first-order quadrupolar Hamiltonian in equation (16.18) has a purely rank $\ell = 2$ orientational dependence and so, in the limit of very fast MAS, a single sharp line at the Larmor frequency is predicted. However, in reality, the MAS rate (~kHz) will almost certainly be much smaller than the satellite broadening and in this slow MAS limit the narrow

Table 16.1. Spin and magnetic quantum number dependent coefficients $A_{I,m_i}^{(\ell)}$ governing second-order quadrupolar broadening for spin $I = \frac{3}{2}$ and $I = \frac{5}{2}$ (See Equation (16.23))

	$A_{I,m_i}^{(0)}$	$A_{I,m_i}^{(2)}$	$A_{I,m_i}^{(4)}$
Spin $I = \frac{3}{2}$			
$m_1 = +\frac{3}{2}$	$\frac{6}{5}$	0	$-\frac{6}{5}$
$m_2 = +\frac{1}{2}$	$-\frac{2}{5}$	$-\frac{8}{7}$	$\frac{54}{35}$
$m_3 = -\frac{1}{2}$	$\frac{2}{5}$	$\frac{8}{7}$	$-\frac{54}{35}$
$m_4 = -\frac{3}{2}$	$-\frac{6}{5}$	0	$\frac{6}{5}$
Spin $I = \frac{5}{2}$			
$m_1 = +\frac{5}{2}$	$\frac{20}{3}$	$\frac{40}{21}$	$-\frac{60}{7}$
$m_2 = +\frac{3}{2}$	$-\frac{4}{5}$	$-\frac{40}{7}$	$\frac{228}{35}$
$m_3 = +\frac{1}{2}$	$-\frac{16}{15}$	$-\frac{64}{21}$	$\frac{144}{35}$
$m_4 = -\frac{1}{2}$	$\frac{16}{15}$	$\frac{64}{21}$	$-\frac{144}{35}$
$m_5 = -\frac{3}{2}$	$\frac{4}{5}$	$\frac{40}{7}$	$-\frac{228}{35}$
$m_6 = -\frac{5}{2}$	$-\frac{20}{3}$	$-\frac{40}{21}$	$\frac{60}{7}$

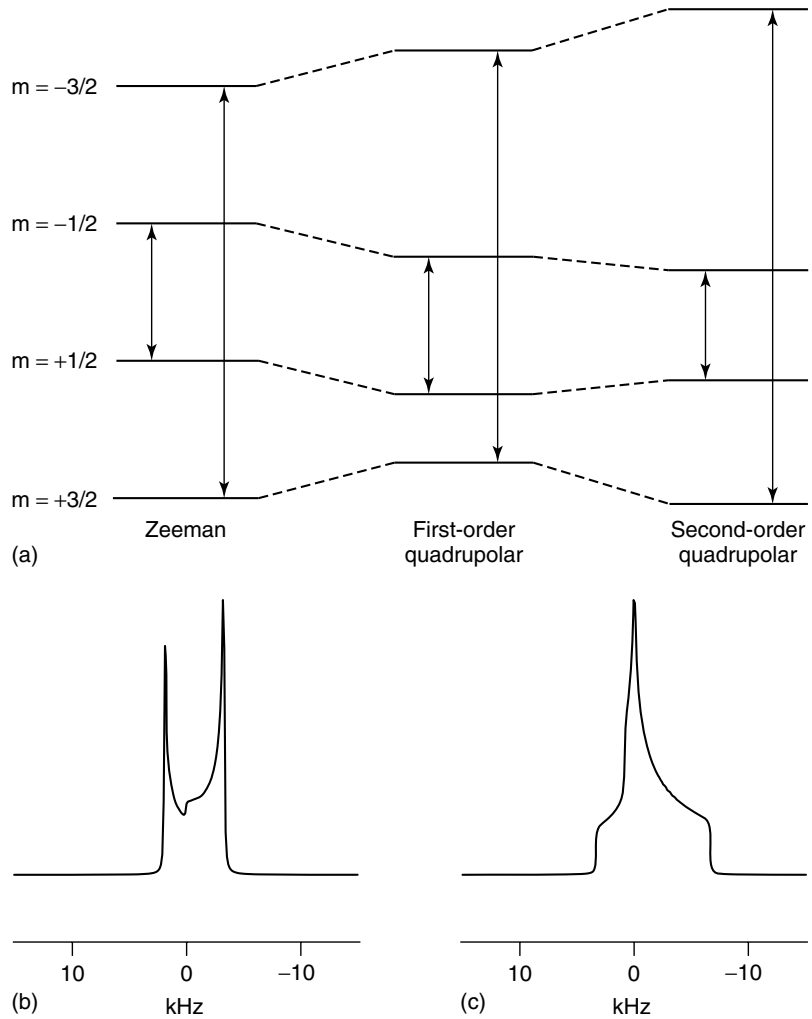


Figure 16.2. (a) Perturbation of the spin $I = \frac{3}{2}$ Zeeman energy levels by the quadrupolar coupling to first- and second-order approximations, showing that the frequencies of the $m = +\frac{1}{2} \leftrightarrow -\frac{1}{2}$ central- and $m = +\frac{3}{2} \leftrightarrow -\frac{3}{2}$ triple-quantum transitions are affected in the second-order (but not first-order) approximation. (b) and (c) Simulations of spin $I = \frac{3}{2}$ second-order quadrupolar broadened central-transition NMR lineshapes with (b) $\eta_Q = 0$ and (c) $\eta_Q = 1$. Other simulation parameters: $C_Q = 2\,\text{MHz}$ and $\omega_0/2\pi = 100\,\text{MHz}$.

centerband at the Larmor frequency will be replicated in a series of spinning sidebands separated by the MAS rate ω_{MAS}. If second-order quadrupolar effects are considered, then the effects of MAS on the orientation-dependent terms in equation (16.24) must be taken into account: $B^{(0)}$ is unaffected, $B^{(2)}$ vanishes completely if we assume that the MAS rate is faster than $(\omega_Q^{PAS})^2/\omega_0$, and $B^{(4)}$ is scaled by $-7/18$, leaving the MAS-averaged second-order correction to the energy as

$$\langle \varepsilon_i^{(2)} \rangle_{MAS} = \frac{\left(\omega_Q^{PAS}\right)^2}{2\omega_0} \left(A_{I,m_i}^{(0)} B^{(0)} - \frac{7}{18} A_{I,m_i}^{(4)} B^{(4)}(\beta', \gamma') \right) \tag{16.25}$$

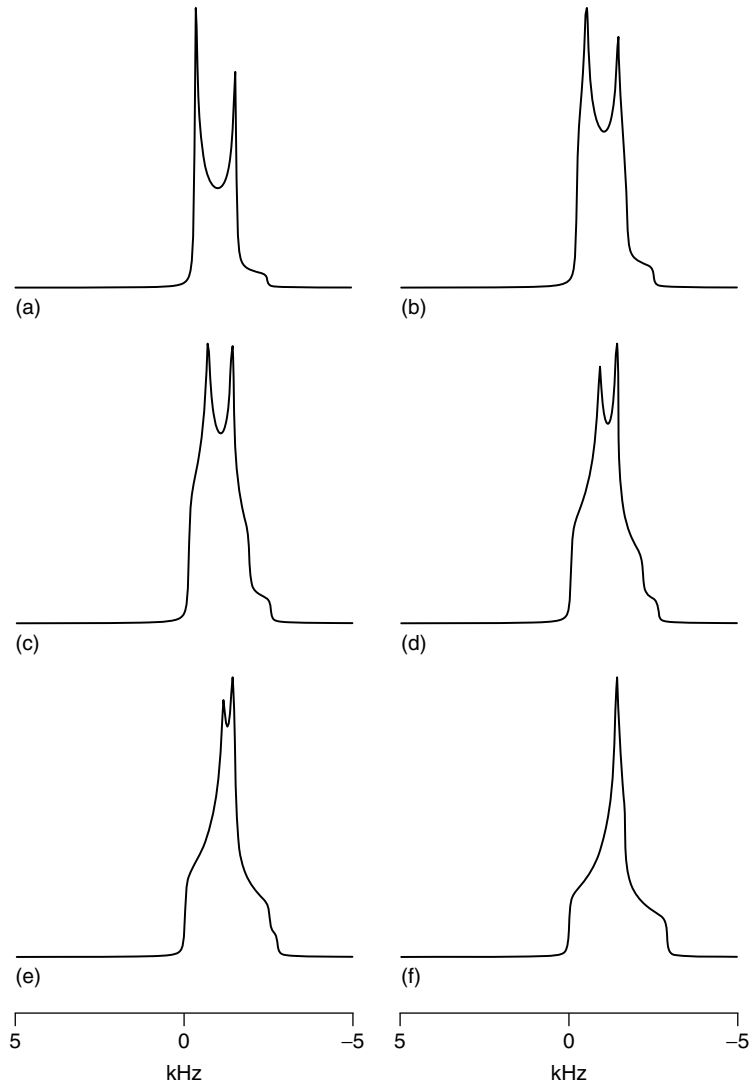


Figure 16.3. Simulations of spin $I = \frac{3}{2}$ second-order broadened central-transition MAS NMR lineshapes with (a) $\eta_Q = 0$, (b) $\eta_Q = 0.2$, (c) $\eta_Q = 0.4$, (d) $\eta_Q = 0.6$, (e) $\eta_Q = 0.8$, and (f) $\eta_Q = 1.0$. Note that these lineshapes are offset from zero frequency by the isotropic second-order quandrupolar shift. Other simulation parameters are $C_Q = 2\,\text{MHz}$ and $\omega_0/2\pi = 100\,\text{MHz}$.

where β' and γ' are Euler angles relating the PAS of the EFG tensor to the "rotor frame" with its z axis coincident with the MAS axis. Hence, the rank $\ell = 4$ part of the second-order powder broadening survives in the MAS spectrum, as shown in Figure 16.3 for the spin $I = \frac{3}{2}$ $m = +\frac{1}{2} \leftrightarrow -\frac{1}{2}$ central transition.

16.5 MEASUREMENT BY NMR

Quadrupolar couplings can be measured by a variety of techniques, including microwave rotational spectroscopy, electron spin resonance (ESR), perturbed angular correlation (PAC) of nuclear radiation, Mössbauer spectroscopy, solution-state NMR relaxation measurements, and nuclear quadrupole

resonance (NQR), also known as zero-field NMR. These are all outside the scope of this article and we concentrate, as in the previous section, on the measurement of quadrupolar couplings in solid-state NMR spectroscopy performed in the high-field limit.

A series of NMR spectra of a single crystal recorded as a function of orientation in a goniometer probehead can be analyzed to yield quadrupolar coupling parameters.[19] Either the satellite transitions or, for a half-integer spin exhibiting second-order effects, the central transition may be followed. Although a powerful method (as it yields the absolute orientation of the EFG tensor in the crystal frame, which is difficult to obtain by other techniques), it is limited by the availability of large crystals of the appropriate material.

The determination of quadrupolar coupling parameters from powder NMR lineshapes is a much more general and widely used approach. Ideally, all transitions are recorded in a single spectrum, most likely using a spin-echo experiment to obtain an undistorted lineshape. This is the approach used for nuclei with small quadrupole moments, such as ^{2}H, ^{6}Li ($I = 1$), ^{7}Li ($I = \frac{3}{2}$), and ^{133}Cs ($I = \frac{7}{2}$). The resulting powder spectra can be fitted using a variety of widely available software and, if present, any additional effects of other spin interactions or dynamics can be taken into account.[20] A ^{2}H NMR example of such a fitting, with dynamic effects included, is shown in Figure 16.4. For most other nuclides, however, the quadrupolar coupling is much larger and the full powder lineshape is too wide to record in a single spectrum. In this case, it can be reconstructed from a series of experiments in which either the radiofrequency or static magnetic field is stepped across the region of interest.[21] Alternatively, for half-integer spin quadrupolar nuclei, the second-order powder lineshape of the central transition can be recorded (i.e., instead of attempting to record the much broader satellite transitions) and fitted to obtain the quadrupolar coupling parameters. Because the central transition is typically several orders of magnitude narrower than the satellite-transition powder lineshape, it is more important to allow for the presence of other spin interactions, such as the chemical shift anisotropy (CSA), in any fitting. Although popular, the analysis of powder lineshapes of static samples has at least two major drawbacks: (i) the sensitivity is low as the signal is spread across a wide frequency range and, more significantly, (ii) if more than one inequivalent species of the observed nuclide is present their lineshapes will overlap and be unresolved, making analysis difficult.

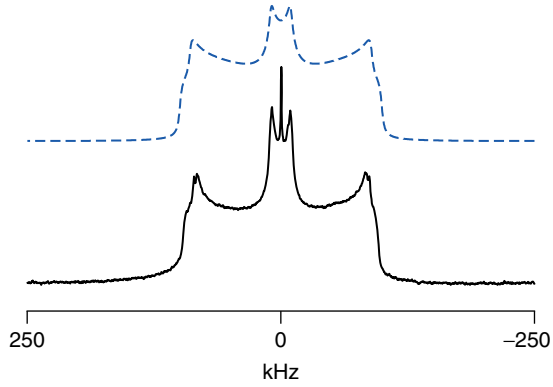


Figure 16.4. ^{2}H ($I = 1$) quadrupolar-echo NMR spectrum of static powdered sodium tetrathionate dihydrate-d_4 ($Na_2S_4O_6.2D_2O$) and computer fitting (dashed line). Experimental parameters: $\omega_0/2\pi = 61.4$ MHz. The fitting includes a dynamic model allowing for 180° flips of the D_2O molecules about their C_2 axes and yields the parameters: $C_Q = 266$ kHz, $\eta_Q = 0$, a D–O–D angle of 105.5°, and rate constant $k = 6.8 \times 10^6\ s^{-1}$.

For half-integer spin quadrupolar nuclei, the nutation behavior of the central transition during a radiofrequency pulse depends largely on the first-order quadrupolar interaction, even though the observed lineshape is unaffected by it.[22] This phenomenon provides a means of measuring quadrupolar parameters from a central-transition powder lineshape even if that lineshape shows no features characteristic of the quadrupolar interaction. Two-dimensional nutation NMR spectra are obtained by incrementing an excitation pulse duration as a function of a time t_1 and recording the resulting free induction decays (FIDs) as a function of t_2 and then performing a two-dimensional Fourier transform with respect to $\{t_1, t_2\}$. Computer fitting of the complex lineshape correlating second-order broadening in F_2 with the nutation pattern in F_1 yields the quadrupolar coupling parameters. An ^{27}Al ($I = \frac{5}{2}$) NMR example of a two-dimensional nutation spectrum is shown in Figure 16.5. As with other methods designed for static samples, nutation spectroscopy is difficult to apply if there are several inequivalent sites for the observed nuclide owing to the lack of site resolution.

In recent years, it has become increasingly popular to study powdered solids by MAS NMR. For

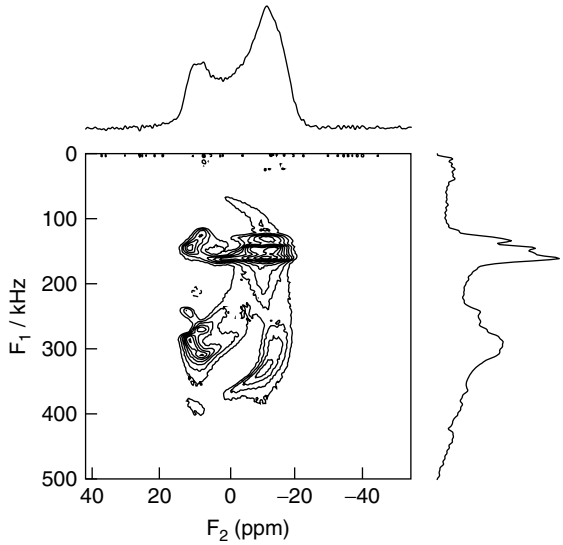


Figure 16.5. Two-dimensional ^{27}Al ($I = \frac{5}{2}$) nutation spectrum of static powdered aluminum acetylacetonate, $Al(C_5H_7O_2)_3$. This correlation spectrum can be analyzed to yield the ^{27}Al quadrupolar coupling parameters $C_Q = 3.0$ MHz and $\eta_Q = 0.15$. Experimental parameters are $\omega_0/2\pi = 104.3$ MHz and radiofrequency field strength $\omega_1/2\pi = 100$ kHz.

nuclei that generally exhibit small quadrupolar couplings, the full static powder lineshape breaks up under MAS into spinning sidebands whose intensities mirror the original static lineshape, thus providing a higher signal-to-noise ratio and often resolving crystallographically inequivalent species, but still allowing extraction of quadrupolar coupling parameters. For nuclei exhibiting larger quadrupolar couplings, full excitation and detection of the satellite transitions is unlikely but, for half-integer spin nuclei like ^{23}Na ($I = \frac{3}{2}$), ^{17}O and ^{27}Al ($I = \frac{5}{2}$), quadrupolar parameters can still be extracted by lineshape analysis of the MAS-averaged second-order broadened central transition. Unfortunately, this second-order broadening means that site resolution is not obtained unless the broadening is unusually small or the chemical shift range is large. For spin $I = \frac{5}{2}$ nuclei, second-order broadened $m = \pm\frac{3}{2} \leftrightarrow \pm\frac{1}{2}$ satellite-transition spinning sidebands are sometimes analyzed as well as, or instead of, the central transition as the broadening is smaller and, hence, there is more chance of resolving multiple sites.[23] Even if MAS lineshapes show no features characteristic of the second-order quadrupolar interaction, the composite quadrupolar parameter $C_Q(1 + {\eta_Q}^2/3)^{\frac{1}{2}}$ can still be extracted by recording spectra at different B_0 field strengths and separating the second-order quadrupolar shift from the chemical shift. Finally, it is worth noting that in very favorable cases it is even possible to extract quadrupolar coupling parameters from MAS NMR spectra of spin $I = \frac{1}{2}$ nuclei, where powder lineshapes due to second-order "cross terms" between the $I - S$ dipolar interaction and the strong quadrupolar interaction of a "remote" $S \geq 1$ nucleus are sometimes observed.[24]

The problem of second-order MAS lineshapes from inequivalent sites overlapping and hence being unresolved has been tackled with some success in recent years with the development of new experimental methods. The double rotation (DOR)[25] and dynamic angle spinning (DAS)[26] techniques were proposed in 1988 and involve rotating the powdered solid at two angles with respect to B_0 (simultaneously in the case of DOR and sequentially in the case of DAS) to remove the rank $\ell = 2$ and 4 components of the second-order quadrupolar broadening. However, neither DOR nor DAS have achieved wide popularity, as specialist, rather complicated probeheads are needed and spinning rates are limited, severely so in the case of DOR. In contrast, the multiple-quantum (MQ)MAS[27] and satellite-transition (ST)MAS techniques,[28,29] proposed in 1995 and 2000, respectively, are purely MAS-based and so can be performed on standard MAS hardware and at high spinning rates. These methods yield two-dimensional NMR spectra with an "isotropic" dimension (F_1) that is free from first- and second-order quadrupolar broadening, yet retains isotropic chemical and second-order quadrupolar shifts, and an "anisotropic" dimension (F_2) that displays MAS-averaged second-order broadened central-transition lineshapes. A ^{87}Rb ($I = \frac{3}{2}$) NMR example of a two-dimensional MQMAS spectrum is shown in Figure 16.6(a). Extraction of quadrupolar coupling parameters can be done in a variety of ways, including (i) fitting the central-transition lineshapes in F_2 to obtain C_Q and η_Q (see the examples of ^{87}Rb central-transition lineshapes and their fittings in Figure 16.6b and 16.6c), (ii) measuring the $\{F_1, F_2\}$ coordinates of the center of mass of a two-dimensional peak and deriving $C_Q(1 + {\eta_Q}^2/3)^{\frac{1}{2}}$, and (iii) measuring the peak positions in the F_1 dimension at two different B_0 field strengths and deriving $C_Q(1 + {\eta_Q}^2/3)^{\frac{1}{2}}$.

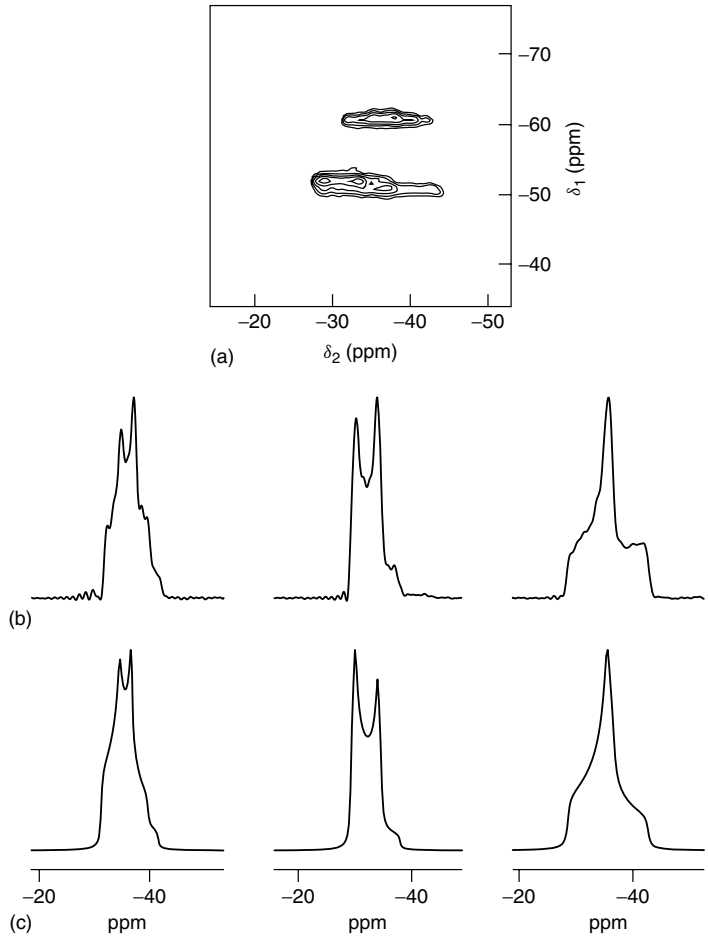


Figure 16.6. (a) Two-dimensional ^{87}Rb ($I = \frac{3}{2}$) MQMAS NMR spectrum of rubidium nitrate, $RbNO_3$. Experimental parameters: $\omega_0/2\pi = 130.9$ MHz. (b) Cross sections parallel to δ_2 through the three second-order broadened ridge lineshapes in (a). (c) Computer fittings of the ^{87}Rb MAS lineshapes in (b), yielding quadrupolar parameters (from left to right): (i) $C_Q = 1.7$ MHz, $\eta_Q = 0.6$; (ii) $C_Q = 1.7$ MHz, $\eta_Q = 0.1$; and (iii) $C_Q = 1.9$ MHz, $\eta_Q = 1.0$.

The principal drawbacks of MQMAS and STMAS are that (i) their application is limited to sites with small and moderate quadrupolar couplings, (ii) peak intensities are not quantitative and F_2 central-transition lineshapes can be very distorted, (iii) the overall sensitivity is poor, especially for MQMAS, and (iv) extensive phase cycling and the need for high resolution in F_1 mean that minimum experiment times for these two-dimensional methods can be rather long. This last problem was the inspiration behind the development of the satellite transitions acquired in real time (START)MAS experiment,[30] which provides isotropic spectra in a real-time, one-dimensional experiment; however, it is limited to spin $I = \frac{3}{2}$ nuclei.

16.6 USE IN NMR CRYSTALLOGRAPHY

16.6.1 Quadrupolar Coupling and Symmetry

The dependence of the quadrupolar coupling parameters upon the EFG tensor, $\boldsymbol{V}$, results in a strong relationship with crystal symmetry.[31] Although this relationship is rarely simple, with a range of factors

affecting the EFG, for two types of local symmetry at the site of the nucleus strong restrictions are imposed upon the nature and symmetry of the EFG tensor, providing almost instant insight into the structure.

16.6.1.1 Cubic Point Symmetry

For the case of cubic point symmetry $V_{XX} = V_{YY} = V_{ZZ}$ and, hence, by the Laplace equation, $V_{ZZ} = eq$ is zero. Therefore, C_Q is zero for regular fourfold tetrahedral, sixfold octahedral and eightfold cubic coordination environments. For example, in MgO, which has the rock salt structure (space group *Fm3m*) C_Q is zero for both ^{17}O and ^{25}Mg (both $I = \frac{5}{2}$).[32] More commonly, however, a quadrupolar coupling of exactly zero is rarely observed as the "perfect" symmetry is often broken either on the short length scale (by distortions and deviations of bond angles and/or bond lengths away from their ideal value) or, on a longer length scale, i.e., when second and third coordination spheres are taken into account. Indeed, even in powdered NaCl, the ^{23}Na NMR resonance, although very narrow, displays a small quadrupolar broadening resulting from the presence of defects and the finite extent of the crystallites and hence a deviation from perfect cubic point symmetry.

16.6.1.2 Axial Point Symmetry

For the case of perfect axial point symmetry $V_{XX} = V_{YY}$ and η_Q is therefore zero. Note this places no additional restriction upon the value of V_{ZZ}. Such a situation occurs when the nucleus in question lies on an n-fold rotation axis, where $n = 3$, 4, 5, or 6. For example, in ZnO, which has a dihexagonal pyramidal structure (space group *P63mc*), there is a C_3 axis passing through the Zn and hence η_Q is zero for ^{67}Zn ($I = \frac{5}{2}$).[33] Similarly, although for TiO_2 the two polymorphs, anatase (space group *I4/amd*) and rutile (space group *P4/mnm*) have tetragonal structures, in anatase η_Q is zero for ^{47}Ti ($I = \frac{5}{2}$) and ^{49}Ti ($I = \frac{7}{2}$) as the Ti is situated on a C_4 rotation axis, whereas in rutile the Ti has *m.mm* point symmetry and η_Q is 0.19.[34] A well-known example of local axial symmetry occurs with the ^2H ($I = 1$) nucleus, which, unless part of a strong hydrogen bond, is usually found to have $\eta_Q \approx 0$ in molecular crystals, with V_{ZZ} oriented along the axially symmetric X–H σ-bond.[35]

Apart from the two special cases described above, the crystal symmetry alone may place constraints upon the orientation of the quadrupolar PAS in the crystal frame. For example, in $RbClO_4$ (space group *Pnma*) the Rb sits on a mirror plane, implying that the EFG PAS must have one principal direction perpendicular to this plane.[36] Thus, experimental determination of the absolute orientation of the EFG tensor, usually by single-crystal NMR, can be used to confirm the crystal space group or, if this is unknown, to suggest a possible space group.

16.6.2 Correlation with Local Structure

In addition to symmetry considerations, the determination of quadrupolar parameters can provide a wider insight into local structure. As with the chemical shift, where the correlations are perhaps better known, the quadrupolar parameters C_Q and η_Q display dependences upon local structural features such as coordination number, bond distances, and bond angles.

At a simple level, it might be expected from the point-charge model that the magnitude of the quadrupolar interaction would increase as the deviation from perfect cubic symmetry increases, i.e., that C_Q values associated with coordination environments such as trigonal-bipyramidal or square-pyramidal would be significantly higher than those associated with tetrahedral or octahedral coordination environments.[37] Indeed, there are many examples in the literature where this is found to be the case. For example, the C_Q of a trigonal ^{11}B ($I = \frac{3}{2}$) species is typically found to be between 2.3 and 2.5 MHz while, in contrast, that of a tetrahedral boron is much smaller, between 0 and 0.5 MHz.[32] This distinction (together with an associated change in chemical shift) has been of great use in the study of borosilicate glasses where it has enabled the relative amounts of each species to be easily determined.

Some care must be taken, however, when attempting to infer coordination number solely from quadrupolar parameters, as many different factors can influence the values observed. For example, the ^{27}Al ($I = \frac{5}{2}$) MAS NMR spectrum of andalusite (a polymorph of Al_2SiO_5) shows two second-order broadened lineshapes corresponding to C_Q values of 15.6 and 5.9 MHz.[38] However, the larger of these values has been assigned to the six-, not five-, coordinated Al species in this material, as a result of a significant distortion of the octahedral coordination environment.

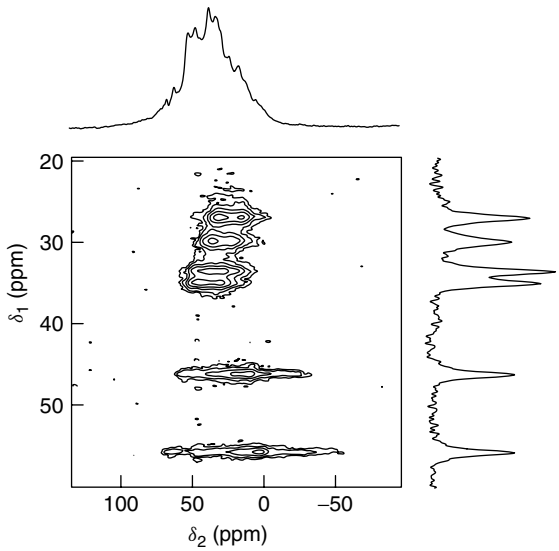


Figure 16.7. Two-dimensional ^{17}O ($I = \frac{5}{2}$) MQMAS NMR spectrum of orthoenstatite, $MgSiO_3$. The ^{17}O MAS spectrum and δ_1 isotropic projection are also shown. Experimental parameters are $\omega_0/2\pi = 54.3$ MHz. Six crystallographically distinct oxygen sites are resolved: four (in the range $\delta_1 = 27–37$ ppm) with smaller second-order broadenings in δ_2 ($C_Q \approx 2–3$ MHz) and two (with $\delta_1 = 47$ ppm and $\delta_1 = 57$ ppm) with larger second-order broadenings in δ_2 ($C_Q \approx 4–5$ MHz). On the basis of these C_Q values, the former are identified as nonbridging oxygens and the latter as Si–O–Si bridging oxygens. (Reproduced from Ref. 43. © American Chemical Society, 2007.)

In this context, it is worth noting that attempts have been made to parameterize the distortion of tetrahedral and octahedral Al sites and correlate these with ^{27}Al C_Q and η_Q values, albeit with limited success.[39]

For a range of nuclides, a great many empirical correlations have been proposed between local structure and quadrupolar parameters, although a majority of these are applicable only to series of similar materials. For example, the ^7Li ($I = \frac{3}{2}$) quadrupolar coupling constant has been found to have a linear dependence upon the C–Li–C bond angle in organolithium compounds.[40] However, there are examples of more generally applicable empirical relationships. One important example is the dependence of the ^{17}O C_Q upon the covalency of the M–O bond, which was discovered during the earliest ^{17}O ($I = \frac{5}{2}$) MAS NMR studies.[41] This dependence has been widely exploited in the study of silicates where "bridging" (Si–O–Si) and "nonbridging" (Si–O–Mg, for example) oxygen species display C_Q values in the ranges 4–6 and 2–3 MHz, respectively.[42] It can be seen in the ^{17}O MQMAS spectrum of orthoenstatite ($MgSiO_3$) in Figure 16.7, for example, that the oxygen species can be grouped into two categories: four with $C_Q \approx 2–3$ MHz (nonbridging oxygens) and two with $C_Q \approx 4–5$ MHz (bridging oxygens).[43] Another example of an apparently general relationship is the strong dependence of the ^2H ($I = 1$) quadrupolar parameters (both C_Q and η_Q) and the length, r_{XY}, of a hydrogen bond X–H···Y.[44]

In recent years, first-principles computation of quadrupolar parameters has been increasingly used to provide support for these correlations with local structure and, indeed, as an aid to discovering new ones (see below).

16.6.3 Comparison with Calculated Parameters

Although very useful, empirical correlations between local structure and quadrupolar parameters have many limitations. These include (i) the additional dependence of C_Q and η_Q upon long-range structure and symmetry, commonly leading to a "fuzziness" or lack of precision in such correlations, (ii) the occurrence of quadrupolar parameters that appear to defy established correlations (e.g., ^{17}O C_Q values of 3.8 and 4.4 MHz in the mineral wadsleyite, β-Mg_2SiO_4,[45] that, based on the well-known correlation discussed above, would indicate that they corresponded to bridging oxygen atoms, whereas, in fact, they arise from nonbridging ones), and (iii) the possible absence of a suitable series of structurally related materials upon which to base the correlation.

These limitations can be overcome by using first-principles computation of quadrupolar parameters, as discussed in the section "Computation of Quadrupolar Parameters". Close agreement between calculated C_Q and η_Q values and experimentally derived ones both confirms the accuracy of the NMR measurements (which is useful if the signal-to-noise ratio is poor or if the lineshapes are distorted, e.g., as occurs with MQMAS and STMAS) and the accuracy of the crystal structure used as the basis for the calculations. This approach has been used, for example, in the ^{17}O MQMAS and STMAS NMR studies of orthoenstatite and wadsleyite referred to above.[43,46] Figure 16.8 shows a comparison of cross

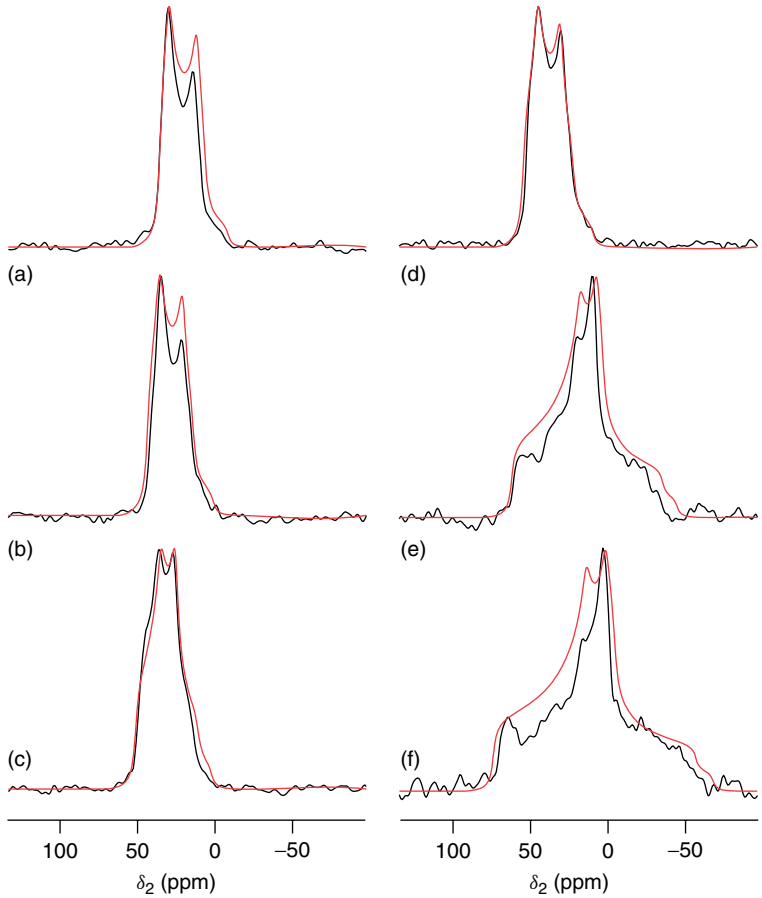


Figure 16.8. Cross sections parallel to δ_2 through the six second-order broadened ridge lineshapes in the ^{17}O MQMAS NMR spectrum of orthoenstatite in Figure 16.7 (black) and lineshapes simulated using quadrupolar and isotropic chemical shift parameters obtained using the first-principles CASTEP code (red). The CASTEP calculated parameters are (a) $C_Q = 3.06$ MHz, $\eta_Q = 0.21$, $\delta_{iso} = 41.0$ ppm; (b) $C_Q = 2.96$ MHz, $\eta_Q = 0.30$, $\delta_{iso} = 47.8$ ppm; (c) $C_Q = 3.03$ MHz, $\eta_Q = 0.61$, $\delta_{iso} = 53.4$ ppm; (d) $C_Q = 3.03$ MHz, $\eta_Q = 0.35$, $\delta_{iso} = 57.4$ ppm; (e) $C_Q = 4.35$ MHz, $\eta_Q = 0.80$, $\delta_{iso} = 62.6$ ppm; and (f) $C_Q = 5.00$ MHz, $\eta_Q = 0.82$, $\delta_{iso} = 74.4$ ppm. (Reproduced from Ref. 43. © American Chemical Society, 2007.)

sections from the ^{17}O MQMAS NMR spectrum of orthoenstatite in Figure 16.7 and lineshapes simulated using quadrupolar and isotropic chemical shift parameters obtained using the first-principles CASTEP code.

More interesting from the perspective of NMR crystallography is the possibility that crystal structures could be refined or optimized by minimizing the differences between the calculated and experimental quadrupolar parameters. Electronic structure calculations often reveal the presence of large forces on the atoms and it is usual to minimize these by optimizing the structure, i.e., displacing the atoms from their positions in the diffraction-based structure, but the status of these purely theoretical structures is controversial. To our knowledge no one has yet successfully optimized structures using the experimental quadrupolar parameters as constraints but evidence is emerging that this will soon be possible. For example, in recent work, it was demonstrated that the agreement between experimental and calculated ^{27}Al quadrupolar parameters for the open-framework aluminophosphate AlPO-14 was extremely poor unless optimization of the structure was undertaken prior to the calculation of the NMR parameters.[47]

This is probably a consequence of the use of an initial structure derived from powder (as opposed to single-crystal) X-ray diffraction.

In addition to the comparative approach described above, first-principles calculations also provide a flexible way to investigate the systematic dependence of NMR parameters on a particular structural feature. This area was pioneered in a study that used a simple cluster model to determine the dependence of the ^{17}O quadrupolar parameters upon the Si–O–Si bond angle,[48] a trend that was later confirmed experimentally in an ^{17}O DAS NMR study.[49] A range of similar work has appeared more recently, with a number of computational studies discussing the dependence of the ^{17}O C_Q upon the Si–O distance and of η_Q upon the Si–O–Si bond angle.[50] The trends predicted by computation can then be utilized to interpret spectra and ultimately determine the structural moieties present in glasses, where the lack of long-range order restricts the ability of diffraction to provide structural models.

16.6.4 Orientation of Quadrupole/EFG Tensors

First-principles calculations provide the absolute orientation of the quadrupole or EFG tensor in the crystal frame. Experimentally, however, this information is only directly available from single-crystal NMR spectroscopy, with NMR of powdered solids usually

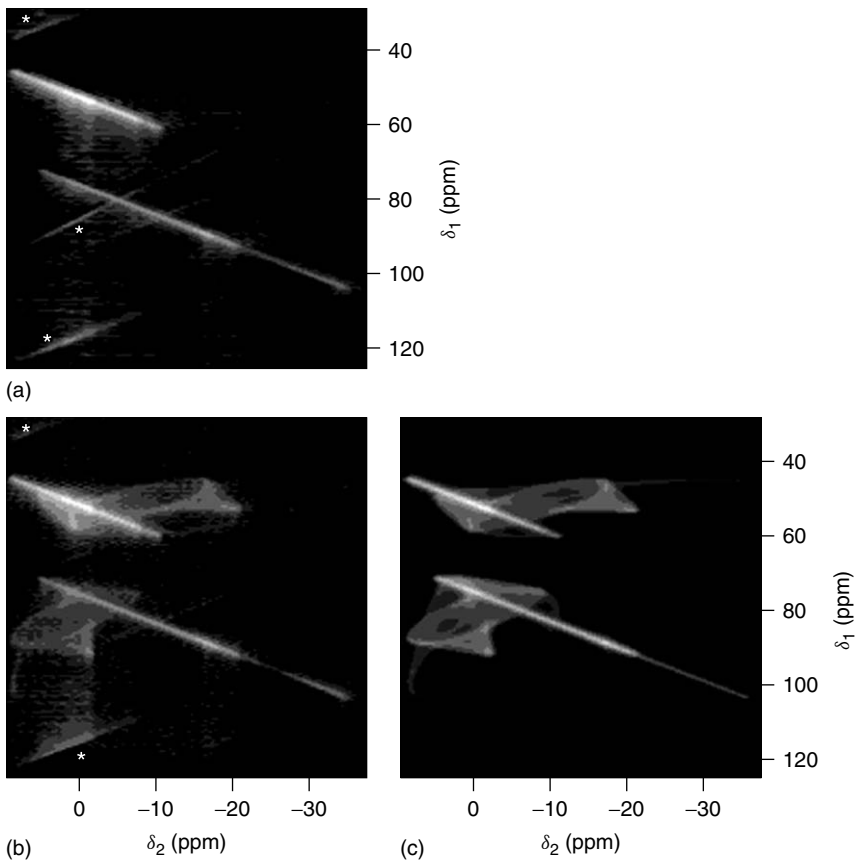


Figure 16.9. (a) Two-dimensional ^{23}Na ($I = \frac{3}{2}$) MQMAS NMR spectrum of sodium metasilicate pentahydrate, $Na_2SiO_3.5H_2O$. (b) As (a), but recorded with a 400 ms mixing time inserted into the pulse sequence. (c) Simulated spectrum with a relative orientation of $\{\alpha, \beta, \gamma\} = \{90^\circ, 35^\circ, 10^\circ\}$ between the two ^{23}Na EFG tensors. Experimental parameters are $\omega_0/2\pi = 105.8$ MHz. (Reproduced from Ref. 54. © American Chemical Society, 2002.)

only providing the magnitudes of V_{XX}, V_{YY}, and V_{ZZ} (through determination of C_Q and η_Q) and not their direction.

In some circumstances, it is possible to obtain information about the orientation of EFG tensors from powder NMR spectra, hence allowing comparison with calculated tensors. This can be achieved using two-dimensional NMR spectroscopy under either static or spinning conditions, correlating the quadrupole tensor with either a dipole–dipole interaction tensor,[51] a shielding tensor,[52] a paramagnetic shift tensor,[53] or another quadrupole tensor.[54] Only the first of these will provide the absolute orientation of the EFG tensor in the crystal frame, but the last two methods can be used to determine the relative orientation of the tensors, allowing comparison with the results of first-principles calculations and, possibly, absolute orientations to be inferred. For example, Figure 16.9 compares (i) a standard ^{23}Na ($I = \frac{3}{2}$) MQMAS NMR spectrum of sodium metasilicate pentahydrate ($Na_2SiO_3.5H_2O$) (Figure 16.9a), (ii) an alternative ^{23}Na MQMAS spectrum of the same material recorded with a 400 ms mixing time inserted into the pulse sequence, allowing spin diffusion between the two inequivalent Na sites to occur (Figure 16.9b), and (iii) a computer-simulated spectrum with a relative orientation of $\{\alpha, \beta, \gamma\} = \{90^\circ, 35^\circ, 10^\circ\}$ between the two ^{23}Na EFG tensors (Figure 16.9c).[54]

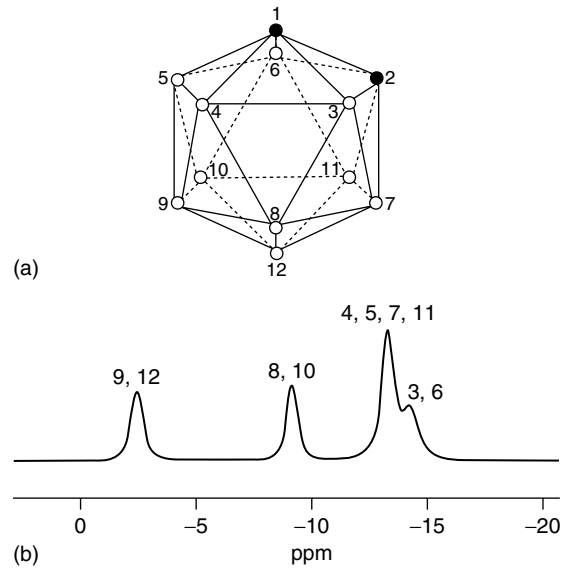


Figure 16.10. (a) Structure of molecule of orthocarborane, $C_2B_{10}H_{12}$, and (b) the ^{11}B ($I = \frac{3}{2}$) MAS NMR spectrum. Experimental parameters are $\omega_0/2\pi = 128.4$ MHz. As a result of fast dynamics in the solid, none of the four ^{11}B peaks shows evidence of second-order quadrupolar broadening, thus indicating that $C_Q = 0$ for all four distinct boron sites.

16.6.5 Effect of Dynamics

Solid-state NMR spectra of quadrupolar nuclei are highly sensitive to the presence of dynamics.[55] Because the quadrupolar interaction is large and usually dominates other interactions such as the chemical shift and dipole–dipole coupling, the effects of dynamics on quadrupolar lineshapes are typically much more evident than in NMR of spin $I = \frac{1}{2}$ nuclei.

The dynamical timescale for which strongly perturbed quadrupolar lineshapes are observed is usually governed by the inverse of the first-order quadrupolar coupling (100 ns–10 μs). For the central-transition lineshapes of half-integer spin quadrupolar nuclei, however, the relevant timescale is the inverse of the second-order quadrupolar interaction (100 μs–1 ms), while under fast MAS conditions (where the MAS rate exceeds the NMR frequency "jump" during the dynamic process), it is the inverse of the MAS rate (10–100 μs). Solid-state dynamics on these "intermediate" timescales typically involve reorientation of complex ions, molecules, or parts of molecules and can be studied both by variable-temperature NMR of static samples (e.g., quadrupolar-echo ^{2}H NMR)[56] or MAS-based techniques (e.g., ^{2}H double-quantum MAS NMR).[57] In favorable cases, the dynamical information obtained can be of a very high order, achieving both elucidation of the mechanism of the motion and measurement of the rate constants involved. As is the case in other areas, it is to be expected that first-principles calculations of NMR parameters will play an increasing role here.

For dynamics on the "fast" timescale, motional effects on the lineshape will not be observed but averaged quadrupolar parameters will be obtained. For example, as shown in Figure 16.10, ^{11}B ($I = \frac{3}{2}$) MAS NMR of solid orthocarborane, $C_2B_{10}H_{12}$, at room temperature reveals four inequivalent boron sites, each with $C_Q = 0$.[58] The obvious crystallographic conclusion from this is that the four borons are located at sites with cubic point symmetry (see the section "Quadrupolar Coupling and Symmetry") but this is clearly incompatible with the known icosahedral cage structure of the $C_2B_{10}H_{12}$

molecule. The answer to this apparent conundrum is that orthocarborane is a "plastic crystal" and the molecules are tumbling rapidly and isotropically in the solid but with their centers of mass remaining fixed in a cubic lattice. Thus, if we focus on the time-averaged structure, then the quadrupolar parameters obtained from lineshape analysis are indicating the true long-range crystal symmetry. From the perspective of an instantaneous "snapshot" of the structure, however, then the C_Q values are misleading us as to the local symmetry of the boron sites (but note that ^{11}B spin-lattice relaxation time measurements or first-principles calculations would reveal the unaveraged quadrupolar parameters).

16.7 CONCLUSIONS

If crystallography is defined as the "experimental science of determining the arrangement of atoms in solids" (Wikipedia) then solid-state NMR measurements of quadrupolar couplings clearly have a role to play. There are strong similarities between the chemical shift and the quadrupolar coupling in this respect as both are single-spin centered tensorial interactions that depend on the electronic environment of the nucleus. The key limitation of the quadrupolar interaction compared with the chemical shift is that it can only be measured for nuclei with $I \geq 1$, whereas chemical shift information is available from nuclei with all spin quantum numbers. However, the following points should also be noted: (i) quadrupolar nuclei are much more common than spin $I = \frac{1}{2}$ nuclei (famously, 75% of all NMR-active nuclides have $I \geq 1$), (ii) as the dominant internal spin interaction, the quadrupolar coupling is usually easier to measure than the chemical shift interaction for spin $I \geq 1$ nuclei, (iii) the quadrupolar coupling, although influenced by local structure to a similar extent to the chemical shift, appears to be a more sensitive reporter of long-range symmetry and order within a crystal, and (iv) as noted in the section "Computation of Quadrupolar Parameters", first-principles calculations of EFG tensors are generally more efficient and (probably) more accurate than those of chemical shift tensors.

Arguably, studies of dynamics represent the most important application of solid-state NMR and, as discussed in the section "Effect of Dynamics", the quadrupolar coupling is a uniquely sensitive probe here. The status of dynamic NMR studies in crystallography is harder to define; however, as diffraction-based crystallography can rarely match the rich detail of dynamic information provided by solid-state NMR and the information that it does provide is on a very different timescale. Perhaps, in the future, as NMR crystallography becomes better established, the definition of crystallography may be widened to "experimental science of determining the arrangement and dynamic behavior of atoms in solids".

REFERENCES

1. P. P. Man, Quadrupolar interactions, in *Encyclopedia of Nuclear Magnetic Resonance*, eds R. K. Harris and David M. Grant, John Wiley & Sons: Chichester, 1996, Vol. **6**, p. 3838.
2. A. J. Vega, Quadrupolar nuclei in solids, in *Encyclopedia of Nuclear Magnetic Resonance*, eds R. K. Harris and David M. Grant, John Wiley & Sons: Chichester, 1996, Vol. **6**, p. 3869.
3. Y. Wu, Double rotation, in *Encyclopedia of Nuclear Magnetic Resonance*, eds R. K. Harris and David M. Grant, John Wiley & Sons: Chichester, 1996, Vol. **3**, p. 1749.
4. P. J. Grandinetti, Dynamic angle spinning, in *Encyclopedia of Nuclear Magnetic Resonance*, eds R. K. Harris and David M. Grant, John Wiley & Sons: Chichester, 1996, Vol. **3**, p. 1768.
5. L. Frydman, Multiple-quantum magic-angle spinning experiments on half-integer quadrupolar nuclei: fundamentals, in *Encyclopedia of Nuclear Magnetic Resonance*, eds R. K. Harris and R. Wasylishen, John Wiley & Sons: Chichester, 2000, Vol. **9**, p. 262.
6. J. P. Amoureux and M. Pruski, MQMAS NMR: Experimental Strategies and Applications, in *Encyclopedia of Nuclear Magnetic Resonance*, eds-in-chief R. K. Harris and R. E. Wasylishen, John Wiley & Sons: Chichester, 2008. DOI: 10.1002/9780470034590.emrstm0319.pub2.
7. Z. Gan, Satellite transition NMR spectroscopy of half-integer quadrupolar nuclei under magic angle spinning, in *Encyclopedia of Nuclear Magnetic Resonance*, eds R. K. Harris and R. Wasylishen, John Wiley & Sons: Chichester, 2000.
8. S. E. Ashbrook and S. Wimperis, Advances in STMAS, in *Encyclopedia of Magnetic Resonance*, eds-in-chief R. K. Harris and R. E. Wasylishen, John Wiley & Sons: Chichester, 2008. DOI: 10.1002/9780470034590.emrstm1032.

9. A. Abragam, *Principles of Nuclear Magnetism*, Clarendon Press: Oxford, 1961, Chapter 6.
10. C. P. Slichter, *Principles of Magnetic Resonance*, 3rd edn., Springer-Verlag: Berlin, 1990, Chapter 10.
11. M. J. Frisch, *et al*. *Gaussian 03*, Gaussian Inc., Wallingford, 2004.
12. J. R. Yates and C. J. Pickard, Computation of magnetic resonance parameters for crystalline systems: principles, in *Encyclopedia of Magnetic Resonance*, eds R. K. Harris and R. Wasylishen, John Wiley & Sons: Chichester, 2008. DOI: 10.1002/9780470034590.emrstm1009.
13. P. Blaha, K. Schwarz, G. K. H. Madsen, D. Kvasnicka, and J. Luitz, *Computer code WIEN2k*, Vienna University of Technology, 2001.
14. M. D. Segall, P. J. D. Lindan, M. J. Probert, C. J. Pickard, P. J. Hasnip, S. J. Clark, and M. C. Payne, *J. Phys. Cond. Matt.*, 2002, **14**, 2717.
15. S. Dahaoui, N. E. Ghermani, S. Ghose, and J. A. K. Howard, *Am. Mineral.*, 2001, **86**, 159.
16. R. N. Zare, *Angular Momentum*, Wiley: Chichester, 1996.
17. P. W. Atkins, *Molecular Quantum Mechanics*, Oxford University Press: Oxford, 1983, Chapter 8.
18. R. R. Ernst, G. Bodenhausen, and A. Wokaun, *Principles of Nuclear Magnetic Resonance in One and Two Dimensions*, Clarendon Press: Oxford, 1987.
19. R. V. Pound, *Phys. Rev.*, 1950, **79**, 685.
20. L. S. Batchelder, Deuterium NMR in solids, in *Encyclopedia of Nuclear Magnetic Resonance*, eds R. K. Harris and David M. Grant, John Wiley & Sons: Chichester, 1996, Vol. **3**, p. 1574.
21. J. A. Tang, J. D. Masuda, T. J. Boyle, and R. W. Schurko, *Chem. Phys. Chem.*, 2006, **7**, 117.
22. A. P. M. Kentgens, *Prog. Nucl. Magn. Reson. Spectrosc.*, 1998, **32**, 141.
23. C. Jäger, W. Muller-Warmuth, C. Mundus, and L. van Wullen, *J. Non-Cryst. Solids*, 1992, **149**, 209.
24. R. K. Harris, Magic angle spinning: effects of quadrupolar nuclei on spin-1/2 spectra, in *Encyclopedia of Nuclear Magnetic Resonance*, eds R. K. Harris and David M. Grant, John Wiley & Sons: Chichester, 1996, Vol. **5**, p. 2909.
25. A. Samoson, E. Lippmaa, and A. Pines, *Mol. Phys.*, 1988, **65**, 1013.
26. A. Llor and J. Virlet, *Chem. Phys. Lett.*, 1988, **152**, 248.
27. L. Frydman and J. S. Harwood, *J. Am. Chem. Soc.*, 1995, **117**, 5367.
28. Z. Gan, *J. Am. Chem. Soc.*, 2000, **122**, 3242.
29. S. E. Ashbrook and S. Wimperis, *Prog. NMR. Spectrosc*, 2004, **45**, 53.
30. M. J. Thrippleton, T. J. Ball, and S. Wimperis, *J. Chem. Phys.*, 2008, **128**, 034507.
31. J. W. Akitt and W. S. McDonald, *J. Magn. Reson.*, 1984, **58**, 401.
32. K. J. D. Mackenzie and M. E. Smith, *Multinuclear Solid-state NMR of Inorganic Materials*, Pergamon: Oxford, 2002.
33. G. Wu, *Chem. Phys. Lett.*, 1998, **298**, 375.
34. T. J. Bastow, M. A. Gibson, and C. T. Forwood, *Solid State Nucl. Magn. Reson.*, 1998, **12**, 201.
35. P. Pulay, E. M. Scherer, P. C. A. van der Wel, and R. E. Koeppe, *J. Am. Chem. Soc.*, 2005, **127**, 17488.
36. T. Vosegaard, J. Skibsted, H. Bildsøe, and H. J. Jakobsen, *J. Magn. Reson.*, 1996, **122**, 111.
37. H. Koller, G. Engelhardt, A. P. M. Kentgens, and J. Sauer, *J. Phys. Chem.*, 1994, **98**, 1544.
38. S. F. Dec, J. J. Fitzgerald, J. S. Frye, M. P. Shatlock, and G. E. Maciel, *J. Magn. Reson.*, 1991, **93**, 403.
39. S. Ghose and T. Tsang, *Am. Mineral.*, 1973, **58**, 748.
40. A. Pepels, H. Günther, J. P. Amoureux, and C. Fernandez, *J. Am. Chem. Soc.*, 2000, **122**, 9858.
41. S. Schramm and E. Oldfield, *J. Am. Chem. Soc.*, 1984, **106**, 2502.
42. S. E. Ashbrook and M. E. Smith, *Chem. Soc. Rev.*, 2006, **35**, 718.
43. S. E. Ashbrook, A. J. Berry, D. J. Frost, A. Gregorovic, C. J. Pickard, J. E. Readman, and S. Wimperis, *J. Am. Chem. Soc.*, 2007, **129**, 13213.
44. L. G. Butler and T. L. Brown, *J. Am. Chem. Soc.*, 1981, **103**, 6541.
45. S. E. Ashbrook, A. J. Berry, W. O. Hibberson, S. Steuernagel, and S. Wimperis, *J. Am. Chem. Soc.*, 2003, **125**, 11824.
46. S. E. Ashbrook, L. Pollès, C. J. Pickard, A. J. Berry, S. Wimperis, and I. Farnan, *Phys. Chem. Chem. Phys.*, 2007, **9**, 1587.
47. S. E. Ashbrook, M. Cutajar, C. J. Pickard, R. I. Walton, and S. Wimperis, *Phys. Chem. Chem. Phys.*, 2008, **10**, 5754.
48. J. A. Tossell and P. Lazzeretti, *Chem. Phys. Lett.*, 1987, **112**, 205.

49. P. J. Grandinetti, J. H. Baltisberger, I. Farnan, J. F. Stebbins, U. Werner, and A. Pines, *J. Phys. Chem.*, 1995, **99**, 12341.
50. T. M. Clark and P. J. Grandinetti, *J. Phys. Cond. Matter*, 2003, **15**, S2387.
51. J. D. van Beek, R. Dupree, and M. H. Levitt, *J. Magn. Reson.*, 2006, **179**, 38.
52. J. S. Shore, S. H. Wang, R. E. Taylor, A. T. Bell, and A. Pines, *J. Chem. Phys.*, 1996, **105**, 9412.
53. S. Antonijevic and S. Wimperis, *J. Chem. Phys.*, 2005, **122**, 044312.
54. N. G. Dowell, S. E. Ashbrook, and S. Wimperis, *J. Phys. Chem. A*, 2002, **106**, 9470.
55. M. J. Duer, *Introduction to Solid-State NMR Spectroscopy*, Blackwell Science: Oxford, 2004, Chapter 6.
56. J. H. Davis, K. R. Jeffrey, M. Bloom, M. I. Valic, and T. P. Higgs, *Chem. Phys. Lett.*, **42**, 390.
57. M. Cutajar, S. E. Ashbrook, and S. Wimperis, *Chem. Phys. Lett.*, 2006, **423**, 276.
58. R. K. Harris, J. Bowles, I. R. Stephenson, and E. H. Wong, *Spectrochimica Acta A*, 1988, **44**, 273.

PART D
Crystal Structure Determination using NMR

Chapter 17

Fundamental Principles of NMR Crystallography

Francis Taulelle

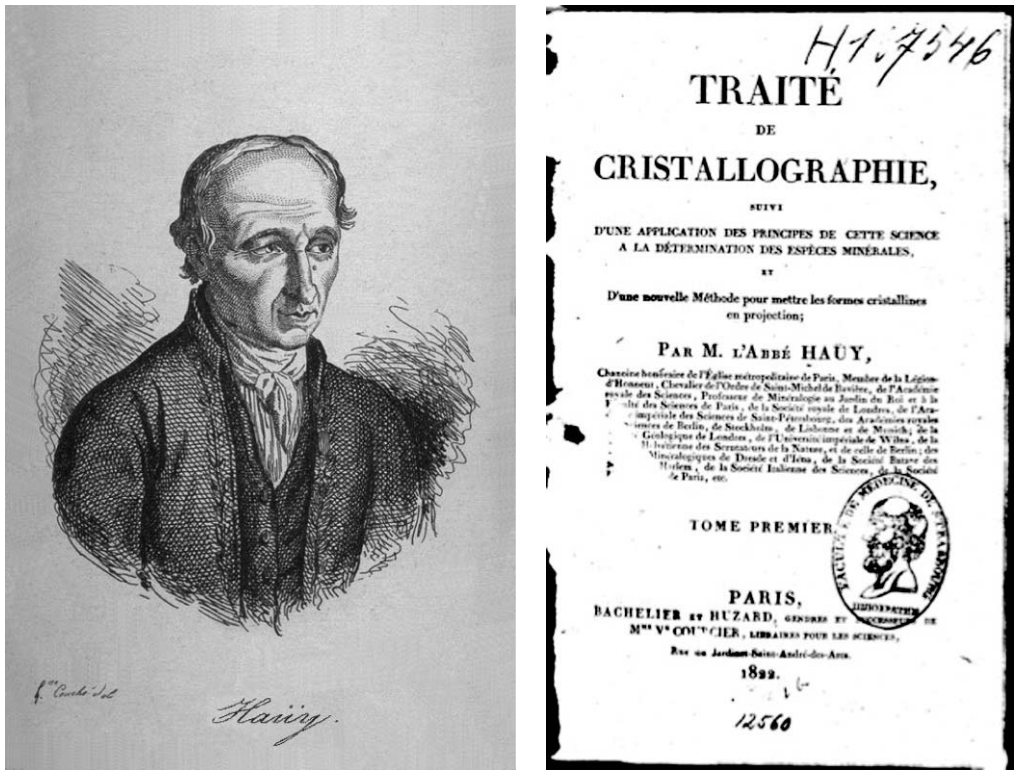
Lavoisier Institute, University of Versailles-Saint-Quentin-en-Yvelines, 78035 Versailles, France

17.1	Introduction	245
17.2	NMR Physical Measurements	248
17.3	Resolving Structures by NMR	257
17.4	NMR Crystallography and Beyond Periodic Structures	261
	References	261

17.1 INTRODUCTION

René Just Haüy (Figure 17.1) edited in 1822 the first "Treatise of Crystallography".[1] In a crucial experiment of cutting crystals into smaller pieces, Haüy inferred that at a certain degree of size the ultimate shape of the smaller cut does not change. Therefore crystals can be composed of elementary units, and the relation between the elementary shapes and their packing leads to an understanding of the morphology. Haüy, a contemporary of Lavoisier, deduced from these experiments the discrete nature of substances. About the same period, three mainstreams in science were converging to describe substances not like continuous matter with properties, but as constituted of "atoms", unbreakable units. The gases, with the emerging thermodynamic description (the theory of perfect gases) were assumed to be composed of spherical objects. On the other hand, Haüy was assuming that the form of crystals could be deduced from the actual shape of an elementary brick, a "molecule intégrante", the integer part of a structure. The third stream in Lavoisier's time comes from the identification that substances are combinations of simpler elements that can be isolated and transformed into other combinations. Spheres in gases, elementary units in crystals, substances as combination of simple ones (elements), those three lines of thoughts, led to the modern notions of atoms and molecules. After Dalton, the "atomic theory" associated "elements" with "atoms", and the conclusion was reached that the elementary unit was the "atom". Mendeleiev, by ranking "elements" in order of mass, was led to the now universally admitted conclusions that substances are composed of atoms, they can combine in discrete units like molecules, or in infinite combinations like crystals. Yet the physical concepts of atoms, molecules, and unit cells were not completely clarified. With Kekulé (who found the geometrical formula of benzene) the arrangement of atoms as a molecule was accepted after over 80 years. On the crystal side, it is only with Bravais, when he replaced the "molecule intégrante" of Haüy by "points", that geometrical crystallography started as a mathematical discipline. Geometrical crystallography considers symmetrical arrangements of "points" in space (the nature of those points being not necessarily fully

NMR Crystallography Edited by Robin K. Harris, Roderick E. Wasylishen and Melinda J. Duer © 2009 John Wiley & Sons, Ltd. ISBN: 978-0-470-69961-4



(a) (b)

Figure 17.1. (a) René Just Haüy, the author of the "Traité de Cristallographie in 1822". (Reproduced from Ecoles des Mines de Paris.) (b) The first page of the "Traité".

defined), a "unit cell", a "molecule", or an "atom". Geometrical crystallography, after Bravais' contributions, resulted in the discovery of the seven crystal systems (triclinic, monoclinic, orthorhombic, tetragonal, rhombohedral, hexagonal, and cubic) and the 14 Bravais lattices. It was not before the last decade of the nineteenth century that, by combining translations, rotations, mirrors planes, and centers of symmetry, Schönflies and Fedorov showed that one could find 230 "space groups". Later, in 1922, Ralph Wyckoff showed that in each space group, some special space regions are left invariant under the application of certain symmetries,[2] defining the concept of special positions (Figure 17.2). During about the same period, the discrete nature of atoms was revealed by J.J. Thompson, by first discovering electron beams, then, with alpha particles, showing the existence of a smaller core, which became the atomic nucleus concept. This model for atoms would be refined by Rutherford, Sommerfeld, Bohr, and Dirac. Meanwhile, Röntgen discovered X rays and their effect on matter. Von Laue explained that patterns observed when irradiating crystals were not projections of objects lighted by the X-ray beam but were caused by the interference phenomenon of electromagnetic radiation with regularly spaced objects, acting as a grating to produce diffraction. A few years later, the Braggs, father and son, determined the first crystal structure (NaCl) by defining the relative arrangement of atoms in a solid. If diffraction is such a powerful tool, it is because it relies on electron density, a common feature found in any atom. As the price to pay for being such a general method for determining positions of atoms in a crystal, two aspects of diffraction make the measurement incomplete. The first aspect is that a strict translational symmetry, the periodicity, is required to produce the diffraction phenomenon. The second aspect is related to the very nature of

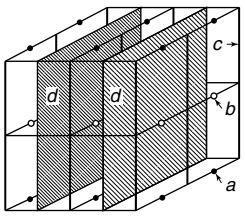


Fig. 66. Space group V_h^{11}
(a) – (b) C_i; (c) C_2; (d) C_s

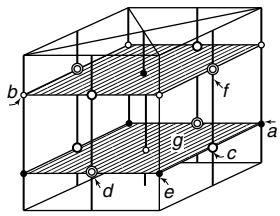


Fig. 67. Space group V_h^{12}
(a) – (d) C_2^h; (e) – (f) C_2; (g) C_s

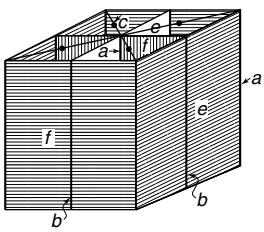


Fig. 68. Space group V_h^{13}
(a) – (b) C_2^v; (c) – (d) C_i;
(e) – (f) C_s

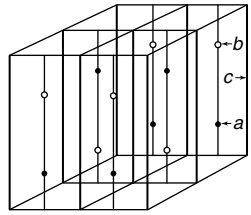


Fig. 69. Space group V_h^{14}
(a) – (b) C_i; (c) C_2

Figure 17.2. An example of special positions in a 3-D space group. The gray locations are left invariant by the operation of an element of symmetry. (Reproduced from R.W.G. Wyckoff, *The Analytical Expression of the Results of the Theory of Space Groups*, Carnegie Institution of Washington, Washington, 1922.)

the diffraction phenomenon. Only the intensity of the electromagnetic wave is measured, not its amplitude and phase. Because of these two limitations of diffraction, the class of materials that can be studied is restricted and the determination of atomic positions requires the use of additional information. Despite these limitations, structure determination by diffraction has unveiled an immense number of crystalline structures, and diffraction will remain an extraordinarily powerful method.

NMR happened to appear when the development of synthetic organic chemistry underwent, after the Second World War, a considerable extension. NMR was very successful at using chemical shifts and J-coupling to determine the structures of molecules. The information content of these two interactions is relatively limited, though the chemical shift is exquisitely sensitive to electronic density changes of the chemical environment and the J-couplings provide information about shared pairs of electrons between atoms (chemical bonds) with a range of two to three bonds usually. With only this information, the topologies of the molecules were achievable with a limited effort of trials. This is the essence of a molecular structural determination.

Experiments using the dipolar interactions, particularly NOE experiments, were developed (particularly by the Wüthrich group) to determine hydrogen–hydrogen distances. By adding the hydrogen–hydrogen distance matrix to an already determined sequence of amino acids, peptide and protein structures can be determined successfully. This is a considerable extension of molecular structure determination but it is still almost limited to a "one molecule" structure determination.

What matters ultimately in crystallography is to be able to collect as many as possible pieces of information available for the crystal considered and to compare them with the $4N$ parameters needed to describe N atoms (one for the nature of each atom and three for its position).

This is the case for a "perfect" crystal, fulfilling a complete periodicity for all atom sublattices.

However, there is much more to measure than this. Atoms or groups of atoms may undergo motion, they may not be periodic, and they may have local symmetry that is not crystal symmetry (such as a fivefold rotation axis or icosahedral symmetry) but they may, nonetheless, constitute "regular" structures. Usually all these additional features are termed "disorder" in diffraction crystallography. However, there is a general need for such structure determination. If the information content is of the order of the Avogadro number (i.e., of the actual number of atoms in the crystal), there is probably no use in trying to determine the structure. If a reduction of the information content is possible, then the structure determination has some sense. The reduction of information provided by the unit cell of a fully periodic crystal is probably a very stringent one: the amount of information needed is restricted at most to the unit cell, but it can be further reduced to the "asymmetric unit". The asymmetric unit, or the fundamental volume for mathematicians, is the subpart of the unit cell that can be used to generate the unit cell by application to it of all the symmetry operations of the space group of the crystal. Now, if for any reason, the crystal is not fully periodic (as zeolites are very often, when the templating agents or the extra-framework cations are considered), or if there are isoelectronic atoms in the same lattice, the additional information about location or motion or nature of the framework or extra-framework moieties should be provided by different means of localization.

Actually, NMR is generally able to collect much more than the $4N$ parameters necessary to establish a crystallographic structure, and is also able to probe pertinently motions or distributions like those in amorphous materials. Owing to its extreme flexibility in accessing crystalline atomic parameters, NMR can definitely address crystal-structure determination. However, the main difference from diffraction is that it involves measuring many different interactions, which is its strength and its weakness – strength because of the multiple ways to access the same set of parameters, weakness because of the multiple experiments that may be needed, with their specific demands on the spectrometer or probes or pulse sequence.

Three aspects of structure determination will be explored here: first, what is the information related to crystal structure available by NMR? Second, what are the relations between the NMR parameters set and the crystal geometry? Third, how can strategies to determine a crystal structure using NMR information be established?

17.2 NMR PHYSICAL MEASUREMENTS

17.2.1 The NMR Phenomenon

By submitting a sample to a constant magnetic field, the nuclear magnetic moments become polarized by this field, and subsequent application of a radio-frequency magnetic field induces transitions between the magnetic states of the nuclei. In addition to the splitting of energy levels that the constant magnetic field induces, all the internal interactions acting on the nuclear magnetic moments add to determination of the energy levels. As these interactions are anisotropic, they depend on their orientation relative to the main magnetic field (the "space part" of the interaction) and they all depend on the magnetic state of the nuclei, and on the orientation of the nuclear magnetic moment relative to the main magnetic field (the "spin part" part of the interaction). The anisotropic character of the interactions leads to a general decomposition as irreducible spherical tensors to systematize their study (see Tables 17.1 and 17.2). Observation of the transitions of the nuclear magnetic states provides all the available information about the internal interactions, and therefore about the structure.

17.2.2 NMR Interactions

The energy levels are defined by application of a constant magnetic field and by the internal interactions of the sample. However, an additional handle on the internal interactions is provided by the manipulation of the orientation of the sample. As the interactions are anisotropic, their effect is dependent on their spatial orientation relative to the external magnetic field and on the orientation of magnetic moments relative to each other. Both can be changed with time by appropriate change of orientation of the sample in space or by application of suitable radio-frequency pulses acting on the orientation of the targeted nuclear magnetic moment.

17.2.3 High-Resolution Solid-State NMR

A general technology of energy-level manipulation arises. As the radio-frequency impulsions applied to the sample generate rotations of the magnetic moments of the nuclei (i.e., of their "spin"), and the mechanical movement of the orientation of the sample generates a rotation of the space part of the interaction, the energy levels can be manipulated by combining orientation manipulation and spin-state manipulation. This leads to a completely new world of exploring the internal interactions. The pulse sequences can produce an average, time-independent, Hamiltonian that contains only a limited part of the information available, not only filtering a limited set of interactions but also a limited fraction of a given interaction. One can, for example, generate experiments in which the isotropic part of the chemical shift is correlated to its anisotropic part, or a heteronuclear correlation is established between the isotropic part of the chemical shift for each nucleus. Even the most popular solid-state NMR experiment, i.e., cross polarization with magic angle spinning (CPMAS), introduces in its pulse sequence three periods that manipulate in different ways the two ensembles of nuclei to generate the desired observation, i.e., the isotropic chemical shift of the low-abundant nucleus. The first period involves polarization of the high-abundance spin, usually the protons. The second period manipulates simultaneously the high- and low-abundance spins, coherently fulfilling the Hartmann–Hahn condition between the two radio-frequency fields, producing a nonvanishing average heteronuclear dipolar interaction between the two types of nuclei. This second

Table 17.1. Construction of spin hamiltonians from spatial and spin components of Various Interactions

Interaction	C^{Λ}	A^{Λ}_{00}	$\hat{T}^{\Lambda}_{00}$	$\hat{H}^{\mathrm{iso}}_{\Lambda}$	$\left[A^{\Lambda}_{20}\right]^{\mathrm{L}}$	$\left[\hat{T}^{\Lambda}_{20}\right]^{\mathrm{L}}$	$\hat{H}^{\mathrm{aniso}}_{\Lambda}$
Chemical shift (CS)	$-\gamma_I$	$-\sqrt{3}\delta^j_{\mathrm{iso}}$	$-\frac{1}{\sqrt{3}}B_0\hat{I}_{jz}$	$\delta^j_{\mathrm{iso}}\omega_0\hat{I}_{jz}$	δ^j_{CSA}	$\sqrt{\frac{2}{3}}B_0\hat{I}_{jz}$	$\omega^j_{\mathrm{CSA}}\sqrt{\frac{2}{3}}\ \hat{I}_{jz}$
Homonuclear dipolar (D)	1	—	—	—	ω^{jk}_{D}	$\frac{1}{\sqrt{6}}\left(3\hat{I}_{jz}\hat{I}_{kz}-\hat{I}_j\cdot\hat{I}_k\right)$	$\omega^{jk}_{\mathrm{D}}\frac{1}{\sqrt{6}}\left(3\hat{I}_{jz}\hat{I}_{kz}-\hat{I}_j\cdot\hat{I}_k\right)$
Heteronuclear dipolar (D)	1	—	—	—	ω^{IS}_{D}	$\sqrt{\frac{2}{3}}\hat{I}_z\hat{\mathrm{S}}_z$	$\omega^{IS}_{\mathrm{D}}\sqrt{\frac{2}{3}}\hat{I}_z\hat{\mathrm{S}}_z$
Homonuclear (J)	1	$-2\pi\sqrt{3}J^{jk}_{\mathrm{iso}}$	$-\frac{1}{\sqrt{3}}\hat{I}_j\cdot\hat{I}_k$	$2\pi J^{jk}_{\mathrm{iso}}\hat{I}_j\cdot\hat{I}_k$	$\omega^{jk}_{\mathrm{J,\,aniso}}$	$\frac{1}{\sqrt{6}}\left(3\hat{I}_{jz}\hat{I}_{kz}-\hat{I}_j\cdot\hat{I}_k\right)$	$\omega^{jk}_{\mathrm{J,\,aniso}}\frac{1}{\sqrt{6}}\left(3\hat{I}_{jz}\hat{I}_{kz}-\hat{I}_j\cdot\hat{I}_k\right)$
Heteronuclear (J)	1	$-2\pi\sqrt{3}J^{IS}_{\mathrm{iso}}$	$-\frac{1}{\sqrt{3}}\hat{I}_z\hat{\mathrm{S}}_z$	$2\pi J^{IS}_{\mathrm{iso}}\hat{I}_z\hat{\mathrm{S}}_z$	$\omega^{IS}_{\mathrm{J,\,aniso}}$	$\sqrt{\frac{2}{3}}\hat{I}_z\hat{\mathrm{S}}_z$	$\omega^{IS}_{\mathrm{J,\,aniso}}\sqrt{\frac{2}{3}}\ \hat{I}_z\hat{\mathrm{S}}_z$
First-order quadrupolar (Q)	$\frac{1}{2I(2I-1)}$	—	—	—	$\left[\mathrm{Q}^j_{20}\right]^{\mathrm{L}}$	$\frac{1}{\sqrt{6}}\left(3\hat{I}^2_{jz}-I(I+1)\right)$	$\omega^j_{\mathrm{Q}}\frac{1}{\sqrt{6}}\left(3\hat{I}^2_{jz}-I(I+1)\right)$

The spin interaction Hamiltonians may be constructed as the product of a constant C^{Λ}, the spatial part in the laboratory frame $\left[A^{\Lambda}_{10}\right]^{\mathrm{L}}$, and the spin part $\left[\hat{T}^{\Lambda}_{10}\right]^{\mathrm{L}}$. (See the discussion in the text regarding the chemical shift Hamiltonian.) The contribution from the $l = 0$ part of interaction Λ is obtained by multiplying columns 2, 3, and 4 of the given row. The result is given in column 5 $\left(\hat{H}^{\mathrm{iso}}_{\Lambda}\right)$. The contribution from the $l = 2$ part is obtained by multiplication of columns 2, 6, and 7, resulting in the expression given in column 8 $\left(\hat{H}^{\mathrm{aniso}}_{\Lambda}\right)$. The tensor components $\left[A^{\Lambda}_{2m}\right]^{\mathrm{P}}$ necessary for obtaining $\left[A^{\Lambda}_{20}\right]^{\mathrm{L}}$ are listed in Table 17.2. The various parameters and constants have the following meaning: for spin species I, γ_I denotes the gyromagnetic ratio and I is the spin number (i.e., total spin angular momentum). The isotropic components A_{iso} (e.g., δ^j_{iso} and J^{IS}_{iso}) are defined as the mean value of the principal values of the spatial tensor:

$$A_{\mathrm{iso}} = \frac{1}{3}\left([A_{xx}]^{\mathrm{P}} + [A_{yy}]^{\mathrm{P}} + [A_{zz}]^{\mathrm{P}}\right)$$

For the first-order quadrupolar interaction, the quadrupolar frequency is defined as

$$\omega^j_{\mathrm{Q}} = \frac{\left[Q^j_{20}\right]^{\mathrm{L}}}{2I(2I-1)}$$

step allows transferring magnetization from the high- and low-abundant spins. The third step is observation of the low-abundant spin, with a decoupling scheme that suppresses the heteronuclear dipolar interaction. The heteronuclear interaction has been used in this sequence in two ways: during "contact" the dipolar interaction is reintroduced, while during decoupling it is suppressed.

This technology has been developed into hundreds of experiments to address the infinite variety of interaction landscapes present in solid materials.

It is not the purpose of the article to indicate the principles and the extension of this technology. The application of these methods of manipulating energy levels (and hence frequencies of transitions) are generically termed as "high-resolution solid-state NMR".

17.2.4 The Structural Parameters

The geometry of a crystal (the relative positions of atoms) is extracted from interactions, which define energy levels. Each interaction involves an energy, i.e., a Hamiltonian operator, when the quantum description of energy is considered. Each interaction contains a space and a spin part. Generally speaking, these energy levels can be written as follows:

$$\hat{H}_{\Lambda} = C^{\Lambda}\left\{A^{\Lambda}_{00}\hat{T}^{\Lambda}_{00} + [A^{\Lambda}_{20}]^{\mathrm{L}}[\hat{T}^{\Lambda}_{20}]^{\mathrm{L}}\right\} \qquad (17.1)$$

Table 17.2. Components A_{2m}, $2 < m < 2$, of second-rank spatial tensors in their principal axis system

Interaction (Λ)	$\left[A_{20}^{\Lambda}\right]^{\mathrm{P}}$	$\left[A_{2\pm1}^{\Lambda}\right]^{\mathrm{P}}$	$\left[A_{2\pm2}^{\Lambda}\right]^{\mathrm{P}}$
Chemical shift (CS)	$\sqrt{\frac{3}{2}}\zeta_{\mathrm{aniso}}^{j}$	0	$-\frac{1}{2}\eta\zeta_{\mathrm{aniso}}^{j}$
Homonuclear dipolar (D)	$\sqrt{6}b^{jk}$	0	0
Heteronuclear dipolar (D)	$\sqrt{6}b^{IS}$	0	0
Homonuclear J	$2\pi\sqrt{\frac{3}{2}}J_{\mathrm{aniso}}^{jk}$	0	$-\frac{1}{2}\eta J_{\mathrm{aniso}}^{jk}$
Heteronuclear J	$2\pi\sqrt{\frac{3}{2}}J_{\mathrm{aniso}}^{IS}$	0	$-\frac{1}{2}\eta J_{\mathrm{aniso}}^{IS}$
First-order quadrupolar (Q)	$\sqrt{\frac{3}{2}}\chi_{\mathrm{Q}}$	0	$-\frac{1}{2}\eta\chi_{\mathrm{Q}}$

The anisotropies A_{aniso} of the spatial tensors (e.g., ζ_{aniso} and J_{aniso}^{jk}) are defined as

$$A_{\mathrm{aniso}} = [A_{zz}]^{\mathrm{P}} - A_{\mathrm{iso}}$$

with A_{iso} given by

$$A_{\mathrm{iso}} = \frac{1}{3}\left([A_{xx}]^{\mathrm{P}} + [A_{yy}]^{\mathrm{P}} + [A_{zz}]^{\mathrm{P}}\right)$$

The asymmetry parameter for each interaction is defined as

$$\eta = [A_{yy}]^{\mathrm{P}} - [A_{xx}]^{\mathrm{P}} \Big/ \left([A_{zz}]^{\mathrm{P}} - A_{\mathrm{iso}}\right)$$

The dipolar coupling constants b^{jk} and b^{IS} are defined by

$$b^{jk} = \mu_0\gamma_I^2\hbar/(4\pi r_{jk}^3) \quad \text{and} \quad b^{IS} = \mu_0\gamma_I\gamma_S\hbar/(4\pi r_{jk}^3)$$

with r^{jk} and r_{IS} being the distances between the two spins in the homonuclear and heteronuclear spin pair, respectively; $\mu_0 = 4\pi \cdot 10^7$ N C^{-2} s^2 is the permeability of vacuum and $\hbar$ is Planck's constant (h = 6.62608·10^{-34} J s) divided by 2π. The quadrupolar tensor $\left(\boldsymbol{Q}^{(2)}\right)$ is defined as the product of the electric field gradient tensor and the quadrupolar moment of the nucleus (eQ). With this definition, the magnitude of the anisotropy of the quadrupolar interaction is given by the quadrupolar coupling constant $\chi_{\mathrm{Q}} = e^2qQ/\hbar$. The following units are employed for the anisotropies: χ_{Q} and b (rad s^{-1}), ζ_{aniso} (ppm), and J_{aniso} (Hz).

with the now classical notation that C^{Λ} is a number defining the relation between the dimensionless A (space part) and T (spin part) terms and the effective energy. Usually, these terms contain the geometrical information, i.e. distances, angles, or connectivity neighbors. The $A_{00}T_{00}$ term defines the isotropic part of an interaction (when it exists) and the $A_{20}T_{20}$ term defines the anisotropic part. The latter can be modulated by space or spin manipulation.

As many interactions (labeled by the exponent "Λ" above) act on a given nucleus, the detailed theoretical description of all the internal interactions is a never-ending story. It all depends on the degree of accuracy of the description relative to the possibility of calculating it. To overcome this intrinsically unlimited level of description, all these interactions (written as irreducible spherical tensors) produce a systematically engineered way of dealing with both the physical measurements of interactions and their relation to the geometry.

As the different interactions may form an extremely complex set of energy levels, their progressive edition is the rational way to unravel their complexity. Actually, the adapted choice of the sequence allows, ideally, the suppression (by proper choice of the sequence) of every interaction but the one of interest. The strategy is therefore unique in comparison to diffraction, for which every diffracting fraction of the sample acting on the radiation beam and all diffraction phenomena take place at the same time. In an NMR investigation, each piece of information carrying structural parameters may be a separate one. Diffraction provides directly higher

statistics on the set of distances, and the separation of the different diffracting lines is best achieved with a single crystal by separating each orientation one by one (i.e., by rotating the crystal). In NMR, the statistics is done in a sense afterwards, because many interactions have the same irreducible spherical tensor for the space part. Thus the geometrical information appears redundantly in the different NMR observables. However, as a counterpart, for NMR, each experiment is different and has its own constraints.

Herein, a fraction of the structural information that is generally available by NMR, is enumerated.

17.2.4.1 Inequivalent Chemical Sites, Inequivalent Crystallographic Sites

When considering an NMR spectrum, the different lines correspond to different atomic sites. The crystallographic multiplicity of the sites (equal to their NMR site area ratio) is information that is readily available in an NMR spectrum. Actually, the chemical shift tensor is sensitive, mainly, to the nature of the chemical environment, and at a secondary level to the crystallographic inequivalence for sites of identical chemical nature. When the resolution in the spectrum is high enough (i.e., using all the possibilities for obtaining the highest resolution – MAS in the highest spinning range, MQMAS when dealing with the quadrupolar fourth rank tensor elements, decoupling of nuclei that may cause dipolar broadening of the acquired signal, refocusing in the indirect dimension for 2Q–1Q correlation, and all other possible high-resolution schemes available), then the number of observed lines is usually the number of crystallographic sites. This can be experienced in another way. When observing a single crystal with a nonspecial orientation, every signal for a nucleus not in a special position has a crystallographic multiplicity equal to the number of general positions in the asymmetric unit, i.e., one. It is quite specific to NMR to be able to provide this information as immediately available from the spectrum of a polycrystalline powder, i.e., without the need for a single crystal and without the need to know the space group of the crystal. The second aspect of resolving the inequivalent sites is (provided the conditions of acquisition are amenable to some reasonable quantification) that the multiplicity of each site is measurable by the integrated area of the relevant signal. Except in difficult situations, even a 5–10% accuracy in quantitation is enough to make the difference in multiplicity between the rational numbers involved in asymmetric unit assessment.

If every nucleus can reasonably be measured by NMR, all the atomic sublattices can be analyzed, and the number of inequivalent sites as well as their multiplicity can be determined.[3]

17.2.4.2 The Crystallochemical Formula

Actually, it was as early as 1922, when Shubnikov recognized that a chemical formula imposes very strong constraints on the possible space group in which a compound may crystallize. The chemical formula imposes a stoichiometric ratio between the different atoms of the formula. A chemical formula associates to each atom contained in a compound its stoichiometric coefficient. A crystallochemical formula splits each atom type into its inequivalent crystallographic sites and associates to each its multiplicity in the unit cell. Consider an example: the mineral chiolite has the chemical formula $Al_3\ F_{14}\ Na_5$ ($A_i\ \nu_i\ A_j\ \nu_j\ A_k\ \nu_k\ \ldots$), whereas $Al_2\ A_4\ F_4\ F_8\ F_{16}\ Na_2\ Na_8$ ($A_i^a\ m_{i,a}\ A_i^b\ m_{i,b}\ A_j^c\ m_{j,c}\ A_j^d\ m_{j,d}\ A_k^e\ m_{k,e}\ \ldots$) represents its crystallochemical formula. In the unit cell, the chemical formula appears twice ($Z = 2$) and the number of times each inequivalent site occurs is indicated by the subscript. The stoichiometric coefficient is related to the multiplicity by the following relation:

$$Z \times \nu_i = \Sigma_{i,k} m_{i,k} \tag{17.2}$$

Stoichiometry, density of the sample (which is related to Z, the number of formula units per unit cell), and the site multiplicity are linked by the above relation. NMR, other spectroscopies (Mössbauer, EPR, etc.), and elemental analysis, can be used alone or in combination to propose the proper crystallochemical formula. The crystallochemical formula is a central concept for crystal-structure determination because the molecular concept is not so general. For a 3-D-connected (network) inorganic crystal, there is no such simple relation between what is in solution and what appears in the crystal. The crystallochemical formula links the unit cell content to its possible distribution in specific site symmetries related to the space group into which the crystal is assigned.

17.2.4.3 Point-Group Symmetries of Sites and Crystal Space Groups

A space group contains an infinite number of general positions as well as special positions sitting on one or several elements of symmetry (rotation axes, mirror planes, center of symmetry). The possible multiplicities of three-dimensional space groups are (1, 2, 3, 4, 6, 8, 12, 16, 24, 48). So, if we generate a list of 10 numbers ranked by the possible multiplicity in the unit cell, for each multiplicity we count the number of special positions having this multiplicity. We can therefore build for each space group this list of 10 numbers. For the general position, a star will indicate that actually an infinite number of such positions can occur. This will happen also for special positions that are loci of points, line or planes, and not simple points. Axes of rotation and mirror planes are such cases of special positions that can accommodate an infinite number of atoms on them. In such cases, we use some typographical convention to differentiate them from a point or from a general position for which a star has been assigned. In Galiulin's work[4] this differentiation is not retained. The list of 10 numbers defines the Wyckoff spectrum of a space group. One has to be aware that the description of every space group has to be limited to its primitive cell description, and the usage of centered cell has to be eliminated, limiting rigorously to 48 (the maximum multiplicity for a general position). Though equivalent, as Bravais' description[5] allows, the centered cell choice for space groups is the actually the dominant choice, but not the unique one to describe space groups. For NMR, as for theoretical calculations, it is much more convenient to describe all space groups in their primitive representation.[6]

Once this precaution has been taken, a unique Wyckoff spectrum can be established. The Wyckoff spectrum is an invariant of the group and can therefore be used to identify it. For 2-D space groups, the relation between the list of Wyckoff spectra and the space groups is biunivocal. For 3-D space groups, this relation is not completely biunivocal: 175 space groups have an biunivocal relation to their Wyckoff spectrum,[7] and the remainder differ by some gliding element of symmetry. It is therefore a quite good property for the discrimination of space groups.

Now, with these two notions in place (i.e., the crystallochemical formula and the Wyckoff spectrum), it becomes easy to explain the procedure of embedding a crystallochemical formula into a space group. First, let us rewrite the crystallochemical formula as a list of 10 numbers (its "multiplicity spectrum"), in the same way that was done above for the Wyckoff spectrum. Then the number of inequivalent sites by their crystallographic multiplicities is collected and the number of times a multiplicity m appears is counted, the latter numbers are finally ranked by multiplicity order.

For chiolite, the crystallochemical formula is $Al_2Al_4F_4F_8F_{16}Na_2Na_8$ $(A_i{}^a m_{i,a} A_i{}^b m_{i,b} A_i{}^c m_{i,c} A_j{}^d m_{i,d} A_j{}^e m_{i,e} A_k{}^f m_{i,f} \ldots)$ which, rewritten under its multiplicity spectrum, is (0,2,0,2,0,2,0,1,0,0). Now, to determine the compatible space groups in which this crystallochemcial formula can be embedded, define a projection operation, involving a sort of scalar product between a crystallochemical formula's multiplicity spectrum and a space group Wyckoff's spectrum, as follows: select one space group and its associated Wyckoff spectrum, then consider the crystallochemical formula's multiplicity spectrum; both are represented by a vector of 10 numbers, respectively (*pj*) and (*mj*). To be able to embed a crystallochemical formula into a space group, it is required to have a number of available sites of rank j greater or equal to the number of sites of rank j in the crystallochemical formula's multiplicity spectrum. So, the condition to fulfill is $pj \geq mj$ and it leads for each (*pj,mj*) pair to a Boolean value *kj*. If this condition is not fulfilled, the crystallographical formula cannot fit into the space group. An embedding spectrum of 10 numbers is built (*kj*) that describes for each rank j if the previous condition is fulfilled. It leads to a list of 1 or 0 values. The projector is represented by this embedding spectrum. At last, the product of all the *kj* provides the answer to the question. If only one 0 occurs in (*kj*) then it is not possible to embed the crystallochemical formula into the considered space group.

This strategy is summed up as follows:

- Ranking of possible multiplicities for each space group (1,2,3,4,6,8,12,16,24,48) (*nj*)
- Space group Wyckoff spectrum of a space group (#128) (0, 2, 0, 3, 0, 3, 0, 1, 0, 0) (*pj*)
- Crystallochemical formula's multiplicity spectrum (0, 2, 0, 2, 0, 2, 0, 1, 0, 0) (*mj*)
- Embedding spectrum (if $mj > pj$ then $kj = 0$ else 1) (1, 1, 1, 1, 1, 1, 1, 1, 1, 1) (*kj*)
- Embedding product $\Pi j\ kj = 1$ or 0 (here 1)

The meaning of the possible use of only point-group site symmetry to determine the space group lies in the fact that it is not a single-site

analysis. A single-site analysis would be limited only to the crystallographic point group of the site considered. Here, the distribution of point groups in a space group is used. The Wyckoff's spectrum is a quite discriminative property. In diffraction, the set of diffracting lines with zero intensity provides a different way to select space groups. The line extinctions arise from the gliding elements of symmetry, a combination of a translation and a rotation, or a mirror plane. In NMR, the special positions change the multiplicity of each site, which is detected. Both criteria produce a list of conditions, a "group invariant" that selects the space groups matching the experimental observations.

Space groups can also be considered in the perspective of the group/subgroup relation. When a space group is considered, say after a diffraction study, the number of inequivalent sites proposed must be compared to the actual number of inequivalent sites measured by NMR. In the case of the MP_2O_7 family of compounds, such a group/subgroup relation has been investigated, and the convergence came out of the match between the possible subgroups and the number of inequivalent phosphorus sites measured by a double-quantum to single-quantum correlation.[8] However, one has to be careful, because such a search may not lead to convergence. Actually, the sensitivity of chemical shifts is high to any local modulation. An approximate periodic distribution of water in the pores of a zeolite-like material, may very well modulate the chemical shift as has been shown in the aluminophosphate nanoporous materials MIL-50.[9] In such cases, one must be careful, because an approximately periodic sublattice may generate a site multiplicity that does not match the number defined by the diffraction space group. These inequivalent sites are usually called "noncrystallographic" to express that their differentiation arises from a nonperiodic interaction.

The group/subgroup relations can also be determined using the point group of one site and comparing it to the crystal point group. If one gets for the site of smallest multiplicity, a lower site symmetry than what the crystal point group indicates, then the group/subgroup relations can be explored to check the compatible space groups.[10]

However, the group/subgroups relation should lead one to think that a consistency between diffraction and NMR space groups will always be obtained. In the case of MIL-74, a metalophosphate compound with a sodalite topology, no space group can describe the structure rigorously.[11] A sodalite topology is made of squares of which two opposite corners can be occupied by the same atom type, and the two other corners by a different atom type (classically, silicon alternated with aluminum atoms). This alternation may be perfect – the sodalite is therefore ordered; or the four corners can be completely statistically occupied – the sodalite is then said to be disordered. The corresponding space groups are $I\bar{4}3$ m and $P\bar{4}3$ m. They are not in a group/subgroup relation. The actual numbers of phosphorus sites would be one in

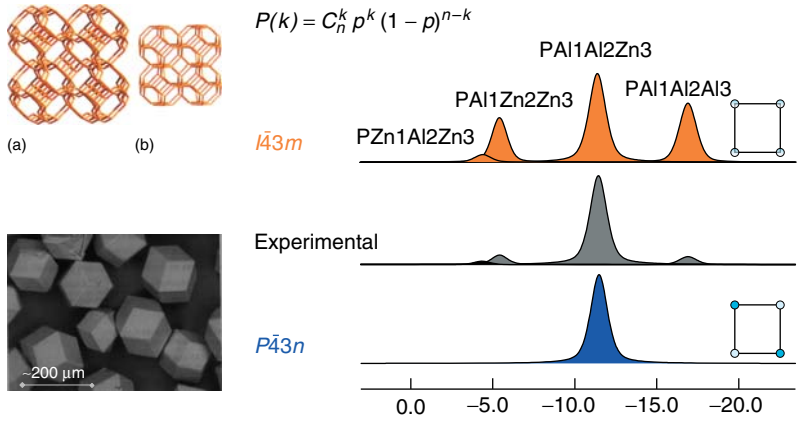


Figure 17.3. For the supersodalite crystal topology MIL-74, the actual distribution of units in the crystal does not correspond to either the "disordered" case of space group $I\bar{4}3$ m, or to the "ordered" case in space group $P\bar{4}3$ m. The crystal, though ordered, cannot be simply described in either of the possible space groups, though it has a reproducible and regular structure. (Reproduced from Ref. 25 © Elsevier, 2004.)

the $I\bar{4}3$ m case and four, with intensities given by a binomial distribution for $P\bar{4}3$ m (Figure 17.3). The actual result on the MIL-74 compound indicates (for the phosphorus atom) a departure from both the single-site model and the binomial distribution. Any of the possible space group choices would provide such a distribution. The reproducibility of these multiplicities and relative intensities precludes a "disorder," but indicates an order that cannot be accounted for by any of the considered space groups. This is mainly due to the low sensitivity of diffraction to the nature of the atom types, but measurement limited to just the electron density. In such a situation, using the 230 crystallographic space groups approach, the crystal has to be described as "between" two space groups, $I\bar{4}3$ m partially ordered, or $P\bar{4}3$ m slightly disordered.[11]

NMR and diffraction can be used to analyze the space groups or point groups of crystals, and obviously some comparison between them should be provided. When doing so, one may have differences with higher or lower symmetry space groups for one technique or the other, depending on the sublattice more sensitive to diffraction or NMR.[12] Usually diffraction is more sensitive to high electronic density sublattices, though NMR is more sensitive to low-atomic sublattices. The conclusion for crystal description is that none of the space groups or point groups proposed by one or the other measurement is either good or bad; they reflect the weighting schemes of the different measures and each of them sheds some light on the regular structure of the crystal. They would be the same only if the crystal is perfectly periodic, with no defects, and if all atoms can be unambiguously assigned to a different electronic density (a quasi-mathematical crystal) – probably a rare case. One should realize that the determination of a space group is limited by the accuracy of the physical measurement, whichever the measurement type. This explains why many crystal structures are described with an apparent space group, containing more elements of symmetry than the geometrical element of symmetry.

Up to now a limited usage of NMR observables has been made. We retained mainly the interactions with nonzero isotropic terms, limiting ourselves just to the isotropic chemical shift and the resolution of sites. There is obviously much more to it with other parts of the interactions.

17.2.4.4 Site Symmetry Determination

In a recent paper,[13] Senker *et al*. have shown that the rotational element of symmetry of the point group of a given site can be determined by using a correlation spectrum of the static sample. This makes use of the anisotropic part of the chemical shift tensor. This specific case demonstrated the ability to determine the element of symmetry at the site of a phosphorus atom. The authors were able to make the distinction between a three-fold axis and a rotoinversion $\bar{3}$ axis, leading to the choice of the space group $R\bar{3}$ (No 148 in the International Tables of Crystallography[14]). Such a procedure shows that observing a site in detail can lead to determination of the point-group site symmetry. As this can be done on different sites, the constraints created by the point group determined are quite severe for space group selection or site assignment.

The quadrupolar interaction and chemical shift anisotropy tensors can carry the same point-group site symmetry.[15] Whichever mode for estimating the quadrupolar interaction is used (a point charge model or a complete ab initio method), the asymmetry parameter η_Q, usually carries long-range order information. The quadrupolar interaction senses long-range order because it involves a direct or an implicit Madelung summation, i.e., an electrostatic energy calculation that has a reciprocal distance dependency, hence being definitely much longer ranged than any interaction having a higher reciprocal power of the internuclear distances. When considering the chemical shift anisotropy, things are slightly different compared to the quadrupolar interaction. As the interaction decreases in space much faster than an electrostatic interaction, one may not sum over a large enough fraction of the crystal space to get the same site symmetry as the crystal itself.

A particularly interesting case of site symmetry determination is the absolute orientation of a space group. Actually, among the 230 3-D crystal space groups, 22 have a mirror relationship, leading to 11 space groups with 11 mirror images. From a diffraction point of view, it is always a delicate problem to assess which, the left-handed or the right-handed, space group should be chosen.[16] This is true for point groups too, leading von Laue to show that among the 32 possible crystallographic point groups, diffraction can only discriminate 11 classes, containing several point groups in each class. The reason for this loss of information comes from the scattering factor measured for an atom j, f_j is the

square of the structure factor $F^2(h,k,l) = F^2(\bar{h}, \bar{k}, \bar{l})$ leading to an additional apparent center of symmetry for the space groups. NMR does suffer from such a limitation, but this property is largely underused. Though recently surveyed,[17] the basis for NMR to determine absolute configuration lies in the fact that NMR can determine all the elements of second-rank tensors, but at least one tensor (the dipolar coupling) is a polar tensor. This property, if used properly, authorizes one to determine absolute configurations of chiral crystals. As this property holds for any nonisotropic medium, it has been shown that a liquid crystal possesses the same property, with the possibility to determine the absolute configuration of a molecule dissolved into it.[17]

17.2.4.5 Distances, Angles, Proximities, Connectivities

The geometrical parameters describing the structure are in the three components involved in the energy-level determination, i.e., in the product for each interaction, the space part, and the spin part. Apart from the dipolar interaction for a spin pair, for which a direct relation to the internuclear distance appears explicitly in the dipolar coupling constant, all the other geometrical parameters are more or less "hidden" in the irreducible spherical tensor representation of the space and spin parts.[18] Additionally, as these are written as quantum descriptions of the energy contributions occurring for the crystal, one may not immediately recognize how the geometry is directly expressed in the NMR measurement. This is clearly in contrast to the diffraction experiment, for which the geometrical meaning is much more direct. However, as the irreducible spherical tensors develop in a systematic mode, few terms are related to each spherical harmonic; i.e., a parameter governing its amplitude but not its shape while the remaining part is the origin and orientation of each of these spherical harmonics. For a long time, many empirical or theoretical rules have been used for the isotropic chemical shift and for some coupling constants. With the advent of more available computing codes for processing what would be the NMR observables from a structural model, one may expect a more systematic use of these computations for making the geometry more amenable to systematic exploration.

However, many semiempirical methods correlate one of the components of the tensor to average distances in a polyhedron, like PO_4 or SiO_4, a bond angle as for <SiOSi> or <POP>, a dihedral angle as for NH–CH bonds (the dihedral angle between the HNC and NCH planes), the Si–O–Si angles from oxygen-17 quadrupolar information, etc. These methods are providing convenient ways to isolate one geometrical parameter and to estimate it from a simple operational relation.

The distance measurement approach is a general technique of structure resolution. Actually, if one considers an existing structure, knowing the positions and nature of atoms in space, one can calculate the distance matrix. This distance matrix (d_{ij}) provides distances between any pair of atoms (i, j). Generally, one cannot invert a distance matrix to get the positions of atoms, except in quite simple cases. This problem is closely related to the Patterson function in diffraction crystallography. Actually, it would be useful to access the vector matrix, which would lead to a more direct way to find a correct distribution of atoms in space. However, the distance matrix can be usually used as a cost function for modeling possible structures. This has its correspondence in diffraction crystallography with the advent of direct methods, for which a distribution of atoms in direct space is provided and adapted to fit the reciprocal space of diffraction. Direct methods allow the phase limitations problem of diffraction to be overcome.

The dipolar and indirect couplings (*see* **Chapters 10**, **11** and **12**) bring information of immediate proximity through space for dipolar coupling or through bonds for indirect coupling. For a pair of isolated dipolar-coupled spins, the dipolar coupling constant brings an unambiguous status of qualitative proximity and can lead to an accurate distance measurement (*see* **Chapters 11** and **12**). For an infinite network of dipolar couplings, things are less obvious but are amenable to calculations (*see* **Chapter 14**). Usually J-couplings can be analyzed easily for a limited number of neighbors, providing the connectivities between atoms. Dipolar coupling of an isolated pair of spins leads generally to very accurate distance determination. However, when dealing with the common situation of an infinite network of dipolar couplings, the determination of distances uses the build-up of polarization transfer,[19] the build-up of the zero quantum experiment,[20] the build-up of spin diffusion experiments (*see* **Chapter 14**) or experiments like REDOR and all its variants.

As in direct methods, it is difficult or impossible to access the distances directly from the build-up curves: no general method of inversion exists for

doing so. However, as in diffraction "direct methods," from distributions of atoms in space, one can use the build-up curves as cost functions for matching the possible atomic positions to them. Depending on the quality of this experimental set of data, highly probable structural models can be produced.

This is what has been undertaken for the proton atomic sublattice (*see* **Chapter 14**). Actually, measuring the homonuclear dipoles for an infinite network of protons raises two challenges. The first one is to get enough resolution by using pulse sequences addressing strong homonuclear interactions with 100% abundant nuclei like protons. Therefore, many homonuclear high-resolution schemes have been developed (*see* **Chapter 22**). The second challenge is to find a way to start with a set of atomic positions that would match the build-up of magnetization originating from the spin-diffusion experiment. Both issues have been successfully addressed (*see* **Chapter 14**). Even with an approximate model of spin diffusion, this approach appears to be very efficient. A relation can be established between the distances determined for the proton sublattice to the unit cell in a manner comparable to what has been achieved by Wüthrich when resolving the structure of peptides in solution, but with the additional constraints that one has to take into account for the infinite periodicity of the crystal. Locating the protons in a unit cell is a considerable extension of structure determination: first, because the determination of position by diffraction of X rays is difficult, owing to the low electron density of hydrogen atoms; second, even when using neutron diffraction, this imposes the use of deuterated compounds and usually fairly large single crystals. In both diffraction methods, the use of a single crystal is still needed. The NMR version of the experiment is run on a polycrystalline powder, with natural abundance hydrogen atoms.

17.2.4.6 Asymmetric Unit and Integrant Unit

When measuring the magnetization of a given family of nuclei through a given pulse sequence, one accesses many interactions available in the crystal. Among them, the observation of all the atomic families and, for each, the multiplicity of each inequivalent site leads to the crystallochemical formula. Further experiments allow connectivities and proximities to be established, through the indirect coupling, the dipolar coupling, and all the other information on chemical shifts, or quadrupolar or hyperfine interactions. Coordination state is a classical example, in aluminum NMR, of a state determined by the chemical shift range; 0–20 ppm indicates an aluminum surrounded by six oxygens, 20–40 ppm an aluminum in a five-coordinate state, 60–90 ppm a four-coordinate state. This type of information also carries the nature of the first sphere coordination, in some cases the second sphere too. For carbon, it is well known that the chemical shift range and anisotropy carries information about the hybridization state, commonly differentiating carbon atoms in sp2 or sp3 hybridization.

With the crystallochemical formula, and all the information about the hybridization state or the coordination level of atoms as well as their connectivities or proximities, it is therefore possible to build a fundamental unit, the integrant unit, required to build up the crystal. As discussed earlier, the integrant unit is the first multiple of the asymmetric unit leading to integer numbers of atoms for the stoichiometry of the unit. Very often, for molecular compounds, of low space-group symmetry, the integrant unit is equivalent to the molecule in the crystal. It is worth noticing that the concept of a molecule is not essential in diffraction crystallography. Actually, atoms are only located by their electron density. The existence of a bond is inferred by subsequently considering interatomic distances. If they are inferior to a known value, then covalent bonding is inferred. For NMR, things are definitely different, the molecule concept allows one to compare the spectrum of a molecule in solution and in a crystal, and the carbon or nitrogen chemical shifts will be comparable but slightly modulated by the difference of the surrounding medium and by the crystallographic inequivalence. On the other hand, the molecule concept is of no use in the case of inorganic, infinitely connected covalent networks, such as zeolites. For them, NMR has to define a unit that would have a meaning for the crystal, which is comparable to that for the molecule. However, one should not expect to observe this unit in solution, or in the molten state. The integrant units the proper structural descriptor when a molecule cannot be defined in a crystal.

With the integrant unit, or the molecular structure, the basic tiles of the crystal, one can start to build up the crystal structure by combining the different possibilities for a compact paving of space with the basic unit. This can be done following different modeling schemes, but one needs to

explore a large number of possible geometries. This leads to the different possibilities for different polymorphs.

17.3 RESOLVING STRUCTURES BY NMR

17.3.1 The Distance Approach and the Pseudo 1-D Problem for Large Molecular Structures

During the early 1980s, molecular structure determination of some peptides was successfully achieved by Kurt Wüthrich's group using a distance matrix between the protons of the molecule.[21] The molecular structure determination needed two steps: first, the determination of the sequence of amino acids, then the proton sublattice determination. Both methods were developed in Wüthrich's group. Later, various structure determination technologies were set up. Though not strictly belonging to NMR crystallography because of the intrinsic lack of translational periodicity (the molecular structure were determined in solution), the method shares most of its features with NMR crystallography, except for its lack of pertinence to the space group determination.

17.3.2 3-D Molecular Approaches

For molecular approaches two steps are necessary to determine the crystal structure. The molecular object must be identified by measuring the necessary 1 and 2-D spectra, allowing for resolution of all the sites, their assignment, and their connectivities. This defines the topological model, the number of molecules in the asymmetric unit. The second stage of the crystal-structure determination is to access the metric (i.e., the atomic positions and unit cell parameters). At this stage, usually one may access a set of distances through many experiments and then combine the metric with the space group knowledge to determine the unit cell as the last step of the crystal-structure determination.

This strategy was first used as an intermediate step between the molecular approach and a crystallographic approach by Cross and colleagues[22,23] using angle determination and, at a later stage, distance measurements to obtain the Gramicidin structure by solid-state NMR.

Use of high-resolution proton NMR with homonuclear decoupling has led to a specific approach for analyzing the build-up of magnetization of spin diffusion by Emsley and his coworkers (*see* **Chapter 14**). Emsley's group developed a combination of INADEQUATE (*see* **Chapter 15**) and proton spin-diffusion to determine proton–proton distances.

One should remember that, in a diffraction experiment, as the square of the diffracted complex amplitudes are measured, the phase of the signal is lost and it is not possible to back Fourier transform the diffracted intensities to get the positions of atoms directly. Many methods are used now to get an estimate of the phase for each site. This limitation has led to the realm of "direct methods" for structure determination.

It is interesting to notice that, though NMR spectroscopy does not, in general, suffer from the phase indetermination, the distance matrix usage reintroduces a similar limitation as for diffraction in that distances are not interatomic vectors and lose the "phase", i.e., the orientation of the vector. As a consequence, modeling the crystal is essential for producing a structure determination out of a distance matrix. The above structure determinations belong to a general class of "direct methods".

17.3.3 3-D Nonmolecular Crystals

The aluminophosphate AlPO4-CJ2,[24] and a natural fluoride, chiolite,[25] have had their structure completely resolved by solid-state NMR via a combination of assignment of the inequivalent crystallographic sites, the integrant unit and the atomic positions and unit cell parameters. Brouwer proposed for zeolites (*see* **Chapter 18**) a method assigning silicon sites and performing distance measurement by using DQ build-up curves between silicon sites. In the last example, the space group used came from the X-ray powder diffractogram. Actually, even if the structure cannot be solved by diffraction, an accurate set of the unit-cell parameters is usually available. However, the concept of integrant unit is also useful here; software for polymorph prediction has been used for the two first examples, by modifying some of the atomic potential to allow for sticking atoms in order i.e., to "fuse" atoms at the sticking points between integrant units. This method called automatic assembling of secondary building units (AASBU)[26] has a considerable impact in the domain of inorganic

nanoporous materials as well as in the metal organic framework domain. Alternative approaches use smaller units instead of the unique integrant unit, when not enough constraints are available. In such cases, the necessary additional information can be gathered from diffraction, or from modeling.[27]

17.3.4 Structure Determination Strategies

To determine a structure from a polycrystalline compound is an art more than pure technology, as has been described in "The art of zeolite structure analysis" by McCusker[28] (*see* **Chapters 18** and **19**). McCusker describes the process of determining a correct structure as a walk in a maze in which one has to find enough information and in a proper order to discover the arrangement of atoms in space of the considered object. If this view is correct for diffraction crystallographers, it also applies to a much broader extent to NMR spectroscopists. The reason for this is the number of experiments (much larger than in diffraction methods) that should be used to unveil the parameters leading to a proper structure.

The variety of situations that need to be considered is so large that different types of strategies will be available for different classes. However, the nature of the steps and their sequence can be grossly classified as follows:

1. Usually, it is very useful to access the space group to reduce the search in space. It can be determined by diffraction or by NMR. Both ways to do it require only a good powder polycrystalline sample. NMR determination requires usually several experiments while diffraction of X rays is limited to one. Consistency of a space group issued from diffraction can be generally checked by a single NMR measurement. If the space group is determined by diffraction, the unit cell parameters are at this stage available; otherwise, they will be determined at a later stage.
2. The number of molecules in the asymmetric unit can be determined or the integrant unit defined (*see* **Chapter 1**). For molecular compounds, this is probably much easier to perform by using NMR. In the latter case, usually the molecular structure can be determined from solution-state NMR, so a comparison between the solution-state and solid-state spectra is a convenient practice. For inorganic compounds, the task may be more elaborate, because the concept of a molecule may not apply at all, and what could be observed in solution does not relate to the crystal arrangement of atoms. Several experiments, enumerating the inequivalence of sites, their multiplicity as well as their topological arrangement, might be necessary to establish the integrant unit.
3. Structure modeling can be performed with an initial "tile" (the molecule, the integrant unit, the asymmetric unit), with or without conformational flexibility of this unit. The packing of space can be looked for by using topological rules like connecting some atoms or points of the unit surface, or just by using energy as a criterion, as in ab initio calculations. Several methods are available for modeling: polymorph predictions using molecules can provide initial guesses; AASBU[26] (a polymorph-predictor-like program, which includes the possibility of having "sticking" atoms to join the integrant unit by shared atoms); a grid-filling topology for tetrahedral networks.[29] This structural model elaboration step is probably the most diverse and most demanding one in terms of computer power and skills. There are several hybrid approaches, in which topology and metric are mixed, such as diffraction based programs Fox[27] or TOPAS.[30]
4. A refinement step of the structure can be carried out to provide an improved set of positions and also a refined set of the unit-cell parameters. Three types of cost functions can be used to refine the structural model: energy, diffraction observables, and NMR observables. Actually, each cost function has a specific weight or accuracy; one can grossly characterize them by saying that the energy being a global parameter is the coarsest refinement, then diffraction as a cost function in Rietveld refinement, then NMR observables. Actually, one will iterate between the different cost functions and may here again define strategies to use as many as possible with different weights in such a way as to lead to the accuracy targeted.

Usually, when solving a structure by diffraction, one must use a lot of additional information, such as the chemical composition, the measured or estimated density, determination of the absence of a center of symmetry, and molecular motifs that can be found in the crystal. Including chemical information in the structure determination is the aim of a specific program, FOCUS.[31] In NMR crystallography, one

must follow a similar attitude and include as much complementary information as necessary to perform a full crystal-structure determination. This is a consequence of the intrinsic nature of incomplete information on objects by a single measurement method.

17.3.5 Structure Refinement

Energy, diffracted intensities, and spectroscopic observables such as NMR interactions can be used. The ranking in term of accuracy is from coarse to accurate: energy, diffraction, and NMR. This is because of the energy range of interactions: all energies together, the periodic part of the energy, the lattice part, and edition of interactions at any level of subtlety by NMR.

17.3.5.1 Refining Using Energy

Once a structure has been determined, topologically or at a mixed level between topology and an estimated metric, then the structure can be submitted to any structural "relaxation" in the available crystal modeling packages. The principle upon which this minimization is carried out is that all contributions to energy are considered and it is the global energy that serves to relax the structure. Nowadays, this strategy is robust enough that many polymorph predictions are really close to the actual experimental results. Additional initial constraints may be added before relaxing the structure in take into account distances or angles determined during the previous resolution steps. These refinement methods, though intrinsically coarser than any other approach, are likely to improve very rapidly in their use to tune the estimation of energy by classes of situation, thus defining better atomic potentials. They are also improving in terms of code availability and computer speed.

17.3.5.2 Refining Using Powder Diffraction

From the structural model, it is possible to simulate the powder diffractogram and to refine unit cell parameters and positions of atoms to fit the complete diffractogram. This is usually the Rietveld method of refinement. The weak aspect of this method was, in the past, to be not always able to get an initial structural model that would be close enough to the experimental structure. Therefore, one fails at refining the structure. With programs like Fox or TOPAS, one may mix the two steps (structure determination and refinement) in a single analysis, making the method more robust. No extension to NMR of these codes has been implemented yet. For the future, this would make an integrated structure determination much easier.

17.3.5.3 Refining Using NMR Observables

When using a modeling program to simulate a structure, one can obviously try to perform quantum calculations of different aspects of the crystal. All the spectroscopic observables, especially, can be derived if one knows how to compute a proper basis set of functions for each atom. The solutions are not unique, and depend very much on which property has to be evaluated. The isotropic chemical shift is reputed for its sensitivity to average distances around an atom, the quadrupolar interaction to the long-ranged charge distribution for ionic compounds, etc. The anisotropic parts of the interactions are related to a more exact description of the crystal arrangement. Each of these calculations is atom dependent and some interactions are easier to calculate than others. But the trend is that with an increased number of crystal structures determined by a wider use of measurements, the ability to compute faster and with a wider variety of atoms in the crystal will increase concomitantly. There is still much work to be done before the codes will appear as flexible "black boxes" for structure determination. However, as many NMR interactions are exquisitely sensitive to geometrical changes of the structure, this is probably one of the current directions of development (*see* **Chapter 3**).

The edition of NMR interactions allows refinement of the structure piecewise. This is one of the most promising manners to navigate the maze of structure determination by ranking the interactions in decreasing accuracy and refining the structure in the same order. As an example, chiolite, a mineral already mentioned in the article, had its structure determined by diffraction. Using this structural model as a starting solution, coordinates of every atom have been explored, with variation of each coordinate independently. Isotropic fluorine chemical shifts have been used as a cost function (Figure 17.4c). As fluorine atoms are not at the center of the AlF_6 polyhedra, their positions determined by diffraction are probably less accurate than the Al positions at the center of the polyhedra. The latter case leads in diffraction to a much better centering of the electron density. One

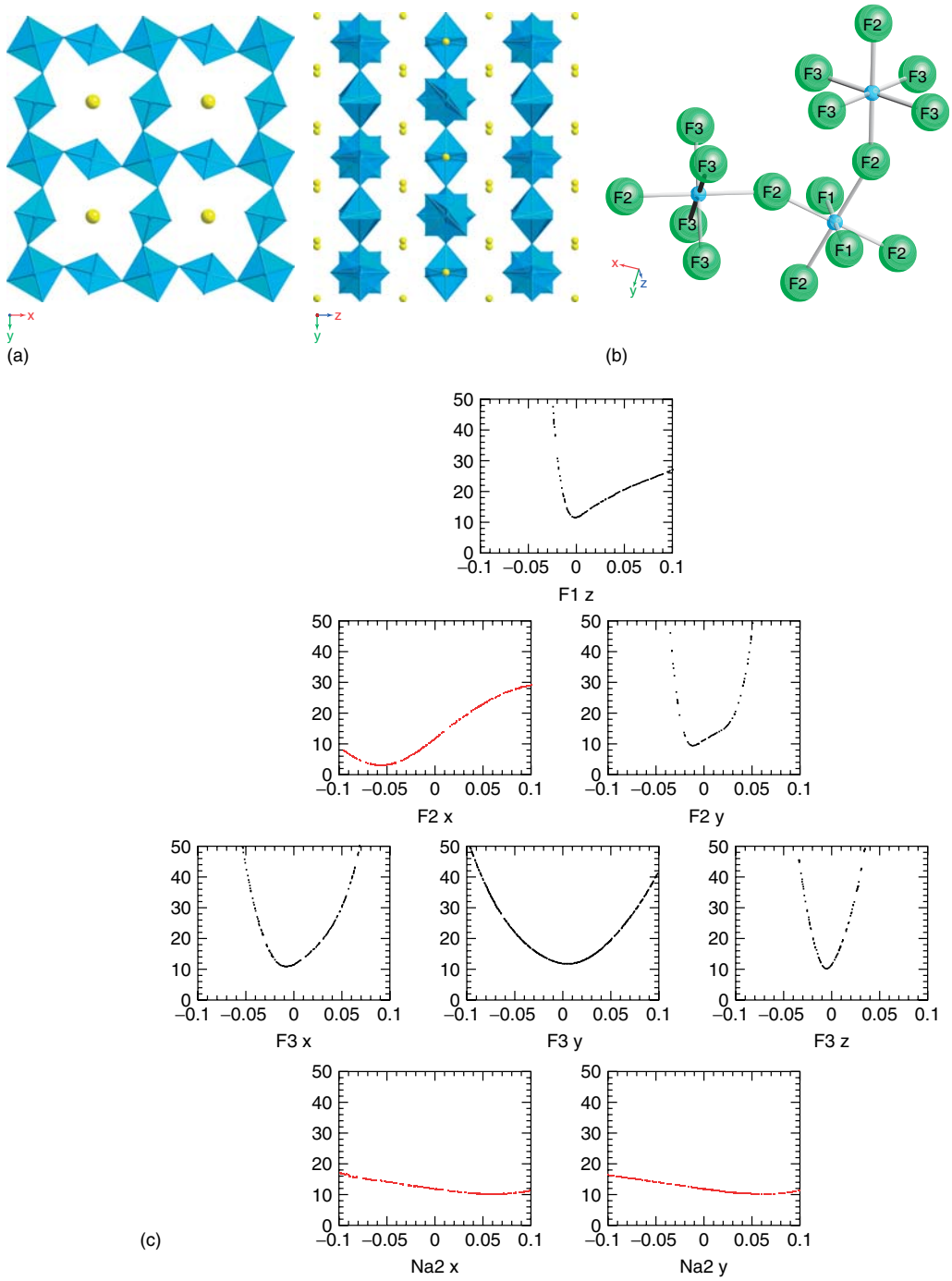


Figure 17.4. The chiolite structure has been redetermined by NMR Crystallography: (a) the framework of AlF_6 polyhedra; (b) the integrant unit used to construct the framework, with its degrees of freedom explored; (c) fluorine calculation of chemical as a cost function for refinement of the atomic positions. (Reproduced from Ref. 25 © Elsevier, 2004.)

can see from the results displayed in Figure 17.4(b) that all atoms but two (one fluoride ion and its neighboring sodium ion) are in almost exact agreement. The two remaining atoms are slightly different from the diffraction results by only one coordinate. This is an example demonstrating that once an approximate solution of the structure has been established – here by diffraction – one may reexplore using other cost functions to further refine the structural model provided here by NMR.

17.3.5.4 Assessing the Quality of a Structural Model

A general problem in structure determination is to assess to quality of the proposed model or its likelihood. Usually, sets of different *R* parameters express the average mean distance between the proposed structure and the actual data. This is a general procedure that requires back-calculation from the proposed structural model to the physical observables and comparison of their distance from the actual measurement. It has been up to now a weakness of NMR crystallography that calculating such a quality for the parameters has to deal with many experiments, implying different types of assumptions on the model to back calculate the data, and different types of inaccuracy due to the quality of the data. However, new theories in this direction allow the development of a proper frame for such an assessment.[32] The principle developed by the authors is that given a data set *D*, a group of assumptions and often constraints or "potentials," one can evaluate from the quality of the data, the likelihood of the structural model. The advantage of such probabilistic methods is that they can easily incorporate data of different types as well as all the assumptions made along the strategy of structure determination.

17.4 NMR CRYSTALLOGRAPHY AND BEYOND PERIODIC STRUCTURES

NMR crystallography is a complete crystallographic system. It is an emerging branch of a much broader "general" crystallography, which includes all the techniques working in reciprocal as well as in direct space. Space groups as well as point groups can be determined by NMR crystallography. Unit-cell determination is related to measurement of distances and angles that can be achieved by NMR. Atomic position resolution is carried out in two steps, i.e., by determination of the topological arrangement of connectivities and proximities, and in a second stage by the determination of an integrant unit with its metric. Assembling the integrant unit leads to the structure determination. The final step is the refinement by using energy, diffraction, or NMR cost functions. This general strategy may have some variations on the way to perform one or the other stages, but is of general validity.

NMR crystallography is not limited by the periodic boundary conditions restrictions that apply to diffraction methods, provided that structures are regular enough to be described by a finite number of rules. Surprisingly, glasses may possess enough local order and their formation can follow a limited set of rules. What is to be revealed is first: is the local order some sort of local invariant? If the answer is yes, is it possible to generate some long-distance organization with few rules? It has been recently shown that double-quantum to single-quantum correlations using dipolar or indirect coupling can probe local groupings of atoms and analyze their distribution throughout the variations of the glass compositions.[33] Such findings point in the direction of formulating some simple rules for the formation of such possible regular objects. Some glasses may well fall into this class.

Many others cases such as nanoporous compounds belong to the class of regular objects with sublattices being described by a different set of rules, one periodic, the other one not. Many natural minerals mix cations or anions in approximately, but not quite, stoichiometric situations. As for MIL-74,[11] they may very well define a class of regular structure for which the minimum in energy does not coincide with the perfectly periodic situation. NMR crystallography will face many of these future challenges by bridging periodic atomic assemblies and not only periodic ones. NMR crystallography is based upon and extends actual crystallography, which is very often restricted to diffraction crystallography of perfectly "ordered" crystals.

REFERENCES

1. R.-J. Haüy, *Traité de Cristallographie*, Bachelier et Huzard: Paris, 1822.
2. R. W. G. Wyckoff, *The Analytical Expression of the Results of the Theory of Space Groups*, Carnegie Institution of Washington: Washington, DC, 1922.

3. F. Taulelle, *Solid State Sci.*, 2004, **6**, 1053–1057.
4. R. V. Galiulin and V. R. Khacgaturiv, *Mathematical Modelling of Composite Objects*, Comp. Centre of RAS: Moscow, 1994.
5. M. A. Bravais, *J. Ecole Polytech.*, 1850, **33**, 1–128.
6. S. F. A. Kettle and L. J. Norrby, *J. Chem. Educ.*, 1993, **70**, 959–963.
7. O. Delgado Friedrichs and D. Huson, *Period. Math. Hung.*, 1997, **34**, 29–55.
8. I. J. King, F. Fayon, D. Massiot, R. K. Harris, and J. S. O. Evans, *Chem. Commun. (Camb.)*, 2001, **18**, 1766–1767.
9. L. Beitone, J. Marrot, T. Loiseau, G. Ferey, M. Henry, C. Huguenard, A. Gansmuller, and F. Taulelle, *J. Am. Chem. Soc.*, 2003, **125**, 1912–1922.
10. E. Gaudin, F. Taulelle, F. Boucher, and M. Evain, *J. Chim. Phys. Phys. Chim. Biol.*, 1998, **95**, 295–301.
11. L. Beitone, C. Huguenard, A. Gansmueller, M. Henry, F. Taulelle, T. Loiseau, and G. Ferey, *J. Am. Chem. Soc.*, 2003, **125**, 9102–9110.
12. L. Allouche, C. Huguenard, and F. Taulelle, *J. Phys. Chem. Solids*, 2001, **62**, 1525–1531.
13. J. Senker, L. Seyfarth, and J. Voll, *Solid State Sci.*, 2004, **6**, 1039–1052.
14. T. Hahn, *International Tables for Crystallography*, D. Reideln Publishing Co.: Boston, 1983, 1987.
15. J. A. Weil, T. Buch, and J. E. Clapp, *Crystal Point Group Symmetry and Microscopic Tensor Properties in Magnetic Resonance Spectroscopy*, Academic Press: San Diego, CA, 1973.
16. H. D. Flack and G. Bernardinelli, *Chirality*, 2008, **20**, 681–690.
17. J. Courtieu, P. Lesot, A. Meddour, D. Merlet, and C. Aroulanda, Chiral liquid crystal NMR: a tool for enantiomeric crystals, in *Encyclopedia of Nuclear Magnetic Resonance*, eds-in-chief D. M. Grant and R. K. Harris, John Wiley & Sons: Chichester, 2002, Vol. **9**, pp 497–505.
18. M. Eden, *Concept Magn. Reson. A*, 2003, **17**, 117–154.
19. C. A. Fyfe and D. H. Brouwer, *J. Am. Chem. Soc.*, 2006, **128**, 11860–11871.
20. S. Dusold, J. Kuemmerlen, T. Schaller, A. Sebald, and W. A. Dollase, *J. Phys. Chem. B*, 1997, **101**, 6359–6366.
21. D. Marion and K. Wuethrich, *Biochem. Biophys. Res. Commun.*, 1983, **113**, 967–974.
22. M. Cotten, R. Q. Fu, and T. A. Cross, *J. Biomol. NMR*, 2000, **16**, 261–268.
23. T. A. Cross and J. R. Quine, *Concept Magn. Reson.*, 2000, **12**, 55–70.
24. F. Taulelle and C. Huguenard, *Stud. Surf. Sci. Catal.*, 2001, **135**, 1414–1421.
25. J. Dutour, N. Guillou, C. Huguenard, F. Taulelle, C. Mellot-Draznieks, and G. Ferey, *Solid State Sci.*, 2004, **6**, 1059–1067.
26. C. Mellot-Draznieks, J. M. Newsam, A. M. Gorman, C. M. Freeman, and G. Férey, *Angew. Chem. Int. Ed.*, 2000, **39**, 2270–2275.
27. V. Favre-Nicolin and R. Cerny, *J. Appl. Crystallogr.*, 2002, **35**, 734–743.
28. L. B. McCusker, *Stud. Surf. Sci. Catal.*, 2004, **154A**, 41–51.
29. D. H. Brouwer, R. J. Darton, R. E. Morris, and M. H. Levitt, *J. Am. Chem. Soc.*, 2005, **127**, 10365–10370.
30. A. A. Coelho, *J. Appl. Crystallogr.*, 2003, **36**, 86–95.
31. R. W. Grosse-Kunstleve, L. B. McCusker, and C. Baerlocher, *J. Appl. Crystallogr.*, 1999, **32**, 536–542.
32. M. Habeck, W. Rieping, and M. Nilges, *Proc. Natl. Acad. Sci. USA.*, 2006, **103**, 1756–1761.
33. K. Glock, O. Hirsch, P. Rehak, B. Thomas, and C. Jager, *J. Non-Cryst. Solids*, 1998, **232-234**, 113–118.

Chapter 18

Interplay between NMR & Single-crystal X-ray Diffraction

Darren H. Brouwer

Department of Chemistry, Redeemer University College, Ancaster, Ontario L9K 1J4, Canada

18.1	Introduction	263
18.2	Background Concepts	263
18.3	Solid-State NMR and X-Ray Diffraction	264
18.4	Examples	266
18.5	Conclusion	273
	References	273

18.1 INTRODUCTION

The aim of this article is to explain and illustrate the complementary relationship between solid-state nuclear magnetic resonance (NMR) spectroscopy and diffraction techniques, specifically single-crystal X-ray diffraction (XRD). The complementarity of XRD and NMR arises from that fact that each technique "observes" the structure from a different "point of view". X-ray diffraction probes the *long-range periodicity* of the electron density in a material, whereas solid-state NMR spectroscopy probes the *ensemble of local environments* around the (NMR active) nuclei in the material. This article will unpack the implications of these two different ways of probing the structure of a material and how the different points of view can be combined advantageously, allowing structural chemists to investigate the detailed structures of materials in a way that could not be achieved by using a single technique alone. Some background concepts about crystal structures, X-ray diffraction, and the general strategy for crystal structure determination are briefly introduced, followed by a discussion of the complementary nature of solid-state NMR and XRD. Then, by using few examples involving zeolites and organic host–guest complexes, the importance of a combined approach with solid-state NMR and single-crystal XRD for detailed structural characterization of materials is illustrated.

NMR Crystallography Edited by Robin K. Harris, Roderick E. Wasylishen and Melinda J. Duer © 2009 John Wiley & Sons, Ltd. ISBN: 978-0-470-69961-4

18.2 BACKGROUND CONCEPTS

18.2.1 Crystal Structures

In a crystal, the constituent atoms and molecules are arranged into a regular repeated pattern in three dimensions. A *unit cell* of a crystal refers to a basic unit or volume of space from which the entire crystal can be constructed by translational repetition of its contents in three dimensions. Within the unit cell is a subunit called the *asymmetric unit* that refers to a volume of space from which the unit cell is constructed by the application of *symmetry*

operators to its contents. The set of symmetry operators that expand the asymmetric unit into the unit cell constitutes the *space group* of the crystal. If an atomic position is within the asymmetric unit, such that only one symmetry operator maps to that location, the atom is said to lie on a *general position* and it will have the lowest site symmetry. A *special position* refers to an atomic position for which more than one symmetry operator maps to it, leading to a higher degree of site symmetry.

18.2.2 X-Ray Diffraction

In an XRD experiment,[1,2] the X rays are scattered by electrons. The periodicity of the electron density in a crystal leads to *coherent* scattering of X rays, giving rise to a set of *reflections* referred to as the *reciprocal lattice*. The positions of the reflections can be used to obtain the unit cell parameters, whereas the *systematic absences* of the reflections reveal the possible space groups of the crystal structure. The intensities and phases of the reflections are related to the distribution of electron density in the unit cell and, thus, the atomic positions. However, only the intensities, and not the phases, are measured in the XRD experiment. If the phases could be measured, the reconstruction of the crystal structure from the XRD reflection data would be essentially a straightforward Fourier transform from this reciprocal space observed in the XRD experiment to the real space of the crystal structure. The lack of phase information, and the consequential complications in reconstructing the crystal structure directly from the XRD data, is referred to as the *phase problem*. Fortunately, there are well-established methods available to overcome the phase problem, particularly, for single-crystal XRD. Powder XRD has additional complications due to the fact that the three-dimensional reciprocal lattice of a single crystallite becomes projected onto a single dimension for a powder, leading to a very high degree of reflection overlap and uncertainty about the intensities of individual reflections.

Structure determination from diffraction data is a process that typically involves a series of three main steps: (1) the positions and systematic absences of the reflections are evaluated to identify the unit cell and possible space groups of the crystal; (2) the structure is *solved* by overcoming the phase problem in some manner using the information contained in the intensities of the reflections and other available data to come up with an initial structural model; and (3) the structural model derived in the second step is *refined* to give the best agreement between the calculated and observed reflection intensity data.

18.2.3 Solid-State NMR

Solid-state NMR has the potential to contribute valuable structural information at each step in the structure determination process described above. The nuclear spin interactions that are probed and manipulated in solid-state NMR experiments provide information about local environments in a site-specific manner. These nuclear spin interactions are as follows: the magnetic shielding interactions arising from the surrounding electrons that give rise to chemical shifts (*see* **Chapter 5**); through-space direct dipole–dipole couplings (dipolar couplings) and through-bond indirect dipole–dipole couplings (J couplings or scalar couplings) with neighboring spins (*see* **Chapter 10**); and the interaction of quadrupolar nuclear spins with the electric field gradient (*see* **Chapter 16**). Each of these nuclear spin interactions is inherently *local*.

The contributions of solid-state NMR to crystal structure determination can be particularly important for materials that can be studied only as powders, such as most zeolites and many pharmaceutical compounds (*see* **Chapter 19**). For example, an approach for structure determination of zeolite crystal structures has recently been demonstrated in which this crucial step of structure solution is achieved using advanced solid-state NMR experiments to probe the distance-dependent dipolar interactions between ^{29}Si nuclei in the zeolite framework.[3]

Although XRD is often successful at the complete structure determination process when data can be collected on suitable single crystals, there still remain situations in which solid-state NMR can make crucial contributions to the detailed structural characterization of single-crystal materials due to its ability to probe the structure on a local level.

18.3 SOLID-STATE NMR AND X-RAY DIFFRACTION

18.3.1 Complementarity of NMR and XRD

Solid-state NMR and X-ray diffraction are complementary techniques due to the fact how each

technique observes or probes the same structure from a different perspective or point of view. As stated in the Introduction section, X-ray diffraction probes the long-range periodicity of the electron density in a material, whereas solid-state NMR probes the ensemble of local environments around the (NMR active) nuclei in the material. The following discussion elaborates on this statement about the complementarity of the techniques.

In the XRD experiment, it is the interaction of X rays with *electrons* and the resulting scattering of the X rays that leads to a diffraction pattern. In the NMR experiment, it is the *nuclei* that are spectroscopically probed with radiofrequency irradiation in the presence of a magnetic field. XRD is most sensitive when heavier atoms with many electrons are present while many of the heavier atoms are not straightforward to observe in the NMR experiments. On the other hand, XRD is quite insensitive to hydrogen atoms, due to low electron density, whereas protons are one of the most sensitive nuclei for NMR; however, solid-state proton NMR is not straightforward (*see* **Chapter 22**).

Owing to the vastly different frequencies of X-ray and radiofrequency radiation, XRD and NMR are different in the *timescales* that they probe. An important feature of NMR spectroscopy is its ability to probe the dynamics present in a material in a variety of different ways over a wide range of time scales (*see* **Chapter 24**). X rays are not sensitive to the time scales that molecular motions occur on. All possible configurations are observed since the molecular motions occur at frequencies well below the frequencies of X rays. (However, the distribution of electron density resulting from thermal motions of the atoms is typically modeled in a single-crystal XRD structure refinement.)

For a (useful) diffraction pattern to be observed in the XRD experiment, it is necessary that the X rays are scattered coherently. This is the case when the electron density is arranged in a periodic manner over length scales much greater than the wavelength of the X rays. Consequently, the main strength of diffraction experiments is in probing the *long-range* structure of a material. On the other hand, an NMR experiment can be thought of as observing (and manipulating) the nuclei in the material so that these nuclei act as probes of their structural environments. The various ways in which the nuclei can interact with their environment (magnetic shielding, direct and indirect dipolar coupling, and interaction of quadrupolar nuclei with electric field gradients) are all short-range interactions in the order of up to 10 Å. Consequently, the main strength of NMR experiments is in probing the *local* structural environments of the detected nuclei.

A diffraction experiment requires the constituents of the structure to act together, or cooperatively, in order for the scattering to be coherent (the structure has to be arranged with periodicity). In solid-state NMR, the constituents of the structure act more or less individually or cooperatively over only very short length scales (in the case of direct and indirect dipole–dipole couplings), such that a *sum* of the ensemble of local environments is observed. Therefore, XRD provides information about periodicity (the shape and size of the repeated unit cell and the symmetry operators that define the asymmetric unit) but does not easily provide information about the contents of the asymmetric unit, at least not until the phase problem is solved. Solid-state NMR does not provide direct information about periodicity (no information about the unit cell, but potentially some information about space group), but it can reveal a great deal of information about the contents of the asymmetric unit. In situations where disorder is present, XRD takes an *average* over the entire crystal, whereas NMR can potentially see the individual disordered configurations since a *sum* of the various local environments is observed (unless there is fast exchange between configurations). For example, NMR can potentially distinguish between "random" disorder and disorder over larger domains within a crystal. Furthermore, NMR has the potential to distinguish between the static and dynamic disorder.

Another important aspect of solid-state NMR that arises out of its ability to probe local structure, as opposed to the long-range periodic arrangement of *all* the atoms that diffraction methods probe, is its *multinuclear* capability. Since the Larmor frequencies of the various nuclides are typically significantly different from each other, there are separate spectral regions for each nuclide that gives NMR spectroscopy unrivalled elemental distinction. It is thus possible to probe the various substructures of the crystal by collecting spectra for the various nuclides present in the material. With double- and triple-resonance techniques it is even possible to probe the relationships between these various substructures and build up a tremendous amount of structural information about the crystal structure.

In summary, combining these complementary strengths of XRD (long-range periodicity of electron density) and solid-state NMR (ensemble of local environments) leads to a powerful approach for full structural characterization of materials.

18.3.2 Ordered Structures

The number of isotropic peaks in a solid-state NMR spectrum reveals the number of crystallographically unique sites in the crystal structure (*see* **Chapter 6**). If a quantitative spectrum can be obtained, then the relative peak areas indicate the relative occupancies of the crystallographic sites. The number of peaks and their relative occupancies can be used to identify the possible space groups[4] (*see* **Chapter 17**) and can potentially be very usefully incorporated into the structure solution step of a crystal structure determination.

For example, in organic molecular crystals such as pharmaceutical compounds,[5] the existence of a single peak in the ^{13}C NMR spectrum for each carbon in the molecule indicates that the asymmetric unit consists of a single molecule, as is the case for form I of finasteride[6] (Figure 18.1a). However, the existence of a splitting or doubling of some or all of the peaks indicates the existence of two crystallographically unique molecules per asymmetric unit, as is the case for the Form II polymorph (Figure 18.1b). The ^{13}C NMR spectra thus reflect the different space groups of the polymorphs: an orthorhombic space group for form I and a monoclinic space group for form II. A combined solid-state NMR and XRD approach ensures consistency and additional confidence that XRD-derived structures of polymorphs are correct.

In high-silica zeolites, the number and relative intensities of the isotropic peaks in the ^{29}Si spectrum indicate the number of crystallographically unique Si sites and their relative occupancies. An interesting example is high-silica ZSM-5 that undergoes a number of temperature-dependent and adsorption-induced crystallographic phase changes which can be monitored by solid-state ^{29}Si NMR (Figure 18.2a–d).[7] The ^{29}Si NMR spectrum of ferrierite (Figure 18.2e) illustrates the crystallographic information that is contained in the intensities of the peaks.[3] There are four unique Si sites on general positions and one Si site on a special position with half occupancy. This is manifested in one of the peaks having half the intensity of the others.

18.3.3 Disordered Structures

The examples presented so far have involved quite well-defined and well-ordered crystal structures. Although solid-state NMR reveals complementary structural information that is useful for verification, consistency, and increasing the confidence of crystal structures obtained by XRD, truth be told, pretty much all of the structure determination can be accomplished by XRD for such well-defined crystal structures, granted that a crystal of suitable dimensions can be obtained. However, many materials are not so well defined and straightforward to fully characterize by single-crystal XRD alone, and this is when a combined approach of solid-state NMR and XRD can become very important.

As a simple example, consider an aluminosilicate zeolite in which the tetrahedral "T-sites" in the crystal structure can be occupied by Si *or* Al. Since XRD probes the average periodic electron density in the structure, it only sees an average T-site since the Si and Al atoms are distributed randomly and it is inherently difficult for XRD to distinguish between T-sites occupied by Si or Al as they differ by only one electron. Consequently, although XRD can define the geometry of an aluminosilicate zeolite framework in terms of the positions of T-sites, the structural picture is not quite complete as XRD is incapable of saying anything about the nature of these T-sites. The ^{29}Si MAS NMR spectrum of an aluminosilicate zeolite (Figure 18.2f) reveals the distribution of Si atoms in the various local environments arising from different number of neighboring Al atoms. This information can be used to determine the Si/Al ratio and to confirm whether or not the distribution of Si and Al atoms is indeed random.[8] By combining both the techniques, a more complete picture of the structure emerges.

18.4 EXAMPLES

In general, for crystal structures that are disordered in some manner, X-ray diffraction tends to give the average structure since it probes the long-range periodic electron density of the material and it cannot distinguish between the disorder being static or dynamic. On the other hand, solid-state NMR probes disordered structures in a different manner since it gives a sum of all the local environments and it

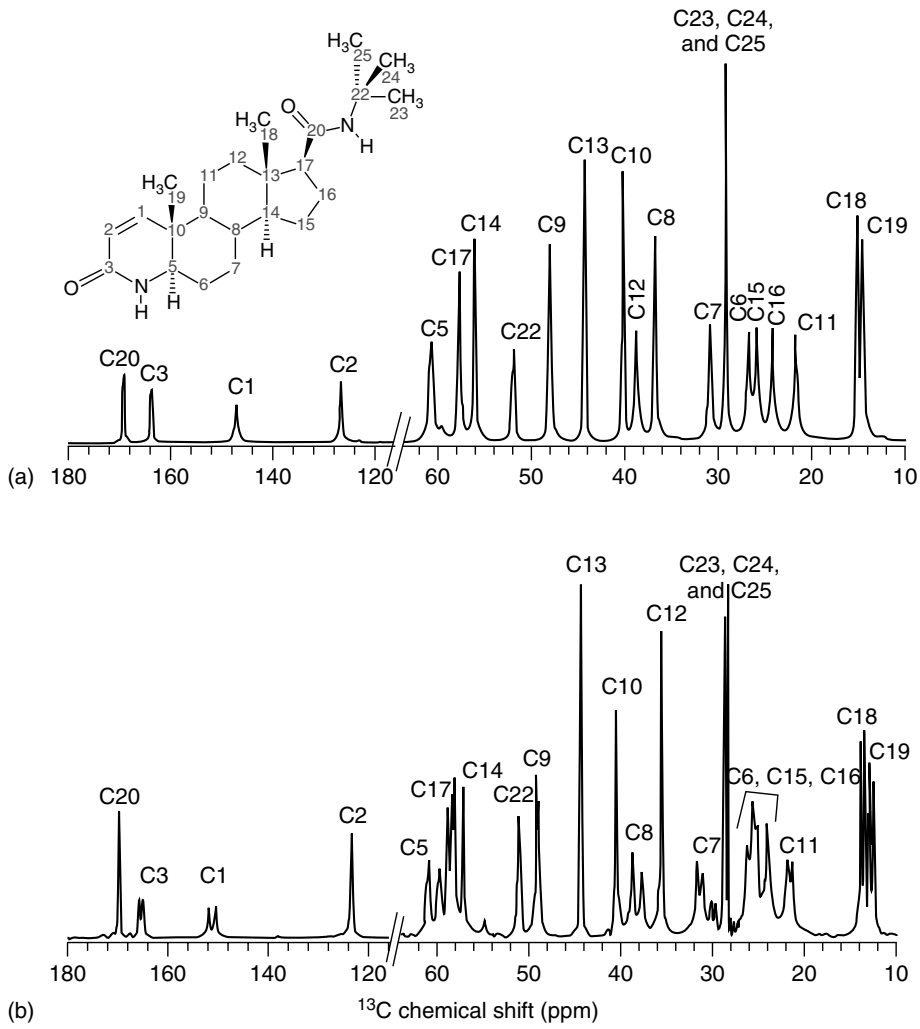


Figure 18.1. ^{13}C CP/MAS NMR spectra of finasteride: (a) form I and (b) form II. (Reproduced from Ref. 6. © Wiley, 1997.)

is sensitive to different time scales. Consequently, solid-state NMR can often reveal some of the important details of disordered structures that XRD tends to miss by taking an average. The remainder of the article illustrates the interplay of solid-state NMR and single-crystal XRD by describing a number of structural studies in which solid-state NMR provided crucial structural information that was inaccessible or difficult to see by single-crystal XRD, leading to a more complete understanding of the structure and dynamics of the materials.

18.4.1 Fluoride-Containing Zeolites

Zeolites that have been synthesized in fluoride-containing media often incorporate fluoride anions into their structures and XRD studies often show the fluoride anions disordered over two (or more) sites. An example is fluoride-containing as-synthesized STF zeolite[9] whose XRD structure in shown in Figure 18.3(a). The XRD structure has eight unique Si sites and the fluoride anions are found disordered over two symmetry-related sites,

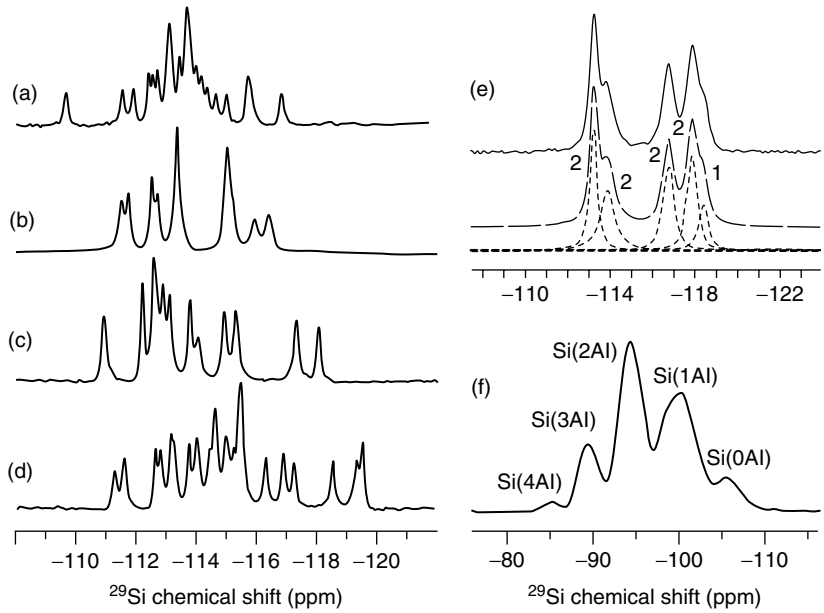


Figure 18.2. ^{29}Si MAS NMR spectra of zeolites. (a–d) Phases changes for high-silica ZSM-5:[7] (a) empty at 403 K, (c) loaded with two molecules *p*-xylene per unit cell, and (d) loaded with eight molecules *p*-xylene per unit cell. (e) As-synthesized high-silica ferrierite with deconvolution by five peaks with indicated relative peak areas. (f) NaY zeolite having Si/Al ratio of 2.6. (Reproduced from Ref. 7. © American Chemical Society, 1990.)

each with 50% occupancy. However, the solid-state ^{29}Si NMR spectrum (Figure 18.3c) indicates the existence of 16 unique Si sites, one of which is in a five-coordinate geometry, as indicated by the unique isotropic chemical shift at 147 ppm, having an additional covalent Si–F bond which leads to the J-coupling doublet that is solely observed in a ^{19}F/^{29}Si INEPT experiment (Figure 18.3d). At the local level, it is likely that only one of the cages in the "fused cage pair" contains a fluorine and the eight unique Si sites become doubled (Figure 18.3b). Solid-state NMR picks this up since it is sensitive to the local structure. The fluorine is distributed over these two sites throughout the crystal structure and since XRD probes the long-range structure, the resulting structure is an average of the two possible configurations of the fused cage pairs.

This averaging of the disorder by XRD leads to the incorrect local geometry of the Si site to which the fluorine is attached: XRD gives a local geometry that is averaged between four-coordinate SiO_4 and five-coordinate SiO_4F. One of the results of this averaging is that the Si–F bond length of 1.87 Å obtained by XRD is longer than it actually is. When the ^{29}Si–^{19}F dipolar coupling constant was measured in a ^{29}Si{^{19}F} REDOR experiment (*see* **Chapter 11**), the resulting estimate of the Si–F bond length was 1.72 ± 0.05 Å (Figure 18.3e). This result provided the impetus for a reexamination of the XRD structure refinement. A disorder between the SiO_4 and SiO_4F geometries was included in the structure refinement, and the expected five-coordinate trigonal bipyramidal geometry was found for SiO_4F, as shown in Figure 18.3(f), with a Si–F bond length of 1.74 Å and elongated Si–O bond lengths.

The fluoride-containing as-synthesized MFI zeolite[10] presents a different case, in which the disorder of the fluorine arises from a dynamic process, rather than a static disorder. The low-temperature ^{29}Si spectrum (Figure 18.4a) indicates the existence of 24 unique Si sites, with the peak near 147 ppm indicating the existence of a five-coordinate SiO_4F unit. However at room temperature (Figure 18.4b), the spectrum indicates 12 unique Si sites in the crystal structure. The broad peak near 125 ppm, halfway between the expected ^{29}Si chemical shifts for four- and five-coordinate environments, suggests a dynamic process involving the fluoride anion.

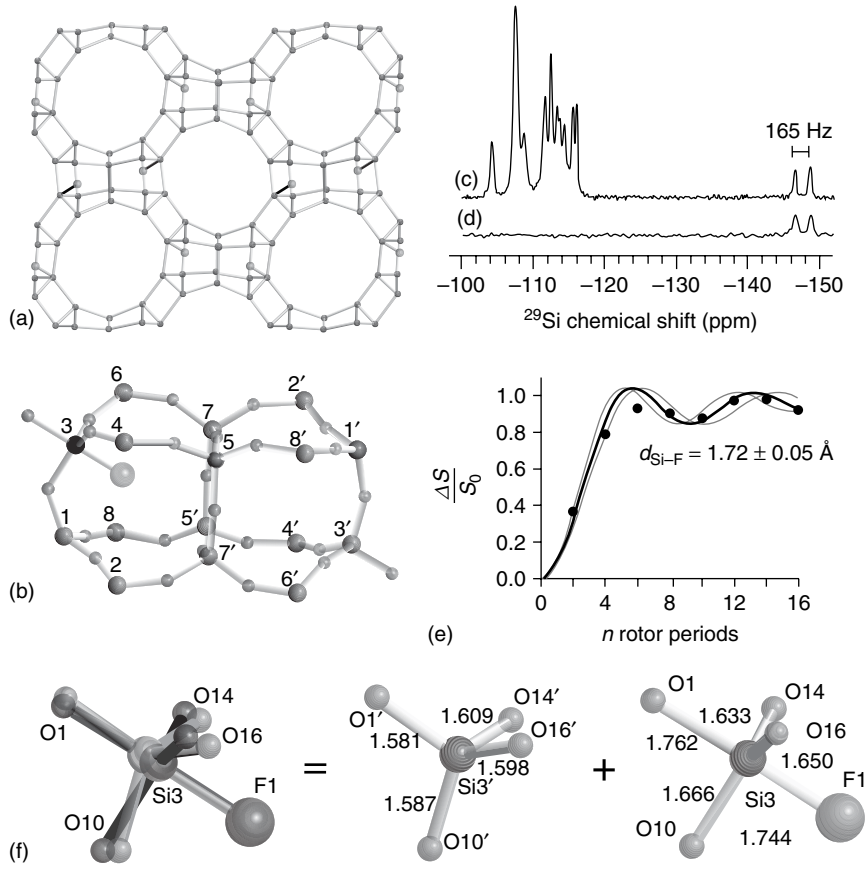


Figure 18.3. Crystal structure and NMR data for fluoride-containing as-synthesized STF zeolite[9]: (a) XRD crystal structure in which the fluorine atoms are disordered over two sites with 50% occupancy. The bridging oxygen atoms and template molecules have been left out. (b) Local structure of one fused cage pair in which only one fluorine site is occupied. (c) ^{1}H/^{29}Si CP/MAS NMR spectrum, (d) ^{19}F/^{29}Si INEPT spectrum, and (e) ^{29}Si{^{19}F} REDOR curve obtained with 15-kHz MAS frequency. (f) Local structure around Si3/Si3′ sites after including SiO_4F/SiO_4 disorder in XRD refinement. (Reproduced from Ref. 9. © American Chemical Society, 2002.)

By employing a 2-D ^{29}Si NMR correlation experiment to assign the peaks and a series of ^{29}Si–^{19}F dipolar recoupling experiments at room temperature, it was possible to locate the time-averaged fluorine position, which had previously been unknown. As depicted in Figure 18.4(c), the solid-state NMR results suggest that at room temperature, the fluorine exchanges between two Si9 sites, causing the Si9 local geometry to alternate between four-coordinate SiO_4 and five-coordinate SiO_4F, and leading to a time-average of the entire crystal structure so that 12 unique Si sites are observed. At low temperature, the ^{29}Si NMR spectrum clearly indicates that the dynamic process has stopped and that the crystal structure has 24 unique Si sites, at least on the local level since there could still be static disorder that could lead to XRD detecting an averaged higher symmetry crystal structure with 12 unique Si sites.

18.4.2 Calixarene Host–Guest Complexes

The structural characterization of the host–guest complex of *t*-butylcalix[4]arene (*t*-BC) with toluene provides another illustrative example of the interplay of solid-state NMR and single-crystal XRD for the

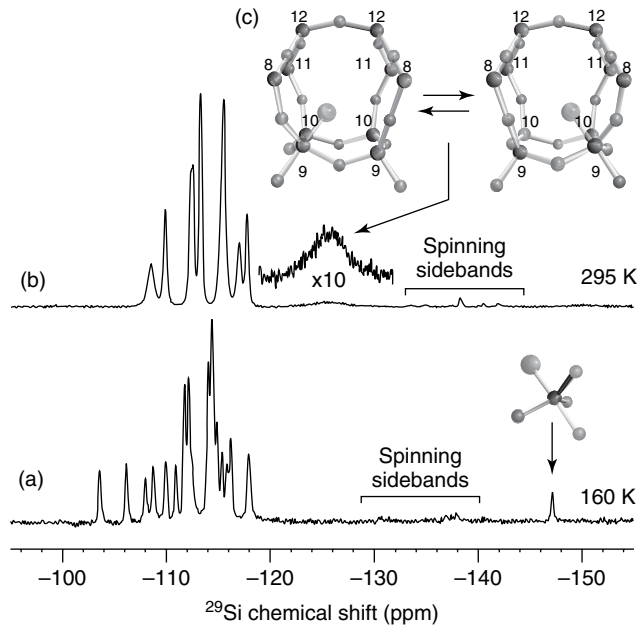


Figure 18.4. $^{1}H/^{29}Si$ CP/MAS NMR spectra of fluoride-containing as-synthesized MFI zeolite[10] at (a) 160 K and (b) 295 K obtained with ~2.5-kHz MAS frequency. (c) At room temperature, the fluorine jumps between "mirror-related" Si9 sites causing these atoms to exchange between SiO_4F and SiO_4 coordination geometries.

characterization of a dynamic and disordered crystal structure.[11,12]

In the initial single-crystal XRD structure of the complex, the toluene molecule was found to lie with its long molecular axis aligned with the fourfold crystallographic axis with its methyl group inserted into the calixarene cavity (Figure 18.5a). However, to satisfy the fourfold crystallographic symmetry of the *P*4/*n* space group, the toluene molecules were disordered over two equivalent sites.

The existence of guest molecule disorder in the structure poses an interesting question: how can toluene, with no more than twofold symmetry, be found in a crystal structure that maintains overall fourfold symmetry? There must be some sort of disorder in the structure, but what is the nature of the disorder? If it is static, then the fourfold symmetry observed by XRD must be a consequence of *space-averaging* of individual toluene–calixerene units of lower symmetry. If the disorder is dynamic, then the higher symmetry must result from *time-averaging* of toluene–calixarene units changing between different lower symmetry forms.

Solid-state NMR provides a method for probing the nature of this structural disorder. Initial solid-state ^{13}C NMR work showed a room-temperature spectrum consistent with the fourfold symmetric structural model, with a single peak for each type of carbon (see Figure 18.5c). ^{2}H NMR experiments on the *t*-BC complex with toluene-d_5 carried out above room temperature (Figure 18.5e) reveal fourfold rotation of the toluene molecules. The disorder observed by XRD at room temperature is therefore clearly due to a dynamic process.

As the temperature is lowered, differential scanning calorimetry indicates that as the guest molecule motions are slowed, the structure undergoes a phase transition to a lower symmetry form around 248 K. Surprisingly, a single-crystal XRD data set collected well below this temperature (150 K) refined to the same fourfold symmetric structure (*P*4/*n* space group) as found previously at room temperature. However, solid-state ^{13}C and ^{2}H NMR, carried out at temperatures below this apparent phase transition, were able to detect changes in the structure and dynamics. The ^{13}C NMR spectrum at 115 K shows an increase in the multiplicity of the carbon resonances (Figure 18.5d), while the ^{2}H NMR spectra at temperatures between 129 and 179 K indicate twofold, rather than fourfold,

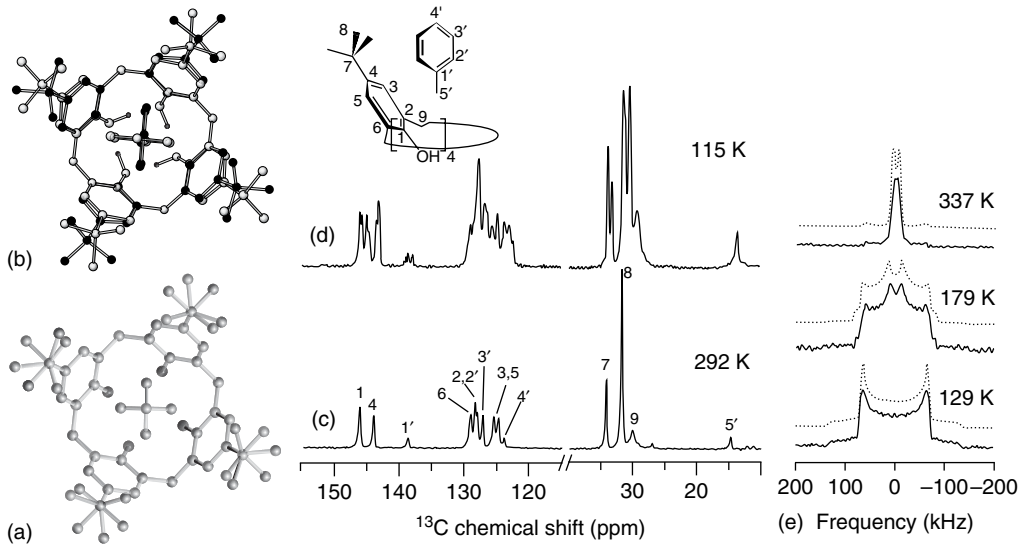


Figure 18.5. Single-crystal XRD crystal structures and solid-state NMR spectra of the tBC-toluene host-guest complex[11,12]: (a) original room-temperature structure and (b) low-temperature structure; (c,d) ^{13}C CP/MAS NMR spectra obtained at 292 and 115 K; and (e) ^{2}H NMR spectra of toluene-d_5/*t*-BC complex (solid lines) with simulated lineshapes (dashed lines) for static aromatic ring (129 K), twofold flips of the aromatic ring (179 K), and fourfold rotation (337 K). (Reproduced from Ref. 12. © Royal Society of Chemistry, 2006.)

rotation about the long axes of the toluene molecules (Figure 18.5e). These spectra indicate that, at the local level of single toluene–calixarene units, the lower temperature leads to local structural units with lowered twofold symmetry. However, since the XRD structure detects fourfold symmetry for the entire crystal, the apparent high crystallographic symmetry found by XRD at 150 K must be a consequence of *space-averaging* of locally twofold symmetric host–guest units.

Armed with this local structure information obtained by solid-state NMR, the XRD refinement of the 150 K data was carried out in the *P*4/*n* space group with a two-component disorder model with each component having distorted twofold local symmetry. The resulting structural model (Figure 18.5b) gives a much-improved agreement factor with the XRD data and resolves the disorder of the *t*-butyl groups. By examining steric effects between the toluene guests and the calixarene *t*-butyl groups, it appears that the two orientations of the toluene molecules are correlated with the two configurations of the calixarene host, as indicated by the light and dark shades in Figure 18.5(b).

The picture of this host–guest structure that emerges from a combined NMR and XRD approach is one of a dynamic structure in which the host and guest motions are correlated. At room temperature, it is likely that as the toluene molecules undergo fourfold rotation in the cavity, the calixarene host "breathes" by switching between the twofold distorted forms. This in-depth understanding of the structure and dynamics of this material was made possible only by employing a combination of the solid-state NMR and single-crystal XRD techniques.

18.4.3 Xenon Absorption in Calixarene

The crystal structures of the low-density guest-free form of *t*-butylcalix[4]arene and its complexes with absorbed xenon were recently investigated by single-crystal XRD and ^{129}Xe solid-state NMR.[13] The unit cell parameters of the complexes with Xe (with low and high loadings) were almost identical to the guest-free form and the observed systematic absences of the reflections were identical, suggesting the same space groups. It was therefore assumed

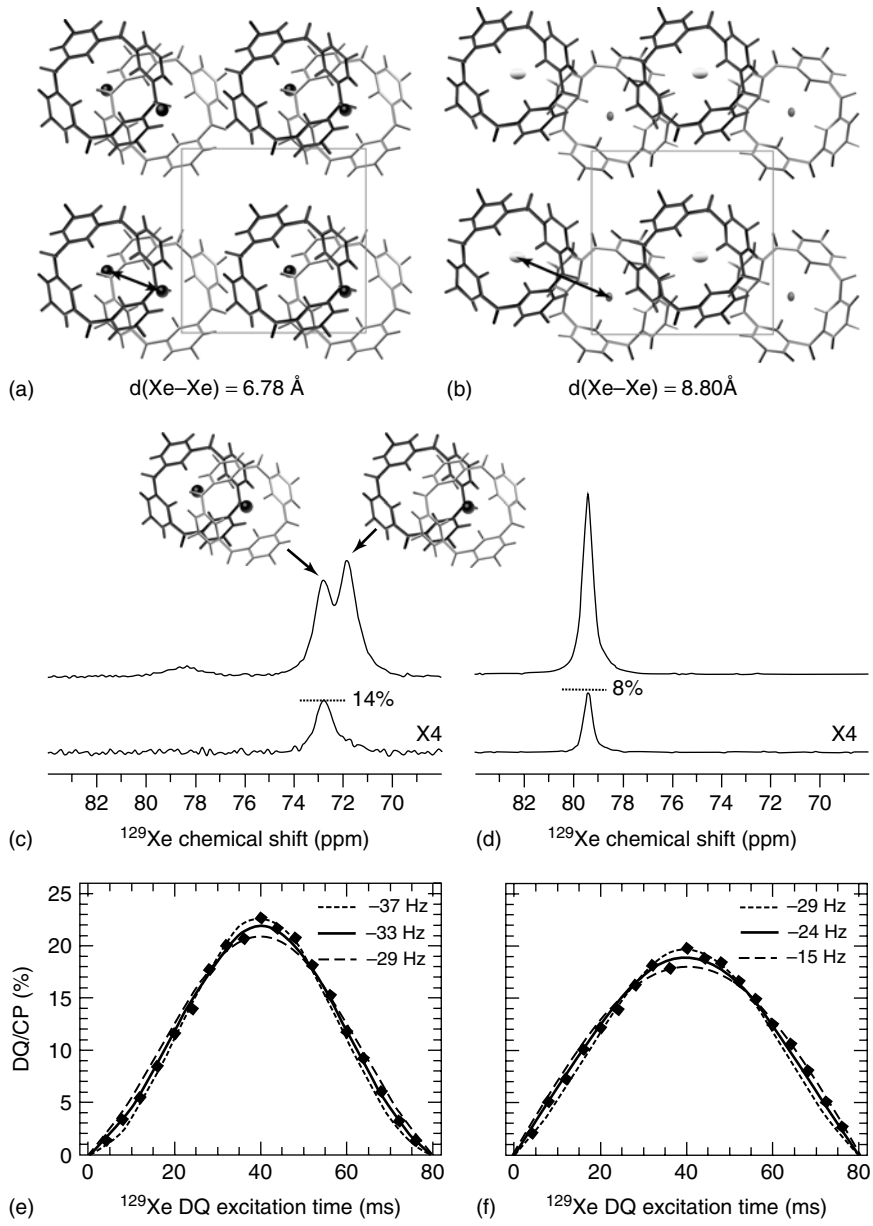


Figure 18.6. Crystal structure and NMR data for tBC with absorbed Xe at (a,c,e) low loading and (b,d,f) high loading. (a,b) Single-crystal XRD structures with closest Xe–Xe distances indicated. The layer of light-grey calixarene molecules point "down", while the adjacent layer of dark-grey calixerene molecules point "up". (c,d) ^{129}Xe CP/MAS NMR spectra (upper) and ^{129}Xe DQ filtered spectra (lower) with indicated DQ filter efficiencies. (e,f) Constant-time ^{129}Xe DQ curves with best-fit ^{129}Xe–^{129}Xe dipolar coupling constants. (Reproduced from Ref. 13. © American Chemical Society, 2008.)

that Xe atoms are absorbed into the cavities of the calixarene host with little change to the host tBC structure. For the sample at low Xe loadings (0.25 Xe atoms per calixarene cavity), this was what was indeed observed: the calixarene molecules in the guest-free and low-loaded structures were almost perfectly superimposable. Since the crystals with higher Xe loading (0.5 Xe atoms per calixarene cavity) showed nearly identical unit cell parameters and the same set of reflections, it was assumed that this structure would be identical to the structure obtained at low loadings, with the exception that the occupancy of the Xe site would be greater. However, this expected structure proved exceedingly difficult to refine, giving poor agreement with the XRD reflection intensity data.

Solid-state ^{129}Xe NMR spectroscopy provided new structural information that allowed the XRD crystal structure determination to move forward. The ^{129}Xe CP/MAS NMR spectra of the low- and high-loaded forms are significantly different (Figure 18.6c,d). The dipolar couplings that exist between Xe atoms in close spatial proximity can be probed by symmetry-based[14] double-quantum (DQ) ^{129}Xe dipolar recoupling experiments. In the guest-free and low-loaded forms, the calixarene molecules are arranged in such a manner that pairs of calixarenes in the adjacent layers form "skewed capsules" (Figure 18.6a). On the basis of the ^{129}Xe DQ NMR spectrum of the low-loaded form (Figure 18.6c), the peaks can be straightforwardly assigned to capsules occupied by one or two Xe atoms, as indicated. From a constant-time ^{129}Xe DQ recoupling curve (Figure 18.6e), the ^{129}Xe–^{129}Xe dipolar coupling constant was estimated to be 33 Hz which corresponds to a Xe–Xe internuclear distance of 6.6 Å, in excellent agreement with the distance in the XRD structure of 6.78 Å. The ^{129}Xe DQ NMR spectrum of the high-loaded form showed a surprising loss of DQ recoupling efficiency (Figure 18.6d) and the constant-time DQ recoupling curve (Figure 18.6f) indicated a weaker dipolar coupling constant of 24 Hz, corresponding to a lengthening of the Xe–Xe distance to approximately 7.4 Å (assuming an isolated spin pair). This result suggested that there was a significant structural rearrangement of the calixarene molecules at higher levels of Xe absorption that caused the Xe atoms to move further apart from one another. With this information, the single-crystal XRD structure determination of the high-loaded form was revisited and a structure was found having quite a dramatic structural rearrangement of the calixarene layers (Figure 18.6b).

It is also worth mentioning that ^{129}Xe NMR spectroscopy, in general, is a powerful technique that complements XRD for the characterization of porous materials.[15,16] For example, a crystal structure determined by XRD may indicate porosity, but there may be concerns about accessibility of the pores or whether or not the pores are occupied by residual solvent molecules. ^{129}Xe NMR provides a method to probe the existence and accessibility of the structure's void space.

18.5 CONCLUSION

In the above discussion of the complementary relationship between NMR and XRD, solid-state NMR tends toward supporting XRD in the process of structure determination. It is worth pointing out the importance of single-crystal XRD in the development of solid-state NMR methodologies, particularly in quantum chemical calculations of NMR parameters. Because NMR parameters are very sensitive to local structure, it is necessary to have the highest quality structural data for performing quantum chemical calculations. No matter how well the calculations work, if the structure is not quite correct, the calculated NMR parameters will be incorrect. For example, in calculations of ^{29}Si shielding tensors in zeolites, using single-crystal XRD structural data over powder XRD data significantly improved, the agreement, with experimentally measured tensors.[17]

Although the examples presented above are far from comprehensive, they do illustrate many of the principles of the interplay between solid-state NMR and single-crystal XRD and diffraction techniques in general. Because the techniques probe the structure differently, they complement each other so that combining the information from single-crystal XRD and solid-state NMR leads to a more complete understanding of the structure of interest.

REFERENCES

1. G. H. Stout and L. H. Jensen, *X-ray Structure Determination – A Practical Guide*, John Wiley & Sons: New York, 1989.
2. C. Giacovazzo, (ed.) *Fundamentals of Crystallography*, Oxford University Press, 1995.

3. D. H. Brouwer, R. J. Darton, R. E. Morris, and M. H. Levitt, *J. Am. Chem. Soc.*, 2005, **127**, 10365.
4. F. Taulelle, *Solid State Sci.*, 2004, **6**, 1053.
5. R. K. Harris, *Analyst*, 2006, **131**, 351.
6. A. Othman, J. S. O. Evans, I. Radosavljevic Evans, R. K. Harris, and P. Hodgkinson, *J. Pharm. Sci.*, 1997, **96**, 1380.
7. C. A. Fyfe, H. Grondey, Y. Feng, and G. T. Kokotailo, *J. Am. Chem. Soc.*, 1990, **112**, 8812.
8. J. Klinowski, S. Ramdas, J. M. Thomas, C. A. Fyfe, and J. S. Hartman, *J. Chem. Soc., Faraday Trans. 2*, 1982, **78**, 1025.
9. C. A. Fyfe, D. H. Brouwer, A. R. Lewis, L. A. Villaescusa, and R. E. Morris, *J. Am. Chem. Soc.*, 2002, **124**, 7770.
10. C. A. Fyfe, D. H. Brouwer, A. R. Lewis, and J.-M. Chézeau, *J. Am. Chem. Soc.*, 2001, **123**, 6882.
11. E. B. Brouwer, G. D. Enright, C. I. Ratcliffe, and J. A. Ripmeester, *Supramol. Chem.*, 1996, **7**, 79.
12. J. A. Ripmeester, G. D. Enright, C. I. Ratcliffe, K. A. Udachin and I. L. Moudrakovski *Chem. Commun.*, 2006, 4986.
13. D. H. Brouwer, I. L. Moudrakovski, K. A. Udachin, G. D. Enright, and J. A. Ripmeester, *Cryst. Growth Des.*, 2008, **8**, 1878.
14. M. H. Levitt, in *Encyclopedia of Nuclear Magnetic Resonance*, eds D. M. Grant and R. K. Harris, (eds), John Wiley & Sons: Chichester, 2002, 165.
15. D. Raftery, *Ann. Rep. NMR Spec.*, 2006, **57**, 208.
16. D. V. Soldatov, I. L. Moudrakovski, E. V. Grachev, and J. A. Ripmeester, *J. Am. Chem. Soc.*, 2006, **128**, 6737.
17. D. H. Brouwer and G. D. Enright, *J. Am. Chem. Soc.*, 2008, **130**, 3095.

Chapter 19

Combined Analysis of NMR & Powder Diffraction Data

Kenneth D. M. Harris and Mingcan Xu

School of Chemistry, Cardiff University, Cardiff CF10 3AT, UK

19.1 Introduction 275
19.2 Introduction to Structure Determination from Powder Diffraction Data 277
19.3 Structure Determination from Powder Diffraction Data Augmented by Information from Solid-State NMR 278
19.4 Structure Determination Directly from Solid-State NMR Data 284
References 286

19.1 INTRODUCTION

Although single-crystal X-ray diffraction is the most powerful technique for the determination of structural information at the atomic level, the requirement for a single-crystal sample of appropriate size and quality imposes a limitation on the scope of this technique. Indeed, many crystalline solids can be prepared only as microcrystalline powders, and are therefore not suitable for investigation by single-crystal X-ray diffraction techniques. To establish the structural properties of such materials, the most direct approach is to use powder X-ray diffraction, although it is important to emphasize that the process of carrying out structure determination from powder X-ray diffraction data is substantially more challenging than that from single-crystal X-ray diffraction data. Nevertheless, as many important materials can be prepared only as microcrystalline powders, the availability of reliable procedures for carrying out structure determination directly from powder X-ray diffraction data has the potential to make considerable impact in several areas of structural sciences. Therefore, much activity has been devoted in recent years to the development and application of new techniques and strategies in this field. Although these techniques are also generally applicable for structure determination using powder neutron diffraction data, they have been applied much more extensively in the case of powder X-ray diffraction data. Therefore, we focus here primarily on structure determination from powder X-ray diffraction data.

Diffraction techniques and solid-state NMR techniques are complementary approaches for probing structural properties of solids, and provide complementary types of information (a good account of the comparisons and contrasts between the types of information provided by solid-state NMR and diffraction techniques is given in **Chapter 1**). In view of the complementarity between these techniques, there are considerable potential benefits to be gained by employing them in tandem in the structural characterization of solids.

Diffraction data from a crystalline solid provide a reciprocal-space representation of the crystal

NMR Crystallography Edited by Robin K. Harris, Roderick E. Wasylishen and Melinda J. Duer © 2009 John Wiley & Sons, Ltd. ISBN: 978-0-470-69961-4

structure, but carrying out Fourier transformation to give a direct-space representation of the crystal structure is nontrivial because of the absence of phase information in the experimental diffraction data. Thus, structure determination from experimental diffraction data is reliant upon techniques that overcome the "phase problem," allowing the crystal structure to be determined from knowledge of the experimental diffraction intensities alone. In the case of single-crystal X-ray diffraction data, the experimental diffraction intensities can, in general, be measured straightforwardly and with a high degree of accuracy. However, in the case of powder X-ray diffraction data, in which diffraction intensity is recorded as a function of a single reciprocal-space variable (the diffraction angle 2θ), the three-dimensional diffraction data are essentially "compressed" into one dimension. As a consequence, there is usually considerable overlap of peaks in the powder X-ray diffraction pattern, which obscures information on the positions and intensities of the diffraction maxima. The intrinsic difficulty in obtaining reliable intensity information from powder X-ray diffraction data can impede, or in many cases prohibit, the ability to carry out successful structure determination. The peak overlap problem is less severe for structures with small unit cells and high symmetry (as there is only a low density of peaks in the powder X-ray diffraction pattern in such cases). But for most organic molecular solids, the problem of peak overlap can be particularly severe as such materials typically have large unit cells and low symmetry, and hence a high density of peaks in the powder X-ray diffraction pattern. In such cases, the process of carrying out structure determination from powder X-ray diffraction data can become correspondingly more challenging.

In contrast to the reciprocal-space representation provided by diffraction data, experimental solid-state NMR data can, in general, be interpreted directly in terms of specific structural features in direct space, as the NMR spectrum is influenced by the local structure in the vicinity of the nucleus under investigation. Thus, in general, specific features of a solid-state NMR spectrum can be interpreted directly in terms of specific features in the crystal structure, and it is often possible to deduce aspects of structural information directly from inspection of the NMR spectrum, or from straightforward analysis of the NMR data. This ability of solid-state NMR to provide direct insights regarding structural properties serves a particularly valuable role when solid-state NMR data are used to assist the process of structure determination from diffraction data (*see* **Chapter 28**). In the case of diffraction data, on the other hand, the Fourier transform relationship between the experimental data and the crystal structure is such that individual features in a diffraction pattern have no direct interpretation in terms of specific features in the structure – in essence, knowledge of specific structural features (for example, structural properties of the type that might be deduced directly from solid-state NMR data) emerges only once the complete structure is actually determined.

In the section "Introduction to Structure Determination from Powder Diffraction Data," we give an elementary introduction to current techniques and strategies for carrying out structure determination from powder X-ray diffraction data, focusing in particular on the techniques that have been developed in recent years for structure solution of organic molecular solids, as it is these techniques that have benefited most from the utilization of information derived from solid-state NMR data. The remainder of the article then surveys two different aspects of the combined application of powder X-ray diffraction and solid-state NMR in structure determination, as follows.

In the section "Structure Determination from Powder Diffraction Data Augmented by Information from Solid-State NMR," we provide a range of examples that illustrate the uses of solid-state NMR in providing information to assist the process of structure determination from powder X-ray diffraction data. Although considerable progress has been made in recent years, structure determination from powder X-ray diffraction data is not yet a routine technique (unlike the relatively automated nature of structure determination from single-crystal X-ray diffraction data), and therefore specific aspects of information provided by other experimental and computational techniques can play a valuable role in the structure determination process. Among the techniques that have been utilized in this regard, solid-state NMR has been particularly important for providing information on a range of structural issues, including the number of molecules in the asymmetric unit, an assessment of the phase purity (including polymorphic purity) of the sample, evidence for the existence of disorder (dynamic or static disorder) in the structure, and information regarding molecular conformation or specific interatomic interactions (*see* **Chapter 22**).

In the section "Structure Determination Directly from Solid-State NMR Data," we consider advances that have been made in recent years toward ab initio crystal structure determination from solid-state NMR data. Again, success in this task can be enhanced considerably by combining such analysis with information from powder X-ray diffraction data for the material of interest. For example, the powder X-ray diffraction data may be used to determine the unit cell dimensions and crystal symmetry, and/or to provide independent validation of the quality of the final structure determined from the solid-state NMR data (for example, to verify that the structure determined from the NMR data is in full agreement with the powder X-ray diffraction data).

19.2 INTRODUCTION TO STRUCTURE DETERMINATION FROM POWDER DIFFRACTION DATA

Crystal structure determination from diffraction data generally involves three stages: (i) unit cell determination and space group assignment, (ii) structure solution, and (iii) structure refinement. The aim of *structure solution* is to obtain an initial approximation to the structure, using the unit cell and space group determined in the first stage, but starting with no knowledge of the actual arrangement of atoms or molecules within the unit cell. If the structure solution is a sufficiently good approximation of the true structure, a good quality structure can then be obtained by *structure refinement*. For powder X-ray diffraction data, structure refinement can be carried out fairly routinely using the Rietveld profile refinement technique, and standard indexing procedures are available for carrying out unit cell determination. In general, structure solution represents the most challenging stage of the structure determination process, and in the case of structure determination from powder X-ray diffraction data, the most important technique developments in recent years have involved advances in structure solution methodology.[1–10] Techniques for carrying out structure solution from powder X-ray diffraction data can be subdivided into *traditional* approaches and *direct-space* approaches.

The *traditional* approach follows a close analogy to the analysis of single-crystal X-ray diffraction data. In this approach, the integrated intensities of individual diffraction maxima are extracted directly from the powder X-ray diffraction pattern to generate a single-crystal-like dataset, which is then used in the types of structure solution calculation that are used for single-crystal X-ray diffraction data. As discussed above, however, peak overlap in the powder X-ray diffraction pattern can limit the reliability of the extracted intensities and can therefore lead to difficulties in subsequent attempts to solve the structure using these intensity data. As noted above, such problems may be particularly severe in cases of large unit cells and low symmetry, as encountered for most organic molecular solids.

The *direct-space* approach,[11] on the other hand, handles the structure solution process as a global optimization problem. In the direct-space approach, trial structures are generated in direct space, independently of the experimental powder X-ray diffraction data, and the quality of each trial structure is assessed by direct comparison between the powder X-ray diffraction pattern calculated for the trial structure and the experimental powder X-ray diffraction pattern. In this regard, we emphasize that the powder X-ray diffraction pattern of any trial structure can be calculated automatically (in contrast, the reverse process is not automatic because of the "phase problem"). Comparison of experimental and calculated powder X-ray diffraction patterns is quantified using an appropriate figure of merit. In several implementations of the direct-space strategy, the weighted powder profile R-factor R_{wp} (the R-factor normally employed in Rietveld refinement) has been used, and has the advantage that it considers the entire digitized intensity profile point by point rather than the integrated intensities of individual diffraction maxima. Thus, the use of R_{wp} takes peak overlap implicitly into consideration. Furthermore, R_{wp} uses the digitized powder X-ray diffraction data directly "as measured", without further manipulation of the type required when integrated peak intensities are extracted from the experimental powder X-ray diffraction pattern.

The direct-space strategy handles structure solution as a global optimization problem, with the aim of finding the trial structure that corresponds to optimal agreement (i.e., lowest R_{wp}) between calculated and experimental powder X-ray diffraction patterns, and is equivalent to exploring a hypersurface $R_{wp}(\Gamma)$ to find the global minimum, where Γ represents the set of variables that define the trial structures. Conventionally, the structural variables in the set Γ comprise, for each molecule in the asymmetric unit, the position $\{x, y, z\}$ and orientation $\{\theta, \phi, \psi\}$ of the whole

molecule, and a set of n variable torsion angles $\{\tau_1, \tau_2, \ldots, \tau_n\}$ to define the molecular conformation. An important feature of the direct-space strategy is that it incorporates reliable prior knowledge of molecular geometry (i.e., bond lengths, bond angles, geometries of well-defined structural units such as phenyl rings, etc.) directly within the structure solution calculation (in contrast, the traditional approach for structure solution generally does not exploit prior knowledge of molecular geometry). In principle, any technique for global optimization may be used to find the lowest point on the $R_{wp}(\Gamma)$ hypersurface, and much success has been achieved using Monte Carlo/Simulated Annealing and Genetic Algorithm techniques in this field. In addition, grid search and differential evolution techniques have also been employed.

In the case of organic molecular solids, structure determination from powder X-ray diffraction data is nowadays carried out extensively, mainly by employing direct-space techniques for structure solution (although there have also been several reports of successful structure solution of such materials using the traditional approach). Indeed, the recent upsurge of activity in this field has coincided with the development of the direct-space strategy for structure solution. Although such techniques are now readily accessible and fairly straightforward to apply, their application is still far from routine, and it is essential that the structural results are subjected to adequate scrutiny before the structure can be confidently assigned as correct. Thus, in carrying out structure determination from powder X-ray diffraction data, it is important (i) to validate the use of an appropriate structural model in the direct-space structure solution calculation (for example, to establish the correct representation of molecular geometry to be used in the calculation and to establish the correct number of molecules in the asymmetric unit), and (ii) to validate the final structure obtained from the Rietveld refinement calculation. In both aspects, utilization of information obtained from other experimental and computational techniques can be particularly important, and as highlighted in the section "Structure Determination from Powder Diffraction Data Augmented by Information from Solid-State NMR," solid-state NMR techniques have proven to be particularly useful in this regard.

Finally, we note that the structure determined from diffraction techniques represents a space-averaged and time-averaged description of the actual structure of the crystalline material under investigation, and therefore diffraction techniques do not provide direct information on the actual distribution of local structural features about the averaged description, nor any direct information on the time-dependence of the structure (i.e., dynamic properties). The complementarity of solid-state NMR with regard to both of these aspects should be noted, as solid-state NMR techniques represent both a valuable source of information on local structural properties and a powerful probe of the dynamic properties of solids across a wide range of motional timescales.

19.3 STRUCTURE DETERMINATION FROM POWDER DIFFRACTION DATA AUGMENTED BY INFORMATION FROM SOLID-STATE NMR

Solid-state NMR can play a particularly important role in regard to direct-space structure solution, as it can provide insights on specific direct-space aspects of the structure, including the tautomeric form of the molecule, the number of molecules in the asymmetric unit, the question of whether the molecules occupy general positions or special positions, direct evidence for the existence of specific interactions (for example hydrogen bonds), quantitative information on specific interatomic distances, and a priori insights on the existence of disorder within the structure (*see* **Chapter 22**). Information on several of these structural aspects can be important in setting up the correct structural model for use in a direct-space structure solution calculation, or in validation of the final structural results obtained from Rietveld refinement.

First we consider the task of setting up a suitable structural model for use in direct-space structure solution calculations. In general, the identity of the molecule(s) present in the structure and the composition (for example in the case of a solvate or cocrystal phase) may be established readily from the application of a range of analytical techniques, including high-resolution solid-state NMR. Another important issue concerns details of molecular geometry, recognizing that in some cases, the molecule may be able to adopt different tautomeric forms. The structure determination of red fluorescein[12] from powder X-ray diffraction data represents an early example of the use of solid-state NMR in conjunction with direct-space structure solution. In this case, high-resolution solid-state ^{13}C NMR data were used

to distinguish the tautomeric form of the molecule present in the crystal structure. Clearly, the use of a geometrically correct representation of the molecule in direct-space structure solution calculations (including correct assignment of the tautomeric form) may be crucial for achieving successful structure solution.

Second, we consider the question of the number of molecules in the asymmetric unit. Following unit cell determination, the number of molecules in the unit cell can generally be deduced straightforwardly from density considerations, but, in general, such information does not lead to a unique assignment of the number of molecules in the asymmetric unit, nor to a unique assignment of the space group. For example, in the case of a monoclinic system with four molecules in the unit cell deduced from density considerations and with no evidence of systematic absences from analysis of peak intensities in the indexed powder X-ray diffraction pattern, the following scenarios cannot be distinguished: space group *P*2 or *Pm* with two molecules in the asymmetric unit, or space group *P*2/*m* with one molecule in the asymmetric unit. In such cases, high-resolution solid-state NMR can often provide valuable independent information on the number of molecules in the asymmetric unit, based on the fact that, for example, the high-resolution solid-state ^{13}C NMR spectrum of an organic material should contain one peak for each crystallographically distinguishable carbon atom in the structure (although we note that, in practice, the actual number of *observed* peaks may be less than this number due to accidental peak overlap). Thus, following the assignment of each peak in the ^{13}C NMR spectrum to a specific carbon environment within the molecule, it is generally straightforward to assess whether there are one, two, or more molecules in the asymmetric unit, or only a fraction of the molecule (indicating that the molecule resides on a special position).

As an example,[13] the high-resolution solid-state ^{13}C NMR spectrum (Figure 19.1) of the 1 : 1 cocrystal formed between benzoic acid (BA) and pentafluorobenzoic acid (PFBA) was found to contain two peaks for the carbon atom of the carboxylic acid group of BA and two peaks for the carbon atom of the carboxylic acid group of PFBA, leading to the conclusion that the asymmetric unit comprises two molecules of BA and two molecules of PFBA. In this case, systematic absences in the powder X-ray diffraction pattern indicated that the structure is

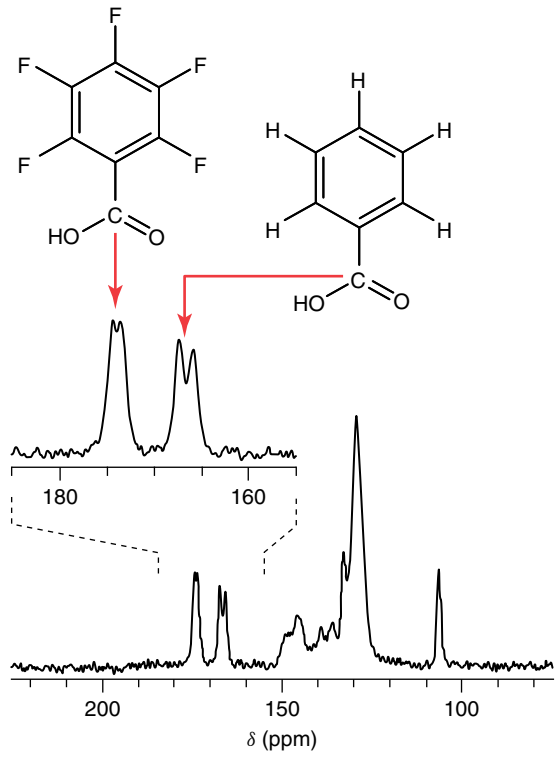


Figure 19.1. High-resolution solid-state ^{13}C NMR spectrum of the 1 : 1 cocrystal containing benzoic acid (BA) and pentafluorobenzoic acid (PFBA). The two peaks at approximately 174 ppm represent the carboxylic acid group of PFBA and the two peaks at approximately 167 ppm represent the carboxylic acid group of BA, indicating that there are two molecules of BA and two molecules of PFBA in the asymmetric unit.

C-centered and has a *c*-glide plane, and density considerations suggested that there are eight molecules of BA and eight molecules of PFBA in the unit cell. The solid-state NMR data, therefore, pointed toward *Cc* as the correct space group (with two molecules of BA and two molecules of PFBA in the asymmetric unit), rather than *C*2/*c* (with one molecule of BA and one molecule of PFBA in the asymmetric unit).

An example of space group assignment in the case of an inorganic material concerns the low-temperature phase of ZrP_2O_7.[14] In this case, the application of 2-D double quantum (DQ) and 1-D ^{31}P NMR techniques led to the assignment of 27 distinct ^{31}P resonances, assigned as 13 $P_2O_7^{4-}$ units with two inequivalent phosphorus sites and one $P_2O_7^{4-}$ unit with two equivalent phosphorus sites. On the basis of this

information, the space group was assigned as orthorhombic *Pbca*, leading to the conclusion (further supported by excellent fits to powder X-ray and neutron diffraction data using this space group) that a previous assignment of the space group as cubic $Pa\bar{3}$ was wrong.

An example in which high-resolution solid-state ^{13}C NMR provided evidence for a molecule residing on a special position was encountered in the structure determination of an early-generation dendrimeric material[15] (tetrakis [(3,5-dimethoxybenzyloxy)methyl] methane; TDMM) (Figure 19.2). In this case, the ^{13}C NMR data supported the assignment (from density and space group considerations) that the molecule is located on a crystallographic twofold rotation axis, with the asymmetric unit comprising half the molecule. Structure determination of a new polymorph (β-phase) of the latent pigment DPP-Boc[16] from powder X-ray diffraction data also relied on information from high-resolution solid-state ^{13}C NMR, which suggested that the asymmetric unit comprises half the DPP-Boc molecule. Thus, the direct-space structure solution calculation in space group $P\bar{1}$ was carried out with the molecular inversion center constrained to reside on a crystallographic inversion center, with variation of the orientation of the whole molecule around this pivot position and variation of four torsion angles within the *t*-butoxycarbonyl group.

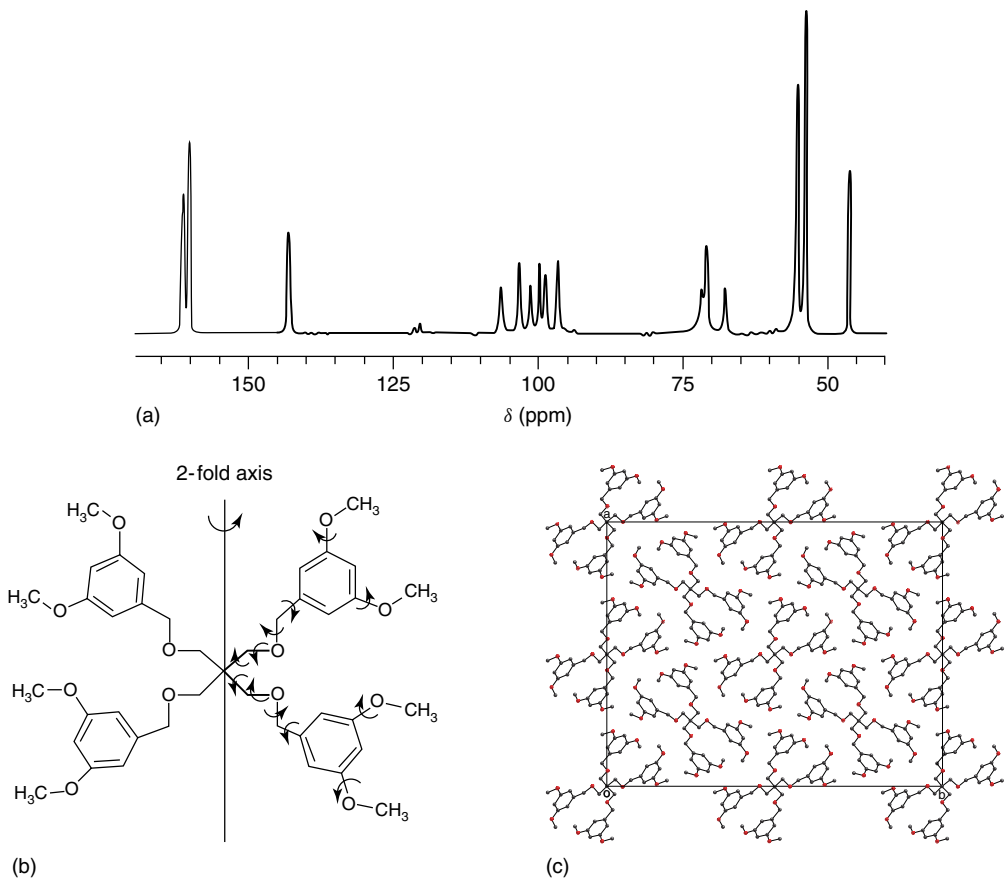


Figure 19.2. (a) High-resolution solid-state ^{13}C NMR spectrum of the early-generation dendrimeric material TDMM, which is consistent with the molecule being located on a twofold rotation axis in the crystal structure as shown in (b). (c) The crystal structure of TDMM determined from powder X-ray diffraction data, viewed along the *c* axis (hydrogen atoms are omitted for clarity).

Another situation in which solid-state NMR may provide important structural insights concerns the direct detection of disorder (dynamic or static disorder) in the crystal structure. In cases of severe disorder, it would generally be necessary to incorporate an appropriate description of the disorder in both the structure solution and structure refinement stages; thus the disorder would need to be incorporated into the structural model used in direct-space structure solution calculations, and a good fit would be obtained in the Rietveld refinement only for a structure solution that embodied an accurate description of the disorder. However, if the disorder concerns a sufficiently localized part of the structure, it may be possible to obtain a reasonable (but not perfect) Rietveld fit using an ordered structural model, which may then be improved by modifying the model to incorporate a description of the disorder. This situation was encountered in structure determination of the β-polymorph of *p*-formyl-*trans*-cinnamic acid from powder X-ray diffraction data[17] (Figure 19.3). The structure was solved and refined as an ordered structure, leading to a good quality of fit in the Rietveld refinement ($R_{wp} =$ 3.27%). However, the high-resolution solid-state ^{13}C NMR spectrum of this material showed evidence for disorder of the formyl group (with the remainder of the structure ordered). Thus, the ^{13}C NMR spectrum has two peaks for the ^{13}C site in the formyl group,[18] whereas all other ^{13}C sites in the molecule give just a single peak. Integration of the two peaks for the formyl group suggests that there are two components with relative populations approximately 69 and 31%. In subsequent Rietveld refinement, the disorder of the formyl group was modeled in terms of two orientations (with the plane of the formyl group in the same plane as the aromatic ring in each case, but differing by 180° rotation about the C–C bond linking the formyl group and the aromatic ring). Rietveld refinement of the disordered model gave an improved fit ($R_{wp} = 2.87\%$), with refined occupancies for the two orientations of the formyl group of 59 and 41%, in relatively close agreement with the relative populations established from the solid-state ^{13}C NMR data. In this case, it is almost certain that, if evidence of disorder had not been obtained from the solid-state ^{13}C NMR data, the Rietveld refinement obtained for the ordered model would probably have been considered to provide an acceptable fit to the experimental powder X-ray diffraction data, and thus the existence of the disorder in this case may not have been apparent from consideration of the powder X-ray diffraction data alone.

Next, we consider the use of solid-state NMR data to establish information on specific interactions or interatomic distances in the crystal structure (*see* **Chapter 22**), in conjunction with structure determination from powder X-ray diffraction data. First, we consider the question of whether an OH group is involved in O–H···O hydrogen bonding, which may be particularly pertinent when an O···O distance in a structure is found to correspond to a relatively long hydrogen bond, and recalling that the H atom of an OH group is generally not located accurately from powder X-ray diffraction data (due to the low X-ray scattering power of hydrogen). A useful technique for assessing this issue is solid-state ^{2}H NMR, carried out on the material in which the OH group in question is deuterated (i.e., OD). The ^{2}H NMR quadrupole coupling constant (χ) can be determined directly from the solid-state ^{2}H NMR spectrum and is very sensitive to the geometry of O–D···O hydrogen bonds. Thus, well-defined correlations between the magnitude of χ and D···O distance have been established.[19,20] In the structure determination of 1-hydroxymethyl-2,4,6-trimethoxybenzene from powder X-ray diffraction data,[21] an O–H···O hydrogen bond involving the hydroxyl group as the hydrogen bond donor was observed to have a relatively long O···O distance (3.18 Å), and additional verification was sought on the validity of this observation. For this purpose, the ^{2}H NMR spectrum was recorded for the material selectively deuterated in the hydroxyl group, leading to a value of $\chi = 240$ kHz (and asymmetry parameter $\eta = 0.075$) for this deuteron. This value of χ is within the range established for OD groups engaged in O–D···O hydrogen bonding interactions, and is consistent with the existence of a long hydrogen bonding interaction, as observed in the crystal structure.

Another example concerns the application of solid-state ^{13}C and ^{15}N NMR techniques, in conjunction with powder X-ray diffraction, in structural studies of anhydrous theophylline.[22] In addition to supporting the assignment that there is one molecule in the asymmetric unit, ^{15}N NMR data provided crucial evidence to distinguish two structures that could not be unambiguously discriminated on the basis of the powder X-ray diffraction analysis, with one structure containing N–H···O hydrogen

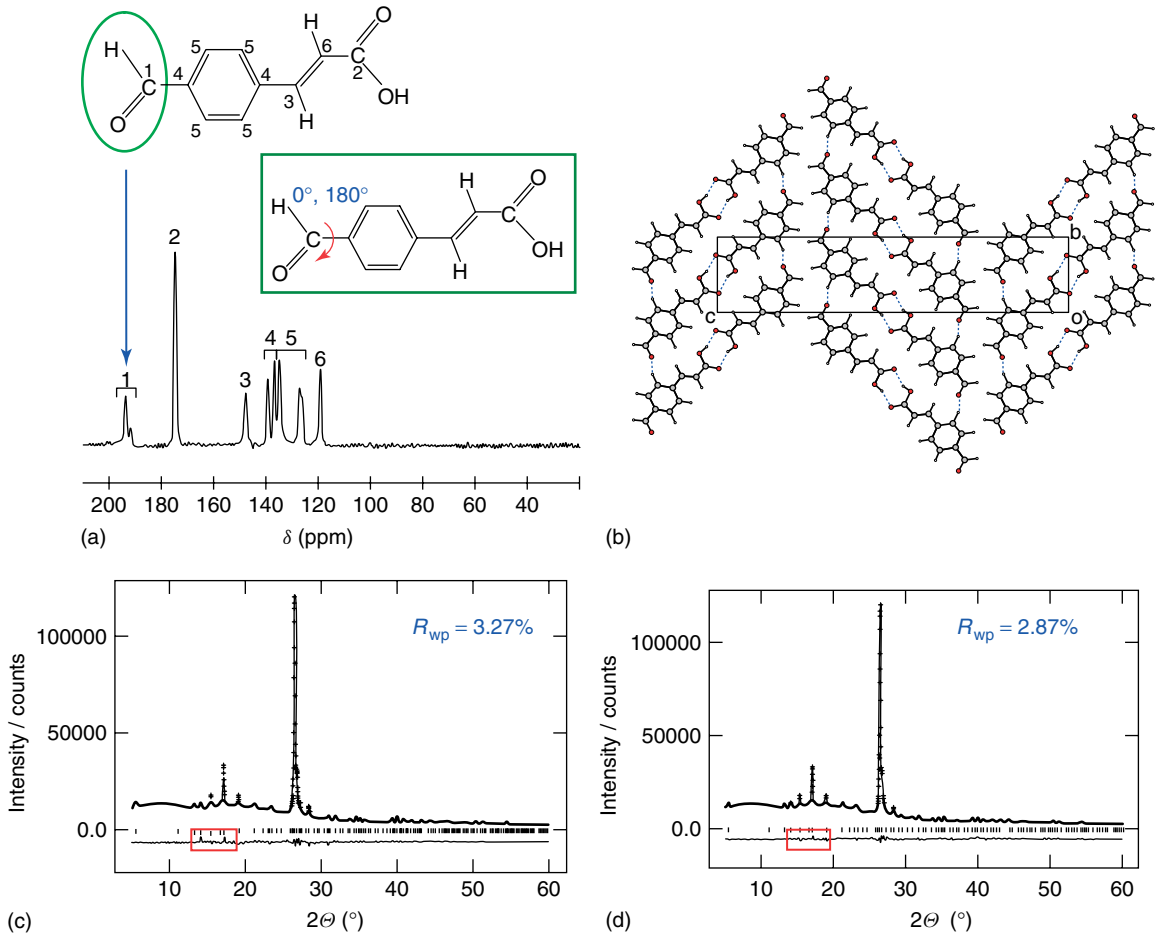


Figure 19.3. (a) High-resolution solid-state ^{13}C NMR spectrum recorded for the β polymorph of *p*-formyl-*trans*-cinnamic acid with the proposed disorder of the formyl group shown in the inset. (b) Crystal structure of the β-polymorph of *p*-formyl-*trans*-cinnamic acid determined from powder X-ray diffraction data, viewed along the *a* axis and with only the major orientation of the formyl group shown. Powder X-ray diffraction profiles for the Rietveld refinement of the β-polymorph of *p*-formyl-*trans*-cinnamic acid are shown in (c) and (d) for the ordered model of the formyl group ($R_{wp} = 3.27\%$) and the disordered model of the formyl group ($R_{wp} = 2.87\%$), respectively. Apart from the description of the order/disorder of the formyl group, all other aspects of the refinement calculations were the same for (c) and (d). The red boxes highlight the region of the powder X-ray diffraction pattern corresponding to the greatest improvement in the quality of fit for the disordered model.

bonding and the other structure containing N–H···N hydrogen bonding. However, comparison between computed isotropic ^{15}N NMR chemical shifts (calculated for small clusters containing the N–H···O and N–H···N hydrogen bonding arrangements) and experimentally observed isotropic ^{15}N NMR chemical shifts was shown to favor the structure with N–H···N hydrogen bonding.

For such cases in which structural questions concern details of hydrogen bonding arrangements, it is clear that powder neutron diffraction may also serve as a complementary technique to powder X-ray diffraction data, as illustrated in the structure determination of ammonium cyanate,[23] in which solid-state ^{15}N NMR was also employed as part of a multitechnique investigation.

Various solid-state NMR approaches have been used in conjunction with structural studies of polymorphs of 2-methyl-4-nitroacetanilide.[24,25] In this work, a number of structural issues were assessed directly from the solid-state NMR data, with a view to using such information to assist the process of direct-space structure solution from powder X-ray diffraction data. The NMR techniques employed in this work included high-resolution ^{1}H (exploiting fast magic angle sample spinning), ^{13}C and ^{15}N NMR. In particular, the ^{1}H NMR studies,[24] in conjunction with DFT calculations (*see* **Chapter 3**), explored the opportunities to exploit correlations between computed isotropic ^{1}H chemical shifts and N–H bond lengths, to allow the N–H bond length in the "white polymorph" to be determined from the experimental ^{1}H NMR data. Subsequent studies[25] established the dependence of computed isotropic ^{13}C chemical shifts (from quantum mechanical calculations, including calculations on the periodic solid) on the value of a key torsion angle within the molecule, allowing the value of the torsion angle in the crystal structure to be established with a reasonable degree of confidence from the values of isotropic ^{13}C chemical shifts observed in the experimental solid-state ^{13}C NMR spectrum. In principle, once equipped with such information, the process of structure solution from powder X-ray diffraction data could be facilitated by constraining the torsion angle in question, thus reducing the number of structural variables required in the direct-space structure solution calculation. Nevertheless, it is important to advocate caution before biasing structure solution calculations in this way, unless absolutely necessary to do so. Thus, while such structural constraints might be valuable in the case of complex structural problems that challenge the limits of direct-space structure solution methodology, it should be noted that the particular example studied (for which the molecular geometry is defined by only three variable torsion angles) should be readily solvable by modern direct-space algorithms without the need to apply any conformational constraints during the structure solution calculation.

Another approach to reduce the dimensionality of variable space in direct-space structure solution calculations from powder X-ray diffraction data is to utilize the direct information on interatomic distances that may be obtained from REDOR NMR measurements, and then to use this information as a means of constraining the molecular conformation during direct-space structure solution calculations.[26] In this work, a sample of cimetidine (of known crystal structure), selectively ^{15}N-labelled in one of the six nitrogen sites of the molecule, was prepared, and REDOR measurements were carried out to establish couplings (and hence distance information) between the ^{15}N-labeled site and natural-abundance ^{13}C sites in the molecule. A number of intramolecular ^{13}C–^{15}N distances determined in this way were used to constrain the molecular conformation in an MD simulation, yielding a conformation close to that present in the known crystal structure. When the molecular conformation established from the solid-state NMR and MD studies was used in direct-space structure solution calculations, the correct structure solution was located more efficiently than when the molecular conformation was handled in the normal manner with variation of all torsion angles. Again, this work primarily serves to demonstrate the potential of methodology that could be valuable in tackling more complex structural problems, while recognizing that the particular example considered in this work could be tackled successfully by allowing full conformational flexibility in the structure solution calculation without the need to constrain the molecular conformation.

Another example of the use of solid-state NMR data to gain insights on hydrogen bonding independently of diffraction data concerns Form II of cortisone acetate,[27] which has one molecule in the asymmetric unit. Cortisone acetate has one hydrogen bond donor (OH group) but four potential hydrogen bond acceptors (C=O groups), and analysis of ^{13}C chemical shift information (including anisotropies and asymmetries) was exploited to assign the specific C=O group that is engaged in (intermolecular) hydrogen bonding with the OH group. Clearly, information of this type may be potentially useful in advance of carrying out structure determination from powder X-ray diffraction data.

Although the examples discussed above have focused on cases of organic molecular solids, we emphasize that solid-state NMR techniques can play an important role in the process of structure determination of many other types of material from powder X-ray diffraction data. An example from the field of extended framework materials concerns the large pore, pure silica polymorph ITQ-4.[28] Laboratory powder X-ray diffraction data were used initially to determine the unit cell parameters, and high-resolution solid-state ^{29}Si

NMR was used to establish that there are four different silicon environments in the asymmetric unit. High-resolution synchrotron powder X-ray diffraction data were then used to solve the structure using the traditional approach, giving the positions of all the framework atoms, which were used as the starting structural model in a Rietveld refinement. This structure represented a new zeolite with an exceptionally large pore volume.

In general, the traditional approach for structure solution from powder X-ray diffraction data has been applied widely for structure determination of inorganic materials, but direct-space strategies can provide a viable alternative for such materials in certain cases. An example concerns structure solution of the γ-phase of $Al_2(CH_3PO_3)_3$, which proved to be difficult using the traditional approach, and a direct-space approach was used instead.[29] For this material, solid-state ^{13}C, ^{31}P and ^{27}Al NMR studies were carried out, indicating that the asymmetric unit contains two inequivalent aluminum sites (with tetrahedral and fivefold coordination) and three inequivalent CH_3PO_3 units, representing a total of five structural fragments in the direct-space structure solution calculation. The final structure determined in this work, shown in Figure 19.4, was found to be lamellar, with the methyl groups protruding from the ends of each sheet.

19.4 STRUCTURE DETERMINATION DIRECTLY FROM SOLID-STATE NMR DATA

In this section, we discuss progress that has been made in recent years toward ab initio crystal structure determination from solid-state NMR data, exploiting advances in solid-state NMR techniques that allow quantitative geometric data to be established. In the examples discussed below, which mainly focus on structure determination of zeolites and organic materials, the solid-state NMR data alone are insufficient to enable complete structure determination to be carried out, and it has been essential to incorporate appropriate information from powder X-ray diffraction data (particularly information on the unit cell and space group) within the structure determination process.

Using magic angle sample spinning and efficient pulse sequences for homonuclear and heteronuclear decoupling, site-resolved NMR spectra can, in general, be recorded readily for spin-1/2 nuclei such as ^{1}H, ^{13}C, ^{15}N, and ^{29}Si in solids,[30] allowing the line broadening due to anisotropic interactions, including dipole–dipole interactions, to be removed effectively. To determine the arrangements of atoms in crystalline solids by solid-state NMR, however, it is crucial to retrieve information on the dipolar coupling between specific pairs of spins.

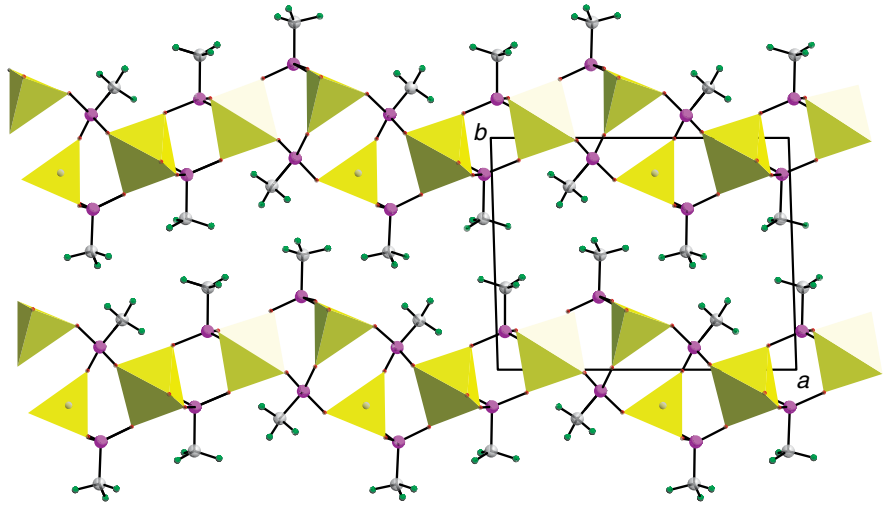


Figure 19.4. Crystal structure of the γ-phase of $Al_2(CH_3PO_3)_3$ determined from powder X-ray diffraction data.

With the advent of efficient recoupling pulse sequences[30,31], it has been demonstrated that zeolite crystal structures can be solved directly from solid-state NMR data.[32] The approach used in such work relies on the excitation of double-quantum-coherence (DQC) among spin-1/2 nuclei, which depends strongly on dipolar coupling among these nuclei. In a 2-D DQ filtered spectrum, nondiagonal cross peaks arise from coupling between the spins[33] and the matrix of intensities (I) of cross peaks depends on the strengths of the dipolar couplings and the recoupling time τ. Experimental build-up curves $I(\tau)$ may be established by measuring the intensity as a function of recoupling time. Analytic expressions for $I(\tau)$ curves can be established theoretically for separated spin pairs,[32] and simulation of $I(\tau)$ curves, therefore, provides a way to determine the arrangement of atoms in a crystal.

Purely siliceous zeolites consist of silicon–oxygen tetrahedra only, and give rise to a great number of structural possibilities because of the multitude of geometric permutations that exist for arranging these tetrahedra in three dimensions. Fortunately, site-resolved ^{29}Si NMR spectra can be readily recorded for such materials[34,35], and as the natural abundance of ^{29}Si is only 4.68%, the ^{29}Si–^{29}Si spin pairs in zeolite structures are relatively well separated from each other. As a consequence, quantitative estimation of internuclear distances is possible, and it has been shown[36] (for the zeolite material sigma-2) that the symmetry-based recoupling pulse sequence can recouple dipolar interactions as low as around 10 Hz.

The structure solution work reported in Ref. 32 was focused on two zeolite materials – ITQ-4 and ferrierite – which were handled as "blind test" examples. Using known unit cell parameters and space group determined from powder X-ray diffraction data, a set of atomic coordinates was found by assessing the agreement between experimental build-up curves and the corresponding data calculated for a given set of atomic coordinates.[32] After the structure was solved by this approach, it was refined subsequently against the powder X-ray diffraction data using the Rietveld technique. Clearly, solid-state NMR data could also be used (instead of the powder X-ray diffraction data) for the final structure refinement by exploiting the fact that ^{29}Si chemical shift tensors are very sensitive to the local atomic arrangement (*see* **Chapter 9**). Such information can be determined from experimental ^{29}Si NMR data, and can be calculated with sufficient reliability for structural models using ab initio Hartree–Fock calculations[37] (*see* **Chapter 3**). Using this approach, it has been shown[38] (for the zeolite material sigma-2) that structure refinement can be carried out by varying the atomic coordinates of the silicon and oxygen atoms in the structure to obtain the best agreement between experimental and calculated ^{29}Si chemical shift tensors.

The success of the techniques that are used to carry out structure solution of zeolites from solid-state NMR data is a consequence of having (i) site-resolved resonances (^{29}Si) and (ii) relatively well separated spin pairs (^{29}Si–^{29}Si). However, relatively well separated spin pairs do not exist in many other types of materials. In the case of organic crystalline materials, for example, there is usually a high density of spins (e.g., ^{1}H), and quantitative estimation of internuclear distances would not be viable from 2-D DQ correlation experiments in such cases. For organic materials, on the other hand, ^{1}H spin diffusion NMR experiments have been shown[39] to represent a promising approach for structure determination. The high natural abundance of ^{1}H (99.99%) typically leads to very strong ^{1}H–^{1}H dipolar coupling, and as ^{1}H spin diffusion in solids (which involves exchange of magnetization among nuclear spins of the same type) is driven by the distance dependent dipolar couplings, it represents a potential basis for the structure determination of organic crystalline materials. However, the situation is complicated by the fact that the rate of ^{1}H spin diffusion also depends on many other factors, including the orientation of internuclear vectors, the chemical shift anisotropies of the two coupled spins, the coupling to other spins, and the rate of magic angle sample spinning.[39] Although it is difficult to derive an analytic expression to allow ^{1}H spin diffusion curves to be calculated for a given set of atomic coordinates, a simple phenomenological multispin kinetic rate matrix approach has been developed in the context of structure determination of small organic molecules in crystalline solids.[40] In this model, the rate of exchange (denoted k_{ij}) between two different ^{1}H environments i and j (assumed to be resolved in the NMR spectrum) is given by equation (19.1):

$$k_{ij} = A \sum_{\lambda} \left(\frac{\mu_0 \gamma_H{}^2 \hbar}{4\pi} \right)^2 \frac{1}{(r_{ij}^n)_\lambda} \qquad (19.1)$$

In this expression, r_{ij} is the internuclear distance between sites i and j, λ indicates the sum over exchange between sites i and j in different molecules in the crystal structure, and A is a phenomenological scaling factor. In principle, n is a variable that depends on the specific molecules, and was confirmed[40] to be close to 6. The peak intensities (denoted I_{ij}) in a 2-D exchange spectrum are then given by equation (19.2):

$$I_{ij}(\tau_{SD}) = \exp[-\boldsymbol{K}\tau_{SD}]_{ij}\ M_{zj}{}^{0} \qquad (19.2)$$

where $\boldsymbol{K}$ is the $N \times N$ matrix of the k_{ij} values for the N resolved sites in the NMR spectrum, τ_{SD} is the spin diffusion mixing time, and $M_{zj}{}^{0}$ is the intensity of the jth peak at $\tau_{SD} = 0$. Thus, using this approach, the intensities of cross peaks in a 2-D exchange spectrum can be calculated for a given trial structure, and provides a basis for carrying out structure solution by finding the structural model that gives the best fit between computed and experimental data.

This approach has been demonstrated, assuming known unit cell parameters and space group (which may be obtained, for example, from powder X-ray diffraction data), by carrying out structure solution of the known structure of β-L-aspartyl-L-alanine.[39] The initial structure was found to deviate significantly from the known structure, partly as a consequence of the phenomenological description, and also because nonprotonated groups are not strongly constrained by the ^{1}H spin diffusion data. However, it was shown that the quality of the structure may be improved significantly by subsequent refinement of the structure on the basis of obtaining the best agreement between computed (from DFT calculations) and experimental ^{1}H or ^{13}C chemical shift data. In the final structure determined by this approach,[41] the average root mean squared atom–atom distances between the structure determined from the solid-state NMR data and the known crystal structure was only 0.13 Å. On the basis of the success achieved to date, this approach (summarized in Figure 19.5) for ab initio structure solution of organic crystalline materials from solid-state NMR data appears to be a particularly promising area for further development and application.

Finally, we consider the structure determination of macromolecules of biological interest from solid-state NMR data. Using complete or selective isotopic labeling (with ^{13}C or ^{15}N), structural properties of macromolecules such as proteins and peptides in amyloid fibrils have been established from ^{13}C or ^{15}N NMR data recorded under conditions of fast magic angle sample spinning.[42–44] In this work, information on interatomic distances and dihedral angles was extracted from dipolar homonuclear and heteronuclear correlation experiments. Although rigorous quantitative estimation of geometrical properties is not feasible, these NMR data nevertheless provide valuable structural insights when single-crystal X-ray diffraction is not applicable, either because of insolubility or because of the fact that single crystals of suitable size and/or quality cannot be grown.

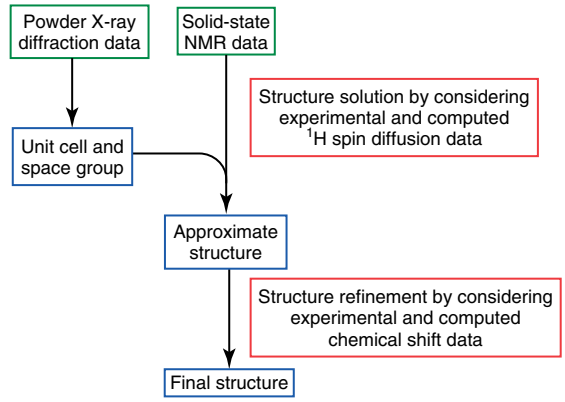


Figure 19.5. Schematic illustration of the strategy developed[39–41] for ab initio structure solution of organic crystalline materials from solid-state NMR data.

REFERENCES

1. K. D. M. Harris and M. Tremayne, *Chem. Mater.*, 1996, **8**, 2554.
2. K. D. M. Harris, M. Tremayne, and B. M. Kariuki, *Angew. Chem. Int. Ed.*, 2001, **40**, 1626.
3. V. V. Chernyshev, *Russ. Chem. Bull.*, 2001, **50**, 2273.
4. Y. G. Andreev and P. G. Bruce, *J. Phys.: Condens. Matter*, 2001, **13**, 8245.
5. W. I. F. David, K. Shankland, L. B. McCusker, and C. Baerlocher, eds, *Structure Determination from Powder Diffraction Data*, OUP/IUCr, 2002.
6. K. D. M. Harris and E. Y. Cheung, *Chem. Soc. Rev.*, 2004, **33**, 526.
7. M. Tremayne, *Philos. Trans. R. Soc.*, 2004, **362**, 2691.
8. S. Karki, L. Fabian, T. Friscic, and W. Jones, *Org. Lett.*, 2007, **9**, 3133.

9. H. Tsue, M. Horiguchi, R. Tamura, K. Fujii, and H. Uekusa, *J. Synth. Org. Chem. Jpn.*, 2007, **65**, 1203.
10. W. I. F. David and K. Shankland, *Acta Crystallogr., Sect. A*, 2008, **64**, 52.
11. K. D. M. Harris, M. Tremayne, P. Lightfoot, and P. G. Bruce, *J. Am. Chem. Soc.*, 1994, **116**, 3543.
12. M. Tremayne, B. M. Kariuki, and K. D. M. Harris, *Angew. Chem. Int. Ed. Engl.*, 1997, **36**, 770.
13. D. Albesa-Jové, B. M. Kariuki, S. J. Kitchin, L. Grice, E. Y. Cheung, and K. D. M. Harris, *ChemPhysChem*, 2004, **5**, 414.
14. I. J. King, F. Fayon, D. Massiot, R. K. Harris, and J. S. O. Evans, *Chem. Commun.*, 2001, 1766.
15. Z. Pan, M. Xu, E. Y. Cheung, K. D. M. Harris, E. C. Constable, and C. E. Housecroft, *J. Phys. Chem. B*, 2006, **110**, 11620.
16. E. J. MacLean, M. Tremayne, B. M. Kariuki, K. D. M. Harris, A. F. M. Iqbal, and Z. Hao, *J. Chem. Soc., Perkin Trans. 2*, 2000, 1513.
17. S. Meejoo, B. M. Kariuki, S. J. Kitchin, E. Y. Cheung, D. Albesa-Jové, and K. D. M. Harris, *Helv. Chim. Acta*, 2003, **86**, 1467.
18. K. D. M. Harris and J. M. Thomas, *J. Solid State Chem.*, 1991, **94**, 197.
19. G. Soda and T. Chiba, *J. Chem. Phys.*, 1969, **50**, 439.
20. A. E. Aliev and K. D. M. Harris, *Struct. Bond.*, 2004, **108**, 1.
21. Z. Pan, M. Xu, E. Y. Cheung, J. A. Platts, K. D. M. Harris, E. C. Constable, and C. E. Housecroft, *J. Solid State Chem.*, 2006, **179**, 3214.
22. E. D. L. Smith, R. B. Hammond, M. J. Jones, K. J. Roberts, J. B. O. Mitchell, S. L. Price, R. K. Harris, D. C. Apperley, J. C. Cherryman, and R. Docherty, *J. Phys. Chem. B*, 2001, **105**, 5818.
23. E. J. MacLean, K. D. M. Harris, B. M. Kariuki, S. J. Kitchin, R. R. Tykwinski, I. P. Swainson, and J. D. Dunitz, *J. Am. Chem. Soc.*, 2003, **125**, 14449.
24. R. K. Harris, P. Y. Ghi, R. B. Hammond, C. Y. Ma, and K. J. Roberts, *Chem. Commun.*, 2003, 2834.
25. R. K. Harris, P. Y. Ghi, R. B. Hammond, C. Y. Ma, K. J. Roberts, J. R. Yates, and C. J. Pickard, *Magn. Reson. Chem.*, 2006, **44**, 325.
26. D. A. Middleton, X. Peng, D. Saunders, K. Shankland, W. I. F. David, and A. J. Markvardsen, *Chem. Commun.*, 2002, 1976.
27. R. K. Harris, *Solid State Sci.*, 2004, **6**, 1025.
28. P. A. Barrett, M. A. Camblor, A. Corma, R. H. Jones, and L. A. Villaecusa, *Chem. Mater.*, 1997, **9**, 1713.
29. M. Edgar, V. J. Carter, D. P. Tunstall, P. Grewal, V. Favre-Nicolin, P. A. Cox, P. Lightfoot, and P. A. Wright, *Chem. Commun.*, 2002, 808.
30. D. D. Laws, H. L. Bitter, and A. Jerschow, *Angew. Chem. Int. Ed.*, 2002, **41**, 3096.
31. M. H. Levitt, Symmetry-based sequences in magic-angle spinning solid-state NMR, in *Encyclopedia of Nuclear Magnetic Resonance*, eds-in-chief D. M. Grant and R. K. Harris, John Wiley & Sons: Chichester, 2002, Vol. **9**, p 165.
32. D. H. Brouwer, R. J. Darton, R. E. Morris, and M. H. Levitt, *J. Am. Chem. Soc.*, 2005, **127**, 10365.
33. P. K. Madhu, E. Vinogradov, and S. Vega, *Chem. Phys. Lett.*, 2004, **394**, 423.
34. C. A. Fyfe, J. M. Thomas, J. Klinowski, and G. C. Gobbi, *Angew. Chem. Int. Ed. Engl.*, 1983, **22**, 259.
35. C. A. Fyfe, H. Strobl, G. T. Kokotailo, G. J. Kennedy, and G. E. Barlow, *J. Am. Chem. Soc.*, 1988, **110**, 3373.
36. D. H. Brouwer, P. E. Kristiansen, C. A. Fyfe, and M. H. Levitt, *J. Am. Chem. Soc.*, 2005, **127**, 542.
37. D. H. Brouwer and G. Enright, *J. Am. Chem. Soc.*, 2008, **130**, 3095.
38. D. H. Brouwer, *J. Am. Chem. Soc.*, 2008, **130**, 6306.
39. B. Elena, G. Pintacuda, N. Mifsud, and L. Emsley, *J. Am. Chem. Soc.*, 2006, **128**, 9555.
40. B. Elena and L. Emsley, *J. Am. Chem. Soc.*, 2005, **127**, 9140.
41. C. J. Pickard, E. Salager, G. Pintacuda, B. Elena, and L. Emsley, *J. Am. Chem. Soc.*, 2007, **129**, 8932.
42. F. Castellani, B. van Rossum, A. Diehl, M. Schubert, K. Rehbein, and H. Oschkinat, *Nature*, 2002, **420**, 98.
43. A. T. Petkova, Y. Ishii, J. J. Balbach, O. N. Antzutkin, R. D. Leapman, F. Delaglio, and R. Tycko, *Proc. Natl. Acad. Sci.*, 2002, **99**, 16742.
44. C. P. Jaroniec, C. E. MacPhee, V. S. Bajaj, M. T. McMahon, C. M. Dobson, and R. G. Griffin, *Proc. Natl. Acad. Sci.*, 2004, **101**, 711.

Chapter 20
Tensor Interplay

David L. Bryce

Department of Chemistry, University of Ottawa, Ottawa, Ontario K1N 6N5, Canada

20.1	Introduction	289
20.2	Tensor Interplay	289
20.3	Concluding Remarks	300
	References	300

20.1 INTRODUCTION

Generally, nuclei embedded in a molecule are subject to multiple nuclear magnetic resonance (NMR) tensor interactions simultaneously. Clearly an understanding of the interplay between various tensor interactions, and how this interplay affects the resulting NMR spectra, is important to maximize the amount of information which may be extracted from such spectra. In this article I will provide, through examples, a pedagogical overview of how interplay between various tensor interactions (nuclear magnetic shielding ($\boldsymbol{\sigma}$), direct dipolar coupling ($\boldsymbol{D}$), indirect nuclear spin–spin coupling ($\boldsymbol{J}$), and nuclear electric quadrupolar coupling ($\boldsymbol{V}$)) manifests itself in solid-state NMR spectra, and how experimental measurements involving more than one tensor relate to local nuclear symmetry and to crystal structure.

NMR Crystallography Edited by Robin K. Harris, Roderick E. Wasylishen and Melinda J. Duer © 2009 John Wiley & Sons, Ltd. ISBN: 978-0-470-69961-4

The most rigorous way in which information regarding tensor magnitudes and orientations may be measured is through a single-crystal NMR study; however, single crystals of suitable size and quality are often not available. In the context of NMR crystallography, one often wishes to apply NMR methods to provide insight into the crystal structure because such data are not available from diffraction methods. In what follows, the discussion will be focused on methods to study tensor interplay in powdered samples.

20.2 TENSOR INTERPLAY

20.2.1 Interplay Between σ and Spin–Spin Coupling Interactions

The most ubiquitous NMR interaction after the dominant Zeeman interaction is the magnetic shielding of the nucleus by the surrounding electrons. The symmetric part of $\boldsymbol{\sigma}$ is characterized by up to three independent principal components and three angular variables, which relate the principal axis system (PAS) of $\boldsymbol{\sigma}$ to a reference frame, e.g., the PAS of a second tensor interaction. Selected relationships between local symmetry and the number of independent elements of $\boldsymbol{\sigma}$ are summarized in Table 20.1.[1] When more than one NMR-active nucleus is present, spin–spin coupling interactions may also affect the NMR spectrum. The dipolar coupling constant, R_{DD},

Table 20.1. Examples of relationships between symmetry and the nuclear magnetic shielding tensor[a]

Symmetry at nucleus	Number of independent components	Nonzero components
O_h, T_d	1	$\sigma_{xx} = \sigma_{yy} = \sigma_{zz} = \sigma_{iso}$
$D_{\infty h}$, $C_{\infty v}$	2	σ_{zz}
C_{nv} $(n > 2)$, C_n $(n > 2)$, S_n		$\sigma_{xx} = \sigma_{yy}$
C_{2v}	3	σ_{xx}, σ_{yy}, σ_{zz}
C_s, C_2, C_{2h}	4	σ_{xx}, σ_{yy}, σ_{zz} σ_{xy}
C_1	6	σ_{xx}, σ_{yy}, σ_{zz} σ_{xy}, σ_{xz}, σ_{yz}

[a]Only the symmetric part of $\boldsymbol{\sigma}$ is discussed. The z axis is the principal axis of symmetry. (Adapted from Robert and Wiesenfeld.[1])

provides the most direct structural information available from an NMR experiment in the form of a motionally averaged internuclear distance:

$$R_{DD} = \left(\frac{\mu_0}{4\pi}\right)\left(\frac{\gamma_1\gamma_2\hbar}{2\pi}\right)\langle r_{12}^{-3}\rangle \qquad (20.1)$$

Experimentally, one can only measure the effective dipolar coupling, $R_{eff} = R_{DD} - \Delta J/3$ (note that this simple equation is only valid when the $\boldsymbol{D}$ and $\boldsymbol{J}$ tensors are coaxial).

VanderHart and Gutowsky's 1968 article described the spectra of coupled spin pairs in stationary powdered samples in the presence of CSA.[2] Zilm and Grant extended this work to consider the more general case of the AB spin pair and presented spectral simulations.[3] The heteronuclear (AX) and homonuclear (A_2, AB) cases are discussed below. The reader is also referred to a useful review of NMR studies of isolated spin pairs in the solid state which has been presented by Power and Wasylishen.[4]

20.2.1.1 CSA and Heteronuclear Coupling

Consider the spectrum of a stationary powdered sample containing effectively isolated AX spin-1/2 pairs. In the limit of zero coupling between the spins, the spectrum of nucleus A is a chemical shift (CS) powder pattern, where the three discontinuities correspond to the principal components of this tensor (Figure 20.1). The same is true for the X nucleus. In the presence of dipolar coupling, the spectrum of the A (or X) nucleus is a superposition of two "effective" powder patterns, with one being "stretched" relative to the pure CS pattern, and the other being "squeezed". Harris and coworkers have described this phenomenon extensively[5,6] and the entire analysis will not be repeated here.

For axially symmetric $\boldsymbol{\sigma}$, $\boldsymbol{D}$, and $\boldsymbol{J}$ tensors, with their largest components lying along the internuclear vector, the resonance frequency of the A nucleus may

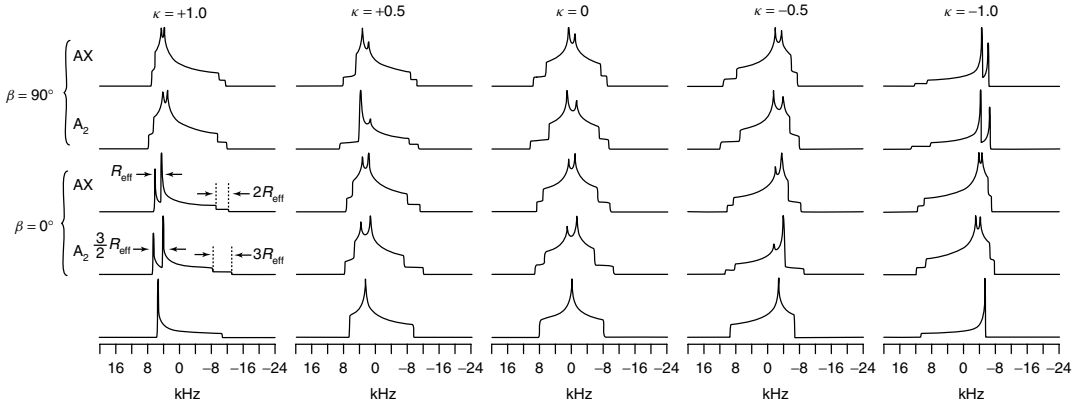


Figure 20.1. Simulated dipolar-chemical shift spectra for A_2 and AX spin systems under stationary conditions (ν_0 = 162 MHz; Ω = 100 ppm; R_{DD} = 1600 Hz). In the lower trace of each column is the spectrum of an isolated spin subject only to CSA. The angle β is that between the dipolar vector and δ_{33}. Span, $\Omega = \sigma_{33} - \sigma_{11} \cong \delta_{11} - \delta_{33}$. Skew, $\kappa = 3(\sigma_{iso} - \sigma_{22})/\Omega \cong 3(\delta_{22} - \delta_{iso})/\Omega$. $\sigma_{33} \geq \sigma_{22} \geq \sigma_{11}$. Spectra are simulated using WSOLIDS1.

be expressed as follows:

$$\nu_A = \nu_A^{iso} - \frac{1}{2}\nu_{0,A}\zeta_A^{eff}(3\cos^2\theta - 1) - J_{AX}\, m_X \tag{20.2}$$

where an effective tensor anisotropy is defined as follows:

$$\zeta_A^{eff} = \zeta_A - \frac{2R_{eff}\, m_X}{\nu_{0,A}} \tag{20.3}$$

Here, ζ_A is equal to $\sigma_A^{\parallel} - \sigma_{A,iso}$, and $\sigma_A^{\parallel}$ is the shielding of the A nucleus when the internuclear vector is along B_0. The angle θ is that between the internuclear vector and B_0.

Shown in Figure 20.1 are simulated dipolar-CS spectra of AX spin pairs in the absence of J coupling, for different symmetries of the shielding tensor; the spectra are superpositions of stretched and squeezed effective powder patterns. The discussion above corresponds to the case where $\beta = 0$ and $\kappa = +1$. In this case, the value of R_{eff} is readily obtained from inspection of the spectrum as the separation between the high-frequency discontinuities. The separation between the shoulders at the low-frequency edge is equal to $2R_{eff}$. Thus, the interplay between shielding and dipolar coupling provides direct evidence for two crystallographic features: (i) an axially symmetric CS tensor suggests the presence of a C_3 axis or higher crystallographic symmetry at the A nucleus and (ii) a bond length is obtained from the measured dipolar coupling constant (assuming $\Delta J \ll R_{DD}$). Eichele and Wasylishen have described a dipolar-splitting method which enables the interpretation of such spectra in cases where $\boldsymbol{\sigma}$ deviates from axial symmetry and its PAS does not coincide with that of $\boldsymbol{D}$.[7]

An example where this tensor interplay was applied to obtain crystallographic information in the absence of conclusive diffraction studies is that of silver cyanide.[8] Shown in Figure 20.2 is the ^{13}C dipolar-CS spectrum of ^{13}C, ^{15}N-enriched (99%) $Ag^{13}C^{15}N$. Analysis of the powder pattern provides evidence for linearity of the AgCN chains at carbon and also provides a carbon–nitrogen bond length of 1.16 ± 0.03 Å (obtained from the measured value of R_{eff} of -1800 ± 50 Hz and small corrections for ΔJ and librational averaging). The inset in the figure also shows the value of the method when ^{15}N is exchanged for the quadrupolar ^{14}N ($I = 1$); three discontinuities are observed due to the three possible spin states, m_X, for ^{14}N.

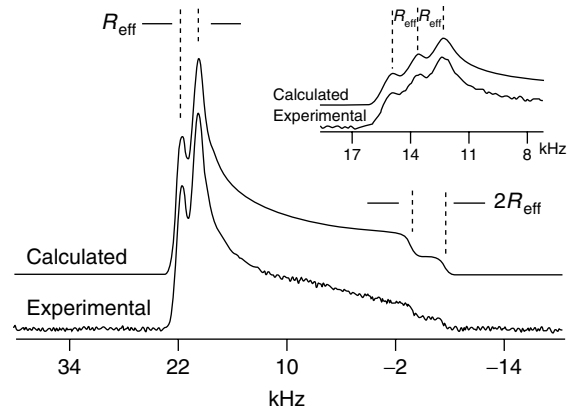


Figure 20.2. Carbon-13 dipolar-CS NMR spectra of stationary $Ag^{13}C^{15}N$, with $R_{eff}(^{13}C, ^{15}N)$ indicated. Inset: high-frequency part of the ^{13}C spectrum of $Ag^{13}C^{14}N$. (Reproduced from Ref. 8. © American Chemical Society, 2002.)

Under MAS conditions, an isolated spin-1/2 nucleus gives rise to a series of spinning sidebands due to CSA. As in the static case, when heteronuclear coupling between A and X is introduced, the spinning sideband manifold splits into two separate manifolds, one being squeezed and the other being stretched relative to the pure CS manifold. Since the heteronuclear dipolar interaction commutes with itself at all times during the rotor cycle, the spectral analysis is relatively straightforward. The centerbands of the two manifolds will be separated by J_{iso}. The sidebands of each of the manifolds may be interpreted to provide information on the CS tensor and R_{eff}. Information on the relative signs of these interactions, and the J coupling, is also available, as detailed by Harris.[5,6,9]

An interesting example of the AX_2 case is presented in Figure 20.3.[6] Shown is the ^{119}Sn MAS NMR spectrum of triisobutyltin fluoride, which reflects the presence of J coupling to two ^{19}F nuclei as well as ^{119}Sn CSA and $^{119}Sn-^{19}F$ dipolar coupling. One of the important crystallographic insights arising from the spectral analysis is that, despite the monomeric formula R_3SnF, the triplet nature of the centerband ($|J_{iso}(^{119}Sn, ^{19}F)| = 1.26$ kHz) reveals a polymeric structure in the solid state, with two equivalent bridging fluorines between each pair of tin atoms.

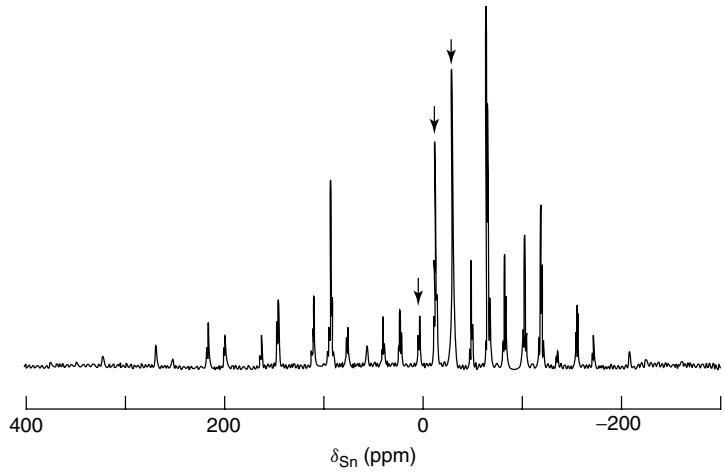


Figure 20.3. Tin-119 MAS NMR spectrum of triisobutyltin fluoride at 74.63 MHz. The centerband triplet is denoted by arrows. (Reproduced from Ref. 6. © American Chemical Society, 1992.)

20.2.1.2 CSA and Homonuclear Coupling

Homonuclear coupling may be divided into A_2 and AB cases. A spin system is labeled as A_2 when the two nuclei are magnetically equivalent in the crystal structure; this ensures that the chemical shifts of the two nuclei are identical for all crystal orientations in the magnetic field. Simulated spectra for various cases are presented in Figure 20.1. Importantly, the splittings discussed above for the $\beta = 0$ and $\kappa = 1$ case for an AX spin pair are a factor of 3/2 larger in an A_2 spin system for a given R_{eff}.

Haeberlen has summarized the conditions under which homonuclear spin pairs are classified as "crystallographically equivalent" versus "magnetically equivalent".[10] Crystallographic equivalence of two spins arises when they are related by any of the symmetry elements of the crystal structure. Magnetic equivalence carries stricter criteria; two spins fulfill the criteria only if their positions in the crystal structure are related by an inversion center or a translation element. Therefore, all magnetically equivalent spin pairs are crystallographically equivalent but the converse is not necessarily true. It is important to note that crystallographically equivalent spin pairs will give rise to very different NMR spectra depending on whether or not they are also magnetically equivalent. Some of the important consequences have been described in reference 10.

For a homonuclear AB pair (neither crystallographically nor magnetically equivalent), general expressions for the four possible transitions must be used to interpret the spectrum:[3,11,12]

$$\nu_1 = \frac{1}{2}(\nu_A + \nu_B + D + A); \quad P_1 = 1 - \frac{B}{D} \tag{20.4}$$

$$\nu_2 = \frac{1}{2}(\nu_A + \nu_B + D - A); \quad P_2 = 1 + \frac{B}{D} \tag{20.5}$$

$$\nu_3 = \frac{1}{2}(\nu_A + \nu_B - D + A); \quad P_3 = 1 + \frac{B}{D} \tag{20.6}$$

$$\nu_4 = \frac{1}{2}(\nu_A + \nu_B - D - A); \quad P_4 = 1 - \frac{B}{D} \tag{20.7}$$

where

$$D = \sqrt{[(\nu_A - \nu_B)^2 + B^2]} \tag{20.8}$$

$$A = J_{\text{iso}} - R_{\text{eff}}(3\cos^2\theta - 1) \tag{20.9}$$

$$B = J_{\text{iso}} + \frac{1}{2}R_{\text{eff}}(3\cos^2\theta - 1) \tag{20.10}$$

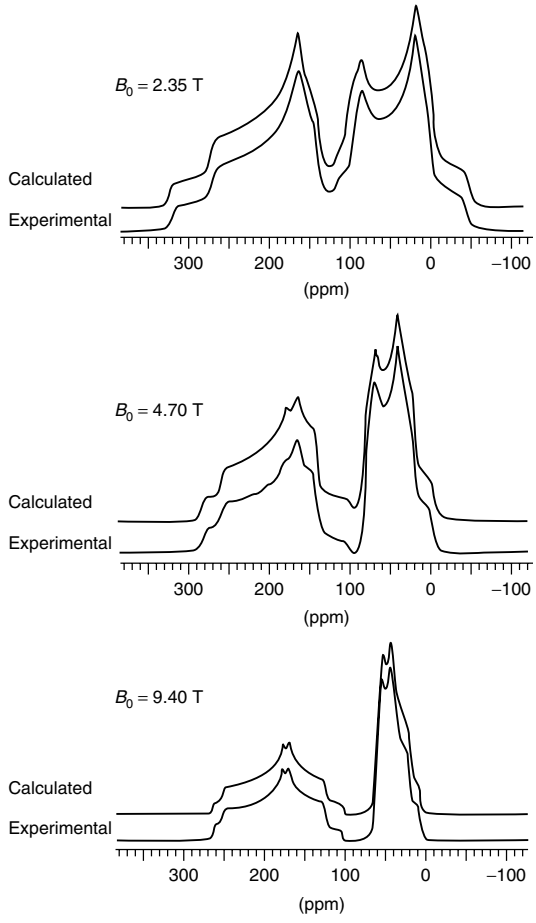


Figure 20.4. Carbon-13 dipolar-CS NMR spectra of stationary phenylacetic-$^{13}C_2$ acid at three magnetic fields. (Reproduced from Ref. 13. © American Chemical Society, 2000.)

Numerical lineshape simulations are more critical for the interpretation of AB powder spectra featuring interplay between $\boldsymbol{\sigma}$, $\boldsymbol{D}$, and $\boldsymbol{J}$ compared with the heteronuclear case. Simulations reveal, in addition to tensor magnitudes, the orientation of the internuclear vector in the PAS of the CS tensor. An experimental example of interplay between $\boldsymbol{\sigma}$ and $\boldsymbol{D}$ for a $^{13}C-^{13}C$ spin pair is presented in Figure 20.4. Proton-decoupled ^{13}C CP NMR spectra of stationary powdered samples of phenylacetic-$^{13}C_2$ acid acquired at three different magnetic field strengths, along with simulations are shown.[13] On the basis that δ_{33} is typically oriented perpendicular to the COO plane for a carbonyl carbon, it was possible to deduce the absolute orientation of the methylene carbon CS tensor in the molecular frame. When such relative tensor orientations are known for particular molecular fragments, it becomes possible to determine the relative orientation of such fragments, e.g., adjacent peptide planes.

MAS NMR spectra of homonuclear spin pairs are more complicated than those for AX systems due to the fact that the homonuclear dipolar interaction does not commute with itself at all times during the rotor cycle. Iterative numerical simulations are therefore typically required to properly simulate and interpret MAS NMR spectra of homonuclear spin pairs.[14] Tensor magnitudes ($\boldsymbol{\delta}$, $\boldsymbol{D}$, $\boldsymbol{J}$) and relative tensor orientations affect the shapes of spinning sidebands as well as their relative intensities.[15,16] For example, iterative fitting of ^{31}P MAS NMR spectra of metal phosphine complexes featuring crystallographically equivalent, but magnetically nonequivalent $^{31}P-^{31}P$ spin pairs provides information on the relative orientations of the shielding, dipolar, and J-coupling tensors.[17] Other interesting examples of the lineshapes that may arise when a spin pair consists of crystallographically equivalent but magnetically nonequivalent nuclei may be found in the literature.[18,19] An example of the MAS rate dependence of the isotropic lineshape is presented in Figure 20.5 for the $^{15}N-^{15}N$ spin pair in *cis*-azobenzene-$^{15}N_2$ dioxide, where the two ^{15}N nuclei are slightly nonequivalent.[15]

20.2.2 Interplay Involving Quadrupolar Nuclei

While both quadrupolar and shielding interactions depend on the local molecular structure, they do so in different ways and therefore contain unique information on the local structure and symmetry. For example, $\boldsymbol{\sigma}$ depends on sums over excited electronic states, while the quadrupolar interaction is a ground-state property which is proportional to the inverse cube of the separation between the nucleus of interest and the charge density contributing to the EFG. Shielding is therefore typically a more local effect, while the EFG may reflect structure and symmetry over longer distances. Various instances of tensor interplay involving quadrupolar nuclei are discussed below.

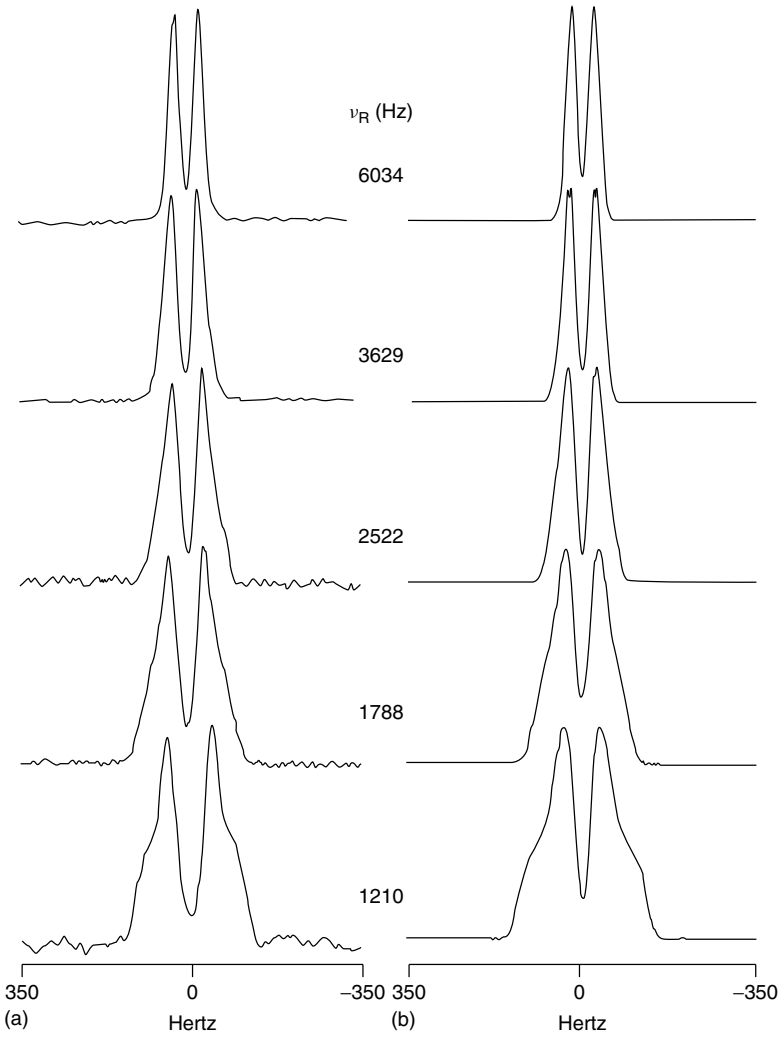


Figure 20.5. Observed (a) and calculated (b) ^{15}N MAS NMR lineshapes for *cis*-azobenzene-$^{15}N_2$ dioxide as a function of MAS rate. B_0 = 4.7 T. (Reproduced from Ref. 15. © Elsevier, 1993.)

20.2.2.1 σ and V Interactions

The framework for interpreting the NMR spectrum of a nucleus experiencing $\boldsymbol{\sigma}$ and $\boldsymbol{V}$ interactions simultaneously was described by Baugher *et al*. for the case of coincident tensor PASs[20] and then extended[21–23] to the general case with anisotropic and asymmetric $\boldsymbol{\sigma}$ and $\boldsymbol{V}$ tensors which are noncoincident. Up to eight independent parameters are required to properly describe the spectrum of a stationary powder sample (three principal components of the CS tensor, C_Q, η_Q, and three Euler angles (see Figure 20.6)). Since the appearance of the spectrum will change due to the opposing dependencies of the shielding (in ppm) and second-order quadrupolar interactions on B_0, it is always prudent to obtain spectra at more than one applied magnetic field strength. A general strategy for extracting the parameters is as follows. First, a MAS NMR spectrum is obtained and fitted to provide δ_{iso}, C_Q, and η_Q (provided the available MAS rate is large enough to properly average the CS anisotropy and

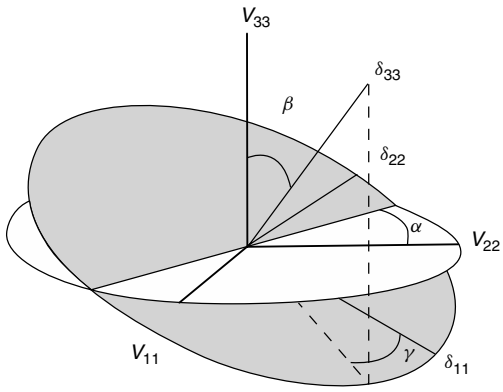


Figure 20.6. Relationship between the orientations of the PASs for the $\boldsymbol{V}$ and $\boldsymbol{\delta}$ tensors in terms of the Euler angles α, β, and γ. The simplest angle to visualize is β, which is always the angle between V_{33} and δ_{33}. Figure adapted from the WSOLIDS1 program. $V_{33} \geq V_{22} \geq V_{11}$; $\delta_{11} \geq \delta_{22} \geq \delta_{33}$.

the first-order quadrupolar interaction). A spectrum of a stationary sample is then acquired and simulated to yield Ω, κ, and three angles relating the PASs of the CS and EFG tensors.

A series of simulated central transition (CT) spectra of an isolated spin-3/2 nucleus under stationary conditions subject to quadrupolar and shielding interactions, which shows the effects of changing the span and skew of the CS tensor as well as the relative orientation of the quadrupolar and CS tensors is presented in Figure 20.7. When $\kappa = +1$ and α, β, $\gamma = 0^\circ$, the effect of CSA is straightforward: the breadth of the powder pattern increases and the position of a central discontinuity moves to lower frequency. In contrast, when $\kappa = -1$ and $\beta = 90^\circ$, increased CSA has a counterintuitive effect in that the total breadth of the pattern *decreases*. These two cases arise frequently (i.e., when nuclei are at sites of particular symmetry). Generally, when dealing with

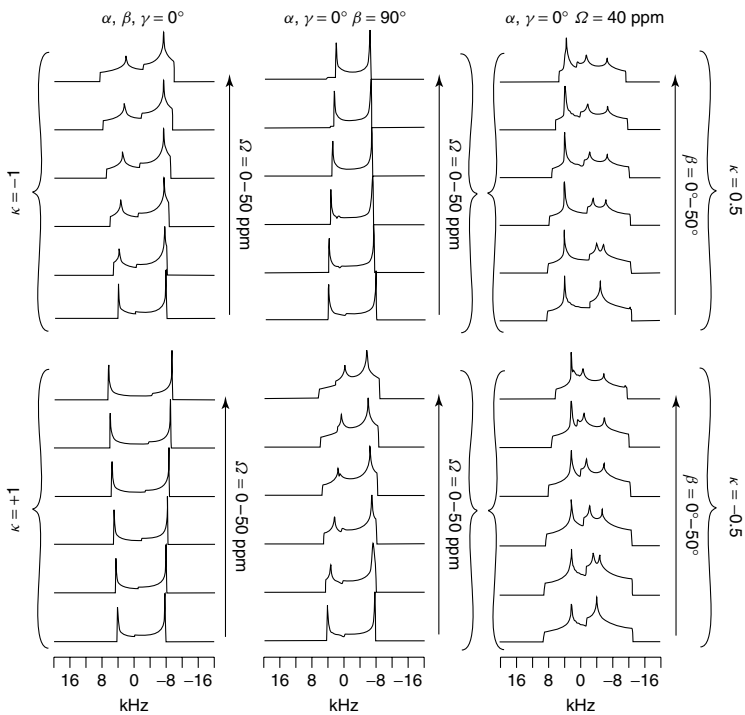


Figure 20.7. Simulated ^{23}Na (I = 3/2) central transition NMR spectra of a stationary powder sample, demonstrating the effect of interplay between quadrupolar and chemical shift interactions on the lineshapes. C_Q = 3.5 MHz; ν_0 = 132.221 MHz; δ_{iso} = 0 ppm. For the left and center columns, η_Q = 0; for the right-hand column, η_Q = 0.5. Where indicated, the span is increased from 0 to 50 ppm in steps of 10 ppm, and the angle β is increased from 0–50° in steps of 10°. Spectra were generated with WSOLIDS1.

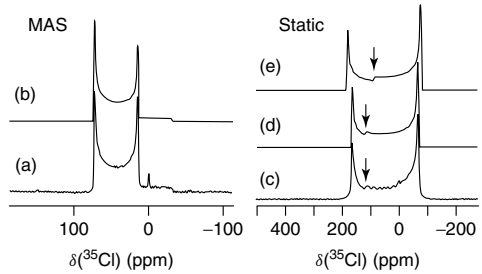


Figure 20.8. Chlorine-35 NMR spectra of solid powdered $SrCl_2 \cdot 6H_2O$ obtained at 21.1 T under MAS and static conditions. Experimental spectra are shown in (a) and (c). Best-fit simulations are shown in (b) and (d) (the latter incorporates both $\boldsymbol{V}$ and $\boldsymbol{\delta}$ interactions). A simulation based solely on the quadrupolar interaction is shown in (e). Arrows denote a key spectral feature, which moves due to interplay between $\boldsymbol{V}$ and $\boldsymbol{\delta}$. (Reproduced from Ref. 24. © Wiley-VCH, 2007.)

experimental spectra, one resorts to lineshape fitting (using a program such as WSOLIDS, Simpson, or DMFit).

^{35}Cl NMR spectra of solid powdered $SrCl_2{\cdot}6H_2O$ obtained at 21.1 T, where ^{35}Cl second-order quadrupolar interactions ($C_Q = 3.91 \pm 0.05$ MHz) dominate over CSA ($\Omega = 45 \pm 20$ ppm) are shown in Figure 20.8.[24] As an illustration of the strategy discussed above, consider the spectrum obtained under MAS conditions. Inspection reveals an axially symmetric second-order quadrupolar lineshape, which is consistent with the chloride ion lying on a C_3 axis in the crystal structure.[25] The spectrum obtained under stationary conditions provides a practical example which demonstrates the sensitivity of the central discontinuity of the spectrum to the small chlorine CSA. As shown in Figure 20.8, the spectrum cannot be properly simulated in the absence of CSA; it is both too broad and the central feature does not coincide with the experimental position. This is a clear example of a situation where the presence of CSA decreases the spectral breadth rather than increasing it. The best fit is obtained with $\Omega = 45$ ppm and $\beta = 90 \pm 10^\circ$, indicating that the direction of greatest shielding is perpendicular to V_{33}. The axial symmetry of the CS tensor and the orthogonality of V_{33} and δ_{33} are additional reporters on the symmetry at Cl.

The ^{95}Mo MAS SSNMR spectrum of the piano-stool compound mesitylenetricarbonylmolybdenum(0) is shown in Figure 20.9.[26] Visual inspection reveals that the spectrum resembles that of a spin-1/2 nucleus: it is dominated by CSA rather than quadrupolar effects (the span of the CS tensor is 775 ± 30 ppm, while $C_Q(^{95}\text{Mo})$ is only −0.96 ± 0.15 MHz). The tensor PASs are coincident, i.e., $\alpha, \beta, \gamma = 0^\circ$. How does the structure around Mo lead to a vanishing EFG and a large CSA? The compound possesses approximate C_{3v} symmetry in the solid state. A point charge analysis shows that a zero EFG will result at Mo if the angles between the Mo–CO vectors and the putative C_3 axis are exactly equal to the magic angle (the aromatic ring must also be planar and perpendicular to the C_3 axis). Therefore, we conclude from the spectrum that the molecular symmetry cannot be exactly C_{3v}. An inspection of the relevant angles shows that there are small deviations ($<2^\circ$) from the magic angle. The information afforded from the large CSA may be interpreted in the context of Ramsey's theory[27] to suggest that there is a small energy gap between appropriate molecular orbitals of appropriate symmetry centered on Mo. A relativistic calculation of $\boldsymbol{\sigma}(^{95}\text{Mo})$ allows for the correlation of the CSA with the electronic structure of the molecule (see Figure 20.9c). In this example, it is seen that the quadrupolar and shielding interactions can report on different aspects of crystal geometry and symmetry. For instance, while the EFG interaction is a sensitive reporter on deviations from C_{3v} symmetry, the CSA will be sensitive to geometrical changes within this point group, e.g., changes in Mo–C bond distances or changes in substituents on the aromatic ring.

20.2.2.2 Residual Dipolar Coupling Involving a Quadrupolar Nucleus

Interplay between $\boldsymbol{V}$, $\boldsymbol{D}$, and $\boldsymbol{J}$ can lead to useful effects on the NMR spectrum of a spin-1/2 nucleus which is coupled to a quadrupolar nucleus.[28–30] Briefly, since the spin states of the quadrupolar nucleus (S) are influenced by the EFG as well as B_0, the dipolar coupling between a quadrupolar nucleus and a spin-1/2 nucleus is not averaged to zero under MAS conditions; what remains is the residual dipolar coupling (d):

$$d = -\frac{3C_Q R_{\text{eff}}}{20\nu_S}[(3\cos^2\beta - 1) + \eta_Q \sin^2\beta \cos 2\alpha] \tag{20.11}$$

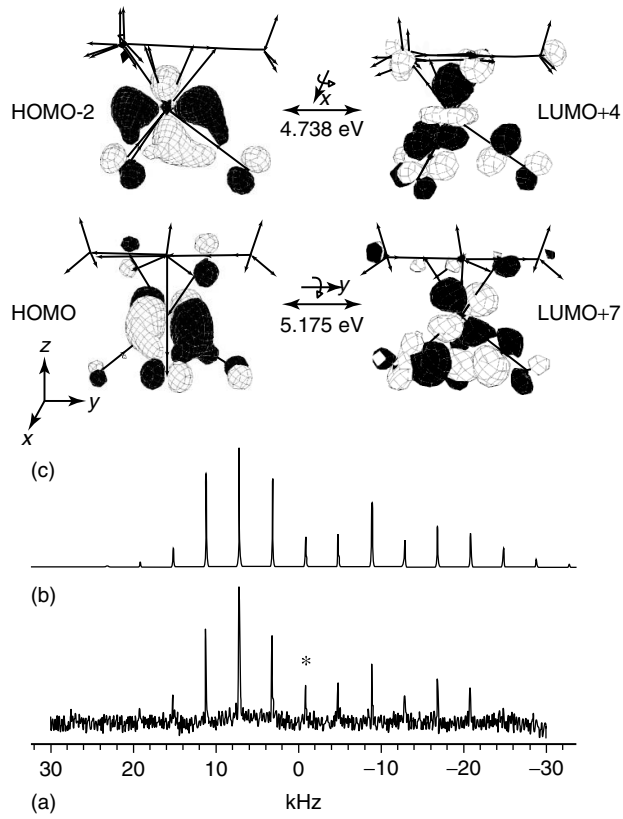


Figure 20.9. (a) Molybdenum-95 NMR spectrum of solid mesitylenetricarbonylmolybdenum(0) obtained at 18.8 T and a MAS rate of 11 kHz. The asterisk denotes the centreband. (b) Simulated spectrum based on quadrupolar and shielding interactions. (c) Molecular orbitals responsible for the large CSA, from zeroth-order regular approximation (ZORA) scalar relativistic calculations. (D. L. Bryce and R. E. Wasylishen, *Phys. Chem. Chem. Phys.*, 2002, ***4***, 3591. Reproduced by permission of the PCCP Owner Societies, 2002.)

To first order, the spectrum of the spin-1/2 nucleus will depend on d and $|J_{iso}|$. Here, α and β are the polar angles describing the orientation of the internuclear vector in the EFG PAS. Spectral analysis can provide the values of these parameters, which is of use for providing structural insights. For example, R_{eff} provides internuclear distance information. The ^{31}P MAS NMR spectrum of a ruthenium phosphine, in which ^{31}P is coupled to ^{99}Ru ($S = 5/2$), is presented as an example in Figure 20.10.[42] Each of the multiplet components is a powder pattern with a lineshape which is also reflective of the tensor interplay; while these patterns can sometimes be observed, they are often obscured due to linebroadening effects.[31] Spectral simulations will provide, under favorable circumstances, all the relevant interaction parameters; however, it is useful to know that the splitting between the two outermost components of the multiplet is equal to $|(2S)(J_{iso})|$, where S is the spin quantum number of the quadrupolar nucleus (assuming that components do not "cross over" each other as a result of the residual dipolar coupling).

An application of the interplay between ***V, D***, and ***J*** that provides crystallographically important structural information is provided by the analysis of ^{113}Cd MAS NMR spectra of a series of cadmium thiocyanate coordination compounds in which the cadmium is bonded to two, three, or four thiocyanate ligands.[32] Analyses of the multiplets resulting from the ^{113}Cd, ^{14}N residual dipolar coupling revealed the number of nitrogen atoms bonded to the cadmium (see Figure 20.11). It was also found that

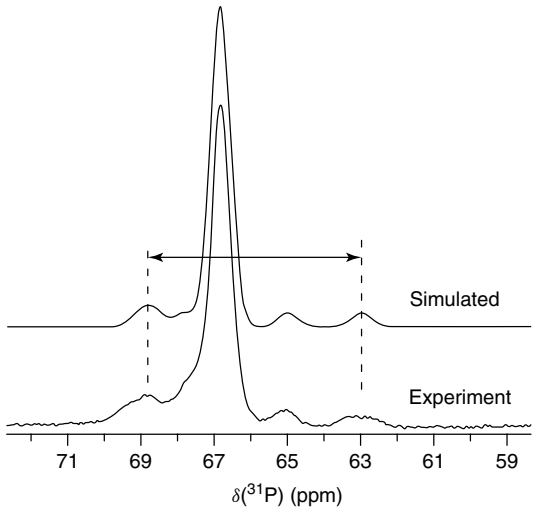


Figure 20.10. One of the phosphorus-31 resonances in the ^{31}P MAS NMR spectrum of RuCl[(2,6-*i*Pr$_2$C$_6$H$_3$)N=CHC$_4$H$_3$N](PPh$_3$)$_2$, along with a simulation which incorporates residual dipolar coupling to the ^{99}Ru nucleus (natural abundance = 12.8%, I = 5/2). The breadth denoted by the arrow is equal to five times $^1J(^{99}\text{Ru}, ^{31}\text{P})_{\text{iso}}$. (A Chelate-Stabilized Ruthenium(a-pyrrolato) Complex: Resolving Ambiguities in Nuclearity and Coordination Geometry through 1H PGSE and 31P Solid-State NMR Studies, Foucault *et al*., Reproduced by permission from American Chemical Society, 2006.)

the value of $^1J(^{113}\text{Cd}, ^{14}\text{N})$ appears to be related to the cadmium–nitrogen internuclear distance.

Wu and Wasylishen reported on the impact of residual dipolar coupling effects on the spectrum of the quadrupolar nucleus.[33] While these effects are typically small compared to quadrupolar broadening effects, they are potentially important in experiments which suppress or eliminate the second-order quadrupolar broadening (e.g., multiple-quantum magic-angle spinning (MQMAS), satellite transition magic-angle spinning (STMAS)).

Facey *et al*. have described an interesting example where interplay between strong ^{2}H–^{2}H homonuclear dipolar interactions and ^{2}H quadrupolar interactions must be considered to describe the ^{2}H MAS NMR spectrum.[34] Average Hamiltonian theory was applied to extract the relevant tensor magnitude and orientation information from the spinning sideband manifold for the transition metal dihydride Os(D$_2$)Cl$_2$(CO)(P^{i}Pr$_3$)$_2$; the D–D internuclear distance was thus obtained.

20.2.2.3 An Example where σ, V, D, and J all Contribute: $\mathbf{Ph_3P^{17}O}$

The ^{17}O NMR spectra of triphenylphosphine oxide are interesting since $\boldsymbol{\sigma}$, ***V***, ***D***, and ***J*** interactions all contribute significantly.[35] Furthermore, since data are available for two different polymorphs of this material, the effect of polymorphism on all the tensors may be evaluated in the context of the structural differences. ^{17}O MAS NMR spectra, in addition to yielding δ_{iso}, C_{Q}, and η_{Q}, feature resolved $J(^{31}\text{P}, ^{17}\text{O})_{\text{iso}}$ spin–spin coupling, which is unusual for a quadrupolar nucleus.[35] The ^{17}O NMR spectra of both polymorphs of stationary powdered Ph$_3$P^{17}O are presented in Figure 20.12; these demonstrate the sensitivity of the various interactions to polymorphism. Additionally, $\Delta J(^{31}\text{P}, ^{17}\text{O})$ was estimated from the spectral analyses to be in the order of −500 Hz.

Figure 20.12(c) shows the individual simulated subspectra for the monoclinic polymorph arising from ^{31}P −^{17}O spin–spin coupling interactions (***J*** + ***D***), ^{17}O CSA, and ^{17}O quadrupolar coupling. Note that the simulated spectrum that incorporates all effects is not simply a sum of these individual subspectra. In fact, each of these subspectra bears no resemblance to the total spectrum, which results from interplay between the four interaction tensors.

20.2.3 Advanced Methods

20.2.3.1 Example: ^{17}O *DOR NMR of* $\mathbf{Ph_3P^{17}O}$

Hung *et al*. applied double rotation (DOR) ^{17}O NMR to determine the utility and sensitivity of this method for characterizing Ph$_3$P^{17}O which, as described above, features contributions from $\boldsymbol{\sigma}$, ***V***, ***D***, and ***J*** interactions.[36] Figure 20.13 shows the ^{17}O DOR NMR spectrum of the monoclinic polymorph of Ph$_3$PO along with various spectral simulations. This demonstrates the sensitivity of ^{17}O DOR NMR to all the various parameters, which were shown to be consistent with those derived from the MAS and static studies.[35] The DOR method was slightly less sensitive in this case to variations in R_{eff} and therefore to the value of ΔJ. DOR holds promise as a complementary high-resolution technique to those described above for the characterization of spin systems subject to multiple simultaneous interactions, as demonstrated for hydroxyl oxygens by Wong *et al*.[37]

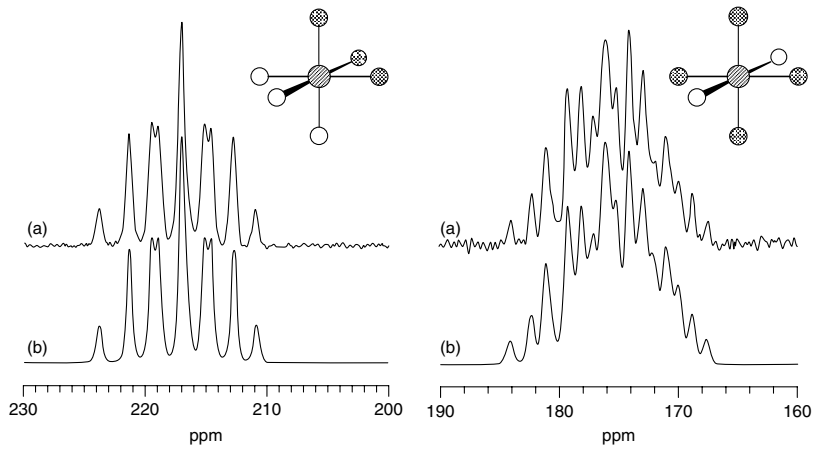


Figure 20.11. Isotropic regions of ^{113}Cd CP/MAS NMR spectra of $Na[Cd(SCN)_3]\cdot 3H_2O$ that exhibits J coupling to three equivalent ^{14}N nuclei (left) and $(Me_4N)_2[Cd(SCN)_4]$ which exhibits J coupling to four ^{14}N nuclei (right). Experimental spectra are shown in (a) and simulated spectra are shown in (b). (Reproduced from Ref. 32. © American Chemical Society, 1994.)

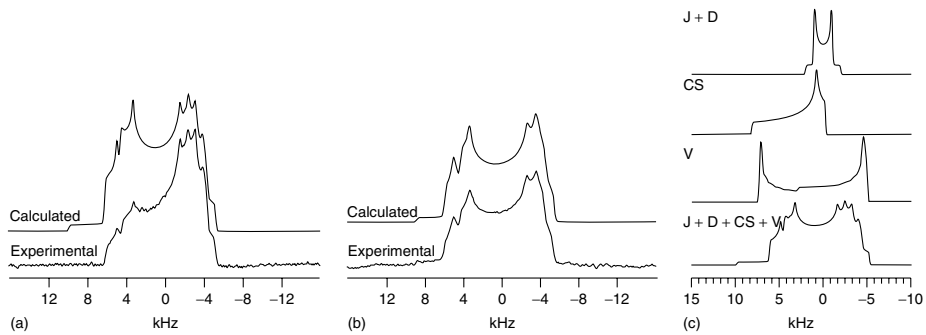


Figure 20.12. Experimental and simulated ^{17}O NMR spectra of stationary powdered samples of $Ph_3P^{17}O$. (a) Monoclinic polymorph. (b) Orthorhombic polymorph. (c) Simulated contributions, for the monoclinic polymorph, from each NMR interaction along with the final spectrum resulting from tensor interplay. (Reproduced from Ref. 35. © American Chemical Society, 2003.)

20.2.3.2 Advanced Pulse Sequences

The discussion thus far has focused on the analysis of 1-D lineshapes arising from powder samples under stationary or MAS conditions. Sophisticated pulsed NMR techniques have been developed to provide specific geometrical information, and multidimensional experiments are often required to reduce spectral congestion in the case of biopolymers. The development and application of advanced pulse sequences to provide structural information is a vast field and a detailed discussion is beyond the scope of this article; however, a short discussion follows. One of the goals of modern pulse sequences is to enable the determination of angles between the principal axes of various tensors, in addition to tensor magnitudes, with the goal of correlating relative tensor orientations to local geometry. Consider two adjacent peptide planes in a protein. One can make use of the knowledge that δ_{33} of the carbonyl carbon is approximately perpendicular to this plane and that δ_{22} lies approximately along the C=O axis: if the relative orientations of the two ^{13}C=O CS tensors can be measured, then the backbone torsion angles ψ and ϕ may also be deduced. Duer provides a pedagogical discussion of such a situation.[38] Various pulse

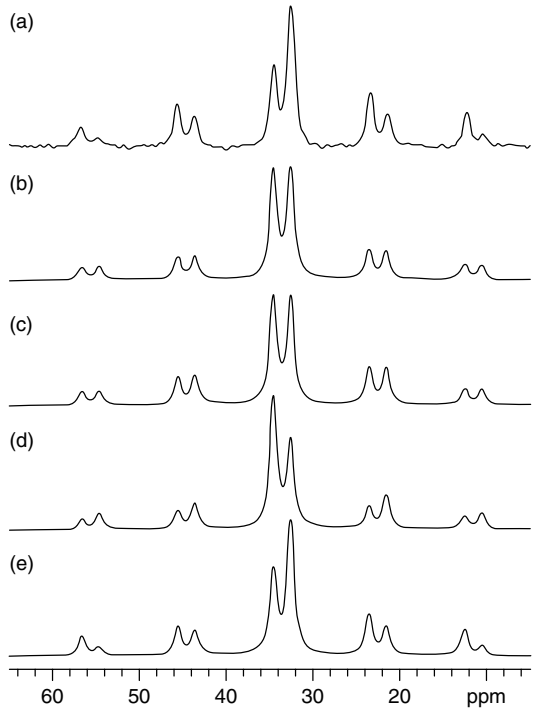


Figure 20.13. (a) Experimental ^{17}O DOR NMR spectrum of $Ph_3P^{17}O$ (monoclinic) obtained at 14.1 T. (b) Simulated spectrum due to quadrupolar and J-coupling interactions. (c) Same as (b) but with the inclusion of CSA. (d) Same as (b) but with the inclusion of dipolar coupling. (e) Simulated spectrum due to ***V, J, D*** and $\boldsymbol{\sigma}$ interactions. (Reproduced from Ref. 36. © Elsevier, 2007.)

schemes are available for the correlation of two CS tensors; typically the resulting 2-D spectra are interpreted through numerical simulation. Schmidt-Rohr and Spiess discuss some of these important experiments as applied to polymers.[39] Dipolar-CS experiments are also useful in providing peptide plane orientations relative to a particular dipolar vector. For example, Jaroniec *et al*. reported on the application of TEDOR and 3-D dipolar-CS correlation methods[40] to determine the high-resolution structure of a peptide fragment of the amyloidogenic protein transthyretin.[41]

20.3 CONCLUDING REMARKS

The interplay between multiple NMR interaction tensors leads to solid-state NMR spectra which are rich with information concerning local symmetry and molecular structure. In addition to furthering the fundamental understanding of how molecular and electronic structure are reflected in the NMR tensors, this information is particularly valuable in cases where diffraction-based methods cannot provide definitive structural information. With NMR, the most direct structural data come from dipolar coupling constants; however, relative tensor orientations can also be interpreted to provide related information. EFG and shielding tensors provide valuable information on the electronic distribution about the nucleus of interest. While some spectra may be interpreted through visual inspection, the majority of cases require lineshape simulations to extract a maximum of tensor information. The ongoing development of ingenious advanced NMR methods that take advantage of the information available from multiple tensor interactions enables spectroscopists to continue to push the boundaries in terms of characterizing spin systems in complex materials and biopolymers.

REFERENCES

1. J. B. Robert and L. Wiesenfeld, *Phys. Rep.*, 1982, **86**, 363.
2. D. L. VanderHart and H. S. Gutowsky, *J. Chem. Phys.*, 1968, **49**, 261.
3. K. W. Zilm and D. M. Grant, *J. Am. Chem. Soc.*, 1981, **103**, 2913.
4. W. P. Power and R. E. Wasylishen, *Ann. Rep. Nucl. Magn. Reson. Spectrosc.*, 1991, **23**, 1.
5. R. K. Harris, K. J. Packer, and A. M. Thayer, *J. Magn. Reson.*, 1985, **62**, 284.
6. H. Bai and R. K. Harris, *J. Magn. Reson.*, 1992, **96**, 24.
7. K. Eichele and R. E. Wasylishen, *J. Magn. Reson. Ser. A*, 1994, **106**, 46.
8. D. L. Bryce and R. E. Wasylishen, *Inorg. Chem.*, 2002, **41**, 4131.
9. R. K. Harris, P. Reams, and K. J. Packer, *J. Mol. Struct.*, 1986, **141**, 13.
10. U. Haeberlen, High resolution NMR in solids, selective averaging, in *Advances in Magnetic Resonance, Supplement 1* , J. S., Waugh, ed. Academic Press: New York, 1976.
11. H. van Willigen, R. G. Griffin, and R. A. Haberkorn, *J. Chem. Phys.*, 1977, **67**, 5855.

12. M. D. Lumsden, G. Wu, R. E. Wasylishen, and R. D. Curtis, *J. Am. Chem. Soc.*, 1993, **115**, 2825.
13. D. L. Bryce and R. E. Wasylishen, *J. Phys. Chem. A*, 2000, **104**, 7700.
14. S. Dusold, W. Milius, and A. Sebald, *J. Magn. Reson.*, 1998, **135**, 500.
15. G. Wu and R. E. Wasylishen, *J. Magn. Reson. Ser. A*, 1993, **102**, 183.
16. G. Wu, B. Sun, R. E. Wasylishen, and R. G. Griffin, *J. Magn. Reson.*, 1997, **124**, 366.
17. S. Dusold, E. Klaus, A. Sebald, M. Bak, and N. C. Nielsen, *J. Am. Chem. Soc.*, 1997, **119**, 7121.
18. K. Eichele, G. Wu, and R. E. Wasylishen, *J. Magn. Reson.*, 1993, **101A**, 157.
19. G. Wu and R. E. Wasylishen, *J. Chem. Phys.*, 1993, **98**, 6138.
20. J. F. Baugher, P. C. Taylor, T. Oja, and P. J. Bray, *J. Chem. Phys.*, 1969, **50**, 4914.
21. W. P. Power, R. E. Wasylishen, S. Mooibroek, B. A. Pettitt, and W. Danchura, *J. Phys. Chem.*, 1990, **94**, 591.
22. J. T. Cheng, J. C. Edwards, and P. D. Ellis, *J. Phys. Chem.*, 1990, **94**, 553.
23. P. J. Chu and B. C. Gerstein, *J. Chem. Phys.*, 1989, **91**, 2081.
24. D. L. Bryce and E. B. Bultz, *Chem. Eur. J.*, 2007, **13**, 4786.
25. P. A. Agron and W. R. Busing, *Acta Crystallogr. Sect. C*, 1986, **42**, 141.
26. D. L. Bryce and R. E. Wasylishen, *Phys. Chem. Chem. Phys.*, 2002, **4**, 3591.
27. (a) N. F. Ramsey, *Phys. Rev.*, 1950, **78**, 699; (b) N. F. Ramsey, *Phys. Rev.*, 1951, **83**, 540; (c) N. F. Ramsey, *Phys. Rev.*, 1952, **86**, 243.
28. P. A. Casabella, *J. Chem. Phys.*, 1964, **41**, 3793.
29. R. K. Harris and A. C. Olivieri, *Prog. Nucl. Magn. Reson. Spectrosc.*, 1992, **24**, 435.
30. R. Gobetto, R. K. Harris, and D. C. Apperley, *J. Magn. Reson.*, 1992, **96**, 119.
31. N. A. Davies, R. K. Harris, and A. C. Olivieri, *Mol. Phys.*, 1996, **87**, 669.
32. K. Eichele and R. E. Wasylishen, *Inorg. Chem.*, 1994, **33**, 2766.
33. G. Wu and R. E. Wasylishen, *Mol. Phys.*, 1998, **95**, 1177.
34. G. Facey, D. Gusev, R. H. Morris, S. Macholl, and G. Buntkowsky, *Phys. Chem. Chem. Phys.*, 2000, **2**, 935.
35. D. L. Bryce, K. Eichele, and R. E. Wasylishen, *Inorg. Chem.*, 2003, **42**, 5085.
36. I. Hung, A. Wong, A. P. Howes, T. Anupõld, J. Past, A. Samoson, X. Mo, G. Wu, M. E. Smith, S. P. Brown, and R. Dupree, *J. Magn. Reson.*, 2007, **188**, 246.
37. A. Wong, I. Hung, A. P. Howes, T. Anupõld, J. Past, A. Samoson, S. P. Brown, M. E. Smith, and R. Dupree, *Magn. Reson. Chem.*, 2007, **45**, S68.
38. M. J. Duer, *Introduction to Solid-State NMR Spectroscopy*, Chapter 3, Blackwell Publishing: Oxford, 2004.
39. K. Schmidt-Rohr and H. W. Spiess, *Multidimensional Solid-State NMR and Polymers*, Chapter 6, Academic Press: London, 1994.
40. C. M. Rienstra, M. Hohwy, L. J. Mueller, C. P. Jaroniec, B. Reif, and R. G. Griffin, *J. Am. Chem. Soc.*, 2002, **124**, 11908.
41. C. P. Jaroniec, C. E. MacPhee, V. S. Bajaj, M. T. McMahon, C. M. Dobson, and R. G. Griffin, *Proc. Natl. Acad. Sci. USA*, 2004, **101**, 711.
42. H. M. Foucault, D. L. Bryce, and D. E. Fogg, *Inorg. Chem.*, 2006, **45**, 10293.

PART E
Properties of the Crystalline State

Chapter 21

Intermolecular Interactions & Structural Motifs

Lindsay S. Cahill[1] and Gillian R. Goward[2]

[1]*Department of Physics, University of Warwick, Coventry CV4 7AL, UK*
[2]*Department of Chemistry, McMaster University, Hamilton, Ontario L8S 4M1, Canada*

21.1	Introduction	305
21.2	Host–Guest Interactions: Zeolites	306
21.3	Aromatic π–π Stacking and Ring-Current Effects	307
21.4	Interactions in Nanostructures	311
21.5	Polymorphs	312
21.6	Ab Initio Calculations	315
21.7	Conclusion	317
	References	317

21.1 INTRODUCTION

Nuclear magnetic resonance (NMR) is a powerful tool for establishing intermolecular interactions in the solid state, and has been used extensively to study structure in this way. The investigation of intermolecular bonding is pivotal in the field of supermolecular chemistry and in the study of polymorphs, enzyme-substrate complexes and hydrogen-bonding arrangements (*see* **Chapter 22**). Two key nuclear interactions have dominated the study of intermolecular interactions by solid-state NMR: magnetic shielding and dipolar coupling. Chemical shifts, both isotropic values and components of the symmetric portion of the shielding tensor, are a significant structural probe. They are highly sensitive to the local structure and to changes in packing arrangements. Dipolar coupling constants, whether heteronuclear or homonuclear, scale with the inverse cube distance between partner nuclei, and can therefore be used to probe local environments. Moreover, when paired with diffraction studies, detailed information regarding both structure and site-specific dynamics on the molecular level can be obtained. The related article, **Chapter 18**, outlines the complementarity between diffraction methods for structure determination and solid-state NMR.

While this article does comment on the interpretation of chemical shifts, it focuses primarily on the application of NMR strategies that take advantage of the dipolar coupling to determine intermolecular interactions that govern the solid-state structural motifs. We begin with examples based on the utilization of cross polarization (CP), and also include recoupling techniques, which take advantage of either homonuclear or heteronuclear dipolar couplings. This article also demonstrates how chemical shifts can help to elucidate interactions in host–guest complexes and can be used to differentiate between polymorphs. Complementary computational methods, such as CASTEP,[1,2] which can be used in combination with experimental data to validate a structural model, is also described

NMR Crystallography Edited by Robin K. Harris, Roderick E. Wasylishen and Melinda J. Duer © 2009 John Wiley & Sons, Ltd. ISBN: 978-0-470-69961-4

throughout the article. While hydrogen bonding is clearly a dominant intermolecular interaction, it has been discussed in another article (*see* **Chapter 22**), and thus, the focus here is on π-stacking, host–guest interactions, and other intermolecular interactions.

21.2 HOST–GUEST INTERACTIONS: ZEOLITES

An understanding of intermolecular interactions is critical in the study of host–guest systems. A central aim in these studies is to determine which parts of a host structure interact with the guest molecule, and what are the strengths of those interactions. Porous aluminosilicate frameworks, known as *zeolite structures*, are an elegant example of host–guest interactions, which find application in molecular sieves, catalysts, and as hosts for gas adsorption. Such structures have been studied extensively by solid-state NMR.

Solid-state NMR studies of the host zeolite structure itself take advantage of the ability of NMR to select ^{29}Si or ^{27}Al nuclei, whereas these atoms have similar X-ray scattering factors making distinction of the ordering of the catalytically important Al sites elusive by X-ray diffraction (XRD) methods. Moreover, single-crystal XRD methods are often limited due to the disorder of the Si and Al atoms in the structure. An early study of the 3-D Si–O–Si connectivity in zeolite ZSM-39 (dodecasil 3 C) with 80% ^{29}Si enrichment was conducted by Fyfe *et al*.[3] Spin-diffusion measurements and ^{29}Si correlation spectroscopy (COSY) experiments correctly established the connectivities that were expected from the XRD structure. It is pertinent to point out that the latter technique only detects through-bond interactions and, unlike dipolar coupling, allows one to distinguish between direct connectivity and intermolecular proximity. This work was later extended to other zeolite structures using natural abundance ^{29}Si COSY and INADEQUATE experiments.[4,5] These 2-D homonuclear correlation studies provide a methodology for constructing the arrangement of atoms in zeolite and other crystalline solids. Fyfe led one of the first groups to directly observe weak through-bond couplings in solids and to demonstrate their value for structure determination. Recently, Brouwer provided the first full crystal structure from NMR, defining both the silicon and oxygen positions.[6] This approach uses ^{29}Si double quantum (DQ) correlation experiments to solve the structure and ^{29}Si chemical shift tensors for refinement. Having established a means for reliably determining the host framework structure, this seminal work was further developed to include the intermolecular connectivity of the host and guest molecules.

The ability to study the structural relationship between the zeolite host and the guest molecule is essential to identify binding sites, and improve upon their selectivity. CP,[7] which transfers magnetization from abundant nuclei, such as protons, to dipolar-coupled heteronuclei, is a versatile method for establishing through-space interactions between the zeolite framework and the target guest molecule. By increasing the contact time in the CP experiment, longer internuclear distances between specific nuclei can be probed. Fyfe *et al*. have used ^{1}H/^{29}Si CP experiments to determine the 3-D structure formed between the ZSM-5 zeolite framework and organic molecules including *p*-xylene,[8] *p*-dichlorobenzene,[9] and naphthalene.[10] Figure 21.1 shows the 1-D ^{29}Si spectra of ZSM-5 and *p*-dichlorobenzene with and without CP. Qualitatively, the peaks of Si sites that are closest to the protons on the organic molecule will experience significant enhancements, as is evident for Si 8 and Si 9, whereas lower relative intensity will be observed for peaks arising from Si sites which are far from the organic guest. Plotting the peak area of the ^{29}Si CPMAS signal versus contact time in a CP buildup curve gives CP time constants that yield Si–H distances. Using the distances determined from the dipolar interaction, the location of the guest molecule in the zeolite framework can be determined.

CP experiments assume that the number of ^{1}H nuclei is much greater than the number of ^{29}Si nuclei, and that the rate constant for transfer of magnetization between ^{1}H and ^{29}Si is much greater than the homonuclear relaxation rate constants. It is important to note that when the interactions of interest are intermolecular, these conditions are often not met, since the IS coupling is invariably small. In such cases, CP drain experiments can be used to measure the absolute CP rate constant values, which are proportional to the internuclear distance.

Detailed information can also be obtained by selectively deuterating the organic guest molecule, as this allows the ^{1}H polarization source to be controlled and placed at different sites. An example of this type of study is the investigation of the location of *ortho*-xylene within ZSM-5, using selective deuteration of the guest.[11] In this way, isolated spin pairs can be chosen, and more

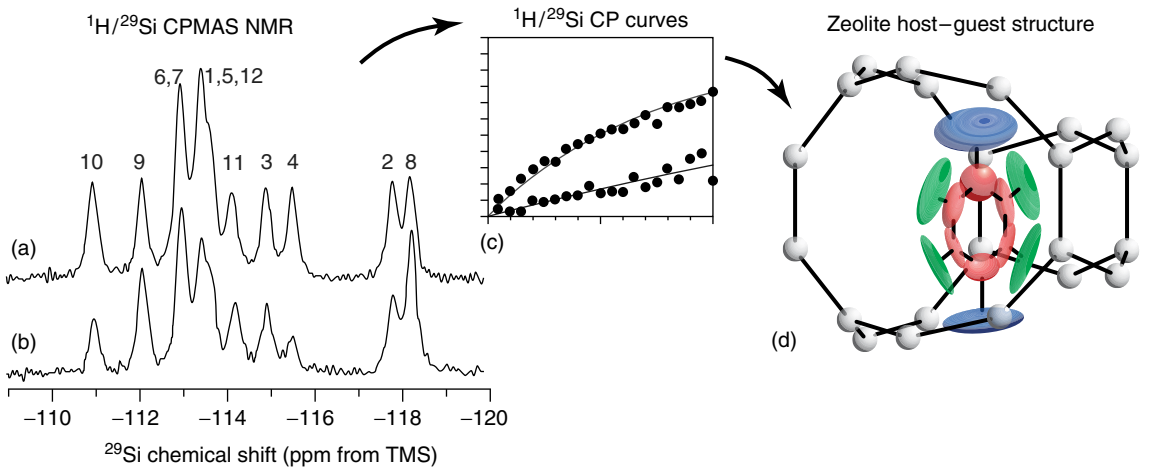


Figure 21.1. Comparison of (a) quantitative ^{29}Si MAS and (b) $^{1}H/^{29}Si$ CPMAS spectra of ZSM-5 loaded with *p*-dichlorobenzene at 280 K. Note that the intensities of the peaks Si 8 and Si 9 are enhanced compared to the others. (c) shows a representative buildup curve, and (d) shows a final structure, resulting from the complete analysis of the CP data. (Reproduced from Ref. 9. © American Chemical Society, 2006.)

structural information becomes available. Here, the CP drain experiment provides the normalized signal difference, measured with and without the CP contact pulse, from which the internuclear distances can be calculated. Using this approach, the locations of the organic sorbate molecules determined by solid-state NMR were in excellent agreement with single-crystal XRD studies. It is important to recognize that motion of the organic sorbate will decrease the efficiency of the CP, giving erroneous internuclear distances. Low-temperature experiments were necessary in these zeolite host–guest studies to ensure investigation of rigid systems.

Proton solid-state NMR has been used to examine adsorbed molecules such as acetonitrile,[12] 1-butene[13] and phenol[14] in zeolites. In this case, the information about the nature of adsorption sites is found by comparing the chemical shifts of the free molecule and the adsorbed guest molecule. The sites that experience the greatest change in chemical shift are, by inference, located closest to the zeolite host framework. Brouwer *et al*. have used ^{1}H NMR to investigate *p-tert*-butylcalix[4]arene, another type of inclusion host–guest complex.[15] They compared the differences in ^{1}H chemical shifts of the free guest molecule and the host–guest complex for toluene and pyridine (Table 21.1). This shift difference was termed a *complexation-induced shift* (CIS) and is highly sensitive to the formation of this host–guest complex because of the magnetic shielding caused by the aromatic rings of the calixarene molecule. Considering a combination of CISs and results from ab initio calculations, it was possible to locate the position, as well as confirm the specific dynamics of the toluene guest molecule in the calixarene cavity, as illustrated in Figure 21.2.

21.3 AROMATIC π–π STACKING AND RING-CURRENT EFFECTS

As described in **Chapter 22** and seen in the above studies of host–guest systems, ^{1}H chemical shifts are immensely sensitive to local environments, and can be used to probe local intermolecular interactions such as π–π stacking. In particular, we discuss several examples where insights into molecular packing motifs are provided through the sensitivity of the ^{1}H chemical shift to ring-current effects of neighboring aromatic systems. A detailed review of the theory underlying ring-current effects can be found in the review by Lazzeretti.[16] In essence, when a proton sits above or below an aromatic moiety, the proton experiences a large shielding effect and the peak moves to lower frequency. Conversely, if a proton interacts with the π electrons in the plane of the aromatic

Table 21.1. Comparison of experimental and ab initio calculated ^{1}H chemical shifts in *p-tert*-butylcalix[4]arene inclusion compounds

	Experimental (ppm)			Calculated (ppm)		
	Solution	Complex	CIS	Free	Complex	CIS
Toluene (2:1)						
H2	6.98	5.10	−1.88	7.36	5.62	−1.79
H3	7.09	4.54	−2.46	7.41	5.40	−2.12
H4	7.00	2.96	−4.13	7.52	3.56	−3.80
H5	2.09	−1.41	−3.50	2.50	−1.48	−3.75
Toluene (1:1)						
H2	6.98	5.46	−1.52	7.36	5.97	−1.39
H3	7.09	6.40	−0.69	7.41	7.02	−0.39
H4	7.00	6.40	−0.60	7.52	6.83	−0.69
H5	2.09	−1.76	−3.85	2.50	−1.87	−4.37
Pyridine (1:1)						
H2	8.74	6.92	−1.82	9.15	7.71	−1.44
H3	7.22	4.46	−2.76	7.30	4.95	−2.35
H4	7.58	4.29	−3.29	7.97	4.75	−3.22

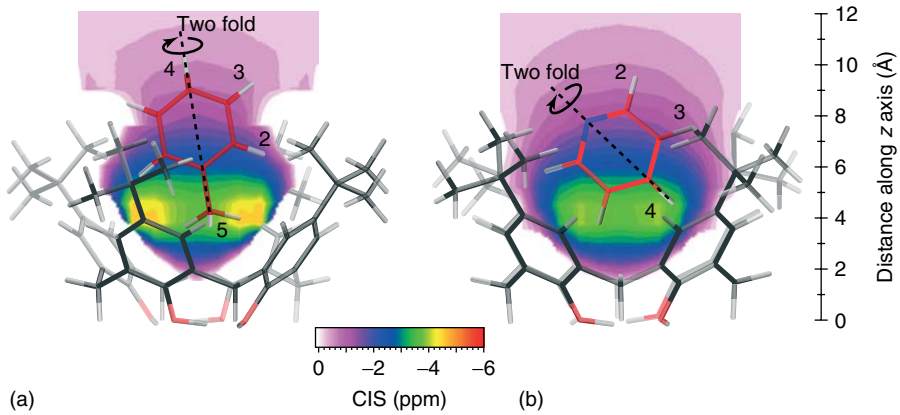


Figure 21.2. Superposition of (a) toluene and (b) pyridine guest molecules on the complexation-induced shift map of the *p-tert*-butylcalix[4]arene cavity. (Reproduced from Ref. 9. © Royal Society of Chemistry, 2006.)

ring, the peak will move to higher frequency. The ring-current effect is found to be quite long range, showing an influence at a distance of 0.7 nm in the hexabenzocoronene systems discussed below.[17]

In some cases, the ^{1}H chemical shifts and through-space couplings alone can present a compelling case for unique 3-D packing motifs. The hexabenzocoronenes (HBCs) are such an example (Figure 21.3a).[18] These molecules can be thought of as small, round pieces of graphite, surrounded by aliphatic side chains. They show a strong propensity to stack as discotic liquid crystals. The preference to form tilted stacks, rather than flat stacks, was determined on the basis of the ^{1}H chemical shifts, resolved under fast magic angle spinning, and correlated through the homonuclear ^{1}H–^{1}H DQ correlation spectrum. This is an excellent example of the power of solid-state NMR to be applied to a material in which the local packing motif was suspected, but ill characterized due to lack of long-range order and molecular dynamics. In this sense, the crystallography of the material is established through the three resolved ^{1}H chemical shifts. The three peaks are unique due to the

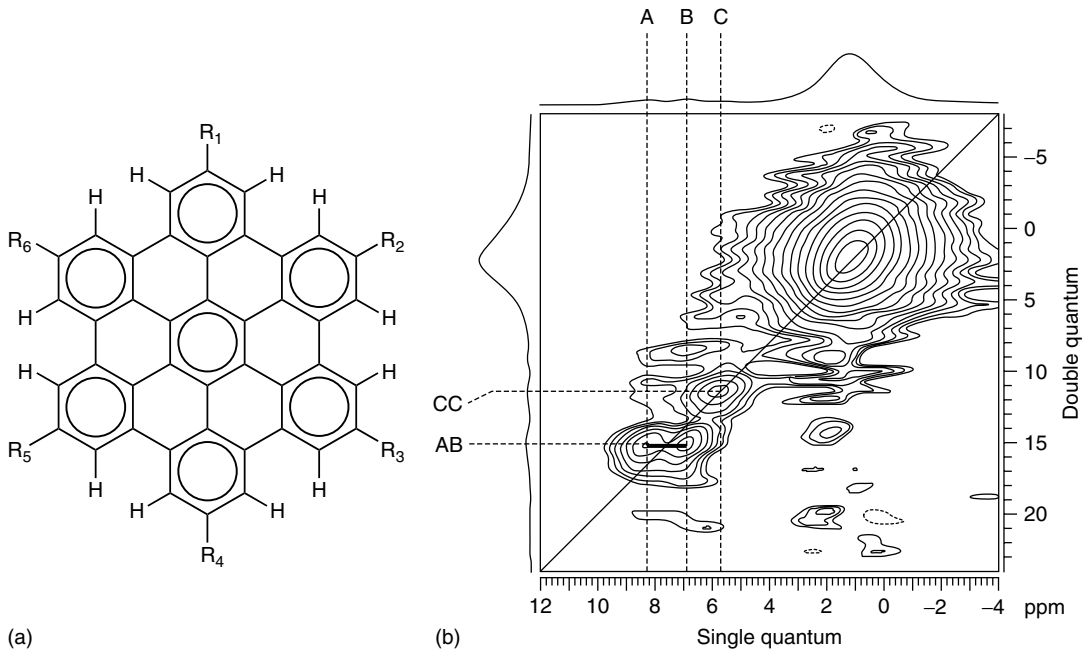


Figure 21.3. (a) Structure of hexa-*n*-dodecylhexa-*peri*-hexabenzocoronene (HBC-C_{12}); (b) rotor-synchronized ^{1}H DQ MAS NMR spectrum of deuterated HBC-C_{12} at 35 kHz using one cycle of the back-to-back (BABA) recoupling sequence. The three aromatic protons are labeled A, B, and C from highest to lowest frequency. (Reproduced from Ref. 18. © American Chemical Society, 1999.)

varying influence of the aromatic ring-current and are a function of the position of the protons with respect to the graphene sheets above and below it.[18] The 2-D ^{1}H–^{1}H DQ correlation spectrum is used to establish the packing motif, illustrated in Figure 21.3(b), where the three peaks are shown in the projection on the *x*-axis, and the correlations among the three peaks allow the intermolecular interactions to be identified. 2-D DQ spectroscopy, as described in detail in, takes advantage of dipolar coupling interactions to generate and select DQ coherences between coupled spins. In the 2-D experiment, correlations appear as diagonal peaks for coupled "like" spins, and off-diagonal peaks represent protons in different local environments. In both cases, the cross peaks are observed at the sum of the single-quantum peak frequencies for the spin pair, in the DQ dimension. This provides the qualitative constraints that can be used to develop a picture of the 3-D packing motif for the molecules. In particular, in the case of HBC–C_{12} (hexa-*n*-dodecylhexa-*peri*-hexabenzocoronene), the intermolecular interaction between protons and aromatic ring structures in adjacent molecules is elucidated.[18] Here, the ^{1}H chemical shift is a sensitive probe of aromatic ring-current effects and is used to determine the stacking arrangement of the HBC molecules. Quantitative distance information is available from ^{1}H DQ spinning sideband patterns. This method gives direct distances between nuclei based on the dipolar coupling constant. Differences in dynamics between crystalline and liquid crystalline phases of HBC–C_{12} were determined.[18] In the latter, the decrease in dipolar coupling for protons in the core of the HBC, compared to the distance expected from the XRD structure, is attributed to mobility. Mobility of the alkyl chains was identified in a similar way.

Quantitative information regarding dynamics can also be acquired using recoupled polarization-transfer heteronuclear multiple-quantum correlation (REPT-HMQC)[19] or rotor-encoded rotational echo (REREDOR)[20] spinning sideband patterns, from which dipolar couplings can be deduced.[21,22] A decrease in ^{1}H-^{13}C dipolar coupling is correlated to local segmental motion of C–H

internuclear vectors through an order parameter *S*. The parameter *S* is calculated by taking the ratio of the reduced coupling (experimental) to the rigid (static) coupling.[23] This approach was used to compare the mobility of HBC–C_{12} and HBC–PhC_{12} where the added phenylene units in the latter case cause a decrease in mobility of the HBC core.

An example of the combination of homonuclear DQ correlation, heteronuclear correlation, and quantum mechanical calculations for determining local structure is given in the case of molecular tweezers, shown on the left in Figure 21.4. These complexes are concave-shaped and can selectively bind guest molecules.[24] This is yet another example of the power of intermolecular ring-current effects on local proton environments, as observed through chemical shifts. The chemical shift resolution is a result of both the chemical shift dispersion caused by the varying proximities and orientations of protons with respect to the aromatic system, and the averaging of the homonuclear dipolar couplings via fast magic angle spinning. In 1,4-dicyanobenzene (DCNB), the aromatic protons are equivalent for an isolated molecule but when complexed with the tweezers, the chemical shifts differ by more than 3 ppm.[24,25] The comparison of two guest molecules, DCNB and 1,2,4,5-tetracyanobenzene (TCNB), within the same molecular tweezer gave rise to distinct 1-D ^{1}H MAS spectra and ^{1}H DQ spectra, on the right in Figure 21.4, indicative of unique conformations for the guest in each case.[26] Intermolecular interactions between protons and benzene rings are observed both between guest and host and between two host molecules. This information is necessary to build up the 3-D packing arrangement of the complexes. The spectra are compared to quantum chemical calculations of the structures, and predicted spectra thereof, to determine the packing motif of each. The tweezers needed to be modeled as a dimer to accurately predict the chemical shifts in the solid state. In

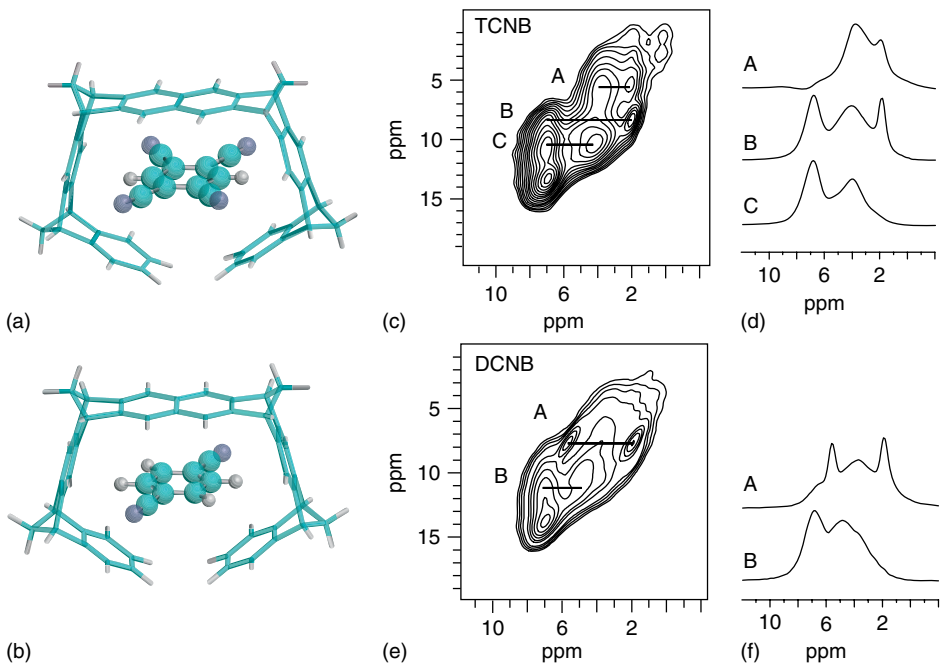


Figure 21.4. Complex with (a) 1,2,4,5-tetracyanobenzene (TCNB) and with (b) 1,4-dicyanobenzene (DCNB: $H_{guest,\,A}$, $H_{guest,\,B}$ point toward the tweezer benzene units of the sidewalls and out of the cavity, respectively). The carbon atoms are represented in green, the nitrogen atoms in blue, and the protons in white. ^{1}H rotor-synchronized DQ MAS spectra at 30 kHz and using one cycle of the BABA recoupling sequence. (c) Complex with 1,2,4,5-tetracyanobenzene (TCNB) and slices (A, B, C) showing (d) the correlation peaks between the resonances. (e) Complex with 1,4-dicyanobenzene (DCNB) and slices (A, B) showing (f) the correlation peaks between the resonances. (Reproduced from Ref. 26. © American Chemical Society, 2007.)

this way, the change in the chemical shifts caused by the influence of the intermolecular interactions can be determined. By comparing these results to calculations on a monomer unit, the influence of intramolecular interactions within the host–guest complex could be separated from the interactions between neighboring complexes. Where possible, quantum chemical calculations such as these can provide convincing support for spectral interpretation in the context of a proposed structure. In this case, the calculations were performed using ab initio packages, Q-Chem, and TURBO-MOLE, and this was one of the first demonstrations of the application of a combined experimental and theoretical approach to provide information regarding intermolecular interactions to elucidate structural arrangements.

Interestingly, there is no direct correlation between the availability of an aromatic ring system, and a strong ring-current influence on the ^{1}H chemical shifts. In a study of the hydrogen-bonded structure, bilirubin, which includes an aromatic functionality, the differences in chemical shift between solution and solid state were on the order of 0.5 ppm.[27] This is equivalent to the error values associated with the ab initio calculations of the solid-state structures. In this case, the structural motifs are governed by the four strong hydrogen bonds, as reflected in the chemical shifts of these protons.

21.4 INTERACTIONS IN NANOSTRUCTURES

Intermolecular interactions driven by π-stacking have also been observed in the unique, and intensively investigated behavior of carbon nanotubes (CNTs). In this case, owing to the absence of protons in the nanotube structure, heteronuclear correlations become key to establishing structural motifs. In one example, functionalization of the CNT is demonstrated through the correlation between the protons of the functional group and the aromatic carbons on the nanotubes.[28] This demonstration of functionalization, based on the through-space dipolar coupling, was probed using a CP transfer of magnetization, to provide structural detail on an insoluble, noncrystalline, yet well behaved and highly intriguing structure. In this case, the only comparable structural information on these molecular architectures has been provided by scanning tunneling microscopy. The 2-D

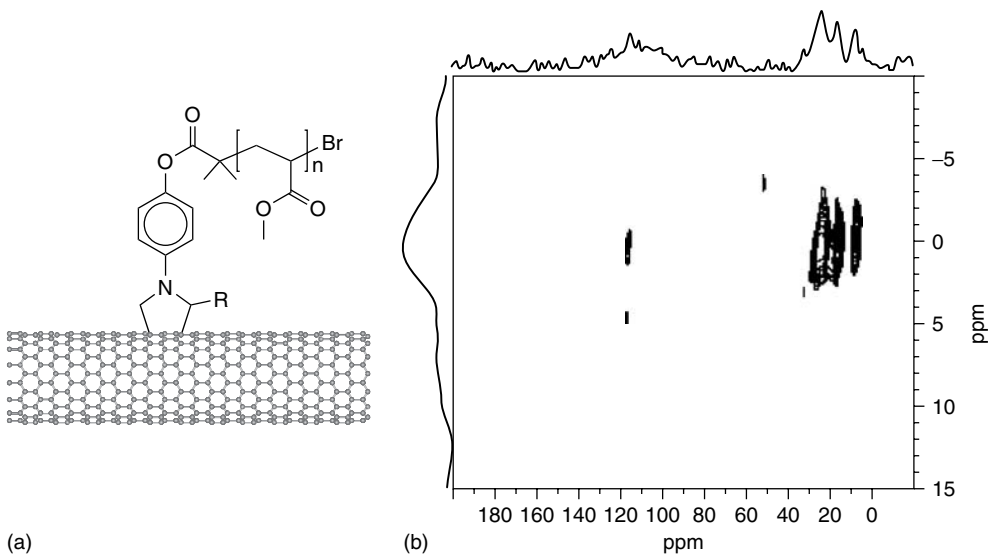


Figure 21.5. (a) Schematic representation of phenol-functionalized carbon nanotubes; (b) $^{1}H-^{13}C$ 2-D correlation spectra of phenol nanotubes acquired by a variant of TEDOR, with 30 kHz MAS, and six rotor periods of recoupling. The number of slices in the indirect dimension was 24, with 512 transients averaged per slice. There is a clear correlation between the ^{13}C resonance of the nanotubes (121 ppm) and the ^{1}H chemical shift of the aliphatic functional group (0.5 ppm). (Reproduced from Ref. 28. © American Chemical Society, 2004.)

$^{1}H-^{13}C$ correlation spectrum, shown in Figure 21.5, highlights the key through-space correlation, diagnostic for the functionalization of the nanotubes.

Another study of host–guest complexes uses $^{1}H-^{13}C$ HETCOR to study CH$\cdots\pi$ through-space interactions to understand the architecture in nanostructure materials of tris(*o*-phenylenedioxy) spirocyclotriphosphazene (TPP) with polyethylene.[29] The HETCOR spectra show a clear interaction between the polymer chains and the aromatic TPP system, indicating that the TPP "paddles" wrap around the linear polyethylene chain.

Similarly, homonuclear recoupling methods have been used to characterize nanostructures. For example, in a recent study, the selective ^{13}C-labeling of the amino acids was used to probe the structure formed upon self-assembly of amyloids, under a variety of pH conditions.[30] The intermolecular $^{13}C-^{13}C$ homonuclear dipolar couplings among the labeled peptides, which become part of the hollow-nanotube structure, were then used to assess the structure of the nano-object. The coupling was probed via the DQF-DRAWS experiment, which produced a buildup curve, from which the interchain distance of 4.6 Å provides the basis of the assessment of the β-sheet structure, as illustrated in Figure 21.6. These are just three examples of the power of heteronuclear correlation experiments to elucidate structure in applications for nanomaterials.

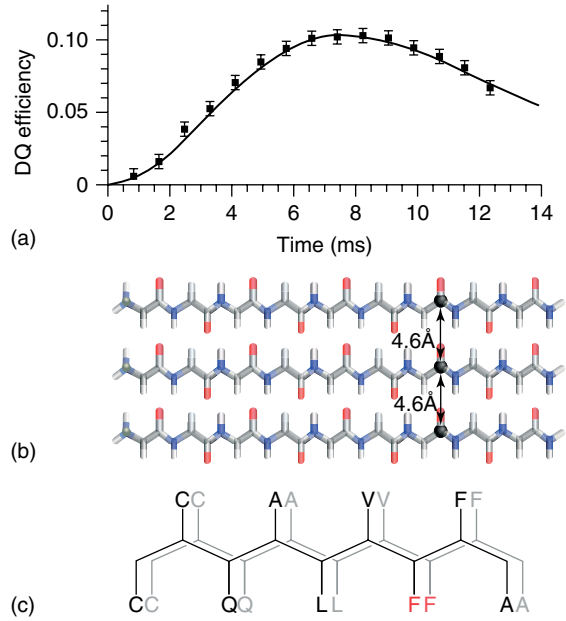


Figure 21.6. (a) ^{13}C DQF-DRAWS of 1-mM peptide assembled in buffered solution at pH 3.3. The solid line is the simulated DQF-DRAWS curve, from which the intermolecular distances between peptides are determined for an infinite array of $^{13}C-^{13}C$ distances of 4.6 Å with a $T_{2\text{-DQ}}$ = 9.4 ms. (b) Three in-register parallel β-strands; black spheres represent the F-19 carbonyl ^{13}C. (c) Schematic β-sheet diagram showing peptide registry and residues displayed on each β-sheet face. The front peptide is colored black and ^{13}C labeled F-19 residues are shaded red. (Reproduced from Ref. 30. © American Chemical Society, 2008.)

21.5 POLYMORPHS

Polymorphs of a material have different crystal structures and therefore differ in the spatial arrangement of the atoms or molecules. Polymorphs can differ in either their intramolecular bonding (changes in the molecular geometry) or intermolecular bonding (different packing motifs). An understanding of what governs the intermolecular interactions is essential to control the generation of polymorphs, an important concern for the pharmaceutical industry. Solid-state NMR has been used at length in the study of polymorphism and there are a number of review articles available by Harris.[31,32] For example, in, Harris demonstrates how the chemical shift is very sensitive to conformation and packing arrangements. In many cases, the NMR spectrum can definitively act as a "fingerprint" for identification of the polymorphic form. ^{13}C CPMAS was first used to study polymorphs where it was demonstrated that the differences between the chemical shifts of several polymorphs can be large. Often the differences in shift arise because of differences in intermolecular interactions, especially hydrogen bonding and aromatic ring-current effects. Examples where this has been revealed by solid-state NMR include the studies of polymorphs of cortisone acetate,[33] dirithromycin,[34] lamivudine,[35] sulfathiazole,[36] aspartame,[37] 4-methyl-2-nitroacetanilide,[38] and testosterone.[39] Figure 21.7 shows the ^{13}C CPMAS spectra of the white and yellow forms of 4-methyl-2-nitroacetanilide. The X-ray structures of these polymorphs are known and the large differences in chemical shifts for C1 and C5 (labeled in the figure) result from large changes in the dihedral angle. These changes will affect the delocalization of the π electrons in the benzene ring. While the different polymorphs are

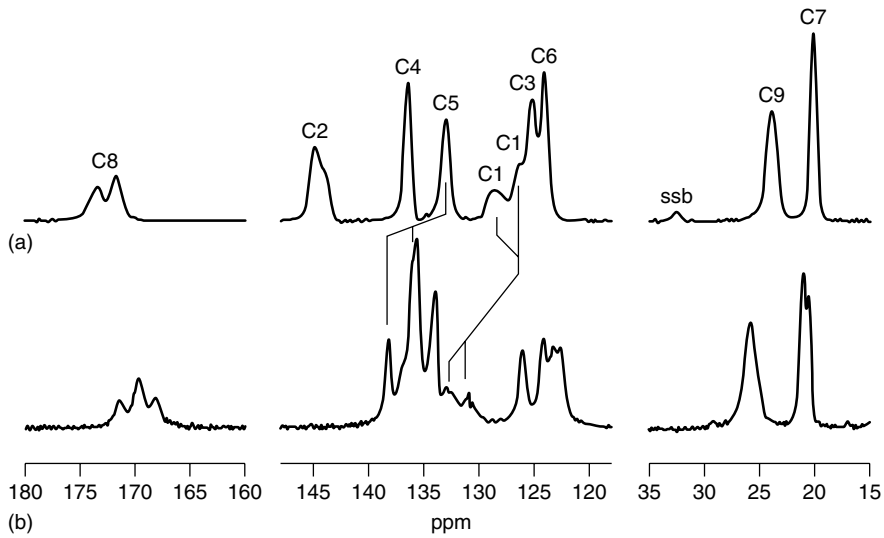


Figure 21.7. $^{1}H/^{13}C$ CPMAS spectra of (a) white and (b) yellow forms of 4-methyl-2-nitroacetanilide. The lines emphasize the large differences in chemical shift for C1 and C5. (Reproduced from Ref. 38. © John Wiley & Sons Ltd, 2006.)

often easily identified by their fingerprint spectra, the exact assignment of the peaks is sometimes only possible with the aid of computational methods.

Even more sensitive to molecular conformation than isotropic chemical shifts are shielding tensors. This was originally recognized for application to polymorphs in the study of cortisone acetate by Christopher *et al*.[33] Both the principal values and orientation of these tensors strongly reflect conformation and packing effects. Full shielding tensors are difficult to determine experimentally, unless performing a single-crystal NMR study. The principal chemical shift values in powders, δ_{11}, δ_{22}, and δ_{33}, can be obtained using 2-D FIREMAT experiments.[40] This technique results in an isotropic spectrum in one dimension and gives shielding information in the other. Slices through the indirect dimension give isolated spinning sideband patterns for each resolved isotropic shift (shown in Figure 21.8 for 4,7-di-*t*-butylacenaphthene). Grant and coworkers used this method to study two polymorphs of dimethyl-3,6-dichloro-2,5-dihydroxyterephthalate.[41] The principal values of the chemical shift tensors of the carbons were obtained and shown to be very sensitive to the intermolecular interactions, both π-conjugation and hydrogen bonding. Figure 21.9 compares isotropic chemical shifts (dotted lines) with chemical shift principal values (solid lines) for the white (W–I) and yellow (Y–I) polymorphs of dimethyl-3,6-dichloro-2,5-dihydroxyterephthalate. It is clear from the larger differences in the chemical shift principal values that they are more sensitive to conformation than the isotropic shifts. This is particularly true for the ester carbon, where the isotropic chemical shifts could not be used to distinguish between polymorphs while the principal values are significantly different. Gaussian calculations of the shielding tensors were performed using the DFT approach. Agreement between experimental and theoretical values was greatly improved by increasing the size of the calculated system from an isolated molecule to a stack of three molecules. This is just one example of the important role that intermolecular interactions play in determining accurate shielding parameters by calculation.

2-D FIREMAT spectra were also used to compare 4,7-di-*t*-butylacenaphthene (Figure 21.8) and 4,7-*t*-butylacenaphthylene where in the former, ring-current effects were found to account for the large difference in the chemical shift tensors.[40] In combination with Gaussian calculations, the intermolecular shielding contribution was determined. Grant *et al*. have also used ^{13}C and ^{15}N chemical shift principal values and $^{1}H-^{13}C$ HETCOR to assign the structure of a polymorph of paclitaxel, the anticancer drug marketed as Taxol®.[42]

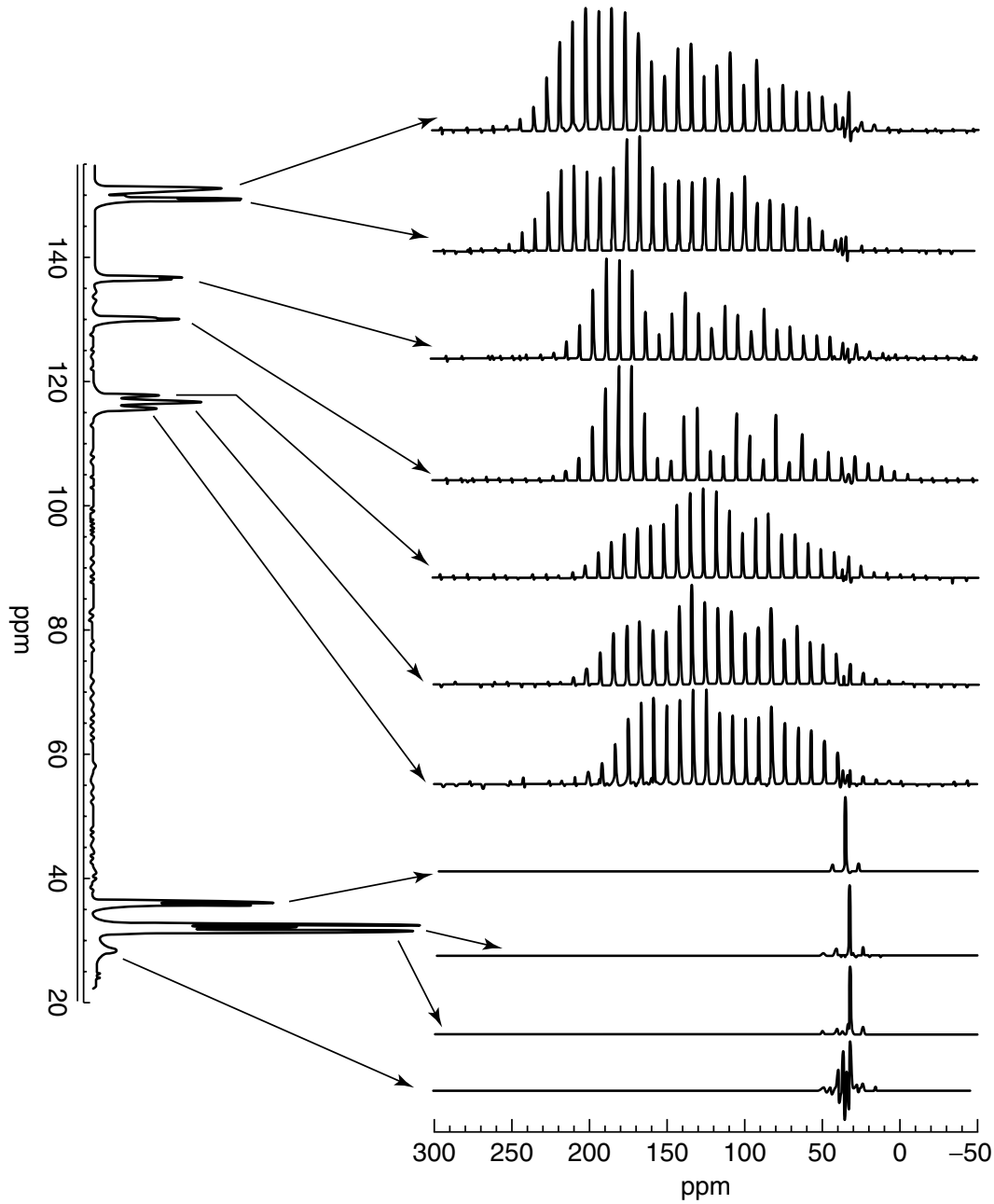


Figure 21.8. 2-D FIREMAT guide spectrum versus spinning sideband spectrum for 4,7-di-*t*-butylacenaphthene, acquired at 850 Hz. (Reproduced from Ref. 40. © American Chemical Society, 2007.)

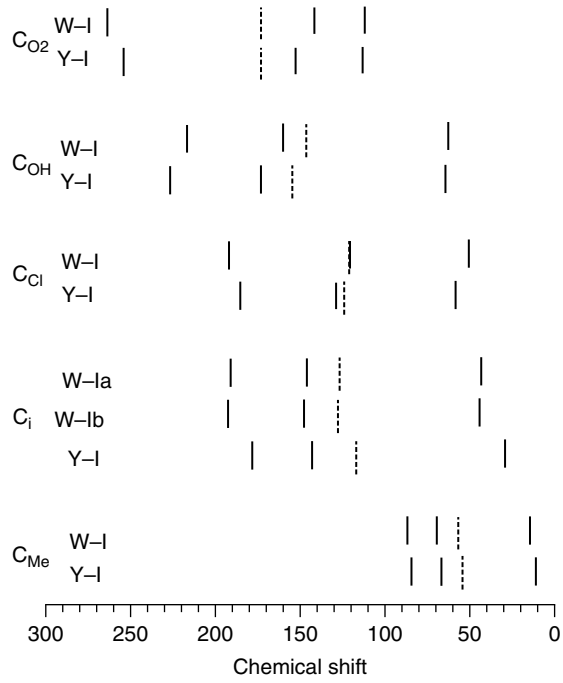


Figure 21.9. Experimental chemical shift principle values and isotropic chemical shifts for white (W–I) and yellow (Y–I) polymorphs of dimethyl-3,6-dichloro-2,5-dihydroxyterephthalate. Solid lines represent the chemical shift principal values and the isotropic chemical shifts are represented by dashed lines. (Reproduced from Ref. 41. © American Chemical Society, 2001.)

The significance of combining an experimental and theoretical approach is emphasized in the study of intermolecular interactions in polymorphs. Using DFT calculations, it has been shown that full shielding tensors can easily be computed. Besides, since packing affects molecular geometry, the impact of intra- and intermolecular interactions can be distinguished using computational methods. Recent advances in the computation of NMR parameters make it possible to study the effect of repetition in the crystal lattice. This is described in the following section.

21.6 AB INITIO CALCULATIONS

The benefits of combining solid-state NMR and first principles quantum mechanical calculations for structural elucidation are widely recognized. This is particularly true when the system of interest has several sites, resulting in a complex and often overlapped solid-state spectrum.[43–48] In studies of crystalline solids using Gaussian calculations, agreement between experiment and computation was improved by increasing the size of the calculated system beyond the isolated molecule under consideration. This was seen for the studies of the dimethyl-3,6-dichloro-2,5-dihydroxyterephthalate polymorphs (Section 21.5) and in molecular tweezers (Section 21.3) where intermolecular interactions were important.[41] Introduced in 2002, gauge-including projector-augmented wave (GIPAW) DFT calculations using the CASTEP code have had a major impact on accounting for interactions between molecules[1,2] (*see* **Chapter 3**). Unlike Gaussian calculations that use the cluster approximation and therefore do not encompass the true periodic structure of a crystal, GIPAW calculations use a plane-wave pseudopotential approach to model the infinite periodic solid. GIPAW uses pseudopotentials to represent the interaction between the core and valence states and the orbitals are expanded using a plane-wave basis set. The CASTEP code accounts for intermolecular effects found within crystalline solids by using its translational symmetry. It has been shown to accurately predict both crystallographic splittings and shift differences between polymorphs.[38] Since the NMR spectra can be considered a fingerprint of the polymorph, matching the experimental to the theoretical result can determine which polymorph is present. Bryce *et al*. recently showed an example of this for determining the crystallographic space group of a polymorph of calcium carbonate.[49] The correct choice in space group is easily illustrated by simulating the ^{43}Ca MAS NMR spectra using the calculated parameters and comparing them to the experimental spectra (Figure 21.10).

The computed magnetic shielding tensors of isolated molecules can be compared to molecules in the crystal lattice to determine the effect of packing arrangements. The computational approach to look at isolated molecules by using a very large unit cell has been described by Harris.[50] Using this method, Yates *et al*. have shown that the differences in shift in maltose anomers result from weak intermolecular CH$\cdots$O hydrogen bonds.[51] The effect solvent molecules have on the chemical shift can also be explored. Pseudopolymorphism, polymorphs with different solvates, is an area of interest where powder XRD is often not able to distinguish between

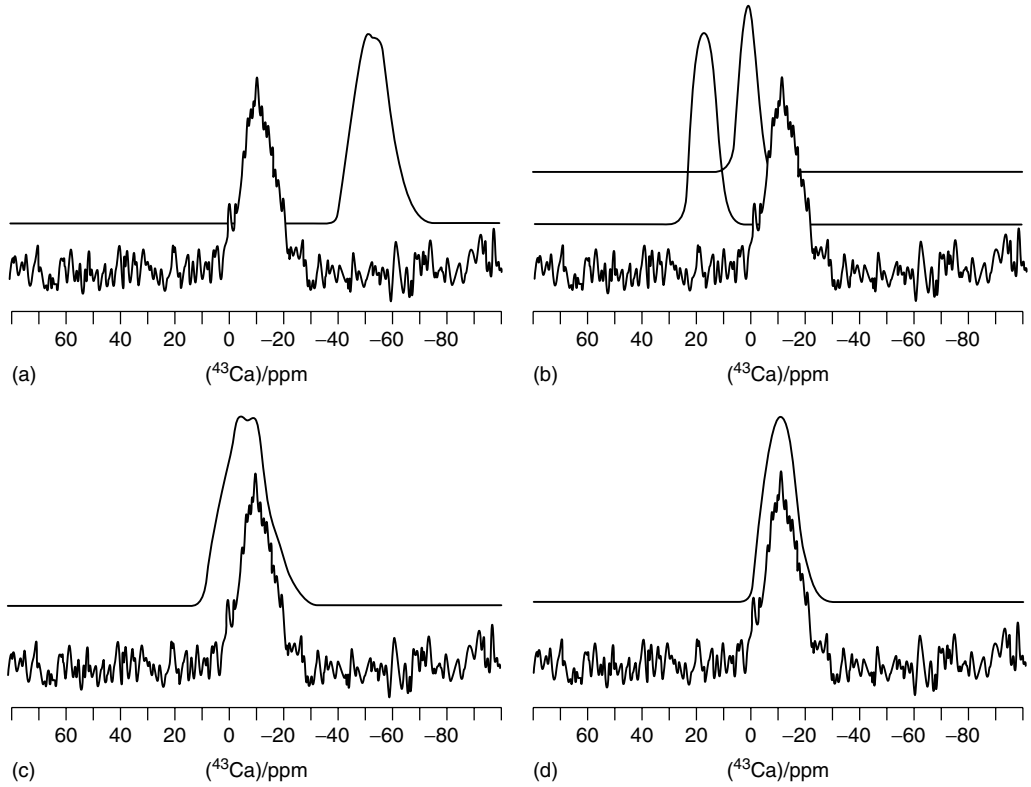


Figure 21.10. Experimental and simulated ^{43}Ca MAS NMR spectra of the vaterite polymorphs of $CaCO_3$ acquired at 21.1 T. The experimental spectrum, shown in the lower trace of each part, is the sum of 4790 scans with a recycle delay of 20 s. The MAS rate was 5 kHz. The spectra shown in the upper trace of each part have been simulated using the NMR parameters calculated using CASTEP for the following structural models of vaterite: (a) Pbnm; (b) local density approximation (LDA)-ortho (middle trace) and generalized gradient approximation (GGA)-ortho (upper trace); (c) hexagonal $P6_3/mmc$; and (d) best-fit simulation. (Reproduced from Ref. 49. © American Chemical Society, 2008.)

them. Often it is difficult experimentally to remove solvent molecules to get a certain stoichiometry but this is easily achieved with computation. The solvent molecules can be artificially removed from the host structure while the remaining molecule has the same geometry (same bond angles and bond distances). This is illustrated in the study of finasteride acetic acid by Harris *et al*.[50] The acetic acid acts as both a H-bond donor and acceptor. As summarized in Table 21.2, the effect on the chemical shifts of the solvent is clear and can be quantified ("solvent effect"). The major changes (C1, C2, and C6) are the regions directly affected by intermolecular hydrogen bonding to the acetic acid molecules. It is clear that even if the crystal structure was unknown, the sites where intermolecular interactions occur would be easily determined. Grant and coworkers investigated two polymorphs of 10-deacetyl baccatin III: a dimethyl sulfoxide (DMSO) solvate and an unsolvated form.[52] Using FIREMAT experiments, the ^{13}C principal tensors values were determined and compared between the two forms. Several differences in the principal values were found and were not accounted for by ab initio calculations of the solvated and unsolvated forms. Adding the DMSO did not significantly influence the shift and it was concluded that there must be conformational differences between the polymorphs to explain the large differences observed experimentally. Again, chemical shift tensors are shown to be rich with

Table 21.2. ^{13}C Chemical shifts (CS) (in ppm) of the finasteride acetic acid solvate calculated using CASTEP code

Position	Computed CS	Computed CS without solvent[a]	Solvent effect	Computed CS without solvent[b]	Reoptimization effect	Solvent effect
1	162.1	158.1	4.0	157.7	−0.4	4.4
2	124.8	127.9	−3.1	128.1	0.2	−3.3
3	166.3	164.9	1.4	165.4	0.5	0.9
5	62.1	62.3	−0.2	62.2	−0.1	−0.1
6	24.3	27.1	−2.8	27.0	−0.1	−2.7
7	30.2	30.2	0.0	30.2	0.0	0.0
8	35.5	35.6	−0.1	35.6	0.0	−0.1
9	49.6	49.4	0.2	49.4	0.0	0.2
10	41.4	42.3	−1.0	42.3	0.0	−0.9
11	19.4	19.6	−0.3	19.6	0.0	−0.2
12	36.7	37.8	−1.1	38.0	0.2	−1.3
13	45.5	45.1	0.5	45.1	0.0	0.4
14	56.1	55.8	0.3	55.8	0.0	0.3
15	25.6	25.6	0.0	25.6	0.0	0.0
16	21.2	22.0	−0.8	22.1	0.1	−0.9
17	57.3	58.7	−1.4	58.8	0.1	−1.5
18	9.9	9.7	0.2	9.6	−0.1	0.3
19	9.2	9.7	−0.5	9.7	0.1	−0.5
20	170.0	169.7	0.3	169.8	0.1	0.2
22	50.6	50.5	0.2	50.4	−0.1	0.2
23	25.0	25.0	0.0	24.9	−0.1	0.1

[a]Proton positions optimized.
[b]Proton positions reoptimized after removal of solvent.

information about molecular conformation and are a powerful method to study intermolecular interactions and structure.

21.7 CONCLUSION

Intermolecular interactions are important for an understanding of structure in the solid state. Advances in NMR crystallography allow one to determine quantitative information about structural parameters, such as bond lengths, from solid-state NMR experiments. In this article, both chemical shifts and dipolar couplings revealed a high sensitivity to neighboring molecules and conformations. This makes them key interactions for solving questions of structure. The determination of shielding tensors using FIREMAT experiments and computation, illustrated the strength of using these values to deduce structural motifs. Site-specific dipolar coupling information is directly related to distance. Dipolar coupling constants can be determined using a variety of techniques including CPMAS and recoupling sequences such as 2-D DQ experiments and HETCOR studies. Quantitative distance information is also contained within DQ spinning sideband patterns.

Materials applications where structural elucidation has benefited from studies of intermolecular interactions include, but are not limited to, host–guest complexes such as zeolites and molecular tweezers, nanomaterials, and polymorphs. The introduction of first principles DFT calculations using the CASTEP code to study the periodic nature of solids has greatly aided the understanding of packing arrangements in solids. Combining experimental and theoretical results are providing answers to many important questions of structure.

REFERENCES

1. M. D. Segall, P. J. D. Lindan, M. J. Probert, C. J. Pickard, P. J. Hasnip, S. J. Clark, and M. C. Payne, *J. Phys.: Condens. Matter*, 2002, **14**, 2717.
2. C. J. Pickard and F. Mauri, *Phys. Rev. B: Condens. Matter*, 2001, **63**, 245101.

3. C. A. Fyfe and Y. Feng, *J. Am. Chem. Soc.*, 1989, **111**, 7702.
4. C. A. Fyfe, H. Gies, Y. Feng, and G. T. Kokotailo, *Nature*, 1989, **341**, 223.
5. C. A. Fyfe, Y. Feng, H. Gies, H. Grondey, and G. T. Kokotailo, *J. Am. Chem. Soc.*, 1990, **112**, 3264.
6. D. J. Brouwer, *J. Am. Chem. Soc.*, 2008, **130**, 6306.
7. D. Rovnyak, *Concepts Magn. Reson.*, 2008, **32A**, 254.
8. C. A. Fyfe, A. C. Diaz, H. Grondey, A. R. Lewis, and H. Forster, *J. Am. Chem. Soc.*, 2005, **127**, 7543.
9. C. A. Fyfe and D. H. Brouwer, *J. Am. Chem. Soc.*, 2006, **128**, 11860.
10. C. A. Fyfe and D. H. Brouwer, *Can. J. Chem.*, 2006, **84**, 345.
11. C. A. Fyfe and J. S. J. Lee, *J. Phys. Chem. C*, 2008, **112**, 500.
12. B. L. Trout, B. H. Suits, R. J. Gorte, and D. White, *J. Phys. Chem. B*, 2000, **104**, 11734.
13. D. Michel, A. Pampel, and J. Roland, *J. Chem. Phys.*, 2003, **119**, 9242.
14. T. Beutel and B.-L. Su, *Chem. Phys. Lett.*, 2005, **416**, 51.
15. D. H. Brouwer, S. Alavi, and J. A. Ripmeester, *Phys. Chem. Chem. Phys.*, 2008, **10**, 3857.
16. P. Lazzeretti, *Prog. NMR Spectrosc.*, 2000, **36**, 1.
17. C. Ochsenfeld, S. P. Brown, I. Schnell, J. Gauss, and H. W. Spiess, *J. Am. Chem. Soc.*, 2001, **123**, 2597.
18. S. P. Brown, I. Schnell, J. D. Brand, K. Mullen, and H. W. Spiess, *J. Am. Chem. Soc.*, 1999, **121**, 6712.
19. K. Saalwachter, R. Graf, and H. W. Spiess, *J. Magn. Reson.*, 1999, **140**, 471.
20. K. Saalwachter and I. Schnell, *Solid State Nucl. Magn. Reson.*, 2002, **22**, 154.
21. M. M. Elmahdy, G. Floudas, M. Mondeshki, H. W. Spiess, X. Dou, and K. Mullen, *Phys. Rev. Lett.*, 2008, **100**, 107801.
22. M. M. Elmahdy, X. Dou, M. Mondeshki, G. Floudas, H.-J. Butt, H. W. Spiess, and K. Mullen, *J. Am. Chem. Soc.*, 2008, **130**, 5311.
23. A. Fechtenkotter, K. Saalwachter, M. A. Harbinson, K. Mullen, and H. W. Spiess, *Angew. Chem. Int. Ed. Engl.*, 1999, **38**, 3039.
24. S. P. Brown, T. Schaller, U. P. Seelbach, F. Koziol, C. Ochsenfeld, F.-G. Klarner, and H. W. Spiess, *Angew. Chem. Int. Ed. Engl.*, 2001, **40**, 717.
25. C. Ochsenfeld, F. Koziol, S. P. Brown, T. Schaller, U. P. Seelbach, and F.-G. Klarner, *Solid State Nucl. Magn. Reson.*, 2002, **22**, 128.
26. T. Schaller, U. P. Buchele, F.-G. Klarner, D. Blaser, R. Boese, S. P. Brown, H. W. Spiess, F. Koziol, J. Kussmann, and C. Ochsenfeld, *J. Am. Chem. Soc.*, 2007, **129**, 1293.
27. T. Metzroth, M. Lenhart, and J. Gauss, *Appl. Magn. Reson.*, 2008, **33**, 457.
28. L. S. Cahill, Z. Yao, A. Adronov, J. Penner, K. R. Moonoosawmy, P. Kruse, and G. R. Goward, *J. Phys. Chem. B*, 2004, **108**, 11412.
29. P. Sozzani, A. Comotti, S. Bracco, and R. Simonutti, *Chem. Commun.*, 2004, **7**, 768.
30. P. Liu, R. Ni, A. K. Mehta, S. Childers, A. Lakdawala, S. V. Pingali, P. Thiyagarajan, and D. G. Lynn, *J. Am. Chem. Soc.*, 2008, **130**, 16867.
31. R. K. Harris, *Solid State Sci.*, 2004, **6**, 1025.
32. R. K. Harris, *Analyst*, 2006, **131**, 351.
33. E. A. Christopher, R. K. Harris, and R. A. Fletton, *Solid State Nucl. Magn. Reson.*, 1992, **1**, 93.
34. G. A. Stephenson, J. G. Stowell, P. H. Toma, D. E. Dorman, J. R. Greene, and S. R. Byrn, *J. Am. Chem. Soc.*, 1994, **116**, 5766.
35. R. K. Harris, R. R. Yeung, B. Lamont, R. W. Lancaster, S. M. Lynn, and S. E. Staniforth, *J. Chem. Soc. Perkin Trans. 2*, 1997, **7**, 2653.
36. D. C. Apperley, R. A. Fletton, R. K. Harris, R. W. Lancaster, S. Tavener, and T. L. Threlfall, *J. Pharm. Sci.*, 1999, **88**, 1275.
37. M. T. Zell, B. E. Padden, D. J. W. Granr, S. A. Schroeder, K. L. Wachholder, and I. Prakash, *Tetrahedron*, 2000, **56**, 6603.
38. R. K. Harris, P. Y. Ghi, R. B. Hammond, C. Y. Ma, K. J. Roberts, J. R. Yates, and C. J. Pickard, *Magn. Reson. Chem.*, 2006, **44**, 325.
39. R. K. Harris, S. A. Joyce, C. J. Pickard, S. Cadars, and L. Emsley, *Phys. Chem. Chem. Phys.*, 2006, **8**, 137.
40. Z. Ma, M. D. Halling, M. S. Solum, J. K. Harper, A. M. Orendt, J. C. Facelli, R. J. Pugmire, D. M. Grant, A. W. Amick, and L. T. Scott, *J. Phys. Chem. A*, 2007, **111**, 2020.
41. M. Strohmeier, A. M. Orendt, D. W. Alderman, and D. W. Grant, *J. Am. Chem. Soc.*, 2001, **123**, 1713.
42. E. Heider, J. K. Harper, and D. M. Grant, *Phys. Chem. Chem. Phys.*, 2007, **9**, 6083.

43. S. E. Ashbrook, A. J. Berry, D. J. Frost, A. Gregorovic, C. J. Pickard, J. E. Readman, and S. Wimperis, *J. Am. Chem. Soc.*, 2007, **129**, 13213.

44. C. Gervais, R. Dupree, K. J. Pike, C. Bonhomme, M. Profeta, C. J. Pickard, and F. Mauri, *J. Phys. Chem. A*, 2005, **109**, 6960.

45. F. Pourpoint, A. Kolassiba, C. Gervais, T. Azais, L. Coury-Bonhomme, C. Bonhomme, and F. Mauri, *Chem. Mater.*, 2007, **19**, 6367.

46. S. E. Ashbrook, M. Cutajar, C. J. Pickard, R. I. Walton, and S. Wimperis, *Phys. Chem. Chem. Phys.*, 2008, **10**, 5754.

47. S. E. Ashbrook, L. Le Polles, R. Gautier, C. J. Pickard, and R. I. Walton, *Phys. Chem. Chem. Phys.*, 2006, **8**, 3423.

48. J. Cuny, S. Messaoudi, V. Alonzo, E. Furet, J.-F. Halet, E. Le Fur, S. E. Ashbrook, C. J. Pickard, R. Gautier, and L. Le Polles, *J. Comput. Chem.*, 2008, **29**, 2280.

49. D. L. Bryce, E. B. Bultz, and D. Aebi, *J. Am. Chem. Soc.*, 2008, **130**, 9282.

50. R. K. Harris, P. Hodgkinson, C. J. Pickard, J. R. Yates, and V. Zorin, *Magn. Reson. Chem.*, 2007, **45**, S174.

51. J. R. Yates, T. N. Pham, C. J. Pickard, F. Mauri, A. M. Amado, A. M. Gil, and S. P. Brown, *J. Am. Chem. Soc.*, 2005, **127**, 10216.

52. J. K. Harper, J. C. Facelli, D. H. Barich, G. McGeorge, A. E. Mulgrew, and D. M. Grant, *J. Am. Chem. Soc.*, 2002, **124**, 10589.

Chapter 22

Hydrogen Bonding in Crystalline Organic Solids

Steven P. Brown

Department of Physics, University of Warwick, Coventry CV4 7AL, UK

22.1	Introduction	321
22.2	NMR Chemical Shifts	321
22.3	Dipolar Couplings	326
22.4	Hydrogen Bond-Mediated *J* Couplings	333
22.5	Hydrogen-Bond Dynamics	334
22.6	Outlook	336
	References	337

22.1 INTRODUCTION

Hydrogen bonding, e.g., OH···O, OH···N, NH···O, and NH···N, is a key interaction that determines both intra- and intermolecular structure.[1] For biomolecules, hydrogen bonding controls secondary structure in proteins or α-helix formation by nucleic acids. For small and moderately sized organic molecules, different intermolecular hydrogen-bonding arrangements lead to distinct three-dimensional packing arrangements, i.e., polymorphism, with this being of particular importance for the pharmaceutical industry, while hydrogen bonding is exploited in supramolecular chemistry to generate novel molecular architectures.

NMR Crystallography Edited by Robin K. Harris, Roderick E. Wasylishen and Melinda J. Duer © 2009 John Wiley & Sons, Ltd. ISBN: 978-0-470-69961-4

The marked sensitivity of NMR parameters to the local electronic environment makes solid-state NMR a powerful probe of hydrogen bonding. Moreover, the atomic specificity of NMR enables the separate probing of the different atoms involved in a hydrogen-bonding interaction. In this article, the focus is on the spin $I = 1/2$ nuclei, ^{1}H and ^{15}N, and the spin $I = 5/2$ nucleus ^{17}O (the only NMR visible isotope of oxygen); for ^{15}N and ^{17}O, the low natural abundance (0.37 and 0.037%, respectively) usually necessitates the preparation of isotopically enriched samples. This article will illustrate the marked sensitivity of the NMR chemical shift to hydrogen bonding. In addition, it will be shown that the presence of hydrogen-bonding interactions can be identified and their strength characterized by solid-state NMR experiments that probe and quantitatively determine dipolar and J couplings.

22.2 NMR CHEMICAL SHIFTS

It is well established that the NMR chemical shift is a very sensitive indicator of hydrogen-bonding strength. For example, the clear correlation between increasing ^{1}H solid-state NMR chemical shift and decreasing OH···O hydrogen-bonding distance for carboxylic acid dimers was presented in the 1980s.[2] In recent years, developments in first-principles methods for calculating NMR parameters, as well

as advances in computing power, have led to an increasing number of studies that combine calculation and experiment, thus allowing systematic investigations of hydrogen-bonding interactions.

22.2.1 ^{1}H Chemical Shifts

Figure 22.1 shows the variation of the absolute ^{1}H shielding, calculated using the density functional theory (DFT) code Gaussian98, with the NH distance in an intermolecular NHO hydrogen bond formed by a methylnitroacetanilide (MNA) dimer.[3] Note that the isotropic chemical shift, δ, as measured experimentally, for example, in an ^{1}H fast MAS experiment, is related to the absolute shielding, σ, as determined by a first-principles calculation, as follows

$$\delta = -[\sigma - \sigma_{\text{ref}}] \qquad (22.1)$$

Thus, the decrease in the calculated absolute shielding observed in Figure 22.1 for an increasing NH distance corresponds to an increase in the isotropic chemical shift with increasing NH distance (and hence increasing hydrogen-bonding strength) up to a value of ~1.6 Å that corresponds to where the hydrogen atom is equidistant between the nitrogen and oxygen atoms. Note that the solid vertical and

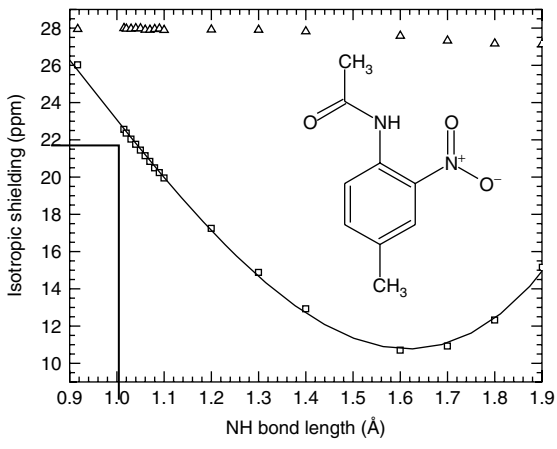


Figure 22.1. The variation with respect to the NH distance of the absolute ^{1}H shielding (squares), as calculated using the DFT code Gaussian98, for an intermolecular NHO hydrogen bond formed by an MNA dimer.[3] The vertical and horizontal lines correspond to the experimental $\delta(^1\text{H})$ of 10.6 ppm as measured for the NH proton in the white polymorphic form of MNA. The triangles correspond to the calculated absolute ^{1}H shielding for the NH proton in the second MNA molecule that is not hydrogen bonded for the considered model dimer. (Reproduced from Ref. 3. © The Royal Society of Chemistry, 2003.)

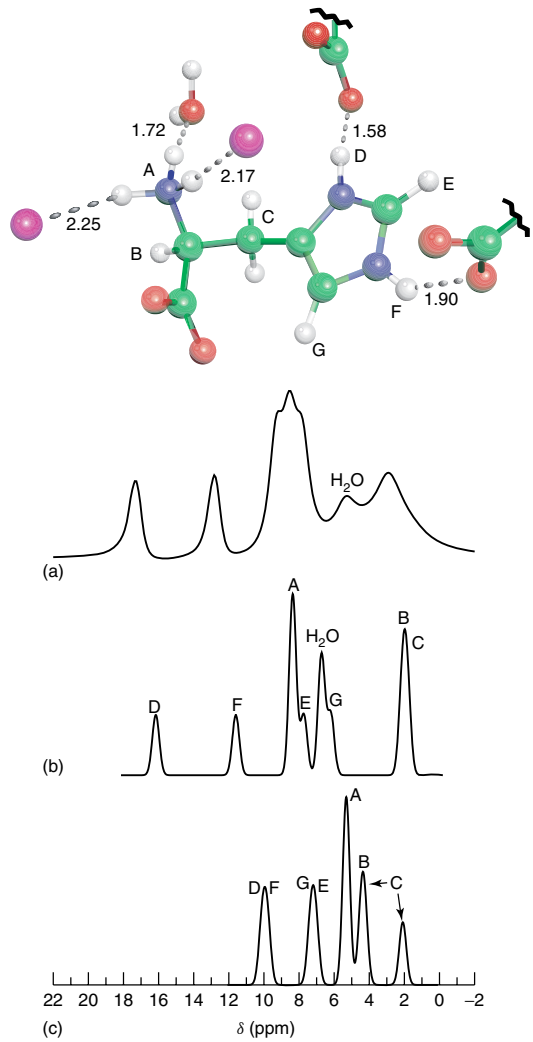


Figure 22.2. A comparison of an experimental ^{1}H (700 MHz) MAS (30 kHz) spectrum (a) of L-histidine·HCl·H_2O with spectra computed using a planewave-based DFT approach employing periodic boundary conditions for the fully periodic crystal structure of L-histidine·HCl·H_2O (b) and an isolated molecule retaining the geometry of the crystal (c). (Reproduced from Ref. 4. © American Chemical Society, 2006.)

horizontal lines in Figure 22.1 correspond to the experimental $\delta(^1H)$ of 10.6 ppm as measured for the NH proton in the white polymorphic form of MNA.

Figure 22.2 compares an experimental ^1H MAS spectrum of L-histidine·HCl·H_2O (a) with spectra computed using a planewave-based DFT approach employing periodic boundary conditions for the fully periodic crystal structure of L-histidine·HCl·H_2O (b) and an isolated molecule retaining the geometry of the crystal (c).[4] For the two ring NH protons [D (δ_1 site) and F (ε_2 site)], the calculated ^1H isotropic chemical shifts are larger for the crystal as compared to the isolated molecule. This is due to intermolecular NH···O hydrogen bonding, with the bigger molecule to crystal change [$\Delta\delta$ = ~6 ppm (D) as compared to ~2 ppm (F)] being observed for resonance D corresponding to the considerably shorter H···O distance.

In the solid state, the RNA base uracil packs as a layered structure with the individual molecules within each plane held together by two NH···O hydrogen bonds to one carbonyl acceptor and two CH···O weak hydrogen bonds[5] to the second carbonyl acceptor (see Figure 22.3). Table 22.1 presents the calculated ^1H isotropic chemical shifts[6] determined using the CASTEP software package, which implements DFT using a planewave basis set and employs the gauge-including projector augmented-wave (GIPAW) method[7] to calculate the shieldings. In addition to hydrogen bonding, the ring currents associated with the aromatic moieties represent a second intermolecular contribution to the solid-state NMR chemical shift. Comparing the calculations for the full periodic crystal and an isolated plane in Table 22.1, intraplanar ring currents are found to contribute changes of −0.7 to −0.9 ppm to the ^1H chemical shifts—larger changes (up to 6 ppm in magnitude) have been calculated for the intermolecular ring currents of, for example, benzene, naphthalene, and hexabenzocoronene (HBC) moieties.[8,9] The furthest right column of Table 22.1 shows the difference of the chemical shifts calculated for an isolated plane and an isolated molecule (with the same geometry as in the crystal structure), and thus corresponds to the effect of intermolecular hydrogen bonding on the chemical shifts. While the $\Delta\delta^{plane-mol}$ values of ~5 ppm for the NH ^1H chemical shifts involved in NH···O hydrogen bonding are similar to that observed for the histidine NH discussed above (Figure 22.2), it is noteworthy that the $\Delta\delta^{plane-mol}$ values of ~2 ppm for the CH ^1H chemical shifts involved in so-called CH···O weak hydrogen bonding are ~40 % of those for the conventional hydrogen bonds. In this context, we note that similar molecule to crystal changes (by up to 1.9 ppm) have been calculated for the CH protons in maltose anomers that also exhibit CH···O hydrogen bonding with OH as the acceptor group.[10]

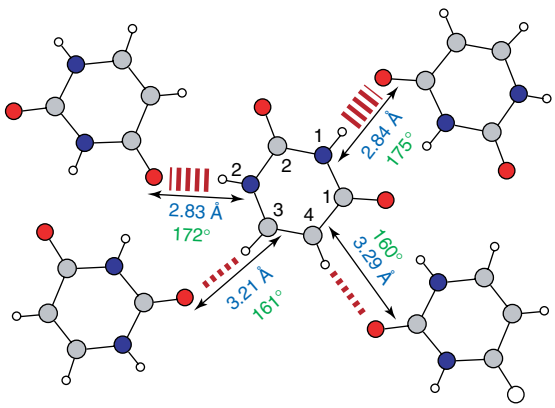


Figure 22.3. The intraplanar arrangement of uracil molecules in the solid state. Color coding: C, black; O, red; N, blue; and H, gray. For the NH···O and CH···O hydrogen bonds, the XHY angle, the H···X distance (in red), and the XY distance (in brackets) are indicated. (Reproduced from Ref. 6. © American Chemical Society, 2008.)

22.2.2 ^{17}O Chemical Shifts

Table 22.1 also demonstrates the marked dependence of the ^{17}O chemical shift to hydrogen bonding: for O_1, which is the acceptor of two NH···O hydrogen bonds (see Figure 22.3), $\Delta\delta^{plane-mol}$ is ~4.5 times bigger than that for O_2, which is the acceptor of two CH···O hydrogen bonds. This marked difference has also been noted by Ida *et al.* who compared quantum-chemical calculations for clusters of uracil molecules with that for an isolated molecule.[11]

The effect of hydrogen bonding on ^{17}O NMR parameters has also been investigated by quantum-chemical calculations for urea, $CO(NH_2)_2$.[12] Specifically, Figure 22.4 shows the calculated quadrupolar and chemical shift parameters for seven different molecular clusters with an increasing number of C=O···HNH hydrogen bonds—the case of eight hydrogen bonds is for a cluster of six molecules around a central urea molecule, representing the complete

Table 22.1. Comparison of experimental solid-state NMR and computed ^{1}H chemical shifts for uracil[6]

Donor and site	Experiment (ppm)	Calculated (ppm)			$\Delta\delta^{\text{plane}-\text{mol}}$ (ppm)
		Crystal	Plane	Molecule	
N–H H_1	11.2	11.7	12.5	7.4	5.1
N–H H_2	10.8	11.2	11.9	6.5	5.4
C–H H_3	7.5	7.2	8.1	6.1	2.0
C–H H_4	6.0	5.5	6.3	4.1	2.2
O_1 (NH)	275	274.4	273.2	407.8	−134.6
O_2 (CH)	245	257.6	256.0	286.0	−30.0

hydrogen-bonding arrangement found in the crystal structure. Besides a decrease in the ^{17}O isotropic chemical shift for increasing hydrogen-bond strength (as observed above for uracil, see Table 22.1), Figure 22.4 investigates the behavior of the separate components of the ^{17}O chemical shielding tensor: both δ_{11} and δ_{22} decrease for increasing hydrogen-bond strength. ^{17}O has a spin $I = 5/2$ nucleus, and it is thus informative to investigate the effect of hydrogen bonding on the quadrupolar parameters. Specifically, Figure 22.4 shows that the quadrupole coupling constant, χ, and its asymmetry,

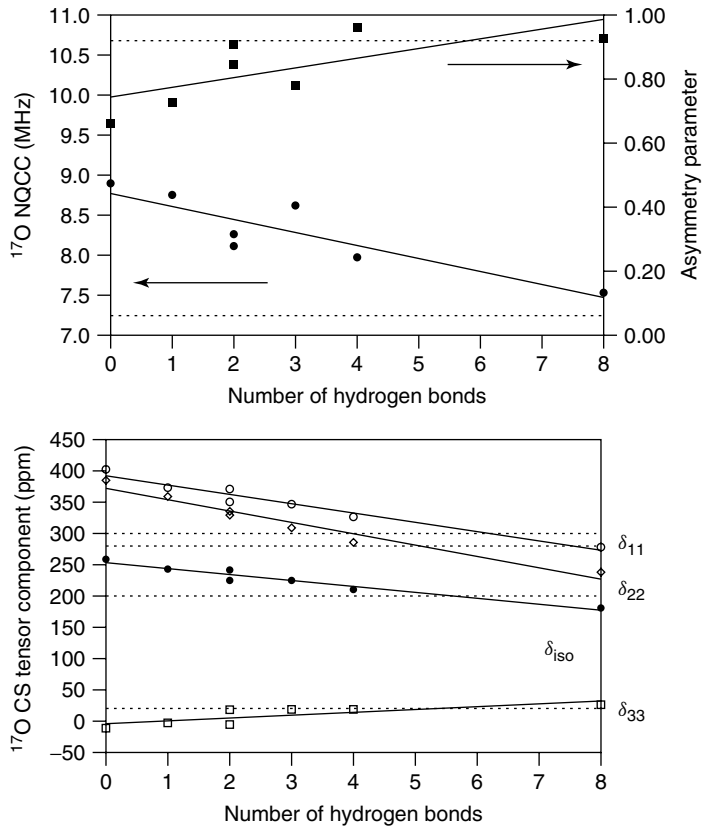


Figure 22.4. Calculated ^{17}O quadrupolar and chemical shift parameters for seven different clusters of urea molecules, $CO(NH_2)_2$, with an increasing number of C–O···HNH hydrogen bonds. (Reproduced from Ref. 12. © Elsevier, 2008.)

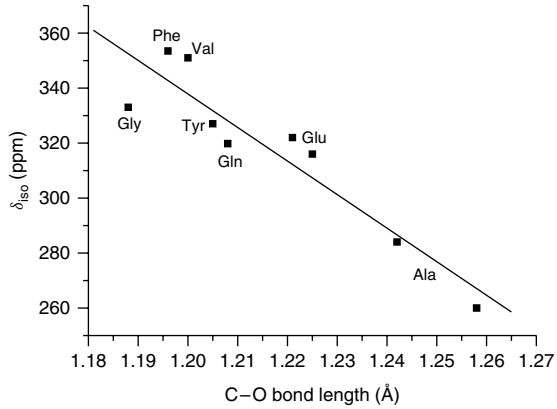


Figure 22.5. The variation in the ^{17}O chemical shift with the C–O bond length for the carbonyl oxygen in a series of amino acids.[13] With the exception of the two Ala points (corresponding to L-alanine in its zwitterionic form), all points correspond to amino acids as hydrochlorides i.e., with a neutral COOH group. (Reproduced from Ref. 13. © American Chemical Society, 2004.)

η, decrease and increase, respectively, for increasing hydrogen-bonding strength. These trends have been confirmed experimentally for amides, carboxylic acids, peptides, polypeptides, and nucleic acid bases.[12]

As a related example, Figure 22.5 shows the dependence of the ^{17}O chemical shift upon the C–O bond length for the carbonyl oxygen in a series of amino acids[13]: a clear correlation between the increasing C–O bond length and decreasing $\delta(^{17}O)$ is observed.

22.2.3 ^{15}N Chemical Shifts

The sensitivity of the ^{15}N chemical shift to hydrogen-bonding strength is illustrated by Figure 22.6, which compares ^{1}H MAS and ^{15}N CP MAS solid-state NMR spectra of the aldimine base (**2a**) alone with the corresponding spectra of the 1:1 complex of the base with four benzoic acid derivatives, 4-chlorobenzoic acid (**2b**), 4-nitrobenzoic acid (**2c**), 3,5-dinitrobenzoic acid (**2d**), and 4-tolylsulphonic acid (**2e**), where the pK_a of the acid equals 3.99, 3.44, 2.82, and −6.65, respectively.[14] Upon decreasing acidity of the acid, both the ^{1}H and ^{15}N chemical shifts for the N1 and H1 protons in the intermolecular NH···O hydrogen bond are observed to increase, while those for the N2 and H2 protons in the intramolecular NH···O hydrogen bond remain effectively unchanged. The correlation of the ^{1}H and ^{15}N chemical shifts in the aldimine (**2**), and also for various aldenamine (**1**) Schiff base adducts, is shown in Figure 22.7. For the intermolecular NH···O hydrogen bond, the largest ^{1}H and ^{15}N chemical shifts correspond to a symmetric N···H···O hydrogen bond (see also Figure 22.1 in Section 22.2.1). For the intramolecular NHO hydrogen bond in the Schiff base adducts, the change from a tolyl (**1**) to a methyl (**2**) substituent leads to a large change in the ^{15}N chemical shift associated with a change from an OH···N to an NH···O hydrogen bond, with the ^{1}H chemical shifts being similar. Note that the aldimine base (**2a**) alone also exhibits OH···N intramolecular hydrogen bonding (see Figure 22.6). In further work, Limbach and coworkers have used the establishment of the clear correlation of the ^{15}N chemical shift with the proton localization in an NH···O hydrogen bond to accurately localize the proton in a critical enzyme hydrogen bond, by means of ^{15}N CP MAS spectra in the presence and absence of a maleate inhibitor.[15]

22.2.4 Using Chemical Shifts in NMR Crystallography: Outlook

This section has demonstrated the marked sensitivity to hydrogen bonding of the chemical shifts of the directly hydrogen-bonded nuclei. The potential to exploit this dependence in NMR crystallography is evident. First, hydrogen atoms in hydrogen bonds can be accurately localized, i.e., detailed structural information (at a precision usually considerably better than that that is possible by diffraction methods) for key parts of the structure can be obtained. Second, the combination of experiment and calculation that benefits from ever-improving capabilities of computational methods offers the prospect of the development of "spectrum to structure" approaches that use NMR chemical shifts to determine crystal structures for organic molecules where single crystals suitable for diffraction studies cannot be obtained.

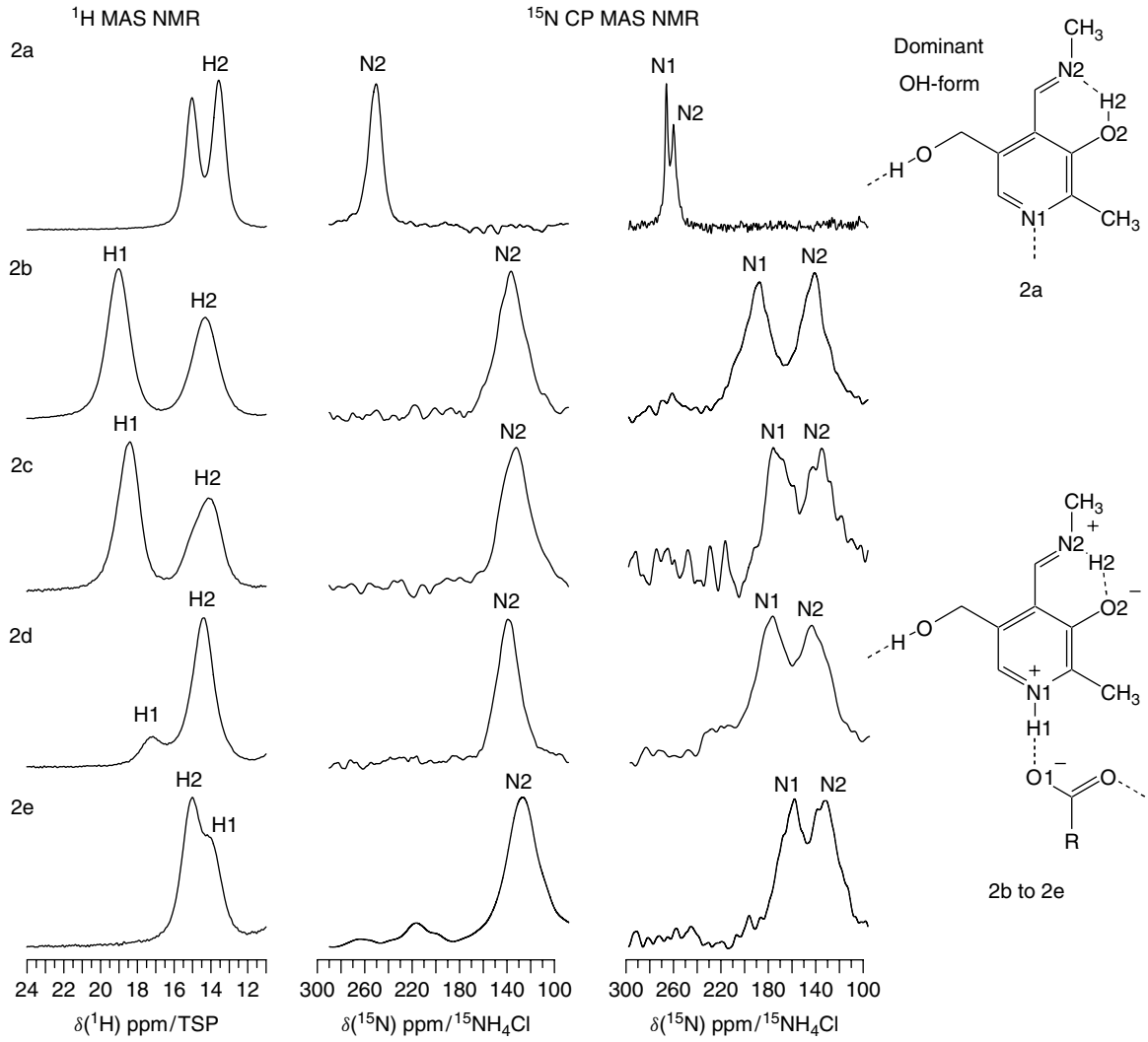


Figure 22.6. ^{1}H (600 MHz) MAS (24 kHz) and ^{15}N (30 MHz) CP MAS solid-state NMR spectra of the aldimine base (labeled **2a**) alone and together with the corresponding spectra of the 1 : 1 complex of the base with four benzoic acid derivatives, namely 4-chlorobenzoic acid (**2b**), 4-nitrobenzoic acid (**2c**), 3,5-dinitrobenzoic acid (**2d**), and 4-tolylsulfonic acid (**2e**).[14] The middle and right columns show ^{15}N spectra of singly ^{15}N and doubly ^{15}N or natural abundance labeled samples, respectively. ^{15}N chemical shifts are referenced with respect to the resonance of solid $^{15}NH_4Cl$. (Reproduced from Ref. 14. © American Chemical Society, 2007.)

22.3 DIPOLAR COUPLINGS

Many applications of solid-state NMR for structure determination rely upon the inherent dependence of the dipolar coupling on the internuclear separation of the two coupled nuclei to the inverse cubed power. Indeed, much effort has been devoted to the development of pulse sequences that recouple specific dipolar couplings that would otherwise be removed by MAS.[16] This section describes the application of such recoupling methods that allow the quantitative determination of hydrogen-bonding distances as well

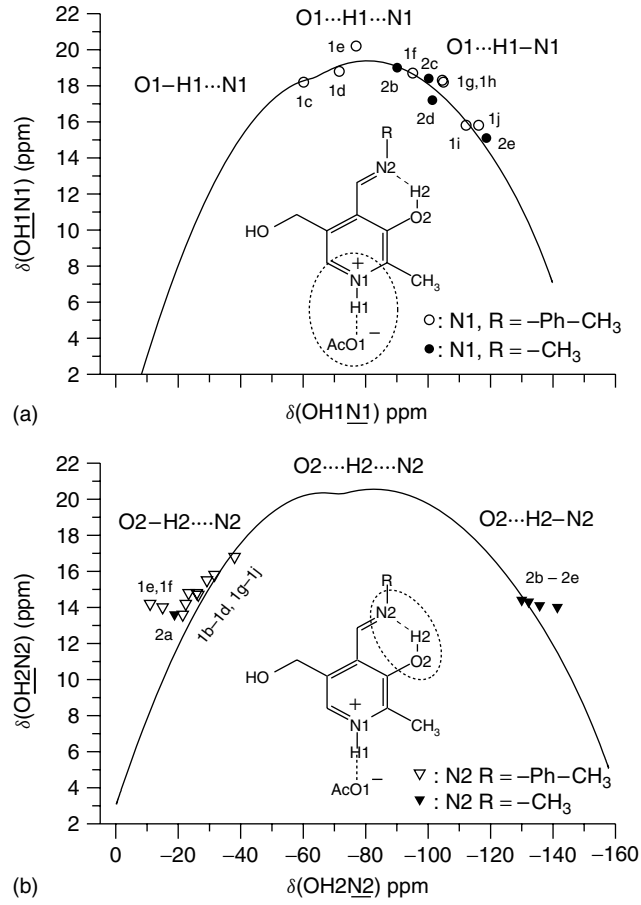


Figure 22.7. The correlation of ^{1}H and ^{15}N chemical shifts for the (a) intermolecular and (b) intramolecular NH···O hydrogen bonds in various aldenamine (**1**) or aldimine (**2**) Schiff base adducts.[14] The ^{15}N chemical shifts are given relative to the ^{15}N resonance of a reference compound (the 5′-triisopropylsilyl ether of *N*-(pyridoxylidene)-tolylamine at 282.5 ppm—referenced with respect to the resonance of solid $^{15}NH_4Cl$). (Reproduced from Ref. 14. © American Chemical Society, 2007.)

as the identification of specific hydrogen-bonding arrangements via the observation of internuclear proximities.

22.3.1 Heteronuclear Dipolar Couplings

22.3.1.1 ^{15}N–^{1}H *Dipolar Couplings*

The two NH protons in L-histidine·HCl·H_2O exhibit NH···O intermolecular hydrogen bonding. The NH···O hydrogen-bonding distance is shorter for the δ_1 NH (see Figure 22.2), and this is reflected in the larger ^{1}H chemical shift (see Section 22.2.1). Zhao *et al*. have presented a two-dimensional experiment by which the ^{15}N–^{1}H dipolar coupling can be determined for the resolved ^{15}N resonances.[17] Figure 22.8(a, b) present slices at the δ_1 and ε_2 resonances obtained using the $R18_2^5$ recoupling sequence. From numerical simulations (see Figure 22.8c, d), the ^{15}N–^{1}H distances are determined as (δ_1 NH) 1.09 ± 0.05 Å and (ε_2 NH) 1.05 ± 0.05 Å, with the longer NH distance corresponding to the stronger hydrogen bond. Schnell and Saalwächter have further shown that the NH distances can be determined for an L-histidine·HCl·H_2O sample at

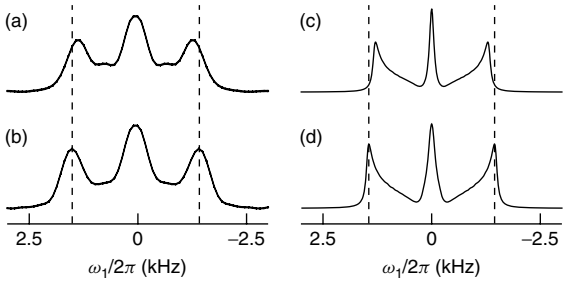


Figure 22.8. (a,b) Slices at the δ_1 and ε_2 ^{15}N resonances extracted from a two-dimensional ^{15}N–^{1}H (400 MHz) spectrum of [U–^{13}C, ^{15}N] L-histidine·HCl·H$_2$O obtained by employing the R18$_2^5$ sequence (ν_r = 20 kHz, ν_1 = 90 kHz) to recouple the ^{15}N–^{1}H dipolar interaction.[17] (c,d) Numerical simulations for ^{15}N–^{1}H dipolar coupling constants of magnitude (c) 9.41 and (d) 10.52 kHz. (Reproduced from Ref. 17. © American Chemical Society, 2001.)

natural abundance from rotor-encoded spinning sidebands observed in a ^{15}N–^{1}H two-dimensional experiment with transferred echo double resonance (TEDOR) magnetization transfer and inverse (^{1}H) detection.[18] In a further example, the N···H distance for an intramolecular N···HO hydrogen bond has been determined as 1.94 ± 0.05 Å from rotor-encoded ^{15}N–^{1}H spinning sidebands obtained using an inversely (^{1}H) detected DIP-HSQC experiment.[19]

22.3.1.2 ^{17}O–^{1}H *Dipolar Couplings*

Brinkmann and Kentgens have shown how ^{17}O–^{1}H dipolar couplings can be determined using the supercycled symmetry-based recoupling sequence, SR4$_1^2$, which is applied to the ^{1}H channel during a ^{17}O spin echo.[20] Experiments were performed for [35–40% ^{17}O]$^{\eta}$ L-tyrosine·HCl, where the phenol O$^{\eta}$ H$^{\eta}$ oxygen forms an intermolecular O$^{\eta}$···H″O″ hydrogen bond with the OH group of the carboxylic acid group. Figure 22.9 shows the change in ^{17}O$^{\eta}$ peak amplitude as a function of the recoupling time for experiments incorporating a selective Gaussian inversion pulse on the (a) phenol OH$^{\eta}$ and (b) carboxylic acid OH″ ^{1}H resonances. From fits to numerical two-spin simulations (solid lines in Figure 22.9), the ^{17}O$^{\eta}$–^{1}H$^{\eta}$ and ^{17}O$^{\eta}$···^{1}H″ distances were determined as 1.03 ± 0.01 and 1.73 ± 0.12 Å, respectively. van Beek *et al.* have described similar ^{17}O–^{1}H experiments, termed phase-shifted recoupling effects a smooth transfer of order (PRESTO-II) and employing R18$_2^5$

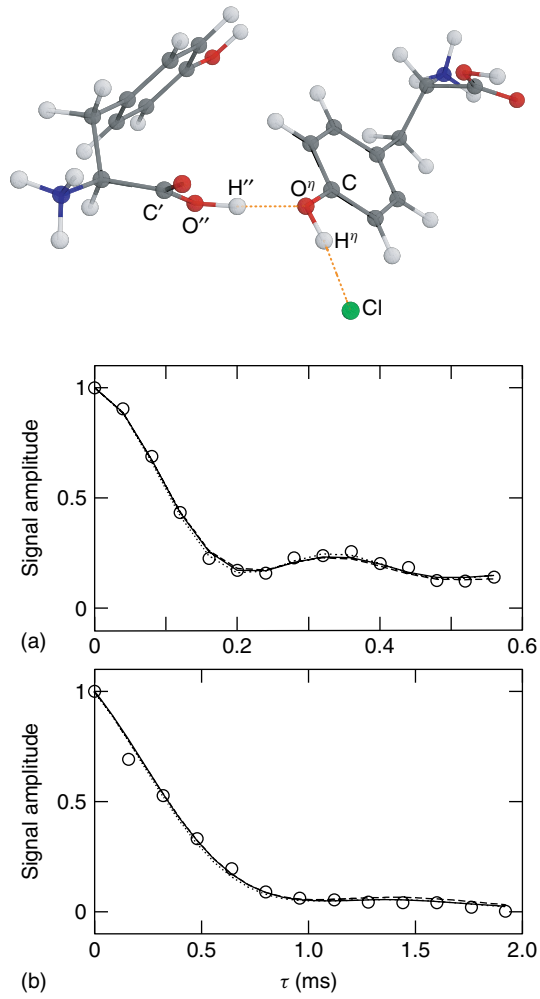


Figure 22.9. The change in ^{17}O$^{\eta}$ peak amplitude for (35–40% ^{17}O)$^{\eta}$ L-tyrosine·HCl as a function of the duration of SR4$_1^2$ recoupling for ^{17}O spin-echo experiments (18.8 T, ν_r = 50 kHz) incorporating a selective Gaussian inversion pulse on the (a) phenol OH$^{\eta}$ and (b) carboxylic acid OH″ ^{1}H resonances.[20] The solid and dotted lines correspond to fits to numerical two-spin simulations and average Hamiltonian calculations (using the fit parameters), respectively. (Reproduced from Ref. 20. © American Chemical Society, 2006.)

recoupling, with application to $Mg(^{17}OH)_2$ and [U–^{13}C,^{17}O]glycine·HCl.[21]

22.3.2 Homonuclear Dipolar Couplings

22.3.2.1 ^{1}H *Double-Quantum Experiments*

^{1}H double-quantum (DQ) spectroscopy has been applied extensively to investigate hydrogen-containing solids, with the observation of DQ peaks indicating a proton–proton proximity within 3.5 Å for a typical organic solid.[22,23] Indeed, the shifting of hydrogen-bonded ^{1}H resonances to high frequency usually results in good resolution under fast MAS (30+ kHz) and moderate magnetic field (500+ MHz). As a consequence, two-dimensional ^{1}H DQ MAS has demonstrated itself as a powerful method for characterizing specific hydrogen-bonding interactions, with applications including distinguishing a pairwise and chainlike structure of benzoxazine oligomers,[24] or the identification of the keto or enol tautomer of a ureido-pyrimidinone moiety.[22] Figure 22.10 compares ^{1}H DQ MAS rotor-synchronized spectra obtained for the diacid $HO_2C(CH_2)_2PO_3H$ in the bulk phase and adsorbed on nano-ZrO_2.[25] For the bulk phase (Figure 22.10a), AA and CC cross peaks demonstrate the formation of distinct carboxylic acid dimers (AA) and phosphonic acid dimers (CC). By comparison, the ^{1}H DQ MAS spectrum for the adsorbed diacid exhibits an AC pair of peaks and no CC cross peak, which is indicative of the phosphonic acid moiety being adsorbed to the ZrO_2, with intermolecular hydrogen bonding between the carboxylic and phosphonic acid ends of the molecules.

Enhanced resolution in ^{1}H solid-state NMR is achieved by combining the physical rotation of MAS with rotations in spin space using RF pulses in the CRAMPS approach. For a dipeptide, line narrowing by a factor of five and nine in the SQ and DQ dimensions, respectively, has been achieved for a ^{1}H DQ CRAMPS experiment[26] utilizing DUMBO (decoupling using mind-boggling optimization) ^{1}H homonuclear decoupling.[27] Figure 22.11 shows ^{1}H DQ CRAMPS spectra of the (a) anhydrous and (b) monohydrate forms of an active pharmaceutical ingredient (API).[28] The different chemical shifts

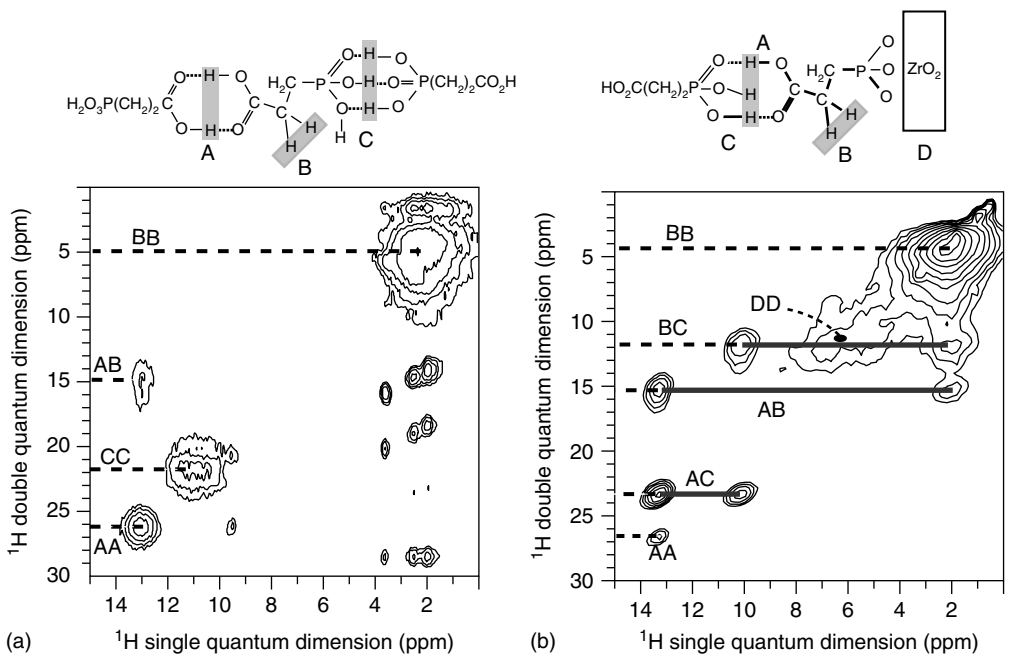


Figure 22.10. ^{1}H (500 MHz) DQ MAS (30 kHz) rotor-synchronized spectra of $HO_2C(CH_2)_2PO_3H_2$ in (a) the bulk state and (b) adsorbed on nanocrystalline zirconia, ZrO_2. (Reproduced from Ref. 25. © American Chemical Society, 2003.)

of the high-frequency hydrogen-bonded resonances (11.4 and 9.8 ppm) are a consequence of different intermolecular hydrogen-bonding arrangements. For these hydrogen-bonded resonances, the observed DQ peaks at (a) $\delta_{DQ} = 11.4 + 8.7 = 20.1$ ppm and (b) $\delta_{DQ} = 9.8 + 8.2 = 18.0$ ppm correspond to an intramolecular proximity to the same nearby proton. The ^{1}H DQ CRAMPS NMR spectra of the pure anhydrous and hydrous forms of the API in Figure 22.11 constitute detailed fingerprints that can be used to demonstrate the presence or absence of a particular pseudopolymorph in a tablet formulation comprising a mixture of the API and excipients. Figure 22.11(c) shows a ^{1}H DQ CRAMPS NMR spectrum of a crushed tablet. Despite the presence of extra peaks (labeled by *) due to excipients (notably resonances due to $CaHPO_4 \cdot 2H_2O$) in the tablet, the spectrum allows the clear identification of only resonances that are characteristic of the anhydrous form of the API, notably the indicated pair of cross peaks at $\delta_{DQ} = 11.4 + 8.7 = 20.1$ ppm.

^{1}H–^{1}H dipolar couplings can be quantitatively determined from an analysis of rotor-encoded ^{1}H DQ MAS spinning sidebands obtained when the t_1 increment is not rotor synchronized.[22,23] For bilirubin, which is an insoluble yellow pigment whose buildup in the body as a consequence of liver malfunction causes jaundice, ^{1}H DQ MAS spinning sidebands (see Figure 22.12) obtained for the NH1 resonance allow the determination of the distance (1.86 ± 0.02 Å) between the NH1 and NH2 protons that form intramolecular NH···O hydrogen bonds to the same carbonyl acceptor.[29]

22.3.2.2 ^{15}N–^{15}N *and* NHHN *Experiments*

Ramachandran and coworkers have shown how specific hydrogen-bonding arrangements between nucleotides can be characterized in ^{15}N-labeled RNA using $^{15}N^{-15}N$ SQ–SQ correlation experiments that probe $^{15}N^{-15}N$ dipolar couplings[30] or ^{1}H–^{1}H dipolar couplings using an NHHN experiment.[31] Figure 22.13 shows the NHHN spectra obtained with different mixing times for a hydrated 100-kDa RNA sample composed of 97 CUG (cytosine-uracil-guanine) repeats.[31] The adoption of Watson–Crick GC (guanine-cytosine) hydrogen-bonding is evident from the buildup of cross-peak intensity between the CN4 and GN1 resonances.

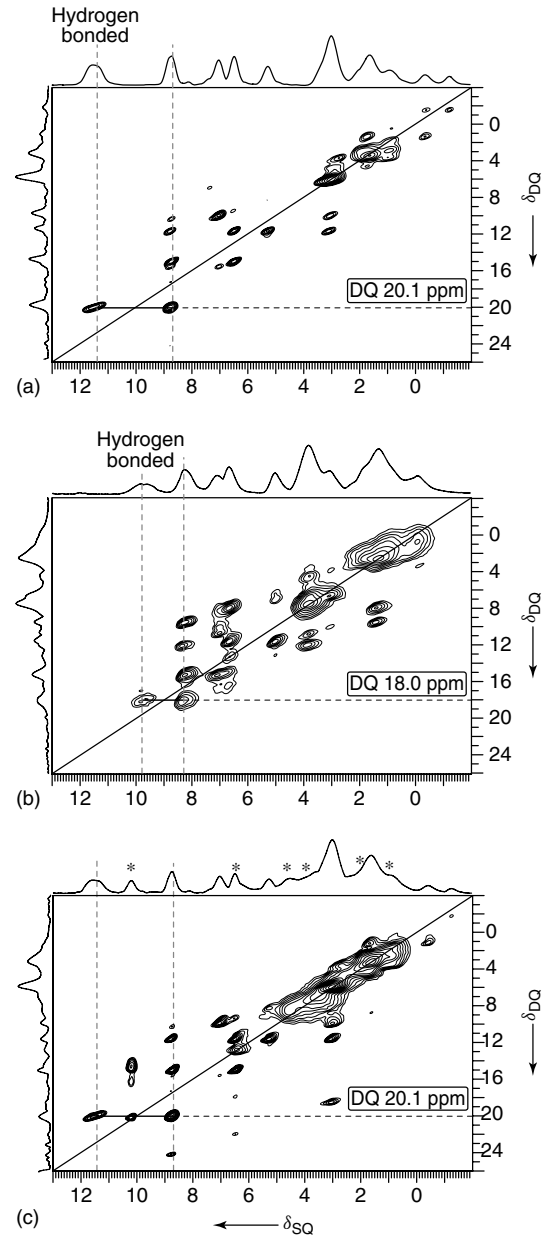


Figure 22.11. ^{1}H (600 MHz) DQ CRAMPS NMR spectra together with skyline projections of (a) anhydrous and (b) monohydrate forms of an active pharmaceutical ingredient, and (c) a crushed tablet containing the API and other excipients (excipient resonances are indicated by asterisk).[28] The pair of DQ peaks corresponding to the intramolecular proximity of the high-frequency hydrogen-bonded proton to the same nearby proton are highlighted.

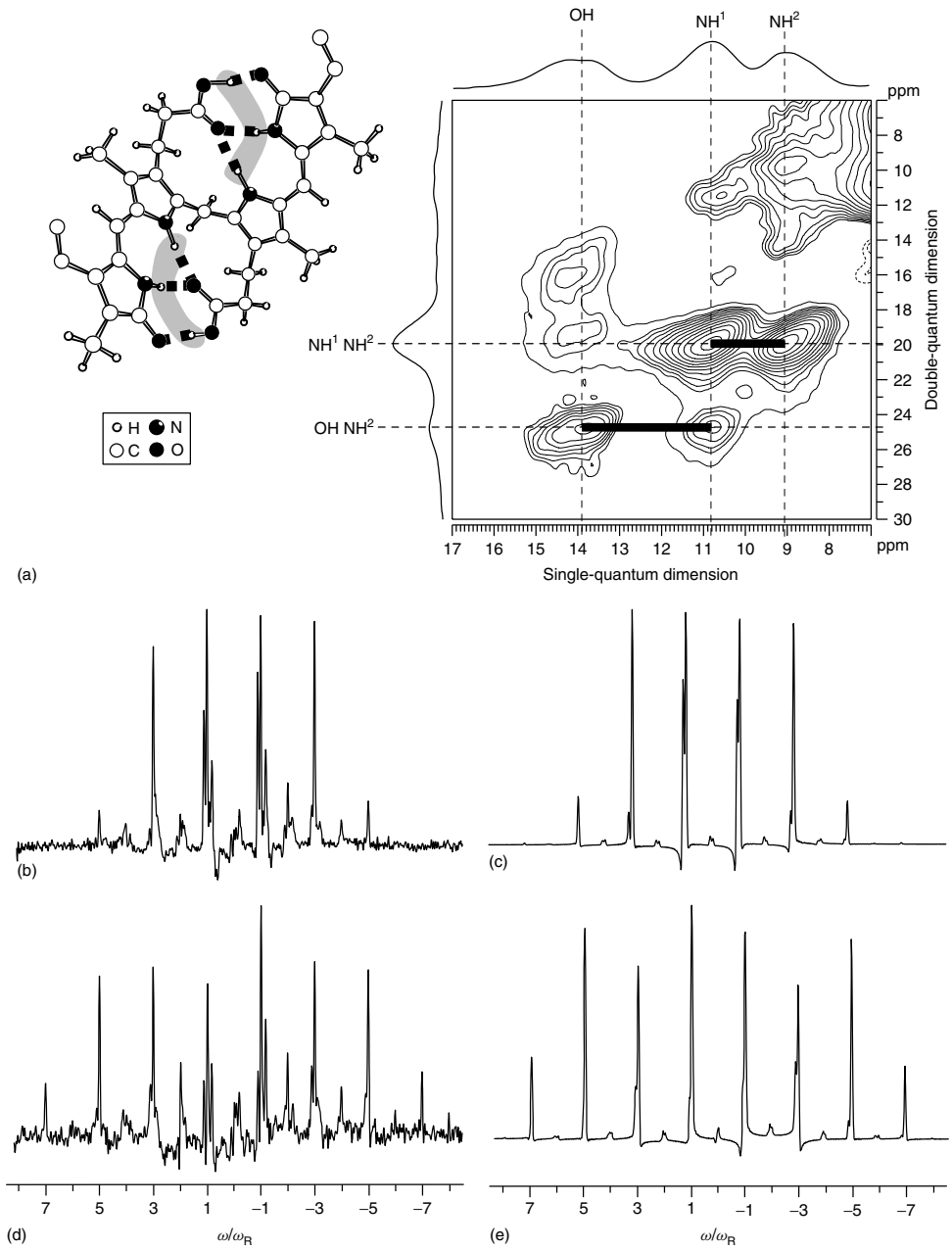


Figure 22.12. (a) ^{1}H (700 MHz) DQ MAS (30 kHz) spectrum of bilirubin. (b,d) Experimental ^{1}H (700 MHz) DQ MAS (30 kHz) NMR spinning-sideband patterns obtained for the NH^{1} hydrogen-bonded resonance of bilirubin, with (c,e) the corresponding best-fit three-spin simulations. (Reproduced from Ref. 29. © American Chemical Society, 2001.)

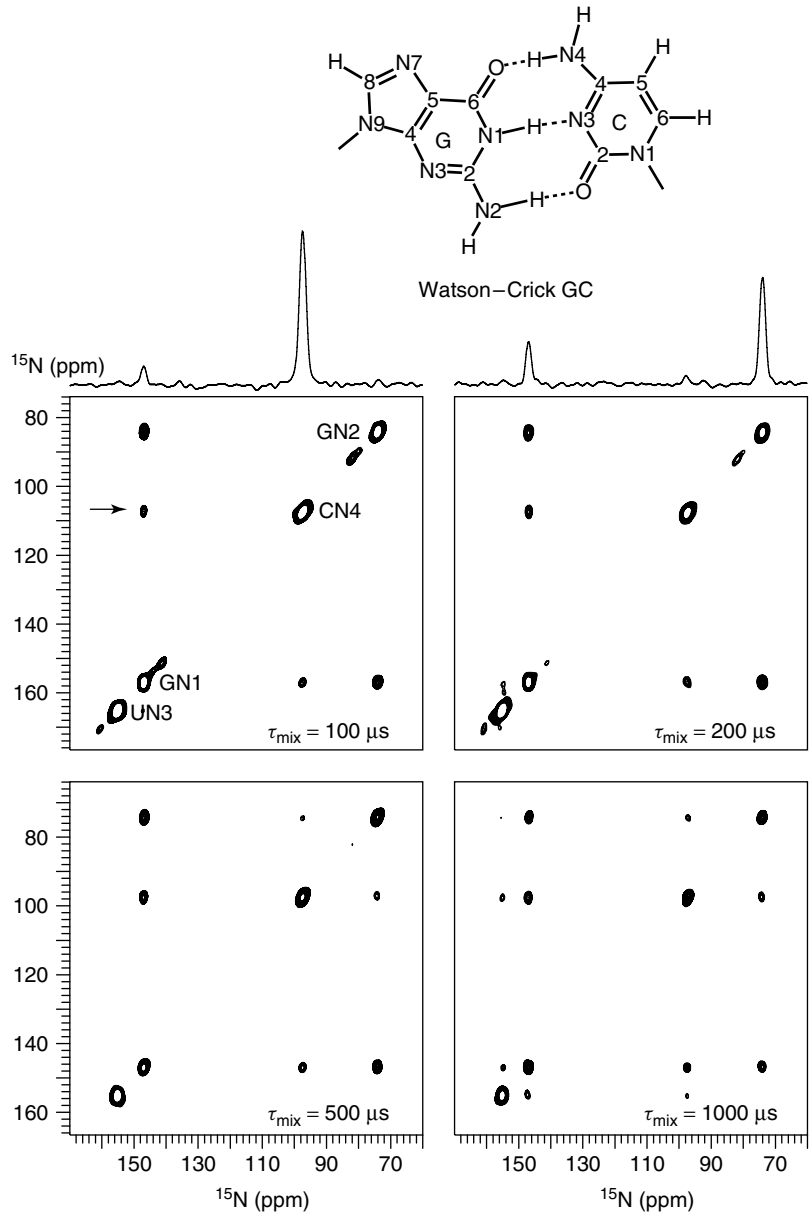


Figure 22.13. NHHN (500 MHz) MAS spectra obtained with different mixing times for a hydrated 100 kDa ^{15}N-labeled RNA sample composed of 97 CUG repeats.[31] Cross peaks between the CN4 and GN1 resonances corresponding to Watson–Crick GC hydrogen bonding are indicated. (Reproduced from Ref. 31 with kind permission from Springer Science and Business Media.)

22.3.3 Using Dipolar Couplings in NMR Crystallography: Outlook

Dipolar couplings with their inherent dependence on internuclear distances are a rich source of structural information to be exploited in NMR crystallography studies. Different solid-state NMR experiments yield either the quantitative or semi-quantitative determination of dipolar couplings. The former allows the accurate localization of specific atoms in the key parts of the structure, while the latter can identify particular structure-determining intermolecular hydrogen-bonding arrangements. Notably, the combination of chemical shift and dipolar coupling information, for example, the identification of assigned proton–proton proximities constitute valuable constraints to be exploited in the development of "spectrum to structure" approaches that combine experiment with calculation.

22.4 HYDROGEN BOND-MEDIATED J COUPLINGS

In solution-state NMR, the observation and measurement of J couplings across hydrogen bonds has enabled the identification of hydrogen-bonded partners, as well as the quantification of hydrogen-bond strengths and geometries.[32,33] In the solid state, the direct detection of intra- and intermolecular hydrogen bonds via the presence of correlation peaks due to $^{2h}J_{NH\cdots N}$ hydrogen bond-mediated J couplings has been demonstrated.[34,35] Figure 22.14 presents ^{15}N refocused INADEQUATE spectra for two fully ^{15}N-labeled deoxyguanosine derivatives, dG(C3)$_2$ and dG(C10)$_2$ with R = (a) C_2H_5 or (b) C_9H_{19}.[35] Of the observed pairs of correlation peaks, three can be assigned to two-bond intramolecular $^2J_{NN}$ connectivities. The pairs labeled in bold italics correspond to intermolecular hydrogen bond-mediated $^{2h}J_{N1-H\cdots N7}$ and $^{2h}J_{N2-H\cdots N7}$ couplings, demonstrating the adoption of (a) ribbonlike or (b) quartetlike self-assembly. The determination of intermolecular hydrogen-bonding arrangements (note that for dG(C10)$_2$, it has not been possible to obtain a single crystal suitable for a diffraction study) clearly demonstrates the potential of exploiting hydrogen bond-mediated J couplings in NMR crystallography.

Multiplet patterns due to such hydrogen bond-mediated J couplings have not been observed

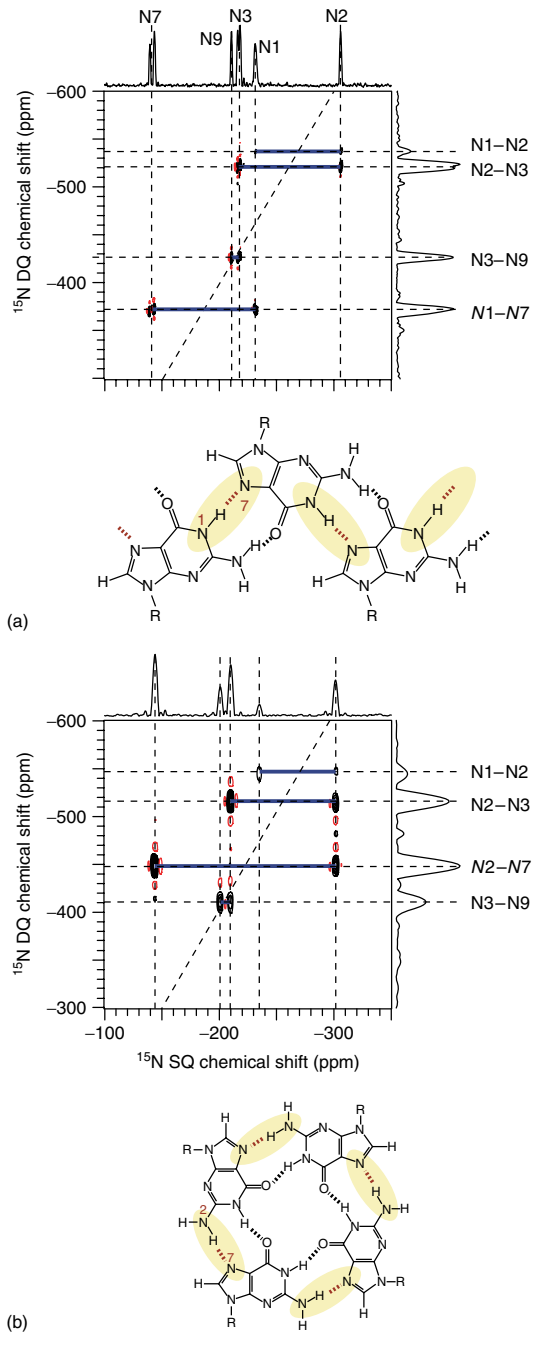


Figure 22.14. ^{15}N refocused INADEQUATE spectra for two fully ^{15}N-labeled deoxyguanosine derivatives with R = (a) C_2H_5 or (b) C_9H_{19}[35] that exhibit ribbonlike or quartetlike self-assembly, respectively. (Reproduced from Ref. 35. © American Chemical Society, 2005.)

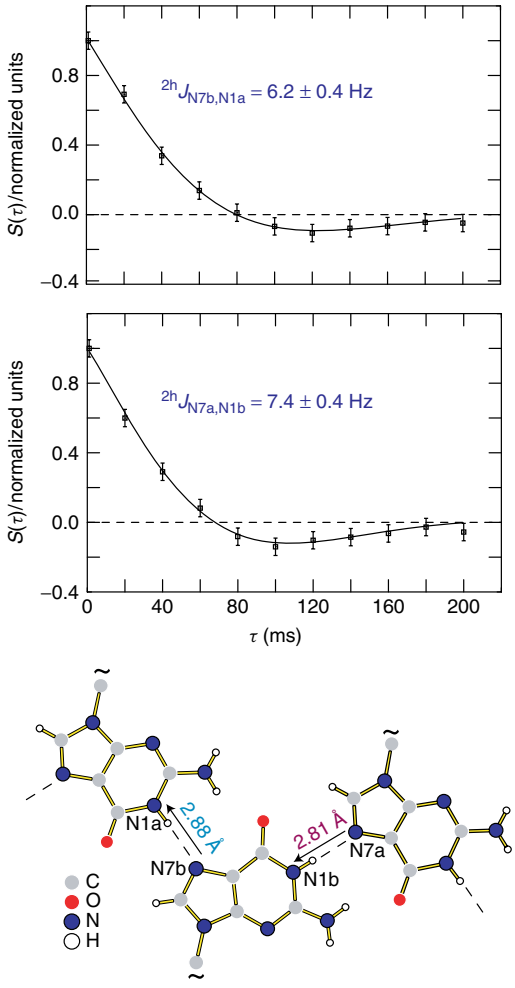


Figure 22.15. ^{15}N CP MAS (at 300 MHz for ^{1}H) spin-echo ($\tau/2-\pi-\tau/2$) data for the two resolved N7 resonances (see the representation of the crystal structure) of $dG(C3)_2$. (Reproduced from Ref. 38. © Royal Society of Chemistry, 2007.)

in one-dimensional solid-state NMR spectra, since the inherent linewidths are significantly larger than the magnitude of the coupling. However, J couplings can be quantitatively determined in the solid state by using a simple $\tau/2-\pi-\tau/2$ spin-echo MAS experiment.[36] Using ^{15}N spin-echo MAS experiments, inter- and intramolecular hydrogen bond-mediated J couplings have been determined.[37,38] Figure 22.15 illustrates the determination of two different $^{2h}J_{NN}$ couplings associated with the different N–H···N hydrogen-bonding distances for the two distinct molecules in the asymmetric unit cell of $dG(C3)_2$ which exhibits ribbon formation.[38] The experimentally determined values of $^{2h}J_{NN}$ = 6.2 ± 0.4 and 7.4 ± 0.2 Hz are in excellent agreement with values of 6.5 and 7.7 Hz calculated using the first-principles DFT code CASTEP.[39] This proof of concept work for the case of a known single-crystal diffraction structure demonstrates the potential of using hydrogen bond-mediated J couplings in "spectrum to structure" studies for organic molecules with unknown crystal structures.

22.5 HYDROGEN-BOND DYNAMICS

Solid-state NMR is well suited to the probing of dynamic processes. This section gives examples of two studies where temperature-dependent chemical shift changes allow the quantitative characterization of the dynamics associated with changes in the hydrogen-bonding arrangement.

Figure 22.16 presents temperature-dependent ^{1}H MAS and double-quantum filtered (DQF)[23] MAS spectra of the HBC derivative, HBC–C_{10}COOH, where all six alkyl chains are capped by a terminal carboxylic acid group,[40] such that the hydrogen bonding as well as aromatic π–π interactions determine the supramolecular assembly. In the solid phase at T = 320 K, the presence of hydrogen-bonded COOH dimers is demonstrated by the observation of an auto COOH peak in the ^{1}H DQ MAS NMR two-dimensional spectrum[23] – see Figure 22.16(c). Considering the COOH peak in the one-dimensional ^{1}H MAS spectra, as shown in Figure 22.16(a), both a shift to low frequency of the peak position, as well as an initial increase followed by a subsequent decrease in the linewidth, are observed upon heating—these effects are represented in Figure 22.17(a,b). These observations are interpreted in terms of a chemical exchange process involving the making and breaking of hydrogen bonds, with the coalescence point corresponding to T = 362 K. The equilibrium constant at a given temperature can be calculated from the observed chemical shift provided that the ^{1}H chemical shifts of the hydrogen-bonded and free states are known. Only the COOH protons in hydrogen-bonded dimers can give rise to a COOH auto peak in the ^{1}H DQ MAS spectrum (Figure 22.16(c)), and thus the chemical shift of the hydrogen-bonded protons can

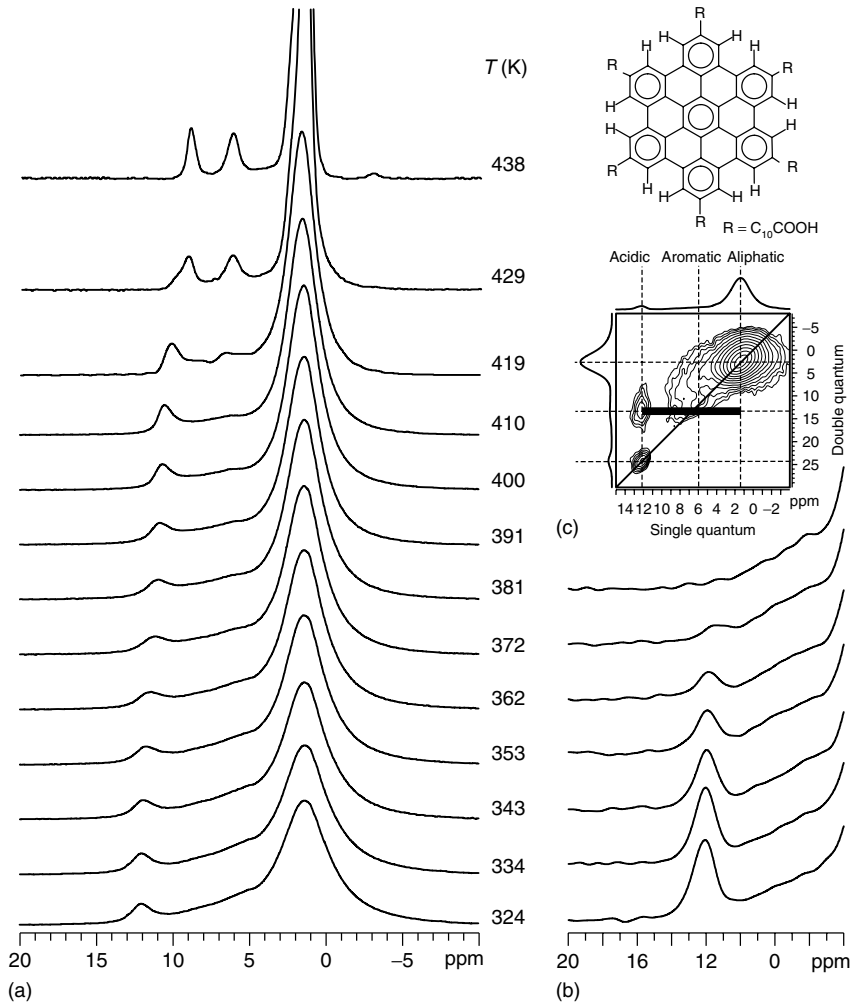


Figure 22.16. ^{1}H (500 MHz) MAS NMR (ν_r = 30 kHz) spectra of HBC–C_{10}COOH[40]: temperature-dependent (a) one-pulse and (b) DQ-filtered spectra; and (c) a rotor-synchronized DQ MAS spectrum (at room temperature), together with skyline SQ and DQ projections. (Reproduced from Ref. 40. © The PCCP Owner Societies, 2000.)

be determined to be 12.1 ppm. The chemical shift of the free COOH protons cannot be so easily identified; however, the initially observed chemical shift of 9.0 ppm for the COOH protons on heating into the liquid-crystalline phase (at T = 438 K) is strikingly low, and it is thus assumed that the chemical shift of the free state can be assigned to this value. A thermodynamic analysis of the temperature-dependent change in the equilibrium constant yields for the opening of the hydrogen-bonded dimers: ΔH = 45 $\pm$ 4 kJ mol^{-1} and ΔS = 113 $\pm$ 11 J K^{-1} mol^{-1}.

In ^{1}H DQF MAS spectra of HBC–C_{10}COOH—see Figure 22.16(b)—the intensity of the COOH peak is observed, upon heating, to reduce faster than expected from the thermodynamic factors alone, and above T = 380 K, no signal is detected—see Figure 22.17(c), where the experimentally observed DQ signal intensities for the COOH protons, relative to the intensity of the T = 324 K spectrum, are shown as crosses, while circles represent the expected reduction, again relative to the T = 324 K case, due solely to the combined temperature dependence of

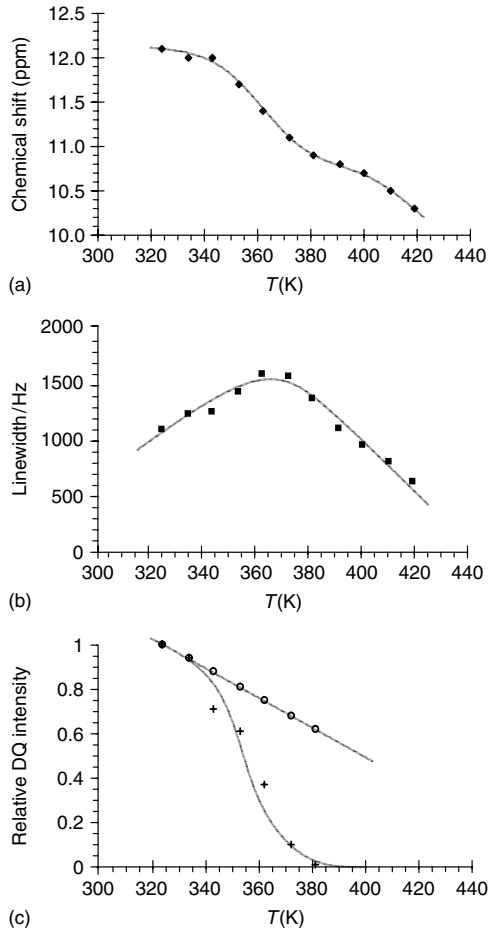


Figure 22.17. The effect of temperature on (a) the observed chemical shift, (b) the linewidth in ^{1}H MAS spectra (Figure 22.16a), and (c) the intensity in ^{1}H DQ-filtered MAS spectra (Figure 22.16b) of the COOH resonance for HBC–C_{10}COOH.[40] In (c), in addition to the crosses, which represent the experimental DQ-filtered intensities, the intensities which are expected on account of solely the combined temperature dependence of the equilibrium constant and the NMR bulk magnetization are shown as circles. Both the experimental and thermodynamically expected intensities are normalized relative to the $T = 324$ K case. (Reproduced from Ref. 40. © The PCCP Owner Societies, 2000.)

the equilibrium constant and the bulk magnetization. To observe a signal in a DQF experiment, the hydrogen-bonded form must exist for the duration of the DQ filter part of the NMR experiment, i.e., 133 μs for the spectra in Figure 22.16(b). It is then apparent that the falloff in the DQ intensity with increasing temperature can be explained by a decrease in the proportion of hydrogen-bonded dimers having lifetimes over 133 μs, until at $T = 381$ K, the concentration is less than that required to observe an NMR signal. In this way, an analysis of the DQF data yields the temperature dependence of the dimer lifetimes, and hence the kinetics of the chemical exchange process involving the making and breaking of hydrogen bonds could be determined: the activation energy and Arrhenius parameter equal 89 ± 10 kJ mol^{-1} and 4.2×10^{16} s^{-1}, respectively.

Figure 22.18(a) presents temperature-dependent ^{15}N CP MAS spectra of polycrystalline *N*,*N*′-diphenyl-6-aminofulvene-1-aldimine, which exhibits an intramolecular NH···N hydrogen bond.[41] Two ^{15}N resonances are observed at each temperature, with the splitting increasing as the temperature is lowered (see Figure 22.18b). This behavior is due to intramolecular proton tautomerism, whereby the equilibrium constant, K_{12}, at each temperature can be calculated from the observed splitting. A plot of $\ln(K_{12})$ against $1/T$ is a straight line (Figure 22.18c), hence allowing the determination from the van't Hoff equation of $\Delta H = 1.4 \pm 0.1$ kJ mol^{-1} and $\Delta S = 2.49 \pm 0.05$ J K^{-1} mol^{-1}.

22.6 OUTLOOK

This article has demonstrated the marked sensitivity of various NMR parameters (^{1}H, ^{15}N, ^{17}O chemical shift, dipolar, and J couplings) to hydrogen bonding in organic solids and has illustrated the potential of solid-state NMR as a crystallographic tool. Solid-state NMR and diffraction methods are complementary approaches: NMR is sensitive to the local environment around a nucleus, while diffraction techniques rely on long-range periodic order. Indeed, for a number of applications to organic solids, well-resolved solid-state NMR spectra indicative of an ordered structure are obtained in cases where it is not possible to obtain single crystals suitable for diffraction studies. Moreover, solid-state NMR studies can localize the atoms in key hydrogen bonds to a great accuracy, and NMR is particularly adept at following dynamic processes. Of much promise are the possibilities that are being opened up by the increasing capabilities (due to advances in methodology and computing power) of methods for calculating solid-state NMR parameters.

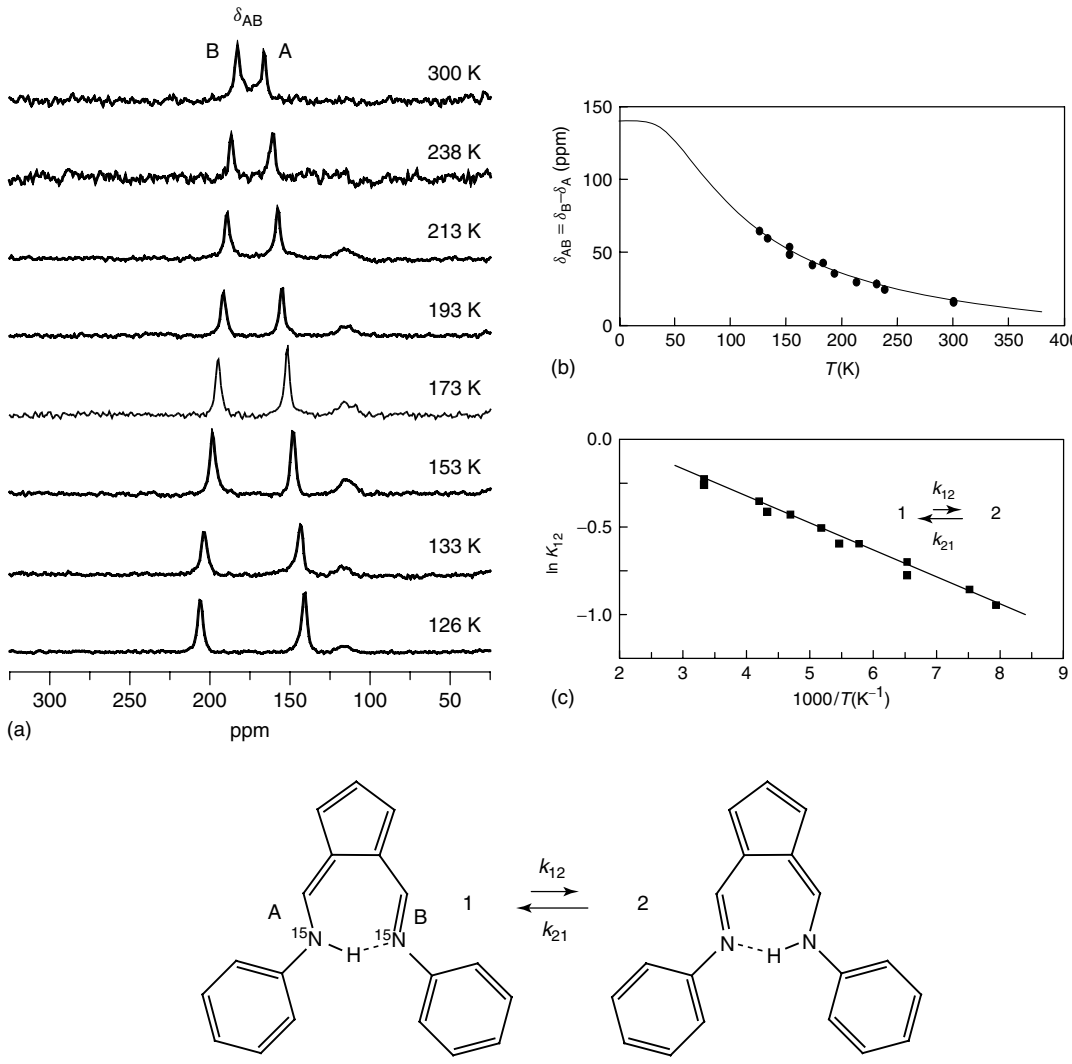


Figure 22.18. (a) Temperature-dependent ^{15}N (30 MHz) CP MAS spectra of polycrystalline *N,N′*-diphenyl-6-amino fulvene-1-aldimine. (b) The change in the splitting of the two ^{15}N signals as a function of temperature; and (c) the corresponding van't Hoff plot.[41] ^{15}N chemical shifts are referenced with respect to the resonance of solid $^{15}NH_4Cl$. (Reproduced from Ref. 41. © American Chemical Society, 2008.)

The dream of these combined experimental and calculation research efforts is the development of reliable and rapid "spectrum to structure" procedures, i.e., to translate the rich information content of solid-state NMR spectra, notably the sensitivity to structure-determining intermolecular interactions, of which hydrogen bonding is the most important, into crystallographic structures.

REFERENCES

1. G. A. Jeffrey, *An Introduction to Hydrogen Bonding*, Oxford University Press: Oxford, 1997.
2. R. K. Harris, P. Jackson, L. H. Merwin, B. J. Say, and G. Hagele, *J. Chem. Soc., Faraday Trans.*, 1988, **84**, 3649.

3. R. K. Harris, P. Y. Ghi, R. B. Hammond, C. Y. Ma, and K. J. Roberts, *Chem. Commun.*, 2003, 2834.
4. J. Schmidt, A. Hoffmann, H. W. Spiess, and D. Sebastiani, *J. Phys. Chem. B*, 2006, **110**, 23204.
5. G. R. Desiraju and T. Steiner, *The Weak Hydrogen Bond In Structural Chemistry and Biology*, Oxford University Press: Oxford, 1999.
6. A. C. Uldry, J. M. Griffin, J. R. Yates, M. Pérez-Torralba, M. D. Santa Maria, A. L. Webber, M. L. L. Beaumont, A. Samoson, R. M. Claramunt, C. J. Pickard, and S. P. Brown, *J. Am. Chem. Soc.*, 2008, **130**, 945.
7. C. J. Pickard and F. Mauri, *Phys. Rev. B*, 2001, **63**, 245101.
8. C. Ochsenfeld, S. P. Brown, I. Schnell, J. Gauss, and H. W. Spiess, *J. Am. Chem. Soc.*, 2001, **123**, 2597.
9. S. P. Brown, T. Schaller, U. P. Seelbach, F. Koziol, C. Ochsenfeld, F. G. Klarner, and H. W. Spiess, *Angew. Chem., Int. Ed. Engl.*, 2001, **40**, 717.
10. J. R. Yates, T. N. Pham, C. J. Pickard, F. Mauri, A. M. Amado, A. M. Gil, and S. P. Brown, *J. Am. Chem. Soc.*, 2005, **127**, 10216.
11. R. Ida, M. De Clerk, and G. Wu, *J. Phys. Chem. A*, 2006, **110**, 1065.
12. G. Wu, *Prog. Nucl. Magn. Reson. Spectrosc.*, 2008, **52**, 118.
13. K. J. Pike, V. Lemaitre, A. Kukol, T. Anupold, A. Samoson, A. P. Howes, A. Watts, M. E. Smith, and R. Dupree, *J. Phys. Chem. B*, 2004, **108**, 9256.
14. S. Sharif, D. Schagen, M. D. Toney, and H. H. Limbach, *J. Am. Chem. Soc.*, 2007, **129**, 4440.
15. S. Sharif, E. Fogle, M. D. Toney, G. S. Denisov, I. G. Shenderovich, G. Buntkowsky, P. M. Tolstoy, M. C. Huot, and H. H. Limbach, *J. Am. Chem. Soc.*, 2007, **129**, 9558.
16. S. Dusold and A. Sebald, in *Annual Reports On NMR Spectroscopy*, Academic Press Inc: San Diego, 2000, Vol. 41, p 185.
17. X. Zhao, J. L. Sudmeier, W. W. Bachovchin, and M. H. Levitt, *J. Am. Chem. Soc.*, 2001, **123**, 11097.
18. I. Schnell and K. Saalwächter, *J. Am. Chem. Soc.*, 2002, **124**, 10938.
19. G. R. Goward, I. Schnell, S. P. Brown, H. W. Spiess, H. D. Kim, and H. Ishida, *Magn. Reson. Chem.*, 2001, **39**, S5.
20. A. Brinkmann and A. P. M. Kentgens, *J. Am. Chem. Soc.*, 2006, **128**, 14758.
21. J. D. van Beek, R. Dupree, and M. H. Levitt, *J. Magn. Reson.*, 2006, **179**, 38.
22. I. Schnell and H. W. Spiess, *J. Magn. Reson.*, 2001, **151**, 153.
23. S. P. Brown, *Prog. Nucl. Magn. Reson. Spectrosc.*, 2007, **50**, 199.
24. I. Schnell, S. P. Brown, H. Y. Low, H. Ishida, and H. W. Spiess, *J. Am. Chem. Soc.*, 1998, **120**, 11784.
25. S. Pawsey, M. McCormick, S. De Paul, R. Graf, Y. S. Lee, L. Reven, and H. W. Spiess, *J. Am. Chem. Soc.*, 2003, **125**, 4174.
26. S. P. Brown, A. Lesage, B. Elena, and L. Emsley, *J. Am. Chem. Soc.*, 2004, **126**, 13230.
27. D. Sakellariou, A. Lesage, P. Hodgkinson, and L. Emsley, *Chem. Phys. Lett.*, 2000, **319**, 253.
28. J. M. Griffin, D. R. Martin, and S. P. Brown, *Angew. Chem., Int. Ed. Engl.*, 2007, **46**, 8036.
29. S. P. Brown, X. X. Zhu, K. Saalwächter, and H. W. Spiess, *J. Am. Chem. Soc.*, 2001, **123**, 4275.
30. J. Leppert, C. R. Urbinati, S. Hafner, O. Ohlenschlager, M. S. Swanson, M. Gorlach, and R. Ramachandran, *Nucleic Acids Res.*, 2004, **32**, 1177.
31. K. Riedel, J. Leppert, O. Ohlenschlager, M. Gorlach, and R. Ramachandran, *J. Biomol. NMR*, 2005, **31**, 331.
32. A. J. Dingley and S. Grzesiek, *J. Am. Chem. Soc.*, 1998, **120**, 8293.
33. S. Grzesiek, F. Cordier, V. Jaravine, and M. Barfield, *Prog. Nucl. Magn. Reson. Spectrosc.*, 2004, **45**, 275.
34. S. P. Brown, M. Pérez-Torralba, D. Sanz, R. M. Claramunt, and L. Emsley, *J. Am. Chem. Soc.*, 2002, **124**, 1152.
35. T. N. Pham, S. Masiero, G. Gottarelli, and S. P. Brown, *J. Am. Chem. Soc.*, 2005, **127**, 16018.
36. L. Duma, W. C. Lai, M. Carravetta, L. Emsley, S. P. Brown, and M. H. Levitt, *ChemPhysChem*, 2004, **5**, 815.
37. S. P. Brown, M. Pérez-Torralba, D. Sanz, R. M. Claramunt, and L. Emsley, *Chem. Commun.*, 2002, 1852.
38. T. N. Pham, J. M. Griffin, S. Masiero, S. Lena, G. Gottarelli, P. Hodgkinson, C. Filip, and S. P. Brown, *Phys. Chem. Chem. Phys.*, 2007, **9**, 3416.

39. S. A. Joyce, J. R. Yates, C. J. Pickard, and S. P. Brown, *J. Am. Chem. Soc.*, 2008, **130**, 12663.

40. S. P. Brown, I. Schnell, J. D. Brand, K. Mullen, and H. W. Spiess, *Phys. Chem. Chem. Phys.*, 2000, **2**, 1735.

41. J. M. Lopez del Amo, U. Langer, V. Torres, G. Buntkowsky, H.-M. Vieth, M. Pérez-Torralba, D. Sanz, R. M. Claramunt, J. Elguero, and H. H. Limbach, *J. Am. Chem. Soc.*, 2008, **130**, 8620.

Chapter 23

Inorganic Non-stoichiometric Crystalline Systems & Atomic Ordering

Mark E. Smith

Department of Physics, University of Warwick, Coventry CV4 7AL, UK

23.1	Introduction	341
23.2	NMR Interactions and Data Analysis	343
23.3	Example Applications	345
23.4	Conclusions	352
	References	352

23.1 INTRODUCTION

In the idealized concept of a perfect crystalline solid, there is a well-defined unit cell with the chemical composition and the atomic coordinates of each distinct site present in the structure well specified, with the three-dimensional solid simply made up by the repeating rules of the associated space group. The opposite structural extreme is the amorphous state with a defined stoichiometry, but there is no unit cell and hence no long-range order. Hence for amorphous solids, the structure needs to be described statistically in terms of the local coordination units (short-range order) and the way the well-defined local units join together (medium-range order). This article deals with "real" crystalline solids, which only rarely demonstrate the idealized perfection of a textbook crystalline solid. To best understand solid materials, a range of characterization techniques should be applied since there is often a high degree of complementarity between the information provided by different approaches, often arising from their sensitivity to different length- and time-scales. The sophistication of all techniques is progressing. For example, diffraction (both X-ray and neutron) has moved well beyond conventional Bragg diffraction that produces the coherent scattering from the lattice to give the typical "average" unit cell for a sample that reflects the long-range repeating nature of a crystalline lattice. Despite the impression often conveyed that diffraction is uninformative regarding the amorphous state, Fourier transformation of the scattered intensity produces the correlation function that can yield information about the local coordination of atoms. With the relatively large momentum transfer ranges often now available, the correlation function can reveal structural information as exemplified by phosphate glasses where the P–O correlations from bridging and nonbridging oxygens can be resolved.[1] Fourier-transforming diffraction data to include both the local correlations and the Bragg diffraction in what is termed *total diffraction* has revealed atomic disorder that would otherwise have been missed from simple Bragg diffraction.[2] Electron microscopy has also developed very considerably, especially as it can now offer atomic-scale resolution with aberration-corrected microscopes. Imaging at close to atomic-scale resolution means that again local ordering can be probed.

NMR Crystallography Edited by Robin K. Harris, Roderick E. Wasylishen and Melinda J. Duer © 2009 John Wiley & Sons, Ltd. ISBN: 978-0-470-69961-4

Comprehensive suites of physical probe techniques can now be employed to understand materials (*see* **Chapter 19**).[3] However, solid-state NMR has a key role to play through its exquisite short-range sensitivity to different environments and its direct quantitative nature, with applications to disorder in crystalline inorganic systems examined here.

In a crystalline material, even for those exhibiting stoichiometry, there are various ways perfect crystalline order can be spoilt. For example, there can be interchange of different atoms between sites. A classic case is the spinel (AB_2O_4) composition where the structure contains two types of cation (A and B) and cation site (i.e., tetrahedral or octahedral coordination) with a range of orderings of the different chemical elements possible over the structurally distinct sites. Another example is that a compound, while stoichiometric, can contain a heterogeneous distribution of elements within a supposedly single structure, thereby forming chemically distinct domains. Such clustering and domain formation can be important in some ferroelectric phases and can also be a precursor to phase-separation behavior. The importance of atomic ordering should not be underestimated, since it may drive much of the underlying thermodynamics of a system. Crystal structures can often accommodate significant amounts of chemical variation to form solid solutions, where the properties are altered in either subtle or quite dramatic ways, especially if direct charge compensation in the atomic substitutions is not there. Then such solid solutions can be accompanied by the creation of, for example, vacancies or interstitials. Variations of structural disorder include incommensurate behavior, where there is some degree of well-defined change of the structure via a modulation of the local structure that imposes a different periodicity on top of the underlying fundamental unit cell/crystallographic periodicity. In the NMR spectrum, this is reflected in an increase in the multiplicity of lines or broadening, depending on the relative effect of incommensurate structure on the NMR interaction parameters.

It is the NMR interaction parameters that convey information about the local surroundings of the nucleus in NMR spectroscopy. Often, the most direct information comes via the chemical shift. In solid solutions where paramagnetic ions are added, the often much greater paramagnetic interactions can be used to enhance such influences in NMR spectra, helping to identify the site of dopant ions. With so many nuclei in the Periodic Table having a spin quantum number greater than 1/2, and the increasingly sophisticated methodology for extraction of the quadrupolar interaction parameters, this interaction is also playing a more important role in describing the local environments.

To date, the application of NMR to study problems concerning nonstoichiometry and atomic ordering in inorganic materials have largely centred on relatively simple NMR techniques. The most important information is to identify the different local environments present, which can be translated into how atoms being added are distributed in the host structure. Hence the number of different peaks along with their structural identity and relative intensity are crucial features. The most direct approach to obtain this information, provided that there is sufficient spectral resolution, can be simply one-dimensional static and MAS spectra. It is relatively straightforward to make such spectra quantitative, which is a key to understanding the distribution of different environments. The relative intensity can quite strongly constrain the nature of local ordering (e.g., random, clustered, etc.). However the information from these spectra relates to the short-range order and does not provide insight into how these different local environments are distributed relative to one another (i.e., the medium-range order). To extend information to a longer length scale requires some form of coupling between the different units, such as through space dipolar coupling or through bond J-coupling. Then two-dimensional (2-D) pulse sequences provide an indication of the coupling of different local units. A whole range of 2-D experiments exist that are based on either dipolar coupling (e.g., REDOR, rotational echo adiabatic passage double resonance (REAPDOR), transfer of population in double resonance (TRAPDOR)), or J-coupling in the refocused INADEQUATE experiment. The connectivity pattern that emerges for the local units gives insight into whether there is a homogeneous distribution or clustering on a length scale longer than the nearest and next-nearest neighbors (nnn). If suitable nuclei exist (typically larger magnetic moments and high natural abundance), spin diffusion or driven diffusion experiments can provide "domain" sizes, but this is much less developed for inorganic materials as compared to organic polymers.

To illustrate how NMR can elucidate local atomic ordering, a range of examples is used to demonstrate (i) atomic disorder within stoichiometric materials, (ii) atomic substitutions, such as layer substitutions

and cation exchange (i.e., at relatively low levels), and (iii) comprehensive solid solutions and creation of defect sites. The focus on inorganic materials does not include semiconductor or metal alloy formation, which, nevertheless, form classic atomic ordering problems, where, although some NMR examples exist, applications are still limited, but NMR should play an increasingly important role. A very elegant example that illustrates both the evolution of structure and atomic ordering is the crystallization of magnesium cordierite ($Mg_2Al_4Si_5O_{18}$) glass.[4,5] Crystallization of the glass occurs effectively almost immediately at 1150 °C, yielding the metastable hexagonal form. The X-ray diffraction (XRD) pattern shows the characteristic, relatively sharp Bragg peaks of the hexagonal phase. The ^{29}Si MAS NMR pattern also changes considerably (Figure 23.1) on crystallization, with the broad featureless line of the glass being replaced by eight much narrower lines. The hexagonal structure contains two structurally distinct tetrahedral Q^4 sites[6,7] (T1 and T2) in the ratio 1 : 2, but with the aluminum and silicon largely disordered over these two sites, as evidenced by the eight ^{29}Si resonances that arise from the effects of the nnn aluminum on the isotropic chemical shift. Annealing drives silicon/aluminum ordering within the structure, reflected in changes in the relative intensity of the different peaks. XRD does not register any real change in the diffraction pattern between initial crystallization and annealing for ~100 h. This is a particularly difficult case because of the very close X-ray scattering factors of silicon and aluminum (since they are next to each other in the periodic table). After heating for 1000 h (Figure 23.1j) a continuous transformation driven by Lowenstein's aluminum avoidance principle to the fully ordered orthorhombic structure has occurred and just two distinct silicons are observed. This very clearly illustrates the sensitivity of NMR to changes in the local environment.

23.2 NMR INTERACTIONS AND DATA ANALYSIS

The NMR interaction parameters contain information about the local environment. The isotropic chemical shift (δ_{iso}) often provides the most direct information. The influences of ^{29}Si on δ_{iso} illustrate the likely sensitivity to ordering effects.[6,7] In nonparamagnetic materials, δ_{iso} is most affected by the coordination number, such that δ_{iso} varies successively by ~50 ppm in going from SiO_4 to SiO_5 to SiO_6. The ^{29}Si δ_{iso} undergoes a similar magnitude of change when the element in the first coordination sphere alters, for example, from Si–O to Si–N to Si–C. Changes in the nnn produce smaller, but readily measurable, changes in δ_{iso} and they form the basis of the effects seen in the cordierite example above. For ^{29}Si changes, typically ~10 ppm, are observed when the connectivity of the local unit changes (i.e., Q^n speciation). In aluminosilicates, these changes are of similar magnitude to the effect of aluminum nnn, which is why in such glasses often featureless, uninformative ^{29}Si MAS NMR signals are recorded. Crystallographically inequivalent sites can cause significantly varying changes in δ_{iso}, depending on the degree of structural variation causing the inequivalence.

Although the presence of paramagnetic centers can often have a detrimental effect on the quality of NMR spectra, in certain situations, the presence of paramagnetic ions within a structure can be beneficial in determining the site of dopant ions in solid solutions. If the electronic relaxation time is sufficiently short (i.e., $<10^{-10}$ s), then the broadening of nearby nuclei will be mitigated to give high-resolution NMR spectra. Then the additional local fields produced by both the Fermi contact and through-space pseudocontact interactions can cause a significant change of shift to nearby nuclei. In lanthanide-doped pyrochlores $Y_2(Sn/Ti)_2O_7$, both the ^{119}Sn[8] and ^{89}Y[9] MAS NMR spectra showed additional, shifted peaks from interaction with the paramagnetic lanthanide species present. The observed shifts were found to be proportional to the number of lanthanide ions substituted, so that the intensities of the different resonances observed allowed the concentration of paramagnetic rare-earth ions to be accurately determined.

The quadrupole interaction also reflects the surroundings, particularly the distortion of the local environment, although identification of the local environment on the basis of the quadrupolar parameters alone is much less straightforward than for δ_{iso}. However, this is a continually developing situation, where rapidly improving calculations can more directly indicate the parameters to be expected from different environments.

The basis on which NMR can provide unequivocal information about the distribution of an element between different local environments is that the spectral differences between them are much greater than the intrinsic linewidths. Hence in the cordierite

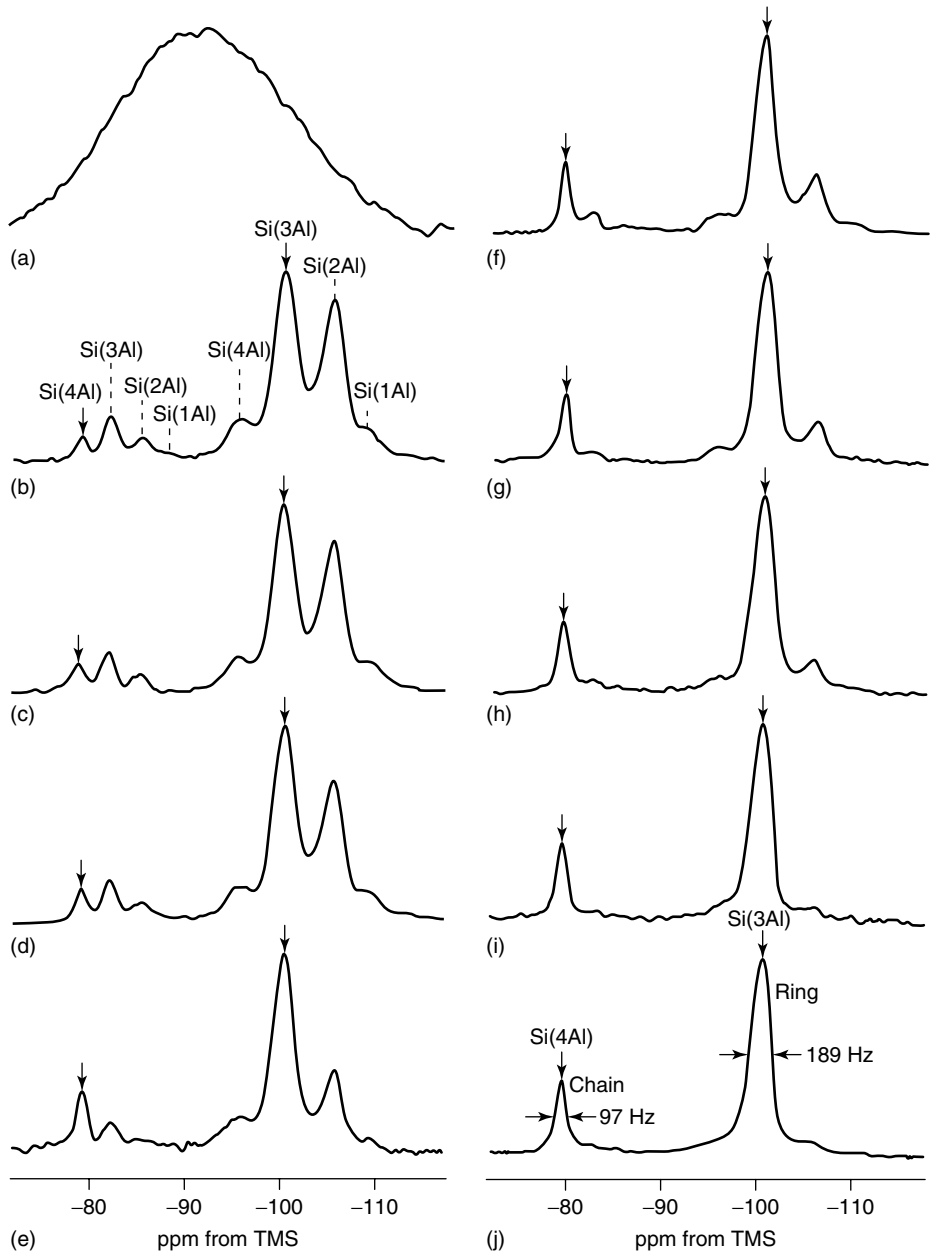


Figure 23.1. ^{29}Si (79.5 MHz) MAS NMR spectra of synthetic cordierite, prepared from glass of the same composition (a), by annealing at 1185 °C for (b) 2 min, (c) 6.5 min, (d) 20 min, (e) 6 h, (f) 23.5 h, (g) 48.5 h, (h) 96 h, (i) 408 h, and (j) approximately 2000 h. (Reproduced from Ref. 5. © American Chemical Society, 1986.)

example of Figure 23.1, in the initial glass, there is a range of nnn silicon/aluminum environments. However, rather than being two well-defined silicon environments, each characterized by a single set bond of lengths and angles, there are much wider variations in the local geometry, causing a range of chemical shifts. This range is comparable to or greater than the differences caused by the nnn effects, thereby obscuring the information about the nnn environments present. On crystallization, there will be very little change in the range of nnn environments present, but a very great decrease in the range of bond lengths and angles, which results in the very great reduction of the intrinsic linewidth associated with each site, thereby revealing the nnn effects. Since NMR is element specific, it provides a view of the structure around each element. In considering different elements that experience different interactions, these have different sensitivity to structural distortion (which can also vary for a given interaction for different nuclei). Often, the quadrupole interaction can be much more sensitive to distributions in bond lengths and angles than the chemical shift. In a solid solution of aluminoborate mullites $Al_{6-x}B_xO_9$, complex ^{27}Al MAS NMR spectra are obtained with seven distinguishable lines across the series.[10] The spectra from this crystalline compound (Figure 23.2) show most of the ^{27}Al resonances exhibiting the tails characteristic of a range of local environments in a glass.[7] This simply indicates that the structural variation in the local environment created in the solid solution is reflected in a sufficient range of interactions to cause such a lineshape (but note that this material does not have any characteristics of a glass). By contrast the ^{11}B MAS NMR spectra from the same series show well-defined second-order quadrupolar lineshapes (if slightly smoothed) for the BO_3 sites and the normal featureless peak for the BO_4.[10]

Once the different sites have been identified from the NMR spectrum and the intensity distribution between them has been deduced, this has to be compared with the structure. Here the directly quantitative nature of solid-state NMR is seen to its maximum advantage. Models of the potential distribution of atoms between the different sites can be proposed and matched to the measured intensity distribution and hence confirm how the atoms in the solid solution are being arranged. This will be explicitly demonstrated in some of the examples that follow.

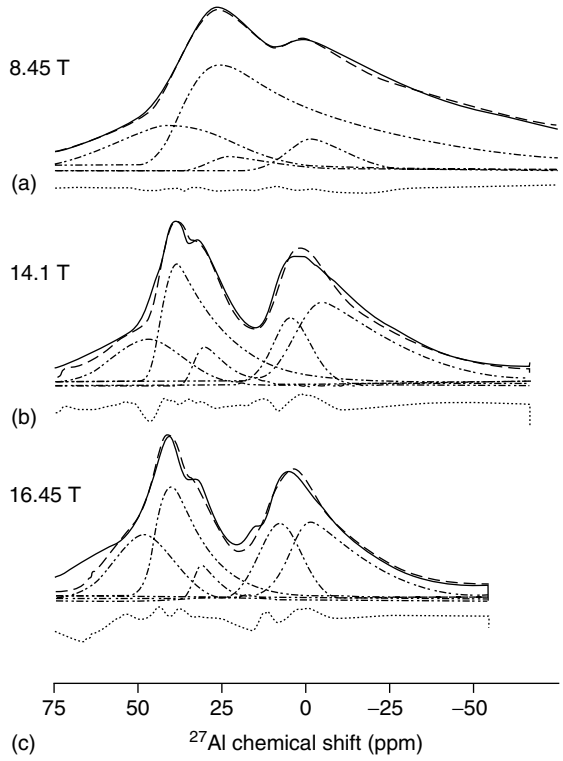


Figure 23.2. ^{27}Al MAS NMR spectra of $Al_4B_2O_9$ at field strengths of (a) 8.45, (b) 14.1 and (c) 16.45 T showing peaks fitted according to the most consistent simulations at all magnetic field strengths. The solid line denotes the experimental spectrum and the broken line the lineshape simulated with the fitted peaks as shown. (Reproduced from Ref. 10. © Springer Verlag, 2007.)

23.3 EXAMPLE APPLICATIONS

23.3.1 Silicates and Aluminosilicates

23.3.1.1 Ordering of Aluminosilicates

One of the original key observations in demonstrating the utility of solid-state NMR in providing new information about materials was determining the silicon/aluminum ordering within zeolites.[6,11] Many zeolites have purely siliceous forms and solid solutions are obtained as aluminum is dissolved into the structure. The ^{29}Si NMR intensity of the different resolved $Q^4(m\text{Al})$ resonances allows the silicon-to-aluminum ratio of the framework to be determined. The same

principles can be applied more widely to determining the silicon–aluminum ordering within aluminosilicates, especially minerals.[7] As was shown for cordierite (see the Section 23.1), although initially a highly disordered distribution might form, it tends to a Lowensteinian (aluminum avoidance) distribution as thermodynamic equilibrium is approached.

Clay minerals are typical layer aluminosilicate structures, with two types of layers: silica-like, made up of SiO_4 units, and gibbsite-like, made up of $AlO_4(OH)_2$. Between these repeated layers are interlayer spaces and these interlayers can have important ion-exchange properties. Structural complexity in clays may arise through atomic substitutions that can occur within these layers. Some examples are aluminum substituting for silicon in the silica-like layers, and iron and magnesium substituting for aluminum in the gibbsite-like layer. These substitutions usually produce a negative layer charge, which then needs to be balanced by cations (e.g., K^+, Ca^{2+}) that reside in the interlayer space. The various layer substitutions and interlayer contents can produce significant changes in the properties of the clay, including its thermal breakdown mechanism. NMR can spot aluminum substitution very clearly in the silica-like layer through the presence of an AlO_4 signal. Fitting the spectral intensities of the different nuclei, especially ^{29}Si, has suggested that, since the AlO_4 units carry a negative charge, they tend to try and sit as far apart as possible within the layer.[7]

23.3.1.2 Mullites

Mullite (central composition $\approx 3Al_2O_3{\cdot}2SiO_2$) is one of the most widely studied ceramic materials and shows significant solid-solution formation. The general formula of mullite is $[Al_2]^6\,[Al_{2+2x}Si_{2-2x}]^4O_{10-x}$ (where the superscripts indicate the coordination) in which columns of octahedral AlO_6 units are cross-linked by double chains of SiO_4 and AlO_4 tetrahedra. The charge imbalance in this structure is compensated by the formation of characteristic oxygen vacancies (x) in conjunction with three distorted tetrahedral Al–O groups (a so-called "tricluster" or Al* unit). It has been inferred that a random distribution of aluminum and silicon occurs in the tetrahedral sites and contrasts with the closely related sillimanite structure, where the corresponding sites are fully ordered. ^{29}Si MAS NMR spectra of mullite often show several peaks, with the strong signal at −88 ppm attributed to a site with sillimanite-type short-range order, i.e., an SiO_4 is surrounded by three AlO_4. The signals at −92 and −95 ppm are ascribed to an SiO_4 surrounded by one SiO_4 plus two AlO_4 or by two SiO_4 and one AlO_4, respectively.[12,13] Various models of demixing and ordering can be examined and it is clear that, by comparing the predicted intensity distribution with the ^{29}Si MAS NMR spectra, within the chains there is moderate ordering with little tendency for the silicon and the aluminum to segregate.[14] Mullite forms during the thermal decomposition of clay minerals. As the layers break apart, nanoscale separation of the silica-rich and alumina-rich parts of the structure occurs (typically at 1000 °C). The alumina phase is initially a transitional (e.g., γ) alumina, but then transforms (~1200 °C) to a mullite phase that is initially very aluminium-rich. With further heat treatment, the migration of silicon into the mullite structure can be followed by ^{29}Si MAS NMR until close to the stoichiometric 3 : 2 composition is reached at higher temperatures.[15]

23.3.2 Simple Solid Solutions Including Spinels and Garnets

In the spinel structure (AB_2O_4), the cations can occupy tetrahedral or octahedral coordinations. In a *normal* spinel, the distribution of the cations over these sites is described as $A^4B_2{}^6O_4$. *Inverse* spinels have the configuration $B^4\,(AB)^6O_4$, with most spinels showing a degree of disorder between these two end members, with formulae expressed as $(A_{1-x}B_x)^4\,(B_{2-x}A_x)^6O_4$, where x is the *degree of disorder*. Since x is related to the octahedral : tetrahedral ratio R, which can be deduced from the NMR spectrum by $x = 2/(1 + R)$, NMR can determine the degree of inversion. This can occur in stoichiometric compounds, but site preferences for nonstoichiometric compounds have also been probed. ^{27}Al MAS NMR is the obvious probe of the aluminum distribution in the classic spinel $MgAl_2O_4$. The thermodynamics of disordering over the cation sites has been followed,[16] including *in situ* measurements up to 1600 °C.[17] For the solid solution $MgAl_{2-x}Ga_xO_4$, the distribution of the magnesium and aluminum over the two sites is almost independent of the gallium content, with a small dependence on the thermal history of a particular sample.[18]

Garnets, specifically $Y_3Al_5O_{12}$ (YAG) are technologically very important materials, with neodymium- and erbium-doped YAG, forming key lasing media. In $YSc_xAl_{5-x}O_{12}$, as scandium was doped into the structure, both ^{27}Al and ^{45}Sc MAS NMR spectra were recorded.[19] The two ^{27}Al resonances (AlO_4, AlO_6) showed a small increase in χ_Q for both sites as scandium was added, but more noticeably there was a blurring of the distinct lineshapes of the resonances, indicating the structural variation caused on doping. ^{45}Sc NMR showed a single resonance characteristic of an octahedral site preference of the dopant ion. Exactly analogous NMR results were obtained for gallium-doped YAG, apart from gallium having a preference for the tetrahedral site.[20] Also in $Y_{3-x}Lu_xAl_5O_{12}$, only small variations in the NMR parameters were observed with a generally increasing distribution of parameters. However, the ^{27}Al multiple-quantum (MQ) data showed variations in the isotropic dimension, indicating that some compositions might tend to be more ordered than a purely random distribution of yttrium and lutetium across the relevant sites.[21]

Magnesium shows almost complete solid solution in γ-$Zn_3(PO_4)_2$, which has a single ^{31}P resonance at 3.9 ppm. In the solid solution with magnesium, four well-resolved ^{31}P peaks appear, spanning a range of only ~4 ppm. The cations are spread over an octahedral site and a five-coordinated site in the ratio 1 : 2. The observation of four resonances indicates that the ^{31}P δ_{iso} is sensitive not only to the nearest cation, but also to the cation in the next site. Hence the intensity distribution in the ^{31}P spectra could be modeled by taking into account both the composition and site preference of the different cations between the five and sixfold sites. Unequivocal evidence was presented for the magnesium having a significant preference for the octahedrally coordinated site, but with some distribution onto the five-coordinated site.[22]

23.3.3 Pyrochlores

The pyrochlore ($A_2B_2O_7$) structure has a rich solid-state chemistry, much of this afforded by the extensive solid–solution formation. In such

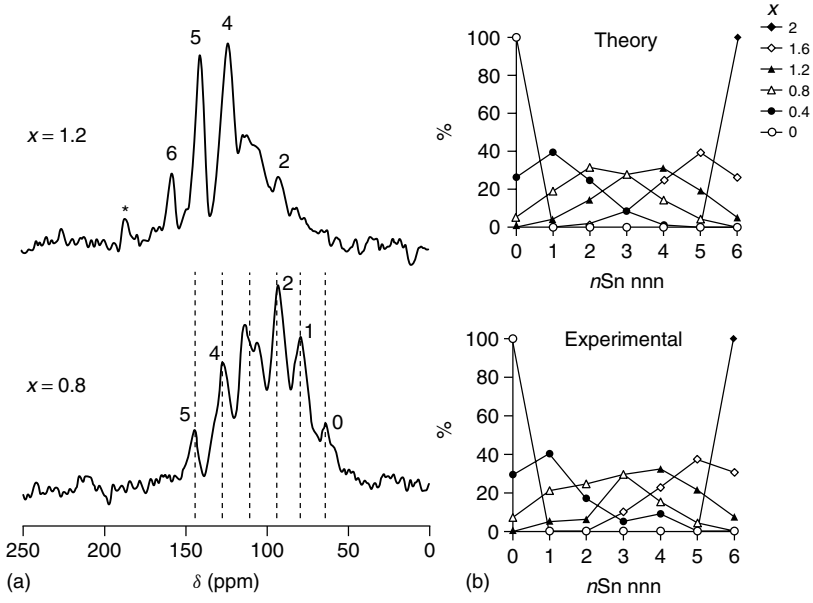


Figure 23.3. (a) ^{89}Y (24.5 MHz) MAS NMR spectra of $Y_2Ti_{2-x}Sn_xO_7$ for x = 1.2 and 0.8. Peak assignments in terms of the number of Sn nnn are given. The gray dashed lines show the predicted positions of resonances based on a 14–16 ppm chemical shift for Sn/Ti substitution. (b) Plot of signal intensities (expressed as %) for a statistical model assuming a random distribution of Sn/Ti on the pyrochlore B site (theory) compared to the data extracted from ^{89}Y MAS NMR spectra (experimental). (Reproduced from Ref. 24. © American Chemical Society, 2006.)

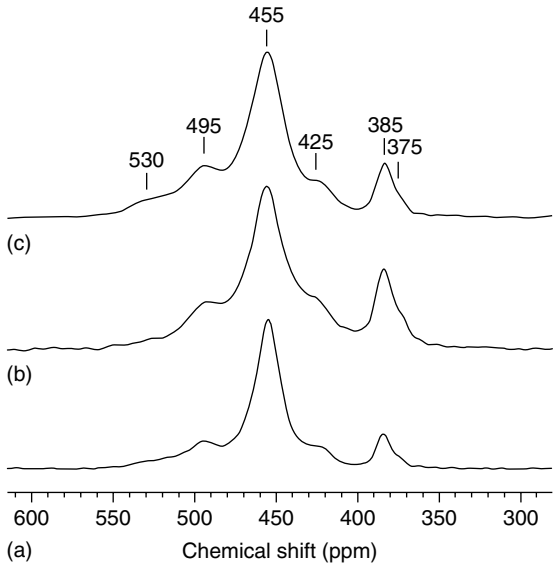


Figure 23.4. ^{17}O MAS NMR spectra of (a) $(Ca_{0.05}Y_{0.95})_2Ti_2O_{6.95}$, (b) $(Ca_{0.1}Y_{0.9})_2Ti_2O_{6.9}$, and (c) $(Ca_{0.15}Y_{0.85})_2Ti_2O_{6.85}$. The different resonances correspond to different local environments around the oxygen sites, with a possible assignment to O1 site with 495 ppm $O(Ti_4/Ti_3(Y,Ca))$, 455 ppm OTi_2Y_2, 425 ppm $OYCaTi_2$, O2 site with 385 ppm OY_4, and 375 ppm OY_3Ca. The peak at 530 ppm is believed to be an impurity. (Reproduced from Ref. 28. © Royal Society of Chemistry, 2004.)

materials, substitution on both the A and B sites can occur. ^{89}Y ($I = 1/2$) NMR has been applied to look at both $(Y_{1-x}La_x)_2Ti_2O_7$[23] and $Y_2(Ti_{2-x}Sn_x)O_7$[24] solid solutions. Despite ^{89}Y being a low-γ nucleus, good-quality data were obtained, with its large chemical shift range ensuring good discrimination between the different local environments. In the lanthanum-doped system, lanthanum dissolution occurs in the yttrium site of the pyrochlore up to $x \sim 0.134$, after which a two-phase pyrochlore/monoclinic mixture occurs. In the single-phase region, several ^{89}Y resonances were observed, and were attributed to differing numbers of lanthanum on the six neighboring A sites, with the intensity distribution following a random distribution. Substitution across the whole composition range is possible on the B site. Distinct ^{89}Y resonances are obtained for each different number n of nnn B site tins (Figure 23.3a). Using a purely statistical analysis, the relative probability (P) of each site (e.g., with n tin nnn on the B site) is $P(n\mathrm{S}n) = \Omega\ \mathrm{p}^n(1-\mathrm{p})^{6-n}$, where Ω is the number of permutations and $n = x/2$. Such an analysis shows that the experimental intensities very closely match that for a random distribution (Figure 23.3b).

^{17}O MAS NMR holds much promise for elucidation of the cation distribution in such systems since oxygen occurs throughout the systems Although it is a quadrupolar ($I = 5/2$) nucleus, in ionic systems χ_Q is sufficiently small and the shift range sufficiently large that different local coordinations around the oxygen are usually readily distinguished.[7,25,26] In the end member $Y_2Ti_2O_7$, there are two resonances at 385 (O1, OTi_2Y_2) and 455 ppm (O2, OY_4), in the intensity ratio 6 : 1. Extended to pyrochlore solid solutions such as $Y_2B_2O_7$ (B = Ti, Zr, Sn), the local $O(Y,B)_4$ environments could be distinguished, with the range of environments and linewidths measured indicating that $Y_2(Zr,Ti)_2O_7$ pyrochlores are more disordered than $Y_2(Sn,Ti)_2O_7$.[27] As calcium is doped for yttrium in $Y_2Ti_2O_7$, in addition to the two main resonances, four other resonances are observed (Figure 23.4) with the line at 530 ppm ascribed to an impurity.[28] By following the magnetization exchange at variable temperature, the oxygen motion is shown to involve jumps between O1 sites and vacancies created by the addition of calcium to the structure.[28]

23.3.4 Paramagnetic Doping of Solid Solutions

The large shift effect that typically occurs by the interaction with added paramagnetic ions (see the Section 23.2) is very useful for probing the site of paramagnetic dopants within lattices. In many practical phosphor applications, the distribution of the dopant should be as uniform as possible (i.e., not clustered) and the new resonances that appear can be modeled to provide information about the uniformity of the distribution, for example, Eu-doped Y_2O_2S.[29] In coloring of zircon ($ZrSiO_4$), vanadium (as V^{4+}) is a common additive. There are several possibilities as to the structural site of the vanadium dopant, i.e., substitute in the ZrO_8 or SiO_4 sites or as an interstitial. ^{29}Si MAS NMR can report on the vanadium site.[30] Crystalline zircon shows a dominant sharp line at −81.6 ppm corresponding to a Q^0 site. As vanadium is added, small but definite additional peaks appear at −75.2 and −105.1 ppm (Figure 23.5a), with spectral analysis also revealing a minor shoulder at −80 ppm.

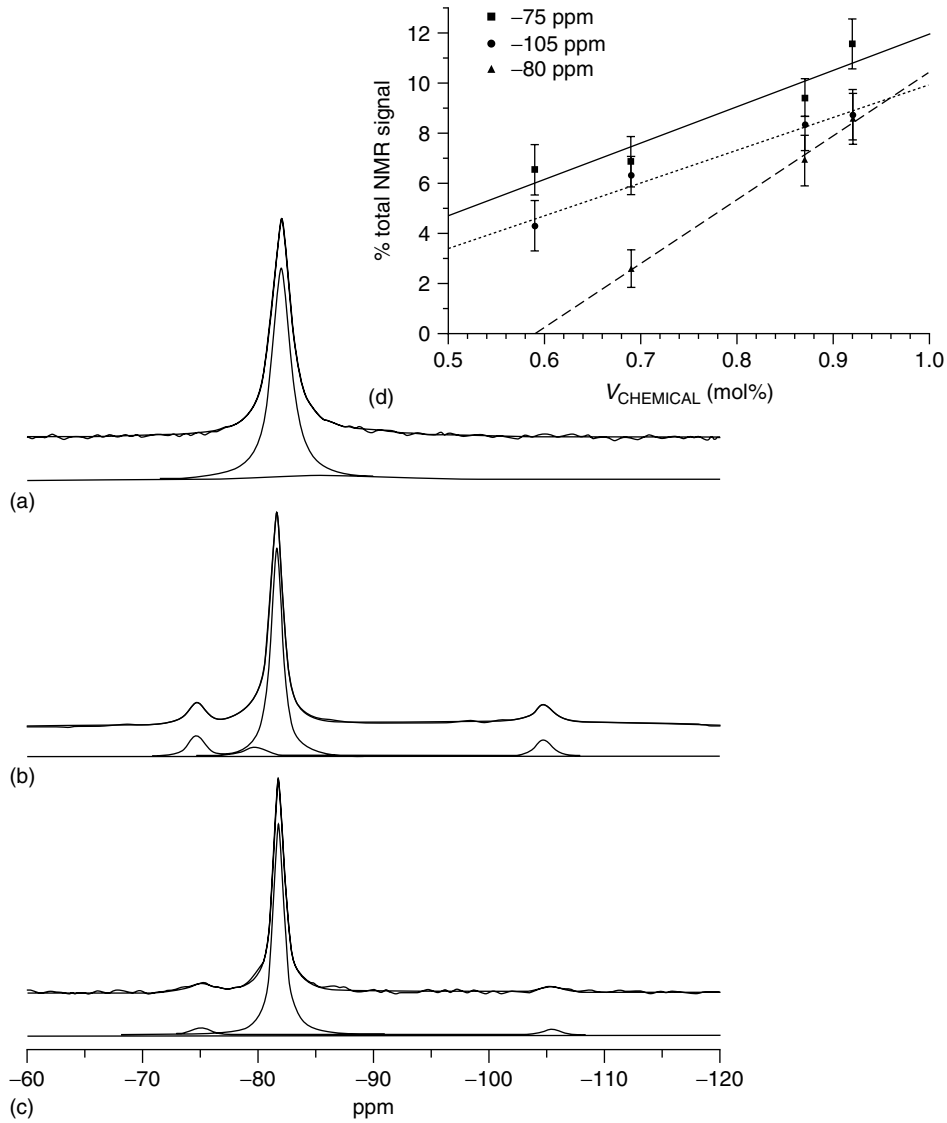


Figure 23.5. (a) Expanded ^{29}Si MAS NMR spectrum at 7.05 T of a naturally occurring sample of zircon with the two-component fit overlaid. The individual Lorentzian and Gaussian components corresponding to crystalline and amorphous zircon in the ratio 9 : 1 are shown below. (b) A four-component fit to the 0.92-mol% vanadium-containing $ZrSiO_4$ sample formed by solid-state reaction. (c) A three-component fit to the 0.59-mol% vanadium-containing $ZrSiO_4$ sample formed by a sol-gel reaction, with the individual components also shown in each case. (d) The integrated intensity of each of the small peaks in the ^{29}Si MAS NMR spectra, with the amount of vanadium left in the zircon sample deduced from chemical analysis. (Reproduced from Ref. 30. © American Physical Society, 2003.)

The source of these peaks (as coming from the interaction with the vanadium) is revealed by their intensity scaling with vanadium content (Figure 23.5d) and by the Curie-like temperature dependence of their positions. The sites were assigned to interactions with vanadium substituting for ZrO_8 (−105.1 ppm) and SiO_4 (−75.2 ppm), as shown by spectral simulations (Figure 23.5c) with some slight preference for the

tetrahedral site. The shoulder at −80 ppm was ascribed to some interstitial vanadium that occurs at higher concentrations (Figure 23.5b).

23.3.5 Doped Fluorite Oxygen-Ion Conductors

Fluorite-structured oxides (e.g., ZrO_2, CeO_2) hold much promise as solid electrolytes. One of the key questions is the vacancy distribution and how this changes with composition. As the Zr^{4+}/Ce^{4+} ion is replaced by lower charged ions such as Y^{3+}, Sc^{3+}, and Ca^{2+}, charge neutrality is maintained through the introduction of vacancies. In Y_2O_3-doped ZrO_2 both ^{17}O and ^{89}Y MAS NMR have been employed. The ^{89}Y MAS NMR spectrum shows a very clear separation of the different coordinations present (Figure 23.6; YO_8, YO_7, and YO_6). The lower coordinations only appear at higher dopant concentration as they are associated with vacancies. Analysis of the intensity suggested that vacancies occur preferentially around the zirconium.[31] For scandium-doped ZrO_2, ^{45}Sc MAS NMR suggested that ScO_7 units were paired with a single associated vacancy.[32] Analysis of the intensity of the different local coordination around oxygens from ^{17}O NMR data in both ZrO_2[33,34] and CeO_2[35] suggests that the vacancy distribution is probably not random, but that there is some pairing of the vacancies. ^{17}O MAS NMR data from doped ceria (Figure 23.7) illustrate very clearly the sensitivity of NMR to the local structural variation that is introduced even in a well-crystalline material because of the atomic disorder of the solid solution.[35] In both the pure CeO_2 and with 5% Y_2O_3 doping, the OCe_4 resonance is dominant, but its width increases by almost 2 orders of magnitude on doping.

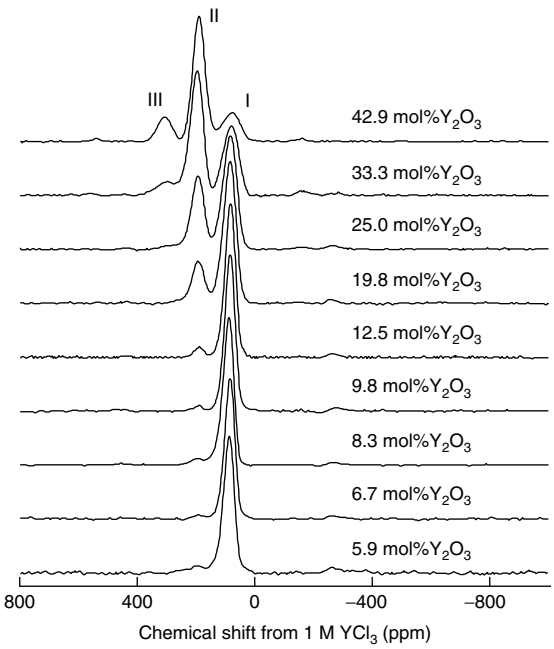


Figure 23.6. ^{89}Y MAS NMR spectra of yttria-stabilized zirconia. The peaks noted as I, II, and III are assigned to yttrium ions with 8, 7, and 6 oxygen neighbors, respectively. (Reproduced from Ref. 31. © Elsevier, 2006.)

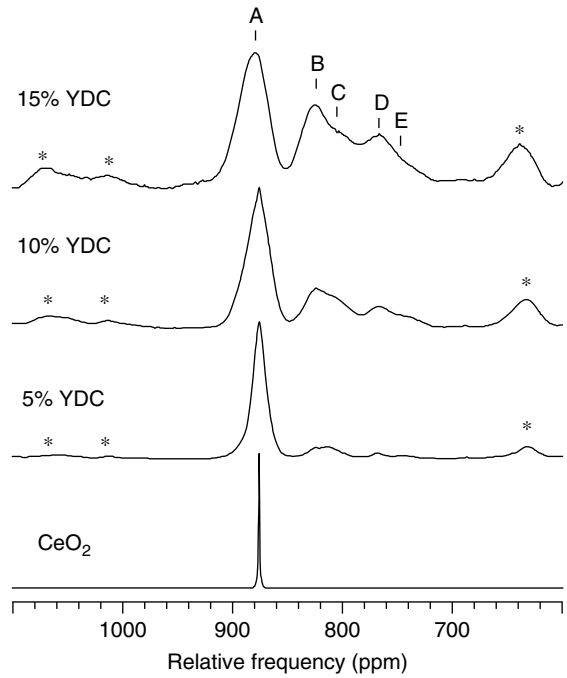


Figure 23.7. ^{17}O MAS NMR of Y_2O_3-doped CeO_2 at 14.1 T with a spinning speed of 20 kHz. Spinning side bands are marked by asterisks. Peak A is assigned to oxygen with 4 Ce neighbors, peaks B and C to oxygen with 3 Ce and 1 Y neighbor, and peaks D and E to oxygen with 2 Ce and 2 Y neighbors. (Reproduced from Ref. 35. © American Chemical Society, 2007.)

23.3.6 Apatites

One of the most important, naturally occurring substituted inorganic phases is calcium hydroxyapatite (HA), $Ca_{10}(PO_4)_6(OH)_2$. In natural HA, several ionic substitutions can be present, such as CO_3^{2-}, F^-, Cl^-, Mg^{2+}, and Na^+. These minor species not only alter the morphology and stability of the HA structure but they also play an important role in the biological response of bone cells. In synthetic samples, the compositional variation has been exploited in many applications from bone substitutes to gas sensors and catalysts. In such systems, very complex substitution mechanisms can be involved, and they provide a good example where a multinuclear solid-state NMR approach can give complementary information from the different nuclei. For example, in carbonate substitution two carbonate species were observed from ^{13}C and this was closely linked to sodium substitution, which was monitored by ^{23}Na.[36] In fluorapatites, strontium substitution into the calcium sites can be detected via its effect on the neighboring ^{19}F resonances, with specific shifts being readily assigned to the numbers of calcium and strontium on neighboring sites.[37] From the data, it was deduced that strontium has some preference for substitution in the Ca(2) site. Apatite-structured silicates (e.g., $La_9M(SiO_4)_6O_{2.5}$, with M = Ca, Sr, Ba) have potential as oxygen-ion conductors and ^{29}Si MAS NMR showed clear changes with composition.[38] Poorly conducting samples had a single resonance, whereas a second site became visible in the better conductors, associated with an SiO_4 adjacent to an interstitial oxygen. Further structural changes with the condensation of two Q^0 into Q^1 species were followed.

23.3.7 Oxynitride Solid Solutions

Oxynitrides offer much opportunity for solid-solution formation, especially if there is a simultaneous substitution of paired charge balancing elements, e.g., a silicon and a nitrogen being replaced by an aluminum and an oxygen. The ^{29}Si δ_{iso} can readily distinguish its local coordination SiO_xN_{4-x} ($0 \leq x \leq 4$), with the shift ranges of these units well documented.[7] In some cases, additional information from the anions (e.g., ^{15}N and ^{17}O) can be very useful. In $Y_4Si_2O_7N_2$, there are "disilicate" ($Si_2O_5N_2$) units, and the ^{15}N NMR data indicated two very different resonances, one corresponding to nitrogen in the bridging position between the two tetrahedral units and one in a terminal position.[39] The solid solutions formed by substitutions into pure compound (e.g., Si_3N_4, AlN) form materials with significant applications as engineering ceramics. As silicon and oxygen are introduced into AlN, to accommodate the excess of nonmetals that is then present, an octahedrally coordinated layer becomes inserted into the structure and ^{27}Al NMR readily picks up the AlO_6 units.[40] The β'-sialon ($Si_{6-z}Al_zO_zN_{8-z}$) solid solution is very extensive, but the ^{29}Si MAS NMR resonance remains at -48.5 ppm throughout the series, indicating that silicon occurs only as SiN_4, so that mixed AlO_xN_{4-x} ($0 \leq x \leq 4$) tetrahedra form.[40] Their presence has been detected by ^{27}Al MAS NMR, but accurate quantification, because of the significant spectral overlap due to residual second-order quadrupole effects, remains elusive.

23.3.8 Perovskite Ferroelectric Phases

An area where local atomic order is likely to be of key importance is in relaxor ferrolectrics. For normal ferroelectrics, a sharp frequency-independent paraelectric/ferroelectric transition is observed. Relaxor ferroelectrics are significantly different, characterized by a broad, frequency-dependent maximum in dielectric permittivity that is also temperature dependent and is manifest as a diffuse transition into the relaxor ferroelectric state. Most known ferroelectric relaxors show chemical/site disorder. The ability of a sample to show nanoscale deviations from the average local structure is thought to be important for relaxor properties. Lead magnesium niobate $PbMg_{1/3}Nb_{2/3}O_3$ (PMN) has niobium and magnesium ions distributed across the octahedrally coordinated B sites in the perovskite lattice, each with six nnn B cations. ^{93}Nb ($I = 9/2$) MAS NMR has proved a very useful probe, with PMN, showing three peaks (Figure 23.8) attributed to different configurations of B cation on the neighboring B site.[41–43] These cations are distributed randomly on these sites, but with ordered domains along the ⟨111⟩ direction. Careful variable-temperature work indicated that each specific configuration of local coordinations shows its own local ferroelectric distortions, with different characteristic transition temperatures, perhaps explaining the broad transition associated with relaxor behavior.[43,44]

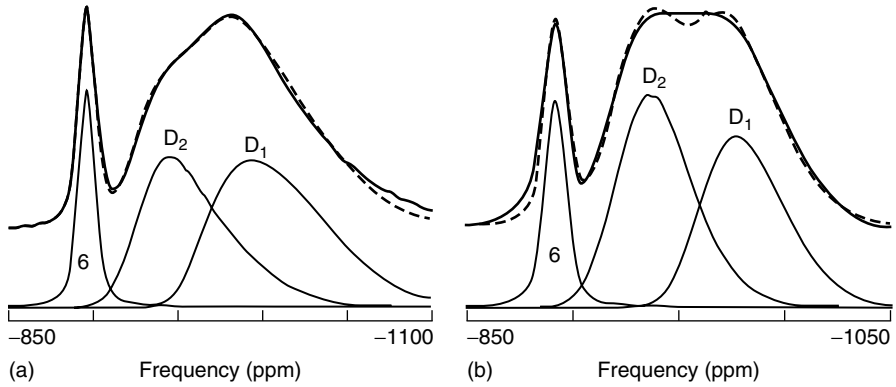


Figure 23.8. ^{93}Nb MAS NMR spectra of PMN with a constrained deconvolution at (a) 14.1 T and (b) 19.6 T. Bold solid lines are the experimental MAS spectra, the thin solid lines are deconvoluted components, with 6, D_1 and D_2, corresponding to different local environments, and the dashed line is the sum of all components. (Reproduced from Ref. 41. © American Physical Society, 2002.)

The situation becomes rapidly more complicated in other solid solutions exhibiting such behavior, such as $PbMg_{1/3}Nb_{2/3}O_3$–$Pb(Sc_{1/2}Nb_{1/2})O_3$ (PMN–PSN)[41,45] and $PbMg_{1/3}Nb_{2/3}O_3$–$PbTiO_3$ (PMN–PT).[42] Again, ^{93}Nb was the key probe nucleus, but showed very different resolution of the different nnn B cation environments, depending on what the different added elements were (e.g., PSN showed much better resolution of some environments than PT). These materials emphasis the advantage that the short-range information NMR provides can be really useful in understanding key properties of materials.

23.4 CONCLUSIONS

Solid solutions and nonstoichiometry are ubiquitous in inorganic materials technology and many of their structural signatures can often be difficult to describe and quantify with conventional characterization approaches. The short-range nature of NMR means that the distinct local environments can usually be identified from their differing chemical shifts. If the chemical shift range is insufficient to distinguish these different environments then other interactions (e.g., quadrupole or chemical shift anisotropy) or paramagnetic additions can be used since they tend to provide greater distinction between sites. Quantification of the different environments then allows an understanding of how the atoms are ordering and dissolving into the structure. Examples described here include solid electrolytes for fuel cells where the controlled introduction of vacancies is important to ionic diffusion processes and ferroelectric relaxors where the specific behavior is thought to be related to atomic/chemical disorder. Although some materials technology examples have been used to illustrate nonstoichiometric materials there is a whole range of other important areas such as the dissolution of water in nominally anhydrous minerals in the earth sciences. There is no doubt that solid state NMR is a leading technique in understanding atomic ordering and such work should become increasingly common.

REFERENCES

1. A. C. Hannon, *Nucl. Instrum. Meth. Phys. Res. A*, 2005, **551**, 88.
2. S. J. Hibble, A. C. Hannon, and I. D. Fawcett, *J. Phys.: Condens. Matter*, 1999, **11**, 9203.
3. G. W. Wallidge, R. Anderson, G. Mountjoy, D. M. Pickup, P. Gunawidjaja, R. J. Newport, and M. E. Smith, *J. Mater. Sci.*, 2004, **39**, 6743.
4. A. Putnis, C. A. Fyfe, and G. C. Gobbi, *Phys. Chem. Miner.*, 1985, **12**, 211.
5. C. A. Fyfe, G. C. Gobbi, and A. Putnis, *J. Am. Chem. Soc.*, 1986, **108**, 3218.
6. G. Engelhardt and D. Michel, *High Resolution Solid State NMR of Silicates and Zeolites*, Wiley: Chichester, 1987

7. K. J. D. MacKenzie and M. E. Smith, *Multinuclear Solid State NMR of Inorganic Materials*, Pergamon: Oxford, 2002
8. C. P. Grey, C. M. Dobson, A. K. Cheetham, and R. J. B. Jakeman, *J. Am. Chem. Soc.*, 1989, **111**, 505.
9. C. P. Grey, M. E. Smith, A. K. Cheetham, C. M. Dobson, and R. Dupree, *J. Am. Chem. Soc.*, 1990, **112**, 4670.
10. K. J. D. MacKenzie, M. E. Smith, T. F. Kemp, and D. Voll, *Appl. Magn. Reson.*, 2007, **32**, 647.
11. J. Klinowski, *Prog. Nucl. Magn. Reson. Spectrosc.*, 1984, **16**, 237.
12. T. Ban and K. Okada, *J. Am. Ceram. Soc.*, 1993, **76**, 2491.
13. I. Jaymes, A. Douy, D. Massiot, and J.-P. Coutures, *J. Non-Cryst. Solids*, 1996, **204**, 125.
14. M. Schmücker, H. Schneider, K. J. D. Mackenzie, M. E. Smith, and D. L. Carroll, *J. Am. Ceram. Soc.*, 2005, **88**, 2935.
15. M. E. Smith, G. Neal, M. B. Trigg, and J. Drennan, *Appl. Magn. Reson.*, 1993, **4**, 157.
16. R. L. Millard, R. C. Peterson, and B. K. Hunter, *Am. Mineral.*, 1992, **77**, 44.
17. H. Maekawa, S. Kato, K. Kawamura, and T. Yokohama, *Am. Mineral.*, 1997, **82**, 1125.
18. T. Ito, A. Yoshiasa, T. Yamanaka, A. Nakatsuka, and H. Maekawa, *Z. Anorg. Allg. Chem.*, 2000, **626**, 42.
19. C. Tien, E. V. Charnaya, S. Y. Sun, R. R. Wu, S. N. Ivanov, and E. N. Khazanov, *Phys. Status Solidi B*, 2002, **233**, 222.
20. N. Gautier, M. Gervais, C. Landron, D. Massiot, and J.-P. Coutures, *Phys. Status Solidi A*, 1998, **165**, 329.
21. E. V. Charnaya, C. Tien, J. J. Lu, R. R. Wu, S. N. Ivanov, and E. N. Khazanov, *J. Phys.: Condens. Matter*, 2001, **13**, 8775.
22. R. J. B. Jakeman, A. K. Cheetham, N. J. Clayden, and C. M. Dobson, *J. Am. Chem. Soc.*, 1985, **107**, 6249.
23. E. J. Harvey, S. E. Ashbrook, G. R. Lumpkin, and S. A. T. Redfern, *J. Mater. Chem.*, 2006, **16**, 4665.
24. S. E. Ashbrook, K. R. Whittle, G. R. Lumpkin, and I. Farnan, *J. Phys. Chem. B*, 2006, **110**, 10358.
25. T. J. Bastow, P. J. Dirken, M. E. Smith, and H. J. Whitfield, *J. Phys. Chem.*, 1996, **100**, 18539.
26. S. E. Ashbrook and M. E. Smith, *Chem. Soc. Rev.*, 2006, **35**, 718.
27. N. Kim and C. P. Grey, *J. Solid State Chem.*, 2003, **175**, 110.
28. N. Kim and C. P. Grey, *Dalton Trans.*, 2004, 3048.
29. T. Harazono, R. Adachi, Y. Shimomura, and T. Watanabe, *Phys. Chem. Chem. Phys.*, 2001, **3**, 2943.
30. N. Dajda, J. M. Dixon, M. E. Smith, N. Carthey, and P. T. Bishop, *Phys. Rev. B*, 2003, **67**, 024201.
31. K. Kawata, H. Maekawa, T. Nemoto, and T. Yamamura, *Solid State Ionics*, 2006, **177**, 1687.
32. N. Kim, C.-H. Hsieh, and J. F. Stebbins, *Chem. Mater.*, 2006, **18**, 3855.
33. T. Viefhaus, T. Bolse, and K. Muller, *Solid State Ionics*, 2006, **177**, 3063.
34. N. Kim, C.-H. Hseih, H. Huang, F. B. Prinz, and J. F. Stebbins, *Solid State Ionics*, 2007, **178**, 1499.
35. N. Kim and J. F. Stebbins, *Chem. Mater.*, 2007, **19**, 5742.
36. H. E. Mason, A. Kozlowski, and B. L. Phillips, *Chem. Mater.*, 2008, **20**, 294.
37. G. Cho, C.-N. Chau, and J. P. Yesinowski, *J. Phys. Chem. C*, 2008, **112**, 6165.
38. J. E. H. Sansom, J. R. Tolchard, M. S. Islam, D. Apperley, and P. R. Slater, *J. Mater. Chem.*, 2006, **16**, 1410.
39. D. S. B. Hauck, R. K. Harris, D. C. Apperley, and D. P. Thompson, *J. Mater. Chem.*, 1993, **3**, 1005.
40. M. E. Smith, *J. Phys. Chem.*, 1992, **96**, 1444.
41. G. L. Hoatson, D. H. Zhou, F. Fayon, D. Massiot, and R. L. Vold, *Phys. Rev. B*, 2002, **66**, 224103.
42. P. Bhattachraya, M. E. Smith, and P. A. Thomas, *Phase Transitions*, 2006, **79**, 79.
43. R. Blinc, *Ferroelectrics*, 2006, **330**, 1.
44. M. Vijaykumar, G. L. Hoatson, and R. L. Vold, *Phys. Rev. B*, 2007, **75**, 104104.
45. R. L. Vold, G. L. Hoatson, and M. Vijaykumar, *Phys. Rev. B*, 2007, **75**, 134105.

Chapter 24
Rotational & Translational Dynamics

Christopher I. Ratcliffe

Steacie Institute for Molecular Sciences, National Research Council Canada, Ottawa, Ontario K1A 0R6, Canada

24.1	Introduction	355
24.2	NMR and Dynamics	356
24.3	Rotational Barriers and Symmetry	356
24.4	Dynamics and Dipolar Coupling	356
24.5	Deuterium NMR Lineshapes	359
24.6	Shielding and Dynamics	366
24.7	Noninteger Quadrupolar Dynamic Averaging	368
24.8	Concluding Remarks	371
	References	371

24.1 INTRODUCTION

The interactions between atoms, molecules, and ions ultimately determine the structural forms of solid materials, and, in turn, the crystal structure itself imposes potential fields around these components, which strongly influence their dynamic behavior while locked in the solid. Translational and rotational motions inside solid materials are quite commonplace, a fact that often comes as a complete surprise to the uninitiated. It is also surprising to know how large an amplitude some motions can have. Yet the evidence from such techniques as inelastic neutron scattering, Raman and infrared spectroscopy, calorimetry, and NMR is incontrovertible. Indeed, NMR is perhaps the foremost technique for the study of such motions.

This article discusses the many ways in which solid-state NMR has been used to explore the interplay between crystal and molecular symmetry and how this affects translational and rotational motions. Brief descriptions of theory are given and different aspects are highlighted with examples.

NMR studies of dynamics can yield structural information (internuclear distances, molecular orientation with respect to a crystallographic axis) and symmetry information, which is complementary to diffraction data. Indeed, there are instances where information from NMR studies of dynamics has been used to improve or direct structural refinements. In turn, crystal structures help in understanding the dynamics. In addition, NMR can provide a wide variety of other information, including activation energies required to cross barriers, rotational rates, or correlation times. It can indicate phase transitions and metastable phases and, in some cases, give insight into possible mechanisms for phase transitions.

NMR is also very useful in resolving problems of crystallographic disorder, since it gives aspects of local structure and is sensitive to dynamics on various timescales, whereas diffraction gives a long-range spatial average of electron density with little or no temporal information. Consequently, only NMR can distinguish between static and dynamic disorder among partially occupied sites, and dynamics among fully populated sites is effectively invisible to diffraction.

NMR Crystallography Edited by Robin K. Harris, Roderick E. Wasylishen and Melinda J. Duer © 2009 John Wiley & Sons, Ltd. ISBN: 978-0-470-69961-4

24.2 NMR AND DYNAMICS

In essence, the study of dynamics in NMR relies upon changes in the magnitude and orientation of the different NMR interaction tensors, principally dipolar, CSA, and quadrupolar, brought about by various motions, which result in modulation of the resonance frequency.[1–4]

Molecular motion in a solid is an incoherent/stochastic process, which can be expressed in terms of an autocorrelation function, effectively a measure of the fraction of molecules whose position and/or orientation is the same at time $(t + \tau)$ as at time (t):

$$G(\tau) = \overline{f(t)f(t+\tau)} \tag{24.1}$$

where $f(t)$ describes the position/orientation of a molecule at time t and the bar represents an ensemble average. Under any motion, $G(\tau)$ decreases with increasing time and in most cases this decay is taken to be an exponential function with a correlation time τ_c:

$$G(\tau) = \exp(-|\tau|/\tau_c) \tag{24.2}$$

For thermally activated processes, τ_c is assumed to have an Arrhenius dependence on the activation energy for the motion (E_a) and on temperature (T):

$$\tau_c = {\tau_c}^0 \exp(E_a/RT) \tag{24.3}$$

Clearly, as T increases the rate of a motion increases and τ_c decreases.

Different techniques are available to probe motions on different timescales:

Lineshapes are sensitive to motional rates comparable to the linewidth, typically of the order of 10^4–$10^7\ s^{-1}$, usually referred to as *intermediate rate*s. Relaxation measurements are used for intermediate and faster rates, and 2-D exchange NMR for slow rates.

Note that a pure translation between equivalent crystallographic sites will not result in any change in any of the interaction tensors, except for intermolecular dipolar coupling.

However, changes in the interaction tensors can occur for translation between crystallographically inequivalent sites, or between equivalent sites where a change in orientation is required (i.e., combined translation and rotation). It is also possible in some circumstances for molecular dynamics to be indirectly detected by spectator nuclei, whose interaction tensors are averaged by motions in their surroundings.

24.3 ROTATIONAL BARRIERS AND SYMMETRY

Different crystal symmetries can have quite drastic effects on the magnitude of barriers to reorientation. This can be illustrated for a simple case as follows:

The energy potential between a single atom rotating about an axis and a fixed external atom can be expressed as a Fourier series periodic in $n\theta$:

$$V = V_0 + \sum_{n=1}^{\infty} \frac{V_n(1 - \cos(n\theta))}{2} \tag{24.4}$$

where θ is the angular coordinate about the rotation axis and V_n is the amplitude of the n-fold component, which decreases as n increases. If three atoms form a rotor group with threefold symmetry, e.g., $–CH_3$ or $–NH_3^+$, the summation of terms for θ, $(\theta + 120^\circ)$, $(\theta + 240^\circ)$ interacting with the fixed external atom leaves only the $V_3, V_6, V_9, \ldots$ terms to describe the potential. Then, if this threefold rotor interacts with three external atoms in a threefold arrangement about the axis, the individual atom–atom potentials are all in phase adding constructively to a substantial threefold barrier, i.e., all three rotor atoms are at closest approach to an external atom at the same time. However, in the case of a fourfold arrangement of external atoms (a symmetry mismatch), even though the individual atom–atom potentials are the same as before, the summation is destructive except for terms where $n = 12, 24, \ldots$, and since the magnitude of the higher order terms diminishes rapidly, the 12-fold barrier will be quite small.

By extension, high-symmetry molecules are often found to reorient with relative ease, and usually this can be traced to a mismatch with the symmetry of their environment, plus the fact that they require little, if any, extra space to perform the rotation, e.g., benzene, NH_4^+, C_{60}, adamantane. Likewise, for molecules with little symmetry in a high-symmetry lattice site, the barrier can be low.

24.4 DYNAMICS AND DIPOLAR COUPLING

24.4.1 Lineshape and Second Moment

The early years of solid-state NMR were dominated by studies of dipolar interactions, due largely to limitations on available magnetic fields and detection

methods, which meant that studies were centered on large γ nuclei, mainly ^{1}H and, to a lesser extent, ^{19}F and ^{31}P. It was soon realized that changes in NMR lineshapes and relaxation times could be used to monitor dynamic processes as a function of temperature.

Proton lineshape second moments (M_2) provide a convenient means of quantifying the spectral changes, since they are also relatively easy to calculate for the static molecule, using the formula developed by Van Vleck.[1,5] For homonuclear interactions

$$M_2 = \tfrac{3}{4}\gamma^4\hbar^2\left(\tfrac{\mu_0}{4\pi}\right)^2 I(I+1)\left(\tfrac{1}{N}\right) \times \sum_{j,k} \frac{\left(1-3\cos^2\theta_{jk}\right)^2}{r^6{}_{jk}} \qquad (24.5)$$

where γ is the magnetogyric ratio of the nuclei under consideration, r is the distance between the nuclei j and k, θ is the angle between the internuclear vector and B_0, and N is the number of interacting spins. I is the nuclear spin, equal to 1/2 for ^{1}H, and μ_0 is the permeability constant. The powder average of this expression is

$$M_2 = \tfrac{3}{5}\gamma^4\hbar^2\left(\tfrac{\mu_0}{4\pi}\right)^2 I(I+1)\left(\tfrac{1}{N}\right)\textstyle\sum_{j,k}\frac{1}{r^6{}_{jk}} \qquad (24.6)$$

and for any dynamic process, expressions can be derived to take into account the averaging effects of rapid jumps between different orientations visited in the motion. For heteronuclear interactions, the formula is modified[6] to

$$M_2 = \tfrac{1}{3}\gamma_I{}^2\gamma_S{}^2\hbar^2\left(\tfrac{\mu_0}{4\pi}\right)^2 S(S+1)\left(\tfrac{1}{N}\right) \times \sum_{\mathrm{j,k}} \frac{\left(1-3\cos^2\theta_{jk}\right)^2}{r^6{}_{jk}} \qquad (24.7)$$

where S is the spin of the nucleus with which the nucleus of spin I is interacting.

A simple example is that of solid benzene,[7] for which ^{1}H M_2 reaches a value of $9.72 \times 10^{-8}\,\mathrm{T}^2$ below 100 K compared to $9.62 \times 10^{-8}\,\mathrm{T}^2$ calculated for the rigid lattice. M_2 reduces rapidly between 100 and 120 K, then levels out at $1.6 \times 10^{-8}\,\mathrm{T}^2$, almost exactly the same number as calculated ($1.7 \times 10^{-8}\,\mathrm{T}^2$) for reorientation about the molecular sixfold axis.

The case of solid triethylenediamine (TEDA)[8] is more complex, as shown in Figure 24.1. Below ~140 K, the molecule is static with $M_2 = 24.7 \times 10^{-8}$ T^2, in full agreement with calculation. Dramatic reduction in M_2 occurs between 190 and 220 K to a plateau level of 5.52×10^{-8} T^2, which is lower than the calculated value of 8×10^{-8} T^2 for the expected reorientation about the coincident threefold axes of the molecule (N–N axis) and the crystal. The discrepancy can be attributed to a further motion, namely, an off-axis wobbling of the N–N axis over ~10–15°. The sudden drop in M_2 at ~350 K occurs at a phase transition and indicates a significant change in the dynamics. The reduced value of $M_2 = 1.1 \times 10^{-8}$ T^2 corresponds to random reorientation of the molecule, which has reduced intramolecular dipolar coupling to zero. At this point, there is a residual intermolecular dipolar coupling, but as T increases toward the melting point at 433 K, M_2 gradually reduces to near zero due to translational diffusion, which completely averages the dipolar couplings. The isotropic reorientation and translational diffusion are typical of a plastic phase (cubic and therefore high symmetry).

The wobbling motion of TEDA is actually a combination of two librational modes of the molecule. In the solid phase, the three rotational degrees of freedom enjoyed by free polyatomic molecules all become restricted to small amplitude oscillations (librations) in the lower levels of the potential wells. These motions produce small variations in orientation, which can reduce NMR linewidths slightly, and since the amplitude of librational motions increases as T increases, small gradual reductions in linewidths over extended temperature ranges are commonly seen.

Barrier heights for rotation among n-fold potential wells can be estimated from M_2 data using the Waugh–Fedin approximation,[9] $V_0 = 155\ T$ in J mol^{-1}, where T is the temperature of the onset of

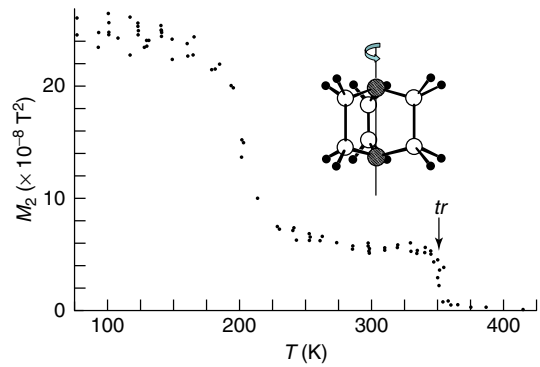


Figure 24.1. Proton NMR second moments, M_2, for solid triethylenediamine. (Reproduced from Ref. 8. © American Institute of Physics, 1965.)

the lineshape narrowing. In the case of TEDA (with $T = 190\,\mathrm{K}$), this formula gives a barrier estimate of $29.5\,\mathrm{kJ\,mol^{-1}}$ for the threefold motion, just slightly less than a value of $30.1\,\mathrm{kJ\,mol^{-1}}$ obtained by a much more complex lineshape analysis.

24.4.2 Spin–Lattice Relaxation

A more acceptable and reliable way to obtain activation energies for motions is by way of relaxation time measurements, most often of the spin–lattice relaxation time T_1, as a function of temperature, which also leads to values of the correlation time. The modified Bloembergen–Purcell–Pound (BPP) theory[10–12] provides the framework for the interpretation of T_1 results. Dipole–dipole relaxation is effected by reorientation of the internuclear vectors in the applied field, and for homonuclear interaction this can be described by the general expression

$$\frac{1}{T_1} = C\gamma^4\hbar^2\left(\frac{\mu_0}{4\pi}\right)^2\frac{f(\omega_0\tau_c)}{\omega_0} \qquad (24.8)$$

where

$$f(\omega_0\tau_c) = \frac{(\omega_0\tau_c)}{(1+(\omega_0\tau_c)^2)} + \frac{4(\omega_0\tau_c)}{(1+4(\omega_0\tau_c)^2)} \qquad (24.9)$$

where ω_0 is the Larmor frequency and τ_c is the correlation time for the motion. C depends on the specifics of the motion, the interproton distances (r), and the number of protons being relaxed (via spin diffusion) by the protons undergoing the motion. In the specific case of threefold reorientation of an equilateral triangle of protons $C = (9/20)r^{-6}$. Similar expressions can be derived for T_2, $T_{1\rho}$, etc., for heteronuclear dipolar coupling, and for other interactions besides dipolar.

The classical BPP plot of $\ln T_1$ as a function of reciprocal temperature for a simple motion shows a minimum at $\omega_0\tau_c \sim 0.616$, with linear slopes on either side (where $\omega_0\tau_c \gg 1$ or $\ll 1$), which are proportional to E_a. The depth of this minimum is related to the dipolar coupling constant and can thus be related to the internuclear distances, e.g., in a CH_3 group. The depth of the minimum also depends on how many other nuclei the rotating group is relaxing via spin diffusion. Phase transitions are quite often apparent in such plots as sudden changes in T_1 associated with drastic changes in the motions.

Figure 24.2 shows the results of ^{1}H T_1 studies on anilinium halides ($C_6H_5NH_3X$).[13] All three salts have a T_1 minimum of ~38 ms, which corresponds to a reorienting $-NH_3^+$ group relaxing all 8H in the anilinium ion via spin diffusion. Fits to the plots using BPP theory give activation energies, 37.1 (Cl), 11.2 (Br), and 8.5 (I) $\mathrm{kJ\,mol^{-1}}$, and correlation time constants $\tau_c^0 \sim 5.7 \pm 1.3 \times 10^{-14}$ s. The E_a values should reflect only the external interaction potential, since the internal rotation barrier is expected to be very small (as is found in toluene). The large barrier for the chloride reflects the fact that the $-NH_3^+$ hydrogen-bonds to chloride ions in a roughly threefold environment, whereas the symmetry match is poor in the other two salts. Above ~200 K, T_1 values for the bromide and iodide deviate from the extrapolated BPP fit, due to second-order phase transitions. In the high-temperature phases of these two salts, the $C_6H_5NH_3^+$ long axis sits in a roughly fourfold environment. Thus, the NH_3^+ group is expected to have a very low barrier and very fast reorientation, which makes relaxation inefficient. The phenyl group, on the other hand, fits into the fourfold environment very well, and the relaxation in these high-temperature phases can be confidently assigned to pseudo-fourfold phenyl group rotation, based on the 178 ms T_1 minimum observed for the iodide.

Another example of the effects of symmetry mismatch is seen in a ^{1}H T_1 study of CH_3NH_3Cl,

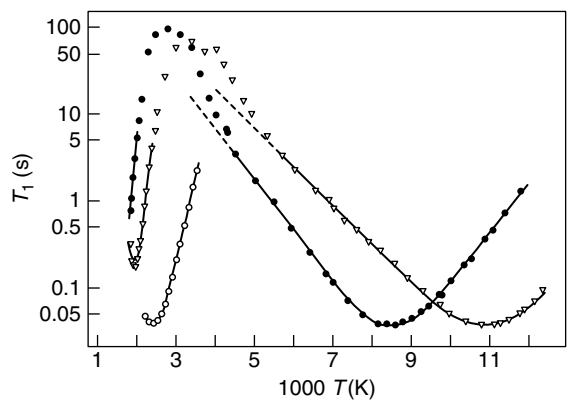


Figure 24.2. Proton spin–lattice relaxation time (T_1) as a function of reciprocal temperature for anilinium chloride (open circles), bromide (filled circles), and iodide (triangles) at 31 MHz.[13] The solid lines represent fits based on the BPP equation. The dashed lines are extrapolations to emphasize the deviations caused by phase changes in the bromide and iodide.

CD_3NH_3Cl and CH_3ND_3Cl.[14] In the room temperature α-phase, where the threefold ion sits on a fourfold crystal axis, the observed E_a is only $4.0\,kJ\,mol^{-1}$ for all three isotopomers, suggesting that this represents rapid rotation of the whole ion. In contrast, the low-temperature β and γ phases show substantial E_a for rotation of NH_3^+ (β-phase $\sim$25, γ-phase = $32\,kJ\,mol^{-1}$), suggesting a closer match of threefold symmetry. The E_a values for CH_3 contrast markedly with a high value for β-phase = $18.6\,kJ\,mol^{-1}$ and a low value for γ-phase = $7.6\,kJ\,mol^{-1}$.

24.4.3 Other Dipolar Effects

24.4.3.1 Dipolar Dephasing

Perhaps the simplest technique for indicating dynamics in a system is the cross-polarization dipolar dephasing (nonquaternary suppression) experiment.[15] This is widely used when obtaining ^{13}C CPMAS spectra, where in the normal experiment signal acquisition with ^1H high-power decoupling is started immediately following the cross-polarization. If instead a short delay, typically 40 μs, is introduced before ^1H decoupling is applied, signals from carbons, which are strongly coupled to protons, rapidly dephase and disappear from the resulting spectrum. However, proton-bearing carbons in groups in motion can also have much reduced dipolar coupling: Methyl groups, which in most materials undergo rapid C_3 rotation at room temperature, invariably appear in the dipolar dephased spectrum. Similarly, rotating phenyl groups typically show resonances for the ortho and meta carbons in the dipolar dephased spectrum, but not for the para carbon.[16] The para C–H bond usually lies along the rotation axis and therefore the dipolar coupling is not averaged by the rotation. Consequently, this technique is also very good for separating dynamic guest resonances from host resonances in complex spectra of inclusion compounds.

24.4.3.2 Interference with Decoupling

Molecular dynamics can interfere with ^1H high-power decoupling in ^{13}C CPMAS experiments for carbons whose static broadening is largely due to C–H dipolar coupling,[17] e.g., in 18-crown-6 complexes.[18] Over a finite temperature range where the rate of the motion is comparable to the frequency of the decoupling field, the incoherent averaging of C–H dipolar coupling caused by the random dynamic process interferes with the coherent averaging effect of the decoupling field, leading to broadening and loss of apparent intensity, sometimes to the point of disappearance into the noise.

24.5 DEUTERIUM NMR LINESHAPES

Deuterium NMR is ideally suited for studies of rotational dynamics,[2,19–21] and D can be substituted readily for H in both organic and inorganic materials. Consequently, it has been and still is a major tool for such studies and, in a number of cases, has been used to aid in crystal structure refinement.

Deuterium (spin $I = 1$) NMR powder lineshapes are dominated by the quadrupolar coupling tensor to first order and the relatively small quadrupole moment means that the lines are typically <320 kHz wide.[22,23]

The two allowed transitions give rise to a symmetric doublet powder line shape (Figure 24.3b), which has either two or three pairs of characteristic features (edges, shoulders, and peaks) separated by frequencies:

$$\Delta\nu_{zz} = \frac{3\chi}{2} \quad \Delta\nu_{yy} = \frac{3\chi(1+\eta)}{4}$$
$$\Delta\nu_{xx} = \frac{3\chi(1-\eta)}{4} \tag{24.10}$$

where χ is the quadrupole coupling constant and $\eta = (\Delta\nu_{yy} - \Delta\nu_{xx})/\Delta\nu_{zz}$ is the asymmetry parameter. The $\Delta\nu_{ii}$ are proportional to the magnitude of the principal axis components of the ^2H quadrupolar coupling tensor, which can be envisaged as an ellipsoid with its largest axis aligned (in most instances) along the bond direction (Figure 24.3a). This has the advantage that the angles describing the tensor orientation can also be directly related to angles in the molecule. Motions that change the orientation of the tensor begin to distort the static lineshape at rates of about $10^4\ s^{-1}$. At intermediate rates, distorted lineshapes develop progressively until at about $10^7\ s^{-1}$ or faster (the fast motion limit (fml)) the line shape can be described by an averaged effective tensor. The averaged and intermediate lineshapes are very sensitive to the details of the motions, providing much information to aid the development of dynamic models and to determine molecular geometry and orientation with respect to crystal axes.

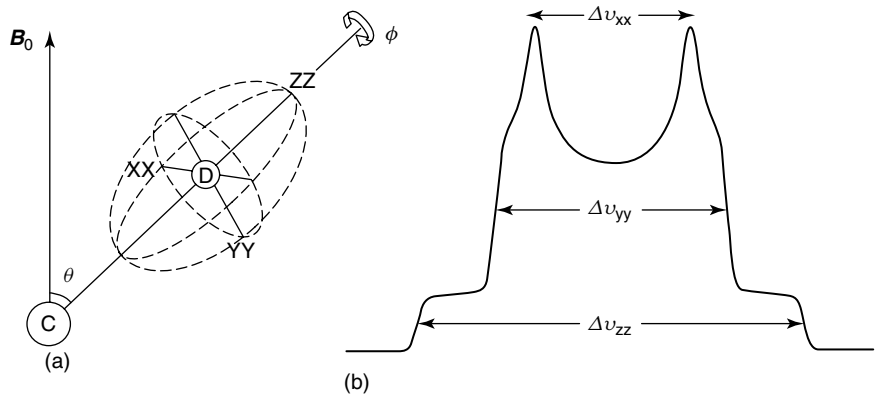


Figure 24.3. (a) Quadrupolar coupling tensor for ^{2}H in a C–D bond, visualized as an ellipsoid with three distinct axes. Its orientation with respect to the applied field and corresponding NMR frequency can be described in terms of the two angles θ and ϕ. (b) The widths of the features in the ^{2}H NMR frequency spectrum corresponding to all crystallite orientations in a powder relate directly to the magnitudes of the principal components of the coupling tensor.

Analytical expressions for determining the line shapes in the fast-motion limit for a particular motion are relatively easy to obtain.[4,24,25] The tensor must first be described in a reference frame in terms of the Euler angles α, β, γ:

$$\boldsymbol{V}(\alpha, \beta, \gamma) = \boldsymbol{R}\boldsymbol{V}_{\mathrm{PAS}}\boldsymbol{R}^{-1} \tag{24.11}$$

where $\boldsymbol{R}$ is the Euler angle rotation matrix describing the coordinate transformation and $\boldsymbol{V}_{\mathrm{pas}}$ is the static tensor in its principal axis system. The fast-motion limit line shape then represents the effective tensor $\boldsymbol{V}_{\mathrm{eff}}$, which is the population weighted average of the tensor components in the reference frame for all the sites (orientations) visited during the motion:

$$\boldsymbol{V}_{\mathrm{eff}} = \sum_{i=1}^{n} \frac{[V_i(\alpha, \beta, \gamma)p_i]}{[p_i]} \tag{24.12}$$

with p_i the population factor of site i.

In order to calculate the dynamic line shapes, it is necessary to know the quadrupolar parameters for the static tensor. A useful rule is that for n-fold symmetric reorientation about an axis where $n > 2$ the averaged tensor has axial symmetry, with its largest principal component (V_{zz}) along the rotation axis. Also note that the dynamic effects are additive in the sense that if one motion is already fast, then the effective averaged tensor for that motion can be used as the tensor to be averaged by the second motion.

Programs are available to calculate intermediate-rate lineshapes once a specific model has been determined. By matching calculated lineshapes with observed lineshapes, it is then possible to pair rates with temperature and obtain an E_a for the motion.

There are some interesting situations where ^{2}H NMR can distinguish motions where ^{1}H dipolar NMR cannot. For instance, 180° flips of an isolated water molecule about its twofold axis do not cause ^{1}H NMR line narrowing because the intramolecular ^{1}H–^{1}H dipolar tensor is unchanged, but they do narrow the ^{2}H lineshape since the quadrupolar tensor, along the bond direction, does change orientation. Another case is for molecular configurations as in the *t*-butyl group, where the methyls can rotate about their C_3 axis and the *t*-butyl group as a whole can rotate about its C_3' axis.[26] Again, because of the different orientations for the interaction tensors, ^{1}H NMR cannot distinguish C_3 from C_3', whereas the ^{2}H lineshapes are quite distinct (Figure 24.4). In situations where the external barrier is very low, C_3' motion occurs at lower temperatures than methyl C_3 motion.

Deuterium relaxation studies can also distinguish between jump reorientation and rotational diffusion. For example, a rotating methyl group will show anisotropic relaxation across the powder pattern for jumps or isotropic relaxation for diffusion.[27]

The inclusion compound of toluene with *p-tert*-butyl-calix[4]arene (*t*BC) provides a simple illustration of the sensitivity of ^{2}H NMR lineshapes to details of dynamics.[28] The lineshapes for $C_6D_5CH_3 \cdot t$BC (Figure 24.5) show three states; static at 129 K, twofold reorientation about the long axis

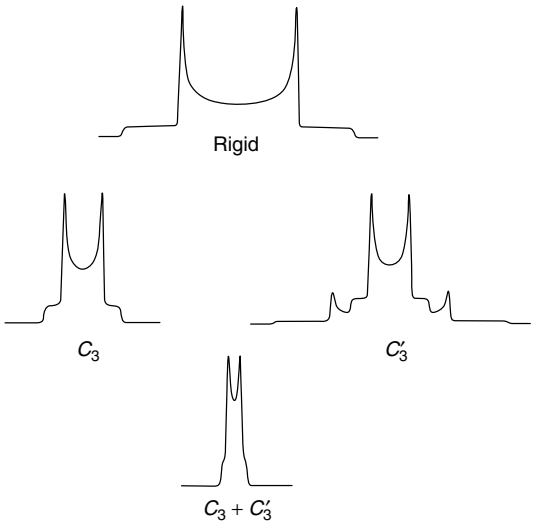


Figure 24.4. Simulated ^{2}H NMR powder spectra for C_3, C_3', and combined $C_3 + C_3'$ motions of a *t*-butyl group or a group with analogous geometry.

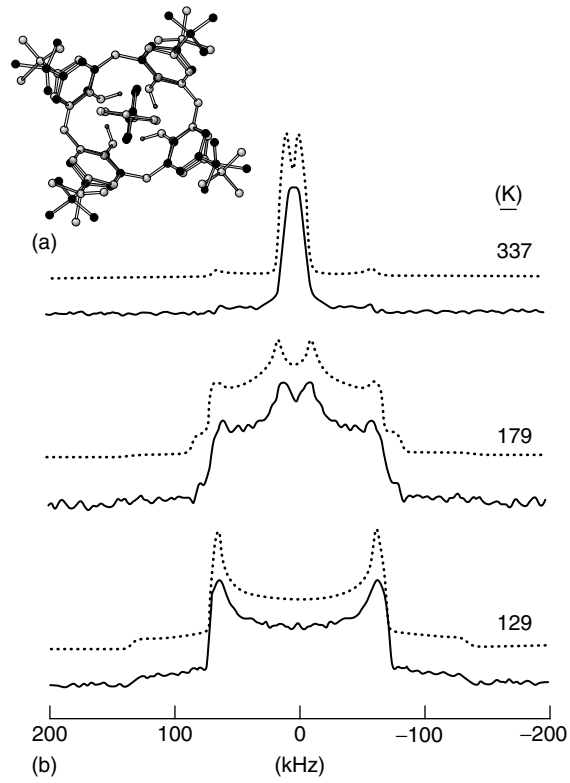


Figure 24.5. (a) View down the fourfold axis of *t*BC·toluene. (b) ^{2}H NMR spectra of $C_6D_5CH_3$, static at 129 K, with rapid 180° flips about the phenyl twofold axis at 179 K, and with rapid rotation about the fourfold calix axis at 337 K. The dotted curves are simulations.[28]

of the molecule at 179 K, and fourfold reorientation about a crystal axis at 337 K. Reorientation of the tensors for ortho- and meta-D atoms gives the narrowed lines. Since the para C–D bond lies along the rotation axis, there is no averaging for the twofold motion.

More detailed analysis suggested that in the fourfold motion, the molecule is actually tilted off the crystal axis by 12°, which disagrees with an early X-ray diffraction (XRD) structural determination that had the molecular and crystal axes coinciding. A new structure determination then found that the toluene is indeed tilted off axis. The final choice of space group in the XRD structure refinement of the low-temperature phase also was influenced by the fact that only twofold motion occurs. (Preliminary refinement indicated a fourfold symmetry axis for the calix, which is clearly incompatible with the dynamics).

Pyridine·*t*BC is another case where ^{2}H NMR studies of dynamics provided feedback, which helped in the structure refinement process.[29] Initial XRD refinement was hindered because of fourfold disorder of the pyridine about the calix axis, and by difficulty in defining the *N* atom position within the pyridine ring since nitrogen and carbon atoms do not differ very much in electron density. The issue was also confused by the fact that benzene and pyridine as guests in inclusion compounds are known to display in-plane motion. In this particular case, however, the ^{2}H NMR showed that the molecule does not undergo in-plane reorientation, since the ortho-, meta-, and para-deuterons retain distinct ^{2}H lineshape features (Figure 24.6). Instead, pyridine executes rapid rotation about its own twofold axis even below 77 K, and then rapid rotation of this axis about the crystal fourfold axis at quite a large tilt angle by 210 K. Because the para-D lies along the molecular twofold axis and is not averaged by 180° flips, the averaging effects of the fourfold motion on the lineshape of this atom directly provide the off-axis tilt angle (53° at 210 K, cf. 47° from final XRD at 150 K). Thus, the information from the dynamic model reduces the choice of nitrogen atom positions from six to two. One of these positions, with the N pointing out of the calix, gave a much improved XRD refinement, whereas the other made it worse.

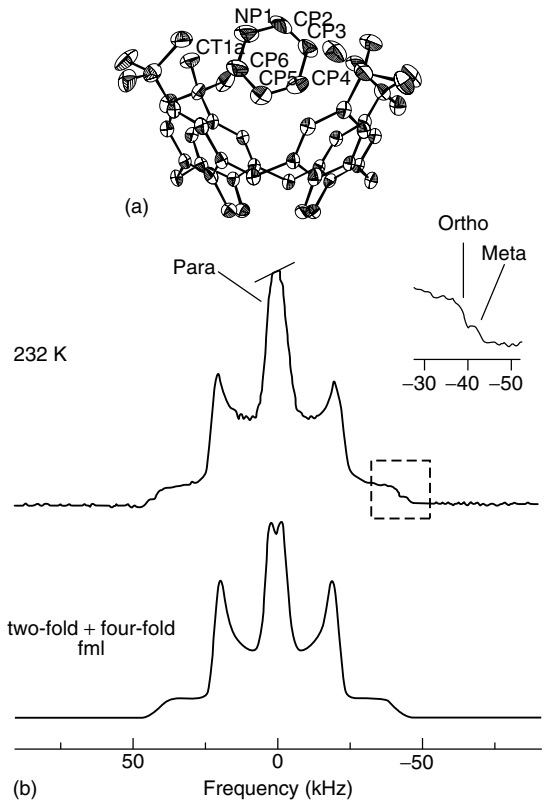


Figure 24.6. (a) The orientation of pyridine inside *t*BC (one of four disordered positions) from the crystal structure. (b) ^{2}H NMR spectra at 46.1 MHz of pyridine-d_5 at 235 K, showing features from ortho-, meta-, and para-D. The lower spectrum is simulated.[29]

A point to note is that in the cases where guest molecules rotate about the calix fourfold axis, there is usually also a small translational component to the motion because the center of gravity of the molecule is off axis.

This complementary approach, where NMR dynamics studies have been used hand-in-hand with XRD data to achieve better structural refinements, is especially useful where there is a high degree of disorder. In such situations, there may be very little difference in the XRD refinement *R*-factor between structures where the disordered molecules are oriented in different ways, i.e., with many local minima in the refinement, so that the structure that best reflects reality might not be arrived at. The dynamic models developed from the NMR results may not be able to give a unique solution but they can restrict the range of orientations to be explored in the X-ray refinement. In other words, the orientations defined in the final XRD model must be able to accommodate the dynamic averaging observed in the NMR.

A case in point is that of the acetone·*t*BC inclusion compound,[30] for which the initial guest positions (with a fourfold disorder about the calix axis) obtained from XRD were incompatible with the dynamically averaged ^{2}H NMR spectrum of the acetone. Consequently, a plausible dynamic model was developed with rapid methyl rotations, twofold exchange of the methyls, and reorientation about the crystal fourfold axis. The only two unknown factors for calculating the lineshape from this model are the two Euler angles α and β defining the orientation of the acetone with respect to the fourfold axis. By using the observed averaged lineshape, it was then possible to calculate ranges of α and β, which were compatible. These ranges proved to be large, but inspection showed that if the acetone were rotated about C=O by $\pm 27^\circ$ from the original XRD position, agreement could be achieved. Refinement at $+27^\circ$ proved to be acceptable. This was not the final refinement as other possible orientations and a further feasible disorder were investigated, which had better *R*-factors, until a structural model was arrived at that was consistent with both data sets. The motion of the acetone is quite complex, with both methyl groups exchanging positions with the ketone oxygen, but in such a manner that one methyl group is always in the calix cavity and the C=O group always points out. Also, the methyl groups both rotate rapidly about their threefold axes at 77 K.

The structure of trimethylene oxide (TMO) clathrate hydrate was refined in a similar way.[31] The hydrate cage occupied by TMO has $\bar{4}$ symmetry and XRD shows that the molecule is disordered over two sites, each of which has eight symmetry-equivalent positions (Figure 24.7). Deuterium NMR shows that the molecule is dynamic, rapidly sampling all 16 sites. The two D atoms on the apical C2 atom behave identically and produce an axial lineshape, and the four D on the C1 and C3 atoms adjacent to oxygen behave identically and produce a nonaxial averaged lineshape. Again, the initial XRD refinement produced orientations that were incompatible with the NMR result. However, by using the NMR result to define the range of possible orientations, it was possible to make adjustments to the original XRD orientations so as to bring the

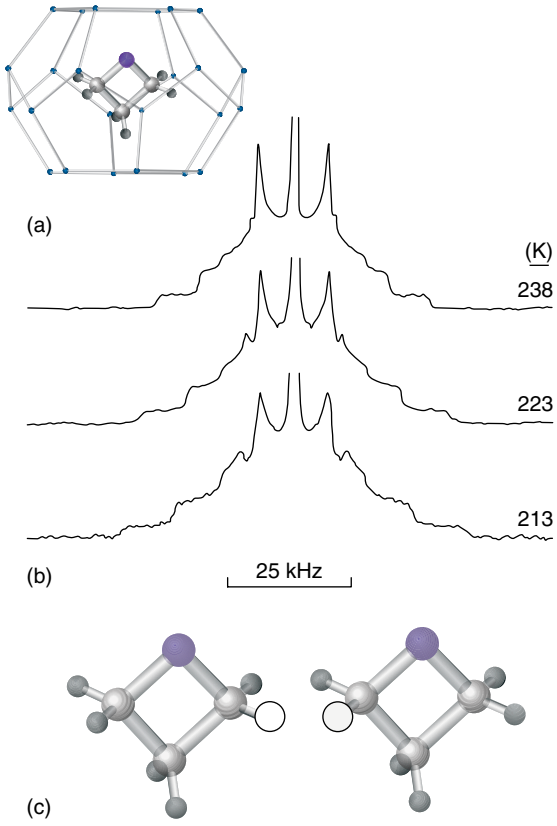


Figure 24.7. (a) Trimethylene oxide (TMO-d_6) in the large cage water framework of its Structure I clathrate hydrate. (b) Corresponding ^{2}H NMR spectra at 46.1 MHz at several temperatures. (c) Nonsuperimposable mirror images of TMO with one D atom labeled in white.[31]

two sets of results into agreement and to still have a good *R*-factor.

This case also shows another peculiarity of symmetry effects: It is surprising that, although this is a rigid molecule and therefore the two types of CD_2 are subject to exactly the same motions, one lineshape is axial but the other is not. If each C–D vector were able to visit all the crystallographically symmetry-equivalent atomic sites, an axial lineshape would result. The reason this does not happen for D on the C1 and C3 atoms is that the molecule is prochiral, i.e., if one of these D could be labeled, the mirror images would be nonsuperimposable (Figure 24.7). Although reflection is an allowed crystal symmetry operation, any specific D atom on C1 or C3 cannot physically occupy its mirror image site. However, the mirror image site of a D on C2 can be visited because the two are also related by rotation.

A comparison of ^{2}H NMR lineshapes of cyclohexane (C_6D_{12}) in the cavities of two different metal cyanide framework compounds highlights the effects of different symmetries on the dynamics of this guest molecule: In $Cd(mtn)Ni(CN)_4 \cdot \frac{1}{2} C_6D_{12}$ clathrate (mtn, *N*-methyl-1,3-diaminopropane) a framework of Cd and Ni bridged by CN and mtn forms a cavity which can be visualized as a square box.[32] Cyclohexane fits into this box, with the threefold axis of its chair form along the fourfold axis of the cavity. Deuterium NMR (Figure 24.8) shows that *n*-fold (probably 12-fold) rotation about the cavity axis already causes averaging at 77 K, with an estimated E_a of $\sim$5.8 kJ mol^{-1}. This *n*-fold reorientation gives a characteristic lineshape consisting of broad and narrow doublets of equal intensity. The six axial C–D are parallel to the rotation axis and therefore do not change orientation, whereas the six equatorial C–D change tensor orientation and are therefore averaged to give the narrow line. The fml for this motion is rapid by $\sim$117 K and the lineshape shows anisotropic T_1 relaxation, indicating that this is a jump motion. Between 230 and 390 K, the ^{2}H lineshapes undergo further changes in which the broad component disappears, leaving only the narrow line. This is due to inversion of the cyclohexane, which flips each C–D between axial and equatorial positions. An E_a of 44.7 ± 1.0 kJ mol^{-1} was determined by comparison of simulated and observed lineshapes.

In $Cd(CN)_2 \cdot C_6D_{12}$ clathrate, the cyclohexane sits within a cavity that has tetrahedral symmetry, formed by a framework of Cd atoms linked by CN.[33] The 77-K lineshapes (Figure 24.8) show cyclohexane already undergoing rapid reorientation about its threefold axis, indicated by the broad and narrow components, but the lineshape is also showing some effects of a pseudoisotropic motion, which is rapid by 140 K. Reorientation of the threefold molecular axis among just the four tetrahedral axes of the cavity produces this pseudoisotropic lineshape. This is not a degree of freedom available to the cyclohexane in the Cd(mtn) compound. In this particular case, inversion cannot be detected because the line is already completely narrowed. The low-temperature motion around the molecular axis in both compounds is considerably faster than in bulk solid cyclohexane, which is still static at 157 K.

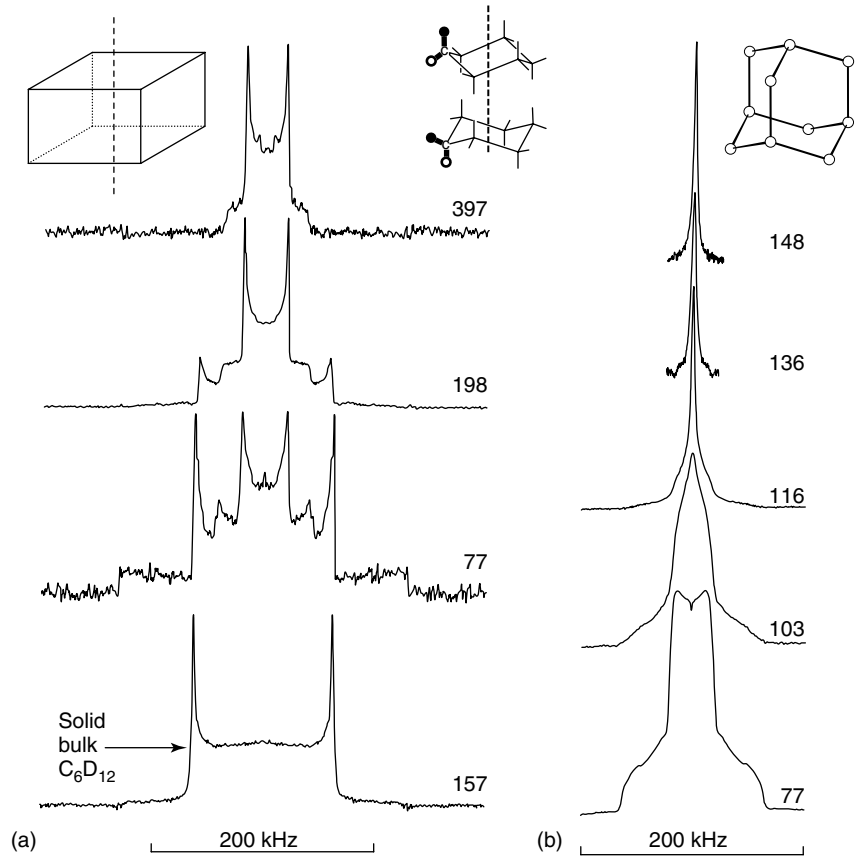


Figure 24.8. Deuterium NMR lineshapes at 27.6 MHz of cyclohexane enclathrated in $Cd(mtn)Ni(CN)_4 \cdot 1/2\, C_6D_{12}$[32] (a) and $Cd(CN)_2 \cdot C_6D_{12}$[33] clathrates (b) at various temperatures (K). The spectrum of solid bulk C_6D_{12} is shown at the lower left.

The 18-crown-6 malononitrile complex $(\text{-}CH_2CH_2O\text{-})_6 \cdot 2CH_2(CN)_2$ is an example of a very large molecule undergoing a reorientation (at room temperature), which is diffraction invisible.[34] Crystallography shows the crown to be in a conformation with close to D_{3d} symmetry, which means that like cyclohexane there are axial C–D bonds (parallel to the threefold axis) and equatorial C–D bonds. Rapid threefold reorientation would cause an averaging of the quadrupole coupling of the equatorial D to give an axial ^2H NMR lineshape with about one-third of the static width, but no averaging for the axial D. This is not observed, but rather a single axial lineshape (indicating that all D behave identically) with approximately one-third of the static width. Since the X-ray structure does not show any disorder, the fml lineshape can only be explained if the molecule rotates within itself, each $\text{–}CD_2CD_2O\text{-}$ unit rotating 60° to an adjacent position in the ring while every D must also switch between axial and equatorial orientations in order to match the crystal structure. The changes in orientation are exactly analogous to combined rotation and inversion as described above for cyclohexane. Jump rates were determined by modeling the intermediate-rate lineshapes at different temperatures and an E_a of $47.6 \pm 0.8\ \text{kJ mol}^{-1}$ was obtained.

The case of the semiclathrate hydrate of tetramethylammonium (TMA) hydroxide pentahydrate, $N(CH_3)_4OH \cdot 5H_2O$, illustrates a number of different aspects of dynamics linked to crystal symmetry. This material has a cubic structure[35] above 315 K (H-form) and an orthorhombic structure below.[36] The structures have different (but related) frameworks of

O atoms linked by hydrogen bonds, forming cavities which are occupied by the TMA ion (Figure 24.9).

The orthorhombic phase shows TMA with one molecular C_3' axis sitting on a crystal C_2 axis (and therefore disordered), so a small sixfold barrier to rotation about this axis is expected. However, pseudotetrahedral jumps of the whole molecule might also be relatively easy. In fact, ^{2}H NMR lineshapes of $N(CD_3)_4^+$ indicate C_3' rotation is already occurring by 70 K,[37] closely followed by pseudoisotropic motion, which is rapid by 130 K. Because the latter motion reduces the effective χ to zero, C_3 methyl motion cannot be observed. Of greater interest is the dynamic behavior of the framework.[38] Below 210 K, several overlapping ^{2}H NMR lineshapes indicate static D atoms in hydrogen bonds of different lengths (Figure 24.9). Motion is evident as T increases ($E_a = 11.3$ kJ mol^{-1} from ^{1}H T_1) and a *single* fml lineshape with large η has developed by 280 K, indicating that all the deuterium atoms are equivalent and hence must be exchanging rapidly between all the different bonds. This can be achieved by a combination of reorientation and translation along H-bonds. The nonaxial tensor is a consequence of the orthorhombic crystal symmetry, and on transformation to the cubic phase the lineshape becomes isotropic. In the cubic phase, the structure is symmetrized in terms of the positions of the oxygen atoms, but there are too few hydrogen atoms to fill every H-bonded side of the cage. However, rapid exchange ensures that all the hydrogen atoms are shared throughout, resulting in partial occupancy of all the bonds on a time average basis. Concerning the phase transition, it is conceivable that reorientational dynamics in the framework of the orthorhombic phase could occasionally bring an O–H bond into alignment such that H transfer across to the adjacent nonbonded oxygen atom might occur (and does so with increasing frequency as T increases), and that this ultimately might drive the phase transition.

Other examples of rapid D exchange among all possible sites in a hydrogen-bonded lattice include

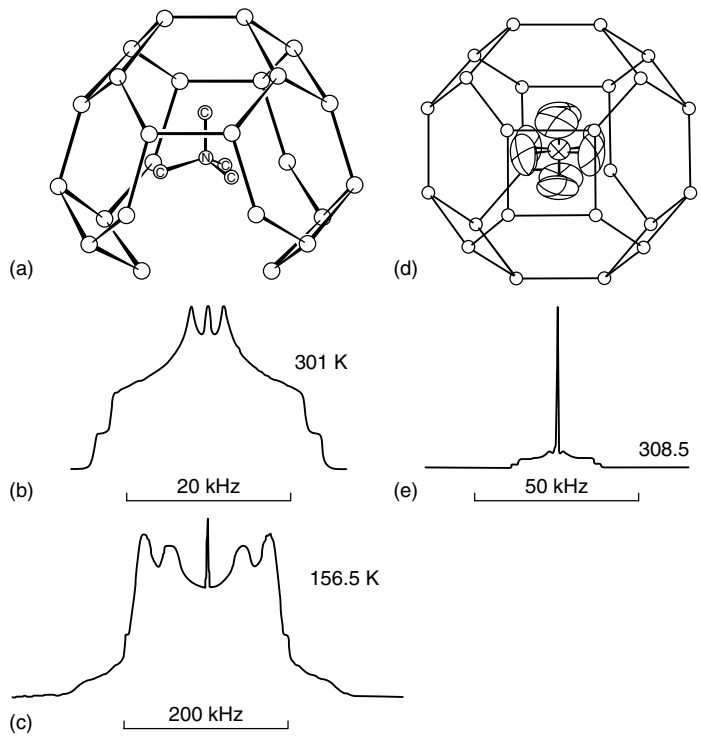


Figure 24.9. TMAOD·5D$_2$O: (a) TMA in a partial cage of the orthorhombic β-phase; dynamic (b) and static (c) ^{2}H NMR spectra at 27.6 MHz in the β-phase. (d) TMA in the full cage of the cubic α-phase; (e) ^{2}H NMR spectrum of mixed α and β-phases.[37]

the proton conductor $D[UO_2]PO_4 \cdot 4D_2O$,[21] and $HClO_4 \cdot 5 \cdot 5H_2O$.[39]

Situations sometimes occur where there is rotation among potential wells of unequal depth. A characteristic of such motions is that they can cause lineshapes to show changes over relatively short temperature intervals, even though they are apparently in the fast-motion limit. This is distinct from the small continuous changes brought about by librational motions, mentioned earlier. The simplest example would be that of a pseudo-fourfold potential, with two wells at 0° and 180°, which are lower in energy than the two at 90° and 270°. The populations of the two pairs of sites depend on the difference in energy (ΔE) and temperature, governed by the Boltzmann distribution. The populations then affect the averaged coupling tensor and lineshape as a continuous function of T. An example is the motion of ethylenediamine-d_4 (en) bridging ligand in phases III and II of the Hofmann-type clathrate $Cd(en)Ni(CN) \cdot 2C_6H_6$.[40] Phase II of D_2S and D_2Se, can be modeled by reorientation among the four diagonals of a cube but with one well deeper than the other three.[41] The latter two cases have the added complication that ΔE reduces asymptotically to zero as T increases in order to account for critical behavior at the II → I phase transition.

There are also 2-D exchange ^2H NMR experiments for looking at slow motions.[42,43] The patterns of the ridges in the 2-D plots contain information about the jump angle i.e., the angle between two orientations. An example is shown in Figure 24.10 for dimethylsulfone, where the jump angle was determined to be 106°. The patterns also allow discrimination between discrete jump motions and rotational diffusion.

24.6 SHIELDING AND DYNAMICS

Shielding is another second-rank spatial interaction, giving rise to anisotropic NMR lineshapes, which can be affected by dynamics in much the same way as for the quadrupolar interactions in ^2H NMR. In this case, the orientation of the static shielding tensor may not be so obvious as for the quadrupole coupling tensor of ^2H, unless it is dictated by molecular symmetry.

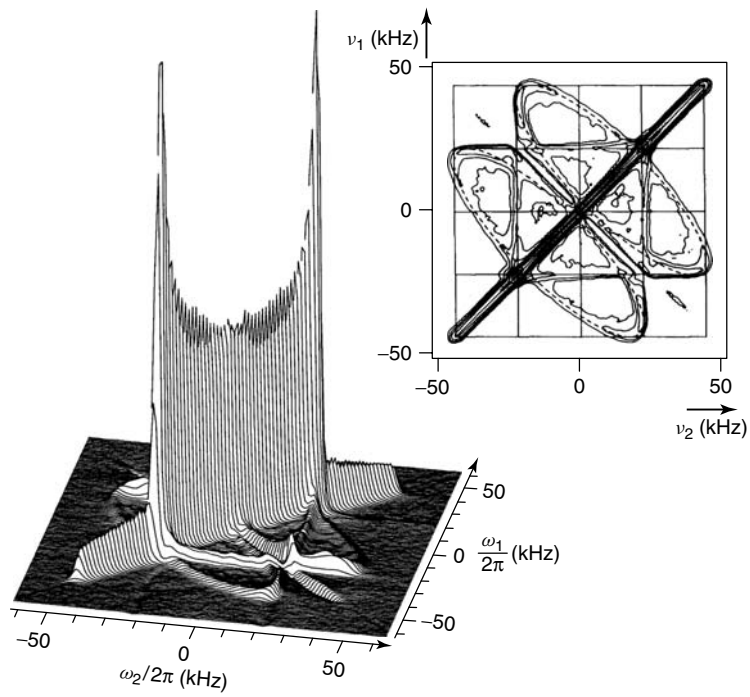


Figure 24.10. Static 2-D exchange ^2H NMR spectrum of dimethylsulfone ($t_{mix} = 3$ ms) at 46.07 MHz,[42,43] shown as stack and contour plots. (Reproduced from Ref. 42 and Ref. 43 © Elsevier, 1986, 1988.)

An early example studied in detail was the dynamics of P_4 molecular units in the β-phase of solid white phosphorus.[4,44,45] The ^{31}P NMR spectrum at 25 K shows a shielding anisotropy lineshape (span = 405 ppm), which corresponds to static molecules. In the region 80–120 K, the lineshape becomes distorted and eventually, at temperatures above 125 K, an isotropic lineshape is observed, indicating rapid isotropic averaging. Jump frequencies determined by comparison with calculated lineshapes compared well with those derived from T_1 measurements, from which an E_a of $\sim$15 kJ mol^{-1} was obtained.

The crystal structure of the 2 CO_2 : 1 *t*BC calix complex shows one CO_2 occupying a fourfold disordered site in the calix cavity and the second CO_2 in an interstitial site with no disorder. As the CO_2 level is decreased, the interstitial site depopulates. Carbon-13 NMR of a sample loaded to 1.8 CO_2 shows that both types of CO_2 sample all sites available to give a single lineshape. This can be modeled well with rapid reorientation in the calix site at an angle of 53.8° with respect to the fourfold axis, together with translational exchange with the interstitial site.[46]

Quite often, spectra will show resonances for guests in cavities which do not have spinning side bands under MAS and no anisotropy when static, whereas bulk guest material will show significant CSA. This lack of sidebands is clearly due to rapid pseudoisotropic reorientation, generally for a lower-symmetry molecule in a high-symmetry cage, e.g., P_4S_3 (C_3 symmetry) in the supercages of the cubic lattice of zeolite NaY,[47] but also high-symmetry molecules in low-symmetry environments, e.g., C_{60} in a nickel tetra-aza-annulenate inclusion compound.[48]

Exchange in solids can also be seen through averaging of isotropic chemical shifts. When CH_3 groups are pushed deep into the cavity of the host molecule, *t*-butyl-calix[4]arene, they experience a decrease in ^{13}C chemical shift due to ring current effects from proximity to four aromatic rings of the host. Carbon-13 CPMAS spectra of toluene in this cavity show two signals, one for the methyl "out" at 21.9 ppm, close to that of liquid toluene (21.3 ppm), the other for methyl "in", reduced to 15.0 ppm.[49] In a series of substituted butane molecules $CH_3-(CH_2)_3-Y$, this difference in shifts between "in" and "out" methyls provides evidence of exchange between the two in the cases of pentane and butyl alcohol.[50] It is found from diffraction that halides strongly prefer the "out" position, so in butyl chloride the methyl is "in" and decreases in shift by 4.3 ppm compared to solution in $CDCl_3$. In contrast, first, pentane shows only one methyl resonance, and second, this is shifted by just −1.4 ppm compared to solution. The implication is that the "in" and "out" methyls exchange rapidly on the NMR timescale, giving an averaged chemical shift. A similar small shift of −1.4 ppm is seen for butyl alcohol, again implying rapid exchange, and, in this case, the X-ray diffraction structural refinement was also insensitive to whether CH_3 or OH was inserted into the cavity.

The inclusion complex of xylene in Dianin's compound is a case where spectator nuclei in the host show sensitivity to motion of the guest. The crystal structure from X-ray diffraction shows a disorder of the xylene molecule over six equivalent sites in the host cavity. While the six Dianin's molecules surrounding the xylene are crystallographically equivalent, at room temperature the ^{13}C resonances are split into several peaks, showing that the local sixfold symmetry has been lost because the xylene is static and occupies just one site (on the timescale of the chemical shift splitting). This is effectively a static disorder in the crystal, which on spatial averaging gives the crystallographic sixfold symmetry.[51] However, by 363 K, xylene is able to rotate among all six sites, the disorder becomes dynamic and the chemical shift differences average out.[52]

Clearly, the Xe atom does not have rotational modes, but translational motions can involve changes in orientation of the ^{129}Xe CSA tensor. A simple example is Xe in the one-dimensional channels of ALPO-11 for which a single lineshape, which changes continuously as a function of Xe loading, is observed.[53]

A curious dynamic situation occurs when zeolite-Y powder is loaded with Xe and quenched to 77 K.[54] Xenon-129 NMR shows that it takes days to years (depending on the Xe loading) for this system to fully equilibrate at 77 K. While Xe motion within any one zeolite particle is very rapid, there is extremely slow transfer of Xe between particles. For equilibrated samples, their ^{129}Xe NMR static spectra consist of a single isotropic lineshape whose shift depends on how much Xe is present. The isotropic line arises due to the high symmetry of the cubic structure framework of zeolite-Y, as the Xe rapidly translates between all possible positions in the space within and between the supercages. When the samples are first quenched to 77 K and Xe condenses into the zeolite pores, thermal gradients produce an inhomogeneous

distribution of Xe among the particles. This gives rise to a range of ^{129}Xe chemical shifts and thus to broad and oddly shaped lines, which eventually revert to an isotropic line as very slow Xe exchange between particles homogenizes the Xe concentration across the sample.

Xenon-129 spectra of Xe in zeolite NaA[55] and AgA[56] show multiple lines corresponding to a distribution of cages occupied by one up to eight Xe atoms. Atoms within a cage are all equivalent through rapid exchange, but exchange between the cages is slow due to the 8-ring faces between cages being occupied by hydrated ions. However, this slow exchange can be monitored very well using 2-D-EXSY NMR (Figure 24.11). Analysis of the intensities of the cross-peaks in the AgA EXSY spectra as a function of temperature[56] leads to exchange rate constants between cages with different occupancies, and an estimated E_a for single Xe transfer of about 45 kJ mol^{-1}. The rate constants increase at loadings above 4 Xe per cage suggesting that the Xe sorption energies decrease for cages with higher occupancy.

24.7 NONINTEGER QUADRUPOLAR DYNAMIC AVERAGING

Examples of detailed studies of dynamics involving noninteger quadrupolar nuclei are relatively few, though there are numerous reports where indications of motions causing quite narrow lines have been

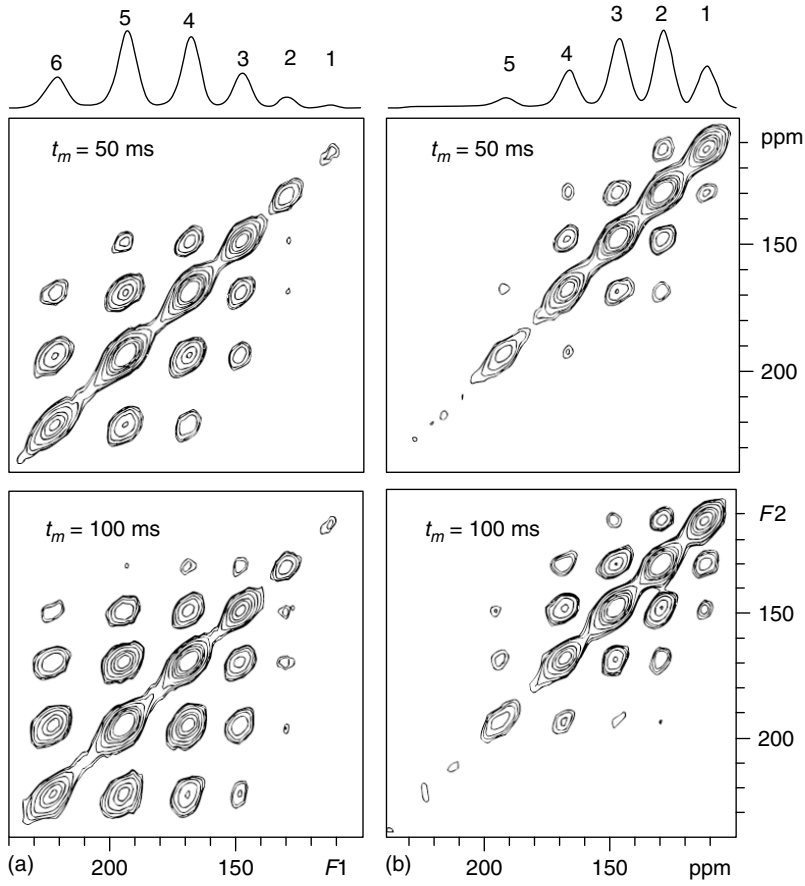


Figure 24.11. ^{129}Xe 2-D-EXSY spectra at 7.04 T of two samples of Xe/AgA zeolite with different loadings at different mixing times t_m. (a) $< n > = 4.0$ Xe per cage; (b) $< n > = 2.4$ Xe per cage.[56]

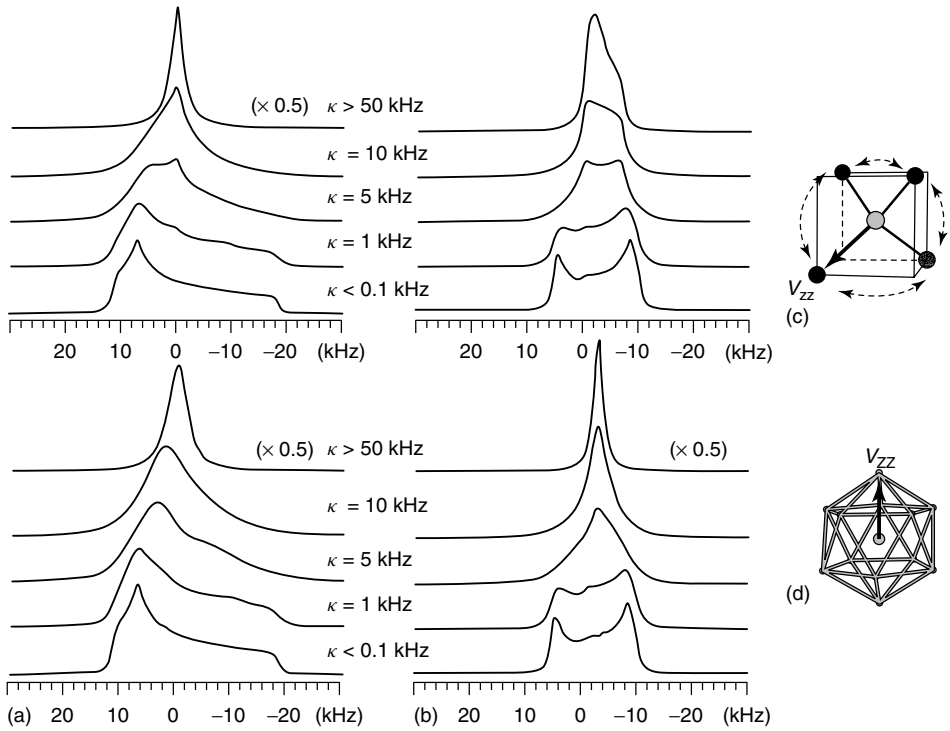


Figure 24.12. A comparison of the averaged lineshapes calculated for different motions for first-order chemical shift anisotropy (a) and second-order noninteger quadrupolar central transitions (b). Four-site exchange about the vertices of a tetrahedron (c). Twelve-site exchange about the vertices of a dodecahedron (d). (Reproduced from Ref. 61. © American Chemical Society, 2002.)

noted, for example, alkali metals in zeolites.[57–59] However, the recent explosion of interest in the NMR of these nuclei and the techniques necessary to observe them means that more situations with dynamics are being reported.

General discussion of first- and second-order[22] correction effects for noninteger quadrupolar nuclei can be found elsewhere.[60] For nuclei with χ small enough that first-order satellite transition lineshapes can be observed, one can obtain information on the coupling tensor before and after dynamic averaging.

In the majority of cases, however, χ will be large and the spectroscopy will focus on the central transition with its second-order shift and lineshape. Because this is much narrower than the satellite transition lineshapes, it shows effects of dynamics at much lower rates than the satellites. (In fact, the rates required to cause averaging of the satellites might never be reached before melting for many materials). There are some aspects peculiar to this situation[61–65]: (i) the central lineshape will change at dynamic rates comparable to χ^2/ω_0 but it retains its center of gravity at the position of the second-order shift and (ii) motions that would cause averaging to an isotropic lineshape for CSA and first-order quadrupolar interactions (as in ^{2}H NMR), e.g., reorientation of the tensor among T_d or O_h directions, do not give isotropic central transition lineshapes for noninteger nuclei, because of the second-order orientation dependence (Figure 24.12). Only for averaging over icosahedral or higher symmetry orientations will an isotropic average be obtained. However, as the dynamic rate increases further (to rates where the satellite lines should begin to average) the central lineshape will begin to change again, still at the second-order shift. Only when the satellites are almost completely averaged does the line move over to the true isotropic shift position (Figure 24.13) as shown in studies of ^{23}Na

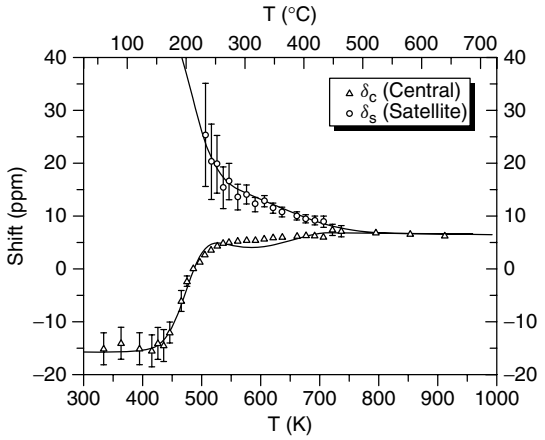


Figure 24.13. Temperature dependence of the ^{23}Na resonance shifts for the central and satellite transitions in $(Na_3PO_4)_{0.94}-(Na_2SO_4)_{0.06}$ solid solution. (Reproduced from Ref. 63. © American Chemical Society, 1999.)

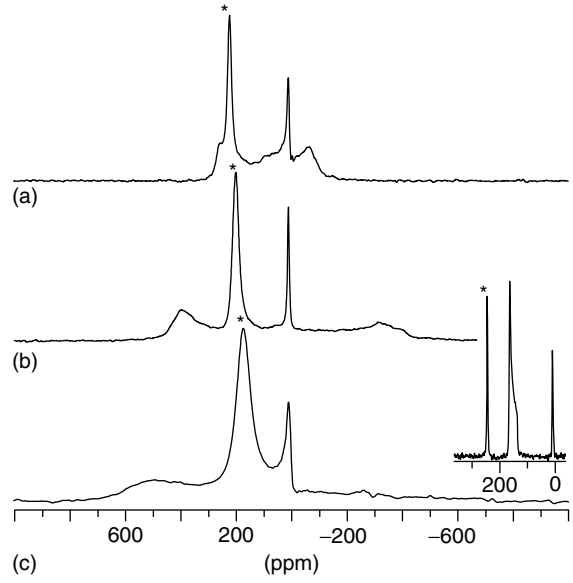


Figure 24.14. Static ^{131}Xe spectra of Xe structure I clathrate hydrate at 14.1 T, 9.4 T, and 7.05 T (a–c).[70] Asterisk indicates the line corresponding to Xe in the small cages. The inset shows the corresponding ^{129}Xe spectrum at 7.05 T.

in $(Na_3PO_4)_{0.94}-(Na_2SO_4)_{0.06}$ solid solution at high temperatures.[63]

A number of papers have presented methods for calculating dynamically averaged lineshapes under static,[61,63–65] MAS and MQMAS,[66] and QCPMG[67] conditions.

Two other complicating factors for studies of dynamics for many noninteger nuclei that have to be taken into account are (i) the chemical shift anisotropy can be a significant interaction and (ii) unless dictated by symmetry the orientation of the coupling tensor may not be known.

The following presents three other interesting examples:

With ^{7}Li (or ^{6}Li), the χ are generally small and second-order effects are not an issue. Dynamic averaging can be seen in the narrowing of the doublet lineshapes of the satellite transitions (much the same as for ^{2}H). An example is the case of *t*-butyl lithium, which has a tetrameric molecular structure in the solid state.[68] The ^{7}Li lineshapes correspond to a χ of 100 kHz below 150 K, but by room temperature have narrowed to a pseudoisotropic lineshape, suggesting that the Li are rapidly exchanging among the four sites on the tetrahedron at room temperature. The whole molecule cannot be tumbling, however, since ^{1}H lineshapes indicate that the *t*-butyl groups are not exchanging. Could it be that the Li_4 tetrahedron rotates independently? Lithium-7 T_1 measurements also indicate a solid–solid phase transition at ~310 K, where there is a sudden change in T_1 equivalent to an increase in exchange rate by a factor of 16. Although the derived E_a values are almost identical at 23.8 and 23.0 kJ mol^{-1} below and above the transition, the dynamics are in the slow and fast regimes respectively.

Sodium-23 NMR of sodocene, whose structure has chains consisting of alternating Na and cyclopentadienyl (Cp) rings gives the surprising observation of an increasing χ (and hence linewidth) as temperature increases.[69] The likely explanation, based on a dynamic model, which is consistent with all the evidence, was achieved with the aid of calculations for an isolated Cp_2Na^- cluster, which showed that χ increases with increasing Na displacement perpendicular to the CpNaCp axis. Thus in the solid, as the amplitudes of vibrational motions perpendicular to the NaCp chain axis increase with temperature, so too does the χ.

Xenon-131 in the small cages of xenon clathrate hydrate (Figure 24.14) is another example of a spectator nucleus, in this case observing the dynamics of the water framework but with an unusual aspect due to the quadrupolar interaction.[70] The ^{129}Xe spectrum is

simple (inset Figure 24.14), and reflects the symmetries of the cages, with an isotropic lineshape for Xe in the small cage and an axially symmetric shielding tensor lineshape for Xe in the large cage. Xenon-131 in the large cage has two static factors contributing to its observed second-order NMR lineshape ($\chi = 2.52$ MHz, $\eta \sim 0.1$); first the cage is nonspherical, and secondly 78% of the large cages have at least one vacant neighboring cage, which distorts the symmetry and leads to the nonzero η. In contrast, the small cage is spherical with T_d symmetry and 79% of these cages have no vacant neighboring cages, so no ^{131}Xe quadrupole coupling is expected. Yet the observed pseudoisotropic line has a second-order shift whose field dependence fits a static χ of ~1.33 MHz. This is the behavior expected for incomplete dynamic averaging, and since the Xe itself is not mobile, the averaging must come from dynamics of the water forming the cage. This water motion is well known from other NMR studies of clathrate hydrates. Water reorientation is apparently fast enough to average the second-order effects, i.e., of the order of the static central transition linewidth of several kHz, but not fast enough to average first-order effects on the MHz scale.

24.8 CONCLUDING REMARKS

This article has briefly covered many of the basics and the most-used aspects of NMR studies of motion in solids, and attempted to show with numerous examples how crystal structure and dynamics influence each other. Owing to space limitation, a number of notable topics, such as the effects of quantum tunneling on ^{1}H NMR of rotating methyl groups with low barriers, and diffusion in ionic conductors, have been omitted. One last aspect of dynamics, which has not been covered here, is its capacity for causing problems with specialized NMR techniques which rely on static interactions, making some inoperative or leading to misleading results.

REFERENCES

1. A. Abragam, *The Principles of Nuclear Magnetism*, Clarendon Press: Oxford, 1961, p 111.
2. M. J. Duer, in *Solid State NMR Spectroscopy Principles and Applications*, ed. M. J. Duer, Blackwell Science: Oxford, 2002, Chap. 6.
3. R. Tycko, in *Nuclear Magnetic Resonance Probes of Molecular Dynamics*, ed. R. Tycko, Kluwer Academic Publishers: Dordrecht, 1994, Chap. 1.
4. H. W. Spiess, Dynamic NMR spectroscopy, in *NMR: Basic Principles and Progress*, eds P. Diehl, E. Fluck, and R. Kosfeld, Springer-Verlag: New York, 1978, Vol. **15**.
5. J. H. Van Vleck, *Phys. Rev.*, 1948, **74**, 1168.
6. C. P. Slichter, *Principles of Magnetic Resonance*, 3rd edn., Springer-Verlag: Berlin, 1989, Chap. 3.
7. E. R. Andrew and R. G. Eades, *Proc. R. Soc. London, Ser. A*, 1953, **218**, 537.
8. G. W. Smith, *J. Chem. Phys.*, 1965, **43**, 4325.
9. J. S. Waugh and E. I. Fedin, *Sov. Phys. Sol. Stat.*, 1963, **4**, 1633.
10. N. Bloembergen, E. M. Purcell, and R. V. Pound, *Phys. Rev.*, 1948, **73**, 679.
11. R. Kubo and K. Tomita, *J. Phys. Soc. Jpn*, 1954, **9**, 888.
12. D. E. Woessner, *J. Chem. Phys.*, 1962, **36**, 1.
13. C. I. Ratcliffe and B. A. Dunell, *Faraday Disc. Chem. Soc. Faraday Symp.*, 1979, **13**, 42.
14. S. Albert and J. A. Ripmeester, *J. Chem. Phys.*, 1973, **58**, 541.
15. S. J. Opella and M. H. Frey, *J. Am. Chem. Soc.*, 1979, **101**, 5854.
16. D. V. Soldatov, A. T. Henegouwen, G. D. Enright, C. I. Ratcliffe, and J. A. Ripmeester, *Inorg. Chem.*, 2001, **40**, 1626.
17. W. P. Rothwell and J. S. Waugh, *J. Chem. Phys.*, 1981, **74**, 2721.
18. G. W. Buchanan, C. Morat, C. I. Ratcliffec, and J. A. Ripmeester, *Chem. Commun.*, 1989, 1306.
19. K. Schmidt-Rohr and H. W. Spiess, *Multidimensional Solid-State NMR and Polymers*, Academic Press: London, 1994.
20. G. L. Hoatson and R. L. Vold, in *NMR Basic Principles and Progress*, eds B. Blumich, P. Diehl, E. Fluck, H. Gunther, R. Kosfeld, and J. Seelig, Springer-Verlag: Berlin, 1994, Vol. **32**, Chap. 1.
21. R. R. Vold, in *Nuclear Magnetic Resonance Probes of Molecular Dynamics*, ed. R. Tycko, Kluwer Academic Publishers: Dordrecht, 1994, Chap. 2.
22. M. H. Cohen and F. Reif, *Solid State Phys.*, 1957, **5**, 321.

23. R. G. Barnes, *Adv. Nuclear Quad. Reson.*, 1974, **1**, 335.
24. M. S. Greenfield, A. D. Ronemus, R. L. Vold, R. R. Vold, P. D. Ellis, and T. E. Raidy, *J. Magn. Reson.*, 1987, **72**, 89.
25. R. J. Wittebort, E. T. Olejniczak, and R. G. Griffin, *J. Chem. Phys.*, 1987, **86**, 5411.
26. J. A. Ripmeester and C. I. Ratcliffe, *J. Chem. Phys.*, 1985, **82**, 1053.
27. D. A. Torchia and A. Szabo, *J. Magn. Reson.*, 1982, **49**, 107.
28. E. B. Brouwer, G. D. Enright, C. I. Ratcliffe, J. A. Ripmeester, and K. A. Udachin, in *Calixarenes 2001*, eds Z. Asfari, V. Bohmer, J. Harrowfield, and J. Vicens, Kluwer Academic Publishers: Dordrecht, 2001, Chap. 16, p 296.
29. E. B. Brouwer, G. D. Enright, C. I. Ratcliffe, G. A. Facey, and J. A. Ripmeester, *J. Phys. Chem. B*, 1999, **103**, 10604.
30. K. A. Udachin, G. D. Enright, C. I. Ratcliffe, and J. A. Ripmeester, *Chem. Phys. Chem.*, 2003, **4**, 1059.
31. K. A. Udachin, C. I. Ratcliffe, and J. A. Ripmeester, *J. Phys. Chem. B*, 2007, **111**, 11366.
32. S. Nishikiori, C. I. Ratcliffe, and J. A. Ripmeester, *J. Phys. Chem.*, 1990, **94**, 8098.
33. J. A. Ripmeester, C. I. Ratcliffe, and E. B. Brouwer, Inclusion compounds, in *Encyclopedia of Nuclear Magnetic Resonance*, eds D. M. Grant and R. K. Harris, John Wiley & Sons: Chichester, 2002, Vol. **9**, p 558.
34. C. I. Ratcliffe, J. A. Ripmeester, G. W. Buchanan, and J. K. Denike, *J. Am. Chem. Soc.*, 1992, **114**, 3294.
35. D. Mootz and R. Seidel, *J. Inclusion. Phenom. Mol. Recognit. Chem.*, 1990, **8**, 139.
36. R. K. McMullan, T. C. W. Mak, and G. A. Jeffrey, *J. Chem. Phys.*, 1966, **44**, 2338.
37. C. I. Ratcliffe and J. A. Ripmeester, *Can. J. Chem.*, 1986, **64**, 1348.
38. C. I. Ratcliffe, S. K. Garg, and D. W. Davidson, *J. Inclusion. Phenom. Mol. Recognit. Chem.*, 1990, **8**, 159.
39. T. H. Huang, R. A. Davis, U. Frese, and U. Stimming, *J. Phys. Chem.*, 1988, **92**, 6874.
40. S. Nishikiori, C. I. Ratcliffe, and J. A. Ripmeester, *J. Phys. Chem.*, 1991, **95**, 1589.
41. M. J. Collins, C. I. Ratcliffe, and J. A. Ripmeester, *J. Phys. Chem.*, 1989, **93**, 1495.
42. C. Schmidt, S. Wefing, B. Blumich, and H. W. Spiess, *Chem. Phys. Lett.*, 1986, **130**, 84.
43. C. Schmidt, B. Blumich, and H. W. Spiess, *J. Magn. Reson.*, 1988, **79**, 269.
44. H. W. Spiess, *Chem. Phys.*, 1974, **6**, 217.
45. H. W. Spiess, R. Grosescu, and U. Haeberlen, *Chem. Phys.*, 1974, **6**, 226.
46. K. A. Udachin, I. L. Moudrakovski, G. D. Enright, C. I. Ratcliffe, and J. A. Ripmeester, *Phys. Chem. Chem. Phys.*, 2008, **10**, 4636.
47. G. S. H. Lee, C. I. Ratcliffe, and J. A. Ripmeester, *Can. J. Chem.*, 1980, **76**, 1660.
48. D. V. Soldatov, P. R. Diamente, C. I. Ratcliffe, and J. A. Ripmeester, *Inorg. Chem.*, 2001, **40**, 5660.
49. E. B. Brouwer, G. D. Enright, C. I. Ratcliffe, and J. A. Ripmeester, *Supramol. Chem.*, 1996, **7**, 79.
50. E. B. Brouwer, K. A. Udachin, G. D. Enright, C. I. Ratcliffe, and J. A. Ripmeester, *Chem. Commun.*, 1998, 587.
51. G. D. Enright, C. I. Ratcliffe, and J. A. Ripmeester, *Mol. Phys.*, 1999, **97**, 1193.
52. E. Zaborowski, S. Vega, P. Speier, H. Zimmerman, and U. Haeberlen, *Mol. Phys.*, 1997, **91**, 1083.
53. J. A. Ripmeester and C. I. Ratcliffe, *J. Phys. Chem.*, 1995, **99**, 619.
54. C. I. Ratcliffe and J. A. Ripmeester, *J. Am. Chem. Soc.*, 1995, **117**, 1445.
55. R. G. Larsen, J. Shore, K. Shmidt-Rohr, L. Emsley, H. Long, A. Pines, M. Janicke, and B. F. Chmelka, *Chem. Phys. Lett.*, 1993, **214**, 220.
56. I. L. Moudrakovski, C. I. Ratcliffe, and J. A. Ripmeester, *J. Am. Chem. Soc.*, 1998, **120**, 3123.
57. M. Hunger, U. Schenk, and A. Buchholz, *J. Phys. Chem., B*, 2000, **104**, 12230.
58. M. Feuerstein, G. Engelhardt, P. L. McDaniel, J. E. MacDougall, and T. R. Gaffney, *Microporous Mesoporous Mater.*, 1998, **26**, 27.
59. K. H. Lim and C. P. Grey, *J. Am. Chem. Soc.*, 2000, **122**, 9768.
60. P. P. Man, Quadrupolar interactions, in *Encyclopedia of NMR*, eds D. M. Grant and R. K. Harris, John Wiley & Sons: New York, 1996, p 3838.
61. R. W. Schurko, S. Wi, and L. Frydman, *J. Phys. Chem., A*, 2002, **106**, 51.
62. T. Kurkiewicz, M. J. Thrippleton, and S. Wimperis, *Chem. Phys. Lett.*, 2009, **467**, 412.

63. M. Witschas and H. Eckert, *J. Phys. Chem., A*, 1999, **103**, 10764.

64. J. H. Kristensen and I. Farnan, *J. Chem. Phys.*, 2001, **114**, 9608.

65. K. Muller, *Phys. Chem. Chem. Phys.*, 2002, **4**, 5515.

66. M. Kotecha, S. Chaudhuri, C. P. Grey, and L. Frydman, *J. Am. Chem. Soc.*, 2005, **127**, 16701.

67. F. H. Larsen, *J. Magn. Reson.*, 2004, **171**, 293.

68. G. H. Penner and Y. C. P. Chang, *Chem. Commun.*, 2000, 1803.

69. C. M. Widdifield, J. A. Tang, C. L. B. Macdonald, and R. W. Schurko, *Magn. Reson. Chem.*, 2007, **45**, S116.

70. I. L. Moudrakovski, C. I. Ratcliffe, and J. A. Ripmeester, *J. Am. Chem. Soc.*, 2001, **123**, 2066.

Chapter 25

Intramolecular Motion in Crystalline Organic Solids

Paul Hodgkinson

Department of Chemistry, University of Durham, Durham DH1 3LE, UK

25.1 Introduction 375
25.2 Dynamics and Structure 376
25.3 Effects of Dynamics on NMR Spectra 378
25.4 Characterization of Dynamics in Solids 381
25.5 Overview 385
References 385

25.1 INTRODUCTION

For the conventional crystallographer, the presence of internal dynamics is an unwelcome complication. Modest amplitude librational motion leads to decreased intensity of Bragg diffraction peaks, which is generally quantified in terms of a "thermal ellipsoid", whose size increases with temperature due to the increased amplitude of motion.[1,2] Large amplitude motions, e.g., "Rigid Unit Modes",[3] which are commonly encountered in framework materials, cause particular problems since the resulting time-averaged atomic positions are misleading and thereby giving rise to incorrect bond lengths. Jumps between distinct and nonequivalent sites cause more severe disruptions of the periodic ordering required for strong Bragg scattering, while jumps between equivalent sites will remain undetected. Modeling, with the attendant risks of oversimplification, is then typically required to interpret the scattering data. Hence single-crystal X-ray diffraction is now routinely carried out at low temperatures, typically 100–120 K, in order to minimize the unwelcome effects of dynamics on Bragg diffraction. Although this usually generates "clean" structures with reduced thermal ellipsoids, the resulting static structures may give a misleading, or at least incomplete, picture of the material and its behavior at ambient temperatures.

In contrast, NMR observables are determined by the local environment rather than by long-range ordering, and so the impact of dynamic processes in solids is less disruptive. Indeed, NMR is an ideal tool for the characterization of dynamic processes, since different NMR parameters are sensitive to different motional processes over an extremely wide range of timescales.[4,5] Hence the complementarity of NMR and diffraction techniques is particularly strong when dynamic processes are present; diffraction studies can provide information with regard to the overall structure of the material (averaged over space and the duration of data acquisition), while NMR can characterize the local molecular-level motional behavior.

The following section discusses the types of motion that can be observed in the NMR studies of crystalline organic solids, and describes how these

NMR Crystallography Edited by Robin K. Harris, Roderick E. Wasylishen and Melinda J. Duer © 2009 John Wiley & Sons, Ltd. ISBN: 978-0-470-69961-4

interact with conventional crystallography. After discussing in qualitative terms how dynamics can manifest themselves in NMR spectra, the main approaches for the detailed quantitative characterization of dynamics in organic solids are briefly surveyed.

25.2 DYNAMICS AND STRUCTURE

When considering dynamics in crystalline solids and their interaction with structure, it is helpful to distinguish between very slow motions (which will not be visible to diffraction-based techniques), motions that are fast compared to the timescale of both NMR and scattering, and intermediate rate motions to which both diffraction and NMR are sensitive.

In contrast to the static structural models provided by diffraction studies, molecular dynamics (MD) simulations of organic solids show that molecular solids are in continuous motion at ambient temperature. Such molecular vibration is generally much faster than the timescale of both NMR and diffraction studies, and so both NMR and Bragg scattering experiments will "observe" structure averaged over the vibrational timescale. It is noteworthy, however, that the nature of the averaging differs subtly between observed parameters. For example, measurements of internuclear distances from neutron Bragg scattering and NMR dipolar couplings are expected to be in relatively good agreement, since both techniques are sensitive to nuclear position. (X-ray diffraction involves scattering from the overall electron density and so systematic differences, of a few percent, are generally observed between interatomic distances derived from XRD studies on the one hand, and neutron scattering and NMR experiments on the other. These differences are particularly marked for H atoms.) However, the dipolar coupling depends on internuclear distance as r^{-3} and so the relevant time-averaged parameter for NMR is $\langle r^{-3} \rangle$ rather than $\langle r \rangle$ for neutron Bragg diffraction. As a result, subtle differences will be observed between distances derived from NMR dipolar couplings and the "true" time-averaged structure, especially if the vibration has a strong anharmonic characteristic. These issues have been successfully addressed for the highly accurate structures of small molecules dissolved in liquid-crystal solvents, where normal mode analysis of the molecular vibration is used to "correct" the distances derived from dipolar coupling measurements for the effects of molecular vibration.[6] Little work in this direction has been performed for molecular solids[7,8] partly because the corresponding vibrational analysis is more challenging for a solid material, but largely because solid-state NMR experiments struggle to match the quality of data provided by liquid-crystal NMR.

These librational motions of molecules within potential minima are, however, of relatively little intrinsic interest. Hence the most significant dynamic processes in crystalline organic solids are intramolecular jump motions. For example, rotational diffusion of methyl groups plays an important role in the NMR of molecular solids, as it provides an effective driving force for spin-lattice relaxation. Similar processes include, e.g., 180° rotation of phenylene rings, or exchange of H atoms between sites. Whole molecular reorientations are commonly observed in host–guest systems; as illustrated below, the solvent molecules in organic solvates are frequently dynamic, and their NMR may show more similarities with solution-state or liquid-crystal NMR than with classic solid-state NMR.

In contrast with solution-state NMR where "asymmetrical" chemical exchange is frequently encountered, these dynamic processes generally involve exchange between sites of the same (or very similar) total energy. In this case, activation barriers for the "forward" and "backward" processes are the same, and a single kinetic parameter is sufficient to characterize the motion. Rare exceptions include systems with high energy "defect" sites, such as the example presented in Figure 25.1, or rearrangements between energetically nonequivalent conformations.[9] (Note that in the former case, the difference in activation barriers between "forward" and "reverse" processes is so large that the motions will be very strongly correlated and it would not be possible to observe the "reverse" process independently.) For the rest of the article, we will assume that dynamic processes can be characterized by a single rate constant. It will also be assumed that dynamic processes can be modeled in classical terms; quantum tunneling effects in hindered rotors[10] lead to deviations from simple Arrhenius-like kinetics, but these effects are generally insignificant at ambient temperatures.

Different dynamic processes may be encountered in other types of material. For example, motion in inorganic network solids, e.g., zeolites, typically has strong diffusional characteristics. Molecular motion in amorphous/glassy materials, such as polymers and

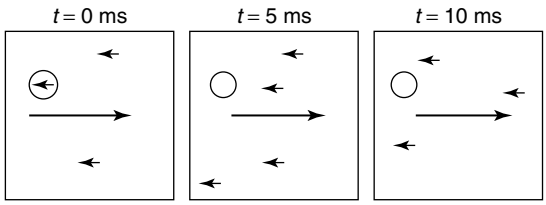


Figure 25.1. Schematic illustration of the compatibility of long-range ordering observed by diffraction methods with local dynamics observed by NMR. The domain has a well-defined overall order (expressed by the large arrow), but with a small fraction of reversed units, which have negligible impact on the diffraction pattern. At the local level, however, individual sites (such as one highlighted) may flip back and forth between orientations over the timescale of an NMR experiment. (Figure adapted from Ref. 11.)

glasses, is often key to their physical properties, but may be extremely difficult to describe compactly, particularly as these materials are frequently heterogeneous. Modeling in terms of a single rate constant will be highly unrealistic in these situations.

Scattering techniques are relatively insensitive to slow processes that do not disrupt the overall long-range ordering, as schematically illustrated in Figure 25.1. Over the timescale of an NMR magnetization transfer experiment (milliseconds and longer), individual units will flip in and out of the net alignment. But the fraction of such "defect units" is very small at any given time, and the drop in Bragg scattering intensity associated with this small fraction would be difficult to detect. Essentially NMR observes that the individual sites all move over the duration of the experiment, while diffraction observes that only a few sites are "different" at any one time. This clearly illustrates the complementary viewpoints of the two techniques.

NMR is most widely applied, however, in the "intermediate" case, where the presence of solid-state dynamics has been inferred from "disorder" in the structure derived from scattering experiments. As discussed below, a wide range of techniques can be applied, depending on the timescale of the motion, in order to characterize the dynamics. Although it is usually possible to separate solution of the overall structure via diffraction from characterization of dynamics via NMR, there are isolated examples where it has been necessary to incorporate NMR information directly into the modeling of the diffraction data.[12]

It is noteworthy that the description of solid structures in terms of space groups becomes more doubtful as the extent of dynamics increases. This is schematically illustrated in Figure 25.2. Although at a local level, the only difference between the two "structures" is the rate at which molecules jump between configurations, diffraction experiments will derive distinct space groups and lattice parameters in the two limits.

The relationship between local structure and long-range ordering becomes particularly fraught in cases where the motional process involves a positional as well as an orientational component. For example, many solvate systems involve channel structures in which guest molecules may be relatively free to translate. Typically, guest molecules occupy well-defined lattice sites at low temperature (even if they are rotationally disordered) and the solid has a well-defined stoichiometry cf. the finasteride system discussed in Section 25.3.3.1. At higher temperatures, the guest molecules may be free to migrate, particularly in structures containing suitable channels. Characterization of the guest, including any desolvation processes, is then difficult by diffraction, since the translational dynamics leads to a loss of Bragg scattering. Although it is also difficult to characterize translational dynamics via conventional solid-state NMR (since the NMR parameters will typically vary subtly only between the limits of full ordering on fixed lattice sites

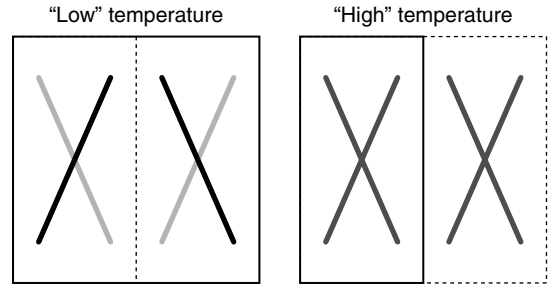


Figure 25.2. Schematic illustration of the interaction of dynamics and space group symmetry. The "molecule" can adopt two essentially equivalent configurations at each lattice site. When the thermal energy is large compared to the energetic barrier between configurations, each molecule is "disordered" between the two sites. At low temperatures, an ordered structure is adopted with a larger unit cell. Note that the unit cell in the high temperature "form" also has higher symmetry.

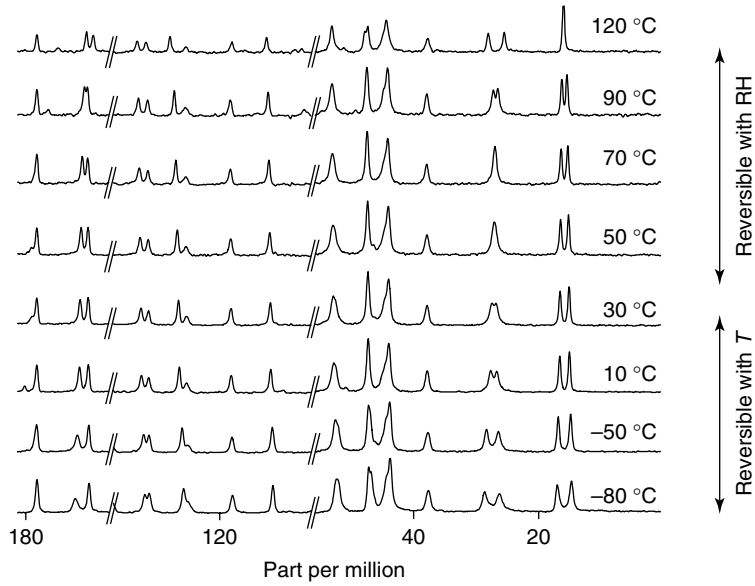


Figure 25.3. Variation of selected regions of the ^{13}C CP/MAS spectrum of sildenafil citrate as a function of temperature. The subtle changes in the spectrum below room temperature are reversible with temperature and are likely to involve exchange of labile protons between citrate ions, water in the channel structures and the sildenafil host. Above room temperature, water is reversibly lost from the channels, leading to changes in the ^{13}C spectrum that are reversed on increasing the relative humidity (RH). Such behavior is very difficult to characterize via diffraction methods.

and full translational disorder), the local nature of NMR spectroscopy means that the changes in guest behavior and its impact on the host can still be monitored via NMR techniques, as illustrated in Figure 25.3.

25.3 EFFECTS OF DYNAMICS ON NMR SPECTRA

Before considering how motional processes in crystalline solids can be characterized, e.g., via relaxation time measurements, it is useful to consider the different ways in which dynamics can influence NMR spectra, since this is often how the presence of dynamics is first inferred.

25.3.1 Motional Averaging

Motions that are fast on the NMR timescale (exceeding the width of the NMR spectrum) will lead to an averaging of the anisotropic components of the different NMR parameters. Consider for simplicity fast rotation about a single axis (or, equivalently, rapid diffusional rotation about a C_n axis with $n > 2$). The magnitude of the anisotropies of affected tensors is scaled by $P_2(\cos\theta) = (3\cos^2\theta - 1)/2$, where θ is the angle between the z principal axis of the tensor and the axis of rotation. The averaged tensor (which is by definition symmetric for this case) is aligned with its z principal axis along the rotation axis. For example, all the H–H homonuclear couplings in a rapidly rotating methyl group are scaled by $P_2(\cos\pi/2) = -1/2$, since the H–H internuclear vectors are perpendicular to the rotation axis, while the ^{13}C–^{1}H heteronuclear dipolar couplings are scaled by $P_2(\cos 109.5^\circ) = -1/3$.

When considering whole molecular reorientation, it is useful to introduce the principal order parameter $S_{zz} = \langle P_2(\cos\theta(t))\rangle$, which scales the magnitude of all the tensor anisotropies. (Additional order parameters are required to fully describe the averaging in the absence of an effective axis of cylindrical symmetry.) In the limit $S_{zz} = 0$, all the anisotropic interactions

are suppressed and the limit of solution-state NMR is recovered. Intermediate values, i.e., $0 < S_{zz} < 1$, essentially correspond to liquid-crystal NMR, where the anisotropic interactions are scaled, but not completely suppressed.

Overall fast motional processes lead to a scaling of the anisotropic interactions (cf. Figure 25.5), with the scaling factor depending on the nature of the motional process. Particularly for quasi-isotropic reorientations, this can lead to a considerable narrowing of the NMR spectrum. Molecular reorientation will, however, only scale intramolecular anisotropic orientations, but will only partially average the interactions between the molecule and its neighbors. For instance, in the plastic crystal adamantane, the adamantane molecules are randomly reoriented on the sites with cubic symmetry. Hence chemical shift anisotropies and intramolecular dipolar couplings are averaged to zero, but the lack of translational motion means that motional averaging has limited impact on the intermolecular dipolar couplings. As a result, adamantane behaves like a conventional crystalline solid, but one in which the strength of the proton coupling network has been reduced by a factor of ~3. Dynamic systems such as adamantane and hexamethylbenzene are, as a result, often used as setup and test samples for organic solid-state NMR.

25.3.2 Chemical Exchange

Jumps between sites of different chemical shift have characteristic effects on spectral linewidths and positions if the jump rate is of a similar order of magnitude to the difference in (isotropic) NMR frequencies.[4] For example, unless the ring is located on a high symmetry site, both "sides" of a *para*-phenylene ring are generally nonequivalent, and distinct ^{13}C resonances ought to be observed for each carbon site. However, reorientation (via 180° flips) around the 1,4-axis interchanges the sites, and, depending on the temperature, distinct resonances will be observed that broaden as the temperature (and jump rate) increases, or averaged resonances will be observed.[13] As seen in Figure 25.4, the

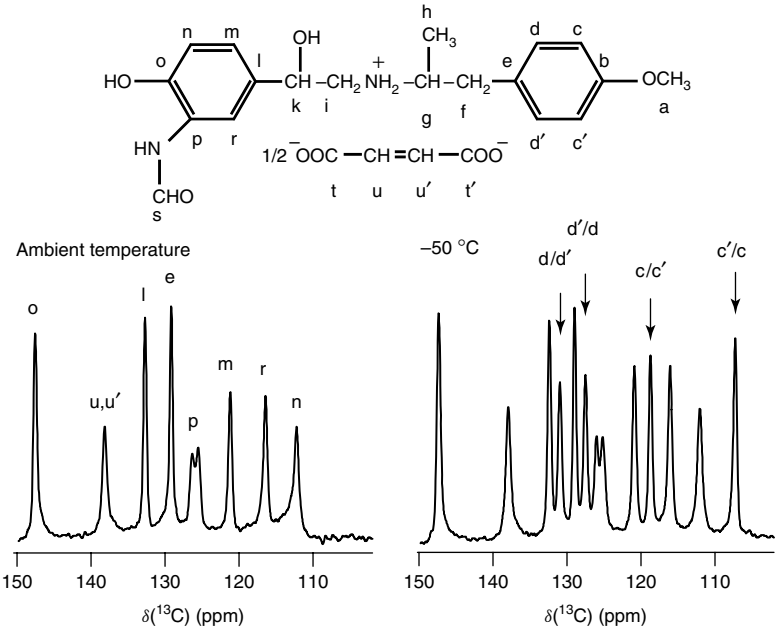


Figure 25.4. Part of the ^{13}C CP/MAS spectrum of formoterol fumarate dihydrate at ambient (left) temperature and (right) −50 °C. Resonance peaks from the c/c′ and d/d′ aromatic carbons are observed at low temperature but apparently disappear (into broad coalesced peaks) at ambient temperature. This is due to flipping of the phenyl ring, which must be interconverting c ↔ c′ and d ↔ d′ resonances at a rate of kilohertz (matching the difference in NMR frequencies) at ambient temperature.

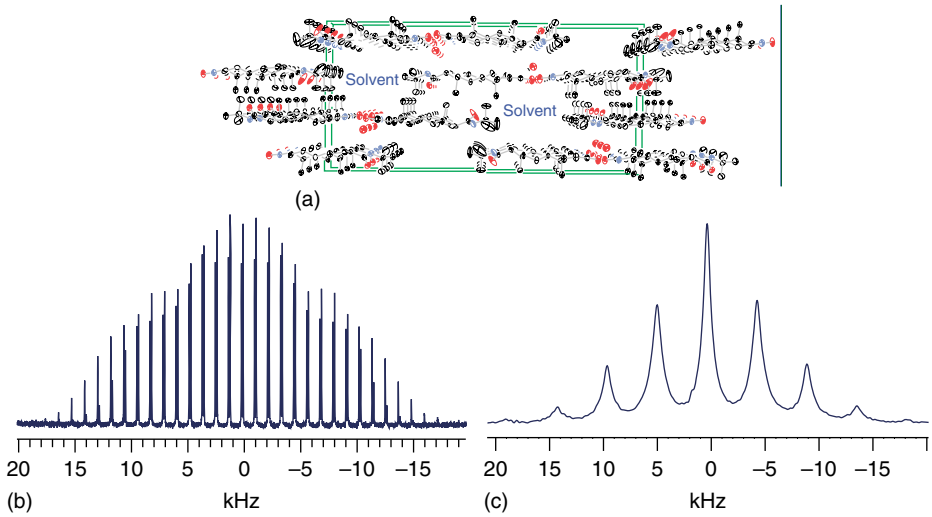


Figure 25.5. (a) Structure of the isomorphous solvates formed by finasteride with a number of small molecule solvents. Ambient temperature ^{2}H MAS spectra of the solvates formed with (b) deuterated THF, and (c) deuterated 1,4-dioxane.

coalesced line may be too broad to be observed at intermediate temperatures/jump rates.

It is noteworthy that other mechanisms can also lead to spectral broadenings in this intermediate timescale. These are discussed in the following subsection.

25.3.3 Timescale Interference

Simple reorientational motions between equivalent sites leave the isotropic chemical shift unchanged and so are not directly observed in 1-D magic-angle spinning spectra. However, unless unusually high symmetries are involved, any motion will modulate the anisotropic components of NMR parameters, such as the chemical shift anisotropy. This modulation can interact with externally imposed modulations that are present in MAS experiments, typically resulting in line-broadening effects. The extent of these effects depends on the magnitude of the modulations and the spectral density of the motion, $J(\nu)$, at the frequency of the external modulation, ν.

In general, spectral densities are poorly characterized in solids,[14] but the dynamics of simple jump/reorientational motions in homogeneous solids, such as molecular crystals, is usually well described in terms of a simple random (Markovian) process with a unique correlation time, τ_c, (analogous to the time constants of relaxation processes). In this case, the (normalized) spectral density is given by

$$J(\nu) = \frac{\tau_c}{1 + (2\pi\nu\tau_c)^2} \tag{25.1}$$

25.3.3.1 Interference with Magic-Angle Spinning

If $J(\nu_{MAS})$ is significant (where ν_{MAS} is the MAS frequency), then interference effects can be observed between the sample spinning and the molecular dynamics, provided the spinning rate is low enough for spinning sidebands to be observed. In the absence of dynamics, the evolution of magnetization under the influence of interactions such as the CSA and the quadrupolar coupling is refocused to form "rotor echoes" in the time-domain signal (which correspond to the spinning sidebands of the frequency-domain spectrum). But the formation of these rotor echoes is disrupted if the tensors reorient during the rotor period. Hence the signal decays more quickly and the MAS spectrum is strongly broadened in the presence of motional processes on the order of the sample spinning frequency.

These effects are illustrated in Figure 25.5. The steroid finasteride forms a series of isomorphous solvates with small molecule solvents such as tetrahydrofuran (THF) and 1,4-dioxane, with the solvent

molecules filling extended tunnels in the structure. ^{2}H MAS spectra of the solvates prepared using deuterated solvents readily show that the solvent molecules are highly dynamic (in the absence of molecular tumbling, the overall spectral envelope would span of the order of 200 kHz), but the nonzero scaling implies that the order parameter is nonzero and the motion must be anisotropic. The sidebands for the dioxane solvate (c), are strongly broadened in comparison with those for the THF (b), where the distinct ^{2}H sites can be resolved. This is presumably due to interference between the magic-angle spinning and chair–chair interconversion of the six-membered ring of dioxane. See also Figure 25.9.

25.3.3.2 Interference with RF Irradiation

Dilute spin spectra (e.g., ^{13}C, ^{15}N) are invariably acquired in the presence of strong ^{1}H heteronuclear decoupling. However, this creates an additional potential source of interference with dynamics,[15] with the relevant frequency being the ^{1}H nutation frequency (typically 10 s of kilohertz). This manifests itself as a broadening of ^{13}C resonances affected by the dynamic process (with directly protonated carbons being much more strongly broadened). Although the interaction of dynamics with RF modulation can potentially be used to characterize dynamic processes, other techniques designed for intermediate timescale motions (including MAS interference) are often easier to apply. For the most part, these interference effects are rarely severe enough to be clearly identified, and in any case can generally be mitigated by changing the sample temperature and so moving the maximum of the spectral density away from the problematic external modulation. See also Ref. 16 and references therein for further details of the interaction between dynamics and heteronuclear decoupling. Note that analogous effects may be observed when applying homonuclear decoupling.[17] This may also be used to characterize dynamics.[18]

25.4 CHARACTERIZATION OF DYNAMICS IN SOLIDS

There are a large number of NMR experiments that can potentially be used for the quantitative characterization of dynamic processes. These experiments[19–21] and their application to organic solids[22] have been well described elsewhere, and so this section simply summarizes the methods available and their ranges of application.

25.4.1 Fast Dynamics

Typical processes: reorientation of weakly hindered entities, e.g., rotational diffusion of methyl groups, small guest molecules in host–guest systems.

25.4.1.1 General Principles

Spin-lattice relaxation times are the functions of the spectral density at (multiples of) the nuclear Larmor frequency, $J(\nu_{\mathrm{NMR}})$, and so are useful probes for motions that are too fast to affect the NMR spectrum directly. In highly dynamic systems, e.g., soft gels or included solvents, it may be feasible to apply variable field relaxometry to measure relaxation parameters, such as T_1, over a wide frequency/magnetic field range at a fixed temperature. However, relaxometry is generally not feasible for most solid materials, and so relaxation studies generally involve measurements at fixed magnetic fields as a function of temperature, with the associated risk that the nature of the dynamics may change over the temperature range, e.g., as phase transitions are approached.

In favorable cases, it is possible to obtain data points either side of the "T_1 minimum", that is, either side of the point where the dynamic process is most efficient for driving the nuclear spin relaxation. Figure 25.6 shows a relatively unusual case where two distinct T_1 minima, due to different motional processes, were observed. Given suitable approximate models, e.g., an n-site jump, the results can then be fitted to derive not only an activation barrier for the process, but also the absolute values of jump rates as a function of temperature. In the majority of cases, the sample and/or equipment limits the temperature range that can be explored, and often only one side of the T_1 minimum can be characterized. Unless the relaxation data are being fitted to a full model of the relaxation (which would be extremely challenging for solid materials), the information that can be readily extracted is then limited to the activation barrier. This is determined from the temperature dependence of the relaxation rates. Specifically, the relaxation *rate* constant, $R_1 = 1/T_1$, in the limits either side of the minimum is proportional to τ_c (slow limit) and $1/\tau_c$

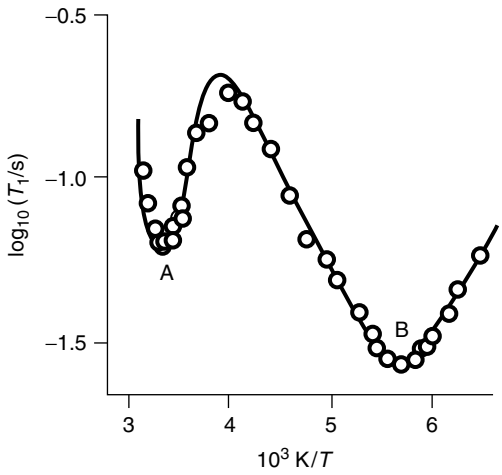


Figure 25.6. Proton T_1 values for solid trimethylphosphine sulfide as a function of temperature, showing minima for two independent molecular motions: minimum A corresponds to overall rotation about the molecular axis, while minimum B is associated with internal rotation of the methyl groups about the C–P bonds. (Figure adapted from Ref. 4.)

(fast limit), where τ_c is the motional correlation time. If we assume that the temperature dependence of τ_c follows Arrhenius behavior, $\tau_c = \tau_0 \exp(-E_a/RT)$, then the empirical activation barrier, E_a, can be simply derived from the magnitude of the gradient of a plot of $\ln R_1$ against inverse temperature. Note in Figure 25.6, how the minimum, B, for the more facile process (methyl group rotation) is less steep, i.e., has a lower activation barrier. Deviations from linear behavior imply that the motion is not a simple thermally activated process that can be described by a single correlation time.

It is often difficult to determine absolute rate constants for the dynamic process in the fast exchange limit since only a single data point (or very limited number of data points) is measured at a given temperature (in contrast to experiments in which entire bandshapes can be fitted). But the temperature dependence of any metric, such as relaxation rate, which is directly related to jump rate can still be used to determine activation barriers. Moreover, in cases where the same motional process is dominant over a wide timescale, it may be possible to use absolute information on jump rates from slow and intermediate regimes to "calibrate" measurements in the fast motional limit.[11]

25.4.1.2 Fast Dynamics from Abundant Spin-$\frac{1}{2}$ Nuclei

Spin-lattice relaxation times can be measured relatively efficiently for high-receptivity abundant nuclei, such as ^{1}H, ^{19}F, and ^{31}P. Although classic solution-state NMR methods, such as the inversion recovery experiment, are useful for highly mobile components, saturation recovery techniques can be applied for systems (such as solids) where the (phenomenogical) T_2 describing the decay of *xy* magnetization is invariably much shorter than T_1. This is particularly useful for samples with long T_1 values since there is no need to wait for the *z*-magnetization to recover between acquisitions.

Spectral resolution may be limited, of course, by strong homonuclear dipolar couplings. Moreover, for ^{1}H especially, efficient "spin diffusion" between the spins due to the dipolar couplings means that all but the most isolated spins generally relax with a common rate, which is determined by relaxation sinks such as rotating methyl groups. As a result, the dynamics cannot be localized to individual parts of a molecular system. Note that care is also required when the system is heterogeneous, since spin diffusion between the different domains may complicate the analysis of the relaxation data;[23] there are several examples in the literature of overinterpreted ^{1}H relaxation experiments.

25.4.1.3 Fast Dynamics from Dilute Spin-$\frac{1}{2}$ Nuclei

Dilute spins such as ^{13}C and ^{15}N are well suited to high-resolution spectroscopy, but are less suited to the study of dynamics in the fast exchange limit since measuring relaxation times for less receptive nuclei is generally very time consuming. However, the resolution of dilute spin solid-state NMR spectra and the lack of spin diffusion between dilute spins generally allows separate T_1's to be determined for each site. Figure 25.7 shows how dilute spin T_1's can be used to estimate separate activation barriers for two methyl groups that cannot be not resolved in the ^{1}H spectrum. Measurement of T_1 values for the sites further away from relaxation sinks (such as methyl groups) may be complicated by the effects of spin diffusion between the protons; unless the protons spin system can be decoupled during the relaxation delays (which are generally too long for this to be practical), multiexponential relaxation may be observed.[22]

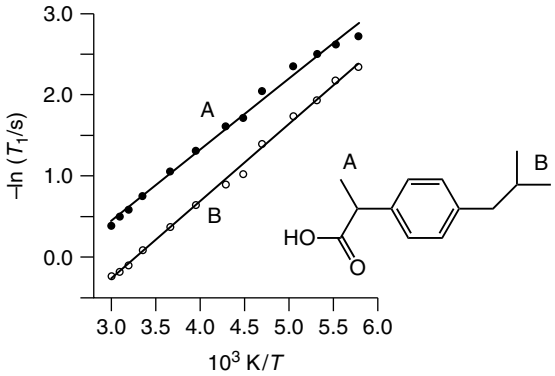


Figure 25.7. Arrhenius-type plot of ^{13}C T_1 values as a function of temperature for the resolved methyl groups, A and B, of solid ibuprofen obtained using the pulse sequence introduced by Torchia.[24] The short ^{1}H T_1 values of the methyl groups greatly facilitate the data acquisition in this case—only 15 min of spectrometer time was required to measure each pair of ^{13}C T_1's.

25.4.1.4 Fast Dynamics from Quadrupolar NMR

The quadrupolar interaction is a potentially valuable probe of dynamics since it only depends on the immediate environment of an individual nucleus (specifically electric field gradients at the nucleus) in contrast, for example, to dipolar interactions, which depend on the relative positions of pairs of nuclei. On the other hand, if quadrupolar couplings are very large, the lifetime of nuclear spin coherences will be extremely short for very mobile components (due to rapid quadrupole-driven relaxation) or the linewidths will be extremely broad (for less dynamic systems). Hence most studies of dynamics in solids use nuclei such as ^{2}H and $^{6/7}$Li, whose quadrupole moments are relatively small.[25,26] ^{2}H is particularly useful in the context of organic solids since it is often easy to introduce at sites of interest, e.g., labile H-bonded protons or included solvent molecules. As a result, deuterium T_1 values have been widely used to study fast timescale dynamics in solids.

Relaxation for half-integer quadrupolar spins, such as ^{17}O ($I = 5/2$), is much more complex, since multiple spin states are involved and so the relaxation behavior is intrinsically multiexponential. However, quantitative information on activation barriers can still be deduced from the temperature dependence of T_1.[11]

25.4.2 Slow Dynamics

Typical processes: dynamics involving bond breaking or significant structural rearrangement.

The timescale limit for NMR is ultimately set by spin-lattice relaxation. This is usually slow in solid materials (seconds in typical organic solids and much longer in highly rigid systems), allowing processes that are extremely slow (by the standards of other techniques) to be observed by solid-state NMR. In solution-state NMR, where anisotropic interactions are averaged away by molecular tumbling, exchange effects are limited to jumps between nonequivalent sites (i.e., with different isotropic chemical shifts). In contrast, solid-state NMR is also directly sensitive to reorientational processes, which only modulate the anisotropic component of interactions.

25.4.2.1 Resolved Sites

In this limit, classical magnetization transfer experiments such as saturation transfer and EXSY canbe readily applied to solids. This is illustrated in Figure 25.8 for the proton shift and rearrangement of solid tropolone. Similar proton shift and ring rearrangement processes in polymorphic drug systems have also been characterized by ^{15}N EXSY.[27] Such use of EXSY for the qualitative study of slow dynamic processes is relatively straightforward. Care is required in *quantitative* applications if the sites

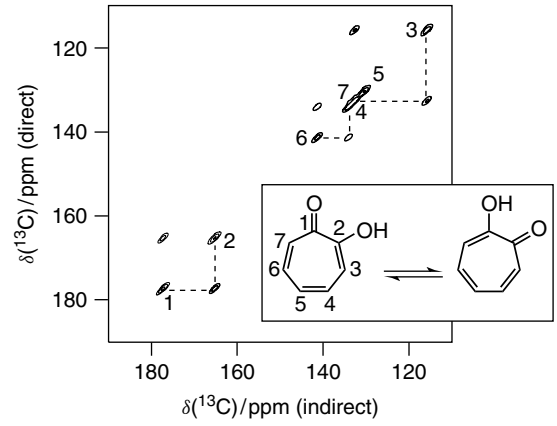


Figure 25.8. A ^{13}C EXSY spectrum from solid tropolone obtained at 30 °C and with a mixing time of 3 s. Dashed lines link peaks related by the exchange process. Example based on Ref. 29.

are associated with a spinning sideband manifold in MAS experiments; unless the mixing time for magnetization transfer is synchronized to a multiple of the rotation period, then the transfer efficiency will be additionally modulated by the spinning. Since the magnetization transfer periods are, by definition, relatively long, active synchronization with the sample rotation is therefore required in such cases.[28]

In the absence of competing transfer mechanisms, such as "spin diffusion" or the NOE, the rate at which magnetization is transferred between sites can simply be identified with the rate of the underlying dynamic processes i.e., a motional model is not required to extract quantitative information. Note that competing mechanisms of magnetization transfer will be largely independent of temperature and so variable temperature experiments can be used to verify that the magnetization transfer is genuinely associated with a dynamic process.

25.4.2.2 Unresolved Sites

Simple magnetization transfer experiments cannot be applied if the isotropic chemical shift is unaffected by the dynamic process, e.g., for reorientations between equivalent sites. However, the anisotropic components of the NMR parameters will be modulated by the dynamics. Hence two-dimensional EXSY-type experiments can show off-diagonal intensities corresponding to sites that have changed orientation during the mixing time. 2-D exchange experiments using ^{2}H NMR under static conditions have, for example, been widely used to study dynamics of polymer samples.[26] The^{13}C CSA is also a valuable probe of dynamics, but magic-angle spinning is necessary in this case for sensitivity reasons, and evidence for exchange is sought from the pattern of off-diagonal sidebands. Careful experimentation is required, however, to produce spinning sidebands that are both in phase and whose intensities are determined only by the exchange dynamics (rather than modulated by the sample spinning).

Two-dimensional experiments are useful for distinguishing between different models of the motional process, since the pattern of off-diagonal intensity is a function of the nature of the exchange process. However, acquiring a series of such 2-D experiments as a function of mixing time in order to extract jump rates is often prohibitively time consuming, and numerous experiments have been devised that allow reorientational dynamics to be studied using just a series of one-dimensional experiments.[30] For example, the centerband only detection of exchange experiment (CODEX) simply involves measurement of centerband intensities as a function of a mixing period. Although less sensitive than full 2-D techniques to the details of the dynamic model, it is often still possible to distinguish between extremely different models of the underlying process.

25.4.3 Intermediate Timescale Dynamics

Typical processes: hindered jumps, e.g., phenylene ring flips, conformational exchange e.g., chair-chair interconversion.

Dynamics on the timescale of the spectral width will have direct effects on the NMR spectrum. In general, analysis requires a full "bandshape analysis", i.e., fitting of the complete spectrum using analytical formulae, or, more generally, numerical simulation of the NMR spectrum.[19,31] Parameters, such as exchange rates, are iteratively adjusted to obtain optimal agreement with the experimental spectrum. This can be quite demanding, particularly if NMR frequencies are also time-dependent due magic-angle spinning, and it may be simpler to restrict attention to the fast and slow exchange limits of this range, and measure the line broadening due to the exchange process.

25.4.3.1 Spectral Fitting

Static ^{2}H lineshapes have been widely used to study dynamics on the kilohertz timescale.[25,32] The spectra can be fitted to extract jump rates, but different motional mechanisms generally have distinct effects on the overall lineshape, potentially allowing distinct motional mechanisms to be distinguished. A number of established computer codes[25] is available for such simulations.

If anisotropies have been effectively suppressed by magic-angle spinning, fitting exchange between sites of different isotropic frequencies will be straightforward since standard solution-state codes can be used. In contrast, fitting spinning sideband manifolds that are influenced by exchange effects is considerably more challenging, since more than one mechanism can contribute to the spectral appearance; the direct effect of chemical exchange, and interference between the dynamics and the magic-angle spinning and (if relevant) ^{1}H decoupling. There are currently no widely available general codes for such simulations.

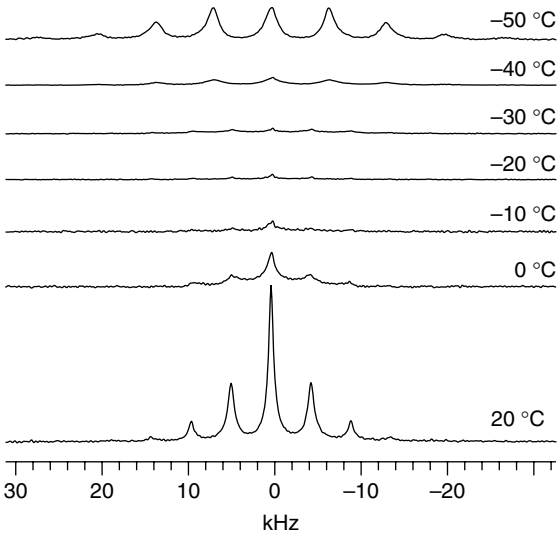


Figure 25.9. ^{2}H MAS spectra of the finasteride. d_8-1,4-dioxane solvate (see Figure 25.8) as a function of temperature. The interference between conformational exchange and sample spinning is maximal around $-20\,^\circ$C. Either side of this point, the broadening due to the interference can be quantified to estimate an activation barrier and absolute exchange rates (slow exchange side).

25.4.3.2 Analysis of Fast/Slow Limits

Although full spectral fitting can provide the most complete and accurate insight into the rate and nature of the dynamic process, it may be sufficient to quantify the line-broadening due to exchange. For example, if the intrinsic linewidth is assumed to be independent of temperature, then the activation barrier can be determined simply from the variation of linewidth with temperature.

These approaches are most applicable when the intrinsic linewidth is small, e.g., for MAS spectra. For example, reorientational processes on the kilohertz timescale can conveniently be studied using ^{2}H MAS spectra,[33,34] as illustrated in Figure 25.9.

25.4.3.3 $T_{1\rho}$ Relaxation

In the usual situation in solids where $T_{1\rho}$ time constants are much shorter (typically millisecond) than T_1 values, the rate of $T_{1\rho}$ relaxation is simply determined by the spectral density at the nutation frequency of the RF used for the spin lock. Hence the measurement of $T_{1\rho}$ relaxation time constants is often a convenient route for probing processes occurring on the kilohertz frequency scale. The principles are essentially the same as using T_1 relaxation to probe motion at the nuclear Larmor frequencies, but the impact of spin diffusion between the protons may be less marked since $T_{1\rho}$ values are generally much shorter; different $T_{1\rho}$ values may well be obtained for ^{1}H sites that are resolved under fast magic-angle spinning, potentially allowing dynamic behavior to be localized.

25.5 OVERVIEW

It is evident from even this very rapid survey of techniques to probe motion on different timescales that NMR is a particularly useful and powerful probe for the characterization of dynamics in solids, especially crystalline solids. Approximate rates can be deduced simply from the timescale of the experiment in which the effects are observed, accurate estimates of activation barriers are straightforward to deduce from their temperature dependence, and absolute values of jump rates can often be readily extracted. In cases where the complete spectral form is being modeled, it may be possible to determine the nature of the motional mechanism, or, rather, distinguish between plausible scenarios.

The utility of such studies is likely to increase as advances in MD techniques allow longer timescale processes to be examined. Such simulations are strongly complementary to experimental NMR measurements since it is often impossible to deduce the nature of the dynamic process on the basis of NMR data alone. Although classic MD techniques are limited to simulations over a few nanoseconds, which are only sufficient to fully capture fast motions on the timescale of the nuclear Larmor frequency, rapid progress is being made in developing techniques to characterize the relatively slow processes that can be probed via NMR.

REFERENCES

1. B. T. M. Willis and A. W. Pryor, *Thermal Vibrations in Crystallography*, Cambridge University Press, 1975.
2. H.-B. Bürgi and J. D. Dunitz, *Acc. Chem. Res.*, 1983, **16**, 153.

3. K. D. Hammonds, M. T. Dove, A. P. Giddy, V. Heine, and B. Winkler, *Am. Mineralogist*, 1996, **81**, 1057.
4. R. K. Harris, *NMR Spectroscopy—A Physicochemical View*, Longman Scientific & Technical, 1991.
5. R. Tycko, in *Nuclear Magnetic Resonance Probes of Molecular Dynamics*, ed R. Tycko, Kluwer Academic Publishers, 1994, Chapter 1.
6. P. Diehl, in *NMR of Liquid Crystals*, ed J. W. Emsley, Reidel, 1985.
7. E. R. Henry and A. Szabo, *J. Chem. Phys.*, 1985, **82**, 4753.
8. Y. Ishii, T. Terao, and S. Hayashi, *J. Chem. Phys.*, 1997, **107**, 2760.
9. G. McGeorge, R. K. Harris, A. S. Batsanov, A. V. Churakov, A. M. Chippendale, J. F. Bullock, and Z. Gan, *J. Phys. Chem. A*, 1998, **102**, 3505.
10. A. J. Horsewill, *Prog. NMR. Spectrosc.*, 1999, **35**, 359.
11. M. R. Hampson, J. S. O. Evans, and P. Hodgkinson, *J. Am. Chem. Soc.*, 2005, **127**, 15175.
12. J. Fatah, J. M. Twyman, S. J. Heyes, D. J. Watkin, A. J. Edwards, K. Prout, and C. M. Dobson, *J. Am. Chem. Soc.*, 1993, **115**, 5636.
13. J. M. Twyman and C. M. Dobson, *J. Chem. Soc. Chem. Commun.*, 1998, 786.
14. P. A. Beckmann, *Phys. Rep.*, 1988, **171**, 85.
15. W. P. Rothwell and J. S. Waugh, *J. Chem. Phys.*, 1981, **74**, 2721.
16. P. Hodgkinson, *Prog. NMR Spectrosc.*, 2005, **46**, 197.
17. P. Jackson and R. K. Harris, *J. Chem. Soc. Faraday Trans.*, 1995, **91**, 805.
18. D. E. McMillan, P. Hazendonk, and P. Hodgkinson, *J. Magn. Reson.*, 2003, **161**, 234.
19. A. D. Bain, *Prog. NMR Spectrosc.*, 2003, **43**, 63.
20. M. J. Duer, in *Solid-State NMR Spectroscopy: Principles and Applications*, ed M. J. Duer, Blackwell Science, 2002, Chapter 6.
21. D. Reichert, *Ann. Rep. NMR Spectrosc.*, 2005, **55**, 159.
22. R. K. Harris, *Analyst*, 2006, **131**, 351.
23. A. M. Kenwright and B. J. Say, *Solid-State Nucl. Magn. Reson.*, 1996, **7**, 85.
24. D. A. Torchia, *J. Magn. Reson.*, 1978, **30**, 613.
25. R. R. Vold, in *Nuclear Magnetic Resonance Probes of Molecular Dynamics*, ed R. Tycko, Kluwer Academic Publishers, 1994, Chapter 2.
26. K. Schmidt-Rohr and H. W. Spiess, *Multidimensional Solid-State NMR and Polymers*, Academic Press, 1994.
27. M. Bauer, R. K. Harris, R. C. Rao, D. C. Apperley, and C. A. Rodger, *J. Chem. Soc. Perkin Trans. 2*, 1998, 475.
28. A. F. de Jong, A. P. M. Kentgens, and W. S. Veeman, *Chem. Phys. Lett.*, 1984, **109**, 337.
29. N. M. Szeverenyi, A. Bax, and G. E. Maciel, *J. Am. Chem. Soc.*, 1983, **105**, 2579.
30. Z. Luz, P. Tekely, and D. Reichert, *Prog. NMR Spectrosc.*, 2002, **41**, 83.
31. J. Sandström, *Dynamic NMR Spectroscopy*, Academic Press, 1982.
32. R. R. Vold and R. L. Vold, *Adv. Magn. Opt. Reson.*, 1991, **16**, 85.
33. S. Vega, in *Nuclear Magnetic Resonance Probes of Molecular Dynamics*, ed R. Tycko, Kluwer Academic Publishers, 1994, Chapter 4.
34. M. Cutajar, S. E. Ashbrook, and S. Wimperis, *Chem. Phys. Lett.*, 2006, **423**, 276.

Chapter 26
Structural Phase Transitions

Kenneth R. Jeffrey and Glenn H. Penner

Department of Chemistry, University of Guelph, Guelph, Ontario N1G 2W1, Canada

26.1	Introduction	387
26.2	The Classification of Phase Transitions	388
26.3	NMR Identification of Phase Changes	395
26.4	The Landau Theory	400
26.5	Pure Quadrupole Resonance	404
26.6	Dynamics at Structural Phase Transitions	404
26.7	Summary	410
	References	411

26.1 INTRODUCTION

This article discusses the application of NMR spectroscopy to the study of structural solid–solid phase transitions. Magnetic phase transitions and transitions involving incommensurate phases are not considered.

Magnetic resonance has proven to be a powerful tool for the study of solid–solid phase transitions. Over 100 magnetic nuclear isotopes can be observed at natural abundance, which allows one to probe different atomic sites of interest during the course of a phase transition. Indeed, a study of solid–solid phase transitions was reported just three years after the appearance of the first papers on NMR spectroscopy.[1]

NMR lineshapes in solids are dominated by a combination of the quadrupolar (Q), magnetic shielding anisotropy (SA) (or chemical shift anisotropy (CSA)), and dipole–dipole (DD) interactions. The anisotropic nature of these interactions is strongly affected by the site symmetry and motional dynamics of the atom. In addition to lineshapes, a variety of relaxation times can be measured. These include spin-lattice relaxation of the Zeeman energy of the spin system, T_{1Z}, spin-lattice relaxation of the quadrupolar energy (nuclear spin $I > 1/2$), T_{1Q}, spin-lattice relaxation in the rotating frame, $T_{1\rho}$, and the spin–spin relaxation time, T_2. Using stimulated echo techniques, it is possible to measure correlation times, τ_c, associated with atomic motion in the ultraslow region, where the correlation time, τ_c, is much greater than the reciprocal of the nuclear spin interaction expressed in frequency units.[2] A wide range of motional timescales ($10^{-1} - 10^{-12}$ s) can be investigated via the associated changes in lineshapes and relaxation times.

At a phase transition there are often significant changes in the macroscopic properties of a substance such as density, molar volume, heat capacity, and conductivity, which can have a profound effect on the usefulness of that substance for a particular application. Properties such as ferroelectricity, piezoelectricity, elastic constants, thermal expansion, etc., often significantly change at a phase transition. Materials may have very useful properties in one phase but not in others. Bulk properties and how they are affected by phase transitions have been studied for centuries; however, a fundamental understanding of the phase transition requires knowledge of what is happening at the microscopic level. NMR spectroscopy is ideally positioned to help the

NMR Crystallography Edited by Robin K. Harris, Roderick E. Wasylishen and Melinda J. Duer © 2009 John Wiley & Sons, Ltd. ISBN: 978-0-470-69961-4

experimentalist study phase transitions at the atomic level. The study of structural phase transitions is important not only from the prospective of the scientific interest in the mechanisms of phase transition but also from a material science point of view.

The purpose of this article is to provide an overview of how phase transitions can affect observable NMR parameters and how NMR spectroscopy can be used to investigate the nature of solid–solid phase transitions. An emphasis is placed on structural phase transitions and the changes in site symmetry and molecular dynamics that accompany these phase transitions.

The application of NMR spectroscopy to the study of solid–solid phase transitions has been extensively reviewed by Odin,[3] Rigamonti,[4] and Bjorkstam.[5] The reader is also referred to the monographs *Magnetic Resonance of Phase Transitions*, edited by Owens *et al*.[6] and *Soft Modes in Ferroelectrics and Antiferroelectrics* by Blinc and Žekš.[7]

26.2 THE CLASSIFICATION OF PHASE TRANSITIONS

Phase transitions have been classified in many different ways. It is useful to summarize some of these ideas.[8]

26.2.1 The Ehrenfest Classification

This classification scheme[9] considers the behavior of the Gibb's free energy, G, at the phase transition. If the first derivatives of G with respect to the temperature and pressure $S = (\partial G/\partial T)_P$ and $V = (\partial G/\partial P)_T$ are discontinuous, the phase transition is considered to be of first order. These transitions are distinctive because there is a latent heat resulting from an enthalpy change and an abrupt volume change. At second-order phase transitions, the second derivatives of G; the heat capacity, the linear expansion coefficient, and the compressibility $C_P = T(\partial^2 G/\partial T^2)_P$ $\alpha = 1/V(\partial^2 G/\partial T \partial P)$ and $\beta = 1/V(\partial^2 G/\partial P^2)_T$ are discontinuous while there is no abrupt change in the volume or a latent heat.

26.2.2 Reconstructive, Displacive, and Order–Disorder Phase Transitions

At a *structural* phase transition, there is a change in the crystal symmetry so that some of the symmetry elements of the high-symmetry phase (usually the high-temperature phase) are missing in the low-symmetry phase. The occurrence of symmetry breaking from the high-to-low symmetry phase is an essential characteristic of a structural phase transition and is associated with certain displacements of the atoms in the crystal. These displacements, often referred to as a *distortion of the high-temperature phase*, are the order parameter describing the phase transition. At a continuous phase transition, the distortion taking place in the low-symmetry phase continuously decreases to zero upon approaching the high-symmetry phase. At a discontinuous or first-order phase transition, there may be a discontinuous change of the order parameter at the transition.

In a *reconstructive* phase transition, strong primary (first-coordination shell) chemical bonds are broken and reconstructed. The transition is first order in the Ehrenfest sense with the occurrence of discontinuous enthalpy and volume changes. Characteristics of first-order transitions such as the coexistence of phases at equilibrium, hysteresis, and metastability are often observed. The space group symmetries of the phases on either side of the transition, G_H and G_L, are not related.[7,10] Any kinetic mechanism for the transition must be based on an intermediate structure whose space group is a subgroup of the two space groups G_1 and G_2. The intermediate state transforms from G_1 into G_2 according to the change of some kinetic order parameter.

Weaker secondary chemical bonds are rearranged during *displacive* phase transitions but the atomic displacements are small as compared to interatomic spacings. The enthalpy and volume changes are small or vanishing so that the phase transition is second order or weakly first order. Cochran[11] and Anderson[12] suggested that displacive transitions are the result of an instability in the crystal against a particular normal mode of vibration in the high-temperature phase. There is now overwhelming evidence for these so-called "soft modes" and their role in displacive phase transitions.[13] When a normal mode frequency decreases due to anharmonic effects upon cooling, there is the possibility that it will become zero at a certain temperature. At that point, the crystalline lattice becomes unstable and undergoes a phase transition to a new stable phase. The mode is called *soft* because the frequency has decreased and the restoring forces have weakened. This concept can be

summarized with the basic relationship

$$\overline{\omega}^2(\boldsymbol{k}_c) = K(T - T_c) \qquad (26.1)$$

When T is below T_c, the imaginary value for $\overline{\omega}$ indicates the instability. The critical wave vector $\boldsymbol{k}_c$ of the soft mode is a high-symmetry point in the first Brillouin zone (at the zone center or boundary) if the transition is to a commensurate phase and $\boldsymbol{k}_c$ measures the phase difference among the atomic displacements from one unit cell to the other. If the instability occurs at the Brillouin zone center $\boldsymbol{k}_c = 0$, the distortion is ferrodistortive and there is no change in the number of atoms in the unit cell at the phase transition. If $\boldsymbol{k}_c \neq 0$, the magnitude and direction of $\boldsymbol{k}_c$ determine the size of the new unit cell. The distortion taking place is referred to as *antiferrodistortive*. There is also a soft mode in the low-temperature phase, which increases in frequency on further cooling.

The low-symmetry structure is a small modification of the high-symmetry phase caused by a distortion corresponding to the eigenvector of the soft mode. The stable low-symmetry structure is equivalent to the high-symmetry structure that remains frozen in normal mode coordinates of wave vector $\boldsymbol{k}_c$ corresponding to the soft mode. It can be shown that the soft mode theory is essentially equivalent to the Landau theory of structural phase transition at least as far as thermal dynamic properties are concerned.[7]

26.2.2.1 Example: K_2ReCl_6

An excellent example of soft modes occurs in the antifluorite crystals, which have been explored extensively by Armstrong *et al*.[14] The antifluoride materials have the chemical formula A_2MX_6 with M being a metal ion, A, an alkali or ammonium ion, and X a halide ion.[14] The bonding within the polyatomic $[MX_6]^{2-}$ ion is much stronger than the ionic interaction between the A^+ and the $[MX_6]^{2-}$. The high-temperature cubic phase structure shown in Figure 26.1 is the same as that for CaF_2, where the $[MX_6]^{2-}$ replaces the Ca^{2+} ion and the A^+ replaces the F^- ion. The $[MX_6]^{2-}$ ions form a face-centered cubic lattice with the six surrounding X atoms situated on the cubic axes at a distance d from the M atom. The A^+ ions are located at eight positions interior to the unit cell. The Brillouin zone is the truncated octahedron shown in Figure 26.2. The locations of important high-symmetry points (Γ, X, K, L) as well as the general points (Δ, Λ, Σ) along the high-symmetry directions are indicated.

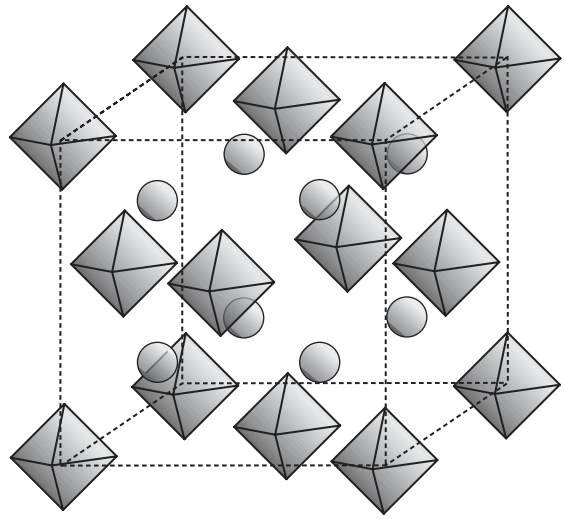


Figure 26.1. Schematic representation of the A_2MX_6 antifluorite structure. The circles depict the A^+ ions and the octrahedra represent $MX_6{}^{-2}$ ions with the M atoms at the center and X atoms at the corners. The $MX_6{}^{-2}$ ions occupy a face-centered cubic lattice.

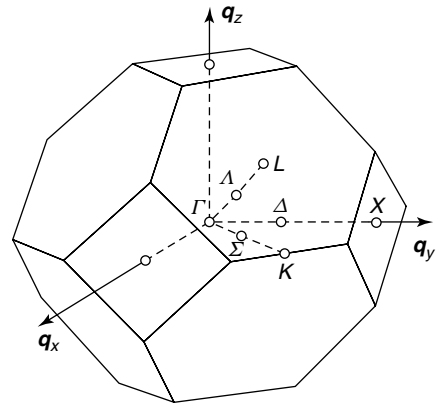


Figure 26.2. The Brillouin zone for the *Fm*3*m* space group, which is a truncated octrahedron. Wave vectors in the x, y, and z directions are denoted as $\boldsymbol{q}_x$, $\boldsymbol{q}_y$, and $\boldsymbol{q}_z$. The high-symmetry points (Γ, X, K, L) and the general points (Δ, Λ, Σ) along high-symmetry directions are shown.

Many of the A_2MX_6 compounds have displacive structural phase transitions and K_2ReCl_6 has transitions at 111, 103, 76, and 12 K.[15] The first two

are of particular interest. The high-temperature phase is cubic as described above for the general A_2MX_6 structure. The chlorine nuclei are situated at sites where the time-averaged electric field gradient is nonzero. It is possible to measure the pure chlorine nuclear quadrupole resonance (NQR) frequencies very accurately and detect any small distortion on the crystalline lattice. The temperature variation of the ^{35}Cl (spin $I = 3/2$) NQR frequencies in K_2ReCl_6 is shown in Figure 26.3.[15]

Above 111 K in the cubic phase, there is only one line observed; the $\pm 3/2$ to $\pm 1/2$ transition for all six chlorines in the $ReCl_6$ octahedron. An X-ray diffraction study[16] of K_2ReCl_6 has shown that at 111 K, the structure changes from cubic ($Fm3m$, $Z = 1$) to tetragonal ($I4/m$, $Z = 1$) and at 103 K, the structure becomes monoclinic ($B2/6$, $Z = 4$). At 111 K, the transition to the tetragonal phase results in two NQR lines, which have the intensity ratio of 2:1. Below 103 K, three lines of equal intensity are observed. The 111 K transition is the result of a soft rotary lattice mode and the rotation of the octahedron about one of the cubic axes is the order parameter. The X-ray experiment was unable to measure the rotation angle of the $[ReCl_6]^{2-}$ ion below the 111 K transition because of the formation of multiple domains. There is also a small tetragonal distortion, which results in a ratio of the long to the short axes of 1.003.

The measurement of the order parameter as a function of temperature in the low-symmetry phase is an important first step in understanding the mechanism of the phase change. There have been numerous examples of measurements of NMR parameters, which are related to the order parameter.[3–5] It is, however, rarely the case where NMR results directly measure the order parameter. In most cases, the NMR parameter measured is linearly or quadratically coupled to the order parameter. One case where a direct measurement was made was the determination of the torsional angle of the MX_6 octahedron in the antifluorite K_2ReCl_6.[14] The rotation of the octahedron about one of the cubic axes has been successfully measured using Zeeman perturbation of the NQR spectra.[17]

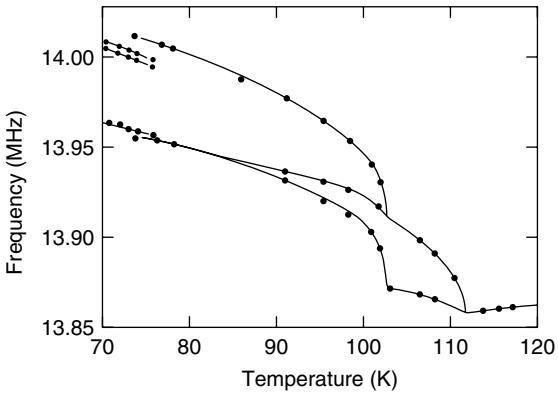


Figure 26.3. The pure quadrupole resonance frequencies as a function of temperature for K_2ReCl_6.

When a single crystal of K_2ReCl_6 is placed in a magnetic field, the degeneracy in the pure quadrupole levels is removed. In the case of $I = 3/2$, the transition frequencies between the Zeeman split states are given by[14]

$$\nu = \nu_{NQR} \pm \left(\frac{\gamma B_0}{2\pi}\right) \cos\theta[3 - (1 + 4\tan^2\theta)^{1/2}] \tag{26.2}$$

where ν_{NQR} is the pure quadrupole resonance frequency, and θ is the angle between the direction of the applied magnetic field and the symmetry axis of the electric field gradient. The $+$ sign refers to the $-3/2 \leftrightarrow 1/2$ transition while the $-$ sign refers to the $3/2 \leftrightarrow 1/2$ transition.

As a first approximation, the electric field gradient at the chlorine nuclear site is a result of the Re–Cl bonding. Although below $T_c = 111$ K, the site symmetry at the chlorine nucleus is no longer C_{4v} and the interaction is no longer axially symmetric, it is reasonable to assume that equation (26.2) is still valid in the tetragonal phase and that $\theta = 0$ corresponds to the magnetic field being aligned parallel to the Re–Cl bond. Therefore, the observation of the NMR frequencies as a function of field provides an accurate method of locating the principal axes of the electric field gradient, that is, the orientation of the Re–Cl bond.

In the cubic phase above T_c, the ^{35}Cl resonance line having the frequency given by equation (26.2) with the $+$ sign was observed. The frequency was fixed and magnetic field varied to obtain the resonance. As the crystal was rotated about the [010] and [001] directions, the center of the resonance traced out the curves described by the $\cos\theta[3 - (1 + 4\tan^2\theta)^{1/2}]$ factor. The minima of the two curves established the position of the crystal when the magnetic field was aligned along the Re–Cl bond.

Below T_c, the single resonance found above T_c was replaced by two. As the crystal was rotated about the [001] direction, the upper field line moved further upfield while the lower field line split as shown

in Figure 26.4. The upper field line is identified with those chlorine nuclei having their Re–Cl bonds along the magnetic field direction; the lower field line with the chlorine nuclei associated with Re–Cl bonds that have rotated by angles of $\pm\varphi$ away from their high-temperature equilibrium positions in the (001) plane. The dashed lines in Figure 26.4 are the least squares fits of equation (26.2) to the data. From Figure 26.4, it is determined that at 106 K, the rotation angle of the $ReCl_6$ octahedra and therefore the order parameter is about 3.1°.

When the structural differences between the high- and low-symmetry phases are related to different chemical occupations of the same crystallographic sites which in turn lead to different symmetry groups in the two phases, the transition is termed as *order–disorder*. The structural phase transition is again second or weakly first order with small or negligible enthalpy and volume changes.

There are two main categories of disorder in solids: (i) disorder in position and (ii) disorder in orientation. Disorder in position occurs when there are more sites that will accommodate a particular atom in the unit cell than there are atoms to fill the sites. An example is lithium lanthanum titanate. This perovskite material will allow the substitution of one La^{3+} for three Li^+ ions creating a two vacant lithium sites in the lattice.[18] Another well-studied example is a large group of materials having the KH_2PO_4 structure, where each PO_4 group is linked to four neighboring PO_4 groups by O–H–O hydrogen bonds. Each hydrogen atom can, in principle, take one of two possible positions.[7]

Orientationally disordered materials have diatomic or polyatomic ions or molecules at particular lattice sites in the unit cell.[19] However, these atomic groups have access to two or more possible orientations, which are distinguishable within the lattice. The λ transition in NH_4Cl is a classic case of an order–disorder phase transition, where the use of an Ising variable is quite appropriate. The two orientations shown in Figure 26.5 are assigned the values $\sigma = \pm 1$ and the order parameter ψ is just the average value of σ over the whole sample. Dynamics often play a critical role in order–disorder phase transitions, but the timescale for the motion is much slower that in the case of soft modes in displacive transitions. For example, in NH_4Cl, the reorientation of the ammonium ion is fundamental to the order–disorder transformation at T_λ. NMR is uniquely suited to monitor the dynamics in these situations because of its sensitivity to slow motions on the order of the reciprocal of the Larmor processional frequency or less. The dynamics of the ammonium ions in NH_4Cl is discussed later in the Section 26.6.2.

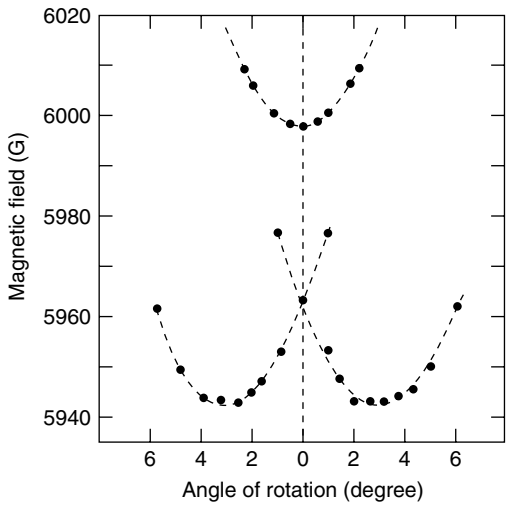


Figure 26.4. The resonance magnetic field as a function of the angle of rotation of a K_2ReCl_6 single crystal at 106 K. The value $\theta = 0$ corresponds to the symmetry position above $T_c = 111$ K.

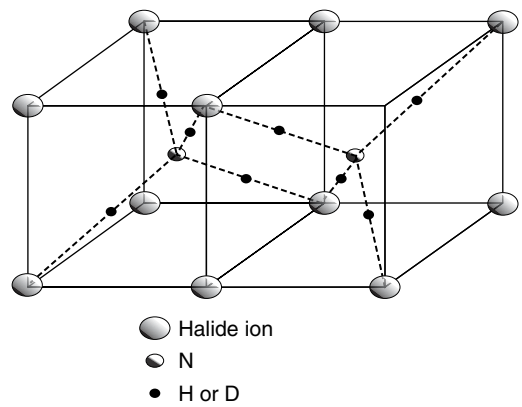


Figure 26.5. The crystal structure of the ammonium halides in the β phase. The two possible orientations of the NH_4^+ ions within the cage of surrounding halide ions are shown. In the β phase, there is a 50% probability of either orientation within any particular cage.

26.2.3 NMR Evidence of Mixed Order–Disorder/Displacive Phase Transitions

At first glance, it might appear that a phase transition cannot be both displacive and order/disorder. Phase transitions can be a mixture of the two and this has been demonstrated for a number of solids.[20] During the past decade, NMR spectroscopy has been used to investigate the coexistence of order–disorder and displacive behavior in a number of phase transitions.

Because the isotropic chemical shift (CS), δ_{iso}, is invariant with respect to rotation and translation, an order–disorder phase transition should not be accompanied by a change in δ_{iso}. On the other hand, a change in δ_{iso} would imply that the phase transition has a displacive contribution. However, it should be pointed out that the change in δ_{iso} during a phase transition may be so small that it can not be measured. Therefore, obtaining the highest resolution in an MAS experiment is of utmost importance when using the magnetic shielding interaction to investigate the displacive nature of a phase transition.

26.2.3.1 Example: Squaric Acid

At ambient temperatures, squaric acid exists in an antiferroelectric phase (space group $P2_1/m$) where the C_4O_4 "squares" are held together by strong hydrogen bonds to form 2-D sheets. The hydrogen bonds are found at the corners of each of the squares (see Figure 26.6). The hydrogen atoms in each hydrogen bond are displaced such that they are covalently bonded to the oxygen of one squaric acid unit and bridge to an adjacent squaric acid oxygen via the hydrogen bond. The arrangement is of the type C–O–H···O=C. At 374 K, squaric acid undergoes a transition to a paraelectric phase (space group $I4/m$). In this phase, the hydrogen bond is symmetric to give an arrangement of the type O···H···O. The crystal structure clearly shows that in the low-temperature phase, the C_4O_4 moiety is not square but has C_1 symmetry and hence all of the carbons are not chemically and magnetically equivalent.[21] Therefore, four spectral peaks should be observed in this phase. In the high-temperature phase, the C_4O_4 unit has D_{4h} symmetry and all carbons are equivalent. As the temperature of the antiferroelectric phase increases and the phase transition temperature is approached, the order–disorder dynamics of the proton cause the ^{13}C peaks to move together and coalesce at the transition temperature. Although the CS of the individual carbons change with temperature and eventually merge, the average value of δ_{iso} will not change if the phase transition is purely order/disorder. Figure 26.7 depicts the predicted variations of δ_{iso} for carbons C_1 (C_2) and C_3 (C_4) with temperature for order–disorder and mixed order–disorder/displacive

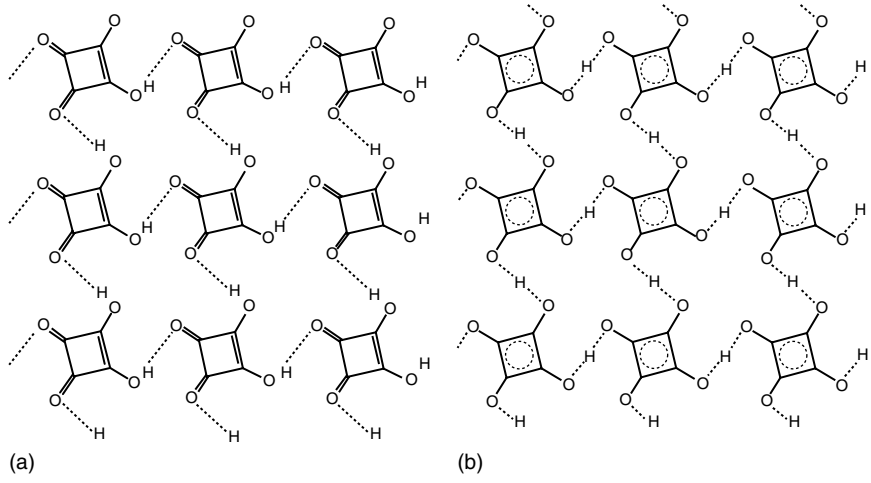


Figure 26.6. Structure of the squaric acid sheets in (a) the low-temperature antiferroelectric phase and (b) the high-temperature paraelectric phase.

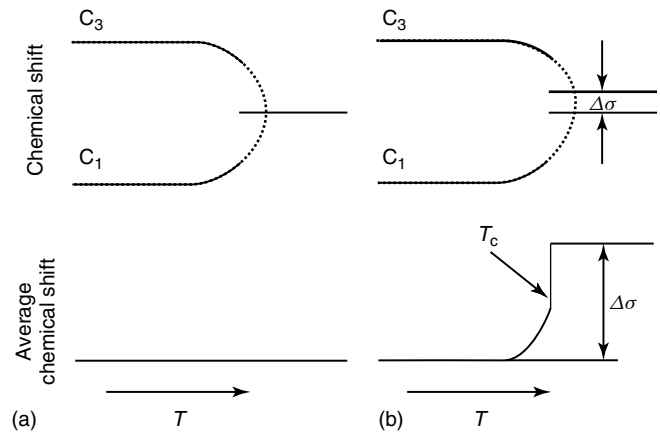


Figure 26.7. The expected change in δ_{iso} at the phase transition temperature for (a) an order–disorder transition and (b) a mixed order–disorder/displacive transition.

phase transitions. The variation of δ_{iso} with temperature follows that expected for an order parameter. The first series of ^{13}C NMR investigations of the phase transition in squaric acid were performed by Mehring and coworkers.[22–24] They observed the temperature dependence of ^{13}C peaks in a single crystal of squaric acid using cross polarization and high power proton decoupling. They fit the CS difference to an equation of the form

$$\Delta\delta = \left(\frac{T_c - T}{T_c}\right)^{\beta} \Delta\delta_0 \qquad (26.3)$$

The β value obtained was about 1/8, whereas a 3-D mean field theory predicts $\beta = 1/2$. The value of 1/8 is consistent with a 2-D Ising model.[25,26] This makes physical sense because the general Landau theory (see the Section 26.4) is based on a 3-D model whereas the squaric acid molecules form 2-D sheets in both phases. These single crystal experiments did not show any change in the average chemical shift as the sample passed through the phase transition. More recently, Dalal and coworkers used CPMAS to observe δ_{iso} and significantly improved the resolution by spinning single crystals of squaric acid.[27,28] They were able to resolve the four inequivalent carbons in the low-temperature phase and clearly demonstrated that there is a change in δ_{iso} at the phase transition supporting the coexistence of order–disorder and displacive behavior during the antiferroelectric–paraelectric phase transition in squaric acid. See Figure 26.8. This is supported by ^{17}O MAS results, also on single crystals.[29,30]

26.2.4 Ferroic Classification of Phase Transitions

The order parameter describes certain degrees of freedom of the system but these may not always have a direct relationship with the physical quantities that experimentalists measure. Measured macroscopic physical quantities such as the polarization, piezoelectric coefficients, and elastic compliance are tensors of various ranks. Although these tensors may have certain anomalies at T_c, they do not in

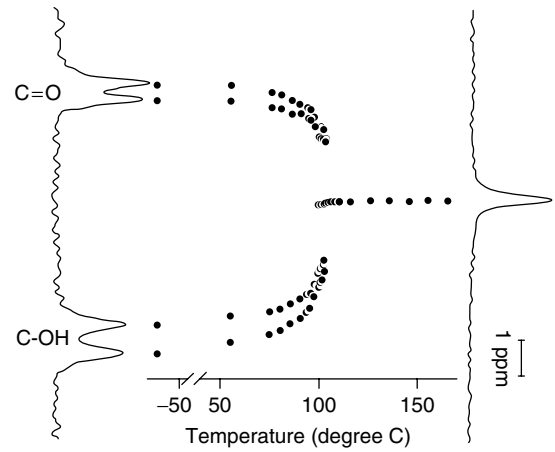


Figure 26.8. Temperature dependence of the average ^{13}C isotropic CS, δ_{iso}, near the paraelectric–antiferroelectric phase transition.

general have the same symmetry properties as the order parameters. However, some of the components of the macroscopic tensors may be secondary order parameters. The form of these tensors is entirely determined by the point group symmetry of the crystalline phases involved in the transition. The study of the change in the tensorial properties brought about by a structural phase transition must be based on the point group symmetry change across the transition. It is crucial to know the symmetry relationship between the tensorial components measured experimentally and the primary order parameter.

Tolédano and Tolédano[31] have suggested the following classification of structural phase transitions. The first division is between ferroic and nonferroic transitions. At a nonferroic transition, there is a change in translational symmetry but no spontaneous macroscopic tensor components are created. The point group symmetry remains the same in both phases and the symmetry breaking at the transition is a result of the decrease in the translational symmetry. An example of such a transition is the transformation of the space group *Pmmm* into *Fmmm*.

At a ferroic transition, there is a change in the point group symmetry (there is also the possibility of a change in the translational symmetry) and spontaneous symmetry-breaking tensor components appear. The classification of ferroics is on the basis of both crystallographic and physical changes at the transition. The crystallographic aspect refers to the change in point group symmetry while the physical aspect focuses on the nature of the physical quantity (electrical, mechanical) involved. Ferroelectrics, ferromagnetics, and ferroelastics are referred to as the *primary ferroics* and respectively correspond to the spontaneous onset of previously unallowed components of polarization (polar vector), magnetization (axial vector), and strain (second rank tensor). Because magnetic transitions are not being considered in this article, the first division in the classification scheme for ferroic phase changes is into ferroelastic and nonferroelastic transitions.

26.2.4.1 Ferroelastics

At a ferroelastic phase transition, a lattice distortion is created, which can build up into a macroscopic spontaneous strain (tensor of rank 2) and this spontaneous strain can be reoriented by an external stress. A ferroelastic crystal shows elastic hysteresis.[32,33] Raising the temperature above that of the phase transition into the paraelastic phase causes the hysteresis to disappear. Ferroelastic phase transitions are accompanied by a combination of elastic constants, which decrease to zero at the transition. This effect implies that the gradient of one of the transverse acoustic modes at wave vector $\boldsymbol{k} = 0$ falls to zero. At a ferroelastic transition, there is a change in crystal system.

One example of a ferroelastic phase transition is the phase transition that occurs in sodium azide (NaN_3) at 293 K, which is a transformation from a rhombohedral structure (β-NaN_3) with space group $R3m$ at high temperature to monoclinic (α-NaN_3) with space group $C2/m$ at low temperature.[34] Both phases have one formula weight per primitive unit cell. The primitive unit cell for the rhombohedral high-temperature structure is shown in Figure 26.9(a). The low-temperature monoclinic structure is shown as a unit cell containing two formula weights in Figure 26.9(b).

The displacements of the atoms that occur at the phase transition are shown in Figure 26.9(a). The transition mainly involves the shearing of the layers of sodium ions making the angle β in the monoclinic unit cell smaller as the temperature decreases and at the same time there is a tilting of the N_3 ion away from the trigonal axis denoted in Figure 26.9(a) as the z axis. In the β phase, the N_3 ion is aligned along the trigonal axis, whereas in the α phase, the ion has tilted away from the axis. In addition to the shearing, there is a contraction along the monoclinic a axis.[34]

The ferroelastic category can be subdivided further into pure ferroelastics where there is only a spontaneous strain created and transitions which are both ferroelectric and ferroelastic where both a spontaneous polarization (first rank tensor/axial vector) and strain appear.

26.2.4.2 Nonferroelastics

Nonferroelastic transitions are characterized by the conservation of the crystal system through the phase change. Within this category, there are ferroelectric and secondary ferroics. A ferroelectric transition is characterized by the spontaneous generation of a macroscopic polarization, $\boldsymbol{P}$, in the low-symmetry phase. The components of $\boldsymbol{P}$ are zero above T_c but nonzero below. There is a loss of a center of symmetry of the unit cell and the creation of a net dipole moment in the unit cell, which gives rise

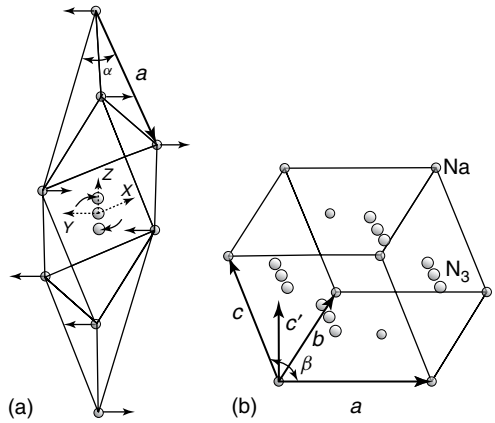


Figure 26.9. The crystal structure of NaN_3. (a) The high-temperature rhombohedral primitive cell for β-NaN_3. The arrows indicated the nature of the distortions taking place at the phase transition. (b) The crystal structure of low temperature α-NaN_3. The monoclinic unit cell shown contains two formula weights. In the high-temperature phase, $a = \sqrt{3b}$ and the c' axis is perpendicular to the ab plane and has the magnitude $3c \sin\beta$. The angle between the c' and a axes is denoted as β'.

to the macroscopic polarization. Crystallographically, the point group of the low-symmetry phase must be compatible with the nonzero components of a vector. This point group symmetry must be one of the polar groups. Above T_c, the point group may be nonpolar (all the components of the macroscopic polarization are zero) or polar (the number of independent components of the polarization must be less than the number below T_c).

The onset of higher order tensor forms gives rise to secondary or higher order ferroics. For example, the onset of piezoelectric modulus components (third rank tensor) and elastic constant components (fourth rank tensor) give secondary ferroics referred to as *ferroelastoelectrics* and *ferrobielactics*.

26.2.4.3 Proper and Improper Ferroics

For each class of ferroics, there are spontaneous tensor components which share with the order parameter the property of being zero above T_c and nonzero below. However, two different scenarios can occur depending upon whether the tensor components constitute the primary order parameter or are a set of secondary order parameter components. In a proper ferroelastic material, the homogeneous deformation of the unit cell is the primary order parameter. Note however that in most, if not all, structural phase transitions there is a small deformation of the unit cell but in many cases the homogeneous strain parameter is a secondary order parameter. The characteristics of the order parameter of improper ferroics are discussed in detail in reference.[31]

26.3 NMR IDENTIFICATION OF PHASE CHANGES

Most studies of phase changes take place as a function of temperature, pressure, or composition of the material. By identifying at what temperature, pressure, or composition a phase transition takes place, measured NMR parameters (spectra, relaxation times, etc.) can often help in the determination of the crystalline space groups on either side of the transition and any change in dynamics that occurs as the material passes through the phase transition. The ultimate aim of study of a structural phase transition is to create a microscopic model that corresponds to all available experimental data about the phase change.

26.3.1 Site Symmetry and Restrictions on EFG and Shielding Tensors

The lineshape of a powder NMR spectrum or the number of lines and their dependence on crystal orientation with respect to $\boldsymbol{B}_0$ in single crystal NMR are usually determined by the dipolar, magnetic shielding and quadrupolar interactions of the observed nucleus. These interactions are anisotropic and represented by second rank tensors. The principal components of the tensors are to some degree determined by the symmetry of the lattice site occupied by the magnetic nucleus. Quadrupolar and shielding interactions are the two most commonly used interactions to probe how the lattice site symmetry changes during a phase transition. In general, the site symmetry increases from a low-temperature to a high-temperature phase. Table 26.1 shows how the lattice point symmetry constrains the anisotropic tensor.

26.3.2 Example: NaN_3

As mentioned in the Section 26.2.4.1, at 293 K, sodium azide (NaN_3) transforms from a

Table 26.1. Relationship between the point symmetry and the EFG shielding tensor of given lattice site

Point group symmetry	EFG shielding tensor restrictions
1 or $\overline{1}$	No restrictions
2 or $\overline{2}$	One of the principal components is parallel to the twofold axis
M	One of the principal components is perpendicular to the mirror plane, while the other two lie in the plane
222, *mmm*, *mm*2	The tensor axes are parallel to the crystal axes
3, $\overline{3}$, 4, $\overline{4}$, 6, $\overline{6}$	The tensor is axially symmetric and one component is parallel to the rotation axis
Cubic	All elements of the EFG tensor are zero and all components of the shielding tensor are equal

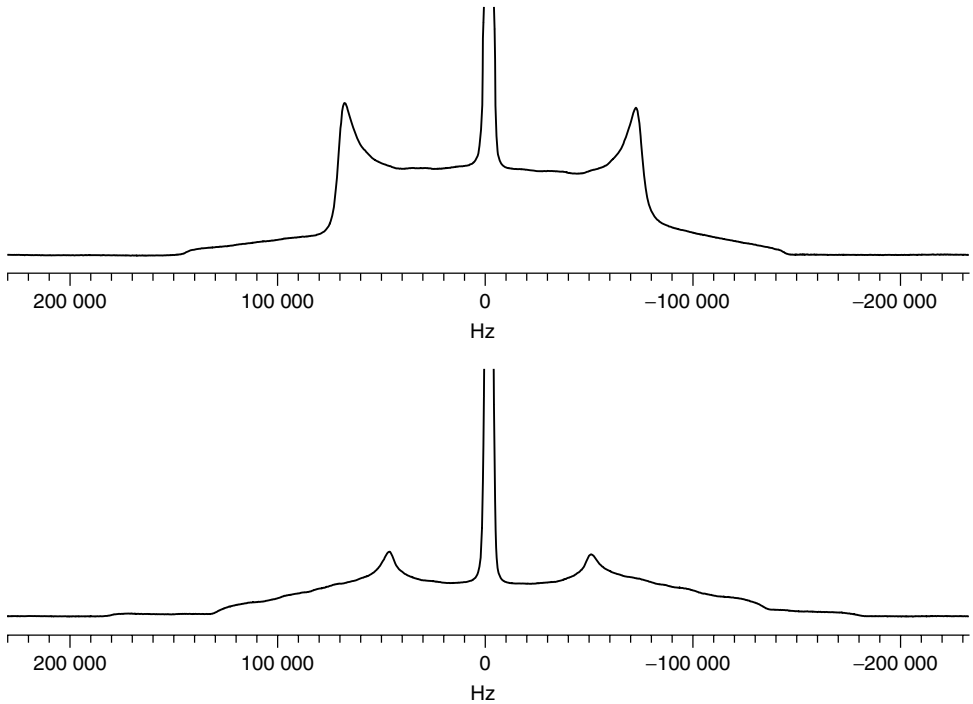


Figure 26.10. ^{23}Na quadrupolar echo spectra of NaN_3 at $B_0 = 11.75$ T. The upper spectrum was taken at 330 K and the lower spectrum was taken at 290 K. The central $1/2 \leftrightarrow -1/2$ transition has been truncated.

low-temperature monoclinic (space group $C2/m$) phase to a high temperature, rhombohedral, (space group $R3m$) phase. The site symmetry of the quadrupolar ^{23}Na nucleus changes from $2/m$ (C_{2h}) to $3m$ (C_{3v}). As can be seen from Table 26.1, there are point symmetry restrictions on the orientation of the sodium EFG tensor in the low-temperature phase. In the high-temperature phase, the EFG tensor must be axially symmetric and one component of the EFG tensor must point along the C_3 axis. Figure 26.10 clearly shows a low-temperature lineshape that is consistent with a nonzero asymmetry parameter, $\eta_Q \neq 0$, whereas the high-temperature spectrum indicates $\eta_Q = 0$.

26.3.3 Example: KSCN

It is important to note that the International Tables for X-ray Crystallography[35] list the sets of equivalent

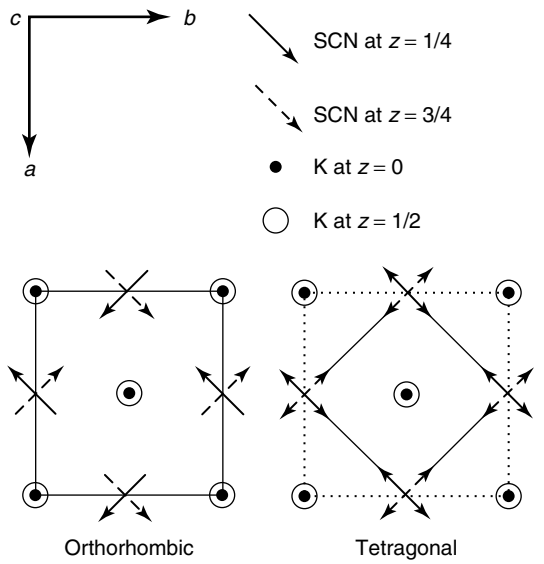


Figure 26.11. In the high-temperature tetragonal phase, the SCN^- ions are randomly oriented head to tail. In the low-temperature orthorhombic phase, there is a small shift of the K^+ ions along the *a* axis and an ordering of the SCN groups. Note that the unit cell (indicated by the solid lines) is twice as large in the orthorhombic phase.

sites and their site symmetries for all 230 space groups. A knowledge of the space group symmetry for the high- and low- temperature phases allows one to predict the number of lines and their intensities in the single crystal NMR spectrum resulting from the static quadrupolar interaction. Difficulties arise when only partial structural information about the phases on either side of the transition is known. The NMR spectrum can be used to check, or clarify, structural data coming from other sources such as X-ray or neutron diffraction. An excellent example is the work of Blinc and his colleagues[36–39] on the alkali thiocyanates.

The order–disorder transition in KSCN from the high-temperature paraelectric tetragonal phase with space group *I*4/*mcm* ($Z = 2$) to an antiferroelectric phase with space group *Pbcm* ($Z = 4$) occurs at $T_c = 413$ K. The crystal structure is shown schematically in Figure 26.11. X-ray data of Yamamoto *et al.*[40] was interpreted in terms of a model where in the tetragonal phase, the SCN^- group can take two opposite orientations with equal probability, which are related by inversion symmetry. The K^+ ions are fixed at their high-symmetry positions. In the orthorhombic phase, there is a probability P_{SCN} of the SCN^- group occupying one of the two possible orientations and the orientational order parameter $P_{SCN} - 1$ was measured. In addition, the K^+ ions are shifted from their high-symmetry locations by an amount Δx along the *a* axis. The temperature dependence of the orientational order parameter and Δx is shown to be proportional to each other. Therefore, the phase transition involves both a displacive and order–disorder component.

The electric field gradient at the *K* site depends on the orientation of the surrounding SCN^- ions and the displacement of the K^+ ions from their positions in the high-symmetry tetragonal phase. It is possible to observe the $1/2 \leftrightarrow -1/2$ NMR transition in the ^{39}K spectrum of KSCN.[36] If the spectra in the orthorhombic phase from a single crystal newly grown at room temperature are observed as a function of angle using the three crystal axes as rotation axes, the angle dependences of the second-order quadrupolar interaction are observed as shown in Figure 26.12. The electric field gradient and the shielding tensors were deduced from these patterns.[36] The values of the two tensors are given in Table 26.2.

Below the transition in the orthorhombic phase, the NMR results agree with the crystal symmetry determined by X-ray diffraction. There are four K^+ sites in the unit cell but the sites are paired. The two sites within each pair are related by inversion symmetry and therefore have the same quadrupolar and magnetic shielding interactions. With a rotation about the *a* axis, the angular dependence of each pair is revealed. The shielding interaction has the same symmetry as the electric field gradient. It is interesting to note that if a newly created crystal is taken above the phase transition and then brought back into the antiferroelectric phase, four domain structures are revealed. Each of these have the structure of the antiferroelectric phase, but the crystal axes are rotated by 90° about the *c* axis.

The splitting observed in the antiferroelectric phase for a rotation about the *a* axis disappears at $T_c = 415$ K with the disappearance of long-range order in the paraelectric phase (see Figure 26.13).

The extra lines due to the domain structure also vanish at the phase transition. The NMR data, therefore, demonstrate that neither the long-range order

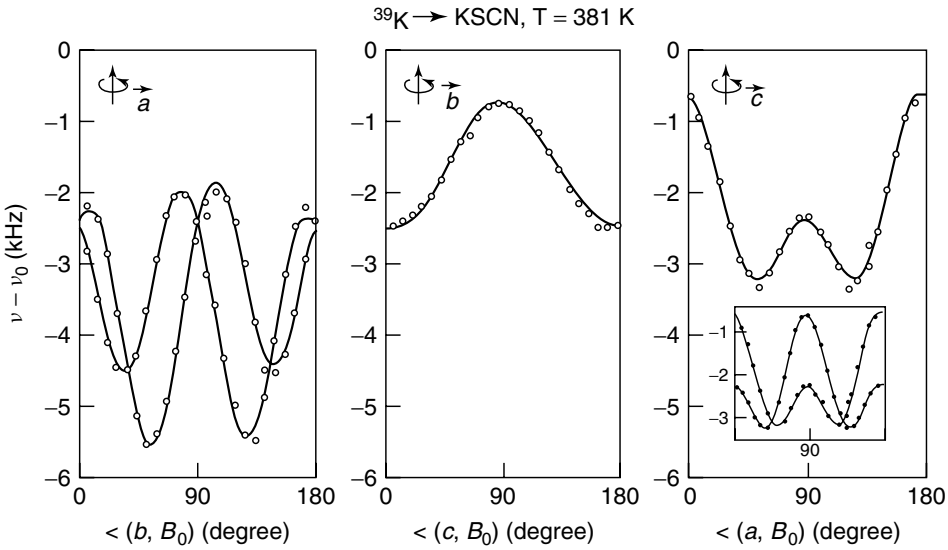


Figure 26.12. The angular dependence of the ^{39}K NMR line shift for KSCN in the low-temperature ferroelectric phase at $T = 381$ K. The rotations are about the *a, b,* and *c* axes in the orthorhombic phase. If the crystal is cooled from the paraelectric phase, domain structure is revealed in the *c* axis pattern as indicated in the inset.

nor the antiferroelectric domain structure persists into the high-temperature phase. However, the electric field gradient tensor in the paraelectric phase does not have the symmetry expected of the high-temperature tetragonal phase. The EFG should be axially symmetric because the K^+ ions lie on a fourfold axis of rotation. Interestingly, the shielding tensor is axially symmetric! Although the 90° domain pattern has disappeared, the number of physically distinct K^+ sites has been reduced from 2 to 1 and the rotation patterns about the *a* and *b* axes are the same as required by the tetragonal symmetry. However, the strong angular dependence shown in the rotation pattern about the *c* axis is not compatible with the proposed structure. The asymmetry parameter is 1 instead of 0.

A possible explanation has been put forward,[39] suggesting that the K^+ ions move between four sites corresponding to displacements along $+a$, $-a$, $+b$, and $-b$ in the four possible domains of the orthorhombic phase. The tetragonal phase then corresponds to a dynamic superposition of the four orthorhombic domains. The frequency of this domain switching, which is determined by the SCN^- ion reorientation, should be slow on the ^{39}K NMR Larmor frequency timescale. Further results from ^{14}N NMR tend to support this model.[39]

26.3.4 Overview of T_1 Changes at Phase Transitions

Relaxation time measurements can provide detailed insight into structural phase transitions. The vast majority of relaxation time studies of phase transitions use the spin-lattice relaxation time, T_1. T_1 measurements are particularly useful for following changes in molecular dynamics that occur during the course of the phase transition. In many of these cases, T_1 can be described by the BPP formalism[41] and the motional correlation time follows Arrhenius behavior. That being the case, a plot of $\ln(T_1)$ versus inverse temperature can provide the activation energy for the motional process below and above the phase transition.

The following behavior has been observed in the temperature dependence of the T_1 around the phase transition temperature:

1. A clean break in the T_1 curve—this is most commonly reported in the literature. As the temperature is increased through the phase transition, the rate of the motional process suddenly increases. Figure 26.14 shows such a case, where the rates for reorientation of the BH_3 and NH_3 groups rapidly increase, by

Table 26.2. The components of the ^{39}K electric field gradient and chemical shift tensors in the crystal fixed $a-b-c$ frame in KSCN. The values of δ are with respect to dilute KCl. the values of σ are with respect to δ_{iso}

Orthorhombic antiferroelectric phase at $T = 381$ K

$$\left(\frac{eQ}{h}\right)\boldsymbol{V} = \begin{vmatrix} -81 & 0 & 0 \\ 0 & 249 & \pm 66 \\ 0 & \pm 66 & -168 \end{vmatrix} \text{ kHz} \qquad \boldsymbol{\sigma} = \begin{vmatrix} -15.5 & 0 & 0 \\ 0 & -7.5 & -22.2 \\ 0 & -22.2 & 23 \end{vmatrix} \text{ ppm}$$

$\chi = 259$ kHz, $\eta_Q = 0.37$ $\qquad \delta_{iso} = -71.4$ ppm

Tetragonal paraelectric phase $T = 415$ K

$$\left(\frac{eQ}{h}\right)\boldsymbol{V} = \begin{vmatrix} -165 & 0 & 0 \\ 0 & 165 & 0 \\ 0 & 0 & 0 \end{vmatrix} \text{ kHz} \qquad \sigma = \begin{vmatrix} -15.5 & 0 & 0 \\ 0 & -15.5 & 0 \\ 0 & 0 & 30.2 \end{vmatrix} \text{ ppm}$$

$\chi = 165$ kHz, $\eta_Q = 1$ $\qquad \delta_{iso} = -128.5$ ppm

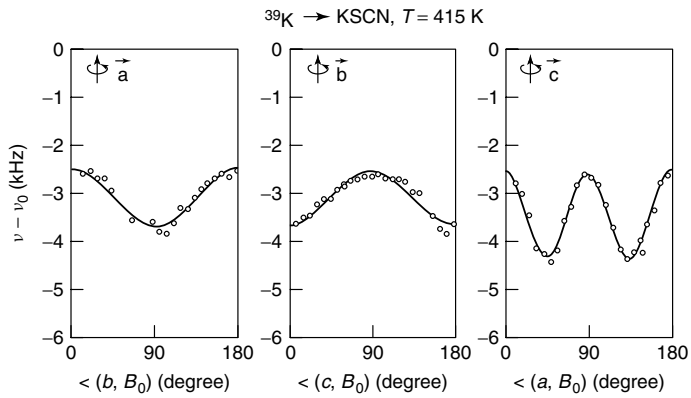


Figure 26.13. Angular dependence of the ^{39}K NMR central transition shifts in the paraelectric phase of KSCN at $T = 415$ K.

differing amounts, as solid BH_3NH_3 transforms from the low-temperature orthorhombic phase to the high-temperature tetragonal phase at 220 K. A sharp break in the T_1 curve usually indicates a first-order phase transition.[42] The discontinuity in the T_1 curve may show hysteresis in the case of a first-order phase transition.

2. No visible break in the T_1 curve—in general, one of two observations is made: (i) there is no detectable change in the slope of the curve and therefore no evidence for a phase transition and (ii) there is a change in the slope of the curve at the phase transition temperature. The absence of a discontinuity at the phase transition temperature is frequently (but not necessarily) associated with a second- order phase transition. Case (i) is observed in the temperature dependence of the ^{23}Na T_1 for NaN_3. In crystalline solids where the only atomic motion is due to the lattice vibrations or phonons energy conservation and the very few phonons in the lattice at the Larmor precessional frequency means that a direct phonon nuclear spin flip process is very rare. Rather a Raman process involving the creation of one phonon coupled with the annihilation of another dominates.[43,44] With this process, energy conservation only demands that the difference in phonon frequency be equal to the Larmor frequency. The temperature dependence enters through the equilibrium phonon occupation numbers and in the high-temperature approximation the transition probability between

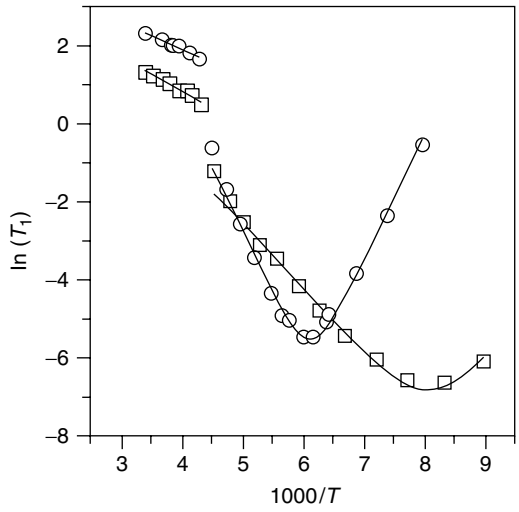


Figure 26.14. The dependence of the deuterium $\ln(T_1)$ as a function of $1/T$ for solid BD_3NH_3 (circles) and BH_3ND_3 (squares).

Zeeman energy states $W \propto T^2$. An example (NaN_3) is given in Figure 26.15. In the case of NaN_3, the acoustic mode responsible for the phase transition does not modulate the ^{23}Na nuclear quadrupole interaction. The T^2 temperature dependence is due to the other phonon modes which do not soften as the phase transition continues uninterrupted through the phase transition temperature. Second-order phase transitions do not show hysteresis.

3. A cusp in the T_1 on one or both sides of the phase transition—a rapid increase in the relaxation rate is observed as the phase transition temperature is approached. This indicates that the spin-lattice relaxation is reflecting the critical slowing down of the order parameter near the phase transition temperature. A good example[45] of this can be found in the temperature dependence of the deuterium T_1 near the phase transition at 353 K for $KDCO_3$. This is illustrated in Figure 26.16.

26.4 THE LANDAU THEORY

One of the most significant developments in the study of phase transition is the exploitation of the Landau theory[13,31,33,46] to describe not only the thermodynamics of phase transitions but also to understand structural transition between phases that have a group–subgroup relationship. The theory gives a phenomenological framework that brings together a wide range of thermodynamic and physical quantities and provides linkages between various experimental measurements. The Landau theory can be considered in its simplest form as a Taylor series expansion of the change in the Gibbs free energy at the phase transition in terms of an order parameter that describes the structural change.

The order parameter ψ can be viewed as a new variable created as a result of the symmetry breaking at the phase transition. In general, the order parameter may have more than one component. In the high-symmetry phase, the Gibb's free energy is a minimum when $\psi = 0$ while in the low-symmetry phase, the minimum occurs at a nonzero value

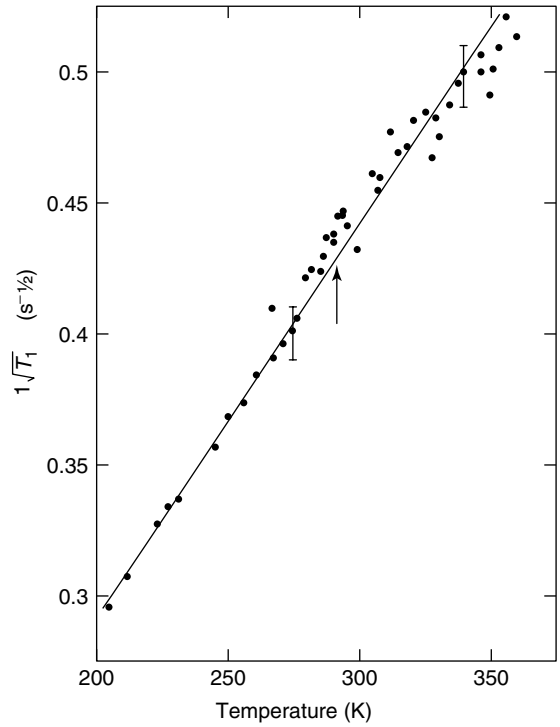


Figure 26.15. The spin-lattice relaxation time of the ^{23}Na $1/2 \leftrightarrow -1/2$ transition in NaN_3. The graph demonstrates the $1/T_1 \propto T^2$ relationship expected when the dominate relaxation mechanism is the quadrupolar spin–phonon interaction. The arrow indicates the phase transition temperature.

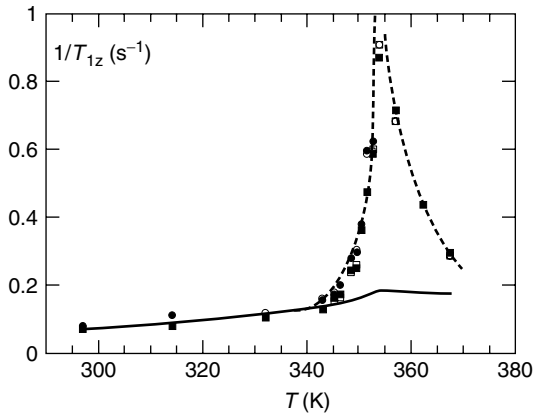


Figure 26.16. The deuterium spin-lattice relaxation rate ($1/T_1$) as a function of temperature for a single crystal of $KDCO_3$. For an explanation of the dashed and solid curves, see the Section 26.6.2.

of ψ. At a continuous phase transition, the order parameter which is nonzero in the low-symmetry phase smoothly decreases to zero as the transition is approached. Symmetry considerations play a very important role in this theory and these are somewhat independent of the Landau equations for the free energy. Because of the condition that G_L be a subgroup of G_H, G_L is a called an isotropy subgroup of G_H and all the isotropy subgroups of any particular space group can be determined by group theoretical methods. Significant information about a structural phase transition can be learned just on the basis of symmetry considerations and the laws of thermodynamics.

26.4.1 Group Theoretical Considerations

Both the experimental and the theoretical understanding of structural phase transitions have benefited from the application of group theoretical methods. Extensions of the Landau theory formulated by Birman *et al.*[47–52] have shown that direct group theoretical conditions must be satisfied if there is a continuous transition between the high- and low-symmetry phases. From these conditions, a hierarchy of constraints can be obtained, which successively restrict the generality of the phase transition. Even if the phase transition is discontinuous, much of the extended Landau theory is applicable. In a series of paper, Stokes and Hatch[53–58] have implemented on computer the direct group theoretical conditions of the Landau theory and have applied them to all the 230 3-D space groups.

In the set of tables "Isotropy Subgroups of the 230 Crystallographic Space Groups" published by Stokes and Hatch,[59] there is information about group–subgroup relationships, representation properties, Landau free energy forms, domain specifications, and Landau or renormalization group theory of continuity conditions. It is interesting to note the prevalence of ferroelastic transitions. Of the 15 239 group–subgroup transitions listed, 553 are purely ferroelectric, 6248 are purely ferroelastic, 4854 are simultaneously ferroelectric and ferroelastic, 708 are ferroelastoelectric, 144 are ferrobielastic, 376 are simultaneously ferrobielastic and ferroelastoelectric, 140 are higher order ferroics, and 2203 are nonferroic.[60]

Both the so-called direct and inverse Landau problems[61] have been discussed. The direct problem addresses the situation where given the space group of the high-symmetry phase, G_H find all possible order parameters and for each of these determine (i) the space group of the low-symmetry phase G_L, (ii) the thermodynamic potential that describes the phase and the transition between them, and (iii) classify these potentials in a suitable way. The Landau theory starts from the premise that G_L is a subgroup of G_H determined by one of the irreducible representations of G_H that satisfy a series of conditions. On the other hand, the inverse Landau problem is given G_H and G_L to find the distortion giving rise to the phase transition.

The work of Stokes and Hatch, especially the web-based tool for exploring structural distortions taking place at phase transitions,[58] is an invaluable aid in interpreting experimental data that is obtained in the region of a phase change.

26.4.2 Interactions between the Order Parameter and Other Variables

The role of strain remains as a fundamental problem in the understanding of structural phase transitions. Changes in the size and shape of the crystal are often associated with many structural phase transitions. All ferroelastic phase transitions involve the coupling of the order parameter to some degree to the elastic strain. Spontaneous strains may

act as the driving-order parameter, as in proper ferroelectrics, or are coupled to a different driving order parameter, as in improper ferroelastics. A general consequence of strain coupling is that the order parameter extends over a characteristic correlation length that is determined by the long-range strain interactions. As a result, mean field behavior dominates and so phase transitions involving spontaneous strains follow models derived from Landau theory very closely.[62–64] A second consequence of the coupling of the strain to the order parameter is that the strain may provide a coupling between the order parameters of two or more phase transitions.

An example of the complexity that arises when there is coupling between the primary order parameter and other degrees of freedom in the system is the case of the $\beta-\gamma$ phase transition in NH_4Br. NH_4Br undergoes two successive phase transitions at 235 and 108 K. The high-temperature β phase has the cubic CsCl structure (space group $Pm3m$), where each ammonium ion is surrounded by eight neighboring bromide ions. A rotation of 90° about any of the three fourfold axes will reconfigure the NH_4^+ ions within the surrounding cage. A rotation of 180° about these same axes does not change the orientation. In addition to these possible reorientational motions, the ammonium ions can rapidly rotate about any of the four threefold axes. This motion does not reconfigure the ion. The tetrahedral NH_4^+ groups are disordered between two possible orientations differing by an inversion. In the lower-temperature γ phase, the NH_4^+ groups become ordered and the unit cell takes on a tetragonal distortion (space group $P4/nmm$). The NH_4^+ groups form ordered $a-a-a-a\ \ldots$ or $b-b-b-b\ \ldots$ chains along the tetragonal axis with neighboring chains being oppositely oriented. There is an antiparallel ordering in the $a-b$ plane and parallel ordering along the tetragonal axis. This ordering contrasts to the case of ammonium chloride where there is a parallel ordering of the pseudospins. The $\beta-\gamma$ phase change is a so-called λ transition because of the shape of the specific heat anomaly.

Bromine NMR is a means of monitoring the displacement of the Br in the tetragonal γ phase. Above the $\beta-\gamma$ phase transition, the bromine site symmetry is cubic and the static nuclear quadrupole interaction vanishes. In the γ phase, the tetragonal distortion causes a quadrupolar splitting of the Zeeman line. To second order the resonance frequencies are given by [41]

$$\begin{aligned}\nu_m &= \nu_0 + \nu_m^{(1)} + \nu_{1/2}^{(2)} \\ &= \nu_0 + \nu_Q\left(m-\frac{1}{2}\right)\left[\frac{1}{2}(3\cos^2\theta-1)\right] \\ &\quad -\frac{3}{16}\left(\frac{\nu_Q^2}{4\nu_0}\right)\times(1-\cos^2\theta)(9\cos^2\theta-1) \\ &\quad \times\delta\left(m-\frac{1}{2}\right) \qquad (26.4)\end{aligned}$$

where $m = 3/2,\ 1/2,\ -1/2$; ν_0 is the Larmor precessional frequency; $\nu_Q = e^2qQ/h$, θ is the angle between the direction of the applied magnetic field and the axis of symmetry of the electric field gradient at the nuclear site; δ is a delta function that indicates that this term is nonzero only when $m = 1/2$. Using an aligned single crystal and recording the complete rotation pattern, it is possible to verify the angular dependence given in equation (26.4) and determine the quadrupolar coupling constant. Figure 26.18 shows the temperature dependence of the ratio of $e^2qQ/(e^2qQ)_o$, where $(e^2qQ)_o$ is the coupling constant measured at the lowest temperature

In the ordered phase, the bromine ions are displaced parallel to the cubic axes from their location in the disordered phase. Because the resultant electric field gradient, eq, is invariant to an inversion of the bromine displacements, a series expansion of eq in powers of the displacement will have only even terms. For sufficiently small displacements, the lowest order term, which is proportional to the square of the bromine ion movement, will dominate. Because X-ray diffraction[65] has shown that the displacement is about 0.015 times the cubic unit cell parameter, the assumption that e^2qQ is proportional to the bromine ion displacement squared should be valid.

Birefringence and neutron diffraction studies of NH_4Br have been carried out by Egert *et al.*[66] in an attempt to measure the temperature dependence of the order parameter in the region just below the $\beta-\gamma$ phase transition. Neutron diffraction shows a series of superlattice lines in the low-temperature phase due to the doubling of the unit cell. The intensity of a suitable superlattice line corrected for temperature factors was considered to be a measure of the long-range ordering of the ammonium ions. It was found that the square of the long-range order determined from neutron diffraction and the birefringence coincided within experimental error. Fitting to those data with a relationship of the form $(1 - T/T_c)^\beta$ produced a critical exponent for the order parameter of

0.25 ± 0.02. In Figure 26.18, the NMR data presented above is shown again with the square of the order parameter data from the neutron diffraction results. Because the two sets of data coincide within 2% over the entire range, it may be concluded that the order parameter associated with the ordering of the ammonium ions is directly proportional to the order parameter associated with the bromine ion displacements reflected in the bromine NMR experiment.

The pattern of small displacements shown in Figure 26.17 exactly corresponds to the eigenvector for a transverse acoustic phonon at the [110] point on the Brillouin zone boundary (M point). As has been shown above, the displacement of the Br^- ion is proportional to the long-range ordering of the pseudospins in the γ phase.[67] This type of transition has the distinction of being a pseudospin-phonon coupled case where the order parameter can be expressed in terms of pseudospins. The NMR results can be interpreted in terms of the Landau theory and the measured value of critical exponent of 1/4 suggests that tricritical behavior is being observed.

An alternative approach to this coupled problem has been developed by Yamada *et al*.[68] The coupled

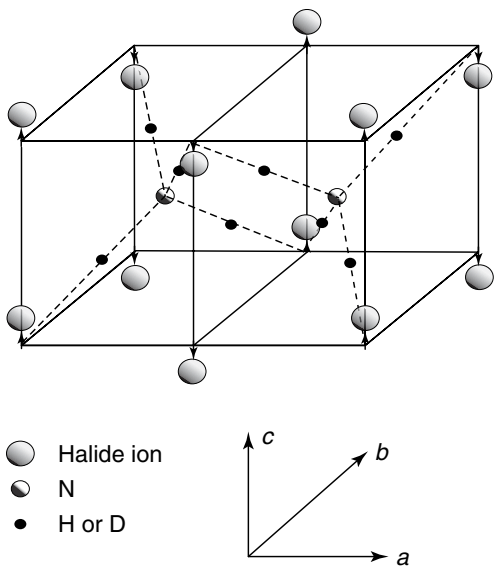


Figure 26.17. The tetragonal structure of NH_4Br. The arrows indicate the distortion of the cubic β phase taking place at the $\beta-\gamma$ phase transition.

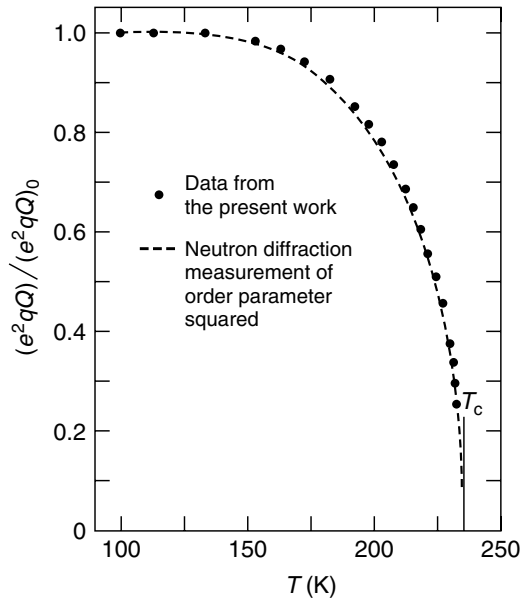


Figure 26.18. The temperature dependence of the quadrupolar coupling constant in the γ phase of NH_4Br.

system is described by a microscopic Hamiltonian

$$H_{\mathrm{PP}} = \frac{1}{2}\sum_{\boldsymbol{q}j}\dot{\psi}(\boldsymbol{q}j)\dot{\psi}(-\boldsymbol{q}j) + \omega(\boldsymbol{q}j)^2 \times\psi(\boldsymbol{q}j)\psi(-\boldsymbol{q}j) - \frac{1}{2}\sum_{ik}J_{ik}\sigma_i\sigma_k + \sum_{\boldsymbol{q}j,i}\frac{\omega(\boldsymbol{q}j)}{\sqrt{\mathrm{N}}}g_{\boldsymbol{q}j,i}\psi_{\boldsymbol{q}j}\sigma_i e^{i\boldsymbol{q}\cdot r_i} \qquad (26.5)$$

The first two terms are the harmonic Hamiltonian describing the phonon energy, the third term is the coupling between pseudospins, and the last term is the pseudospin-phonon coupling. J_{ik} is the pseudospin coupling coefficient while $g_{\boldsymbol{q}j,\,i}$ is the pseudospin-phonon coupling strength. Futhermore, the spontaneous strain giving rise to the tetragonal distortion is introduced into the model by having the coefficient J_{ik} dependent on the strain variables. The model makes predictions of the phase diagram and the temperature order parameter. The dynamics arising from this model have been derived based on the Onsager theory[69] of irreversible processes.[70] A comparison of various static properties such as the long-range ordering of the pseudospins with the theoretical predictions has been carried out.[70]

26.4.3 Shortcomings of the Landau Theory

The Landau theory has been widely used in the study of structural phase transitions. First, the theory provides a good empirical description of the experimentally observed behavior in the region of the phase change. From the experimental measurements of the temperature dependence of the order parameter and thermodynamic data, it is quite easy to obtain estimates for the coefficients in the expressions of the Landau free energy. A second reason for the success of the Landau theory is that the Landau free energy provides a model free energy that can provide the first step toward a microscopic theory of the phase transition. Even when the numerical predictions are not accurate, many of its qualitative aspects are useful because they are based on rigorous symmetry principles. The use of group theory places very powerful constraints on the formulation of the Landau free energy.

The Landau approach, however, leads to a mean field theory. The Landau free energy does not contain information about any individual atom but only about the order parameter, which is an average over all atoms. Any individual atom is assumed to interact with the average behavior of the surrounding atoms. The theory does not take into account fluctuations.

Because the Landau theory involves a Taylor series expansion, it might be argued that it should be valid in a region close to T_c. Experimentally, it is found that the Landau expression for the temperature dependence of the order parameter holds for a range of temperatures but at temperatures very close to the T_c the modification

$$\psi = A(T_c - T)^{\beta} \tag{26.6}$$

applies with $\beta < 1/2$ typically (but not exactly equal to) 1/3 for 3-D systems. The temperature boundary defining the region, where mean field theory is no longer applicable, is called the Ginsburg interval.[13] The existence of this interval is due to fluctuations in the order parameter and the long-range order of these fluctuation increases as the transition temperature is approached. There are many phase transitions where the Ginzburg interval is so close to zero that it can not be observed.[46] For instance, when the order parameter is coupled to the any spontaneous strain at T_c, the fluctuations are suppressed and the mean field is applicable over an extended region.

The mean field expression for the order parameter $\psi = \mathrm{A}(T_c - T)^{1/2}$ cannot work at low temperature because of the third law of thermodynamics. $\partial\psi/\partial T = 0$ at $T = 0\,\mathrm{K}$. Therefore, the Landau free energy is not a valid function, but a high-temperature approximation. Modification of the original Landau theory has been put forward, which leads to the correct low-temperature behavior.[62]

26.5 PURE QUADRUPOLE RESONANCE

There have been numerous studies[3,4] of phase transitions using the pure nuclear quadrupole resonance (NQR) frequencies or quadrupolar splittings of NM R lines to monitor small differences in the local electric field gradients. Because these frequencies can typically be measured to parts in 10^5 or better (ratio of the resonance frequency to the line width), nuclear spins of a particular species situated in inequivalent sites will in general have well-separated resonance frequencies. The intensity of each line is proportional to the number of contributing spins and therefore, the ratio of intensities of the lines measures the ratio of the number of spins associated with the inequivalent sites. At a phase transition, where the crystal structure changes, modifications to the local electric field gradients are reflected in the observed spectrum. At a continuous phase transition, the change in quadrupolar frequencies will be continuous but a discontinuity appears in the derivatives of the frequencies with respect to temperature. If the transition is first order, the change in frequencies is discontinuous. From the study of the quadrupolar spectrum as a function of temperature on both the high- and low-temperature sides of the phase transition, it is often possible to determine (i) the order of the transition, (ii) the number of inequivalent sites, and (iii) the ratio of the number of nuclei in these sites.

In a series of three papers[71–73], Armstrong and his colleagues have illustrated how group theoretical methods can be used to develop a classification scheme for the pattern of NQR lines arising from the distortions of the cubic antifluorite structure.

26.6 DYNAMICS AT STRUCTURAL PHASE TRANSITIONS

Models have been developed to explain the observed behavior of T_1, $T_{1\rho}$, or T_2 at structural phase transition, which is naturally divided into two

categories depending upon where the transition is predominantly displacive or order–disorder. Because displacive phase transition involves the softening of a lattice vibration, the timescale of the atomic displacements is much faster than typical NMR Larmor frequencies and the amplitudes of the vibrations are very small. The contribution from the direct interaction of the nuclear spin system and the spectrum of phonon in the lattice is very small because energy conservation demands the phonon energy be equal to the Larmor frequency. There are very few phonons in a crystalline lattice with such a low frequency. As van Kranendonk[43,44] has pointed out there is the possibility of a first-order Raman process and an anharmonic Raman process where energy conservation only demands that the difference in phonon energies be equal to the NMR frequency. Therefore, enhanced relaxation often observed at displacive phase transitions was originally considered to arise from the phonon Raman and the anharmonic Raman processes associated with the soft mode responsible for the phase transition. However, as is discussed in the Section 26.6.1, there is evidence that the enhanced spin-lattice relaxation is not in fact influenced by the soft mode. In conjugation with the mode softening there are other aspects of the dynamics which influence the measured values of the spin-lattice relaxation. The effects of overdamped phonon modes, precursor phenomena[74] and central frequency peaks[13] in the phonon spectra on the direct relaxation mechanism seem to be the largest effects and these act through the direct term.

Order–disorder transitions are very different in the sense that large-scale movement of atoms from one lattice site to another is involved. These large atomic motions are very effective in causing relaxation because the spin interactions are changed significantly. At a structural phase transition, certain aspects of the atomic motion may change quite dramatically leading to very noticeable changes in the spin relaxation and line shapes. In some cases such as that for NH_4Cl discussed in the Section, 26.6.2, the "cusp" in T_1 at the λ transition in the ^{35}Cl spin-lattice relaxation rate is a direct result of the static ordering taking place at the phase change.

There have been numerous discussions of the nuclear spin relaxation associated with structural phase transitions over the past 40 years (see, for example, Refs 3–5 and 75–77).

26.6.1 Relaxation at a Displacive Transition; The ^{23}Na and ^{93}Nb Spin-Lattice Relaxation in $NaNbO_3$

The influence of the Raman two phonon process on spin lattice relaxation at a displacive phase transition is considered first.[75] One of the principal characteristics of spin-lattice relaxation due to the Raman and anharmonic Raman phonon processes is the T^2 temperature dependence. The transition probability resulting from spin-lattice relaxation between the Zeeman levels m and $m + \mu$ can be written as

$$W_{m,m+\mu} = KT^2 + \frac{2\pi}{\hbar^2}|Q_{\mu m}|^2 BT^2 \int_{SM} \frac{\rho_{SM}^2(\omega)}{\omega^4} d\omega \tag{26.7}$$

where K and B are constants and $Q_{\mu m} = \langle m|Q_\mu|m + \mu\rangle$ are the matrix elements of the nuclear quadrupole tensor. The first term is the relaxation due to all of the phonon modes excluding the soft mode (SM). Far from the phase transition, the typical T^2 dependence is observed. The second term describes the influence of the soft mode. As pointed out by Bonera *et al.*[75] the exact temperature dependence of this term significantly depends on the form assumed for the phonon density spectrum $\rho_{SM}(\omega)$. For instance if an Einstein model with frequency spread $\Delta\omega$ is assumed and the soften of the mode goes as $\omega_{SM}^2 = A(T - T_c)$, then it is found that

$$W_{m,m+\mu} \propto \frac{T^2}{(T - T_c)^2} \tag{26.8}$$

Other models for ρ give quite different results but all those that have been considered display a peak in the relaxation rate at T_c.

For crystals undergoing displacive phase transitions, the distortion of the high-symmetry phase is a pattern of time-averaged atomic displacements, which are continuous variables as a function of temperature in the low-symmetry phase. These time-averaged displacements are the order parameter. However, the atomic displacements $\varphi_l(t)$ are in fact time dependent oscillating about some mean position. The $\varphi_l(t)$ are often referred to as the *critical variables*.[4] In the soft mode model, the $\varphi_l(t)$ are the time-dependent positions of the atoms in the unit cell participating in that particular mode of oscillation.

The calculation of the direct relaxation process can be performed by starting with the relationship

$$W_{m,m+\mu} = \left(\frac{1}{\hbar^2}\right) |Q_{\mu m}|^2 J_\mu(\mu\omega_{\mathrm{L}}) \tag{26.9}$$

where the spectral density function

$$J_\mu(\omega) = \int_{-\infty}^{\infty} \exp(\mathrm{i}\omega t) \left\langle V_\mu(0) V_{-\mu}(t) \right\rangle \mathrm{d}t \tag{26.10}$$

involves the correlation functions for the electric field gradient tensor components. Of particular interest is the contribution to the electric field gradient components $V_\mu(t)$ from the critical variables. $V_\mu(t)$ can be written directly in terms of the critical variables

$$V_\mu(\mathrm{t}) = \sum_n a_n^\mu \varphi_n(t) \tag{26.11}$$

Because the quadrupolar interaction is relatively short range, it is often possible to limit the summation over n to nearest neighbors. Now the spectral density functions can be written as

$$\begin{aligned} J_\mu(\omega) &= \frac{1}{N} \int_{-\infty}^{\infty} \sum_{\boldsymbol{q}} \sum_{n,m} a_n^\mu \mathrm{a}_m^\mu \left\langle \varphi_{\boldsymbol{q}}(t) \varphi_{-\boldsymbol{q}}(0) \right\rangle \\ &\quad \times \exp(\mathrm{i}\boldsymbol{q} \cdot \boldsymbol{R}_{nm}) \exp(\mathrm{i}\omega t) \mathrm{d}t \\ &= \sum_{\boldsymbol{q}} A_{\boldsymbol{q}}^\mu \mathrm{S}(\boldsymbol{q}, \omega) \end{aligned} \tag{26.12}$$

It has been convenient to introduce the dynamic structure factor for the critical variables

$$S(\boldsymbol{q}, \omega) = \int_{-\infty}^{\infty} \left\langle \varphi_{\boldsymbol{q}}(t) \varphi_{-\boldsymbol{q}}(0) \right\rangle \exp(\mathrm{i}\omega t)\, \mathrm{d}t \tag{26.13}$$

where

$$\varphi_{\mathrm{l}}(t) = N^{1/2} \sum_{\boldsymbol{q}} \varphi_{\boldsymbol{q}}(t) \exp(\mathrm{i}\boldsymbol{q} \cdot \boldsymbol{R}_{\mathrm{ll}'}) \tag{26.14}$$

The factors $A_{\boldsymbol{q}}^\mu$ present a complication. They describe how a particular mode of oscillation contributes to the time dependence of the electric field gradient at a site within the unit cell. Usually, some form of theory has to be invoked to calculate these factors. The dynamic structure factor, $S(\boldsymbol{q}, \omega)$, is related to the imaginary part of the collective susceptibility $\chi(\boldsymbol{q}, \omega)$ by the fluctuation dissipation theorem so that nuclear spin transition probability can be written as

$$\begin{aligned} W_{m,m+\mu} &= \left(\frac{2k_B T}{\hbar^2 N \mu \omega_{\mathrm{L}}}\right) |Q_{\mu m}|^2 \\ &\quad \times \sum_{\boldsymbol{q}} A_{\boldsymbol{q}}^\mu \mathrm{Im}\left[\chi(\boldsymbol{q}, \mu\omega_{\mathrm{L}})\right] \end{aligned} \tag{26.15}$$

The calculation of the transition probabilities involves the determination of two factors: the collective susceptibility, χ, and the coefficients $\mathrm{A}_{\boldsymbol{q}}^\mu$.

There are several approaches to obtain an expression for the dynamic collective susceptibility arising from the critical variables $\varphi_{\mathrm{l}}(t)$. The dominant contribution to the nuclear spin relaxation will come from the soft mode whose frequency approaches zero at the transition. The Landau theory as presented in the Section 26.4 has to be modified to consider the fluctuations, the so-called Landau–Ginzburg theory.[76] Alternatives include the use of the pseudospin model or to simply treat the soft mode as a damped harmonic oscillator.[7]

To proceed further, it is appropriate to consider a specific example. $NaNbO_3$ is a cubic perovskite above 910 K. As in many perovskites, there is a cubic to tetragonal phase transition involving rotational antiferrodistortive tilts of the NbO_3 octahedra about the principle cubic axes. In the temperature region immediately above the transition, there is experimental evidence for the softening of a large part of the phonon branch from the R–M points in the Brillouin zone corresponding to rotational fluctuations which are only two-dimensionally correlated within parallel planes. At the transition itself, there is a crossover from 2-D to 3-D behavior of the fluctuations and the onset of a ferrodistortive ordering among adjacent planes which corresponds to a freezing in of a pure M_3 mode. $NaNbO_3$ is particularly noteworthy because there is a succession of other phase transitions as the temperature is reduced. At the cubic to tetragonal transition, there is a very significant increase in the ^{23}Na spin-lattice relaxation rate as shown in Figure 26.19.[78] The ^{93}Nb relaxation rate however is virtually temperature independent throughout this region. Calculations of the $\mathrm{A}_{\boldsymbol{q}}^\mu$ coefficients[4] using a point charge model and considering only nearest neighbor atoms accounts for strong interaction with the soft mode for ^{23}Na and the much weaker interaction for ^{93}Nb. The temperature dependence of the ^{23}Na spin-lattice relaxation in the transition region is well described by a relationship of the form

$$\mathrm{W}_{m,m+\mu} \propto \ln\left(\frac{T_{\mathrm{c}}}{|T - T_{\mathrm{c}}|}\right) \tag{26.16}$$

This relationship can be derived on the basis of the simplest Landau–Ginsburg equation applicable to a uniaxial ferroelectric, where polarization is an axis of spatial anisotropy.[76] In the case of $NaNbO_3$,

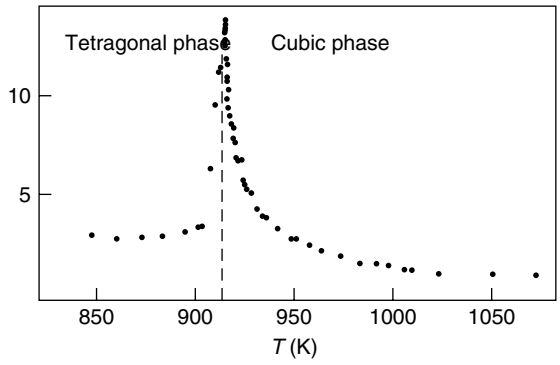


Figure 26.19. The temperature dependence of the ^{23}Na spin-lattice relaxation rate near the cubic to tetragonal phase transition in $NaNbO_3$.

the anisotropy arises because of the softening of the whole phonon branch between the *R* and *M* points as mentioned above.

26.6.2 Relaxation at an Order–Disorder Transition; The ^2H and ^{35}Cl Spin-Lattice Relaxation in NH_4Cl

The lambda transition in ammonium chloride (249.4 K) has been the subject of many experimental investigations using a wide variety of techniques as well as theoretical studies. Spin-lattice relaxation time measurements [^1H [79–81]; ^2H;[79] ^{35}Cl[82,83]] and corresponding theory[81,84,85]) have been explored by a number of scientists. To illustrate the general picture, an emphasis is placed on the ^2H and ^{35}Cl results. The ^2H data displayed on Figure 26.20 shows a well-developed T_1 minimum as predicted by BPP theory.

The time-dependent motion responsible for the observed spin-lattice relaxation is the reorientation of the ammonium ion. Except for the discontinuity at T_λ, the data is well described by the relationship

$$\frac{1}{T_1} = \frac{3\pi^2}{10}\left(1+\frac{\eta_Q^2}{3}\right)\left(\frac{e^2qQ}{h}\right)^2 \times \left[\frac{\tau_c}{1+\omega_o^2\tau_c^2} + 4\frac{\tau_c}{1+4\omega_o^2\tau_c^2}\right] \quad (26.17)$$

The T_1 minimum occurs when $\omega_o\tau_c = 0.6158$ and using the values of the quadrupole coupling constant $e^2qQ/h = 180.2$ kHz and asymmetry parameter $\eta_Q = 0.00 \pm 0.01$ obtained from deuterium NMR spectra,[86] the value of T_1 at the minimum is predicted to be 0.435 ms as compared to the measured value 0.455 ms. Because of the agreement between these two values, it is possible to state that the reorientation of the ammonium ion averages out the entire static deuteron quadrupolar interaction and therefore, each deuteron samples a group of sites having on average at least tetrahedral symmetry. Using the known values for e^2qQ/h and η_Q, equation (26.17) can be used to determine the correlation time τ_c at each temperature. Above T_λ, it is possible to fit the data to an Arrhenius relation

$$\tau_c = \tau_c^o \exp\left(\frac{E_a}{RT}\right) \quad (26.18)$$

and obtain a value of $E_a = 19.7\ kJ\ mol^{-1}$ and $\tau_c{}^o = 6 \times 10^{15}$ s. The data below 195 K produces $E_a = 19.7\ kJ\ mol^{-1}$ and $\tau_c{}^o = 17 \times 10^{15}$ s. Right at T_λ and

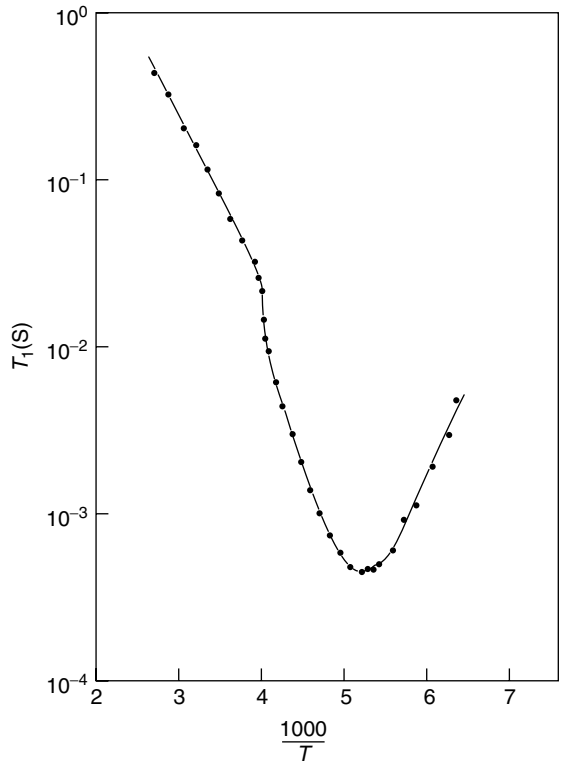


Figure 26.20. The ^2H spin-lattice relaxation time T_1 as a function of reciprocal temperature for ND_4Cl. The data was taken with a Larmor frequency equal to 9.5 MHz.

in the temperature region just below, standard BPP theory does not account for the observed results.

The ^{35}Cl data displayed in Figure 26.21 shows quite a different result. There is a marked cusp in the relaxation time at T_λ but no evidence of a T_1 minimum due to ammonium ion reorientation. Measurement of the ratio of T_1 for ^{35}Cl and ^{37}Cl[82] produced a value of 1.60 ± 0.04. The ratio of the squares of the quadrupole moments for the two isotopes is 1.61 indicating that the relaxation is due to the chlorine nuclear quadrupole interaction.

Above T_λ, the T_1 data are accurately represented by an Arrhenius equation of the form

$$\frac{1}{T_1} = A\tau_c \tag{26.19}$$

where τ_c is given by equation (26.18). The activation energies obtained by least squares fits to the data are about the same for NH_4Cl ($18.4 \pm 0.5\,kJ\,mol^{-1}$) and ND_4Cl ($17.6 \pm 0.5\,kJ\,mol^{-1}$) and these values agree with that obtained from deuterium NMR on ND_4Cl. Above T_λ, the chlorine spin-lattice relaxation is due to the reorientation of the ammonium ion as is the case for the deuterium results. Below T_λ, the relaxation time rapidly increases indicating that the ammonium ion reorientation is no longer an effective relaxation mechanism. This fits with the picture that has been developed for the mechanism driving the lamba transition. Above T_λ, the ammonium ion can reorient by rotating by 90° about three axes parallel to the [100], [010], and [001] directions and possibly by 120° about the body diagonals, the four axes parallel to the [111], [1$\bar{1}$1], [$\bar{1}$11], [$\bar{1}\bar{1}$1]. Below T_λ, the fourfold reorientation is reduced to simply a twofold reorientation though 180°. Now the tetrahedron is ordered and is unable to change its configuration within the surrounding cage of chlorine ions.

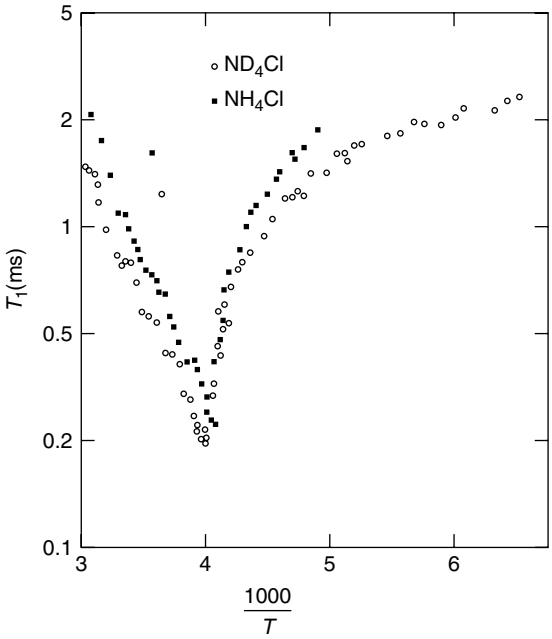


Figure 26.21. The ^{35}Cl spin-lattice relaxation time for ND_4Cl (squares) and NH_4Cl (open circles) as a function of reciprocal temperature in the region of the lambda transition.

There is no doubt that the dominating relaxation mechanism is the reorientation of the ammonium ion. The ammonium ion has a net charge of +1, no molecular dipole or quadrupolar moment but does have an octapole and hexadecapole moment. From the electrostatic potential due to a single octapole, it is straight forward to derive the electric field gradient tensor components. These can be written in terms of a variable $\sigma = \pm 1$ representing the two possible configurations of the tetrahedral ammonium ion within the cage of surrounding chlorine ions. The electric field gradient at a chlorine nuclear site depends on the sum of these components due to all the neighboring ammonium ions. The electric field gradient tensor components are therefore

$$V_\mu = \sum_l A^l_\mu \sigma_l \tag{26.20}$$

It is convenient to use spherical tensors so that $\mu = -2 \ldots 2$ and l labels the surrounding ammonium ions. V_μ will be time dependent if the allowed reorientation of the ammonium ions results in a change in the configuration of the tetrahedron. Motion of the ammonium ion about any threefold axis or a 180° reorientation about any of the cubic axes will not cause quadrupolar relaxation of the chlorine nucleus but will relax the deuterons. A succession of these rotations will average the static quadrupole interaction at the deuteron site to zero even though the configuration of the tetrahedron has not changed. The spectral density functions governing the relaxation can be written

$$J_\mu(\omega) = \frac{1}{\hbar}\int_{-\infty}^{\infty} \exp(i\omega t) \sum_{ll'} A^l_\mu A^{*l'}_\mu \langle \sigma_l(0)\sigma_{l'}(t)\rangle \, dt \tag{26.21}$$

Itoh and Yamagata[87] determined the spectral density functions under the following assumptions

1. There is no cooperative motion. The configuration of a particular ammonium ion is independent of the configuration of the neighboring ions.
2. In the ordered state, if the degree of long-range order is p (where p varies between 0 and 1), the probability that an ammonium ion will take the favored configuration is $(1 + p)/2$ while the probability of taking the unfavored configuration is $(1 - p)/2$.
3. The summations over l and l' in equation (26.21) are taken only over nearest neighbors.

The resulting spectral density functions are

$$J_\mu(\omega) = \frac{1}{\hbar}(1 - p^2)\sum_l A_\mu^l A_\mu^l \frac{2\tau_c}{1 + \omega^2\tau_c^2} \quad (26.22)$$

After expressing the A_μ^l factors in terms of the octapole moment of the ammonium ion, the spin lattice relaxation rate becomes

$$\frac{1}{T_1} = \frac{655\,360}{2187}\left(\frac{e^2qQ}{\hbar}\right)^2\left(\frac{\gamma\Omega}{a^6}\right)^2(1 - p^2)\tau_c \quad (26.23)$$

in the high-temperature region ($\omega_o\tau_c < 1$). Ω is the octapole moment of the ammonium ion, the factor γ takes into account antishielding effects and a is the cubic unit cell dimension. Above T_λ where $p = 0$, $1/T_1 \propto \tau_c$ and the observed Arrhenius behavior is predicted. Below T_λ, $p \to 1$ and the ammonium ion reconfiguration no longer determines the chlorine spin-lattice relaxation. The sharp rise in T_1 observed in Figure 26.21 at T_λ is therefore a direct result of the ordering of the tetrahedral.

It is instructive to use an alternative approach to evaluate the spectral density functions. Michel[84] suggested that the dynamics of the kinetic Ising model[88,89] can be applied to obtain an expression for the spectral density functions. Initially, the collective coordinates

$$\sigma_l(t) = N^{-1/2}\sum_{\boldsymbol{q}} \sigma(\boldsymbol{q}, t)\exp(i\boldsymbol{q}\cdot r_l) \quad (26.24)$$

are introduced and a dynamic scattering function

$$S(\boldsymbol{q}, \omega) = \int_{-\infty}^{\infty} \langle\sigma(\boldsymbol{q}, 0)\sigma(-\boldsymbol{q}, t)\rangle \exp(i\omega t)\,dt \quad (26.25)$$

is defined. Then, the spectral density functions become

$$J_\mu(\omega) = \left(\frac{1}{N\hbar}\right)\sum_{\boldsymbol{q}} A_\mu^{\boldsymbol{q}} A_\mu^{*\boldsymbol{q}} S(\boldsymbol{q}\omega) \quad (26.26)$$

in the random phase approximation where

$$A_\mu^{\boldsymbol{q}} A_\mu^{*\boldsymbol{q}} = \sum_{ll'} A_\mu^l A_\mu^{*l'} \exp(i\boldsymbol{q}\cdot(r_l - r_l')) \quad (26.27)$$

Because the electric field gradient rapidly decreases with distance, only the gradient arising from the nearest neighbor ammonium ions needs to be considered in the summation above. The resulting expression contain factors such as $[1 - \cos(q_x a)\cos(q_y a)]$ and $[1 - \cos(q_z a)]$. Because the reconfiguration of the ammonium ions results in a ferrodistortion, the principal effects of the critical slowing down of the ammonium reorientation should occur at $q = 0$. However, the factors mentioned above indicate that the quadrupolar relaxation is not sensitive to the critical dynamical behavior at the phase transition. The observed cusp in the chlorine relaxation at T_λ is a result of the static ordering of the ammonium ions.

In contrast to the situation in NH_4Br, the results shown in Figure 26.16 for $KDCO_3$ indicate that both static ordering and critical fluctuations contribute to the observed cusp in the spin-lattice relaxation at T_c. The solid line shown in Figure 26.16 is a calculation of the contribution to the relaxation due to the ordering of the hydrogen bonds. The difference between the experimental data and this line was shown[45] to fit to an expression of the form

$$\frac{1}{T_1} \propto \ln\left(\frac{T_c}{|T - T_c|}\right) \quad (26.28)$$

which is indicative of critical behavior in anisotropic systems.[4,75,76]

26.6.3 Molecular Dynamics and Lineshape Changes at Phase Transitions

Phase transitions are frequently accompanied by a change in atomic or molecular dynamics. This may include translational or rotational motion or both. Molecular rotational dynamics, which change with solid–solid phase changes, have been extensively studied by NMR spectroscopy; in particular, by deuterium NMR spectroscopy. Hence, there are many examples of the use of NMR spectroscopy to follow

molecular dynamics at phase transitions (see, for example, Ref. 90).

The temperature dependence of the ^{2}H and ^{31}P spectra of solid potassium phosphide (KPH_2) and its deuterated analog (KPD_2) illustrate, in a rather straightforward way, how NMR lineshape changes due to changes in molecular dynamics accompany phase transitions.[91] In the case of potassium phosphide, it is the phosphide anion which is undergoing different modes of reorientation in different phases. KPD_2 undergoes two solid–solid phase transitions at about 154 and 373 K.[92]

The temperature dependent deuterium lineshapes show that in the lowest temperature phase the phosphide ion is undergoing two-site 180° flipping, which exchanges the two P–H bonds. The rate of exchange increases with temperature. Since such an exchange process leaves the orientation of the ^{31}P CSA tensor unchanged (the directions of the principal tensor components are simply reversed by the exchange), the ^{31}P powder pattern is the same as that expected for a static phosphide ion.

At the phase transition, the crystal symmetry changes from an unknown phase to monoclinic (space group $P2_1/n$) with a concomitant change in ^{2}H and ^{31}P lineshapes. At first glance, the ^{31}P spectrum appears to be converted to that expected for isotropic reorientation of the phosphide ion (see Figure 26.22a). However, the ^{2}H spectrum yields a Pake doublet, which is consistent with in-plane reorientation of the ion. Figure 26.22(b) shows how the ^{31}P spectrum should look like for the motion of the ion about its three inertial axes. As one can see, the in-plane motion happens to average δ_{11} and δ_{33} such that their average is nearly coincident with δ_{22}, yielding a narrow featureless lineshape.

As the temperature of a sample of potassium phosphide rises above the phase transition at 373 K, the crystal structure becomes cubic. In this phase, the phosphide anion is reorienting between equivalent positions within the cubic lattice to yield a pseudo-isotropic lineshape in the ^{2}H and ^{31}P spectra.

The analogous alkali metal amides (MNH_2) have also been shown by NMR spectroscopy to change reorientational dynamics with each phase transition.[93]

26.7 SUMMARY

In this article, we have shown that magnetic resonance spectroscopy is an invaluable tool for the investigation of structural phase transitions. We have attempted to show both classical and modern examples of how one can use different aspects of

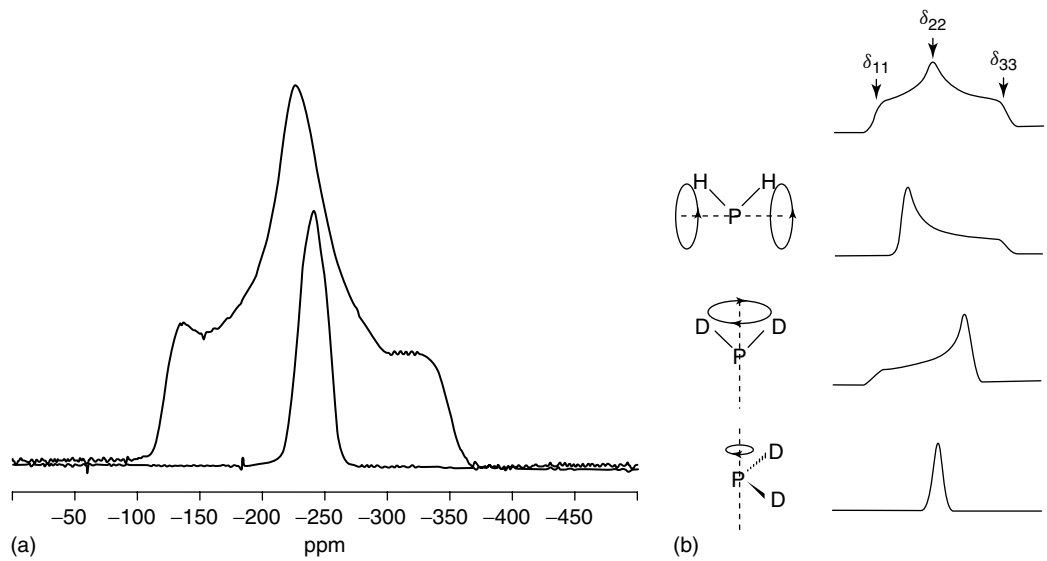


Figure 26.22. (a) The powder spectrum of KPH_2 at 120 K (upper trace) and at 295 K (lower trace). The spectra were obtained with cross polarization from, and decoupling of, protons. (b) Simulated ^{31}P powder spectra of KPH_2 for different types of rotational motion of the phosphide anion.

magnetic resonance spectroscopy, such as lineshape, CS, T_1, and NQR frequency, to gain useful insight into the nature of a structural phase transition.

REFERENCES

1. N. L. Alpert, *Phys. Rev.*, 1949, **75**, 398.
2. K. Schmidt-Rohr and H. W. Spiess, *Multidimensional Solid-State NMR and Polymers*, Academic Press: London, 1994.
3. C. Odin, *Prog. NMR Spectrosc.*, 2006, **59**, 118.
4. A. Rigamonti, *Adv. Phys.*, 1984, **33**, 115.
5. J. L. Bjorkstam, *Adv. Magn. Res.*, 1974, **7**, 1.
6. F. Owens, C. Poole, and H. Farach, eds, *Magnetic Resonance of Phase Transitions*, Academic Press: New York, 1979.
7. R. Blinc and R. Žekš, *Soft Modes in Ferroelectrics and Antiferroelectrics*, North Holland Amsterdam: Netherlands, 1974.
8. M. Catti, *Lecture Notes from the International School on Mathematical and Theoretical Crystallography*, Université Henri Poincaré: Nancy 1, 2005.
9. H. B. Callen, *Thermodynamics and an Introduction to Thermostatistics*, 2nd edn., John Wiley & Sons: New York, 1985.
10. H. T. Stokes and D. M. Hatch, *Phys. Rev.*, 2001, **B 65**, 144114.
11. W. Cochran, *Adv. Phys.*, 1960, **9**, 387.
12. P. W. Anderson, in *Fizika Dielectrikov*, ed G. I. Skanavi, Acad. Nauk, SSR: Moscow.
13. A. D. Bruce and R. A. Cowley, *Structural Phase Transitions*, Taylor and Francis Ltd: London, 1981.
14. R. L. Armstrong, *Phys. Rep.*, 1980, **57**, 344.
15. G. P. O'Leary, *Phys. Rev. Lett.*, 1969, **23**, 782.
16. G. P. O'Leary and R. G. Wheeler, *Phys. Rev.*, 1970, **B1**, 4409.
17. A. G. Brown, R. L. Armstrong, and K. R. Jeffrey, *Phys. Rev.*, 1973, **B1**, 121.
18. M. Sommariva and M. Catti, *Chem. Mater.*, 2006, **18**, 2411.
19. R. M. Lynden-Bell and K. H. Michel, *Rev. Mod. Phys.*, 1994, **66**, 721.
20. N. S. Dalal, O. Gunaydin-Sen, and A. Bussmann-Holder, *Struct. Bonding*, 2007, **124**, 23 (see also other papers in this volume).
21. D. Semminsen, Z. Tun, R. J. Nelmes, R. K. McMullan, and T. F. Koetzle, *Z. Kristallogr.*, 1995, **210**, 934.
22. M. Mehring and D. Suwelack, *Phys. Rev. Lett.*, 1979, **42**, 317.
23. J. D. Becker, D. Suwelack, and M. Mehring, *Solid State Commun.*, 1978, **25**, 1145.
24. M. Mehring and J. D. Becker, *Phys. Rev. Lett.*, 1981, **47**, 366.
25. L. Onsager, *Phys. Rev.*, 1944, **46**, 597.
26. M. E. Fischer, *Rev. Mod. Phys.*, 1974, **46**, 597.
27. A. N. Klymachyov and N. S. Dalal, *Z. Phys. B*, 1997, **104**, 651.
28. A. N. Klymachyov and N. S. Dalal, *Ferroelectrics*, 1998, **206–207**, 103.
29. N. S. Dalal, K. L. Pierce, J. Palomar, and R. Fu, *J. Phys. Chem. A*, 2003, **107**, 3471.
30. N. S. Dalal, O. Gunaydin-Sen, R. Achey, and K. L. Pierce, *Ferroelectrics*, 2006, **3–12**, 337.
31. J.-C. Tolédano and P. Tolédano, *The Landau Theory of Phase Transitions*, World Scientific Publishing Company: Singapore, 1987
32. R. A. Cowley, *Phys. Rev.*, 1976, **13**, 4877.
33. E. K. H. Salje, S. A. Hayward, and W. T. Lee, *Acta Crystallogr.*, 2005, **A61**, 3.
34. G. E. Pringle and D. E. Noakes, *Acta Crystallogr.*, 1968, **B24**, 262.
35. International Union of Crystallography *International Tables for X-ray Crystallography*, Kynoch Press Birmingham, 1965.
36. R. Blinc, J. Seliger, A. Apih, J. Dolinšek, I. Zupanšiš, O. Plyushch, A. Fuith, W. Schranz, H. Warhanek, B. Topiš, and U. Haeberlen, *Phys. Rev.*, 1991, **B43**, 569.
37. R. Blinc, J. Seliger, A. Apih, J. Dolinšek, A. Fuith, W. Schranz, and H. Warhanek, *Phys. Rev.*, 1995, **B52**, 833.
38. R. Blinc, J. Seliger, A. Apih, J. Dolinšek, W. Schranz, A. Fuith, and H. Warhanek, *Solid State Commun.*, 1995, **93**, 609.
39. R. Blinc, A. Apih, J. Seliger, A. Fuith, W. Schranz, and H. Warhanek, *Phase Trans.*, 1999, **67**, 617.
40. S. Yamamoto, M. Sukuno, and Y. Shinnaka, *J. Phys. Soc. Jpn.*, 1987, **56**, 4393.
41. A. Abragam, *The Principles of Nuclear Magnetism*, Oxford University Press: Oxford, 1961.
42. G. H. Penner, Y.-C. P. Chang, and H. M. Grandin, *Inorg. Chem.*, 1999, **38**, 2868.

43. J. van Kranendonk, *Physica*, 1954, **20**, 781.
44. (a) J. van Kranendonk and M. Walker, *Phys. Rev. Lett.*, 1967, **18**, 701.; (b) J. van Kranendonk and M. Walker, *Can. J. Phys.*, 1968, **46**, 2441.
45. C. Odin, *Mag. Reson. Chem.*, 2007, **46**, 9.
46. M. T. Dove, *Structure and Dynamics*, Oxford University Press: Oxford, 2003.
47. J. L. Birman, *Phys. Rev. Lett.*, 1966, **17**, 1216.
48. F. E. Goldrich and J. L. Birman, *Phys. Rev.*, 1968, **167**, 528.
49. J. L. Birman, in *Group Theoretical methods in Physics*, eds P. Karmer and A. Riecker, Springer: New York, 1978.
50. M. V. Jaric and J. L. Birman, *Phys. Rev.*, 1977, **B16**, 2564.
51. M. V. Jaric, *Phys. Rev.*, 1981, **B23**, 3460.
52. M. V. Jaric, *Phys. Rev.*, 1982, **B25**, 2015.
53. H. T. Stokes and D. M. Hatch, *Phys. Rev.*, 1984, **B30**, 3845.
54. H. T. Stokes and D. M. Hatch, *Phys. Rev.*, 1985, **B31**, 7462.
55. H. T. Stokes and D. M. Hatch, *Phys. Rev.*, 1991, **B43**, 11010.
56. H. T. Stokes, D. M. Hatch, and H. M. Nelson, *Phys. Rev.*, 1993, **B47**, 9080.
57. H. T. Stokes and D. M. Hatch, *Phys. Rev.*, 2001, **B65**, 014113.
58. B. J. Campbell, H. T. Stokes, D. E. Tanner, and D. M. Hatch, *Appl. Cryst.*, 2006, **39**, 607.
59. H. T. Stokes and D. M. Hatch, *Isotropy Subgroups of the 230 Crystallographic Space Groups*, World Scientific Singapore: Singapore, 1988.
60. H. T. Stokes and D. M. Hatch, in *Phase Transitions in Ferroelastic and Co-elastic Crystals*, eds E. K. H. Salje, Cambridge University Press: Cambridge, 1990.
61. E. Ascher and J. Kobayashi, *J. Phys. C., Solid State Phys.*, 1977, **10**, 1349.
62. E. K. H. Salje, *Phase Transitions in Ferroelastic and Co-elastic Crystals*, Cambridge University Press: Cambridge, 1990.
63. M. A. Carpenter, *Rev. Mineral. Geochem.*, 2000, **39**, 35.
64. S. A. T. Redfern, *Rev. Mineral. Geochem.*, 2000, **39**, 105.
65. A. Bonilla, C. W. Garland, and N. E. Schmaker, *Acta Crystallgr.*, 1972, **A26**, 156.
66. G. Egert, I. R. Jahn, and D. Renz, *Solid State Commun.*, 1971, **9**, 775.
67. H. Terauchi, Y. Noda, and Y. Yamada, *J. Phys. Soc. Jpn.*, 1972, **32**, 1560.
68. Y. Yamada, M. Mori, and Y. Noda, *J. Phys. Soc. Jpn.*, 1972, **32**, 1565.
69. H. Mori, *Prog. Theor. Phys.*, 1965, **33**, 424.
70. Y. Yamada, H. Terauchi, and D. L. Huber, *J. Phys. Soc. Jpn.*, 1972, **32**, 1560.
71. R. G. C. McElroy, R. L. Armstrong, and M. Sutton, *J. Mag. Res.*, 1980, **38**, 253.
72. M. Sutton and R. L. Armstrong, *J. Mag. Res.*, 1982, **47**, 68.
73. R. M. Morra and R. L. Armstrong, *J. Mag. Res.*, 1984, **60**, 1.
74. R. L. Armstrong, *Prog. NMR Spect.*, 1989, **21**, 151.
75. G. Bonera, F. Borsa, and A. Rigamonti, *Phys. Rev. B*, 1970, **2**, 2784.
76. H. Theveneau and P. Papon, *Phys.Rev. B*, 1976, **14**, 3810.
77. R. L. Armstrong, *Magnetic Resonance in Condensed Matter-Recent Developments*, eds R. Blinc and G. Lahajnar, I. Stefan Institute: Ljubljana.
78. A. Avogadro, G. Bonera, and A. Rigamonti, *J. Mag. Reson.*, 1975, **20**, 399.
79. D. E. Woessner and B. S. Snowden, *J. Phys. Chem.*, 1967, **71**, 952.
80. N. J. Trappeniers and W. Mandema, *Physica*, 1966, **32**, 1170.
81. T. Kodama, *J. Mag. Reson.*, 1972, **7**, 137.
82. P. A. Speight and K. R. Jeffrey, *J. Mag. Reson.*, 1973, **10**, 195.
83. D. F. Cooke and K. R. Jeffrey, *J. Mag. Reson.*, 1975, **18**, 455.
84. K. H. Michel, *J. Chem. Phys.*, 1973, **58**, 142.
85. R. G. Petschek and B. I. Halperin, *Phys. Rev. B*, 1979, **19**, 166.
86. M. Linzer and R. A. Forman, *Bull. Am. Phys. Soc.*, 1966, **11**, 33.
87. J. Itoh and Y. Yamagata, *J. Phys. Soc. Jpn.*, 1962, **17**, 481.
88. R. J. Glauber, *J. Maths. Phys.*, 1963, **4**, 294.

89. M. Suzuki and R. Kubo, *J. Phys. Soc. Jpn.*, 1968, **24**, 61.

90. G. Facey, R. E. Wasylishen, M. J. Collins, C. I. Ratcliffe, and J. A. Ripmeester, *J. Phys. Chem.*, 1986, **90**, 2047.

91. G. H. Penner, K. R. Jeffrey, R. E. Wasylishen, and N. Burford, unpublished results.

92. H. Jacobs and K. M. Hassiepen, *Z. Anorg. Allg. Chem.*, 1985, **531**, 108.

93. (a) M. Müller, J. Senker, B. Asmussen, W. Press, H. Jacobs, W. Kockelmann, H. M. Mayer, and R. M. Ibberson, *J. Chem. Phys.*, 1997, **107**, 2363; (b) M. Müller, B. Asmussen, W. Press, J. Senker, H. Jacobs, H. Büttner, and H. Schober, *J. Chem. Phys.*, 1998, **109**, 3559; (c) J. Senker, H. Jacobs, M. Müller, W. Press, P. Müller, H. W. Mayer, and R. M. Ibberson, *J. Phys. Chem.*, 1998, **102**, 931; (d) J. Senker, H. Jacobs, M. Müller, W. Press, and G. Neue, *J. Phys, Chem. B.*, 1999, **103**, 4497.

PART F
Applications of NMR to Crystalline Solids

Chapter 27
Structural Biology

David A. Middleton

School of Biological Sciences, University of Liverpool, Liverpool L69 7ZB, UK

27.1	Introduction	417
27.2	Sample Preparation	418
27.3	Assignment Strategies	419
27.4	Structural Restraints	421
27.5	Alternative Isotope Labeling Patterns	429
27.6	Structure Calculation and Refinement	430
27.7	Dynamics	430
27.8	Prospects	431
	References	432

27.1 INTRODUCTION

An important advance in solid-state NMR has been the development of strategies to elucidate the three-dimensional folds of biological macromolecules—including integral membrane proteins and polypeptide aggregates—that are resilient to conventional methods of structural analysis. This recent step forward has come about as the result of (predominantly wide-bore) high-field magnet and probe-head technologies converging with sophisticated sample preparation techniques and multidimensional experiments exploiting ^{13}C- and ^{15}N-labeled (more accurately, *enriched*) proteins. After a prolonged gestation, biological solid-state NMR has thus emerged as a formidable, realistic, and versatile tool in structural biology, which is capable of providing atomic models of protein drug targets, such as ion channel complexes[1] and seven-transmembrane (7TM) receptors[2,3] and which has also unveiled the first details of ordered protein aggregates associated with widespread human disorders.[4]

Two procedures have been widely adopted in the biological solid-state NMR community. One strategy is to measure anisotropic interaction tensor orientations for proteins embedded in lipid bilayers that are uniaxially aligned at defined angles relative to the external magnetic field. In the other strategy, magic-angle spinning (MAS) is employed to eliminate or scale the effects of anisotropic interactions to provide site-specific distances and angles for dynamically constrained proteins of any size in various forms and environments. MAS NMR studies on highly ordered precipitates of soluble proteins—*protein NMR crystallography*—has played a vital role in establishing the tools and concepts for biomolecular structural analysis. Measurements on structurally well-characterized proteins have demonstrated the validity of NMR crystallography as a feasible alternative to diffraction methods for the complete de novo structure determination of biomacromolecules in natively solid or solid-like environments and for soluble proteins in solid precipitates.

The ability of NMR crystallography to solve protein structures was first demonstrated with the example of the 30-amino acid SH3 domain

NMR Crystallography Edited by Robin K. Harris, Roderick E. Wasylishen and Melinda J. Duer © 2009 John Wiley & Sons, Ltd. ISBN: 978-0-470-69961-4

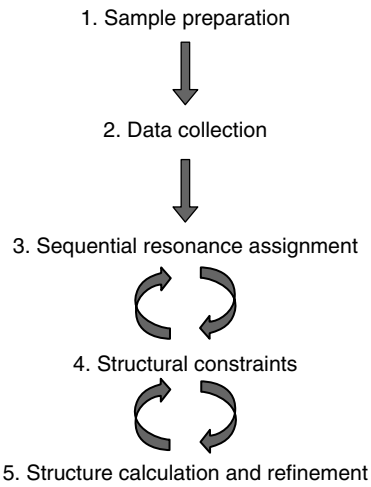


Figure 27.1. A general scheme for protein structure determination by NMR crystallography.

of α-spectrin.[5] Since then, proteins including ubiquitin,[6–8] the immunoglobulin binding domain of protein G,[9] and the domain-swapped dimeric protein Crh[10] have provided valuable test-beds on which the precision and accuracy of NMR crystallographic constraints against known protein X-ray structures of varying size and complexity are evaluated. The experimental protocol, which broadly follows the scheme outlined in Figure 27.1, will be familiar to those with an appreciation of the NMR structural analysis of proteins in solution, although the specific experiments are necessarily different to those practiced in solution NMR. As expected for a technique in its early stages of development, however, protein NMR crystallography currently embraces a rather diverse collection of approaches and methodologies and it remains to be seen which of these will endure to become standard tools in structural biology.

With this in mind, this article briefly outlines some of the methods that have featured most commonly at each of the experimental stages as shown in Figure 27.1. For convenience, much of the detailed description is restricted to experiments on highly ordered proteins that are uniformly labeled with ^{13}C and ^{15}N (by recombinant expression), taking account of the fact that, until recently, proton observation has been hampered by the effects of strong homonuclear coupling. This situation is changing, however, aided by recent developments harnessing deuterated proteins to attenuate strong couplings and to improve proton resonance line widths, particularly at high MAS rates. In recognition of these developments, a section has been included on experiments exploiting alternative isotope labeling schemes, including deuteration.

27.2 SAMPLE PREPARATION

For a realistic chance of successful structure determination, the protein must be obtained in a form having sufficient order to yield main-chain ^{13}C and ^{15}N line widths of ideally less than 0.5 ppm. Lyophilized preparations of soluble proteins or frozen solutions are usually, if not always, too heterogeneous to give sufficiently resolved spectra. Unfortunately, the relationship between resolution and molecular order in crystalline preparations is complex and poorly understood. In some cases, crystals with dimensions of several micrometers (microcrystals) are necessary for sharp lines; in other cases, crystals on the nanometer scale (nanocrystals) are sufficient. Sometimes the NMR line widths for nanocrystals and microcrystals are comparable. The example in Figure 27.2 illustrates how the resolution of a ^{13}C spectrum can be affected by preparing the same protein under different conditions. Screening a range of conditions, guided by light microscopy and electron microscopy as well as NMR, is useful for obtaining the best sample empirically.

Nanocrystals or microcrystals suitable for protein NMR crystallography have been prepared using standard precipitants (e.g., polyethylene glycol (PEG) and 2-methyl-2,4-pentandiol (MPD)) or with specific crystallization buffers evaluated by screening.[11] In practice, crystals can be yielded using vapor diffusion methods (i.e., sitting or hanging drop), but such procedures are laborious and require harvesting and combining many such drops to provide sufficient sample (2–15 mg). An attractive alternative is to obtain protein precipitates by batch precipitation from an initially highly concentrated solution or with solvent evaporation to rapidly concentrate the protein.

Sample packing and maintenance in the MAS rotor is also critical. It is desirable to remove the excess moisture, by centrifugation, from the precipitated protein to maximize the concentration within the center of the MAS rotor, which typically holds samples of 20–50 μl. Multidimensional experiments require several days or weeks to complete, and measures must

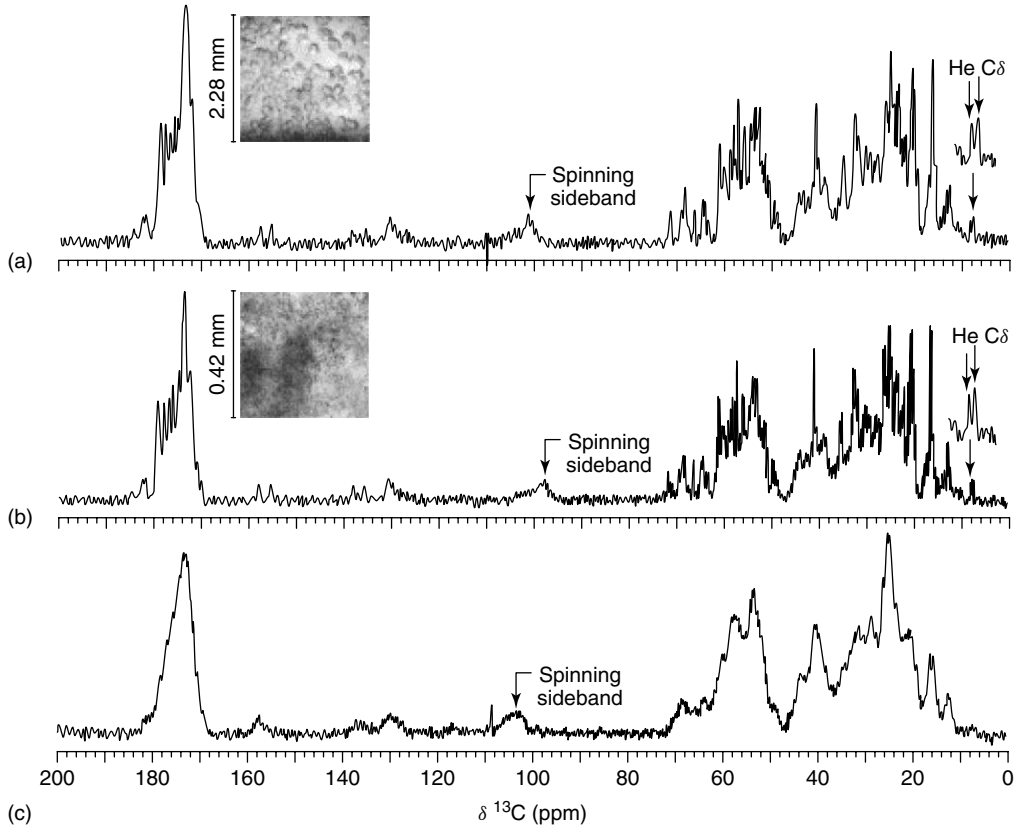


Figure 27.2. An example of the effect of sample preparation on the resolution of ^{13}C CP-MAS solid-state NMR spectra of proteins in the solid state. (a) A spectrum of polycrystalline ubiquitin composed of crystals grown in a sitting drop. Inset shows crystals at 5× magnification using a light microscope. The crystals measure approximately 200 μm across the widest point. (b) A spectrum of ubiquitin nanocrystals produced using rapid batch crystallization looks practically identical to that of the polycrystalline sample. Inset shows crystals at 225× magnification under a light microscope. (c) A spectrum of lyophilized ubiquitin shows poor resolution, indicating structural heterogeneity in the sample. (Reproduced from Ref. 11. © Elsevier, 2003.)

be taken to prevent the effects of high radiofrequency power and frictional heating from dehydrating the sample, which has deleterious effects on resonance line widths and structural integrity. These measures include effective sealing of the sample within the rotor to prevent escape of moisture and performing experiments at reduced temperature (below -10°C).

27.3 ASSIGNMENT STRATEGIES

The key step in protein structure determination by NMR crystallography is to assign all or most of the ^{13}C and ^{15}N resonances to specific amino acid types and, ultimately, to all the residues along the polypeptide chain. Assigning a spectrum to specific amino acids, without identifying their position within the primary sequence, can be achieved extensively, if not completely, using a series of two-dimensional carbon–carbon dipolar correlation spectra with longitudinal mixing schemes, such as proton-driven spin diffusion (PDSD), dipolar-assisted rotational resonance (DARR), or radio-frequency-driven recoupling (RFDR), for example, which mediate through-space homonuclear polarization transfer via dipolar interactions (Figure 27.3a). Other radiofrequency mixing schemes using symmetry-based sequences and rotationally synchronous fields can also be used. The

duration of the mixing period is varied so that the spectra are relatively simple at short mixing periods, displaying only cross peaks between directly bonded spins, whereas longer mixing times introduce cross peaks correlating entire intraresidue spin systems and sometimes weak interresidue couplings as well. A combination of experiments at short and long mixing times can usually help to identify specific amino acid types; for example, proline, isoleucine, threonine, and serine have characteristic chemical shifts and coupling patterns. For a protein of modest size (<30 amino acids) and with line widths of <0.5 ppm,

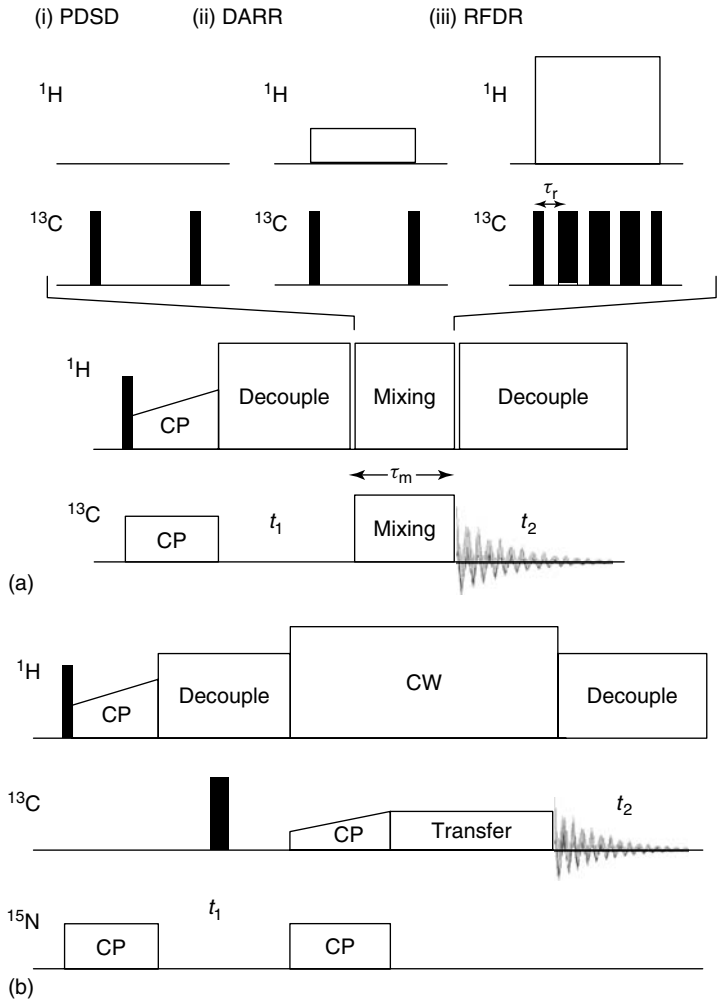


Figure 27.3. Pulse schemes for NMR crystallography experiments to assist ^{13}C and ^{15}N resonance assignment for uniformly labeled proteins. (a) A two-dimensional ^{13}C–^{13}C correlation experiment with a longitudinal mixing period. The inset shows examples of three mixing schemes. (b) A two-dimensional NCACB(CX) or NCOCA(CX) experiment, with broadband CP from ^{1}H to ^{15}N and frequency-selective cross polarization from ^{15}NH(i) to ^{13}CA(i) (or ^{13}CO($i-1$)). A ^{13}C–^{13}C transfer block after the second CP step transfers magnetization from CA(i) to CB(i) (CX(i)) or from CO($i-1$) to CA($i-1$) (CX($i-1$)). Narrow solid bars represent 90° pulses and broad solid bars represent 180° pulses. The 180° pulse at the ^{13}C frequency at the center of t_1 refocuses the effect of ^{13}C–^{13}5N J-modulation. A three-dimensional version of this experiment can be made by inserting an extra ^{13}C chemical shift evolution period immediately before the homonuclear transfer block.

it is possible to identify the signals from all amino acids of a specific type.

When dipolar couplings are weak or scaled by dynamics, through-bond carbon–carbon correlation spectra in which polarization transfer is mediated through scalar couplings can, in principle, provide additional information. These may be obtained using the through-bond spectroscopy (TOBSY) SSNMR method or solid-state variants of the INADEQUATE and INEPT experiments. The refocused INADEQUATE experiment (*see* **Chapter 15**) provides greater frequency dispersion in the indirect dimension because the double-quantum (DQ) coherences generated evolve at the sum of frequencies of the J-coupled spin pair, but require a number of delays on the order of $1/4J_{CC}$ ($\sim$5 ms) and thus efficient proton decoupling is required to minimize loss of coherence via transverse relaxation.

It is possible to identify sequential cross peaks (i.e., between residues i and $i \pm 1$) correlating C$\alpha(i)$–C$\alpha(i \pm 1)$ or carbonyl CO(i)–C$\alpha(i \pm 1)$ or to observe longer range constraints on tertiary structure from two-dimensional carbon–carbon (C–C) dipolar correlation spectra.[8–12] However, complications arise for uniformly ^{13}C/^{15}N labeled proteins because strong couplings ($\sim$2 kHz) between the directly bonded ^{13}C spins of each amino acid spin system impede polarization transfer to more distant sites (i.e., dipolar truncation). Moreover, cross peaks may be misleadingly interpreted as correlations between remote spins by direct through-space coupling, when instead they are the result of relayed magnetization transfer along a network of spins. Both effects can be suppressed to some extent by sparsely labeling the protein so as to limit the probability of ^{13}C spins being bonded to each other (see section "Alternative Isotope Labeling Patterns").

Multidimensional heteronuclear (^{15}N–^{13}C) correlation experiments are the mainstay of any sequential assignment strategy.[13] Main-chain amide nitrogens form the bridge between adjacent amino acids, and thus by utilizing heteronuclear polarization transfer between N(i) and either CO$(i-1)$ or C$\alpha(i)$, a series of inter- and intraresidue connectivities can be established. A convenient form of ^{13}C–^{15}N transfer is to apply narrow-band or frequency-specific cross polarization (CP) for rare spin signal enhancement and to shorten recycle times, using adiabatic passage CP or SPECIFIC CP.[14] Under MAS at rate ω_r, polarization transfer between spins I and S occurs if the applied fields (ω_{1I} and ω_{1S}) and chemical shift offsets (Ω_I and Ω_S) satisfy the following condition:

$$\sqrt{\Omega_I^2 + \omega_{1I}^2} \pm \sqrt{\Omega_S^2 + \omega_{1S}^2} = n\omega_r \qquad (27.1)$$

Thus, by appropriate selection of the transmitter frequencies and fields, the CP step can be tailored to facilitate highly selective and efficient transfer between ^{15}N and ^{13}C and thereby generate subspectra displaying selective correlations between either N(i) and CO$(i+1)$ or N(i) and C$\alpha(i)$. With an additional homonuclear transfer step, the ^{13}C dimension can be expanded to give Cα–Cβ(CX) and CO–Cα(CX) correlations, where CX denotes carbon sites beyond Cα and Cβ but within the same amino acid spin system. A general scheme for these so-called NCACB and NCOCA procedures is shown in Figure 27.3(b).

By combining two-dimensional C–C spectra with NCOCA and NCACB spectra, and with knowledge of amino acid intraresidue coupling patterns, the ^{13}C and ^{15}N chemical shifts can be assigned to specific amino acid residues by walking through the spectra according to sequential connectivities. The case is illustrated with the simple case of the hypothetical tripeptide segment Ala$_i$-Ser$_{i+1}$-Val$_{i+2}$ in Figure 27.4. Analogous experiments that utilize polarization transfer via scalar couplings rather than dipolar interactions may be useful for observing cross peaks that are attenuated in the dipolar experiments because of motion.[15]

The assignment of spectra becomes more challenging as the protein size increases because of crowding and resolution, and strategies to simplify the spectra of uniformly labeled samples by generating amino-acid-specific subspectra have been proposed. For example, a methyl filtering block has been introduced into two-dimensional ^{13}C–^{13}C and ^{15}N–^{13}C correlation experiments to generate spectra specifically for leucine.[16]

27.4 STRUCTURAL RESTRAINTS

An ensemble of three-dimensional structures is derived from a variety of complementary measurements on fully or partially assigned ^{13}C/^{15}N spectra. Measurements take the form of chemical shifts and main-chain torsional angles to estimate local secondary structure, and distance-dependent dipolar couplings that place constraints on short- and long-range internuclear distances defining the global protein fold.

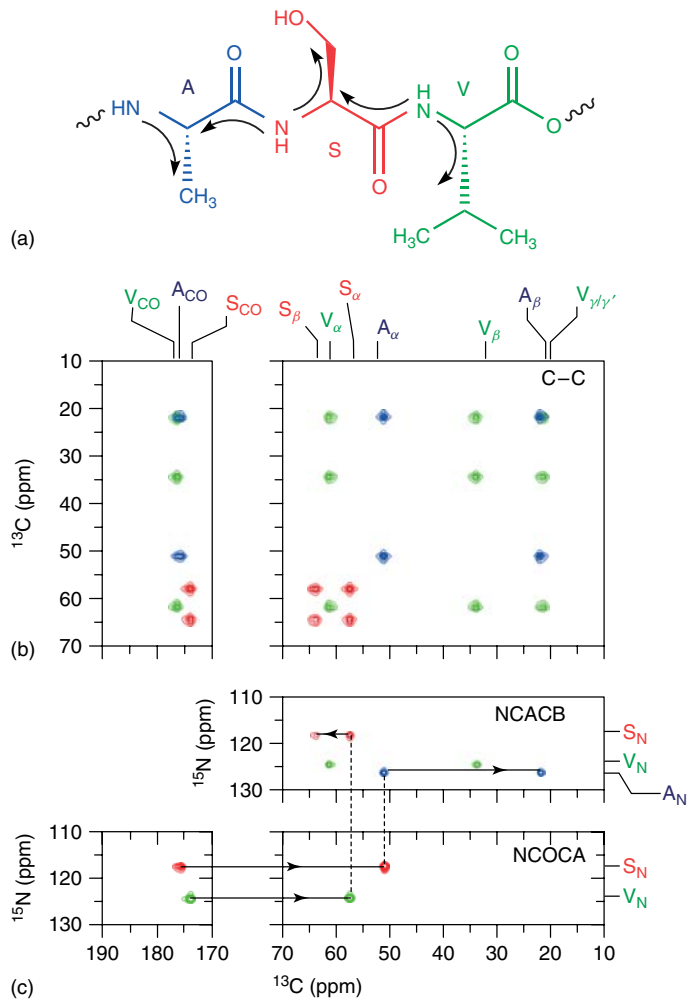


Figure 27.4. A simulated example of an assignment protocol using NMR crystallography. The trivial case of the tripeptide segment Ala-Ser-Val is given. (a) A $^{13}C-^{13}C$ correlation experiment with full-exchange within each amino acid spin system (obtained using an experiment such as in Figure 27.3(a)) shows the characteristic cross-peak patterns used to identify the spin systems for alanine (A: blue), serine (S: red), and valine (V: green). In this case, sequential cross peaks are not observed. (b) An NCACB-type experiment correlates ^{15}N of residue i with the α-carbon (CA) and β-carbon (CB) of residue i. (c) An NCOCA-type experiment correlates ^{15}N of residue i with carbonyl carbon CO and CA of residue $i-1$. It is now possible to sequentially assign the spectra by "walking" along the cross peaks. Thus, CA of A ($A\alpha$) is correlated with N of A (A_N) in the NCACB spectrum and $A\alpha$ is correlated with N of S (S_N) in the NCOCA spectrum. Similarly, $S\alpha$ is correlated with S_N in the NCACB spectrum and $S\alpha$ is correlated with V_N in the NCOCA spectrum. Chemical shifts are taken from the average values for random coil proteins (Biological Magnetic Resonance Data Bank).

27.4.1 Secondary Structure

Isotropic ^{13}C and ^{15}N chemical shifts are sensitive to main-chain geometry, providing a convenient means of estimating local secondary structure from assigned $^{13}C/^{15}N$ spectra. One simple secondary structure predictor is the reduced chemical shift value $\Delta\delta$, calculated from measured chemical values for $C\alpha$ and $C\beta$ and from average random coil (RC) database values for each specific amino acid type (e.g., taken

from the Biological Magnetic Resonance Data Bank) according to the following relationship:

$$\Delta\delta = \{\delta_{C\alpha}(\text{meas}) - \delta_{C\alpha}(\text{RC})\} - \{\delta_{C\beta}(\text{meas}) - \delta_{C\beta}(\text{RC})\} \quad (27.2)$$

Correlation between $\Delta\delta$ and local secondary structure is greatest for β-sheet regions of proteins, with $\Delta\delta$ being large and negative.[17] This approach is thus suited to β-sheet-rich proteins such as amyloid fibrils.

The statistical analysis routine TALOS[18] is used more routinely to provide quantitative estimates of main-chain (ϕ and ψ) torsional angles for triplets of amino acids with reference to a large database of ^{1}H, ^{15}N, and ^{13}C chemical shift values for identical triplets in proteins of known structure. Values are most accurate for structurally well-defined regions of proteins, containing long α-helical or β-strand stretches, but are less reliable for loop or turn regions; dynamics, crystal packing, and conformational heterogeneity can also cause deviations from predicted values.

Chemical shift anisotropy (CSA) values potentially contain information about secondary structure, but so far have been underexploited in structural studies of proteins in the solid state. Theoretical studies predict that the CSA for Cα in α-helical conformations is larger in magnitude than for β-sheet conformations, and solid-state NMR studies of small peptides have also quantified the dependence of tensor parameters on backbone dihedral angles. Recent three-dimensional experiments to obtain site-specific CSA values from uniformly labeled proteins have recently been demonstrated and these may extract further structural information.[19]

Protein backbone geometry can be quantified directly using multidimensional experiments to monitor the time evolution of multiple quantum coherences under the local fields of bonded spins. These experiments generate time-dependent signal amplitudes that are sensitive to the relative orientations of specific C–H and N–H dipolar vectors or to the orientations of pairs of C–N dipolar vectors (Figure 27.5). Torsional angle ϕ, defined formally by the bonded backbone atoms CO($i-1$)–N(i)–Cα(i)–CO(i), can be measured in an experiment that is sensitive to the absolute value of the main-chain angle θ, defined as H(i)–N(i)–Cα(i)–CO(i)[20] (Figure 27.5a). For L-amino acids, the measured angle θ is related to ϕ by $\phi = \theta + 60^{\circ}$. The absolute value of angle ψ, defined as N(i)–Cα(i)–CO(i)–N($i+1$), can be measured by following the evolution of Cα–CO double-quantum coherences during t_1 under the influence of N–Cα and CO–N dipolar couplings[21] (Figure 27.5b). In both cases, a series of experiments is performed to obtain signal amplitudes over a range of t_1 times; the normalized amplitudes are compared with numerically simulated curves to obtain a range of values for ϕ (from θ) and ψ. Examples of the modulation of signal amplitudes over t_1 are given in Figure 27.6(a) and (b). From the statistical plots in Figure 27.6(c) and (d), it is clear that the angular sensitivity of the curves is greatest over the range from $\pm 130^{\circ}$ to $\pm 180^{\circ}$ for θ (i.e., ϕ ranges from -70° to -170°, the β-sheet region of the Ramachandran plot) and over the range $\pm 130^{\circ}$ to $\pm 180^{\circ}$ for ψ, and are essentially invariant in the region from 30° to 100°. Moreover, the amplitudes are sensitive only to the absolute value of the torsional angles. These shortcomings can be allayed in part by combining with additional experiments measuring the relative orientations of dipolar and chemical shielding tensors,[22] or the projection angles defined as H(i)–N(i)–N($i+1$)–H($i+1$)[23] and H(i)–Cα(i)–N($i+1$)–H($i+1$),[24] to resolve degeneracies in the conformational solutions. Alternative methods for ^{13}C (or ^{15}N) detection of ^{1}H spin-diffusion rates between Hα(i) and Hα($i+1$) can provide sensitivity in the helical region of Ramachandran space.[25,26] These latter methods are described further in section "Higher Order Structural Constraints".

27.4.2 Side-Chain Geometry

Methods for determining the conformation of amino acid side groups generally involve precise measurements or estimates of through-space distances between main-chain and side-chain ^{13}C and ^{15}N sites. Such measurements exploit the well-known relationship between the internuclear distance r_{IS} separating spins I and S and the dipolar coupling constant D_{IS}:

$$D_{IS} = \left(\frac{\mu_0}{4\pi}\right)\frac{\gamma_I \gamma_S h}{(2\pi r_{IS}^3)} \quad (27.3)$$

which is inherent in the NMR signal amplitudes or line shapes. All the other terms in equation (27.3) take their usual values. Under even modest MAS

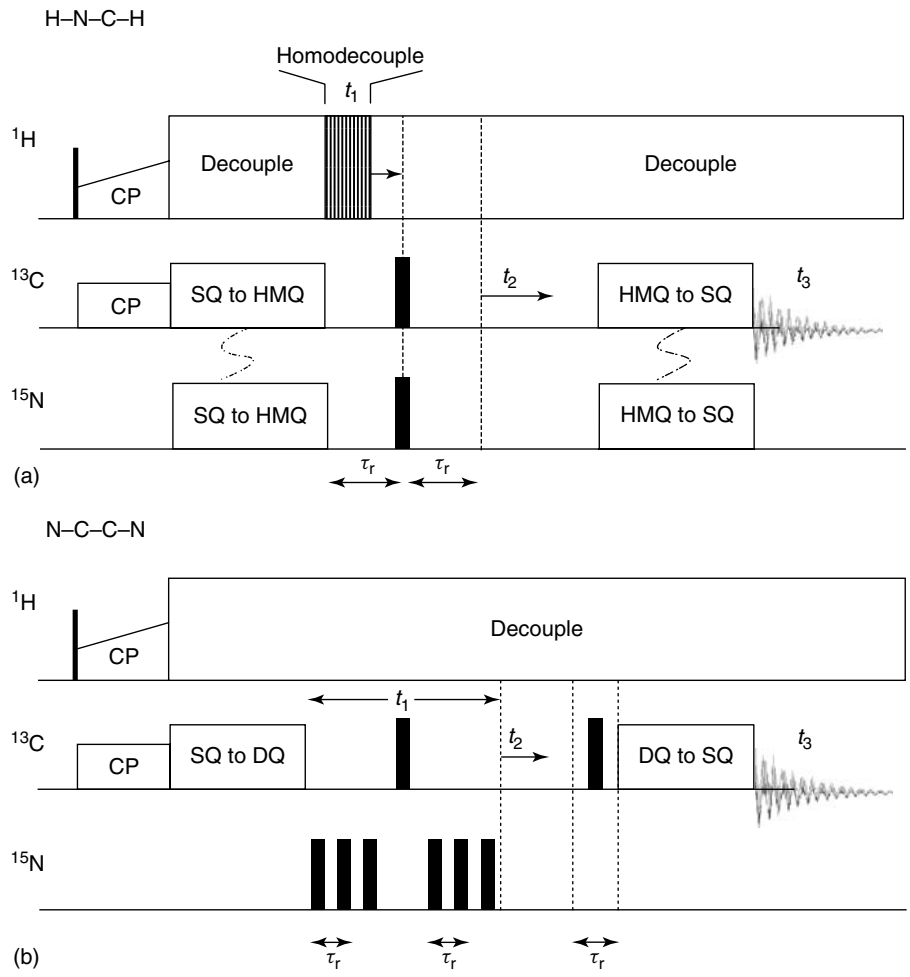


Figure 27.5. Generalized examples of two pulse schemes used to measure the main-chain torsional angles ϕ and ψ for peptides and proteins in the solid state. (a) An H–N–C–H experiment, which is sensitive to the relative orientations of correlated N–H and C–H dipolar vectors. Heteronuclear multiple quantum (HMQ) coherences between N($i+1$) and C$\alpha(i)$ are excited by recoupling the ^{13}C–^{15}N dipolar interaction, using a REDOR pulse train, for example, and is converted back to ^{13}C single quantum (SQ) coherence for observation. Proton homonuclear decoupling during t_1 (where t_1 is less than or equal to one rotor period τ_r) can be achieved using a frequency-switched Lee–Goldburg block. (b) An N–C–C–N experiment, which is sensitive to the relative orientations of correlated ^{13}C–^{15}N dipolar vectors. Double-quantum (DQ) coherence can be excited using a symmetry-based pulse sequence such as C7 or POST-C7.

rates, however, weak dipolar interactions are averaged to zero and thus homonuclear and heteronuclear dipolar recoupling experiments must be employed to restore these interactions and collect data from which the distance information is extracted.

Side chains of amino acids other than glycine and alanine are conformationally variable and defined by torsional angles χ_1 (N(i)–C$\alpha(i)$–C$\beta(i)$–X$\gamma(i)$) and χ_2 (C$\alpha(i)$–C$\beta(i)$–X$\gamma(i)$–X$\delta(i)$), where heavy atom Xδ = C, N, S, or O (the conformations of lysine and arginine are further defined by χ_3 and χ_4). Evaluation of known protein structures indicates that χ_1 is statistically predisposed to take values of -60° (gauche(+)), $+60^\circ$ (gauche(−)) or 180° (trans). Side chains tend to adopt the same three angles ($\pm 60^\circ$, 180°) about χ_2 since these

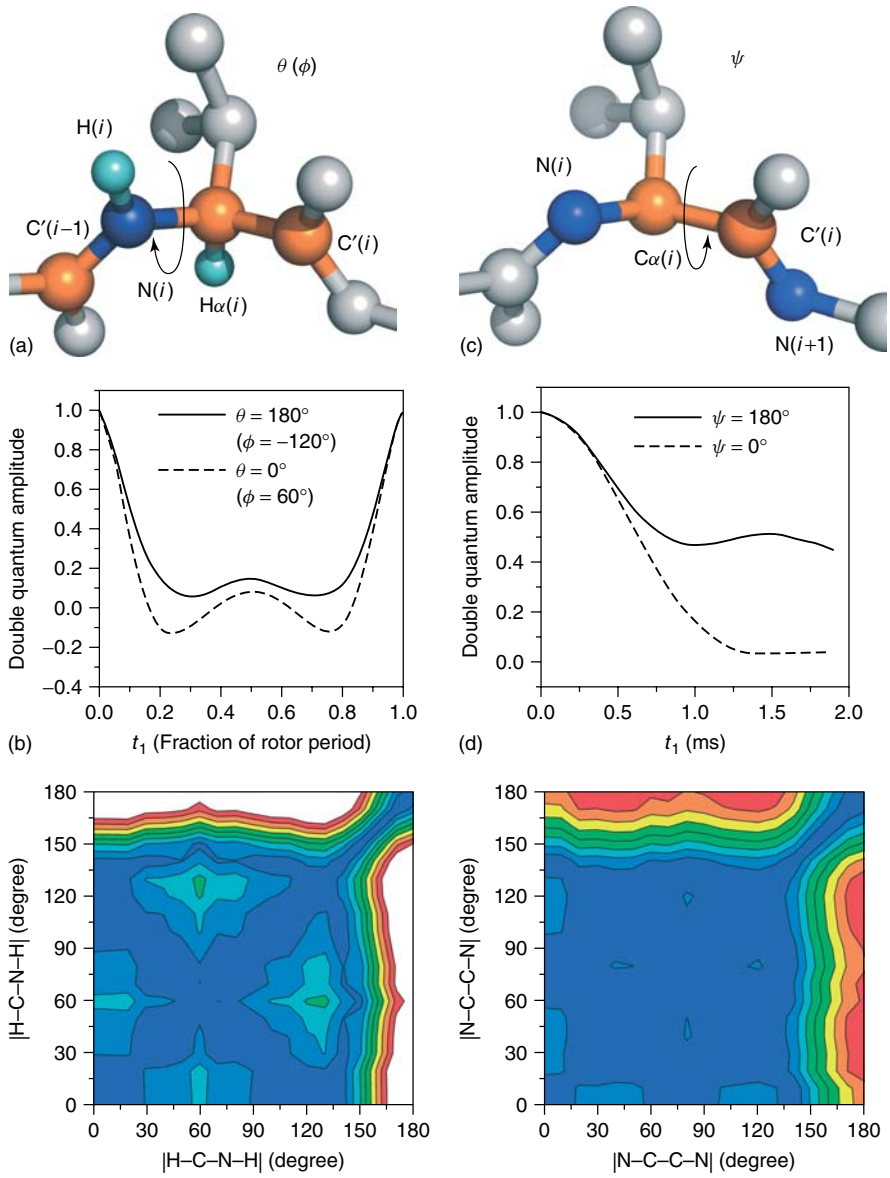


Figure 27.6. Sensitivity of the H–N–C–H and N–C–C–N experiments in Figure 27.5 to the backbone torsional angles ϕ and ψ. (a) Measurement of angle θ ($H^N(i)$–N(i)–Cα(i)–Hα(i)) using the scheme in Figure 27.5(a) gives angle ϕ according to the relationship $\phi = \theta + 60^\circ$. Signal amplitudes (expressed as a fraction of one cycle of sample rotation under MAS) for two extreme angles θ (0°, 180°) corresponding to angles ϕ of 60° and 240° (−120°) (bottom). (b) Angular sensitivity of the H–N–C–H experiment shown in two-dimensional root mean square deviation (RMSD) plot. Blue regions indicate the range of angles for which there is little or no change in the measured signal amplitude curves. (c) Angle ψ is measured directly using the scheme in Figure 27.5(b). Signal amplitudes (expressed as a fraction of one cycle of sample rotation under MAS) for angles ψ of 0° and 180° (bottom). (d) Blue regions in the RMSD plot again indicate the range of angles for which there is little or no change in the measured signal amplitude curves.

correspond to staggered configurations. For a specific residue, the value of χ_1 can, in principle, be obtained by measuring the distance $r_{NC\gamma}$ between its main-chain nitrogen N(i) and, if appropriate, Cγ(i), according to the following geometric relationship:

$$\chi_1 = \cos^{-1}\left\{\frac{r_1^2 + r_2^2 + r_3^2 - r_{NC\gamma}^2 - 2r_1r_2\cos a_1 - 2r_2r_3\cos a_2 + 2r_1r_3\cos a_1\cos a_2}{2r_1r_3\sin a_1\sin a_2}\right\} \quad (27.4)$$

where r_1, r_2, and r_3 are the N–Cα, Cα–Cβ, and Cβ–Cγ bond lengths, respectively, and a_1 and a_2 are the N–Cα–Cβ and Cα–Cβ–Cγ bond angles, respectively.

Distance $r_{NC\gamma}$ can be measured from uniformly labeled proteins using experiments such frequency-selective REDOR (*see* **Chapter 11**), which reinstates dipolar interactions between selected pairs of spins. This approach is not very practicable when applied to uniformly labeled proteins because it requires many individual measurements to be performed by carefully adjusting the transmitter frequencies each time. Moreover, distance $r_{NC\gamma}$ gives only the absolute value of χ_1, making individual measurements impossible to distinguish between gauche(+) and gauche(−) conformations, for example, where both correspond to a distance $r_{NC\gamma}$ of ~3.0 Å. These problems have been overcome using a three-dimensional z-filtered transferred-echo double resonance (TEDOR) experiment[27] (*see* **Chapter 11**) in which the intensities of cross-peaks correlating main-chain ^{15}N and side-chain ^{13}C sites reflect two internuclear distances, i.e., N(i)–Cγ(i) (i.e., $r_{NC\gamma}$) and N($i+1$)–Cγ(i) (Figure 27.7). The advantage of this approach is that multiple distances can be measured from a uniformly ^{13}C and ^{15}N labeled protein and the sign of χ_1 can in each case be determined by triangulation, if the backbone conformation is already known.

Distance measurements are sensitive up to ~4.5 Å for ^{13}C–^{15}N and thus $r_{NC\gamma}$ can in principle access the entire conformational space of χ_1 and much of the conformational space of χ_2 (i.e., from the distance N(i)–Cδ(i)), although certain [χ_1,χ_2] combinations place N(i)–Cδ(i) beyond the upper limit of detection. Longer range distances between pairs of protons in specific C–H groups can also be estimated using CHHC rare spin-detected spin-diffusion measurements by exploiting the large gyromagnetic ratio of protons.[26] However, the accuracy is compromised for distances between protons in CH groups and in CH_2 or CH_3 groups.

27.4.3 Higher Order Structural Constraints

The above-described methods create a two-dimensional map of secondary structural elements along the protein sequence, which is then used to generate an ensemble of three-dimensional structural models of the overall protein fold by obtaining medium- and long-range constraints defining tertiary (and, for protein complexes, quaternary) contacts. Such constraints usually take the form of through-space interactions between side groups, main-chain sites, or both, which are distant from one another in the primary sequence but close together in the folded protein (Figure 27.8a and b).

A convenient method for observing long-range contacts is to monitor rates of proton spin diffusion (*see* **Chapter 14**), which have a $1/r^6$ proton distance dependence and are thus analogous to solution-state NOESY experiments. For uniformly ^{15}N- and ^{13}C-labeled proteins, direct observation of protons is not straightforward (although recent advances have made this possible, as described in the following section) and two-dimensional CHHC and NHHC experiments[26] have been developed to detect protons indirectly with ^{13}C or ^{15}N observation. In these experiments, nonselective CP from ^{1}H to ^{13}C (or ^{15}N) is followed by ^{13}C (or ^{15}N) chemical shift evolution in t_1 before reverse CP from ^{13}C (or ^{15}N) to ^{1}H. The ^{1}H magnetization is stored longitudinally and is allowed to diffuse within the proton network for a mixing period t_m before a final CP step to the observed ^{13}C (or ^{15}N). In a two-dimensional CHHC spectrum, proton–proton interactions between sites C_i–H_i and C_j–H_j are detected as a cross peak correlating the frequencies of C_i and C_j. Three-dimensional variants of these experiments provide additional resolution and constraints. The build up of cross-peak intensities as a result of

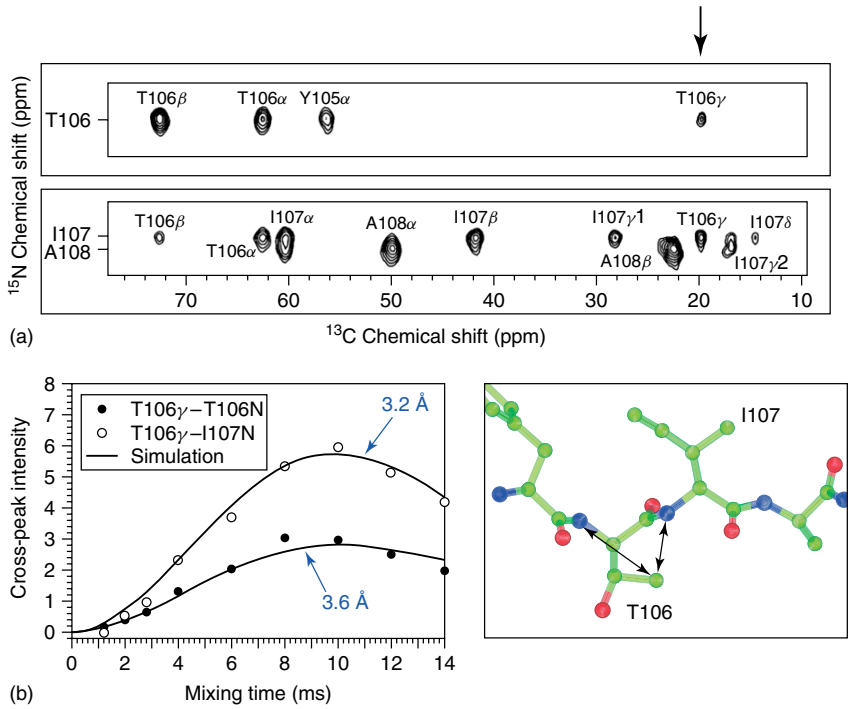


Figure 27.7. A *z*-filtered ^{13}C,^{15}N-TEDOR experiment for determining side-chain conformations in uniformly labeled polypeptides. (a) Strips from the two-dimensional ^{13}C,^{15}N chemical shift correlation spectrum of the short peptide TTR(105–115). Cross peaks correlating Cγ of residue T106 with N of T106 and residue I107 are denoted by the arrow. (b) Experimental and simulated intensities for T106N–T106Cγ and T107N–T106Cγ cross peaks as a function of TEDOR mixing time (left) and a model showing the corresponding measured distances (right). (Adapted from Jaroniec, C. P.; MacPhee, C. E.; Bajaj, V. S.; McMahon, M. T.; Dobson, C. M.; Griffin, R. G., High-resolution molecular structure of a peptide in an amyloid fibril determined by magic angle spinning NMR spectroscopy. *Proceedings of the National Academy of Sciences of the United States of America* 2004, **101**, (3), 711–716 © National Academy of sciences, 2004.)

spin diffusion during t_m can be approximated by an exponential process[28]:

$$I_{ij} = 1 - \exp\left(\frac{-t_m}{T_{\mathrm{SD}}}\right) \tag{27.5}$$

Under MAS at frequency ω_{r} the spin-diffusion time constant T_{SD} for a specific proton pair is, to the lowest approximation, given by the H_i–H_j distance r_{ij} and the zero quantum line-shape function $J^{\mathrm{ZQ}}(\Delta, \omega_{\mathrm{r}})$, which is evaluated at the isotropic chemical shift difference Δ of I spin 1 and 2, according to

$$\frac{1}{T_{\mathrm{SD}}} = \left(\frac{\mu_0}{4\pi}\right)^2 \frac{\hbar^2 \gamma_H^4}{r_{ij}^6} J^{\mathrm{ZQ}}(\Delta, \omega_{\mathrm{r}}) \tag{27.6}$$

Calculated curves agree with the experimental build-up curves most closely at short mixing times and for short H_i–H_j distances (of up to 3.5 Å) because transfer between pairs of protons at short mixing times is essentially direct. Multiple spin effects dampen the magnetization build-up curves at longer mixing times, however, and, in addition, the predicted curves begin to deviate from the experimental data at longer ^{1}H–^{1}H distances (>5 Å). Nevertheless, even qualitative information about long-range distances can provide valuable constraints on tertiary structure.

Quaternary structure is defined as the molecular organization of individual, usually independently folded, polypeptide chains in a multisubunit complex. Protein NMR crystallography can be used in principle to highlight protein–protein contacts at the interfacial sites by mapping chemical

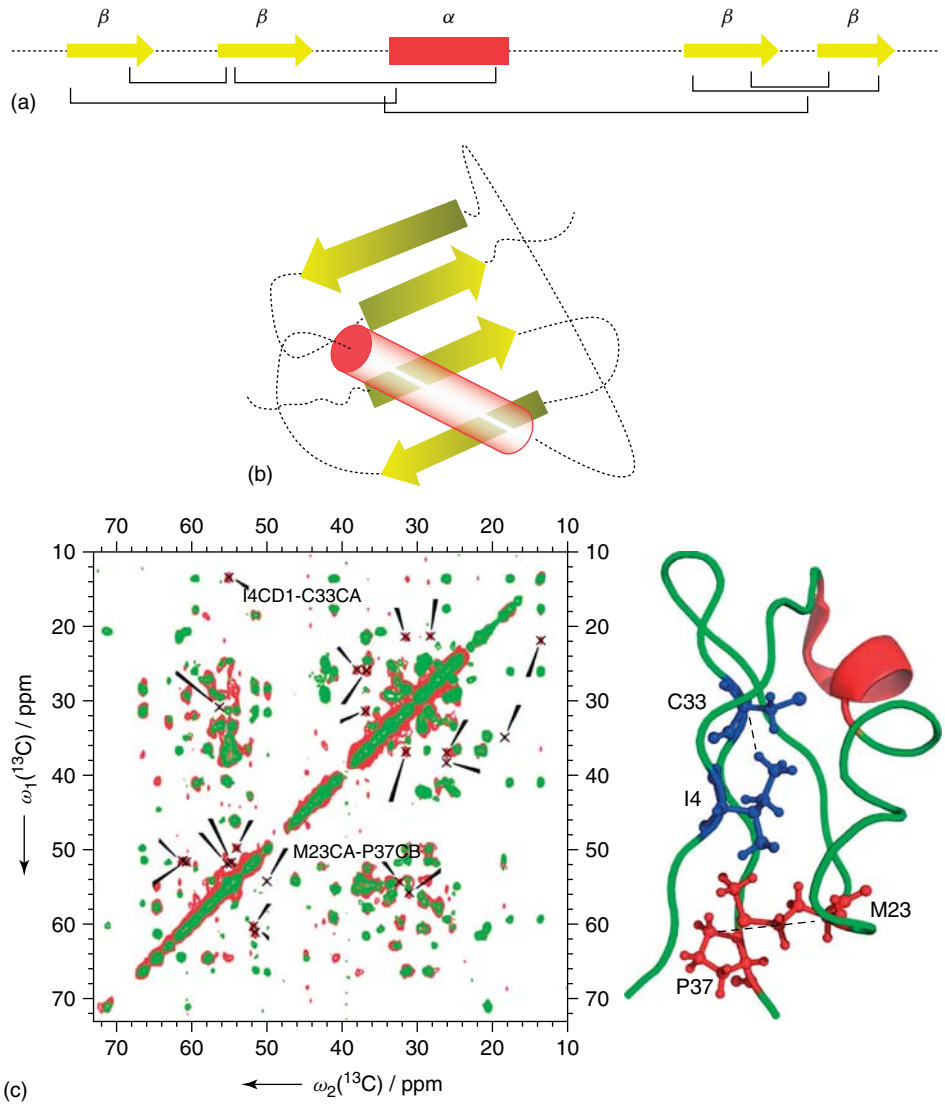


Figure 27.8. Example of the procedure to generate a tertiary structural model of a protein from a two-dimensional map of secondary structure. (a) Secondary structural map of a hypothetical protein showing underneath (as solid lines) long-range connectivities typical of those identified in a CHHC experiment, for example. (b) A three-dimensional model of the protein in (a) created from the long-range constraints shown. (c) Experimental $^{13}C-^{13}C$ (green) and CHHC (red) spectra of the 38-residue kaliotoxin (KTX) peptide in the solid state. Spectrum reproduced from Ref. [26] by permission of Wiley-VCH. Cross peaks correlating long-range $^{1}H-^{1}H$ interactions are arrowed. The model to the right-hand side of the spectrum shows the NMR crystallographic structure of KTX (accession code PDB1XSW) highlighting two long-range interactions corresponding to the labeled cross-peaks I4CD1-C33CA (blue) and M23CA-P37CB (red) identified from the CHHC spectrum. (Reproduced from Ref. 26. © Wiley-VCH, 2005.)

shift changes or by measuring intermolecular distances across an interaction surface. For homodimers and higher oligomers comprising identical polypeptide chains, it is possible to combine crystallographic mixtures of sequentially identical molecules but having different labeling patterns: for example, a mixed dimer containing individually ^{15}N- and ^{13}C-labeled molecules could be exploited to measure close ^{13}C–^{15}N contacts that occur exclusively at molecular interfaces.[29] In such cases, caution must be taken to distinguish the artificial "crystallographic" interface from the actual physiological interface, although the latter is more likely to involve more intimate contacts and intercalated residues (e.g., domain swapping).

One potentially useful, but so far underexploited, application of protein NMR crystallography is in the structural investigation of ligand recognition sites within proteins. Receptor–ligand complexes can be formed by soaking small molecules into preformed hydrated precipitates—a procedure that is performed routinely in X-ray crystallography—but here without the ultimate requirement for diffracting crystals. Binding of small molecules and peptides can induce small but selective movements in the ^{13}C and ^{15}N chemical shifts of resonances for a protein target, thus providing detailed information about protein–ligand contact sites that can guide ligand design, for example.[30]

27.5 ALTERNATIVE ISOTOPE LABELING PATTERNS

Although it is desirable to carry out structure determination by NMR crystallography on a single uniformly ^{13}C and ^{15}N labeled protein, issues of spectral crowding, resolution, and overlap present major obstacles to both assignment and structure determination of proteins of even modest size. Isotope labeling strategies have consequently lain at the heart of method development in protein NMR crystallography. Table 27.1 summarizes some common methods for isotope labeling proteins.

Spin dilution, by supplementing the bacterial growth media with [2-^{13}C]- or [1,3-^{13}C]glycerol as the sole carbon source, lowers the probability of two ^{13}C spins being bonded to each other, thereby reducing line broadening effects of one-bond J-couplings and strong dipolar coupling (owing to the $1/r^3$ distance dependence) and the effects of dipolar truncation.[5] Other approaches include amino-acid-specific labeling proteins (e.g., with mixtures of uniformly ^{15}N,^{13}C labeled and Cα, Cβ labeled amino acids) to give long-range interresidue cross peaks,[31] or "unlabeling", in which nonlabeled amino acids are added to the labeled growth medium. These selective methods require suitable auxotrophic bacterial strains that are deficient in the enzyme machinery to synthesize (or metabolize) the amino acids in which the growth medium is supplemented.

Protons were long neglected in SSNMR studies of biomolecules because their abundance and high gyromagnetic ratio promote strong homonuclear couplings that severely broaden the resonance lines. Even with high-frequency (>50 kHz) MAS and/or CRAMPS methods, the resolution is suitable only for small molecules having less than around 30 unique protons. Direct proton observation has recently been exploited in protein NMR crystallography by combining ^{15}N or ^{13}C/^{15}N labeling with deuteration to remove the vast majority of the proton network.[32–34] If the exchangeable amide protons are then fully or partially replaced by back substitution, the residual proton spins are dilute and only weakly coupled to one another and, thus, can be observed directly or indirectly without employing homonuclear decoupling schemes under fast MAS. Using experiments with ^{1}H–^{15}N–^{1}H transfer schemes and ^{1}H–^{1}H mixing by spin-diffusion or double-quantum excitation, NMR crystallography variants of solution-state (e.g., ^{1}H–^{15}N HSQC) experiments may be obtained with high resolution in the proton dimension.[32] Quantitative ^{1}H–^{1}H distance information can be obtained from the build up of peak intensities under DQ mixing, as the theoretical treatment of the exchange pathways is simplified in predominantly deuterated systems. Proton-observed ^{1}H, ^{13}C, ^{15}N spectra have also recently been used to solve the structure of a 50 amino acid protein from hundreds of ^{1}H–^{1}H distance restraints obtained at high field (750 MHz) and rapid MAS (~40 kHz).[35] Sensitivity was enhanced by almost 20-fold relative to direct ^{15}N detection and this approach could be applied to larger proteins if combined with methyl labeling, for instance, to allow measurements of CH_3–CH_3 and CH_3–NH distance constraints.

Table 27.1. Some isotope labeling strategies for protein structure determination using commercially available precursors

Labeling agent	Incorporation sites	Reasons for use
[$^{13}C_6$]glucose	Uniform ^{13}C	Routine assignment and structure determination
[1-^{13}C]glucose	Alternate ^{12}C–^{13}C–^{12}C and methyl ^{13}C	Simplification of relaxation analysis; removal of ^{13}C–^{13}C scalar coupling effects
[d_7]glucose/[^{15}N] ammonium chloride	Uniform ^{15}N and perdeuteration	^{1}H–^{15}N correlation (with amide proton back substitution)
[4,4′-$^{13}C_2$]-α-ketoisovalerate	Selective methyl labeling: [^{13}C-δ-Me]Leu, [^{13}C-γ-Me]Val	Simplification and assignment
[3,3′-$^{2}H_2$,4-^{13}C]-α-ketobutyrate	($^{13}C^{1}H$-δ_1-Me)Ile and selective methyl protonation	Simplification
[2-^{13}C]glycerol	Fractional ^{12}C–^{13}C–^{12}C	Simplification of relaxation analysis; removal of ^{13}C–^{13}C scalar coupling effects

27.6 STRUCTURE CALCULATION AND REFINEMENT

The short-, medium-, and long-range constraints (e.g., from magnetization build-up curves) are combined with backbone and side-chain torsional angle measurements to generate an ensemble of structures, often comprising several hundred three-dimensional models. These processes are normally carried out iteratively as the boundaries between the experiments required for assignment, structure determination, and refinement are loosely defined.

In practice, structural models are generated using programs used routinely in solution NMR, such as CNS/XPLOR, which incorporate the NMR constraints as force fields in molecular dynamics simulations combined with simulated annealing and energy minimization based on the known conformational preferences of proteins. A more manageable number of structures (10–50) can be selected by eliminating high-energy structures from the ensemble. In the first round of calculations, the remaining models usually exhibit substantial conformational variability, depending on how stringent the relationship is between cross-peak intensities and distance range, but a common structural fold may nevertheless emerge. Some constraints may be violated and it may be necessary to adjust the distance range specified by the constraints for further iterations. The early structural models may also assist in the assignment of ambiguous resonances in the spectrum by identifying coupling patterns, which can be introduced into further rounds of structure calculation. Back calculation of spectra from the structures can also help to validate or eliminate structural models, as do programs such as PROCHECK that highlight any deviations from preferred geometries. Finally, a small (<20) number of structures are derived, with precision determined by the backbone root mean square deviation (RMSD) within the ensemble and accuracy defined by the RMSD between the mean structure and the crystal structure if available. Figure 27.9 shows examples of recent protein structures determined using NMR crystallographic constraints and their similarity with the X-ray crystal structures. Recently reported RMSD values are less than 1.0 Å within structural ensemble and less than 2.0 Å between mean NMR and X-ray structures. The accuracy is largely limited by errors in the relative orientations of helices and strands (i.e., defined by loop regions).

27.7 DYNAMICS

One clear advantage of NMR crystallography over diffraction methods is the ability to monitor protein dynamics by analysis of relaxation and residual anisotropic interactions. Information about side-group mobility, such as the rotational dynamics of valine and leucine methyl groups and phenylalanine, tyrosine, and tryptophan aromatic rings, can provide a useful indicator of buried and exposed regions of proteins and their various interactions. Longitudinal relaxation rates from

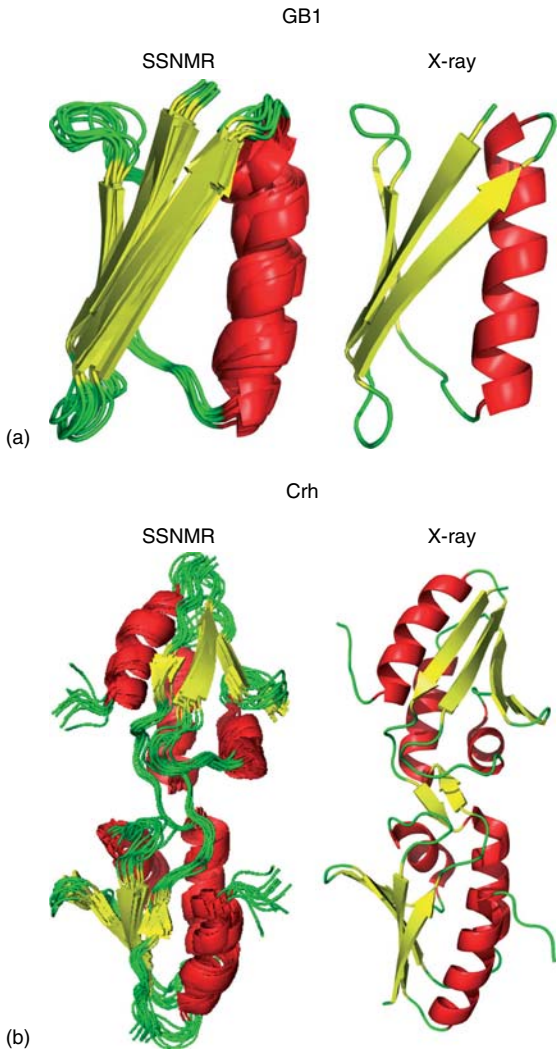


Figure 27.9. The three-dimensional structural ensembles for the immunoglobulin binding domain of protein G (GB1) (a) and Crh (b) determined by NMR crystallography (left) and X-ray diffraction (right). PDB accession codes for GB1 are PDB2JU6 for the NMR structures and PDBGI9 for the crystal structure. Accession codes for Crh are PDB2RLZ for the NMR structures and PDB1MU4 for the crystal structure.

multidimensional heteronuclear correlation methods may be interpreted qualitatively or quantitatively in a model-free manner to provide information about local main-chain and side-chain dynamics that augment prior structural analyses.[36–39] Imaginative isotope labeling strategies can again play a valuable role here: for instance, supplementing bacterial expression systems with specifically ^{13}C-enriched α-ketoisovalerate enables ^{1}H–^{13}C spin pairs to be incorporated into valine and leucine methyl groups amidst an extensively ^{2}H-labeled background.[40] This approach allows ^{13}C relaxation measurements to be interpreted straightforwardly in terms of the rates of side-group rotation about the valine Cα–Cβ and leucine Cβ–Cγ bonds.

Deuterium is a valuable nucleus with which local dynamics can be explored. Direct measurements of deuterium relaxation rates provide information about rapid dynamic processes with correlation times on the order of 10^{-8}–10^{-12} s, while the deuterium Pake pattern line shape reports on the amplitudes and modes of motional processes occurring on time scales greater than 10^{5}–10^{6} s^{-1}. Deuterium line shapes, which are dominated by the quadrupolar interaction and span a range of up to ~250 kHz, can be analyzed from experiments on static samples or under MAS. The example in Figure 27.10 highlights the sensitivity of ^{2}H MAS NMR line shapes to aromatic ring rotations. The amplitudes of motion along the main-chain and side groups of proteins can also be measured from residual ^{1}H–^{13}C dipolar anisotropies. Above the fast motional limit, at which the rate of the motional process exceeds the frequency of the measured interaction (~23 kHz for ^{1}H–^{13}C dipolar coupling), the order parameter S describes the extent of the angular excursions of the dipolar tensor from the principal rotational axis. The order parameter can take values from 0 (the isotropic limit) to 1 (the rigid limit) and is the ratio of the observed anisotropy to the maximum anisotropy at the rigid extreme. Heteronuclear dipolar interactions can be encoded within the third dimension of a homonuclear correlation experiment, thereby allowing extensive site-specific measurements of order parameters.[41]

27.8 PROSPECTS

Protein NMR crystallography has gained momentum as a viable alternative technique to X-ray diffraction in structural biology. In the quest for new structures, methods for analysis of larger proteins and complexes will become increasingly important. The utilization of protons, both indirectly as in the CHHC experiments and directly through the use of isotopic dilution, is likely to become more widespread. Moreover,

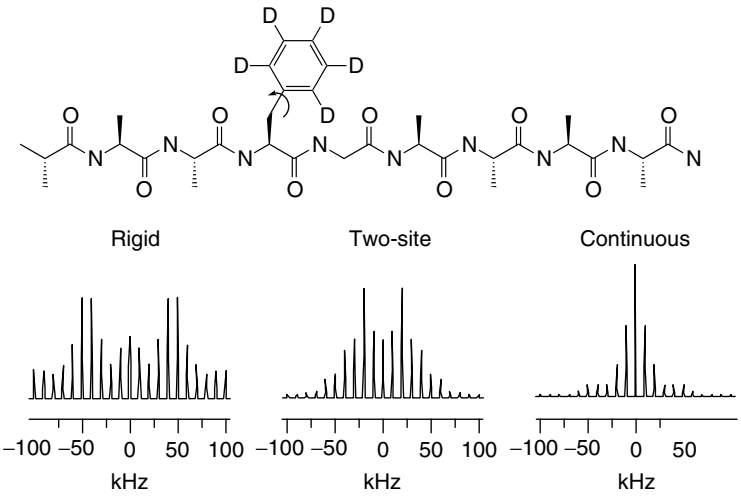


Figure 27.10. Simulated ^{2}H MAS NMR spectra (10 kHz spinning) for a fully deuterated phenylalanine ring undergoing different modes of motion. Simulated spectra are shown for the ring fixed in space or undergoing rapid ($k = 10^7$ s^{-1}) rotation about the C_β–C_γ bond, either as two-site 180° jumps or continuous rotation. In proteins, rings are either rigid or undergo two-site jumps (π-flips.)

recent advances in proton solid-state NMR spectroscopy provide an ideal opportunity to explore hydrogen bonding, which underpins all protein folds and macromolecular interactions. Much progress has been made in developing NMR crystallographic methods for characterizing hydrogen bonding in small organic molecules, but analogous methods tailored to the more demanding requirements of proteins are scarce at present. One promising approach is to incorporate carbonyl ^{17}O-labeled amino acids into specific residues of proteins and to measure hydrogen bond lengths using ^{17}O–^{1}H dipolar recoupling methods.[42] Finally, automation of the assignment and structural calculation processes will help to improve the throughput of structure determination. The increasing commercial availability and robustness of triple resonance MAS probes for standard bore magnets will open up many of these techniques to users who have not had routine access to solid-state facilities.

REFERENCES

1. A. Lange, K. Giller, S. Hornig, M. F. Martin-Eauclaire, O. Pongs, S. Becker, and M. Baldus, *Nature*, 2006, **440**, 959–962.
2. M. Etzkorn, S. Martell, O. C. Andronesi, K. Seidel, M. Engelhard, and M. Baldus, *Angew. Chem. Int. Ed.*, 2007, **46**, 459–462.
3. J. J. Lopez, A. K. Shukla, C. Reinhart, H. Schwalbe, H. Michel, and C. Glaubitz, *Angew. Chem. Int. Ed.*, 2008, **47**, 1668–1671.
4. C. Wasmer, A. Lange, H. Van Melckebeke, A. B. Siemer, R. Riek, and B. H. Meier, *Science*, 2008, **319**, 1523–1526.
5. F. Castellani, B. van Rossum, A. Diehl, M. Schubert, K. Rehbein, and H. Oschkinat, *Nature*, 2002, **420**, 98–102.
6. S. G. Zech, A. J. Wand, and A. E. McDermott, *J. Am. Chem. Soc.*, 2005, **127**, 8618–8626.
7. K. Seidel, M. Etzkorn, H. Heise, S. Becker, and M. Baldus, *Chembiochem*, 2005, **6**, 1638–1647.
8. T. Manolikas, T. Herrmann, and B. H. Meier, *J. Am. Chem. Soc.*, 2008, **130**, 3959–3966.
9. W. T. Franks, B. J. Wylie, H. L. F. Schmidt, A. J. Nieuwkoop, R. M. Mayrhofer, G. J. Shah, D. T. Graesser, and C. M. Rienstra, *Proc. Natl. Acad. Sci. U.S.A.*, 2008, **105**, 4621–4626.
10. M. Etzkorn, A. Bockmann, F. Penin, D. Riedel, and M. Baldus, *J. Am. Chem. Soc.*, 2007, **129**, 169–175.
11. R. W. Martin and K. W. Zilm, *J. Magn. Reson.*, 2003, **165**, 162–174.

12. K. Seidel, A. Lange, S. Becker, C. E. Hughes, H. Heise, and M. Baldus, *Phys. Chem. Chem. Phys.*, 2004, **6**, 5090–5093.
13. A. T. Petkova, M. Baldus, M. Belenky, M. Hong, R. G. Griffin, and J. Herzfeld, *J. Magn. Reson.*, 2003, **160**, 1–12.
14. M. Baldus, A. T. Petkova, J. Herzfeld, and R. G. Griffin, *Mol. Phys.*, 1998, **95**, 1197–1207.
15. L. Chen, J. M. Kaiser, T. Polenova, J. Yang, C. M. Rienstra, and L. J. Mueller, *J. Am. Chem. Soc.*, 2007, **129**, 10650–10651.
16. S. Jehle, M. Hiller, K. Rehbein, A. Diehl, H. Oschkinat, and B. J. van Rossum, *J. Biomol. NMR*, 2006, **36**, 169–177.
17. S. Luca, D. V. Filippov, J. H. van Boom, H. Oschkinat, H. J. M. de Groot, and M. Baldus, *J. Biomol. NMR*, 2001, **20**, 325–331.
18. G. Cornilescu, F. Delaglio, and A. Bax, *J. Biomol. NMR*, 1999, **13**, 289–302.
19. B. J. Wylie, W. T. Franks, D. T. Graesser, C. M. Rienstra, *J. Am. Chem. Soc.*, 2005, **127**, 11946–11947.
20. M. Hong, J. D. Gross, and R. G. Griffin, *J. Phys. Chem. B*, 1997, **101**, 5869–5874.
21. V. Ladizhansky, C. P. Jaroniec, A. Diehl, H. Oschkinat, and R. G. Griffin, *J. Am. Chem. Soc.*, 2003, **125**, 6827–6833.
22. M. Hong, J. D. Gross, W. Hu, and R. G. Griffin, *J. Magn. Reson.*, 1998, **135**, 169–177.
23. B. Reif, M. Hohwy, C. P. Jaroniec, C. M. Rienstra, and R. G. Griffin, *J. Magn. Reson.*, 2000, **145**, 132–141.
24. C. M. Rienstra, M. Hohwy, L. J. Mueller, C. P. Jaroniec, B. Reif, and R. G. Griffin, *J. Am. Chem. Soc.*, 2002, **124**, 11908–11922.
25. C. Gardiennet, A. Loquet, M. Etzkorn, H. Heise, M. Baldus, and A. Bockmann, *J. Biomol. NMR*, 2008, **40**, 239–250.
26. A. Lange, S. Becker, K. Seidel, K. Giller, O. Pongs, and M. Baldus, *Angew. Chem. Int. Ed.*, 2005, **44**, 2089–2092.
27. C. P. Jaroniec, C. E. MacPhee, V. S. Bajaj, M. T. McMahon, C. M. Dobson, and R. G. Griffin, *Proc. Natl. Acad. Sci. U.S.A.*, 2004, **101**, 711–716.
28. A. Lange, S. Luca, and M. Baldus, *J. Am. Chem. Soc.*, 2002, **124**, 9704–9705.
29. M. Etzkorn, A. Bockmann, A. Lange, and M. Baldus, *J. Am. Chem. Soc.*, 2004, **126**, 14746–14751.
30. S. G. Zech, E. Olejniczak, P. Hajduk, J. Mack, and A. E. McDermot, *J. Am. Chem. Soc.*, 2004, **126**, 13948–13953.
31. M. Hiller, V. A. Higman, S. Jehle, B. J. van Rossum, W. Kuhlbrandt, and H. Oschkinat, *J. Am. Chem. Soc.*, 2008, **130**, 408–409.
32. V. Chevelkov, K. Rehbein, A. Diehl, and B. Reif, *Angew. Chem. Int. Ed.*, 2006, **45**, 3878–3881.
33. V. Agarwal, A. Diehl, N. Skrynnikov, and B. Reif, *J. Am. Chem. Soc.*, 2006, **128**, 12620–12621.
34. E. K. Paulson, C. R. Morcombe, V. Gaponenko, B. Dancheck, R. A. Byrd, K. W. Zilm, *J. Am. Chem. Soc.*, 2003, **125**, 15831–15836.
35. D. H. Zhou and C. M. Rienstra, *Angew. Chem. Int. Ed.*, 2008, **47**, 7328–7331.
36. Y. Xue, M. S. Pavlova, Y. E. Ryabov, B. Reif, and N. R. Skrynnikov, *J. Am. Chem. Soc.*, 2007, **129**, 6827–6838.
37. M. Hologne, Z. J. Chen, and B. Reif, *J. Magn. Reson.*, 2006, **179**, 20–28.
38. B. Reif, Y. Xue, V. Agarwal, M. S. Pavlova, M. Hologne, A. Diehl, Y. E. Ryabov, and N. R. Skrynnikov, *J. Am. Chem. Soc.*, 2006, **128**, 12354–12355.
39. N. Giraud, A. Bockmann, A. Lesage, F. Penin, M. Blackledge, and L. Emsley, *J. Am. Chem. Soc.*, 2004, **126**, 11422–11423.
40. V. Agarwal, Y. Xue, B. Reif, and N. R. Skrynnikov, *J. Am. Chem. Soc.*, 2008, **130**, 16611–16621.
41. J. L. Lorieau and A. E. McDermott, *J. Am. Chem. Soc.*, 2006, **128**, 11505–11512.
42. A. Brinkmann and A. P. M. Kentgens, *J. Am. Chem. Soc.*, 2006, **128**, 14758–14759.

Chapter 28
Organic & Pharmaceutical Chemistry

Marek J. Potrzebowski

Center of Molecular and Macromolecular Studies, Polish Academy of Sciences, 90-362 Łódź, Poland

28.1 Introduction 435
28.2 Search for the Stereochemistry of Organic Compounds and Pharmaceuticals in the Solid State by Means of XRD and SSNMR 436
28.3 Polymorphism of Organic Compounds and Pharmaceuticals 439
28.4 Molecular Disorder 445
28.5 Cryocrystallography and Solid-State NMR 448
28.6 Conclusions 451
References 451

28.1 INTRODUCTION

Structural characterization of condensed matter represents a key challenge for researchers dealing with scientific disciplines such as organic and pharmaceutical chemistry as well as new materials engineering.[1] Understanding the properties of substances and knowledge of their three-dimensional structure are essential in accounting for the relationship between morphology and functions. There are a number of experimental techniques that are dedicated to the study of solid-state structures.[2] Usually, the first choice for researchers is a diffraction method, which provides a comprehensive and in many cases unequivocal set of structural data. Unfortunately, many materials are not amenable to structure determination based on single-crystal diffraction methods (neutron/X ray). This may be due to a variety of reasons such as the inability to grow large single crystals, inherent disorder within a crystal, or defects caused by impurities. Phenomena such as phase transitions, polymorphism, and sorption/desorption processes have significant influences on the structure of materials.

Much effort has recently been expended by X-ray crystallographers and theoreticians to introduce methods that allow the prediction of crystal structures of organic compounds by means of an *ab initio* approach.[3–5] Three collaborative workshops (1999, 2001, and 2004) were held at the Cambridge Crystallographic Data Center to test how well available methods perform when given only the atomic connectivity for a compound. A blind test was conducted on selected organic compounds with rigid geometry and torsional flexibility. The results of *ab initio* crystal structure prediction (CSP) were not fully satisfying. In particular, problems occur for compounds with flexible skeletons and those showing a tendency to form polymorphs.[6] Of course, the prediction problem is greatly simplified if powder diffraction data and information on unit-cell dimensions or space groups are known.

Significant recent progress has been made in diffraction methods for powdered solids.[7] Powder

NMR Crystallography Edited by Robin K. Harris, Roderick E. Wasylishen and Melinda J. Duer © 2009 John Wiley & Sons, Ltd. ISBN: 978-0-470-69961-4

diffraction patterns contain essentially the same information as with single crystals. In the latter case, diffraction data are distributed in three-dimensional space, whereas the diffraction data of powders are "compressed" into a one-dimensional pattern. As a consequence, there is usually considerable overlap of peaks in the powder diffraction diagram. Progress in overcoming peak overlap relies either upon finding improved techniques for extracting individual peak intensities from the overlapped data or the formulation of new structure-solution strategies. In consequence, within the last 15 years it has became possible to determine molecular structures of organic compounds and pharmaceuticals directly from powder X-ray diffraction (PXRD) data.

Although at first glance diffraction techniques seem to form a complete approach that provides a broad spectrum of structural information about condensed matter, these methods are not free from drawbacks and limitations. Burgi and Capelli very recently highlighted these limitations, concluding that "first, it is not the chemically interesting bond lengths and angles that are determined in a single-crystal diffraction experiment but the probability distributions of the atoms in the unit cell and second, it is not the "crystal structure" that is determined, but rather an average unit cell, i.e., the time and space average of the distributions of atoms over the entire crystals".[8]

Solid-state nuclear magnetic resonance (SSNMR) spectroscopy is a technique that gives a "fingerprint" of local structure and represents the local electronic environment for each nucleus.[9] The simplest piece of information to obtain from high-resolution spectra recorded under magic-angle spinning (MAS) is the isotropic chemical shifts of solids. The other NMR parameters, such as the chemical shift anisotropy, quadrupole interaction, and dipolar coupling constants, are relatively easily accessible. They provide information about electron distribution, local molecular motion, intra- and intermolecular interactions, and changes of local conformation.[10]

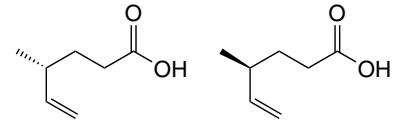
From the short review presented above, it is apparent that there is no "perfect technique" that is able to answer all structural questions related to the analysis of solid materials. Each of them is oriented to different aspects of structure. However, in a complementary approach joining SSNMR, XRD, and theoretical calculations, it is possible to obtain a very precise picture of matter. Such a *hybrid* strategy opens up new perspectives in structural studies of novel materials. In this article, we will show how these complementary methodologies can be used in structural studies of pharmaceuticals and organic compounds.

28.2 SEARCH FOR THE STEREOCHEMISTRY OF ORGANIC COMPOUNDS AND PHARMACEUTICALS IN THE SOLID STATE BY MEANS OF XRD AND SSNMR

Chiral products are commonly used in the pharmaceutical industry,[11–13] but the role of enantiopure organic compounds in other sectors such as flavor and aroma chemicals, agricultural chemicals, and specialty materials continues to rise. The worldwide revenues from chiral products in 2002 were estimated to be US$7 billion and it is predicted that they will grow to approximately US$15 billion by the end of 2009.[14]

It is well known that, in the case of chiral drugs possessing at least one stereogenic center, frequently only one of the two enantiomers is an active pharmaceutical ingredient (API), while the other may be inactive or even toxic.[15] A convincing example of the distinct physiological properties of different stereoisomers is given by the antiepileptic drug vigabatrin (**1a**), which inhibits the catabolism of γ-aminobutyric acid (GABA). Its *S*(+) form **1b** is highly toxic. The two structures are presented in Figure 28.1.

For analytical chemistry, the challenge is to develop methodology that provides detailed information about the absolute configuration of each chiral center and to establish optical purity. If single



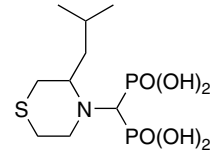
(**1a**) (**1b**)

Figure 28.1. The different stereoisomers of vigabatrin.

crystals of an API or an organic compound are available, X-ray crystallography (single-crystal X-ray diffraction (SXRD)) is the most efficient method to determine the relative stereochemistry and, under some circumstances, absolute configuration.[16] The first experimental determination of absolute configuration of a chiral molecule was achieved by Bijvoet *et al*. in 1951.[17] Employing anomalous X-ray scattering, which involves using X rays with a wavelength near the absorption edge of one of the atoms, the phase change at this atom relative to X rays scattered by other atoms is observed. The diffraction pattern is no longer truly centrosymmetric, but pairs of spots (Bijvoet pairs) in the pattern that are related by a center of symmetry become unequal in intensity. Nowadays, with modern X-ray equipment the assignment of absolute configuration for organic single crystals is a routine procedure. On the other hand, it has to be stressed that while SXRD is a useful method for the assignment of the stereochemistry of pure compounds (APIs), it is useless for the analysis of mixtures of stereoisomers and for establishing enantiomeric excess (ee). The problem of racemization of chiral drugs during handling, storing, and manufacture is well established.[15] Thus, methods that would enable the assignment of enantiomeric excess for final pharmaceutical products, e.g., tablets, are highly desirable.

SSNMR is a technique for which the methodology is being developed, slowly but surely, for the study of chiral organic compounds and APIs using the specific properties of condensed matter.[18] It is well known that the molecular packing and symmetries in crystals of enantiomers and racemates are not the same. Racemic crystals tend to be denser and more stable than their chiral counterparts. Wallach formulated this rule while investigating the differences in behavior of racemic crystals and homochiral molecules.[19] Since then, many researchers have exhaustively discussed the validity of this statement and, even though Wallach's rule has many exceptions, it expresses a general trend. Dunitz and coworkers have discussed, in a comprehensive review, the influence of enantiomeric interactions on conformational and crystal packing forces in racemic crystals and their chiral counterparts.[20]

The existence of different types of crystals, and consequently of diastereotopic intermolecular interactions, results in variation of physical properties



(**2**)

Figure 28.2. Structure of *N*-[(diphosphono)methyl]-3-isobutyl-thiomorpholine.

such as melting point, solubility, and intermolecular distances between chemically equivalent nuclei. Hence, the crystal and/or powdered samples of racemates and enantiomers should be easily recognizable by SSNMR spectroscopy, which gives observable differences in isotropic chemical shifts. SSNMR seems to be useful for the determination of the enantiomeric purity of chiral compounds.

This approach has been exploited by Jacobsen and coworkers for investigating chiral species of organophosphorus compounds.[21] In the cited paper, the authors reported ^{31}P CPMAS (cross-polarization/magic-angle spinning) NMR spectra for racemic and optically active forms of *N*-[(diphosphono)methyl]-3-isobutyl-thiomorpholine (**2**) shown in Figure 28.2. For this compound, the stereogenic center is localized on the ring but a prochiral phosphate group was employed as the stereochemical probe. The racemate and the chiral isomers gave well-resolved signals.

Figure 28.3(a) shows a spectrum that comprises two spinning sideband patterns of (−)-**2** with isotropic chemical shifts at 3.79 and 7.10 ppm, assigned to the inequivalent phosphorus atoms within the same molecules. This is in agreement with X-ray studies of the sample, which show that the crystallites belong to the space group $P2_12_12_1$, with one molecule in the asymmetric unit. A very similar spectrum of a racemic sample is shown in Figure 28.3(c), but the isotropic chemical shifts of the two spinning sideband patterns are different (−0.69 and 14.54 ppm). From NMR studies, it is apparent that molecular packing of the racemate and enantiomer is different. The spectrum in Figure 28.3(b) displays an almost enantiomerically pure (+) sample of **2**. The two dominant spinning sideband patterns are, as expected, identical to those in Figure 28.3(a). The low-intensity lines in Figure 28.3(b) are identical to the resonances observed in Figure 28.3(c). Simple integration (or deconvolution) of the MAS NMR signals in the

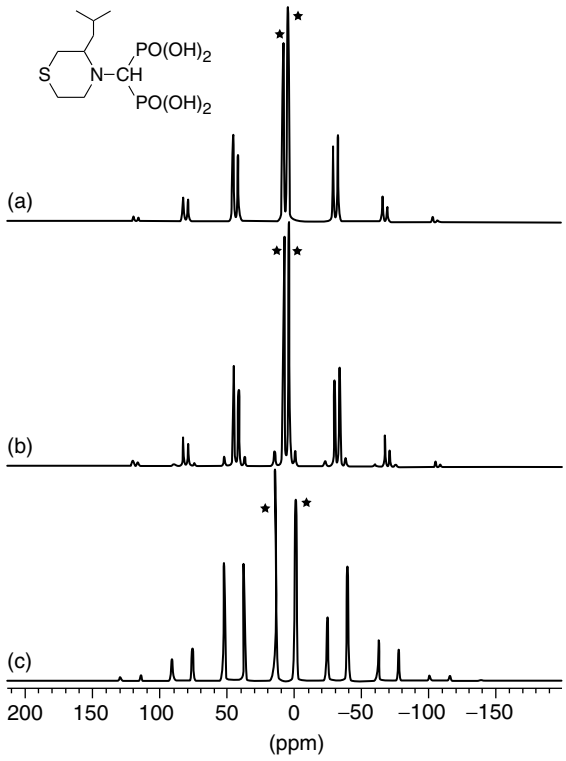


Figure 28.3. Phosphorus-31 CPMAS NMR spectra of (a) (−)-**2**, (b) (+)-**2**, and (c) racemic-2. The spinning speed was 4.6 kHz and the number of transients was 120 for all samples. (Reproduced from Ref. 21. © John Wiley & Sons Ltd, 1990.)

spectrum of Figure 28.3(b) can be used to determine the enantiomeric purity of this sample.

A slightly more advanced methodology was employed for establishing the enantiomeric excess for the P-chiral oxazaphosphorine derivatives (cyclophosphamides **3–5**) shown in Figure 28.4, which are used in oncology as therapeutic agents.[22] In this project, the authors used the one-dimensional exchange spectroscopy by sideband alternation (ODESSA) pulse sequence for measuring dipolar interactions between chemically equivalent sites. This one-dimensional SSNMR experiment utilizes the fact that the differences in distance between chemically equivalent but magnetically nonequivalent nuclei produce a difference in the rate constants of spin diffusion, W_{ij}.[23,24]

From the analysis of the ^{31}P SSNMR spectra of cyclophosphamides, it was apparent that δ_{iso} values and spinning sidebands patterns for the racemate–enantiomer pairs are almost the same so that differentiation between the racemate and enantiomer is not possible.

Proton-driven spin-diffusion rate constant (W_{ij}) measurements from ODESSA experiments were exploited to distinguish the enantiomer from the racemate. The W_{ij} values were obtained by measurement of the changes in intensities of the sidebands as a function of the mixing time τ_{mix} (Figure 28.5).

In order to answer the question of whether the ODESSA experiment can be applied for the determination of enantiomeric excesses, mixtures of the racemate and (−)-cyclophosphamide (−)-**3** in different proportions were prepared and the samples with 5, 10, 25, 40, 50, and 60% ee values were obtained. For each sample, the ODESSA experiment was run. It was found that the amplitude of the ODESSA decay increases with the amount of enantiomeric excess.

The variety of molecular phenomena to which tensors are sensitive prompted Grant's group to test whether the analysis of principal values could provide sufficient information to establish stereochemistry.[25] The sensitivity of ^{13}C tensor principal values to stereochemical differences in the natural product terrein (**6**) (Figure 28.6), which is a bioactive fungal metabolite with two stereocenters and a relatively simple structure, was investigated by Harper *et al*. Terrein (**6**) can form only four stereoisomers and has limited conformational flexibility, which make this compound a reasonably easy model for investigation of the relationship between relative stereochemistry and tensor shift. The five π replicated magic angle turning (FIREMAT) technique was employed to obtain the values of ^{13}C δ_{ii} parameters.

Figure 28.7 shows the spectrum of (**6**) performed with a spinning speed of 468 Hz. Such a slow sample spinning was necessary to obtain a sufficient number of spinning sidebands, needed for the calculation of ^{13}C δ_{ii} values. FIREMAT method is able to very efficiently separate overlapped spinning sideband systems and to establish isotropic and anisotropic values for each specific site. To investigate the sensitivity of ^{13}C tensors to stereochemistry, an approach was used in which computer generated models of a variety of conformers are made for each diastereomer and tensors computed for energy-minimized structures. From a complementary approach, it was concluded that it is sufficient to use only shift tensor values

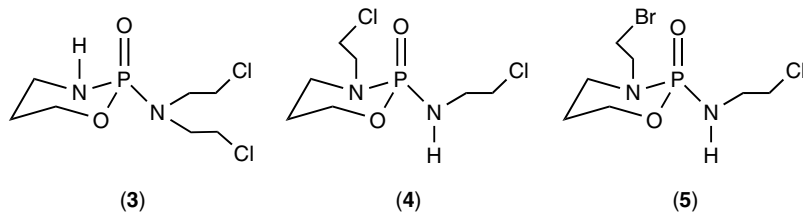


Figure 28.4. P-chiral oxazaphosphorine derivatives.

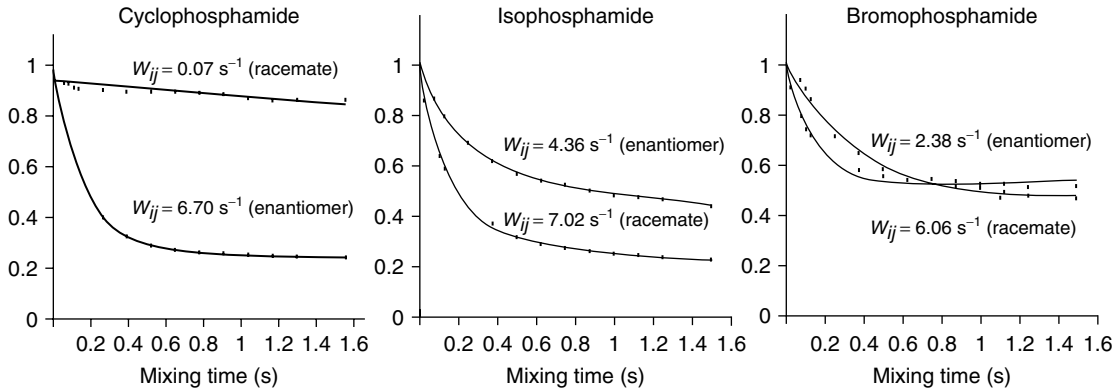


Figure 28.5. Intensity changes of the entire set of ^{31}P spinning sidebands for oxazaphosphorinane drugs in the ODESSA experiment as a function of mixing time. (Reproduced from Ref. 22. © Wiley VCH, 2002.)

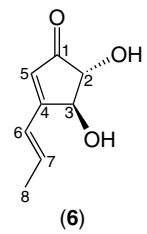


Figure 28.6. The structure of terrein. The atomic numbering used is shown.

at carbons 2 and 3 (Figure 28.6), the stereocenters, to characterize both stereochemistry and molecular conformations. It was noted that the use of only tensor principal values allows for the determination of relative stereochemistry. The presented methodology can be useful for investigating the stereochemistry of compounds that are difficult to crystallize. Other applications of SSNMR for studying stereochemistry are reported elsewhere.[18]

28.3 POLYMORPHISM OF ORGANIC COMPOUNDS AND PHARMACEUTICALS

A number of organic compounds and APIs exhibit polymorphism.[26] When polymorphism exists as a result of differences in crystal packing, it is called *packing polymorphism*. This phenomenon can also result from the existence of different conformers of the same molecule (conformational polymorphism). In other words, polymorphism is the ability of a compound to adopt two or more crystalline phases that differ in the conformation and/or arrangement of molecules in the crystal lattice. *Pseudopolymorphism* is a term that is used to describe the crystalline solid adducts containing solvent molecules within the crystal structure, in either stoichiometric or nonstoichiometric proportions, giving rise to unique differences in physical and pharmaceutical properties. If the incorporated solvent is water, the solvate is termed a *hydrate*. The various

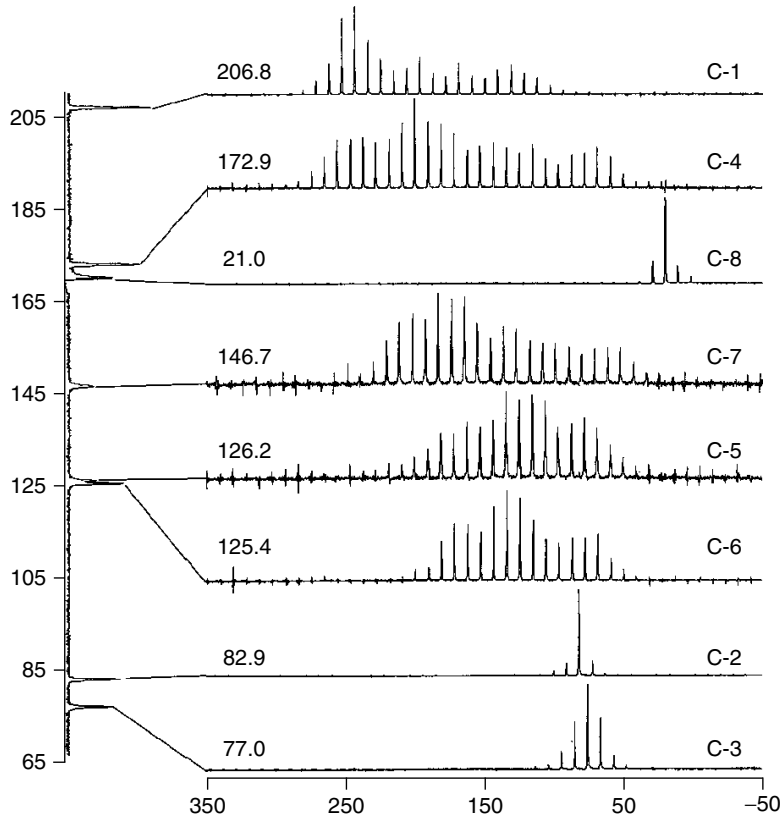
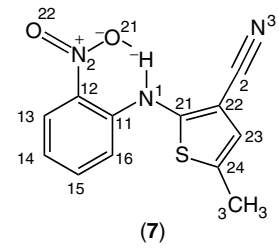


Figure 28.7. FIREMAT spectrum of terrein. Isotropic peaks are shown along the left side of the figure and corresponding tensor sideband patterns displayed horizontally. Assigned carbon numbers and corresponding isotropic shifts are listed on each sideband pattern. The isotropic peak displayed near 170 ppm (carbon 8) is aliased from its true position at 21.0 ppm for convenience in data collection. (Reproduced from Ref. 25. © American Chemical Society, 2001.)

crystalline forms of a polymorphic substance can have very different chemical, biological, or physical properties such as density, hardness, refractive index, melting point, solubility, dissolution rate, and even color. An interesting example of an organic compound coexisting at room temperature as red, orange, and yellow (ROY) polymorphs is 5-methyl-2-[(2-nitrophenyl)amino]-3-thiophenecarbonitrile (**7**) (Figure 28.8). It is the top system in the current Cambridge Structural Database for the number of polymorphs with solved crystal structures.[27]



(**7**)

Figure 28.8. Structure of 5-methyl-2-[(2-nitrophenyl) amino]-3-thiophenecarbonitrile.

Today, polymorphism is a great challenge for the pharmaceutical industry. According to FDA regulations, all known polymorphs of an API have to be recognized and fully characterized.[28] The FDA does not allow a company to market a new form without establishing the exact characteristics of the polymorph. Moreover, patent law protects the individual polymorphs. Early knowledge of all important new API crystalline forms might protect companies from serious problems.

SSNMR is an analytical technique that systematically extends the repertoire of novel approaches, allowing better understanding of the nature of polymorphism. This field was recently exhaustively reviewed, and a number of papers have been published.[29–35] Significant contributions regarding SSNMR studies of organic compounds and pharmaceuticals come from Harris's group. A number of APIs were investigated by employing mostly 1-D high-resolution NMR. Isotropic chemical shifts, chemical shift tensor (CST) parameters, and measurements of relaxation times have been reported for several systems including sulfathiazole (**8**), theophylline (**9**), indomethacin (**10**), nifedipine (**11**), and carbamazepine (**12**) (Figure 28.9).[36–43]

Recently, new 2-D SSNMR applications in structural studies of polymorphs were published. One- and two-dimensional approaches to the study of three polymorphs of aspartame (L-aspartyl-L-phenylalanine methyl ester), a commonly used sweetener in low-calorie food products, were reported by Zell *et al*.[44] Three distinct forms of aspartame, two hemihydrate polymorphs (aspartame · 0.5 H_2O) and a dihemihydrate (aspartame · 2.5 H_2O), are known to exist. A two-dimensional radio frequency driven recoupling (RFDR) spin-exchange experiment with a spinning speed of up to 26 kHz on uniformly labeled aspartame gave complementary assignments for short- and long-range interactions (Figure 28.10). Studies of neotame [*N*-(3,3-dimethylbutyl)-L-aspartyl-L-phenylalanine methyl ester] provided an interesting example of changes of polymorphic forms related to very high sample spinning rates.[45]

The separation of the isotropic and anisotropic parts of spectra with heavily overlapped systems is still a challenge for SSNMR spectroscopy. The 2-D PASS (phase adjusted spinning sidebands) experiment[46–48] has found a few remarkable applications in structural studies of polymorphs. The power of the method in the analysis of crowded spectra of organic compounds for the extraction of values of ^{13}C principal elements of CSTs was very recently demonstrated by Olejniczak and Potrzebowski.[49] In the cited paper, the authors investigated two crystallographic modifications of quercetin (3,3′,4′,5,7-pentahydroxyflavone) (**13**), one of the most important compounds belonging to the flavonoid group (Figure 28.11). Quercetin and other flavonoids have been shown to modify antiprostanoid and anti-inflammatory responses, to protect low-density lipoprotein from oxidation, and to promote relaxation of cardiovascular smooth muscle. Moreover, many of the flavonoids play a role as antioxidants and scavengers of free radicals.

The crystal and molecular structure of one of the polymorphs of quercetin was established by XRD.

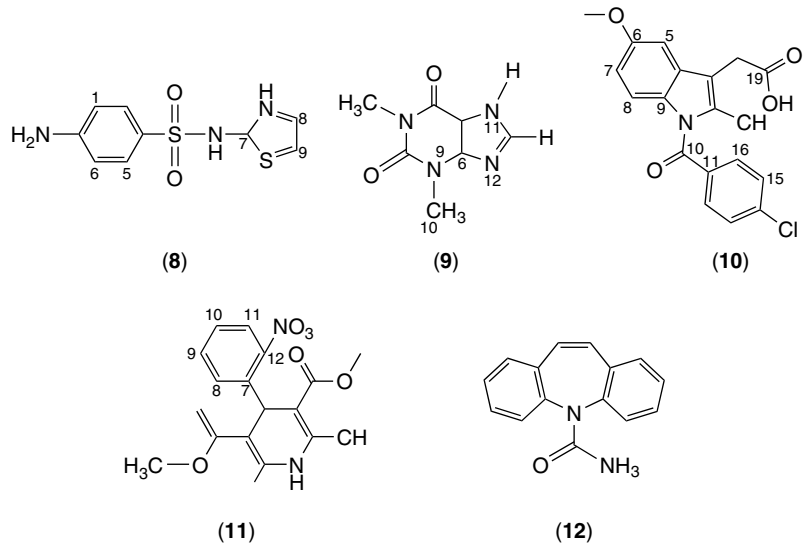


Figure 28.9. Structures of systems **8**–**12**.

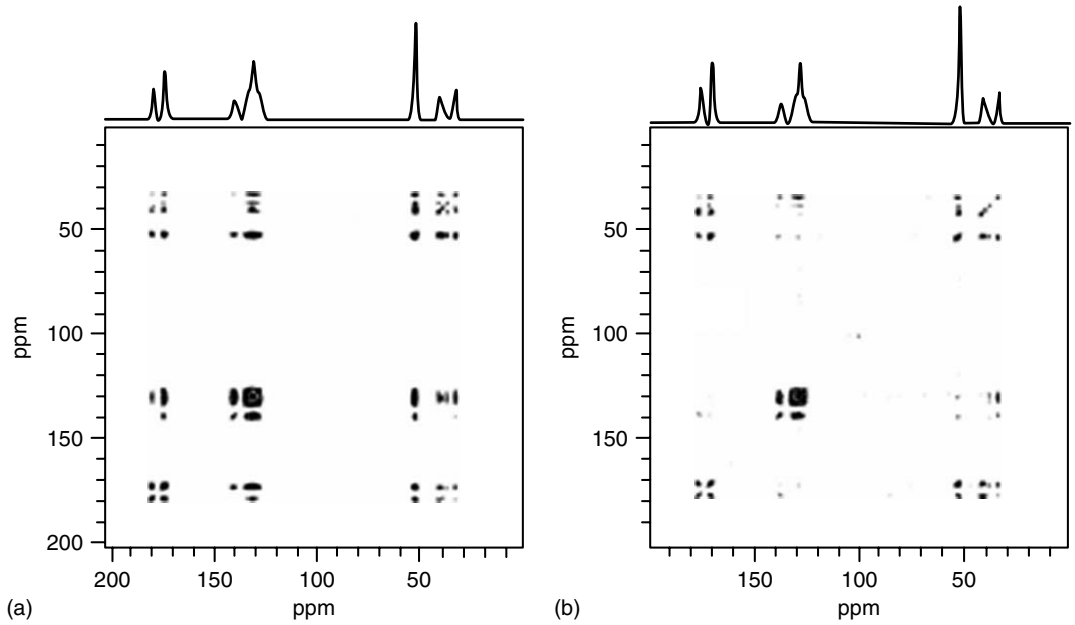


Figure 28.10. Two-dimensional RFDR spectrum of 20% uniformly ^{13}C labeled aspartame (Form II), diluted in unlabeled aspartame, acquired at a spinning speed of 26 with 263 kHz ^{1}H decoupling and a mixing time 0.02 s (128 rotor cycles). (Reproduced from Ref. 45. © Elsevier, 2000.)

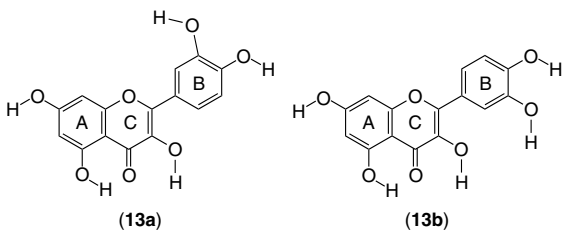
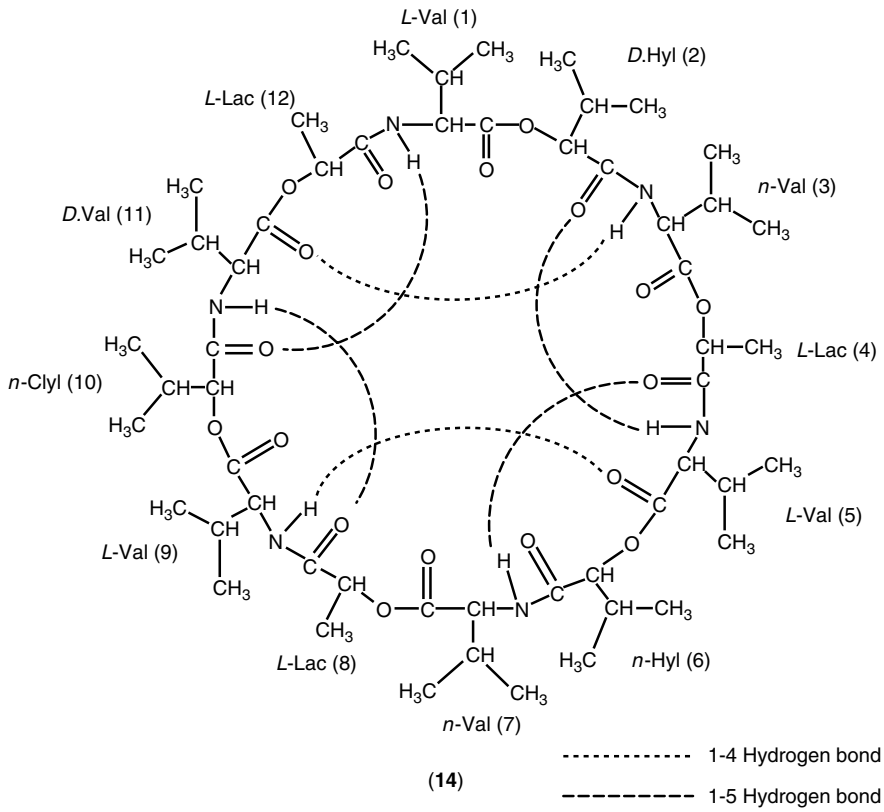


Figure 28.11. The structure of quercetin.

In the solid phase, **13a** crystallizes as the dihydrate in a fairly planar conformation with molecular geometry as shown in Figure 28.11. The geometry of polymorph **13b** was unknown. Comparative analysis of ^{13}C δ_{ii} parameters for the two polymorphs obtained by means of the 2-D PASS sequence revealed significant differences. Experimental ^{13}C CST values were compared with ^{13}C NMR shielding parameters computed for different models with optimized geometry employing the gauge-including atomic orbitals (GIAO) density functional theory (DFT) method. The best-fitted ^{13}C CST data enabled the authors to predict the most reliable molecular structure of polymorph **13b**.

The 2-D methodology was employed by Raftery and coworkers to investigate the conformational polymorphism of ROY.[50] Using 2-D PASS, spectral editing techniques, and DFT-based calculations of the local fields, the authors proved the sensitivity of all carbon and nitrogen sites to the change of molecular conformations. It has been found that chemical shift and dipolar coupling information obtained from these experiments varies noticeably between forms. This observation can be used to quantitatively determine the molecular structure in these materials, including the coplanar angle between the phenyl and thiophene rings. The influence of motion on the methyl and nitro chemical shifts was also investigated. The accuracy of the information obtained from local field analysis and the model structure calculation showed the capabilities of SSNMR as a quantitative structural method.

Similar sets of structural information as in the case of 2-D PASS can be obtained by means of the FIREMAT sequence, briefly characterized in the previous section. Grant and coworkers have employed this methodology to study two different crystalline polymorphs of valinomycin (**14**) (Figure 28.12), which exists in triclinic and monoclinic forms.[51]

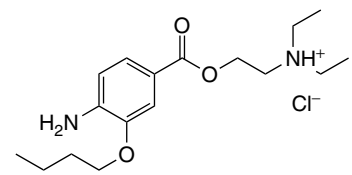


(**14**)

Figure 28.12. Structural formula of valinomycin. The hydrogen bonding is indicated by the dashed lines. (Reproduced from Ref. 51. © Springer Science and Media, 2004.)

The two polymorphs of the crystal are remarkably similar; however, there are distinct differences in the isotropic chemical shifts between the two spectra. For the triclinic form, the carbon CST components for the α carbons adjacent to oxygen in the lactic acid and hydroxyisovaleric acid residues and the ester carbonyls of the valine residue were obtained using the FIREMAT experiment. From the measured components, it was found that the behavior of the isotropic chemical shift, δ_{iso}, for valine residue ester carbonyl carbons is predominately influenced by the intermediate component, δ_{22}.

Oxybuprocaine hydrochloride (**15**) (Figure 28.13) is a drug compound acting as a local anesthetic and is therapeutically used in eye-drop formulations for the diagnosis of eye diseases by ophthalmic examination. Harris and coworkers have shown that this compound exists in at least three polymorphic forms.[52–53] For cases with two or more molecules in the asymmetric unit, there is an inherent difficulty in structural assignment of experimental chemical shifts because from one-dimensional spectra it is not feasible to decide which resonances belong to the same independent molecule. The two-dimensional solid-state incredible natural abundance double quantum transfer experiment (INADEQUATE) pulse sequence can be applied to obtain the necessary links. The NMR



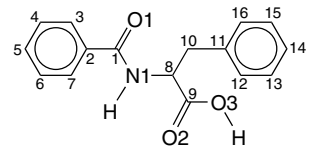
(**15**)

Figure 28.13. The structure of oxybuprocaine hydrochloride.

data, combined with quantum mechanical computation of shielding, allows an explanation the nature of the polymorphism to be made.

Several methodological papers were published employing *N*-benzoyl-phenylalanine (*N*−BzPhe) (**16**) as a model compound for the development of two-dimensional SSNMR spectroscopy in structural studies of polymorphs.[54,55] The racemic form of *N*-BzPhe is well defined by X-ray crystallography, while the L-enantiomer crystallizes as a complex mixture of different crystallographic modifications. In many cases, various polymorphs display a range of different hydrogen-bonding arrangements, constructed from different types of hydrogen-bonded arrays. The existence of several different potential hydrogen-bond donor and hydrogen-bond acceptor groups in the molecule leads to several possible geometric permutations for hydrogen-bonding arrangements in the solid state. The *N*-BzPhe sample belongs to this category of polymorphs.

For ^{13}C and ^{15}N selectively enriched model samples, the homonuclear ^{13}C–^{13}C POST C7 correlation (Figure 28.14a) and heteronuclear ^{13}C–^{15}N HETCOR experiments (Figure 28.14b) were employed to assign the number of polymorphs in the domain, the change of conformation, and the hydrogen-bonding



(**16**)

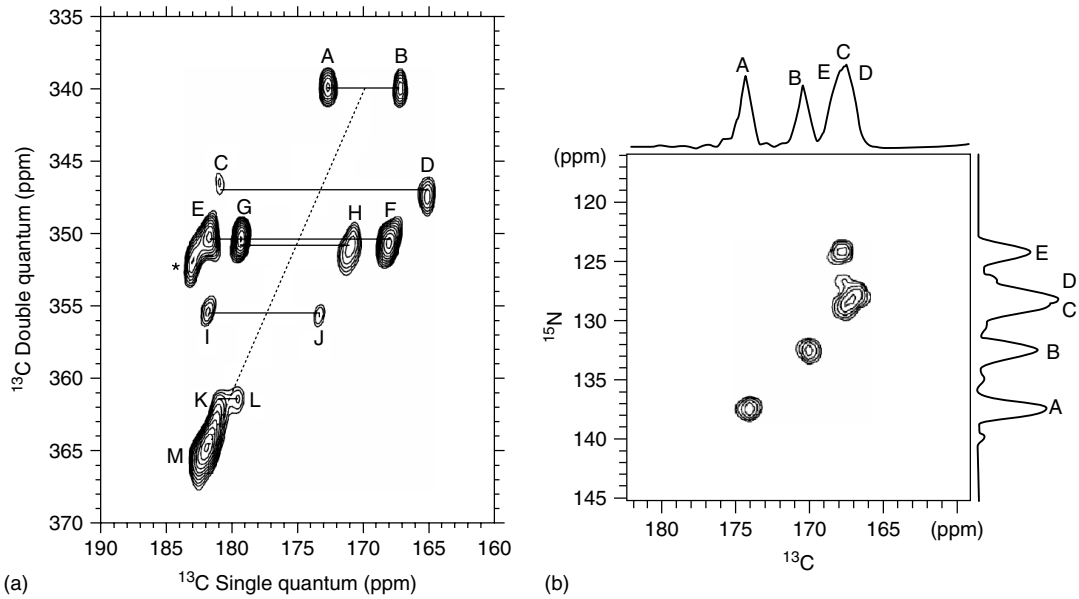


Figure 28.14. (a) POST-C7 2-D correlation spectrum of N–BzPhe selectively labeled by ^{13}C (99%) at C1 and C9 positions, carried out with τ_{exc} 3 ms, 12 kHz MAS frequency, B_0 of 14.1 T, and 5 °C. Horizontal lines join correlated resonances, and the dashed line indicates the spectrum diagonal, at a ratio of 2 : 1. The spectrum was recorded with 100 kHz decoupling during signal acquisition in both t_1 and t_2 but no decoupling during the POST-C7 sequences. A total of 64 t_1 increments were made, with 512 acquisitions per increment. (Reproduced from Ref. 54. © American Chemical Society, 2005). (b) ^{13}C–^{15}N correlation of L-enantiomer of N–Bz–Phe selectively labeled by ^{13}C (99%) at C1 and ^{15}N (95%) at N1. The spectrum was recorded on a BRUKER DSX 400 MHz spectrometer. (Reproduced from Ref. 55. © American Chemical Society, 2008.)

pattern. The structural constraints and obtained values of chemical shift anisotropy (CSA) parameters were used in the prediction of the geometry of polymorphs with unknown molecular structure. In the work reported above,[49–55] *ab initio* and DFT calculations were carried out in order to deduce the most reliable conformations. Much effort is currently being made to introduce algorithms allowing efficient computing and structure prediction of polymorphs. The method relying on DFT and using plane waves together with pseudopotentials in a gauge-including projector-augmented wave (GIPAW) is one of the most promising approaches.[56] This has been implemented in the CASTEP code.[57] A number of other examples of the formation of polymorphs and further techniques applied for their study are published in a recent thematic issue of *Crystal Growth and Design*.[58]

28.4 MOLECULAR DISORDER

Two kinds of molecular disorder can be distinguished: dynamic (related to molecular motion in the crystal lattice) and static. Subtle structural features, e.g., deviation from perfect periodicity (static distortion), have influence on the physical properties of condensed matter.[59]

Most solid materials contain some level of disorder. It is not always possible to investigate the local distortion of structure by means of XRD methods, which reflect long-range order. Hence, SSNMR spectroscopy, representing the local electronic environment for each nucleus, seems to be a more sensitive technique for the study of this phenomenon. The literature describing NMR applications for the study of disordered organic compounds and pharmaceuticals is very extensive.[60–62] Significant contributions in this field come from Emsley's group.[63–67] In many cases, simple analysis of broadening of isotropic resonance lines is a source of important information. The result is that a given atom in a molecule will find itself in slightly different structural environments in going from one molecule to another. The result is a corresponding variation in the isotropic chemical shift from one molecule to another, resulting in an inhomogeneous broadening of the NMR resonance. A similar broadening can arise from differences in magnetic susceptibility in different parts of the sample. Even under fast MAS and strong heteronuclear decoupling conditions, disordered solids often yield ^{13}C, ^{31}P, and/or other linewidths of several hundred hertz. This broadening is not always a disadvantage. If it can be measured, in favorable cases it can be interpreted in terms of structure.

An example that justifies the above-mentioned statement is the SSNMR study of the hetero-organic compound *N*,*N*-bis-(diphenylphosphino)-*N*-((*S*)-*R*-methylbenzyl)amine (**17**).[66] For this sample, there are eight chemically distinct phosphorus atoms in the crystal structure, arising from four inequivalent molecules per unit cell. Each ^{31}P resonance is inhomogeneously broadened owing to a slight structural disorder. Figure 28.15 shows a ^{31}P MAS NMR spectrum of **17**, while

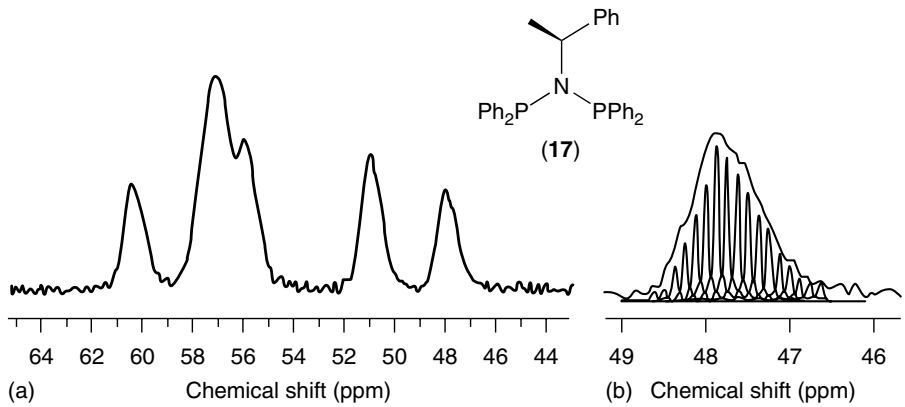


Figure 28.15. A typical CPMAS NMR spectrum (a), in this case a ^{31}P spectrum of **17**. Each peak is broadened by a distribution of chemical shifts, as illustrated schematically in (b). (Reproduced from Ref. 66. © American Chemical Society, 2003.)

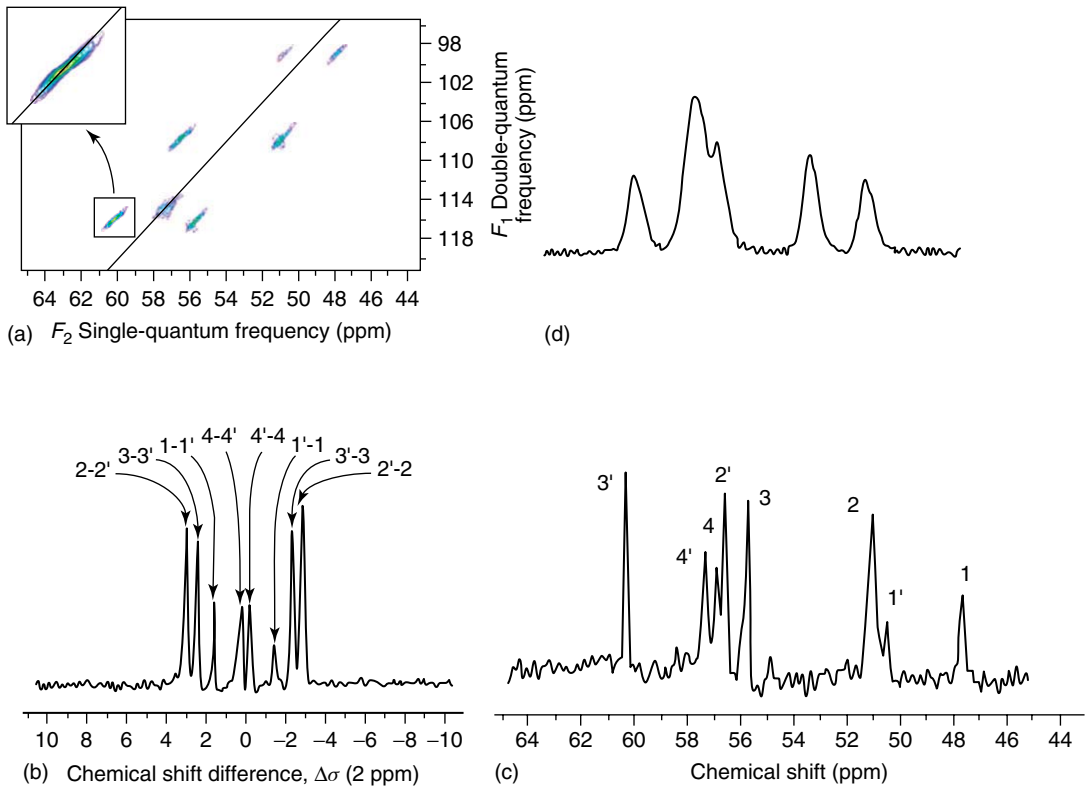
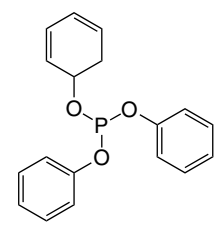


Figure 28.16. (a) Contour plot of a two-dimensional refocused INADEQUATE spectrum of **17**. The spectrum was recorded with 856 increments in t_1 for a spectral width of 12.0 kHz (rotor-synchronized acquisition) in both F_1 and F_2 with 32 transients per increment. The recycle time was 6 s between free induction decays, and the τ period in the INADEQUATE sequence was 4.0 ms. (b) Projection of (a) onto the single-quantum axis after the spectrum was sheared along F_1. The resulting high-resolution spectrum yields narrow peaks at the chemical shift differences between *J*-coupled spin pairs. In (c) a spectrum is shown that is constructed by adding traces taken through the 2-D spectrum parallel to F_2 at double-quantum frequencies of 98.5, 107.8, 114.6, and 116.0 ppm. (d) Reproduces the normal 1-D spectrum on the same scale for comparison. (Reproduced from Ref. 66. © American Chemical Society, 2003.)

Figure 28.16 shows the 2Q–1Q spectra recorded under MAS using the refocused INADEQUATE pulse sequence.

This case clearly demonstrates that, under appropriate conditions, strong correlations can be observed between the changes in chemical shifts induced by disorder for adjacent nuclei in solids. This approach was also used for the investigation of other disordered systems, including cellulose and L-alanine.[66]

Sehnet and Senker have reported a concerted approach for the determination of the local environment in ordered and disordered phases in the solid-state investigation of triphenyl phosphite (TPP) (**18**) (Figure 28.17).[68]



(**18**)

Figure 28.17. The structure of triphenyl phosphate (TPP).

TPP forms two different crystalline (c1 and c2) and two amorphous (aI and aII) states. Of the crystalline phases, c1 is the commonly found modification,

whereas c2 can be crystallized only from an ionic liquid. The amorphous phases can be distinguished between the structural glass (aI with $T_g = 205\,\mathrm{K}$) and the second phase aII, which is produced via annealing of the supercooled liquid in the temperature range 210–230 K. Combining isotope labeling, *ab initio* calculations, and SSNMR spectroscopy, structure proposals were generated using molecular modeling methods (DFT, semiempirical, or force field methods).

The concerted approach was successfully applied to unravel the distribution of conformers in one ordered (c1) and two disordered phases (aI and aII) of TPP. The combination with 2-D exchange spectroscopy has a strong potential for the investigation of local order in disordered materials.

Over 25 years ago, Gavezzotti and Simonetta wrote in a review article: "A common view among chemists, and even X-ray crystallographers, is that a molecular crystal is made up of frozen chemical entities that can at most undergo very small translational and librational motions. This is because most of the solid-state investigation techniques, as well as the theoretical models for the interpretation of their results, see the molecules in such a way."[69] In spite of the fact that today knowledge about molecular dynamics in organic crystals is much more common, the development of techniques dedicated to analysis of such processes is still very much needed. NMR spectroscopy is a powerful approach for quantifying molecular dynamics at multiple atomic sites and over multiple timescales. Extensive studies by SSNMR spectroscopy of spin relaxation and lineshapes in organic compounds have been performed in order to characterize the amplitudes, timescales, and energetics of intramolecular conformational modes and to elucidate the relationships between conformational dynamics, structure, and function.[70] It is known that molecular motion can cause disordering of solid materials. An interesting example of this kind of disorder was reported by Sebald and colleagues.[71,72] Employing L-tyrosine-ethylester (TEE) (**19**) with ^{13}C in low natural abundance and in fully ^{13}C enriched form, the authors proved that the phenyl rings undergo π flips with a rather low activation energy. Figure 28.18 shows the different modes of motion of the ethylester residue of TEE.

It is concluded from this study that NMR experiments (homonuclear ^{13}C recoupling) faithfully reproduce those molecular structural features, known from SXRD, that are defined by short range ^{13}C–^{13}C interactions. Unfortunately, SSNMR fails to uniquely

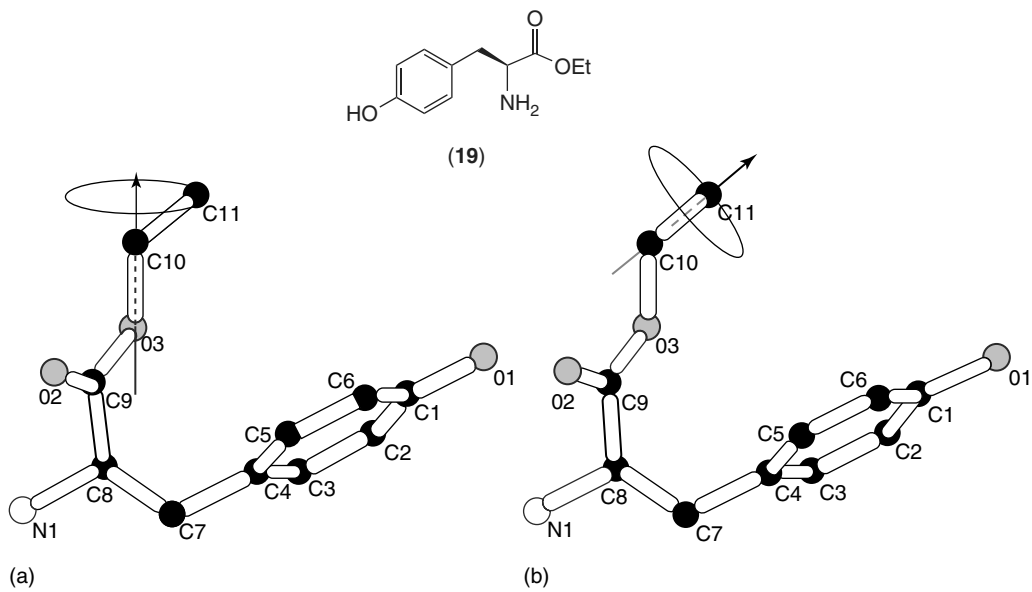


Figure 28.18. Two models of dynamic disorder affecting the ester tail in solid L-tyrosine-ethylester. (a) Rotation of the $^{13}C10$–$^{13}C11$ bond vector around the O3–$^{13}C10$ bond direction. (b) Nutation of the $^{13}C10$–$^{13}C11$ bond vector around its mean direction. (Reproduced from Ref. 71. © American Chemical Society, 2003.)

characterize the complete molecular conformation defined by intermediate-range $^{13}C-^{13}C$ interactions due to large scale molecular motion of phenyl ring and ethyl group.

So far, we discussed examples of molecular disorder for one-component systems. Interesting cases of this phenomenon can be found for more complex samples, e.g., inclusion complexes. The disorder can be caused by molecular dynamics of guest molecules involving, for instance, rapid reorientation of guests about the tunnel axis or by changes in the host:guest ratio during the release of guest molecules from the crystal lattice while the complexes are being stored.[73,74]

28.5 CRYOCRYSTALLOGRAPHY AND SOLID-STATE NMR

SXRD is by far the most commonly used technique available for the determination of the crystal and molecular structure of crystalline solids. This technique enables the acquisition of complete and detailed structural information, including the relative position of atoms, as well as some aspects of their motion in the solid state. The dynamic processes discussed in the Section 28.4 are common in crystal lattices and in many cases can make X-ray data analysis difficult and/or ambiguous. Today, the method that eliminates many of the problems related to dynamic disorder of condensed matter is low-temperature X-ray crystallography (cryocrystallography). Recently, this subject was exhaustively reviewed by Goeta and Howard.[75]

The increased popularity of cryocrystallography has come about not only as a result of the number and variety of currently marketed cooling devices but also because it is generally accepted that structural information obtained in this way is of better quality than that obtained at room temperature. Although this approach seems to be very attractive, it is not free from drawbacks and limitations. Juers and Matthews have concluded that there is a risk that structures determined at low temperature may suggest conclusions based on aspects of the structure that are not necessarily consistent with data obtained at room temperature.[76] Dunlop, Irvin, and Hazes have stated that high-quality cryogenic synchrotron data is extremely valuable but that room-temperature structures are still desirable, especially if the research question involves features that are sensitive to temperature-induced changes.[77] This problem is particularly important in the crystallography of proteins. Moreover, it is well known that very small changes in the relative orientation of molecules in the crystal can cause major changes in the crystal reciprocal lattice. This has to be taken into consideration when X-ray structural data serve as a template in docking calculations.[78]

SSNMR spectroscopy employing a variable temperature (VT) approach provides a relatively easy way for measurement of the dynamic processes and mechanisms of phase transitions. When the X-ray data are combined with results of VT SSNMR and differential scanning calorimetry (DSC) measurements, the thermal processes and other properties of condensed matter may be completely characterized.

An example of the power of this complementary approach is the structural study of 2-thio-(5, 5-dimethyl-1,3,2-dioxaphos phorinanyl)-2′-oxo-dineopentylthiophosphate (**20**).[79] DSC and low-temperature XRD studies showed that **20** undergoes a reversible phase transition at 203 K related to the change of symmetry of the crystallographic unit (Figure 28.19). These changes are easily followed by the ^{31}P CPMAS experiment. Figure 28.20 shows the different spectral patterns below and above the phase transition temperature.

SSNMR spectroscopy was used to establish the dynamic processes of aliphatic groups and the phosphorus skeleton. ^{13}C and ^{31}P VT NMR studies, as well as measurements of ^{13}C relaxation times T_1 and $T_{1\rho}$ revealed the different modes of molecular motion for each neopentyl residue directly bonded to a phosphorus atom. It was further concluded that the molecular dynamics of the aliphatic groups causes different van der Waals interactions in the crystal lattice and is the driving force of the phase transition for compound **20**.

Similar observations were reported for L-selenomethionine (**21**), investigated by low-temperature XRD of a single crystal, VT SSNMR, and DSC.[80] From SXRD, it was concluded that **21** crystallizes in the $P2_1$ space group with two molecules (A and B) in the asymmetric unit, while SSNMR was used for investigating the structure and dynamics of **21** in the crystal lattice, as well as the mechanism of the phase transition observed at 313 K. Above this temperature, only one molecule in the asymmetric unit is observed. The distinct molecular motion of side chains for A and B molecules of **21** was apparent from measurements of relaxation parameters (^1H $T_{1\rho}$, ^{13}C T_1) and analysis

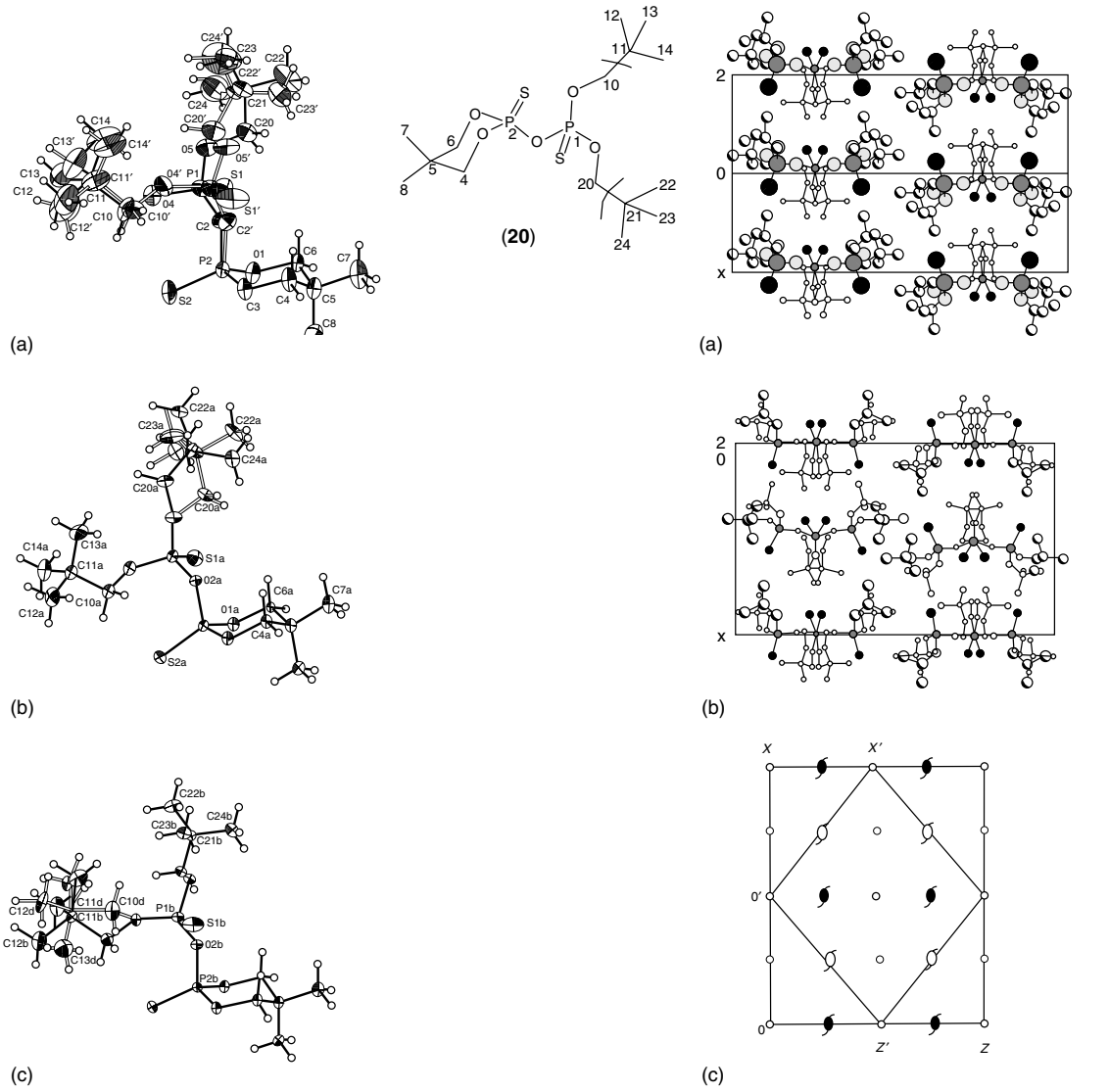


Figure 28.19. (Left) ORTEP plot of compound **20**, with displacement ellipsoids drawn at the 50% probability level. (a) Molecule in structure I (high temperature), (b) molecule A in structure II (low temperature), and (c) molecule B in structure II (low temperature). Hydrogen atoms are represented by spheres of size unrelated to the thermal vibration. The open bonds connect atoms with lower occupational factors in disordered moieties. (Right) Crystallographic bases of phase transition for sample **20**. (a) Molecular arrangement in the crystal lattice in structures I and (b) molecular arrangement in the crystal lattice in structures II. The gliding plane *n* and *c* are located horizontally and perpendicularly to the picture plane. The hydrogen atoms are not shown. Only the conformations with higher occupational factors are visible. Larger radii of atoms indicate the disordered fragments. (c) Diagram of symmetry elements in superposed structures I and II structure I is drawn with thicker lines. The *a* and *c* unit cell parameters in structure II are approximately equal to the diagonals in structure I. The new *c* parameter corresponds to the shorter diagonal started from the origin, which creates the *n* gliding plane of the $P2_1/n$ space group. The new a parameter corresponds to the longer diagonal, which does not contain the origin. The symmetry elements that vanish during the phase transition are marked by open symbols. (Reproduced from Ref. 79. © American Chemical Society, 2006.)

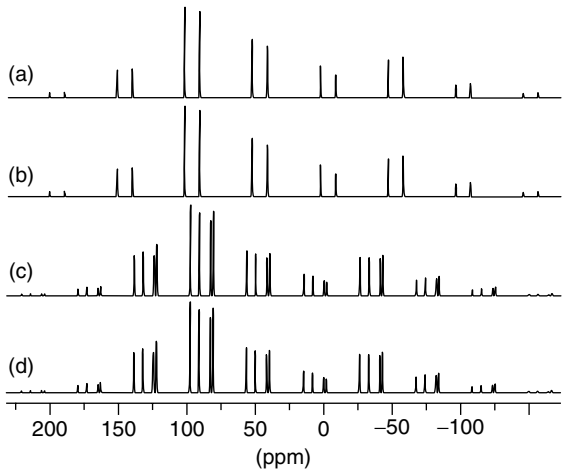


Figure 28.20. (a) Experimental ^{31}P CPMAS NMR spectrum of **20** recorded at 290 K with spinning rate 5 kHz. (c) Experimental ^{31}P CPMAS NMR spectrum of **20** recorded at 190 K with spinning rate 4 kHz. Figures (b) and (d) show appropriate theoretical spectra obtained employing the SIMPSON program. (Reproduced from Ref. 79. © American Chemical Society, 2006.)

of CSA data taken from the 2-D PASS experiment. The ^{13}C δ_{ii} and ^{77}Se δ_{ii} parameters were correlated with theoretical shielding parameters obtained by means DFT GIAO calculations in order to explain the nature of the phase changes.

The complementary approach combining cryocrystallography, VT SSNMR, and DSC was employed by Turner and coworkers in structural studies of 4-iodobenzoic acid dimers **22** in the solid state.[81] Diffraction data were collected from crystalline specimens of **22** at 103, 123, 148, 173, 198, 248, and 298 K, while the ^{13}C CPMAS spectra were recorded in the temperature range 178–248 K. It is found that the position of the electron density associated with the proton varies with temperature in that the population of the disordered sites changes with varying temperature.

In some cases, SSNMR can explain the poor refinement of X-ray data and suggest a way to optimize the conditions of the XRD experiment, in particular the choice of the temperature of measurement. This is the case for structural studies of the tripeptide Tyr-D-Ala-Phe, **23**, the "message" domain of opioid peptides, dermorphin (Tyr-D-Ala-Phe-Gly-Tyr-Pro-Ser-NH_2), deltorphin I (Tyr-D-Ala-Phe-Asp-Val-Val-Gly-NH_2) and deltorphin II (Tyr-D-Ala-Phe-Glu-Val-Val-Gly-NH_2).[82] Dermorphin binds to the μ-selective opioid receptor and induces, for example, long-lasting analgesia, especially on the central nervous system (up to a 1000-fold greater than that from morphine).

The room-temperature XRD study of **23** gave poor refinement (a large value of the R factor). From SS-NMR measurements, it was concluded that at ambient temperature the phenyl ring of phenylalanine undergoes large-amplitude molecular motion (a case of dynamic disorder). The dynamic process in the crystal lattice was apparent from ^{13}C T_1 measurements, analysis of the CP kinetics, and from data obtained from a dipolar dephasing experiment. It was further confirmed by a 2-D PASS experiment used to assign principal elements of the CST ^{13}C δ_{ii}. It is known that dynamic processes that are fast on the NMR timescale can reduce the value of chemical shift anisotropies represented by the span parameter Ω ($\Omega = |\delta_{11} - \delta_{33}|$). The XRD measurement at 100 K "froze" the molecular motions of aromatic rings and local vibrations in the crystal lattice, yielding an unambiguous refinement of the structure with a small R value (Figure 28.21).

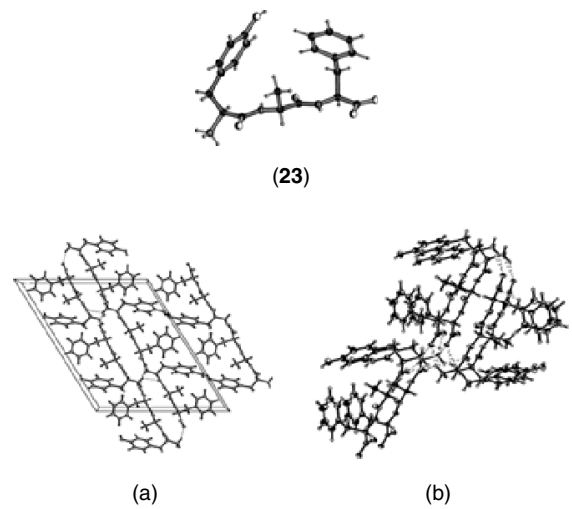


Figure 28.21. (a) Unit cell containing four molecules of tripeptide **23**, and (b) a depiction of six molecules of tripeptide **23**. Both pictures reflect their interactions between molecules, with ellipsoids at 50% probability. The measurements were carried out at 100 K. R_{obs} is found to be 0.0394. (Reproduced from Ref. 82. © American Chemical Society, 2004.)

28.6 CONCLUSIONS

X-ray crystallography and SSNMR are the most commonly used techniques in structural studies of organic solids and APIs. There are a number of features that differ between the two methods. First, the techniques are based on different physical phenomena; second, the measured set of data is entirely dissimilar; third, the interpretation of the collected results is significantly different; and so on. However, in the complementary approach, the two methods provide a full picture describing the structure and dynamics of the condensed matter. Together, they form the method of choice for the investigation of intermolecular interactions.

SSNMR spectra are in many cases similar to those recorded in the liquid phase, but they usually contain a wider range of information. Analysis of the tensorial nature of chemical shifts provides subtle structural information about local environment. Strategies based on dipolar recoupling indicate a number of ways in which dipolar coupling constants can be measured, yielding direct data on internuclear distances. The repertoire of SSNMR is rapidly growing. From the short discussion of this technique it is apparent that the recently introduced term *NMR crystallography* is fully justified.

REFERENCES

1. J. I. Gersten, and F. W. Smith, *The Physics and Chemistry of Materials*, Wiley Publishers, 2001.
2. C. E. Hughes, S. Hamad, K. D. M. Harris, C. R. A. Catlow, and P. C. Griffiths, *Faraday Discuss.*, 2007, **136**, 71.
3. J. P. M. Lommerse, W. D. S. Motherwell, H. L. Ammon, J. D. Dunitz, A. Gavezzotti, D. W. M. Hofmann, F. J. J. Leusen, W. T. M. Mooij, S. L. Price, B. Schweizer, M. U. Schmidt, B. P. van Eijck, P. Verwer, and D. E. Williams, *Acta Crystallogr., B*, 2000, **56**, 697.
4. W. D. S. Motherwell, H. L. Ammon, J. D. Dunitz, A. Dzyabchenko, P. Erk, A. Gavezzotti, D. W. M. Hofmann, F. J. J. Leusen, J. P. M. Lommerse, W. T. M. Mooij, S. L. Price, H. Scheraga, B. Schweizer, M. U. Schmidt, B. P. van Eijck, P. Verwer, and D. E. C. Williams, *Acta Crystallogr., B*, 2002, **58**, 647.
5. G. M. Day, W. D. S. Motherwell, H. L. Ammon, S. X. M. Boerrigter, R. G. Della Valle, E. Venuti, A. Dzyabchenko, J. D. Dunitz, B. Schweizer, B. P. van Eijck, P. Erk, J. C. Facelli, V. E. Bazterra, M. B. Ferraro, D. W. M. Hofmann, F. J. J. Leusen, C. Liang, C. C. Pantelides, P. G. Karamertzanis, S. L. Price, T. C. Lewis, H. Nowell, A. Torrisi, H. A. Scheraga, Y. A. Arnautova, M. U. Schmidt, and P. Verwer, *Acta Crystallogr., B*, 2005, **61**, 511.
6. A. Gavezzotti, *Cryst. Eng. Comm.*, 2002, **4**, 343.
7. K. D. M. Harris and E. Y. Cheung, *Chem. Soc. Rev.*, 2004, **33**, 526.
8. H. B. Burgi and S. C. Capelli, *Helv. Chim. Acta*, 2003, **86**, 1625.
9. S. P. Brown and H. W. Spiess, *Chem. Rev.*, 2001, **101**, 4125.
10. R. K. Harris, *Solid-State Sci.*, 2004, **6**, 1025.
11. C. A. Challener and V. T. Brookfield, *Chiral Intermediates and Chiral Drugs*, Ashgate, 2001.
12. H. Y. Aboul-Enein, *The Impact of Stereochemistry on Drug Development and Use*, John Wiley & Sons: New York, 1997.
13. C. Brown, *Chirality in Drug Design and Synthesis*, Academic Press: New York, 1990.
14. A. M. Rouhi, *Chiral Chem. Chem. Eng. News*, 2004, **82**, 47.
15. I. Ali, V. K. Gupta, H. Y. Aboul-Enein, P. Singh, and B. Sharma, *Chirality*, 2007, **19**, 453.
16. J. P. Glusker, M. Lewis, and M. Rossi, Eds, *Crystal Structure Analysis for Chemists and Biologists*, VCH Publishers, 1994.
17. J. M. Bijvoet, A. F. Peerdeman, and A. J. van Bommel, *Nature*, 1951, **168**, 271.
18. M. J. Potrzebowski, A. Jeziorna, and S. KaYmierski, *Concepts Magn. Reson. A*, 2008, **32A**, 201.
19. O. Wallach, *Liebigs Ann. Chem.*, 1895, **286**, 90.
20. C. P. Brock, W. B. Schweizer, and J. D. Dunitz, *J. Am. Chem. Soc.*, 1991, **113**, 9811.
21. K. V. Andersen, H. Bildsoe, and H. J. Jacobsen, *Magn. Reson. Chem.*, 1990, **28**, 47.
22. M. J. Potrzebowski, E. Tadeusiak, K. Misiura, W. Ciesielski, G. Bujacz, and P. Tekely, *Chem. Eur. J.*, 2002, **8**, 5007.
23. P. Tekely, M. J. Potrzebowski, Y. Dusausoy, and Z. Luz, *Chem. Phys. Lett.*, 1998, **291**, 471.
24. P. Tekely, C. Gardinet, M. J. Potrzebowski, A. Sebald, D. Reichert, and Z. Luz, *J. Chem. Phys.*, 2002, **116**, 7607.

25. J. K. Harper, A. E. Mulgrew, J. Y. Li, D. H. Barich, G. A. Strobel, and D. M. Grant, *J. Am. Chem. Soc.*, 2001, **123**, 9837.
26. S. R. Byrn, *In Solid State Chemistry of Drugs*, Academic Press: New York, 1982.
27. S. Chen, I. A. Guzei, and L. Yu, *J. Am. Chem. Soc.*, 2005, **127**, 9881.
28. http://www.fda.gov/cder/Guidance/6154dft.htm 2007.
29. R. K. Harris, *J. Pharm. Pharmacol.*, 2007, **59**, 225.
30. R. T. Berendt, D. M. Sperger, P. K. Isbester, and E. J. Munson, *TrAC, Trends Anal. Chem.*, 2006, **25**, 977.
31. S. Datta, D. J. W. Grant, and R. K. Harris, *Analyst*, 2006, **131**, 351.
32. D. D. Sharmistha and J. W. Grant, *Nat. Rev. Drug Discov.*, 2004, **3**, 42.
33. M. J. Potrzebowski, *Eur. J. Org. Chem.*, 2003, **8**, 1367.
34. D. E. Bugay, *Adv. Drug Deliv. Rev.*, 2001, **48**, 43.
35. U. Holzgrabe, B. W. K. Diehl, and I. Wawer, *J. Pharm. Biomed.*, 1998, **17**, 557.
36. R. K. Harris, R. R. Yeung, R. B. Lamont, R. W. Lancaster, S. M. Lynn, and S. E. Staniforth, *J. Chem. Soc., Perkin Trans. 2*, 1997, **12**, 2653.
37. R. K. Harris, A. M. Kenwright, R. A. Fletton, and R. W. Lancaster, *Spectrochim. Acta A*, 1998, **54**, 1837.
38. D. C. Apperley, R. A. Fletton, R. K. Harris, R. W. Lancaster, S. Tavener, and T. L. Threlfall, *J. Pharm. Sci.*, 1999, **88**, 1275.
39. E. D. L. Smith, R. B. Hammond, M. J. Jones, K. J. Roberts, J. B. O. Mitchell, S. L. Price, R. K. Harris, D. C. Apperley, J. C. Cherryman, and R. Docherty, *J. Phys. Chem. B*, 2001, **105**, 5818.
40. J. M. Rubin-Preminger, J. Bernstein, R. K. Harris, I. R. Evans, and P. Y. Ghi, *Cryst. Growth Des.*, 2004, **4**, 431.
41. D. C. Apperley, A. H. Forster, R. Fournier, R. K. Harris, P. Hodgkinson, R. W. Lancaster, and T. Rades, *Mag. Res. Chem.*, 2005, **43**, 881.
42. R. K. Harris, P. Hodgkinson, T. Larsson, and A. Muruganantham, *J. Pharm. Biomed.*, 2005, **38**, 858.
43. R. K. Harris, P. Y. Ghi, H. Puschmann, D. C. Apperley, U. J. Griesser, R. B. Hammond, C. Y. Ma, K. J. Roberts, G. J. Pearce, J. R. Yates, and C. J. Pickard, *Org. Process Res. Dev.*, 2005, **9**, 902.
44. M. T. Zell, B. E. Padden, D. J. W. Grant, M. C. Chapeau, I. Prakash, and E. J. Munson, *J. Am. Chem. Soc.*, 1999, **121**, 1372.
45. M. T. Zell, B. E. Padden, D. J. W. Grant, S. A. Schroeder, K. L. Wachholder, I. Prakash, and E. J. Munson, *Tetrahedron*, 2000, **56**, 6603.
46. O. N. Antzutkin, *Prog. Nucl. Magn. Reson. Spectrosc.*, 1999, **35**, 203.
47. O. N. Antzutkin, S. C. Shekar, and M. H. Levitt, *J. Magn. Reson.*, 1995, **115**, 7.
48. O. N. Antzutkin, Y. K. Lee, and M. H. Levitt, *J. Magn. Reson.*, 1998, **135**, 144.
49. S. Olejniczak and M. J. Potrzebowski, *Org. Biomol. Chem.*, 2004, **2**, 2315.
50. J. R. Smith, W. Z. Xu, and D. Raftery, *J. Phys. Chem. B*, 2006, **110**, 7766.
51. T. Kameda, G. McGeorge, A. M. Orendt, and D. M. Grant, *J. Biomol. NMR*, 2004, **29**, 281.
52. R. K. Harris, S. Cadars, L. Emsley, J. R. Yates, C. J. Pickard, R. K. R. Jetti, and U. J. Griesser, *Phys. Chem. Chem. Phys.*, 2007, **9**, 360.
53. U. J. Griesser, R. K. R. Jetti, M. F. Haddow, T. Brehmer, D. C. Apperley, A. King, and R. K. Harris, *Cryst. Growth Des.*, 2008, **8**, 44.
54. C. E. Hughes, S. Olejniczak, J. Heliński, W. Ciesielski, M. Repisky, O. Andronesi, K. Fehér, M. J. Potrzebowski, and M. Baldus, *J. Phys. Chem. B*, 2005, **109**, 23175.
55. S. Olejniczak, J. Miku3a-Pacholczyk, C. E. Hughes, and M. J. Potrzebowski, *J. Phys. Chem. B*, 2008, **112**, 1586.
56. C. J. Pickard and F. Mauri, *Phys. Rev. B*, 2001, **63**, 245101.
57. S. J. Clark, M. D. Segall, C. J. Pickard, P. J. Hasnip, M. J. Probert, K. Refson, and M. C. Payne, *Z. Kristallogr.*, 2005, **220**, 567.
58. G. Desiraju, *Cryst. Growth Des.*, 2008, **8**, 3, and other papers in this issue.
59. S. Ravy, P. Launois, R. Moret, and J. P. Pouget, *Z. Kristallogr.,* 2005, **220**, 1059.
60. T. N. Pham, J. M. Griffin, S. Masiero, S. Lena, G. Gottarelli, P. Hodgkinson, C. Fillip, and S. P. Brown, *Phys. Chem. Chem. Phys.*, 2007, **9**, 3416.
61. F. Malz, Y. Yoneda, T. Kawada, K. Mereiter, P. Kosma, T. Rosenau, and C. Jager, *Carbohydr. Res.*, 2007, **342**, 65.

62. M. Mirmehrabi, S. Rohani, K. S. K. Murthy, and B. Radatus, *J. Cryst. Growth*, 2004, **260**, 517.

63. S. Cadars, J. Sein, L. Duma, A. Lesage, T. N. Pham, J. H. Baltisberger, S. P. Brown, and L. Emsley, *J. Magn. Reson.*, 2007, **188**, 24.

64. S. Cadars, A. Lesage, M. Trierweiler, L. Heux, and L. Emsley, *Phys. Chem. Chem. Phys.*, 2007, **9**, 92.

65. S. Cadars, A. Lesage, and L. Emsley, *J. Am. Chem. Soc.*, 2005, **127**, 4466.

66. D. Sakellariou, S. P. Brown, A. Lesage, S. Hediger, M. Bardet, C. A. Meriles, A. Pines, and L. Emsley, *J. Am. Chem. Soc.*, 2003, **125**, 4376.

67. A. Lesage, M. Bardet, and L. Emsley, *J. Am. Chem. Soc.*, 1999, **121**, 10987.

68. J. Sehnet and J. Senker, *Chem. Eur. J.*, 2007, **13**, 6339.

69. A. Gavezzotti and M. Simonetta, *Chem. Rev.*, 1982, **82**, 1.

70. A. G. Palmer, J. Williams, and A. McDermott, *J. Phys. Chem.*, 1996, **100**, 13293.

71. X. Helluy and A. Sebald, *J. Phys. Chem. B*, 2003, **107**, 3290.

72. K. Seidel, M. Etzkorn, L. Sonnenberg, C. Griesinger, A. Sebald, and M. Baldus, *J. Phys. Chem. A*, 2005, **109**, 2436.

73. M. J. Potrzebowski, W. M. Potrzebowski, A. Jeziorna, W. Ciesielski, J. Gajda, G. D. Bujacz, M. Chruszcz, W. Minor, *J. Org. Chem.*, 2008, **73**, 4388.

74. M. J. Potrzebowski and S. Kazmierski, *Top. Curr. Chem.*, 2005, **246**, 91.

75. A. E. Goeta and J. A. K. Howard, *Chem. Soc. Rev.*, 2004, **33**, 490.

76. D. H. Juers and B. W. Matthews, *Q. Rev. Biophys.*, 2004, **37**, 105.

77. K. V. Dunlop, R. T. Irvin, and B. Hazes, *Acta Crystallogr., D*, 2005, **61**, 80.

78. E. Skrzypczak-Jankun, O. Y. Borbulevych, M. I. Zavodszky, M. R. Baranski, K. Padmanabhan, V. Petricek, and J. Jankun, *Acta Crystallogr., D*, 2006, **62**, 766.

79. M. J. Potrzebowski, G. D. Bujacz, A. Bujacz, S. Olejniczak, P. Napora, J. Helinski, W. Ciesielski, and J. Gajda, *J. Phys. Chem. B*, 2006, **110**, 761.

80. J. Gajda, J. Pacholczyk, A. Bujacz, E. Bartoszak-Adamska, G. Bujacz, W. Ciesielski, and M. J. Potrzebowski, *J. Phys. Chem. B*, 2006, **110**, 25692.

81. C. L. Nygren, C. C. Wilson, and J. F. C. Turner, *J. Phys. Chem. A*, 2005, **109**, 2586.

82. M. M. Slabicki, M. J. Potrzebowski, G. Bujacz, S. Olejniczak, and J. Olczak, *J. Phys. Chem. B*, 2004, **108**, 4535.

Chapter 29
Inorganic & Materials Chemistry

Ray Dupree

Physics Department, University of Warwick, Coventry CV7 4AL, UK

29.1	Introduction	455
29.2	Space-Group Assignment	456
29.3	Toward Full Structural Determination using NMR	456
	References	461

29.1 INTRODUCTION

NMR has long been used to obtain structural information about inorganic materials with a very early example being the use of the dipole interaction to give the proton–proton distance in calcium sulfate dihydrate (gypsum), $CaSO_4{\cdot}2H_2O$[1] (*see* **Chapter 1**). Although the distance between isolated spin pairs can be readily obtained from the strength of the dipole interaction, in most cases, the spins are not isolated and then the second moment, M_2, can be used to give structural information.

$$M_2 = \frac{\int_{-\infty}^{\infty} \omega^2 f(\omega)\,\mathrm{d}\omega}{\int_{-\infty}^{\infty} f(\omega)\,\mathrm{d}\omega} = \frac{3}{4}\gamma^4\hbar^2 I(I+1) \times \frac{1}{N}\sum_{j,k}\frac{(1-3\cos^2\theta_{jk}{}^2)}{r_{jk}^6} \qquad (29.1)$$

NMR Crystallography Edited by Robin K. Harris, Roderick E. Wasylishen and Melinda J. Duer © 2009 John Wiley & Sons, Ltd. ISBN: 978-0-470-69961-4

Usually it can only be used to confirm, or otherwise, a proposed structure or to confirm motion or phase changes in a material although the distance between adjacent protons in a benzene ring was determined by comparing C_6H_6 and $C_6H_3D_3$ in another classic early study.[2] Other early works identified the chemical shift as being sensitive to the local environment, but for many years it was used mostly in solution as a "fingerprint" technique. With the advent of high-resolution solid-state NMR, the advantages of using the NMR chemical shift for characterizing inorganic materials quickly became apparent; different coordinations often have very different shift ranges, e.g., ∼0–20 ppm for ^{27}Al aluminum surrounded by six oxygens, ∼50–90 ppm for four-coordinate aluminum, etc. Furthermore, the number of inequivalent sites in the structure and their multiplicity (if the resolution is high enough) comes directly from the spectrum. Although the chemical shift is most sensitive to the local environment, the effects of different atoms/elements in the next neighbor shell can often be readily observed. For example, in silicates, silicon is usually tetrahedrally bonded. This bonding is often described in terms of Q units, where Q denotes a silicon bonded to four oxygen atoms. A superscript n, where $n = 0$–4 indicates the number of Q units connected to the Q unit in question, so that Q^4 indicates a silicon bonded through oxygen to four other silicons and Q^2 to two other silicons. The shift difference between a Q^4 and a Q^3 unit is ∼10 ppm, while replacement of one Si by Al in a Q^4 unit to become a Q^4 (1Al) changes the shift by about 5 ppm. These changes in shift have been used

for determining the Si/Al ratio in zeolites and for studying ordering in minerals. A number of examples are given in **Chapter 30**.

29.2 SPACE-GROUP ASSIGNMENT

NMR can be very useful in space-group assignment since it often involves "simple" determination of the number of sites and their occupancy. Early examples are the use of ^{29}Si in zeolites.[3] Although, in principle, the determination of the number of sites is straightforward, in practice there can be considerable overlap of the many lines that occur for structures where powder diffraction is unable to uniquely determine the space group. The AM_2O_7 system, where A = Zr, Sn, Ti, etc., and M = P, V, As, is a good example of the ability of NMR to provide space-group assignment. These compounds are made up of corner sharing AO_6 octahedra and MO_4 tetrahedra linked together by M_2O_7 units. At high temperatures, these compounds are usually cubic; this constrains the M–O–M bonds to be 180°, whereas energetically preferred bond angles are considerably less. Thus at lower temperatures (i.e., room temperature), a lower symmetry structure is often observed with a tripled ($3 \times 3 \times 3$) unit cell. From symmetry, a $3 \times 3 \times 3$ structure can adopt one of 12 possible space groups containing between 11 (*Pa*/3) and 216 (*P*1) different M sites.[4] An early experiment on ZrP_2O_7 observed 12 ^{31}P resonances and interpreted one of these as an impurity.[4] However, a later ^{31}P 2-D exchange experiment showed that all the peaks belonged to the same phase. A ^{31}P 2-D double quantum (DQ) experiment was then used to determine the directly linked PO_4 tetrahedra and showed that there were 27 distinct ^{31}P resonances of equal intensity from 13 $P_2O_7^{4-}$ units with two inequivalent P sites and one $P_2O_7^{4-}$ with two equivalent sites, giving a space-group *Pbca*.[5] An even more complex example is SnP_2O_7 where X-ray and neutron diffraction had shown that the structure was $P2_13$ (which would have 11 P sites) or lower.[6] The 1-D ^{31}P spectrum was broad, with more than 17 overlapping resonances covering ~20 ppm. The 2-D ^{31}P DQ spectrum, using the POSTC7 sequence, indicated that there were at least 27 pairs of peaks with at least 38 of the 54 resonances (27 pairs) showing different ^{31}P isotropic shifts, i.e., there must be at least 38 different sites. A refocused INADEQUATE experiment (*see* **Chapter 15**) was then used to determine the through-bond connectivity. This showed that there were at least 98 distinct ^{31}P resonances and, by fitting the 1-D MAS spectrum allowing only the intensity to change, it was shown that there were 108 crystallographically inequivalent P sites and thus the space group was either $P2_1$ or *Pc*. X-ray diffraction (XRD) gave an equally good fit to either of these.

29.3 TOWARD FULL STRUCTURAL DETERMINATION USING NMR

Recently, it has become possible in some cases to obtain a complete structure using only the unit cell parameters and space group, if available, from diffraction measurements. There are two approaches, one based solely on NMR to obtain distance and connectivity information and the other by combining the results obtained for the NMR parameters with first-principles calculations.

29.3.1 Using Distance Measurements

A simplified version of the basic algorithm for obtaining the crystal structure based upon NMR distance measurements is shown in Figure 29.1. First, the number and occupancy of the sites and the intersite connectivity must be determined using, e.g., an INADEQUATE experiment. This is followed by distance measurements based upon the dipole interaction. For the case of ^{29}Si, the natural isotopic abundance is 4.7% and this very much simplifies the situation since it enables the ^{29}Si–^{29}Si dipole interaction to be treated as that between isolated spin pairs. The Si–Si distances can then be determined by following the buildup of a DQ homonuclear recoupling experiment.[7] The intensities of the DQ correlation peaks as a function of recoupling time are highly sensitive to Si–Si distances and, using a symmetry-based $SR26_4^{11}$ homonuclear recoupling sequence, it was shown that distances of up to 8 Å can be determined.[8] The structure is then determined by finding the set of Si coordinates in the asymmetric unit, which minimizes the residual between the experimental and calculated DQ curves. The comparison is considerably helped by there being an analytical expression for the DQ buildup.[9] Only Si–Si distances are obtained, but in a fully siliceous sample, each Si is linked via an O

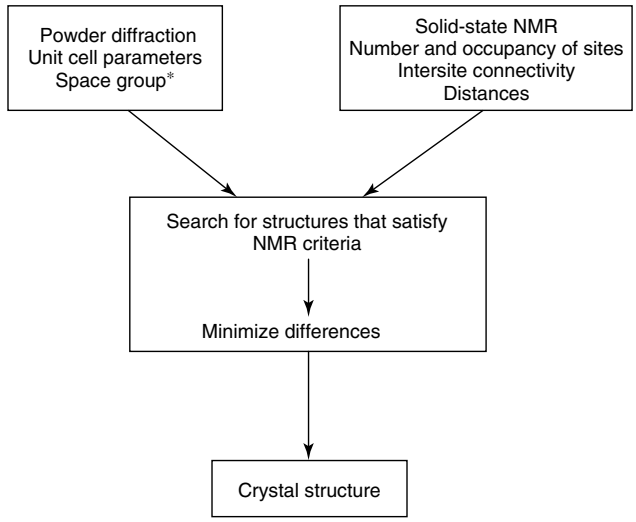


Figure 29.1. Simplified schematic algorithm for solution of crystal structures using solid-state NMR. * The space group is sometimes determined by combination of NMR and XRD data.

to other Si atoms with the distance between linked Si atoms known to be ~3.1 Å and this (soft) constraint is fed into the minimization. As a first example, the structure of the zeolite ITQ-4 was determined and found to be in good agreement with that found by XRD. The method was then tested on a more complex sample where the unit cell parameters and space group (*Pnnm*) were determined by standard powder XRD, but it was insufficient to solve the structure because of severe preferred orientation effects and the presence of occluded organic templates. The sample was found to have 5 Si sites in the ratio 2 : 2 : 2 : 2 : 1 and after finding the "best" NMR structure, oxygen atoms were added midway between the silicon and the geometry optimized for comparison with the XRD data. Once again, agreement between the NMR structure and that refined against the XRD data was found to be very good and the structure was found to be ferrierite.

Distance information has also been used to locate guest species in zeolite frameworks. For zeolites synthesized from fluoride-containing media, the situation is relatively simple since, once again, the distances between silicon and fluorine can be treated as isolated or nearly isolated pairs. In tetrapropylammonium fluoride silicalite-1, a combination of $^{19}F \rightarrow {}^{29}Si$ cross polarization, $^{19}F/^{29}Si$ REDOR, and $^{19}F/^{29}Si$ TEDOR was used to locate the fluoride ion in the structure.[10] At short CP times, the oscillations in the CP buildup are from "isolated" spin pairs but at longer times the effects of the extended ^{19}F network becomes more important. Thus only the three shortest (up to ~3.4 Å) F–Si distances were determined from the CP behavior. However, as the structure of silicalite is known and the Si resonances assigned, the location of the fluorine could be determined. Although REDOR and TEDOR were able to give distances to two further Si atoms at distances up to ~3.9 Å, they were not able to give any information about the shortest Si–F bond because of its short T_2 indicating the importance of using more than one technique to obtain distance information where feasible. The additional distances obtained using REDOR and TEDOR confirmed the CP data and the position of the F atom in the structure.

The situation of isolated spin pairs, while ideal for distance measurements, is very restrictive. However, distance information can also be obtained from the second moment M_2 (defined earlier for a homonuclear system) and this has been used to locate guest molecules in zeolites via the $^{1}H/^{29}Si$ CP behavior.[11] Initially, *p*-xylene in ZSM-5 was studied as the structure of the fully loaded form (eight molecules per unit cell) was known.[12] The full CP curve was used since the rate of cross polarization between spins I and

S, k_{IS}, is given by

$$k_{IS} = C\frac{M_2^{IS}}{\sqrt{M_2^{II}}} \tag{29.2}$$

where the heteronuclear second moment $M_2{}^{IS}$ is

$$M_2^{IS} = \frac{1}{5}\gamma_I^2\gamma_S^2\hbar^2\sum\frac{1}{r_{IS}^6} \tag{29.3}$$

i.e., k_{IS} depends sensitively on distance. However, the full CP signal is very sensitive to motion since long contact times up to 60 ms must be used; only when the sample was cooled to 273 K did k_{IS} become directly proportional to the calculated second moment. For a lower loaded sample with only three molecules per unit cell, it was necessary to cool to 193 K, but once this was done reliable values for k_{IS} could be obtained. To determine its position, the *p*-xylene molecule was located at a specific position inside the zeolite and the second moment calculated from the Si–H distances. The molecule was then rotated and translated into other positions and the second moments recalculated. The proportionality of k_{IS} to the calculated moment for all Si sites was used as a filter to find acceptable solutions. Calculated CP spectra at a contact time of 10 ms were then used to find those positions that agreed best with experiment. Only one of these was able to satisfy the symmetry requirements and thus the position of the molecule in the zeolite was determined. The method was improved in a later paper[11] by using a CP "drain" experiment[13] to determine k_{IS}. The advantage of this experiment, which compares signal with and without a contact pulse on the I spins, is that it gives k_{IS} directly and avoids complications due to $T_{1\rho}$ of either the I or S spins. A low loaded *p*-dichlorobenzene/ZSM-5 was investigated with M_2^{IS} being calculated for 4×10^6 locations of the molecule. As before, only those locations where there was a good correlation between the calculated M_2^{IS} and the experimental CP rate constants for each Si site, and also agreement with the experimental spectrum, were regarded as acceptable. Good agreement with single-crystal XRD structure was obtained and with this method an error ellipsoid for the position was produced rather like the thermal ellipsoid obtained from scattering experiments.

29.3.2 Using First-Principles Calculations

An alternative approach to determining crystal structure based upon first-principles calculations is shown in the schematic in Figure 29.2 (*see* **Chapter 3** for further discussion). The unit cell and, ideally, space group are provided by powder diffraction and the NMR parameters are calculated from first principles. Differences between the calculated and measured parameters are now taken to indicate that the structure is likely to be incorrect. It is clearly important to have

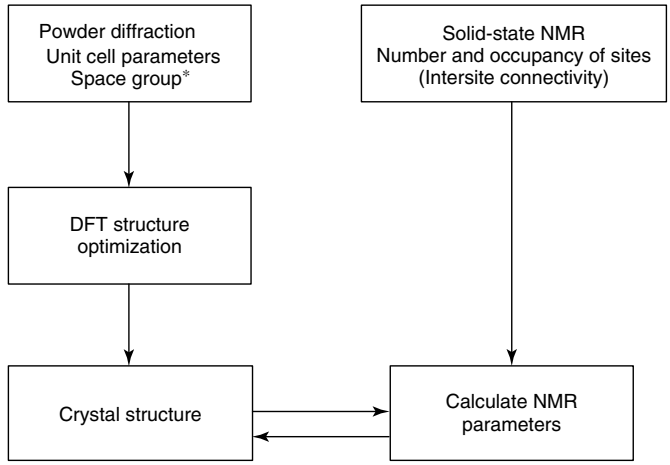


Figure 29.2. Simplified schematic algorithm for solution of crystal structures using solid-state NMR combined with DFT calculations of NMR parameters. Usually the intersite connectivity is not required.

as many parameters as possible so that ideally all nuclei in the sample should have their NMR parameters measured and for quadrupolar nuclei the electric field gradient (EFG) provides additional information. Early work in this direction compared two structures of siliceous ferrierite.[14] The space group of ferrierite was known to be *Pnnm* with 5 Si sites, 10 O sites, and 108 atoms in the unit cell. The calculation of the NMR parameters was carried out using a four-shell cluster (for O), cut from the diffraction structure, centered on the atom in question and terminated with hydrogen, since at that time no suitable periodic code was available. Ferrierite is a particularly testing material since the shifts of nine of the ^{17}O sites (measured by a combination of DOR and MQMAS) lie within an 8 ppm range. It was found that subtle differences between the two structures completely changed the calculated NMR spectrum of both nuclei and that, although the single-crystal structure gave reasonable agreement with the ^{29}Si spectrum, the calculated ^{17}O shifts were not in sufficiently good agreement with experiment to allow assignment of more than 3 of the 10 lines. With the development of methods for calculating the NMR parameters using periodic boundary conditions, a new calculation on ferrierite was carried out using the GIPAW (gauge-included projector augmented wave) method.[15] Both the isotropic shift and the quadrupolar coupling constant χ_Q were calculated and used for the assignment. While an assignment (based on minimization of a χ^2 from the combined error in these parameters) was possible, the assignment became much clearer with a much reduced χ^2 after optimization of the structure using density functional theory (DFT). Although there were significant differences in the calculated NMR parameters between the optimized and single-crystal structure, the simulated diffraction patterns were virtually identical indicating that ^{17}O NMR is much more sensitive to the local geometry than X-ray diffraction. Further examples of the sensitivity of ^{17}O to local environment in oxides are $PbZrO_3$ where the ^{17}O shift changed linearly with Zr–O bond length by ~800 ppm $Å^{-1}$[16] and a more thorough investigation of structural effects in α-ZrW_2O_8 and the $P2_1/n$ phase of WO_3.[17] In these materials, the NMR parameters were calculated using CASTEP – a code that uses the periodic structure and the GIPAW method. For α-ZrW_2O_8, which has four O sites with shifts covering a range of ~300 ppm, it was found that while changes in the unit cell parameters had no significant effect on the spacing of the ^{17}O lines, the shifts were extremely sensitive to changes in the individual internal coordinates, being ~705 ppm $Å^{-1}$ for a change in one W–O distance. For $P2_1/n$ WO_3, which has six O sites with shifts varying by ~120 ppm, the three high-quality neutron diffraction structures appeared very similar but gave distinctly different calculated ^{17}O spectra, all of which only qualitatively agreed with experiment. The structure was optimized using DFT and a new spectrum calculated. This was different from the other calculated spectra but was still only qualitatively in agreement with experiment. Interestingly, the powder diffraction pattern calculated for the optimized structure was indistinguishable from that of the original "GSAS" structure even though their calculated oxygen spectra were significantly different, indicating once again that ^{17}O NMR could help distinguish between different structural models even when diffraction data cannot. It is also noteworthy that the optimized structure gave a much better linear correlation of ^{17}O shift with mean W–O distance than the GSAS structure, with the standard deviation dropping from 9.5 to 2.3 ppm (slope 1700 ppm $Å^{-1}$).

A refinement strategy using only ^{29}Si NMR has been developed recently for siliceous zeolites.[18] As indicated earlier, use of the isotropic shift alone leaves a rather underdetermined problem since even for a relatively complex multisite material there are only a small number of experimental parameters. Furthermore, the chemical shift is a tensor and the full tensor values are much more likely to provide information about the local geometry and thus the structure. The difficulty is that for ^{29}Si in fully siliceous materials the chemical shift anisotropy (CSA) is small (span ~10–25 ppm) and difficult to measure. This was overcome partly by doing experiments at high field (900 MHz), and also by using a 2-D CSA recoupling sequence so that the anisotropy could be correlated with the isotropic shift.[19] The reliability of this method for two systems with a relatively small number of sites was confirmed by doing a slow spinning MAS experiment, which is clearly impractical in systems with a large number of overlapping sites. Using this recoupling experiment, the CSA of 15 of the 24 sites in ZSM-5 (previously assigned by a 2-D correlation experiment[3]) could be determined even though in this material there are 18 lines within a range of 3 ppm. The shift tensors were also calculated on clusters representing these samples in the same way as carried out earlier for ferrierite.[14] The clusters were centered on the atom of interest and were extracted from the crystal structure. They extended out

to three coordination spheres and were terminated by hydrogen atoms. Good agreement between the experimental and calculated principal components of the ^{29}Si shift tensor was found for α quartz, for clathrasil Sigma-2 (provided the single-crystal structure rather than the synchrotron powder diffraction structure was used) and for ZSM-5. However, for ZSM-12, where there was only a synchrotron powder diffraction structure, very poor agreement between experimental and calculated values was observed (rms shift deviation = 8.3 ppm compared with 2.1 ppm for ZSM-5, a much more complicated structure but based on single-crystal diffraction data), suggesting that the crystal structure was of low quality. Furthermore, the Si–O distances covered a wider range and were much more variable than in other zeolites where a single crystal structure was available. In a later paper, further refinement of the structure was carried out by minimizing equation (29.4)

$$\chi^2 = \chi^2_{CS} + \chi^2_{dist} \tag{29.4}$$

where $\chi^2{}_{CS}$ reflects the quality of the agreement between the experimental and calculated chemical shift tensor components and $\chi^2{}_{dist}$ that for distances.[18] The real distances are not known, so the refinement is against target average distances Si–O, O–O and Si–Si distances determined from single-crystal structures of zeolites. First, a distance least squares (DLS) optimization of the structure was performed, which not only dramatically reduced $\chi^2{}_{dist}$ but also $\chi^2{}_{CS}$ with the rms(CS) deviation becoming 2.9 ppm. Further refinement using both $\chi^2{}_{CS}$ and $\chi^2{}_{dist}$ decreased χ^2 from 385 to 81 and the rms(CS) deviation to 0.3 ppm. A comparison of the calculated powder diffraction pattern for the refined structure with that of the starting structure revealed only small differences, which could have been due to preferred orientation effects known to be present in the sample. Without a single-crystal diffraction study, the accuracy of the NMR refined structure cannot be assessed; however, when the same refinement strategy was used for Sigma-2, a simpler system for which there was a high-quality single-crystal XRD structure, excellent agreement between the two approaches was found.[20]

An alternate way of combining NMR experiments and calculations to determine crystal structure has been proposed in which the number of inequivalent sites, their multiplicity, and connectivity are determined by NMR to identify a "fragment" and AASBU (automated assembly of secondary building units) is used to build a 3-D structure.[21] This is discussed in more detail in **Chapter 17**. It was applied to chiolite, $Na_5Al_3F_{14}$, to show via MAS that there are 2 Al sites, 3 F sites, and 2 Na sites and combined with $^{19}F \rightarrow {}^{23}Na$ and $^{19}F \rightarrow {}^{27}Al$ CP- HETCOR (heteronuclear correlation) to determine the basic "fragment". Two possibilities emerged for corner-sharing AlF_6 octahedra connected via F(2) as cis or trans and the ASSBU method was used to derive candidate crystal structures. The cis unit was found to give more chiolite-type structures and was used together with the powder diffraction pattern to correctly derive the crystal structure.

29.3.2.1 Outlook

For NMR to be useful in determining crystal structures (or at the very least providing useful information), resolution of the different sites in the material is a prime requirement. This has meant that, to date, most work on inorganic materials has been carried out using spin $I = 1/2$ nuclei, particularly ^{29}Si and ^{31}P. For samples containing these nuclei, the techniques developed recently hold out much hope of providing "real" crystallographic information, i.e., the full structure in cases where diffraction techniques have not been successful. The majority of NMR active nuclei in inorganic materials are not spin 1/2 and are thus affected by the quadrupole interaction; however ^{17}O, which is ubiquitous in these systems, has a relatively small EFG in "ionic" materials such that MAS is sufficient to narrow the lines and give high resolution as discussed earlier.[16–17] In this situation, ^{17}O has considerable potential to give crystallographic information, particularly when combined with calculation. Even when oxygen is more covalently bonded with a higher EFG, techniques such as MQMAS and DOR are able to produce high-resolution spectra for highly crystalline samples.[14] Thus despite the need for enrichment, it is likely that ^{17}O studies will become more important. The ability of *ab initio* codes to calculate NMR parameters means that they are likely to become much more widely used in structural investigations. This is particularly the case since, even for situations where one code such as CASTEP has weaknesses, e.g., transition metal ions, others such as WIEN2k can be used at least for structural optimization and calculation of the EFG. A very recent example is β-Pb_2ZnF_6[22] whose structure was unknown but related to Ba_2ZnF_6. A combination of ^{19}F, ^{207}Pb, and ^{67}Zn NMR and the powder XRD allowed the space

group, $P4_2/ncm$, to be determined together with a "first" structure. This structure was optimized using WIEN2k and validated from the ^{67}Zn EFG. Before optimization the calculated asymmetry parameter, η_Q, was 0.64 compared with 0.10 ± 0.05 from experiment. After optimization the calculated value was 0.06, i.e., in very good agreement with experiment. By using the approaches described in this article, it is anticipated that structure refinement using NMR will become an important tool for accurate structure determination of inorganic materials that are difficult to be fully characterized by traditional diffraction techniques.

REFERENCES

1. G. E. Pake, *J. Chem. Phys.*, 1948, **16**, 327–336.
2. E. R. Andrew and R. G. Eades, *Proc. R. Soc. London, Ser. A*, 1953, **218**, 537–552.
3. C. A. Fyfe, H. Grondey, Y. Feng, and G. T. Kokotailo, *J. Am. Chem. Soc.*, 1990, **112**, 8812–8820.
4. V. Korthuis, N. Khosrovani, A. W. Sleight, N. Roberts, R. Dupree, and W. W. Warren, *Chem. Mater.*, 1995, **7**, 412–417.
5. I. J. King, F. Fayon, D. Massiot, R. K. Harris, and J. S. O. Evans, *Chem. Commun.*, 2001, 18, 1766–1767
6. F. Fayon, I. J. King, R. K. Harris, R. K. B. Gover, J. S. O. Evans, and D. Massiot, *Chem. Mater.*, 2003, **15**, 2234–2239.
7. D. H. Brouwer, R. J. Darton, R. E. Morris, and M. H. Levitt, *J. Am. Chem. Soc.*, 2005, **127**, 10365–10370.
8. D. H. Brouwer, P. E. Kristiansen, C. A. Fyfe, and M. H. Levitt, *J. Am. Chem. Soc.*, 2005, **127**, 542–543.
9. K. T. Mueller, *J. Magn. Reson., A*, 1995, **113**, 81–93.
10. C. A. Fyfe, D. H. Brouwer, A. R. Lewis, and J. M. Chezeau, *J. Am. Chem. Soc.*, 2001, **123**, 6882–6891.
11. C. A. Fyfe and D. H. Brouwer, *J. Am. Chem. Soc.*, 2006, **128**, 11860–11871.
12. C. A. Fyfe, A. C. Diaz, H. Grondey, A. R. Lewis, and H. Forster, *J. Am. Chem. Soc.*, 2005, **127**, 7543–7558.
13. E. O. Stejskal, J. Schaefer, and R. A. Mckay, *J. Magn. Reson.*, 1984, **57**, 471–485.
14. L. M. Bull, B. Bussemer, T. Anupold, A. Reinhold, A. Samoson, J. Sauer, A. K. Cheetham, and R. Dupree, *J. Am. Chem. Soc.*, 2000, **122**, 4948–4958.
15. M. Profeta, F. Mauri, and C. J. Pickard, *J. Am. Chem. Soc.*, 2003, **125**, 541–548.
16. A. Baldwin, P. A. Thomas, and R. Dupree, *J. Phys.: Condens. Matter*, 2005, **17**, 7159–7168.
17. A. Soleilhavoup, M. R. Hampson, S. J. Clark, J. S. O. Evans, and P. Hodgkinson, *Magn. Reson. Chem.*, 2007, **45**, S144–S155.
18. D. H. Brouwer, *J. Magn. Reson.*, 2008, **194**, 136–146.
19. D. H. Brouwer and G. D. Enright, *J. Am. Chem. Soc.*, 2008, **130**, 3095–3105.
20. D. H. Brouwer, *J. Am. Chem. Soc.*, 2008, **130**, 6306–6307.
21. J. Dutour, N. Guillou, C. Huguenard, F. Taulelle, C. Mellot-Draznieks, and G. Férey, *Solid State Sci.*, 2004, **6**, 1059–1067.
22. C. Martineau, F. Fayon, C. Legein, J. Y. Buzare, M. Body, D. Massiot, and F. Goutenoire, *J. Chem. Soc., Dalton Trans.*, 2008, **44**, 6150–6158.

Chapter 30
Geochemistry

Brian L. Phillips

Department of Geosciences, Stony Brook University, Stony Brook, NY 11794-2100, USA

30.1 Introduction 463
30.2 Al, Si Order/Disorder 464
30.3 Al Coordination in Minerals 471
30.4 Anion Order/Disorder in Minerals 473
30.5 Order/Disorder of Cations Other than Al, Si 475
30.6 Vacancy Defects 477
30.7 Speciation and the Structural Role of H 478
30.8 Structural Environment of other Minor Components 480
30.9 Potential Future Applications 481
References 482

30.1 INTRODUCTION

The crystal structure of most of the approximately 4200 (according to the International Mineralogical Association) distinctly named crystalline substances found in nature are known, most having been solved by traditional single-crystal X-ray diffraction (XRD) methods. This knowledge of the atomic arrangement of minerals forms the fundamental basis of much of geochemistry. In the Earth Sciences, this phenomenal success of diffraction methods has led to the adoption of a narrow meaning for "crystallography," focused on the relationships among crystal structures, three-dimensional periodicity, macroscopic crystal forms, and physical properties. However, minerals can only very rarely be considered pure substances, reflecting the chemical heterogeneity of natural systems, so that the crystal structure averaged over the coherent scattering length for X-rays represents an incomplete picture of the arrangement of atoms in a mineral. Complete analysis of a typical major mineral in a rock will reveal a dozen or more chemical constituents present at minor-to-trace concentrations. Furthermore, most rock-forming minerals exhibit extensive formation of solid solutions, reflecting the ability of crystalline solids to accommodate ions of similar size and charge and also to compensate charge locally via coupled substitution. This chemical variability is often essential to geochemical studies that aim to deduce the formation conditions and/or subsequent P,T history of a rock. Many geothermometers and geobarometers are based on experimental studies of the partitioning of major, minor, and trace elements and order/disorder effects. In materials from low-temperature, near-surface settings, trace-element patterns are used extensively as proxies to infer the conditions existing at the time of formation such as temperature and pH. The ability to relate experimental results from laboratory studies of mineral stability, order/disorder, and compositional variation to materials found in nature depends critically on an essential similarity of the atomic arrangement.

The introduction of high-resolution solid-state NMR spectroscopy in the early 1980s led to the solution of many long-standing problems in the

NMR Crystallography Edited by Robin K. Harris, Roderick E. Wasylishen and Melinda J. Duer © 2009 John Wiley & Sons, Ltd. ISBN: 978-0-470-69961-4

structure and composition of mineral systems that could not be solved directly by XRD methods, either because of weak scattering factors (e.g., H), scattering factors that are very similar (e.g., Al and Si), concentrations too low to significantly affect cell parameters, or short-range order/disorder effects at distance scales shorter than that for coherent X-ray scattering. This is especially true of minor components, which can affect macroscopically measured parameters such as the unit cell dimensions, but play a structural role that can only indirectly be inferred from diffraction. The goal in this article is to provide an overview of these applications of NMR crystallography in geochemistry, adopting the broader definition described by Harris (*see* **Chapter 1**) of the determination of the atomic arrangement in crystalline solids. The focus is on applications that complement the information on long-range structure (e.g., symmetry, multiplicity, and polymorphism) available from diffraction, which naturally fall along deviations from ideal structure and pure compositions—defects and disorder. A number of studies have employed NMR spectroscopy to examine the more traditionally defined crystallographic properties of minerals, particularly in the context of understanding phase transitions.[1] For the present purpose, the scope is limited to studies focused on determining atomic arrangement in crystalline or quasi-crystalline earth materials and their direct synthetic analogs. Beyond this immediate subject there exists an extensive literature describing the NMR properties of minerals. These studies have been important both as tests for NMR methodology and for the relationships developed between NMR parameters and local structural environment that have been essential to the application of NMR for determining the atomic arrangements in amorphous materials. Such data up to about 1995 have been compiled by Stebbins.[2] Reflecting the enormous breadth of the field of geochemistry itself, there are also many significant applications of NMR spectroscopy to materials and processes of geochemical interest besides crystallography that are also omitted from present consideration, including

- structure and composition of natural organic matter[3–7] and other soil constituents;[8,9]
- structure and dynamics of geologically relevant melts and related glasses;[10–13]
- speciation and chemical exchange kinetics in aqueous solutions;[14]
- adsorption phenomena;[5,15–18]
- dynamical disorder and diffusional transport, in both low-temperature fluid-dominated settings[19–21] and in minerals at elevated temperatures.[22–24]

Finally, rather than providing a comprehensive review, the aim herein is to give a broad overview of the types of crystallographic problems in geochemistry for which solid-state NMR spectroscopy has proven useful, and to close with a few comments on potential future developments.

30.2 Al, Si ORDER/DISORDER

By far the most common application of NMR crystallography in geochemistry has been the characterization of the Si,Al distribution in aluminosilicate minerals. Silicon and aluminum are the second and third most abundant elements in Earth's crust, and aluminosilicate minerals account for over 90% of its volume. The aluminosilicate minerals contain both Si and Al in tetrahedral coordination with oxygen (e.g., Al[4]) and the coupled substitutions that accompany the incorporation of Al[4] in a mineral are a major contribution to the rich and complex structural chemistry of the rock-forming silicates. The stability of a mineral depends not only on its composition but also on the state of Al,Si order. Kirkpatrick reviewed the application of NMR to determine the extent of Si,Al order in minerals, so the focus here is on more recent developments although some earlier work is included for completeness. The unique contribution of NMR crystallography has involved the ability to distinguish and quantify short-range from long-range Si,Al order. In this context, long-range order (LRO) refers to the occupancy of crystallographically distinct tetrahedral positions (T), which in some instances can be inferred from the average T–O distance or refined occupancies from single-crystal diffraction data. Short-range order (SRO) corresponds to the distributions of small clusters of cations, such as pairs (Si–O–Si vs. Si–O–Al vs. Al–O–Al) or larger "star" clusters denoted by the standard $Q^m(n\mathrm{Al})$ notation, where Q^m is a 4-coordinated Si linked through oxygen bridges to m tetrahedrally coordinated cations, n of which are Al and $m - n$ are Si. Energetically, variations in SRO have much larger effects than predicted by mixing models of the simple Bragg–Williams type based on LRO patterns and site occupancies.

The utility of NMR in this context lies mostly in the systematics of ^{29}Si NMR chemical shifts. As described by Engelhardt, the ^{29}Si chemical shift increases by about 5 ppm for each increment in n and decreases by about 10 ppm with each increase in m. In aluminosilicates containing only a single T crystallographic position, the ^{29}Si NMR spectrum can contain from 1 to $i+1$ peaks with intensities that reflect the population distribution of $Q^m(n\text{Al})$ clusters (Figure 30.1). Comparison of the apparent Si/Al ratio of the cations adjacent to Si with that from chemical analysis indicates the extent of avoidance of Al–O–Al type pairs, the so-called Loewenstein rule, which has been found to be a good approximation in most cases although exceptions are noted below. In favorable systems, partially ordered minerals containing multiple T-positions yield distinct ^{29}Si NMR peaks, which can be integrated to yield LRO in terms of T-site occupancies. For example, the crystal structure of low albite ($NaAlSi_3O_8$) contains four T-positions and its ^{29}Si NMR spectrum shows three peaks in a 1 : 1 : 1 ratio,[25–27] reflecting the nearly complete LRO of Al onto one of the T-positions. However, the presence of both significant short-range disorder and multiple crystallographic positions can yield complex ^{29}Si NMR spectra that are difficult to interpret uniquely.

It has also been shown that the pairwise tetrahedral cation clusters can be easily distinguished in ^{17}O-NMR spectra, especially with the aid of MQ-MAS methods,[28,29] because the Si–O–Si, Si–O–Al, and Al–O–Al clusters exhibit distinct ^{17}O quadrupolar coupling parameters. However, application of ^{17}O NMR is only feasible for synthetic or altered materials enriched in ^{17}O. The results from NMR studies have been used to quantify the thermochemical effects of Si,Al disorder, which have been incorporated into thermodynamic solid-solution models, and used extensively to constrain computational studies. A brief summary using examples of specific mineral systems follows.

30.2.1 Framework Aluminosilicates

The framework aluminosilicates contain Si and Al tetrahedra linked through bridging oxygens to four other tetrahedral cations ($m = 4$), and include several groups of rock-forming silicates, including the feldspars, which comprise over 50% of Earth's crust by volume. Minerals of the leucite group

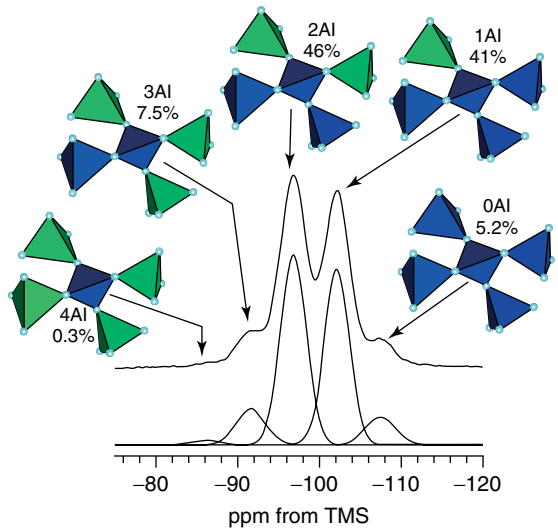


Figure 30.1. ^{29}Si NMR spectrum of analcime (top) containing a single tetrahedral T-position with a disordered Si[4],Al[4] distribution, with a least-squares fit to Gaussian curves (bottom) and assignments to local $Q^4(n\text{Al})$ configurations. Results indicate a framework Si/Al = 2.55 and somewhat more SRO than required by Al-avoidance.

(including analcime, leucite, pollucite, and wairakite) illustrate both the potential application and the difficulties of applying ^{29}Si NMR spectroscopy to measure the extent of Si,Al disorder. Analcime ($Na_xAl_xSi_{3-x}O_6{\cdot}H_2O$; typically $0.85 \leq x \leq 1$) is normally cubic (*Ia3d*) at ambient conditions, its crystal structure containing a single T-position occupied statistically by Si and Al. Silicon-29 NMR spectra of numerous specimens have been published[30–34] and all show a relatively simple pattern of quasi-equally spaced, well-resolved peaks corresponding to the $Q^4(n\text{Al})$ local Si environments. Most specimens give five peaks, corresponding to $0 \leq n \leq 4$, with intensities that reflect the composition (Si/Al ratio) and the extent of SRO, although an exceptionally well-ordered specimen gives only three peaks[33] owing to a very low abundance of $Q^4(4\text{Al})$ and $Q^4(0\text{Al})$. The breadth of the intensity distribution among the $Q^4(n\text{Al})$ peaks reflects the extent of short-range Si,Al disorder. For example, with an ideal stoichiometric Si/Al = 2 and absence of Al–O–Al linkages, complete SRO would yield only a single peak for $Q^4(2\text{Al})$, whereas complete disorder would yield the full set of five peaks with intensities governed by the binomial distribution.

Comparison of Si/Al ratios calculated from the intensities of the $Q^4(n\text{Al})$ peaks with those from chemical analysis indicates that Al–O–Al avoidance generally holds. While ^{17}O MQMAS spectra of one sample enriched via reaction with ^{17}O-enriched water under hydrothermal conditions shows the presence of a few percent Al–O–Al,[35] data for another sample[36] showed no Al–O–Al resonance within detection limits.

The entropic effects of the Si,Al SRO detected by NMR can be quantified using a cluster-variation approach[31,37] and show a large range of values for samples of different provenance and composition.[31,34] These data have now been incorporated into models for analcime solid solution[38] with better predictive ability for the stability of analcime with respect to other minerals.

In contrast, leucite (ideally, $KAlSi_2O_6$), which has the same framework topology as analcime, is metrically tetragonal below about 700 °C owing to collapse of the framework about the K-containing cavities, giving three distinct *T*-positions. Whether long-range Si,Al order occurs over the three sites has been a long-standing problem, XRD studies being complicated by the presence of pervasive transformation twinning at ambient conditions. The ^{29}Si NMR spectra of natural leucite specimens[30,33,39,40] contain a series of eight partially resolved peaks, corresponding to three overlapping sets of five peaks arising from $Q^4(n\text{Al})$ environments, one set for Si occupying each of the three crystallographic *T*-positions. The incomplete resolution makes simultaneous determination of the LRO and SRO difficult. ^{27}Al MAS NMR could be helpful for determining the LRO, in that features for three peaks are clearly resolved,[33,40] corresponding to Al on each *T*-position linked to four adjacent Si[4] (no significant population of Al–O–Al linkages). However, determination of the LRO from the ^{27}Al spectrum is somewhat uncertain owing to the partial overlap of two peaks and possibly asymmetrical peak shapes arising from the quadrupolar interaction.

The Si,Al SRO for a natural leucite was determined by ion exchanging Cs for K via reaction in molten salt, which does not significantly alter the aluminosilicate framework. The Cs-exchanged leucite is cubic above about 100 °C, with a single *T*-position, and ^{29}Si NMR spectra taken at 150 °C are much simpler than those of the original K-leucite,[31] containing only five peaks corresponding to the set of $Q^4(n\text{Al})$ environments for a single *T*-position. The intensity distribution indicates a much smaller degree of Si,Al SRO compared to analcime of similar composition, consistent with the higher crystallization temperature for natural leucite. The Si,Al distribution was found to be nearly random after exclusion of Al–O–Al linkages, but the decrease in configuration entropy arising from Al–O–Al avoidance alone is much greater than that calculated from application of the Bragg–Williams equation to any of the proposed long-range Si,Al ordering schemes.

The LRO of tetragonal leucite was determined by ion-exchanging K, Rb, and Cs for Na in an analcime with a very high degree of Si,Al SRO, at temperatures above the cubic–tetragonal transition.[41] The ^{29}Si NMR spectra are simplified compared to that of natural leucite because of dominance of the $Q^4(2\text{Al})$ and absence of $Q^4(4\text{Al})$ and $Q^4(0\text{Al})$ peaks for each of the three sites. The NMR data showed that the apparent LRO, reflected in the Si occupancies of the three *T*-positions, varied with the identity of the alkali cation, and that the site occupancies determined by ^{29}Si NMR were consistent with the relative intensities of the corresponding peaks in ^{27}Al MAS NMR spectra. These results suggest a decoupling of the SRO from the local orientation of the tetragonal distortion and emphasize that the short-range interactions dominate the thermodynamics of ordering in this system.

Other examples of the determination of SRO in frameworks with long-range Si,Al disorder on a single *T*-position include the zeolite chabazite. Natural specimens give well-resolved ^{29}Si NMR spectra[34,42] containing the five $Q^4(n\text{Al})$ peaks, with intensities that reflect the framework Si/Al ratio (from 1.76 to 3.1) and only a small amount of Si,Al SRO beyond Al–O–Al avoidance.[34] In contrast, NMR experiments have revealed the existence of nearly complete SRO (and hence, LRO) in some frameworks having Si/Al $\approx$1 that appear to exhibit long-range Si,Al disorder by XRD methods. For example, the crystal structure of the feldspathoid sodalite contains a single *T*-position with average occupancy ($Si_{0.5}Al_{0.5}$). Natural specimens yield ^{29}Si NMR spectra[43] that show only a single peak for $Q^4(4\text{Al})$, indicating the absence of a significant concentration of Si–O–Si linkages, and hence Al–O–Al by inference from mass balance. This result indicates the existence of nearly perfect alternation of Si and Al tetrahedra in the framework but which likely reverses at antiphase boundaries over distances shorter than the coherent X-ray scattering length.

In frameworks containing multiple crystallographic *T*-positions, measurement of Si,Al SRO from ^{29}Si NMR spectra remains straightforward if the sites are sufficiently similar. For example, β-eucryptite ($LiAlSiO_4$), which has a quartz-like framework topology, contains two inequivalent Si-positions that exhibit nearly identical ^{29}Si chemical shifts, reflecting their very similar average Si–O–Al bond angles. As a result, fully ordered β-eucryptite gives a ^{29}Si NMR spectrum containing only a single, narrow peak,[44] corresponding to $Q^4(4Al)$ Si in the two unresolved crystallographic sites. This property allowed measurement of the energetics of reducing Al–O–Al linkages in the aluminosilicate framework. Samples crystallized from glass of the same composition and annealed for short periods contain additional $Q^4(n\text{Al})$ peaks, $n < 4$, due to Si,Al disorder. The 1 : 1 Al : Si ratio of the framework requires that each Si–O–Si linkage detected in the ^{29}Si spectrum be balanced by an Al–O–Al linkage. Consequently, the decrease in the concentration of Al–O–Al linkages with annealing time could be quantified from changes in the ^{29}Si spectrum. The resulting values show an excellent correlation with enthalpies of dissolution obtained for splits of the same samples, from which a value of $-26\,\text{kJ mol}^{-1}$ was obtained for the enthalpy change of the short-range ordering reaction:

$$\text{Al–O–Al} + \text{Si–O–Si} = 2[\text{Al–O–Si}] \qquad (30.1)$$

although the lack of resolution of the crystallographic sites prevents simultaneous determination of the LRO.

The feldspars ($M^{n+}Al_nSi_{4-n}O_8$) illustrate potential difficulties and strategies for quantifying Si,Al order in a low-symmetry framework. Both albite ($NaAlSi_3O_8$) and microcline ($KAlSi_3O_8$) occur in well-ordered versions that contain four inequivalent *T*-positions with one nearly fully occupied by Al. The ^{29}Si NMR spectra correspondingly contain three well-resolved peaks for the crystallographic Si-positions. The presence of Si,Al disorder is clearly evident in ^{29}Si NMR spectra of natural feldspars crystallized at high temperatures[25–27] and in disordered samples prepared by annealing well-ordered specimens at elevated temperatures,[27,45,46] which is manifested by much broader, poorly resolved peaks representing sums of multiple overlapping peaks (difficult to interpret uniquely).

In the case of anorthite ($CaAl_2Si_2O_8$), however, the 1 : 1 Al : Si ratio of the framework allows information on the SRO to be obtained using a spectral moment analysis despite the presence of 16 inequivalent *T*-positions in the low-temperature triclinic structure. The ^{29}Si NMR spectrum of well-ordered end-member anorthite[47] contains seven relatively sharp peaks, one with doubled intensity, corresponding to the eight inequivalent Si-positions, all of which represent $Q^4(4Al)$ environments arising from the long-range alternation of Si and Al tetrahedral required to satisfy Al–O–Al avoidance. Synthetic samples contain additional peaks and show an overall broadening and shift of intensity to more negative chemical shifts, indicating the presence Si with fewer than four adjacent Al due to short-range disorder.[48] Using spectral data for a well-ordered natural sample as representing complete SRO and assuming a -5 ppm shift for each Si–O–Si linkage, the short-range Si,Al disorder could be quantified in terms of the number of Al–O–Al linkages per formula unit by comparing the first spectral moment with that of the maximally ordered natural material. As described above for β-eucryptite, these NMR results show a strong linear correlation with the enthalpies of dissolution for the same samples, which yielded an enthalpy change of $-39\,\text{kJ mol}^{-1}$ for the ordering reaction represented by equation (30.1).

Results for the synthetic Sr analog of anorthite ($SrAl_2Si_2O_8$) support the use of the spectral moment approach. In this case, the larger Sr atom reduces the framework distortion so that the structure is monoclinic at ambient conditions, containing only two inequivalent Si-positions. These sites give ^{29}Si NMR peaks with chemical shifts that differ by <2 ppm, so that $Q^4(3Al)$ and $Q^4(2Al)$ peaks are well resolved from those for the $Q^4(4Al)$.[49] In this case, the concentration of Al–O–Al linkages could be determined both from integrating the $Q^4(n\text{Al})$ peaks and from a moment analysis, which gave similar results.

Spectral complexity characteristic of such low-symmetry frameworks can prevent quantitative characterization of Si,Al order where $Q^4(n\text{Al})$ with $n < 4$ environments result from both Si,Al disorder and compositional effects. In the plagioclase feldspar series ($Na_xCa_{1-x}Al_{2-x}Si_{2+x}O_8$), of which anorthite is the Ca-end member, solid solution exists at high temperatures, but at lower temperatures the subsolvus phase relationships are extraordinarily complex. The ^{29}Si NMR spectra of well-ordered intermediate compositions show distinct changes across the series[50] but are difficult to interpret. A complicating factor is the presence of incommensurate phases at intermediate compositions, which

typically yield complex, nonanalytical peak shapes that depend sensitively on the details of the structural modulation, including waveform and dimensionality.

In minerals containing topologically distinct *T*-positions, the occupancies corresponding to LRO can also be determined along with SRO if the resonances are well resolved, which is more likely if the framework contains structurally distinct tetrahedra. For example, cordierite ($Mg_2Al_4Si_5O_{18}$) contains six-membered rings of tetrahedra (*T*2) in a plane approximately perpendicular to the *c*-direction that are linked by tetrahedra (*T*1), forming chains of four-membered rings (2 *T*1 + 2 *T*2) along *c*. Fully ordered cordierite is orthorhombic and contains three distinct Si-positions, two of which correspond to four of the ring tetrahedra (*T*2), which are Q^4(3Al), and the other a *T*1-type connecting site linked only to Al tetrahedra (Q^4(4Al)). Silicon-29 NMR spectra of well-ordered orthorhombic cordierite thus contain two peaks in the crystallographic 1 : 4 intensity ratio separated by over 20 ppm.[51] The two crystallographic Si-positions in the rings are very similar and are not resolved in the NMR spectra. Cordierite containing Si,Al disorder gives spectra with two well-resolved sets of $Q^4(n\text{Al})$ peaks,[51,52] corresponding to connecting (*T*1(*n*Al)) and ring sites (*T*2(*n*Al)), which do not overlap because of the large difference in average Si–O–*T* angle between the *T*1- and *T*2-type sites. Samples initially formed after crystallization from glass are hexagonal, having no LRO apparent by XRD, but analysis of the NMR intensities reveals significant partitioning of Al into the connecting *T*1 sites, with Si occupancy of 0.2 for *T*1 compared to 0.33 for ordered cordierite, and 0.556 for complete disorder.[53] Annealing samples below the hexagonal–orthorhombic transition temperature gradually reduces the degree of both short-range and long-range disorder, which correlates well with changes in the enthalpies of dissolution. Subsequent detailed analysis of the NMR data with the aid of Monte Carlo simulations[54] yielded values for the SRO in terms of the concentration of Al–O–Al linkages, from which a value of -40 kJ mol^{-1} for the enthalpy of the ordering reaction (equation (30.1)) was obtained, which is nearly identical to that measured for anorthite.

Natural specimens of minerals with structures similar to that of cordierite appear by ^{29}Si NMR to be well ordered,[55] in agreement with LRO determined from structure refinements of XRD data. In the double-ring structure of milarite, Si occupies only the ring sites, giving a single ^{29}Si NMR peak, whereas in armenite Si occurs in both ring and connecting tetrahedra giving three narrow peaks in crystallographic ratios: one connecting site (Q^4(4Al)) and two ring sites, of type Q^4(3Al) and Q^4(2Al). Although armenite contains 10 inequivalent Si-positions, only the topochemically distinct Si sites are resolved in the NMR spectrum.

The potential for quantifying long-range Si,Al disorder from ^{29}Si NMR data for minerals in which crystallographic Si sites are less well resolved is demonstrated in studies of zeolites from the natrolite group. In this case, Si,Al disorder results in additional peaks arising from local variation in the number of adjacent Si,Al due to differences in occupancy of the neighboring sites. For example, well-ordered natrolite ($Na_2Al_2Si_3O_{10}\cdot 2H_2O$) yields two narrow ^{29}Si peaks,[56,57] one each for the crystallographic sites Si1 (Q^4(2Al)) and Si2 (Q^4(3Al)), that are separated by about 7.5 ppm. In specimens with incomplete Si,Al LRO, this peak separation is sufficient to resolve additional low-intensity peaks offset by the $\sim 5 \cdot \Delta n$ ppm increment for Si,Al substitution on adjacent tetrahedra, including Si2 with $n = 1$, 2, and 4 adjacent Al and Si1 having $n = 3$ Al neighbors.[57] In addition, it is necessary to assign signal intensity for Si that occupy the Al-position (Al1), which was done by noting that the average *T*–O–*T* bond angle for the Al1 site is similar to that of Si2 from which coincidence of $Q^4(n\text{Al})$ peaks for Si on Al1 and Si2 could be inferred. Consideration of the connectivity of the framework crystallographic sites and assumption of a simple disordering scheme that preserves Al–O–Al avoidance (involving a simultaneous swap of both Al onto trans Si1- and Si2-positions across a four-membered [–Al–Si1–Al–Si2–] ring) allowed derivation of expressions for Si occupancies in terms of the relative intensity of only two peaks. Self-consistency of the model (peak assignments + disordering scheme) was verified from mass balance constraints by comparing the resulting apparent Si/Al ratio from the $Q^4(n\text{Al})$ distributions with the chemical composition. Configurational entropies could then be calculated for the long-range Si,Al distribution using the Bragg–Williams approximation. This approach becomes more difficult with increasing number of crystallographic sites, as found for the related minerals scolecite and mesolite (three and five distinct Si-positions, respectively), but is relatively straightforward for the higher-symmetry frameworks of tetranatrolite and gonnardite, which were shown to exhibit significant Si,Al disorder.[57]

The usefulness of ^{17}O-NMR methods to measure short-range Si,Al order was illustrated for the zeolite mineral stilbite, with approximate composition $Na_{0.5}Ca_2Al_{4.5}Si_{13.5}O_{36} \cdot 10.8H_2O$. The crystal structure of stilbite contains five distinct *T*-positions, but no long-range order of Si and Al is apparent by XRD. The ^{29}Si NMR spectra are correspondingly complex[29], as one would expect for a case of five overlapping sets of $Q^4(n\text{Al})$ peaks. However, distinct signals for Si–O–Si, Si–O–Al, and Al–O–Al are clearly resolved in ^{17}O MQMAS spectra for a sample that was equilibrated with ^{17}O-enriched water under hydrothermal conditions.[28] Comparison of the integrated intensities in the isotropic projection indicated that about 3% of the oxygen atoms are of type Al–O–Al,[29] which is surprisingly large for the relatively low formation temperature and low Si/Al ratio of this mineral.

30.2.2 Phyllosilicates: Micas and Clay Minerals

These layered aluminosilicates contain two-dimensional sheets of tetrahedrally coordinated Si or Al, each connected to three other tetrahedra (the tetrahedral sheet) arranged in a pattern of six-membered pseudohexagonal rings. In contrast to many of the framework aluminosilicates, crystal structures of most phyllosilicates contain only a single crystallographic *T*-position and lack three-dimensional long-range Si,Al order, making quantification of the Si,Al SRO by ^{29}Si NMR methods relatively straightforward. In those minerals for which structure refinements indicate the presence of multiple crystallographic *T*-positions (e.g., kaolinite), the sites are typically very similar and give ^{29}Si NMR peaks separated by much less than the shifts from Al,Si substitution on adjacent tetrahedra.[58,59] As a result, ^{29}Si NMR spectra of phyllosilicates typically contain a series of between one and four peaks separated by 3–5 ppm, corresponding to Q^3 (nAl), with $0 \leq n \leq 3$. The potential for ^{29}Si NMR to determine the state of Si,Al order in the tetrahedral sheet was recognized at an early stage, where comparison of the Si/Al ratio from chemical analysis with that calculated from the intensities of the Q^3 (nAl) peaks for a variety of synthetic[60,61] and natural[62,63] phyllosilicates having tetrahedral Si/Al > 1 showed that Al–O–Al avoidance applies generally for these materials. Subsequent, ^{29}Si studies have confirmed this result[64–67] and more recent ^{17}O MQMAS results do not show an obvious signal for Al[4]–O–Al[4] environments.[68,69] In the case of the mica margarite ($CaAl_2(Si_2Al_2)O_{10}(OH)_2$; Si/Al ≈ 1) Al–O–Al avoidance requires Si,Al alternation in the tetrahedral sheet, and the ^{29}Si NMR spectra correspondingly contain a single peak, for Q^3 (3Al),[62,70,71] indicating nearly complete Si,Al order within each tetrahedral sheet. However, aluminous clintonites, having Si/Al ratios ranging from 1/3 to 1/4 clearly contain Al–O–Al linkages.[72] For these materials, ^{29}Si NMR spectra contain only one peak, for Q^3 (3Al), which indicates the absence of Si–O–Si linkages and ^{27}Al MAS and MQMAS data indicate the presence of multiple Al[4] signals, which are assigned to Al(Si,2Al) and Al(2Si,Al) environments.

A more detailed analysis of ^{29}Si NMR data shows that the distribution of intensity among Q^3 (nAl) peaks in phyllosilicates indicates additional SRO beyond that expected for a random Si,Al distribution after accounting for the absence of Al–O–Al linkages. Herrero *et al.*[71,73,74] showed that in many phyllosilicates this tetrahedral Si,Al SRO can be described well by a homogeneous dispersion of charge (HDC), meaning that each six-membered ring of tetrahedra contains as close to the bulk average Al-content as possible. The resulting SRO is somewhat less than that for an ordering pattern, which minimizes the concentration of Al–O–Si–O–Al linkages, also known as *Dempsey's rule* or *maximum dispersion of charge* (*MDC*). The tetrahedral Si,Al distribution in a variety of natural[67] and synthetic[64,65] materials appears to be consistent with the HDC model. In aluminous clintonites, the HDC model also appears to apply, but in this case to the distribution of Si in tetrahedral sheets that are composed principally of Al[4], leading to the dominance of Al(1Si,2Al) and Al(2Si,Al) environments, reduction of Al(3Al) and Al(3Si), and absence of Si–O–Si linkages.[72] The success of Al–O–Al avoidance plus HDC SRO models in describing the Si,Al distribution in well-ordered phyllosilicates has encouraged application of similar methods to determine layer composition from ^{29}Si NMR spectra of compositionally complex phases.[75,76] As for framework aluminosilicates, cluster-variation methods have been developed to quantify the contribution of tetrahedral Si,Al disorder to the configurational entropy,[77,78] which appears to be small owing to the considerable SRO. The Q^3 (nAl) distributions from ^{29}Si NMR data have also played an important

role as constraints for computational studies of Si,Al order[79–81] in phyllosilicates.

30.2.3 Other Aluminosilicates

Application of NMR spectroscopy to determine the extent of Si,Al order in less-polymerized aluminosilicates, including amphiboles and pyroxenes, can be difficult because ^{29}Si chemical shift differences between Si environments are smaller, between both $Q^m(n\text{Al})$ and $Q^{m\pm1}$ (nAl) and Si having n and $n \pm 1$ adjacent tetrahedral Al, and the chemical shift is more sensitive to substitution on adjacent octahedral and other highly coordinated sites. However, with careful peak assignments and spectral modeling, it has been possible to determine basic features of Si,Al order in these materials.

In amphiboles, the characteristic double tetrahedral chain contains Q^2 and Q^3 tetrahedral sites and a key question has been the extent of long-range Si,Al order among them. These sites are resolved in ^{29}Si NMR spectra of Al-free tremolite ($Ca_2Mg_5Si_8O_{22}(OH)_2$), which contain two peaks of approximately equal intensity but separated by only about 3.5 ppm.[82–84] Amphiboles with Al substitution in the tetrahedral chain yield more complex ^{29}Si NMR spectra, with up to six overlapping peaks corresponding to Q^2 (nAl) and Q^3 (nAl), $0 \leq n \leq 2$, because of the similarity in chemical shifts for Q^3 (nAl) and Q^2 ([$n-1$]Al) environments. For a series of tremolites containing 0.3–1 Al[4] per eight tetrahedra, charge balanced by an approximately equal amount of octahedral Al^{3+} for Mg^{2+} substitution, the approach of Jenkins *et al.*[85] was to focus on the best-resolved peak, assigned to Q^2 (1Al). With this assignment, the changes in relative intensity with composition were best explained by a model in which Al[4] was disordered over the Q^2 and Q^3 sites. A similar conclusion was reached by Welch *et al.*[84] for a synthetic Al-rich pargasite ($NaCa_2(Mg_4Al)(Si_6Al_2)O_{22}(OH)_2$), in which up to one-fourth of the Al[4] occurs on the Q^2 site. In this case, fits of the ^{29}Si NMR spectra were interpreted with the aid of spectra for a series of Al-free samples having various substitutions on the larger *A* (Na, K, Rb) and *M*4 (Na, Ca, Sr) sites. By assuming the absence of SRO beyond avoidance of Al[4]–O–Al[4] linkages, expressions were derived from mass balance constraints that allow the calculation of populations for some environments (e.g., for Q^2 (1Al)), from the composition (the number of Si atoms per formula unit) and the relative intensity of the peak for a complementary configuration (e.g., Q^2 (0Al)). In this way, it could be shown that for pargasite, the peaks corresponding to Q^3 (2Al) and Q^2 (1Al) coincide. Using similar self-consistency constraints, it was found that data for an amphibole with lower Al[4] content ($NaCa_2Mg_5(Si_7Al)O_{22}F_2$; fluor-edenite), gave the best agreement of the observed intensities for an ordering model in which all Al[4] occupies Q^3 sites.

In pyroxenes, which contain single chains of Q^2 tetrahedra, analysis of ^{29}Si NMR spectra to determine Si,Al order is further complicated by the sensitivity of the chemical shift to substitution on adjacent octahedral sites. For example, diopside ($CaMgSi_2O_6$) gives a single ^{29}Si NMR peak for Q^2(0Al), but addition of about 5% Al according to the coupled Tschermak substitution:

$$Si^{4+}[4] + Mg^{2+}[6] = Al^{3+}[4] + Al^{3+}[6] \quad (30.2)$$

yields two additional small peaks of equal intensity, one shifted by +3.7 ppm for Q^2 (1Al) and another by −4.3 ppm for Q^2 (0Al) linked to Al[6] (i.e., Q^2 (0Al)[Al] vs. Q^2 (0Al)[Mg]).[86] The extent of Si,Al order in more Al-rich samples was then evaluated by comparing distributions of local Si environments with those calculated for various model assumptions, which included Al substitution on both adjacent tetrahedral and octahedral sites. For up to about 75% Al substitution, it was found that SRO distributions according to Al-avoidance give reasonable fits to the NMR intensities, but that agreement is markedly improved if SRO is also introduced between the tetrahedral and octahedral occupancies such that adjacent Al[4] are accompanied by Al[6], and conversely Si[4] neighbors by Mg[6]. At more aluminous compositions, some disorder was noted that indicates the presence of Al[4]–O–Al[4] linkages. At the fully Al-substituted end-member (Ca-Tschermakite; $CaAl(AlSi)O_6$), complete SRO would require perfect alternation of Al and Si in the tetrahedral chains, but the ^{29}Si NMR spectrum contains three peaks (for $Q^2(n\text{Al})$, $n = 0, 1, 2$), the intensities of which indicate the presence of 0.175 Al–O–Al linkages per formula unit.

In less-polymerized structures, lack of correlation in Si,Al order between structural units can produce apparently contradictory long- and short-range ordering patterns, as illustrated by comparison of NMR and diffraction data for sillimanite. The structure of sillimanite (Al_2SiO_5) contains a double chain of

tetrahedra for which most previous work indicated long-range alternation of Al and Si tetrahedra. However, a neutron diffraction study found Si,Al disorder over the tetrahedral positions in the unit cell. Subsequent investigation of the same sample by ^{29}Si NMR[87] showed only a single peak in the spectrum, consistent with complete Si,Al SRO. This discrepancy between the apparent long-range disorder observed by diffraction and SRO by NMR was explained by incoherence in the phase of the Si,Al alternation pattern between chains. In this case, the three-dimensional long-range spatial average appears disordered, whereas in the individual one-dimensional chains the ordering appears to be nearly complete.

30.3 Al COORDINATION IN MINERALS

In addition to being the third most abundant element in the crust, aluminum is the only major crustal element that commonly occurs in both four- and six-coordination by oxygen; Al[4] and Al[6], respectively. As a result, the structural role of Al is important in the crystal chemistry of rock-forming minerals and their solid solutions. For example, in tetrahedral coordination, Al^{3+} substitution for Si^{4+} creates a negative charge that must be balanced by another substitution, whereas occurrence in octahedral coordination in the place of Mg^{2+} or of divalent transition elements such as Fe^{2+} creates a net positive charge. Determining the distribution of the Al directly by diffraction methods can be difficult, especially in disordered intermediate compositions or if Al is present as a minor component. The distinct chemical shift ranges for Al[4], Al[5], and Al[6] in oxides makes ^{27}Al NMR extremely useful for quantitatively determining the distribution of Al among different sites even in compositionally complex minerals.

30.3.1 Al[4]/Al[6] in Phyllosilicates

Substitution of Al plays a central role in determining the layer charge in micas and clay minerals and hence in their physical and chemical properties. In principle, the distribution of Al between the tetrahedral and octahedral sheets can be determined in most phyllosilicates from an accurate chemical analysis by assuming a fully occupied tetrahedral sheet and apportioning the remaining cations to create a balanced structural formula of the mineral consistent with its crystal structure. However, it can be very difficult to obtain natural materials, especially clay minerals, in pure form and synthetic analogs also often contain impurities, so it is sometimes difficult to obtain an accurate analysis of the clay mineral itself. NMR spectroscopy can provide a check of the chemical analysis by providing either accurate Al[4]/Al[6] ratios through integration of ^{27}Al NMR spectra, or the tetrahedral occupancy ratio Al[4]/(Al[4]+Si[4]), from the intensity distribution of Q^3 (nAl) peaks in ^{29}Si NMR spectra (assuming absence of Al[4]–O–Al[4] linkages).

The usefulness of ^{27}Al NMR for measuring Al[4]/Al[6] ratios in clay minerals was clearly demonstrated in the study by Woessner,[88] in which excellent agreement was found for a wide range of clay minerals between the Al[4]/(Al[4] + Al[6]) ratio obtained from the integration of ^{27}Al MAS NMR spectra and the structural formula deduced from chemical analysis. (Earlier ^{27}Al NMR studies met with only limited success, primarily because of nonquantitative acquisition conditions and overlap of spinning sidebands and centerbands at low spinning rates.) However, disagreement was found for several montmorillonites for which the published chemical analysis indicated the presence of substantial amounts of Al[4], but very little or no corresponding Al[4] signal was found in the ^{27}Al NMR spectra obtained after careful purification. Similarly, for some saponites, which contain significant Al[4] substitution for Si, the ^{27}Al NMR spectra contain signal for only Al[4], even though the structural formulae contain substantial Al[6]. These inconsistencies between inferred chemical composition and ^{27}Al NMR were explained by chemical variability among samples, with analyses of previous studies unrepresentative of the material studied by NMR.

In studies involving synthetic samples, NMR has proven useful for checking the validity of mechanisms for balancing chemical substitutions in mineral solid solutions, particularly the Tschermak substitution equation (30.2), which plays an important role in several series of rock-forming silicates. For example, a series of micas along the phlogopite–eastonite join, $KMg_3(Si_3Al)O_{10}(OH)_2$–$K(Mg_2Al)(Si_2Al_2)O_{10}(OH)_2$, was studied by Circone *et al.*[64] using both ^{29}Si NMR, to determine the Al[4] content of the tetrahedral sheet, and ^{27}Al NMR to measure the Al[4]/Al[6] ratio. The Al[4]/(Al[4] + Si) ratios determined from

^{29}Si NMR are in excellent agreement with those obtained from chemical analyses performed by electron microprobe analysis (EMPA), which could avoid corundum and other impurities in the synthesis products. This result was interpreted to indicate adherence to Al–O–Al avoidance, even for samples near the eastonite end-member (Al[4]/Si[4] = 0.92). Agreement was generally also good for Al[4]/Al[6] ratios obtained by integrating ^{27}Al NMR spectra and fitting a separate Al[6] peak to a signal arising from corundum impurity. However, poorer agreement was found for some intermediate compositions, which could be explained by the presence of unresolved Al[6] signal owing to the relatively slow spinning rates employed.

With wide availability of suitable instrumentation, especially moderate-to-high fields and sufficiently fast spinning rates, ^{27}Al NMR spectroscopy is now a standard tool in the methodology for determining the structural chemistry of both natural,[67,75,89–95] and synthetic[65,76,96,97] phyllosilicates. For example, spectra collected for a series of kaolinite and halloysite samples[94] showed the presence of very little Al[4], 0.4–0.5% in kaolinite and 0–0.9% in halloysite. Halloysite is similar to kaolinite, but contains more water, which had been postulated to indicate the existence of hydrated interlayer cations to balance Al[4] substitution. These ^{27}Al NMR results showed clearly that layer charge due to Al[4] substitution in the tetrahedral sheet does not distinguish halloysite from kaolinite. Similarly, an ^{27}Al study of palygorskite[95] revealed the presence of only Al[6], although Al had generally been thought to occur as both Al[4] and Al[6] in this mineral. This result suggested that the Al substitution occurs principally in the octahedral sheet as $3Mg^{2+} = 2Al^{3+} + \square$, where $\square$ represents a vacant octahedral site.

In a study of a series of aluminous phlogopite micas with varying F^- substitution for OH^-, ^{27}Al MQMAS experiments proved useful for resolving the mica Al[4] and Al[6] peaks from those of aluminous impurity phases, including kalsilite and corundum.[98] The ^{27}Al chemical shift and quadrupolar coupling parameters derived from the MQMAS spectra were used to fit high-field MAS data, from which relative abundances of Al[4] and Al[6] were obtained. These results showed that Al[6] is favored in OH-rich compositions and that impurities were more abundant at high F-content. For synthetic aluminous chlorites, ^{27}Al NMR spectra contain well-resolved, narrow peaks for Al[4] and Al[6] in a 1 : 1 intensity ratio,[65] indicating that the Tschermak substitution equation (30.2) is the principal mechanism for alumina incorporation.

The high sensitivity of ^{27}Al NMR allows the Al[4]/Al[6] ratio to be measured in phyllosilicates even at trace-to-minor concentrations. In talc, nominally $Mg_3Si_4O_{10}(OH)_2$ but often containing small amounts of Al^{3+} and Fe^{3+}, the distribution of Al between the tetrahedral and octahedral sheet could be determined for samples ranging from 0.02 to 4 wt% Al_2O_3,[89] yielding tetrahedral occupancies of from 0.00072 to 0.0646 per four tetrahedra. These data, combined with Mossbauer data for the distribution of Fe^{3+}, allowed the expression of detailed structural formulae, which showed that the small amount of negative charge caused by substitution of the trivalent ions in the tetrahedral sheet is balanced by Al^{3+} and Fe^{3+} substitution for Mg^{2+} in the octahedral sheet.

30.3.2 Al Distribution in Other Minerals

Consideration of the distribution of Al among coordination environments in other mineral systems has focused primarily on ^{27}Al NMR methods, even for other silicates. For example, Kohn *et al*.[99] determined the Al substitution mechanism in the orthopyroxene enstatite ($MgSiO_3$) from ^{27}Al MAS NMR. It had previously been shown that orthopyroxene can incorporate large amounts of H under upper-mantle $P - T$ conditions, which has potentially important implications for water transport and content of the mantle. Several potential mechanisms for incorporation of H involve coupled substitution of H^+ with Al^{3+} (e.g., $2Mg^{2+} = Al^{3+} + H^+$) from which it was proposed that the distribution of Al between the tetrahedral and octahedral sites could provide information on the water activity at crystallization conditions. However, for a series of samples containing between 3 and 6 wt% Al_2O_3 and H : Al ratios of 0–6.9, careful quantitative analysis of high-field (21 T) ^{27}Al NMR data revealed that all samples contained essentially equal amounts of Al[4] and Al[6]. This result showed that the Tschermak substitution equation (30.2) is the principal mechanism for Al incorporation in enstatite at all water contents, even though the ^{27}Al spectra clearly show distinct differences between anhydrous and H-containing samples.

In the mineral spinel ($MgAl_2O_4$), the distribution of Al between four- and six-coordinated sites serves as a measure of the extent of Mg,Al disorder, which can be measured using ^{27}Al NMR methods.

In the ordered normal spinel at low temperatures Al occupies only the octahedral site, but increasing Mg,Al disorder at higher equilibration temperature is indicated by the presence of ^{27}Al NMR signals for both Al[4] and Al[6]. For temperatures up to 1000 °C, the fraction of aluminum occupying tetrahedral sites can be determined by integrating ^{27}Al MAS NMR data for quenched samples,[23,100] which show an increase in the fraction of Al[4] with temperature up to 0.3 at 1100 °C, in good agreement with thermodynamic models. However, cation diffusion prevents the state of disorder from being quenched in at temperatures above 1000 °C. At higher temperatures, up to 1600 °C, the Al[4] fraction could be estimated from *in situ* static (nonspinning) NMR measurements,[23] by correlating the Al[4] fraction with the average chemical shift of the partially resolved spectrum.

For garnets along the Tschermak substitution vector equation (30.2) between pyrope ($Mg_3Al_2Si_3O_{12}$) and majorite ($Mg_3[MgSi]Si_3O_{12}$), only octahedral Al was detected in ^{27}Al NMR spectra.[101,102] Garnets contain eight-, six-, and four-coordinated cation sites in a 3 : 2 : 3 ratio (occupied in pyrope by Mg, Al, and Si, respectively) and Mg,Si rich garnets are thought to be important at elevated pressure in the upper mantle. The absence of Al[4] signal in ^{27}Al MAS NMR spectra of synthetic samples suggests that disorder occurs only on the octahedral sites.

The distinct chemical shift range for Al[5] in oxides makes ^{27}Al NMR spectroscopy valuable for detecting such species in complex and poorly crystalline materials. Observation of ^{27}Al NMR peaks with chemical shifts between 30 and 40 ppm has shown the presence of Al[5] in pyrophyllite dehydroxylate,[103] allophane,[104] naturally occurring amorphous Al-oxyhydroxides[105] and the chemically complex mineral vesuvianite.[106] In the latter case, the crystal structure contains a five-coordinated square-pyramidal site, which had been assigned to Mg in refinements of XRD data for samples of similar composition.

Aluminum-27 NMR has also played an important role in determining the distribution of trace-to-minor amounts of Al in high-pressure phases. Although aluminum is nearly five times less abundant in the Earth's mantle compared to the crust, its occurrence in the minerals thought to exist under conditions of elevated temperature and pressure can have a large effect on their physical properties. In the lower mantle, the dominant mineral is thought to be a perovskite-structured phase with composition near $MgSiO_3$, in which Si occupies the octahedral *B* site and Mg the larger *A* site. Solid solution with Al_2O_3 could play an important role in determining the chemical and physical properties, but the charge balance mechanism for the substitution is not understood. The ^{27}Al MAS NMR spectra of a stoichiometric Al-rich magnesium–silicate perovskite[107] contain a relatively narrow peak for Al[6] plus a much broader second-order quadrupolar powder pattern at more negative shifts, which is assigned to Al substitution for Mg in the larger *A* site. The observed 1 : 1 intensity ratio of the two ^{27}Al resonances at high field (18.8 T) is consistent with a coupled substitution of $Si^{4+}(B) + Mg^{2+}(A) = Al^{3+}(B) + Al^{3+}(A)$, analogous to the tetrahedral/octahedral Tschermak substitution equation (30.2). In studies of nonstoichiometric compositions having excess Mg (e.g., $MgSi_{1-x}Al_xO_{3-x/2}$),[108,109] the same two signals for Al on the *B* and *A* sites were observed (but in ratios near 2 : 1) plus an additional signal at more positive chemical shifts. These results suggest that in Mg-silicate perovskite Al also occurs in lower coordination environments, consistent with the presence of oxygen vacancies that could also serve to balance the charge arising from Al incorporation. In contrast, aluminous stishovite (SiO_2, with Si in octahedral coordination) synthesized under water-saturated conditions yields only a single, relatively narrow ^{27}Al NMR peak for Al[6].[109] A small ^{27}Al{^{1}H} REDOR effect was observed at a short dephasing time (50 μs), indicating that charge could be balanced by interstitial H^+, giving a substitution $Si^{4+}[6] = Al^{3+}[6] + H^+$. For rutile ($TiO_2$), which is isostructural with stishovite, samples grown in a H-containing environment also gave an ^{27}Al NMR peak for Al[6][110] that could be distinguished even in the presence of a large signal for corundum, indicating Al substitution onto the Ti site.

30.4 ANION ORDER/DISORDER IN MINERALS

Substitution of fluoride for structural hydroxyl is a common simple substitution in minerals, including several groups of rock-forming silicates, many of which exhibit limited to complete OH^-, F^- solid solution. Based primarily on compositional data and vibrational spectroscopy, it has long been recognized that in some mineral groups, such as phyllosilicates and amphiboles, the anion distribution is not random,

expressing, for example, a high affinity of F^- for Mg^{2+}. A number of studies have applied NMR spectroscopic methods to determine the distribution of hydroxyl and fluoride, through observation of not only ^1H and ^{19}F but also by observing the effects on the resonance of cations as well. The quantitative nature of NMR intensities and the availability of double-resonance methods to substantiate peak assignments makes NMR useful for characterization of ordering of OH^-, F^- and other anions in minerals.

Most natural clay and other phyllosilicate minerals contain sufficient F (from 10 to >10 000 ppm) for direct observation of the ^{19}F-resonance, even under modest experimental conditions. In phyllosilicates, the monovalent anion occurs in the octahedral sheet at vertices linking octahedral cations, in the center of the six-membered, pseudohexagonal silicate rings of the tetrahedral sheet. In the trioctahedral series, the OH^-, F^- are bonded to three octahedral cations, e.g., [3Mg]OH, whereas in dioctahedral minerals one of every three octahedral sites is vacant, owing to the presence of mainly trivalent cations in the octahedral sheet, so that each OH^-, F^- is bonded to two cations and is adjacent to a vacancy (e.g., [□, 2Al]OH = [2Al]OH). Fluorine-19 MAS NMR spectroscopic data obtained for a range of well-characterized natural and synthetic phyllosilicates[111,112] show, overall, a broad range of ^{19}F chemical shifts, but with relatively narrow regions corresponding to specific local configurations of cations directly bonded to F. Thus, distinct peaks can be identified in the spectra for [2Al]F and [AlMg]F environments in dioctahedral sheets and for [3Mg]F and [2MgLi]F in trioctahedral sheets. For both montmorillonite and palygorskite containing substantial fluoride, the NMR data show evidence for strong ordering of F^- into Mg-octahedra.[112] The montmorillonites contain substantial Mg^{2+} substitution for Al^{3+} in the dioctahedral sheet, but the ^{19}F spectra contain only a single peak, near −153 ppm for [□AlMg]F environments, even though [□2Al]-type anion sites should dominate overall. Data for a F-rich palygorskite containing 10 wt% Al_2O_3, mostly as Al[6], also showed one peak, but at −175.3 ppm for [3Mg]F, whereas a significant population of [2MgAl]F environments would be expected for a random OH^-, F^- distribution.

The distribution of OH^-, F^- and extent of order can also be determined from ^1H NMR, as shown for a series of synthetic phlogopite samples prepared with varying Al-content and OH^-/F^- ratios.[76] The ^1H MAS NMR spectra of these micas contain peaks for structural hydroxyl at 0.7 and 1.8 ppm. The relative intensity of the peak at 1.8 ppm increases with Al-content and this peak is absent in Al-free samples, indicating assignment to [2MgAl]OH environments and that at 0.7 ppm to [3Mg]OH. Comparison of the relative intensities to a model for a random OH^-, F^- distribution calculated from the chemical composition indicates a strong preference of OH^- to occur in [2MgAl]OH environments. Results of two-dimensional $^{27}Al\{^1H\}$ heteronuclear correlation (HETCOR) experiments strongly support this interpretation,[98] showing an Al[6] cross-peak only for the ^1H signal at 1.8 ppm, whereas the Al[4] resonance shows cross-peaks for both ^1H signals, reflecting the proximity of Al[4] to both types of octahedral groupings. Conversely, ^{19}F MAS NMR spectra of the same samples[76] contain only two peaks from the phlogopite phase, at −174 ppm for [3Mg]F and −150 ppm for [2MgAl]F. In an analysis similar to that for the ^1H results, the variation of intensity ratios of the two types of F-environments with chemical composition differ substantially from that expected for a random OH^-, F^- distribution and indicate strong preference of F^- for [3Mg]F sites.

The potential for characterizing anion order/disorder based on the effects of anion substitution on the NMR spectra of the cation is illustrated by ^6Li NMR spectra of minerals along the amblygonite–montebrasite series ($LiAlPO_4F$—$LiAlPO_4OH$).[113] This series exhibits complete F^-, OH^- solid solution, in which fluoride or hydroxyl bridges two corner-linked Al-octahedra and is bonded to one Li atom. For a series of natural specimens, two ^6Li NMR peaks occur that are very well resolved at high field (18.8 T) and could be assigned to Li–OH and Li–F based on variation in peak intensity with composition (i.e., F^-/OH^- ratio) and supported by $^6Li\{^1H\}$ and $^6Li\{^{19}F\}$ CPMAS spectra. In this case, interpretation of the ^6Li spectra is simplified because each Li is bonded to only one monovalent anion (F^-/OH^-) and the coordination of Li changes from six if bonded to F^- ($Li[O_5F]$) to five when linked to OH^- ($Li[O_4OH]$), resulting in a relatively large chemical shift difference. Comparison of relative intensities with EMPA data indicates that the ^6Li NMR peaks quantitatively reflect the F^-/OH^- ratio of the sample. In this structure, the Li–H and Li–F approximate isolated spin-pairs so that the distances between Li and H for $Li[O_4OH]$ polyhedra and between Li and F for $Li[O_5F]$ octahedra could be

determined from both $^{6}Li\{^{1}H\}/^{6}Li\{^{19}F\}$ REDOR data, and from the characteristic oscillations of the corresponding $^{6}Li\{^{1}H\}/^{6}Li\{^{19}F\}$ CPMAS intensity with contact time. These distances are in very good agreement with refinements of neutron diffraction data using partially occupied split Li and OH^{-}/F^{-} positions, thus providing support for the structural model. The observation of significant intensity for the $Li[O_5F]$ environments in $^{6}Li\{^{1}H\}$ CPMAS spectra and correspondingly the appearance of the $Li[O_4OH]$ peak in $^{6}Li\{^{19}F\}$ data indicate dipolar coupling between the OH^{-} and F^{-}-bearing Li sites. This result indicates that the OH^{-}/F^{-} are intimately mixed and not segregated into largely OH^{-}- or F^{-}-rich domains.

A somewhat different approach for using NMR data from the cation to examine the F^{-}, OH^{-} anion distribution was taken in a study of zunyite by ^{27}Al NMR.[114] The structure of this mineral contains Al[4]-centered oxy/hydroxy-bridged $Al[4](Al[6])_{12}$ clusters that closely resemble the Keggin-type "Al_{13}" polyoxometalate. Most specimens contain significant substitution of fluoride for hydroxyl that appears to be related to the presence of two Al[6] resonances in ^{27}Al NMR spectra, which are distinguished primarily by peak width. Comparison of ^{27}Al quadrupolar coupling parameters obtained from MQMAS spectra with those calculated from a cluster model suggests that the broader resonance, which exhibits a large quadrupolar interaction, corresponds to Al[6] bonded to fluoride, whereas the narrower peak can be assigned to Al bonded only to hydroxyl (based on the smaller quadrupolar coupling obtained from the cluster calculation for this configuration). Comparison of the relative intensities of the two Al[6] resonances with $F^{-}:OH^{-}$ ratios from chemical analysis indicated that F^{-} were dispersed, such that only $Al[O_4(OH)_2]$- and $Al[O_4(OH)F]$-type octahedra occur in the Keggin-like moiety of the structure, with no significant fraction of Al bonded to two bridging fluoride groups.

Fluorine-19 NMR data for a mixed fluor/chlorapatite ($Ca_5(PO_4)_3(F,Cl)$)[115] provide an example in which multiple peaks can occur even in the presence of complete order, and illustrate the importance of double-resonance methods for correct spectral interpretation. The structure of apatite features large unidimensional channels containing the monovalent anion, which is bonded to three Ca atoms. For an apatite near the composition $Ca_5(PO_4)_3(F_{0.5}Cl_{0.5})$, refinement of single-crystal synchrotron XRD data appears to indicate a long-range ordered F,Cl distribution within the channels. The centerband of the ^{19}F NMR spectrum, however, exhibits a complex lineshape that appears to indicate the presence of distinct F sites. However, comparison of $^{19}F\{^{35}Cl\}$ TRAPDOR (transfer of populations in double resonance; control and difference spectra show no difference in the spectral profile, indicating that the resolved features are unrelated to the local anion distribution near F. Quantitative comparison of experimental TRAPDOR dephasing curves with those calculated for spin clusters with geometry constrained by crystal structure data showed that there could be no significant population of F farther from Cl than the 2.6 Å intracolumn anion spacing. Experimental conditions (i.e., TRAPDOR dephasing periods) could be chosen such that no significant TRAPDOR effect would occur for F–Cl distances corresponding to two intrachannel anion spacings (5.3 Å) or from the interchannel distance (9 Å). These results show the absence of F-rich clusters, consistent with locally ordered F,Cl distribution within the apatite channels.

30.5 ORDER/DISORDER OF CATIONS OTHER THAN Al, Si

A range of NMR techniques has been applied to obtain information on the distribution and ordering of cations, in addition to Al[4],Si[4] order/disorder described above. Although spectral interpretation is often not as straightforward as for tetrahedral Al,Si order, these applications illustrate other potential applications of NMR crystallography. For example, the distribution of Al and Mg in octahedral sites linked by hydroxyl groups can be determined from ^{1}H NMR spectra of the corresponding hydroxyl bridges, which show a tendency for Al-octahedra to be dispersed if possible. In phyllosilicates, the structural hydroxyl groups link three octahedral sites and can potentially probe the distribution in terms of clusters of three mutually edge-shared octahedra. For a series of aluminous phlogopites having between 3 and 27% of the sites in the octahedral sheet occupied by Al (the balance being Mg), ^{1}H NMR spectra show two hydroxyl peaks, indicating the presence of only [3Mg]OH and [2MgAl]OH environments and the avoidance of adjacent Al-octahedra.[76] A similar distribution was observed in a series of layered double hydroxides (LDHs) with compositions

between brucite ($Mg(OH)_2$) and a hydrotalcite-like composition ($Mg_2Al(OH)_6(NO_3) \cdot nH_2O$).[116] The LDHs consist essentially of an Al-substituted trioctahedral sheet, with the excess positive charge balanced by interlayer anions (e.g., carbonate). Proton NMR spectra of intermediate compositions between brucite and hydrotalcite, taken at very high spinning rates (60 kHz), contain only two peaks for hydroxyl, in addition to a peak for the interlayer water. The hydroxyl peaks correspond to [2MgAl]OH and [3Mg]OH environments. These assignments were confirmed by $^1H\{^{27}Al\}$ TRAPDOR results, in which the TRAPDOR difference spectrum was found to be dominated by the peak assigned to [2MgAl]OH, and by agreement of the relative peak intensities with the bulk composition. This result suggests an ordered Mg,Al distribution, because random Mg,Al mixing would be expected to produce observable concentrations of [Mg2Al]OH as well. For the $Mg:Al = 2:1$ composition, the presence of only a single hydroxyl resonance in the ^1H NMR spectra, for [2MgAl]OH, showed that Mg,Al order is nearly complete.

Similar hydroxyl distributions were found for the amphibole pargasite,[117] in which the octahedral sites have a Mg : Al ratio of 4 : 1. The octahedra in amphiboles are arranged by edge-sharing into chains, with an alternating width of two (M1–M1) and three (M2–M3–M2) octahedra, where M1, M2, and M3 represent crystallographically distinct positions. Since the hydroxyl groups connect the two M1 octahedra to an adjacent M3 site, the ^1H NMR data provide information on the Mg,Al occupancy of the crystallographic positions. The ^1H NMR spectra contain two peaks of nearly equal intensity, corresponding to [3Mg]OH and [2MgAl]OH. By consideration of the bulk 4 : 1Mg : Al ratio in the octahedra, this result indicates that Al must occur on both the M2 and M3 positions. From the nearly equal intensities of the two hydroxyl peaks, occupancies of (2/3Mg + 1/3 Al) for M2 (twofold multiplicity) and (1/2Mg + 1/2 Al) for M3 could be determined, implying that M1 is fully occupied by Mg. A similar conclusion was drawn from ^{27}Al NMR data for aluminous tremolite amphiboles.[118] On the basis of the observation of only two Al[6] resonances in ^{27}Al MQMAS spectra, it was concluded that Al occurs on only two of the octahedral sites and thus one is fully occupied by Mg.

In a novel application of ^{27}Al NMR, the loss of signal intensity with increasing Fe-content was shown to indicate clustering of Fe at higher Fe-content.[119] Interaction with the unpaired electron spins of paramagnetic Fe^{3+} leads to very large frequency shifts for nearby ^{27}Al nuclei, which, in turn, causes an apparent loss of signal intensity in the normal chemical shift range. For clay minerals containing small amounts of Fe, the loss of ^{27}Al NMR signal correlates well with Fe-content from chemical analysis, corresponding to about 10% signal loss with each 1 wt% Fe_2O_3. However, deviation from this correlation at higher Fe-concentrations indicates that excess ^{27}Al signal is observed. From a spherical "wipe-out" model, in which it is assumed that signal is unobservable for Al within about 0.65 nm of an Fe-center, it was concluded that clustering of Fe^{3+} at higher Fe-content leads to a decrease in the unobservable ^{27}Al signal fraction, compared to the correlation found at low Fe-content.

Investigation of the ordering of alkaline earth cations in mixed pyrope-grossular garnet ($Mg_3Al_2Si_3O_{12}$–$Ca_3Al_2Si_3O_{12}$) illustrates how the choice of probe nucleus can provide information on different aspects of the ordering interactions. In the garnet structure, Ca and Mg occupy large eight-coordinated sites resembling a twisted cube. Each oxygen is bonded to one tetrahedral cation (Si), one octahedral cation (Al), and two eight-coordinated sites but at distinct bond distances. For intermediate compositions along the pyrope-grossular series ($(Ca,Mg)_3Al_2Si_3O_{12}$), synthesized ^{17}O-enriched, four peaks are resolved in the isotropic projections of ^{17}O MQMAS spectra[120] corresponding to the local configurations [Ca_sCa_l], [Ca_sMg_l], [Mg_sCa_l], and [Mg_sMg_l], where the subscripts "s" and "l" denote the adjacent cation position at shorter and longer distance. The relative intensities of the ^{17}O peaks are consistent with a random distribution of Ca,Mg neighbors about the oxygen. In contrast, ^{29}Si NMR data for similarly prepared garnets indicate the presence of some short-range Ca,Mg order in the distribution of cubic sites linked to a common tetrahedron.[121,122] The tetrahedral sites share edges with two cubic sites in a trans configuration and corners with four additional cubic sites, giving rise to 15 possible local configurations (Mg_iCa_{2-i})–(Mg_jCa_{4-j}) with $0 \leq i \leq 2$ (edge-shared) and $0 \leq j \leq 4$ (corner-linked). The ^{29}Si NMR chemical shift is sensitive to Ca,Mg substitution on both the corner-linked and edge-shared sites, giving approximately +3.5 and +1 ppm for each increment in i and j, respectively. Intermediate compositions give ^{29}Si NMR spectra containing resolved features for as many as 13

of the 15 possible configurations, which could be assigned on the basis of comparison of spectra for a number of compositions across the series.[121] Comparison of relative intensities of the ^{29}Si NMR peaks with populations calculated for random Ca,Mg distributions, based on compositions determined by EMPA, indicate small but consistent deviations in favor of clustering of Ca and Mg. For example, at the 85% pyrope composition, NMR data indicate about 4–5% more (Mg_2)–(Mg_4) and 4% less (Mg_2)–(Mg_3Ca) than expected for a purely random distribution.[122] The degree of disorder, expressed as the ratio of intensities, generally increases with increasing synthesis temperature. The effect on the configurational entropy could be estimated from the populations derived from peak intensities, which was shown to be of the order $1-2\,J\,mol^{-1}\,K^{-1}$. The contrasting results of ^{17}O and ^{29}Si NMR are consistent with subsequent computational studies[123–125] that suggest that the Ca,Mg order is dominated by third-neighbor interactions, across the Si tetrahedron, but insensitive to the first-neighbor interactions between adjacent edge-sharing Ca,Mg polyhedra.

Silicon-29 MAS NMR also proved to be a useful probe of the ordering for octahedrally coordinated cations (Si,Mg,Al) in garnets along the series between pyrope $(Mg_3Al_2Si_3O_{12})$ and majorite ($Mg_3[MgSi]Si_3O_{12}$; enstatite composition), which corresponds to coupled substitution on the octahedral position: $Mg^{2+}[6] + Si^{4+}[6] = 2\,Al^{3+}[6]$. In the garnet structure, the Si tetrahedron shares corners with four adjacent octahedral sites. The ^{29}Si chemical shift is sensitive to substitution on the adjacent octahedra, but with an apparent pairwise additivity rule,[48] the constants of which could be determined from near-end-member compositions. For the majorite end-member, the spectral region for tetrahedral Si is dominated by three peaks, for Si(4Mg), Si(2Mg2Si), and Si(4Si) environments, consistent with the presence of three distinct tetrahedral sites owing to LRO of Si[6] and Mg[6] onto distinct octahedral positions. The observation of smaller, additional Si[4] peaks indicates the existence of some long-range disorder, which could be quantified from the spectral intensities in terms of octahedral site occupancies.

For compositions intermediate between pyrope and majorite, the large number of local configurations cannot be fully resolved. However, the observed spectra could be fitted with a physical model using chemical shifts calculated from best-fit pairwise additivity constants and peak widths that were constrained to values consistent with the better-resolved peaks at the edges of the spectral profile. This model allowed the spectra to be fitted allowing only variation in the peak intensities, representing 11–13 adjustable parameters, compared to 21 parameters needed for an unconstrained fit to the seven resolved spectral features. The fitted intensities differ by less than 5% from those expected for a random Si[6],Mg[6] distribution, indicating the absence of a large degree of SRO. This result from the model fit is consistent with the intensities of the relatively well-resolved Si(4Mg) and Si(4Si) peaks at the edges of the spectral profile, and the lack of a large intensity deviation from random at the predicted position for the (Mg,2Al,Si) environment, especially at the 50% pyrope composition, which could potentially be accommodated with a fully ordered Si(Mg,2Al,Si) arrangement.

30.6 VACANCY DEFECTS

Crystallographic application of NMR spectroscopy to determine the local structural configuration and charge balance mechanism for vacancy defects has made use of spectral effects of both nuclei adjacent to the defect and those of a substituting species. As protonation of oxygen is thought to be an important charge balance mechanism for vacancies at normal cation sites in oxides, NMR methods are particularly well suited for such problems. The small size and charge of H^+ and stabilization by hydrogen bonding interactions can allow accommodation of vacancies without large disruption of the crystal structure, leading to an increased range in chemical composition of minerals. For example, such H-bearing defects in nominally anhydrous minerals[126] could play an important role in the water budget of the deep Earth.

NMR studies of the so-called 10 Å phase revealed the presence of essential Si-vacancies that could not be detected by conventional crystallographic methods and provide an illustration of an application in which vacancies can be detected via an NMR signal from adjacent Si nuclei and terminating protons. The "10 Å phase" is a high-pressure product of water and talc ($Mg_3(OH)_2Si_4O_{10}$; a 2 : 1 trioctahedral phyllosilicate) and is essentially talc with interlayer water and a correspondingly increased c cell dimension (from 9.4 to 10 Å). The occurrence of vacancies at the

Si-position in the tetrahedral sheet is indicated by the appearance in ^{29}Si NMR spectra of a distinct peak for Q^2-type Si environments,[127] whereas talc contains only Q^3 sites. The Q^2 signal was observed in samples prepared from oxides/hydroxides as well as from a well-crystalline talc that contained no significant concentration of Q^2, suggesting that the vacancies are intrinsic to the 10 Å phase structure. That the vacancies are compensated by protonation of adjacent oxygens was shown by a combination of ^{1}H and ^{2}H NMR.[128] Particularly useful were two-dimensional ^{29}Si{^{1}H} HETCOR spectra that show the presence of a silanol proton strongly coupled to the Q^2 Si.

For phases of the alunite group ($AAl_3(SO_4)_2(OH)_6$; $A = Na^+$, K^+, H_3O^+), ^{27}Al and ^{1}H NMR data provided important information on the configuration of vacancy defects.[129] The presence of vacancies can be inferred from chemical analyses that are often deficient in both monovalent *A*-cation and Al and contain excess water. The structure of alunite contains a sheet of $Al[O_2(OH)_4]$ octahedra in which each octahedron is corner-linked to four other octahedra via hydroxyl bridges. A minor resonance observed in ^{27}Al MAS NMR spectra of nonstoichiometric alunite was shown by ^{27}Al{^{1}H} HETCOR to be strongly coupled to structural water molecules. The absence of this extra ^{27}Al peak in well-ordered samples suggests that the additional Al environment corresponds to sites adjacent to a vacancy at the Al-position. One possible source of the excess water is substitution of hydronium ion onto the *A* site, but no signal from hydronium was observed in ^{1}H or ^{2}H NMR spectra. This result, considered with the strong coupling observed between Al adjacent to defects and structural water, suggests that the water molecules result from protonation of terminal hydroxyls at the vacancy. Comparison of the NMR results with chemical analysis indicates that protonation of all four dangling hydroxyl groups at the Al-site vacancy is charge balanced by a vacancy at the monovalent *A* site ($A = Na^+$ or K^+), indicating a coupled substitution $Al^{3+} + A^+ = 4H^+$, which differs from that proposed previously, based solely on compositional data (e.g., $Al^{3+} = 3H^+$), which would leave one terminal hydroxyl at the defect site. The coupled H/vacancy substitution was also suggested to explain the presence of additional excess water, which could occupy the vacant *A*-site positions.

Evidence for proton substitution at Mg-vacancies in Mg-phosphate end-member phosphoellenbergite was obtained from ^{1}H and ^{31}P NMR data.[130] Comparison of chemical analyses of phosphoellenbergite and the crystal structure from refinement of XRD data suggest the presence of about 10% vacancies at the Mg-position, which occurs in a chain of face-shared Mg-octahedra, and excess H; $(Mg_{0.9}\square_{0.1})_2Mg_{12}P_2P_6O_{38}H_{8.4}$. In addition to the main hydroxyl peak, small but distinct resonances were observed in ^{1}H MAS NMR spectra for H in a moderately strong hydrogen bond. A small extra resonance is also present in ^{31}P spectra for hydrogen phosphate groups associated with the defects. The ^{31}P-assignment to protonated phosphate could be made on the basis of observation of a rapid cross-polarization rate in a series of CPMAS spectra taken at varying contact time. This excess H was attributed to charge balance of Mg^{2+} vacancies in the chains of face-sharing Mg-octahedra.

30.7 SPECIATION AND THE STRUCTURAL ROLE OF H

Despite the importance of H in most geochemical systems (more than half of the ca. 4200 named mineral species recognized by the IMA contain H as an essential component), to date, there have been relatively few applications of ^{1}H NMR to address crystallographic problems regarding hydrogen, especially considering its high sensitivity. This somewhat limited application of ^{1}H NMR can be attributed to generally poor resolution in phases in which H is abundant and to interference in materials with low H-content from H at grain-boundaries, surfaces, and in fluid inclusions. However, more recent studies have begun to overcome these difficulties to make use of the extremely useful correlations that allow the hydrogen bond distance to be estimated from ^{1}H chemical shifts. The crystallographic information obtained about H from NMR in systems of geochemical interest has focused on determining the speciation of H (principally whether hydroxyl or molecular water), estimation of hydrogen-bond distances, and determination of H–H distances. Proton NMR has also been successfully applied to probe the distribution of octahedral cations linked by hydroxyl groups; these types of applications are discussed above with anion (in the Section 30.4) and octahedral cation (in the Section 30.5) order/disorder.

Determination of hydrogen-bond length, typically stated as $d(O\cdots O)$, relies on correlations with ^{1}H

NMR chemical shift.[131–135] NMR is particularly useful for identifying strong hydrogen bonds ($d(O\cdots O) < 2.7$ Å), giving ^{1}H chemical shifts higher than 10–12 ppm, because IR bands for such species can be broad, with ill-defined maxima.[136] For example, silanols (Si–OH) that donate strong hydrogen bonds have been identified in ussingite[136] and magadiite[137] on the basis of the ^{1}H chemical shift. The absence of a ^{1}H NMR peak at a high chemical shift in spectra of sorensenite (obtained by CRAMPS) was taken as evidence for a relatively weak hydrogen bond,[138] whereas the ^{1}H spectra of the structurally related mineral pectolite[139] contains signal from a strongly hydrogen-bonded silanol. Excess hydroxyl in a triclinic Na-amphibole was determined to be moderately strongly hydrogen-bonded based on the ^{1}H chemical shifts (5.5 and 6.1 ppm),[140] which decreased with increasing temperature indicating a weakening of the hydrogen bond. In the 10 Å phase (described in the Section 30.6), the 7.8-ppm chemical shift of the silanol protons, identified in two-dimensional ^{29}Si{^{1}H} HETCOR spectra, indicate they donate moderate hydrogen bonds to the interlayer water. However, the very low chemical shift of the interlayer water molecules themselves, 3.2 ppm, indicates that they are isolated and do not donate hydrogen bonds under ambient conditions.

In disordered phases, the distribution of chemical shifts in broad peaks can be interpreted to indicate a range of hydrogen-bond environments. Hydrous wadsleyite (β-Mg_2SiO_4, with a spinel-type structure), which is stable under conditions in the Earth's mantle transition zone and can contain up to several wt.% H_2O, gives a complex ^{1}H NMR spectrum that was fitted to a sum of six curves.[141] The NMR peaks were assigned to groups of possible structural positions by correlating the ^{1}H chemical shifts with O–O distances from the crystal structure, including some with strong hydrogen bonds ($d(O\cdots O = 2.65$ Å). In "phase D", which is a disordered hydrous Mg-silicate stable at high pressure, the large breadth of the ^{1}H resonance in CRAMPS spectra[142] indicates disorder in the hydrogen-bond lengths. The peak for protons in phase D was also identified from ^{29}Si{^{1}H} HETCOR data, which showed cross-peaks between the broad ^{29}Si resonance and a ^{1}H NMR peak centered near 12 ppm. This chemical shift indicates that the hydrogen bonding, $d(O\cdots O) = 2.55$ Å, is stronger than suggested by structure refinements of XRD data using partial occupancies. This result shows that the oxygen positions in the X-ray structure data represent an average over hydrogen-bonded and non-hydrogen-bonded positions.

Several studies have used homonuclear H–H dipolar interactions to measure interhydrogen distances. The high-pressure hydrous magnesium silicate phases A, B, and superhydrous B contain paired hydroxyl groups. Nonspinning ^{1}H powder spectra of these phases were fitted with simulated spectra for dipolar-coupled H–H pairs,[143,144] which yield highly accurate H–H distances because of the r^{-3} dependence of the spectral width. However, in all cases, significant deviations from a symmetrical Pake doublet were observed owing to the effects of chemical shift anisotropy (CSA). The CSA and its orientation with respect to the internuclear vector must be included in the lineshape simulation, but could be estimated from the crystal structure data assuming an axially symmetric CSA oriented along the OH vector. Cho and Rossman used a spectral moment method based on the van Vleck equations to determine the H–H distances of isolated H-clusters in garnet.[145] From multiple-quantum NMR experiments, it was determined that the H-content of a natural grossular specimen (nominally $Ca_3Al_2Si_3O_{12}$) containing the equivalent of 0.2 wt% H_2O was dominated by clusters of two H-atoms. Analysis of the spectral second moment indicated an average H–H distance of 1.69 Å in the clusters. Multiple-quantum data for other grossular specimens showed the presence of clusters of four H, indicating some H-incorporation according to the "hydrogarnet" substitution at the tetrahedral site, $[SiO_4]^{4-} = [H_4O_4]^{4-}$. Similar data for a synthetic, fully substituted hydrogarnet ($Ca_3Al_2H_{12}O_{12}$) indicated clusters of four H, as expected, with average intracluster H–H distance of 2.16 Å.

For disordered phases and those containing minor-to-trace amounts of H as defects, MAS NMR methods have been applied successfully to determine the distribution of H between hydroxyl and molecular water, principally based on the breadth of the spinning sideband pattern.[133,139] Relatively isolated molecular water gives a broad spinning sideband envelope, approximating a Pake doublet, whereas relatively isolated hydroxyl groups give smaller sideband patterns. Using this method, the speciation of trace amounts of H could be determined in natural, nominally anhydrous feldspar minerals,[146] at H-concentrations as low as 40 ppm (as H_2O). Microcline (Al,Si ordered $KAlSi_3O_8$) gives broad ^{1}H

spinning sideband envelopes, corresponding to about 1000–1400 ppm of quasi-isolated water molecules, whereas sanidine (Si,Al disordered $KAlSi_3O_8$, from higher crystallization temperatures) and plagioclase feldspars were found to contain primarily structural hydroxyl (170–510 ppm). However, most of the H present in albite (Si,Al ordered $NaAlSi_3O_8$; 40–280 ppm H_2O) occurs in fluid inclusions, which gives a sharp ^1H MAS NMR peak near 4.7 ppm that broadens considerably with decreased temperature. In disordered phases in the alunite group ($MAl_3(SO_4)_2(OH)_2$; $M = Na^+$, K^+, H_3O^+), it was possible to distinguish and quantify ^1H signals of hydronium, Al-OH hydroxyl, and Al-OH_2 bound water.[129] Proton NMR spectra of opal and other poorly crystalline silica[147–149] contain signals for both molecular water and hydroxyls, presumably representing silanol groups.

The nominally anhydrous calcium carbonate minerals also contain measurable amounts of H, so ^1H NMR spectra of sedimentary and biogenic carbonates typically yield relatively strong signals for hydroxyl and molecular water.[150] However, for calcite precipitated at low temperatures, indirect ^{13}C-detected ^1H NMR spectra from $^{13}C\{^1H\}$ HETCOR experiments combined with detailed CP kinetics[151] show that the only H in close proximity to C occurs in hydrogen carbonate groups. The $^{13}C\{^1H\}$ HETCOR spectra contain only a single, narrow ^1H peak near 7 ppm, whereas the strongest peaks observed in single-pulse ^1H MAS spectra are absent, indicating that they correspond to H far from C. The variation in intensity of the $^{13}C\{^1H\}$ CPMAS spectra with contact time show an oscillation characteristic of an isolated $^{13}C-^1H$ spin pair. Fitting the CP oscillations yields a C–H distance of 1.9 Å, consistent with a hydrogen carbonate group. The ^1H chemical shift indicates a moderately strong hydrogen bond, having an O–O distance somewhat shorter than that of the bulk crystal structure, indicating structural relaxation near the hydrogen carbonate defect.

30.8 STRUCTURAL ENVIRONMENT OF OTHER MINOR COMPONENTS

Although most applications of NMR crystallography in geochemistry have focused on the atomic arrangement of major components, the more sensitive NMR nuclei can be utilized to gain information on the structural environment of minor or trace components as well. Such information can have important implications for trace-element systematics that are used in geochemistry to infer physicochemical conditions during crystallization. For example, the coordination of boron that occurs as an impurity in calcium carbonate minerals, was determined from single-pulse ^{11}B NMR data[152] of samples containing 59–600 ppm B, by making use of the observation that signals from B in trigonal (B[3]) and tetrahedral (B[4]) coordination to oxygen differ in both chemical shift and quadrupolar coupling.[153] Fractionation of the stable isotopes of boron impurities in calcite and aragonite had been shown to depend on the pH of the solution from which the carbonate mineral precipitated, although the chemical form and coordination of the B-containing defects was not known. The ^{11}B MAS NMR spectra of calcite are dominated by a broad quadrupolar powder pattern characteristic of trigonal B[3]. Fitting the spectra with a calculated quadrupolar powder pattern indicated the presence of an additional, small narrow peak typical for tetrahedral B[4], and that the trigonal B[3] accounted for 80–90% of B. However, both synthetic and coral skeletal aragonite contain only tetrahedral B[4]. Transformation of coral aragonite to calcite by heating in air at 450–500 °C results in a change in the B coordination from tetrahedral to predominantly trigonal. This change and the observation of different coordination states in aragonite and calcite suggest that the boron occurs as a defect in the $CaCO_3$ mineral structure, and not in fluid inclusions or as a trace B-rich phase.

NMR spectroscopy has also proven useful for constraining the possible mechanisms for carbonate substitution in apatite-group minerals. Sedimentary apatite typically contains a significant amount of carbonate, and carbonate-rich fluorapatite is a principal sink for phosphorus in marine sediments. The structural environment and charge-balancing mechanisms for carbonate substitution in apatite are not fully understood, although it is known that carbonate can occur in the channels parallel to *c* ("A-type"), at a phosphate site ("B-type"), or both together ("AB" type). The A-type and B-type carbonates exhibit distinct ^{13}C chemical shifts, which can be resolved and quantified in ^{13}C NMR spectra.[154] The bulk chemistry of natural carbonate-rich fluorapatite is complex (nominally, $Ca_5(PO_4)_3F$, with typically 0.4–0.9 carbonate ion per formula unit) but appear to indicate that carbonate and fluoride content are positively correlated (e.g., $Ca_5(PO_4)_{3-x}(CO_3)_xF_{1+0.4x}$), which has been proposed as evidence for substitution of a

tetrahedral "CO_3F^{3-}" species at the phosphate site in apatite. However, ^{13}C NMR data were shown to be inconsistent with such short C–F distances.[155] Static spin-echo ^{13}C spectra of both natural and synthetic carbonate-rich fluorapatite having 0.12–0.6 carbonate per formula unit (5 Ca) show an axially symmetric CSA powder pattern very similar to that obtained for $BaCO_3$ and consistent with a planar trigonal carbonate ion. In addition, the ^{13}C chemical shifts obtained from MAS spectra are very similar to those of crystalline carbonates. Calculations of powder patterns incorporating a carbonate-like CSA with ^{13}C–^{19}F dipolar coupling corresponding to C–F bond distances of 1.38 and 2.0 Å differ substantially from the experimental spectra. Only at C–F distances approaching 3 Å did the effect of ^{19}F dipolar coupling on the ^{13}C powder pattern become small, indicating relatively weak C–F coupling and absence of tetrahedral "CO_3F^{3-}" complexes.

For carbonate-rich hydroxylapatite, NMR results indicate that several types of substitution mechanisms can occur in the same sample. Analyses indicate substantial amounts of Na in the sample, while observation of a strong $^{23}Na\{^{31}P\}$ REDOR effect[156] showed that the Na is incorporated into the apatite structure, suggesting that it plays a role in a coupled carbonate substitution. In addition, the presence of hydrogen carbonate groups was inferred from two-dimensional $^{13}C\{^1H\}$ HETCOR data. These spectra show the presence of two distinct ^1H NMR peaks, at 5.5 and 1.3 ppm, in addition to the main hydroxyl resonance. HETCOR data taken at a variety of contact times showed a rapid buildup of cross-peak intensity for these two extra ^1H peaks, indicating short C–H distances consistent with protonated carbonate. The ^{13}C NMR peaks for both A-type and B-type carbonate show a common cross-peak for a minor ^1H resonance at 1.3 ppm, providing evidence for a coupled substitution of carbonate into both channel and phosphate sites (e.g., $2(CO_3^{2-}) = PO_4^{3-} + OH^-$).

30.9 POTENTIAL FUTURE APPLICATIONS

In future, NMR crystallography is likely to continue to play an important role in geochemistry, especially for light elements that remain difficult subjects for the elementally specific X-ray spectroscopies (principally, those with atomic numbers of P and lower). The most successful and widespread of the applications described above focus on systems amenable to detailed and quantitative interpretation of conventional, principally one-dimensional, experiments. These applications take advantage of the good resolution of resonances that can be assigned on the basis of careful correlations with model compounds and/or spectral changes with chemical composition. The use of the more basic double-resonance and indirect detection methods, such as HETCOR, REDOR, and TRAPDOR, has generally lagged that in other disciplines, but is likely to expand and, with it, the types of geochemical system from which crystallographic information can be obtained by NMR. CPMAS has of course been used to some effect in this context, but mostly in a qualitative manner, for example, whether a resonance corresponds to an atom "close to" or "far from" H, and often without consideration of CP kinetics and spin diffusion in detail. The information from two-dimensional correlation and double-resonance experiments (for example, whether resolved pairs of resonances correspond to species in close spatial proximity) can be used to assign peaks in ambiguous situations, establish the nature of local structural configurations at substitution sites, and even determine whether a species occurs in the phase of interest or as an impurity phase. This type of information and associated spectral editing are exceptionally useful in the heterogeneous, disordered, and chemically and structurally complex materials that are of primary interest in geochemistry. Investigation of hydrogen environments by NMR spectroscopy is also likely to expand with improvements in resolution and specificity available from a combination of ultrafast spinning rates (40–60 kHz), indirect detection, and heteronuclear and homonuclear correlation methods. With these techniques, useful crystallographic information can be obtained even in the presence of ^1H NMR signals from matrix effects, such as grain boundary defects, fluid inclusions, hydroxylated surfaces, and adsorbed surface water. Additional future development is also expected to result in obtaining useful crystallographic information from more difficult nuclei of geochemically important elements. For example, improved detection schemes have been developed for nuclides with very large chemical shift anisotropy, such as ^{207}Pb, and a combination of very high magnetic fields with sensitivity and resolution-enhancement schemes should improve prospects for quadrupolar nuclei such as ^{43}Ca,[157,158] ^{25}Mg,[116,159–161] ^{39}K,[162,163] and ^{87}Sr.[164,165] Finally,

recent success in obtaining solid-state NMR spectra for probe nuclei (e.g., ^{6,7}Li, ^{2}H) in Fe-rich materials such as goethite[166–168] and jarosite,[169] along with development of models for understanding hyperfine shifts,[170] may lead to more widespread applications of NMR crystallography to paramagnetic Fe- and Mn-bearing minerals that are important constituents of many geochemical systems.

REFERENCES

1. B. L. Phillips, in *Transformation Processes in Minerals*, eds S. A. T. Redfern and M. A. Carpenter, Reviews in Mineralogy & Geochemistry, Mineralogical Society of America, Washington, DC, 2000, Vol. **39**, p 203.
2. J. F. Stebbins, in *Mineral Physics and Crystallography. A Handbook of Physical Constants*, ed. T. J. Ahrens, AGU Reference Shelf, American Geophysical Union, Washington, DC, 1995, Vol. **2**, p 303.
3. C. M. Preston, *Soil Sci.*, 1996, **161**, 144.
4. P. G. Hatcher, K. J. Dria, S. Kim, and S. W. Frazier, *Soil Sci.*, 2001, **166**, 770.
5. L. A. Cardoza, A. K. Korir, W. H. Otto, C. J. Wurrey, and C. K. Larive, *Prog. Nucl. Mag. Reson. Spectr.*, 2004, **45**, 209.
6. P. N. Nelson and J. A. Baldock, *Biogeochemistry*, 2005, **72**, 1.
7. J. D. Mao, L. Tremblay, J. P. Gagne, S. Kohl, J. Rice, and K. Schmidt-Rohr, *Geochim. Cosmochim. Acta*, 2007, **71**, 5483.
8. B. J. Cade-Menun, *Talanta*, 2005, **66**, 359.
9. R. Lookman, P. Grobet, R. Merckx, and W. H. Van Riemsdijk, *Geoderma*, 1997, **80**, 369.
10. J. F. Stebbins, in *Structure, Dynamics, and Properties of Silicate Melts*, eds J. F. Stebbins, P. F. McMillan, and D. B. Dingwell, Reviews in Mineralogy, Mineralogical Society of America, Washington, DC, 1995, Vol. **32**, 191.
11. J. F. Stebbins, in *Solid State NMR: Principles and Applications*, ed. M. Duer, Blackwell Scientific: Oxford, 2001, p 391.
12. J. F. Stebbins, J. V. Oglesby, and S. K. Lee, *Chem. Geol.*, 2001, **174**, 63.
13. S. Kohn, in *Spectroscopic Methods in Mineralogy*, eds A. Beran and E. Libowitzky, *EMU Notes in Mineralogy*, European Mineralogical Union, 2004, Vol. **6**, p 399.
14. W. H. Casey, *Chem. Rev.*, 2006, **106**, 1.
15. Z. R. Hinedi, S. Goldberg, A. C. Chang, and J. P. Yesinowski, *J. Colloid Interface Sci.*, 1992, **152**, 141.
16. Y. Kim and R. J. Kirkpatrick, *Geochim. Cosmochim. Acta*, 1997, **61**, 5199.
17. J. P. Nordin, D. J. Sullivan, B. L. Phillips, and W. H. Casey, *Geochim. Cosmochim. Acta*, 1999, **63**, 3513.
18. T. J. Van Emmerik, D. E. Sandstrom, O. N. Antzutkin, M. J. Angove, and B. B. Johnson, *Langmuir*, 2007, **23**, 3205.
19. C. A. Weiss, R. J. Kirkpatrick, and S. P. Altaner, *Geochim. Cosmochim. Acta*, 1990, **54**, 1655.
20. Y. Kim, R. J. Kirkpatrick, and R. T. Cygan, *Geochim. Cosmochim. Acta*, 1996, **60**, 4059.
21. X. Q. Hou, R. J. Kirkpatrick, P. Yu, D. Moore, and Y. Kim, *Am. Mineral.*, 2000, **85**, 173.
22. J. F. Stebbins, I. Farnan, E. H. Williams, and J. Roux, *Phys. Chem. Min.*, 1989, **16**, 763.
23. H. Maekawa, S. Kato, K. Kawamura, and T. Yokokawa, *Am. Mineral.*, 1997, **82**, 1125.
24. M. Mookherjee, M. D. Welch, L. Le Polles, S. A. T. Redfern, and D. E. Harlov, *Phys. Chem. Min.*, 2005, **32**, 126.
25. E. Lippmaa, M. Magi, A. Samoson, G. Engelhardt, and A. R. Grimmer, *J. Am. Chem. Soc.*, 1980, **102**, 4889.
26. R. J. Kirkpatrick, R. A. Kinsey, K. A. Smith, D. M. Henderson, and E. Oldfield, *Am. Mineral.*, 1985, **70**, 106.
27. B. L. Sherriff and J. S. Hartman, *Can. Mineral.*, 1985, **23**, 205.
28. Z. Xu and J. F. Stebbins, *Solid State NMR*, 1998, **11**, 243.
29. J. F. Stebbins, P. D. Zhao, S. K. Lee, and X. Cheng, *Am. Mineral.*, 1999, **84**, 1680.
30. J. B. Murdoch, J. F. Stebbins, I. S. E. Carmichael, and A. Pines, *Phys. Chem. Min.*, 1988, **15**, 370.
31. B. L. Phillips and R. J. Kirkpatrick, *Am. Mineral.*, 1994, **79**, 1025.
32. D. K. Teertstra, B. L. Sherriff, Z. Xu, and P. Cerny, *Can. Mineral.*, 1994, **32**, 69.
33. S. C. Kohn, C. M. B. Henderson, and R. Dupree, *Am. Mineral.*, 1995, **80**, 705.
34. P. S. Neuhoff, J. F. Stebbins, and D. K. Bird, *Am. Mineral.*, 2003, **88**, 410.

35. X. Cheng, P. D. Zhao, and J. F. Stebbins, *Am. Mineral.*, 2000, **85**, 1030.
36. P. Zhao, P. S. Neuhoff, and J. F. Stebbins, *Chem. Phys. Lett.*, 2001, **344**, 325.
37. C. P. Herrero, *Chem. Phys. Lett.*, 1990, **171**, 369.
38. P. S. Neuhoff and L. S. Ruhl, *Chem. Geol.*, 2006, **225**, 373.
39. I. W. M. Brown, C. M. Cardile, K. J. D. Mackenzie, M. J. Ryan, and R. H. Meinhold, *Phys. Chem. Min.*, 1987, **15**, 78.
40. B. L. Phillips, R. J. Kirkpatrick, and A. Putnis, *Phys. Chem. Min.*, 1989, **16**, 591.
41. S. C. Kohn, C. M. B. Henderson, and R. Dupree, *Am. Mineral.*, 1997, **82**, 1133.
42. D. E. Akporiaye, I. M. Dahl, H. B. Mostad, and R. Wendelbo, *J. Phys. Chem.*, 1996, **100**, 4148.
43. B. L. Sherriff, H. D. Grundy, and J. S. Hartman, *Eur. J. Mineral.*, 1991, **3**, 751.
44. B. L. Phillips, H. W. Xu, P. J. Heaney, and A. Navrotsky, *Am. Mineral.*, 2000, **85**, 181.
45. W. H. Yang, R. J. Kirkpatrick, and D. M. Henderson, *Am. Mineral.*, 1986, **71**, 712.
46. Y. Xiao, R. J. Kirkpatrick, R. L. Hay, Y. J. Kim, and B. L. Phillips, *Mineral. Mag.*, 1995, **59**, 47.
47. H. Zhu, R. C. Newton, and O. J. Kleppa, *Am. Mineral.*, 1994, **79**, 134.
48. B. L. Phillips, R. J. Kirkpatrick, and M. A. Carpenter, *Am. Mineral.*, 1992, **77**, 484.
49. B. L. Phillips, M. D. McGuinn, and S. A. T. Redfern, *Am. Mineral.*, 1997, **82**, 1.
50. R. J. Kirkpatrick, M. A. Carpenter, W. H. Yang, and B. Montez, *Nature*, 1987, **325**, 236.
51. C. A. Fyfe, G. C. Gobbi, J. Klinowski, A. Putnis, and J. M. Thomas, *J. Chem. Soc. Chem. Commun.*, 1983, 556.
52. A. Holscher and W. Schreyer, *Eur. J. Mineral.*, 1989, **1**, 21.
53. A. Putnis and R. J. Angel, *Phys. Chem. Min.*, 1985, **12**, 217.
54. M. T. Dove and V. Heine, *Am. Mineral.*, 1996, **81**, 39.
55. T. Armbruster, *Am. Mineral.*, 1999, **84**, 92.
56. E. Lippmaa, M. Magi, A. Samoson, M. Tarmak, and G. Engelhardt, *J. Am. Chem. Soc.*, 1981, **103**, 4992.
57. P. S. Neuhoff, S. Kroeker, L. S. Du, T. Fridriksson, and J. F. Stebbins, *Am. Mineral.*, 2002, **87**, 1307.
58. P. F. Barron, R. L. Frost, J. O. Skjemstad, and A. J. Koppi, *Nature*, 1983, **302**, 49.
59. S. Hayashi, T. Ueda, K. Hayamizu, and E. Akiba, *J. Phys. Chem.*, 1992, **96**, 10922.
60. M. Lipsicas, R. H. Raythatha, T. J. Pinnavaia, I. D. Johnson, R. F. Giese, P. M. Costanzo, and J. L. Robert, *Nature*, 1984, **309**, 604.
61. D. Plee, F. Borg, L. Gatineau, and J. J. Fripiat, *J. Am. Chem. Soc.*, 1985, **107**, 2362.
62. J. Sanz and J. M. Serratosa, *J. Am. Chem. Soc.*, 1984, **106**, 4790.
63. P. F. Barron, P. Slade, and R. L. Frost, *J. Phys. Chem.*, 1985, **89**, 3880.
64. S. Circone, A. Navrotsky, R. J. Kirkpatrick, and C. M. Graham, *Am. Mineral*, 1991, **76**, 1485.
65. M. D. Welch, J. Barras, and J. Klinowski, *Am. Mineral.*, 1995, **80**, 441.
66. H. J. Jakobsen, N. C. Nielsen, and H. Lindgreen, *Am. Mineral.*, 1995, **80**, 247.
67. D. L. Carroll, T. F. Kemp, T. J. Bastow, and M. E. Smith, *Solid State NMR*, 2005, **28**, 31.
68. S. K. Lee, J. F. Stebbins, C. A. Weiss, and R. J. Kirkpatrick, *Chem. Mat.*, 2003, **15**, 2605.
69. S. K. Lee and C. A. Weiss, *Am. Mineral.*, 2008, **93**, 1066.
70. R. A. Kinsey, R. J. Kirkpatrick, J. Hower, K. A. Smith, and E. Oldfield, *Am. Mineral*, 1985, **70**, 537.
71. C. P. Herrero, J. Sanz, and J. M. Serratosa, *J. Phys. C*, 1985, **18**, 13.
72. J. Sanz, C. P. Herrero, and J. L. Robert, *J. Phys. Chem. B*, 2003, **107**, 8337.
73. C. P. Herrero, M. Gregorkiewitz, J. Sanz, and J. M. Serratosa, *Phys. Chem. Min.*, 1987, **15**, 84.
74. C. P. Herrero, J. Sanz, and J. M. Serratosa, *J. Phys. Chem.*, 1989, **93**, 4311.
75. S. K. Lausen, H. Lindgreen, H. J. Jakobsen, and N. C. Nielsen, *Am. Mineral.*, 1999, **84**, 1433.
76. M. Fechtelkord, H. Behrens, F. Holtz, C. A. Fyfe, L. A. Groat, and M. Raudsepp, *Am. Mineral.*, 2003, **88**, 47.
77. C. P. Herrero and J. Sanz, *J. Phys. Chem. Solids*, 1991, **52**, 1129.
78. V. L. Vinograd and A. Putnis, *Phys. Chem. Min.*, 1998, **26**, 135.

79. M. C. Warren, M. T. Dove, E. R. Myers, A. Bosenick, E. J. Palin, C. I. Sainz-Diaz, B. S. Guiton, and S. A. T. Redfern, *Mineral. Mag.*, 2001, **65**, 221.
80. E. J. Palin, M. T. Dove, S. A. T. Redfern, A. Bosenick, C. I. Sainz-Diaz, and M. C. Warren, *Phys. Chem. Min.*, 2001, **28**, 534.
81. V. L. Vinograd, *Phys. Chem. Min.*, 1995, **22**, 87.
82. K. A. Smith, R. J. Kirkpatrick, E. Oldfield, and D. M. Henderson, *Am. Mineral.*, 1983, **68**, 1206.
83. M. Raudsepp, A. C. Turnock, F. C. Hawthorne, B. L. Sherriff, and J. S. Hartman, *Am. Mineral.*, 1987, **72**, 580.
84. M. D. Welch, S. X. Liu, and J. Klinowski, *Am. Mineral.*, 1998, **83**, 85.
85. D. M. Jenkins, B. L. Sherriff, J. Cramer, and Z. Xu, *Am. Mineral.*, 1997, **82**, 280.
86. R. L. Flemming and R. W. Luth, *Am. Mineral.*, 2002, **87**, 25.
87. J. F. Stebbins, C. W. Burnham, and D. L. Bish, *Am. Mineral.*, 1993, **78**, 461.
88. D. E. Woessner, *Am. Mineral.*, 1989, **74**, 203.
89. F. Martin, E. Ferrage, S. Petit, P. de Parseval, L. Delmotte, J. Ferret, D. Arseguel, and S. Salv, *Eur. J. Mineral.*, 2006, **18**, 641.
90. R. Badreddine, D. Vandormael, A. M. Fransolet, G. J. Long, W. E. E. Stone, and F. Grandjean, *Clay Min.*, 2002, **37**, 367.
91. F. Martin, P. Micoud, L. Delmotte, C. Marichal, R. Le Dred, P. De Parseval, A. Mari, J. P. Fortune, S. Salvi, D. Beziat, O. Grauby, and J. Ferret, *Can. Mineral.*, 1999, **37**, 997.
92. J. Cuadros, C. I. Sainz-Diaz, R. Ramirez, and A. Hernandez-Laguna, *Am. J. Sci.*, 1999, **299**, 289.
93. I. Tkac, P. Komadel, and D. Muller, *Clay Min.*, 1994, **29**, 11.
94. R. H. Newman, C. W. Childs, and G. J. Churchman, *Clay Min.*, 1994, **29**, 305.
95. N. Guven, J.-B. d'Espinose de la Caillerie, and J. J. Fripiat, *Clays Clay Min.*, 1992, **40**, 457.
96. S. Lantenois, R. Champallier, J. M. Beny, and F. Muller, *Appl. Clay Sci.*, 2008, **38**, 165.
97. L. Delevoye, J. L. Robert, and J. Grandjean, *Clay Min.*, 2003, **38**, 63.
98. M. Fechtelkord, H. Behrens, F. Holtz, J. L. Bretherton, C. A. Fyfe, L. A. Groat, and M. Raudsepp, *Am. Mineral.*, 2003, **88**, 1046.
99. S. C. Kohn, B. M. Roome, M. E. Smith, and A. P. Howes, *Earth Planet. Sci. Lett.*, 2005, **238**, 342.
100. R. L. Millard, R. C. Peterson, and B. K. Hunter, *Am. Mineral.*, 1992, **77**, 44.
101. P. McMillan, M. Akaogi, E. Ohtani, Q. Williams, R. Nieman, and R. Sato, *Phys. Chem. Min.*, 1989, **16**, 428.
102. B. L. Phillips, D. A. Howell, R. J. Kirkpatrick, and T. Gasparik, *Am. Mineral.*, 1992, **77**, 704.
103. J. J. Fitzgerald, S. F. Dec, and A. I. Hamza, *Am. Mineral.*, 1989, **74**, 1405.
104. C. W. Childs, S. Hayashi, and R. H. Newman, *Clays Clay Min.*, 1999, **47**, 64.
105. G. Furrer, B. L. Phillips, K. U. Ulrich, R. Pothig, and W. H. Casey, *Science*, 2002, **297**, 2245.
106. B. L. Phillips, F. M. Allen, and R. J. Kirkpatrick, *Am. Mineral.*, 1987, **72**, 1190.
107. J. F. Stebbins, S. Kroeker, and D. Andrault, *Geophys. Res. Lett.*, 2001, **28**, 615.
108. J. F. Stebbins, H. Kojitani, M. Akaogi, and A. Navrotsky, *Am. Mineral.*, 2003, **88**, 1161.
109. J. F. Stebbins, L. S. Du, K. Kelsey, H. Kojitani, M. Akaogi, and S. Ono, *Am. Mineral.*, 2006, **91**, 337.
110. J. F. Stebbins, I. Farnan, and U. Klabunde, *J. Am. Ceram. Soc.*, 1989, **72**, 2198.
111. L. Huve, L. Delmotte, P. Martin, R. Ledred, J. Baron, and D. Saehr, *Clays Clay Min.*, 1992, **40**, 186.
112. A. Labouriau, Y. W. Kim, S. Chipera, D. L. Bish, and W. L. Earl, *Clays Clay Min.*, 1995, **43**, 697.
113. L. A. Groat, B. C. Chakoumakos, D. H. Brouwer, C. M. Hoffman, C. A. Fyfe, H. Morell, and A. J. Schultz, *Am. Mineral.*, 2003, **88**, 195.
114. B. Zhou, B. L. Sherriff, and F. Taulelle, *Can. Mineral.*, 2003, **41**, 891.
115. F. M. McCubbin, H. E. Mason, H. Park, B. L. Phillips, J. B. Parise, H. Nekvasil, and D. H. Lindsley, *Am. Mineral.*, 2008, **93**, 210.
116. P. J. Sideris, U. G. Nielsen, Z. H. Gan, and C. P. Grey, *Science*, 2008, **321**, 113.
117. M. D. Welch, W. Kolodziejski, and J. Klinowski, *Am. Mineral.*, 1994, **79**, 261.
118. F. C. Hawthorne, M. D. Welch, G. Della Ventura, S. X. Liu, J. L. Robert, and D. M. Jenkins, *Am. Mineral.*, 2000, **85**, 1716.
119. P. A. Schroeder, *Clays Clay Min.*, 1993, **41**, 668.

120. K. E. Kelsey, J. F. Stebbins, L. S. Du, J. L. Mosenfelder, P. D. Asimow, and C. A. Geiger, *Am. Mineral.*, 2008, **93**, 134.
121. A. Bosenick, C. A. Geiger, T. Schaller, and A. Sebald, *Am. Mineral.*, 1995, **80**, 691.
122. A. Bosenick, C. A. Geiger, and B. L. Phillips, *Am. Mineral.*, 1999, **84**, 1422.
123. A. Bosenick, M. T. Dove, and C. A. Geiger, *Phys. Chem. Min.*, 2000, **27**, 398.
124. C. L. Freeman, N. L. Allan, and W. van Westrenen, *Phys. Rev. B*, 2006, **74**.
125. V. L. Vinograd and M. H. F. Sluiter, *Am. Mineral.*, 2006, **91**, 1815.
126. S. C. Kohn, *Am. Mineral.*, 1996, **81**, 1523.
127. M. D. Welch, A. R. Pawley, S. E. Ashbrook, H. E. Mason, and B. L. Phillips, *Am. Mineral.*, 2006, **91**, 1707.
128. B. L. Phillips, H. E. Mason, and S. Guggenheim, *Am. Mineral.*, 2007, **92**, 1474.
129. U. G. Nielsen, J. Majzlan, B. Phillips, M. Ziliox, and C. P. Grey, *Am. Mineral.*, 2007, **92**, 587.
130. F. Brunet and T. Schaller, *Am. Mineral.*, 1996, **81**, 385.
131. B. Berglund and R. W. Vaughan, *J. Chem. Phys.*, 1980, **73**, 2037.
132. J. P. Yesinowski and H. Eckert, *J. Am. Chem. Soc.*, 1987, **109**, 6274.
133. H. Eckert, J. P. Yesinowski, L. A. Silver, and E. M. Stolper, *J. Phys. Chem.*, 1988, **92**, 2055.
134. E. Brunner and U. Sternberg, *Prog. Nucl. Magn. Reson. Spectrosc.*, 1998, **32**, 21.
135. X. Xue and M. Kanzaki, *J. Phys. Chem. B*, 2007, **111**, 13156.
136. E. A. Johnson and G. R. Rossman, *Phys. Chem. Min.*, 2004, **31**, 115.
137. G. G. Almond, R. K. Harris, and P. Graham, *J. Chem. Soc. Chem. Comm.*, 1994, 851.
138. A. Sebald, L. H. Merwin, W. A. Dollase, and F. Seifert, *Phys. Chem. Min.*, 1990, **17**, 9.
139. J. P. Yesinowski, H. Eckert, and G. R. Rossman, *J. Am. Chem. Soc.*, 1988, **110**, 1367.
140. F. Camara, R. Oberti, G. Della Ventura, M. D. Welch, and W. V. Maresch, *Am. Mineral.*, 2004, **89**, 1464.
141. S. C. Kohn, R. A. Brooker, D. J. Frost, A. E. Slesinger, and B. J. Wood, *Am. Mineral.*, 2002, **87**, 293.
142. X. Y. Xue, M. Kanzak, and A. Shatskiy, *Am. Mineral.*, 2008, **93**, 1099.
143. B. L. Phillips, P. C. Burnley, K. Worminghaus, and A. Navrotsky, *Phys. Chem. Min.*, 1997, **24**, 179.
144. H. Kagi, J. B. Parise, H. Cho, G. R. Rossman, and J. S. Loveday, *Phys. Chem. Min.*, 2000, **27**, 225.
145. H. Cho and G. R. Rossman, *Am. Mineral.*, 1993, **78**, 1149.
146. E. A. Johnson and G. R. Rossman, *Am. Mineral.*, 2003, **88**, 901.
147. H. Graetsch, I. Topalovic, and H. Gies, *Eur. J. Mineral.*, 1994, **6**, 459.
148. H. Graetsch and I. Topalovic-Dierdorf, *Chem. Erde Geochem.*, 1996, **56**, 387.
149. M. Paris, E. Fritsch, and B. O. A. Reyes, *J. Non-Cryst. Solids*, 2007, **353**, 1650.
150. S. J. Gaffey, *Am. Mineral.*, 1995, **80**, 947.
151. J. Feng, Y. J. Lee, R. J. Reeder, and B. L. Phillips, *Am. Mineral.*, 2006, **91**, 957.
152. S. Sen, J. F. Stebbins, N. G. Hemming, and B. Ghosh, *Am. Mineral.*, 1994, **79**, 819.
153. G. L. Turner, K. A. Smith, R. J. Kirkpatrick, and E. Oldfield, *J. Magn. Reson.*, 1986, **67**, 544.
154. K. Beshah, C. Rey, M. J. Glimcher, M. Schimizu, and R. G. Griffin, *J. Solid State Chem.*, 1990, **84**, 71.
155. P. Regnier, A. C. Lasaga, R. A. Berner, O. H. Han, and K. W. Zilm, *Am. Mineral.*, 1994, **79**, 809.
156. H. E. Mason, A. Kozlowski, and B. L. Phillips, *Chem. Mater.*, 2008, **20**, 294.
157. D. L. Bryce, E. B. Bultz, and D. Aebi, *J. Am. Chem. Soc.*, 2008, **130**, 9282.
158. D. Laurencin, A. Wong, J. V. Hanna, R. Dupree, and M. E. Smith, *J. Am. Chem. Soc.*, 2008, **130**, 2412.
159. K. Shimoda, Y. Tobu, M. Hatakeyama, T. Nemoto, and K. Saito, *Am. Mineral.*, 2007, **92**, 695.
160. N. G. Dowell, S. E. Ashbrook, and S. Wimperis, *J. Phys. Chem. B*, 2004, **108**, 13292.
161. S. Kroeker and J. F. Stebbins, *Am. Mineral.*, 2000, **85**, 1459.
162. F. H. Larsen, J. Skibsted, H. J. Jakobsen, and N. C. Nielsen, *J. Am. Chem. Soc.*, 2000, **122**, 7080.
163. I. L. Moudrakovski and J. A. Ripmeester, *J. Phys. Chem. B*, 2007, **111**, 491.

164. G. M. Bowers, A. S. Lipton, and K. T. Mueller, *Solid State NMR*, 2006, **29**, 95.

165. G. M. Bowers, R. Ravella, S. Komarneni, and K. T. Mueller, *J. Phys. Chem. B*, 2006, **110**, 7159.

166. K. E. Cole, Y. Paik, R. J. Reeder, M. Schoonen, and C. P. Grey, *J. Phys. Chem. B*, 2004, **108**, 6938.

167. U. G. Nielsen, Y. Paik, K. Julmis, M. A. A. Schoonen, R. J. Reeder, and C. P. Grey, *J. Phys. Chem. B*, 2005, **109**, 18310.

168. J. Kim, U. G. Nielsen, and C. P. Grey, *J. Am. Chem. Soc.*, 2008, **130**, 1285.

169. U. G. Nielsen, J. Majzlan, and C. P. Grey, *Chem. Mat.*, 2008, **20**, 2234.

170. Y. Paik, J. P. Osegovic, F. Wang, W. Bowden, and C. P. Grey, *J. Am. Chem. Soc.*, 2001, **123**, 9367.

Index

2-D EXSY *see* Exchange spectroscopy
2-D FIREMAT *see* Five π replicated magic angle turning
2Q-HORROR *see* Double-quantum homonuclear rotary resonance
2QF-COSY *see* Uniform-sign cross-peak double quantum filtered correlation spectroscopy
3-D TEDOR *see* Transferred echo double resonance
3-D ZF-TEDOR *see* *Z*-filtered transferred echo double resonance (ZF-TEDOR)

AASBU *see* Automated assembly of secondary building units
Ab-initio calculations
  chemical shifts 81–97
  inorganic/materials chemistry 458–460
  intermolecular interactions 315–317
  magnetic shielding 56–58
  organic molecules 286
  spin diffusion 198–199
ABMS *see* Anisotropy of the bulk magnetic susceptibility
Absolute orientation, space groups 254–255
Absorption, xenon in calixarenes, combined studies 271–273
Abundant spin-1/2 nuclei, fast dynamics 382
Accuracy 87, 261
Acetone, *tert*-butylcalix[4]arene inclusion 362
ADF *see* Amsterdam Density Function
AHT *see* Average Hamiltonian theory
Alkane carbons 104
Aluminosilicates 266, 345–346, 465–471
Aluminum
  chemical shifts 256
  coordination in minerals 471–473
  geochemistry 464–473
  inorganic non-stoichiometric crystalline systems 343–346
  Lowenstein's avoidance principle 343, 345–346
Ambuic acid 118, 120
Amino acids
  assignment strategies 419–421
  bond lengths 102, 325
  dihedral angles 106
  dynamics 430–431
  side chain geometry 106, 423–426
Ammonium bromide, phase transitions 402–403
Ammonium cations 117
Ammonium hydrochloride, phase transitions 407–409
Amphiboles 470
Ampicillin 92–93
Amsterdam Density Function (ADF) package 57
Anderson and Weiss (A–W) approach 182–183, 189–190
Anions, geochemistry 463–465
Anisole 104–105
Anisotropic jump motions
  fast motion 181–182
  intermediate motions 182–183
Anisotropy 65–67
  concepts and conventions 65–67
  crystal structure 113–124
  fast processes 379
  gauge-including projector augmented wave modeling 92–93
  hydrogen bonding 116–118
  jump reorientation 182–183, 360
  powder patterns 72–74
  shielding 132–133
  structure refinement 259–260
Anisotropy of the bulk magnetic susceptibility (ABMS) 88
Antiferrodistortive phase transitions 389
Antiferroelectric-paraelectric phase transitions, squaric acid 392–393
Antiferroelectric phases
  potassium thiocyanate 396–398
  squaric acid 392
Antifluorite crystals 389–391
Apatite atomic ordering 351
Aperiodic structures 261
Aromatic carbons 102, 107–108, 379
Aromatic ring-currents 307–311
Aromatic π–π stacking 307–311
  nanostructures 311–312
Aspartame polymorphisms 441
Assignment strategies
  amino acids 419–421
  calculated chemical shifts 87–88
Asymmetric units 90–91, 256–257
  definition 65, 263
  structure determination 279

Asymmetry
  crystal structure 113–124
  gauge-including projector augmented wave modeling 92–93
  hydrogen bonding 116–118
  powder patterns 72–74
Asymmetry parameter
  anisotropic interactions 65–67
  long-range order 254
Atomic ordering
  aluminosilicates 345–346
  apatites 351
  clay minerals 346
  fluorite-structured oxides 350
  garnets 346–347
  inorganic non-stoichiometric crystalline systems 341–353
  mullites 346
  oxynitride solid solutions 351
  paramagnetic doping 343, 348–350
  Perovskites 351–352
  pyrochlores 347–348
  spinels 346–347
  Yttrium aluminum garnet 347
Autocorrelation functions 356
Automated assembly of secondary building units (AASBU) 257–258, 460
Averaged dipolar couplings 181–182
Average Hamiltonian theory (AHT)
  homonuclear dipolar recoupling 164–165
  rotary resonance recoupling 141–142
  rotational echo double resonance 145
  shift evolution assisted selective homonuclear recouplings 173
A–W *see* Anderson and Weiss

Bacteria, protein labeling 429
Bacteriorhodopsin (bR) 150–151
Basis set computation 82–83
Benzene 357
Bloch's theorem 30–31
Bloembergen–Purcell–Pound (BPP) theory 358
Bond angles 103
Bond lengths 255–256
  amino acids 325
  carbon 102
  chemical shifts 101–103
  combined studies 281
  heavy atoms 102
  indirect coupling 130–131
  inorganic/materials chemistry 456–458
  structure resolution 257
Bond stretching 102
BPP *see* Bloembergen–Purcell–Pound
bR *see* Bacteriorhodopsin
Bravais lattices 65
Brillouin zone computation 82–83
Bronchiolitis 252
tert-Butylcalix[4]arene (*t*-BC)
  host–guest complexes 269–271
    deuterium lineshapes 360–362
    pyridine inclusion 306–308, 361–362
    xenon absorption 271–273

Calcium clustering 476–477
Calcium hydroxyapatite 351
Calcium sulfate dihydrate (gypsum) 4
Calixarenes
  host–guest complexes 269–271
  pyridine inclusion 306–308, 361–362
  xenon absorption 271–273
Candidate structures 122
Carbamazepine 89
Carbohydrates 120
Carbon–carbon bonds 102
Carbon–hydrogen bonds 102
Carbon nanotubes (CNTs) 311–312
Carbons
  alkanes 104
  aromatic 102, 106–107, 117–118, 379
  carbonyl 100, 116–117, 323–325
  hydrogen positions 85
  methanol 11
  methyl benzenes 107
  spectrum temperature effects 379
Carbonyl carbons 100, 116–117, 323–325
Carbonyl groups 283
Carboxylic acid groups 100
  hydrogen bonding 116, 118, 334–336
Carr–Parrinello Molecular Dynamics (CPMD) code 58
Carr–Purcell–Meiboom–Gill (CPMG) experiment 129
Cartesian tensors 19–20, 22
CASTEP code
  GIPAW 87
  intermolecular interactions 315–317
  quadrupolar coupling 225
Cations, geochemistry 471–473, 475–477
Centreband only detection of exchange experiment (CODEX) 384
Chemical equivalence 64
Chemical exchange 379–380
Chemical shift anisotropy (CSA)
  heteronuclear coupling and structure 290–291
  homonuclear coupling and structure 292–293
  homonuclear dipolar recoupling 164
  noninteger nuclei 370
  polymorphisms 445
  powdered solids 43, 44–46
  protein secondary structure 423
  Ramsey's theory 296
  reliability of calculations 46–49
  slow dynamics 384
Chemical shift-dependent dipolar recoupling 133–134
Chemical shifts
  see also Isotropic chemical shifts
  aluminum 256
  amino acids 325
  ammonium cations 117
  anisotropy 113–124
  asymmetry 113–124
  bond angles 103

bond lengths 101–103, 325
bond stretching 102
carbonyl carbons 116–117
carboxylic acid groups 116
computation 81–97
delta-function pulse recoupling 169–170
dihedral angles 103–106
direct structural encoding 115–118
γ-effect 103–104
electrostatic field effects 115–116
experimental results, versus computation 87
gauge-including projector augmented wave models 81–97
Hamiltonians 23
heterocyclic aromatic compounds, hydrogen bonding 117–118
homonuclear dipolar recoupling 168–170
hydrogen bonding 95–96, 116–118, 321–326
hydrogen in organic structures 322–323
hydrogen tensors 117
hydroxy hydrogens 119
magnesium/calcium clustering 476–477
magnetic shielding 53–61
molecular-level structure 99–111
nitrogen in hydrogen bonding 117, 325
organic crystalline structures 321–326
oxygen atoms 83
protonation 100
Ramachandran angles 106
selectivity and evolution periods 172–173
silicon with magnesium/calcium clustering 476–477
spherical tensors 23
steric crowding 106–108
structural phase transitions 392
structure refinement 259
tautomers 100–101
tensors 7, 23, 92–93, 113–114, 117
uracil 324
CHHC *see* Proton spin-diffusion with carbon detection
Chiolite 259–261
Chirality 436–439
deuterium lineshapes 363
site symmetry determination 254–255
Cholesteryl acetate 219
CIS *see* Complexation-induced shifts
Clay minerals 346, 469–470
Cluster models of shielding 57–58
CNS/XPLOR, protein folding 430
Cocrystal structure determination 279
CODEX *see* Centreband only detection of exchange experiment
Coherent scattering 264
Combined rotation and multiple-pulse spectroscopy (CRAMPS) 210
dipolar dephasing 359
geochemistry 479
homonuclear dipolar couplings, hydrogen bonding 329–330
hydrogen bonding
carboxylic acid groups 336
homonuclear dipolar couplings 329–330
polymorphs 312–315
structural biology 429
zeolite host–guest interactions 306–307
Commutation properties 74–77
Complexation-induced shifts (CIS) 307
Complimentary studies 263–274, 362–366, 448–450
Conformational information 8–16
Connectivity
fundamental principles 255–256
indirect coupling 209–222
Constant time (CT) recoupling
symmetry-based, homonuclear dipolar recoupling 171
3-D transferred echo double resonance 156
Continuous gauge transformation (CSGT) 56
Continuous radiofrequency recoupling 166–168
Coordination
aluminum 471–473
quadrupolar coupling 234–235
Core states
Lamb formula 34
periodic systems 34–36
Correlation spectroscopy (COSY) 209, 210–215
zeolite host–guest interactions 306
Cortisone acetate 10, 14, 283
COSY *see* Correlation spectroscopy
2QF-COSY *see* Uniform-sign cross-peak double quantum filtered correlation spectroscopy
Coulomb gauge 55–56
Coupling interactions 125–241
dipolar 127, 129–131
indirect 129
Covalent bonding 256
CPMAS *see* Cross-polarization with magic angle spinning
CPMD *see* Carr–Parrinello Molecular Dynamics
CPMG *see* Carr–Purcell–Meiboom–Gill
CRAMPS *see* Combined rotation and multiple-pulse spectroscopy
Critical values, displacive phase transitions 405–406
Cross-polarization (CP)
dipolar coupling 183–190
dipolar dephasing 359
indirect coupling 209–222
zeolite host–guest interactions 306–307
Cross-polarization with magic angle spinning (CPMAS)
concepts 8
mineral substitutions 474–475, 478
principles 248
stereochemistry 437–438
18-Crown-6 malonitrile complex 364
Crystalline organic solids
chemical exchange 379–380
intramolecular motion 375–386
motional averaging 378–379
Crystalline systems
atomic ordering 341–353
chemical shift computations 81–97
incredible natural abundance double-quantum transfer experiment 210–212
inorganic non-stoichiometric 341–353
long-range order 64–65
Lowenstein's aluminum avoidance principle 343, 345–346
organic

Crystalline systems (*continued*)
hydrogen bonding 321–339
chemical shifts 321–326
spin diffusion 195–207
spin systems and interactions 64–67
Crystallinity 3–4
Crystallochemical formula 251
Crystallographically equivalent, definition 292
Crystallographic space groups 65
Crystallographic splitting, α-testosterone 90–91
Crystallography
concepts 3–18
definition 3
fundamental principles 245–262
history 245–248
Crystal packing
chemical shift calculation 93–94
gauge-including projector augmented wave modelling 93–94
Crystal space groups
see also Space groups
absolute orientation 254–255
concepts 252–254
group/subgroup relationships 253–254
Crystal structure
see also Lattice structure
anisotropy 113–124
asymmetric unit 256–257
asymmetry 113–124
complete derivation 121–122
direct encoding 115–118
electrostatic field effects 115–116
fundamental principles 13–16, 245–262, 263–264
heteronuclear scalar couplings 216–217
hydrogen bonding 116–118, 119
indirect coupling 209–222
integrant units 256–257
polar effects 119
prediction 122
proton spin-diffusion 203–205
quadrupolar coupling 233–239
refinement 119–121
shift tensors 115–118
Crystal-structure determination
see also Structure determination
crystallochemical formula 251
dipolar coupling and magnetic shielding 289–293
double rotation 298
fundamental principles 245–262
inorganic/materials chemistry 456–460
inorganic non-stoichiometric systems 341–353
nuclear magnetic resonance versus X-ray diffraction 254
organic/pharmaceutical compounds 448–450
proton spin-diffusion 203–205
tensor interplay 289–301
CSA *see* Chemical shift anisotropy
CSGT *see* Continuous gauge transformation
CT *see* Constant time
Cubic symmetry
antifluorite crystals 389–391
magnetic shielding tensors, single crystals 68
quadrupolar coupling 234
Cubic to orthorhombic phase transitions 364–365
CUG *see* Cytosine-uracil-guanine
Cyclohexane 363
Cytosine-uracil-guanine (CUG) repeats 330–332

DARR *see* Dipolar-assisted rotational resonance
DAS *see* Dynamic angle spinning
DCNB *see* 1,4-Dicyanobenzene
Decoupling, interference 359
Decoupling using mind-boggling optimization (DUMBO)
heteronuclear scalar couplings 217
homonuclear dipolar coupling 329–330
hydrogen bonding 329–330
spin diffusion 197
Delta-function pulses
chemical shift dependent recoupling 169–170
homonuclear dipolar recoupling 165–166
Dempsey's rule, phyllosilicates 469–470
Density functional theory (DFT) 30
hydrogen chemical shifts 322–323
inorganic/materials chemistry 459
magnetic shielding 56–58
polymorphisms 315, 442, 445
quadrupolar coupling 225
Dephasing 359
Deshielding, definition 53
Desolvation 94–95
Deuterium lineshapes 359–366
protein folding dynamics 431
DFT *see* Density functional theory
Diamagnetic spin orbits (DSO), indirect coupling calculation 37
Diamagnetism 53–61
1,4-Dicyanobenzene (DCNB) 310–311
Differential scanning calorimetry (DSC) 180–181, 270–271
Diffraction refinement 119–121
Dihedral angles 103–106, 118–119, 121–122
Dilute spin-1/2 nuclei, fast dynamics 382
Dimethyl sulfoxide (DMSO) 316–317
Dipolar alphabet 132
Dipolar-assisted rotational resonance (DARR)
homonuclear dipolar recoupling 175
structural biology 419–420
Dipolar chemical shift correlation (DIPSHIFT)
molecular-level mobility 183–185, 189–190
pulse sequence 186
Dipolar coupling 127
amino acid side chain geometry 423–426
anisotropic shielding 132–133
characterization 131–134
chemical shift correlation 183–185, 189–190
concepts 7, 8, 12
conformational information 9–10
constant 127
dynamics 356–359
dynamic solid-state nuclear magnetic resonance 177–193

fast motion 181–182
Hamiltonians 23–24
heteronuclear 70, 183–190, 327–329
homonuclear 70, 183–190
hydrogen bonding 183–190, 327–334
indirect 333–334
Lee–Golberg cross-polarization 184–186, 189–190
magnetic shielding and structure 289–293
magnetic shielding tensors 70–72
molecular-level mobility 177–193
nitrogen–nitrogen 330–332
proton lineshape second moments 357
separated local field recoupling 183–190
spin-lattice relaxation 358–359
temperature dependence 179, 180–181
wideline spectra anomalies 43
Dipolar coupling with a windowless sequence (DRAWS) 137
Dipolar dephasing 359
Dipolar exchange nuclear magnetic resonance 191
Dipolar recoupling
heteronuclear 137–161
homonuclear 163–176
delta-function pulses 165–166
magic angle spinning 133–134
Dipolar recoupling enhanced by amplitude modulation (DREAM) 168
Dipolar recovery at the magic angle (DRAMA) 134
homonuclear dipolar recoupling 165–168
Dipolar-rotational spin echoes (DRSE) 183–190
DIPSHIFT *see* Dipolar chemical shift correlation
Direct coupling, Pake doublets 132–133
Direct dipolar coupling constant, definition 127
Direct dipolar coupling 66, 71–73
Direct encoding 115–118
Direct-space structure solutions 277–284
Disorder
combined studies 266, 270–271, 362–366
geochemistry 479–480
hydrogen bonding 479–480
organic/pharmaceutical compounds 445–448
sodalite topology 253
structure determination 281
through-bond correlations 213
Displacive phase transitions
antifluorite crystals 389–391
classification 388–391
critical values 405–406
dynamics 405–407
perovskites 405–407
sodium niobate 405–407
Distortion of the high temperature phase 388
DMSO *see* Dimethyl sulfoxide
Dopant ions 343
DOR *see* Double rotation
Double-quantum-coherence (DQC) 285
Double-quantum (DQ) correlation 211
hydrogen bonding 329–330
molecular level mobility 190–191
zeolite host–guest interactions 306
Double-quantum filtered magic angle spinning (DQF MAS) 334–336
Double-quantum homonuclear rotary resonance (2Q-HORROR) 166–168
Double-quantum magic angle spinning (DQMAS)
hydrogen bonding 330
carboxylic acids 334–336
molecular-level motion 190–191
Double rotation (DOR)
quadrupolar coupling 232
structure determination 298
DPP-Boc, structure determination 280
DQ *see* Double-quantum
DQC *see* Double-quantum-coherence
DQF-DRAWS, nanostructures 312
DQF MAS *see* Double-quantum filtered magic angle spinning
DQMAS *see* Double quantum magic angle spinning
DRAMA *see* Dipolar recovery at the magic angle
DRAWS *see* Dipolar coupling with a windowless sequence
DREAM *see* Dipolar recoupling enhanced by amplitude modulation
DSC *see* Differential scanning calorimetry
DSO *see* Diamagnetic spin orbits
DUMBO *see* Decoupling using mind boggling optimization
Dynamic angle spinning (DAS), quadrupolar coupling 232
Dynamic order parameter, expression 181–182
Dynamics 365–373
amino acids 430–431
autocorrelation functions 356
Bloembergen–Purcell–Pound theory 358
characterization 381–385
chemical exchange in organic solids 379–380
combined studies 362–366
crystalline organic solids 375–386
deuterium lineshapes 359–366
dipolar coupling 356–359
disorder 445–448
displacive phase transitions 405–407
fast processes 381–383
host–guest complexes 270–271
hydrogen bonding 334–336
intermediate processes 384–385
line broadening 385
noninteger quadrupolar dynamic averaging 368–371
order–disorder phase transitions 405, 407–409
phase transitions 409–410
polymorphs 312–315, 383–384
protein folding 430–431
quadrupolar coupling 238–239
relaxation times in organic solids 380–381
rotational barriers 356
shielding 366–368
slow processes 383–384
spin-lattice relaxation 358–359
structural motifs 309–310
structural phase transitions 404–410
Dynamic solid-state nuclear magnetic resonance 177–193

γ-Effect, chemical shifts 103–104
EFGs *see* Electronic field gradients
Ehrenfest classification 388
Electric field gradients (EFGs) 29, 36
  displacive phase transitions 406
  order-disorder phase transitions 408–409
  phase transitions 395–398
  powdered solid wideline spectra 43
  quadrupolar coupling 225, 237–238
  structure determination 293
  tensor orientation 237–238
Electronic charge density 30
Electronic density 254
Electron paramagnetic resonance (EPR) 29, 38
Electrons, indirect nuclear spin-spin coupling 127
Electron transfer, anisotropy and asymmetry 115–116
Electrostatic field effects, lattice structure encoding 115–116
Enantiomer determination 436–439
Encoding
  direct 115–118
  indirect 118–119
γ-Encoding, rotary resonance recoupling 142–143
Energy refinement 259
EPR *see* Electron paramagnetic resonance
Euler angles 67
Euler rotations 67
Exchange-correlation functionals 83
Exchange spectroscopy (EXSY) 368
  disorder 446–447
  slow dynamics 383–384
Exchange theory, dynamic solid-state nuclear magnetic resonance 180
Experimental characterization
  magic angle spinning 44–49
  spinning sideband analysis 44–46
  tensors 41–50
EXSY *see* Exchange spectroscopy

Fast dynamics
  characterization 381–383
  motional averaging 378–379
  quadrupolar coupling 383
  spin-1/2 nuclei 382
Fast motion 180–182
  double quantum experiments 190–191
Fermi-contact (FC) term 37
Ferrierite
  chemical shift computations 85
  structure determination 285
Ferrobielectics 395
Ferroelastic phase transitions 394
  Landau theory 410–413
Ferroelastoelectrics 395
Ferroelectric phases, atomic ordering 351–352
Ferroic phase transitions
  classification 393–395
  definition 394
FID *see* Free induction decay

Finasteride 5–6, 317
  GIPAW modeling 87–88
  isomorphous solvates 380–381
  solvent modelling 94–95
Finite pulse radiofrequency-driven recoupling (fpRFDR) 166
FIREMAT *see* Five π replicated magic angle turning
First principles
  chemical shifts 81–97
  inorganic/materials chemistry 458–460
  intermolecular interactions 315–317
  organic molecules 286
  spin diffusion modelling 198–199
Five π replicated magic angle turning (FIREMAT)
  dimethyl sulfoxide 316–317
  polymorphs 313–315, 442–443
  stereochemistry 438–439
Flavonoids, polymorphisms 441–442
Flexibility, crystal structure derivation 122
Flip-flop term, dipolar alphabet 132
Floquet theory, rotational echo double resonance 145
Fluorapatite 481
Fluoride-containing zeolites 267–269
Fluoride-substitution 473–475
Fluorine-exchanges 269
Fluorite-structured oxides, atomic ordering 350
Flurbiprofen 85, 86
FOCUS (computer program) 258
Formoterol fumarate 379
Formyl group orientation 281–282
β-*p*-Formyl-*trans*-cinnamic acid 281–282
Fox (computer program) 258, 259
FpRFDR *see* Finite pulse radiofrequency-driven recoupling
Framework aluminosilicates 465–469
Free induction decay (FID) 44–45, 180
Frequency-selective homonuclear dipolar recoupling 171–173
Frequency-selective rotational echo double resonance (FS-REDOR) 148–151
  Hamiltonians 148
  pulse sequence 148
Frequency-switched Lee–Goldberg (FSLG)
  magnetization transfer 130–131
  molecular level mobility 186
FSLG *see* Frequency-switched Lee–Goldberg

Garnets
  aluminum coordination 473
  atomic ordering 346–347
Gauge-including atomic orbitals (GIAO)
  magnetic shielding theory 56
  polymorphisms 442, 445
Gauge-including projector augmented wave (GIPAW) models 35, 36
  CASTEP code 87
  crystalline systems 81–97
  crystal packing 93–94
  inorganic/materials chemistry 459
  intermolecular interactions 315–317
  magnetic shielding 58

metallic systems 38
molecular-level mobility/rigidity 89
multinuclear aspects 88–89
polymorphisms 445
shielding constants 86–87
shielding tensor components 92–93
signal assignment 87–88
temperature effects 83–85
theory 82
GAUSSIAN (computer program) 225
γ-Effect, chemical shifts 103–104
Generalized gradient approximation (GGA), concept 83
General position, definition 264
Genetic algorithm structure refinement 278
Geochemistry 463–486
aluminosilicates 469–471
aluminum 464–473
coordination 471–473
framework aluminosilicates 465–469
future applications 481–482
homogeneous dispersion of charge 469–470
hydrogen 478–480
minor component resolution 480–481
phyllosilicates 469–470
silicon 464–471
vacancy defects 477–478
Geometry
bond lengths 101–103
chemical shifts 99–111
dihedral angles 103–106
optimization 85–86, 119–121
protein backbones 423
protein secondary structure 423
Ramachandran angles 106
side chains 423–426
structural parameters 249–257
tautomers 100–101
GGA *see* Generalized gradient approximation
GIAO *see* Gauge-including atomic orbitals
Gibbs free energy, Ehrenfest classification 388
GIPAW *see* Gauge-including projector augmented wave
Glycylisoleucine 10
Green functions 33
Group/subgroup relationships 253–254
Landau theory 401
Gypsum *see* Calcium sulfate dihydrate

Habit, definition 5
Half-integer spin quadrupolar nuclei, wideline spectra 43
Hamiltonians 24–26
construction 249
dipolar coupling 23–24
expansion of magnetic shielding terms 55–56
Fermi-contact operator 37
frequency-selective rotational echo double resonance 148
heteronuclear dipolar recoupling 138–141
heteronuclear scalar couplings 216
homonuclear dipolar recoupling 164–165
incredible natural abundance double-quantum transfer experiment 210
isolated spin-spin coupling 129
phase transitions 403
quadrupolar coupling 24, 224, 226
rotary resonance recoupling 141–143
rotational echo double resonance 143, 145–146
spherical tensors 23–26
spin-dipolar operator 37
Hartree–Fock theory
magnetic shielding 56–58
quadrupolar coupling 225
HBC-C *see* Hexa-*n*-dodecylhexa-*peri*-hexabenzocoronene
HDC *see* Homogeneous dispersion of charge
Heavy atoms 38–39, 102
HETCOR *see* Heteronuclear chemical shift correlation spectroscopy
Heterocyclic compounds
aromatic 117–118
nitrous 101
Heteronuclear chemical shift correlation spectroscopy (HETCOR) 209, 217–220
3-D transferred echo double resonance 152–157
amino acid assignment 421
geochemistry 474, 478, 479–480
mineral substitutions 474, 478
nanostructures 312
polymorphisms 444–445
polymorphs 313–315
protein folding, dynamics 431
Heteronuclear dipolar coupling
characterization 132
chemical shift anisotropy and structure 290–291
hydrogen bonding 327–329
proton lineshape second moments 357
single crystals 70
site resolved 183–190
Heteronuclear dipolar recoupling 137–161
frequency-selective rotational echo double resonance 148–151
multi spin systems 147–157
rotary resonance recoupling 141–143
rotational echo double resonance 143–146
spin-1/2 nuclei 138–141
symmetry-based pulse sequences 146–147
Heteronuclear indirect coupling, characterization 129–130
Heteronuclear multiple quantum correlation (HMQC) 39, 424
Heteronuclear scalar couplings
Hamiltonian 216
measurement 216–217
Heteronuclear through-bond spectroscopy 216–220
Hexabenzocoronenes (HBCs) 308–310
Hexa-*n*-dodecylhexa-*peri*-hexabenzocoronene (HBC-C) 309
Hexamethylbenzene (HMB) 180–181
High-resolution solid-state nuclear magnetic resonance 248–249
High silica zeolites 266
History, crystallography 245–248
HMB *see* Hexamethylbenzene
HMQC *see* Heteronuclear multiple quantum coherence

HNCH experiments, amino acid side chain geometry 423–426
Homogeneous dispersion of charge (HDC), phyllosilicates 469–470
Homogeneous nuclear spin, definition 44
Homonuclear coupling
  aromatic π–π stacking 308
  chemical shift anisotropy and structure 292–293
Homonuclear decoupling
  frequency-switched Lee–Goldberg, magnetization transfer 130–131
  magnetization transfer 130–131
Homonuclear dipolar coupling
  characterization 132
  hydrogen bonding 329–333
  organic crystalline structures 329–333
  proton lineshape second moments 357
  single crystals 70
  site resolved 183–190
Homonuclear dipolar recoupling 163–176
  chemical shift dependent 168–170
  delta-function pulses 165–166, 169–170
  dipolar-assisted rotational resonance 175
  frequency-selective 171–173
  Hamiltonians 164–165
  proton-assisted recoupling 175
  radiofrequency-assisted diffusion 175
  radiofrequency-driven recoupling 165–168
  rotational resonance 168–169
  selective 172–173
  stochastic 173–175
  symmetry-based constant time recoupling 171
  symmetry principles 170–171
  theory and notation 163–165
Homonuclear indirect coupling, characterization 129
Homonuclear scalar coupling, measurement 213–216
Homonuclear through-bond correlation spectroscopy 210–216
2Q-HORROR *see* Double-quantum homonuclear rotary resonance
Host–guest complexes
  calixarenes 269–271, 360–362
  combined studies 269–271
  dipolar dephasing 359
  isotropic chemical shifts 11–12
  organic solids 377–378
  zeolites 306–307
Hydrate, definition 439
Hydrogen
  geochemistry 478–480
  minerals 478–480
  organic structures 322–323
Hydrogen bonding
  ammonium cations, chemical shifts 117
  anisotropy and asymmetry 116–118
  carbonyl carbons 323–325
    chemical shifts 116–117
  carbonyl groups 283
  carboxylic acid groups
    chemical shifts 116
    dynamics 334–336
  chemical shift computations 84
  chemical shifts 322–323
    organic crystalline structures 321–326
  density functional theory 322–323
  direct encoding 116–118
  disorder 479–480
  dynamics 334–336
  gauge-including projector augmented wave modelling 95–96
  geochemistry 478–480
  heteronuclear dipolar couplings, organic crystalline structures 327–329
  hydrogen tensors, chemical shifts 117
  indirect dipolar coupling 333–334
  indirect encoding 119
  neutron diffraction 282
  nitrogen-15 117, 325
  nitrogen–hydrogen dipolar coupling 327–328
  nitrogen–nitrogen dipolar coupling 330–332
  organic molecules 119, 321–339
  oxygen-17 323–325
  oxygen–hydrogen dipolar coupling 328–329
  structure determination 281–283, 321–339
  tensor lengths 117–118
  uracil packing 323
Hydrogen-hydrogen interactions, chemical shifts 106–107
Hydrogens
  carbohydrates 120
  chemical shift computations 85
Hydroxy hydrogens, chemical shifts 119
Hydroxylapatite 481
Hydroxyl distributions 475–476

IBMS *see* Isotropic bulk magnetic susceptibility
IGAIM *see* Individual gauges for atoms in molecules
IGLO *see* Individual gauge for localized orbitals
INADEQUATE *see* Incredible natural abundance double-quantum transfer experiment
Incredible natural abundance double-quantum transfer experiment (INADEQUATE)
  disorder 446
  Hamiltonian 210
  hydrogen bond mediated indirect dipolar coupling 333–334
  inorganic/materials chemistry 456–457
  polymorphisms 443–444
  solid-state 209, 210–215
  structural biology 421
  zeolite host–guest interactions 306
Independent spin species 68
Indirect coupling
  bond lengths 130–131
  calculation 36–38
  characterization 129–131
    solids 129–131
  connectivity 209–222
  heteronuclear 129–130
  homonuclear 129
  hydrogen bonds 333–334
  isotropic spin-spin coupling constant 128
  solid state NMR 66

solution-state NMR 64
spin echo modulation 215–216
theory 127–129
Indirect encoding 118–119
Indirect spin-spin coupling 7, 8
Individual gauge for localized orbitals (IGLO) 56
Individual gauges for atoms in molecules (IGAIM) 56
INEPT *see* Insensitive nuclei enhanced by polarization transfer
INEPT-HSQC *see* Insensitive nuclei enhanced by polarization transfer heteronuclear single-quantum coherence
Inequivalency of sites 251
structure resolution 257–258
Inhomogeneous nuclear spin, definition 44
Inorganic chemistry 455–461
future prospects 460–461
space-group assignment 456
Inorganic molecules, structure determination 258, 279–278, 456–460
Inorganic non-stoichiometric crystalline systems
atomic ordering 341–353
Lowenstein's aluminum avoidance principle 343, 345–346
Insensitive nuclei enhanced by polarization transfer heteronuclear single-quantum coherence (INEPT-HSQC) 218–220
Insensitive nuclei enhanced by polarization transfer (INEPT), indirect coupling 131
Integrant unit
fundamental principles 256–257
structure resolution 257–258
Interatomic distances
see also Bond lengths
combined studies 281
Interference
decoupling 359
radiofrequency irradiation 381
relaxation times 380–381
Intermediate dynamics 384–385
Intermediate motion 180, 182–183
Intermolecular interactions 305–319
ab-initio calculations 315–317
aromatic $\pi-\pi$ stacking 307–312
magnetic shielding 57–58
nanostructures 311–312
ring-current effects 307–311
Intramolecular motion 375–386
Inversion symmetry 68–70
Isolated spin systems
direct coupling 132
synthesis 70
Isopropylamine-ALPO-14 13
Isotropic bulk magnetic susceptibility (IBMS) 87
Isotropic chemical shifts
see also Chemical shifts
concepts 7, 8
host-guest systems 11–12
inorganic non-stoichiometric crystalline systems 343
structural phase transitions 392
structure refinement 259
Isotropic indirect spin-spin coupling, concepts 7, 8
Isotropic relaxation, rotational dynamics 360–362
Isotropic shift, gauge-including projector augmented wave modelling 92–93
Isotropic spin-spin coupling constant ($J(N, N')$)
characterization 129–131
definition 128
ITQ-4 457
structure determination 285
IUPAC recommendation, calculating shielding 54

Jump reorientation anisotropy 360

Knight shift 38, 43
k-point, chemical shift computations 82–83
Kronecker delta terms, heteronuclear dipolar recoupling 140
KSCN *see* Potassium thiocyanate
KT3 functional, concept 83

Labeling
deuterium 359–366, 431
structural biology 429
uniformly carbon-13, nitrogen-15 138, 147–153, 156
Lambda transitions 407–409
Lamb formula 34
Landau theory 400–404
group/subgroup relationships 401
limitations 404
Lanthanide-doped pyrochlores 343
Large molecular structures 257
Large-span tensors 117
Lattice structure
see also Crystal structure
aluminum coordination 471–473
anion order/disorder 473–475
anisotropy and asymmetry 113–124
cation order/disorder 471–473, 475–477
electrostatic field effects 115–116
magnetic shielding 57–58
Lattice vibrations, chemical shift computations 84
Layered double hydroxides (LDHs) 475–477
Lead magnesium niobate 351–352
Lee–Golberg cross-polarization (LG-CP) 184–186, 189–190
pulse sequence 186
Levitt's *C* and *R* sequences, homonuclear dipolar recoupling 170–171
LG-CP *see* Lee–Golberg cross-polarization
Libematrix 198
Ligand recognition sites 429
Line broadening
dynamics 385
temperature effects 379–380
Lineshape effects
dipolar coupling and dynamics 356–358
phase transitions 409–410
quadrupolar coupling 226–230

Liquid crystals 307–309
REPT-HMQC 185, 188
Lithium lanthanum titanate 391
Localized orbitals local origin (LORG) 56
Local-level structure
aperiodic structures 261
quadrupolar coupling 234–235
Local symmetry effects 63–67
chemical shifts 103
long-range order 64–65
Long-range order (LRO) 64–65
aluminosilicates 465–469
aperiodic structures 261
asymmetry parameter 254
definition 64–65
quadrupolar interactions 254
LORG *see* Localized orbitals local origin
Lowenstein's aluminum avoidance principle 343, 345–346

Magic angle spinning indirect heteronuclear multiple quantum correlation (MAS-J-HMQC) 130–131, 217–218
Magic angle spinning indirect heteronuclear single quantum correlation (MAS-J-HSQC) 130–131, 217–218
Magic angle spinning (MAS)
cross-polarization 306–307
definition 74
double-quantum experiments 190–191, 334–336
Hamiltonians 74–77, 138–141
heteronuclear coupling 291, 293
homonuclear coupling 291, 293
hydrogen bonding dynamics 334–336
indirect coupling 209–222
isotropic spin-spin coupling constants 129–131
magnetic shielding 74–77, 294–296
molecular level mobility 177–193
protein tertiary structure 427–428
quadrupolar coupling 228–230, 231–235, 294–296
relaxation time interference 380–381
residual dipolar coupling and structure 296–298
self-commuting Hamiltonians 76–77
structural biology sample preparation 418–419
structure determination 284–286
Magnesium clustering 476–477
Magnetic dilution 156
Magnetic equivalence 64, 292
single crystals 68–70
Magnetic resonance parameters 29–40
Magnetic shielding 53–61
ab-initio calculation methods 56–58
cluster models 57–58
density functional theory 56–58
dipolar coupling 289–293
dynamics 366–368
intermolecular effects 57–58
periodic boundary conditions 58
phase transitions 395–398
quadrupolar coupling 294–296
Raleigh–Schrödinger perturbation theory 55–56
relativistic effects 57
theory 55–56
Magnetic shielding tensors 66
magic angle spinning 74–77
polycrystalline powders 72–77
single crystals 67–72
special site symmetry 68
stationary 72–74
Magnetization transfer 130–131
Maleic acid 71–72
Maltose 39, 93–94
MAS *see* Magic angle spinning
MAS-J-HMQC *see* Magic angle spinning indirect heteronuclear multiple quantum correlation
MAS-J-HSQC *see* Magic angle spinning indirect heteronuclear single quantum correlation
Materials chemistry 455–461
future prospects 460–461
space-group assignment 456
Matrix elements
Cartesian tensors 19–20
spherical tensors 26
Maximum dispersion of charge (MDC) 469–470
MDC *see* Maximum dispersion of charge
Measurement
heteronuclear scalar couplings 216–217
homonuclear scalar couplings 213–216
quadrupolar coupling 230–233
Melding of spin-locking and dipolar recovery at the magic angle (MELODRAMA) 134
Mercury, tensorial shielding 10–11
Metallic systems, shielding 38
Methanol 11
Methoxy group steric crowding 107–108
Methoxy substituted benzenes, steric crowding, chemical shifts 107–108
Methylated cyclohexanes 107
Methyl benzene carbons 107
Methylene carbons 104
Methyl groups
dipolar dephasing 359
in and out differentiation 367
rotation 362
steric crowding 106–107
Methylnitroacetanilide 87, 95–96
2-Methyl-2,4-pentadiol (MPD) 418–419
MFI zeolites 268–269
Micas 469–470
Minerals
aluminum coordination 471–473
anion order/disorder 473–475
calcium 476–477
cation order/disorder 471–473, 475–477
magnesium 476–477
speciation 478–480
vacancy defects 477–478
Modelling
spin diffusion 197–201
first principles 198–199
numerically 197–198
phenomenological description 199–201

3-D Molecular crystallography 257
Molecular-level information 8–13
Molecular-level mobility 7, 12–13
  basics 179–181
  chemical shift computations 84–85
  crystalline organic solids 375–386
  dipolar coupling 177–193
  double quantum experiments 190–191
  dynamic order parameter 181–182
  fast motion 180–182
  GIPAW 89
  intermediate motion 180, 182–183
  slow motion 180
  stochastic reorientation motion 177–178
Molecular tweezers, host–guest complexes 310
Monte Carlo/Simulated annealing 278
Motional averaging 378–379
MQMAS *see* Multiple-quantum magic-angle spinning
Mullites, atomic ordering 346
Multiple-quantum magic-angle spinning (MQMAS)
  anion order/disorder 476
  inequivalency 251
  quadrupolar coupling 232–233
Multispin systems 147–157

Nanostructures 311–312
Napthaline 119–120
NCACB experiments 420, 421
NCCN experiments 423–426
NCOCA experiments 420, 421
Neutron diffraction
  geometry optimization 85–86
  hydrogen bonding 282
NHHN experiments 330–332
Nitrogen
  heterocyclic compounds 101
  hydrogen bonding 117, 325
  protonation 101
Nitrogen–hydrogen dipolar coupling, hydrogen bonding 327–328
Nitrogen–nitrogen dipolar coupling, hydrogen bonding 330–332
NOEs *see* Nuclear Overhauser effects
Noncrystallographic sites, definition 253
Nonequivalent sites, chemical exchange 379–380
Nonferroelastic phase transitions 394–395
Noninteger quadrupolar dynamic averaging 368–371
3-D Nonmolecular crystallography 257–258
Nonperiodic structures 261
Nonquaternary suppression 359
Nonuniform labeling 429
NQR *see* Nuclear quadrupolar resonance
Nuclear magnetic resonance (NMR) principles 3–18, 248
Nuclear Overhauser effects (NOEs) 173–175
Nuclear quadrupolar coupling *see* Quadrupolar coupling
Nuclear quadrupolar resonance (NQR) 404
Nuclear quadrupole moment computation 224–226
Nuclear spin, sideband analysis 44–46
Nuclear spin interaction tensors, experimental characterization 41–50
Nuclear spin-spin coupling, concepts 127–136

Octafluoronapthalene 88
One-dimensional exchange spectroscopy by sideband alternation (ODESSA) 438
Optimization 258, 259–261
  assessing accuracy 261
  genetic algorithm techniques 278
  Monte Carlo/Simulated annealing 278
  organic/pharmaceutical compounds 448–450
  protein folding 425, 430
  root mean square deviation 425, 430
  using energy 259
  X-ray diffraction data 278
  zeolites 459–460
Order 341–353
  combined studies 266
Order–disorder phase transitions 388, 392–393, 397
  dynamics 405, 407–409
  identification 392–393
Order parameters 401–403
Organic chemistry 435–453
  combined studies 448–450
  disorder 445–448
  polymorphisms 439–445
  stereochemistry 436–439
Organic molecules
  see also Proteins
  chemical exchange 379–380
  combined studies 279–283
  dipolar coupling 326–333
  hydrogen bonding 119, 321–339
  intramolecular motion 375–386
  motional averaging 378–379
  relaxation time interference 380–381
  structure determination 258, 285–286
  X-ray diffraction structure solution 278
Orientation
  absolute 254
  formyl groups, β-*p*-formyl-*trans*-cinnamic acid 281–282
  quadrupolar coupling tensors 237–238
Orthocarborane 238
Orthoenstatite 40
Orthorhombic phases 364–365, 396–398
Oxybuprocaine hydrochloride 8–9, 105, 443–444
Oxygen
  chemical shift computations 83
  crystal structure refinement 120
  hydrogen bonding 323–325
Oxygen–hydrogen dipolar coupling, hydrogen bonding 328–329
Oxygen magic angle spinning (OMAS) 40
Oxynitride solid solutions 351

Packing polymorphisms, definition 439
Pake doublets 4, 132–133

PAR *see* Proton-assisted recoupling
Paraelectric phases
  potassium thiocyanate 396–398
  squaric acid 392
  transitioning from, antiferroelectric phases 392–393
Paramagnetic doping
  atomic ordering 343, 348–350
  fluorite-structured oxides 350
Paramagnetic effects, inorganic non-stoichiometric crystalline systems 343
Paramagnetic spin orbits (PSO), indirect coupling calculation 37
Paramagnetism, direction 55
PAS *see* Principle axis system
2-D PASS *see* Phase adjusted spinning sidebands
Patterson function 255
PAW *see* Projector augmented wave
PBE *see* Perdew, Burke and Ernzerhof…
PDSD *see* Proton-driven spin diffusion
Pentaerythritol 103
Pentafluorobenzoic acid (PFBA) 279
Peptide fragment dihedral angles 106
Perdew, Burke and Ernzerhof (PBE) calculations 83
Periodic boundary conditions 58
Periodic systems
  core states 34–36
  position operators 33–34
  pseudopotentials 34–36
  shielding 32–33
Permutationally offset stabilized (POST) C7 correlation 444–445
Perovskites
  displacive phase transitions 405–407
  ferroelectric phases 351–352
  order–disorder phase transitions 391
PFBA *see* Pentafluorobenzoic acid
Pharmaceutical chemistry 435–453
  combined studies 448–450
  disorder 445–448
  polymorphisms 439–445
  stereochemistry 436–439
Phase
  spinning sidebands 75–77
  X-ray diffraction 264
Phase adjusted spinning sidebands (2-D PASS) 441
Phase modulated Lee–Goldberg (PMLG) sequences 197
Phase-shifted recoupling effects a smooth transfer of order (PRESTO II) 328–329
Phase transitions 387–413
  classification 388–395
  combined studies 270–271
  displacive 388–391
  dynamics 404–410
  Ehrenfest classification 388
  electric field gradients 395–398
  ferroelastic 394
  ferroic 393–395
  group/subgroup relationships 401
  Hamiltonians 403
  identification 392–393, 395–400
  Landau theory 400–404
  magnetic shielding 395–398
  molecular dynamics 409–410
  nonferroelastic 394–395
  nuclear quadrupolar resonance 404
  order–disorder 388, 391–393
  order parameters 401–403
  paraelectric/ferroelectric 351–352
  phonons 399, 403, 405–407
  pseudospin-phonon coupling 403
  quadrupolar coupling 395
  reconstructive 388
  relaxation times 398–400
  site symmetry restrictions 395
  spin-lattice relaxation 358–359
Phenylalanine 432
Phonons 399, 403, 405–407
Phyllosilicates 469–472
PISEMA *see* Polarization inversion spin exchange at the magic angle
Planewave basis set 31
Plane-wave cutoff energy 83
Planewave-pseudopotential technique 30–32, 82–83
  Bloch's theorem 30–31
  density functional theory 30
  pseudopotential approximation 31–32
  supercell approximation 31
Plastic crystals 239
PMLG *see* Phase modulated Lee–Goldberg
Point charges 115–116
Point-group symmetry 64, 252–255
Point symmetry
  concepts 263–264
  quadrupolar coupling 234
Polar effects 116–119
Polarization inversion spin exchange at the magic angle (PISEMA), molecular-level mobility 183
Polycrystalline powders, magnetic shielding tensors 72–77
Polyethylene glycol (PEG), structural biology 418–419
Polymorphisms 5
  chemical shifts 91
  dynamics 383–384
  FIREMAT 313–315
  GIPAW 91
  organic/pharmaceutical compounds 439–445
  structure determination 281–283, 312–315
Poly(styrene-*co*-dimethylsiloxane) 185
Poly(styrene-*co*-sulfone) 184
Polytypoids 14
Position operator calculation 33–34
POST *see* Permutationally offset stabilized
Potassium phosphide 410
Potassium thiocyanate (KSCN) 396–398
Powder diffraction
  combined with nuclear magnetic resonance 275–287
  structure determination 277–278
  structure refinement 259
Powdered solids
  Chemical shift anisotropy 46–49
  electric field gradients 43
  spinning sideband analysis 44–46
  wideline spectra 42–43
Powder patterns
  anisotropy and asymmetry 72–74
  direct dipolar coupling 73

magnetic shielding tensors 72–74
quadrupolar coupling 231
spinning sidebands 75–77
structure refinement 120
PRESTO II *see* Phase-shifted recoupling effects a smooth transfer of order
Primary ferroics 394
Principle axis system (PAS) calculation 46
PROCHECK (computer program) 430
Projector augmented wave (PAW) method 35–36, 38
Protein folding
dynamics 430–431
quaternary structure 427–429
secondary structure 422–426
side chain geometry 423–426
structural restraints 421–429
tertiary structure 426–427
Protein nuclear magnetic resonance crystallography 417–433
Proteins
see also Organic molecules
backbone geometry 423
dihedral angles, chemical shifts 106
spin diffusion 201
structural restraints 421–429
structure determination 417–433
Proton-assisted recoupling (PAR) 175
Protonation
carboxylic acids, chemical shifts 100
chemical shifts 100–101
nitrogen, chemical shifts 101
Proton-driven spin diffusion (PDSD)
see also Spin diffusion
crystalline systems 196–197
modelling 197–201
structural biology 419–420
structure determination 201–203
Proton spin-diffusion with carbon detection (CHHC) 197, 201–203
Proton spin-diffusion (PSD)
see also Spin diffusion
crystalline systems 196
full crystal structure determination 203–205
modelling 197–201
Proximity 255–256
PSD *see* Proton spin-diffusion
Pseudo 1-D crystallography 257
Pseudopolymorphism, definition 439
Pseudopotentials
approximation 31–32
calculation, periodic systems 34–36
projector augmented wave method 35–36
Pseudospin-phonon coupling, phase transitions 403
PSO *see* Paramagnetic spin orbits
Pulse sequences
amino acid side chain geometry 424
cross-polarization 420
dipolar-assisted rotational resonance 420
dipolar chemical shift correlation 186
dipolar recovery at the magic angle 165
double-quantum homonuclear rotary resonance 167–168
frequency-selective rotational echo double resonance 148
incredible natural abundance double-quantum transfer experiment 211
Lee–Goldberg cross-polarization 186
multiple-quantum coherence 218, 424
NCACB/NCOCA experiments 420
proton-driven spin diffusion 420
radiofrequency-driven recoupling 420
rotational echo double resonance 144, 424
spin diffusion 198
spin echo modulation 216
stochastic homonuclear dipolar recoupling 174
structure determination 299–300
wide-line separation 185
3-D *z*-filtered transferred echo double resonance 152
Pyridine 308, 361–362
Pyrochlores 347–348
Pyroxenes 470

Q-Chem (computer program) 311
Quadrupolar broadening coefficients 228
Quadrupolar coupling (Q) 7, 66, 223, 224–226, 230–233
coordination number 234–235
crystal structure 233–239
deuterium lineshapes 359–360
dynamics 238–239, 383
fast dynamics 383
framework aluminosilicates 465–469
Hamiltonians 24, 224, 226
indirect 129–130
inorganic non-stoichiometric crystalline systems 343
lineshape effects 226–230
long-range order 254
magic angle spinning 228–230, 231–235
magnetic shielding and structure 294–296
measurement 230–233
phase transitions 389–391, 404, 406
powder patterns 231
protein folding 431
residual dipolar coupling 296–298
splitting 227–228
structure determination 293–298
structure refinement 259
symmetry 14–15, 233–234
temperature effects 238–239
tensors 70
orientation 237–238
wideline spectra 42
Wigner rotation matrix elements 228
Zeeman energy perturbation 226–230
Quaternary structure 427–429
Quercetin 441–442

R^3 *see* Rotary resonance recoupling
Racemization 436–439
RAD *see* Radiofrequency-assisted diffusion
Radiofrequency-assisted diffusion (RAD), homonuclear dipolar recoupling 175
Radiofrequency-driven recoupling (RFDR)
  delta-function 169–170
  frequency-selective 171–172
  homonuclear dipolar recoupling 165–172
  polymorphisms 441
  structural biology 419–420
Radiofrequency (RF) interference 381
Raleigh–Schrödinger (RS) perturbation theory 55–56
Ramachandran angles 106
Raman two phonon processes 405
Ramsey's theory 296
REAPDOR *see* Rotational-echo, adiabatic passage, double resonance
Receptor–ligand complexes 429
Reciprocal lattices 264
Reconstructive phase transitions 388
Recoupled polarization-transfer heteronuclear multiple-quantum correlation (REPT-HMQC) 185, 188, 309–310
REDOR *see* Rotational echo double resonance
Red, orange, yellow (ROY) polymorphs 105, 440
Reduced Wigner matrices 140
Relativistic effects 38–39, 57
Relaxation times 7–8
  dynamic solid-state nuclear magnetic resonance 180
  interference 380–381
  phase transitions 398–400
Relaxor ferroelectrics 351–352
REPT-HMQC *see* Recoupled polarization-transfer heteronuclear multiple-quantum correlation
REREDOR *see* Rotor-encoded rotational echo
Residual dipolar coupling 296–298
RF *see* Radiofrequency
RFDR *see* Radiofrequency-driven recoupling
Rietveld refinement 281
Rigidity, gauge-including projector augmented wave modelling 89
Rigid solids, heteronuclear scalar couplings 216–217
Ring-current effects 307–311
Ring rotation, dynamic solid-state nuclear magnetic resonance 180–181
RMSD *see* Root mean square deviation
RNA, hydrogen bonding 323, 330–332
Root mean square deviation (RMSD), protein folding 425, 430
Rotary resonance recoupling (R^3)
  γ-encoding 142–143
  heteronuclear dipolar recoupling 141–143
Rotational dynamics 365–373
  barriers 356
  combined studies 270–271
  dipolar coupling 356–359
  protein folding 430–431
  second moments 356–358
Rotational echo, adiabatic passage, double resonance (REAPDOR) experiments 133
Rotational echo double resonance (REDOR) 137, 143–146
  amino acid side chain geometry 424
  dipolar coupling 133
  frequency-selective 148–151
  Hamiltonians 143, 145–146
  heteronuclear recoupling 143–146
  mineral substitutions 475
  structure determination 283
Rotational resonance 77, 168–169, 171–172, 175
Rotational resonance in the tilted rotating frame (RRTR) 172
Rotor-encoded rotational-echo double-resonance (REREDOR) 185, 187, 309–310
Rotor synchronization 143–146
ROY *see* Red, orange, yellow
RRTR *see* Rotational resonance in the tilted rotating frame
RS *see* Raleigh–Schrödinger theory

Sample preparation
  structural biology 418–419
    labeling patterns 429
Satellite-transition magic angle spinning (STMAS) 232–233
Satellite transitions acquired in real time (START) 233
Scalar coupling
  heteronuclear 216–217
  homonuclear 213–216
Scalar spin-spin coupling constants
  see also Isotropic spin-spin coupling constant
  characterization 129–131
SCT *see* Semiconstant time
SD *see* Spin-dipolar
SDR *see* Stochastic dipolar recoupling
SEASHORE *see* Shift evolution assisted selective homonuclear recouplings
Secondary structure, protein folding 422–426
Second moments
  dipolar coupling and dynamics 356–358
  inorganic/materials chemistry 455
SEDRA *see* Simple excitation for the dephasing of rotational echo amplitudes
Selective labeling 156
Selenium-77 14
Self-commuting Hamiltonians 76–77
Semiconstant time (SCT) pulse sequences 156–157
Separated local field (SLF) recoupling 183–190
Shielding 53, 55–56
  calculation 54, 56–58
  constants 86–87
  dynamics 366–368
  periodic systems, principles 32–33
  tensors 85, 92–93
Shift evolution assisted selective homonuclear recouplings (SEASHORE) 172–173

Shorten recycle times, using adiabatic passage cross-polarization (SPECIFIC CP) 421
Short range order (SRO)
  aluminosilicates 465–469
  geochemistry 464–465
Side chain geometry 423–426
Signal assignment 87–88
Silicate atomic ordering 351
Silicon
  geochemistry 464–471
  inorganic systems 343–346
  magnesium/calcium clustering 476–477
  zeolites 306–307
Sillimanite 470–471
Simple excitation for the dephasing of rotational echo amplitudes (SEDRA) 166, 169–170
Single crystals
  dipolar coupling 70–72
  magnetic shielding tensors 67–72
  principle axis 446
Single-crystal X-ray diffraction (SXRD) 263–274, 448–450
  phase problem 264
  stereochemistry 436
Single site analysis 253
Site resolved dipolar coupling
  heteronuclear 183–190
  homonuclear 183–190
Site symmetry 68, 254–255
  chirality 254–255
  concepts 13–16
  quadrupolar coupling 14–15
  special 68
Slow dynamics 383–384
Slow motion 180, 191
Small-span tensors 117
Sodalite topology 253
Sodium azide 395–396
Sodium niobate 405–407
Soft mode transitions 388, 389–391
Solid benzene 357
Solid-state nuclear magnetic resonance (SSNMR) 264
  anisotropy and asymmetry 113–124
  combined with single-crystal X-ray diffraction 263–274
  direct encoding 115–118
  dynamic 177–193
  hydrogen bonding 116–118, 119
  indirect encoding 118–119
  polar effects 116–118, 119
  structural biology 417–433
  structure determination 99–111, 121–122
  structure refinement 119–121
Solution-state NMR 63–64
Solvates 94–95
Solvents
  isotropic chemical shifts 11–12
  modelling 94–95
Space filling 65
Space groups 90–91, 252–254
  see also Crystal space groups
  absolute orientation 254–255
  assignment 456
  group/subgroup relationships 253–254
Space packing 258
Spatial disorder 7
Spatial spin diffusion 196
Spatial tensors versus spin tensors 23
Special positions, definition 264
Special site symmetry 68
Speciation 478–480
Spectral density functions 406, 408–409
Spectral fitting 384
Spectral spin diffusion 196–197
Spherical tensors
  Cartesian tensors 22
  Hamiltonians 23–26
  rankings 21–22
Spin diffusion 198
  see also Proton-driven spin diffusion; Proton spin-diffusion
  crystalline systems 195–207
  experiments 197
  mechanism 196–197
  modelling 197–201
    first principles 198–199
    numerically 197–198
    phenomenological description 199–201
  protein structure 201
  structure determination 201–205
Spin dilution 429
Spin-dipolar (SD) operator 37
Spin-echo magic angle spinning 334
Spin echo modulation 215–216
Spinels 346–347, 472–473
SPINEVOLUTION (computer program) 198
Spin interactions
  local symmetry effects 63–67
    solid-state NMR 64–67
    solution-state NMR 63–64
Spin-lattice relaxation 358–359, 405–409
Spinning sidebands 44–46, 75–77
Spin-1/2 nuclei
  fast dynamics 382
  heteronuclear dipolar recoupling 138–141
Spin polarization 38
Spin species
  independent 68
  mixed 68
Spin-spin coupling 127–136
  direct 127, 129–131
  indirect 127–131
  isotropic indirect 7, 8
Spin systems
  solution-state NMR 63–64
  symmetry 63–67
Splitting 227–228
Squaric acid 392–393
SRO *see* Short range order
π–π Stacking 311–312
Standard precipitants 418–419
START *see* Satellite transitions acquired in real time
Static sample spin diffusion 201
Stereochemistry 436–439

Steric crowding 106–108
Sternheimer antishielding factor 225
STF zeolites 267–268
STMAS *see* Satellite-transition magic angle spinning
Stochastic dipolar recoupling (SDR) 173–175
Stochastic reorientation motion 177–178
Stoichiometry 251
Structural biology 417–433
  future prospects 431–432
  labeling patterns 429
  sample preparation 418–419
  structural restraints 421–429
Structural motifs 305–319
aromatic π–π stacking 307–311
dynamics 309–310
Structural parameters 249–257
Structural phase transitions 387–413
  classifications 388–395
  dynamics 404–410
Structure determination 150–151, 245–262
  see also Crystal-structure determination
  aromatic π–π stacking 307–311
  asymmetric unit 279
  bond lengths 255
  combined studies 275–287
  crystallochemical formula 251
  dipolar coupling and magnetic shielding 289–293
  disorder 281
  distance approach 257
  distance measurements 456–458
  double rotation 298
  dynamics 359–366, 376–378
  hydrogen bonding 281–283
  inequivalency of sites 257–258
  inorganic materials 279–278, 341–353, 456–460
  integrant unit 257–258
  magic angle spinning 284–286
  NMR with XRD 254, 278–284
  non-stoichiometric systems 341–353
  organic compounds 285–286, 376–378, 448–450
  pharmaceutical compounds 448–450
  phase transitions 387–413
  phyllosilicates 469–470
  polymorphs 281–283
  powder diffraction 277–278
  proteins 417–433
    folding 421–430
  quadrupolar coupling 293–298
  REDOR 283
  RNA 323
  structural motifs 307–311
  tensor interplay 289–301
  XRD with NMR 254, 278–284
  zeolites 284–286, 306–307
Structure solution 277–278
Subgroup relationships 253–254
Substitutions
  aluminum 471–473
  anions 473–475
  calcium 476–477
  cations 471–473, 475–477
  magnesium 476–477
Supercell approximations 31
SXRD *see* Single-crystal X-ray diffraction
Symmetry 13–16, 63–67
  Bravais lattices 65
  chemical shift anisotropy
    heteronuclear coupling 290–291
    homonuclear coupling 292–293
  deuterium lineshapes 360–366
  dipolar coupling and magnetic shielding 289–293
  heteronuclear coupling 146–147, 290–291
  homonuclear coupling 170–171, 292–293
  local level 63–79
  magnetic shielding
    dipolar coupling 289–293
    quadrupolar coupling 294–296
    tensors 68–70, 290
  phase transitions 395–398
  quadrupolar coupling 233–234, 294–296
  rotational barriers 356
  solution-state NMR 63–64
Synthesis of isolated spin systems 70

TALOS, protein secondary structure 423
Tautomers 100–101
t-BC *see tert*-Butylcalix[4]arene
TCNB *see* 1,2,4,5-Tetracyanobenzene
TDMM *see* Tetrakis[(3,5-dimethoxybenzyloxy)methyl] methane
TEDA *see* Triethyldiamine
TEDOR *see* Transferred echo double resonance
TEE *see* L-Tyrosine-ethylester
Temperature
  chemical exchange 379–380
  chemical shifts 83–85
  dipolar coupling 179, 180–181
  host–guest complexes 270–271
  paramagnetic doping 349
  phase transitions 351–352
  quadrupolar coupling 238–239
  spin-lattice relaxation 358–359
Tensors 7, 19–27
  anisotropic interactions 65–67
  axially symmetric 290–291
  chemical shifts 113–114
  components 250
  computation 32–33
  degeneracy 118–119
  direct encoding 115–118
  electric field gradients 237–238
  GIPAW 92–93
  Hamiltonians 23–26
  hydrogen bonding 116–118
  indirect encoding 118–119
  magnetic shielding 54–55, 67–77, 290
  nuclear spin interaction 41–50
  orientation 237–238
  periodic system shielding 32–33
  quadrupolar coupling 70, 237–238, 360
  site symmetry 14–15
  spatial versus spin 23

spherical matrix elements 26
structure determination 121–122, 289–301
structure prediction 122
structure refinement 85, 119–121
Terbutaline sulfate 89
tert-butylcalix[4]arene (*t*-BC)
host–guest complexes 269–271
xenon absorption 271–273
Tertiary structure, protein folding 426–427
Testosterone 90–91
1,2,4,5-Tetracyanobenzene (TCNB) 310–311
Tetragonal-orthorhombic phase transitions 396–398
Tetragonal symmetry 389–391, 396–398
Tetrakis[(3,5-dimethoxybenzyloxy)methyl]methane (TDMM) 280
Tetramethylammonium hydroxide pentahydrate ($TMAOH.5H_2O$) 364–365
Three spin recoupling 175
Threonine 427
Through-bond spectroscopy (TOBSY) 213
disorder 213
double-quantum correlation 211
heteronuclear 216–220
homonuclear 210–216
structural biology 421
Thymol 202
Tidal patterns 223
Time-dependent Hamiltonians 74–77
Time domain signal 182–183
$TMAOH.5H_2O$ *see* Tetramethylammonium hydroxide pentahydrate
TMO *see* Trimethylene oxide
TOBSY *see* Through-bond correlation spectroscopy
TOCSY *see* Total correlation spectroscopy
Toluene
tert-butylcalix[4]arene inclusion 269–270
chemical shifts 308
TOPAS (computer program) 258, 259
Total correlation spectroscopy (TOCSY) 209
TPP *see* Triphenyl phosphate; Tris(*o*-phenylenedioxy)spirocyclotriphosphazene
Traditional ab-initio methods, magnetic shielding 56–58
Traditional structure solution, X-ray diffraction 277
Transfer, magnetization, magic angle spinning experiments 130–131
Transfer of populations in double resonance (TRAPDOR), anion order/disorder 475
Transferred echo double resonance (TEDOR) 138
3-D 152–157
λ-Transitions 407–409
Translational dynamics 365–373
Transverse relaxation times, dynamic solid-state nuclear magnetic resonance 180
TRAPDOR *see* Transfer of populations in double resonance
Triethyldiamine (TEDA) 357
Trimethylene oxide (TMO) 362–363
Triphenyl phosphate (TPP) 446–447
Tris(*o*-phenylenedioxy)spirocyclotriphosphazene (TPP) 312
True crystals, definition 82
Tschermak substitutions 472–473
TURBO-MOLE (computer program) 311
Two dimensional nutation nuclear magnetic resonance spectra 231
L-Tyrosine-ethylester (TEE) 447–448

Uniformly carbon-13, nitrogen-15 (U-^{13}C, ^{15}N) labeled molecules 138, 147–153, 156
Uniform-sign cross-peak double quantum filtered correlation spectroscopy (2QF-COSY) 211, 213
Unit cells
definition 263
spin diffusion 205
temperature effects 84
Uracil 323, 324
Urea 323

Vacancy defects 477–478
Valinomycin 442–443
Virtual desolvation 94–95

WAHUHA *see* Waugh, Huber, and Haberlen sequence
WALTZ *see* Wonderful alternating phase technique for zero residual splittings
Wannier orbitals 33–34
Waugh, Huber, and Haberlen (WAHUHA) sequence 43, 164
Wavefunctions, pseudopotential approximation 31–32
Wide-line separation (WISE) 185
molecular-level mobility 183, 185
Wideline spectra 42–43
anomalies 43
half-integer spin quadrupolar nuclei 43
WIEN2k (computer program) 225
Wigner rotation matrices 140, 228
Wonderful alternating phase technique for zero residual splittings (WALTZ) 213
Wyckoff spectrum 252

Xenon 271–273, 367–368
X-ray diffraction (XRD)
direct-space structure solution 277–278
fundamental principles 264
inorganic/materials chemistry 456–457
interplay with nuclear magnetic resonance 263–274
examples 266–273
utility 264–266
limitations 5–7
organic/pharmaceutical compounds 448–450
phase problem 264
powder diffraction, structure determination 277–278
stereochemistry 436
structure refinement 120
traditional structure solution 277

X-ray diffraction (XRD) (*continued*)
versus nuclear magnetic resonance 254

Yttrium aluminum garnet (YAG), atomic ordering 347

Zeolites
aluminosilicate 266
fluoride containing 267–269
host–guest interactions 306–307
ITQ-4 457
MFI 268–269
structure determination 266–269, 284–286, 457–458
structure refinement 121, 459–460
ZSM-5 306–307, 457–458
Zeolite-Y 367–368
Zeroth-order regular approximation (ZORA) 57
heavy elements 39
z-Filtered transferred echo double resonance (ZF-TEDOR) 152–157, 426
Zircon 348–350
ZORA *see* Zeroth-order regular approximation

NMR Abbreviations and Acronyms

ABMS	Anisotropy of the Bulk Magnetic Susceptibility
ADRF	Adiabatic Demagnetization in the Rotating Frame
APT	Attached Proton Test
ARP	Adiabatic Rapid Passage
BIRD	BIlinear Rotation Decoupling
BLEW	A windowless multiple-pulse decoupling sequence
BR-24	Burum & Rhim (pulse sequence)
CIDNP	Chemically Induced Dynamic Nuclear Polarization
CIS	Complexation-Induced Shift
CODEX	Centerband only Detection of Exchange Experiment
COSY	Correlation Spectroscopy
CP	Cross Polarization
CPMAS	Cross Polarization with Magic Angle Spinning
CPMG	Carr-Purcell pulse sequence, Meiboom-Gill modification
CRAMPS	Combined Rotation and Multiple-Pulse Spectroscopy
CS	Chemical Shift
CSA	Chemical Shift Anisotropy
CST	Chemical Shift Tensor
CT	Central Transition
CT	Contact Time
CW	Continuous Wave
CYCLOPS	CYCLically Ordered Phase Sequence
D	Dipolar
DANTE	Delays Alternating with Nutations for Tailored Excitation
DAS	Dynamic Angle Spinning
DD	Dipole-Dipole
DEPT	Distortionless Enhancement by Polarization Transfer
DNP	Dynamic Nuclear Polarization
DOR	Double Rotation
DQ	Double Quantum
DQC	Double-Quantum Coherence
DQF	Double-Quantum Filtered
DRSE	Dipolar-Rotational Spin Echoes
DUMBO	Decoupling Using Mind-Boggling Optimization
EFG	Electric Field Gradient
ENDOR	Electron-Nucleus DOuble Resonance
EPR	Electron Paramagnetic Resonance
ESR	Electron Spin Resonance
EXSY	EXchange SpectroscopY
FC	Fermi-Contact
FFT	Fast-Fourier Transform
FID	Free Induction Decay
FIREMAT	Five π Replicated Magic Angle Turning
FSLG	Frequency-Switched Lee Goldburg
FT	Fourier Transform
HDOR	Heteronuclear Dipolar-Order Rotor-Encoding
HETCOR	Heteronuclear Correlation
HMQC	Heteronuclear Multiple Quantum Coherence
HOHAHA	HOmonuclear HArtman-HAhn
HSQC	Heteronuclear Single-Quantum Correlation
IBMS	Isotropic Bulk Magnetic Susceptibility
INADEQUATE	Incredible Natural Abundance Double Quantum Transfer Experiment
INEPT	Insensitive Nuclei Enhanced by Polarization Transfer
INEPT-HSQC	Insensitive Nuclei Enhanced By Polarization Transfer-Heteronuclear Single-Quantum Correlation
LG-CP	Lee-Goldberg CP

MAS	Magic Angle Spinning
MAS-J-HMQC	Magic Angle Spinning-J-Heteronuclear Multiple Quantum Correlation
MAS-J-HSQC	Magic Angle Spinning-J-Single Quantum Correlation
MLEV-4	A broadband decoupling sequence
MQ	Multiple-quantum
MQMAS	Multiple-Quantum Magic-Angle Spinning
MREV	Mansfield, Rhim, Elleman, & Vaughan (pulse sequence)
MRI	Magnetic Resonance Imaging
NICS	Nucleus Independent Chemical Shift
NOE	Nuclear Overhauser Effect
NOESY	(Two-dimensional) NOE SpectroscopY
NQCC	Nuclear Quadrupole Coupling Constant
NQR	Nuclear Quadrupole Resonance
ODESSA	One-Dimensional Exchange Spectroscopy by Sideband Alternation
PAS	Principal Axis System
PDSD	Proton-Driven Spin Diffusion
PFG	Pulsed Field Gradient
PMLG	Phase-Modulated Lee Goldburg
PRESTO-II	Phase-Shifted Recoupling Effects a Smooth Transfer of Order
PSD	Proton Spin-Diffusion
Q	Quadrupolar
QF	Quadrupole moment/Field gradient (interaction or relaxation mechanism)
2QF-COSY	Double-Quantum-Filtered Correlation Spectroscopy
REAPDOR	Rotational Echo Adiabatic Passage Double Resonance
REDOR	Rotational-Echo Double-Resonance
RELM	Rotor-Encoding of Longitudinal Magnetization
REPT-HMQC	Recoupled Polarization-Transfer Heteronuclear Multiple-Quantum Correlation
REREDOR	Rotor-Encoded Rotational Echo
RF	Radio Frequency
RFDR	Radio Frequency Driven Recoupling
SA	Shielding Anisotropy
SD	Spin-Dipolar
SECSY	Spin Echo Correlation SpectroscopY
SEDOR	Spin Echo DOuble Resonance
SEFT	Spin Echo Fourier Transform
SLF	Separated-Local Field
SPI	Selective Population Inversion
SPT	Selective Population Transfer
SR	Spin-Rotation (interactive or relaxation mechanism)
ssb	Spinning Sidebands
SSNMR	Solid-State Nuclear Magnetic Resonance
STMAS	Satellite Transition Magic-Angle Spinning
TEDOR	Transferred Echo Double Resonance
TOCSY	Total Correlation Spectroscopy
TOSS	TOtal Suppression of Sidebands
TRAPDOR	Transfer of Population in Double Resonance
UC2QF-COSY	Uniform-Sign Cross-Peak Double-Quantum-Filtered Correlation Spectroscopy
UE	Unpaired Electron relaxation mechanism
VAS	Variable Angle Spinning
WAHUHA	WAugh, HUber, & HAeberlen (pulse sequence)
WALTZ-16	A broadband decoupling sequence
WISE	Wide-Line Separation
ZQ(C)	Zero Quantum (Coherence)